

# MICROBEAM ANALYSIS

# 1986

A. D. Romig Jr. and W. F. Chambers, *Editors*

Proceedings of the 21st Annual Conference  
of the  
Microbeam Analysis Society  
Albuquerque, New Mexico, 11-15 August 1986



*San Francisco Press, Inc.*

Box 6800, San Francisco, CA 94101-6800

*Printed in the U.S.A.*

#### PUBLISHER'S NOTICE

Microbeam Analysis Society (MAS) and its publisher, San Francisco Press, Inc., are not responsible for the information and views presented in this volume by the several contributors.

San Francisco Press, Inc., also publishes the Proceedings of the Annual Meeting of the Electron Microscopy Society of America (EMSA), the proceedings of the triennial workshop on Analytical Electron Microscopy (AEM), and the Electron Microscopy Safety Handbook. Information on back issues follows. *MAS and EMSA members prepaying by personal check get a 20% discount from the prices listed below.* Overseas orders must be prepaid. California purchasers please add sales tax.

##### **Microbeam Analysis**

1975, 1976 (spiral bound)	\$25 each
1977 (full-length papers, Boston meeting)	\$25
1979, 1980, 1981	\$25 each
1982	\$42.50
1983, 1984	\$30
1985	\$40
1986	\$55

##### **EMSA Proceedings**

1983, 1984, 1985	\$45 each
1986	\$55

##### **Analytical Electron Microscopy**

1981	\$25
1984	\$40

<b>Electron Microscopy Safety Handbook</b>	<b>\$15</b>
--	-------------



## Foreword

It has been our privilege to serve as technical program chairmen for the 21st Annual Conference of the Microbeam Analysis Society (Albuquerque, New Mexico, 11-15 August, 1986), a joint conference with the Electron Microscopy Society of America. The 1986 joint conference is the largest ever in several respects: There were approximately 650 technical contributions. The MAS program, including special presentations without manuscripts and specified joint papers published in the EMSA proceedings, numbers over 250 contributions. This proceedings contains over 180 papers. In addition to the size of the technical program, we are especially pleased with the quality of the contributions. We extend our sincere appreciation to our colleagues who organized and chaired the various sessions and so helped make the excellence of this year's program possible. These individuals are listed in the Table of Contents with the session they organized.

In addition to our standard fare of sessions, several special sessions and tutorials were scheduled. Perhaps foremost is the Special Presidential Symposium, organized by C. Gordon Cleaver (GE Nuclear, Vallecitos, Calif.) and Kurt F. J. Heinrich (National Bureau of Standards, Gaithersburg, Md.), in which many of the founders of microanalysis and scanning microscopy have been brought together to reflect on the Historical Perspective of Microanalysis. A videotape of the presentations is available. In addition, this year's program contains a very extensive program in the biological sciences, including a symposium on the Microscopy and Pathobiology of Inhaled Toxicants, organized by S. Rothenburg and J. Harkema (Inhalation Toxicology Institute, Albuquerque, N.M.), and a special symposium on Frontiers of Biological Microanalysis organized by P. Ingram (Research Triangle Institute, Research Triangle Park, N.C.). For the first time, this year's program also has included the symposium on Atom Probe Field Ion Microscopy, principally organized by G. Kellogg (Sandia National Laboratories, Albuquerque, N.M.). We welcome the APFIM community to the MAS/EMSA program, and hope that mutual interests will continue the bonds between the groups. A number of special sessions emphasizing the applications of microanalysis to materials problem solving have been included. For the sake of brevity, we do not list the details here, but suggest that the potential reader scan the Table of Contents that follows.

The coordination between MAS and EMSA has been exceptional this year. Such cooperation has doubtless contributed to the strength of the 1986 program. We sincerely appreciate the cooperation of EMSA technical program chairman L. W. Hobbs (MIT) and his technical program committee in assembling the 1986 program. A program of this magnitude would not have been possible without such extensive cooperation. Many of the sessions given during the 1986 conference were jointly sponsored and the reader may need to refer to both proceedings to find specific information of interest.

A number of organizations and individuals deserve special acknowledgment, including the MAS/EMSA Local Arrangements Committee, which assisted us with many of the final programmatic details, and the Council of the Microbeam Analysis Society, which strongly encouraged our efforts. We must also express our sincere appreciation to Sandia National Laboratories and its management, who fully supported our efforts to assemble this program.

For those who will participate in the 21st Annual conference of the Microbeam Analysis Society, we hope the oral presentations and discussions will be fruitful and enlightening; these proceedings should prove to be a valuable reference and reminder of the conference. For those unable to attend, we hope the published Proceedings will provide a rich source of information on the art and science of microanalysis in 1986.

Alton D. Romig Jr., Technical Program Chairman  
William F. Chambers, Technical Program Chairman  
Microbeam Analysis Society

*Sandia National Laboratories, Albuquerque, New Mexico, 1986*



# TABLE OF CONTENTS<sup>†</sup>

	<i>Page</i>
Foreword .....	iii
Officers of the Microbeam Analysis Society .....	iv
Sustaining Members' Information .....	v

## T-1. TUTORIALS

*Strategy for interpretation of contrast mechanisms in SEM—D. E. Newbury .....	1
*An introduction to biological x-ray microanalysis— P. Echlin .....	6
*Nuclear-microprobe analysis: Applications—B. L. Doyle .....	15

## 1. RAMAN AND IR SPECTROSCOPY (org. F. Adar, James Brash)

*Thin films, colloids, and diamond anvils: The microRaman advantage—L. A. Farrow, C. J. Sandroff .....	22
The characterization of graphitic and nongraphitic carbon by laser Raman microprobe analysis— W. L. Johnson III .....	26
Analysis of inclusion precipitates in $Al_2O_3:Ti^{+3}$ —R. C. Powell, J. L. Caslavski, Z. AlShieb, J. M. Bowen ..	29
Micro-Raman spectroscopy of fluid inclusions in a hopper crystal in halite—K. L. Higgins, C. L. Stein .....	31
Raman spectroscopy of carboranes and polycarboranesiloxanes—J. A. Shelnett .....	35
Micro-Raman characterization of atherosclerotic and bioprosthetic calcification—E. S. Etz, B. B. Tomazic, W. E. Brown .....	39
The use of infrared and Raman microspectroscopy for the analysis of failed circuit boards—P. L. Lang, J. E. Katon .....	47
Raman and FTIR analysis of the interaction between a model organic pesticide and a soil constituent— J. M. Bowen, A. E. Ratcliffe, M. G. Rockley, A. W. Hounslow, C. R. Powers .....	50

## 2. MICROANALYSIS IN JOINING (org. M. J. Cieslak)

Use of analytical electron microscopy in evaluating ferrite stability in austenitic stainless-steel welds— J. M. Vitek, S. A. David .....	53
A microanalytical study of segregation during solidification and heat treatment of 12Cr-1Mo weldments— J. C. Lippold, A. D. Romig Jr., W. R. Sorenson .....	57
Electron microscopy analysis of weld heat-affected zone liquation cracking in Alloy 903— W. A. Baeslack III, W. Lata .....	64
A microstructural study of high-energy-density dissimilar metal welds—J. Cieslak, C. R. Hills, T. J. Headley .....	69
A microstructural analysis of Alloy 718 welds to Kovar and 304—G. A. Knorovsky, T. J. Headley .....	73

---

†An Author Index begins on p. 667.

\*Invited paper.

### 3. AUGER ELECTRON SPECTROSCOPY AND SECONDARY ION MASS SPECTROSCOPY (org. I: R. K. Lewis; II: Diana Daniel)

*Self-regulated potential at insulating surfaces in the presence of a strong electrostatic extraction field— G. G. Slodzian, M. Chaintreau, R. Dennebouy .....	78
Absolute ionization probabilities in secondary ion emission from clean metal surfaces—A. Wucher, H. Oechsner .....	79
Development of an imaging time-of-flight SIMS instrument—A. R. Waugh, D. J. Fathers, D. R. Kingham .....	82
Comparison of several nuclear reaction techniques for hydrogen depth profiling in solids—F. Xiong, F. Rauch, C. Shi, R. P. Livi, T. A. Tombrello .....	85
Optimization techniques for raster-gate SIMS depth profiles—B. C. Lamartine .....	88
Quantitative SIMS microanalysis of trace elements in geological samples using in situ ion-implanted standards—L. A. Streit, R. L. Hervig, P. Williams .....	91
Matrix effects in SIMS analysis of biological tissue—M. S. Burns .....	95
Diffusion profiles of boron and arsenic measured by spreading resistance and SIMS—G. G. Sweeny, A. R. Alvarez .....	97
An ion microprobe system for three-dimensional SIMS imaging—D. R. Kingham .....	99
Computer control software for the resistive anode encoder detector and the CAMECA IMS-3F ion microprobe—R. L. Crouch, C. J. Hitzman .....	101
Improved Auger data analysis programs for physical electronics Auger spectrometer systems— R. A. Mulford, F. S. Austin .....	104
High-resolution scanning ion microprobe analysis of retinal tissue—M. S. Burns, R. Levi-Setti, J. Chabala, Y. L. Wang .....	107
Electron-stimulated desorption microscopy—G. Gillen, P. Williams .....	109
*Sequential ISS-AES measurement for surface composition analysis of Au-Cu Alloy with Auger SEM— R. Shimizu, A. Kurokawa .....	113
Angular dependence of the Auger lineshape of graphite—J. W. Rogers Jr., J. E. Houston, R. R. Rye .....	115

### 4. GEOLOGICAL AND GEMOLOGICAL APPLICATIONS (org. P. H. Hlava, R. C. Gooley)

*Gems under the microbeam: New applications to gemology—C. M. Stockton .....	117
Kimberlitic garnets: Metamerism related to composition—W. L. Mansker, J. T. Springfield, K. Keil .....	123
Garnet suites in U.S. kimberlites and lamproites—W. L. Mansker .....	126
Form and composition of secondary mineralization in fractures in Columbia River basalts— J. P. McKinley, S. A. Rawson, D. G. Horton .....	127
Alteration products of basaltic glass, Hanauma Bay, Oahu, Hawaii—R. Cowan, R. C. Ewing .....	131
Effects of irradiation and dry heating on bentonite: A TEM and x-ray diffraction study— C. C. Allen, S. A. Rawson .....	135
Trace element analyses of olivine in lunar highland rocks: Implications for the origin of the lunar crust—M. G. Bersch, G. J. Taylor, K. Keil .....	138
TEM study of the microstructure of metamict minerals—T. J. Headley, R. C. Ewing .....	141
High-resolution TEM of microlite from the Harding pegmatite, Taos County, N. M.—G. Lumpkin, R. C. Ewing .....	145
The use of microtomed thin sections for the analysis of geologic materials with Auger electron spectrometry—G. P. Meeker, R. H. Fleming .....	148

Elements Cu through Ge: Cosmochemical significance and microanalysis in meteorites—A. Kracher, M. L. Pierson .....	151
Automation of mineral identification from electron microprobe analyses—D. G. W. Smith .....	153
Advancements in nuclear microprobe trace element analysis—P. S. Z. Rogers, C. J. Duffy, T. Benjamin ..	157
EDS microanalysis applied to the study of the pyrite complex ore from Rio Tinto, Huelva (Spain)—F. A. Calvo, J. M. Guilemany, J. M. Gómez de Salazar, A. Ureña, A. Aguilar .....	164
A study on apatite of granitoid by SIMS—Y. K. Liu, S. T. Zhou, Y. Q. Zhang, J. F. Yu .....	167

## 5. SPECIAL BIOLOGICAL SYMPOSIUM HONORING T. A. HALL: FRONTIERS OF BIOLOGICAL MICROANALYSIS (org. P. Ingram, D. E. Johnson)

*Capabilities and limitations of microprobe methods in biology (Keynote)—T. A. Hall .....	169
*Proton microscopy—G. J. F. Legge .....	170
*X-ray fluorescence with synchrotron radiation—K. W. Jones, B. M. Gordon, A. L. Hanson, J. G. Pounds, G. Schidlovsky .....	175
*The present state of laser microprobe mass analysis (LAMMA) as applied to biomedical samples—R. Kaufmann .....	177
*Photoelectron imaging—O. H. Griffith, G. F. Rempfer .....	180
*Quantitative compositional mapping of biological cryosections—C. E. Fiori .....	183
*Quantitative electron energy loss spectroscopy and elemental mapping in biology—R. D. Leapman .....	187
*Frontiers of secondary ion mass spectrometry in biological analysis—M. S. Burns .....	193
*Field-ion tomography—J. A. Panitz .....	196
*Quantitative electron probe analysis in biology—A. P. Somlyo, A. V. Somlyo, M. Bond, H. Shuman .....	199
Quantitative elemental characterization of cultured heart cells by electron probe x-ray microanalysis and ion-selective electrodes—A. LeFurgey, S. Liu, M. Lieberman, P. Ingram .....	205
Regulation of transepithelial Na transport as revealed by electron-microprobe analysis—R. Rick, A. Dörge, K. Thurau .....	209
Characterization of subcellular elemental distribution changes occurring concomitant with mammalian sperm development—K. N. Colonna, G. Oliphant .....	214
Quantitative electron probe x-ray microanalysis and flame atomic absorption spectroscopy of human mononuclear blood cell magnesium—G. R. Hook, J. M. Hosseine, R. J. Elin, C. E. Fiori .....	217
*X-ray microanalysis of secretory cells—G. M. Roomans .....	221
AEM of secretion-related elemental distributions—K. Izutsu, D. E. Johnson .....	225
X-ray microanalysis of rat papillary muscle—M. E. Cantino, L. E. Wilkinson, E. Wang, D. E. Johnson ...	226
Elemental concentrations of thymocytes in vivo and in vitro—A. Warley .....	227
*Cryoultramicrotomy—H. K. Hagler .....	231
*Biological absorption-edge imaging with synchrotron radiation—B. J. Panessa-Warren .....	233
Water measurement in biological tissue—R. R. Warner, N. E. Morgan, T. A. Eby, M. C. Myers, D. A. Taylor .....	238
Mass thickness images of frozen hydrated and freeze-dried sections—D. A. Kopf, A. LeFurgey, L. A. Hawkey, B. L. Craig, P. Ingram .....	241
The distribution of elements in developing roots of <i>Lemna minor</i> L—P. Echlin, T. L. Hayes .....	245
Localization of potassium in <i>Nicotiana</i> leaves at five stages of growth—S. E. Taylor, P. Echlin .....	248

## 6. NEW INSTRUMENTATION AND TECHNIQUES IN ELECTRON MICROSCOPY (org. R. McConville, J. L. Lehman, T. Akiba, P. Bovey)

*Recent developments in Hitachi TEM—S. Isakozawa, M. Kubozoe .....	251
Unattended image analysis of multiple samples in the SEM—R. M. Edwards, J. Lebedzik, G. Stone .....	254
Advanced vacuum systems for AEM—G. S. Venuti, R. R. Warner .....	261
An electromagnetic/electrostatic dual cathode system for electron beam instruments—J. G. Bradley, D. B. Wittry, J. M. Conley, A. L. Albee .....	265

## 7. ELECTRON MICROPROBE QUANTITATION AND AUTOMATION (org. D. E. Newbury, K. F. J. Heinrich)

A general equation for predicting x-ray intensities from stratified samples in the electron microprobe— R. Packwood .....	268
*Universal EPMA correction procedure now in sight—V. D. Scott, G. Love .....	271
Comparison of algorithms for x-ray mass absorption coefficients—K. F. J. Heinrich .....	279
Aspects of quantitative microanalysis of light elements by EDXS—P. J. Statham .....	281
Quantitative electron-probe microanalysis of boron in some binary borides—G. F. Bastin, H. J. M. Heijligers .....	285
Continuum radiation produced in pure-element targets by 10-40keV electrons: An empirical model— J. A. Small, S. D. Leigh, D. E. Newbury, R. L. Myklebust .....	289
On the potential application of artificially structured materials for x-ray microanalysis—A. D. Romig Jr. ....	293
Alkali metal loss in glass from a characterizing electron probe—T. M. Walker, D. G. Howitt .....	299
*The development of EPMA quantitative analysis in China—Y. K. Liu .....	302

## 8. MATERIALS APPLICATIONS (org. J. J. Friel)

The initiation of pitting corrosion in martensitic stainless steels—W. R. Cieslak, R. E. Semarge, F. S. Bovard .....	303
Characterization of residues from a zinc plant—R. Lastra Q. ....	307
A relatively inert material for casting uranium and uranium alloys—L. R. Walker, C. E. Holcumbe, W. M. Swartout, K. A. Thompson .....	312
In situ STEM studies of the interaction between molybdenum disulfide and oxygen—R. T. K. Baker, R. D. Sherwood .....	317
Oxidation kinetics of Pb-Sn eutectic solder films by AES analysis—G. Di Giacomo .....	321
Low-voltage, high x-ray spatial resolution microanalysis of aluminum zinc—J. J. Friel .....	325
Cu-Nb composite wire strength: An electron microscope study—F. C. Laabs, A. R. Pelton, W. A. Spitzig .....	328
Fracture observation in polymer systems using SEM—C. C. Garrison .....	331
PIXE analysis of solders on ancient gold artifacts with a nuclear microprobe—M. Piette, G. Demortier, F. Bodart .....	333
Characterization of oxide scale formed on Incoloy 800 tubes in the molten salt electric experiment (MSEE)—J. J. Stephens, R. E. Semarge, R. W. Bradshaw .....	337

## 9. SPECIAL ATOM-PROBE FIELD-ION MICROSCOPY SYMPOSIUM (org. G. L. Kellogg, O. T. Inal, J. A. Panitz, J. J. Hren)

*Atom-probe field-ion microscopy (Tutorial)—M. K. Miller .....	343
*Chemistry on an atomic scale of solid-state processes—D. N. Seidman .....	348
*Atom-probe study of semiconductors and conducting polymers—O. Nishikawa .....	351
*Phase transition studies through field-ion microscopy—O. T. Inal, H.-r. Pak, M. M. Karnowsky .....	357
*FIM/IAP depth profiling of nitrogen-implanted field emitters—S. D. Walck, J. J. Hren .....	361
*Applications of atom-probe field-ion microscopy to segregation and clustering studies in materials science—M. G. Burke, S. S. Brenner .....	363
*APFIM studies of phase transformations—M. K. Miller .....	370
*The application of APFIM to early stage decomposition of the superalloy NIMONIC PE16—W. Wagner, W. Hein, H. P. Degischer, R. P. Wahi, H. Wollenberger .....	375
APFIM study of antiphase and grain boundaries in Ni <sub>3</sub> Al—J. Horton, M. K. Miller .....	378
*A direct view of atomic interactions and diffusion on metals—J. D. Wrigley, G. Ehrlich .....	382
*Surface reactions investigated by field desorption—J. H. Block, N. Kruse, G. Abend .....	389
Field-ion microscope observations of surface self-diffusion and atomic interactions on Pt—G. L. Kellogg .....	399
Theory of surface structure determination by field-ion microscopy: Comparison with scanning tunneling microscopy—D. R. Kingham .....	403

## 10. ANALYTICAL ELECTRON MICROSCOPY

### I: Imaging and Diffraction (org. E. L. Hall, D. B. Williams)

CBED point group analysis of thin precipitates in metallic systems—J. M. Howe, M. Sarikaya .....	405
Digital CBED patterns collected by EELS—P. M. Budd, P. J. Goodhew, S. H. Vale .....	409

### II: Electron Energy Loss Spectroscopy (org. D. B. Williams, E. L. Hall)

*Pushing toward the limits of detectability in EELS—P. Kruit .....	411
Analysis of semiconductor EELS in the low-loss regime—M. K. Kundmann .....	417
White lines in the EELS of 3d transition metals—P. Rez, W. G. Waddington, I. P. Grant, C. J. Humphreys .....	421
Progress toward precise composition determination of Al-Li alloys by EELS—D-R Liu, D. B. Williams ...	425
*Practical methods for quantitative and fine structure analysis of energy loss spectra— M. M. Disko .....	429

### III: X-ray Analysis (org. D. B. Williams, E. L. Hall)

*Microanalysis limits using energy-dispersive x-ray spectroscopy in the AEM—C. E. Lyman .....	434
*A high-purity germanium x-ray detector on a 200kV AEM—E. B. Steel .....	439
*Standardized definitions of x-ray analysis performance criteria in the AEM—D. B. Williams .....	443
Boron analysis with a windowless x-ray detector—P. M. Budd, P. J. Goodhew .....	449
Thin-film analyses of silicate standards at 200 kV: The effect of temperature on element loss— I. D. R. MacKinnon, G. R. Lumpkin, S. B. van Deusen .....	451
Improved spatial resolution for EDX analysis with intermediate voltages—K. Rajan, J. McCaffrey, P. B. Sewell, G. L'Esperance .....	455

## 11. SPECIAL BIOLOGICAL SYMPOSIUM: APPLICATIONS IN FORENSIC SCIENCE (org. S. Basu, S. J. Rothenberg)

*Hair comparison in the SEM-EDX based upon increased sulfur intensity along the length of hair: Evidence of a "sulfur pump"—S. Basu .....	457
Gunshot residue analysis in bullet wounds with the SEM-EDX—S. Basu .....	461
SEM, Fourier transform infrared microscope, and the light microscope in the analysis of particulate evidence in the crime laboratory—T. A. Kubic .....	463

## 12. DESTRUCTIVE LASER MICROPROBE (org. D. S. Simons, J. A. Small)

LIMA analyses: Quantification of binary metallic systems—A. W. Harris, E. R. Wallach .....	464
Light-element analysis by LIMA—V. L. Kohler, A. W. Harris, E. R. Wallach .....	467
Determination of elemental relative sensitivity factors in the analysis of geological samples by LIMS— F. Radicati di Brozolo .....	471
Laser probing under atmospheric conditions for LIMA—A. Ishimori, T. Yamamoto, T. Yamada .....	473
Laser ionization mass analysis at high masses—T. Dingle, B. W. Griffiths, S. J. Mullock .....	475

## 13. QUANTITATIVE IMAGE PROCESSING AND ANALYSIS (org. J. J. McCarthy)

*Characterization of the geometry of microstructures—R. T. DeHoff .....	479
*Large-field x-ray compositional mapping with multiple dynamically focused wavelength-dispersive spectrometers—C. R. Swyt, C. E. Fiori .....	482
*Evolution of automated electron microscopy—R. J. Lee, J. S. Walker, J. J. McCarthy .....	485
A technique for the 3-d representation of carbon black—P. J. Hood, D. G. Howitt .....	487
Quantitative and low-magnification mapping by the electron microprobe—K. A. Thompson, L. R. Walker .....	491
Defocus modeling for compositional mapping with wavelength-dispersive x-ray spectrometry— R. L. Myklebust, D. E. Newbury, R. B. Marinenko, D. S. Bright .....	495
A multifunctional minicomputer program providing quantitative and digital x-ray microanalysis of cryosectioned biological tissue for use by the inexperienced analyst—R. V. Heyman, A. J. Saubermann .....	498
Image processing for the location and isolation of features—J. Ch. Russ, J. C. Russ .....	501
Automatic editing of binary images for feature isolation and measurement—J. C. Russ, J. Ch. Russ .....	505
Shape and surface roughness characterization for particles and surfaces viewed in the SEM—J. Ch. Russ, J. C. Russ .....	509
Models for particle shapes viewed in SEM projected images—J. C. Russ, T. M. Hare .....	513
Bright-field image correction with various image processing tools—D. S. Bright, E. B. Steel .....	517
Euclidian distance mapping for shape characterization of alloy grain boundaries—D. S. Bright, D. E. Newbury .....	521

## 14. ADVANCES IN SCANNING ELECTRON MICROSCOPY

### I. High-resolution SEM and Metal Coating (org. K.-R. Peters, J. B. Pawley)

Development of ultrahigh-resolution SEM (S-900)—M. Sato, Y. Nakaizumi, I. Matsui, K. Kanda .....	525
*Introduction to charging effects of insulators by incident electron beams—J. Cazaux .....	527
*The control of vacuum-deposited ultra thin films—J. A. Trahan .....	532



## II: (org. O. C. Wells)

*Dynamic observation of magnetic domains in iron alloys with high-voltage SEM—H. Mase, T. Ikuta, R. Shimizu .....	535
--	-----

## 15. SPECIAL BIOLOGICAL SYMPOSIUM: MICROSCOPY AND PATHOLOGY OF INHALED TOXICANTS (org. S. J. Rothenberg, J. R. Harkema)

*AEM and pulmonary toxicology: An overview—V. L. Roggli, S. D. Greenberg .....	539
*Inhalation of asbestos fibers induces macrophage migration and subsequent incorporation of tritiated thymidine by epithelial and interstitial cells—A. R. Brody, L. H. Hill, D. B. Warheit .....	541
Comparison of sodium hypochlorite digestion and low-temperature ashing preparation techniques for lung tissue analysis by TEM—J. A. Krewer, J. R. Millette .....	544
Particle contents of urban lungs: An update—L. E. Stettler, S. F. Platek, R. D. Riley, D. H. Groth, J. P. Mastin .....	547
Particulate analysis samples from amosite workers—R. F. Dodson .....	551
The role of fiber number, size, and mass in asbestos-induced lung disease—K. E. Pinkerton, V. L. Roggli .....	553
*Toxicology of ozone inhalation as revealed by electron microscopy—W. S. Tyler .....	557
Species variation in tracheobronchial epithelial populations: Considerations for selecting model species for toxicologic investigations—C. G. Plopper, A. T. Mariassy, D. W. Wilson, J. A. St. George, N. K. Tyler, D. M. Hyde, J. Heidsiek, S. J. Nishi .....	561
Histochemical and cytochemical evaluation of secretory cells in nonhuman primates exposed to ozone— J. A. St. George, D. L. Cranz, S. J. Nishio, J. R. Harkema, D. L. Dungworth, C. G. Plopper .....	564
Ozone-induced injury to tracheal epithelium in vitro: Morphologic correlation of injury with dose— K. J. Nikula, D. W. Wilson .....	567
Oxygen free radicals stimulate secretion of mucin by rodent airway epithelium in vitro—K. B. Adler, J. E. Schwarz, J. E. Repine .....	571
Ultrastructural evaluation of human nasal epithelium: An experimental tool in inhalation toxicology— J. L. Carson, A. M. Collier .....	574
Ultrastructural changes in nasal epithelium of monkeys exposed to ambient levels of ozone— J. R. Harkema, C. G. Plopper, D. M. Hyde, J. A. St. George, D. W. Wilson, D. L. Dungworth .....	577
Morphologic changes in the upper respiratory tract of rodents exposed to toxicants by inhalation— J. A. Popp, K. T. Morgan, J. Everitt, X. Z. Jiang, J. T. Martin .....	581
Inorganic particulate matter from lungs of individuals without occupational exposure—J. P. Mastin, W. J. Furbish, E. R. DeLong, V. L. Roggli, P. C. Pratt, J. D. Shelburne .....	583
Analytical scanning electron microscopy in the investigation of unusual exposures—V. L. Roggli .....	586
Pulmonary damage in guinea pigs caused by inhaled ultrafine zinc oxide: Evaluation by light and electron microscopy and analysis of pulmonary lavage fluid—M. W. Conner, W. H. Flood, A. E. Rogers, M. O. Amdur .....	589
SEM of tracheal respiratory epithelium exposed in vitro to $\text{Ni}_3\text{S}_2$ —G. L. Finch, T. L. Hayes, B. T. Mossman, M. J. W. Chang, G. L. Fisher .....	591
Microscopical examinations of mucociliar epithelium of rats exposed to sodium combustion products— A. Giovanetti, P. Pagano .....	594
Morphometric alterations in the lung induced by inhaled bacterial endotoxin—R. C. Lantz, R. Burrell, D. E. Hinton .....	597

## 16. APPLICATIONS IN CHEMICAL PROCESSING (org. C. E. Lyman)

*The Fe/MgO (001) system studied by AES, XPS, and TEM—R. A. Hubert, J. M. Gilles .....	599
Electron spectroscopy in fundamental catalytic studies—D. W. Goodman, J. E. Houston .....	602
Application of AEM to ruthenium catalyst synthesis—W. M. Targos, H. Abrevaya .....	605
Application of SIMS to the study of potassium and copper promoters in iron oxide catalysts— E. J. Karwacki Jr. ....	609
Microdistribution of kerogen and mineral phases in raw and retorted oil shales—J. B. Hall, P. P. Hruskoci, T. L. Marker, S. M. Polomchak .....	613
Controlled-atmosphere catalyst characterization by XPS, XAS, and AEM—D. G. Castner, I. Y. Chan .....	617
Surface analysis of catalysts—N. Shah, A. G. Dhere, P. J. Reucroft, R. J. De Angelis .....	620
Microstructure of small bimetallic particles—A. G. Shastri, J. Schwank .....	623

## 17. MICROELECTRONICS—ELECTRON BEAM TECHNIQUES (org. T. D. Kirkendall)

*Electron-beam techniques for studying electronic materials and devices—D. B. Wittry .....	625
*Voltage contrast from cleaved silicon wafers in the SEM—O. C. Wells, B. B. Davari, C. Y. Wong .....	631
*Diagnostic analysis of GaAs high-electron-mobility devices and integrated circuits—A. Christou, W. T. Anderson .....	636
Electron-probe x-ray microanalysis of $Al_xGa_{1-x}As$ epitaxial layers: Technique and accuracy considerations—T. P. Rammel .....	641
Microbeam quantitative analysis of mixed oxides in a tungsten matrix—R. R. Seaver, H. K. A. Kan .....	646
In-process inspection and metrology of semiconductor wafers with the use of an automated low-voltage SEM—M. H. Bennett, G. E. Fuller .....	649
Applications of SEM and XPS in plasma etching of single-crystal silicon—R. Sellamuthu, J. Barkanic, E. Karwacki, R. Jaccodine .....	653
Microcircuit trace cutting with focused ion beams—G. W. Stupian, M. S. Leung .....	656
Multiple applications of TEM/STEM to the inspection of components used in the manufacture of computers—R. Flutie, N. Riel .....	659
Electron beam lithography with a conventional SEM—P. E. Russell, T. North, T. M. Moore .....	663
Author Index .....	667

## Officers of the Microbeam Analysis Society

### *MAS Executive Council*

<i>President:</i>	Gordon Cleaver, General Electric Co., Vallecitos Nuclear Center, Pleasanton, Calif.
<i>President Elect:</i>	Charles E. Fiori, National Institutes of Health, Bethesda, Md.
<i>Past President:</i>	Dale E. Newbury, National Bureau of Standards, Gaithersburg, Md.
<i>Treasurer:</i>	A. D. Romig Jr., Sandia National Laboratories, Albuquerque, N.M.
<i>Secretary:</i>	John T. Armstrong, California Institute of Technology, Pasadena, CA 91125, (818) 356-6253

### *Directors*

Gary Aden, Kevex Corp., Foster City, Calif.  
Joseph H. Doyle, Rockwell International, Golden, Colo.  
Ron Gooley, Los Alamos Scientific Laboratory, Los Alamos, N.M.  
Tom Huber, JEOL (USA) Inc., Peabody, Mass.  
Ronald R. Warner, Procter & Gamble Co., Cincinnati, Ohio  
David B. Williams, Lehigh University, Bethlehem, Pa.

### *Honorary Members*

L. S. Birks, Naval Research Laboratory, USA  
I. B. Borovskii, Academy of Sciences, USSR  
Raymond Castaing, University of Paris (Orsay), France  
V. E. Cosslett, University of Cambridge, Great Britain  
Peter Duncumb, Tube Investments Research Laboratories, Great Britain  
T. A. Hall, University of Cambridge, Great Britain  
K. F. J. Heinrich, National Bureau of Standards, USA  
Gunji Shinoda, Osaka University, Japan



## Sustaining Members' Information

AMRAY, INC.  
160 Middlesex Turnpike  
Bedford, MA 10730

Product Contact: Greg Cameron, (617) 275-1400

Product Line: Manufacturer of Scanning Electron Microscopes.

### Regional Sales Offices:

George Bruno, New England, (617) 275-8310  
Ken Benoit, New Jersey, (609) 662-3922  
Ed Griffith, New Jersey, (609) 662-3922  
Tom Richards, North Carolina, (609) 662-3922  
Ken Lindberg, Jr., Florida, (305) 767-4220  
Bill Wehling, Texas, (214) 247-3542  
Mark Reynolds, Ohio, (216) 579-0035  
Fred Feuerstein, Illinois, (312) 695-6117  
Don Brayton, Southern California, (408) 748-1300  
Gerry O'Loughlin, Northern California, (408) 748-1300

BIO-RAD POLARON INSTRUMENTS, INC.  
2293 Amber Drive  
Hatfield, PA 19440

Product Contact: Brian Kyte (800) 524-8200 (in PA, (215) 822-2665)

Product Line: Complete range of preparation equipment and accessories for all areas of electron microscopy, including vacuum evaporators, carbon coaters, sputter coaters, and plasma ashers.

CAMBRIDGE INSTRUMENTS, INC.  
40 Robert Pitt Drive  
Monsey, NY 10952

Product Contact: Peter W. Boutell (914) 356-3331

Product Line: Research scanning electron microscopes and accessories, research production beam microfabrication systems, image analysis.

### Regional Sales Offices:

Duane Bellingham, PO Box 637, Williamstown, MA 01267, (413) 458-5232  
Roger Attle, 40 Robert Dr., Monsey, NY 10952, (914) 356-3331  
Mike Webber, 3945 Fairington Dr., Marietta, GA 30066, (404) 926-9636  
Richard Russel, 3105 Ira Rd., Box 2626, Bath, OH 44210, (216) 666-5331  
John Pong, 26011 Falbrook, El Toro, CA 92630, (714) 380-9597  
Barbara Stanton, 2840 San Tomas Expressway #106, Santa Clara, CA (408) 970-9292  
Blaise Fleischmann, 6436 Barnaby St. N.W., Washington, D.C. 20015 (202) 362-4131  
John Watkins, 625 Scott St. #504, San Francisco, CA 94117, (415) 922-8652  
Richard Feller, 415 Kewnilworth Ave., Glen Ellyn, IL 60137, (312) 858-2332

CAMECA INSTRUMENTS, INC.  
2001 West Main Street  
Stamford, CT 06902

Product Contact: Thomas C. Fisher (203) 348-5252

Product Line: The IMS-4F is an advanced secondary ion mass spectrometer. The SX microprobes include the SX-50 and SX MACRO and are scanning electron microprobes with full microprocessor control.

Regional Sales Offices:

Robert P. Johnson, Western Regional Sales Manager (707) 255-9228

DAPPLE SYSTEMS

355 West Olive, Suite 100  
Sunnyvale, CA 94806

Product Contact: Bill Stewart (408) 733-3283

Product Line: Microcomputer-based analytical instrumentation including measurement and processing systems and energy-dispersive x-ray analysis.

DENTON VACUUM, INC.

2 Pinoak Ave.  
Cherry Hill, NJ 08003

Product Contact: George Ericcson (609) 424-1012

Product Line: Carbon Coaters, Sputter Coaters, High Vacuum Evaporators, Plasma Etchers.

Regional Sales Offices:

RADCO, PO Box 254, Wycoff, NJ 07481, (201) 444-4425  
Westport Instruments, PO Box 957, Los Altos, CA 94022, (415) 941-6595  
Accurate Marketing, 5656 Tenth Ave., Delta (Tsawwassen), B.C. V4L 1C1 (604) 943-7122  
Danielson Associates, PO Box 157, Downers Grove, IL 60515, (312) 960-0086  
Tyler Griffen, 46 Darby Road, Paoli, PA 19301, (215) 644-7710  
Scientific Instruments, PO Box 11628, Atlanta, GA 30342, (404) 237-7106  
The Buhrke Company, 570 Price Ave., Suite 202, Redwood City, CA 94063, (415) 369-7545

EDAX INTERNATIONAL, INC.

P.O. Box 135  
Prairie View, IL 60069

Product Contact: Marilyn Tillman (312) 634-0600

Product Line: Energy-dispersive x-ray analysis systems for x-ray microanalysis and image collection, display, and processing in SEMs, TEMs, and electron microprobes.

Regional Sales Offices:

Eugene Martin, Silver Spring, MD, (301) 598-8881  
Vic Balmer, Vermilion, OH, (216) 967-4148  
Richard Feller, Bannockburn, IL, (312) 634-0600  
Frank Gibson, Spring, TX, (713) 350-8654  
Brad Lawrence, San Jose, CA, (408) 729-6442

EG&G ORTEC

100 Midland Road  
Oak Ridge, TN 37830

Product Contact: Rick Seymour (615) 482-4411, Ext. 131

Product Line: Energy-dispersive systems for electron optical microscopes of all types. Image analysis systems.

Regional Sales Offices:

Karen Robbins, 100 Midland Rd., Oak Ridge, TN 37830, (615) 482-4411  
Ron Walker, 340 Melvin Dr., Northbrook, IL 60062, (312) 498-5858  
Alan Welco, 23342 South Pointe Dr., Laguna Hills, CA 92653, (714) 770-6222

GATAN, INC.  
6678 Owens Drive  
Pleasanton CA 94566

Product Contact: Kevin Scudder, GATAN, Inc., 780 Commonwealth Drive, Warrendale, PA 15086, (412) 776-5260

Product Line: Materials science specimen preparation equipment for TEM. Electron energy loss spectrometers. Specialized TEM specimen holders. TEM TV-imaging systems. Camscan scanning electron microscopes.

Regional Sales Offices:  
Dana Clough (415) 463-0200

GW ELECTRONICS, INC.  
6981 Peachtree Industrial Boulevard  
Norcross, Georgia 30092

Product Contact: Bob Lewis (404) 449-0707

Product Line: Electronic accessories for scanning electron microscopes.

INSTRUMENTS S.A., INC.  
173 Essex Avenue  
Metuchen, NJ 08840

Product Contact: Bruce D. Perrulli (201) 494-8660

Product Line: MOLE/Molecular Laser Raman Microprobe, providing molecular and crystalline characterization with one-micron spatial resolution.

INTERNATIONAL SCIENTIFIC INSTRUMENTS, INC.  
1457 McCarthy Blvd.  
Milpitas, CA 95035

Product Contact: David Jimenez (408) 945-2233

Product Line: International Scientific Instruments, Inc. (ISI) markets a full range of scanning electron microscopes, electron beam testing systems, and electron optical line width measuring equipment.

Regional Sales Office:  
International Scientific Instruments, Inc., Avon Park South, 20 Tower Lane, Building 2, Avon, CA 06001

JEOL USA, INC.  
11 Dearborn Road  
Peabody, MA 01960

Product Contact: Robert T Santorelli (617) 535-5900

Product Line: SEM/TEM/X-ray Microprobes/Scanning Auger Microprobe

Regional Sales Offices:  
Dave Angle, Rose Lake, 3622 Pinecrest Ave., Coldwater, MI 49036, (513) 232-7350

John Bonnici, JEOL U.S.A., Inc., 24 Brunswick Woods Dr. East Brunswick, NJ 08816  
 (201) 254-5600, 5603  
 Thayer Brickman, Jack Francis, Dave Lewis  
 JEOL U.S.A., Inc., 3500 W. Bayshore Rd., Palo Alto, CA 94303, (415) 493-2600  
 Mike Craig, 517 E. 88th Ave., Suite 1023, Thornton, CO 80229, (303) 979-0169  
 Ron Espeseth, 10 S. Cottenet St., Irvington, NY 10533 Office, (914) 747-2664  
 Home (914) 591-7010  
 T.V. Gildea, JEOL U.S.A. Inc., 11 Dearborn Road, Peabody, MA 01960, (617) 535-5900  
 Ray Gundersdorff, 6236 Gilston Park Road, Catonsville, MD 21228  
 Local D.C. (301) 621-5360, Baltimore (301) 788-2142  
 Richard Lois, One Kingwood Place, Suite 122B, 600 Rockmead Drive Kingwood, TX 77339  
 (713) 358-2121  
 Lewis McDonald, 1011 Camden Court, Atlanta, GA 30327, (404) 255-7940  
 Daniel Montag, 4371 Wilshire Blvd., Apartment B104, Mound, MN 55364, (612) 472-5775  
 Jean-Pierre Slakmon, Soquelec, Ltd., 5757 Cavendish Blvd., Suite 101, Montreal, Quebec  
 Canada H4W 2W8, (514) 482-6427  
 Robert Steiner, JEOL U.S.A., Inc., 9801 West Higgins Road, Suite 220 Rosemont, IL 60018  
 (312) 825-7164

KEVEX CORPORATION  
 1101 Chess Drive  
 Foster City, CA 94404

Product Contact: Drew Isaacs (415) 573-5866

Product Line: Materials analysis systems for qualitative and quantitative x-ray and image analysis. Product line includes instrumentation for x-ray energy-dispersive analysis, wavelength-dispersive analysis, Auger and electron energy-loss spectrometry, and digital image acquisition and feature analysis. X-ray detectors and digital beam control available for most models of microprobe, SEM, TEM and STEM.

#### Regional Sales Offices:

9989 Windsor Way, San Ramon CA 94583, (415) 828-2188  
 2119 Edsel Avenue, Los Angeles, CA 90066, (213) 306-1033  
 6417 Glenmoor Avenue, Galand TX 75043, (214) 226-0182  
 19635 Cottonwood Trail, Strongsville, OH 44136, (216) 238-8666  
 8912 N. Skokie Boulevard, Suite 2N, Skokie IL 60077, (312) 676-9313  
 56 Slater Road, Glatonsbury, CT 06033, (203) 633-3102  
 16 Barberry Hill Road, Gainesville, GA 30506, (404) 887-9965  
 PO Box 200, Mercer Island, WA 98040, (206) 232-3444  
 4536 Stuart Street, Denver, CO 80212, (303) 969-0202  
 PO Box 559, Harvey's Lake, PA 18618, (717) 639-2330  
 1631 Valencia Way, Reston, VA 22040, (703) 648-9590

KRISEL CONTROL, INC.  
 16 Farsta Court  
 Rockville, MD 20850

Product Contact: Christos Hadidiacos (301) 762-1790

Product Line: Automation equipment for electron microprobe/microscope, featuring on-line data acquisition and reduction with Alpha and ZAF correction schemes. Single-crystal automation system for on-line data collection, centering, calculation of orientation matrix, and refinement of cell parameters for an x-ray diffractometer.

LINK ANALYTICAL.  
 240 Twin Dolphin Drive  
 Redwood City, CA 94065



Product Line: Link Systems manufactures a complete line of energy-dispersive x-ray fluorescence and microanalytical systems including high-performance detectors, image processing facilities and automation packages.

Regional Sales offices:

Joe Eddlemon, 9209 Oak Ridge Highway, Oak Ridge, TN 37830  
Jack Enderlein, 34 Pine Cone Ct., Vincentown, NJ 08088  
Dr. Victor Buhrke, 1500 Old County Road, Belmont, CA 94002  
Jim Johnson, PO Box 205, 500 E. NW Highway, Mt. Prospect, IL 60056  
Thomas Flanagan, PO Box 25, 17 Sherman Road, Millis, MA 02054  
Graham R. Bird, 6249 Corporate Drive, Houston, TX 77036

WALTER C. McCRONE ASSOCIATES, INC.  
2820 South Michigan Avenue  
Chicago, IL 60616

Product Contact: John Gavrilovic (312) 842-7100

Product Line: Analytical and consulting services -- ultramicroanalysis, small-particle analysis, light microscopy, analytical electron microscopy, scanning electron microscopy, electron microprobe analysis, secondary ion mass spectrometry, micro x-ray diffraction, organic microanalysis for small particles and subnanogram samples. Failure analysis on solid-state devices, bond failures, corrosion problems, thin-film analysis. Microscopy supplies and accessories, microscope sales (Olympus microscope dealer), light microscopy supplies. Asbestos consulting and testing, analysis of suspect materials for asbestos by light microscopy and/or electron microscopy, building surveys, air sampling, monitoring during abatement projects.

Regional Sales Offices:

Ian M. Stewart/Bonnie L. Betty, McCrone Accessories and Components, 2508 S. Michigan Ave.  
Chicago, IL 60616, (312) 842-7100  
Richard L. Hatfield, McCrone Environmental Services, 5500 Oakbrook Parkway, Suite 200  
Norcross, GA 30093, (404) 449-8474 or 8461

MICRON, INC.  
3815 Lancaster Pike  
Wilmington, DE 19805

Product Contact: James F. Ficca, Jr. (302) 998-1184

Product Line: Scanning electron microscopy, electron microscopy, electron probe x-ray analysis, transmission electron microscopy, quantitative image analysis, x-ray diffraction, x-ray fluorescence, optical microscopy and metallography, microhardness, optical emission spectroscopy, differential scanning calorimetry, ultra microtomy, sample preparation.

MICROSPEC CORPORATION.  
45950 Hotchkiss Street  
Fremont, CA 94539

Product Contact: Joseph Carr (415) 656-8820

Product Line: Fully focusing, fully scanning wavelength-dispersive x-ray spectrometer systems for attachment to scanning electron microscopes.

NISSEI SANGYO AMERICA, LTD.  
HITACHI SCIENTIFIC INSTRUMENT DIVISION  
460 Middlefield Road

Product Contacts: Bill Roth - SEM  
Hideo Naito - SEM  
Gary Palmer - TEM (415) 961-0461, (415) 969-1100

Product Line: Scanning electron microscopes, transmission electron microscopes, electron probes, x-ray analysis.

Regional Sales Offices:

NSA/Hitachi, 2086 Gaither Rd., Rockville, MD 20850, (301) 840-1650  
NSA/Hitachi, 4312 Myra Ave., Cypress, CA 90630, (714) 527-3505  
NSA/Hitachi, PO Box 145, 4444 FM-1960, Suite 28, Houston, TX 77068, (713) 893-2067  
NSA/Hitachi, Tokone Hills, Lakeville, CT 06039, (617) 756-5331  
NSA/Hitachi, 1701 Golf Rd., Suite 401, Rolling Meadows, IL 60008, (312) 364-2462

PERKIN-ELMER  
PHYSICAL ELECTRONICS DIVISION.  
6509 Flying Cloud Drive  
Eden Prairie, MN 55344

Product Contact: Marlin A. Braun (612) 828-6318

Product Line: Full line of analytical instruments for surface and thin film analysis, including scanning Auger microprobes, Auger, ESCA, and SIMS, and components including LEED and ion guns, for research and production applications. Contract services for all of these techniques.

Regional Sales Offices:

Guy R. Messenger, 7310 Ritchie Highway., Suite 520, Glen Burnie, MD 21061, (301) 761-3053  
Edward T. Grabey, 5 Progress St., Edison, NJ 08820, (201) 561-6730  
Tom J. Swanson, 564 Forbes Ave., Suite 1312, Pittsburgh, PA 15219, (412) 261-6760  
Christopher J. Macey, 2 Taunton St., Plainville, MA 02762, (617) 695-7181  
John J. Kadlec, 1011 S. Sherman St., Richardson, TX 75081, (214) 669-4419  
Jude H. Koenig, Meredith J. Bigley, 151 Bernal Rd., Suite 5, San Jose, CA 95119  
(408) 629-4343  
Elm W. Sturkol, 325 Canyon Center, 1881 Ninth St., Boulder, CO 80302, (303) 449-4573  
Dave Harris, Bill Stickle, 1161-C San Antonio Rd., Mt. View, CA 94043, (415) 967-2600  
Europe: Bahnhofstrasse 30, D-8011 Vaterstetten, West Germany, Tel. 011-49-8106-3810  
TLX. 522909, Hans J. Projahn  
Hong Kong: 303 Fourseas Bldg., 208-212 Nathan Rd., Tsimshatsui, Kowloon,  
Hong Kong., Tel. 3-7210788, TLX 37753 HKPHIHX, Dr. John P. Chan  
Japan: ULVAC PHI, Inc., 2500 Hagisono, Chigasaki-shi, Kanagawa-ken,  
Japan, Tel. 0467-85-6522, TLX. 3862157  
India: Blue Star, Ltd., Sahas, 414/2 Vir Savarkar Marg., Probhadev 1,  
Bombay 400 025, India

PHILLIPS ELECTRONIC INSTRUMENTS, INC.  
85 McKee Drive  
Mahwah, NJ 07430

Product Contact: John S. Fahy (201) 529-3800

Product Line: Transmission analytical electron microscopes, scanning analytical electron microscopes, and analytical accessories for electron microscopes.

Regional Sales Offices:

A. Hugo, 55 Virginia Ave., West Nyack, NY 10994  
D. Ahr, 6231 Executive Blvd., Rockville, MD 20852  
H. Ittner, 155 N.E. 100th St., Suite 403, Seattle, WA 98125

B. Smick, Suite D45, 2525 East Oakton, Arlington Heights, IL 60005  
Ms. Jo Long, 7302 Harwin Dr., Suite 106, Houston, TX 77036  
S. Spiers, 3000 Scott Blvd., Suite 113, Santa Clara, CA 95050

POLAROID CORPORATION  
575 Technology Square  
Cambridge, MA 02139

Product Contact: Elinor Solit

Product Line: Photographic films and cameras. Batteries, chemicals, and optics

Regional Sales Offices:  
Industrial Hot Line: (800) 225-1618  
Atlanta, GA: (404) 346-1717  
Cleveland, OH: (216) 433-4884  
Dallas, TX: (214) 258-8100  
Oakbrook, IL: (312) 654-5200  
Paramas, NJ: (210) 265-6900  
Santa Ana, CA: (714) 641-1200

PRINCETON GAMMA-TECH, INC.  
1200 State Road  
Princeton, NJ 08540

Product Contact: Douglas P. Skinner (609) 924-7310

Product Line: Princeton Gamma-Tech develops and manufactures energy-dispersive spectroscopy instrumentation, x-ray fluorescent analytical systems, high-performance germanium photon detectors, high-resolution digital imaging units, and radioisotope-based chemical analyzers.

Regional Sales Offices:  
Scientific Systems Sales Corp., 333 Jericho Turnpike, Jericho, NY 11753, (516) 822-4880  
Scientific Systems Sales Corp., 14300 Gallant Fox Lane, Bowie, MD 20715, (301) 262-4104  
Scientific Systems Sales Corp., 10 Tower Office Park, Woburn, MA 01801, (617) 938-9111  
BASS, Inc., 1217 Hampton Lane, Mundelein, IL 60060, (312) 680-8316  
PGT, T. Griffin, 701 Morewood Pkwy, Rocky River, OH 44116, (216) 331-1020  
PGT, J. W. Binns, 7 Hopscotch Lane, Savannah, GA 31411, (912) 598-1402  
PGT, D. Berger, 568 Weddell Dr., Sunnyvale, CA 94089, (408) 734-8124  
Westport Instruments, PO Box 957, Los Altos, CA 94022, (415) 941-6595  
PGT, Dr. D. White, 773 North Hidden Drive Orange, Orange City, CA 92669, (714) 633-9070  
PGT, D. Cannon, PO Box 36157, Denver, CO 80236, (303) 978-0786

SPI SUPPLIES  
DIVISION OF STRUCTURE PROBE, INC.  
535 E. Gay Street  
PO Box 656  
West Chester, PA 19381-0656

Product Contact: Charles A. Garber, Ph.D. (215) 436-5400

Product Line: SPI Supplies: Small instruments and consumable supplies for electron microprobe and electron microscope laboratories including sputter coaters, table-top vacuum evaporators, and microprobe standards. Structure Probe: Independent laboratory providing SEM/EDS, TEM, probe, Auger, XPS, XRD, and other services for industry and government. Member of American Council of Independent Laboratories; accredited by American Association for Laboratory Accreditation.

Laboratories:

230 Forrest St., Metuchen, NJ 08840, (201) 549-9350  
63 Unquowa Rd., Fairfield, CT 06430, (203) 254-0000  
1015 Merrick Rd., Copiague, L.I., NY, (516) 789-0100

Regional Sales Offices:

SPI Supplies/Canada, PO Box 187, Station "T", Toronto, Ont.,  
Canada M6B 4A1, (416) 787-9193

C. M. TAYLOR CORPORATION

289 Leota Avenue  
Sunnyvale, CA 94086

Product Contact: Dr. Charles M. Taylor (408) 245-4229

Product Line: Standards for microbeam analysis by SEM, microprobe, and ion probe using energy-dispersive, wavelength-dispersive, and mass spectrometers. Standards available exceed 175 different metals, alloys, glasses, and compounds or minerals. Bence-Albee standards are available. Manufacture many types of sample holders, polishing jigs, and other equipment for sample preparation. Also offer electron microprobe analytical services using a MAC-5 instrument, with FRAME B or Bence-Albee correction procedures.

M. E. TAYLOR ENGINEERING, INC.

11506 Highview Ave.  
Wheaton, MD 20902

Product Contact: Gene Taylor ((301) 942-3418

Product Line: Scintillators, BSE and SE detectors, unique SEM supplies. SEM contract work, consulting and adhesion testing of coatings through our SEMicro Division.

Regional Sales Office:

Dave Ballard, SEMicro, 15817 Crabbs Branch Way, Rockville, MD 20855, (301) 330-0077

TRACOR NORTHERN, INC.

2551 West Beltline Highway  
Middleton, WI 53562

Product Contact: John Benson (608) 831-6511

Product Line: Wide range of instrumentation and software for qualitative and quantitative x-ray analysis. Products include data acquisition, reduction, and automation equipment for electron microprobe, SEM, TEM, and STEM. Features include simultaneous EDS/WDS data acquisition and reduction, and digital beam control for digital mapping, line scans, digital image processing, and particle location, sizing, and elemental characterization. Flexible packaging allows instrumentation to be used also for ELS, Auger, ESCA, SIMS, etc. Other products are used in nuclear, optical, signal averaging, and medical applications.

Regional Sales Offices:

Dennis Masaki, 6313 Odana Rd., Suite 2N, Madison, WI 53719, (608) 274-1666  
Don Dunkin, 4001 G, Greentree Executive Campus, Marton, NJ 08053, (609) 596-6335  
Larry Williams, 3040 Holcomb Bridge Rd., Suite F1, Norcross, GA 30071, (404) 449-4165  
Mike Ivey, 70 Whitney Place, Fremont, CA 93539, (415) 656-9898

VICKERS INSTRUMENTS (CANADA), INC.

2930 Baseline Road  
Nepean, Ont., Canada K2H 8T5

Product Contact: Bryce Hanna (613) 820-9437

Product Line: Scanning electron microscopes and systems for the non-destructive inspection and precision critical-dimension measurement of semiconductors.

Regional Sales Office:

Vickers Instruments, Inc., 800 W. Cummings Park, Suite 1900, Woburn,  
MA 01801, (617) 932-3800, or toll-free, 1-800-VICKERS

CARL ZEISS, INC.  
One Zeiss Drive  
Thornwood, NY 10594

Product Contact: William I. Miller, III (914) 747-1800

Product Line: Carl Zeiss makes a complete line of optical and electron microscopes. Included are the Laser Scan Microscopes, the fully digital scanning electron microscope DSM 950, and the EM 902, the only TEM with electron spectroscopic imaging and integrated EELS systems.

Regional Sales Offices:

Ed Boyle, 211 S. Lynn Blvd., Upper Darby, PA 10982, (215) 853-2575  
Frank Coccia, 183 Lake Shore Dr., Pasadena, MD 21122, (301) 437-7382  
Eckhardt Dorneich, 1805 S. Courtland Ave., Park Ridge, IL, (312) 825-2554  
Donald Hesler, 77 Jerome Court, Walnut Creek, CA 94598, (415) 945-0503  
Dietrich Voss, PO Box 2025, Willis, TX 77378, (409) 856-7678  
Richard McMahon, 49 Clough Rd., Dedham, MA 02026, (617) 326-1722



## T-1 Tutorials

### STRATEGY FOR INTERPRETATION OF CONTRAST MECHANISMS IN SCANNING ELECTRON MICROSCOPY: A TUTORIAL

D. E. Newbury

The information carried by signals in the scanning electron microscope (SEM) arises through the operation of contrast mechanisms. Contrast may be defined as the difference in the detected signal between two arbitrarily selected locations in an image normalized by the larger of the two signals. Contrast occurs because the electron-specimen interaction and/or the electron collection varies in response to differences in the properties of the specimen at those two locations. Knowledge of the characteristics of a particular contrast mechanism is vital in the selection of proper SEM operating conditions if that contrast is to be viewed in the final image.<sup>1</sup> A useful strategy for operating the SEM to view a specific contrast mechanism consists of four stages: (1) selection of beam characteristics, e.g., energy, current; (2) selection of specimen characteristics, e.g., surface preparation, orientation to the beam; (3) selection of the detector; e.g., matching to the desired signal, orientation relative to the specimen; and (4) selection of signal processing to display the final image. Interpretation of information in the final image depends on the microscopist's understanding of the characteristics of the contrast mechanism and how those characteristics are modified by the detector. In this paper, the organization and utilization of information for image interpretation are described.

#### *Types of SEM Contrast Mechanisms*

A wide variety of contrast mechanisms can be observed in the SEM, a direct result of the rich variety of interactions the beam electrons can undergo. These mechanisms include topographic contrast, by which the three-dimensional shape of an object can be recognized; atomic number contrast, which reveals compositional differences; channeling contrast, in which the crystallographic orientation of a specimen can be recognized; three types of magnetic contrast, which reveal domain structure; voltage contrast, in which variations in the surface potential can be imaged; and electron-beam-induced conductivity and voltage effects in semiconductors. Extensive studies on the nature of these contrast mechanisms have been reported in the literature and are summarized in SEM textbooks.<sup>2-5</sup> Despite the obvious differences in the nature of the information which these contrast mechanisms can convey, a common approach can be employed to classify the characteristics of the contrast mechanisms for use in image interpretation.

#### *Classification of Contrast Mechanisms and Detectors*

A useful system for classifying the characteristics of contrast mechanisms can be based on the key parameters that affect the SEM detectors: the type of signal carrier (secondary or backscattered electrons, specimen current, photons, acoustic waves), and the nature of the contrast encoding mechanism: number effects, trajectory effects, and energy effects. Number effects arise because of specimen properties that modify the number of electrons leaving the specimen. Trajectory effects occur because the directions of electron emission from the specimen surface or the subsequent flight path may be modified by the specimen properties. Energy effects result from the restriction of certain contrast information to a specific portion of the energy distribution of a signal. Table 1 contains the classification of the principal contrast mechanisms according to this scheme. The terms "strong," "intermediate," and "weak" have been used to give some sense of the magnitude of a particular response. Specific values of the response can often be calculated, but exact materials and conditions must be specified.

---

The author is with the Center for Analytical Chemistry, National Bureau of Standards, Gaithersburg, MD 20899.

## *Image Interpretation*

The information in Tables 1 and 2 forms the basis for a strategy for interpretation of SEM images. The strategy consists of matching the detector response characteristic (for example, sensitivity to number effects) to the nature of the contrast mechanism. In this discussion, only general, qualitative observations on this process will be made. In some special cases, detailed calculations of the contrast by analytic equations or Monte Carlo electron trajectory simulations are possible and can be used to determine contrast quantitatively.

In order to interpret an image properly and extract useful information on the nature of the specimen, it is often necessary to have a series of images taken with two or more detectors so as to take advantage of the different characteristics of each. As an example of this situation, we examine a multiphase rock sample nearly flat but with some surface topography in the form of scratches, in the SEM with various detector configurations. The variable composition and slight surface structure of the specimen mean that both number and trajectory effects can operate in SEM images. If the image is prepared with a variety of detector configurations, the different contrast mechanisms can be at least partially separated and examined.

Figure 1 shows the specimen imaged with the conventional Everhart-Thornley detector biased positively so as to collect both secondary electrons and backscattered electrons. The detector position is located at the top of the image, so that the light-optical analogy of the illumination is top lighting.<sup>2</sup> In forming this image, backscattered electrons have been collected both as a component that is directly scattered into the solid angle of collection of the detector, and as a component that is collected indirectly through the mechanism of remote generation and subsequent collection of secondary electrons from the walls and polepiece of the SEM specimen chamber. The directly collected backscattered component carries principally trajectory effects; the indirectly collected component is effectively integrated over a wide range of directions, and thus carries principally number effects. The convolution of the number and trajectory effects of the electron-specimen interaction with the number and trajectory response characteristics of the positively biased E-T detector results in a mixture of both compositional and topographic contrast components in Fig. 1. Since the surface topography of the specimen is slight, the main source of contrast is the compositional differences from one region to another.

Figure 2 shows the same specimen area as Fig. 1 but with the E-T detector biased negatively. The E-T detector now exclusively detects backscattered electrons that have been scattered into the solid angle subtended by the scintillator, resulting in strong sensitivity to trajectory effects. Backscattered electrons intercepted by the polepiece and walls of the chamber are now lost to the signal. Comparison of Figs. 1 and 2 reveals that although the images are superficially similar, the - E-T image has much stronger topographic contrast than the + E-T image, which brings the fine surface scratches into visibility. Surface scratches parallel to the detector face are seen in high contrast, because the sides of the scratches preferentially scatter electrons either directly toward the E-T detector or away, which results in strong contrast. The visibility of scratches perpendicular to the detector face (example indicated by arrows) is much poorer, because the sides of the scratch scatter electrons parallel to the face of the detector producing low contrast.

Comparison of Figs. 1 and 2 also reveals surface contamination in Fig. 1 (arrows) that does not appear in Fig. 2. This difference is a result of the relative sampling depths of the secondary and backscattered electrons. In Fig. 1, the component of secondary electrons that contributes to the image is highly sensitive to the top 20 nm of the sample. In Fig. 2, the backscattered electrons sample depths down to about 25% of the electron range, which gives a sampling depth of about 250 nm. The presence of surface contaminants is often difficult to recognize in a single + E-T image, which contains contributions from the sampling depths of both the secondary-electron and backscattered-electron components. Comparison of a + E-T image with a backscattered-electron image can reveal surface-dependent structures by the differences between the two.

Figure 3 was prepared with a 4-segment solid-state detector operated with the signal from all four segments added together. The detector segments cover such a large solid angle that only number effects are significant; trajectory effects are almost completely suppressed. The result is that only atomic number contrast is observed in most of the



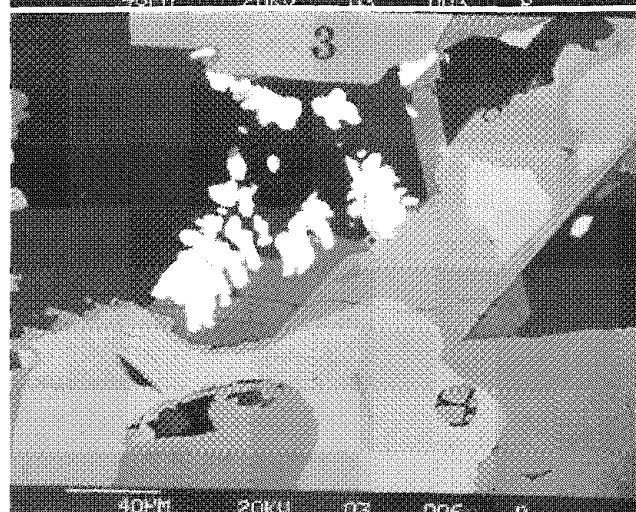
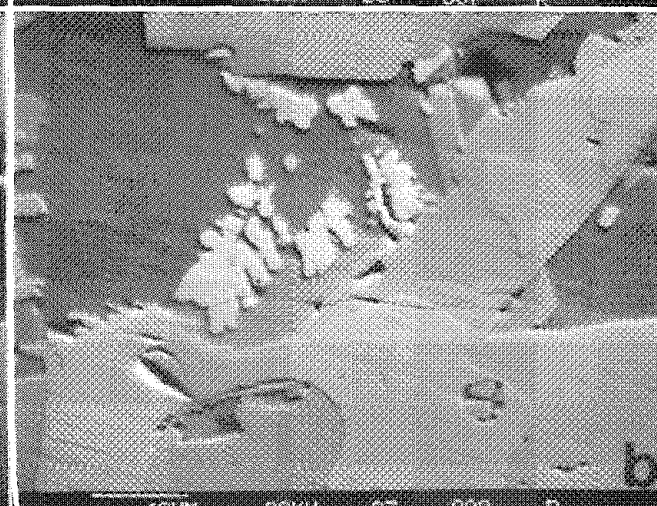
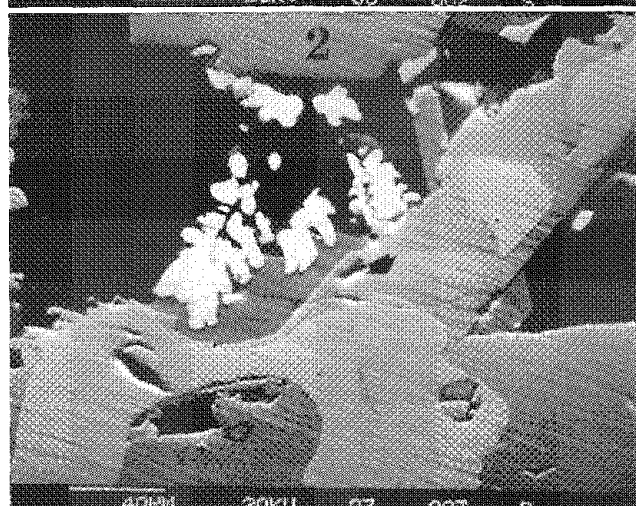
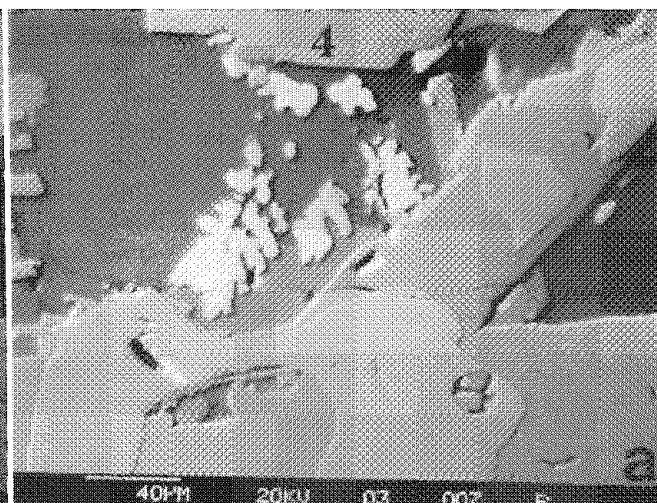
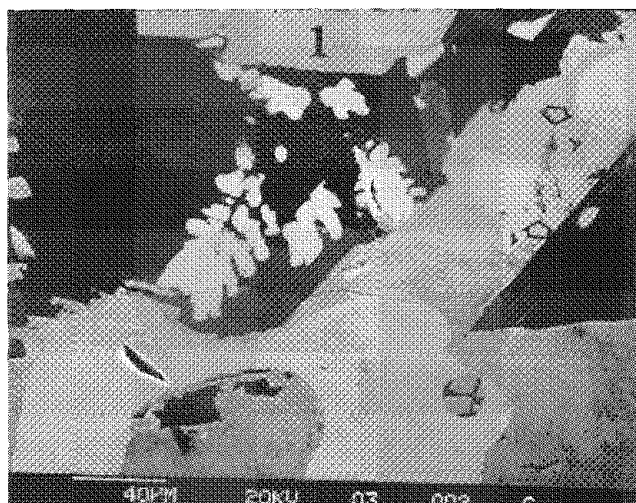


FIG. 1.--SEM image of multiphase rock. Beam energy, 20 keV; specimen tilt,  $0^\circ$  (beam normal to surface). Detector: Everhart-Thornley, biased positively. Arrows denote surface contamination.

FIG. 2.--SEM image of area in Fig. 1 but with Everhart-Thornley detector biased negatively. Note absence of surface contamination.

FIG. 3.--SEM image of same area as in Fig. 1 but prepared with four-segment solid-state detector with signals from all four detectors summed.

FIG. 4.--SEM image of same area as in Fig. 1 but prepared with segmented solid-state detector. Subtraction of signals: (a) upper left minus lower right; (b) upper right minus lower left.

image. The only topographic information remaining is the deep cracks and holes in the specimen that appear dark because they act to trap the beam electrons and thus produce a number effect. Atomic number contrast is emphasized by the solid-state detector because of the energy response and the fact that with increasing atomic number the fraction of high-energy backscattered electrons increases.

In Fig. 4 the signals from the segments of the detectors are subtracted. The detectors are arranged along the diagonals of the image. In Fig. 4(a), the subtraction is upper left - lower right. The atomic number contrast is reduced compared to Fig. 3; with careful scaling of the responses of the individual detectors, the atomic number contrast can be eliminated entirely. In this example, the relative gains were not balanced, so that some atomic number contrast remains even in the difference signal. The topography associated with edges that run perpendicular to the detector axis is greatly enhanced. Again, there is reduced sensitivity to edges that run parallel to the detector axis. This effect is emphasized in Fig. 4(b), in which the subtraction is upper right - lower left. The scratches observed in Fig. 2 are now seen in strong contrast, since the relative sense of the signals from opposite faces of the scratches is reversed in the two detectors, so that taking a difference produces a large result.

The specimen current (SC) signal can be used to produce an image that exclusively reveals number effects. In Fig. 5, a two-phase lead-tin eutectic alloy is observed with the negatively biased E-T detector (Fig. 5a) and with the SC signal (Fig. 5b). Note that in order to maintain consistency in the sense of contrast between these images, the contrast sense has been reversed in the SC image by means of subsequent signal processing. Although the area of the specimen is the same in the two images, the appearance is dramatically different. The - E-T image is dominated by trajectory effects and reveals the undulating nature of the surface, whereas the SC image shows purely number effects that reveal the compositional structure. The SC image also contains intriguing structures that consist of bright areas with soft edges (examples labeled "B" in Fig. 5b). These image structures can be interpreted as arising from islands of the lead-rich phase which are buried beneath and do not intersect the surface. The edges of these islands are not sharply defined in the image because the scattering of the beam electrons during penetration effectively broadens the beam and degrades the lateral spatial resolution.

Figures 1-5 show that the exact form of an SEM image of a specimen can vary substantially through the choice of the detector and the detector orientation, with each of these images possibly carrying unique and valuable information. When the additional variables of beam energy and beam incidence angle (or specimen tilt) are included, the variety of possible images that can be prepared from a single area of a specimen is increased many-fold. The microscopist rarely has the luxury of time to prepare all these images in order to select those which carry the information of interest. To maximize the efficiency of SEM analysis, a working knowledge of the information in Tables 1 and 2 is vital if proper interpretation of the nature of the specimen is to be obtained.

### Conclusions

The character of an SEM image depends on the nature of the operative contrast mechanism and the detector that collects the signal. Proper image interpretation depends on analyzing the contrast in terms of the expected properties of the mechanism and the known properties of the detector. Key concepts include the type of contrast encoding (number, trajectory, or energy) and the detector response. A selection of images of the same area prepared with a variety of detectors often provides the most comprehensive characterization of the specimen.

### References

1. D. E. Newbury, "Imaging strategy in the scanning electron microscope: A tutorial," *SEM/1981*, 71-78.
2. J. I. Goldstein, H. Yakowitz, D. E. Newbury, E. Lifshin, J. W. Colby, and J. R. Coleman, *Practical Scanning Electron Microscopy*, New York: Plenum, 1975.
3. O. C. Wells, *Scanning Electron Microscopy*, New York: McGraw-Hill, 1974.
4. J. I. Goldstein, D. E. Newbury, P. Echlin, D. C. Joy, C. Fiori, and E. Lifshin, *Scanning Electron Microscopy and X-ray Microanalysis*, New York: Plenum, 1981.
5. D. E. Newbury, D. C. Joy, P. Echlin, C. E. Fiori, and J. I. Goldstein, *Advanced Scanning Electron Microscopy and X-ray Microanalysis*, New York: Plenum, 1986.

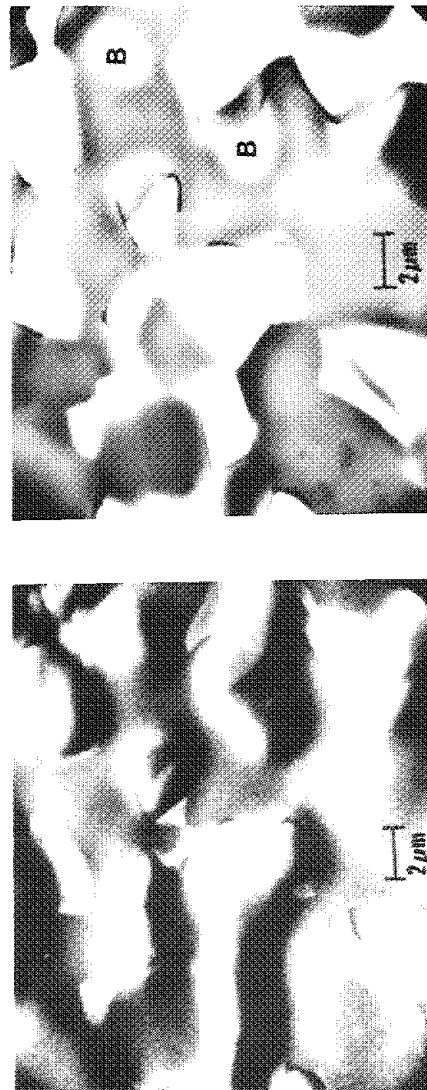
TABLE 1

Contrast Mechanism	Signal Detected	Number	Contrast Encoding: Trajectory	Energy	Detector	Signal Detected	Number	Sensitivity: Trajectory	Energy
Topographic I	SE	Strong (1)	Weak	No	E-T, +	SE	Strong	Weak	None
Topographic II	BSE	Strong (2)	Strong	Yes		BSE	Intermed.	Strong	Slight
Atomic number	BSE	Strong (3)	Weak	Yes	E-T, -	BSE	Weak	Very Strong	Weak
Channeling	BSE	Strong	Weak	Yes		BSE	Intermed.	Intermed.	Intermed.
Magnetic Type I	SE	None	Strong	No	Large Asymmetric Scintillator	BSE	Strong	Weak	Intermed.
Type II	BSE	Weak	Weak	Yes	Large Symmetric Scintillator	BSE	Strong	Weak	Intermed.
Type III	SE, polar.	Intermed.	No	No	Scintillator Array	BSE	Strong	Weak	Intermed.
Voltage	SE	No	Strong	No	mode +	BSE	Strong	Weak	Intermed.
EBIC	SC	Strong	No	No	mode -	BSE	Weak	Strong	Weak
					Low Loss	BSE	Weak	Very Strong	Energy Selecting
					Conversion SE-to-BSE	BSE	Strong	None	Inverse
					Annular solid state	BSE	Strong	Weak	Strong > 5 keV
					Segmented solid state	BSE	Strong	Weak	Strong
					mode +	BSE	Weak	Strong	Weak
					mode -	BSE	Strong	None	None
					Specimen current	SE, BSE	Strong	Strong	None

Abbreviations:

E-T = Everhart-Thornley detector

FIG. 5.--SEM images of two-phase lead-tin eutectic alloy; beam energy, 20 keV; specimen tilt, 0°. (a) Detector: Everhart-Thornley, biased negatively; (b) specimen current, with contrast inversion applied through subsequent signal processing.



## AN INTRODUCTION TO BIOLOGICAL X-RAY MICRONALYSIS

Patrick Echlin

X-ray microanalysis is a method of chemical analysis in which it is possible directly to relate the elemental composition of a small region of cells or tissue with their morphological appearance. One achieves this analysis by focusing a fine beam of electrons onto a preselected area of a specimen and collecting, measuring, and analyzing the x rays which are emitted. These x rays are characteristic of the atoms that make up the sample. The main advantages of the method are that the analysis is carried out in situ, and a photographic record can be made of the precise region which is analyzed.

### *The Physics and Technology of X-ray Microanalysis*

X rays are emitted from *any* specimen when it is irradiated with high-energy radiation such as a flux of electrons or x rays. Nearly all biological x-ray microanalysis is carried out by means of a high-energy beam of electrons that can be **easily** focused onto the area of interest on the sample. The same beam of electrons can be used to provide topographical information about the specimen. In order for the x rays to be produced, the energy of the incident or primary electron beam has to be greater than a minimum value known as the critical excitation potential. This increases with atomic number, but because most of the elements of biological interest are of low atomic number (i.e.,  $Z = 11-20$ ) the primary-beam energy need be no more than 10-15 keV.

The interactions of electrons with matter can generally be divided into two classes:

1. Inelastic scattering, where the incident electron transfers energy to the sample with only a small change in its trajectory.
2. Elastic scattering, where there is a significant change in trajectory of the incoming electron without any substantial change in energy.

During inelastic scattering of the electron beam, x rays can be formed by two distinctly different processes.

1. *Characteristic x rays.* These are produced when the incident electron beam displaces or removes inner shell orbital electrons and leaves the atom in an excited state with a vacancy in the electron shell. The vacancy is filled by an electron from one of the series of shells of orbiting electrons that surround the nucleus. These shells are designated K, L, M, etc., decreasing in energy as the **distance from the nucleus increases**. Each shell has a set number of permitted energy states, which may be occupied by orbital electrons. The energy difference resulting from these electron transitions is emitted as an x ray, characteristic of the electron orbital and the atom from which it was derived. The energy of the x-ray photon is the potential energy difference between the two orbitals involved in the transition and has an important bearing on whether it can be detected. Very-low-energy x-ray photons (e.g., from lithium) would be largely absorbed by the specimen; a few x-ray photons would escape from light elements up to  $Z = 10$  and many of them would be absorbed before they reached the detecting system. It is only when we get to elements such as sodium and above that there is a sufficient flux of emitted x rays to make x-ray microanalysis a practical proposition.

Figure 1 shows that a number of different x rays can be derived from a given element and they can be conveniently named. If an electron was ejected from the inner K shell and the vacancy filled from the L shell, the resulting x ray is referred to as a  $K\alpha$  x-ray photon; a transition from the M shell to the K shell is a  $K\beta$  x-ray photon. Vacancies in L shells give L x rays; in M shells, M x rays; etc.

Thus each element has a distinct x-ray fingerprint depending on the number of electron orbitals, a consequence of its atomic number. For example, nitrogen ( $Z = 7$ ) only has K

---

The author is at the Department of Botany, University of Cambridge, Cambridge, England CB2 3EA.

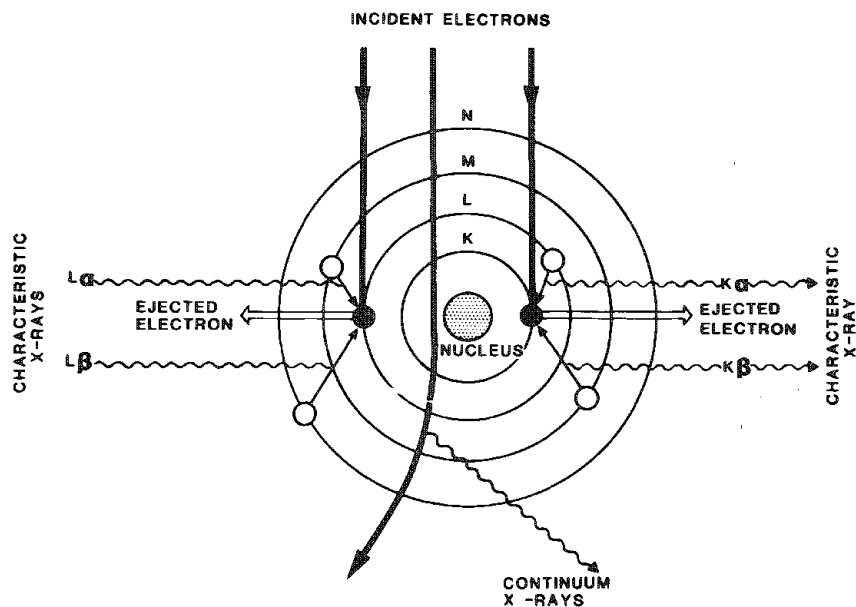


FIG. 1.--Production of x rays.

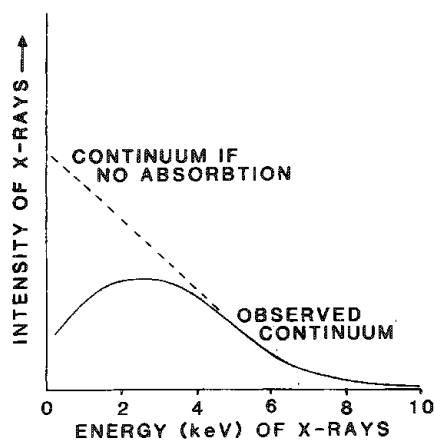


FIG. 2.--Continuum radiation.

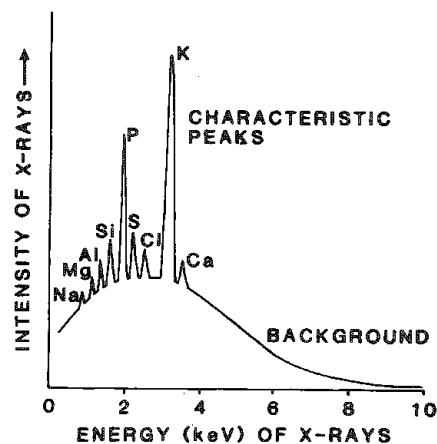


FIG. 3.--Background and characteristic peaks.

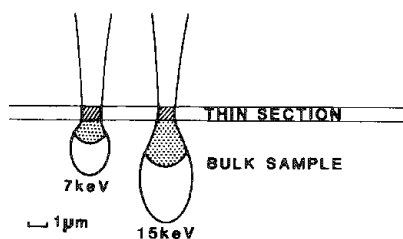


FIG. 4.--Beam penetration into samples.

and L electron orbitals and so can only yield  $K\alpha$  x rays; phosphorus ( $Z = 15$ ) has K, L, and M orbitals and so yields  $K\alpha$  and  $K\beta$  x rays; and calcium ( $Z = 20$ ) has four orbitals and so yields K and L x rays.

The x-ray fingerprints for all the elements have been characterized and are available as tables or slide rules, or are embedded in the software of the computer-driven analytical programs. For light elements it is not possible to detect L and M x rays, although K and L x rays are a characteristic feature of most metals, and heavy elements such as lead or gold have a bewildering array of K, L, and M x-ray lines. The characteristic x-ray fingerprint for each element is the basis of the x-ray analytical technique, as there is a direct relationship between the intensity of characteristic x rays from an element in the specimen and the number of atoms of that element within the irradiated microvolume.

2. *Continuum Radiation or Background.* As seen in Fig. 2, the primary beam electrons may pass close to the nucleus of the sample atom, and experience a large change in direction but suffer only a small energy loss. In the majority of collisions the energy loss is less than 1 keV, although the energy distribution extends all the way to the energy of the incoming beam. Most of these low-energy x rays are either absorbed by the specimen or remain undetected by the x-ray analyzer. The continuum intensity is proportional to the total mass of the irradiated microvolume of the sample.

It will be seen that x-ray production from the irradiated microvolume is primarily a consequence of the characteristic and continuum radiation. Figure 3 shows the visible manifestation of these interactions as a spectrum of the background radiation overlaid with the characteristic peaks of the elements that are sufficiently high on the periodic table to be detected.

### *The Intensity of Characteristic X Rays*

Although the intensity of x-ray emission is linearly proportional to the beam current, several other factors also play a part and their effects vary according to whether the sample is in the form of a bulk sample (i.e., does not transmit the incoming electron beam) or a thin section (transmits the incoming electron beam with negligible loss of energy).

1. *Bulk Specimens.* The intensity of x rays is proportional to:

- (a) the number of atoms encountered by the primary electron beam;
- (b) the fraction of electron interactions that result in the emission of characteristic x rays (the fluorescent yield); and
- (c) the ionization cross section (the probability that ionization of the inner shell electron will occur), which increases rapidly with energy from zero to the critical excitation potential and reaches a plateau potential for a given element.

Below this figure the x-ray yield drops away rather rapidly. Above this figure there is no improvement in x-ray emission and the primary beam penetrates deeper into the sample. This penetration has two important consequences for x-ray microanalysis:

- (a) The further the beam penetrates into the sample the larger the size of the volume from which x rays are emitted, which in turn decreases the spatial resolution.
- (b) The deeper the electrons penetrate into the sample, the longer the path length for the x rays, many of which are absorbed by the specimen. Absorption is a particular problem for light elements and for this reason the voltage of the primary beam for bulk samples should be no more than 15 keV. Figure 4 shows these effects in bulk samples and thin sections.

2. *Thin Sections.* Most of the electrons pass through the section without loss of energy and absorption is negligible, and the characteristic x-ray yield is simply a function of fluorescent yield, ionization cross section, and the number and atomic weight of the atoms in the sample.

### *The Production of X Rays*

The first golden rule of biological x-ray microanalysis is that the x rays generated within the specimen are not necessarily the x rays emitted from the specimen. There are cogent reasons for this state of affairs that depend on three interrelated factors: the

atomic-number effect on the generation of x rays; the absorption of primary x rays; and the fluorescence effect resulting in the secondary generation of additional x rays.

1. *The Atomic-number Effect (Z)*. This is a measure of the back scattering of the primary beam from the surface of a bulk specimen and the amount of stopping power of the specimen matrix. The latter is important in determining how many characteristic x rays are likely to be generated before the energy of the incident electron beam decays to zero. In biological x-ray microanalysis the atomic-number effect has only become a problem with the infrequent bulk specimens of high atomic-weight. The atomic number effect is of little consequence in thin sections.

2. *The Absorption Effect (A)*. The primary generated x rays passing through the samples are absorbed exponentially with distance. This can be a problem with bulk samples where low-energy x rays may be generated deep in the sample. In thin sections absorption is negligible.

3. *The Fluorescence Effect (B)*. This effect occurs when the generated x rays have sufficient energy to interact with other inner-shell orbital electrons of the specimen and produce secondary x rays of a lower energy. This is only a serious problem in bulk specimens in which a small amount of high-atomic weight material is embedded in a low-atomic-weight matrix. The fluorescence effect is of negligible proportions in thin sections.

### *Spatial Resolution*

The spatial resolution in bulk samples depends on the volume through which electrons diffuse and spread in the specimen. Figure 4 shows that this diffusion is a function of accelerating voltage and specimen density, and to a much lesser extent of the beam diameter. Thus, for a given accelerating voltage, the spatial resolution is much lower in a bulk biological sample (between 1 and 3  $\mu\text{m}$ ). In most biological thin sections the mean atomic number and density is so low that beam spread is negligible and the spatial resolution depends primarily on beam diameter. In these circumstances the resolution is typically 20-100 nm.

### *Specimen Surface Topography*

X-ray photons travel in straight lines and care must be taken to insure that there is a direct line of sight between the region of the specimen being analyzed and the x-ray detecting system. Most metallic and geological specimens can be prepared with a smooth surface, but that is rarely the case with bulk biological specimens and surface irregularities can easily obscure and absorb emitted x rays. The x-ray collection efficiency may be substantially improved if the specimen is tilted toward the detector. The surface topography effects rarely present a problem with thin sections which are assumed, sometimes erroneously, to be flat.

In terms of the production, collection, and (as we shall see later) quantification of x rays, the use of thin sections is preferable to the use of bulk samples. There are minimal problems of absorption, the spatial resolution is improved, and the quantitation is more straightforward than with bulk samples. However, bulk samples are much easier to prepare and when this preparation is centered on one of the low-temperature methods, there is a much greater degree of certainty of retaining the elements of biological interest than in a thin section.

### *Instrumentation*

Two pieces of equipment are needed to carry out x-ray microanalysis: a source of high-energy electrons and a means of detecting and measuring the x-ray photons. The source of high-energy electrons is conveniently provided by one of the various types of electron-beam instruments such as transmission and scanning electron microscopes and their derivatives. The only requirement for these instruments is that they produce a narrow beam of electrons that may be brought to focus at various points on the specimen. Two features of x rays, their energy and wavelength, are the principal determinants behind the design of instruments to detect, measure, and quantify the x-ray photons.

1. *Wavelength-dispersive Analysis*. X rays, in common with all electromagnetic radiation, have a range of wavelengths and radiate in all directions from the specimen. A



small proportion of these x rays impinge on a diffracting crystal which reflects and focuses a given wavelength of x-ray photons into a proportional counter. The counter converts the x-ray photons into electrical signals of varying intensity that may be processed, counted, and quantified. The range of wavelengths and thus the number of elements that can be detected can be varied by use of a series of crystals of varying lattice spacings and by changes in the angle of the crystal relative to the specimen at the detector.

Because the analysis is restricted to one element at a time per spectrometer, most instruments have more than one spectrometer, each with several different crystals. Although the analysis is a time-consuming process, wavelength spectrometers have a useful, if limited, part to play in the study of biological samples.

(a) The x-ray resolution is very good and is equivalent to 1-10 eV, which eliminates many of the problems associated with characteristic peak identification and overlap. (The relationship between the wavelength  $\lambda$  and energy E of x rays is given by  $E\lambda = 12.396$ , where E is in keV and  $\lambda$  is in Angstroms.)

(b) The peak-to-background ratio is high, which improves the limits of detection.

(c) Light elements down to Z = 4 are more easily detected.

However, these advantages must be set against several limitations. The overall efficiency of collection (the proportion of x rays measured to x rays emitted) is low. It may improve either by an increase in the beam current (which damages biological samples), or by an increase in the probe diameter (which decreases spatial resolution). The long analysis times, typically 30-60 min, can also result in beam damage to the specimen. But the major limitation is that only one or two elements can be analyzed at a time. This is a significant constraint with biological material, where one may wish to carry out multi-element analysis in a beam-sensitive matrix.

*2. Energy-dispersive Analysis.* These instruments take advantage of the fact that x-ray photons also have discrete energies. The detector is a lithium drifted, p-type silicon crystal that converts the x-ray photons into a series of variable electrical charges which are amplified, measured, counted, and quantified. The detector, which is kept under vacuum and cooled with liquid nitrogen to reduce electronic noise, is isolated from the vacuum of the microscope by a thin 8.0 $\mu$ m beryllium window. The presence of this window prevents the cold detector from becoming contaminated and absorbs the back-scattered electrons. The window unfortunately also absorbs some of the light-element x-ray photons, which limits the usefulness of these detectors for the analysis of elements below sodium. However, most energy-dispersive detectors also operate in a so-called windowless and thin-window mode, which obviates some of these problems.

Energy-dispersive analysis has a number of advantages with respect to wavelength systems:

(a) All elements may be analyzed simultaneously.

(b) The analysis time is short, 2-5 min.

(c) The overall efficiency of collection is improved because the detector can be moved to within a few millimeters of the sample and thus intercepts a much larger solid angle of x-ray photons. A consequence of this improved efficiency is reduced beam currents and smaller probe sizes.

However, energy-dispersive analyzers also have their limitations. The x-ray resolution is poor (ca 150 eV) and decreases with increasing energy of the x-ray photons. Although this dependence creates problems with identification of all the peaks, spectral overlaps, poorer peak to background ratios, and hence poorer minimum detection limits, these effects may be partially alleviated by the use of computers to massage a resultant spectrum gently. Low-energy x-ray photons are absorbed by the beryllium window, and at high rates of x-ray production the counting statistics and the subsequent processing of the signal may give rise to spectral artifacts.

Ideally, biological microanalysis should be carried out on an electron-beam instrument fitted with both types of spectrometers. The high spatial resolution and improved limits of detection (particularly with light elements) of the wavelength analyzer complements the multielement analytical capabilities of the energy-dispersive systems.



## *The Process of X-ray Microanalysis*

To the novice, the process of x-ray microanalysis can be fraught with difficulty, although these difficulties are readily overcome once they are recognized and appreciated. The difficulties center around the second golden rule of microanalysis, which states that the x rays emitted by the specimen are not necessarily solely those collected and analyzed by the detector. This rule implies that the total x-ray signal is either not representative of the sample in that certain signals are deleted and/or contains spurious signals that are not derived from the specimen.

The principal reasons for the loss of x rays are faulty specimen preparation, absorption either within the specimen or due to poor specimen-detector geometry, mass loss due to high beam currents during analysis, and charging due to an excess overvoltage being applied to a poorly conducting sample. These problems may be alleviated by adequate sample preparation and by minimizing the energy input into the sample sufficient to give an adequate signal.

The spurious signals are derived from additions made to the sample during preparation (i.e., fixatives, buffers, stains, and thin films of coating material) and scattering from the regions of the microscope immediately surrounding the specimen (i.e., support grid and film, microscope stage and column, and even parts of the x-ray detector). At best, all these spurious signals can be eliminated; at worst, considerably alleviated.

1. *Qualitative Analysis.* X-ray microanalysis can be carried out at varying degrees of sophistication. In many instances it is sufficient to perform a simple qualitative analysis in which the presence (or absence) of an element is confirmed and directly related to a morphological feature. One can obtain the information by mapping the distribution of the element in the whole sample; running transect scan lines across various regions of the sample and expressing the differences in elemental concentration as varying peak heights; or analyzing discrete parts of the sample by means of a point or reduced raster. At best this approach can tell us that some regions of a sample contain more of an element than another; at worst, that an element is either present or absent.

2. *Quantitative Analysis.* Some analyses require a more sophisticated approach, in which detailed information is needed on either the relative or absolute concentration of elements in the sample. This process is called quantitative analysis and requires that considerable attention be paid to specimen preparation, the process of x-ray acquisition, and the way of ensuing data are corrected and quantified.

A wide range of quantitative procedures are available for converting the collected x rays to relative or absolute concentrations. Space does not permit more than a cursory overview of the two main methods that have been applied to the quantitative analysis of biological samples.

a. *The continuum method for thin sections.* Quantitative procedures for thin sections are reasonably straightforward because in nearly all biological thin sections the measured x-ray intensity is proportional to the amount of element in the analyzed microvolume. The very thinness of the sample precludes any absorption of generated x rays; and since most biological samples are of low atomic number, the atomic number and fluorescence effects are negligible. The spatial resolution is good because there is little beam spread within a thin sample. The quantitative procedure simply combines two well-established relationships of x-ray optics:

(i) the intensity of the continuum or background radiation is proportional to the total mass thickness of the analyzed microvolume; and

(ii) the peak intensity of the characteristic x-ray radiation of an element is proportional to the concentration of that element in the analyzed microvolume.

Thus, the first relationship gives a measure of the total size of the microvolume, and the second provides a measure of the concentration of element(s) within the same microvolume.

b. *The peak-to-background ratio for bulk samples.* Since the characteristic and background x rays of the same energy are generated within nearly the same depth distribution, they are subject to the same local composition-related absorption, secondary fluorescence, and atomic-number effects. This assumption only holds true for homogeneous samples as the characteristic and background x-ray signals vary with changes in the average atomic number

of the sample. However, this particular method is most appropriate for frozen hydrated bulk biological material, where water forms by far the most abundant constituent of the tissue, so that we have what may be considered a homogeneous sample. The ratio of peak area to background immediately under the peak is more or less independent of sample geometry and small variations in the beam current. Provided the peaks are properly characterized and the background below the peak is measured correctly, the accuracy of the method approaches that which may be obtained by use of the continuum method.

Full details of these two methods of quantitation are given in one or more of the references at the end of this article. In using the two procedures, one must pay considerable attention to applying corrections for spurious signals from the sample and to either providing standards made up in a matrix which more closely approximates the matrix of the biological material, or having an accurate measure of the chemical constitution of the matrix containing the analyzable elements. Care must also be taken to operate the microscope (and x-ray analyzer) under reasonably standard and reproducible conditions of beam stability, analysis time, and low contamination, and to insure that a sufficiently high number of characteristic counts are measured to give a peak-to-background ratio of at least three to one. In addition, the analyst must quickly learn to distinguish x-ray spectra that are truly derived from the sample from spectral artifacts due to faulty preparation, specimen support, instrument background, and incomplete spectrum processing.

The accuracy of these two analytical techniques depends greatly on the care taken with the preparative methods and the accuracy by which the x-ray spectra are deconvoluted. Most analysis gets to within 10% (not as good as may be achieved with metallic samples) but still reasonable for biological material. The sensitivity does show some variation, depending on the atomic number of the element being analyzed and on whether the sample is a section or a bulk specimen. An average figure would be between 0.1 and 0.01% concentration.

### *Specimen Preparation*

The quality of x-ray microanalysis is no better than the attention paid to specimen preparation, which is nowhere more exacting than with biological samples. Without going into great detail, we may divide the methods into those which rely on wet chemical methods and those which are based on low-temperature manipulations. In addition, most specimens fall into one of two main categories: thin sections and bulk samples. Thin sections by their nature allow high spatial resolution and more accurate quantitation. These advantages are offset by difficulties of preparation, particularly with frozen hydrated samples, and an increased chance of specimen damage. Bulk samples are much easier to prepare, particularly with frozen hydrated material, and appear to suffer less damage during analysis. However, the spatial resolution is not as good and quantitation is less accurate.

1. *Wet Chemical Specimen Preparation.* These methods are based on the tried and tested methods devised for morphological studies in various forms of electron microscopes. The approach revolves around the premise that structure is a manifestation of the form and interrelationship of molecules and macromolecules in the cell, and that the specimen preservation should be aimed at stabilizing these organic building blocks. Although this approach results in images of consummate elegance and complexity, it does so at the expense of the smaller molecular species, electrolytes, and atoms. From an analytical point of view this approach is disastrous, as the methods both introduce foreign elements into cells and remove vital elements from cells.

A brief catalog of the disasters occasioned by the wet chemical approach should dissuade all but the most intransigent and misinformed biologists from adopting this approach.

Fixation, dehydration, and embedding all cause rapid and gross changes in membrane permeability, and elements from the processing chemicals invariably end up as part of the specimen. Subsequent staining of the sample can only exacerbate the problem. As if total loss of element was not sufficient cause for concern, these procedures can initiate the insidious redistribution of natural elements within tissues that further complicates the analysis. Attempts have been made to precipitate some of the more mobile natural elements in situ, but it is by no means certain that these procedures are effective.

Unless it can be shown quite unequivocally that a given chemical-based preparative protocol causes no changes in the sample, these methods should not be used in biological microanalysis. In a very few instances, specimens can be examined direct without the need

of any preparation. Under these circumstances the main artifact is that related to the distortions which result from air drying a highly hydrated sample.

2. *Low-temperature Preparative Techniques.* There appear to be four main advantages of using low temperatures in the x-ray microanalysis of biological materials. (a) By lowering the temperature but still maintaining the liquid state, chemical reaction rates and transport processes such as viscosity and diffusion are slowed down. This slowing down makes such processes more amenable to study in situ. (b) Water and many organic materials when in the solid state show an increase in mechanical strength and allow these materials to be sectioned, fractured, or dissected to reveal subsurface details. (c) There is a diminution in the amount of the sort of damage to the specimen that is an inevitable consequence of the use of some of the imaging and analyzing systems. (d) There is no need to use the deleterious chemical methods that are frequently required to stabilize and strengthen organic samples during specimen preparation for examination at ambient temperatures.

The conversion of liquid water to solid ice should aim at vitrification in which all the constituent atoms, molecules, and ions remain in their relative position in the specimen before and after cooling. In spite of a variety of fast cooling methods, it is most unlikely that such a perfect state can ever be achieved in a heterogeneous, multiphase specimen and it is only rarely achieved in homogeneous single-phase samples.

There are several options with regard to further treatment of the sample after it has been rapidly cooled: (a) sectioning, (b) fracturing, (c) chemical substitution, and (d) freeze-drying. Before deciding which of these options will be used, one must decide whether the specimen is to be examined in the frozen-dried or the frozen-hydrated state, and whether the external surface or the internal contents are the subject of the investigation. A frozen-dried specimen is one in which the solid water has been removed by sublimation under vacuum.

#### *Specimen Damage*

Early texts and papers frequently refer to x-ray microanalysis being a nondestructive procedure. That may be the case for polished metals and ceramics, but it is not true for most organic and biological samples. Even the low beam currents (0.1 to 2.0 nA) used in energy-dispersive analysis cause significant losses (up to 90%) in both the light-element organic matrix and in the heavier detectable elements. This thermally induced mass loss and elemental loss is progressive with time, and though low temperatures appear to ameliorate the problem, they do not prevent it. The situation with ionizing radiation is even more insidious; there, low temperatures offer no protection. Recent studies show that considerable losses (90%) occur in frozen-hydrated sections and that the presence of water (ice) exacerbates the process. The same losses do not appear to occur in bulk frozen samples. Losses of these proportions, unless significantly reduced, seriously limit the effectiveness of quantitative analytical procedure. One can only hope that the losses are the same in the specimen as in the standard, and that the characteristic peaks and associated backgrounds diminish in proportion to each other.

#### *Devising an Experimental Protocol for Biological X-ray Microanalysis*

Several interrelated factors should be considered before any attempt is made to carry out x-ray microanalysis of biological materials; wherever possible answers should be provided to the following questions.

1. What kind of electron beam instrumentation is available for analysis?
2. What type of x-ray microanalyzer is available for analysis?
3. What type of sample is available for analysis?
4. What type of analysis is required?

#### *Criteria for Use in Judging the Efficacy of a Preparative Technique*

Having established the dimensions of the analytical problem and the availability of the instrumentation which should provide some answers, we can now consider the criteria we should adopt in designing the methods of specimen preparation that are vital for adequate analysis:

1. losses and gains within the sample during preparation
2. changes in the chemical identity of the sample
3. redistribution of elements in the sample
4. preparative procedures should not mask the elements being analyzed
5. the effect of some of the ancillary methods on the analysis
6. preservation and identification of the natural structural relationships of the sample

Biological x-ray microanalysis still remains a powerful analytical adjunct for measuring the elemental concentrations of cells and tissue. However, it must be used with caution, for in untutored hands it can provide erroneous information. It must be accepted that some elemental losses and redistribution invariably occur during specimen preparation, and that this deterioration of the specimen continues in the microscope. Low-temperature preparative and analytic methods offer the only hope forward.

### References

As this is a tutorial paper only three key references are given in order of complexity. Each reference contains many further references that deal with specific parts of the microanalytical process.

1. A. J. Morgan, *X-ray Microanalysis in Electron Microscopy for Biologists*, London: Oxford University Press, Royal Microscopical Society, 1985 (£5.95). An excellent introductory text written specifically for biologists. It is reasonably priced and covers most of the practical aspects.

2. J. I. Goldstein, D. E. Newbury, P. Echlin, D. C. Joy, C. E. Fiori, and E. Lifshin, *Scanning Electron Microscopy and X-ray Microanalysis*, New York: Plenum Press, 1981 (\$39). Provides much more detail than Ref. 1, and in addition to providing the theory, also provides detailed practical information about the preparation and analysis of specimens.

3. D. E. Newbury, D. C. Joy, P. Echlin, C. E. Fiori, and J. I. Goldstein, *Advanced Scanning Electron Microscopy and X-ray Microanalysis*, New York: Plenum Press, 1986 (\$45). This book takes over where the previous book leaves off. It is an up-to-date advanced text on the subject, with particular emphasis on microanalysis, quantitation, and low-temperature specimen preparation.

## NUCLEAR-MICROPROBE ANALYSIS: APPLICATIONS

B. L. Doyle

Nuclear-microprobe analysis is a relatively small but growing field that utilizes high-energy (MeV) beams of finely focused ( $1\mu\text{m}$ ) ions to examine the atomic composition of the near-surface region of solids. With this analytic technique, every element in the periodic table is detectable, for most cases at trace amounts; for many cases, concentrations can be nondestructively determined in three dimensions. Although this technique has been used for approximately 15 years,<sup>1</sup> its utility remains relatively untapped by the general materials analysis community, mainly because of the unavailability of moderately priced accelerators and beam-focusing systems. This situation is currently changing rapidly and has already sparked a renaissance in the area of ion-beam analysis that will probably result in an increased interest in nuclear microprobes.

This paper is a tutorial on nuclear-microprobe analysis. A previous paper, presented to MAS in 1981, comprehensively surveyed ion-beam analysis techniques, focusing geometries, and data-collection/analysis systems, and the reader is urged to refer to it for details.<sup>2</sup> The emphasis of the present paper is on applications to materials problems. A recent study of TiC-coated graphite tiles used in the main movable limiter in the Tokamak Fusion Test Reactor (TFTR) at the Princeton Plasma Physics Laboratory is the central topic, because most of the ion-beam analysis techniques available on our probe were used in this investigation.

### *Experimental*

We begin with a brief overview of ion-beam techniques used in nuclear-microprobe analysis, primarily to introduce terminology; for more detailed information on ion-beam analysis, see Refs. 2-5. Recognizing that nuclear microprobe analysis is not a panacea for all materials problems, we present the strengths and weaknesses of each of these analysis methods. The various techniques are diagrammed in Fig. 1.

Rutherford backscattering spectrometry<sup>6</sup> (RBS) and elastic recoil detection<sup>7,8</sup> (ERD) are based on the simple elastic scattering that occurs during nucleon-nucleon collisions. In RBS (Fig. 1a), a beam of light ions (e.g.,  $^1\text{H}$  or  $^4\text{He}$  at a few MeV) strikes the sample and the energy distribution of the particles backscattered at a specific angle is measured with an Si surface barrier detector. In this example, the proton (p) penetrates some distance into the solid and then scatters from an Au atom. The depth distribution of the Au in the solid is obtained from the intensity and energy of the backscattered protons, and the scattering cross section and energy loss rate. For targets with two or more elements, the energy spectrum of the backscattered particles is ambiguous in that it contains both depth (through energy loss) and mass (through collision kinematics) information. In principle, RBS is capable of determining depth-concentration profiles of any element heavier than the mass of the incident beam; however, this mass/depth ambiguity, in addition to other considerations such as low scattering cross sections for light elements ( $Z < 8$ ) and the reduced mass resolution caused by kinematics at high masses ( $Z > 30$ ), place additional restrictions on the utility of this technique. Through careful selection of the ion beam, energy, and target-detector geometries, these obstacles can be usually overcome. For RBS, typical values for sensitivity, resolution, and profiling depth vary over 1-1000 ppm, 25-5000 Å, and 0.1-50  $\mu\text{m}$ , respectively, depending on the incident beam used and the sample composition.

With ERD, the RBS experiment is simply turned around, with heavy ions used to depth profile lighter elements (Fig. 1b). In this example, Si ions are accelerated onto a

---

The author is at Sandia National Laboratories, Albuquerque, NM 87185. The work was supported by the U.S. Department of Energy under contract DE-AC04-76DP00789. The author thanks N. D. Wing for his assistance in the development in the Sandia nuclear microprobe and the collection of the data used in this report.

target which contains H (i.e., protium, p). In this case the Si knocks protons out of the target in a forward direction. By measuring the energy distribution of these proton recoils, the hydrogen concentration versus depth is obtained by much the same methods as in RBS. ERD also suffers from the same mass/depth ambiguity as RBS, but is capable of depth profiling the elements from hydrogen to oxygen. Typical sensitivity, resolution, and profiling depth values for ERD range over 10-1000 ppm, 200-800 Å, and 0.1-1 µm, respectively. From the above discussion it is clear that RBS and ERD are complementary techniques.

Other ion-beam analyses similar to RBS utilize the generation and detection of nuclear-reaction products to signal the detection of light elements ( $Z < 9$ ).<sup>9</sup> These techniques are nuclear reaction analysis (NRA) and resonant nuclear reaction analysis (RNRA) (Figs. 1c and d). Because of the large reaction cross sections for many of these interactions, sensitivities better than 1 ppm are common.

Of all the atomic events that occur during MeV ion-atom collisions, the generation of characteristic x rays is the most useful for nuclear microprobe analysis.<sup>10-12</sup> This technique is virtually identical to electron microprobe analysis (EMA), except that high-energy proton or alpha particles are used to cause the inner-shell ionization that results in an x ray produced by the atomic decay. This technique is called proton (helium) induced x-ray emission or PIXE (HIXE), depending on the incident ion (Fig. 1e). The primary advantage of PIXE over EMA is the elimination of primary electron bremsstrahlung, which results in a background for PIXE about three orders of magnitude lower than that found in EMA. The thick-target yield for x rays generated with protons or alpha particles is about an order of magnitude greater than that for electrons, so that the sensitivity of PIXE, which approaches 1 ppm for almost all elements with  $Z > 11$ , is from three to four orders of magnitude better than the 1000ppm sensitivity found for EMA. The only drawbacks of PIXE compared to EMA are (1) additional beam-induced target heating, (2) radiation damage (usually not a problem except for single crystals), and (3) the current unavailability of "turn-key" data collection/analysis systems.

Many lens types are in use in the various nuclear-microprobe laboratories around the world,<sup>11-17</sup> but the only new developments since 1981 have been the invention of the achromatic magnetic quadrupole doublet lens<sup>18</sup> and the introduction of the electrostatic "Russian" quadrupole quadruplet lens.<sup>19</sup> The ion lens used on the Sandia nuclear microprobe is a magnetic quadrupole doublet and is described in detail in Ref. 2. This system is attached to an EN tandem Van de Graaff accelerator with a maximum terminal voltage of 5 MV which allows the use of 10MeV H<sup>+</sup>, 15MeV He<sup>++</sup>, etc. The smallest-diameter beam obtained to date on this system is 2 µm; the current record is held by the Melbourne group, which has recently obtained a spot size of 0.3 µm.<sup>20</sup>

Several new materials analysis techniques have recently been utilized on nuclear microprobes: (1) channeling contrast microscopy,<sup>21</sup> which can be used to study near surface crystalline quality; (2) transmission ion energy-loss microscopy,<sup>22,23</sup> which is sensitive to sample electron density and may evolve into a micro-CAT scanner in the near future; (3) three-dimensional concentration profiling<sup>24</sup> of both light and heavy elements using all of the depth-sensitive ion-beam techniques; and (4) the use of external ion microbeams (i.e., outside of the vacuum system) for both RBS and PIXE (external ion-beam analysis, X-IBA) to study samples that are either too large or otherwise unsuitable for insertion into standard target chambers.<sup>25</sup>

## Applications

The results of nuclear-microprobe analysis presented in this section have been selected from data on TiC-coated graphite tiles used on the main movable limiter in TFTR.<sup>26,27</sup> The coatings on these tiles had an adhesion problem during plasma discharges; our goal was to isolate the cause of this coating spallation and find a remedy. Our task was to determine the TiC coating thickness across the plasma-facing portion of the limiter and to determine the identity and abundance of impurities that were either deposited by the tokamak plasma or already present in the bulk of these coatings. Complicating the situation was the requirement that much of this analysis had to be nondestructive so as to preserve the tiles for future use in TFTR. Figure 2 shows the Sandia nuclear microprobe in the process of performing external PIXE (X-PIXE) on the first movable limited used in TFTR. To facilitate handling, the limiter was left in its packing crate (about 6×2×1 ft and over 200 lb). The samples studied in this report were actually the individual tiles that made

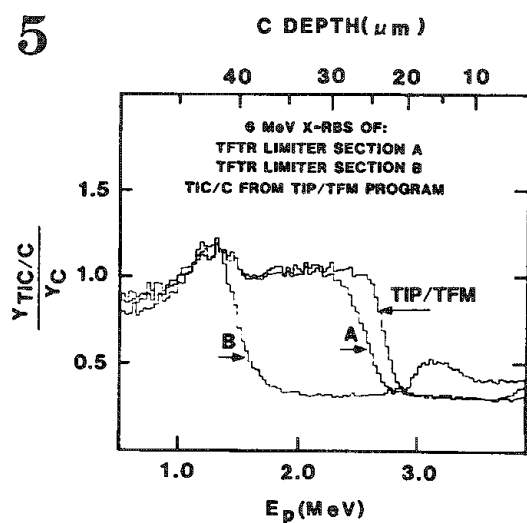
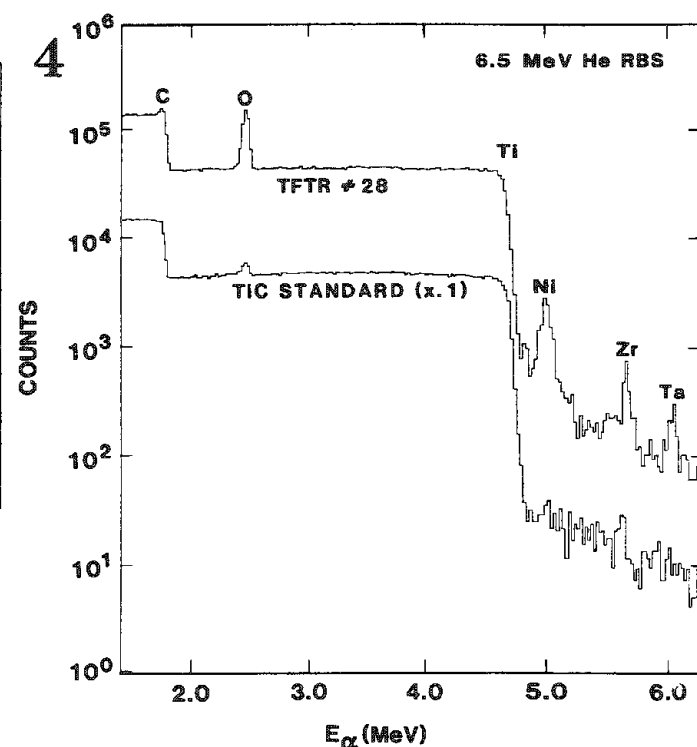
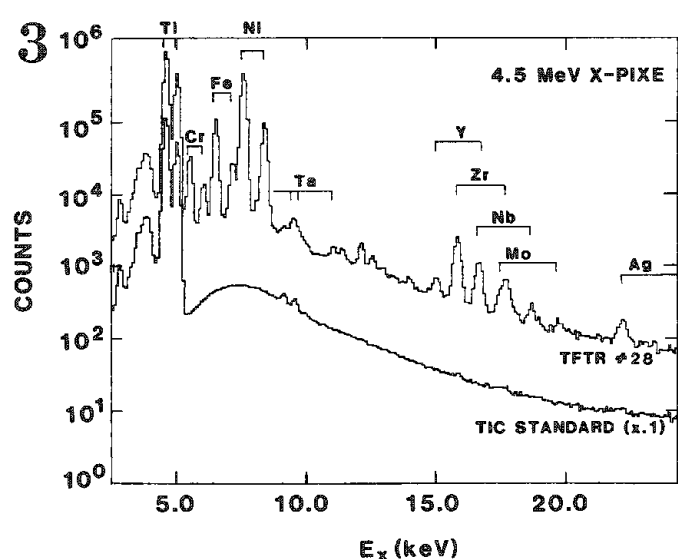
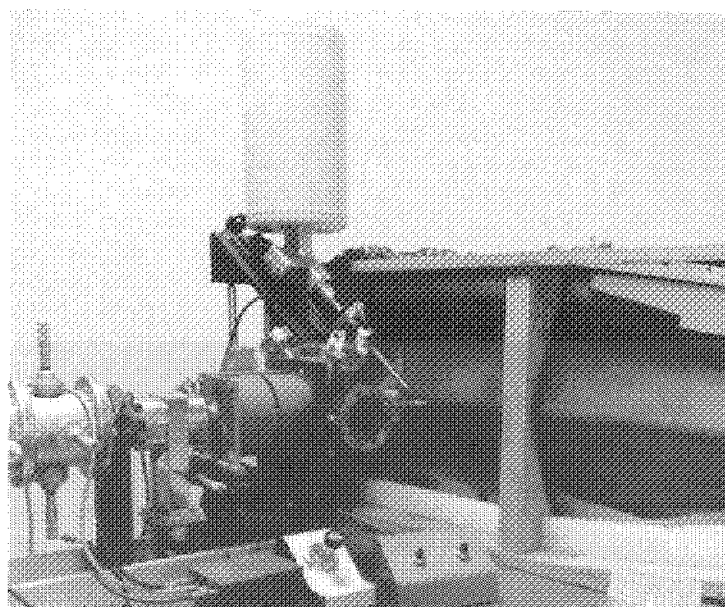
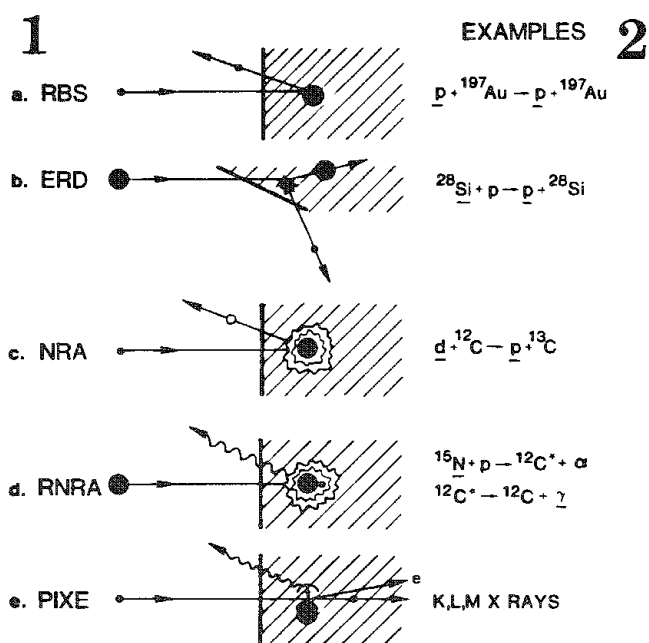


FIG. 1.--Various ion-beam analysis techniques, for examples listed (right). Underlining indicates incident and detected particles.

FIG. 2.--Sandia nuclear microprobe during X-PIXE examination of first movable limiter used in TFTR tokamak.

FIG. 3.--X-PIXE spectra for TiC-coated graphite tile used in TFTR (top) and control standard (bottom). Bands labeled with atomic symbols indicate  $K\alpha$  and  $K\beta$  x rays of respective elements, except for Ta, for which L x rays are indicated.

FIG. 4.--6.5 MeV RBS spectra for samples of Fig. 3.

FIG. 5.--X-RBS spectra of TiC-coated graphite tiles used in TFTR.

up the second movable limiter used in TFTR (which was the same size as this one), but Fig. 2 dramatically shows the importance of X-IBA as a nondestructive analysis technique for large specimens.

Two spectra taken with 4.5MeV X-PIXE are plotted in Fig. 3. The upper spectrum is for the TFTR TiC-coated graphite tile No. 28, taken in a region where the coating had remained intact. An Sn absorber was used in front of the Si(Li) detector to reduce the intensity of the Ti K x rays. The bottom spectrum is for a TiC coated tile not exposed to the plasma. RBS depth profiles were also measured for these tiles (both in and out of the vacuum); two in vacuo RBS spectra for the same regions examined in Fig. 3 are plotted in Fig. 4. Analysis of both sets of data (PIXE and RBS) shows that all the impurities identified in Figs. 3 and 4 reside in the very near surface region ( $< 1000 \text{ \AA}$ ) except Zr, which appears (in data not shown here) to diffuse into the TiC coating at concentrations less than 1000 ppm. These data also indicate that all the impurities, except for a surface oxide, resulted from tokamak plasma exposure and were not introduced during the manufacture of the tiles. The order-of-magnitude deposition levels measured on the exposed tile surfaces were O,Ni:  $10^{18}/\text{cm}^2$ ; Cr,Fe:  $10^{17}/\text{cm}^2$ ; Nb,Ta:  $10^{16}/\text{cm}^2$ ; Zr,Ag,Y:  $10^{15}/\text{cm}^2$ ; Mo:  $10^{14}/\text{cm}^2$ . From these data and similar results on several other TFTR tiles, it was concluded that impurities in the TiC coatings did not cause the detachment problem.

In Fig. 5 the results of 6MeV proton X-RBS analysis are shown where the ratio of the RBS spectrum for three TiC coated graphite samples to that for pure graphite is plotted as a function of both backscatter proton energy (bottom scale) and C depth (top scale). In regions of TiC, this ratio is approximately 0.3; in regions of pure C, it is close to 1. The ratios would be exactly 0.5 and 1, respectively, if the stopping power of protons in TiC and C were the same. The thickness of these various coatings can therefore simply be read off this figure at the point where the ratio takes on a value of approximately 0.75. Measurement A was taken on a tile that did not suffer any significant coating loss, and this coating (25  $\mu\text{m}$  thick) is very close to that measured for a control coating, TIP/TFM. B is for a region of TiC on a tile where over 90% of the coating had detached; this coating thickness (40  $\mu\text{m}$ ) is outside the limits specified to the manufacturer. It is well known that detachment is a problem often encountered for thick TiC coatings; the data strongly suggest that this effect played some part in the coating spallation problem which plagued the limiter tiles in TFTR.<sup>28</sup> Related studies of these tiles indicated that another (and perhaps the main) reason for the coating detachment was that the graphite substrates had not been properly prepared prior to the TiC coating step.<sup>29</sup>

An X-PIXE linescan is shown in Fig. 6 for a tile that suffered severe coating detachment. Although all the elements labeled in Fig. 3 were recorded, only the areal densities of Ti and Ni are plotted. The point of contact with the plasma, or apex, of the limiter is to the right in this figure, and the sharp increase in Ti at 11 cm indicates the only region on this limiter where the TiC coating remained following the use of this tile in TFTR. The corresponding decrease in Ni found at 11 cm is an experimental artifact caused by increased analyzer deadtime due to the high count rate of Ti x rays. Subsequent examination of similar regions where the TiC remained indicated that the amount of Ni impurities was usually greater in these areas--data of little relevance to the detachment process but nevertheless interesting because of the light they shed on impurity transport in tokamaks. Ni is the main impurity in TFTR because the vacuum vessel walls and much of the interior of this tokamak are constructed of Inconel. The most interesting aspect of the Ni linescan in Fig. 6 is that the least amount of Ni seems to be deposited near the apex of this limiter, which is the innermost point of contact between any in-vessel component and the magnetically confined plasma. At first it was thought that the plasma was eroding the Ni overlayer deposited in this region; however, similar deuterium linescans showed that the amount of deuterium ( $10^{17}/\text{cm}^2$ ) was also smaller in the apex region than in other areas on the same limiter but further removed from the plasma. The main conclusion reached from these data was that the Ni impurities were being transported through the tokamak as ions and were therefore confined to the magnetic-field lines which have a point of tangency with the apex of the limiter tiles. This point of tangency results in a low projected flux of plasma impurities such as Ni (or H isotopes, for that matter), near the region of the apex.

An obvious overlap between EMA and nuclear microprobe analysis is the capability of picturing the near-surface composition of materials in the form of elemental maps. Such an image is shown for a severely damaged TiC-coated tile in Fig. 7. Darker regions in



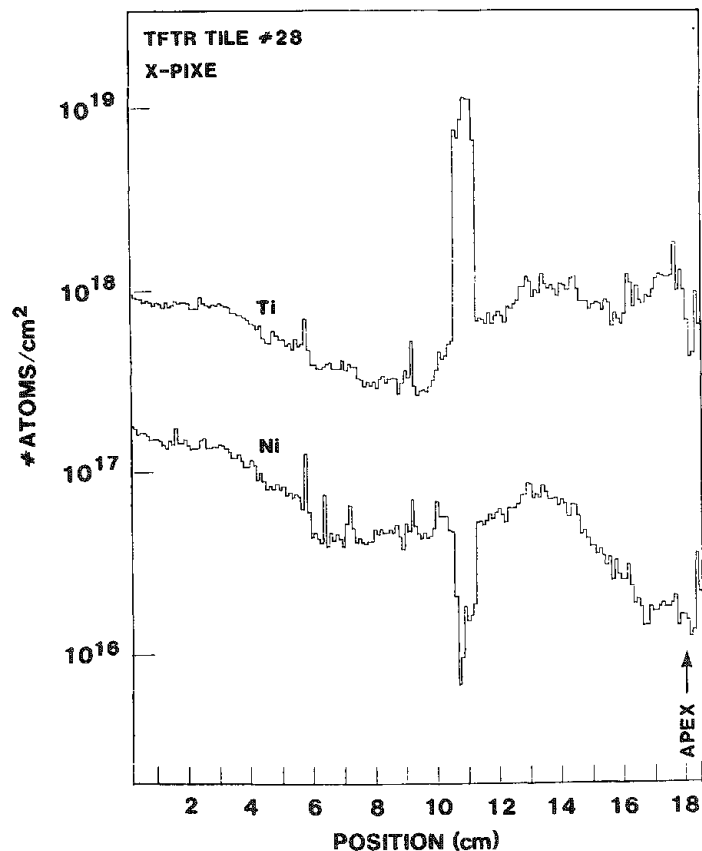


FIG. 6.--X-PIXE linescan measurement of Ti and Ni area densities for heavily damaged TiC-coated graphite limiter tile. Point labeled APEX indicates innermost point of contact between this component and magnetically confined tokamak plasma.

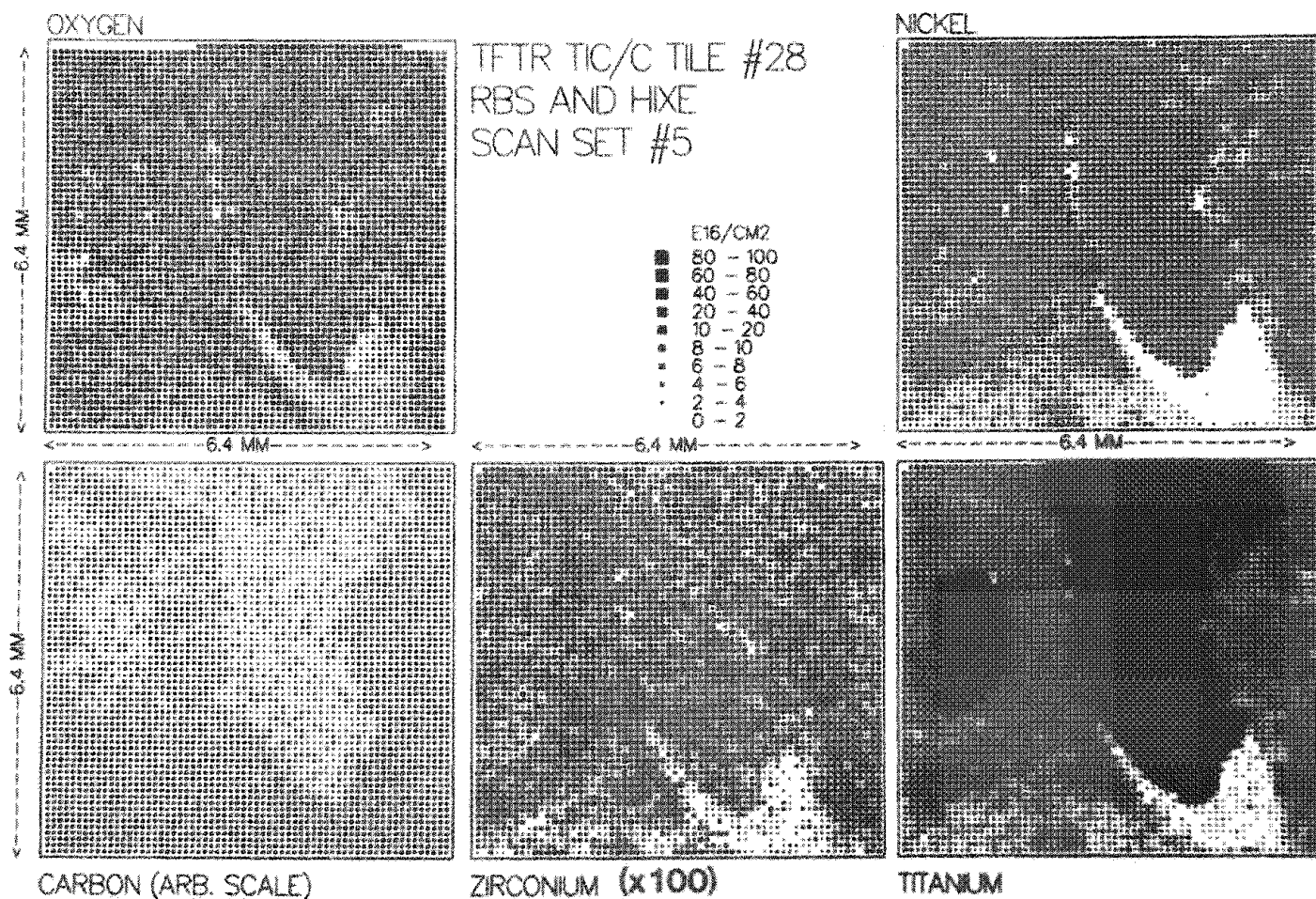


FIG. 7.--2D elemental maps of C, O, Ti, Ni, and Zr near damaged region of TiC-coated limiter tile.

both Figs. 7 and 8 indicate an increase in the abundance of the element under investigation. The C and O was measured by He RBS; the Ti, Ni, and Zr areal densities were determined by HIXE. A peninsula and island of TiC still coating the graphite can be seen in this figure. The Ni areal density is especially useful in determining the evolution of the coating loss. Areas with neither coating loss nor early spallation have a larger Ni overlayer than those which suffered coating detachment at a later time. That is because the Ni deposition (from Inconel erosion) is thought to be nearly continuous and so preserves the history of the coating erosion. The area of low Ni content at the bottom of the TiC peninsula indicates a region of recent coating removal.

A unique aspect of nuclear-microprobe analysis is that by a combination of depth-sensitive techniques such as RBS or ERD with lateral scanning, three-dimensional concentration profiles can be determined. Figure 8 displays such a 3D profile of Ti in the same region of the TiC coated graphite tile depicted in Fig. 7. These data clearly show that the coating in this region is uniform in thickness and that large sheets of the coating had indeed been removed, probably in single events; and that for most cases the coating had become detached at or near the Ti interface. In addition, the presence of a thin ( $<1\mu\text{m}$ ) surface layer of Ti provides a direct display of the erosion/redeposition process that is known to occur in the plasma edge of fusion reactors.

### Conclusions

Nuclear-microprobe analysis is a small but expanding field that is proving to be very useful for probing the near surface region of solids. Benefits of the nuclear microprobe include: (1) trace-element detection, (2) depth-sensitivity/selectivity, (3) light-element (even H) detection, (4) isotope selectivity, (5) ex vacuo analysis, (6) nondestructive analysis, and (7) the unique capability of measuring three-dimensional concentration profiles.

### References

1. J. A. Cookson and F. D. Pilling, AERE Report R6300, 1972.
2. B. L. Doyle et al., *Microbeam Analysis--1981*, 79-86.
3. J. A. Cookson, *Nucl. Instr. and Meth.* 197: 255, 1982.
4. W. Reuter, *Nucl. Instr. and Meth.* 218: 391, 1983.
5. J. W. Mayer and E. Rimini, Eds., *Ion Beam Handbook for Materials Analysis*, New York: Academic Press, 1977.
6. Ref. 5, 21-65.
7. B. Terreault et al., *J. Vac. Sci. Technol.* 14: 492, 1977.
8. B. L. Doyle and P. S. Peercy, *Appl. Phys. Lett.* 34: 881, 1979.
9. Ref. 1, 109-309.
10. Ref. 1, 311-484.
11. J. A. Cookson, *Nucl. Instr. and Meth.* 181: 115, 1984.
12. G. J. F. Legge, *Nucl. Instr. and Meth.* B3: 561, 1984.
13. R. Nobiling, *Nucl. Instr. and Meth.* 218: 197, 1983.
14. G. J. F. Legge, *Nucl. Instr. and Meth.* 197: 243, 1982.
15. J. A. Cookson, *Nucl. Instr. and Meth.* 165: 447, 1979.
16. C. J. Maggiore, *SEM/1980*, I, 439.
17. B. W. Martin, *SEM/1980* I, 419.
18. F. W. Martin and R. Goloskie, *Appl. Phys. Lett.* 40: 191, 1982.
19. S. H. Sie and C. G. Ryan, *Nucl. Instr. and Meth.* B15: 664, 1986.
20. G. J. F. Legge et al., *Nucl. Instr. and Meth.* B15: 669, 1986.
21. J. C. McCallum and C. D. McKensie, *IEEE Trans.* NS-30: 1228, 1983.
22. R. M. Scalock, et al., *Nucl. Instr. and Meth.* 218: 217, 1983.
23. J. C. Overley et al., *Nucl. Instr. and Meth.* B15: 654, 1986.
24. B. L. Doyle, *Nucl. Instr. and Meth.* B15: 654, 1986.
25. B. L. Doyle, *Nucl. Instr. and Meth.* 218: 29, 1983.
26. B. L. Doyle, *J. Vac. Sci. Technol.* A3: 1374, 1985.
27. J. F. Dylla et al., *J. Vac. Sci. Technol.* A3: 1105, 1985.
28. M. Ulrickson et al., *J. Nucl. Mater.* 133/134: 253, 1985.
29. A. W. Mullendore et al., to be published *Proc. 2nd Intern. Conf. Fusion Reactor Materials*, 1986, Chicago.

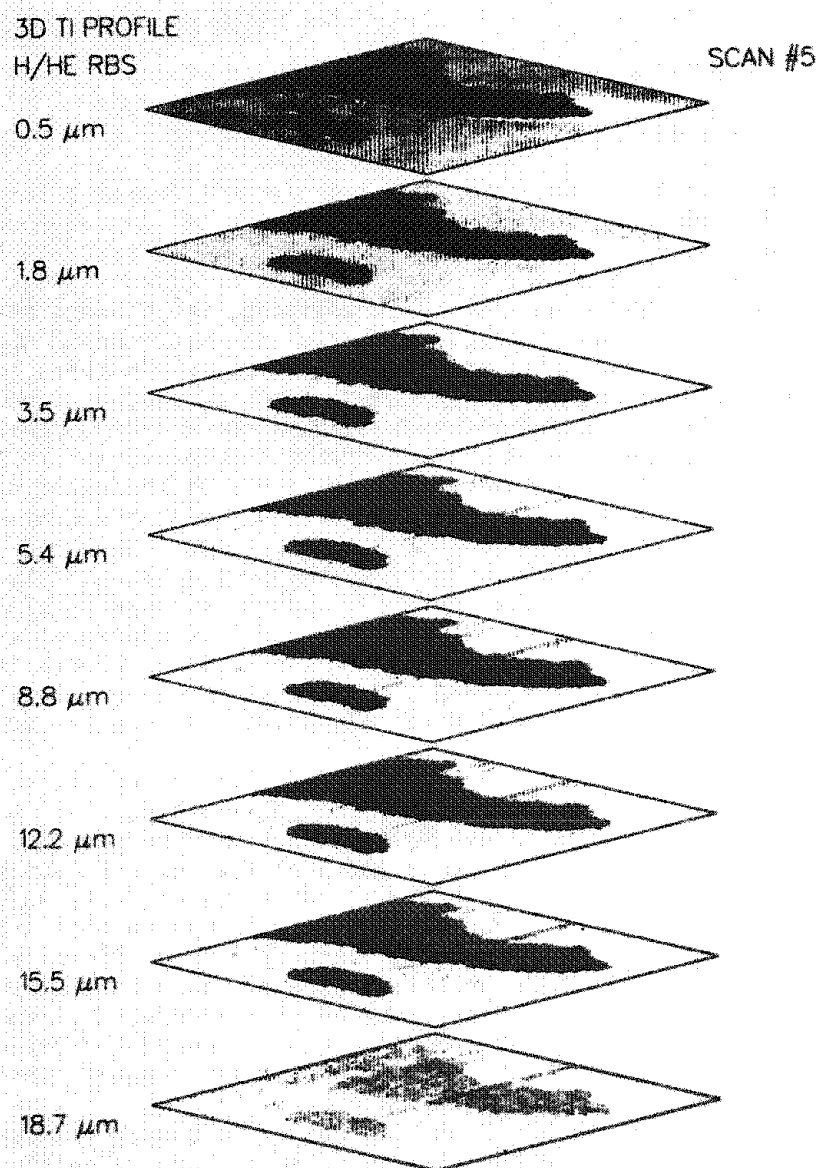


FIG. 8.--3D concentration profile of Ti in same region examined in Fig. 7.--Darker regions indicate increase in Ti abundance.

## Raman and IR Spectroscopy

### THIN FILMS, COLLOIDS, AND DIAMOND ANVILS: THE MICRORAMAN ADVANTAGE

L. A. Farrow and C. J. Sandroff

The micro-Raman technique, with its ability to concentrate the exciting laser radiation onto a sample spot of the order of  $1\text{ }\mu\text{m}$  with a power density of the order of kilowatts/cm<sup>2</sup>, has facilitated the investigation of a new class of disordered solids made by aggregating colloidal microcrystallites into a powder or a thin film. Excellent spectra on very small samples are obtained under ambient conditions. In addition, the diamond anvil cell technique is greatly expedited when used in conjunction with the micro-Raman apparatus to obtain further information on these materials at pressures up to 40 kbars.

Figure 1 shows the apparatus schematically. Excitation radiation at  $6471\text{ }\text{\AA}$  is provided by a Coherent Model 20 Kr<sup>+</sup> laser. Laser plasma lines are removed by dispersion through a pair of Pellin-Broca prisms followed by a spatial filter. Polarization in the plane of the sample is selected by a polarization rotator. The amplitude of the exciting radiation is stabilized to within  $\pm 5\%$  by a Quantum Electronics Model 307 noise reducing system, and is then directed into the microscope objective by means of a beamsplitter and thus concentrated onto the sample. Depending on the objective, the spot size can attain the diffraction limit of  $\sim 1\text{ }\mu\text{m}$ . Since the laser beam going into the microscope is of the order of 3 mm at the  $1/e^2$  points, the increase in power density can be six orders of magnitude. Back-scattered Raman signal is collected by the same objective, passed through the beamsplitter, directed into a Jobin-Yvon double monochromator, and detected by a specially selected red-enhanced photomultiplier. All scanning and data collection are computer controlled. Further details are given elsewhere.<sup>1</sup>

In general, Raman spectroscopy has proved to be effective in the study of the nature of disordered or amorphous materials.<sup>2-4</sup> Such noncrystalline substances are usually fabricated by melt-quenching or vapor deposition. In this work we have prepared colloidal suspensions of the layered semiconductor PbI<sub>2</sub> and evaporated the solvent gently to form a finely powdered precipitate composed of microcrystalline subunits with well-characterized dimensions.<sup>5</sup> Often the amount of powder gathered is only enough to fill a capillary holder 1 mm in diameter to a length of 2 or 3 mm, a volume of 2 or 3 mm<sup>3</sup>. The microscope is able to concentrate the full power of the beam on this very small sample volume, with the result that clear spectra are easily obtained. Sometimes the precipitate takes the form of a thin film  $\sim 1\text{ }\mu\text{m}$  thick deposited on a glass disk placed at the bottom of the vessel holding the colloidal suspension. Since the Raman signal is proportional to power density, once again clear spectra from such a film are easily obtained.

In Fig. 2, we compare the Raman spectra of bulk PbI<sub>2</sub> to a sample made by allowing colloidal microcrystallites of the layered material to aggregate into a solid. The PbI<sub>2</sub> layer structure consists of two hexagonally close-packed layers of iodine sandwiching a similar layer of lead.<sup>6-9</sup> Dominant in the bulk (Fig. 2a) are two strong bands, one at  $93\text{ cm}^{-1}$  corresponding to the totally symmetric vibrational stretch, and the other at  $71\text{ cm}^{-1}$  corresponding to the doubly degenerate shear mode; the lead sheet remains stationary for both bands.<sup>6-9</sup> Figure 2(b) shows the markedly different Raman spectrum for the aggregate. The shear mode at  $71\text{ cm}^{-1}$  has disappeared, and the bulk dominant mode at  $93\text{ cm}^{-1}$  has been virtually suppressed. Even more striking is the series of strong bands at lower shift frequencies, bands that do not appear at all in the bulk.

Some insight into the origin of these latter bands may be found by considering the Raman spectra arising from the bulk crystal phenomenon of polytypism.<sup>10</sup> Here the strongly bound "sandwich" of iodine-lead-iodine is weakly bound to other such structures to form crystals whose unit cells consist of stacks of two, three, or more layers. In such crystal polytypes, very weak Raman features appear at low frequencies, corresponding to inter-layer vibrations. For a single crystal whose unit cell consists of a single layer sandwich with no stacking (2-H polytype), these low frequencies are not Raman active and the

---

The authors are with Bell Communications Research, 600 Mountain Avenue, Murray Hill, NJ 07974.

TABLE 1.--Raman frequencies in  $\text{PbI}_2$  ( $\text{cm}^{-1}$ ).

2H	polytype		aggregate
	4H <sup>†</sup>	6H <sup>†</sup>	
---	14 m	12 m	16 s
---	29 w	29 m	28 s
---	47 w	46 m	45 s
---	---	50 m	50 s
---	---	65 m	66 m
---	72 m	71 s	---
70 s	74 m	73 w	---
93 s	96 s	94 s	93 vw
105 m	106 m	109 m	103 m

<sup>†</sup>Ref. 9.

vw: very weak; W: weak;  
m: moderate; s: strong.

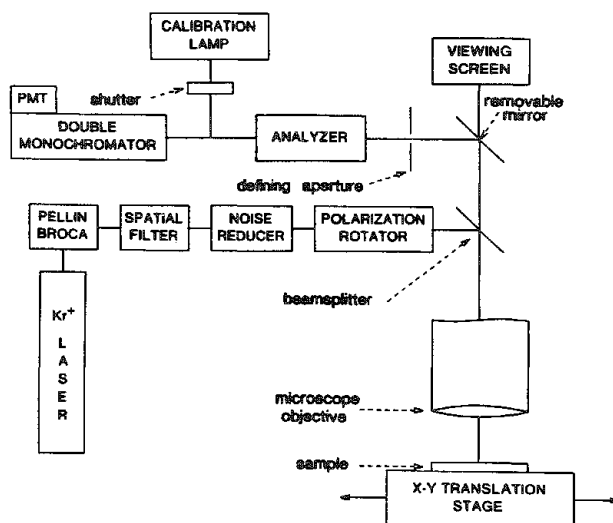


FIG. 1.--Experimental apparatus.

spectrum reveals only intralayer dynamics (Fig. 2a). That low-frequency modes appear in the aggregate (Fig. 2b) suggests a structure with many domains of small lateral extent<sup>5</sup> ( $\sim 29$  Å) and short stacks composed of an average of three  $\text{PbI}_2$  layer sandwich subunits. This structure also suggests that the two-dimensional symmetry of the bulk crystal is destroyed in these small domains as excess iodine binds to the large number of lead atoms located at the periphery of the microcrystallites. Hence the strong or total suppression of the bulk 2-D symmetry modes at 71 and 93  $\text{cm}^{-1}$  (Fig. 2a) in the aggregate spectrum (Fig. 2b). Table 1 compares the frequencies of the weak polytype bands determined for bulk spectra with the strong bands found for the aggregate, as well as the relative strengths of the intralayer 2-D symmetry modes.

A similar series of low frequency bands was noted in Raman spectra of the bulk crystal under pressure.<sup>11</sup> Initially the spectrum was unchanged from Fig. 2(a): near 5 kbar for 2H polytype and near 8 kbar for 4H polytype a phase change was observed, accompanied by the appearance of the low frequency bands. We have performed similar experiments on the aggregate material using a diamond anvil cell, two views of which are presented in Fig. 3. The top view shows the small viewing port, about 1 mm in diameter, in the depression at the center. If a microscope objective with a long-working length of about 5 mm is used in the apparatus of Fig. 1, the exciting laser beam can be readily directed into this port and the emerging Raman scattered light similarly collected. The side view of the diamond anvil cell is also presented in a photomicrograph in Fig. 3. The two diamonds, each about 1/3 karat, are clearly visible. The distance from the top of one diamond to the bottom of the other is 0.15 in. The sample is placed in a small chamber on the "anvil" formed between diamonds, along with a tiny ruby chip. As the three cap screws shown in the top view are tightened to increase the pressure, the characteristic Raman peak of the ruby shifts such that each  $1\text{cm}^{-1}$  displacement towards the red represents 1.33 kbar of additional pressure in the sample chamber.

Figure 4(a) shows the spectrum of the  $\text{PbI}_2$  aggregate in the diamond anvil cell at the minimum available cell pressure of  $<0.5$  kbar. It is immediately obvious that the layered symmetry modes of the bulk crystal at 72 and 93  $\text{cm}^{-1}$  have returned and are larger than the still present lower frequency modes. This result is in strong contrast to Fig. 2(b), where both symmetry modes are virtually suppressed; and in some contrast to Fig. 2(a), where the low-frequency modes are totally absent. The spectrum of Fig. 4(a) is maintained up to and including a pressure of 8 kbar. At 13 kbar, the phase change is observed, as shown in Fig. 4(b). Once again, the layer symmetry modes are strongly suppressed.

The virtual disappearance in Fig. 2(b) of the dominant bulk bands present in Fig. 2(a) implies that the structure of the aggregate is such that the 2-D layered symmetry of the single crystal has been lost, as discussed above. To our knowledge this is the first direct spectroscopic evidence for distortion in the intrinsic structure of microcrystalline domains due to edge effects, and it could be a general feature in a broad class of disordered materials. However, even at very low pressures ( $\sim 0.5$  kbar) in the diamond

anvil cell, 2-D symmetry is restored, as is evident when we note that the bulk crystal modes of Fig. 2(a) are also present in Fig. 4(a). Some of the low frequency modes of the aggregate of Fig. 2(b) are still present, although they are no longer dominant. This finding is consistent with the idea of loose microcrystalline packing of small domains in the aggregated solid of Fig. 2(b), which are then sufficiently compressed in the diamond cell that the bulk modes reappear (Fig. 4a). As pressure is increased further, the spectrum remains essentially unchanged until 13 kbar (Fig. 4b), when a structural phase transition occurs; once again the 2-D symmetry is destroyed, the bulk modes disappear, and the low-frequency bands become dominant.

This study of Raman spectra of colloid aggregates, and the observation of changes in the spectra induced by pressure in a diamond anvil cell, has been greatly facilitated by the use of the micro-Raman apparatus, which concentrates the laser beam into a very small spot with accompanying high power density. Other applications in thin films and heterostructures, as well as extension of the work reported here, are now in progress.

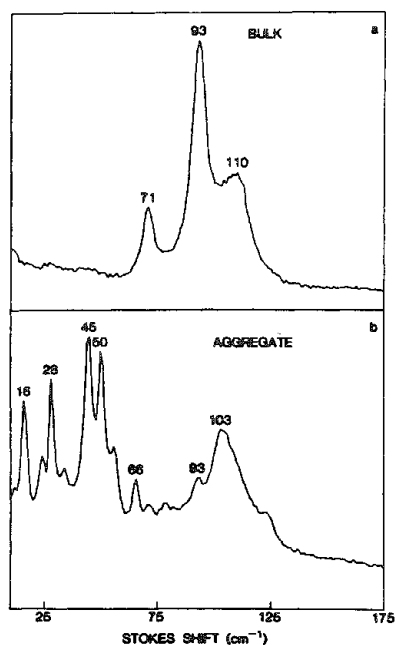


FIG. 2.--Raman spectra of  $\text{PbI}_2$  (Stokes shift in  $\text{cm}^{-1}$  vs intensity in arbitrary units). (a) Single crystal 2H polytype. (b) Material aggregated from colloidal suspension. Many intense low-frequency modes are present that do not appear in the bulk. High-frequency modes at 71 and  $93 \text{ cm}^{-1}$  are virtually absent in aggregate.

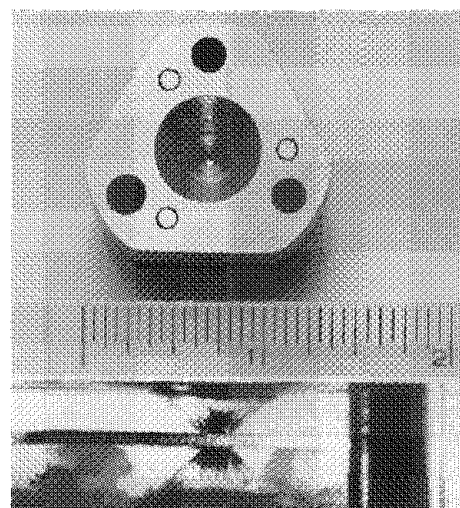


FIG. 3.--Diamond anvil cell in top and side views. Ruler refers to top view; side view is photomicrograph such that distance from top of one diamond to bottom of other is 0.15 in.

## References

1. J. B. Hopkins and L. A. Farrow, *J. Appl. Phys.* 59: 1103, 1986.
2. P. M. Bridenbaugh, G. P. Espinosa, J. E. Griffiths, J. C. Phillips, and J. P. Remeika, *Phys. Rev. B* 20: 4140, 1979.
3. J. E. Griffiths, G. P. Espinosa, J. P. Remeika, and J. C. Phillips, *Phys. Rev. B* 25: 1272, 1982.
4. J. E. Griffiths, M. Malyj, G. P. Espinosa, and J. P. Remeika, *Phys. Rev. B* 30, 6978, 1984.
5. C. J. Sandroff, D. M. Hwang, and W. M. Chung, *Phys. Rev. B* 33: 5953, 1986.
6. R. Zallen and M. L. Slade, *Solid State Comm.* 17: 1561, 1975.
7. A. Grisel and Ph. Schmidt, *Phys. Stat. Sol.* B73: 587, 1976.
8. W. M. Sears, M. L. Klein, and J. A. Morrison, *Phys. Rev. B* 19: 2305, 1979.
9. M. Y. Khilji, W. F. Sherman, and G. R. Wilkinson, *J. Raman Spec.* 13: 127, 1982.
10. J. I. Hanoka and V. Vand, *J. Appl. Phys.* 39: 5288, 1968.
11. A. Jayaraman, R. G. Maines, and T. Chattopadhyay, *Phys. Rev. B* (submitted).

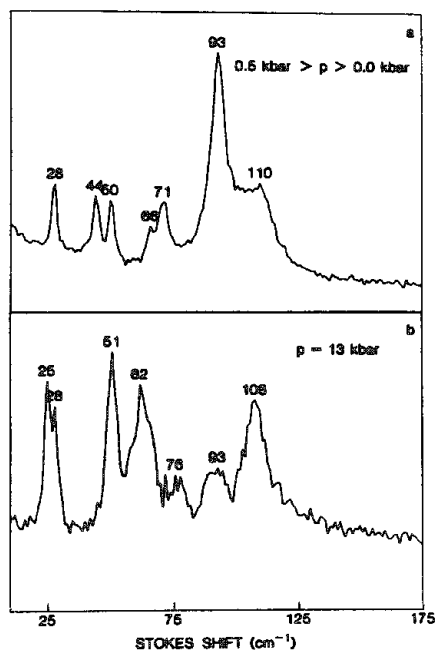


FIG. 4.--Raman spectra of  $\text{PbI}_2$  aggregate under pressure in diamond anvil cell. (a)  $< 0.5 \text{ kbar}$ . (b)  $13 \text{ kbar}$ .

## THE CHARACTERIZATION OF GRAPHITIC AND NONGRAPHITIC CARBON BY LASER RAMAN MICROPROBE ANALYSIS

W. L. Johnson III

Carbon has seven allotropes and is known to exist in a wide range of disordered forms. The use of Raman spectroscopy to characterize the structure of graphitic and nongraphitic carbon is the subject of this paper. Hexagonal graphite consists of hexagonally tessellated or checkered layers of  $sp^2$  hybridized carbon atoms in an AB-AB layer sequence held together by Van der Waals bonding. The less stable rhombohedral graphite is similar, but has an ABC-ABC layer sequence.<sup>1</sup>

Graphitic and nongraphitic carbon can be synthesized from organic raw materials by a thermal degradation process characterized by aromatic  $C_6$  ring formation accompanied by cross linking and the loss of volatiles. Graphitizability is a function of initial molecular structure and its thermal degradation mechanism. During the graphitization process, the crystallite size  $L_a$ , the stack height  $L_c$ , and the number of layers in a stack  $N$  increase and the interlayer distance  $d$  decreases to a limiting value of  $3.35 \text{ \AA}$ .<sup>2</sup>

The Raman spectrum of hexagonal graphite consists of a single peak at  $1580 \text{ cm}^{-1}$ , and weak lines at  $2450 \text{ cm}^{-1}$  and  $3250 \text{ cm}^{-1}$ , respectively. When disorder is introduced into the graphite structure, nongraphitic carbon is produced, the  $2720 \text{ cm}^{-1}$  and  $1580 \text{ cm}^{-1}$  bands broaden, and additional bands at about  $1360 \text{ cm}^{-1}$ ,  $1620 \text{ cm}^{-1}$ , and  $2850 \text{ cm}^{-1}$  appear.<sup>3</sup> Recently, the Raman spectrum of disordered, graphitizable carbon has been found to have an additional peak at  $1500 \text{ cm}^{-1}$  attributed to interstitial disorder. For graphitizable carbons, the  $1500 \text{ cm}^{-1}$  band was found to persist up to  $1670 \text{ C}$  and to higher temperatures for nongraphitizable carbons.<sup>4</sup>

### Experimental

All of the Raman spectral measurements were performed on an Instruments SA Ramanor U-1000 molecular optics laser examiner (MOLE) equipped with a Prism modular controller and data-management system. The power level of the laser ( $514.532 \text{ nm}$ ) was kept to  $80 \text{ mW}$  or less to prevent sample destruction. Spectra were measured at a  $300 \mu\text{m}$  slit width with dwell times of 2 or 4 s per point and at a resolution of 1 or  $2 \text{ cm}^{-1}$ . All spectra reported here were run with a light scrambler to produce an averaged spectrum. All spectra were measured over the  $1700\text{--}1200 \text{ cm}^{-1}$  regime.

The following materials were obtained for analysis: WCA cloth from Union Carbide; CCA-3 cloth, CCA-4 cloth, GCA-4 cloth, F064 resin, USP 33 filter, and USP 27 filter from U.S. Polymeric; and pyrolytic carbon from HITCO.

### Discussion

Carbon fibers made from pitch, polyacrylonitrile (PAN), and rayon become more ordered as they are heat treated. This "graphitization" process produces crystallites of increasing size as the heat treatment temperature is raised. Figure 1 shows the effect of increasing  $L_a$  on the first-order Raman spectrum. As  $L_a$  increases, the band at  $1580 \text{ cm}^{-1}$  gradually dominates the bands at  $1620$  and  $1360 \text{ cm}^{-1}$ .<sup>5</sup> When the  $I_{1350}/I_{1580}$  ratio is determined for each of the spectra shown in Fig. 1, a plot of  $L_a$  vs the  $I_{1350}/I_{1580}$  ratio can be made that enables estimates of  $L_a$  to be made (Fig. 2). Table 1 shows the results of Raman measurements for a number of carbon materials along with estimated crystallite sizes. Considering that highly oriented pyrolytic graphite (HOPG) has crystallite sizes of the order of  $10\,000 \text{ \AA}$ , it is readily apparent that even "graphitized" PAN is not very graphitic. Because graphite is anisotropic, crystal orientation effects are expected,

---

The author is at Morton Thiokol, Inc., Box 241, Elkton, MD 29192. He wishes to express his thanks to Dr. F. Adar of Instruments SA, Metuchen, N.J. and to M. Andersen of W. C. McCrone Associates, Inc., Chicago, for their effort on this project as well as for valuable discussions concerning the use of this technique.



but their magnitude is difficult to predict. Although orientation effects are important with pitch fibers and HOPG, no effect was observed for the carbon materials reported here. This effect is most likely related to the small crystallite size of these materials.

TABLE 1.--Laser Raman microprobe analysis of carbon.

Material	$I_{1350}/I_{1580}$	Estimated $L_a$ (Å)
USP 27 carbon filler	0.88±0.13	46
USP 37 carbon filler	0.83±0.08	45
Pyrolytic carbon	0.87±0.18	46
WCA cloth	0.52±0.16	76
(carbonized rayon, as received)		
WCA cloth (1500 C)	0.53±0.01	76
(carbonized rayon)		
WCA cloth (2200 C)	0.66±0.13	60
(graphitized rayon)		
WCA cloth (prepreg fiber)	0.69±0.16	58
(carbonized rayon)		
CCA-3 cloth	0.63±0.12	65
(carbonized rayon)		
CCA-4 cloth	0.63	65
(carbonized PAN)		
GCA-4 cloth	0.11±0.10	260
(graphitized PAN)		
F064 (carbonized carbon filled phenolic resin)	1.56	30

Because of the small crystallite size of these materials, their spectra consist of broad bands centered at 1580  $\text{cm}^{-1}$  and 1350  $\text{cm}^{-1}$ . For the more ordered materials such as WCA cloth, a shoulder at 1620  $\text{cm}^{-1}$  was found (Fig. 3). The 1500  $\text{cm}^{-1}$  band is apparently present in some spectra, but not all. Figures 4 and 5 show the spectra of USP 27 and USP 33 carbon fillers. It can be seen that the surface structure of these two carbon blacks is very similar. Note that the 1500  $\text{cm}^{-1}$  band appears to be absent even though these carbon blacks are highly disordered. When the spectrum of pyrolytic carbon (Fig. 6) is compared to the carbon filler spectra, it appears that the two materials have similar spectra except that the spectrum of pyrolytic carbon also has a peak at 1500  $\text{cm}^{-1}$ . This result suggests that the pyrolytic carbon surface has small crystallites and interstitial disorder, whereas the carbon blacks have just small crystallites on their surfaces.

### Conclusions

The Raman spectrum of disordered graphite contains considerable structural information and is a useful method for demonstrating the surface differences of various types of carbon. As the crystallite size decreases, the orientation effect in the Raman spectrum becomes insignificant.

### References

1. Jerry Donahue, *The Structure of the Elements*, New York: Wiley, 1974, 257, 259.
2. L. C. Blackman, *Modern Aspects of Graphite Technology*, New York: Academic Press, 1970, 2-18.
3. R. P. Vidano and D. B. Fishbach, *Ext. Abs.*, 15th Carbon Conference, 1981, 468.
4. J. N. Rouzard, A. Oberlin, and C. Beny-Bassez, *Thin Solid Films* 105: 75, 1983.
5. P. Lespade, R. Al-Jishi, and M. S. Dresselhaus, *Carbon* 20: 427, 1982.
6. P. L. Walker Jr. and P. A. Thrower, Eds., *Chemistry and Physics of Carbon*, New York: Marcel Dekker, 1981, vol. 17, 235.

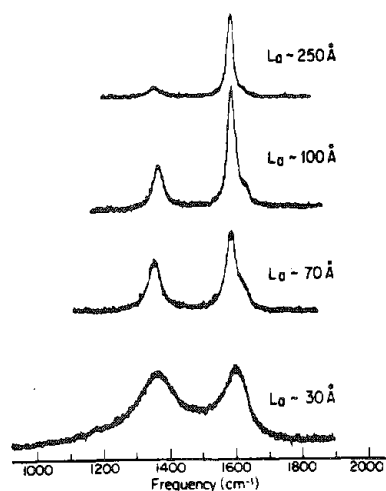


FIG. 1.--Experimental first-order Raman spectra of carbon materials.

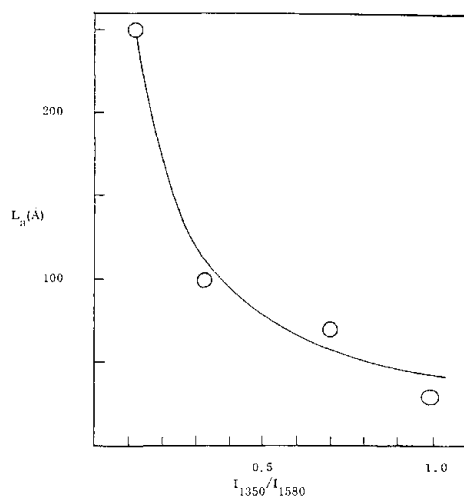


FIG. 2.--Plot of  $L_0$  vs  $I_{1350}/I_{1580}$ .

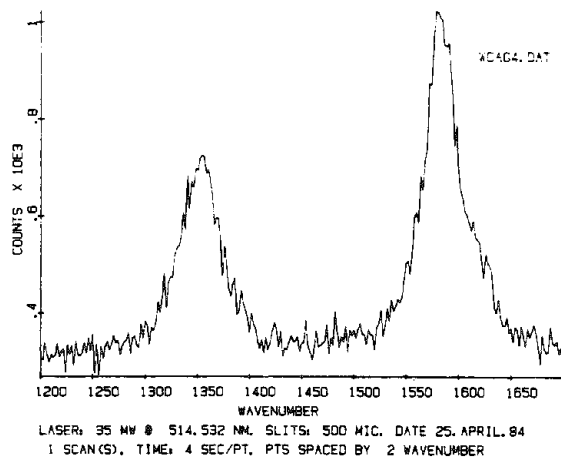


FIG. 3.--Raman spectrum of WCA cloth.

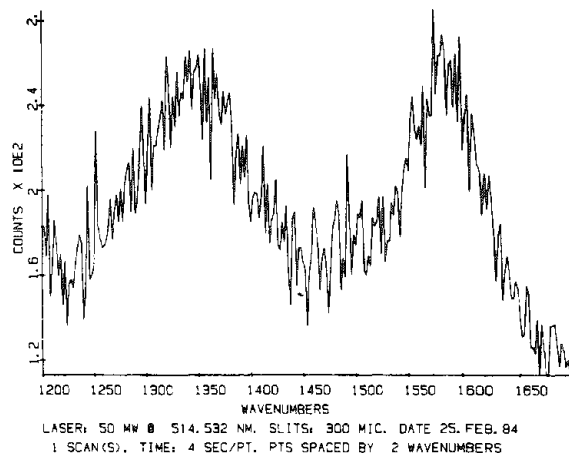


FIG. 4.--Raman spectrum of USP

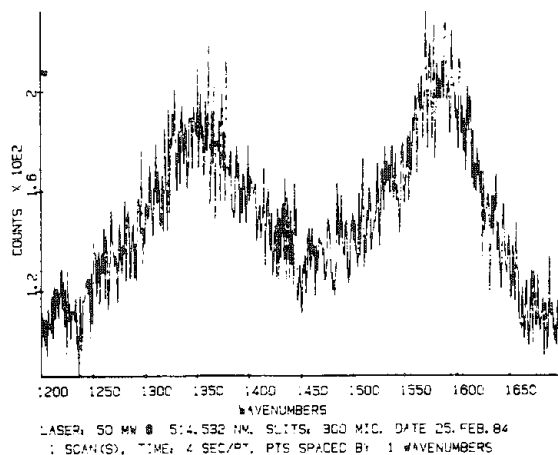


FIG. 5.--Raman spectrum of USP 33 filler

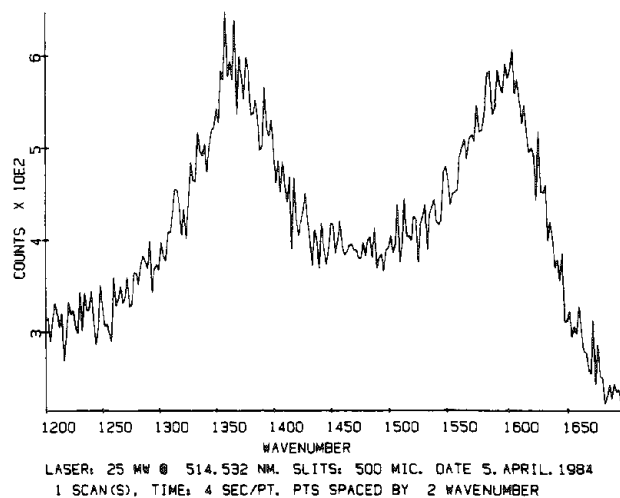


FIG. 6.--Raman spectrum of pyrolytic carbon.

## ANALYSIS OF INCLUSION PRECIPITATES IN $\text{Al}_2\text{O}_3\text{:Ti}^{+3}$

R. C. Powell, J. L. Caslavski, Zuhair AlShieb, and J. M. Bowen

In this study we describe the characterization of the crystal defects found in a large crystal of artificial sapphire ( $\text{Al}_2\text{O}_3\text{:Ti}^{+3}$ ) prepared by the Czochralski method as modified by Caslavski.<sup>1</sup> This crystal type is of interest owing to its application as a material for tunable lasers, for which the crystal must be of high optical quality and high purity, and must have high  $\text{Ti}^{+3}$  concentrations distributed uniformly throughout the crystal. The crystal was found to have a distribution of chemical and structural defects, which were analyzed by Raman microprobe spectroscopy and electron microscopy.

### *Experimental*

The Raman Microprobe was a Ramanor U-1000 with computer-controlled data acquisition manufactured by Instruments SA equipped with a Spectra Physics Argon ion laser. The scanning electron microscope was a JEOL 355 with a Tracor Northern 2000 EDAX attachment for quantitative elemental analysis. The microprobe allowed the analysis of specific areas of the sample as small as 5  $\mu\text{m}$  in diameter, which was the resolution of the focus of the laser beam through the microscope. The sample consisted of a crystal block that had been polished to on one side to expose some of the inclusions to the air. EDAX and Raman spectra were taken of four kinds of regions: the inclusions, precipitates in the inclusions, surface discolorations, and uncontaminated regions of the sample.

### *Results and Interpretation*

The uncontaminated surface of the crystal was found to have no chemical impurities by the SEM/EDAX analysis, and the micro-Raman spectrum of these regions is the same as that of undoped  $\text{Al}_2\text{O}_3$  (Fig. 1). These spectra also revealed a strong background fluorescence in the spectral region consistent with  $\text{Ti}^{+3}$  emission at around 580 nm.<sup>2</sup> The inclusions appeared as voids a few microns in diameter. The SEM/EDAX analysis of the interior of the inclusions did not indicate the presence of any impurities; however, analysis with the Raman microprobe revealed areas of differing color at the inclusion bottom which produced varying Raman spectra. The background fluorescence of the  $\text{Ti}^{+3}$  varied remarkably in the inclusion but was generally less intense than that found at the crystal surface. When the microprobe was focused onto some of the precipitate at the bottom of the inclusion, the spectrum seen in Fig. 2 was observed; it is shown in comparison with the Raman spectrum of  $\text{TiO}_2$  in the rutile configuration. The band positions of the two spectra are well enough correlated to identify that the inclusion precipitate contains  $\text{TiO}_2$ . The difference in the relative band intensities of the two spectra are due to the fact that the  $\text{TiO}_2$  precipitate spectra are of small unoriented crystals, unlike the spectrum of the oriented crystal of pure  $\text{TiO}_2$ .

### *Conclusions*

From the results of the above analysis, it appears that as the  $\text{Al}_2\text{O}_3\text{:Ti}^{+3}$  crystal cools the doped titanium can precipitate out in the form of rutile, which could explain some optical features found in UV and fluorescence spectra.<sup>1</sup> However, Raman analysis was found to be valuable in the analysis and finally in the changes of the crystals-growing procedure.

### *References*

1. R. C. Powell, J. L. Caslavski, Zuhair AlShieb, and J. M. Bowen, *J. Appl. Phys.* 58: 2331, 1985.
2. E. D. Nelson, J. Y. Wong, and A. L. Schawlow, in H. M. Crosswhite and H. W. Moses, Eds., *Optical Properties of Ions in Crystals*, New York: Wiley-Interscience, 1967.

---

The authors are at the Oklahoma State University School of Geology, Stillwater, OK 74078.

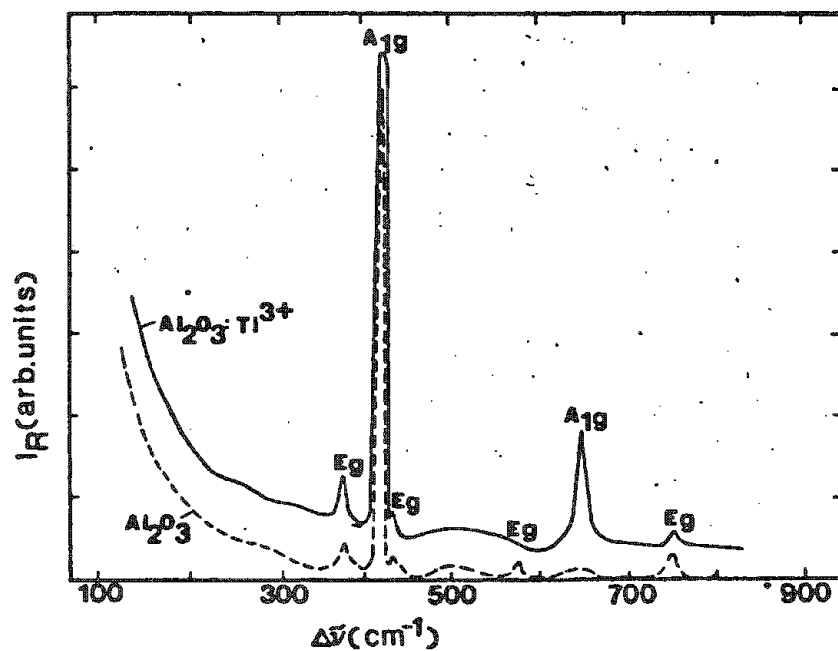


FIG. 1.--Micro-Raman spectra of uncontaminated region of crystal and of undoped  $\text{Al}_2\text{O}_3$ .

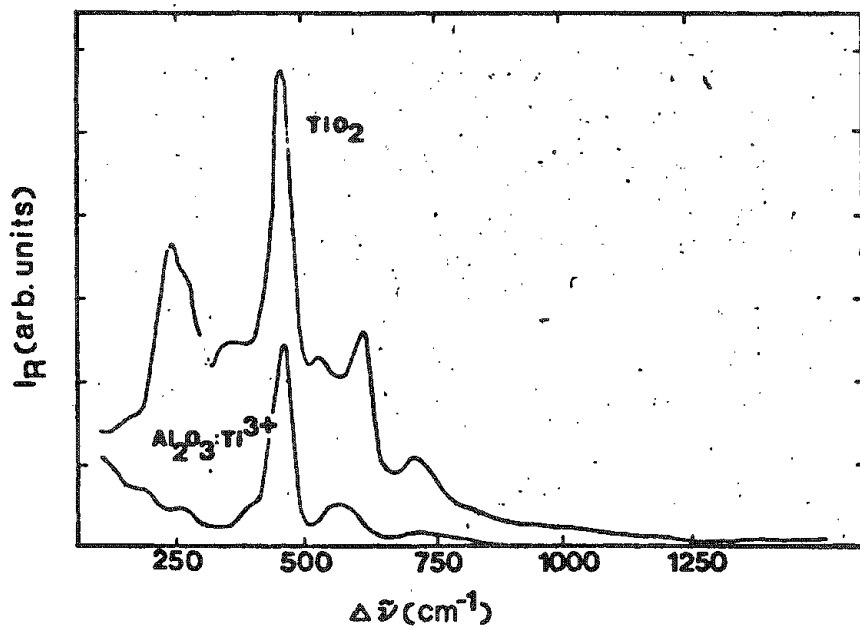


FIG. 2.--Micro-Raman spectra of  $\text{TiO}_2$  rutile and of interior of inclusion.

## MICRO-RAMAN SPECTROSCOPY OF FLUID INCLUSIONS IN A HOPPER CRYSTAL IN HALITE

K. L. Higgins and C. L. Stein

Raman microscopy has been used successfully to analyze for dissolved sulfate in fluid inclusions in naturally occurring halite.<sup>1,2</sup> Hopper crystals are crystals of halite (NaCl) whose structure is produced by crystal growth at the surface of a brine reservoir. Crystal growth supported by surface tension occurs in a series of steps that result in a pyramidal or hopper shape. Brine is trapped by defects in the growing crystal faces as microscopic fluid inclusions. The abundance of these inclusions produces the milky-white parallel bands that characterize the appearance of hopper crystals (Fig. 1).<sup>3,4</sup> The transparency of the salt and its lack of Raman activity make it an ideal medium to study inclusions by Raman microscopy. The small size of these inclusions ( $\sim 1$ -10  $\mu\text{m}$  on an edge) precludes the use of most other analytical techniques. In this study we characterized the hopper crystal by obtaining a profile of the sulfate ( $\text{SO}_4^{2-}$ ) concentrations in brine inclusions in the bands formed in the hopper crystal structure. In addition, the same sample contained large areas of clear recrystallized halite in which fluid inclusions are not as abundant as those in hopper crystals but are several orders of magnitude larger (frequently several millimeters on an edge). These larger inclusions were also analyzed for their sulfate content.

The sample for this study came from a thick halite unit in the Salado Formation (Permian age) in the Delaware Basin, southeastern New Mexico. The Waste Isolation Pilot Plant (WIPP) is located at a depth of approximately 2150 ft from the surface. The WIPP is a proposed nuclear waste facility intended to demonstrate the feasibility of nuclear waste storage in bedded salt deposits. This study of fluid inclusions was undertaken to better characterize the fluid compositions within the WIPP facility host rock. Of primary concern to the WIPP project is the presence of fluid in the repository host rock, particularly because of the possibility of fluid movement and hence corrosion of waste canisters and/or backfill material. In addition, there are few data on fluid inclusions in halite hopper crystals; this study contributes to their understanding.

### *Analytical Methods*

The micro-Raman apparatus employed a modified Zeiss microscope, double monochromator, and photon-counting detection.<sup>2</sup> The 514.5nm Argon ion laser line was used for excitation. The microscope objective had a magnification of 40 $\times$ , a numerical aperture of 0.60, and a working distance of 2 mm.

The samples were analyzed by measuring the ratio of the integrated Raman intensity of the  $\nu_1$  sulfate band (980  $\text{cm}^{-1}$ ) to that of the water band at 3400-3500  $\text{cm}^{-1}$  as was done in our earlier work.<sup>2</sup> Eleven standard solutions were made by addition of anhydrous  $\text{Na}_2\text{SO}_4$  to NaCl-saturated brine. They were each placed in a small beaker, illuminated by the laser through a sapphire cover, and analyzed. Sulfate concentrations of the standard solutions were independently analyzed by ion chromatography and ranged from 0 to 19.8 parts per thousand (ppt). The data from the standards were fit by linear regression (Fig. 2), where sulfate concentration = (568)  $\cdot$  (normalized sulfate intensity) - .596, with a correlation coefficient of 0.97. A factor of 8.3 is required to convert g/100 ml to ppt in saturated brine. Repetitive analysis of a single inclusion containing an average of 6.56 ppt sulfate yielded an estimated standard deviation of  $\pm 14\%$  relative.

---

The authors Higgins and Stein are at Sandia National Laboratories (Div. 1823), Albuquerque, NM 87185. This work was performed at Sandia National Laboratories supported by the U.S. Department of Energy under Contract DE-AC04-76-DP00789. The authors gratefully acknowledge the aid of R. Merrill for his ion chromatography analyses and of D. R. Tallant for his technical advice. The manuscript was greatly improved by the careful reviews given by K. J. Ward and C. Nelson.

## Results

Fluid inclusions were analyzed along a cross section of the hopper crystal in clear, colorless halite. Sulfate values ranged from ~13.5 ppt in the outermost (most recently formed) band, decreasing rapidly and then remaining more or less constant at ~2-3 ppt near the interior (initially formed part) of the hopper crystal (Fig. 3). The bands examined spanned a distance of ~2400  $\mu\text{m}$ . Significant variation in sulfate concentration exists within a given band; for example, the sulfate values in inclusions in the band at 517  $\mu\text{m}$  range from 3.1 to 6.3 ppt. This range is greater than the standard deviation of measurement but much smaller than the variation in values from the outside to the inside of the hopper structure.

The large inclusions in the recrystallized halite which occur in close proximity to the hopper crystal were also analyzed. The sulfate concentrations of these inclusions were between ~5 and 10 ppt.

## Discussion

These results are consistent with the generally accepted geological interpretation of hopper crystal formation, i.e., by rapid evaporation in a concentrated brine in a very shallow basin. In a typical evaporite sequence, the general order in which minerals participate is carbonates  $\rightarrow$  sulfates  $\rightarrow$  halite  $\rightarrow$  complex salts.<sup>5</sup> The concentration of sulfate in the evaporating brine at the point at which halite precipitation begins is ~22 ppt, in contrast to a normal seawater sulfate value of ~2.9 ppt.<sup>5</sup> The interior portion of the hopper crystal used in this study was obviously growing in contact with a solution that was at saturation with respect to NaCl, but fluid inclusions from the interior of this hopper crystal have normal seawater sulfate values.

This type of crystal most likely grew in a brine pan in which abundant NaCl had already precipitated. Fresh seawater entering this pan would rapidly saturate with NaCl, which would then precipitate before any reactions involving the precipitation of sulfate minerals occurred. Primary fluid inclusions (e.g., those in the hopper crystals) consequently would have sulfate concentrations close to that of seawater; with increasing hopper crystal growth in a shallow basin, the brine would become more concentrated in its remaining dissolved components. (Primary fluid inclusions are intracrystalline fluid compositions that have not been modified by contact with other fluids after formation of the host mineral.<sup>6</sup>) This hypothesis is supported by the higher sulfate content of fluid inclusions in the outer bands of the hopper crystal used in this study.

After halite deposition, as the salt recrystallized, fluid inclusions from hopper crystals probably coalesced to form larger inclusions.<sup>6,7</sup> The sulfate concentrations (approximately 5-10 ppt) reported here are from larger inclusions that were in close proximity to the hopper crystal and suggest a homogenization of the fluids from the hopper crystal inclusions.

## Conclusions

Several statements regarding fluid inclusion in halite hopper crystals may be made from this study. First, sulfate concentrations in the hopper crystal fluid inclusions examined here suggest that hopper crystals are in fact primary growth features. The distribution of sulfate values shown in Fig. 3 makes it difficult to explain the origin of these inclusion fluids as the result of water diffusing along crystal planes after crystal growth.

Second, these hopper crystals must have grown in very shallow water, with periodic influxes of fresh seawater. This depositional environment would explain the continuous precipitation of halite from a solution that is saturated with NaCl but with normal seawater sulfate concentrations.

The third point addresses the comparison between the large fluid inclusions immediately adjacent. Sulfate concentrations of the large inclusions fall between the extremes of the sulfate analyses of the hopper crystal inclusions. This observation supports the origin of large fluid inclusions in recrystallized halite from the coalescence of hopper crystal fluid inclusions. A detailed explanation of the role of water in the mechanics of NaCl recrystallization is beyond the scope of this paper. However, our results suggest that it is unnecessary to invoke a mechanism for recrystallizing halite that involves dissolution and precipitation resulting from the addition of fresh water.

Overall, the micro-Raman technique yields in situ and nondestructive measurements of the concentration of dissolved species in the fluid entrapped in inclusions in optically transparent crystals. The results can be used to interpret mineral growth phenomena. These data were previously very difficult to attain because of the extremely small size of the inclusions in hopper crystals.

#### References

1. J. Dubessy et al., "The determination of sulfate in fluid inclusions using the M.O.L.E. Raman microprobe: Application to a Keuper halite and geochemical consequences," *Geochim. Cosmochim. Acta.* 47: 1-10, 1983.
2. D. R. Tallant, C. L. Stein, and K. L. Higgins, "Raman microscopy through transparent materials," *Microbeam Analysis--1983*, 297-300.
3. L. F. Dellwig, "Origin of the Salina Salt of Michigan, *Jour. Sed. Pet.* 25: 83-110.
4. W. T. Holser, "Mineralogy of evaporites," in R. G. Burns, Ed., *Marine Minerals* (Mineralogical Society of America Short Course Notes) 6: 211-294, 1979.
5. K. B. Krauskopf, "Evaporites," in *Introduction to Geochemistry*, New York: McGraw-Hill, 318-353.
6. E. Roedder, *Fluid Inclusions* (Mineralogical Society of America Reviews in Mineralogy, vol. 12), 1984.
- E. Roedder and H. E. Belkin, "Applications of studies of fluid inclusion in Permian Salado salt, New Mexico, to problems of siting the waste isolation pilot plant," in G. J. McCarthy, Ed., *Scientific Basis for Nuclear Waste Management*, New York: Plenum Press, 1979, vol. 1, 313-321.
7. R. Petrovic, "Coalescence of fluid inclusions and their removal from minerals exposed to confining pressure greater than the pressure of the fluid in inclusions," *Proc. COFFI* 2: 20, 1969.
8. L. P. Knauth, Arizona State University, Tempe, Ariz., personal communication.

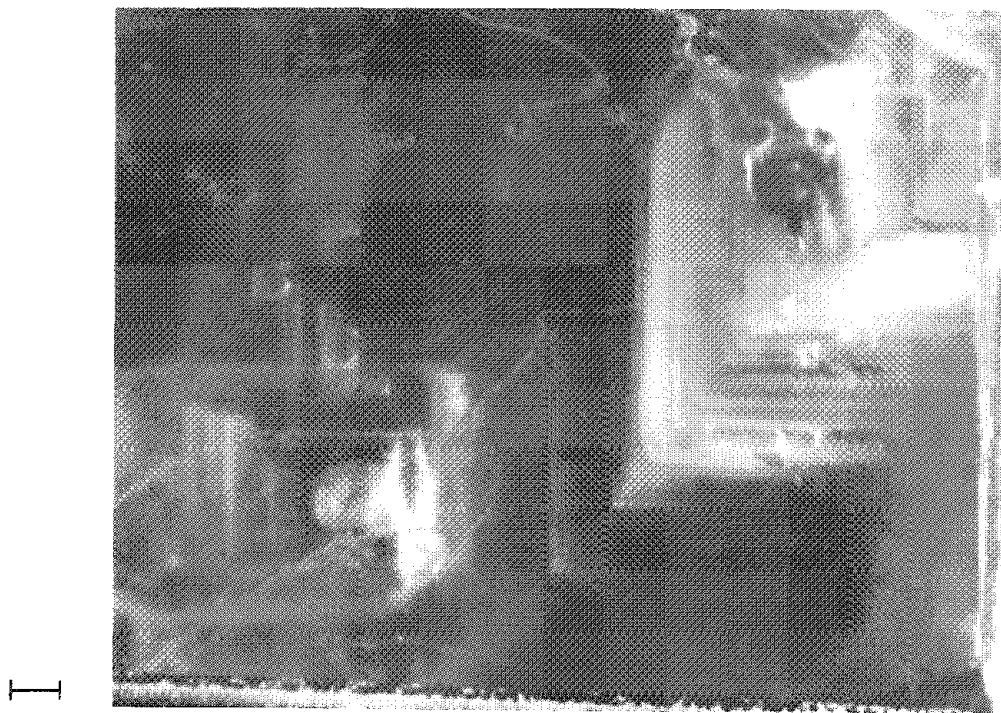


FIG. 1.--Photomicrograph of halite containing hopper crystal (upper right) and large fluid inclusions (lower left). Scale bar = 1 mm.

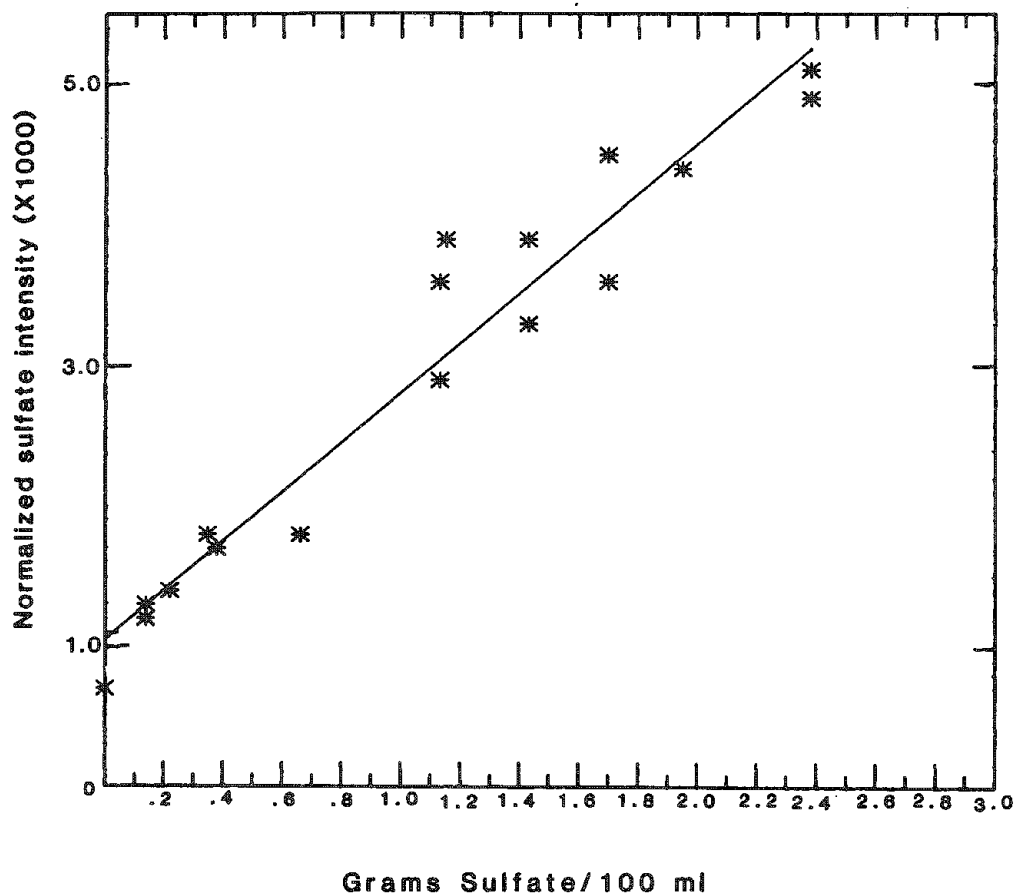


FIG 2.--Calibration of technique using standard solutions analyzed by ion chromatography vs  $\text{SO}_4^{2-}:\text{H}_2\text{O}$  peak intensity ratios.

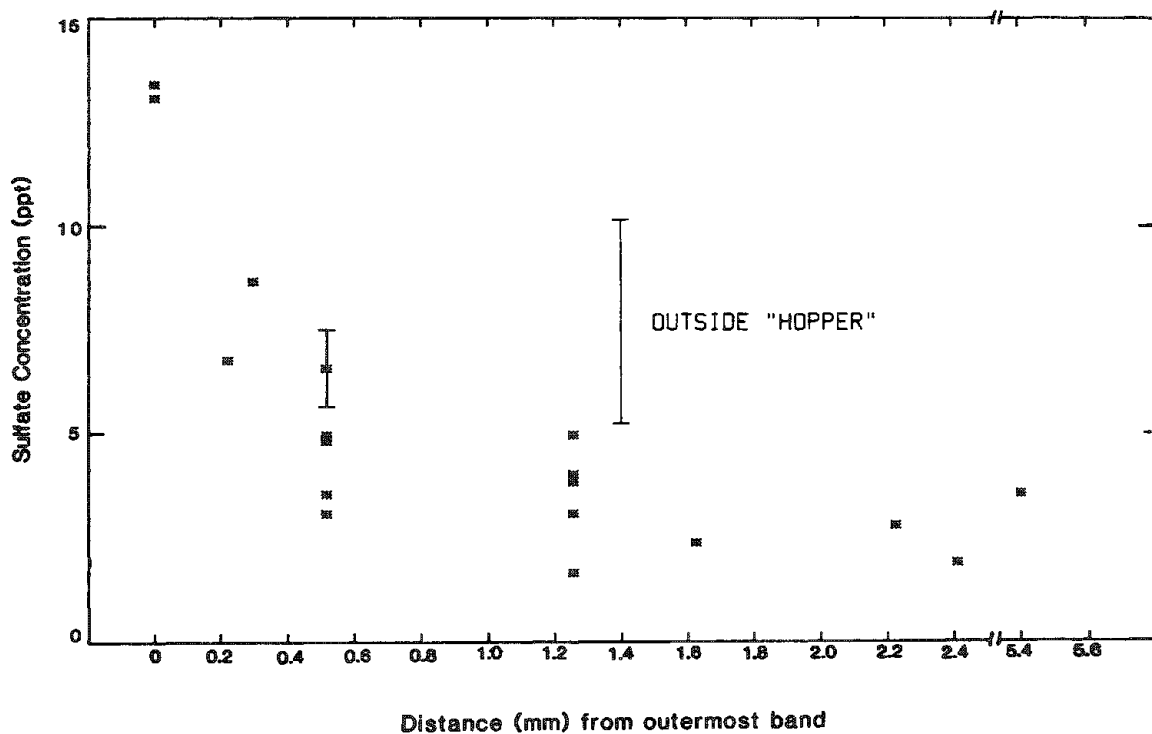


FIG. 3.--Sulfate concentrations (in parts per thousand) in fluid inclusions from cross section of hopper crystal.



## RAMAN SPECTROSCOPY OF CARBORANES AND POLYCARBORANESILOXANES

J. A. Shelnutt

Raman spectra of some m-carboranesiloxane polymers are compared with each other and with the spectrum of o-carborane and boron carbide. The comparisons and additional polarization studies allow the assignment of some vibrations to the icosahedral 1,7-dicarboryl units, siloxy (-Si-O-Si-) polymer connecting units, and substituent groups of the silicon atoms. The Raman investigation is directed toward understanding the interaction of carborane icosahedral units of boron-carbide semiconductor materials. However, these exceptionally heat-resistant polymers are interesting in themselves and have not previously been studied by Raman spectroscopy.

The class of compounds based on the  $B_{12}$  icosahedron are of considerable interest because of their unusual properties. In particular, the material has useful high-temperature electronic properties, heat resistance, and hardness.<sup>1,2</sup> To exploit these properties, a detailed understanding of their structure is needed so that structure-property relationships can be developed and used to tailor the materials to a particular application.

Recently,<sup>3</sup> Raman spectroscopy was used to characterize surface impurities on boron carbide--a high-temperature semiconductor and thermoelectric. More important, the frequency of a group of overlapping Raman lines common to the spectra of a series of icosahedral solids was found to correlate with the structure of the icosahedral units of the crystal for the series  $B_{12}$ ,  $B_{12}As_2$ ,  $B_{12}P_2$ , and  $B_xC$ .<sup>3</sup> To gain a better understanding of the effect of chains linking the  $B_{12}$  icosahedra in the crystalline materials and the effect of carbon-atom substitution in the icosahedra, we examined a series of carboranes and polycarboranes by Raman spectroscopy.

The dicarboranes investigated are composed of 10 borons and 2 carbon atoms arranged in a nearly icosahedral structure. Each boron and carbon atom is bonded to 5 other atoms in the icosahedron by 3-center bonds familiar in boron chemistry.<sup>4</sup> Each boron is also bonded radially to a hydrogen atom by normal 2-center bonds. The two carbon atoms are similarly connected to hydrogens in the parent carborane and to Si atoms of siloxy linking chains in the polycarborane siloxanes.<sup>5</sup> For o-carborane the carbon atoms are adjacent to one another; for m-carborane, they are next nearest neighbors.

The Raman spectra of the carboranes show some similarities with each other, but also differences primarily due to the differences in the siloxane linkages. Vibrations of the  $B_{10}C_2$  icosahedral units of the carboranes can be identified and show some gross features common to the icosahedral crystalline materials.

### *Material and Methods*

All carboranes and poly-m-carboranes were obtained commercially and used without further purification. The poly-m-carboranes were sold under the trade name Dexsil by Supelco. Those examined are Dexsil 300 and Dexsil 400. Dexsil 300 is the methyl silicone (methyl substituents on the Si-atoms) and Dexsil 400 is the methyl phenyl silicone. Dexsil 300 has three siloxy units between m-carboranes and Dexsil 400 has four siloxy units.

Raman spectra were obtained on a Raman difference spectrometer described previously.<sup>6</sup> The  $90^\circ$  scattering geometry was used. Excitation was with  $Kr^+$  laser at 413.1 nm, ~250 mW. The carborane samples were in the form of a waxy lump or viscous liquid for the pure samples or as a solution in  $CS_2$  or toluene.

Spectra with scattered light, analyzed parallel and perpendicular to the incident polarization direction, were obtained simultaneously by means of a rotating 2-compartment cell and solutions of the carboranes.<sup>7</sup> A sheet of polarized material attached to the cell transmitted light parallel to the polarization of the incident beam; a second sheet of the same polarized material was oriented at  $90^\circ$  to the first and attached to the cylindrical surface of the other compartment of the cell. As the cell rotated (at 100 Hz),

---

The author is at the Process Research Division, Sandia National Laboratories, Albuquerque, NM 87185.

alternately parallel and perpendicular polarizations were detected and the signal from the photomultiplier tube was gated electronically to generate the polarized Raman spectra.

### Results and Discussion

The low-frequency Raman spectrum of o-carborane in CS<sub>2</sub> is shown in Fig. 1, and spectra of two m-carboranesiloxane polymers in CS<sub>2</sub> are shown in Fig. 2. The frequencies, polarization, and some assignments of the vibrations are listed in Table 1. The spectrum of o-carborane in Fig. 1 shows both parallel and perpendicular polarizations. Two polarized ( $\rho = I_{\perp}/I_{\parallel} \approx 0$ ) totally symmetric modes are identified at 712 and 768 cm<sup>-1</sup>. All other vibrational modes in the low-frequency region are depolarized ( $\rho \approx 3/4$ ). The vibrations in the 400-1350cm<sup>-1</sup> region are expected to involve B-B, C-B, and C-C stretches and B-B-B, B-C-B, C-B-B, -B-H, -C-H angular motions. No Raman lines are detected in the 1350-2500cm<sup>-1</sup> region for o-carborane.

Figure 2 shows that the polymers also have many Raman lines in the 400-1350cm<sup>-1</sup> region, but also exhibit lines in the 1350-1600cm<sup>-1</sup> region. The lines in the latter region are associated with the siloxane linkages and Si side chains and tentative assignments of some of these lines are given in Table 1. In particular, two strong lines associated with the phenyl groups of the methyl phenyl polymer occur at 1593 and 1569 cm<sup>-1</sup>. Other prominent modes typical of Si-CH<sub>3</sub> vibrations occur at about 1409 and 1261 cm<sup>-1</sup>.

In the icosahedral region (400-1350 cm<sup>-1</sup>) two prominent polarized modes at 773 and 707 cm<sup>-1</sup> of the m-carborane polymers apparently correspond to the 768 and 712 cm<sup>-1</sup> totally symmetric modes of the o-carborane icosahedron. Borane (B<sub>12</sub>H<sub>12</sub><sup>2+</sup>),<sup>8</sup> which has full icosahedral symmetry, has a strong A<sub>1g</sub> breathing mode at 743 cm<sup>-1</sup> that can probably be related to the 773 and 768 cm<sup>-1</sup> A<sub>1</sub> modes in the effective C<sub>2v</sub> symmetry of the carborane icosahedra. The neutral carborane is apparently stabilized relative to borane by the positive charges contributed by the carbon atom. The other A<sub>1</sub> mode could arise from splitting of the weak, 5-fold degenerate H<sub>g</sub> mode of borane at 770 cm<sup>-1</sup>.<sup>8</sup>

The shift in the stretching mode frequency of 768 cm<sup>-1</sup> for o-carborane to 773 cm<sup>-1</sup> for the poly-m-carboranes may result from the substitution of electron withdrawing siloxy groups for hydrogens at the carbon atoms.<sup>9</sup> (Both m-carborane and o-carborane have been reported to have the same frequency for the putative breathing mode in the solid at 774 cm<sup>-1</sup>.)<sup>10</sup> The kinematic effect of replacing light H atoms with heavy siloxy side chains would be to *lower* the breathing mode frequency, but a higher frequency is observed for the polymers.

The high-frequency B-H and C-H stretching regions are shown in Figs. 3 and 4. The polarized Raman spectra show the B-H stretching region of carborane (Fig. 3) to consist of several bands including strongly polarized lines at 2624 and 2604 cm<sup>-1</sup>. The lines probably correspond to the A<sub>1</sub> mode arising from the A<sub>1g</sub> B-H stretch of borane at 2518 cm<sup>-1</sup> and an A<sub>1</sub> component of the H<sub>g</sub> mode of borane at 2475 cm<sup>-1</sup>.<sup>8</sup> Note that the frequencies are about 100 cm<sup>-1</sup> higher for the carboranes than for borane dianion.

The B-H stretching region is also complex for the carboranyl polymers (Fig. 4). For example, Dexsil 400 shows two strong polarized modes at 2607 and ~2620 cm<sup>-1</sup> and at least two less strongly polarized modes at lower frequency (2581 and ~2596 cm<sup>-1</sup>). Although the spectra in the polymer B-H regions are not as well resolved as for o-carborane, the pattern of Raman lines is the same. The lower resolution for the polymers is probably a result of inhomogeneous broadening.

In the C-H stretching region the carboranyl C-H vibration occurs at 3070 cm<sup>-1</sup>. This polarized line is of course absent in the polymers. The phenyl C-H stretch is observed at 3053 cm<sup>-1</sup> for Dexsil 400 but is absent from the methylsilicone. The symmetric (2905 cm<sup>-1</sup>, p) and antisymmetric (2965 cm<sup>-1</sup>) methyl C-H stretch are observed in both polymers.

It is interesting to compare the Raman spectra of the carboranes with those of the crystalline icosahedral borides.<sup>3</sup> In all of the crystalline materials (B<sub>x</sub>C, B<sub>12</sub>As<sub>2</sub>, B<sub>12</sub>P<sub>2</sub>; B<sub>12</sub>) the Raman frequencies are below 1200 cm<sup>-1</sup> and mostly above 400 cm<sup>-1</sup>. Lacking the hydrogens of the carboranes, only the icosahedral vibrations and those associated with the interconnecting chains (C-B-C, As-As, P-P) are expected for the crystals, and no high-frequency modes (above 1600 cm<sup>-1</sup>) are observed. We have seen that the icosahedral modes of the carboranes are all in the 400-1200cm<sup>-1</sup> region (except for the 1330cm<sup>-1</sup> line) consistent with the range of frequencies observed in the crystals. Also the only line identified that is associated with the siloxy inter-icosahedral linkage is the Si-O-Si mode<sup>11</sup> at 1083 cm<sup>-1</sup>--also in the 400-1200cm<sup>-1</sup> region. Other modes in the 1200-1600cm<sup>-1</sup> region of

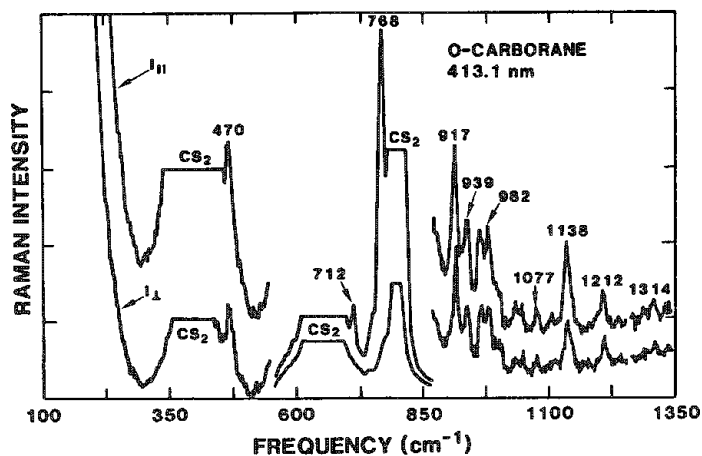


FIG. 1.--Raman spectra of 1,7-dicarbaborane polarized parallel ( $I_{||}$ ) and perpendicular ( $I_{\perp}$ ) to incident light in 100-1350  $\text{cm}^{-1}$  region.

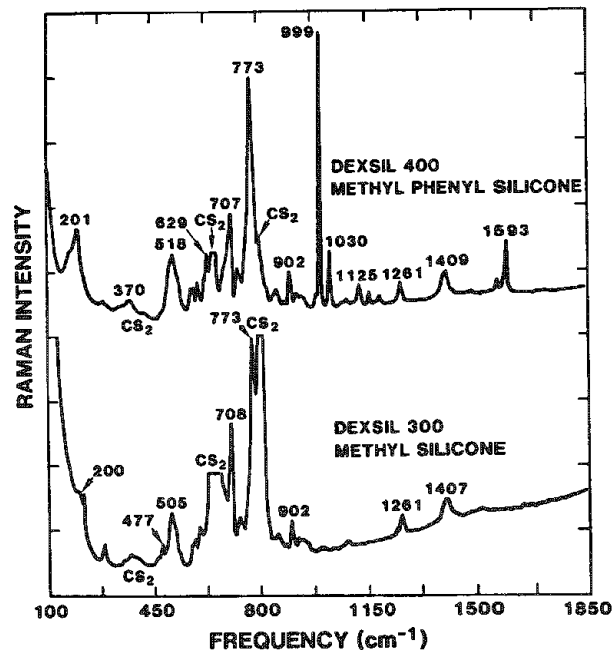


FIG. 2.--Raman spectra ( $I_{\text{total}}$ ) of poly-m-carborane methyl phenyl silicone (top) and poly-m-carborane methyl silicone (bottom) in 100-1850  $\text{cm}^{-1}$  region.

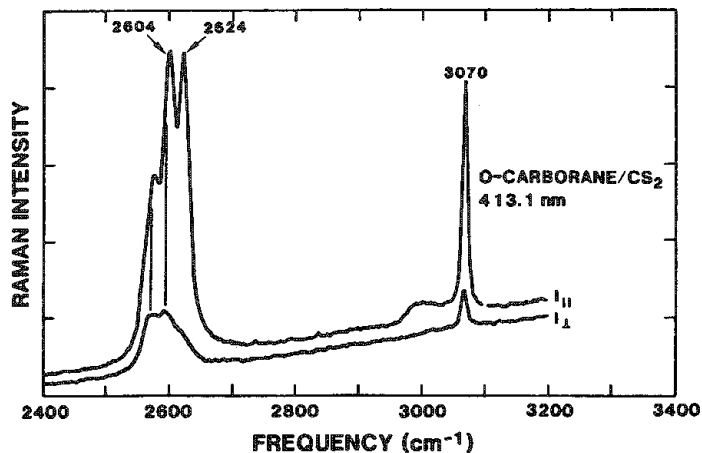


FIG. 3.--Polarized Raman spectra of o-carborane in carbon disulfide in B-H and C-H stretching region.

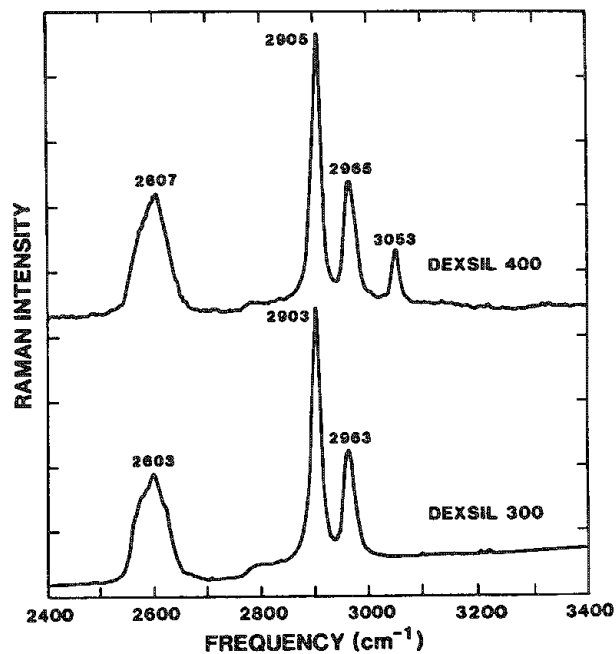


FIG. 4.--Raman spectra of Dexsil 400 (top) and Dexsil 300 (bottom) in B-H and C-H stretching region.

the carboranes are associated with side chain substituents of the Si atoms,<sup>11</sup> which have no analog in the crystalline materials.

The Raman spectra of the crystalline materials and the carboranes share an additional similarity. The borides all possess a complicated feature composed of several overlapping lines in the 900-1200cm<sup>-1</sup> region. The actual frequency of this feature depends on the material and has been shown to correlate with the structure of the boron icosahedra in the crystals.<sup>3</sup> In the carboranes the vast majority of the modes identified with the motions of the icosahedron are in the 900-1200cm<sup>-1</sup> region. The structure sensitive feature in the crystals is probably associated with this group of icosahedral vibrations. Normal coordinate calculations for the carboranes<sup>12,13</sup> should provide a more detailed analysis of the vibrational structure of both the carborane, polycarboranesiloxanes, and crystalline icosahedral borides.

## References

1. D. Emin, T. L. Aselage, C. H. Beckel, and I. A. Howard, Eds., *Boron-rich Solids*, in press, 1986.
2. V. I. Matkovich, Ed., *Boron and Refractory Borides*, Berlin: Springer-Verlag, 1977.
3. J. A. Shelnutt, B. Morosin, D. Emin, A. Mullendore, G. Slack, and C. Wood, in Ref. 1.
4. W. N. Lipscomb, *J. Less-common Met.* 82: 1, 1981.
5. R. N. Grimes, *Carboranes*, New York: Academic Press, 1970, 183.
6. J. A. Shelnutt, *J. Phys. Chem.* 87: 605, 1983.
7. D. L. Rousseau, *J. Raman Spectrosc.* 10: 94, 1981.
8. E. L. Muetterties, R. E. Merrifield, H. C. Miller, W. H. Knoth Jr., and J. R. Downing, *J. Am. Chem. Soc.* 84: 2506, 1962.
9. J. Hansh and L. Albert, *Substituent Constants for Correlation Analysis in Chemistry and Biology*, New York: Wiley-Interscience, 1979.
10. S. S. Bukalov, L. A. Leites, and V. T. Aleksanyan, *Acad. Sci. USSR (trans. Izv. Akad. Nauk, Ser. Khim.* 4: 929), 1968.
11. N. B. Colthup, L. H. Daly, and S. E. Wiberley, *Introduction to Infrared and Raman Spectroscopy*, New York: Academic Press, 1975, ch. 13.
12. C. Beckel and J. A. Shelnutt (unpublished results).
13. T. P. Klimova, L. A. Gribov, and V. I. Stanko, *Opt. Spectrosc.* 36: 650, 1974 (trans. *Opt. Spektrosk.* 36: 1112, 1974).

TABLE 1.--Raman line frequencies and polarization for carboranes.

Assignment	Pol.	Frequencies (cm <sup>-1</sup> )			Assignment	Pol.	Frequencies (cm <sup>-1</sup> )		
		Dexsil 300	Dexsil 400	o-Carborane			Dexsil 300	Dexsil 400	o-Carborane
$\nu(\text{Si-OH})$		3480			$\phi$	dp	- 995		
$\nu(\text{C-H})$				3070		p		999	
$\nu(\phi_{\text{C-H}})$	p		3054			dp			982
$\nu_a(\text{CH}_3)$	dp	2963	2963			dp			967
$\nu_s(\text{CH}_3)$	p	2903	2905		$\text{B}_{10}\text{C}_2$	dp	940	940	939
$\nu_1(\text{B-H})$	p	- 2620	- 2620	2624	$\text{B}_{10}\text{C}_2$	dp	923	920	917
$\nu_2(\text{B-H})$	p	2603	2607	2604		p	902	904	
$\nu_3(\text{B-H})$	dp	- 2595	- 2596	2595		dp	882	883	
$\nu_4(\text{B-H})$	dp	- 2580	2581	2572		dp	858	857	
			1714			p		- 845	
$\nu(\phi_{\text{C...C}})$	dp		1593			p		- 825	
$\nu(\phi_{\text{C...C}})$	dp		1569					813	
		1519					- 785	780	
$\nu(\text{Si-CH}_3)$		- 1430	1486		$\text{B}_{10}\text{C}_2$ , breathing	p	773	773	768
$\nu(\text{Si-CH}_3)$	dp	1407	1425			dp	- 765	- 765	
			1409		$\text{B}_{10}\text{C}_2$	p	732	731	747
			1324	1330	$\text{B}_{10}\text{C}_2$	p	708	707	712
$\nu(\text{Si-CH}_3)$	p	1262	1262			dp	- 695	- 695	
$\nu(\text{Si-CH}_3)$	dp	1260	1260		$\phi$	p		629	
			1238			dp	- 625	621	
			1192			dp	601	601	
			- 1182						- 595
	dp		1157			p	584	584	- 585
$\nu(\text{Si-}\phi)$	dp			1138		dp	575	- 575	- 575
$\text{B}_{10}\text{C}_2$	p		1124			dp	534	534	
$\nu(\text{Si=O-Si})$	dp	1105	- 1105	1111			520	519	
$\text{B}_{10}\text{C}_2$	p	1083	1083				505	518	
$\text{B}_{10}\text{C}_2$	dp	- 1075	- 1075	1077			- 485	- 485	
	dp			1048		dp	477		470
$\text{B}_{10}\text{C}_2$	dp	1038	- 1040	1036		p	396		
$\phi$	p		1030				371	373	
$\text{B}_{10}\text{C}_2$	dp	1005	- 1005	1003			293		
						dp	200	201	212

## MICRO-RAMAN CHARACTERIZATION OF ATHEROSCLEROTIC AND BIOPROSTHETIC CALCIFICATION

E. S. Etz, B. B. Tomazic, and W. E. Brown

In previous applications of Raman microprobe spectroscopy to the study of biological tissues, we have examined the processes of mineralization in tooth and bone with a view to correlating the information on molecular composition gained from the microscopic domain with the elemental data available largely from bulk chemical analysis.<sup>1-3</sup> In these studies, we and other workers have found these tissues to be stable under carefully controlled conditions of laser irradiance. Similarly, sample fluorescence has not been a problem in the successful analysis of such biological tissues.<sup>4-5</sup>

The most general interest in the study of mineralizing tissues is to gain a more complete understanding of biological and pathological calcification. Following this earlier work, we have now applied Raman microprobe analysis to the study of two types of cardiovascular calcification: (i) atherosclerotic calcification in man and (ii) bioprosthetic calcification of heart-assist devices implanted in animals. These studies are part of a larger research program to obtain comprehensive physicochemical information on these two types of pathological mineral deposits found in different living organisms and associated with different host materials.<sup>6</sup> At present there is a special urgency about gaining a fuller understanding of the pathogenesis of biomineralization as this may lead to a more successful application in man of bioprosthetic cardiovascular devices.

This report describes the use of the Raman microprobe for the study of such cardiovascular deposits. These studies are designed to gain information on the composition and structure of the apatitic phase in native deposits, and of deposits with the organic matrix removed by a deproteination treatment. Other goals are to obtain information on the type of carbonate substitution of  $\text{CO}_3^{2-}$  for either  $\text{PO}_4^{3-}$  or  $\text{OH}^-$  (or both) in these biological calcium phosphates, and to quantify carbonate contents based on a method of relative quantitation employing calibration data derived from the measurement of synthetic carbonate apatites of known composition.<sup>2</sup>

### *The Analytical Context: Biological and Pathological Calcification*

There is broad medical interest in comprehensive characterization of the various types of phosphate minerals in human tissues.<sup>7</sup> The most abundant mineral in human tissues is a basic calcium phosphate idealized as hydroxyapatite (HAP),  $\text{Ca}_{10}(\text{PO}_4)_6(\text{OH})_2$ . But other calcium phosphates, for example,  $\text{CaHPO}_4 \cdot 2\text{H}_2\text{O}$  (brushite),  $\text{Ca}_8\text{H}_2(\text{PO}_4)_6 \cdot 5\text{H}_2\text{O}$  (octacalcium phosphate, OCP), and  $\beta\text{-Ca}_3(\text{PO}_4)_2$  ( $\beta$ -tricalcium phosphate,  $\beta$ -TCP), have been identified with or without association with apatite.<sup>7</sup> With age, and in most cases of pathological calcifications, the phosphate minerals incorporate carbonate, forming relatively stable phases of biological "carbonate apatites." Some of the vexing problems concerning the biological apatites are (i) variable stoichiometry (i.e., Ca/P ratios may range from  $\sim 1.5$  to  $\sim 1.8$  compared to 1.67 for pure HAP); (ii) the presence (structural or surface) of various ion impurities, e.g.,  $\text{Na}^+$ ,  $\text{Mg}^{2+}$ ,  $\text{F}^-$ ,  $\text{HPO}_4^{2-}$ ,  $\text{CO}_3^{2-}$ ; and (iii) the co-existence of possible precursor phosphates, such as OCP,  $\beta$ -TCP, and ACP (amorphous calcium phosphate).

The biological apatites are uniquely similar in that they all contain carbonate in varying amounts, putatively a substitute for phosphate in the apatite structure. The incorporation of  $\text{CO}_3^{2-}$  into biological apatites appears to be coupled with that of  $\text{Na}^+$  and results in the predominant (but not exclusive) substitution of  $\text{CO}_3^{2-}$  for  $\text{PO}_4^{3-}$  (i.e., Type-B carbonate apatite). Substitution of  $\text{CO}_3^{2-}$  for  $\text{OH}^-$  results in Type-A carbonate

---

Author Etz is with the Center for Analytical Chemistry at the National Measurement Laboratory, U.S. National Bureau of Standards, Gaithersburg, MD 20899; authors Tomazic and Brown are at the Paffenbarger Research Center, American Dental Association Health Foundation, National Bureau of Standards. We wish to acknowledge the technical assistance of Erik Etz, 1985 Summer Student at the American Dental Association Research Center at NBS, in performing some of the carbonate determinations on biological apatites.

apatites where complete substitution results in the compound of formula  $\text{Ca}_{10}(\text{PO}_4)_6\text{CO}_3$ , containing 5.8 wt% carbonate.<sup>8-10</sup> Type-B carbonate apatites of variable composition may be represented by the general empirical formula  $\text{Ca}_{10-x-y}(\text{PO}_4)_{6-x}(\text{HPO}_4, \text{CO}_3)_x(\text{OH})_{2-x-2y}$ .

Like bone and other mineralized skeletal tissues, cardiovascular calcified deposits comprise two phases, organic and inorganic. They are considered abnormal or pathological calcifications. Dental calculi and urinary stones are other examples of pathological calcification, and in fact almost any tissue in the body can calcify. In several forms of pathologically calcified tissues, the mineral is nonphosphatitic, consisting of calcium oxalates, uric acids, and its salts. Raman microprobe analysis has been used in the study of urinary calculi to characterize various crystalline and amorphous mineral and organic constituents.<sup>11</sup>

Atherosclerotic calcification in man has been studied for some time.<sup>12,13</sup> Calcification of the human aortic wall is a common occurrence in the later stages of cardiovascular disease. Calcified atherosclerotic plaques occur in the media and predominantly in the intima layers of the aortic wall. Several analytical methodologies (including x-ray and electron-diffraction studies, spectroscopic analysis, and wet chemical analysis) indicate that the inorganic matrix of these deposits basically consists of a polycrystalline form of biological apatite. Other types of data (petrographic microscopy, solubility, morphology, pyrolysis, thermogravimetric analysis) indicate that it is an apatitic hydrolyzate of OCP.<sup>6</sup> Severe conditions of human atherosclerotic calcification result in hardening of blood vessels (arteries), ulcerations, and ultimately, the total breakdown of the tissue.<sup>13</sup>

Calcification of synthetic elastomers used in cardiac assist systems (e.g., blood pumps) or total artificial hearts has been a problem as it leads to diminished function or complete failure of the implanted device. The alteration of the mechanical and performance properties of elastomeric implants in the cardiovascular system is viewed as resulting from the simultaneous action of many factors among which are (i) the adsorption of blood lipids, (ii) calcification, (iii) dynamic fatigue, and (iv) enzymatic attack.<sup>14</sup>

Among the most frequently used biopolymers are the segmented polyether urethanes ("Biomer" polymers) which are currently extensively studied as candidates for various heart assist devices and total replacements. The in vivo performance of these polyether urethanes has been tested, for example, when they are used as blood sacks for the left or right ventricular assist device (LVAD, RVAD) and total artificial hearts in sheep and calves. Deterioration and failure brought on by calcification and other contributing factors has led to numerous studies of the composition and structure of these calcific deposits.<sup>15,16</sup> The calcified deposits have been found to consist of various forms of "impure" biological hydroxyapatite as the mineral phase with the organic matrix consisting of lipids, lipoproteins, phosphoproteins, cholesterol, cholesterol esters, and possibly also free fatty acids. In this complex biological/organic matrix the mineral phase forms and deposits as a highly substituted ( $\text{Na}^+$ ,  $\text{Mg}^{2+}$  replacing  $\text{Ca}^{2+}$ ), nonstoichiometric hydroxyapatite, containing carbonate. Contrary to the composition of urinary calculi, these deposits are thought not to contain free calcium carbonate phases, either as calcite or aragonite.

#### *Samples and Their Measurement*

*Synthetic Calcium Phosphates.* These consist of a series of synthetically prepared calcium phosphates known to have roles in biological mineralization. The compounds examined in this work are pure preparations of hydroxyapatite (HAP), octacalcium phosphate (OCP),  $\beta$ -tricalcium phosphate ( $\beta$ -TCP), and an amorphous calcium phosphate (ACP), approximating  $\text{Ca}_9(\text{PO}_4)_6$ . The carbonate apatites studied are of the Type-A and Type-B variety. The Type-A carbonate apatite, a high-temperature product, is a polycrystalline material (powder) prepared under conditions that yield complete substitution of hydroxyl by carbonate, as described above. A series of Type-B carbonate apatites, ranging in carbonate contents from ~1.5 to ~16 wt%, were used as calibration standards in the relative quantitation scheme employed for the determination of carbonate concentrations. These standards have all been prepared in vitro and were characterized by powder x-ray diffraction and wet chemical analysis, and on the basis of their infrared absorption spectra.<sup>2,7</sup>

*Cardiovascular Calcified Deposits.* Calcified atherosclerotic deposits were obtained from autopsies, removed, and isolated from human abdominal aortas (the plaque was isolated from the intima layer). The bioprosthetic calcified deposits consisted of scrapings removed from the "Biomer" surfaces of a blood pump (i.e., a part of a left ventricular

assist device, LVAD) implanted in a sheep. Details of the origins and medical histories of these samples, their isolation, and the purification procedures have been described.<sup>6</sup> The purified deposits consist of homogenized powders suitable for bulk wet chemical analysis and microchemical analysis. For the comprehensive physicochemical analysis of these samples, it was necessary to isolate the inorganic matrix by efficient removal of the organic matrix. It was important in this procedure to preserve the identity of the inorganic matrix. Several procedures were employed in which the deproteinization method by hydrazine treatment was considered the most appropriate.<sup>6</sup> Hydrazine treatment results in practically complete deproteinization of these calcified deposits. Chemical data show that the hydrazine-treated material contained, at most, 2-4% organic residue, as determined by bulk analysis. Carbonate determinations were performed on milligram quantities of these powders by an established microchemical method. X-ray powder-diffraction data and FT/IR spectroscopy further contributed to the characterization of these samples.<sup>6</sup> All bulk chemical measurements and microanalyses of these deposits were performed also on raw or native calcified deposits in which the organic matrix was left intact.

*Raman Microprobe Measurements.* Particle samples of these calcified deposits (homogenized powders, native and deproteinized) were prepared by dry dispersion of these powders on lithium fluoride substrates, which are devoid of Raman scattering. Microprobe measurements were performed on single particles (size range 5-50  $\mu\text{m}$ ) of the dispersed powders by the monochannel (PMT detection) scanning instrument developed at the National Bureau of Standards.<sup>17</sup> All spectra of these samples were excited with 514.5nm radiation of an  $\text{Ar}^+/\text{Kr}^+$  gas laser and recorded with  $5\text{cm}^{-1}$  spectral resolution. The measurements of these samples were carried out under nearly identical conditions of laser irradiance (power densities ranging from 5 to 20 mW measured at the sample in a beam spot  $\sim 10\text{ }\mu\text{m}$  in diameter), signal integration times, and scan rates. The synthetic calcium phosphate standards were totally insensitive to laser irradiation and thus stable even at 80 mW ( $\sim 10\text{ }\mu\text{m}$  beam spot), and showed no fluorescence. The native nondeproteinized powders of the calcified deposits showed some mild luminescence upon initial exposure to the laser spot, which quickly diminished upon continued irradiation and yielded acceptable spectral background levels. Power densities in excess of 30 mW directed at these proteinaceous calcified deposits invariably resulted in sample degradation and destruction.

### *Results of Spectroscopic Measurements*

*Synthetic Calcium Phosphates.* As a basis for obtaining detailed knowledge of the vibrational fingerprints of various calcium phosphates, we examined the spectra of a series of synthetic preparations of these compounds, including HAP prepared by various methods, brushite, OCP, and ACP. Qualitatively, these compounds can be differentiated on the basis of their Raman spectra (phosphate bands show differences in frequency position, the multiplicity of bands, bandwidths, and shapes), though detailed correlations of these spectral differences must await further work, including a rigorous correlation with x-ray diffraction data and the results of FT-IR measurements.

Figure 1 shows the micro-Raman spectra of three of the synthetic calcium phosphates: a stoichiometric HAP, a Type-B carbonate apatite with a  $\text{CO}_3^{2-}$  content (from bulk chemical analysis) of 4.3 wt%  $\text{CO}_3^{2-}$ , and a Type-A carbonate apatite containing 5.8 wt%  $\text{CO}_3^{2-}$ , with formula  $\text{Ca}_{10}(\text{PO}_4)_6\text{CO}_3$ . The general features of the Raman spectra of HAP have been discussed in previous work.<sup>1-3</sup> In the case of stoichiometric HAP, the internal vibrational modes of the phosphate group give rise to bands with shifts at  $961\text{ cm}^{-1}$  ( $\nu_1$ , P-O symmetric stretch),  $432$  and  $455\text{ cm}^{-1}$  ( $\nu_2$  modes),  $582$ ,  $593$  and  $610\text{ cm}^{-1}$  ( $\nu_4$  modes), and at  $1030$ ,  $1048$ , and  $1079\text{ cm}^{-1}$  ( $\nu_3$  modes). In addition, the spectrum of HAP shows a sharp band of medium intensity at  $3573\text{ cm}^{-1}$  indicative of O-H stretching. Weaker, less well defined bands are observed in the low-frequency lattice region ( $< 350\text{ cm}^{-1}$ ) for this polycrystalline sample. The internal vibrations of the  $\text{PO}_4^{3-}$  group are observed at about the same frequencies (variations of  $\pm 3\text{--}8\text{ cm}^{-1}$ ) for the other calcium phosphates, with qualitative differences in band shapes, the splitting of bands, etc.

Relative to the Type-B carbonate apatites (Fig. 1), additional spectral contributions arise from the normal vibrations of the  $\text{CO}_3^{2-}$  ions in addition to those from the  $\text{PO}_4^{3-}$  ions. In crystalline calcium carbonate with the calcite structure, lattice modes are expected at  $156$  and  $283\text{ cm}^{-1}$  (these are generally quite prominent) and internal modes at  $714\text{ cm}^{-1}$  ( $\nu_4$ ),  $1086\text{ cm}^{-1}$  ( $\nu_1$ , C-O symmetric stretching), and at  $1432\text{ cm}^{-1}$  ( $\nu_3$ ).<sup>18</sup> Thus,

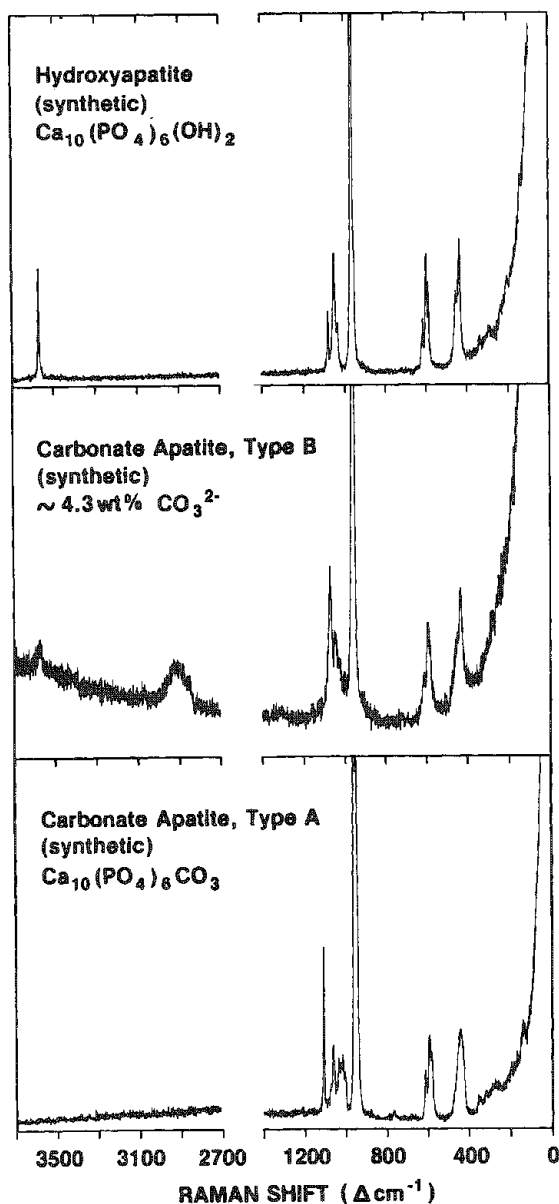


FIG. 1.--Microparticle spectra of three synthetic apatites. Top, stoichiometric, polycrystalline hydroxyapatite,  $\text{Ca}_{10}(\text{PO}_4)_6(\text{OH})_2$ ; middle, Type-B carbonate apatite (substitution of  $\text{CO}_3^{2-}$  for  $\text{PO}_4^{3-}$ ) of  $\sim 4.3\text{wt}\%$  carbonate; bottom, Type-A carbonate apatite (substitution of  $\text{CO}_3^{2-}$  for  $\text{OH}^-$ ) of near stoichiometric composition,  $\text{Ca}_{10}(\text{PO}_4)_6\text{CO}_3$ , with  $\sim 5.8\text{wt}\%$  carbonate. Excitation at 514.5 nm; LiF substrate; partial spectral range.

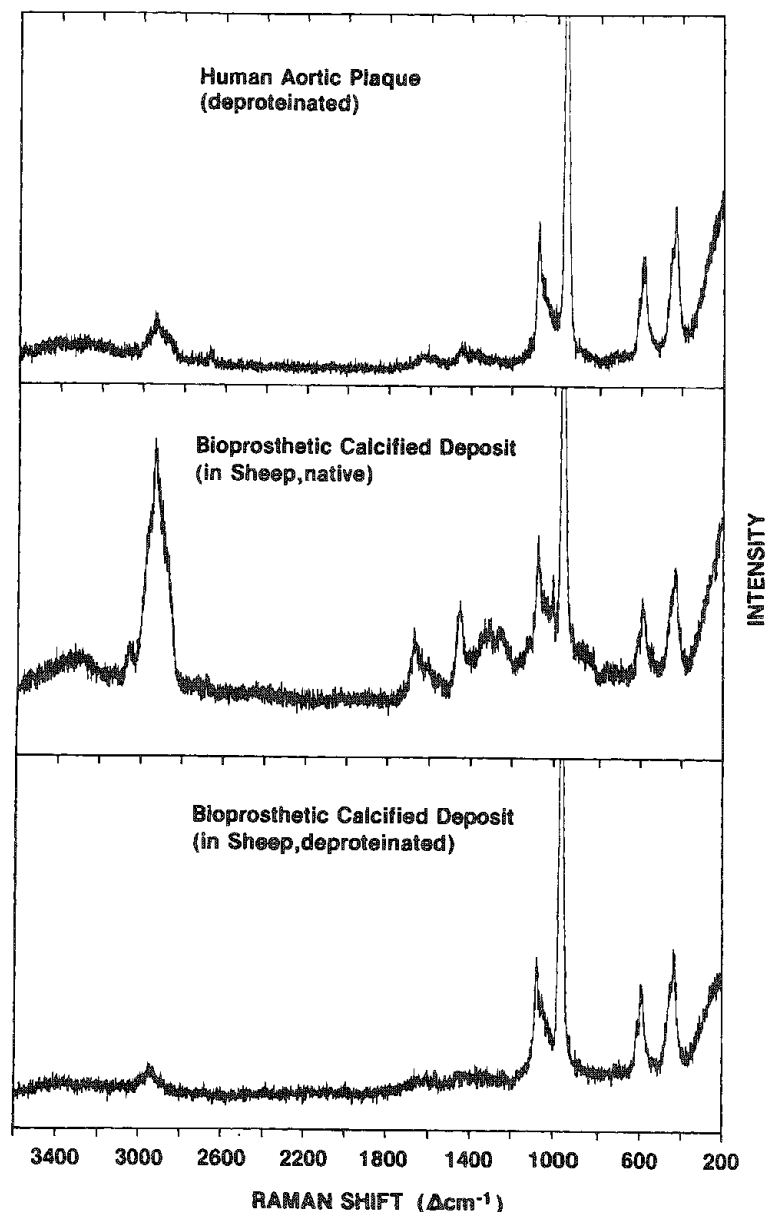


FIG. 2.--Microparticle spectra of two types of cardiovascular mineralized deposits: Atherosclerotic and bioprosthetic calcification. Top, human (abdominal) aortic plaque deproteinated by hydrazine treatment; middle, native calcified deposit from heart assist device (LVAD) implanted in sheep; bottom, deproteinated calcified deposit from heart assist device (LVAD) implanted in sheep. Excitation at 514.5 nm; LiF substrate.



carbonate of the trigonal calcite structure is usually readily recognized by the appearance of the very strong Raman band at  $\sim 1085\text{ cm}^{-1}$ . As the carbonate ion symmetry is lowered by incorporation into other crystal lattices, these frequencies shift and band shapes and intensities are altered due to different structural environments. Thus, for the Type-B carbonate apatites (composition range,  $\sim 1.5$ - $\sim 16\text{ wt}\%$   $\text{CO}_3^{2-}$ ), the carbonate  $\nu_1$  stretch appears at  $\sim 1074\text{ cm}^{-1}$ . The other carbonate modes in these synthetic carbonate apatites are quite weak. The weak band centered at  $\sim 2920\text{ cm}^{-1}$  and the feature at  $\sim 3575\text{ cm}^{-1}$  are attributed to O-H stretching modes of the hydroxyl ions in the carbonate apatite ("bonded" hydroxyl modes rather than "free" modes due to water molecules). Our correlation of the spectra of these synthetic, Type-B carbonate apatites is not complete, but it is evident that the increase in carbonate contents is accompanied by a decrease in the phosphate band ( $\nu_1$ ) intensity. Also, the phosphate bands become broader with increasing carbonate content; furthermore, small shifts in the vibrational frequencies are observed.

In the spectrum of the Type A carbonate apatite of near stoichiometric composition ( $\sim 5.8\text{ wt}\%$   $\text{CO}_3^{2-}$ ), the  $\nu_1$  carbonate stretch appears as a very sharp band of medium intensity at  $1110\text{ cm}^{-1}$ . The weak band at  $\sim 768\text{ cm}^{-1}$  may be assigned to a  $\nu_4$  carbonate vibration. The spectrum shows the  $\nu_1$  phosphate band at  $961\text{ cm}^{-1}$  as in pure HAP, which possibly indicates that carbonate substitution for hydroxyl does not change the internal  $\text{PO}_4^{3-}$  vibrations. The position of the  $\nu_1$   $\text{CO}_3^{2-}$  band at  $1110\text{ cm}^{-1}$  correlates well from x-ray diffraction results with the presence of a distorted carbonate ion in this environment. No bands are detected in the  $2800$ - $3600\text{ cm}^{-1}$  region, which indicates the absence of any hydroxyl vibrations in this carbonate apatite. Thus, Type-A carbonate apatites are readily distinguished from Type-B varieties on the basis of their Raman vibrational spectra, an observation that has also been reported from infrared studies of both types of carbonate apatites.<sup>10</sup> A component of the carbonate ion  $\nu_3$  vibration is observed for both synthetic and biological Type-A carbonate apatites at  $1540 \pm 5\text{ cm}^{-1}$  in the infrared. By comparison, the  $\nu_3$   $\text{CO}_3^{2-}$  vibration of Type-B carbonate apatites (synthetic and biological) is observed as a doublet with band positions at  $\sim 1420$  and  $\sim 1470\text{ cm}^{-1}$  in our bulk infrared measurements of these samples.<sup>6,19</sup>

*Determination of Carbonate Contents.* As in previous work on the composition of the mineral phase in bone,<sup>2,3</sup> the present spectroscopic studies are directed at examining the extent and microscopic distribution of carbonate contents in these cardiovascular calcified deposits. Our studies of the mineralized phases in bone have indicated the feasibility of obtaining quantitative data on  $\text{CO}_3^{2-}$  contents in chick bone by an empirical approach to the quantitation of Raman scattered intensities. The various theoretical and experimental factors to be considered in any scheme of quantitative analysis of the spectra of particles have been described. We have shown that absolute quantitation (from fundamental principles) of Raman data remains a distant goal even for the simplest of scattering systems. Yet useful results can be obtained with sufficient accuracies (typically,  $\pm 1\%$  absolute uncertainty in  $\text{CO}_3^{2-}$  concentrations, determined from single particles) by use of relative quantitation schemes. This approach has involved calculating  $\text{CO}_3^{2-}$  contents from the intensity ratios of the  $\sim 1074\text{ cm}^{-1}$  carbonate band and the  $\sim 961\text{ cm}^{-1}$  phosphate band, with appropriate corrections for the spectral "background" at each of these analytical frequencies. That required establishing a calibration curve, relating the observed intensity ratios to known carbonate contents of a series of Type-B carbonate apatites with  $\text{CO}_3^{2-}$  contents varying from  $\sim 1.5$  to  $\sim 16\text{ wt}\%$ . This method of carbonate quantitation by use of relative band intensity ratios (peak heights rather than band areas) has furnished good results for tissues of bone and density-fractionated bone powders.<sup>2,3</sup> The same approach is used here for the determination of carbonate contents, at the microscopic level, of these cardiovascular calcified deposits.

*Cardiovascular Calcified Deposits.* Raman spectra were obtained from microparticles of both types of cardiovascular deposits, and in each case from powdered samples of the native materials and samples of the same materials deproteinized by the hydrazine treatment. Some of the results of these spectral scans are shown in Fig. 2. Readily recognized in each of these spectra (by comparison with the spectra of Fig. 1) are the prominent features attributed to the  $\text{PO}_4^{3-}$  group of the biological apatite. The frequency positions of these phosphate fundamentals are in each case very close (within  $\pm 4\text{ cm}^{-1}$ ) to the corresponding vibrations observed for the synthetic apatites. Thus, the  $\nu_1$   $\text{PO}_4^{3-}$  vibration peaks at  $962\text{ cm}^{-1}$  in the spectrum of aortic plaque and at  $964\text{ cm}^{-1}$  in the spectra of (native and deproteinized) bioprosthetic plaque. For all spectra of these samples, the carbonate  $\nu_1$

vibration peaks at  $1075 \pm 1 \text{ cm}^{-1}$ , and in these spectra the intensity of this band is relatively more pronounced than it is in the spectrum of the Type-B carbonate apatite (Fig. 1). The spectrum of the aortic plaque shows additional minor spectral contributions from the residual organic matrix, which was not entirely removed by the hydrazine treatment. The spectrum of the bioprosthetic, native calcified deposit shows the Raman bands due to the organic matrix more clearly. These bioprosthetic deposits contain up to 50 wt% (dry weight, bulk analysis) of the proteinaceous material and other biological compounds. Thus, the complex organic pattern in these spectra is difficult to interpret and does not allow assignments to be made with reference to specific vibrating species. In connection with our earlier work on the organic matrix of tooth and bone,<sup>2,3</sup> we have made some general vibrational assignments of the organic bands consistent with other vibrational data of such proteinaceous matrices. Thus, the features in the  $1200\text{--}1700\text{cm}^{-1}$  region are principally attributed to the amide (amide I, II, and III) and methylene ( $\text{CH}_2$ ) groupings, whereas the pronounced broad band with peak maximum at  $\sim 2940 \text{ cm}^{-1}$  is assigned to C-H stretching vibrations. The weak, broad band with maximum at  $\sim 3325 \text{ cm}^{-1}$  is attributed to O-H stretching from water. The spectrum of the deproteinated bioprosthetic calcified deposit retains all the features of the apatitic mineral phase plus some very weak remnants of the incompletely removed organic matrix.

Preliminary results from the quantitation of carbonate concentrations of the mineral phase of these calcified deposits show that these range from 5.8 to 7.5 wt%, when these materials are analyzed with the spatial resolution of the Raman microprobe, on a particle-to-particle basis. The micro-Raman data for carbonate contents of the deproteinated aortic plaque indicate an average concentration of 6.2 wt%  $\text{CO}_3^{2-}$ , based on the spectra of five arbitrary particles, whereas carbonate contents of the deproteinated bioprosthetic plaques averaged out to 6.4 wt%, based on an equal number of particle measurements. A similar variation in composition is reflected in the molar Ca/P ratios, obtained by x-ray microanalysis and wet chemical analysis, which for these mineral phases range from 1.60 to 1.83.

Chemical composition data of two biological tissues, mature human bone and chick bone, and the related cardiovascular calcified deposits, are compared in Table 1. These values are the mean data from bulk chemical analysis and indicate the overall close similarity in the compositions of these bone tissues and that of the pathologic calcified tissues. This close similarity is reflected also in the qualitative appearance of the spectra of these biological minerals despite their differences in origin, host material, and biological processes of formation. The principal features in the spectra of mature chicken bone (tibia, unfractionated)<sup>2,3</sup> whose mineral phase also consists of an "impure" carbonate-substituted (Type-B) hydroxyapatite ( $\sim 6.2 \text{ wt}\% \text{ CO}_3^{2-}$  in whole bone consisting of approximately 30 wt% organic matrix) are virtually identical to the spectra of the native (i.e., not deproteinated) calcified deposits. As for the spectra of mature, whole chick bone, this qualitative likeness appears to extend also to the composition of the organic matrix where the spectra of the native, calcified deposits (Fig. 2, middle) all show a pronounced, sharp band at  $1004 \text{ cm}^{-1}$  that has been attributed by some workers to phenylalanine and by some others to organic phosphate.<sup>3</sup> It remains to be determined which assignment is correct and why this band is so prominent in the bone spectra and now in the spectra of the aortic plaques and the bioprosthetic calcified deposits.

### *Perspective and Conclusions*

The application of the Raman microprobe to this study of cardiovascular calcification has furnished new results in support of other physicochemical characterization studies aimed at elucidating the composition and formation of the mineral phase in these pathological calcified deposits.<sup>6</sup> Aside from limited electron microprobe analysis of these deposits furnishing the data on Ca and P concentrations at the microscopic level, micro-Raman is the only technique available at present to yield molecular information with commensurate spatial resolution of several micrometers. These studies have provided a consistent picture concerning the composition of these calcified deposits, as consisting of a microcrystalline mineral phase present in a complex, bio-organic host material, with the mineral best described as a carbonate-bearing (Type-B) "impure" biological apatite different from a stoichiometric calcium hydroxyapatite. The chemical results for both atherosclerotic and bioprosthetic deposits indicate substantial substitution of Ca by Na and Mg (Table 1),

relative to the calcium contents of mature vertebrate bone. The Raman microprobe results indicate that, at the microscopic level, these calcified deposits clearly show a fair degree of heterogeneity in composition, also born out by the data on Ca/P ratios from x-ray microanalysis. The heterogeneous nature of these deposits can be expected since the formation and maturation of calcium phosphate phases are a reflection of a changeable reaction environment. Contrary to some predictions that such mineralized deposits may also contain carbonate moieties substituted for hydroxyl in the structure of the biological apatite, we did not detect in our spectra the presence of Type-A carbonate apatite.<sup>10</sup> Detection sensitivities in these measurements for  $\text{CO}_3^{2-}$  in A-type sites appear to be at the ~1 wt% level of the apatitic phase.

The laser microprobe mass analysis (LAMMA) technique has recently been applied to the closely related problem of compositional analysis of various types of biological concretions.<sup>20</sup> These studies have demonstrated that the LAMMA technique (albeit destructive) can provide a practical method for obtaining chemical compound information from the microanalysis of human urinary calculi (e.g., kidney stones). The LAMMA negative-ion mass spectra have furnished signals indicating the presence of intact, nonfragmented carbonate ( $\text{CO}_3^{2-}$ ) ions in addition to various phosphorus-oxygen species (e.g.,  $\text{PO}_2^-$ ,  $\text{PO}_3^-$ ). These studies have employed a relative quantitation procedure (based on a calibration curve derived from synthetic standards) that relates the negative-ion signal of  $\text{CO}_3^-$  (mass = 60) and the intensity of the  $\text{PO}_2^-$  ion (mass = 63) for determining carbonate contents in these complex apatitic matrices. With the inherent spatial resolution of LAMMA on the order of a few micrometers, these workers also find a gross heterogeneity of these calcified stones. However, under the conditions of destructive analysis, LAMMA does not permit the recognition of Type-A and Type-B carbonate in the apatitic structure.

In conclusion, further micro-Raman studies are being directed at a full integration of the technique with other methods of analysis (at present including LAMMA studies as well) employed in the comprehensive characterization of these cardiovascular calcified deposits. Detailed analysis of our FT-IR spectra obtained from these samples is expected to yield corroborative results and may especially help in the interpretation of the vibrational pattern attributed to the organic matrix of these calcified deposits. With respect to the mineral or apatitic phase, the vibrational spectra (micro-Raman and FT/IR) will come under close scrutiny to possibly reveal the presence of other calcium phosphates, such as OCP (and its hydrolyzates) that have been invoked as precursors or participants in the formation of cardiovascular calcified deposits.<sup>6</sup>

Concerning the detection and determination of "localized" carbonate contents in these deposits by Raman microsampling, further work needs to be done to place the method of relative quantitation on a more concrete footing. Especially for carbonate concentrations exceeding ~7 wt% (Type-B carbonate apatites), our samples of synthetic carbonate apatites prepared to serve as standards have been found to be themselves heterogeneous at the single-particle level, which makes our quantitative procedures uncertain in that concentration regime and beyond. Thus, the exact trend of the  $\text{CO}_3^{2-}/\text{PO}_4^{3-}$  intensity ratios with carbonate contents needs to be more thoroughly established.

## References

1. F. S. Casciani, E. S. Etz, D. E. Newbury, and S. D. Doty, "Raman microprobe studies of two mineralizing tissues: Enamel of the rat incisor and the embryonic chick tibia," *SEM/1979* II, 383.
2. E. S. Etz, "Empirical quantitation in Raman microprobe analysis," *Microbeam Analysis--1981*, 73.
3. M. D. Grynpsas, E. S. Etz, and W. J. Landis, "Studies of calcified tissues by Raman microprobe analysis," *Microbeam Analysis--1982*, 333.
4. J. L. Abraham and E. S. Etz, "Molecular microanalysis of pathological specimens in situ with a laser Raman microprobe," *Science* 206: 716, 1979.
5. H. Buiteveld, F. F. M. deMul, J. Mud, and J. Greve, "Identification of inclusions in lung tissue with a Raman microprobe," *Appl. Spectrosc.* 38: 304, 1984.
6. B. B. Tomazic, W. E. Brown, L. A. Queral, and M. Sadovnik, "Physicochemical characterization of cardiovascular calcified deposits: I. Isolation, purification, and instrumental analysis," to be published in *Atherosclerosis*.
7. R. Z. LeGeros and J. P. LeGeros, "Phosphate minerals in human tissues," in

J. O. Nriagu and P. B. Moore, Eds., *Phosphate Minerals*, New York: Springer Verlag, 1984, chap. 12, 351-385.

8. N. S. Chickerur, M. S. Tung, and W. E. Brown, "A mechanism for incorporation of carbonate into apatite," *Calc. Tissue Int.* 32: 55, 1980.

9. M. Nishimo, S. Yamashita, T. Aoba, M. Okazaki, and Y. Moriwaki, "Laser-Raman spectroscopic studies of human enamel and precipitated carbonate-containing apatites," *J. Dent. Res.* 60: 751, 1981.

10. J. C. Elliott, D. W. Holcomb, and R. A. Young, "Infrared determination of the degree of substitution of hydroxyl by carbonate ions in human dental enamel," *Calc. Tissue Int.* 37: 372, 1985.

11. D. Daudon, M. F. Protat, R. J. Reveilland, and H. Jaeschke-Boyer, "Infrared spectrometry and Raman microprobe in the analysis of urinary calculi," *Kidney Int.* 23: 842, 1983.

12. A. Bigi, E. Foresti, A. Incerti, A. Ripamonti, and N. Roveri, "Structural and chemical characterization of the inorganic deposits in calcified human aortic wall," *Inorg. Chim. Acta* 55: 81, 1980.

13. H. C. Anderson, "Calcified diseases: A concept," *Arch. Pathol. Lab. Med.* 107: 341, 1983.

14. P. Vondracek and B. Dolezal, "Biostability of medical elastomers: A review," *Bio-materials* 5: 209, 1984.

15. W. S. Pierce, J. H. Donochy, G. Rosenberg, and R. E. Baier, "Calcification inside artificial hearts: Inhibition by Warfarin-sodium," *Science* 208: 601, 1980.

16. D. L. Coleman, D. Lim, T. Kessler, and J. D. Andrade, "Calcification of nontextured implanted blood pumps," *Trans. Am. Soc. Artif. Intern. Organs* 27: 97, 1981.

17. E. S. Etz, "Raman microprobe analysis: Principles and applications," *SEM/1979 I*, 67.

18. W. P. Griffith, "Raman spectroscopy of terrestrial minerals," in C. Karr Jr., Ed., *Infrared and Raman Spectroscopy of Lunar and Terrestrial Minerals*, New York: Academic Press, 1975, chap. 12, 299-323.

19. R. Z. LeGeros and M. S. Tung, "Chemical stability of carbonate and fluoride-containing apatites," *Caries Res.* 17: 419, 1983.

20. P. F. Schmidt, B. Hagen, and D. B. Leusmann, "Laser microprobe mass analysis of carbonate in apatite of biological concretions," *Microbeam Analysis--1985*, 331.

TABLE 1.--Chemical composition data of some biological tissues and calcified deposits. (Average values from bulk chemical analysis.)

Biological tissue or mineral	wt% Ca	wt% P	wt% (Ca + PO <sub>4</sub> )	Ca/P	wt% CO <sub>3</sub>
Human whole bone (mature; femoral shaft)	26.3	11.6	62.0	1.75	~4-~6
1-yr whole chicken bone (tibia)	25.5	11.5	60.7	1.71	6.3
Human (abdominal) aortic plaque (deproteinated)	34.7	15.8	82.0	1.76	7.0
Bioprosthetic (LVAD) calcified deposit in sheep (deproteinated)	34.1	16.3	83.0	1.67	7.1

## THE USE OF INFRARED AND RAMAN MICROSCOPY FOR THE ANALYSIS OF FAILED CIRCUIT BOARDS

Patricia Lang and J. E. Katon

The isolation and identification of particulates which cause or contribute to electronic failure is becoming increasingly important as our society grows more dependent on electronics to serve its needs. Particles that contaminate printed circuit boards (PCBs) can lead to short or open circuits, the results may range from a "downed" instrument to a loss of lives. Since the size of these contaminants is small, infrared and/or Raman microscopy must be used if molecular information of a selective nature is to be obtained. Once the particle is identified, the source of the contamination can be pursued.

One cause of circuit board failure is contamination by residues left from the soldering process. Water-soluble and activated rosin flux residues are particularly corrosive to copper, and although manufacturers take precautions to clean these residues from the PCBs, it is not unusual that the cause of electronic malfunction or failure can be traced to their presence.<sup>1</sup> In addition, polyglycols commonly used in water fluxes to increase flux retention at high temperatures may react with fiberglass substrates to degrade their insulation properties.<sup>2</sup>

In an effort to identify these contaminants we have built a spectral library of a variety of rosin fluxes, water-soluble fluxes, inorganic fluxes, residue removers, and metal surface activators. We have obtained infrared and Raman spectra on the bulk fluxes as well as the residues.

### *Infrared Analysis*

General sample preparation of the macro reference fluxes involved allowing a few drops of the flux solution to evaporate on a microscope slide until the residue just started to solidify. The residue was transferred onto a CsI plate by rolling a disposable pipet across the residue and then smearing it across the plate with the pipet. Infrared spectra were recorded on a Digilab FTS-14C/D Spectrometer.

These same residues were allowed to dry for several days at room temperature, after which time their infrared spectra were obtained with an Analect AQS-20M system which consists of an fX-6260 FTIR Spectrometer and an fXA-515 microscope module. Sample preparation consisted of removing a few of the particulates from the slide under a stereoscope with the aid of a sharp probe and placing them on a 6mm-diameter KCl window held in a center-holed metal slide. It was not uncommon to find an inhomogeneous residue. These inhomogeneities may result from a combination of flux, activators, thickening agents, and impurities.

We have examined small pieces of failed double-sided PCBs, most of which have obvious corroded solder joints and copper dendrites. However, no flux residue was visually apparent. We recorded the infrared spectra of the outer solder mask material and the middle fiberglass substrate to add to our reference files. Since the supplier of this particular group of boards suspected a water-soluble flux, we attempted first to extract these particles by covering the board with water and then pouring it off onto a warm slide where it was allowed to evaporate. The spectra of any residual solids were then obtained. In an attempt to recover any organics present, we extracted particles with chloroform by covering the corroded solder joint with chloroform and rolling the tip of a capillary tube around the joint until the chloroform evaporated. The spectra of residual solids which were left on the capillary tip were obtained.

Although the spectra of several particles from each board were recorded, many were identical or very similar to each other. Extractions from each of the boards produced similar results. It should be noted that residual solids may be the result of being dispersed (rather than soluble) in the water or chloroform. Figures 1 and 2 are repre-

---

The authors are at the Molecular Microspectroscopy Laboratory, Department of Chemistry, Miami University, Oxford, OH 45056.

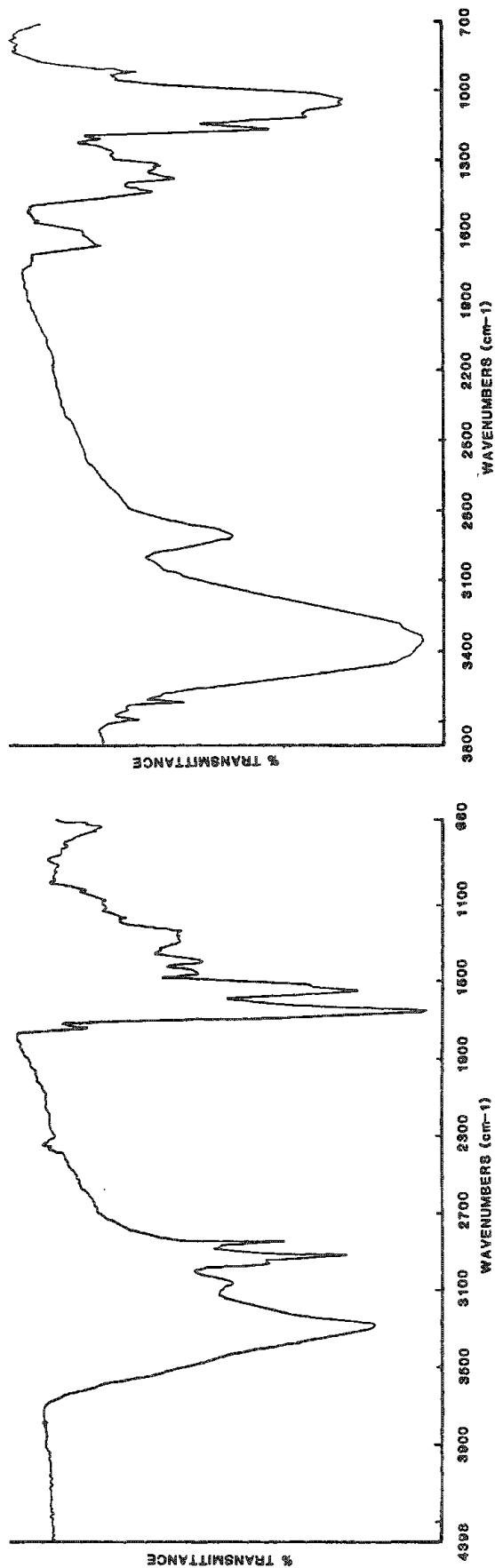


FIG. 1.--Spectrum of polyamide removed from PCB.

FIG. 2.--Spectrum of cellulosic removed from PCB.

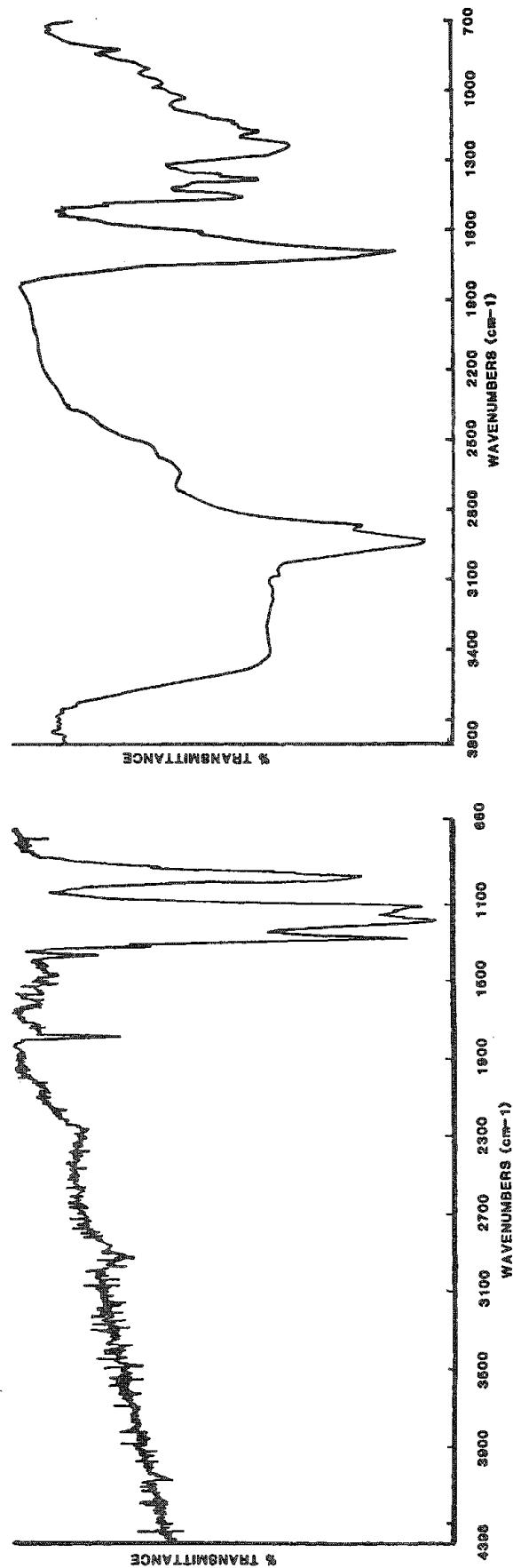


FIG. 3.--Spectrum of substance removed with chloroform extraction.

FIG. 4.--Spectrum of rosin flux residue removed from PCB.

sentative spectra of many of the particles removed from either the chloroform or water extraction. Figure 1 is the spectrum of a polyamide and matches a reference spectrum of a skin sample which we had obtained using the same instrument. In light of this finding, it seems appropriate to suggest that this contaminant was not the cause of PCB failure.

The spectrum shown in Fig. 2 is very similar to that of a cellulose fiber, a typical finding in office dust. Although the boards were received and stored in plastic bags, this spectrum, as well as other "cellulose-looking" spectra, were repeatedly obtained from the particles extracted from the boards. These spectra also match spectra obtained from residues of solder flux removers. We might speculate that a starchy substance was used as a thickening agent for these flux removers. Since starch and cellulose absorb moisture, it is possible that an excess of either contaminant could contribute to corrosion on a PCB.

Figure 3 shows the spectrum of particle obtained from a chloroform extraction. It is very similar to that of a polyfluorochlorocarbon. Since a weak C-H stretch is seen, it is reasonable to suggest that the substance contains a small amount of hydrogen. Halogenated hydrocarbons are a possible source for free halide ions, a potential threat to the PCB's copper circuitry.

A nonfunctioning PCB from a different source visibly showed an excess of residue around several solder joints. An infrared spectrum of the material, which was simply removed with a sharp probe, is shown in Fig. 4. The spectrum can be easily identified as abietic acid, the main constituent of rosin flux. Although none of the solder joints were visibly corroded, the outer layer of the insulating coating was soft and noticeably degraded in several areas near the solder joints.

#### *Raman Analysis*

The Raman spectra of all the flux reference solutions were obtained by capillary sampling with an ISA Ramanor U1000 spectrometer and the 514nm line from an argon laser used as the excitation wavelength. The Raman spectrum of many of the reference residues were obtained by means of the corresponding microscope attachment. However, the Raman spectrum of a large portion of the fluxes and the flux residues could not be obtained due to fluorescence.

Attempts to analyze the boards in situ failed due to excessive fluorescence.

#### *Conclusion*

Although in situ analysis of failed PCBs seems the ideal method, it has not as yet been a successful route via Raman microspectroscopy in this laboratory. Preliminary studies using longer wavelength excitation from a dye laser are currently under way. Infrared reflectance microspectroscopy on these PCBs will be attempted in the near future.

Another route for possible studies involves using a detergent to extract possible polyglycols which may be embedded in the fiberglass substrates.

#### *References*

1. B. C. Chung, M. P. Cassidy, and G. W. Graham, "Evaluation of flux performance, cleaning and reliability," *The Western Electric Engineer*, Jan. 1983, 30-36.
2. F. M. Zado, "Effects of non-ionic water soluble flux residues," *The Western Electric Engineer*, Jan. 1983, 41-48.

## RAMAN AND FTIR ANALYSIS OF THE INTERACTION BETWEEN A MODEL ORGANIC PESTICIDE AND A SOIL CONSTITUENT

J. M. Bowen, A. E. Ratcliffe, M. G. Rockley, A. W. Hounslow, and C. R. Powers

In this study, FTIR and Raman spectroscopic analyses were used to determine the adsorption interaction between the highly polar organophosphonate dimethyl methylphosphonate (DMMP), a relatively non-toxic phosphonate pesticide model compound,<sup>1</sup> and a clay mineral, calcium montmorillonite (SAZ-1). The DMMP molecule appears to interact with the interlamellar exchangeable cation in the montmorillonite clay and to displace water from the clay mineral interlamellar spaces. This finding was confirmed by XRD observation of a primary-lattice-distance expansion of 3.3 Å during the adsorption process. Some evidence for a secondary interaction of the DMMP with the natural organic matter associated with the clay minerals was obtained.

### *Experimental*

The clay mineral used was calcium montmorillonite (SAZ-1),<sup>2</sup> which was used without further treatment. The DMMP, obtained from Aldrich Chemicals as the 97% pure compound, was used without further purification. Infrared absorption spectra were obtained with an IBM IR/32 Fourier transform infrared spectrometer; Raman spectra were recorded on a ISA Ramanor U-1000 Laser Raman Microprobe. XRD spectra were obtained on a Nicolet powder x-ray diffractometer, from very thin clay films sedimented onto a ceramic filter.

Adsorption of the DMMP on to the clay was accomplished by vapor deposition at 40 C.

### *Results and Interpretation*

After adsorption of the DMMP by the clay there is a marked decrease in the broad 3430cm<sup>-1</sup> band in the OH stretching region and the 1635cm<sup>-1</sup> HOH bend when they are ratioed against the 1000cm<sup>-1</sup> Si-O stretch, which indicates that as the adsorption proceeds, it is the hydrogen bonded water, held primarily in the interlamellar spaces of the clay mineral, that is lost during the adsorption process. XRD diffraction patterns of the clay and DMMP-clay complex show that in response to the DMMP atmosphere the SAZ-1 expanded reproducibly to an interlamellar spacing of 3.3 Å, which is similar to the calculated thickness of the DMMP molecule if it is constrained to the flattened disk-shaped configuration of the electronic ground state.

Our results indicate that two bonding mechanisms are possible between the DMMP and the clay. The first is a direct coordination of the DMMP to the interlamellar cation by an ion-induced dipole interaction; the second, an indirect coordination or hydrogen bonding through a water molecule in the first coordination sphere of the cation.<sup>3</sup> The DMMP band that undergoes the largest frequency shift after adsorption, 21 cm<sup>-1</sup> to lower wavenumber, is the P=O stretching mode at 1244 cm<sup>-1</sup>. This bond must therefore be the site of the major specific interaction between the clay mineral and the DMMP.

The magnitude of the spectral shift should depend on the polarizing power of the cation if the interaction of the sorbate with the cation is not through a water bridge. If it is through the first hydration sphere, the shift should be small and little affected by the cation.<sup>3</sup> To establish this result, the calcium ions in the SAZ-1 were exchanged for potassium ions and the band shifts re-measured. The P=O shift in the potassium exchanged SAZ-1 was found to be only 6 cm<sup>-1</sup> downshift found in the calcium containing SAZ-1. Therefore, the interaction must be a direct ion-induced dipole coordination between the DMMP P=O functional group and the exchangeable cation.

No other band is similarly shifted so far in frequency, which indicates that no other interactions are evident. As a result of the interaction through the phosphonate oxygen, the DMMP molecule should undergo electronic rearrangement and leave the P atom with a partial positive charge, which should result in a strengthening of the P=O bond as a result of backbonding. This phenomenon is observed in the 6 and 7cm<sup>-1</sup> band shift to higher wavenumber for the 791 and 824cm<sup>-1</sup> PC<sub>2</sub> stretches, respectively. Other bands were shifted in ways that support this conclusion (Figs. 1 and 2).

In the course of this work, Raman spectra were found to be superimposed on a broad

---

The authors are at Oklahoma State University School of Geology, Stillwater, OK 74078.



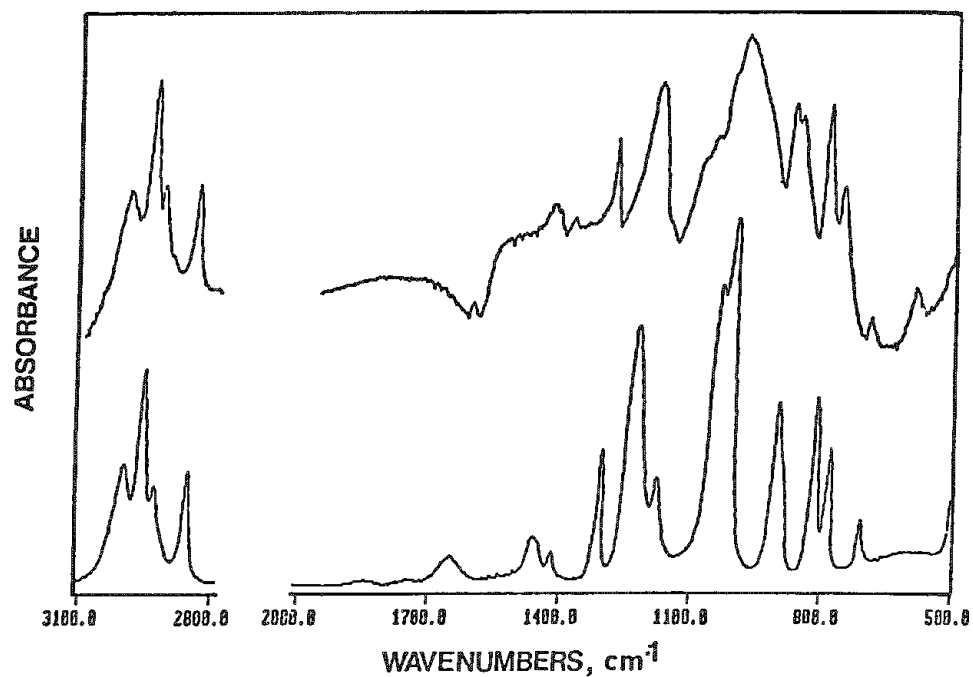


FIG. 1.--FTIR difference spectra of DMMP-clay complex compared with that of pure DMMP.

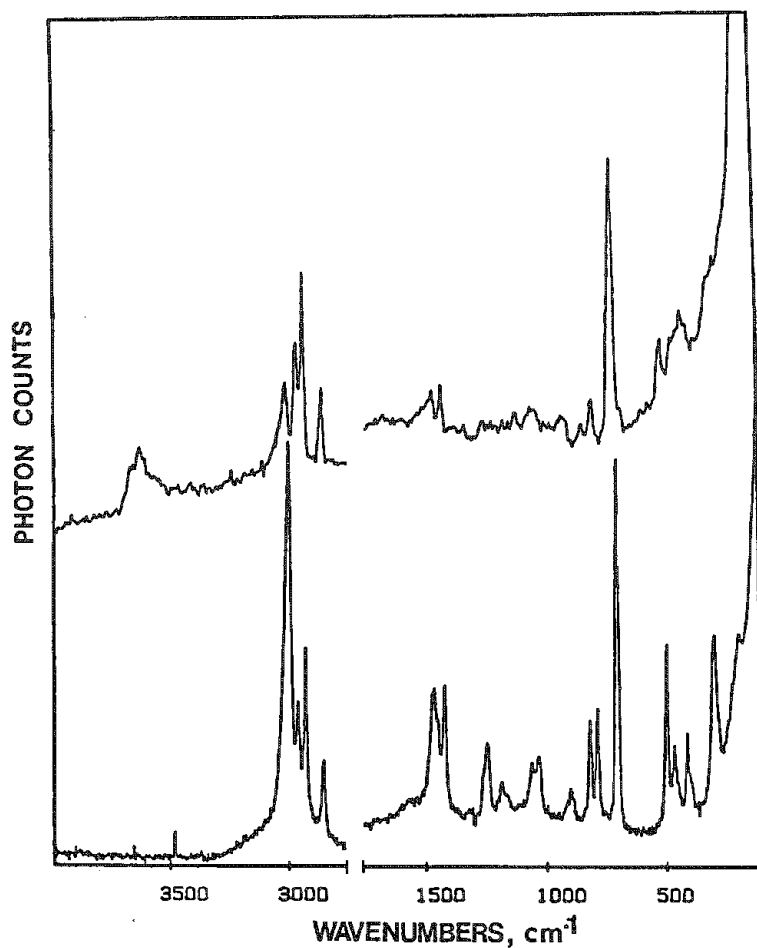


FIG. 2.--Raman spectra of DMMP-clay complex compared with that of pure DMMP.

emission background centered at  $600\text{ cm}^{-1}$  (Fig. 3). Emission is found in some minerals and is thought to be associated with acene moieties in natural soil organic material,<sup>4</sup> such as humic acids. The breadth of these bands and their lack of vibronic structure seem to indicate very large, high-molecular-weight aromatic structures. However, without additional studies, broadband emission from emission centers in minerals cannot be ruled out. This emission was noticeably quenched by adsorption of DMMP. The fact that the quenching takes place, and that quenching by charge-transfer or Forster dipole-dipole mechanisms are short-range effects, suggests that the emission originates from the exterior surface or from the interlamellar spaces. This quenching effect represents a second interaction of the DMMP with the clay, but detailed mechanistic understanding awaits more experimentation.

### Conclusions

It has been shown that the specific interactions between DMMP, a pesticide-like organic compound, and a natural montmorillonite clay mineral can be determined directly and rapidly by use of FTIR and Raman techniques, even when the vibrational modes are near the intense bands associated with the Si-O stretch. It was also determined with other techniques including FTIR-PAS as well as the use of very thin unsupported clay films, that for this particular type of experiment the use of KBr disks in the IR study is an applicable option.

### References

1. R. L. Hilderbrand, *The Role of Phosphonates in Living Systems*, Boca Raton, Fla.: CRC Press, 1983.
2. H. Van Olphen and J. J. Fripiat, *Data Handbook for Clay Materials and Other Non-metallic Minerals*, Elmsford, N.Y.: Pergamon Press, 1979. (Source of SAZ-1: Department of Geology, University of Missouri, Columbia, MO 65201.)
3. V. C. Farmer, "The characterization of adsorption bonds in clays by infrared spectroscopy," *Soil Science* 112: 62-68, 1971.
4. S. A. Visser, "Fluorescence phenomena of humic matter of aquatic origin and microbial cultures," in R. F. Christman and E. T. Gjessing, Eds., *Aquatic and Terrestrial Humic Materials*, Ann Arbor, Mich.: Ann Arbor Science, 1983, 183-202.

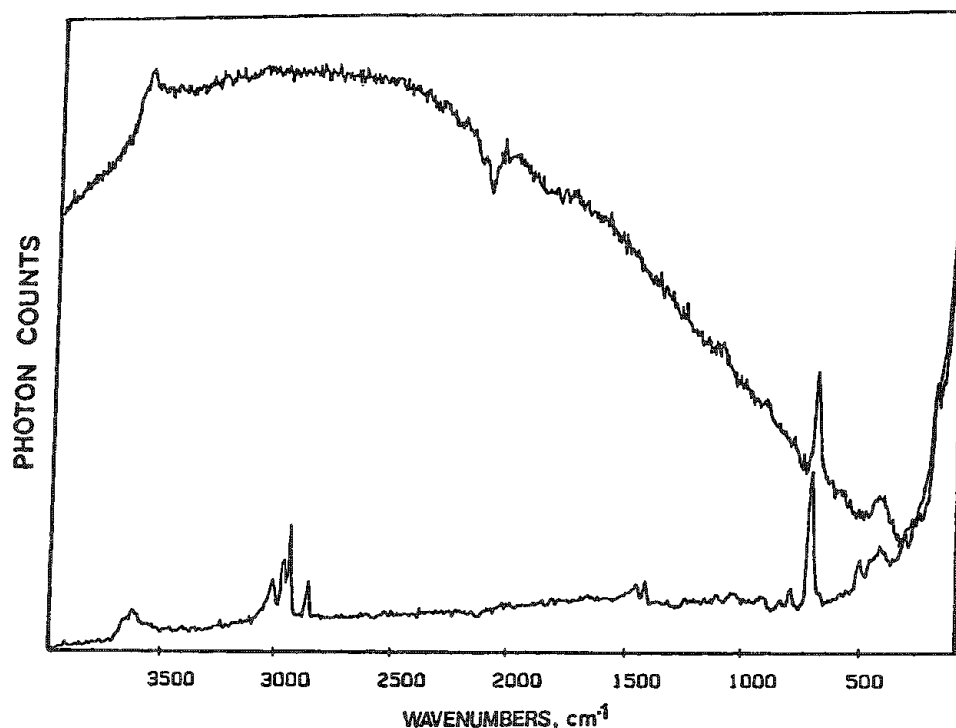


FIG. 3.--Raman spectra of Ca montmorillonite before and after adsorption of DMMP.

## Microanalysis in Joining

### USE OF ANALYTICAL ELECTRON MICROSCOPY IN EVALUATING FERRITE STABILITY IN AUSTENITIC STAINLESS-STEEL WELDS

J. M. Vitek and S. A. David

Stainless-steel weld filler metals are prone to hot-cracking during welding. Although the mechanisms that control hot-cracking are not completely understood, it has been shown that if the primary mode of solidification is ferrite formation rather than austenite formation, the tendency for hot-cracking is substantially reduced.<sup>1-3</sup> Type 308 stainless steel is a typical example of such a filler metal, which solidifies as primary ferrite and is relatively immune to hot-cracking problems. During further cooling, the primary ferrite transforms to austenite.<sup>4</sup> Although ferrite is not an equilibrium phase below approximately 900 C for type 308 stainless steel, the cooling rates encountered during welding are sufficiently high so that 5-15% ferrite is retained at room temperature.<sup>4</sup> Consequently, when such duplex austenite plus ferrite weld microstructures are subjected to elevated temperature applications, the residual ferrite is unstable and transforms. The stability of retained ferrite has been the subject of an ongoing investigation at the Oak Ridge National Laboratory. Analytical electron microscopy has been extensively employed to investigate ferrite stability. The ability to do chemical analyses of ferrite on a fine scale has proved to be invaluable. The results have provided critical data leading to new insights into the stability of ferrite during welding and also during service at elevated temperatures. Such information is important in being able to predict weld microstructures based on thermal histories. The object of this paper is to consider three cases in which the use of analytical electron microscopy has paved the way for a basic understanding of ferrite stability in duplex type 308 stainless-steel welds.

#### Procedure

Two alloys were used in the investigation; their compositions are listed in Table 1. In addition to a standard type 308 austenitic stainless steel, a modified alloy with controlled residual element (CRE) additions, to be referred to as type 308CRE, was employed. Although the type 308CRE alloy behaves differently during aging with regard to precipitation,<sup>5,6</sup> the two alloys show similar behavior with respect to ferrite stability, so that results from the two alloys may be combined.

TABLE 1.--Compositions of alloys used in this study (wt.%).

	Cr	Ni	Mn	Si	C	P	S	Ti	B
Type 308	20.21	9.36	1.75	0.46	0.05	0.018	0.008	<0.01	0.002
Type 308 CRE	19.96	9.98	1.96	0.62	0.04	0.011	0.015	0.57	0.002

The type 308 stainless steel was evaluated in the as-solidified condition. Gas tungsten arc (GTA) and autogenous laser welding, as well as a hammer-and-arc splat cooling process, were used to provide a range of cooling rates and to investigate the composition and stability of ferrite as a function of cooling rate. Further details on each of these methods are provided elsewhere.<sup>5,8</sup> The type 308CRE material was also evaluated after aging of initially homogenized material. A homogenization treatment of 1080 C/1 h was used and yielded a duplex austenite plus ferrite microstructure.<sup>6</sup>

The authors are at the Metals and Ceramics Division, Oak Ridge National Laboratory, Oak Ridge, TN 37831. They wish to acknowledge the technical assistance of W. H. Smith, K. F. Russell, and R. W. Reed; and to thank Brenda Hickey and Frances Scarboro for preparation of the manuscript. The research was sponsored by the Division of Materials Sciences, U.S. Department of Energy, under contract DE-AC05-84OR21400 with Martin Marietta Energy Systems, Inc.

Thin wafers were cut from the various materials and 3mm-diam. disks were electrodischarge machined from these wafers. After mechanical grinding to a thickness of 0.25 mm (0.010 in.), the specimens were electropolished in a Tenupol twin-jet polisher. A polishing solution of 58.5% methanol, 35% ethylene glycol, 6% perchloric acid, and 0.5% glycerin was used at -10 C. The polishing conditions were set at 25 V and 120 mA. Analytical microscopy was performed on a JEM 100CX electron microscope with an energy-dispersive spectrometer (EDS). Compositions were determined by a standardless technique with calculated conversion factors. Only the major constituents (iron, chromium, and nickel) were analyzed, and the results for these three elements were normalized to 100%. Measurements were made in areas less than 300 nm thick so that absorption effects among these three elements were inconsequential and could be ignored.

## Results and Discussion

*Metastable Equilibrium of Ferrite.* During the aging of duplex austenite plus ferrite welds, the ferrite typically becomes enriched in chromium and depleted in nickel as partial dissolution of ferrite takes place.<sup>5-7</sup> This phenomenon was investigated in detail by analysis of the ferrite compositions as a function of aging time and temperature.<sup>7</sup> It was found that the ferrite chromium content approached a limiting value at any given temperature (Fig. 1). This limiting composition was typically achieved as a result of chromium enrichment of the ferrite. However, under certain conditions, for which the initial chromium level was high, the equilibrium composition was reached as a result of chromium depletion and nickel enrichment. These results indicate that the limiting ferrite composition corresponds to a metastable equilibrium between the ferrite and austenite matrix. The approach to metastable equilibrium occurs independently of any subsequent transformations. Eventually, the ferrite was found to transform to sigma phase. Using a plot of ferrite composition in metastable equilibrium vs temperature (Fig. 2), one can predict the behavior of ferrite and its compositional changes as a function of heat treatment. This valuable information could be determined only by analytical electron microscopy and the ability to evaluate compositions of minor constituent phases on a fine scale.

*Cooling-rate Effects.* In addition to the changes in composition that occur after aging, the composition of ferrite in as-solidified materials has been found to depend on cooling rate. As the cooling rate increases, the chromium content of the ferrite decreases and the nickel concentration increases. For splat-quenched foils, with cooling rates on the order of  $10^6$  C/s, a chromium content of 26 wt.% was measured. The ferrite in laser-welded samples, which were cooled at lower rates, contained 29 wt.% Cr. The lowest cooling rates correspond to GTA weld specimens in which the ferrite contained 30 wt.% Cr. These results indicate that even under the most rapid cooling rates considered, significant partitioning of chromium and nickel still occurs. (In order to make a proper comparison, considering only iron, chromium, and nickel, the normalized base material composition in wt.% is approximately 69 Fe, 20.7 Cr, and 10.3 Ni.) The dependence of composition on cooling rate can be understood by reference to the metastable equilibrium ferrite concentration as a function of temperature that was described above and plotted in Fig. 2. If one assumes the ferrite is in equilibrium at some high temperature, the composition of the ferrite changes during cooling in order to remain in (metastable) equilibrium. As the temperature decreases, the ferrite composition varies according to the equilibrium limits in Fig. 2 as long as this equilibrium can be maintained. Eventually, a condition is reached where insufficient time is available for the ferrite composition to adjust in order to maintain metastable equilibrium. Little composition change occurs beyond this point and the ferrite composition is frozen in. As the cooling rate increases, the point at which equilibrium can no longer be maintained occurs sooner. Thus, high cooling rates should quench in high-temperature ferrite compositions (lower chromium, higher nickel), whereas low cooling rates quench in ferrite compositions corresponding to lower temperatures (higher chromium, lower nickel). That is exactly the behavior found.

It is interesting to compare the results on laser welds with those on GTA welds and splat-quenched samples. It has been shown that the mode of solidification changes to primary austenite formation in type 308 stainless steel at very high solidification rates.<sup>9</sup> Both laser welds and splat-quenched material exhibited this change in solidification mode, which shows that comparable solidification rates for the two processes exist. These

solidification rates are orders of magnitude greater than those for more conventional welding techniques. It therefore comes as something of a surprise that the ferrite compositions measured on laser-welded samples are close to those measured on GTA welds and significantly richer in chromium than the ferrite composition in splat-quenched samples. These composition results indicate that although the cooling rate during solidification of laser welds is high enough to produce a structure comparable to that formed by splat-quenching, the cooling rate decreases significantly during solid-state cooling. Thus, the solid-state cooling rate during laser welding approaches that found in GTA welds and is significantly lower than the solid-state cooling rate of splat-quenched materials. This conclusion is reasonable since the laser-welded materials involve a much greater volume of molten material than the splat-quenched foils, and the heat is removed through the lower-conductivity austenitic stainless steel in the laser welds rather than through a high-conductivity substrate as employed in the splat-quenching process.

*Sigma Phase Transformation.* The use of analytical electron microscopy and the ability to evaluate the compositions of minor, and even rare, constituents directly has been very helpful in gaining an insight into the sigma phase transformation.<sup>10</sup> In particular, the composition of ferrite was determined after aging of homogenized type 308CRE stainless steel 10 000 h at 650 C. Under these conditions, nearly all of the ferrite has transformed to sigma phase. However, a few grains of ferrite were observed to be untransformed. These areas were analyzed by EDS; typical spectra are shown in Fig. 3. Analysis of the spectra yielded the following results (wt.%): Ferrite, 60 Fe, 37 Cr, 3 Ni; Sigma, 57 Fe, 38 Cr, 4 Ni. The results indicate the ferrite has been enriched in chromium after aging for 10 000 h at 650 C to such a degree that its composition is basically identical to that of the sigma phase. Thus, no further diffusion is necessary to form sigma phase, and yet the ferrite has not transformed. This result, in combination with other arguments,<sup>10</sup> indicates the sigma-phase transformation is nucleation controlled, and the compositional changes necessary to form sigma phase can only be of secondary importance. Such a clear conclusion could not be made without the use of analytical electron microscopy. Since the residual ferrite is such a minor constituent after aging so long at 650 C, no other technique could identify and evaluate the ferrite composition so precisely.

### Summary

Analytical electron microscopy provides a means of readily evaluating compositions on a scale of 1  $\mu\text{m}$  and less. This unique capability is extremely valuable in that small regions, as well as minor phase constituents in a microstructure, can be evaluated. The technique has been employed extensively on welds of type 308 stainless steel that contain 15% or less ferrite in an austenite matrix. Three cases were examined in which the evaluation of ferrite composition has led to a better understanding of ferrite stability in these duplex weld structures. Following the ferrite composition as a function of aging has shown that the ferrite approaches a metastable equilibrium during aging, independent of any subsequent phase transformations. An evaluation of ferrite composition as a function of cooling rate has shown that during solid-state cooling, the ferrite composition varies in order to maintain metastable equilibrium as much as possible, until eventually a fixed composition is quenched-in. Analytical electron microscopy has also shown that the solid-state cooling rates of laser welds are comparable to those prevalent in more conventional welding processes. Finally, the ability to measure ferrite composition after long-term aging when the ferrite phase is only a very minor constituent has provided new insight into the mechanism of the ferrite-to-sigma phase transformations.

### References

1. J. C. Borland and R. N. Younger, *Brit. Welding J.* 7: 22-60, 1960.
2. F. C. Hull, *Welding J.* 46: 399s-409s, 1967.
3. Y. Arata, F. Matsuda, and S. Katayama, *Trans. Jap. Welding Res. Inst.* 5: 35-51, 1976.
4. S. A. David, G. M. Goodwin, and D. N. Braski, *Welding J.* 58: 330s-336s, 1979.
5. J. M. Vitek and S. A. David, *Welding J.* 63: 246s-253s, 1984.
6. J. M. Vitek and S. A. David, to be published.
7. J. M. Vitek and S. A. David, *Scripta Metall.* 19: 23-26, 1985.

8. J. M. Vitek, A. DasGupta, and S. A. David, *Metall. Trans.* A14: 1833-1841, 1983.
9. S. A. David and J. M. Vitek, in S. Steeb and H. Warlimont, Eds., *Proc. International Conf. on Rapidly Quenched Metals*, Amsterdam: Elsevier, 1985, 847-850.
10. J. M. Vitek and S. A. David, *Welding J.* 65: 106s-111s, 1986.

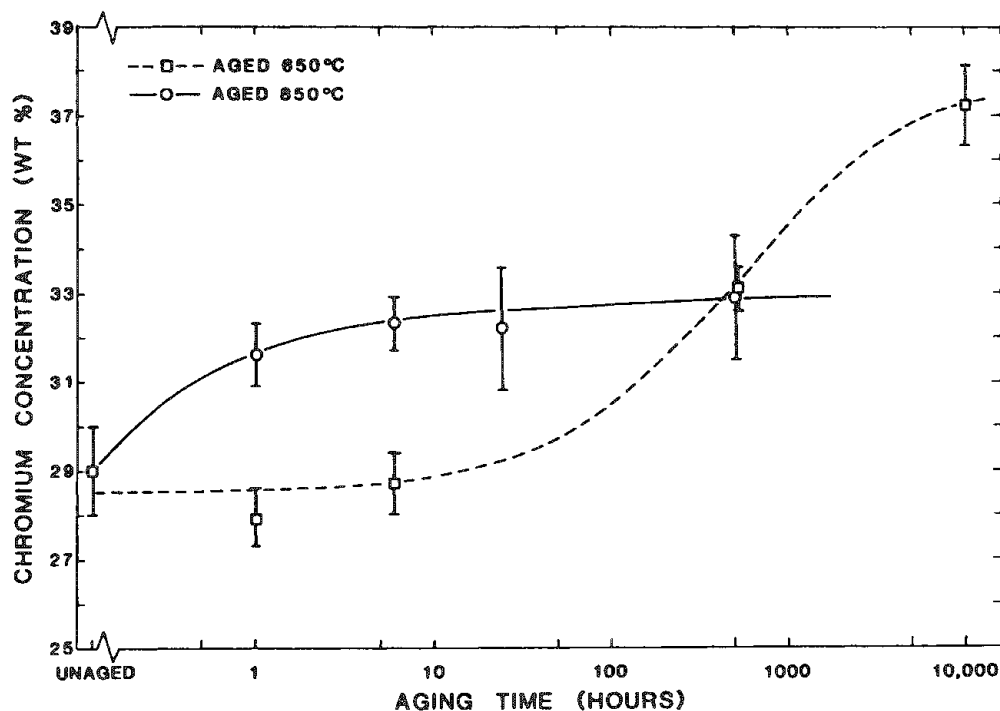


FIG. 1.--Variation of chromium concentration of ferrite as a function of aging time at two different temperatures.

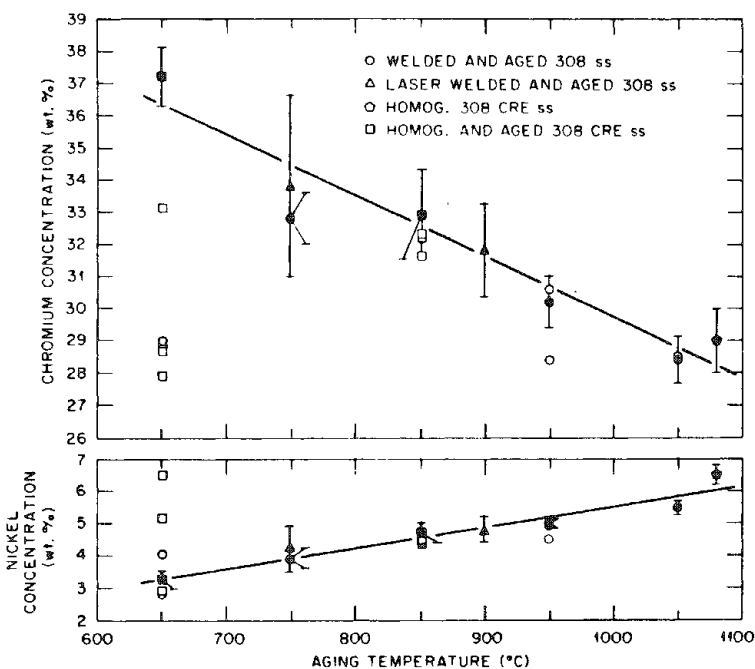


FIG. 2.--Metastable equilibrium composition of ferrite as a function of temperature for types 308 and 308 CRE stainless steels. Data points for longest aging times are filled in.

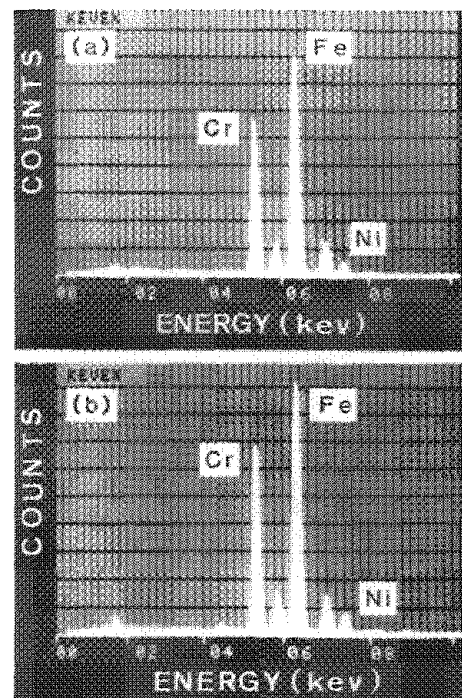


FIG. 3.--EDS spectra of (a) ferrite and (b) sigma phase in type 308 CRE stainless steel aged 10 000 h at 650 C.

## A MICROANALYTICAL STUDY OF SEGREGATION DURING SOLIDIFICATION AND HEAT TREATMENT OF 12Cr-1Mo WELDMENTS

J. C. Lippold, A. D. Romig Jr., and W. R. Sorenson

The 12Cr-1Mo stainless steels are being considered in many engineering applications as potential replacements for austenitic stainless steels. These steels possess comparable strength and creep resistance at elevated temperature and can provide significant material cost savings relative to 300-series stainless steels.<sup>1</sup> However, these potential benefits are balanced by the additional precautions that must be taken when using 12Cr-1Mo steels in welded structures. Nominal weld cooling rates result in the formation of untempered martensite ( $\alpha'$ ) in the weld fusion zone and heat-affected zone (HAZ).<sup>1,2</sup> A postweld heat treatment (PWHT) in the temperature range from 600 to 750 C is required to temper this martensite and thereby reduce the as-welded hardness and restore the toughness of the weld region.<sup>3,4</sup>

Alloy element partitioning during weld solidification results in the formation of a high temperature ferrite ( $\delta$ ) which is retained upon cooling.<sup>2,5</sup> The presence of ferrite in the microstructure may further compromise the properties of welded 12Cr-1Mo steels, particularly if it persists after PWHT. The purpose of this investigation was to utilize microanalytical techniques to characterize the as-welded fusion zone microstructure in a 12Cr-1Mo steel and determine the effect of PWHT on the evolution of this structure, particularly with respect to ferrite formation/dissolution and carbide precipitation.

### *Experimental Procedure*

The composition of the material used in this investigation was 12.1 Cr, 1.04 Mo, 0.51 Ni, 0.57 Mn, 0.45 W, 0.28 V, 0.17 Si, 0.20 C, 0.027 N, 0.016 P, and 0.003 S (all in wt.%). The material was in the form of 10mm-thick plate. Autogenous, bead-on-plate welds were made with the welding conditions shown in Table 1. No preheat was applied prior to welding and the welds were allowed to cool in air to room temperature. A number of welds were subjected to a PWHT at 600 C for 1 h followed by air cooling.

Transverse weld sections were mounted for metallographic examination and electron probe microanalysis (EPMA). Vilella's reagent was used to reveal the microstructural details of the fusion zone. EPMA was performed at 15 kV at a beam current of 15 nA. Under these conditions, in an iron-based specimen, the volume of x-ray generation is approximately 1  $\mu$ m in diameter. Specimens for analytical electron microscopy (AEM) were sliced from transverse sections of the weld fusion zone with a slow-speed diamond saw. After grinding to a thickness of approximately 125  $\mu$ m, 3 mm-diameter disks were mechanically punched from the slices. These disks were electrojet thinned in 10% perchloric (in methanol) at -50 C at 15 V and 18 mA. Final cleaning was performed by ion milling. Extraction replicas for carbide analysis were prepared with standard replication techniques.<sup>6</sup>

A JEOL 100C analytical electron microscope (AEM) equipped with a side-entry EDS x-ray detector and a Tracor Northern TN2000 multichannel analyzer were used to examine the thin foil specimens. The AEM was operated at 100 kV with a nominal beam diameter of 18 nm. All analyses were performed in regions of the foil which satisfied the thin film criterion.<sup>7</sup> X-ray data were converted into weight percents with the Cliff-Lorimer ratio technique.<sup>8</sup> The sensitivity factors used in the Cliff-Lorimer data reduction technique were

TABLE 1.--Welding conditions.  
Process: Gas tungsten-arc welding (GTAW)  
Current: 150 A  
Voltage: 10 V  
Travel speed: 2.54 mm/s  
Shielding gas: Argon

Author Lippold is with the Edison Welding Institute, Columbus, OH 43212. Authors Romig and Sorenson are with Sandia National Laboratories, Albuquerque, NM 87185. This work was supported by the U.S. Department of Energy under Contract Number DE-AC04-76DP00789.

experimentally determined from alloys and compounds of known composition. The compositional results were calculated with a standard computerized data reduction scheme.<sup>7</sup>

## Results and Discussion

**EPMA and Optical Metallographic Analysis: As-welded Microstructure.** The as-welded fusion zone microstructure of the martensitic stainless steel evaluated in this investigation is shown in Fig. 1. Ferrite ( $\delta$ ) is evident along prior solidification subgrain boundaries within the untempered martensite ( $\alpha'$ ) matrix. EPMA of the as-welded structure revealed a distinct variation in composition between the ferrite and the surrounding martensite. In addition, the composition of the martensite varies as a function of the location in the weld solidification structure. The results of EPMA point analysis are shown in Table 2. Note that the ferrite is enriched in ferrite-forming elements (Cr, Mo, V, and W) relative to the martensitic structure. In addition, solidification boundary regions devoid of ferrite are enriched in these same elements relative to the core of the solidification subgrain.

The distribution of Cr, Mo, and W across a ferrite-free solidification subgrain boundary is illustrated by the EPMA traverse shown in Fig. 2. Alloying element enrichment is evident over a 4  $\mu$ m-wide band centered on the boundary. The shape of the compositional profile is representative of partitioning during weld solidification,<sup>9</sup> despite solid-state diffusion which undoubtedly modified the original profile during cooling from the solidification temperature range. Diffusion during cooling tends both to reduce the peak boundary composition and to decrease the extent of enrichment along the boundary. The degree of "compositional smoothing" is a function of the rate of cooling and the nature of the solidification and transformation products that are present at high temperatures. However, the transformation of the primary ferrite to austenite ( $\gamma$ ) at a temperature slightly below the solidification temperature range in 12Cr-1Mo steel inhibits compositional smoothing due to significantly lower diffusivity in austenite relative to ferrite.<sup>10</sup> This austenite persists on cooling to a temperature of approximately 240 C at which point the martensite transformation begins.<sup>11</sup>

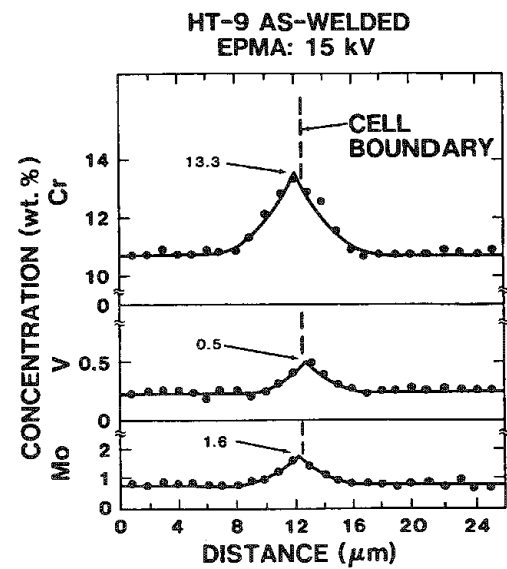
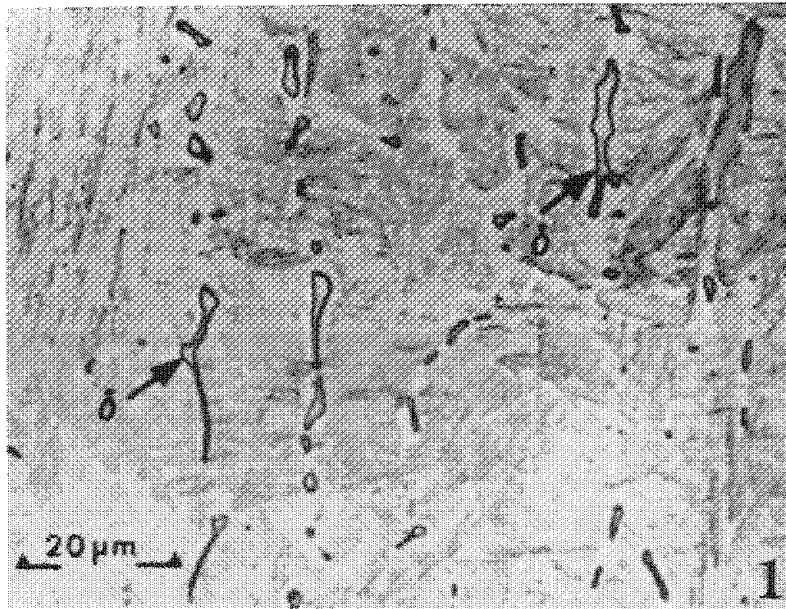
TABLE 2.--EPMA results: As-welded condition (all compositions in wt.%).

Element	Subgrain Core	Subgrain Boundary	Ferrite
Cr	10.65	13.32	14.00
Mo	0.85	1.61	1.91
V	0.28	0.47	0.60
W	0.54	0.71	0.88
Si	0.19	0.21	0.25
Mn	0.41	0.51	0.44
Ni	0.47	0.58	0.43

**AEM Analysis: As-welded and Tempered Microstructures.** The AEM was used for a more careful study of the nature of alloying element partitioning along solidification subgrain boundaries and at the ferrite-martensite interface in both as-welded and tempered samples. A transmission electron micrograph of a solidification subgrain boundary and the boundary ferrite in the as-welded structure are shown in Fig. 3. Compositional traverses, with the AEM operated in the scanning transmission electron microscope (STEM) mode, were performed across both ferrite-free cell boundaries and the ferrite-martensite interfaces (Fig. 3). Only Cr and Mo were present at concentration levels sufficient for reliable analysis in the AEM. Compositional profiles measured across ferrite-free cell boundaries in both the as-welded and tempered condition are shown in Figs. 4(a) and (b), respectively. Compositional profiles measured across ferrite-martensite interfaces in as-welded and tempered specimens are shown in Figs. 5(a) and (b), respectively.

The as-welded compositional profile in Fig. 4 corroborates the segregation pattern measured by EPMA. However, AEM indicates that the alloying element enrichment is actually restricted to a 2  $\mu$ m-wide region centered on the solidification subgrain boundary. In addition, the peak Cr and Mo concentrations at the boundary are higher than those detected by EPMA (Fig. 2) and illustrate the advantages of AEM in detecting actual concentration profiles. PWHT at 600 C results in a slight decrease in the maximum Cr and Mo concentration at the boundaries. It is evident that diffusion of both Cr and Mo, and probably W and V, is quite sluggish at this temperature. Homogenization of the compositional gradients established during solidification would require either extremely long times at 600 C or a PWHT at a higher temperature.





2

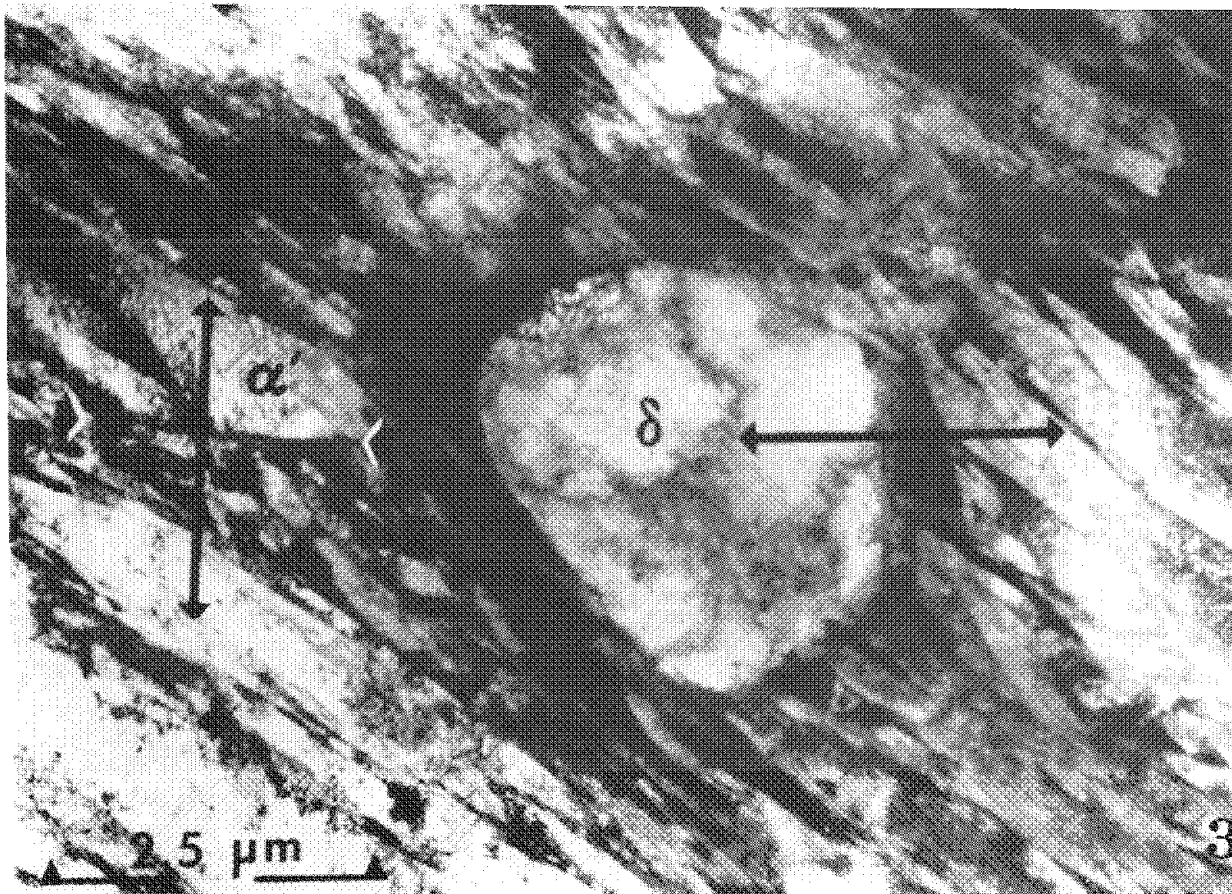


FIG. 1.--As-welded fusion zone microstructure. Arrows indicate ferrite along solidification subgrain boundaries.

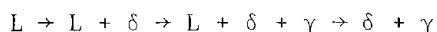
FIG. 2.--Results of EPMA traverse across ferrite-free solidification subgrain boundary in as-welded microstructure.

FIG. 3.--TEM image of as-welded microstructure. Ferrite-free cell boundary and cell boundary ferrite are visible in microstructure. Positions of STEM traverses are indicated.

AEM traverses across ferrite-martensite interface in both as-welded and tempered samples (Fig. 5) corroborate the Cr and Mo enrichment in the ferrite observed previously with EPMA. In addition, AEM revealed the presence of Cr and Mo compositional profiles in the martensite (originally austenite) and ferrite, which are a maximum at the interface. The shape of these profiles suggests the growth of the high-temperature austenite into the ferrite (ferrite dissolution) during cooling from the solidification temperature range. Under isothermal conditions, and assuming binary alloy type behavior, the austenite would grow at a constant composition; the composition at the ferrite-austenite interface would be that given by the equilibrium tie-line; and a steep compositional gradient would exist in the ferrite as a consequence of the rejection of Cr from the austenite into the ferrite. However, in this case, the diffusion is nonisothermal, and the solubility of Cr in both the ferrite and austenite increase with decreasing temperature,<sup>12</sup> which causes a continual readjustment of the interface composition with temperature, and an apparent increase in Cr content in the austenite as the ferrite-austenite interface is approached. The profile in the ferrite is also shallower and shorter than in the austenite due to the increase in Cr solubility in the austenite with decreasing temperature<sup>12</sup> and the more rapid diffusion in open structured (body centered cubic) ferrite.<sup>10</sup> Hence, the observed AEM profile shown in Fig. 5(a) can be predicted via nonisothermal diffusion.<sup>13</sup>

Upon PWHT at 600 C, diffusional leveling of Cr and Mo at the ferrite-martensite interface is clearly evident by AEM (Fig. 5). The profile is typical of a classical single phase diffusion couple, with the starting profile represented by the as-welded condition. Note that the composition gradient in the ferrite is very shallow as the ferrite dissolves and Cr and Mo diffuse into the surrounding martensite. The more rapid diffusion of alloying elements in the highly dislocated martensite also explains the extent of the Cr and Mo profiles in the heat treated fusion zone microstructure.<sup>13</sup>

*Predicted Solidification and Transformation Behavior.* Solidification and transformation behavior of martensitic stainless steels can be estimated with the Fe-Cr-C phase diagram. Reference to a series of constant carbon sections of the Fe-Cr-C ternary diagram may be useful for understanding the solidification sequence during *equilibrium* cooling.<sup>12</sup> As a first approximation, one can refer to the section at 0.20 wt.% C, which predicts



However, the alloy under study contains significant amounts of Mo, W, Si, and V, which are relatively strong ferrite stabilizers; and only small amounts of Ni, Mn, and N, which are relatively weak austenite stabilizers. Considering the effects of these other alloying elements, it is useful to examine sections of the Fe-Cr-C ternary with greater ferrite stability.<sup>12</sup> In such a case, one might postulate:

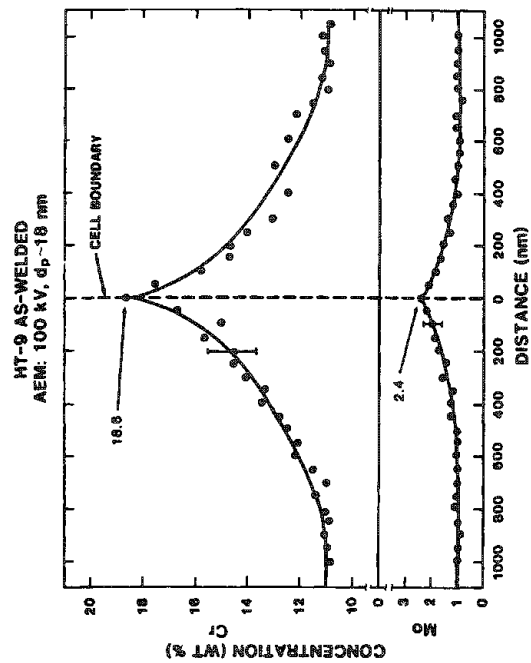


In the present study, the microstructural evidence *suggests* primary solidification of ferrite with a subsequent solid-state transformation of the solute-lean ferrite to austenite. Such a sequence is consistent with the segregation of the ferrite forming elements to the solidification subgrain boundaries. The solute-enriched ferrite at the cell boundaries remains stable on further cooling to room temperature. It is not possible to identify the precise transformation sequence unambiguously from microstructural evidence alone. However, future differential thermal analysis results may assist in positive identification of the solidification sequence.

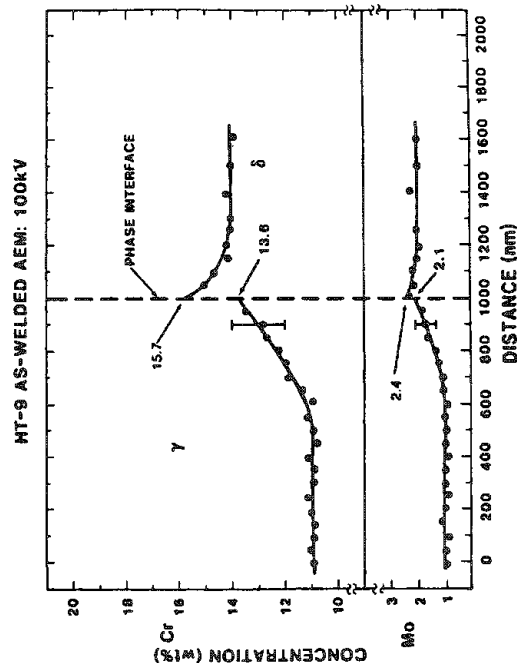
Cooling in the solid state is sufficiently rapid to cause the austenite to transform to martensite. Therefore, the final stages of solid-state transformation behavior in the alloy are,



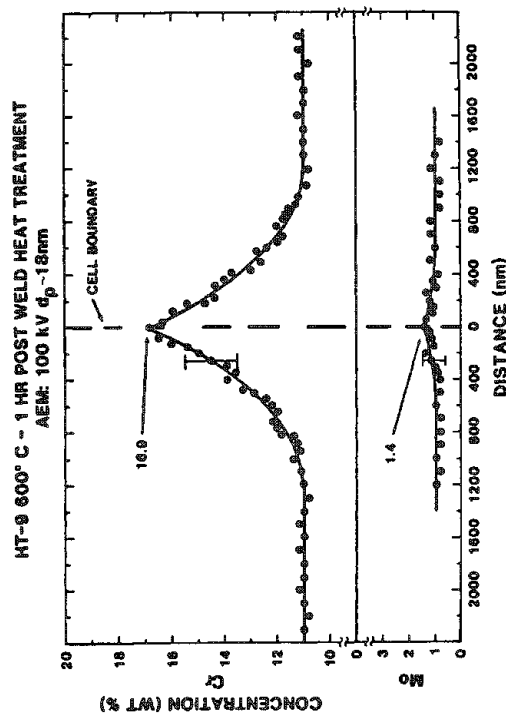
However, the rapid heating and cooling rates associated with welding may alter the solidification and transformation sequence predicted under equilibrium conditions resulting in nonequilibrium transformation products and composition gradients in the as-welded microstructure.



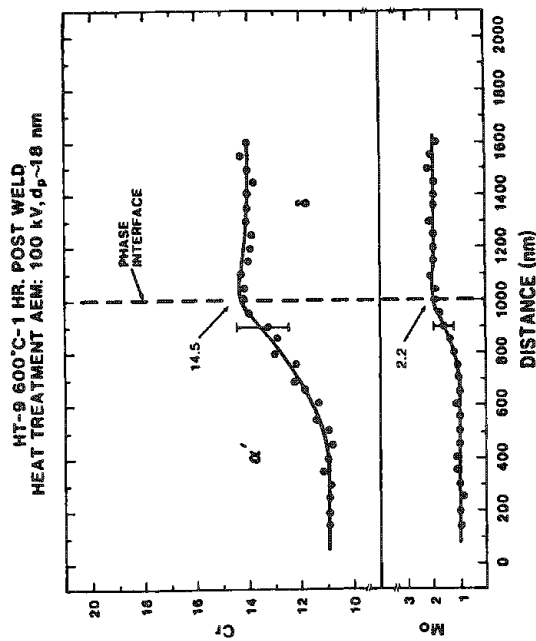
(a)



(a)



(b)



(b)

FIG. 4.--Results of STEM traverses across ferrite-free solidification subgrain boundaries: (a) as-welded condition. (b) 600 C PWHT condition.

FIG. 5.--Results of STEM traverses across ferrite-martensite interface: (a) as-welded condition, (b) 600 C PWHT condition.

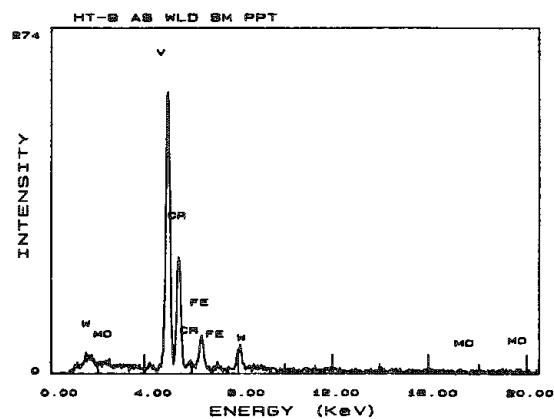
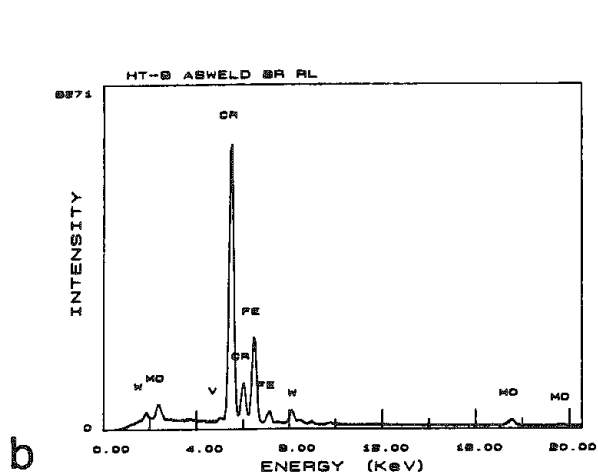
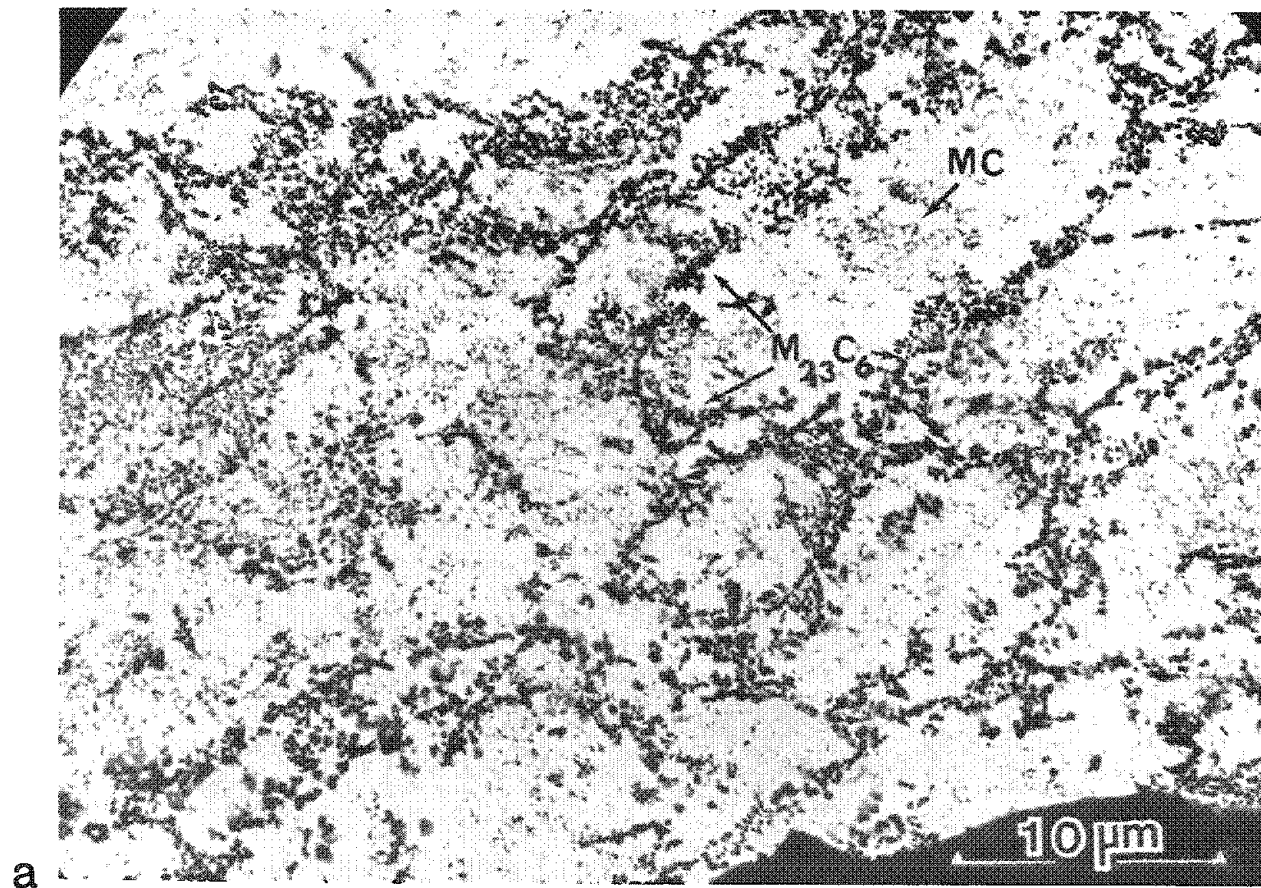


FIG. 6.--Carbide distribution and identification in as-welded condition: (a) extraction replica, (b) EDS spectrum of grain boundary Cr-rich  $M_{23}C_6$  carbides, (c) EDS spectrum of Mo-rich MC carbides.

*Carbide Dissolution.* The nature and distribution of alloy carbides is also influenced by the degree of partitioning during solidification and the modification of this segregation pattern during weld cooling and subsequent PWHT. An extraction replica illustrating the distribution of carbides in the as-welded microstructure is shown in Fig. 6(a). Carbides which have formed on cooling from the solidification temperature range are concentrated along the solidification subgrain boundaries. EDS analysis of these carbides (Fig. 6b) revealed that they are primarily Cr-rich  $M_{23}C_6$ . V-rich MC carbides were also identified (Fig. 6c) and were most prevalent within the solidification subgrains. Neither Mo- nor W-rich carbides were observed in the as-welded fusion zone microstructure.

Examination of extraction replicas from heat treated samples indicated that PWHT at 600 C has little effect on either the nature or distribution of the carbides. The imperceptible change in carbide distribution is consistent with tempering data for this alloy,<sup>2,3</sup> which indicates that only a small decrease in hardness occurs upon tempering at 600 C. Since the reduction in martensitic hardness by PWHT (tempering) is associated with the formation of carbides, the density and distribution of alloy carbides is a good indication of the relative level of tempering. These results suggest that higher PWHT temperatures are required to temper the fusion zone in 12Cr-1Mo welds. Even at higher PWHT temperatures, however, it would be expected that alloy carbides would form preferentially in the segregated regions at the solidification subgrain boundaries.

### Summary

Microstructural evidence suggests that the solidification of welds in 12Cr-1Mo steels proceeds according to the following sequence.



During solidification as primary ferrite, ferrite forming elements (Cr, Mo, V, W) segregate to solidification subgrain boundaries, thereby stabilizing the ferrite and inhibiting transformation to austenite upon cooling. The as-welded fusion zone microstructure consists of a mixture of retained high-temperature ferrite, untempered martensite, and alloy carbides. PWHT at 600 C results in "smoothing" of the segregation profiles established during solidification, both along solidification subgrain boundaries and at ferrite-martensite interfaces. Carbides in the as-welded microstructure are concentrated along the Cr- and Mo-rich subgrain boundaries. PWHT had little influence on the nature or distribution of carbides.

### References

1. C. H. Kreischer, T. Cothren, and A. E. Near, *Welding J.* 40: 489s, 1961.
2. J. C. Lippold, *J. Nuc. Matls.* 103/104: 1127, 1981.
3. J. C. Lippold, in J. W. Davis and D. W. Michel, Eds., *Proc. Topical Conference on Ferritic Alloys for Use in Nuclear Energy Technologies*, Snowbird, Utah, 1983.
4. J. Z. Briggs and T. D. Parker, *The Super 12% Chromium Steels*, New York: Climax Molybdenum Company, 1965.
5. R. Castro and J. J. de Cadenet, *Welding Metallurgy of Stainless and Heat-Resisting Steels*, Cambridge: Cambridge University Press, 1968, 49.
6. K. C. Tyompson-Russell and J. W. Edington, *Electron Microscope Specimen Preparation Techniques in Materials Science*, London: Macmillan Press, 1977.
7. A. D. Romig Jr., *X-ray Microanalysis in the Analytical Electron Microscope*, Sandia National Laboratories Report SAND82-2938, 1983.
8. G. Cliff and G. Lorimer, *Proc. 5th European Conference on Electron Microscopy*, London: Institute of Physics, 1972, 140.
9. J. C. Lippold and W. F. Savage, *Welding J.* 61: 388s, 1982.
10. R. A. Perkins, R. A. Padgett, and N. K. Tunala, *Metall. Trans.*, 4: 2535, 1973.
11. J. C. Lippold, *Microstructural Characterization of Autogenous GTA Welds in a 12Cr-1Mo-0.3V Steel*, SAND80-8236, 1980.
12. D. Peckner and I. M. Bernstein, *Handbook of Stainless Steels*, New York: McGraw-Hill, 1977, 6-5.
13. A. D. Romig Jr. and J. I. Goldstein, *Metall. Trans.* 12A: 243, 1981.

## ELECTRON MICROSCOPY ANALYSIS OF WELD HEAT-AFFECTED ZONE LIQUATION CRACKING IN ALLOY 903

W. A. Baeslack III and William Lata

Weld heat-affected zone (HAZ) liquation cracking results from the formation of a liquid film at grain boundaries during the weld heating cycle and the inability of this film to accommodate thermally induced stresses experienced during cooling.<sup>1</sup> Over the years, field experience and numerous weldability studies<sup>2-6</sup> have shown austenitic Fe and Ni-base alloys that contain a few percent Nb and/or Ti to be particularly sensitive to this form of weld cracking. In the present study, weld HAZ liquation cracking in the austenitic Fe base Alloy 903 was characterized by scanning electron microscopy (SEM) techniques. Results indicated that cracking was associated with the presence of a low-melting Laves phase eutectic at grain boundaries.

### *Background*

Alloy 903 is an Fe-Ni-Co superalloy designed to provide a coefficient of thermal expansion (COE) lower than that of other superalloys. Small quantities of Nb, Ti, and Al in the alloy (totaling about 7 wt%) promote age hardening by the formation of both gamma prime (Ni<sub>3</sub>Al,Ti) and gamma double prime (Ni<sub>3</sub>Nb). This combination of a low COE and excellent room and elevated-temperature strengths (comparable to Alloy 718) have made Alloy 903 extremely useful in high performance aerospace applications where close tolerance control is required over a wide range of temperatures. Field experience has shown Alloy 903 to be sensitive to both HAZ and weld metal liquation cracking. A continuing weldability study of liquation and weld metal hot cracking on the 900 series of low COE alloys has confirmed a HAZ liquation cracking sensitivity in Alloy 903 comparable to that of several well-known "crack-susceptible" alloys. The present morphological study represented an important part of this overall investigation by providing some initial insight into the underlying liquation mechanisms which represent a requisite for cracking.

### *Experimental Procedure*

A commercial heat of mill-annealed Alloy 903 plate 6.4 mm thick was evaluated in this study. The analyzed chemical composition is provided in Table 1. The generation of representative weld HAZ liquation cracks was accomplished by Spot Varestraint testing,<sup>8</sup> which also provided a quantitative analysis of cracking susceptibility. Welding parameters employed in testing were 110 A current, 12 V, electrode negative, argon shielding, 2% augmented strain, 50 ms delay time.

Subsequent to testing, weld HAZ regions which experienced cracking were removed for metallographic examination. The specimens were then mounted in epoxy, polished down to 0.03  $\mu$ m alumina, and etched using a solution comprised of equal parts concentrated lactic, nitric, and hydrofluoric acids. After preliminary examination by light microscopy, the specimens were carbon coated and characterized by an ETEC Autoscan SEM. Energy-dispersive x-ray analysis (EDX) was performed with a JEOL 35A equipped with a Kevex EDAX system. As a complement to the microstructural characterization, SEM fractographic analysis was performed on liquation crack surfaces. Crack surfaces were exposed by careful diamond sawing and fracturing at room temperature.

### *Results and Discussion*

The unaffected base alloy microstructure exhibited a nearly equiaxed austenite grain morphology consistent with mill annealing. Also apparent in the microstructure was a bi-modal distribution of Nb-rich carbides comprised of coarse particles dispersed randomly throughout the austenite grains and much finer particles decorating austenite grain boundaries.

---

The authors are with the Department of Welding Engineering at The Ohio State University, Columbus, OH 43210.

The weld fusion boundary macrostructure is illustrated via light microscopy in Fig. 1. The relatively shallow temperature gradient experienced by this region during the weld thermal cycle promoted a wide region of partial melting immediately adjacent to the fusion boundary and noticeable grain growth. Two intergranular cracks located primarily in this grain-coarsened region are also evident.

SEM analysis more clearly delineated the solid-state and liquidation-related metallurgical phenomena that occurred in the HAZ (Figs. 2a-d). Figure 2(a) illustrates the fine equiaxed austenite grain structure shown farthest from the fusion line in Fig. 1. Somewhat unexpected, this region exhibited a noticeably finer grain size than that of the unaffected base metal, which indicates the occurrence of recrystallization during the weld thermal cycle. As shown, the fine Nb-rich carbides remained at the original prior-austenite grain boundaries. The driving force for recrystallization in the mill-annealed base metal structure was unclear. However, the analysis of transverse sections through continuous and spot GTA welds showed that this effect was not an artifact of specimen preparation or testing. At distances nearer the fusion line, higher peak temperatures promoted noticeable growth of the fine austenite grains and solid-state dissolution of fine carbides. Figures 2(b) and (c) illustrate HAZ regions progressively closer to the fusion boundary and clearly illustrate the onset of a constitutional liquation reaction between coarse, Nb-rich carbides and the austenite matrix.<sup>9</sup> Figure 2(c) shows the more extensive liquation reaction and indicates considerable liquation of the adjacent austenite matrix. Finally, within a distance of approximately five austenite grain diameters from the fusion line, extensive grain boundary liquation was observed (Fig. 2d). The extent of this liquation was widely variable, particularly in regions near original coarse carbides. Note that regions of intragranular liquation were also observed in the highest peak temperature region directly adjacent to the fusion boundary.

SEM examination of the resolidified liquated regions in the HAZ at increased magnification (Fig. 3) indicated the presence of a secondary constituent near the center of the resolidified austenite. Previous investigators have reported a similar second constituent morphology in resolidified HAZ regions and determined them to be a complex Laves phase ( $A_2B$  stoichiometry). EDX analysis of pertinent alloying elements in the region shown in Fig. 3 is given in Table 2, and supports the results of earlier studies by indicating the secondary constituent to be a complex  $(Fe, Ni, Co)_2(Nb, Ti)$  Laves phase.

Cracking was observed primarily in the grain coarsened region where grain boundary liquation was not clearly discernible, which suggests the presence of a very thin intergranular liquid film. The jagged crack edges and variability in the crack width were both characteristic of liquation versus solid state, ductility-dip type cracks. Figure 4 illustrates the tip of the upper crack shown in Fig. 1, and shows evidence of the strong capillarity effects that promoted crack backfilling and healing by liquid from the near HAZ and possibly from the fusion zone. Indeed, this strong crack-healing effect, combined with the copious amounts of grain-boundary liquid, may have accounted for the absence of cracking in the HAZ region directly adjacent to the fusion boundary.

The low-magnification fractograph in Fig. 5(a) illustrates the liquation crack surface as it follows the contour of the weld fusion boundary below the plate surface. Observation of this surface at increased magnification indicated intergranular liquation fracture.<sup>10</sup> The transition from a fine rippled pattern on the intergranular fracture surface near the trailing end of the crack (Fig. 5b) to a distinctly dendritic-appearing surface near the front of the crack resulted from an increased quantity of grain boundary liquid closer to the fusion boundary. EDX analysis of both liquation crack morphologies showed varying degrees of Nb enrichment as compared to the mechanically fractured regions (Fig. 5c).

The SEM analysis described above correlates HAZ cracking with the presence of a complex, low-melting Laves eutectic liquid at HAZ grain boundaries. Although the constitutional liquation of coarse Nb-rich carbides represented one source of this eutectic liquid, it appears unlikely that the extensive grain boundary liquation experienced in the near HAZ could have resulted entirely from the liquation of these relatively widely distributed carbides. Thus, it appears likely that additional mechanisms may have contributed to the liquation phenomena. Previous work on Alloy 800<sup>6</sup> suggests that additional Nb enrichment at grain boundaries may have resulted from the dissolution of the fine carbides and the assimilation of matrix Nb into migrating grain boundaries by a "sweeping up" effect. However, this initial SEM analysis was insufficient to confirm the operation



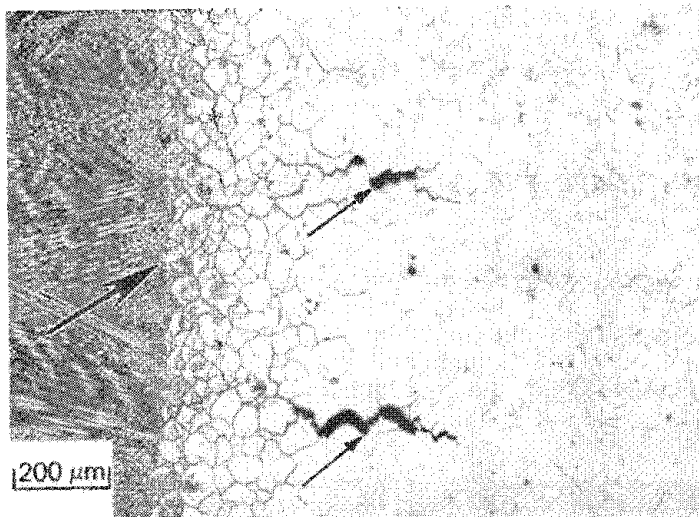
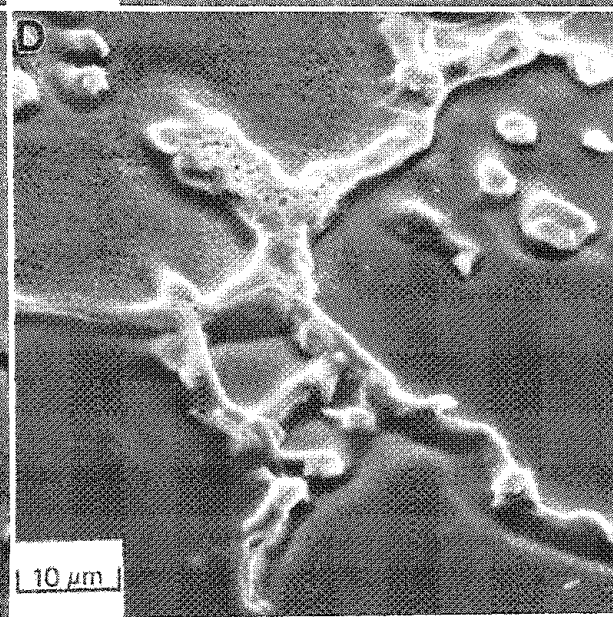
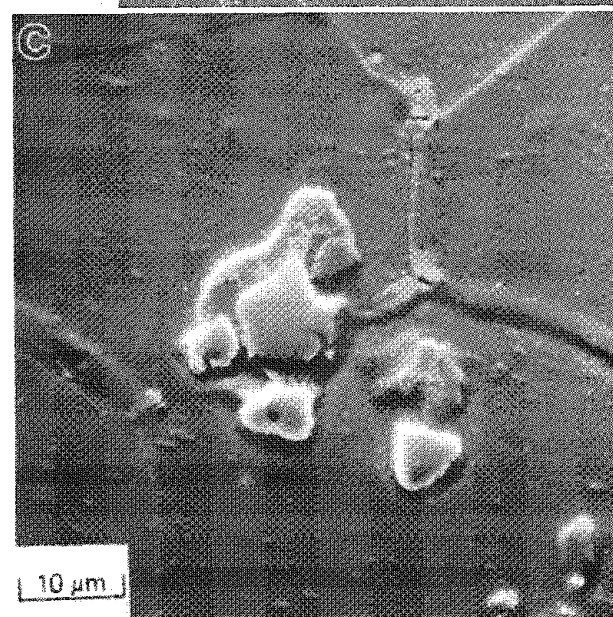
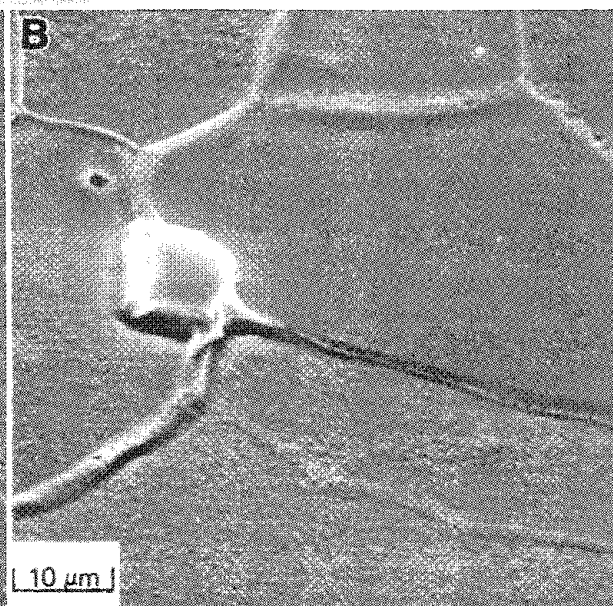
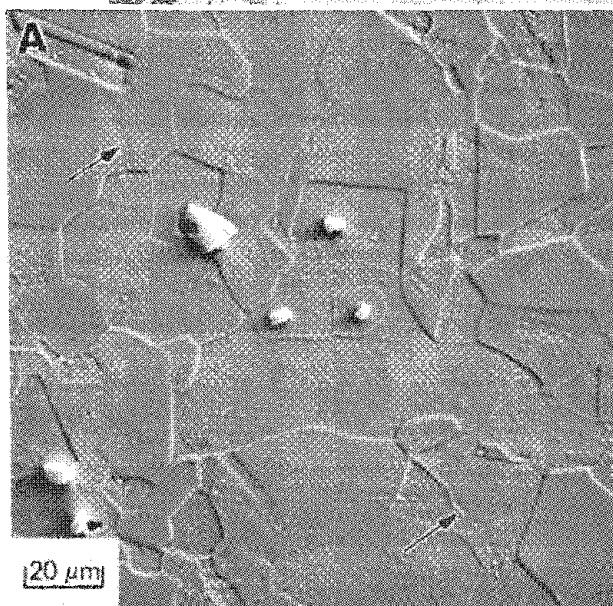


FIG. 1.--Light micrograph of weld fusion boundary region; large arrow indicates fusion boundary, small arrows indicate HAZ liquation cracks.

FIG. 2.--SEM micrographs of weld HAZ at decreasing distances from fusion boundary: (A) recrystallized austenite grains, small arrows indicate fine Nb-rich carbides at prior-austenite grain boundaries; (B) onset of constitutional liquation reaction between coarse Nb-rich carbide and matrix in grain-coarsened region; (C) more extensive constitutional liquation reaction; (D) extensive grain boundary liquation.





of such a mechanism. In continuing studies on Alloy 903 and subsequent generations of low COE superalloys, more extensive microbeam analysis techniques are being used on actual and simulated weld structures to identify more effectively the operative liquation mechanism.

### Conclusions

This study has shown HAZ liquation cracking in Alloy 903 to result from the presence of a low-melting Laves phase eutectic at grain boundaries and the inability of these liquated boundaries to withstand the thermally induced stresses experienced during weld cooling. Microstructure and fractographic analysis suggests the simultaneous operation of liquation mechanisms.

### References

1. B. Hemsworth, T. Boniszewski, and N. F. Eaton, "Classification and definition of high temperature welding cracks in alloys," *Metal Construction and Brit. Welding J.*, Feb. 1982, 5-16.
2. R. H. Dudley, Ph.D. thesis, Rensselaer Polytechnic Institute, Troy, N. Y., 1962.
3. J. A. Brooks, "Effect of alloy modifications on HAZ cracking of A-286 stainless steel," *Welding J.*, Nov. 1974, 517s-524s.
4. Y. Nakao, H. Oshice, S. Koga, H. Nishihara, and J. Sugitani, "Effect of Nb/C on the sensitivity of liquation cracking in 25Cr-20Ni-1.5Nb Fe-base heat resisting alloys," *JRWI*, Dec. 1982, 21-27.
5. D. S. Duvall and W. A. Owzarski, "Further heat-affected zone studies in heat resistant nickel alloys," *Welding J.*, Sept. 1967, 423s-432s.
6. J. C. Lippold, "An investigation of heat-affected zone hot cracking in alloy 800," *Welding J.*, Jan. 1983, 1s-11s.
7. D. F. Smith and E. F. Clatworthy, "The development of high strength, low expansion alloys," *Metal Progress*, March 1981, 32-35s.
8. G. M. Goodwin, W. F. Savage, and E. F. Nippes, "Effects of minor elements on hot-cracking tendencies of Inconel 600," *Welding J.*, Aug. 1977, 238s-244s.
9. J. J. Pepe and W. F. Savage, "Effects of constitutional liquation in 18Ni maraging steel weldments," *Welding J.* Sept. 1967, 411s-422s.
10. F. Matsuda and H. Nakagawa, "Some fractographic features of various weld and cracking and fracture surfaces with scanning electron microscope," *Trans. JWRI*, 1977, 81-90.

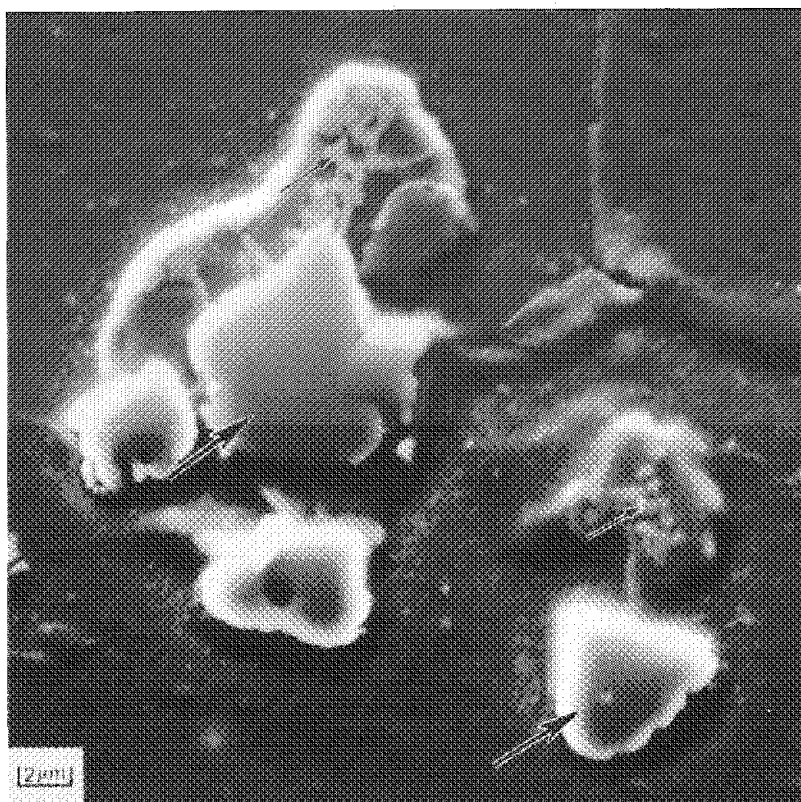


FIG. 3.--Higher magnification SEM micrograph of weld HAZ region shown in Fig. 2(c). Large arrows indicate Nb-rich carbide, small arrows indicate Laves phase.

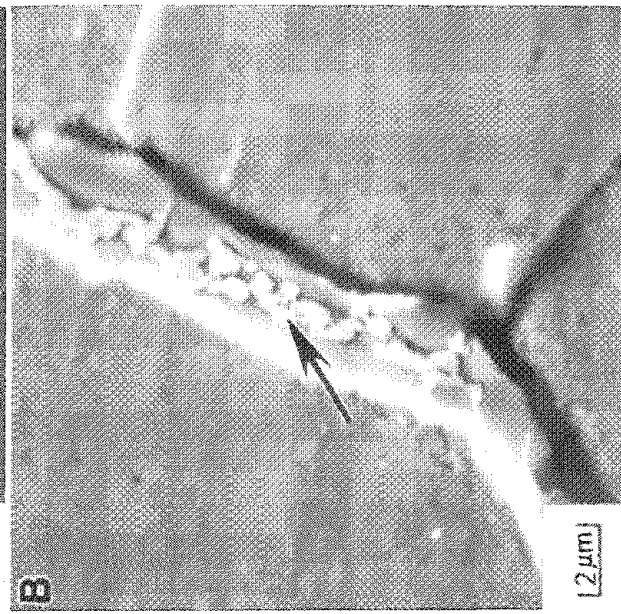
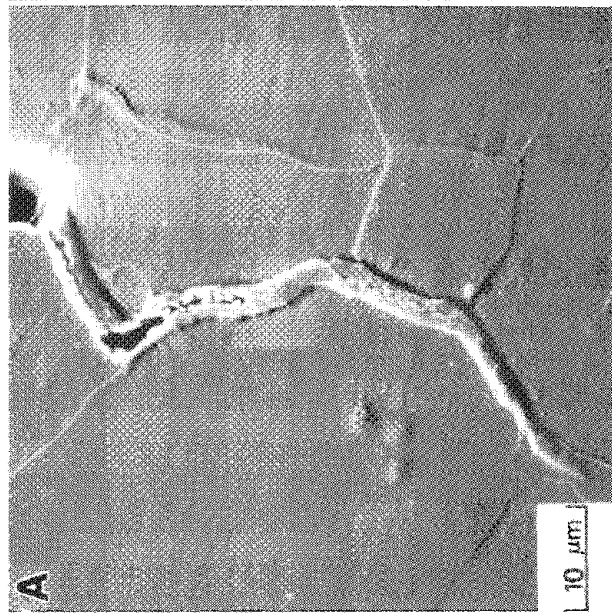


FIG. 4.--SEM micrographs of backfilled tip of HAZ liquation crack. Arrow in (B) indicates Laves phase.

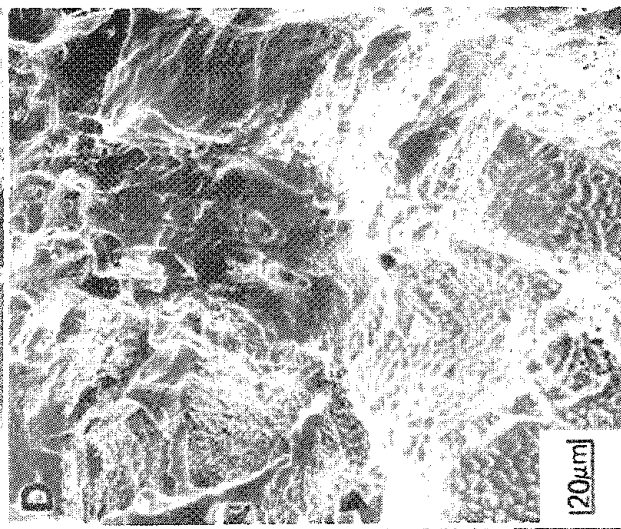
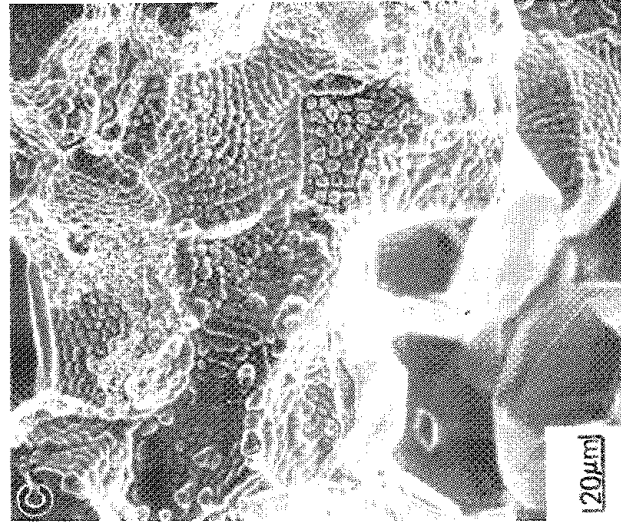
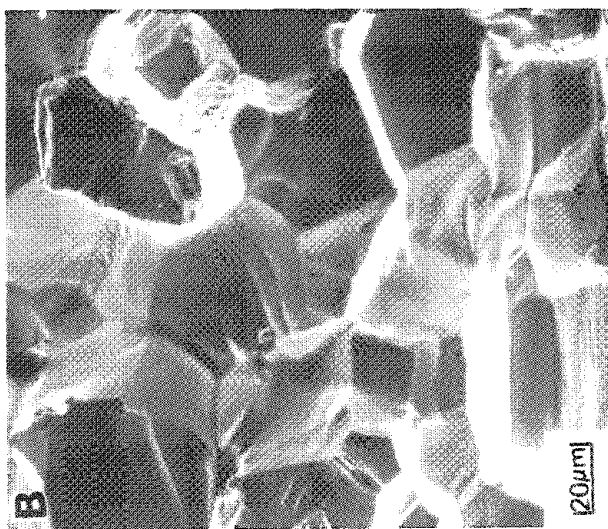
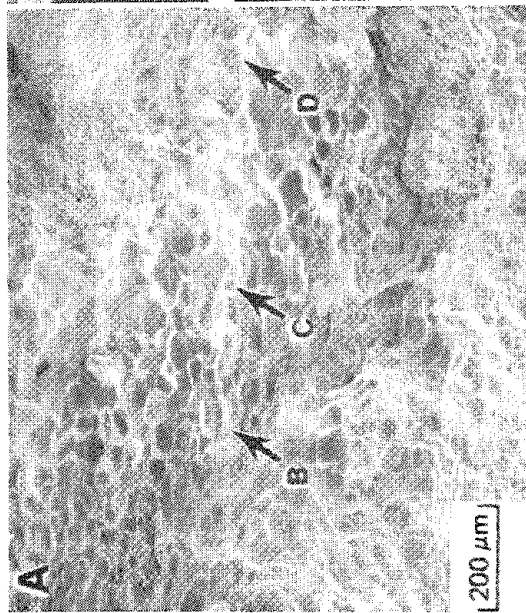


FIG. 5.--SEM fractographs of liquated crack surface. Arrows in (A) indicate regions shown at increased magnification in (B)-(D).

## A MICROSTRUCTURAL STUDY OF HIGH-ENERGY-DENSITY DISSIMILAR METAL WELDS

M. J. Cieslak, C. R. Hills, and T. J. Headley

The combination of two alloys during dissimilar metal fusion welding creates a new alloy which may have a microstructure and properties substantially different from either parent alloy. Often, specific alloying elements which are relatively innocuous, relative to weld metal properties, in the parent alloys may interact to degrade the properties of the dissimilar metal weld. In the present examples, continuous-beam high-energy-density CO<sub>2</sub> laser welds were made between two different sets of alloys, 304 stainless steel and Inconel 625, and 15-5 PH stainless steel and HP 9-4-20 steel. Microstructures were examined by a variety of investigative techniques--optical microscopy, scanning electron microscopy (SEM), and analytical electron microscopy (AEM)--which revealed minor solidification constituents in each type of weld metal.

### *Experimental*

The composition of the four alloys used are given in Table 1. Welding of these alloys was performed with a Photon Sources Versa Lase 1200 CO<sub>2</sub> laser welder. The 304/625 welds were simple linear square-butt welds made between two 3.2mm-thick sheets. These welds were made with 700 W power and a 12.7cm focusing lens at sharp focus and a travel speed of 25 cm/min. The weld was shielded with argon gas. The 15-5 PH/HP 9-4-20 welds were made on a ring-and-disk type specimen described in detail elsewhere.<sup>1</sup> A laser power of 350 W and 9.5cm focus length lens at sharp focus, at a travel speed of 150 cm/min, were the welding variables. Again, argon shielding of the weld was employed.

After welding, specimens were metallographically prepared and etched and subsequently examined by optical microscopy and SEM (Hitachi 520 operated at 25 kV). The 304/625 welds were etched electrolytically with both 10% oxalic acid in water and 10% chromic acid in water. The 15-5 PH/HP 9-4-20 welds were etched with a combination of Frye's reagent (40 ml HCl + 30 ml H<sub>2</sub>O + 25 ml ethanol + 5 gal CuCl<sub>2</sub>) and a mixed-acid Kovar etch (150 ml acetic acid + 50 ml HNO<sub>3</sub> + 3 ml HCl + 1 ml HF). Thin foils were prepared from the 304/625 welds and two-stage plastic extraction replicas were made from the polished and etched weld metal surface of the 15-5 PH/HP 9-4-20 welds for analysis in the transmission electron microscope (TEM) (JEOL 200CX and JEOL 100C, the latter equipped with an energy-dispersive spectrometer (EDS) for x-ray analysis). Foils for TEM were thinned from 3mm-diameter disks in a 10% HClO<sub>4</sub> in methanol electrolyte with a dual-jet thinning apparatus at -40 C and 15 V.

### *Results and Discussion*

The welding conditions described above produced welds that were approximately 1-2 mm deep. All welds were observed to solidify to an austenitic matrix with subsequent solid-state transformation of the 15-5 PH/HP 9-4-20 welds to martensite.<sup>1</sup>

*15-5 PH/HP 9-4-20 Welds.* The 15-5 PH/HP 9-4-20 welds exhibited extensive amounts of fusion-zone hot cracking, as can be seen in Fig. 1. This optical macrograph shows the weld, containing numerous hot cracks, between the 15-5 PH ring and the HP 9-4-20 disk. The HP 9-4-20 disk is on the outer radius of the weld and etches black as it is not a stainless alloy. The laser-energy rampdown area which terminates the weld can also be seen as a weld overlap region at the bottom of the figure.

Extraction replicas were made from this weld surface. TEM micrographs from these extractions are shown in Fig. 2. Extensive population of solidification grain boundaries by second phase particles was observed. Selected-area electron-diffraction patterns were consistent with a face-centered-cubic crystal structure having a lattice parameter of approximately 0.445 nm. A representative EDS spectrum obtained from this phase is shown

---

The authors are at the Sandia National Laboratories, Albuquerque, NM 87185. This work was performed at Sandia National Laboratories, supported by the U.S. Dept. of Energy under contract DE-AC04-76DP00789. The authors would like to acknowledge the assistance of A. D. Romig Jr. and R. D. Lujan at Sandia and Kevin Baughn at Allied Bendix Aerospace in Kansas City.

in Fig. 3. It was assumed that the Cu signal could be attributed to the copper-grid replica holder. A very strong Nb signal was obtained from this phase. The FCC crystal structure and lattice parameter are consistent with NbC (0.447 nm).<sup>2</sup> The EDS data of Fig. 3 were reduced by the standardless ratio technique and calculated k-factors<sup>3</sup> to weight percentages. This result is shown in Table 2, which gives both the metal species content and the absolute phase chemistry assuming an ideal stoichiometry of MC.

The dendritic-type morphology of the NbC seen in Fig. 2(b) is identical to the NbC/austenite eutectic constituent identified by several investigators<sup>4-6</sup> studying the weldability of austenitic stainless steels containing Nb. Ogawa and Tsunetomi<sup>4</sup> suggested that this NbC/austenite eutectic-type reaction occurring at ~1315 C was responsible for the hot cracking observed in the Nb-bearing stainless steels they studied. This mechanism is also a reasonable explanation for the present case. Nb from the 15-5 PH reacts with the relatively high carbon content of the HP 9-4-20 to form the NbC/austenite constituent during the terminal stages of solidification. Similar welds made between PH13-8 Mo stainless steel, a Nb-free alloy, and HP 9-4-20 did not hot crack.<sup>1</sup>

*304/625 Welds.* The linear butt-welds did not show evidence of hot cracking. This type of weld geometry provides very little restraint on the solidifying metal, in contrast to the high restraint condition of the 15-5 PH/HP 9-4-20 welds. Direct comparison of the hot-cracking susceptibility between these two alloy combinations should therefore not be inferred from these observations. However, a large amount of a minor phase was found both in interdendritic regions and along solidification grain boundaries in the weld metal, as can be seen in Fig. 4, which shows an SEM image of the fusion zone. This microstructure was examined in finer detail in the TEM. Figure 5 shows a bright-field, dark-field pair taken of the minor phase found in the 304/625 weld metal. Selected-area electron-diffraction patterns were consistent with a hexagonal Laves phase.

A Laves/austenite eutectic-type constituent has been identified previously in the nickel/base alloy Inconel 718<sup>7</sup> (5 wt.% Nb), and the iron-base alloy IN-519<sup>8</sup> (1.5 wt.% Nb). In a study of gas-tungsten arc weldability of 304L/625 dissimilar metal welds, Patterson and Milewski<sup>9</sup> suggested, without confirming, the possibility of the formation of a Laves-containing eutectic constituent in the weld metals they studied. Their Auger electron spectroscopy data taken on hot-cracked surfaces revealed Nb enrichment over nominal concentrations. Figure 6 is a higher-magnification bright-field image showing the development of a lamellar eutectic-type structure between the Laves and austenite in the 304/625 laser welds in this study.

EDS spectra were collected from various Laves particles in the fusion zone and reduced to weight percentages by the same technique as described above. These data are shown in Table 3. It can be observed that both Nb and Mo are heavily segregated to the Laves phase. A random weld metal matrix data point is shown for comparison purposes.

### Summary

Electron microscopy analysis of two different CO<sub>2</sub> laser welded dissimilar metal combinations revealed the presence of minor constituents that could be attributed to terminal solidification events. In the case of the 15-5 PH/HP 9-4-20 welds, a NbC/austenite eutectic-type constituent was identified that accounted for the observed fusion-zone hot cracks in these welds. The identity of the interdendritic constituent first observed optically by Patterson and Milewski<sup>9</sup> in 304L/625 GTA welds has been confirmed as Laves phase. It was further determined that this phase is enriched in Mo and Nb relative to the austenite matrix.

### References

1. M. J. Cieslak, "Hot-cracking mechanism in 15-5 PH/HP 9-4-20 laser welds," (submitted to the *Welding J.*).
2. *Powder Diffraction File: Inorganic Phases*, JCPDS International Center for Diffraction Data, 1601 Park Lane, Swarthmore, PA 19081, 1982, File No. 10-181.
3. A. D. Romig Jr., *Sandia Report SAND82-2938*, 1983.
4. T. Ogawa and E. Tsunetomi, *Welding J.* 61: 82-93s, 1982.
5. A. M. Ritter, *Equilibrium Phases in Nitronic 50 and Nitronic 50W Stainless Steels*, M.S. Thesis, Rensselaer Polytechnic Institute, Troy, N.Y., 1982.

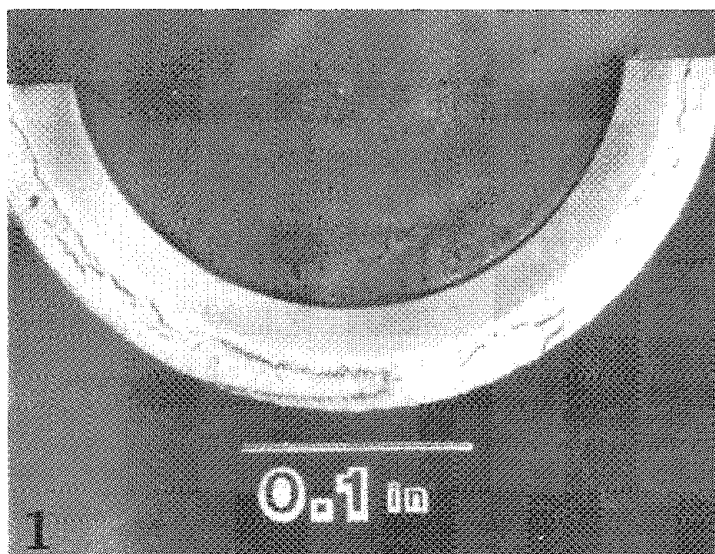


TABLE 1.--Alloy compositions.\*

Element	15-5 PH	HP 9-4-20	304	Inconel 625
Al	0.002	0.03	0.01	0.41
C	0.03	0.17	0.04	0.01
Co	0.13	4.56	-	-
Cr	14.78	0.74	19.07	20.43
Cu	3.34	0.10	0.25	0.01
Fe	75.41	83.78	68.40	3.64
Mn	0.61	0.30	1.83	0.06
Mo	0.15	0.98	0.90	8.71
Nb	0.39	0.02	0.01	3.49
Ni	4.51	9.09	8.49	62.77
P	0.028	0.010	0.028	0.013
S	0.001	0.007	0.022	0.003
Si	0.54	0.11	0.89	0.06
V	0.06	0.10	0.06	-

\*All values in Weight Percent

TABLE 2.--NbC chemistry.

NbC Metal Species Content	
Element	Content - Weight Percent
Nb	85.7 ± 3.1*
Cr	9.8 ± 1.1
Fe	3.6 ± 0.4
V	0.9 ± 0.2

NbC Absolute Phase Chemistry	
Element	Content - Weight Percent
Nb	75.0 ± 2.7
Cr	8.5 ± 1.0
Fe	3.1 ± 0.3
V	0.8 ± 0.2
C	12.6

\*Limits denote twice the absolute error determined from 4 analyses.

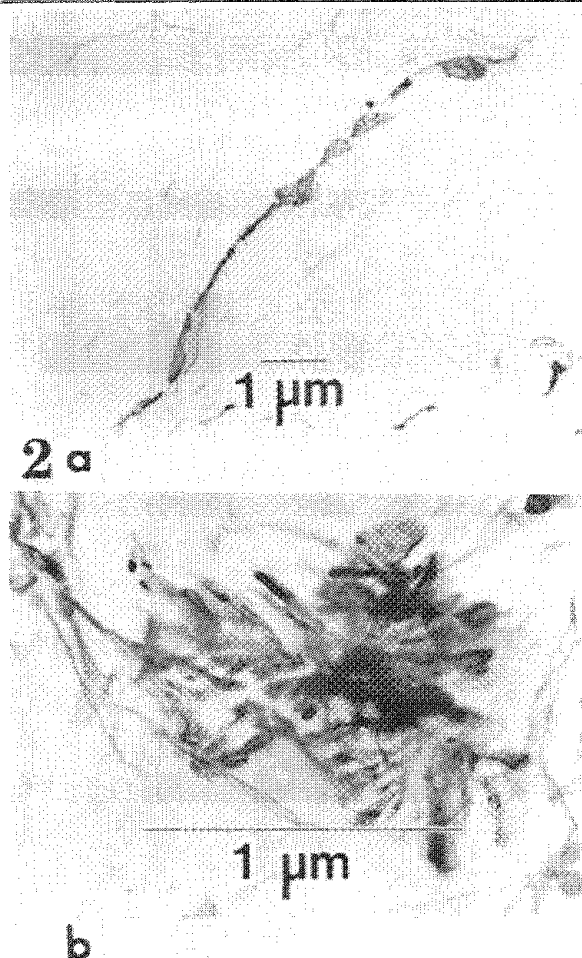


FIG. 1.--Optical photomicrograph of 15-5 PH/HP 9-4-20 CO<sub>2</sub> laser weld test specimen surface after metallographic preparation. Note copious fusion-zone hot cracks. FIG. 2.--(a) Extraction replica TEM image of solidification grain boundary NbC in 15-5 PH/HP 9-4-20 CO<sub>2</sub> laser weld; (b) higher magnification of same phase.

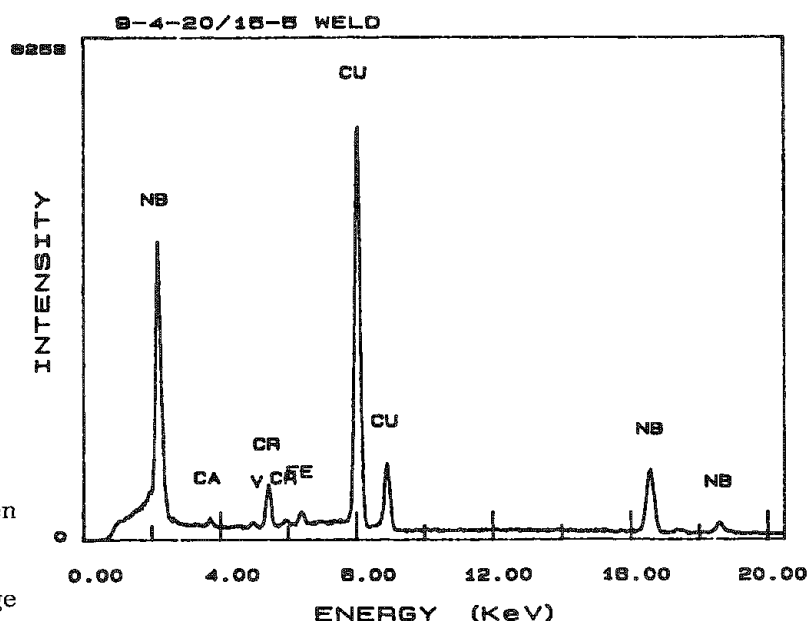


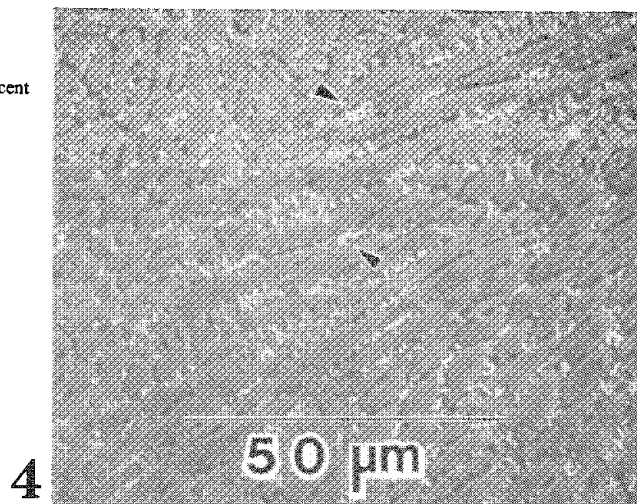
FIG. 3.--EDS spectrum from NbC found in 15-5 PH/HP 9-4-20 CO<sub>2</sub> laser weld.



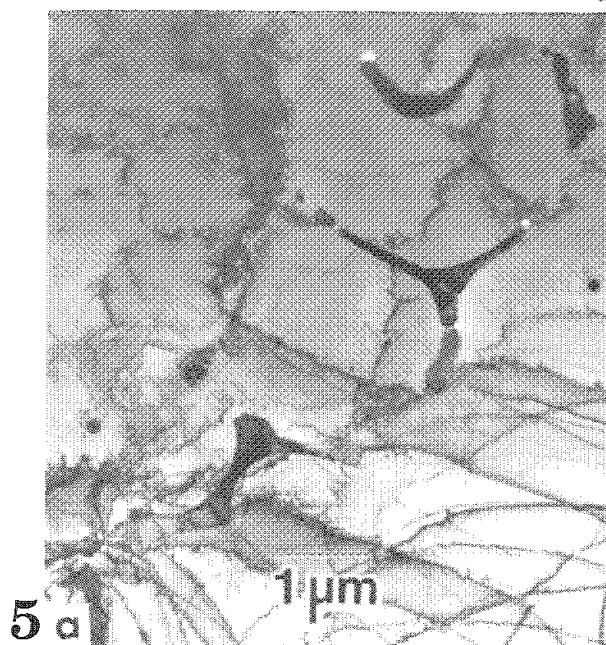
6. G. Jolley and J. E. Geraghty, *Solidification and Casting of Metals*, The Metals Society, 1979, 411-415.
7. R. Vincent, *Acta Metallurgica* 33: 1205-1216, 1985.
8. Y. Nakao, H. Oshige, S. Koga, H. Nishihara, and J. Sugitani, *J. Japan Welding Soc.* 51: 21-27, 1982.
9. R. A. Patterson and J. O. Milewski, *Welding J.* 64: 227-231s, 1985.

TABLE 3.--Laves chemistry.

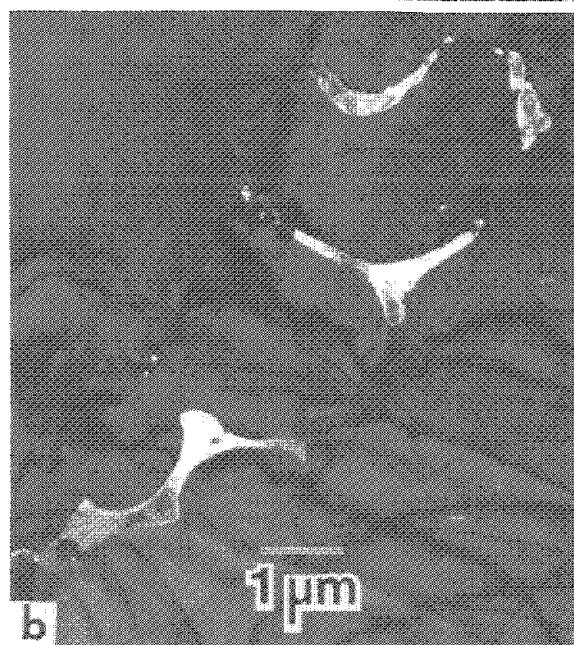
Element	Content - Weight Percent	Random Weld Matrix Point	
		Element	Content - Weight Percent
Fe	19.8 ± 2.4*	Fe	31.2
Cr	16.6 ± 1.0	Cr	21.6
Ni	32.5 ± 1.0	Ni	41.6
Si	1.0 ± 0.4	Si	0.0
Ti	0.1 ± 0.3	Ti	0.1
Nb	18.9 ± 2.0	Nb	1.9
Mo	11.1 ± 2.0	Mo	3.5



4



5 a

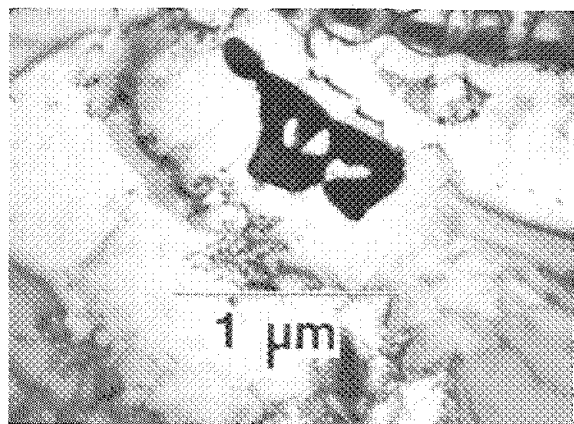


b

FIG. 4.--SEM image of fusion zone in 304/625 CO<sub>2</sub> laser-weld specimen; lighter appearing interdendritic structure (arrows) is Laves phase.

FIG. 5.--(a) Bright-field, (b) dark-field pair TEM images of Laves phase found in fusion zone of 304/625 CO<sub>2</sub> laser weld.

FIG. 6.--Higher-magnification TEM image showing development of lamellar-type structure between Laves and austenite in 304/625 CO<sub>2</sub> laser weld.



6

## A MICROSTRUCTURAL ANALYSIS OF ALLOY 718 WELDS TO KOVAR AND 304

G. A. Knorovsky and T. J. Headley

Hermetic miniature electromechanical and electrochemical components require headers containing glass-to-metal seals through which electrical feedthroughs are made. Recent developments in glass-ceramic technology have provided a high-strength, high-corrosion-resistance lithium aluminosilicate glass-ceramic,<sup>1</sup> which is compatible with Alloy 718 (Ni-18.6Cr-18.5Fe-5Nb-3.1Mo-0.9Ti-0.4Al). This material offers designers a high-strength header material option they have not previously had. However, to take advantage of this option one must be able to closure-weld the header to various structural materials commonly used in these applications. In this study we report on the correlation between weld microstructure determined by analytical electron microscopy (AEM) and weldability ratings given by the Varestraint test for dissimilar welds involving Alloy 718 and either Kovar (Fe-29Ni-17Co) or 304 (Fe-18Cr-10Ni) stainless steel.

### *Experimental*

The Varestraint test compares hot-cracking resistance of different materials by providing a reproducible set of thermal gradient and strain conditions. When these conditions are established, the amount of cracking noted in the test specimen is a direct indication of the material's susceptibility to hot-cracking. One provides the thermal gradient by establishing a moving molten puddle on the test specimen via an inert gas shielded arc. The strain is established by rapid bending of the specimen around a radiused die block when the arc has translated to the appropriate position. (For details, see Ref. 2.) For our experiments we used a split specimen of approximately half Alloy 718 and half Kovar or 304. The composite was approximately 140 × 25 × 3 mm, and the two halves were joined by a shallow electron beam weld along the bottom of the specimen. The position of the tungsten electrode was varied laterally with respect to the joint axis in order to vary the fraction of each material melted during the welding process. This fraction was later established by optical metallography of a specimen cross section normal to the direction of the weld. Samples for AEM were sliced from the fusion zone of gas-tungsten-arc (GTA) welds with a low speed wafering saw, manually ground on SiC papers to ~125  $\mu$ m, from which 3mm disks were punched and electropolished at 15 V in a 10% solution of perchloric acid in methanol cooled to ~-65 C. Ion milling was then used to increase the electron-transparent area and remove any chemical residue. Specimens were examined in either a JEOL-200CX TEM at 200 kV or a JEOL-100C AEM operated at 100 kV which was equipped with a low-take-off-angle x-ray detector and a Tracor Northern TN2000 multichannel analyzer. Energy-dispersive spectroscopy (EDS) data were obtained in the STEM mode with a ~18nm probe, which resulted in a spatial resolution of ~50 nm. Quantitative compositions were obtained from EDS data via the Cliff-Lorimer standardless-ratio technique with a data reduction routine developed by Romig.<sup>3</sup> An absorption correction was not used; thin-foil conditions always applied. Ni, Cr, Fe, Nb, Ti, Si, and Mo compositions were determined. A  $\pm 5\%$  relative error can be expected for AEM-determined chemical compositions. Positive identification of phases was accomplished by matching computer-generated and experimental selected area diffraction (SAD) patterns. Scanning electron microscopy was performed on metallographically polished and etched specimens to determine total volume fraction of minor microconstituents. TEM was used to determine the fractions of this total attributable to the various phases present.

### *Results*

Varestraint data, presented as total crack length at 2.5% augmented strain vs % Kovar or 304 in the weld, are given in Fig. 1. For comparison purposes, the weldability of the 304 used is considered excellent. Three minor phases were seen in appreciable amounts:

The authors are at Sandia National Laboratories, Albuquerque, NM 87185. The work was sponsored by the U.S. Department of Energy under Contract DE-AC04-76-DP00789. They wish to thank Dr. M. J. Cieslak for many interesting discussions, Mr. R. D. Lujan for SEM assistance, and Mr. A. J. Romero for metallographic assistance.

FIG. 1.--Varestraint data: Total crack length at 2.5% augmented strain vs Kovar or 304 diluted into weld.

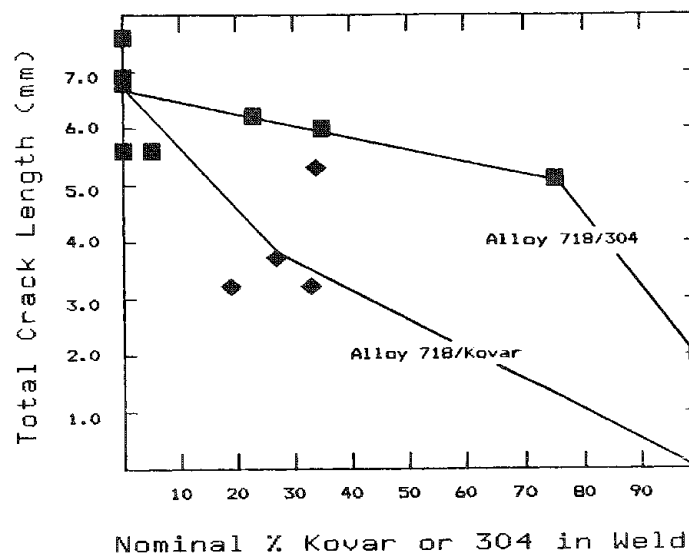


FIG. 2.--Volume % of MC-type carbide and total minor microconstituent content in weld vs % Kovar diluted into weld. Error bars show range of data.

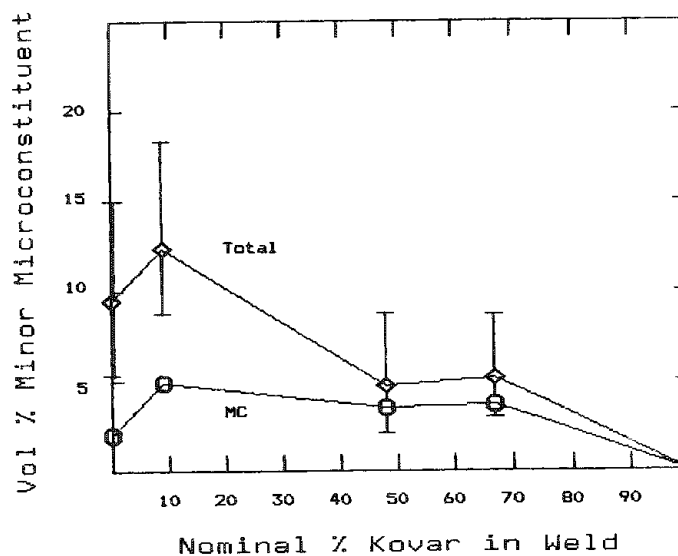
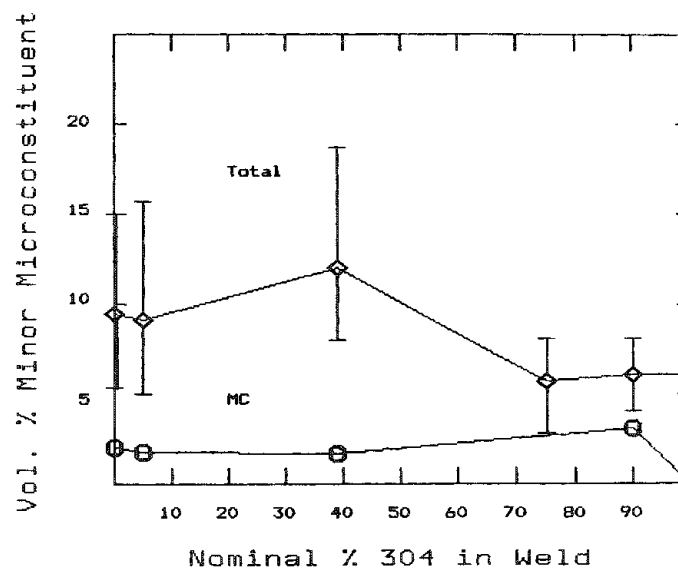


FIG. 3.--Volume % of MC-type carbide and total minor microconstituent content in weld vs % 304 diluted into weld. Error bars show range of data.





MC-type carbide, hexagonal Laves phase, and (in welds with high amounts of 304 dilution) bcc delta ferrite. Figures 2 and 3 summarize the volume percentages of the MC carbide, and total minor microconstituent content as a function of the weld dilution. Figures 4, 5, and 6 show bright-field images and SAD patterns associated with the phases found. The Laves phase was found in an eutectic-like lamellar structure along with fcc austenite. Compositions (in wt.%) of the Laves phase and interlamellar austenite (when it could be determined) are given in Table 1. The MC-carbide tended to form Chinese-script morphologies, so it, too, was probably formed as an eutectic-like reaction. The M in the MC-type carbide was usually ~80% Nb, ~10% Ti, and the remainder split among Ni, Fe, Cr, and Mo. Occasionally, Ti-rich carbides were encountered.

TABLE 1.--AEM compositions.

Interlamellar fcc*	Ni	Fe	Cr	Nb	Mo	Si	Ti	Co
718	57.8	13.7	15.3	8.8	2.5	0.2	1.6	-
718-rich/304	55.5	14.4	14.2	10.1	2.4	0.1	2.0	-
718/304 (~55/45)	42.9	32.0	17.9	4.3	1.7	0.2	1.1	-
718-rich/Kovar	54.3	17.0	12.2	10.6	1.9	0.2	2.2	1.6
Laves phase**								
718	45.0	12.2	13.8	22.5	4.7	0.7	1.1	-
718-rich/304	43.8	12.9	13.5	23.3	4.2	0.8	1.4	-
718/304 (~55/45)	30.7	25.1	13.6	24.6	3.8	1.1	1.1	-
718-rich/Kovar	34.0	23.9	5.6	23.7	1.7	0.5	1.4	8.7
718/Kovar (~52/48)	33.9	23.4	5.2	24.7	1.8	0.5	1.4	9.1
718/Kovar-rich	41.8	15.8	11.3	22.8	3.4	0.6	1.7	2.5

\*Clean analyses were not obtained for interlamellar fcc in the high Kovar content samples due to high magnetic astigmatism in the STEM images.

\*\*Laves phase was not identified in the 718/304-rich sample.

### Discussion

The weldabilities of the dissimilar metal combinations are intermediate to those of the individual materials, with the 718/Kovar system hot-cracking susceptibility generally lower than the 718/304 system. The volume fraction of minor microconstituents remains essentially constant for the 718/304 combination until about 50% dilution, after which it decreases, whereas the 718/Kovar minor microconstituent content is maximum at 718-rich compositions and decreases as the Kovar content increases. The 718/304 system generally contains more fcc/Laves eutectic. The MC carbide fraction remains almost constant for both systems regardless of dilution. Apparently the formation of the fcc/MC carbide eutectic occurs until the interstitial content is exhausted, followed by the formation of the fcc/Laves eutectic. Differential thermal analysis results on Alloy 718<sup>4</sup> support this interpretation. Table 1 shows that the Nb content of the fcc interlamellar phase at near 50/50 718/304 is reduced from the values obtained for 718 or 718-rich/304 mixtures. Calculations based on the Scheil equation for nonequilibrium solidification<sup>5</sup> show that the fraction of eutectic formed should remain approximately constant, since the Nb partition coefficient and nominal composition also decrease.

The presence of low-melting-temperature fcc/Laves eutectic appears to be associated with the high hot-cracking susceptibility of 718-rich alloys. The susceptibility seems to increase as the amount of fcc/Laves eutectic increases from about 2 to about 10 vol.%. Sometimes a phenomenon known as "eutectic healing" occurs at high volume fractions of eutectic, where the crack susceptibility decreases to a low value. That does not seem to be the case here.

Recent work has implied that the formation of topologically close packed (TCP) phase-containing low-melting eutectics (Laves is a TCP phase) can cause hot-cracking susceptibility in Ni-base alloy welds.<sup>6</sup> As part of that study, a new PHACOMP approach was found to predict successfully when TCP phases formed on solidification.<sup>7</sup> A simplified version of the new PHACOMP calculation was applied to the Alloy 718/Kovar and Alloy 718/304 systems. The critical parameter  $M_d$  was found to remain constant as the 304 content of the

weld increased, and decrease as the Kovar content increased. A simple rule of mixture calculation was found to determine weld nominal composition, without taking into account segregation. This simplification allows only relative TCP phase formation tendencies to be determined. Also, the calculation is strictly valid only for systems where Ni is the predominant alloying element and may be expected to break down when Fe content increases, or when solidification to a bcc structure occurs. With these limitations in mind, the microstructural and hot-cracking susceptibilities seem to agree well with the predictions of the theory for these two systems.

#### Summary

Weldability and microstructure have been studied in the Alloy 718/304 and Alloy 718/Kovar systems by a combination of Varestraint and AEM techniques. Minor phases found include Laves and MC-type carbides (both as part of eutectic constituents) and ferrite in 304-rich welds. The 718/Kovar system showed generally lower hot-crack susceptibility than the 718/304 system. A New PHACOMP approach was used to rationalize how microstructure and hot-crack susceptibility varied with alloy dilution during welding.

#### References

1. H. L. McCollister and S. T. Reed, "Glass-ceramic seals to Inconel," U.S. Patent 4 414 282, 1983.
2. C. D. Lundin et al., "The Varestraint test," *WRC Bull.* 280, 1982.
3. A. D. Romig, *SAND 82-2938*, Sandia National Laboratories, Albuquerque, N.M., 1983.
4. G. A. Knorovsky et al., "Alloy 718: A solidification diagram," submitted to *Met. Trans.*
5. M. C. Flemings, *Solidification Processing*, New York: McGraw-Hill, 1974.
6. M. J. Cieslak et al., "The use of new PHACOMP in understanding the solidification microstructure of nickel base alloy weld metal," submitted to *Met. Trans.*
7. M. Morinaga et al., *Superalloys 1984*, 523.

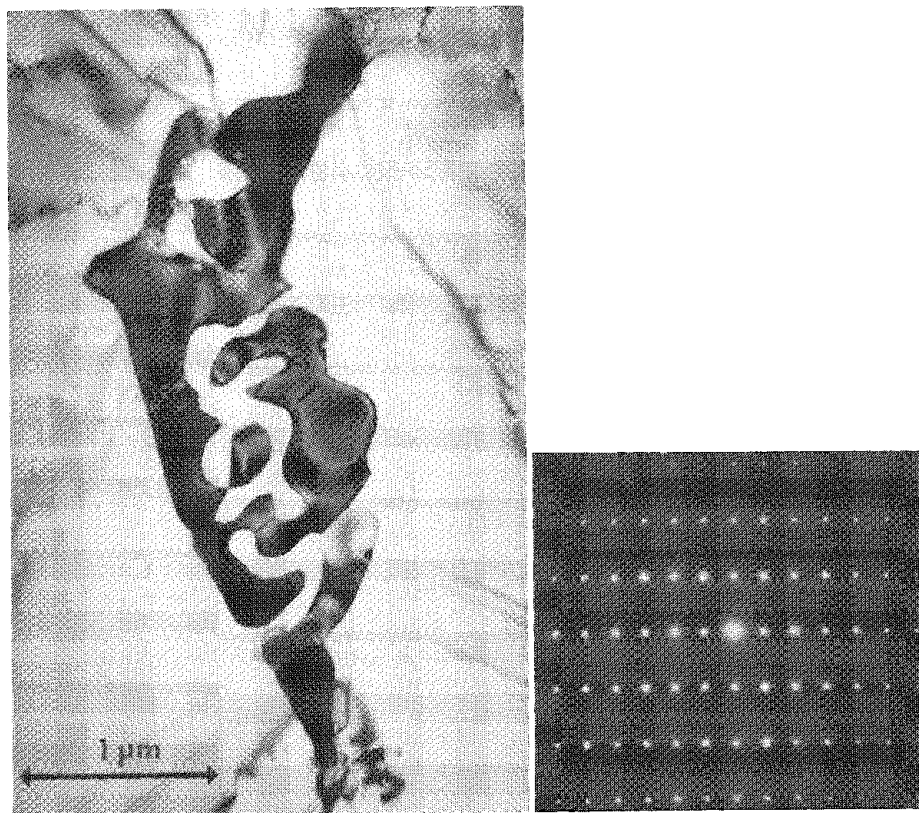


FIG. 4.--Bright-field image with SAD of fcc/Laves eutectic constituent.

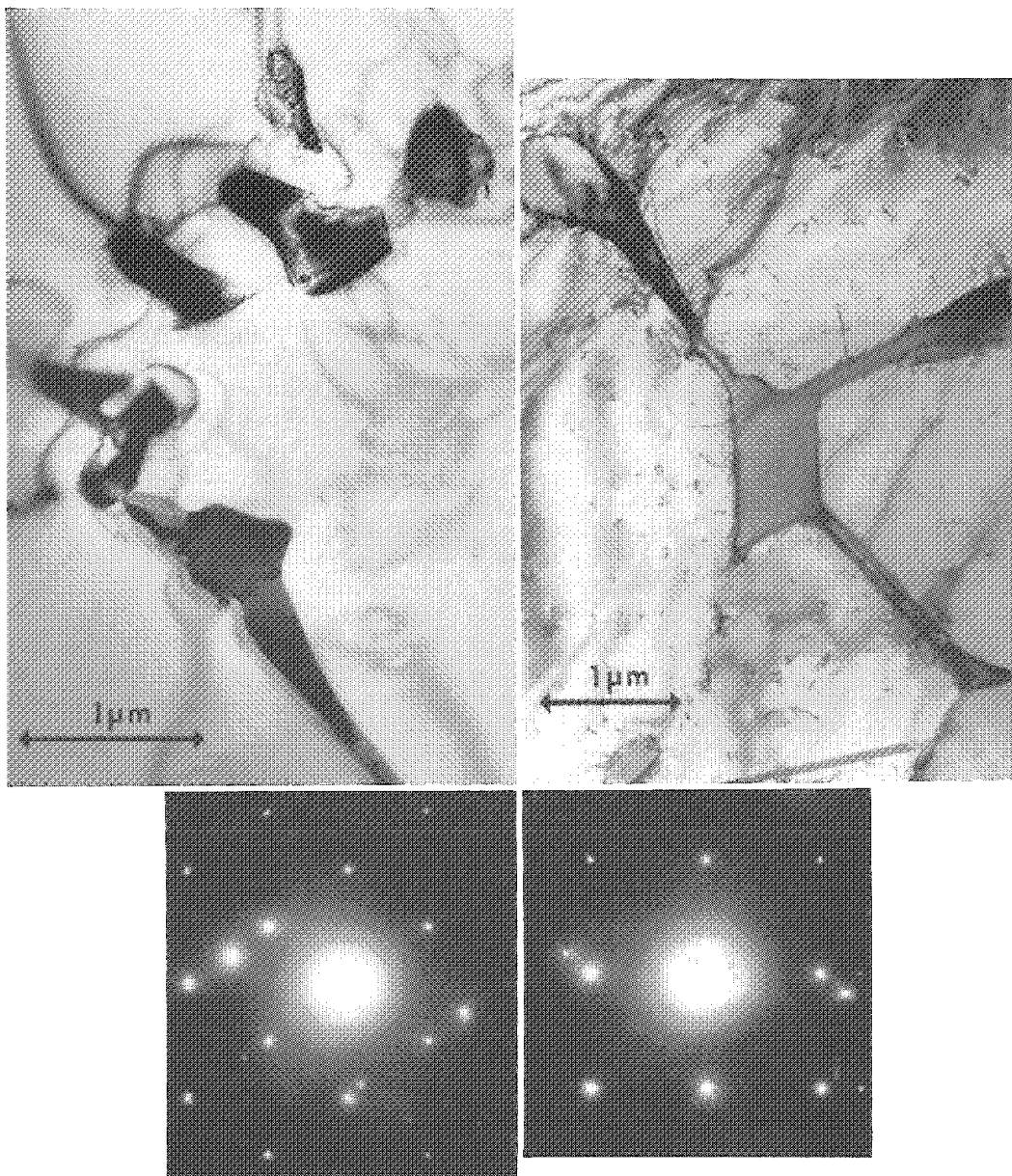


FIG. 5.--Bright-field image with SAD of fcc/MC carbide Chinese script eutectic constituent.

FIG. 6.--Bright-field image with SAD of bcc ferrite.

## Auger Electron Spectroscopy and Secondary Ion Mass Spectroscopy

### SELF-REGULATED POTENTIAL AT INSULATING SURFACES IN THE PRESENCE OF A STRONG ELECTROSTATIC EXTRACTION FIELD

G. Slodzian, M. Chaintreau, and R. Dennebouy

To achieve high collection efficiencies of sputtered secondary ions, a strong electrostatic field is applied at the sample surface. However, when insulating samples have to be examined, the existence of such a field makes it difficult to use the conventional "low-energy electron spraying" to prevent electrical charging-up efforts.

In the case of negative secondary ions, the sample surface is at a negative potential and it is then possible to direct an auxiliary high-energy electron beam perpendicularly toward the surface: electrons are slowed down and can be made to reach the surface with vanishingly small energies. Thus, by use of the principle of reversibility, the emission objective lens simultaneously serves as an image-forming system and as an electron mirror providing low-energy electrons in the vicinity of the surface.

When the primary ion beam strikes the surface, secondary ions and electrons are ejected. Since the yield of secondary electrons is usually much higher than unity, a positive charge tends to build up that is immediately neutralized by the low-energy electrons available near the surface. The fraction of the incoming electronic flux that is not used to cancel the positive charge brought in by the primary ion beam or left behind by the secondary particles is reflected. Indeed, any slight negative local charging-up builds up an additional repulsive potential and prevents further charging-up by low-energy electrons. Thus, as long as the incoming electronic flux is higher than the fluxes of secondary and primary particles, the reflected beam plays the part of a buffer which allows the potential to be self-regulated at each point of the surface no matter how heterogeneous the sample is. By analyzing the energy of the outgoing electrons one can evaluate the reflected and the secondary components. This possibility provides us with a completely new means for measuring secondary electron yields on insulators under ion bombardment in steady conditions.

The numerous applications already known for conducting materials can now be repeated for insulation when negative secondary ions are used. In the case of positive secondary ions, such a similar set-up is much more difficult to put in practice. However, a simple device has been developed that provides a bombarding flux of electrons exactly proportional to the primary ion flux. When some conductivity can be induced by electron bombardment of a few kilo-electrons of energy, this device provides means to operate under stable conditions.

---

The authors are at the Laboratoire de Physique des Solides, Bâtiment 510, Université de Paris-Sud, 91405 Orsay, France.

# ABSOLUTE IONIZATION PROBABILITIES IN SECONDARY ION EMISSION FROM CLEAN METAL SURFACES

A. Wucher and H. Oechsner

The energy spectra of sputtered positive secondary ions and the corresponding neutral species have been measured for sputter-cleaned polycrystalline Ta, Nb, and Cu. By division of the measured energy distributions, the absolute values of the energy-dependent ionization probability  $\alpha^+(E)$  could be determined. The results are compared with predictions of current secondary-ion formation models. It is found that available analytical expressions for the dependence of  $\alpha^+$  on the velocity of the ejected particles do not describe the experimental data.

Ion-induced ejection of atomic or molecular species from solids has become of great importance for surface analysis as far as the charged fraction of the flux of such particles is concerned. With respect to the analytical applications of Secondary Ion Mass Spectrometry (SIMS), detailed knowledge of the mechanisms leading to the formation of secondary ions is necessary in order to correlate SIMS intensities to the composition of the sample.

In the picture commonly used, the formation of secondary ions  $X^+$  is governed by two closely coupled processes: the collision kinetics leading to the sputtering of a species  $X$ , and the electronic interactions determining the charge state of the sputtered particle. The latter is usually characterized by the ionization probability  $\alpha_X^+(E)$ , which is a function of the kinetic energy  $E$  of the sputtered particle and which in addition strongly depends on the chemical environment (matrix) from which the particle is ejected.

## Experimental Method and Results

An attempt to determine  $\alpha_X^+(E)$  experimentally requires a knowledge of the energy distributions of sputtered atomic and molecular secondary ions  $X^+$  and the corresponding neutral species  $X$ , which can be provided by energy-resolved in situ SIMS and SNMS measurements. In SNMS (Secondary Neutral Mass Spectrometry), the sputtered neutrals pass through a slab of a special low-pressure rf plasma, the electron component of which serves as a postionizing medium.<sup>1</sup>

In the present investigation, polycrystalline Ta, Nb, and Cu targets were sputter-cleaned in an ultrahigh-vacuum environment (base pressure  $6 \times 10^{-8}$  Pa) by bombardment with 2keV,  $45^\circ$   $Ar^+$  ions. The residual steady-state surface concentration of impurities and adsorbates was determined by SNMS and in situ Auger Electron Spectroscopy (AES) to be in the order of 1 at%. The SIMS and SNMS energy spectra of sputtered secondary ions  $Me^+$  and  $MeO^+$ , or postionized secondary neutral particles  $Me^0$  and  $MeO^0$ , respectively, were measured under the bombarding conditions mentioned above. The experimental setup is described in detail in Ref. 2.

Since for clean metal surfaces the SIMS- and SNMS-intensities of a species  $X$  are given by

$$I_{X^+}(E) = I_p K_X^+ Y_X(E) \alpha_X^+(E) \quad (1)$$

and

$$I_{X^0}(E) = I_p K_X^0 Y_X(E) \quad (2)$$

where  $I_p$  primary ion current,  $K_X^+$  is the geometry and transmission factor for SIMS,  $K_X^0$  is the proportionality factor containing geometry, transmission, and postionization probability for SNMS,<sup>2</sup> and  $Y_X(E)$  is the energy differential partial sputter yield for species  $X$ , we obtain

$$\alpha_X^+(E) = [I_{X^+}(E)/I_{X^0}(E)] (K_X^0/K_X^+) \quad (3)$$

The authors are in the Fachbereich Physik, Universität Kaiserslautern, Erwin-Schrödinger-Strasse, D-6750 Kaiserslautern, Federal Republic of Germany.

Equation (2) is valid if the measured SNMS energy distributions are corrected for energy-dependent plasma influences such as the spatial distributions of plasma density and potential, as well as heavy-particle scattering, by a well-established procedure described elsewhere.<sup>2-4</sup> For Ta, the absolute value of  $K_{Ta}^0/K_{Ta}^+$  can be taken from previous measurements.<sup>5</sup> For Nb and Cu these values were obtained by a comparison of the energy-integrated SNMS and SIMS intensities with literature data for sputter yields and secondary ion yields taken from Refs. 6 and 7, respectively. Hence, according to Eq. (3), the absolute values of the spectral ionization probabilities  $\alpha_x^+(E)$  could be obtained for  $x = Ta, Nb, Cu$ . The results are shown in Fig. 1.

#### Comparison with Theory

A large amount of theoretical work has been devoted to the formation of secondary ions emitted from clean metal surfaces.<sup>8-14</sup> Most of the various models can be divided into two groups that essentially yield the expressions

$$\alpha_x^+(E) = \frac{2}{\pi} \exp\left\{-\pi \frac{C(I-\phi)}{\hbar\gamma v_{\perp}}\right\} = \frac{2}{\pi} \exp(v_0/v_{\perp}) \quad (4)$$

and

$$\alpha_x^+(E) = \left(\frac{\hbar\gamma v_{\perp}}{\Delta_0}\right)^{2n} \quad (5)$$

where  $I$  is the ionization potential of the sputtered particle,  $\phi$  is the work function of the bombarded metal surface,  $\gamma$  is the characteristic decay length of the electron hopping integral between metal states  $\epsilon_k$  and valence state  $\epsilon_a$  of the sputtered particle,  $\Delta_0$  is the original width of  $\epsilon_a$  for distance  $z = 0$  between sputtered particle and surface, and  $v_{\perp}$  is the normal component of particle velocity  $v$  corresponding to energy  $E$ .

Both types of predicted velocity dependences can be examined by logarithmic plots of  $\alpha^+$  vs  $\log v$  or  $v^{-1}$ , respectively, as shown in Fig. 2. As can be seen, neither Eq. (4) nor Eq. (5) describe the experimental results in the entire velocity interval covered by the present investigations. The observed deviations in the low-velocity region in Fig. 2(b) have been reported previously<sup>15,16</sup> and explained theoretically.<sup>17</sup> The parameters  $2n$ ,  $v_0$ , and  $C$ , as evaluated from the straight-line fits indicated in Fig. 2, are shown in Table 1.

TABLE 1

Sample	$2n$	$V_0$ (cm/s)	$C$	Validity interval of $v_{\perp}$ (cm/s)
Ta	0.9	$5.8 \times 10^5$	0.006	$5-10 \times 10^5$
Nb	0.9	$3.9 \times 10^5$	0.006	$5-8 \times 10^5$
Cu	1.9	$2.1 \times 10^5$	0.023	$7-14 \times 10^5$

For Cu the values for  $2n$  and  $v_0$  from Table 1 agree well with  $2n = 2.1$  and  $v_0 = 2.2 \times 10^6$  cm/s, which can be obtained from measurements in Ref. 18. If  $2n$  and  $v_0$  from Table 1 are inserted into Eqs. (4) and (5), respectively, the absolute order of magnitude of  $\alpha^+(E)$  is theoretically estimated to be of the order of  $10^{-2}$  for Cu and  $10^{-1}$  for Ta and Nb. On the other hand, the absolute experimental values for  $\alpha_x^+(E)$  have been found to be of the order of  $10^{-4}$ . As a consequence, we must conclude that analytical approaches yielding expressions similar to Eqs. (4) and (5) do not describe the experimental results in an appropriate manner.

However, reasonable agreement can be found with recent computer simulations of the secondary ion emission process that takes into account the dynamical disorder of the ion bombarded surface.<sup>19</sup> This finding indicates that the concept of significantly altered electronic states during the emission of sputtered particles is more appropriate than the naive assumption of an undisturbed metal surface.

## References

1. H. Oechsner and W. Gerhard, *Phys. Lett.* 40A: 211, 1972.
2. A. Wucher and H. Oechsner (to be published).
3. H. Oechsner, *Z. Phys.* 238: 433, 1970.
4. F. Bernhardt, H. Oechsner, and E. Stumpe, *Nucl. Instr. Meth.* 132: 329, 1976.
5. H. Oechsner and Z. Sroubek, *Surf. Sci.* 127: 10, 1983.
6. H. H. Andersen and H. L. Bay, in R. Behrisch, Ed., *Sputtering by Particle Bombardment: I*, Springer Topics in Applied Physics, vol. 47, 1981.
7. A. Benninghoven, *Surf. Sci.* 53: 569, 1975.
8. G. Blaise and A. Nourtier, *Surf. Sci.* 90: 495, 1979.
9. Z. Sroubek, *Nucl. Instr. Meth.* 194: 533, 1982.
10. A. Blandin, A. Nourtier, and D. W. Hone, *J. Physique* 37: 369, 1976.
11. R. Brako and D. M. Newns, *Surf. Sci.* 108: 253, 1981.
12. J. K. Nørskov and B. I. Lundquist, *Phys. Rev.* B19: 5661, 1979.
13. H. D. Hagstrum, in N. H. Tolk, J. C. Tully, W. Heiland, and C. W. White, Eds., *Inelastic Ion Surface Collisions*, New York, 1977.
14. M. Cini, *Surf. Sci.* 54: 71, 1976.
15. R. F. Garret, R. J. MacDonald, and D. J. O'Connor, *Surf. Sci.* 138: 432, 1984.
16. M. L. Yu, *J. Vac. Sci. Technol.* 20: 417, 1982.
17. N. D. Lang, *Phys. Rev.* B27: 2019, 1983.
18. T. R. Lundquist, *J. Vac. Sci. Technol.* 15: 684, 1978.
19. B. J. Garrison, A. C. Diebold, J.-H. Lin, and Z. Sroubek, *Surf. Sci.* 124: 461, 1983.

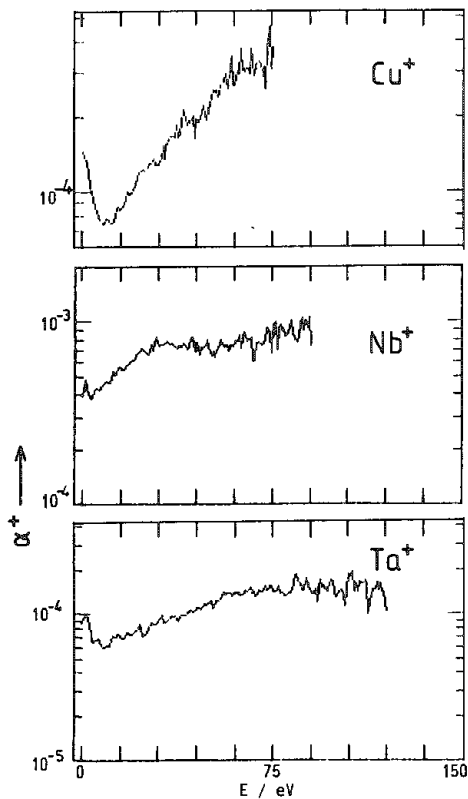


FIG. 1.--Ionization probability for atoms sputtered from polycrystalline Cu, Nb, and Ta as a function of particle emission energy  $E$ . Samples were previously cleaned by bombardment with 2keV,  $45^\circ$   $\text{Ar}^+$  ions.

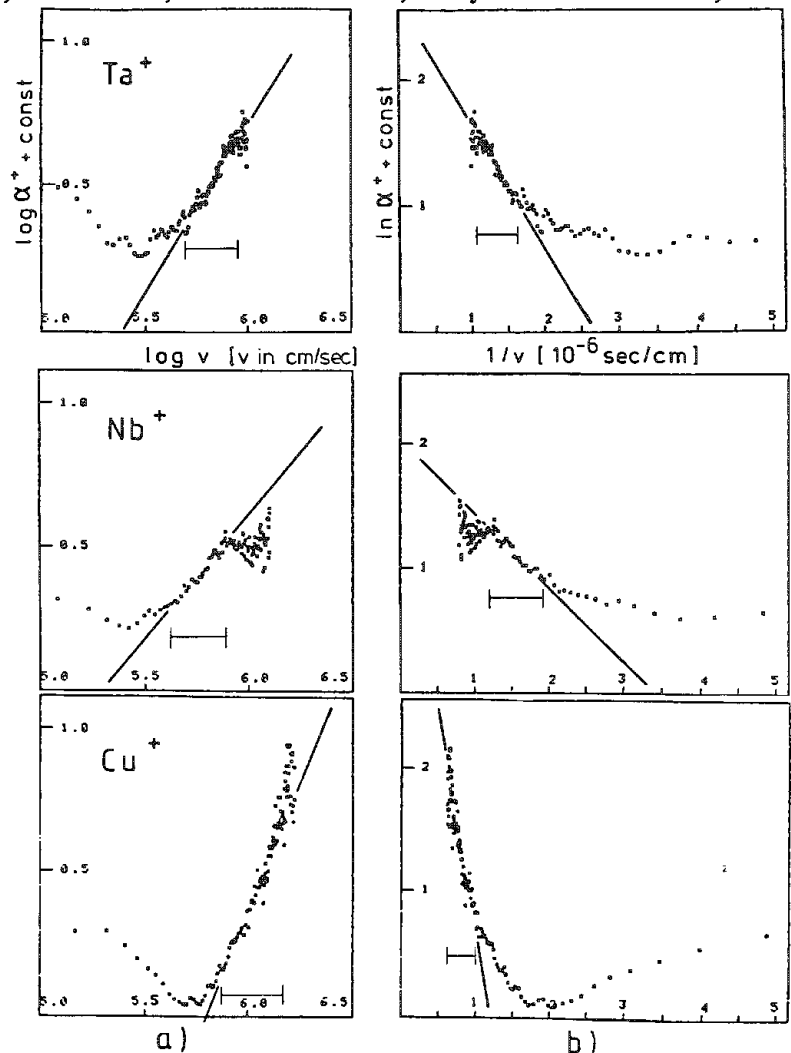


FIG. 2.--Velocity dependence of the ionization probability for atoms ejected from sputter-cleaned Ta, Nb, and Cu in two different logarithmic plots. The straight lines are obtained by least-square fits in the validity region indicated by (|—|).

## DEVELOPMENT OF AN IMAGING TIME-OF-FLIGHT SIMS INSTRUMENT

A. R. Waugh, D. J. Fathers, and D. R. Kingham

Time-of-flight secondary ion mass spectrometry (ToFSIMS) offers the ultimate in detection sensitivity for surface analysis and provides parallel detection of all masses. The exceptional mass spectra that may be obtained with ToFSIMS have been well demonstrated by Benninghoven<sup>1</sup> and others. We report here on the development of the first IMAGING ToFSIMS instrument. The instrument is capable of acquiring a full mass spectrum and up to 8 mass selected images of a sample at the same time.

### *Instrument*

The instrument basically consists of:

- (i) a pulsed primary ion gun,
- (ii) sample handling facilities and high stability stage,
- (iii) an energy focusing time-of-flight mass spectrometer,<sup>2</sup>
- (iv) a chevron channelplate detector, and
- (v) a framestore datasystem for data acquisition and analysis and for instrument control.

A block diagram (Fig. 1) illustrates the instrument components.

### *Primary Ion Gun*

The primary ion gun uses a gallium liquid metal ion source,<sup>3</sup> which is a very high brightness, almost point, source. The maximum primary ion energy is 30 kV and the gun can operate in continuous or pulsed mode (achieved by beam chopping). The ultimate minimum probe size is 1000 Å or better and the minimum pulse duration is 10 ns or less.

### *Mass Spectrometer*

The mass spectrometer of the Poschenreider type has two linear flight tubes and an energy focusing, electrostatic sector analyzer. Energy focusing is achieved by use of a torodial electrostatic field which causes higher-energy ions to have a longer flight path precisely compensating for their higher velocity compared to lower energy ions of the same mass. The total flight path is 2.3 m.

### *Framestore Datasystem*

The major hardware components of the framestore datasystem are a DEC LSI-11 (11-73) computer, a 20Mb fixed Winchester disk, a 10Mb removable Winchester disk, a 512 × 512 pixel by 8 bit framestore, a dedicated control keyboard, and special interfaces for instrument control. System software enables acquisition of ion-induced SEM images as well as time-of-flight SIMS images and mass spectra. Up to 8 128 × 128 pixel images can be acquired simultaneously with a mass spectrum of up to 16 000 channels. All 8 images and any 2000 channels of the mass spectrum can be displayed simultaneously via the framestore. Up to 255 primary ion pulses are made at each pixel of the image per frame and many frames may be acquired sequentially. The software and data acquisition subsystem allow great flexibility in the mass selection for images. Each of the 8 images may be the sum of up to 20 mass windows, so that, for example, an element and various clusters containing that element can be added directly into a single image. This feature is of potentially great value for organic SIMS imaging.

---

The authors are at VG Scientific Ltd., East Grinstead, England RH19 1UB.



### *Data Acquisition Subsystem*

The data acquisition subsystem is a CAMAC unit containing discriminator, 8-channel time to digital converter (TDC), delay generators, and a fast processor with 4k words internal memory and 16k words in an add on memory module (Fig. 1). The TDC has 1 ns channel width and 24 bits range (16 ms) and so is not a limiting factor on the mass resolution or the mass range. The fast processor allows the TDC to be read and cleared for the next pulse in a few microseconds, which allows a pulse repetition rate of 20 kHz.

The fast processor calculates the ion mass from each measured flight time and adds the data to both the spectrum histogram memory and the image memory. Data are transferred back to the framestore datasystem at the end of each line of the image.

### *Mass Range and Mass Resolution*

The data collection rate of the instrument is obviously a function of the primary pulse repetition rate: the rate used in a given experiment is set by the maximum mass expected. For example, with a flight path of 2.3 m and 5kV extraction voltage a particle of mass 290 a.m.u. has a flight time of 40  $\mu$ s.

The mass is given by

$$m = 2eVt^2/d^2 \quad (1)$$

where  $m$  is the ion mass,  $e$  the elementary charge (singly charged ion),  $V$  the extraction voltage,  $t$  the flight time, and  $d$  the path length.

Allowing 10  $\mu$ s to clear the flight tube and read the TDC between pulses, one can detect a maximum mass of 290 a.m.u. with a pulsing frequency of 20 kHz. Figure 2 shows the flight time as a function of the maximum mass that can be detected with the corresponding pulse frequency shown (allowing 10  $\mu$ s clearance time).

The mass range of the instrument is simply extended by reducing the pulse repetition rate: the gradual reduction in the detection efficiency of the channelplate detector at high mass sets a practical upper limit to the mass range.

The mass resolution can be determined from Eq. (1):

$$m/\Delta m = t/2\Delta t \quad (2)$$

and substituting for  $t$  leads to

$$m/\Delta m = [dm^{1/2}/2(2eV)^{1/2}]\Delta t \quad (3)$$

If we assume that  $\Delta t$  is simply the primary pulse width, this result shows that the mass resolution ( $m/\Delta m$ ) increases with the square root of the mass. Figure 3 shows the theoretical mass resolution as a function of mass. It may be seen that in principle a 10ns pulse width allows unit mass resolution at mass 13 800.

### *Instrument Capabilities*

The instrument is capable of analyzing organic and inorganic materials with extreme sensitivity. The parallel detection of a time-of-flight mass spectrometer allows a mass spectrum to be acquired over a wide mass range with a primary ion dose which is lower by a factor of  $10^4$  to  $10^6$  than that required for a quadrupole or magnetic sector mass spectrometer. This circumstance allows high spatial resolution images as well as a mass spectrum to be acquired under Static SIMS conditions. The low primary-ion dose and high sensitivity suggests an application of the instrument to very small area depth profiling.

The instrument is configured to allow a pulsed laser to be fitted for laser microprobe mass analysis with the same mass spectrometer. In combination these two techniques are remarkably powerful, with the speed of analysis in laser microprobe mode complemented by the precision and sensitivity of time-of-flight SIMS.

### *Conclusions*

The first imaging time-of-flight SIMS instrument has been described. It uses a pulsed primary ion beam from a liquid metal ion gun for maximum current density in a sub-

micron spot. The energy focusing mass spectrometer insures a very high detection efficiency for secondary ions leading to exceptional Static SIMS performance with submicron resolution Imaging SIMS.

### References

1. A. Benninghoven, "Ion formation from organic solids," in A. Benninghoven, Ed., *Springer Series in Chemical Physics*, Berlin: Springer, 1983, vol. 25, 640.
2. W. P. Poschenreider, *Int. J. Mass Spec. Ion Phys.* 9: 357, 1972.
3. A. R. Bayly, A. R. Waugh, and P. Vohralik, *Spectrochimica Acta* 40B: 717, 1985.

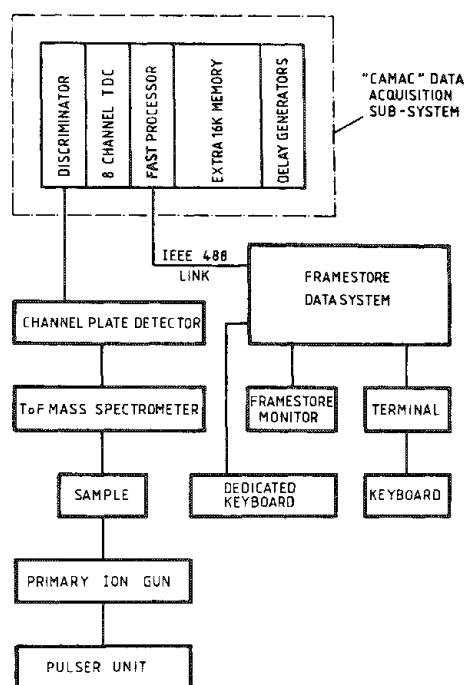


FIG. 1.--Block diagram of time-of-flight SIMS instrument.

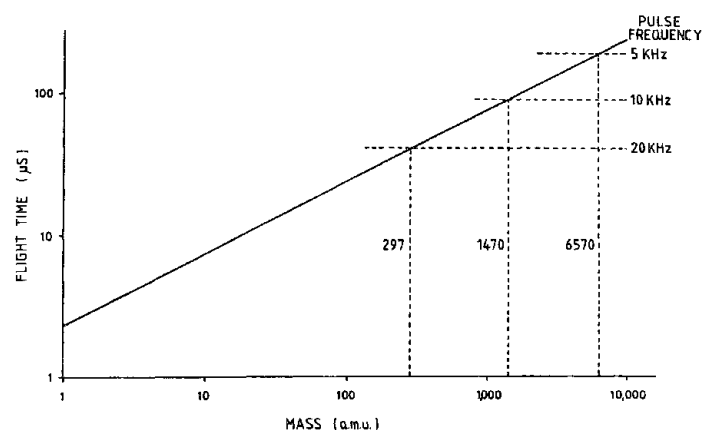


FIG. 2.--Flight time as function of mass. Pulse frequencies indicated allow for 10ns dead time between pulses.

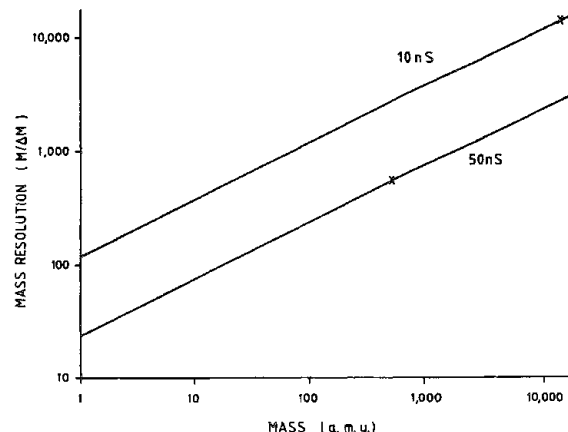


FIG. 3.--Mass resolution of time-of-flight SIMS instrument, for primary ion pulse width of 10 ns and 50 ns, as function of mass. Crosses indicate points at which mass (in a.m.u.) is equal to mass resolution.

## COMPARISON OF SEVERAL NUCLEAR REACTIONS TECHNIQUES FOR HYDROGEN DEPTH PROFILING IN SOLIDS

Fulin Xiong, F. Rauch, Chengru Shi, R. P. Livi, and T. A. Tombrello

Over the past decade nuclear resonant reaction analysis (NRRA) techniques have been widely employed for the study of hydrogen depth profiling in materials in a variety of scientific and technical problems. It has been found that the presence of hydrogen can have dramatic effects on the physical, chemical, and electrical properties of many solids.<sup>1</sup> These studies have normally used ion beams of  $^{19}\text{F}$  at the resonance energy of 16.44 MeV,<sup>2</sup> and  $^{15}\text{N}$  at 6.385 MeV.<sup>3</sup> Recently, an intensive study of hydrogen analysis and profiling with the  $^1\text{H}(^{19}\text{F}, \alpha\gamma)^{16}\text{O}$  reaction at the resonance energy of 6.42 MeV has been carried out in the Caltech Tandem Laboratory and a comparison has been made with the NRRA techniques used previously. It has been found that this method has an excellent depth probe capability and resolution as well as adequate sensitivity. These characteristics guarantee its applicability for most of purposes for hydrogen study in solids.

### *Experiment*

The NRRA techniques for hydrogen depth profiling have been well described elsewhere<sup>1-4</sup> and shall not be repeated in detail here. In the measurement the characteristic  $\gamma$  rays emitted promptly from the excited residual nucleus ( $^{16}\text{O}^*$  or  $^{12}\text{C}^*$ ) are detected. Measuring  $\gamma$ -ray yields as the incident-beam energy is varied gives a direct indication of hydrogen concentration as a function of depth in the target. For convenience we shall use the notations of NL for the profile technique with a  $^{15}\text{N}$  ion beam at the low-energy resonance, FL for  $^{19}\text{F}$  ion beam at the low-energy resonance, and FH for  $^{19}\text{F}$  at the high-energy resonance.

Our experiment has been done on the Caltech EN-Tandem Accelerator. The ion beams of  $^{15}\text{N}$  and  $^{19}\text{F}$  generated in the accelerator were magnetically analyzed and directed through a collimator onto the target which was mounted in a scattering chamber under a  $5 \times 10^{-7}$  Torr vacuum. An  $8 \times 5$  in. NaI(Tl) scintillation detector placed at  $90^\circ$  to the incident beam direction about 5 cm from the target was used for  $\gamma$ -radiation detection. The pulses from the detector were amplified and analyzed in a MCA system.

For the purpose of our work, the geological minerals elbaite and zoisite with known hydrogen concentrations<sup>5</sup> were used as standards. A tantalum foil was used for the study of the depth resolution on the surface, as it is believed that there are only a few monolayers of hydrocarbon contamination on the surface, with very little hydrogen inside. To investigate the energy straggling and determine depth resolutions inside the material, we employed Si crystals with evaporated Ag surface layers of thicknesses of 65, 200, and 300 nm, respectively. There was a thin hydrocarbon layer at the interface between the Ag layer and the Si crystal, since evaporation was deliberately done under a vacuum of  $5 \times 10^{-5}$  Torr.

### *Results and Discussion*

The hydrogen depth profiles of elbaite are shown in Fig. 1. The hydrogen profiles of the Ta foil and the results of profiles on the Ag-coated Si samples are presented in Figs. 2 and 3. From these figures one has a clear overview of the characteristics of the three NRRA techniques for hydrogen depth profiling.

*Sensitivity.* From the yield curves of elbaite (Fig. 1) we see that the average yields by the three techniques are  $Y(\text{NL}):Y(\text{FL}):Y(\text{FH}) = 1:1.1:12.5$ , which are close to the values calculated from the known resonance parameters (1:1.35:13.2). One can conclude that the analysis sensitivity is in the order of  $S(\text{NL}) < S(\text{FL}) < S(\text{FH})$ . However, one should notice

---

The authors are at the Division of Physics, Mathematics, and Astronomy, California Institute of Technology, Pasadena, CA 91125. This work was supported in part by NSF Grant DMR 83-18274.

that the off-resonance yield in using the FH beam is significantly large (the ratio of off-resonance yield to resonance yield is only approximately 1:3), but it is much smaller in NL and FL. This result is caused in thick hydrogen-containing layers by the presence of the resonances at lower energies; thus, for such samples, the sensitivity of the FH technique is somewhat reduced. In addition, the high-energy  $^{19}\text{F}$  beam can induce reactions with other light elements (e.g., Li, Be, and B) and gives the same  $\gamma$  rays as from the hydrogen reaction; that may be a reason the profile curve tilts up while the beam energy is increasing.

*Depth Resolution.* By profiling the hydrogen contamination on the surface of the Ta foil, the FWHM of surface peaks of 14, 48, and 90 keV for NL, FL, and FH were observed, respectively. These numbers can be taken as representing the surface depth resolutions under our experimental conditions, which are typical in many laboratories. Compared with the known resonance widths there exists a large difference from our experimental FWHM value for the NL method (1.8 vs 14 keV). Various factors<sup>6,7</sup> broaden the natural resonance width. The Doppler effect from thermal motion may be the factor that dominated the NL resonance width broadening. For FL and FH profiles the Doppler effect has become almost negligible, as their natural resonance widths are so large. Using the energy loss of the incident beam in the target material,<sup>8</sup> we can convert the FWHM values (in keV) to a depth resolution, at the surface of a silicon target: 9.6, 24.0, 46.2 nm for NL, FL, FH techniques, respectively.

By profiling the Ag-coated Si crystalline samples with the three techniques, one can clearly observe the effects of beam energy straggling in the targets. Due to the poor depth resolution it was hard to separate the interface peak at 65 nm from the surface peak in the FL profile. Even worse, the interface peak was totally covered by the surface peak when FH was used. It can be seen that deeper inside the target the depth resolution is further broadened by beam energy straggling as well as by the factors that affect the surface depth resolution. From the experimental behavior of this broadening as a function of depth in the Ag-coated Si samples illustrated in Fig. 4, the depth resolution of NL is seen to widen quickly inside the sample since the resonance width of NL is narrower, whereas for FH it is only a small change because the peak is already so broad.

*Depth Probe Range.* The depth probe range for depth profiling depends mainly on the gap between the resonance used to the next higher one. These gaps are 7.1, 2.7, and 1.2 MeV for the NL, FL, and FH resonances, respectively. Conversion to the depth scale in a Si target yields 4.8, 1.3, and 0.5  $\mu\text{m}$ .

*Availability of the Technique.* All three techniques can be achieved with most tandem accelerators, and the production of a beam of  $^{19}\text{F}$  is particularly easy and economical as it requires only freon-12 and helium-4 for ion source; however, the  $^{15}\text{N}$  beam requires that the ion source of the accelerator be operated with a rare isotope of nitrogen-15 of high enrichment. Both the NL and FL techniques can of course be used on smaller single-ended accelerators by use of multiple-charged ions.

## Conclusions

The results of our work have illustrated the capabilities and characteristics of the three NRRA techniques for hydrogen depth profiling and concentration analysis. The best choice among the three techniques clearly depends on the chemical composition and hydrogen concentration of the sample, on the depth to be probed, and on the accelerator available. Use of  $^{15}\text{N}$  beam allows a superior depth resolution but a relatively low yield. Use of a high-energy  $^{19}\text{F}$  beam provides a high yield but the poorest depth resolution and the smallest depth probe range. Use of a low-energy  $^{19}\text{F}$  beam is roughly comparable to the  $^{15}\text{N}$  beam in sensitivity and depth range but the depth resolution is poorer; however, it is suitable for many purposes of hydrogen depth profiling. Moreover, the low-energy  $^{19}\text{F}$  resonance can also be used with lower-energy accelerators like the  $^{15}\text{N}$  resonance, but with a much cheaper ion source gas.

In the data reduction, care should be taken with the off-resonance reaction yields and, for some target materials,  $\gamma$ -ray yields from nuclear reactions with other light elements. One should also deal carefully with the surface hydrocarbon contamination contributions, which are always present under normal vacuum conditions and which may be greatly minimized by baking, if it is permissible, in a UHV system before profiling.

## References

1. G. Amsel and W. A. Lanford, *Ann. Rev. Nucl. Part. Sci.* 34: 435, 1984.
2. D. A. Leich and T. A. Tombrello, *Nucl. Inst. and Meth.* 108: 67, 1973.
3. W. A. Lanford, H. P. Trautvetter, J. F. Ziegler, and J. Keller, *Appl. Phys. Lett.* 28: 566, 1976.
4. C. A. Barnes, J. C. Overley, Z. E. Switkowski, and T. A. Tombrello, *Appl. Phys. Lett.* 31: 239, 1977.
5. G. R. Rossman, Caltech, private communication for the composition of the tourmaline samples: elbaite:  $\text{Na}(\text{Li}, \text{Al})_3\text{Al}_6(\text{BO}_3)_3\text{Si}_6\text{O}_{18}(\text{OH})_4$ , (0.3 wt% hydrogen); zoisite:  $\text{Ca}_2\text{Al}_3(\text{SiO}_4)_3(\text{OH})$ , (0.22 wt% hydrogen).
6. G. Amsel and B. Maurel, *Nucl. Inst. and Meth.* 218: 183, 1983.
7. G. Amsel, Ed., C. Cohen, and B. Maurel, *Nucl. Inst. and Meth.* B14: 226, 1986.
8. J. E. Ziegler, Ed., *Handbook of Stopping Cross Sections for Energetic Ions in All Elements*, 1980.

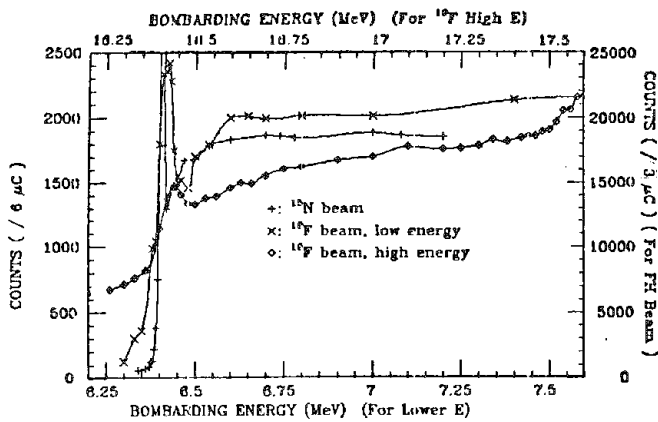


FIG. 1.--Hydrogen depth profiles of elbaite (0.3 wt% H) by three NRRA techniques with  $^{15}\text{N}$  and  $^{19}\text{F}$  ion beams.

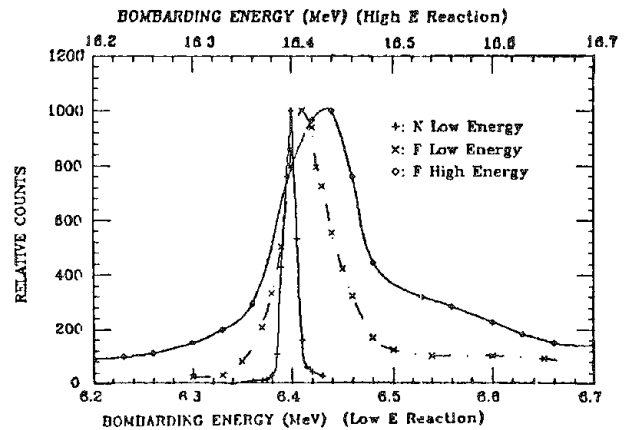


FIG. 2.--Hydrogen depth profiles on surface of Ta foil by three NRRA techniques for comparison of surface depth resolution.

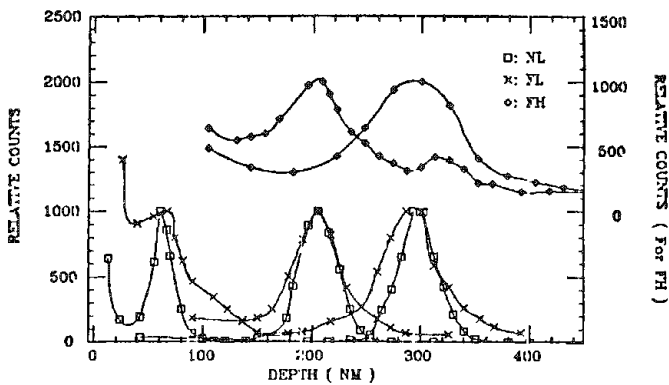


FIG. 3.--Hydrogen depth profiles with three NRRA techniques of Si crystals with Ag layers of 65, 200, and 300 nm on surface.

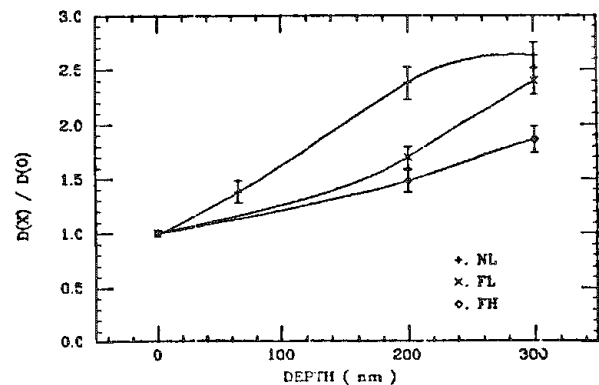


FIG. 4.--Depth resolution broadening of NRRA techniques on interface of Ag-coated Si crystal from our experimental results.

## OPTIMIZATION TECHNIQUES FOR RASTER-GATE SIMS DEPTH PROFILES

B. C. Lamartine

SIMS depth profiling efficiency has been enhanced by the use of primary beam neutral trapping, rastering, and, more recently, electronic gating. Commercial systems employing such features have become available. Model calculations of raster crater shape and profile resolution have been reported by Wittmaack.<sup>1</sup> In that paper it was noted that beam spot size, which determines useful gate, raster, and profile resolution, can be measured from the completed sputter crater. This work develops an alternative scheme to optimize profiles of ion implants using spot-size measurements from straightedge current profiles of the primary ion beam and deflection (magnification) factors measured from grid-current images. It will be shown that the dynamic range of an implant profile can be optimized for any combination of primary ion energy and beam spot size.

### *Experimental*

A commercial Atomika A-DIDA 3000-30 SIMS instrument was modified to include a UTI 100C residual gas analyzer for leak detection, three standard SEM/TEM electroformed mesh image calibration grids, a Faraday cup, and a straightedge made from a section of a razor blade. Addition of a commercial target phosphor also proved useful for obtaining rough ion beam focus before more precise beam measurements were made. High (500nA) and low (1nA) current  $O_2^+$  beams of potentials between 2 and 15 kV were passed through a differential pumping stage, momentum analyzer, neutral trap, and focus optics before bombardment of the specimen. Thus conditioned, the primary beam was brought to best focus by inspection of an oscilloscope output of collected current versus x or y deflector voltage. Scans of the straightedge and grids were taken in both x and y directions to minimize astigmatism. The straightedge current profiles were used to calculate spot size and, by a small motion of the sample manipulator, to calculate beam deflections. Use of the line scan over a grid was more convenient and gave more reproducible results. All deflections reported herein were obtained from grid line scans.

The target chamber was prepared for SIMS operation by residual gas mass analyses. No components of the gas mass spectrum indicated a leak to the atmosphere. The vacuum integrity was further investigated by helium gas probing at all flanges and welds. No change in helium background was detected in the gas analyzer. With the primary ion beam in operation at high current, the target chamber pressure was never greater than  $5 \times 10^{-10}$  Torr.

Samples used for SIMS profiling were standard boron implants<sup>2</sup> in silicon (110) (11B<sup>+</sup>, 40 keV,  $1 \times 10^{16}$  ions  $cm^{-2}$ ,  $R_p = 130.2$  nm,  $\Delta R_p = 44.3$  nm)<sup>3,4</sup> with a 5° implant axis inclination. No background subtraction of the SIMS profiles was performed.

### *Results*

Integrated current profiles such as Fig. 1 permitted calculation of the beam radius  $\rho$ , defined as half the distance required to measure the transition from 0 to 100% collected current. Figure 2 is typical of line scans over the electroformed grid. Such data were used to calculate deflections. Having obtained deflections at different incident ion energies, the area of any square raster could be calculated from Fig. 3, given the deflection voltage range.

According to the model of Wittmaack,<sup>1</sup> a raster-gate profile with minimal edge effects must behave according to:

$$\xi_0 - \delta \geq 3 \quad (1)$$

$$\text{where } \xi_0 = \chi_0 / \rho, \chi_0 = \frac{1}{2} \text{ raster width} \quad (2)$$

---

The author is at Motorola, Inc., Semiconductor Research and Development Laboratory, MS A112, 5005 East McDowell Road, Phoenix, AZ 85008.

$$\delta = \frac{1}{2} \text{ gate width} \quad (3)$$

In practice  $\xi \geq 3$ , so that a flat crater bottom is formed from a Gaussian beam.

With the information obtained from spot size measurements and deflection factors, one can use the profiling model to trade dynamic range (due to crater effects and SIMS signal from the beam tail when the beam is outside the electronic gate) for profiling time (due to effective current density as a result of raster square size). Figure 4 shows a series of depth profiles of the boron/silicon implants taken with  $O_2^+$ , 500 nA at 12 keV. The beam spot radius was 59.4  $\mu\text{m}$ . Curve (a) shows a high peak count rate, low dynamic range, and low profiling time. Curves (b) and (c) show increasing dynamic range and profiling time; and curve (d) is past optimum in that no significant increase in dynamic range is observed, but the profiling time is longer. For this series of implants, then, the optimum profiling conditions occur in the ranges:

$$4.83 \leq \xi_0 \leq 5.67 \quad (4)$$

$$3.38 \leq (\xi_0 - \delta) \leq 3.97 \quad (5)$$

The values of  $\xi_0$  are sufficiently high to produce acceptably flat crater bottoms, as verified by profilometer measurements. Values of  $\xi_0 - \delta$  are in agreement with the model in that  $\xi_0 - \delta \approx 3$  is predicted for a  $10^{-2}$  change in ion intensity for breakthrough of an overlayer. Since the implant is a different profiling problem, we find the agreement to be very good.

### Conclusions

The model of raster-gate depth profiling, first demonstrated successfully on layer structures, has been extended for optimum profiling of implant structures. Values of  $\xi_0$  and  $\xi_0 - \delta$  are in reasonable agreement with previous layer structure experiments. Use of the results of this work permits the experimenter to choose optimum implant profiling conditions if the acceleration energy and beam spot size are known.

### References

1. K. Wittmaack, *Appl. Phys.* 12: 149, 1977.
2. W. K. Hofker, *Philips Res. Repts. Suppl.* No. 8, 1975.
3. J. Lindhard, M. Scharff, and M. Schiott, *Mat. Fys. Medd, Dan. Vid. Selsk* 33: 1, 1963.
4. J. F. Gibbons, W. S. Johnson, and S. W. Mylroie, *Projected Range Statistics for Semiconductor and Related Mat'ls*, New York: Academic Press, 1975, 2d ed.

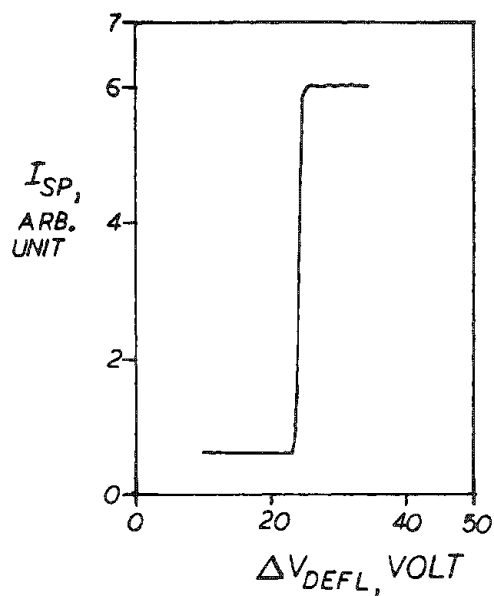


FIG. 1.--Typical integrated current profile. Beam conditions: 15 keV  $O_2^+$ , 1 nA. Full transition width, rather than FWHM, was measured to avoid influence of beam tailing in depth profile.

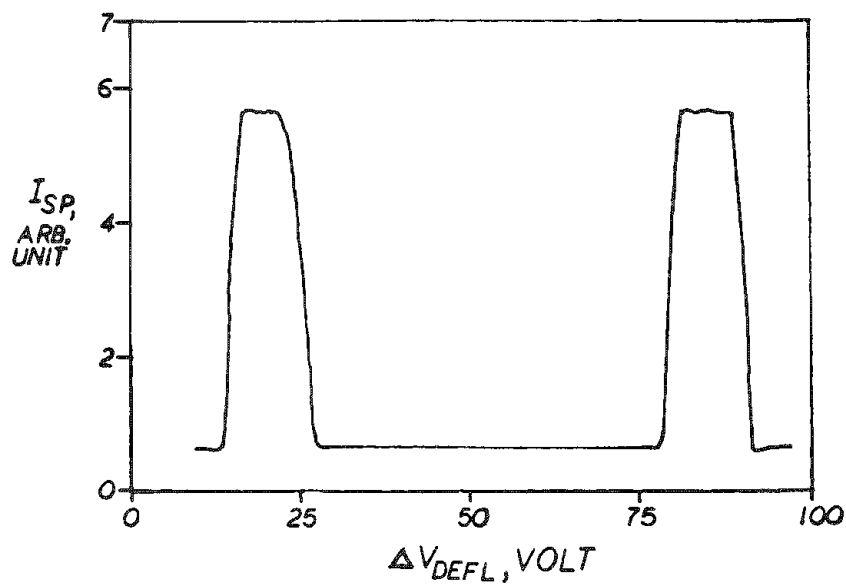


FIG. 2.--Example of line scan over electroformed mesh. Leading edge-leading edge distance was 333  $\mu m$ .

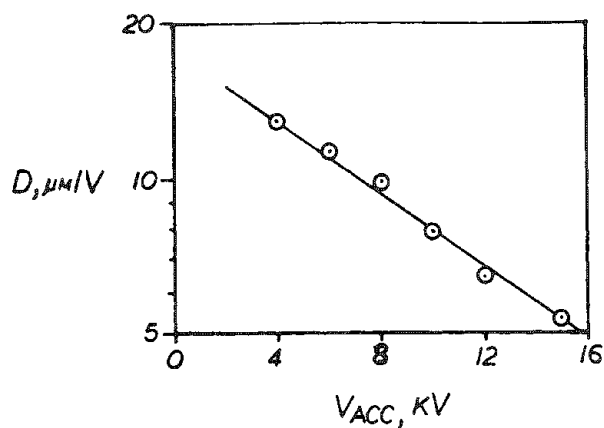


FIG. 3.--Measured deflection factors for Motorola's A-DIDA 3000-30.

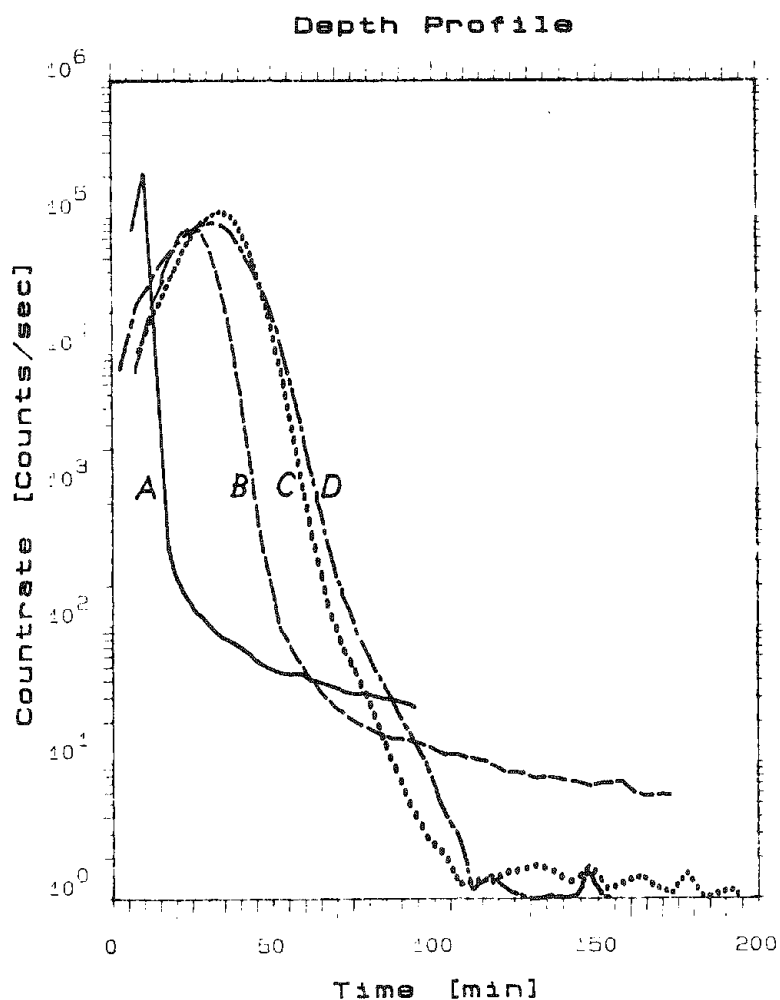


FIG. 4.--SIMS depth profiles of boron implants. (a)  $\xi_0 = 3.00$ ,  $\delta = 0.90$ ; (b)  $\xi_0 = 3.78$ ,  $\delta = 1.52$ ; (c)  $\xi_0 = 4.83$ ,  $\delta = 1.45$ ; (d)  $\xi_0 = 5.67$ ,  $\delta = 1.70$ .



## QUANTITATIVE SIMS MICROANALYSIS OF TRACE ELEMENTS IN GEOLOGICAL SAMPLES USING IN SITU ION-IMPLANTED STANDARDS

Lori A. Streit, R. L. Hervig, and Peter Williams

Secondary ion mass spectrometry (SIMS) is currently the only technique available for microanalysis of trace elements ( $<0.01$  wt.%) in minerals. It has been demonstrated that quantitative analysis using SIMS is possible if suites of well-documented standards are available to establish working curves.<sup>1</sup> However, preparation and analysis of standards is not simple; the only techniques capable of analyzing trace levels are bulk analysis techniques, for which standards are typically made as glasses to insure the homogeneity that is essential when bulk analysis is compared with microanalysis. Havette has recently pointed out that ion migration due to charging may occur to differing extents in glasses and crystals.<sup>2</sup> Because most minerals are crystalline, the use of glass standards to quantify mineral samples may be questionable. Ion implantation has long been advocated as a means of preparing SIMS standards for trace elements,<sup>3,4</sup> because the standard can be introduced directly into the analytical sample, so that ion yield matrix effects, and even charge-induced effects, should be identical for the intrinsic analyte and the superimposed implant. The difficulty for geochemical work is that many elements of geochemical interest are not routinely available in commercial ion implanters. Wittmaack first used the primary ion column of a SIMS instrument as a low-energy ion implanter,<sup>5</sup> and Lareau and Williams<sup>6</sup> and Smith and Morrison<sup>7</sup> have shown that this approach may be used to make ion-implanted standards in conducting or semiconducting samples. The present paper describes the extension of the in situ implantation approach to quantify trace elements in insulators and geological samples. Techniques have been developed for potassium analysis which in principle can be applied to all alkali metals, providing elemental analyses that would not be easily achievable with an electron probe. Results are presented for NBS standard glasses and a mineral.

### *Experimental*

Ion implantation and subsequent depth-profile analyses were performed with a Cameca IMS 3f ion microanalyzer<sup>8</sup> equipped with a primary mass filter.<sup>9</sup> The mass filter allows selection of ion beams from either of two ion sources operating simultaneously, which permits rapid transition (approximately 5 min) between implantation and analysis. An alkali surface ionization source supplied a  $^{41}\text{K}^+$  ion beam for implantation, and a duoplasmatron source generated the  $^{16}\text{O}^-$  ion beam used for analysis. The mass resolution of the mass filter was sufficient to give a  $^{41}\text{K}^+$  beam with negligible ( $<1\%$ ) contamination by  $^{39}\text{K}^+$ .

The samples selected for these experiments were two glasses, NBS 610 and NBS 620, and a Lake County plagioclase. They were all prepared identically: polished on a buffing wheel with  $0.05\ \mu\text{m}$  alumina, cleaned by sonication in distilled water followed by ethanol, and finally coated with approximately  $300\ \text{\AA}$  of Au/Pd alloy. Sample analysis consisted of three steps: presputter, implantation, and depth profiling. In order to obtain a steady-state secondary ion signal, the analytical ion beam,  $^{16}\text{O}^-$  at  $17\text{keV}$  impact energy, was used to presputter a  $500 \times 500\ \mu\text{m}$  area for 20 min. This procedure exposed a clean surface, established a steady-state charging level and the sample voltage offset level required to compensate for this (typically  $+90\ \text{V}$ ), and established a steady-state level of the analyzing beam in the near-surface region of the sample.<sup>6</sup>

Precise measurement of all implant parameters was necessary. The implant beam,  $^{41}\text{K}^+$  (5 nA) at  $17\text{keV}$  impact energy, was rastered over a nominal area  $500 \times 500\ \mu\text{m}$  for a time to give a nominal dose  $\sim 4 \times 10^{13}$  atoms/ $\text{cm}^2$ . The precise dose was determined from measurements of the implant time, ion current, and implanted area. Implant time was controlled by the real-time clock of the instrument control computer (HP9836) and the primary current was measured with an electrometer (Keithley 600B) while

---

The authors are in the Department of Chemistry, Arizona State University, Tempe, AZ 85287. This work was supported in part by NSF Grant DMR 8206028.

the ion beam was directed into a Faraday cup constructed in the sample holder. The implanted area was determined by measurement of a crater sputtered by the implant beam with an optical microscope. Depth profiles of  $^{39}\text{K}^+$  and  $^{41}\text{K}^+$  were recorded during sputtering through the implant profile with a  $^{16}\text{O}^-$  beam rastered over a  $250 \times 250 \mu\text{m}$  area centered within the presputtered region. The analysis raster was made smaller than the presputter raster to ease alignment problems; the different raster sizes probably accounted for small signal variations at the beginning of the depth profiles. A sample voltage offset was used to reject low-energy molecular ion signals (e.g.,  $\text{NaO}^+$ ,  $\text{MgO}^+$ ). Secondary ions were accepted from a circular area  $62 \mu\text{m}$  in diameter centered within the sputtered area. Sputtering was continued to obtain crater depths of  $2000 \text{ \AA}$  to allow precise depth measurement. The presputtering procedure assured that sputtering rates were constant over the entire sputtering time. Crater depths were measured with both a Dektak stylus profilometer and a Zeiss interferometer. The two measurements agreed within 3%.

### *Results and Discussion*

Results are presented in Table 1. Nominal values for the NBS standards were taken from the NBS standard reports (these are considered preliminary data by NBS), and for the Lake County plagioclase from isotope dilution analyses with external standards published by Meyer et al.<sup>10</sup> The use of  $^{41}\text{K}$  as the implant species allowed superimposition of a significant level of the implant on the intrinsic level without raising the total K content to a point where ion yields might be affected,<sup>11</sup> and allowed us to monitor  $^{39}\text{K}$  throughout the profile. A typical depth profile is shown in Fig. 1. Small variations were sometimes seen in the  $^{39}\text{K}$  signal near the surface, possibly a result of differences in sample charging due to the different analysis and presputter raster sizes. The  $^{41}\text{K}$  signal should be identically influenced by such effects although the  $^{40}\text{CaH}$  contribution to the background may not be; the data reported in Table 1 are uncorrected and therefore may be high by about 5%. Note that the profile is far from being a symmetric Gaussian profile, such as may be obtained for high-energy implants. The profile shape is distorted by ion-beam mixing effects and perhaps charge-induced migration. That does not affect the calibration procedure, which simply compares the profile integral (background-subtracted) with the average  $^{41}\text{K}$  concentration over the analyzed depth given by the quotient of the implanted dose and the crater depth.<sup>12</sup> The resultant calibration factor was used to convert the count rate for  $^{39}\text{K}$  to a concentration. Isotope fractionation effects should be small and were ignored.

The results in Table 1 indicated that in situ ion implantation can allow SIMS analyses accurate to within 10%. Reproducibility between two replicate analyses is demonstrated with the Lake County plagioclase to better than 2%. Several difficulties were overcome to obtain these analyses. The major problem was the charging of the insulating sample. Havette and Slodzian have discussed this problem in detail.<sup>13</sup> We reduced charging in the present case by using a negative primary beam, applying a metallic coat to the sample, presputtering for an extended period, and using an energy offset to minimize residual charging effects. It was found to be important to assure analysis conditions similar to those used to presputter; a small misregistration of the analyzing raster on the presputtered area could result in further erosion of the metal coat at one edge of the crater, and a consequent small drift in secondary ion signals. The beam current used for analysis was also found to be important. Use of an analysis raster smaller than the presputter raster eased this problem. Havette and Slodzian have commented that beam currents cannot be too high if charging is to be controlled;<sup>13</sup> a current of 60 nA was offered the best compromise between charging effects and a reasonable analysis time in the present work. With this current, a profile typically took 1 h to complete.

Low-energy molecular interferences arising from  $\text{NaO}^+$  and  $\text{MgO}^+$  signals were made negligible by the use of a sample voltage offset. However, a  $^{40}\text{CaH}^+$  interference at mass 41 did not exhibit a narrow energy distribution, and could not be eliminated in this way. The CaH contribution was eliminated by subtraction of the constant mass 41 signal determined at the end of the profile; if the CaH signal varied near the surface as did the K signals, this procedure would introduce a small error (typically < 5%). Migration of the potassium away from the analyzing beam did not appear to be a problem in the present work; other work in our laboratory indicates that potassium analysis in geological samples presents no unusual difficulties, since linear calibration curves in K-rich glasses can be obtained routinely.<sup>14</sup>

## Conclusion

These preliminary studies demonstrate that SIMS analysis using standards prepared by in situ ion implantation can accurately quantify trace elements in geological samples and other insulators.

TABLE 1.--Preliminary quantitative in situ ion implantation results for geological samples.

Sample	Nominal Value	Analysis Technique	SIMS Analysis	Percent Error
NBS610	250ppma	Isotope Dilution	280ppma	7.2
NBS620	1800ppma	X-ray Fluorescence Spectrometry	1860ppma	4.0
Lake County Plagioclase	540ppma	Isotope Dilution	590ppma 605ppma	7.4 10.2

## References

1. N. Shimizu, "Energy filtering and quantitative SIMS analysis of silicates for major and trace elements," *Secondary Ion Mass Spectrometry, SIMS II*, Berlin: Springer-Verlag, 1979, 62-63.
2. A. Havette, "Mineralogical application of the ion microscope elementary analysis," *SEM/1985 II*, 585-594.
3. R. P. Gittins, D. V. Morgan, and G. Dearnaley, "The application of the ion microprobe analyser to the measurement of the distribution of boron ions implanted into silicon," *J. Phys.* D5: 1654-1663, 1972.
4. M. Croset and D. Dieumegard, "Quantitative secondary ion mass spectrometry analysis of oxygen isotopes and other light elements in silicon oxide films," *Corrosion Science* 16: 703-715, 1976.
5. K. Wittmaack, "Oxygen-concentration dependence of secondary ion yield enhancement," *Surf. Sci.* 112: 168-180, 1981.
6. R. T. Lareau and P. Williams, "In-situ ion implantation for quantitative SIMS analysis," *Mat. Res. Soc. Symp. Proc.* 48: 273-279, 1985.
7. H. E. Smith and G. H. Morrison, "On-line ion implantation for quantification in secondary ion mass spectrometry: Determination of trace carbon in thin layers of silicon," *Anal. Chem.* 57: 2663-2668, 1985.
8. J. M. Gourgout, "Use of the IMS-3f high mass resolving power," *Secondary Ion Mass Spectrometry, SIMS II*, Berlin: Springer-Verlag, 1979, 286-290.
9. J. J. Le Goux and H. N. Migeon, "Principles and applications of a dual primary ion source and mass filter for an ion microanalyser," *Secondary Ion Mass Spectrometry, SIMS III*, Berlin: Springer-Verlag, 1981, 52-56.
10. C. Meyer, D. H. Anderson, and J. G. Bradley, "Ion microprobe mass analysis of plagioclase from 'non-mare' lunar samples," *Proc. Lunar Sci. Conf.* 5: 685-706, 1974.
11. P. Williams, K. M. Stika, J. A. Davies, and T. E. Jackman, "Quantitative SIMS analysis of hydrogenated amorphous silicon using superimposed deuterium implant standards," *Nucl. Inst. Meth.* 218: 299-302, 1983.
12. D. Leta and G. H. Morrison, "Ion implantation for quantitative ion microprobe analysis," *Anal. Chem.* 52: 277-280, 1980.
13. A. Havette and G. Slodzian, "Experimental procedures for quantitative analysis of silicate minerals," *Secondary Ion Mass Spectrometry, SIMS III*, Berlin: Springer-Verlag, 1981, 288-291.
14. R. L. Hervig, Arizona State University, unpublished.

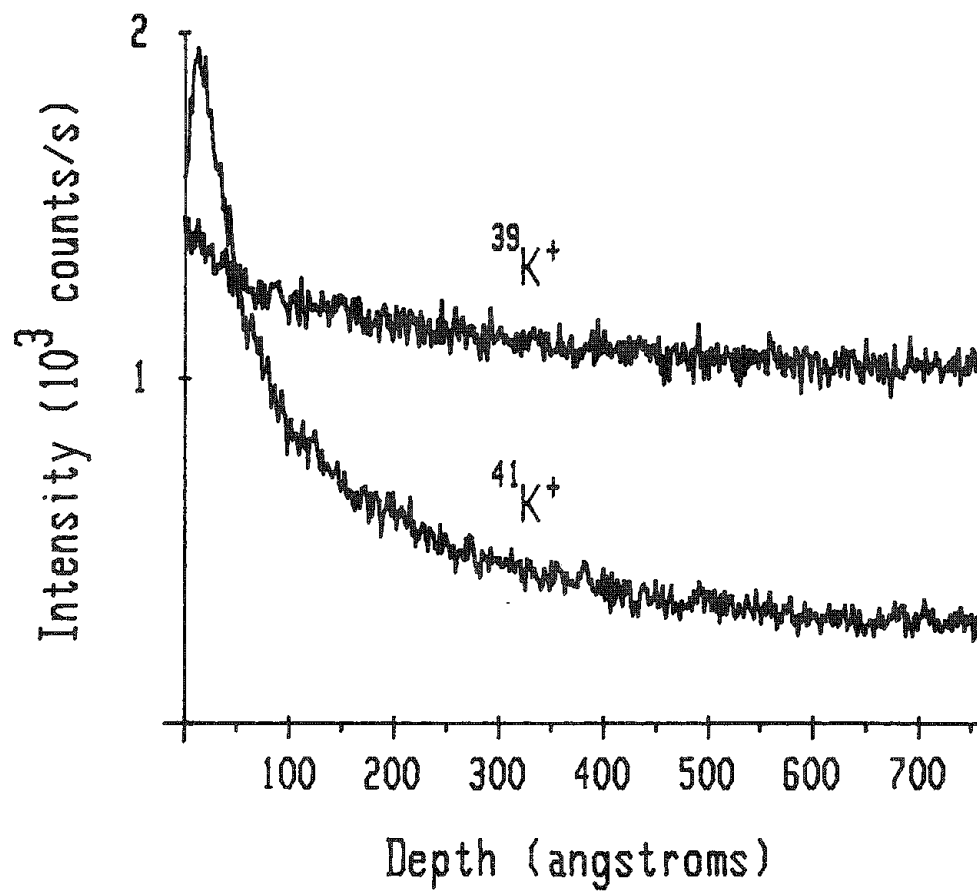


FIG. 1.--Typical implant profile of potassium in Lake County plagioclase.

## MATRIX EFFECTS IN SIMS ANALYSIS OF BIOLOGICAL TISSUE

Margaret Burns

Differential sputtering effects have been reported for muscle tissue prepared with and without heavy metal staining.<sup>1</sup> Studies with plant tissue showed differential sputtering rates of cell walls, nuclei, and cytoplasm.<sup>2</sup> Quettier and Quintana<sup>3</sup> showed that both  $C^+$  and  $C^-$  ion currents were higher in an organic matrix than a mineral one, an example of enhanced ion emission due to the chemical microenvironment.

We have made some observations on sputtering and ion emission of a highly heterogeneous tissue, retina, that suggest that both differential sputtering and ion emission effects may be occurring.

### *Materials and Methods*

Retinas from adult toads were prepared either by conventional EM techniques, involving fixation with glutaraldehyde and postfixation with osmium, or by freezing at  $-130^\circ\text{C}$  and freeze-drying at  $-30^\circ\text{C}$ . Tissues were then embedded in epoxy resin, sectioned at  $10\ \mu\text{m}$  with a dry glass knife, supported on boron-doped silicon wafers, and overcoated with 99.999% Au prior to analysis.

Either the Cameca IMS300 or Cameca IMS3f were operated with a primary  $O_2^+$  primary beam at currents from 30 to 100 nA, and positive secondary ions were imaged for the elements of interest. Scanning electron microscopy was performed on a JEOL 35 instrument.

### *Results*

As previously reported, structures that give very high emission of sodium, potassium, and calcium are the melanin granules of the retinal pigment epithelium and choroid.<sup>4</sup> When this material was examined after sputtering, prominent cone formation was observed in a distribution that corresponded to the melanin granules of the choroid and retinal pigment epithelium (Fig. 1), in both fixed and freeze-dried specimens, although it appeared to be qualitatively less marked when the tissue had not been stained with osmium, which enhances the normal electron density of melanin granules (Fig. 2). We also observed that red blood cells, which have an inherently high iron content, also exhibited cone formation.

Subjecting freeze-dried tissue to osmium vapors dramatically altered the ion emission of calcium in the nuclear layers. Freeze-dried retina exhibits a paucity of calcium emission in the nuclear layers, yet when it was exposed to osmium vapors, the nuclei were highly emissive in calcium, as they are when tissue is fixed with osmium. This is not a diffusion of ions in general, since barium does not translocate from its selective site in the choroidal melanocytes. We interpret this result as enhanced ion emission of calcium from sites which take up heavy metal stains.

### *Discussion*

The simultaneous occurrence of increased ion emission from structures that are refractory to sputtering maybe explained by increased surface area to react with oxygen, which results in increased ion emission compared with adjacent tissue. It is clear that increased sputtering rates cannot be assumed to be equivalent to increased ion emission, as in this case the opposite is true. The sputtering differences may be due to variations in density of the organelles, although these density differences are small. Linton et al.<sup>5</sup> demonstrated etch resistance in freeze-dried nuclear and plasma membranes, which are largely lipid and are thus less dense than the cell cytosol. It seems that subtle matrix effects may be as bothersome in analysis of biological tissue as in other materials.

---

The author is at the Department of Ophthalmology, School of Medicine, University of California, Davis, CA 95616. This work was supported in part by a Research to Prevent Blindness Research Manpower Award.

## References

1. M. E. Farmer, R. W. Linton, P. Ingram, J. R. Sommer, and J. D. Shelburne, *J. Microscopy* 124: RP1, 1981.
2. A. J. Patkin, S. Chandra, and G. H. Morrison, *Anal. Chem.* 54: 2507, 1982.
3. A. Quettier and C. Quintana, *Compt. Rend. Acad. Sci. (Paris)* 289: 433, 1979.
4. M. S. Burns, D. M. File, K. T. Brown, and D. G. Flaming, *Brain Res.* 220: 173, 1981.
5. R. W. Linton, M. E. Farmer, P. Ingram, and J. D. Shelburne, *SEM/1982* III, 1191.

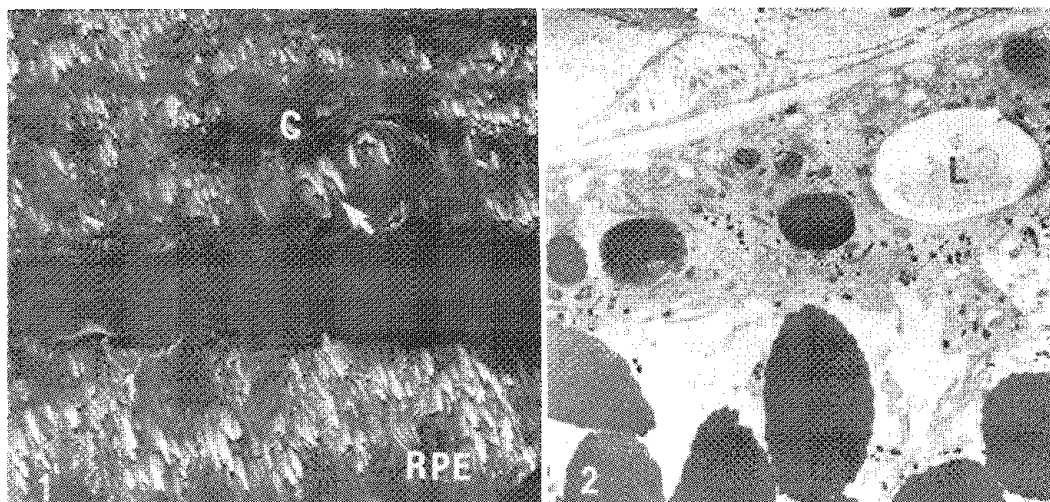


FIG. 1.--SEM image of retina and choroid after 90 min of oxygen sputtering. Raised cone structures correspond to distribution of melanin granules in retinal pigment epithelium (RPE) and choroid (C). Cone formation from red blood cell (arrow) in choriocapillaris is also apparent.

FIG. 2.--TEM image of retinal pigment epithelium showing pigment granules located circumferentially around lipid droplet L.

## DIFFUSION PROFILES OF BORON AND ARSENIC MEASURED BY SPREADING RESISTANCE AND SECONDARY ION MASS SPECTROMETRY

G. G. Sweeney and A. R. Alvarez

As design rules are scaled down in integrated circuit fabrication, vertical scaling of impurity profiles must also be pursued. It follows that the ability to measure, understand, and control impurity profiles becomes more important. That is true both in the vertical and lateral dimensions. Because of the difficulty inherent in lateral profile measurement, this paper is restricted to a discussion of vertical impurity profiles; in particular, shallow junction profiles, typical of advanced bipolar and MOS processes.

The techniques most commonly used to measure impurity profiles in silicon are the spreading resistance probe (SRP) and secondary ion mass spectrometry (SIMS). SRP is a two-point measurement of the spreading resistance under the point contacts. From the raw spreading resistance data, one obtains resistivity, and therefore impurity concentration.

SRP measures the electrically active impurity concentration; i.e., concentration of impurity atoms on substitutional sites in the silicon lattice. The SIMS measurement generates an impurity profile by detection of secondary ion emission from a host substrate. If suitable standards exist, the ion count is transformed into a quantitative measure of the impurity profile in the host. Although these techniques profess to measure impurity profile, each actually measures a slightly different property of the material.

In this investigation, As and  $\text{BF}_2$  ions implanted into silicon were subjected to isochronal anneals and the resulting impurity profiles were measured by SRP and SIMS. The profiles obtained were compared to each other as well as to computer simulations using SUPREM.

### *Experimental*

Both phosphorus and boron doped (100) wafers with nominal impurity concentrations of  $1 \times 10^{15} \text{ cm}^{-3}$  were implanted through 10 nm of  $\text{SiO}_2$  with As and  $\text{BF}_2$ . The screen oxide was used in order to eliminate potential surface dopant depletion during subsequent anneals, minimize possible contamination during implantation, and minimize initial ion channeling. Table 1 provides details of the implants and anneals.

Implantation was carried out with a Varian-Extrion implanter at  $7^\circ$  off angle. Four-point probe sheet resistance measurements were made on all wafers. Wafers were scribed in half and SRP and SIMS measurements were made on pieces from each wafer. The SRP wafer halves received an additional 1  $\mu\text{m}$  plasma oxide (350 C) deposition to improve measurement accuracy.

The SRP measurements were performed on a Solid State Measurements, Inc., 100-C. The measurement conditions were: probe load = 7 g, bevel angle = 1.4%, X-step = 1  $\mu\text{m}$  (effective probe step of 17.5 nm), and probe separation = 25  $\mu\text{m}$ . The angle measurement was made by use of optical interference (SAM). The SIMS measurements were performed on a Cameca IMS-3f. Measurement conditions varied depending on whether As or B was being analyzed. A 10keV (14.5keV effective) primary Cs beam at 200 nA was used to analyze the As doped wafers. A 15keV primary  $\text{O}_2$  beam at 3  $\mu\text{A}$  was used to analyze the B doped wafers. The silicon sputter rate was approximately 2 nm/s. Dectak measurements were made on each sample to determine the crater depth.

### *Conclusions*

Isochronal anneals of  $\text{BF}_2$  and As implants were used to correlate SRP and SIMS measurements. The results indicate a convergence of the profiles as the anneal temperature is increased. Significant discrepancies in junction depth measurement exist between the two techniques at 800 C as expected. A significant portion of electrically inactive boron and arsenic remains even after a 30min 900 C anneal. A kink in the SIMS boron profile

was explained by use of a model proposed by Hofker.<sup>1</sup> SIMS and SRP measurements are complementary; at times both may be necessary to characterize fully shallow, highly doped junctions. SUPREM-3 results, even without modifications to default coefficients, are in fair agreement with the data. The fit to the data can be improved by modification of the default coefficient. Additional experiments are in progress to further evaluate the algorithms and calibration procedures for both SIMS and srp.

#### References

1. W. K. Hofker, *Implantation of Boron in Silicon*, Thesis, University of Amsterdam, 1975.

TABLE 1.--Summary of implants and anneals.

Ion	Dose(cm <sup>-2</sup> )	Energy(keV)	Temp(C)	Time(min)
BF <sub>2</sub>	5 × 10 <sup>15</sup>	60	800	30
BF <sub>2</sub>	5 × 10 <sup>15</sup>	60	900	30
BF <sub>2</sub>	5 × 10 <sup>15</sup>	60	1000	30
As	5 × 10 <sup>15</sup>	80	800	30
As	5 × 10 <sup>15</sup>	80	900	30
As	5 × 10 <sup>15</sup>	80	1000	30



## AN ION MICROPROBE SYSTEM FOR THREE-DIMENSIONAL SIMS IMAGING

D. R. Kingham

Secondary ion mass spectrometry (SIMS) is generally recognized as a technique with excellent depth resolution and remarkable sensitivity. The ultimate depth resolution is a single atomic layer and concentration detection limits for most elements are in the ppm to ppb range. The lateral spatial resolution of the technique has been dramatically improved in recent years, due mainly to the use of liquid metal ion sources<sup>1</sup> to give microfocused ion beams. A primary ion beam probe size of 500 Å has been achieved with a commercial ion microprobe,<sup>2</sup> and Levi-Setti et al.<sup>3</sup> have reached 200 Å probe size.

Three-dimensional materials analysis by SIMS has been reviewed by Rudenauer<sup>4</sup> and an example of the use of a direct imaging ion microscope for 3-D SIMS is given by Bryan et al.<sup>5</sup> A microprobe system has the advantage over an ion microscope at high lateral spatial resolution because the mass spectrometer collection efficiency remains at a constant high value independent of spatial resolution. In addition, the smallest probe size of ion microprobe gives spatial resolution that is an order of magnitude better than that achievable with an ion microscope.

### *Method*

SIMS images in our ion microprobe system are acquired directly in digital format and are displayed via a framestore.

Three-dimensional imaging is achieved by a sequence of mass-selected two-dimensional images. As SIMS is a consumptive technique each successive image is at an increasing depth from the original sample surface. The selected mass can be changed cyclically between images to give a complete multielement three-dimensional matrix containing all the available information on the lateral and depth distribution of all elements of interest. A retrospective linescan or image at any chosen orientation through the three-dimensional matrix can be software reconstructed in seconds. The key feature, particularly for a consumptive technique such as SIMS, is that all the available information be stored at acquisition time. The data can then be processed in a wide variety of different ways that are independent of data acquisition.

### *Mass Spectrometers*

Our present system has a high-transmission quadrupole mass spectrometer and the system is being further developed for use with either a time-of-flight or magnetic-sector mass spectrometer. Both magnetic-sector and quadrupole mass spectrometers are set to detect a single mass, whereas a time-of-flight mass spectrometer can detect all masses quasi-simultaneously. Magnetic-sector and quadrupole mass spectrometers are both suitable for three-dimensional SIMS analysis; the magnetic sector has the advantage of better collection efficiency and very high mass resolution (ultimate mass resolution  $M/\Delta M = 40\,000$ ). A time-of-flight mass spectrometer, however, requires a pulsed primary ion beam so that the mean sputtering rate is reduced by a factor of about 10 000; for an analysis to be completed in a reasonable time total analyzed volumes should not exceed a few cubic microns. The applicability of time-of-flight SIMS to three-dimensional analysis is thus restricted to analysis of very small volumes with high sensitivity. The main application of time-of-flight SIMS is surface analysis (Static SIMS), again with high sensitivity.

### *Summary*

Three-dimensional SIMS imaging with an ion microprobe system is now possible with a lateral spatial resolution of 500 Å or better. Magnetic-sector, time-of-flight, and quadrupole mass spectrometers can be used on the system; time-of-flight offers the best

performance for very small analyzed volumes and high sensitivity, and magnetic sector offers good collection efficiency and exceptional mass resolution.

#### *References*

1. A. R. Bayly, A. R. Waugh, and K. Anderson, *Nucl. Instrum. Methods* 218: 375, 1983.
2. A. R. Bayly, A. R. Waugh, and P. Vohralik, *Spectrochimica Acta* 40B: 717, 1985.
3. R. Levi-Setti, G. Crow, and Y. L. Wang, *Proc. SIMS-V*: 148, 1985.
4. F. G. Rudenauer, *Surface and Interface Analysis* 6: 131, 1984.
5. S. R. Bryan, W. S. Woodward, R. W. Linton, and D. P. Griffis, *J. Vac. Sci. Technol.* A3: 2102, 1985.

## COMPUTER CONTROL SOFTWARE FOR THE RESISTIVE ANODE ENCODER DETECTOR AND THE CAMECA IMS-3F ION MICROPROBE

R. L. Crouch and C. J. Hitzman

Recent advances in computer control software allow for rapid image acquisition and processing by use of the resistive anode encoder (RAE) detector and stigmatic imaging secondary ion mass spectrometry (SIMS). A sample consisting of alternative 500 Å layers of GaAs and AlGaAs has been analyzed to illustrate the various capabilities of the software package. Data are presented showing that one can achieve enhanced depth resolution at a depth of 12 500 Å by selecting a portion of the image area acquired by the RAE and plotting a selected area depth profile.

### *Experimental*

A depth profile of doubly charged Al ions was obtained by use of mass filtered  $O_2^+$  bombardment and positive secondary ion mass spectrometry. A primary beam current of approximately 2  $\mu A$  rastered over a 500  $\mu m^2$  area was employed. The secondary beam optics were adjusted for best image quality in the plane of the detector and a 150  $\mu m$  image field was used.

The RAE is a device that can measure charge impact position on a resistive film.<sup>1</sup> An ion strikes the front side of a dual microchannel plate assembly and produces a pulse of  $10^6$ - $10^7$  electrons from the reverse side. This charge pulse impacts a layer of resistive material and the charge is collected by four electrodes at the corners. The anodic pulses detected at the four corners differ in magnitude depending on the impact position of the original pulse. Computation of the position is accomplished via analog electronics. Following conversion to a digital signal consisting of pulse and position, the information is stored and processed by use of IBM PC/AT-based software. The end result is a 16-level pseudocolor image of the sample. Image acquisition time is determined by the ion arrival rate (maximum rate = 50 000 ions/s) and the required accuracy of the pixel intensities (contrast). Lateral resolution of approximately 1  $\mu m$  has been demonstrated with a 150  $\mu m$  image field.

### *Results*

The image depth profile through alternating GaAs/AlGaAs layers is shown in Fig. 1. The upper curve was obtained by use of the total ion counts from the RAE images. At a depth of about 1  $\mu m$ , the depth resolution begins to degrade, with several of the AlGaAs layers appearing to be closer together than at shallower depths. The lower curve was plotted from the same images as the upper curve except that ion counts from a portion of each image were used. This selected area depth profile shows improved depth resolution over the entire depth profile and in particular the region below 1  $\mu m$ . RAE images corresponding to a peak and a valley in the profile at a depth of about 1.2  $\mu m$  are shown in Fig. 2. In addition, the images show the area selected for the lower depth profile in Fig. 1. Figure 3 is a cross section of the sample reconstructed from the RAE image depth profile and shows the alternating layers of the sample. Cross section reconstruction is a feature of the computer control software.

### *Discussion*

Examination of the RAE images in Fig. 2 reveals that the loss of depth resolution at lower depths is probably due to uneven sputtering of the analytical crater, as shown by the nonuniformity of the sputtered ion distribution in the image field. By selecting a portion of the image field, one can reduce the effects of uneven sputtering, which can be

---

R. L. Crouch is Analytical Representative and C. J. Hitzman is Analyst for Charles Evans & Associates, 301 Chesapeake Drive, Redwood City, CA 94063.

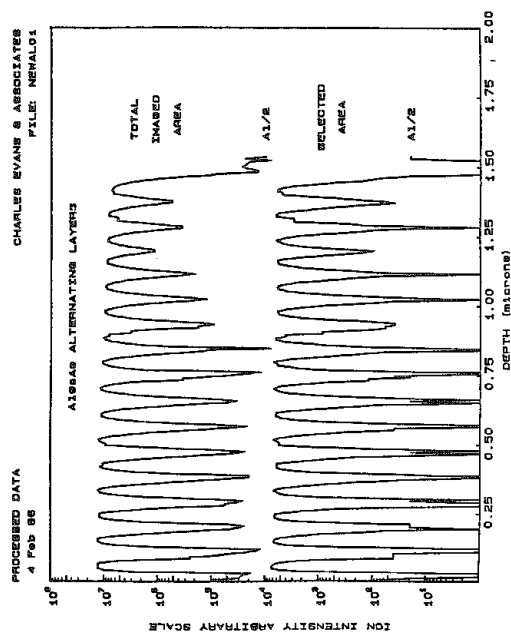
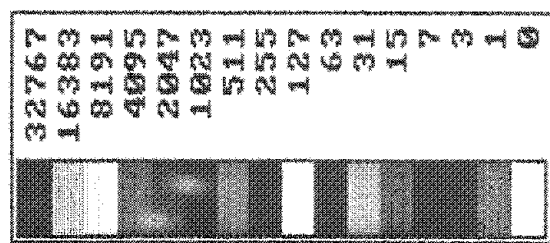
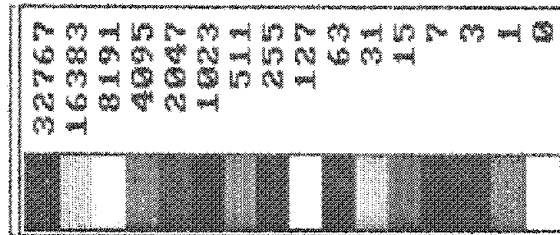


FIG. 1.--RAE depth profiles of alternating layers of AlGaAs/GaAs. Top, total image area depth profile; bottom, selected area depth profile.



\RAE\  
DP07411  
1 byte  
Log base 2



\rae\  
DP07416  
1 byte M  
Log base 2

FIG. 2.--Images at depth of  $\sim 1.2 \mu\text{m}$  from peak (top) and valley (bottom) in profile. Area shown is that selected for bottom curve in Fig. 1.

done under software control as shown here, rather than repeating the analysis with different instrument conditions (which would have the same effect).

The cross section in Fig. 3 is useful in showing the lack of uniform spacing between the alternating AlGaAs layers. Based on the defined thickness of the layers, the cross-sectional depth resolution appears to be about 200 Å. If the narrow spacing were due to uneven sputtering, the cross section would appear as consisting of slanting layers with the slant angle increasing with depth. The narrow spacing is probably a property of the sample in this case.

### Conclusion

Approximately 300 RAE images were acquired to obtain an image depth profile of a sample consisting of alternating GaAs/AlGaAs layers. Off-line processing of the data leads to improved results (in this case better depth resolution was obtained) obviating the need for re-analysis of the sample.

### References

1. R. W. Odom et al., *Anal. Chem.* 55: 574, 1983.

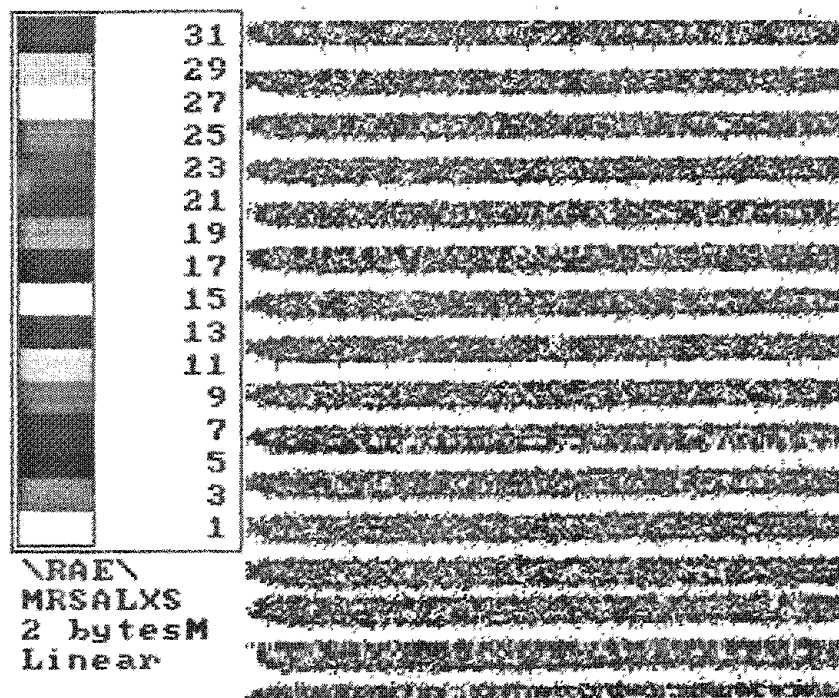


FIG. 3.--Cross section of alternating layers reconstructed from RAE depth profile images.

## IMPROVED AUGER DATA ANALYSIS PROGRAMS FOR PHYSICAL ELECTRONICS AUGER SPECTROMETER SYSTEMS

R. A. Mulford and F. S. Austin

The signal obtained with an Auger electron spectrometer consists of small peaks superimposed on a large scattered electron background. To minimize the effect of the background, it has become traditional for Auger spectra to be presented as the derivative  $dN/dE$  of the signal vs energy  $E$ . Empirically, it is found that the peak-to-peak height on a differentiated spectrum is approximately linearly proportional to the concentration of the element, and results are often reported in this format. Elemental concentrations can be estimated from these peak-to-peak heights by a standardless procedure and sensitivity factors derived from measurements of pure elements or known compounds.<sup>1</sup> Many factors outside the scope of this report influence the accuracy of these estimates. Despite its limitations, however, the standardless peak-to-peak approach is widely used because once the analyst decides that it is suitable for a particular application, the procedure is simple and highly suitable for computer automation. Most commercial instruments provide quantitative output by an algorithm based on this method. Unfortunately, many workers have found that the software supplied by the manufacturer is not sufficiently flexible to provide accurate peak-to-peak height measurements of complex spectra. To improve this situation, a set of utility computer programs for data reduction that run on Physical Electronics (PHI) Auger Multiprobes equipped with the standard computer automation package (MACS) has been developed. These programs will run on PHI systems equipped with HP 2623 or HP 2648 terminals, and will handle all types of Auger data acquisition that are standard with these instruments (SUR, MUL, or PRO). The philosophy behind the programs has been developed over a period of several years use, and although the specifics apply only to users of PHI spectrometers, the methods should be of general interest.

### *Data Analysis*

The programs are designed to run in a stand-alone manner after the spectra are acquired. Data are collected in the normal fashion and saved to disk with the software included with the PHI instruments (ESAU), except that it is not necessary to specify the elements that are present before the analysis is performed. The spectrum can be divided into any convenient arrangement of energy regions, and more than one Auger peak can be present in each energy region. After data acquisition is complete, the user exits the ESAU program and runs Program AC, the data analysis program. The AC program reads the raw  $N(E)$  spectra from the data disk and displays a  $dN(E)/dE$  spectrum on the graphics terminal (correctly scaled to fill the screen). The operator then interactively specifies the Auger peaks that are to be read. Each energy region of the spectrum is differentiated numerically (by the method of Savitzky and Golay<sup>2</sup>) and displayed in sequence automatically. Results for the peak-to-peak heights are written to disk, together with the energy of the peak minimum, the computed atom and weight fractions, and the sensitivity factors that were used. A typical output file is listed in Table 1. These data can then be used by other utility programs to produce, for example, a tabular summary or an average of a series of spectra. Another use is to plot a depth profile from a series of individual datafiles acquired after different amounts of ion sputtering.

The interactive windowing capability for reading the Auger peaks is a major feature of the program. When the operator recognizes that a particular Auger peak is present, the peak name is typed. The default energy limits for this peak are read from a table and a "window" is marked on the graphics display in reverse video (Fig. 1). The left and right (energy) limits of the window are adjusted by the operator (using the keyboard) until the maximum and minimum values within the window are correct. Throughout this procedure, the reverse video display of the window on the graphics terminal is continuously updated.

---

The authors are at General Electric Company, Knolls Atomic Power Laboratory, Schenectady, NY 12301.

TABLE 1.--Sample output file from Program AC.

TEST		6-FEB-86		5 KV	
POINT	1	FILE1	0.00=SPU (MIN)		6-FEB-86
ELEMENT		ENERGY	DATA	SFACT	AT-PCT
CR2		530.	281.8	0.310	17.5
FE2		650.	81.1	0.191	8.2
NI1		846.	1039.2	0.270	74.3
POINT	2	FILE1	0.00=SPU(MIN)		6-FEB-86
ELEMENT		ENERGY	DATA	SFACT	AT-PCT
CR2		529.	340.8	0.310	17.8
FE2		651.	89.4	0.191	7.6
NI1		847.	1246.0	0.270	74.6

When all peaks present in an energy region have been read, the operator proceeds to the next region and the process is repeated. The details of the program operation and the format of the element table, which contains default window limits and elemental sensitivity factors, have been discussed elsewhere.<sup>3</sup> Often it is necessary to analyze a series of similar spectra. Therefore the program remembers the window boundaries for all elements read on the first spectrum, and these windows are marked automatically on the subsequent spectra. These spectra can either be from another physical area (point) saved as part of the same datafile (which is automatically displayed if it exists), or a point from a new file name entered by the operator. The subsequent spectra are quickly displayed, one after the other, on the screen with the previously defined energy windows marked, and action is necessary only if one of the windows must be adjusted. Thus, the operator can examine an extensive series of spectra and read accurate peak-to-peak heights in an efficient manner.

#### *Discussion and Conclusions*

The program described in this report has several advantages. First, the peak windows are specified after data acquisition, so that it is not necessary to know what elements are present in order to specify the analysis parameters. The energy (peak) windows can be adjusted as required for each individual spectrum, after data are acquired. This adjustment is essential unless all samples are flat, polished coupons, but it is not possible to make it with the standard PHI instrument. Second, the energy regions that are acquired can be larger than the Auger peak windows. This feature avoids many sources of error because the effect of end points on the numerical differentiation is avoided, it is easier to measure peaks correctly that lie on a steeply sloping background, and it is more straightforward to analyze closely spaced peaks such as oxygen and chromium. In addition, the operator can qualitatively assess the signal-to-noise ratio by observing the background signal adjacent to the Auger peak. The operator never sees the background if the energy regions are narrow and centered on a peak, as is the common practice. Third, the output of the analysis includes the raw peak-to-peak heights and the actual sensitivity factors used, in addition to the computed quantitative results, and all values are stored on disk for additional analysis and archival purposes. Fourth, it is easier for the operator to examine all spectral data from a series of analyses to insure that the peak windows are appropriate. This feature is essential for reliable results when the Auger peaks are small, near the limit of detectability, or when peak heights exhibit a large change in value, as often occurs during a depth profile. Finally, the programs are written in FORTRAN, in a modular fashion, and can easily be customized for particular applications. Listings of the FORTRAN source code are available from NTIS.<sup>4</sup> To compile the programs, the user needs a license for FORTRAN (available from DEC, the manufacturer of the PDP 11 computer used in the PHI spectrometers). It is not necessary to have the PHI FORTRAN linking software, because these programs run separately and are not linked into the ESAU operating system. The compiled AC program can reside on the same system disk used for the ESAU program, making it convenient to run either program.

## References

1. L. E. Davis, N. C. MacDonald, P. N. Palmber, G. E. Riach, and R. E. Weber, *Handbook of Auger Electron Spectroscopy*, Perkin-Elmer Corp., Eden Prairie, Minn., 1972.
2. A Savitsky and M. J. E. Golay, "Smoothing and differentiation of data by simplified least squares procedures," *Anal. Chem.* 36: 1627-1639, 1964.
3. R. A. Mulford and F. S. Austin, "Customized Auger data analysis and display using the Physical Electronics Model 595 Auger spectrometer," KAPL-4189, NTIS, Springfield, VA 22161, 1985.
4. R. A. Mulford, F. S. Austin, and R. W. Merchant, "An improved set of Auger data analysis programs for Physical Electronics Auger spectrometer systems," KAPL-4193, NTIS, Springfield, VA 22161, 1986.

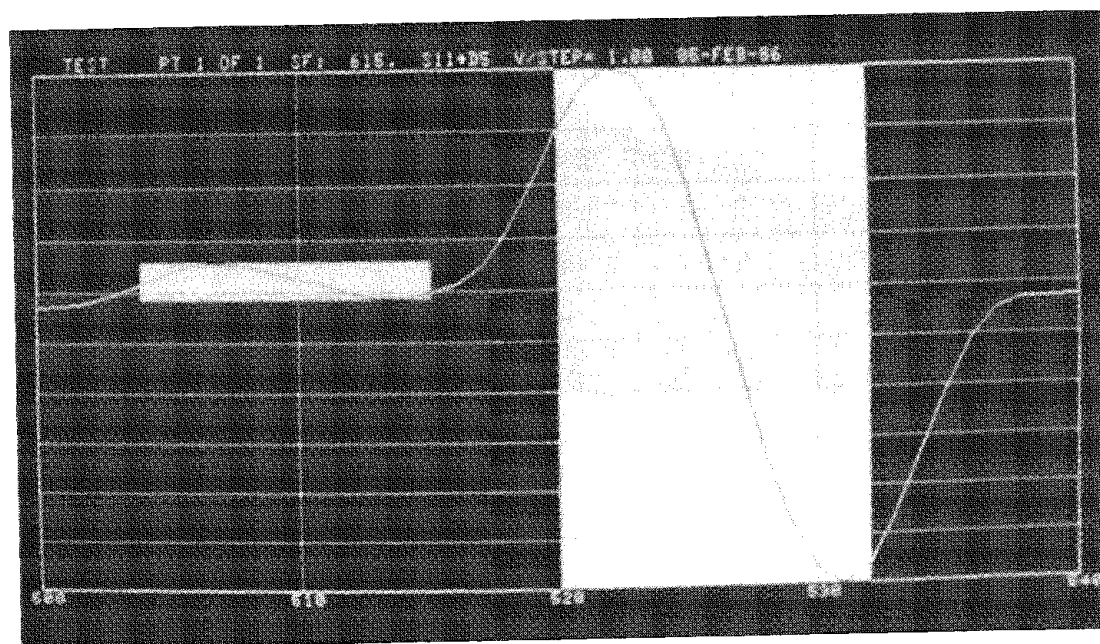


FIG. 1.--Example of graphical display of Auger spectrum from Program AC with peak windows for oxygen and chromium marked.



## HIGH-RESOLUTION SCANNING ION MICROPROBE ANALYSIS OF RETINAL TISSUE

Margaret Burns, Riccardo Levi-Setti, Jan Chabala, and Y. L. Wang

Many problems of elemental localization of interest to biologists occur in the submicron range. The high-resolution ion microprobe with liquid metal primary ion sources has the potential spatial resolution (20 nm) to analyze subcellular compartments of tissue.<sup>1</sup> We investigated basic parameters of bombardment and ion emission from retina, a tissue well characterized by  $O_2^+$  bombardment in a conventional SIMS instrument.<sup>2</sup>

### *Experimental*

*Tissue Preparation.* Adult dark-adapted toad eyes (*Bufo marinus*) were prepared as previously described<sup>2</sup> by freezing at -135 C, freeze-drying at -30 C, dry embedding in eopoxy resin, and microtoming with a dry glass knife; 10 $\mu$ m sections were pressed onto boron-doped silicon wafers and coated with ca 50 nm of 99.999% Au.

*Instrument Operation.* The scanning ion microprobe (SIM) was operated with a 40keV  $Ga^+$  beam of 1 to 10 pA and 40nm-diameter probe size. Secondary ions are separated with an RF quadrupole mass filter at a resolving power of 0.5 amu. Mass-analyzed ions are detected by a channel electron multiplier (CEM) and elemental maps are obtained by display of the individual CEM pulses as counts on a CRT. Images are recorded on Polaroid film in scans containing 1024  $\times$  1024 pixels. Depending upon the abundance and secondary ion yield of the element, images are generated in 50 to 500 s. Secondary electrons can be imaged to form a topographic map (ISE).

### *Results*

Initial images of sodium and potassium from the retina-choroid interface demonstrated an inverse diffuse banding pattern for these elements (Figs. 1 and 2). The choroid is largely extracellular (high Na content) and the retinal-retinal pigment epithelium (RPE) is largely cellular (high K content). With continued bombardment the diffuse image changed to more discrete localization of Na, K, and Ca (Figs. 3-5). The location and relative intensity of these ions was similar to observations on retina with  $O_2^+$  bombardment in a Cameca IMS300.<sup>2</sup> The scalloped emission seen in Na, K, and Ca corresponds to the location of melanin granules in the RPE cell. The dimension of these elliptical potassium-rich structures is ca 1  $\times$  2-3  $\mu$ m. The punctate emission in the Ca image is due to the lower concentration and lower ionization of calcium, so that the full dimensions are not brought out in the exposure taken.

Three explanations for the difference of the image with time are possible. The uniform Au coating may contain Na and K, or the microtoming process may redistribute Na and K over the entire specimen surface. Since Na and K are discretely located, these possibilities are unlikely. A third reason is that the specimen surface getters the abundant ions K and Na. We have previously observed surface enrichment of Na and K in following depth profiles of these ions.<sup>3</sup> In our current studies recoating with Au-Pd or oxygen flooding increased the total signal and transiently regenerated the diffuse pattern.

Elements tend to migrate onto the nearest stable structure during freeze-drying, so the presence of filamentous strands in an aqueous compartment such as a choroidal vessel is not unexpected. An ISE image (Fig. 6) shows increased brightness at a line corresponding to Bruch's membrane and decreased brightness of the filamentous strands, yet both areas were highly emissive for Na, K, and Ca.

---

Author Burns is at University of California, Davis, CA 95616. Authors Levi-Setti, Chabala, and Wang are at the Enrico Fermi Institute and Department of Physics, University of Chicago, IL 60637. The work was supported by the NSF Materials Research Laboratory at the University of Chicago.

## Conclusions

1. Scanning ion microprobe with  $\text{Ga}^+$  liquid metal source gives the same qualitative elemental distribution as is obtained with  $\text{O}_2^+$  bombardment.
2. Disturbance in the sample surface is an important factor in the images obtained.
3. The higher resolution achieved requires better preparative procedures, such as development of a cold transfer stage.

## References

1. R. Levi-Setti et al., "High-resolution topographic and isotopic imaging with a 40keV  $\text{Ga}^+$  scanning ion microprobe," *Microbeam Analysis--1985*, 209-218.
2. M. S. Burns et al., "Localization of calcium and barium in toad retina by secondary ion mass spectrometry," *Brain Res.* 220: 178-183, 1981.
3. M. S. Burns and D. M. File, "Quantitative microlocalization of diffusible ions in normal and cataractous rat lens," Submitted, *J. Microscopy*.

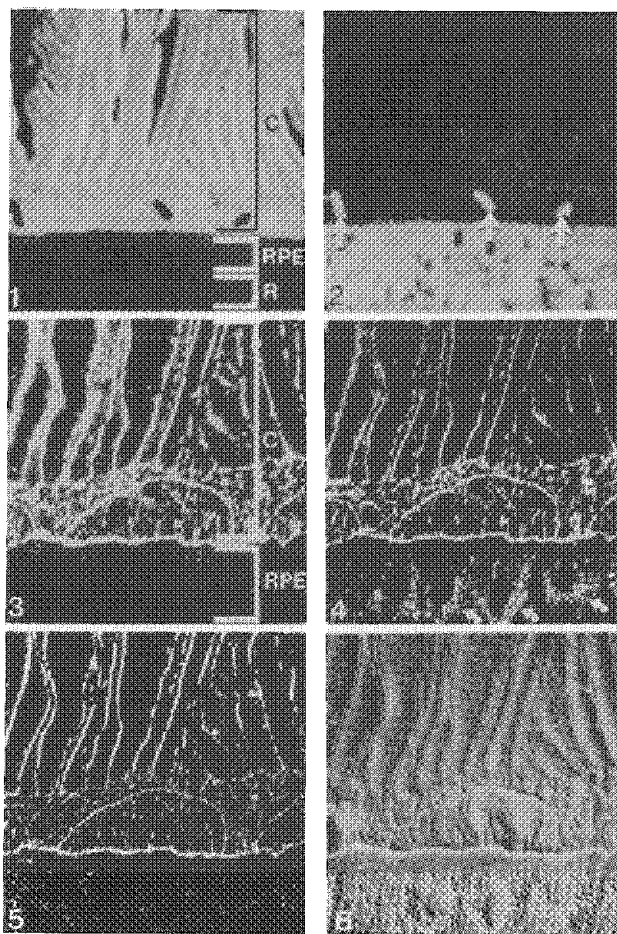


FIG. 1.--Initial  $\text{Na}^+$  image of choroid (C) and retinal pigment epithelium (RPE) and retina (R), 160  $\mu\text{m}$  full scale, 2.3 e6 counts, 64 s.

FIG. 2.--Initial  $\text{K}^+$  image of same area. Note  $\text{K}^+$  emission from red blood cells in choroidal capillaries (arrows). 1.77 e6 counts, 64 s.

FIG. 3.--Later  $\text{Na}^+$  image of choroid (C) and RPE. Diffuse image has become more discrete. Note filamentous strands in large choroidal vessel. 80  $\mu\text{m}$  full scale, 4.3 e6 counts, 128 s.

FIG. 4.--Later  $\text{K}^+$  image of same area as Fig. 3. Melanin granules (arrows) in RPE are clearly shown. 1.55 e6 counts, 128 s.

FIG. 5.-- $\text{Ca}^+$  image of same area as Fig. 3. 1.5 e4 counts, 512 s.

FIG. 6.--ISE showing topographic detail after bombardment, 32 s.

## ELECTRON-STIMULATED DESORPTION MICROSCOPY

Greg Gillen and Peter Williams

The desorption of surface adsorbates by energetic electron impact is a well-known phenomenon. In the past, most of the work done on electron stimulated desorption (ESD) has been of a fundamental nature. Relatively few publications have discussed the practical applications of surface imaging with the use of electron-desorbed ions.<sup>1-7</sup> It has been previously demonstrated that the Cameca IMS-3F ion microscope can be used to image distributions of electron-desorbed ions with high spatial resolution.<sup>6</sup> The present work is a continuation of this earlier study. We have produced high-resolution images of a number of adsorbates and intrinsic contaminants using electron-desorbed ions. Elements imaged include hydrogen, oxygen, fluorine, and chlorine. The low-energy spread of electron-desorbed ions results in high-resolution ion images that often contain more topographical detail than sputtered-ion images. Because the ESD yield is highly sensitive to the local bonding environment, subtle variations in surface features can often be discerned that are not otherwise visible. In instances where the concentration of ESD-active species is low, "imaging gases" can be used for selective enhancement of ESD yields.

### *Experimental*

The instrument used for this work was a Cameca IMS-3F ion microscope. In this instrument, secondary ions, whether produced by ion impact or ESD, are accelerated to 4.5 keV. They are then stigmatically focused through a transfer optics system and are mass analyzed by a double-focusing mass spectrometer.<sup>11</sup> The image produced by the mass-selected ions can then be displayed by a channel plate electron multiplier-fluorescent screen assembly, or the ions can be deflected into a Faraday cup or electron multiplier to measure signal intensities. A signal of  $\sim 10^5$  cps gives a visible image. Lateral resolution depends on the sample and signal intensity and in favorable cases may be  $\sim 1 \mu\text{m}$ . Electron irradiation was achieved by use of an electron gun (Cliftronic, Inc., N.J., model CE-558). A lens and deflector assembly was built to allow focusing of the electron beam. Focusing was optimized by imaging the  $\text{F}^+$  signal from a deposited aluminum test grid on a silicon wafer. The gun was operated at accelerating potentials in the range of 7-10 kV, which gave an impact energy (taking into account the 4.5kV accelerating potential on the sample) of 11.5-14.5 keV. Typical electron currents were 50  $\mu\text{A}$  with an average beam size of  $\sim 1 \text{ mm}^2$ . If a sample did not contain enough intrinsic ESD-active species to be imaged, various gases could be sprayed onto the sample through a leak valve connected to a capillary needle pointing directly at the sample. Gases used to date have included  $\text{H}_2\text{O}$ ,  $\text{D}_2\text{O}$ , acetic acid, oxygen, freon ( $\text{CCl}_2\text{F}_2$ ),  $\text{CO}$ , and  $\text{SF}_6$ .

### *Results and Discussion*

Figure 1 is a  $\text{H}^+$  ESD image of a mixture of inorganic salts (0.02 M Sn, Cu, Co, Ni, and Ba nitrates) which were evaporated from aqueous solution onto a silicon wafer. The  $\text{H}^+$  signal originates mainly from the crystals. An analysis of the same area by SIMS did not produce enough secondary ions to form a useful image. We have found that ESD  $\text{H}^+$  images frequently highlight specific features of the sample in contrast to SIMS ion images of  $\text{H}^+$ , which are often rather featureless.

---

The authors are at the Department of Chemistry, Arizona State University, Tempe, AZ 85287. This work was supported in part by NSF Grant DMR8206028.

Figure 2 is an example of the use of imaging gases to introduce ESD-active species onto a sample. The picture shows an  $O^+$  ESD image of a polycrystalline niobium surface. The niobium was sputtered with argon for 15 min prior to analysis to remove most of the surface contamination. Oxygen was leaked into the sample chamber to a pressure of  $2 \times 10^{-5}$  Torr (the effective pressure at the sample surface was higher by at least an order of magnitude), which caused the  $O^+$  ESD signal to increase by almost two orders of magnitude. Three different grains are clearly visible in the image. For comparison, a  $Nb^+$  sputtered ion image of the same area is shown in Fig. 3 (note that the magnification has been changed). The ESD image gives much higher contrast than the sputtered ion image. In the niobium sputtered ion image, the boundaries of each grain are visible; otherwise, the grains are featureless. The reason for the improved ESD image contrast is not clear. It has been shown that grains in niobium are strongly stepped with the step distance and direction varying from grain to grain.<sup>3</sup> Stepped surfaces are known to give high ESD yields<sup>8</sup> and may explain the features in the image. However, the image contrast may also be the result of sputter-induced topography or residual surface contamination.

It was found that ESD image contrast depends on the ESD-active species being imaged. Williams has mentioned that the low-energy spread of electron-desorbed ions makes them very susceptible to small field irregularities at surface asperities.<sup>6</sup> Figure 4 is an  $H^+$  ESD image of a mischmetal sample (unseparated rare earths) on which several surface scratches are visible. Figure 5 is a  $Cl^+$  ESD image of the same area. (Chlorine is a ubiquitous impurity in this sample and is believed to result from the chloro-fluorocarbon based diamond polishing compound used.) The scratches are more visible in the  $Cl^+$  ESD image. This is presumably the result of the low mean energy of the  $Cl^+$  (about half that of  $H^+$ ), which makes this species more sensitive to surface field irregularities. For comparison to the ESD images, Fig. 6 is a  $NbO^+$  sputtered-ion image of the same area. The ESD images show more detail and have areas of lower signal intensity, which are only faintly visible in the  $NbO^+$  image. The ability to see these areas indicates that ESD is useful for revealing surface contamination.

ESD sensitivities varied with the chemical nature of the sample. On several of the samples studied, a comparison between the sensitivity of SIMS and ESD for production of positive secondary ions was made. The primary species for the SIMS measurements was  $Ar^+$  (impact energy 8 keV). Positive-ion count rates were compared and corrections were made for differences in current density between the electron and ion beams. On niobium, ESD sensitivities were two orders of magnitude greater than SIMS for  $O^+$  and  $F^+$  and one order of magnitude greater for  $Cl^+$ . For  $H^+$  from niobium, the SIMS sensitivity was better by a factor of 5. On the inorganic salt crystals (Fig. 1), ESD sensitivity for  $H^+$  was over two orders of magnitude higher than SIMS. The low ESD yield of  $H^+$  on niobium surfaces has been observed before.<sup>10</sup> For deposited aluminum layers on silicon, the  $F^+$  ESD signal was over an order of magnitude higher than the sputtered  $F^+$  ion signal. It has been suggested that sputtered  $H^+$ ,  $F^+$ , and  $Cl^+$  arise largely from noncollisional ESD-like processes.<sup>9</sup> The present results indicate that the efficiency of this process is relatively low in the samples studied here.

### Conclusion

Our results indicate that ESD is generally more efficient than inert gas sputtering in producing positive secondary ions of the halogens and oxygen, and may also be more efficient for production of  $H^+$ , depending on the sample. A general feature of ESD images in the ion microscope is that they are often more sensitive to sample topography than typical sputtered ion images. Electron-stimulated desorption is very dependent on the local bonding environment, which results in images that highlight specific features of the sample and may reveal local regions of contamination. Finally, imaging gases were found to be generally useful for introducing ESD active species onto a sample.

### References

1. G. Rork and R. E. Consoliver, "Scanning electron probe surface mass spectrometer," *Surface Sci.* 10: 291-295, 1968.
2. A. Joshi and L. E. Davis, "Scanning electron stimulated desorption (SESD): A complementary tool for surface analysis," *J. Vac. Sci. Technol.* 17: 1310-1313, 1977.
3. H. Poppa and E. Bauer, "ESD ion imaging of adsorbates," *Surface Sci.* 97: L309-L312, 1980.

4. L. A. Larson et al., "Energy-selective SESD imaging utilizing a CMA," *J. Vac. Sci. Technol.* 17: 1364-1366, 1980.
5. H. F. Dylla et al., "Scanning electron-stimulated desorption microscopy of model-biological surfaces," *Nature* 291: 401-404, 1981.
6. P. Williams et al., "Ion microscopy using electron desorbed ions," *Appl. Surf. Sci.* 16: 345-350, 1983.
7. H. F. Dylla and J. H. Abrahams, "Scanning electron stimulated desorption microscopy," in Patrick Echlin, Ed., *Analysis of Organic and Biological Surfaces*, New York: Wiley, 1984, 209.
8. T. E. Madey, "The role of steps and defects in electron stimulated desorption: Oxygen on stepped W(110) surfaces," *Surf. Sci.* 94: 483-506, 1980.
9. P. Williams, "Ion-stimulated desorption of positive halogen ions," *Physical Rev.* B23: 6187-6190, 1981.
10. E. Bauer and H. Poppa, "On the origin of electron stimulated desorption of  $H^+$  from metal surfaces," *Surf. Sci.* 99: 341-355, 1980.
11. R. Castaing and G. Slodzian, "Analytical microscopy by secondary imaging techniques," *J. Phys.* E14: 1119-1127, 1981.

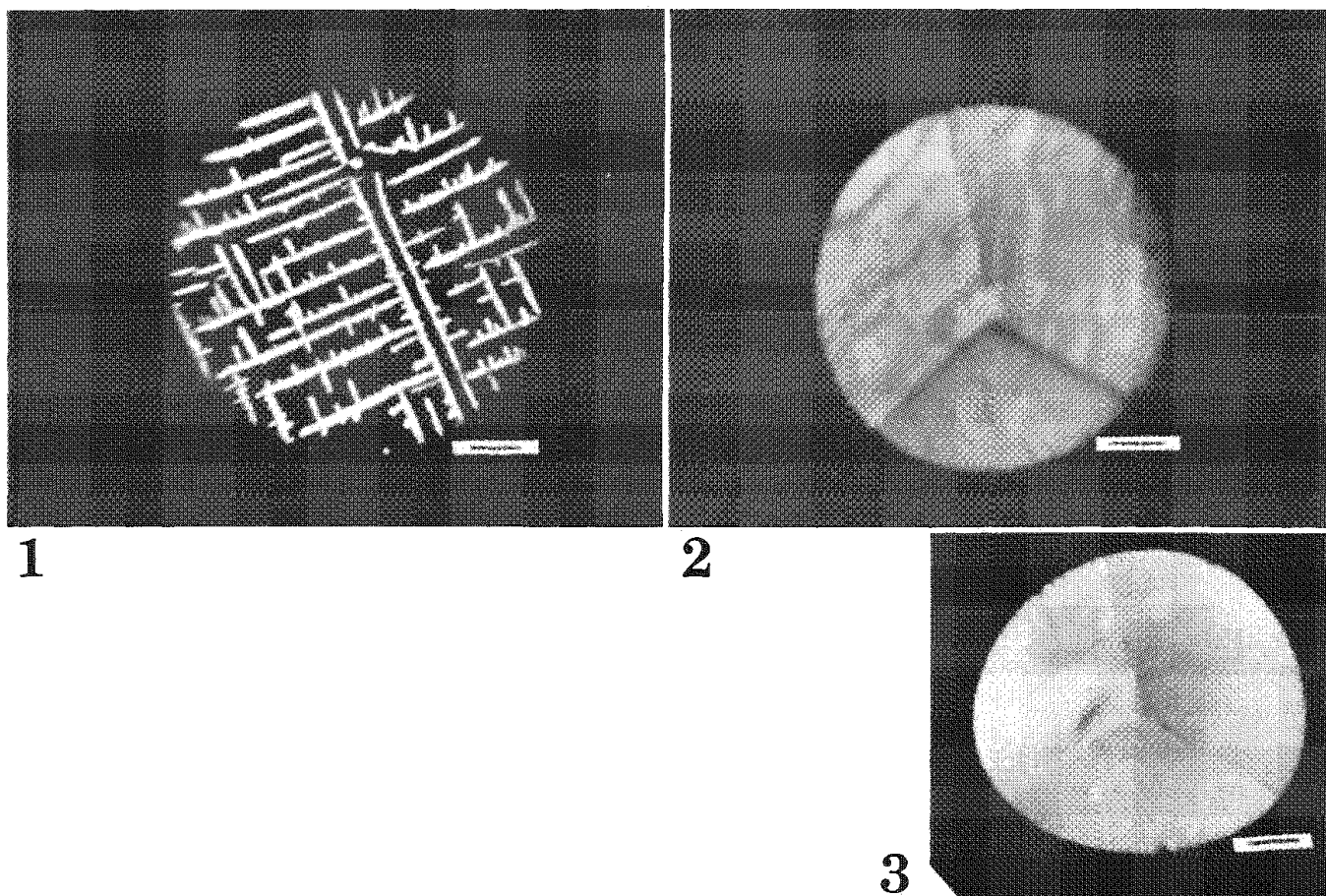
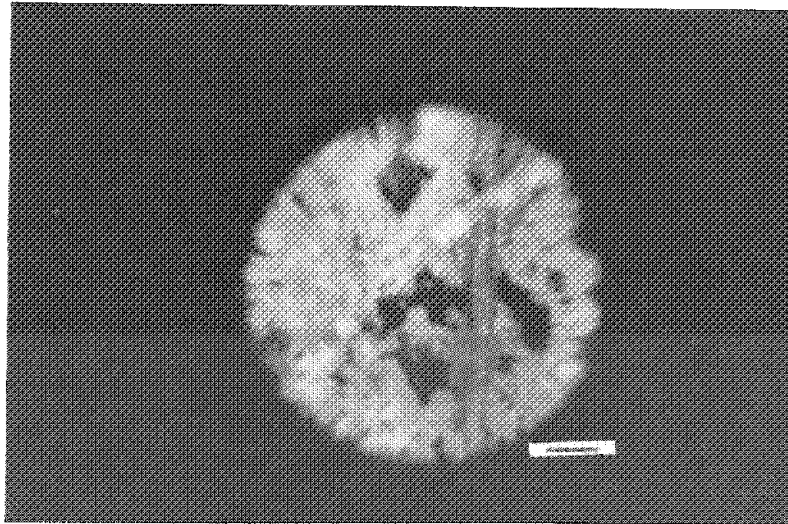
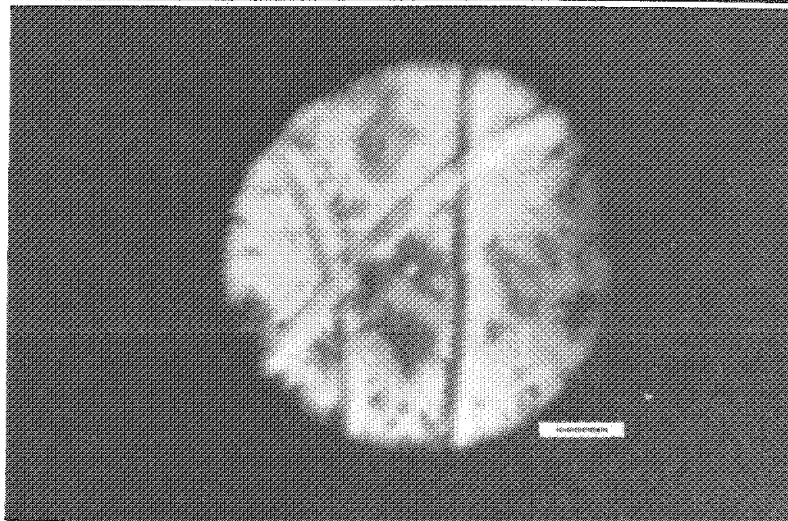


FIG. 1.-- $H^+$  ESD image of inorganic salt mixture evaporated onto silicon. Bar = 50  $\mu m$ .  
 FIG. 2.-- $O^+$  ESD image of polycrystalline niobium metal. Bar = 20  $\mu m$ .  
 FIG. 3.--Lower-magnification  $Nb^+$  sputtered ion image of niobium metal (same area as in Fig. 2). Bar = 50  $\mu m$ .

4



5



6

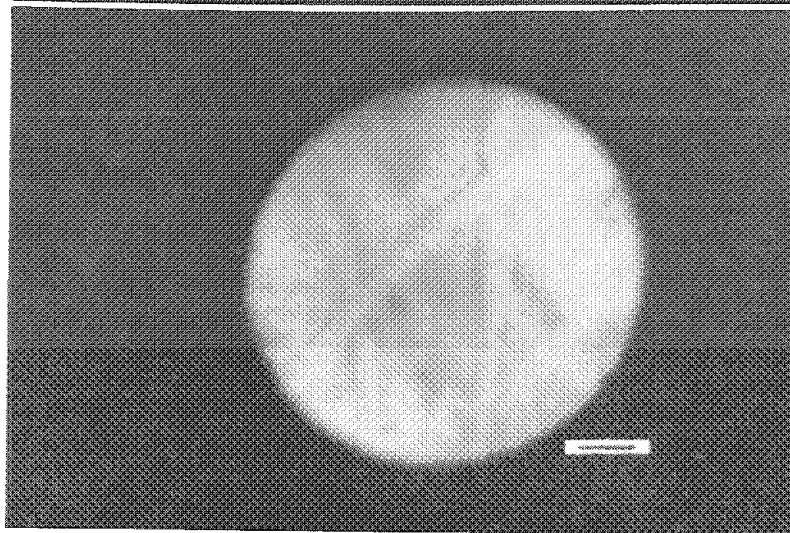


FIG. 4.-- $\text{H}^+$  ESD image of mischmetal surface. Bar = 50  $\mu\text{m}$ .

FIG. 5.-- $\text{Cl}^+$  ESD image of mischmetal surface (same area as in Fig. 4). Bar = 50  $\mu\text{m}$ .

FIG. 6.-- $\text{NdO}^+$  sputtered ion image of mischmetal surface (same areas as Figs. 4 and 5). Bar = 50  $\mu\text{m}$ .



## SEQUENTIAL ISS-AES MEASUREMENT FOR SURFACE COMPOSITION ANALYSIS OF Au-Cu ALLOY WITH AUGER SEM

Ryuichi Shimizu and Akira Kurokawa

Continuous measurement of ion scattering spectroscopy (ISS) and Auger electron spectroscopy (AES) has been achieved in a single energy scan of a cylindrical mirror analyzer by the introduction of a floating high-voltage power supply to the conventional AES system. This technique was applied for Au-Cu alloys, to study the surface composition of sputtered surface by ISS and AES sequentially. The result has confirmed that the AES hardly indicates any surface composition change due to  $\text{Ar}^+$  ion bombardment but the ISS does reveal an obvious Au enrichment of Au atoms on the topmost atomic layer. Further confirmation was also obtained from in situ ISS measurements for both the sputtered and sputter-deposited Au-Cu alloys.

One of the authors (R. S.) has shown a new capability of the scanning Auger electron microprobe attached to a differential pumping type of ion gun; that both the measurements of Auger electron spectroscopy (AES) and ion scattering spectroscopy (ISS) can be achieved in a single energy scan of a cylindrical mirror analyzer (CMA) by the introduction of a floating high-voltage power supply to the conventional AES system.<sup>1</sup> Furthermore, the use of a mixed ion beam (e.g.,  $\text{He}^+$  and  $\text{Ar}^+$ ) can provide the further capability of ion sputtering and ISS being performed simultaneously.<sup>2</sup> Since a sample surface is sputtered in surface analysis (e.g., for surface cleaning and depth analysis), this capability permits not only depth analysis with higher depth resolution by ISS, but also in-depth composition analysis of the subsurface layers by combination of ISS and AES, and leads to more comprehensive understanding of the in-depth composition of the sample surface, which is often modified by ion bombardment.

The present paper reports an experimental arrangement for the sequential ISS-AES measurements with a commercial scanning Auger microprobe, JAMP-3, and the ISS-AES measurements of surface compositions of both Au-Cu (43 at.%) alloy and a sputter-deposited layer.

### *Experimental*

Figure 1(a) shows the sample holder for the sequential ISS-AES measurement with a commercial scanning Auger microprobe, JAMP-3. The block diagram (Fig. 1b) indicates that the present sequential measurement can easily be done simply by introducing a floating high-voltage power supply to the energy-sweeping system of the conventional AES.

A special differential pumping type ion gun,<sup>3</sup> which has been developed for the present sequential measurement, is attached to the JAMP-3. The high brightness of the ion gun provides an ion beam few tens microns in diameter with current intensity of  $10^{-8}$  A if the analysis chamber is kept in ultrahigh vacuum.

The angle of incidence of the ion beam was  $39.2^\circ$  with respect to the sample normal in the case of Fig. 1(a) and was nearly normal in the case of in situ measurements of sputtered and sputter-deposited layer shown in Fig. 3. The scattering angle was  $129^\circ$ . The central disk of the sample holder can be rotated (Fig. 1a)  $360^\circ$  around the axis normal to the disks, independently of the sample holder on which the slit is set. We can thus not only perform ISS and AES measurements for a few samples mounted on the disk under the same experimental condition merely by rotating the disk, but we can also adjust the geometrical arrangement of the slit with ease simply by taking the sample holder out of the analysis chamber.

### *Results and Discussion*

Figure 2 shows the ISS and AES-spectra obtained by the continuous energy scan of the CMA from the positive to the negative with help of a floating high voltage as shown in

---

The authors are at the Department of Applied Physics, Osaka University, Suita, 565 Japan.

Fig. 1(b). The measurement was repeated for Au, Au-Cu, and Cu samples under the same experimental conditions, as follows. The sample surface was bombarded with a mixed ion beam of 3 keV  $\text{He}^+$  and  $\text{Ar}^+$  ions for ISS and sputtering; the intensity and beam diameter were  $\sim 5 \times 10^{-6}$  A and 0.2 mm, respectively. Both the ISS and AES spectra were obtained in 300 s in a single energy scan with an energy window of the CMA 5 eV and time constant 50 ms.

Since we used the same Au-Cu alloy sample of atomic concentration of Cu-43% as in previous work for quantitative surface analysis by ISS and AES, the set of both ISS and AES spectra for the three samples (Au, Cu, Au-Cu) permits us to make similar quantitative arguments on the surface concentration of the Au-Cu alloy under ion bombardment. The results have again led to the same conclusion, that the AES spectra reveal hardly any surface composition changes from the bulk composition due to the ion bombardment, whereas the ISS spectra clearly indicate the enrichment of Au atoms on the topmost surface layer, as reported so far.

Figure 3 shows the in situ ISS measurements of both the sputtered surface of Au-Cu (43 at.%) alloys and sputter-deposited layer surface on a Ta substrate. Taking into account the standard spectra from Fig. 2 for coarse assessment, the result clearly indicates that the composition of the topmost atomic layer of Au-Cu alloys is Au rich, and that of the sputter deposited layer is nearly equal to that of the bulk composition. This result leads to the conclusion that the sputtered-deposited layer reflects the bulk composition satisfying the mass balance law and any remarkable surface segregation of Au atoms onto the topmost atomic layer has not been observed on the sputter-deposited layer.

## References

1. R. Shimizu, I. Ogoh, A. Mogami, Y. Sakai, J. P. Duraud, and C. LeGressus, *Proc. 9th Intern. Vac. Congr. and 5th Intern. Conf. Solid Surfaces*, Asociacion Espanola del Vacio y sus Aplicaciones, Madrid, 1983, 69.
2. H. J. Kang, R. Shimizu, and T. Okutani, *Surface Science* 116: L173, 1982.
3. S. Nishihara, R. Shimizu, and Y. Yamauchi, *Proc. 9th Symp. Ion Sources and Ion-Assisted Technol.*, Ionics, Tokyo, 1985, 543.

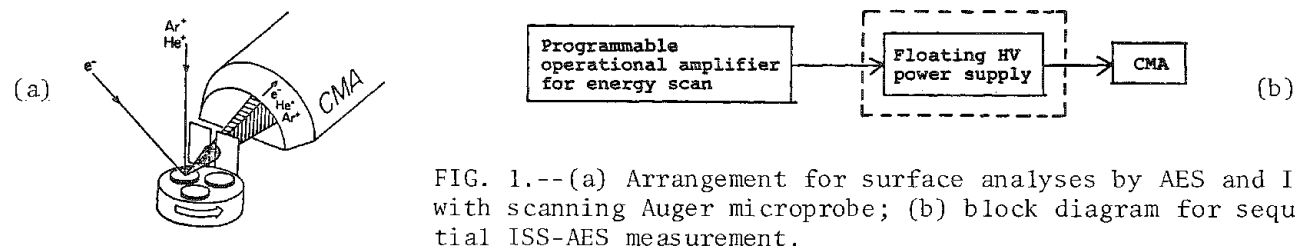


FIG. 1.--(a) Arrangement for surface analyses by AES and ISS with scanning Auger microprobe; (b) block diagram for sequential ISS-AES measurement.

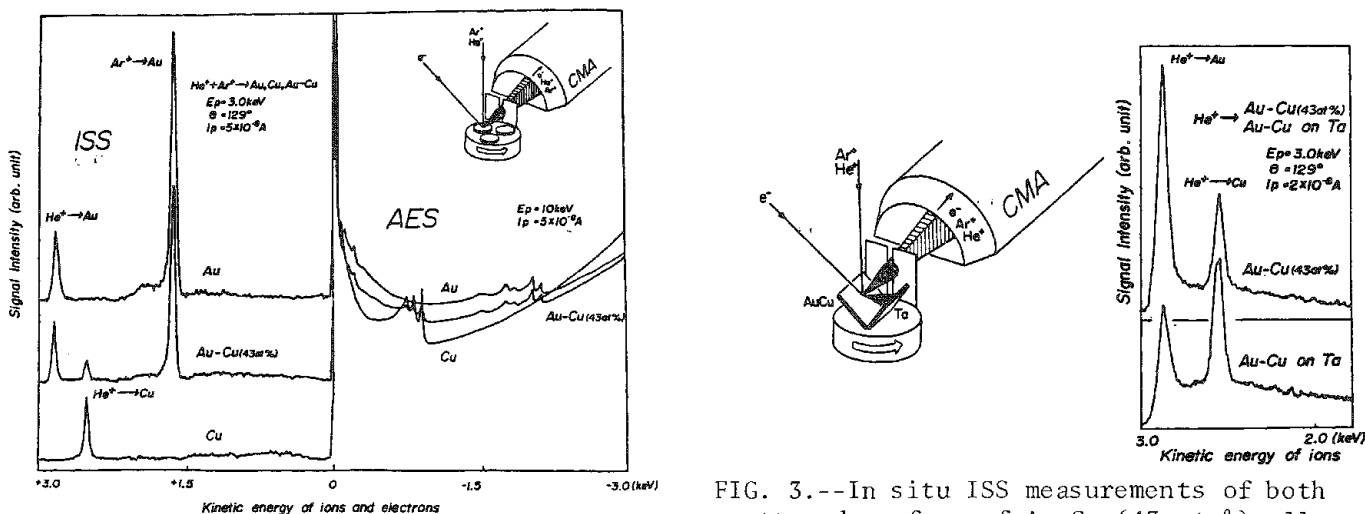


FIG. 2.--ISS and AES spectra obtained for Au, Cu, and Au-Cu (43 at.%) alloy samples by sequential measurement.

FIG. 3.--In situ ISS measurements of both sputtered surface of Au-Cu (43 at.%) alloy and sputter-deposited layer surface on Ta substrate.



## ANGULAR DEPENDENCE OF THE AUGER LINESHAPE OF GRAPHITE

J. W. Rogers Jr., J. E. Houston, and R. R. Rye

The Auger lineshape of graphite is of interest as a model for the study of initial-state, core-hole screening and final-state, hole-hole correlation effects in aromatic systems. As such, it has been the subject of considerable recent study.<sup>1</sup> We have obtained the Auger spectra from POCO (amorphous) and HOPG (highly oriented pyrolytic) graphite. The former is angle-integrated in nature whereas the latter has a strong variation in intensity as a function of the polar angle of emission (the angle between the detector and the surface normal). The spectra were corrected for the effects of secondary-electron background and extrinsic losses. Considerable care was taken to insure that the absolute energy scale was accurate and that the lineshape was as free as possible from experimental and data-reduction artifacts.

A preliminary discussion of the angle-integrated (POCO) graphite lineshape is necessary before one can discuss the angular dependence of the HOPG lineshape.<sup>1</sup> In Fig. 1, the C(KVV) lineshape for POCO graphite (curve a) is compared to a model (curve b) which consists of the self-convolution of the graphite one-electron density of states including atomic values for the symmetry-determined Auger matrix elements and assuming no initial-state screening and noninteracting final-state holes. The one-electron partial DOS ( $\sigma_s$ ,  $\sigma_p$ ,  $\pi_p$ ) were determined empirically<sup>2</sup> from x-ray emission spectra, x-ray photoemission spectra, and an assumed electron configuration of  $sp^2\pi$ . The model lineshape differs considerably from that of the experiment with intensity missing in the model function at both the high- and low-energy ends of the spectrum, and there are significant differences in relative intensity throughout the main body of the line.

To characterize these discrepancies, we have considered both the static and dynamic aspects of initial- and final-state screening which are included in the model lineshape of Fig. 1(c). The static polarization effect of initial-state screening has a negligible influence on the lineshape. However, valence electron shake-up into the core excitonic level (valence/core exciton) places charge in an energy region where very little exists in ground-state graphite and gives rise to significant new intensity (Fig. 1g) in the Auger lineshape just below the Fermi level. This process results in a dramatic improvement between the measured (Fig. 1a) and model (Fig. 1c) lineshapes in the high-energy region.

The distorting effect on the predicted lineshape resulting from the hole-hole interaction in the Auger final state has been modeled<sup>1</sup> on the Cini expression<sup>3-4</sup>; the  $\sigma^*\sigma$ ,  $\sigma^*\pi$ , and  $\pi^*\pi$  contributions are shown in Figs. 1(d), 1(e), and 1(f), respectively. We find effective hole-hole interaction energies of 2.2 eV for two holes in the  $\sigma$  band, 1.5 eV for one hole each in the  $\sigma$  and  $\pi$  bands, and 0.6 eV for both holes in the  $\pi$  band. The application of the Cini expression results in considerable improvement of the model lineshape of Fig. 1(c) in the region below the principal maximum.

The final area of disagreement in the model lineshape consists of a shoulder-like feature (centered at ~240 eV) on the low-energy side of the Auger line that is not accounted for by localization effects. We suggest, on the basis of more recent work by Cini and D'Andrea,<sup>5</sup> that this structure is due to a plasmon effect intrinsic to the two-hole final state in the Auger process.

The Auger lineshape from the HOPG graphite as a function of polar angle is shown in Fig. 2. Considerable angular variation is apparent throughout the body of the line. Modeling of these differences indicates that the Auger intensity at a particular polar angle (at a given energy) is a strong function of the angular momentum of the exiting Auger electron which results from conservation of angular momentum between the initial and final states of the Auger process. The angular momentum of the Auger electron can be predicted independently for each of the self-folds of the partial DOS.<sup>6</sup> The sum of the self-folds

---

The authors are at Sandia National Laboratories, Albuquerque, NM 87185. This work was performed at Sandia National Laboratories and was supported by the U.S. Department of Energy under contract DE-AC04-76DP00789.

at a given polar angle gives the model lineshape. The comparison of this model with the experimental lineshape from Fig. 2 will be discussed with reference to other processes<sup>7</sup> that can give rise to an angular dependence of the lineshape.

#### References

1. J. E. Houston, J. W. Rogers Jr., R. R. Rye, F. L. Hutson, and D. E. Ramaker, *Phys. Rev. B* (in press); J. E. Houston, D. E. Ramaker, J. W. Rogers Jr., R. R. Rye, and F. L. Hutson, *Phys. Rev. Lett.* 56: 1302, 1986.
2. J. S. Murday, B. I. Dunlap, F. L. Hutson II, and P. Oelhafen, *Phys. Rev.* 24: 4764, 1981.
3. M. Cini, *Solid State Commun.* 20: 605, 1976.
4. M. Cini, *Phys. Rev.* B17: 2788, 1978.
5. M. Cini and A. D'Andrea, *Phys. Rev.* B29: 6540, 1984.
6. E. Umbach and Z. Hussain, *Phys. Rev. Lett.* 52: 457, 1984.
7. W. F. Egelhoff, *Phys. Rev.* B30: 1052, 1984.

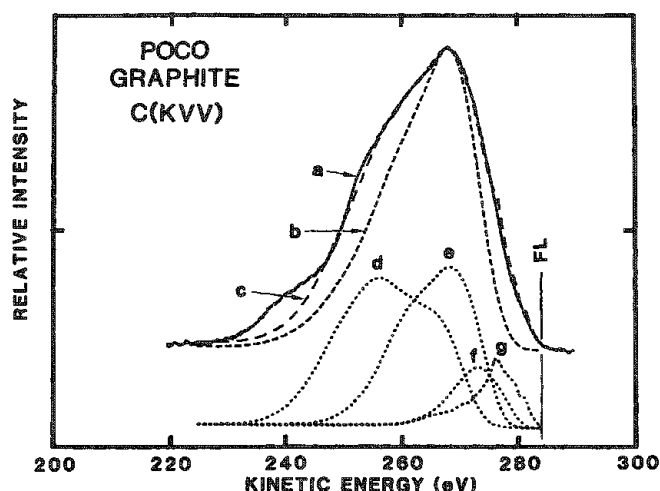


FIG. 1.--Comparison of experimental C(KVV) Auger lineshape (curve a) of POCO graphite,<sup>1</sup> model lineshape (curve b) using one-electron approximation with no hole-hole interaction, and model lineshape (curve c) which includes initial-state screening, Fermi level valence/core excitonic state, and hole-hole interaction distortion calculated through use of Cini expression.<sup>3,4</sup> Contributions to model lineshape of curve c from  $\sigma^*\sigma$ ,  $\sigma^*\pi$ , and  $\pi^*\pi$  self-folds distorted with Cini expression are shown as curves d, e, and f, respectively, and contribution of valence/core excitonic state is shown as curve g. Curve c is sum of d, e, f, and g. Fermi level (FL), after addition of C(1s) binding energy (284.6 eV), is also shown.

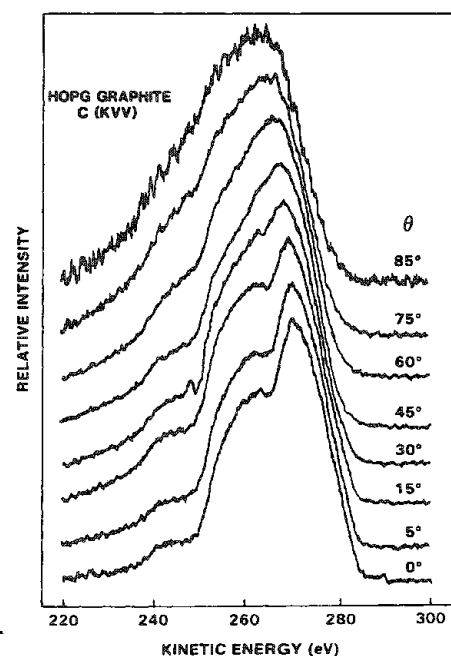


FIG. 2.--C(KVV) lineshape from HOPG graphite as function of polar angle  $\theta$ , the angle between detector and surface normal.

## Geological and Gemological Applications

### GEMS UNDER THE MICROBEAM: NEW APPLICATIONS TO GEMOLOGY

C. M. Stockton

Gemology is the study of gems. As such, one would think that it is a subfield of mineralogy. However, because of the rarity and value of gemstones, their study is concerned with situations and questions that are uniquely associated with the jewelry industry. Microbeam analysis, with its essentially nondestructive nature, is well suited for gemological applications, but has become widely used in gemological research only in the last 5-10 years. The following discussion reviews some of the special problems in gemology to which microbeam techniques have recently been applied.

#### *The Framework of Gemology*

The mineralogic study of gems has been limited by the sometimes exorbitant cost and general scarcity of most of the specimens. However, the expansion of the gem trade that occurred around the turn of the century, especially in the USA, brought about an urgent need for jewelers to know a great deal more about what they were buying and selling. Europe, with its history of gems associated with the nobility and its proximity to the ancient and commercial sources of gemstones, had a tradition of scholarly study of gems. In the USA, on the other hand, the organized study of gems was instigated by a few talented jewelers who, unlike the scientists in this country, had both the access to the samples and an impelling need for the knowledge. As a result, gemology developed in the USA as a service to the jewelry industry and is still taught primarily in trade schools like the Gemological Institute of America (GIA).

Because of the value and rarity of the specimens, gemological testing requires nondestructive techniques; prior to the development of the microprobe, that meant a strong reluctance to do chemical analysis, and until quite recently compositional data on gem quality minerals have been extremely scarce. The bulk of chemical data on gems even now has been collected by nongemologically oriented researchers who are concerned with questions quite different from those in the gem trade. As a result, the chemical data obtained are usually not related to other types of data in such a way as to be useful in solving gemological problems.

The result of this independent evolution of gemology is that techniques like microbeam analysis that are commonplace in most scientific endeavors are relatively new to gemology, because our researchers have not been scientists in the formal sense until quite recently. To my knowledge, GIA is still the only organization dedicated to gemology that is in possession of an electron microscope--an ISI Super III--even now. For microprobe analysis, we have had access to the automated MAC instrument at the California Institute of Technology's Division of Earth and Planetary Sciences.

#### *Sample Preparation*

Virtually all gemological samples must be recovered intact from their mounts. Fortunately, these samples are usually faceted, crystalline gems that provide one or more surfaces suitably polished for microprobe analysis. Specimens must be mounted so that a flat, polished surface is held perpendicular to the incident electron beam by a material from which the gem can be detached after analysis is completed. The method we currently use is a modification of a mounting technique recommended to us by Caltech's George Rossman. The cleaned stone is placed flat surface down on a sheet of powder paper on a glass slide and within a metal retaining ring; orthodontic resin is poured inside the ring and over the sample to a depth of about 1/8 in. depending on sample size. When the resin sets, the paper is peeled off to expose the sample surface surrounded by resin inside the metal ring, and the mount is coated as desired. When analysis is completed, one can remove the sample

---

The author is at the Gemological Institute of America (Research Department), Santa Monica, CA 90404.

by soaking the entire mount for 12-24 h in acetone. Gold and carbon coatings can be removed from the sample surface with alcohol or, if persistent, with a polishing compound such as cerium oxide on a dampened Q-tip. Unfortunately, orthodontic resin is somewhat volatile and is prone to outgassing, so we are still searching for a better soluble mounting medium.

One special case of sample preparation is used in imaging the structure of opal.<sup>1,2</sup> Because the polishing done to the surface of a gem opal destroys the top layer of its structure, we etch a small area of the surface with 5% hydrofluoric acid for about 30-60 s. The acid is confined to a small spot by a dam of casting wax built on the opal's surface. The wax simply chips off by hand after etching is completed. The etching removes the top one micron or so of silica spheres, leaving a barely visible dull spot and exposing the structure of stacked spheres (Fig. 1). After examination, the etched area is re-polished, which results in a loss of usually less than 0.01 ct (0.002 g) of sample weight, a negligible amount even to a gemologist.

### *Gemological Applications*

Most of the problems unique to gemology involve either forensics or product knowledge. One such problem is the identification of synthetic gem materials. Ideally, a synthetic gem would be in all ways identical to its natural counterpart, but differences in their growth environments invariably result in subtle chemical differences between natural and synthetic stones. For example, natural and synthetic emeralds can be distinguished by microprobe<sup>3,4</sup> because nonessential minor elements such as Na, Mg, and Fe are present in much higher levels in natural emeralds than in synthetics (Table 1). Chlorine is present in hydrothermal synthetic emeralds as a residue from the coloring compound used in the manufacturing process, but is essentially absent in natural emeralds.

Analysis of included material frequently permits us to establish the natural or synthetic origin of a gem. Synthetic rubies are often extremely difficult to distinguish from natural ones, but their inclusions are quite distinct. For example, an included needle that came to the surface of one stone was identified as titanium oxide, or rutile, and indicated that the ruby was natural because rutile is a common inclusion in natural ruby but is never found in synthetics. The microprobe can also detect inclusions of gold and platinum from the crucibles in which many synthetic gems are grown and thereby indicate the laboratory origin of a stone.<sup>5</sup>

An unusual problem that was recently resolved through microprobe analysis involved a number of rubies with large, irregular inclusions exposed at their surface.<sup>6</sup> Optical testing indicated that the inclusions were glass. While natural glass inclusions are occasionally encountered in rubies, the sudden abundance and large size of these inclusions seemed suspicious. Microprobe analyses of natural glass inclusions and of the unknown material showed significant differences (Table 2) and it was in fact established that the unknown glass was an artificial material applied to fill cavities in natural rubies so that the larger gems could be cut than would otherwise have been possible. Buyers unaware of this ploy were thus led to pay hundreds of dollars per carat for glass as well as ruby.

Gemologists have traditionally used spectral features associated with iron and cobalt to distinguish, respectively, natural and synthetic blue spinel. However, a stone that was tentatively identified as synthetic on the basis of its strong cobalt-related spectral features and vibrant "cobalt-blue" color, also contained what looked like natural crystalline inclusions. Microprobe analysis of this stone revealed a chemical composition typical of natural blue spinel accompanied by minor amounts of cobalt (Table 3). Further study of this and other samples revealed that  $\text{Co}^{2+}$ , considered diagnostic of synthetic origin for blue spinel, does occasionally occur as a coloring agent in natural blue spinel. Gemological methods of identifying blue spinel were revised accordingly.

A major problem in gemology is that of classification; the terminology applied to gems can radically affect values. One such instance involved the appearance, about ten years ago, of a new type of garnet from East Africa. This material looked much like other, less rare garnets but had anomalous optical and physical properties. A study of the chemistry of these and other gem quality garnets was required before the new type of garnet could be clearly identified and characterized to distinguish it from less valuable types. To this end, we analyzed more than 500 gem-quality garnets (mostly from GIA's permanent collection) and clearly identified a natural compositional range ( $\text{Mg}_3\text{Al}_2\text{Si}_3\text{O}_{12}$ - $\text{Mn}_3\text{Al}_2\text{Si}_3\text{O}_{12}$ ) in the

TABLE 1.--Ranges of chemical compositions for 38 natural and 24 synthetic (6 hydrothermal and 18 flux) emeralds.

Wt. %	Origin of emerald		
	Natural	Hydrothermal Synthetic	Flux Synthetic
Na <sub>2</sub> O	nd- 2.3	nd	nd- 0.1
MgO	nd- 3.1	nd	nd
FeO*	tr- 2.0	nd	nd- 0.5
Al <sub>2</sub> O <sub>3</sub>	11.7-18.2	18.1-18.8	18.1-20.1
V <sub>2</sub> O <sub>3</sub> *	tr- 2.0	nd- 0.7	nd- 0.2
Cr <sub>2</sub> O <sub>3</sub> *	tr- 2.1	0.3- 0.8	0.2- 2.2
SiO <sub>2</sub>	63.3-66.5	65.8-66.6	65.7-67.4
Cl	nd	tr- 0.3	nd

\*Total Fe as FeO, V as V<sub>2</sub>O<sub>3</sub>, and Cr as Cr<sub>2</sub>O<sub>3</sub>.

Traces below microprobe detection limits were detected by EDXRF.

TABLE 2.--Compositions of natural and synthetic glass inclusions in two natural rubies.

Wt. %	Origin of glass inclusions	
	Synthetic	Natural
Na <sub>2</sub> O	nd	0.4
MgO	10.6	1.9
Al <sub>2</sub> O <sub>3</sub>	33.3	26.4
SiO <sub>2</sub>	42.8	56.8
K <sub>2</sub> O	nd	0.6
CaO	7.3	6.5
FeO*	1.7	1.5
TiO <sub>2</sub>	0.1	0.4
MnO	0.1	nd
Total	95.9	94.5

\*Total Fe as FeO.

TABLE 3.--Compositions for natural and flux synthetic blue spinels that contain cobalt as coloring agent.

Wt. %	Origin of spinel	
	Natural	Synthetic
MgO	27.7	26.4
Al <sub>2</sub> O <sub>3</sub>	70.6	72.7
FeO	0.7	nd
CoO	0.1	0.2
ZnO	0.2	nd
Total	99.3	99.3

\*Total Fe as FeO.

TABLE 4.--Microprobe analyses of various minerals in maw-sit-sit.

Wt. %	Ureyite	Alkali Amphiboles		Pyroxene	Chlorite
Na <sub>2</sub> O	13.3	9.3	10.2	13.8	nd
MgO	0.3	11.9	16.3	0.7	26.4
Al <sub>2</sub> O <sub>3</sub>	4.1	7.9	4.8	4.8	20.6
SiO <sub>2</sub>	51.9	53.6	55.3	54.1	32.2
K <sub>2</sub> O	nd	nd	0.1	nd	0.1
CaO	0.3	0.4	0.7	0.8	0.4
TiO <sub>2</sub>	0.1	0.1	nd	0.2	nd
Cr <sub>2</sub> O <sub>3</sub> <sup>1</sup>	25.6	7.1	1.3	14.0	0.1
FeO <sup>1</sup>	0.6	2.8	4.6	10.7	1.1
NiO	nd	nd	0.2	nd	0.5
Total	96.2	93.1	93.5	99.1	81.4
H <sub>2</sub> O <sup>2</sup>	3.8	6.9	6.5	-	18.6

1-Total Fe as FeO and Cr as Cr<sub>2</sub>O<sub>3</sub>.

2-H<sub>2</sub>O by difference.

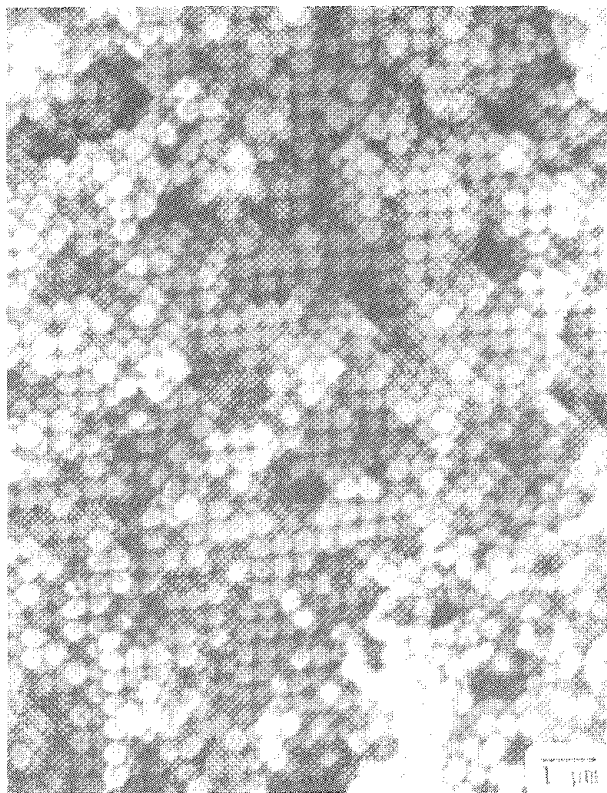


FIG. 1.--Structure of opal revealed by SEM to be stacked spheres.

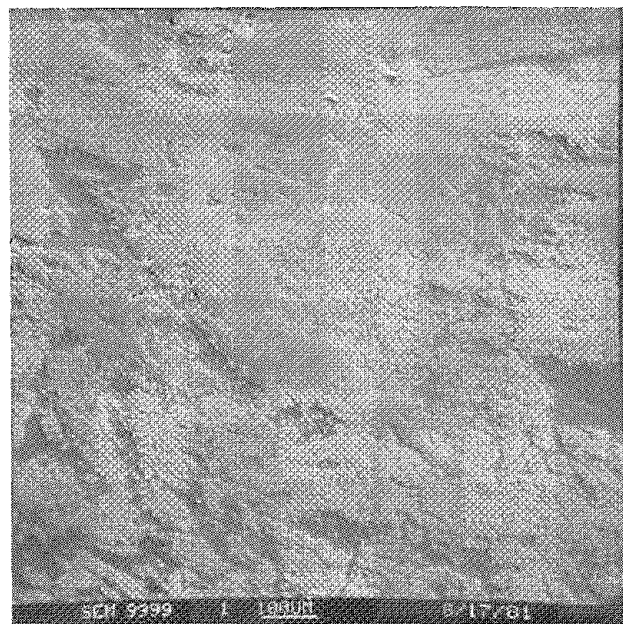


FIG. 3.--SEM micrograph of maw-sit-sit showing complex intergrowth of mineral phases.

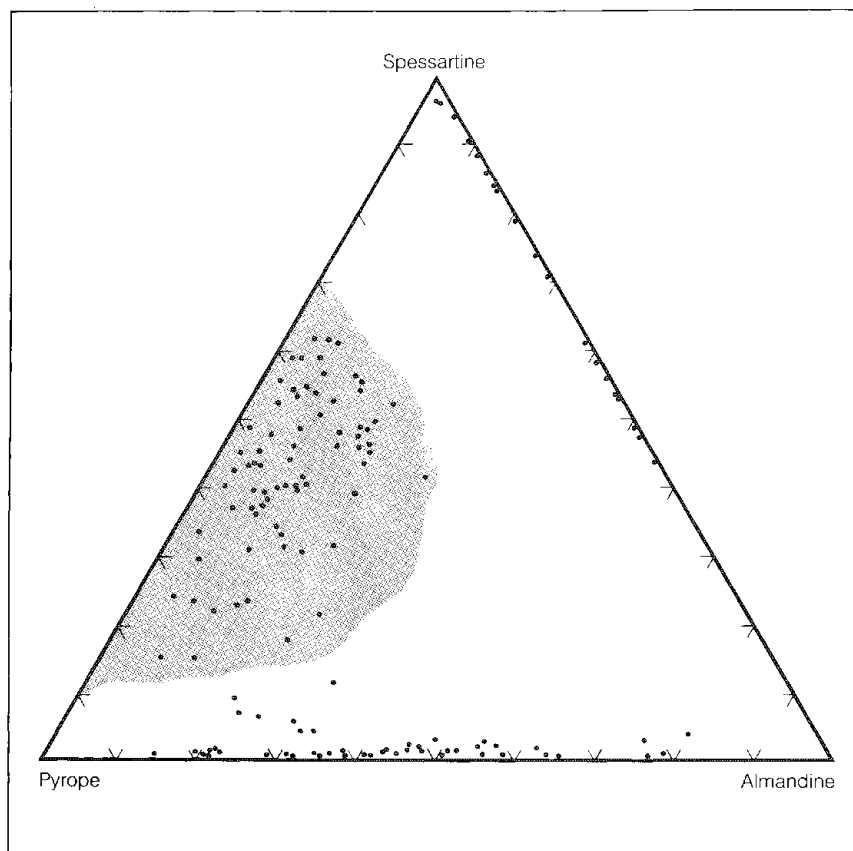


FIG. 2.--Ternary diagram of pyrope-almandine-spessartine compositions observed in gem garnets. Recently characterized new compositional range is shaded.

garnet solid solution series that was unknown ten years ago (Fig. 2).<sup>8</sup>

Another problem to which we are applying microbeam techniques is that of the characterization of nonhomogeneous gem materials. One example is a mottled black, green, and white material known as "maw-sit-sit" that has been confused in the gem trade with jadeite. X-ray powder diffraction of a black patch originally pointed to the material being ureyite [ $\text{NaCr}(\text{Si}_2\text{O}_6)$ ], which had previously been known only from meteorites.<sup>9</sup> Microprobe analysis (Table 4) confirmed it as the first known terrestrial occurrence of this rare mineral. Scanning electron microscopy shows a complex intergrowth of the ureyite with at least one other mineral, white in color (Fig. 3), thereby producing the green color. (The black color of the ureyite is actually a very, very dark green.) Elemental mapping (done by Paul Hlava of Sandia National Laboratories; Fig. 4) enabled us to locate and analyze other phases and to determine the proportions of these to the ureyite in a representative sample of maw-sit-sit. A number of phases have been identified, including ureyite, chlorite, a range of alkali amphiboles, and a ureyite-aegirine pyroxene (Table 4).

A problem in which the SEM has played a truly significant part is in the detection of plastic impregnation of opal.<sup>1,2</sup> Certain types of opal can be treated with plastic to improve the appearance and quality of the phenomenal play of color on which their value depends. The plastic fills the spaces between the stacked silica spheres, thereby changing the refractive index of the intersphere spaces and altering the diffraction effect that produces the play of color. Virtually worthless opal can in this way be turned into apparently fine gem material and there is no simple optical or physical test that can detect the treatment. However, the plastic used (at least, until just a few months ago) is resistant to hydrofluoric acid, whereas the opal silica spheres are not. If plastic is present in an opal, etching will remove layers of silica spheres and leave behind a tell-tale honeycomb of plastic. The structure present can be seen easily at 12 000 to 20 000 $\times$  in an electron microscope (Fig. 5) and identifies the nature of the material.

### Conclusions

The value of microbeam analysis to gemology has been well established over the past ten years. Much has been done in this area, but much more remains to be done. There is now a need for a variety of researchers to become involved in the extensive documentation and characterization of gem materials through microbeam techniques, but with correlation to other properties such as color and clarity (i.e., how much included material is contained in a specimen as well as its crystallinity and homogeneity) that makes the data useful to gemological researchers. Moreover, the problem of sample availability has been overcome because custodians of gem collections (such as those at GIA and various museums worldwide) are now convinced of the value and nondestructive nature of microbeam techniques of analysis and are willing to lend their precious specimens for this type of study.

### References

1. P. J. Darragh et al., "Opals," *Scientific American*, April 1976, 84-95.
2. D. V. Manson, "Plastic impregnated gem opal," *Gems & Gemology*, 1978, 49-57.
3. H. W. Schrader, "Contributions to the study of the distinction of natural and synthetic emeralds," *J. Gemmology*, 1983, 530-543.
4. C. M. Stockton, "The chemical distinction of natural and synthetic emeralds," *Gems & Gemology*, 1984, 141-145.
5. M. O'Donoghue, *A Guide to Man-made Gemstones*, New York: Van Nostrand Reinhold, 1983, 55.
6. R. E. Kane, "Natural rubies with glass-filled cavities," *Gems & Gemology*, 1984, 187-199.
7. J. E. Shigley and C. M. Stockton, "'Cobalt-blue' gem spinels," *Gems and Gemology*, 1984, 34-41.
8. C. M. Stockton and D. V. Manson, "A proposed new classification for gem-quality garnets," *Gems & Gemology*, 1985, 205-218.
9. D. V. Manson, "Recent activities in GIA's research department," *Gems & Gemology*, 1979, 217-218.



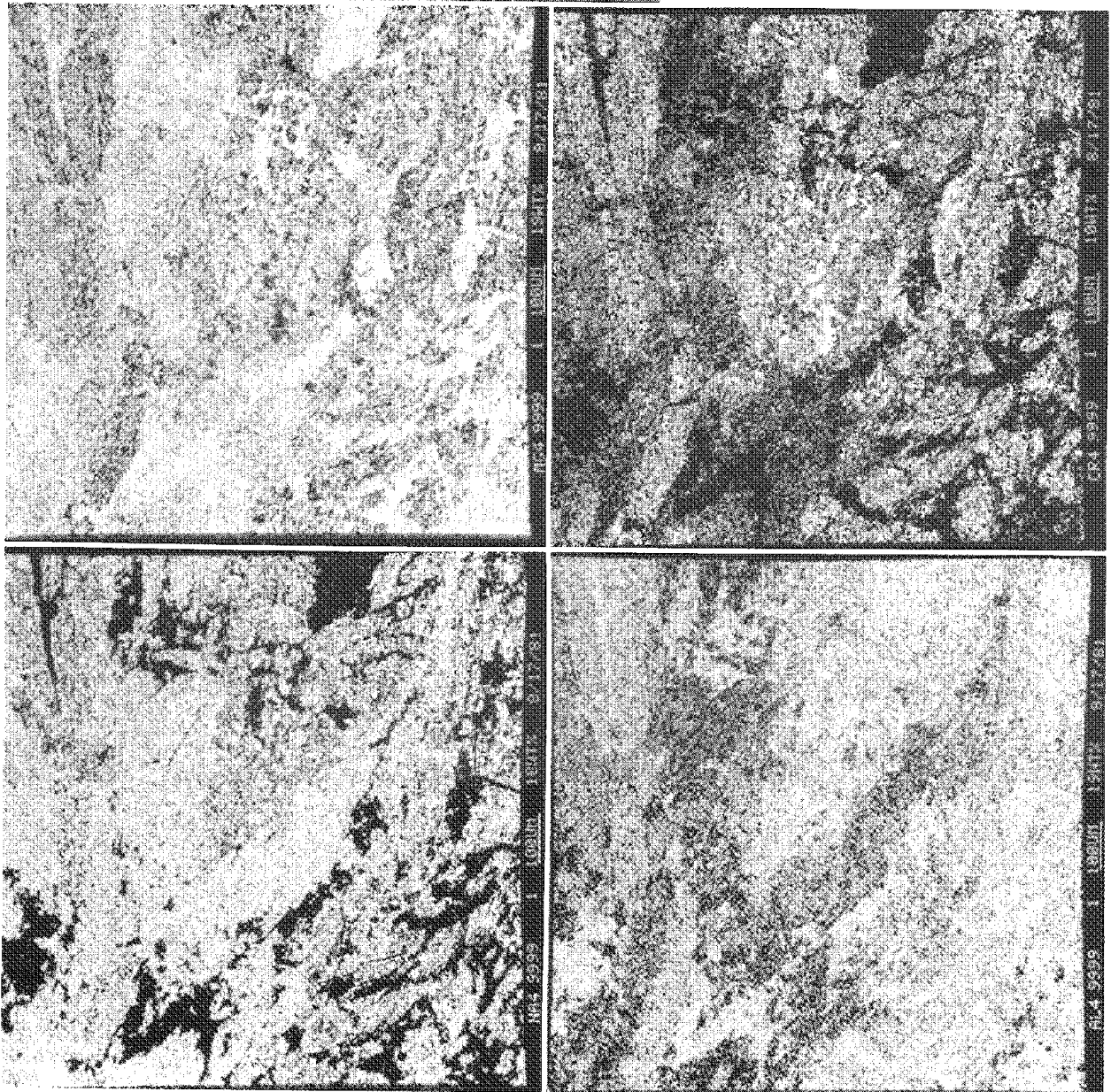


FIG. 4.--Elemental maps of same region of maw-sit-sit specimen shown in Fig. 3.

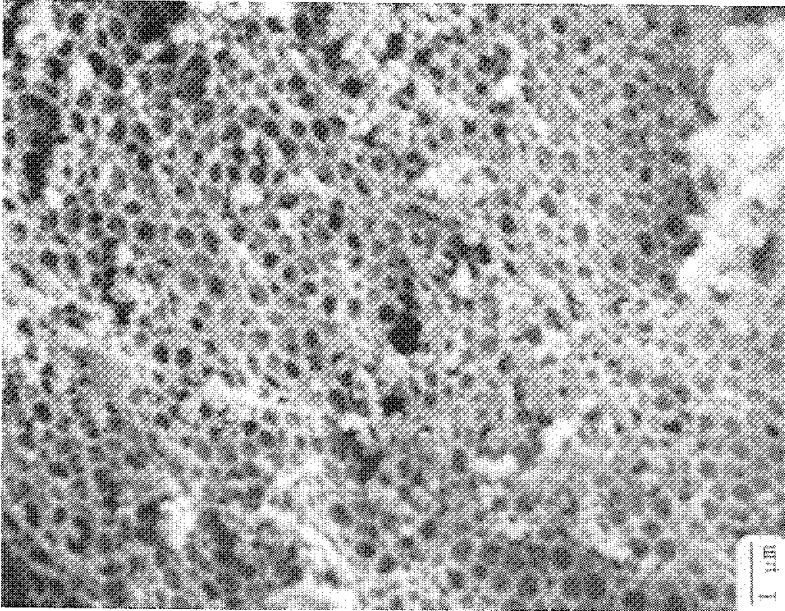


FIG. 5.--Hydrofluoric acid has removed top layer of silica spheres and left behind network of plastic in this SEM micrograph.



## KIMBERLITIC GARNETS: METAMERISM RELATED TO COMPOSITION

W. L. Mansker, J. T. Springfield, and Klaus Keil

Kimberlites contain a diverse population of accidental and cognate garent xenocrysts. Many of these garnets exhibit metameric color changes when viewed in incandescent, then daylight illumination. An artificial illumination technique incorporating incandescent and simulated daylight permits classification of the garnets into metameric categories. Microanalysis of the categorized garnets indicates that metameric changes are influenced primarily by  $\text{Cr}^{+3}$ ,  $\text{Ca}^{+2}$ , and  $\text{Fe}^{+3}$ . Relative compositional variations of these components give rise to color-additive metameric effects. Comparison is made with garnet inclusions occurring in diamond, and a technique is presented for rapid visual field evaluation of garnets regarding kimberlite prospects and their diamond-bearing potential.

Chrome-pyrope garnets are routinely used as indicator minerals for kimberlite in heavy mineral stream sediment and soil surveys. The garnets are typically selected, under artificial light for additional time-consuming refractive-index, specific-gravity, and microprobe determinations to verify their kimberlitic affinity. Although garnet color has been suggested as a means of kimberlitic definition,<sup>1,2</sup> considerable experience is required for discerning critical garnet colors from the multiplicity of colors exhibited by garnets from various terranes. Color-changing (i.e., metameric) chrome-pyropes have been described by others,<sup>3,4</sup> and suggested as a criterion for determining diamond-affiliate garnets.<sup>4</sup> Unfortunately, prior descriptions of garnet metamerism have been ambiguous and nonspecific regarding light sources used during garnet examination.

### *Method*



Garnets for this study were selected from heavy mineral concentrates produced from several U.S. kimberlite occurrences. The garnets were surveyed under both artificial incandescent and 'D' phosphor (daylight) fluorescent illumination, and tentatively categorized into suites, based on observed metameric color change. The samples were prepared as grain mounts and doubly-polished to a uniform thickness (about 300  $\mu\text{m}$ ). The polished grains were then reevaluated and finally classified as to metameric color type. Microanalyses were made using an ARL-EMX-SM electron microprobe, operated at 200nA sample current and 15keV excitation potential. Standard instrumental and matrix effects corrections were made. Structural formula calculations included recasting of atomic proportions, assigning  $\text{Fe}^{+2}$  to  $\text{Fe}^{+3}$  as required to satisfy tetrahedral site deficiencies. Average microanalyses, structural formulas, and endmembers for the garnets of this study, and for high chrome-low calcium (Type 10) and low-chrome garnet inclusions in diamond, are given in Table 1.



### *Discussion*

Metameric color changes may be summarized as: purple (incandescent) > dark green, medium blue, light blue, or light greenish yellow (fluorescent), and orange (incandescent) > medium orange, or light orangish yellow (fluorescent). Microanalytical data indicate that the major compositional components related to metameric changes (Fig. 1) are  $\text{Cr}^{+3}$ ,  $\text{Ca}^{+2}$ , and  $\text{Fe}^{+3}$ . High  $\text{Cr}^{+3}$ , with a concomitant decrease in  $\text{Ca}^{+2}$ , yields a purple > green metameric couplet, corresponding to garnets with a high knorringite endmember component. Lower  $\text{Cr}^{+3}$  and  $\text{Fe}^{+3}$ , with a concomitant increase in  $\text{Ca}^{+2}$ , produces a purple > blue metameric couplet, corresponding with typical pyrope-almandine garnets, which dominate the population of kimberlitic garnets. Increased  $\text{Fe}^{+3}$  tends to produce additively purple > greenish yellow; or orange > yellow, or orange (slight metamerism) couplets. This group

---

Author Mansker is at INEX (Applied Geologic Research, Development and Exploration), 8704 Gutierrez NE, Albuquerque, NM 87111; author Springfield is at Condor Minerals Management, 3379 Gunnison Drive, Ft. Collins, CO 80526; author Keil is at University of New Mexico (Institute of Meteoritics), Albuquerque, NM 87131. Partial support by NASA grant NAG 9-30 (Klaus Keil, Principal Investigator) is gratefully acknowledged by the authors.

TABLE 1.--Average microanalyses, recast (Fe + 3) structural formulas and endmembers for kimberlitic garnets (A through G), and garnet inclusions in diamond (  and  ).

	A	B	C	D	E	F	G		
SiO <sub>2</sub>	40.1	41.1	41.3	41.5	41.4	41.4	41.3	41.9	40.2
Al <sub>2</sub> O <sub>3</sub>	15.7	19.5	21.0	20.8	20.5	20.6	22.5	17.1	21.5
Cr <sub>2</sub> O <sub>3</sub>	10.1	5.95	3.72	3.61	2.46	2.39	1.14	8.2	0.10
CaO	7.74	5.34	5.29	5.10	5.35	4.94	4.54	2.54	8.19
FeO	7.29	7.75	8.44	7.76	8.92	8.82	11.2	6.27	17.0
MgO	18.3	19.8	19.6	20.7	20.6	20.7	19.1	23.1	11.7
MnO	0.42	0.44	0.47	0.35	0.34	0.33	0.39	0.21	0.32
TiO <sub>2</sub>	0.54	0.15	0.16	0.37	0.98	0.90	0.36	0.10	0.61
TOTAL	100.2	100.0	100.4	100.2	100.6	100.1	100.5	99.4	99.6
Recast Structural Formula Based on 12 Oxygens									
Si	2.9560	2.9699	2.9723	2.9690	2.9635	2.9708	2.9619	3.0199	3.0118
Al	1.3214	1.6323	1.7553	1.7245	1.6947	1.7146	1.8656	1.4738	1.9120
Fe+3	0.0597	0.0194	0.0242	0.0513	0.1132	0.1011	0.0503	0.0532	0.0477
Cr	0.5890	0.3402	0.2118	0.2043	0.1393	0.1357	0.0647	0.4676	0.0059
Ca	0.6115	0.4135	0.4080	0.3910	0.4104	0.3799	0.3489	0.1962	0.6576
Ti	0.0299	0.0082	0.0087	0.0199	0.0528	0.0486	0.0194	0.0054	0.0344
Fe+2	0.3898	0.4490	0.4838	0.4131	0.4208	0.4283	0.6215	0.3248	1.0177
Mg	2.0108	2.1327	2.1026	2.2074	2.1980	2.2141	2.0418	2.4816	1.3066
Mn	0.0262	0.0269	0.0287	0.0212	0.0206	0.0201	0.0237	0.0128	0.0203
Total	7.9943	7.9921	7.9954	8.0017	8.0134	8.0131	7.9979	8.0353	8.0140
Garnet Endmembers									
Spess	0.86	0.89	0.96	0.69	0.67	0.66	0.78	0.43	0.68
Andrad	4.39	1.43	1.58	3.60	8.20	7.33	3.54	2.92	4.09
Knorr	29.1	16.9	10.5	10.1	6.86	6.70	3.18	23.3	0.30
Pyrope	37.0	53.8	59.0	62.7	65.2	66.0	64.1	59.0	43.2
Gross	15.8	12.3	11.9	9.41	5.27	5.13	7.95	3.59	17.8
Almand	12.9	14.7	16.0	13.6	13.8	14.1	20.4	10.8	33.9

includes primarily crustal and eclogitic garnets. MnO and TiO<sub>2</sub> content of the garnets show no consistent correlation with metamerism. The data presented are compatible with elemental absorption spectra, which predict Cr<sup>+3</sup> absorption at 410-420 and 560-570 nm, and with previously published absorption data on chrome pyrope garnets.<sup>3</sup> The role of Ca<sup>+2</sup> and Mn<sup>+2</sup> as chromophores, or metameric enhancers, and the role of Fe<sup>+3</sup> as a possible quencher of metamerism, have not been evaluated. Pending absorption determinations for the garnets of this study will perhaps clarify the behavior of these components.

Based on the results of this study, a field technique in which a battery-operated 'D' phosphor fluorescent lamp is used, has proved to be effective in classifying garnets. This technique allows rapid visual evaluation of heavy mineral concentrates for kimberlitic garnets and facilitates prioritization of prospective kimberlites.

### References

1. B. C. Hearn and E. S. McGee, "Garnets in Montana diatremes: A key to prospecting for kimberlites," *U.S. Geological Survey Open File Report 82-722*, 1982, 43 pp.
2. J. P. Padgett and M. E. McCallum, "Relationship between geochemistry and color of garnet xenocrysts from Colorado-Wyoming kimberlites" (Abstract), *Terra Incognita* 2(No. 3), 1982.
3. G. I. Smirnov, "Mineralogy of Siberian kimberlites," *International Geology Rev.* 1(No. 12): 21-39, 1959.
4. N. V. Sobolev, *Deep-Seated Inclusions in Kimberlites and the Problem of the Composition of the Upper Mantle*, Washington, D.C.: American Geophysical Union (translation), 1977.

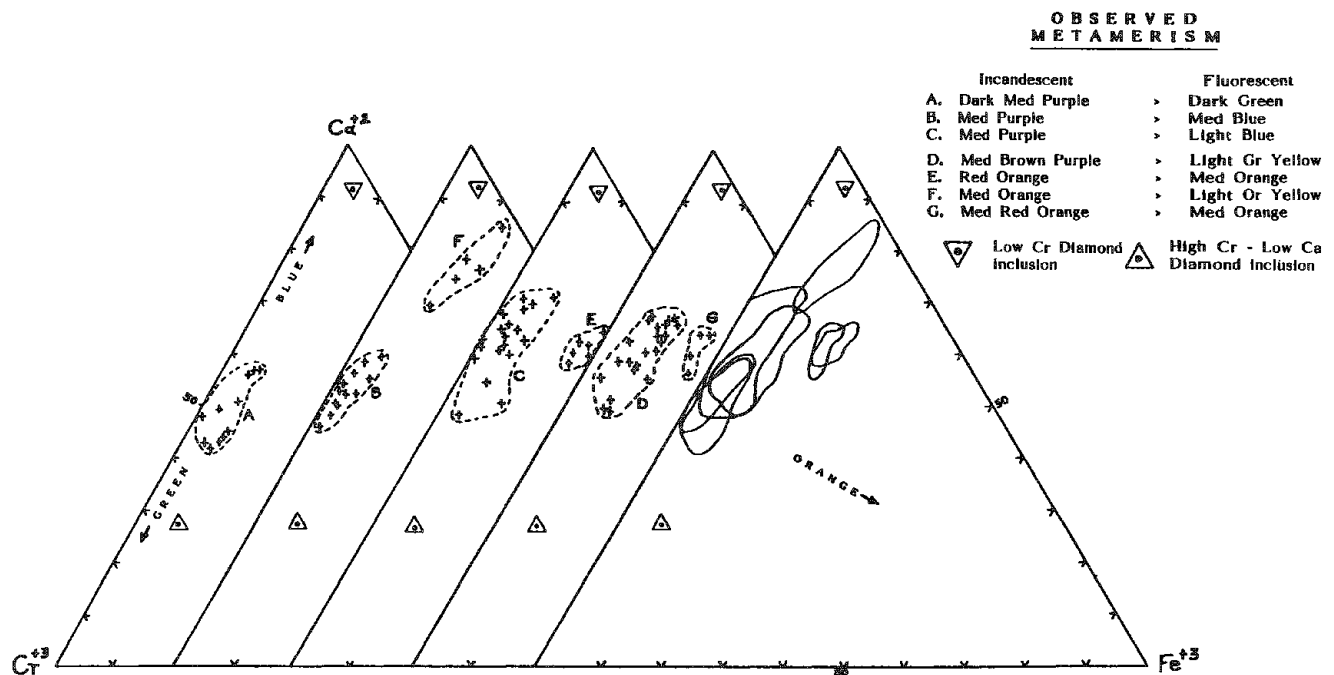


FIG. 1.--Normative plot of atomic Cr<sup>+3</sup>, Fe<sup>+3</sup> (calculated), and Ca<sup>+2</sup> chromophores affecting garnet metamerism.

## GARNET SUITES IN U.S. KIMBERLITES AND LAMPROITES

W. L. Mansker

Garnet xenocrysts in U.S. kimberlites and lamproites show a range of compositions reflecting derivation from various crustal and mantle sources beneath the continent. Lamproitic rocks contain abundant lower crustal and low chrome upper mantle pyropic garnets, and a relative paucity of high chrome, low calcium pyropes. Kimberlites, on the other hand, in addition to crustal and upper mantle garnet suites, contain a higher proportion of apparent deeper-seated, high chrome, low calcium garnet species. Lamproites are tectonically associated with once-active mobile belts, whereas kimberlites appear more confined to thicker, stable cratonic areas. Inferences can be made regarding source depth, chemical evolution, and upper mantle processes based upon garnet suites, in conjunction with overall compositional attributes.

### *Method*

Garnets for this study were selected from heavy mineral suites collected from either bulk rock samples, or alluvial samples known to drain the occurrences. The garnets were prepared as grain microprobe mounts, polished, and analyzed by an ARL-EMX-SM electron microprobe. Operating conditions were 15 keV excitation potential and 200 nA sample current. Standard corrections were made for instrumental and matrix effects. Structural formula calculations included recasting of atomic proportions, assigning  $\text{Fe}^{+2}$  to  $\text{Fe}^{+3}$  as required, to satisfy tetrahedral site deficiencies.

### *Discussion*

Analytical data for the garnets of this study indicate that kimberlites contain a higher proportion of high chrome pyropes, relative to low chrome pyropes and crustal garnet species, which tend to dominate lamproite occurrences. The lamproites exhibit a lower population of all xenocrystal garnet types, relative to kimberlites, which may bias the compositional data. However, the observed garnet compositional data are compatible with inferences that can be made regarding comparative kimberlite vs. lamproite chemistries, and tectonic settings regarding mantle source depth and degree of chemical evolution. The relative paucity of high-chrome pyropes in lamproites may be related to shallow source lamproite derivation, or upper mantle reaction processes (e.g., metasomatism) affecting such garnets.

---

The author is at INEX (Applied Geologic Research, Development and Exploration), 8704 Gutierrez NE, Albuquerque, NM 87111. He gratefully acknowledges Cominco American, Inc., for permission to present the data, and absolves Cominco American, Inc., regarding the interpretations presented, which are solely those of the author.

## FORM AND COMPOSITION OF SECONDARY MINERALIZATION IN FRACTURES IN COLUMBIA RIVER BASALTS

J. P. McKinley, S. A. Rawson, and D. G. Horton

Columbia River basalts in the Pasco structural basin, Washington State, are under study as a possible repository for high-level nuclear waste. The work described here was conducted as part of the program to assess the basalts for their suitability as a repository host. This paper presents the results of electron-optical petrographic examination, x-ray diffraction, and microprobe compositional analysis of fracture-filling and near-fracture secondary mineralization in Columbia River basalts.

Each flow is nominally divided into three morphologic units: flow top, colonnade, and entablature. Textural variations within the morphologic units indicate differences in cooling histories, with a progression toward more rapid cooling from colonnade to entablature to flow top.<sup>1</sup> Below the flow top, entablature and colonnade may alternate throughout the thickness of a given flow. Colonnade is made up of distinct polygonal columns, whereas entablature contains irregular, more closely spaced fractures. Cooling fractures are filled with secondary mineralization.

Petrographically, the basalts consist of augite, which may be rimmed by pigeonite, plagioclase of intermediate composition, titanomagnetite, and glassy mesostasis (Fig. 1). The relative abundance of mesostasis varies from 15 to 20 modal percent in colonnade, to 40 to 55 modal percent in entablature.<sup>2</sup> Outcrop samples of Cohasset flow entablature also contain 5 to 8 modal percent alteration products, randomly distributed throughout in <1mm flecks.<sup>3</sup>

### *Experimental Techniques*

Samples were chosen from pieces of reference Cohasset flow entablature for analysis of alteration products, and from drill core from Hanford Site borehole RRL-2, for analysis of fracture-fill and near-fracture secondary minerals. Portions of fracture-bearing core were first cut for preparation of polished thin sections. Fractures were then broken and scraped for material from which to make random and oriented x-ray diffraction mounts.

A Rigaku D/MAX-rA Rotaflex system was used to analyze x-ray diffraction mounts that were both randomly oriented and preferentially oriented (air-dried and glycol-solvated). Electron microprobe analyses were performed with a Cameca MBX microprobe with Tracor Northern automation. The beam was slightly defocused (2-3 $\mu$ m dia.) and rastered over a 100 $\mu$ m<sup>2</sup> area on the sample surface.

### *Results*

Secondary mineralization in and around fractures includes fracture fill and abundant alteration of adjacent basalt. An alteration rind penetrates the basalt to a depth of as much as 0.75 cm from the fracture face. This rind shows a textural progression from maximum alteration at the fracture face to essentially unaltered basalt outboard of the rind. Experimental studies of basalt-synthetic groundwater interaction have shown that, under the conditions of the experiments, glassy mesostasis is preferentially altered, with only limited alteration of coexistent mineral phases.<sup>4-5</sup> Observed alteration of basalt near fractures indicates that pyroxene, as well as mesostasis, undergoes early hydrothermal alteration. The alteration of mesostasis and pyroxene in preference to plagioclase and titanomagnetite is evident at the edge of the alteration rind (Fig. 1). Plagioclase-mesostasis boundaries and pyroxene-plagioclase boundaries are relatively straight and unaltered; pyroxene-mesostasis boundaries show the effects of alteration. Pyroxene grain boundaries in contact with mesostasis are ragged and embayed. At the

---

The authors are with the Basalt Waste Isolation Project, Rockwell Hanford Operations, Richland, WA 99352. The authors would like to thank S. B. Kunkler and S. K. Showalter for technical assistance.

fracture face (Fig. 2), all mesostasis is altered, and in some places replaced by clay. All boundaries of pyroxene grains are ragged and embayed; plagioclase shows some ragged edges, but in general retains relatively straight crystal-lath boundaries.

X-ray diffraction analysis shows the fracture-fill to contain trioctahedral smectite as the only phyllosilicate phase (Fig. 3). Accompanying the smectite in some samples are minor amounts of zeolite, pyrite, quartz, and opal CT. Minor amounts of basaltic pyroxene and plagioclase were incorporated in the x-ray mounts during scraping.

Electron microprobe analyses were performed on fracture-filling zeolite and smectite and on smectite within the basalt alteration rind, for samples collected from well depths of 480 to 930 m (Table 1). Alteration products within reference Cohasset-flow entablature were also analyzed. The analyses are tabulated in pairs for smectites, representing fracture-fill and near-fracture clay compositions. Standard deviations ( $2\sigma$ ) are given for each element oxide, as is the number of analyses included for each sample. The analyses were also reduced, as appropriate, to chemical mineral formulas for smectites and heulandite-group zeolites (Table 2).<sup>6</sup> The analyses indicate that the trioctahedral phase is Fe-saponite, with little sample-to-sample variation. The mesostasis smectite lacks exchangeable Na and contains little exchangeable K relative to fracture-filling smectite.

FIG. 1.--Backscattered electron image of basalt near limit of fracture-face alteration rind. Textural relationships of basalt phases are illustrated. Dashed lines mark boundary between mesostasis and plagioclase laths. Px = pyroxene (augite), Pl = plagioclase, Ti = titanomagnetite, M = mesostasis. Also shown is onset of alteration involving mesostasis and pyroxene.

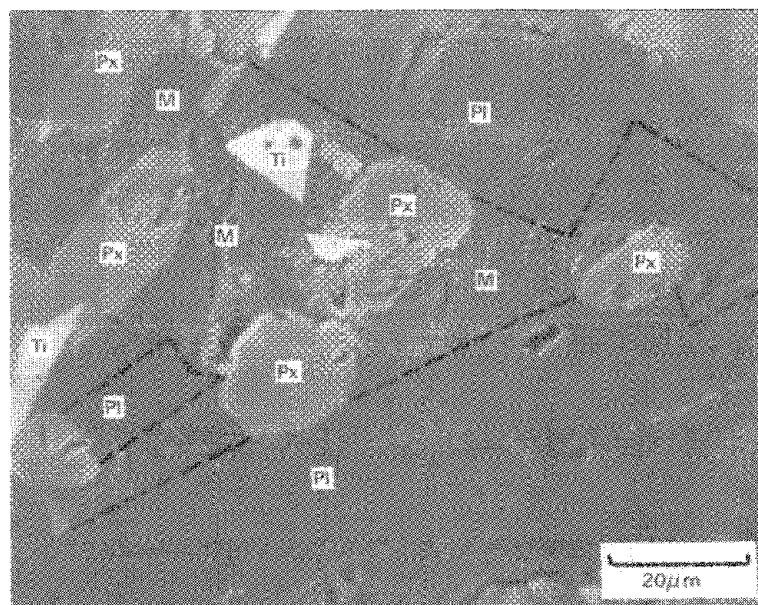
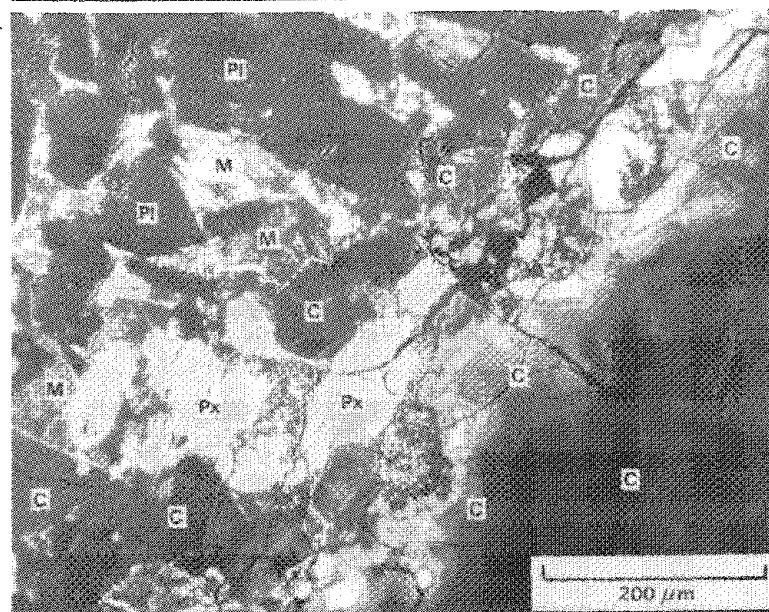


FIG. 2.--Backscattered electron image showing fracture-face texture. Letters are keyed as in Fig. 1, with the addition of C = clay. All mesostasis is altered and in some places replaced by clay. All pyroxene boundaries are ragged and embayed, and plagioclase shows some ragged edges.



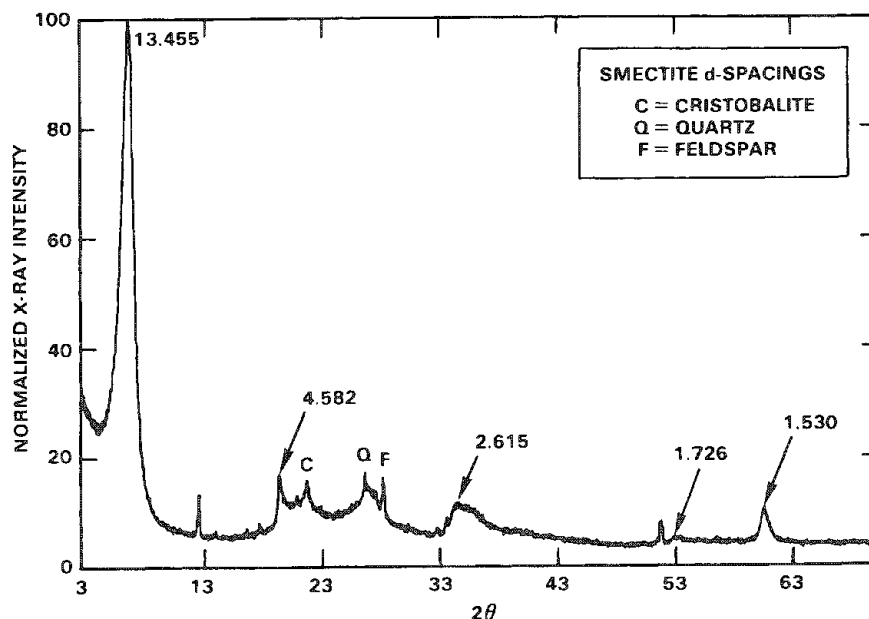


FIG. 3.--X-ray diffractogram of randomly oriented 2-45 $\mu$ m fraction of fracture fill from sample 2227.6.

TABLE 1.--Microprobe analyses of fracture-filling and near-fracture clay minerals and zeolite in samples from Hanford borehole RRL-2 and of alteration in reference Cohasset flow entablature (RCE) basalt. Sample numbers are depths in feet.

Sample	Composition (wt%)										Number of Points
	SiO <sub>2</sub>	TiO <sub>2</sub>	Al <sub>2</sub> O <sub>3</sub>	FeO	MnO	MgO	CaO	Na <sub>2</sub> O	K <sub>2</sub> O	Total	
Smectite, sample 1,620.9											
Fracture-fill	49.87	0.01	2.61	16.19	0.14	16.07	0.98	0.17	0.64	86.68	25
2 $\sigma$	1.76	0.01	0.66	1.49	0.02	0.93	0.15	0.02	0.06		
Near-fracture	44.23	0.25	5.23	22.26	0.21	12.04	1.37	0.43	0.62	86.64	26
2 $\sigma$	0.72	0.31	0.40	0.45	0.03	0.49	0.49	0.04	0.04		
Smectite, sample 2,485.7											
Fracture-fill	44.82	0.20	4.87	27.39	0.21	7.17	1.90	0.46	1.21	88.23	27
2 $\sigma$	0.22	0.02	0.06	0.35	0.03	0.17	0.06	0.02	0.06		
Near-fracture	44.37	0.44	4.90	24.96	0.12	8.34	1.65	0.57	1.38	86.73	25
2 $\sigma$	0.39	0.06	0.20	1.17	0.01	0.82	0.18	0.04	0.19		
Smectite, sample 3,109.0											
Fracture-fill	48.56	0.48	3.17	17.46	0.09	13.62	1.25	0.99	0.72	86.34	27
2 $\sigma$	0.60	0.09	0.27	0.81	0.02	0.58	0.28	0.03	0.05		
Near-fracture	46.42	0.79	3.34	17.20	0.00	13.78	0.68	1.24	0.59	84.04	26
2 $\sigma$	0.63	0.15	0.26	0.71	--	0.63	0.08	0.07	0.03		
Smectite, sample RCE-1											
Alteration	46.76	0.17	3.82	19.07	0.16	13.69	2.00	0.00	0.27	85.94	24
2 $\sigma$	0.39	0.30	0.57	0.74	0.03	0.71	0.30	--	0.02		
Smectite, sample RCE-4-2											
Alteration	47.70	0.01	3.71	16.77	0.18	15.51	1.69	0.00	0.29	85.86	24
2 $\sigma$	0.53	0.01	0.38	0.93	0.03	0.43	0.42	--	0.03		
Zeolite, sample 1,936.0											
Fracture-fill	67.76	0.01	13.01	0.11	0.02	0.08	1.40	2.13	4.54	89.06	24
2 $\sigma$	0.43	0.01	0.14	0.03	0.01	0.01	0.02	0.19	0.16		

Note: 2 $\sigma$  = 2 standard deviations.

## Conclusions

Examination of basalt alteration rinds suggests that pyroxene is altered, along with mesostasis, from the inception of hydrothermal alteration along cooling fractures in Columbia River basalts. The only phyllosilicate secondary mineral in fractures is trioctahedral smectite of Fe-saponite composition, throughout the examined thickness of the basalt column. This smectite is compositionally distinct from the minor amounts of mesostasis smectite found in otherwise unaltered outcrop samples of basalt.

## References

1. P. E. Long and B. J. Wood, *Structures, Textures, and Cooling Histories of Columbia River Basalt Flows*, RHO-BW-SA-212, Richland, Wash.: Rockwell Hanford Operations, 1984.
2. P. E. Long et al., *Relationships Between Internal Structures and Petrographic Textures of Basalt Flows: Example from a Continental Flood Tholeiite Province*, RHO-BWI-SA-67 A, Richland, Wash.: Rockwell Hanford Operations, 1980.
3. C. C. Allen et al., *Characterization of Reference Umtanum and Cohasset Basalt*, SD-BWI-DP-053, Richland, Wash., Rockwell Hanford Operations, 1985.
4. C. C. Allen et al., *Experimental Approaches to Determining the Extent of Equilibrium in a Basaltic Hydrothermal System*, RHO-BW-SA-436, Richland, Wash.: Rockwell Hanford Operations, 1985.
5. D. L. Lane et al., "The basalt/water system: Considerations for a nuclear waste repository," in G. McVay, Ed., *Scientific Basis for Nuclear Waste Management*, New York: North-Holland Publishing Co., 1984, vol. VII, 95-103.
6. W. A. Deer et al., *An Introduction to the Rock-forming Minerals*, New York: Wiley, 1966.

TABLE 2.--Weight percent compositions recalculated as mineral formulas. Smectite cations on basis of 22 charge total, zeolite cations on basis of 144 charge total.

Fracture	Chemical composition (wt%)									
	Si	Al IV	Al VI	Ti	Fe(2+)	Mn	Mg	Ca	Na	K
Smectite, sample 1,620.9										
Fracture-fill	3.82	0.18	0.06	0.00	1.04	0.01	1.83	0.08	0.03	0.06
Near-fracture	3.55	0.45	0.04	0.02	1.49	0.01	1.44	0.12	0.07	0.06
Smectite, sample 2,485.7										
Fracture-fill	3.64	0.36	0.10	0.01	1.86	0.01	0.87	0.17	0.07	0.13
Near-fracture	3.62	0.38	0.10	0.03	1.71	0.01	1.02	0.14	0.09	0.14
Smectite, sample 3,109.0										
Fracture-fill	3.78	0.22	0.07	0.03	1.14	0.01	1.58	0.10	0.15	0.07
Near-fracture	3.72	0.28	0.04	0.05	1.15	0.00	1.65	0.06	0.19	0.06
Smectite, sample RCE-1										
Alteration	3.69	0.31	0.05	0.01	1.26	0.01	1.61	0.17	0.00	0.03
Smectite, sample RCE-2-4										
Alteration	3.71	0.29	0.05	0.00	1.09	0.01	1.80	0.14	0.00	0.04
Zeolite, sample 1,936.0										
Fracture-fill	29.52	6.68	--	0.00	0.04*	0.01	0.05	0.65	1.80	2.52

\*Fe3+.



## ALTERATION PRODUCTS OF BASALTIC GLASS, HANAUMA BAY, OAHU, HAWAII

Rachel Cowan and R. C. Ewing

Natural basaltic glasses are similar to synthetic borosilicate nuclear waste form glasses with respect to their alteration products.<sup>1</sup> Therefore, the alteration and hydration of basaltic glasses may provide a means of verification of models that are used to predict the long-term (>10 000 years) durability of borosilicate waste form glasses. In an effort to understand long-term effects of alteration on basaltic glasses, we have examined products in two different environments--seawater and freshwater--in a sequence of pyroclastic deposits in Hanauma Bay, Hawaii.

Hanauma Bay is in the extreme southeastern corner of the island of Oahu within the alkali olivine tephra deposits and minor lavas of the Koko Crater Group. The age of the Koko Crater Group is 30 000-40 000 years.<sup>2-4</sup> Thus, the lower ash deposits, currently sub-aerial, have been submerged and seawater alteration extends at least 6 m above current sea level. The Hanauma Bay maar crater has been breached by the sea and the fine-grained tephra deposits have been extremely altered by seawater as well as fresh water at the higher elevations, forming palagonite, a hydrolitic replacement product of basaltic glass (sideromelane), and authigenic cementation minerals such as smectite, zeolite [phillipsite,  $(\frac{1}{2}\text{Ca}, \text{NaK})_3(\text{Al}_3\text{Si}_5\text{O}_{16}) \cdot 6\text{H}_2\text{O}$ ; analcime,  $\text{Na}(\text{AlSi}_2\text{O}_6)\text{H}_2\text{O}$ ; erionite,  $(\text{Na}_2\text{K}_2\text{CaMg})_{4-5}(\text{Al}_9\text{Si}_{27}\text{O}_{72}) \cdot 27\text{H}_2\text{O}$ ]; and calcite,  $\text{CaCO}_3$ ]. The purpose of this study is to distinguish between the alteration products formed during palagonitization in seawater and freshwater environments.

Samples include: (1) Hr-br-1a, subaerial, collected 65 m from the ocean and 40 m above current sea level; (2) HW-w-2a, subaerial, collected 7 m from the ocean and 6 m above current sea level; (3) HW-1, partially submarine, covered by sporadic ocean waves at high tide; and (4) HW-1u, submarine, from the same layer as HW-1, but 0.5 m below sea level. An additional series of samples, HR unit, were collected down a 25m cliff face which has only been altered by freshwater.

### *Analytical Procedure*

Six alteration zones were distinguished in the tephra deposits of Hanauma Bay on the basis of color in hand specimen. The samples were friable and in order to preserve the delicate alteration and authigenic phases, special sample-preparation techniques were used in three steps: (1) the exclusive use of either isopropyl alcohol and/or acetone during the entire preparation procedure to protect the hydrous phases, (2) re-impregnation of the sample with Buchler glue after polishing with 1000 grit to prevent additional plucking of phases; and (3) the use of kerosene as a lubricant during all polishing steps.

Ten elements were analyzed sequentially, the most volatile first (Na). In the calibration for Na, the counting time was reduced to minimize loss of Na. An Na diffusion test was conducted on the glass of HW-w-1a. A broad electron beam (30  $\mu\text{m}$ ) was used for a time equivalent to a ten-element analysis (2.5 min). The Na content of basaltic glass was analyzed at 4s intervals and the results indicate minimal diffusion. A focused electron beam (1  $\mu\text{m}$ ) caused up to 70% loss of Na (Fig. 1a). The same Na diffusion test was completed on palagonite in HW-w-1a. The broad electron beam (10  $\mu\text{m}$ ) caused minimal diffusion and the focused electron beam caused up to 50% loss of Na (Fig. 1b). The relatively large size of the basaltic glass shards allowed for the use of a defocused electron beam (30-40  $\mu\text{m}$ ), operated at 20 nA. Smaller palagonite rinds and particles were analyzed using a smaller electron beam (10-12  $\mu\text{m}$ ) operated at 5 nA.

Standards for basaltic glass analyses were Mn-doped diopside (Mn), apatite (P), and a synthetic glass standard (Si, Al, Ti, Fe, Mg, Ca, Na, K). The calibrations were independently checked by analysis of USNM-113716. Standards for palagonite analyses were Mn-doped

---

The authors are at the Department of Geology, University of New Mexico, Albuquerque, NM 87131. This study was supported by a DOE Thesis Research Program on Nuclear Waste Management grant from Argonne National Laboratory. All work was completed in the UNM Electron Microbeam Analysis Facility of the Institute of Meteoritics. We have benefited greatly from the critical comments and advice of M. J. Jercinovic.

diopside (Mn), apatite (P), benitoite (Ti), cordierite (Al), fayalite (Fe), A209 augite (Mg), and a synthetic glass standard (Si, Ca, Na, K). Analyses were performed with a fully automated, five-spectrometer JEOL 733 Superprobe. The JEOL 733 utilizes the Sandia TASK 8<sup>5</sup> operating system, which includes a Bence-Albee correction scheme for differential matrix effects. Fe is analyzed as total FeO. The low totals for the palagonite (Table 1) are due to their high water content.

### *Results and Discussion*

The results of the EMPA (Table 1) are summarized in Fig. 2. The samples represent seawater alteration (HW-w-2a, HW-1, and HW-1u) and freshwater alteration (HR-br-1a). Weight percent values are recalculated to mass per unit volumes by use of the density ranges of basaltic glass (2.75-2.85 g/cm<sup>3</sup>) and palagonite (1.93-2.14 g/cm<sup>3</sup>) reported for the Honolulu Series.<sup>2</sup> Figure 2 shows the ratio of the palagonite to glass plotted for each oxide of the four samples. The conversion of basaltic glass to palagonite is assumed to be an isovolumetric process. Thus, a value less than 1.0 indicates elemental loss as a result of alteration. The vertical range of the data bars is due to the range of densities used in the calculations.

Ti(1.05-1.38) is the only element that consistently increases with the alteration of glass to palagonite. Fe(0.99-1.37) increases from sideromelane to palagonite in all environments except the near-ocean (0.85-0.97). The relative insolubilities of Ti and Fe oxides in most natural waters account for their increase. Si is most depleted in the submarine (0.41-0.47) and partially submarine environments (0.35-0.40) and is the least depleted in the subaerial environment (0.62-0.78). Al variation generally follows Si. Environments most depleted in Al are either submarine or near-ocean (0.34-0.38 and 0.42-0.48). The environment least depleted in Al is subaerial (0.54-0.62). Na and K show a greater depletion in the subaerial environment (Na, 0.06-0.07, and K, 0.31-0.36) and, relatively, much less depletion in the near-ocean (Na, 0.47-0.54, and K, 0.70-0.80) and submarine environments (Na, 0.22-0.64, and K, 0.24-0.55). Mn is completely depleted in the submarine or partially submarine samples (0.0). In the near-ocean environment there is a much greater depletion in Mn (0.16-0.18) relative to the subaerial environment (0.72-0.83). There is no distinction based on the Mg-content between the palagonites of the subaerial and submarine environments. There is a significant accumulation of Mg in the partially submarine environment (1.45-1.66). There is no distinction that can be made between the subaerial and subaqueous environments based on the Ca content of the palagonite. P is retained in the subaerial environment (0.38-0.44) relative to the greater depletion of P in the near-ocean (0.22-0.24) and submarine environments (0.30-0.35 and 0.19-0.21).

SEM analyses (Hitachi S-450 with Tracor Northern 4000 EDS) were completed on a series of samples collected at regular intervals (5 m) in a 25m-thick section of a cliff in the HR unit, a freshwater alteration zone, 65 m from the ocean. Zeolites, identified by EDS and morphology, consistently overlie clays. The top of the section contained abundant phillipsite (Ca rich) and minor analcime, and the zeolites comprised up to 2 vol.% of the sample. At 5, 10, and 15m intervals down the section, increasing amounts of analcime occurred, and the total zeolite content increased to 3-4 vol.%. At the bottom of the section (20 and 25 m), an ubiquitous zeolite, tentatively identified as erionite (based on its distinctive morphology), occurred as overgrowths on the analcime, and the total zeolite content increased to 5-10 vol.% (Fig. 3). These results contrast with the work of Hay and Iijima,<sup>6</sup> in which they observed chabazite  $[\text{Ca}(\text{Al}_2\text{Si}_4\text{O}_{12}) \cdot 6\text{H}_2\text{O}]$  but not erionite.

### *Conclusions*

The four samples from subaqueous, near-ocean, and subaerial environments were distinctly different in palagonite composition (Fig. 2). These results verify the existence of two different alteration environments at Hanauma Bay--a freshwater and a seawater environment. In general, the freshwater environment is characterized by less depletion of Si, Al, Mn, and P and greater depletion of Na and K as compared to the seawater environment. The only previous study of the Hanauma Bay palagonite was limited to visual inspection of the HR unit, and a freshwater alteration environment was suggested.<sup>2</sup> EMPA of the HR unit palagonite supports the freshwater-alteration hypothesis because Si is less depleted and there are more severe depletions in Na and K than from seawater alteration. Seawater alteration usually results in only minor loss or increase of K.<sup>7</sup>

## References

1. W. Lutze et al., "Alteration of basalt glasses: Implications for modelling the long-term stability of nuclear waste glasses," *Nature* 314: 252-255, 1985.
2. R. L. Hay and A. Iijima, "Petrology of palagonite tuff of Koko Crater, Oahu, Hawaii," *Contrib. Mineral. Petrol.* 17: 141-154, 1968.
3. J. W. Gramlich et al., "Potassium-argon dating of holocene basalts of the Honolulu volcanic series, *Geol. Soc. Amer. Bull.* 82: 1399-1404, 1971.
4. M. A. Lanphere and G. B. Dalrymple, "Age and Sr isotope composition of the Honolulu volcanic series, Oahu, Hawaii," *Amer. J. Sci.* 280A: 736-751, 1980.
5. W. F. Chambers, *SANDIA TASK8: A Subroutined Electron Microprobe Automation System*, Sandia Report SAND85-2037, Albuquerque, N.M.: Sandia National Laboratory, 1985.
6. R. L. Hay and A. Iijima, "Nature and origin of palagonite tuffs of the Honolulu Group on Oahu, Hawaii," *Geol. Soc. Amer. Mem.* 116: 331-376, 1968.
7. S. P. Jakobsson, "Environmental factors controlling the palagonitization of the Surtsey tephra, Iceland," *Bull. Geol. Soc. Denmark, Sp. Issue*, 27: 141-154, 1978.

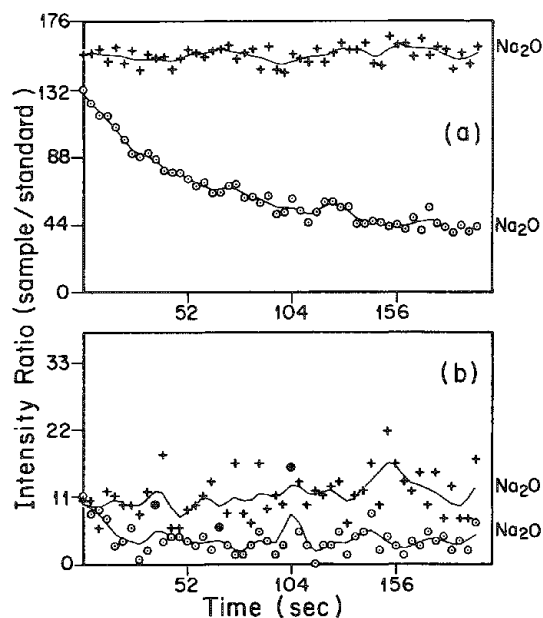


FIG. 1.--Change in Na concentration vs time in (a) glass sample, 30µm beam (upper curve) and 1µm beam (lower curve); (b) palagonite sample, 10µm beam (upper curve) and 1µm beam (lower curve).

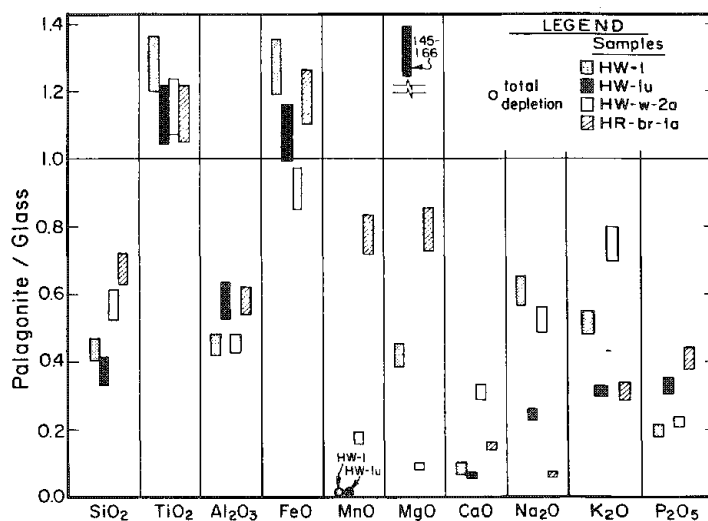


FIG. 2.--Ratio of elemental concentration in palagonite and glass. (See text for details of calculations.)

TABLE 1.--Chemical composition of basaltic glass and associate palagonite (wt%) determined by electron microprobe analysis.

OXIDE	HW-1u		HW-1		HW-w-2a		HR-br-1a	
	GLASS	PALAGONITE	GLASS	PALAGONITE	GLASS	PALAGONITE	GLASS	PALAGONITE
SiO <sub>2</sub>	46.05	27.93	46.67	24.31	47.37	36.88	46.87	43.37
TiO <sub>2</sub>	2.49	4.43	2.19	3.42	2.30	3.66	2.54	3.95
Al <sub>2</sub> O <sub>3</sub>	14.75	9.14	15.16	12.21	14.98	7.41	14.35	11.45
FeO	11.61	20.52	12.00	17.58	11.63	14.56	11.25	18.29
MnO	0.13	*	0.09	*	0.21	0.05	0.16	0.17
MgO	6.21	3.61	4.97	10.61	4.91	0.65	6.36	6.90
CaO	12.47	1.37	11.59	1.05	11.37	4.82	12.05	2.49
Na <sub>2</sub> O	3.93	3.30	4.15	1.38	4.06	2.82	3.87	0.37
K <sub>2</sub> O	1.15	0.82	1.05	0.45	1.19	1.23	1.00	0.46
P <sub>2</sub> O <sub>5</sub>	0.59	0.16	0.62	0.28	0.51	0.16	0.60	0.34
TOTAL	99.38	71.27	98.49	71.29	98.53	72.31	99.07	87.90

\*below limit of detection

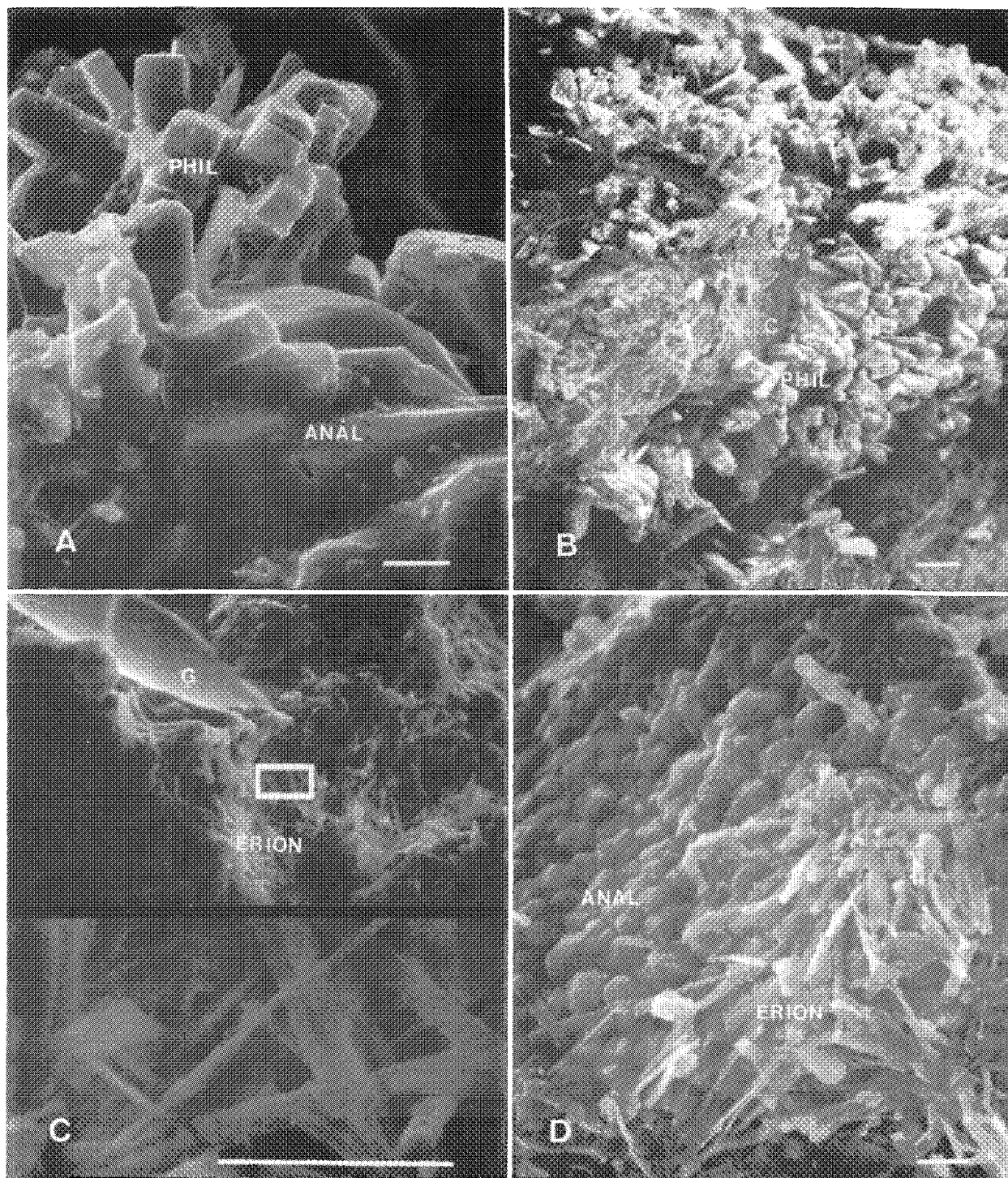


FIG. 3.--Scanning electron micrographs of zeolites in HR unit arranged in order of increasing depth: A, 0m interval, radiating cluster of columnar phillipsite (PHIL) as overgrowths on analcime (ANAL), bar = 5  $\mu$ m; B, 5m interval, phillipsite (PHIL) clusters on clay (C), bar = 50  $\mu$ m; C, 25m interval, interwoven fibrous rods of erionite (ERION) next to unaltered glass surface (G), bar = 5  $\mu$ m; D, 25m interval, fibrous, elongate rods of erionite (ERION) on analcime (ANAL), bar = 5  $\mu$ m.

## EFFECTS OF IRRADIATION AND DRY HEATING ON BENTONITE: A TRANSMISSION ELECTRON MICROSCOPY AND X-RAY DIFFRACTION STUDY

C. C. Allen and S. A. Rawson

The Basalt Waste Isolation Project (BWIP) is investigating the Columbia River basalts in southeastern Washington for suitability as a medium for the permanent disposal of high-level nuclear waste. Bentonite, the subject of the present study, has been proposed as an important component of the packing material surrounding individual waste containers.<sup>1</sup>

This work addresses the effects of gamma radiation and high temperature on the swelling ability of bentonite. Bentonite is a potentially useful packing material, due in part to its ability to swell when wet. A layer of bentonite surrounding each waste container is predicted to retard inward movement of groundwater, and similarly to retard outward movement of radionuclides should the container become breached.

No previous work has been reported on the combined effects of irradiation and dry heating on bentonite. Krumhansl exposed clay derived from bentonite to  $3 \times 10^{10}$  rad of  $^{60}\text{Co}$  gamma radiation at ambient temperature, and reported that no crystallographic changes occurred.<sup>2</sup> Allen et al. showed that heating of bentonite to temperatures as high as 370 C for up to a year did not irreversibly damage the clay's structure nor its ability to swell.<sup>1</sup> Interaction with liquid water in a hydrothermal environment has been shown to cause changes in the crystal structure and chemical composition of bentonite's clay component.<sup>1</sup> The material's swelling ability can be adversely affected by interaction with steam.<sup>3</sup>

### *Experimental*

The starting bentonite, designated B079, was a sample of BWIP reference material, characterized by Palmer et al.<sup>4</sup> It was composed predominantly of sodium montmorillonite clay (85 wt.%), along with quartz, feldspar, cristobalite, illite, calcite, and gypsum. The bentonite was used "as received" from the supplier, sieved to -400 mesh.

The bentonite was sealed in a test cell at atmospheric pressure and ambient relative humidity, heated to 300 C, and exposed to a  $^{60}\text{Co}$  gamma ray flux of  $5.83 \times 10^6$  R/hr for two weeks. The estimated total absorbed dose was  $3.5 \times 10^9$  rad. Irradiation and heating were performed in a gamma pit operated by the Westinghouse Hanford Company under the direction of the Pacific Northwest Laboratory. Following this treatment the sample, designated S0185, was placed in a plastic bottle and stored in a vacuum desiccator.

### *Sample Preparation*

Samples for transmission electron microscopy (TEM) were prepared by ultrasonically suspending bentonite in ethanol for approximately 5 min. The suspension was then allowed to settle for one minute, in order to isolate the clay-size fraction. A drop of the suspension was placed on a copper TEM grid, to which a carbon support film had been applied. The grid was allowed to air dry in a horizontal orientation, and a conductive coating of gold and palladium was applied. Clay particles from samples prepared in this manner were preferentially oriented with their C-axes normal to the grid. The orientation yielded turbostratic electron diffraction patterns, composed of rings corresponding to only the  $\langle h k 0 \rangle$  d-spacings.

Clay samples for TEM were also prepared such that the C-axes of individual particles were parallel to the grid. This orientation permitted imaging of individual basal layers by the lattice fringe technique. Several drops of an ethanol suspension of clay were allowed

---

The authors are with the Basalt Waste Isolation Project, Rockwell Hanford Operations, Richland, WA 99352. They acknowledge the aid of D. T. Reed for initiating the irradiation and heating experiment, providing the samples, and performing peer review. Capable technical support was provided by R. R. Adee, S. K. Showalter and J. R. Smith.

to dry on a solid epoxy substrate. Additional liquid epoxy was then poured over the clay and allowed to harden. The epoxy "sandwich" was trimmed and then sectioned using a diamond-bladed ultramicrotome. The sections, 800-1000 Å thick, were cut normal to the epoxy-clay interface. Individual sections, floating on water, were caught on TEM grids, which were subsequently carbon coated.

The crystal structure of the bentonite was investigated by x-ray diffraction (XRD) techniques. Approximately 0.5 g of the -400 mesh material was backloaded into an aluminum holder in order to yield a randomly oriented packed powder mount. Oriented mounts of reacted and unreacted bentonite were prepared by precipitating the material onto a 0.45 µm filter and pressure transferring the filtrate onto a standard glass slide after the method of Drever.<sup>5</sup>

### *TEM Analysis*

The TEM analyses were run on a JEOL JEM 200-CX. Images of six individual clay particles from the irradiated and heated bentonite showed them to be unchanged in large-scale morphology from particles of the starting clay. Electron diffractograms yielded crystal d-spacing measurements for the starting clay and the treated material which were identical within the ±2% precision of the technique. Figure 1 is a lattice fringe image of the <001> basal planes in montmorillonite from the irradiated and heated bentonite, showing its layer structure. This is very similar to images of the starting material, with the layers in both samples being regular, continuous, and undistorted. Irradiation and heating apparently did not disrupt the clay structure at the scale of individual silicate layers.

The major element chemical compositions for clay particles from both the starting bentonite and the treated material were assessed by a Tracor-Northern System 3 energy-dispersive spectrometer (EDS). The spectra were indistinguishable, which shows that no measurable migration of elements occurred as a result of irradiation and heating.

### *XRD Analysis*

Samples of irradiated and heated bentonite, as well as the unreacted starting material, were analyzed by means of a Rigaku D/MAX-rA Rotaflex system. X-ray diffraction peaks for unreacted bentonite included d-spacings diagnostic for sodium montmorillonite, quartz, feldspar, and illite (Fig. 2a). The <001> d-spacing for sodium montmorillonite was approximately 11.1 Å, which indicates a limited degree of dehydration in the starting material. General montmorillonite reflections were observed at 4.50, 2.57 and 1.50 Å.

The major effect of irradiation and heating on the XRD pattern of randomly oriented bentonite was a decrease in the clay's <001> basal spacing to 9.65 Å (Fig. 2a). Peaks for the second- and fifth-order reflections were identified at approximately 4.8 and 1.93 Å, respectively. This decrease in basal spacing was attributed to the loss of loosely bound interlayer water. The <hk0> peaks showed no shifts, in agreement with the TEM electron diffraction results, which suggests that no other distortion of the crystal lattice occurred. This is evidence against the loss of significant amounts of structural water from the treated clay.

The Drever technique<sup>5</sup> for preparing oriented mounts involved the suspension of clay particles in de-ionized water for approximately 90 min. This treatment was sufficient to introduce interlayer water to both the unreacted and the irradiated and heated montmorillonite. The basal spacing of the oriented mounts for both samples was 12.2 Å (Fig. 2b). It can be concluded that structural contraction indicated by the diffractograms of randomly oriented material was caused primarily by the loss of interlayer water. Furthermore, upon rehydration for 90 min, this water loss proved entirely reversible.

### *Conclusions*

The analyses reported here strongly indicate that the effects of irradiation and dry heating to which this bentonite sample was subjected were minor. Interlayer water was driven out of the clay, but neither structural water loss nor collapse were detectable. Very similar effects were seen in samples that had only been heated. The loss of interlayer water proved reversible, and the swelling ability of the bentonite was apparently not compromised.

The present experiment was conservative in terms of conditions expected in a dry

basalt repository. The absorbed gamma dose of  $3.5 \times 10^9$  rad was more than an order of magnitude greater than that expected after the entire 1000-year containment period.<sup>6</sup> The 300 C temperature was also considerably higher than that expected at any time during repository operation.<sup>1</sup> Further tests are being designed, which will assess irradiation effects in hydrothermal and steam environments.

## References

1. C. C. Allen et al., "Experimental studies of packing material stability," in G. L. McVay, Ed., *Materials Research Society Symposium Proceedings*, vol. 26, North-Holland, 1984, 105-112.
2. J. L. Krumhansl, *Observations Regarding the Stability of Bentonite Backfill in a High-level Waste (HLW) Repository in Rock Salt*, Report SAND83-1293, Albuquerque, NM: Sandia National Laboratories, 1985.
3. R. A. Couture, "Rapid increases in permeability and porosity of bentonite-sand mixtures due to alteration by water vapor," in C. M. Jantzen, J. A. Stone, and R. C. Ewing, Eds., *Materials Research Society Symposium Proceedings*, vol. 44, Materials Research Society, 1985, 515-522.
4. R. A. Palmer et al., *Characterization of Reference Materials for the Barrier Materials Test Program*, RHO-BW-ST-27 P, Rev. O, Richland, Wash.: Rockwell Hanford Operations, 1982.
5. J. I. Drever, "The preparation of oriented clay mineral specimens for x-ray diffraction analysis by a filter-membrane peel technique," *American Mineralogist* 1973, 553-554.
6. D. T. Reed, *Effect of Alpha and Gamma Radiation on the Near-field Chemistry and Geochemistry of High-level Waste Packages*, RHO-BW-SA-406 P, Richland, Wash.: Rockwell Hanford Operations, 1985.

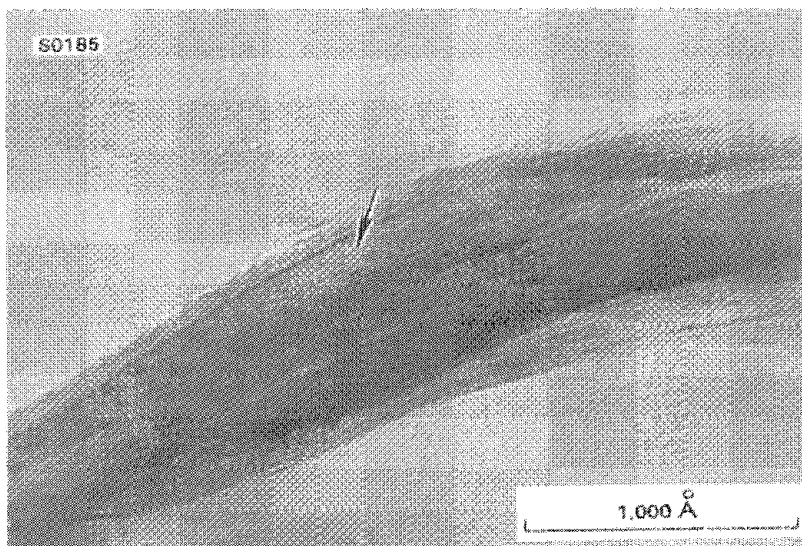


FIG. 1.--Lattice fringe image of montmorillonite from irradiated and heated bentonite (S0185).|| Arrow indicates <001> basal planes.

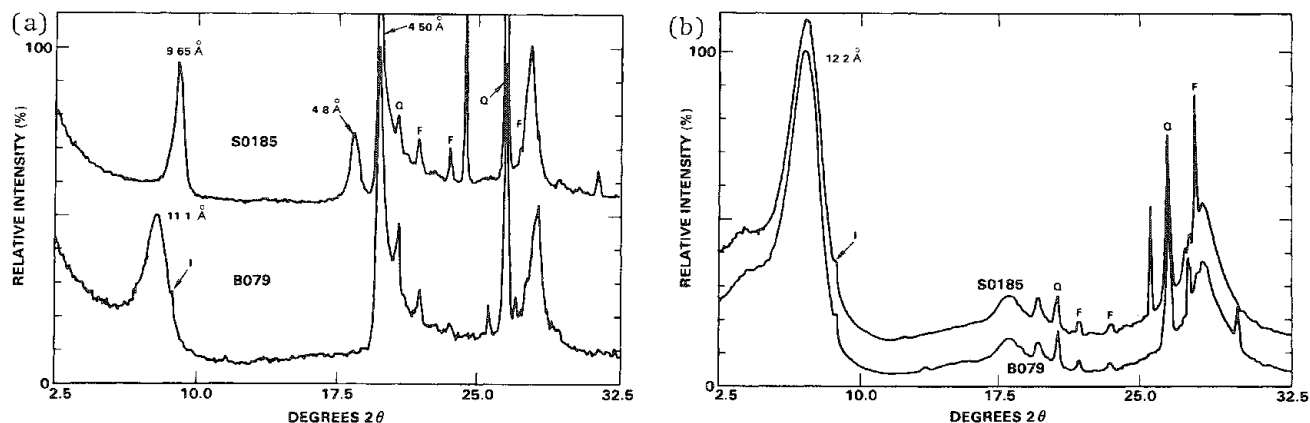


FIG. 2.--X-ray diffractograms of samples of unreacted bentonite (B079) compared to irradiated and heated bentonite (S0185). Montmorillonite peaks labeled with d-spacings: Q = quartz, F = feldspar, I = illite. Patterns vertically offset for clarity. (a) Randomly oriented samples, (b) oriented samples.



## TRACE ELEMENT ANALYSES OF OLIVINE IN LUNAR HIGHLAND ROCKS: IMPLICATIONS FOR THE ORIGIN OF THE LUNAR CRUST

M. G. Bersch, G. J. Taylor, and K. Keil

Samples of the oldest lunar crust comprise two distinct groups: ferroan anorthosites<sup>1</sup> have very calcic plagioclase (An<sub>94-98</sub>) and relatively iron-rich mafic minerals (*mg* 50-70). [The magnesium number, or *mg*, is an abbreviation for the molar ratio  $[\text{MgO}/(\text{MgO} + \text{FeO})] \times 100$ . The Mg-rich rocks range from those with calcic plagioclase (An<sub>95</sub>) and high *mg* (~85) mafic minerals to those with less calcic plagioclase (An<sub>86</sub>) and lower *mg* (~65).<sup>2</sup>

Most lunar petrologists think that the ferroan anorthosites formed by flotation in a magma ocean which surrounded the primitive moon, and the Mg-rich rocks formed from magmas which intruded the anorthosite crust.<sup>3</sup> However, this proposition is not universally accepted.<sup>4,5</sup> Even if the story is basically correct, many questions remain: Was the magma ocean a total or partial melt of bulk lunar material? Do the ferroan anorthosites represent one magma or one magma type? What processes operated in the magma ocean? Could the Mg-rich rocks have formed from the magma ocean? How many magmas are represented in the collection of Mg-rich rocks? What were the source rocks for these magmas?

To address these and other questions, we are measuring concentrations of minor elements in olivines and pyroxenes in pristine highland rocks. Following an initial investigation of this type,<sup>6</sup> we believe such a study has merit because it may avoid the sampling problems inherent in whole-rock analyses of cumulate rocks. Most whole rock analyses of pristine highland rocks are done on samples of about 100 mg and uneven sampling of minor minerals can cause large variations in minor and trace element contents.<sup>7</sup> By analyzing individual grains we hope to avoid problems associated with sample size.

### *Analytical Procedures*

Analyses of major and minor elements were made on a JEOL 733 Superprobe with an automated spectrometer system using a defocused beam 5, 10, or 20  $\mu\text{m}$  in diameter, at 15 keV accelerating voltage and 0.2  $\mu\text{A}$  beam current. The automation system used with our JEOL 733 is Sandia TASK 8.<sup>8</sup>

Peak positions were determined automatically by step scanning across the peak position. Count times are up to 30 s per step. Initial peak positions and background positions were determined by wavelength-dispersive scans across the peak and visual determination of the amount of offset. Analysis times vary with concentration. However, count times are up to 1200 s for both peak and background, i.e., 2400 s total. A typical olivine analysis takes 1 h; a typical pyroxene analysis takes 30 min. We tried to obtain at least six acceptable analyses in each sample, though some anorthosites are so poor in mafic silicates that we had to settle for one or two grains.

These conditions resulted in low detection limits (Table 1) and high precision (Table 2 and 3). As examples of the precision, Table 2 shows averages of analyses of one thin section, 67435,14, on two different days. Table 3 shows analyses of two sections of the same rock, 76335,27 and 76335,29.

### *Discussion*

*Mg-rich Rocks.* In the samples studied to date (mostly troctolites), TiO<sub>2</sub> varies by over a factor of six with little change in *mg* (Fig. 1). Similarly, Al<sub>2</sub>O<sub>3</sub> varies by a factor of five (Fig. 2). (Low-Ca pyroxenes show the same features as do olivines.) Although slight negative trends are apparent in the diagrams, consistent with fractional crystallization, the ranges are too large compared to the small range in *mg* to be accounted for by fractional crystallization of a single magma type. This finding confirms previous

---

The authors are with the Department of Geology and Institute of Meteorites, University of New Mexico, Albuquerque, NM 87131. This work was supported in part by NASA grant NAG 9-30 to K. Keil.



TABLE 1.--Typical detection limits.\*

Ca	-	13 ppm
Al	-	18 ppm
Ti	-	25 ppm
Cr	-	13 ppm
Mn	-	14 ppm
Ni	-	14 ppm
P	-	14 ppm
Na	-	13 ppm

TABLE 2.--Average of 10 olivine analyses of same section of rock 67435,14 done on different days (ppm).

MnO	882	883
Cr <sub>2</sub> O <sub>3</sub>	549	544
Al <sub>2</sub> O <sub>3</sub>	516	473
CaO	945	950
TiO <sub>2</sub>	234	239
P <sub>2</sub> O <sub>5</sub>	160	159
Na <sub>2</sub> O	390	372
	*	*

TABLE 3.--Average olivine analyses in two different sections of same rock (76335,27; 76335,29; ppm).

MnO	1479	1486
Cr <sub>2</sub> O <sub>3</sub>	226	245
Al <sub>2</sub> O <sub>3</sub>	154	191
CaO	380	310
TiO <sub>2</sub>	278	312
P <sub>2</sub> O <sub>5</sub>	182	195
Na <sub>2</sub> O	30	32
	*	*
Grains	7	10

\*Calculated by Sandia task 8 (see ref. 8).

\*Below detection limit (13 ppm).

\*Below detection limits (13 ppm).

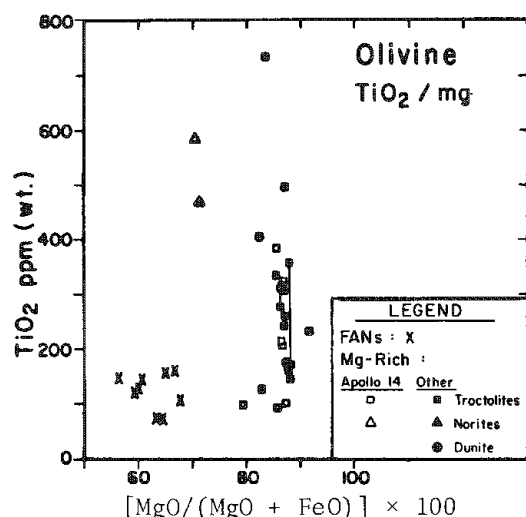


FIG. 1.--TiO<sub>2</sub> content vs molar ratio 100 x MgO/(MgO + FeO) for olivines in rocks from lunar highlands. Note clear separation of ferroan anorthosites (FAN) from Mg-suite rocks (others) and large range in TiO<sub>2</sub> among troctolites.

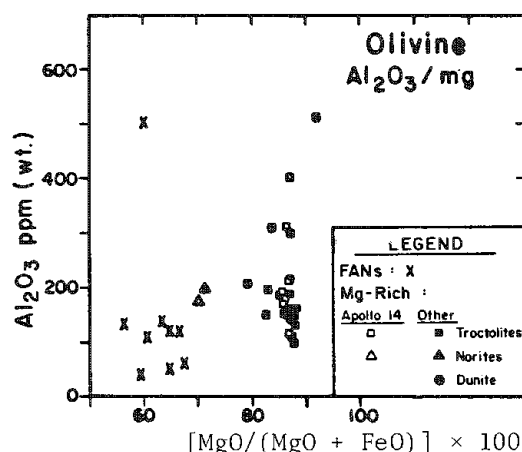


FIG. 2.--Al<sub>2</sub>O<sub>3</sub> content vs molar ratio 100 x MgO/(MgO + FeO) for olivines in rocks from lunar highlands. Note large range in Al<sub>2</sub>O<sub>3</sub> among troctolites.

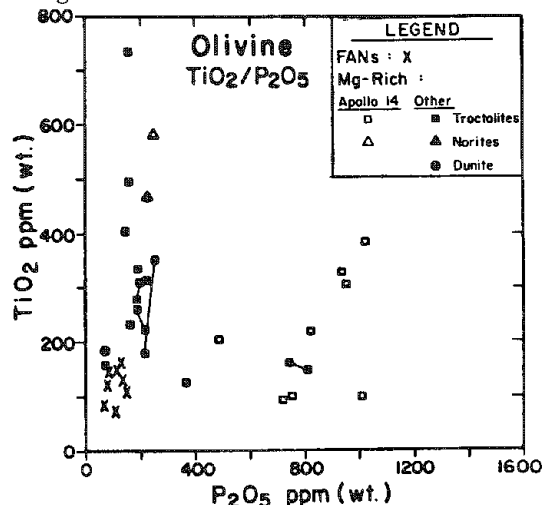


FIG. 3.--TiO<sub>2</sub> vs P<sub>2</sub>O<sub>5</sub> for olivines in rocks from lunar highlands. Note systematic enrichment of P<sub>2</sub>O<sub>5</sub> in Apollo 14 samples, consistent with bulk rock increases in P<sub>2</sub>O<sub>5</sub> and large-ion lithophile elements in Apollo 14 region.

suggestions that numerous separate parent magmas are represented by our collection of Mg-suite rocks. These magmas might have differed in Ti content by a factor of six, thus explaining the six-fold variation of Ti concentrations in olivine, but it is unlikely that Al could have varied by that much in magmas that consistently produced rocks composed of roughly equal amounts of olivine and plagioclase. Perhaps variations in intensive variables such as oxygen fugacity caused changes in the partitioning of Ti and Al between melt and olivine.

The east-west dichotomy among pristine rocks<sup>9</sup> is shown clearly in Fig. 3. P<sub>2</sub>O<sub>5</sub> is significantly greater in olivine in Apollo 14 troctolites than in the others. This result is consistent with the overall greater contents of incompatible elements in pristine samples from Apollo 12 and 14, which is probably the result of assimilation of greater amounts of KREEP.<sup>9,10</sup> Aluminous mare basalts from Apollo 14 also show the effects of assimilation.<sup>11</sup>

*Ferroan Anorthosites.* Olivines in this suite have lower concentrations of Ti, Al, and P than have most of the Mg-suite samples (Figs. 1-3). This finding is consistent with the bulk concentrations of these elements and of incompatible elements in general,<sup>3,7</sup> However, the data do not form clear trends, which suggests that the processes operating in the magma ocean (assuming there was one) were more complicated than simple fractional crystallization. Complex magma mixing processes may have operated in an initially totally molten system,<sup>7,12</sup> or in a partially molten one.<sup>13-15</sup>

## References

1. E. Dowty, M. Prinz, and K. Keil, "Ferroan anorthosite: A widespread and distinctive lunar rock type," *Earth Planet. Sci. Lett.* 24: 15, 1974.
2. J. L. Warner, C. H. Simonds, and W. C. Phinney, "Genetic distinction between anorthosites and Mg-rich plutonic rocks: New data from 76225," *Lunar Science VII*: 915, 1976.
3. P. H. Warren, "The magma ocean concept and lunar evolution," *Ann. Rev. Earth Planet. Sci.* 13: 201, 1985.
4. D. Walker, "Lunar and terrestrial crust formation," *J. Geophys. Res.* 88: B17, 1983.
5. J. Longhi and L. Ashwal, "Two-stage models for lunar and terrestrial anorthosites: Petrogenesis without a magma ocean," *J. Geophys. Res.* 90: C571, 1985.
6. J. V. Smith, E. C. Hansen, and I. M. Steele, "Lunar highland rocks: Element partitioning among minerals II: Electron microprobe analyses of Al, P, Ca, Ti, Cr, Mn and Fe in olivine," *Proc. Lunar Planet. Sci. Conf.* 11: 555, 1980.
7. P. W. Warren and G. W. Kallemeyn, "Pristine rocks (8th foray): 'Plagiophile' element ratios, crustal genesis, and the bulk composition of the Moon," *J. Geophys. Res.* 89: C16, 1984.
8. W. F. Chambers, *Sandia Task 8: A Sub-routine Electron Microprobe Automation System*, SAND Report, 85-2037.
9. P. H. Warren and J. T. Wasson, "Further foraging for pristine nonmare rocks: Correlations between geochemistry and longitude," *Proc. Lunar Planet. Sci. Conf.* 11: 431, 1980.
10. P. H. Warren, G. J. Taylor, K. Keil, C. Marshall, and J. T. Wasson, "Foraging westward for pristine nonmare rocks: Complications for petrogenetic models," *Proc. Lunar Planet. Sci.* 12B: 21, 1981.
11. T. Dickinson, G. J. Taylor, K. Keil, R. A. Schmitt, S. S. Hughes, and M. R. Smith, "Apollo 14 aluminous mare basalts and their possible relationship to KREEP," *J. Geophys. Res.* 90: C365, 1985.
12. J. Longhi and A. E. Boudreau, "Complex igneous processes and the formation of the primitive lunar crustal rocks," *Proc. Lunar Planet. Sci. Conf.* 10: 2085, 1979.
13. J. Longhi, "A model of early lunar differentiation," *Proc. Lunar Planet. Sci. Conf.* 11: 289, 1980.
14. J. Longhi, "Preliminary modeling of high pressure partial melting: Implications for early lunar differentiation," *Proc. Lunar Planet. Sci.* 12B: 1001, 1981.
15. D. N. Shirley, "A partially molten magma ocean model," *J. Geophys. Res.* 88: A519, 1983.

## TEM STUDY OF THE MICROSTRUCTURE OF METAMICT MINERALS

T. J. Headley and R. C. Ewing

Metamict minerals are a special class of "amorphous" materials first described by Broegger in 1893.<sup>1</sup> Their physical and chemical properties have been summarized by Ewing and Haaker.<sup>2</sup> Initially crystalline, they have sustained a loss of crystallinity (usually defined on the basis of x-ray diffraction) due to alpha-recoil events associated with the decay of constituent U and Th (typically 1-15 wt.% as oxides). The alpha decay event results in a high-energy alpha particle ( $\sim 5.5$  MeV) and a recoil nucleus ( $\sim 0.1$  MeV). Most of the energy of the recoil nucleus is lost through collisions producing several thousand atomic displacements (range  $\sim 10$  nm). This recoil-displacement damage is the primary mechanism by which the physical and structural properties of minerals are converted to the metamict state. For most crystalline materials, saturation of the radiation damage is reached in the range of  $10^{25}$  to  $10^{26}$  alpha-recoil events per cubic meter. In the past 10 years, interest in the structure of metamict minerals gained impetus from the nuclear waste form community, where concerns over radiation damage effects in proposed crystalline waste forms led to investigations of metamict minerals as natural analogs. There was renewed interest in whether the metamict state is truly amorphous or microcrystalline on a scale beyond the detection limit of x-ray diffraction techniques. Only limited use has been made of the higher resolution capability of the TEM to study a small number of metamict mineral types. In this paper we briefly outline some of our observations made by transmission electron microscopy on the structure of a wide range of metamict minerals.

### *Experimental*

The minerals selected for examination by TEM were chosen to study (1) the fully metamict structure ("x-ray diffraction amorphous") and (2) the transition from the crystalline to the metamict state (zircon and zirconolite). A wide range of composition and pre-metamict structure types was examined, including silicates, complex Nb-Ta-Ti oxides, and zirconolite. General information on the compositional variations and structure types has been summarized by Ewing and Chakoumakos.<sup>3</sup> Localities, sample numbers, and sources are given in the figure captions. The zircons examined (for which there is a calculated alpha-recoil dose) are described in Refs. 4 and 5. A complete description of the zirconolite samples is given in Ref. 6.

Specimens for electron microscopy were prepared by grinding under butanol and collecting the thin flakes on holey carbon substrates. The specimens were examined at 200 or 100 kV in a JEM-200CX or Philips EM400 electron microscope, respectively. Conventional bright-field imaging, selected-area electron diffraction (SAED), centered dark-field imaging, and high-resolution lattice imaging were used to characterize the metamict structures.

### *Results*

TEM revealed a minor (less than 10%) crystalline fraction in all of the "x-ray diffraction amorphous" specimens examined (due to alteration, crystallization, or impurities).

---

Author T. J. Headley is at Sandia National Laboratories, Albuquerque, NM 87185; author R. C. Ewing is at the University of New Mexico, Geology Department, Albuquerque, NM 87131. This work was supported by the U.S. Department of Energy under contract DE-AC04-76DP00789 (SNLA) and Grant DE-FG04-84ER45099 (UNM). Specimens used in this study were provided by J. S. White of the National Museum of Natural History in Washington, D.C.; H. J. Schubnel of the Muséum National d'Histoire Naturelle et Minéralogie in Paris; Robert Middleton of the Philadelphia Academy of Sciences; William Sinclair of the Australian National University; Virginia Oversby of Lawrence Livermore National Laboratory; Robert Zartmann of the U.S. Geological Survey; and Kathleen Affholter of Virginia Polytechnic Institute and State University.

Nevertheless, the predominant portion of each specimen displayed electron diffraction patterns containing an intense inner diffraction halo and one or two faint outer halos, characteristic of amorphous materials. Despite the wide range of compositions and pre-metamict structure types, the final electron diffraction patterns are remarkably similar (Fig. 1), with an "equivalent d-spacing" for the most intense inner halo of between 0.302 and 0.352 nm. The electron diffraction pattern of a borosilicate glass is shown for comparison. Centered dark-field imaging was used to investigate whether these patterns were produced by diffraction from small, randomly oriented microcrystallites instead of amorphous structures. The images, obtained with the objective aperture positioned on an arc of the first broad diffraction ring, contained bright coherently scattering spots 0.6-0.8 nm in size (Fig. 2). This observation eliminates the possibility that the metamict structures consist of microcrystallites of  $\sim 2.5$  nm or larger, because such crystallites would have been readily resolved as bright spots. The interpretation of bright spots in the  $< 1$  nm size range is not straightforward; however, they are consistent with either microcrystalline or random network models of the amorphous state.<sup>7</sup> High-resolution lattice imaging did not reveal any regions of fringes characteristic of small crystallites. These metamict structures are therefore interpreted to be amorphous to  $\leq 1$  nm scale.

The transition from the highly crystalline to the completely metamict state with increasing alpha-event dose was studied in zircon ( $\text{ZrSiO}_4$ ) and zirconolite (nominally  $\text{CaZrTi}_2\text{O}_7$ ). The total alpha-event doses of the samples were either calculated based on the ages and U and Th concentrations or estimated based on density determinations (see Ref. 8, Fig. 1), x-ray powder diffraction analysis, and precession photographs. The sequence of transition microstructures is similar for zircon and zirconolite and proceeds as follows: (a) Isolated defects, interpreted as individual alpha-recoil tracks with interstitials, are present in the crystalline matrix; SAED patterns exhibit sharp diffraction maxima. (b) Alpha-recoil damage tracks overlap and small regions of amorphous material are present; a faint diffraction halo appears in the SAED pattern. (c) Amorphous regions increase in size leaving remnant crystallites ( $\leq \sim 20$  nm size) in an amorphous matrix; a strong diffraction halo occurs along with somewhat diffuse diffraction maxima. (d) Complete metamictization, no remnant crystalline material; only broad diffraction halos are present in the SAED pattern. This sequence of microstructures is shown for zircon as a function of increasing alpha-event dose in Fig. 3. There is one important difference between the transition structures of zircon and zirconolite. In zircon ( $\text{ZrSiO}_4$ ), the remnant crystallinity retains tetragonal symmetry until complete loss of atomic periodicity. In zirconolite ( $\text{CaZrTi}_2\text{O}_7$ ), the remnant crystallites transform at high alpha-event doses from a low-symmetry, monoclinic structure to a higher-symmetry face-centered-cubic fluorite structure.<sup>6,9</sup> This transition is illustrated in the SAED patterns of Fig. 4.

An unusual feature of the microstructure of the metamict Nb-Ta-Ti oxides and zirconolite is the presence of near-spherical microvoids 3 nm to  $\sim 2$   $\mu\text{m}$  in size (Fig. 5). Generally they are irregularly distributed, present in some flakes but absent in others. The microvoids in Fig. 5(a) are typical, but they also may be very abundant (5b), distorted (5c) and, very rarely, assume the shape of negative crystals (5e) or are finely disseminated through the material (5f). Porosity of this type was not observed in the silicates, but there was an irregular-shaped porosity seen in one sample of allanite (5d). Because of their remarkably spherical shape, it is suggested that these microvoids are caused by nucleation and growth of helium bubbles resulting from internal alpha-particle decay after the mineral has become metamict. Helium has been measured during the release of gases from metamict zirconolite from Sri Lanka.

### Conclusions

The transformation from the crystalline to the metamict state is one in which a true structural change occurs in the material at the atomic level as a result of alpha-recoil events. Prior to reaching saturation doses, the material consists of a mixture of crystalline and amorphous regions; however, the final saturation damage effect is one in which the electron diffraction patterns contain broad, diffuse halos that are consistent with scattering from material with a nonperiodic atomic arrangement. To the limits of detecting small crystallites in the TEM (1-1.5 nm), there was no evidence for long-range periodic structure or the formation of domain structures. Void formation accompanies the process of metamictization for complex Nb-Ta-Ti oxides and zirconolite.

## References

1. W. C. Broegger, *Amorf. Salmonses Store Illustrerede Konversationlexicon* 1: 728, 1893.
2. R. C. Ewing and R. F. Haaker, *Nucl. and Chem. Waste Management* 1: 51, 1980.
3. R. C. Ewing and B. C. Chakoumakos, in P. Cerny, Ed., *Mineralogical Association of Canada, Short Course Handbook 8*, 1982, 239-265.
4. R. C. Ewing, R. F. Haaker, and W. Lutze, in W. Lutze, Ed., *Scientific Basis for Nuclear Waste Management: V*, North-Holland, 1982, 389-397.
5. T. J. Headley, G. W. Arnold, and C. J. M. Northrup, *ibid.*, 379-388.
6. R. C. Ewing and T. J. Headley, *J. Nucl. Materials* 119: 102, 1983.
7. M. L. Rudee, in H.-R. Wenk, Ed., *Electron Microscopy in Mineralogy*, Springer-Verlag, 1976, 476-487.
8. H. D. Holland and D. Gottfried, *Acta Crystall.* 8: 291, 1955.
9. W. Sinclair and A. E. Ringwood, *Geochem. J.* 15: 229, 1981.
10. T. J. Headley, R. C. Ewing, and R. F. Haaker, *Nature* 293: 449, 1981.

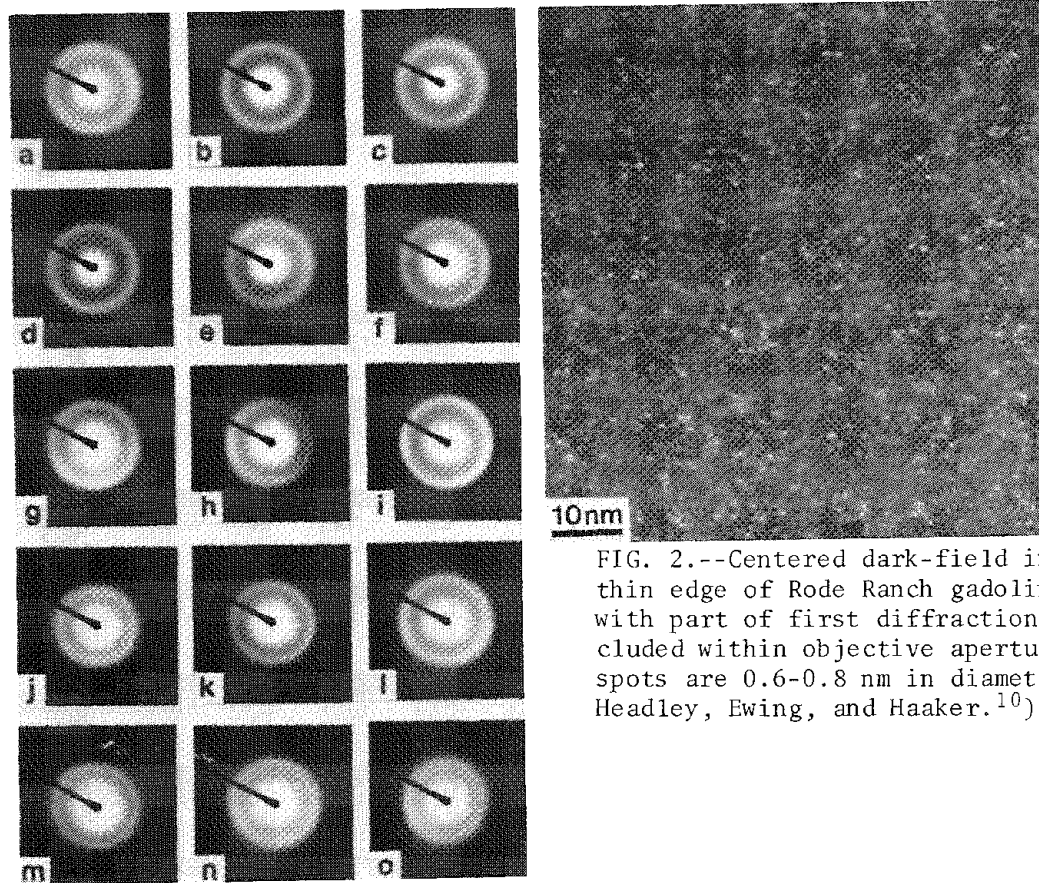


FIG. 2.--Centered dark-field image from thin edge of Rode Ranch gadolinite (#2) with part of first diffraction halo included within objective aperture. Bright spots are 0.6-0.8 nm in diameter. (From Headley, Ewing, and Haaker.<sup>10</sup>)

FIG. 1.--Selected area diffraction patterns of metamict: (a) fergusonite; (b) euxenite, Iveland, Norway, #R17; (c) ampingabeite, Ampangabe, Madagascar; (d) polycrase, Minas Gerais, Brazil, #R6; (e) priorite, Ahi-Trombe, Madagascar, #R11; (f) aeschynite, Morefjaer, Norway, #84647 USNM; (g) blomstrandine, Koabuland, Iveland, Norway, #R12; (h) samarskite, Spruce Pine, N.C., USA, #R10; (i) zirconolite, Sri Lanka, #83800, Harvard Museum; (j) zircon, Madagascar, #111.631, Muséum d'Histoire Naturelle et de Minéralogie, Paris; (k) thorite, Norway, #87367 USNM; (l) gadolinite, Sweden, #12984, Philadelphia Academy of Science; (m) yttrianite, Baringer Hill, Tex., USA, #19968, Philadelphia Academy of Science; (n) allanite, Arendal, Norway, #M14864, Field Museum of Natural History, Chicago; (o) borosilicate glass, Hahn-Meitner Institut, Berlin.

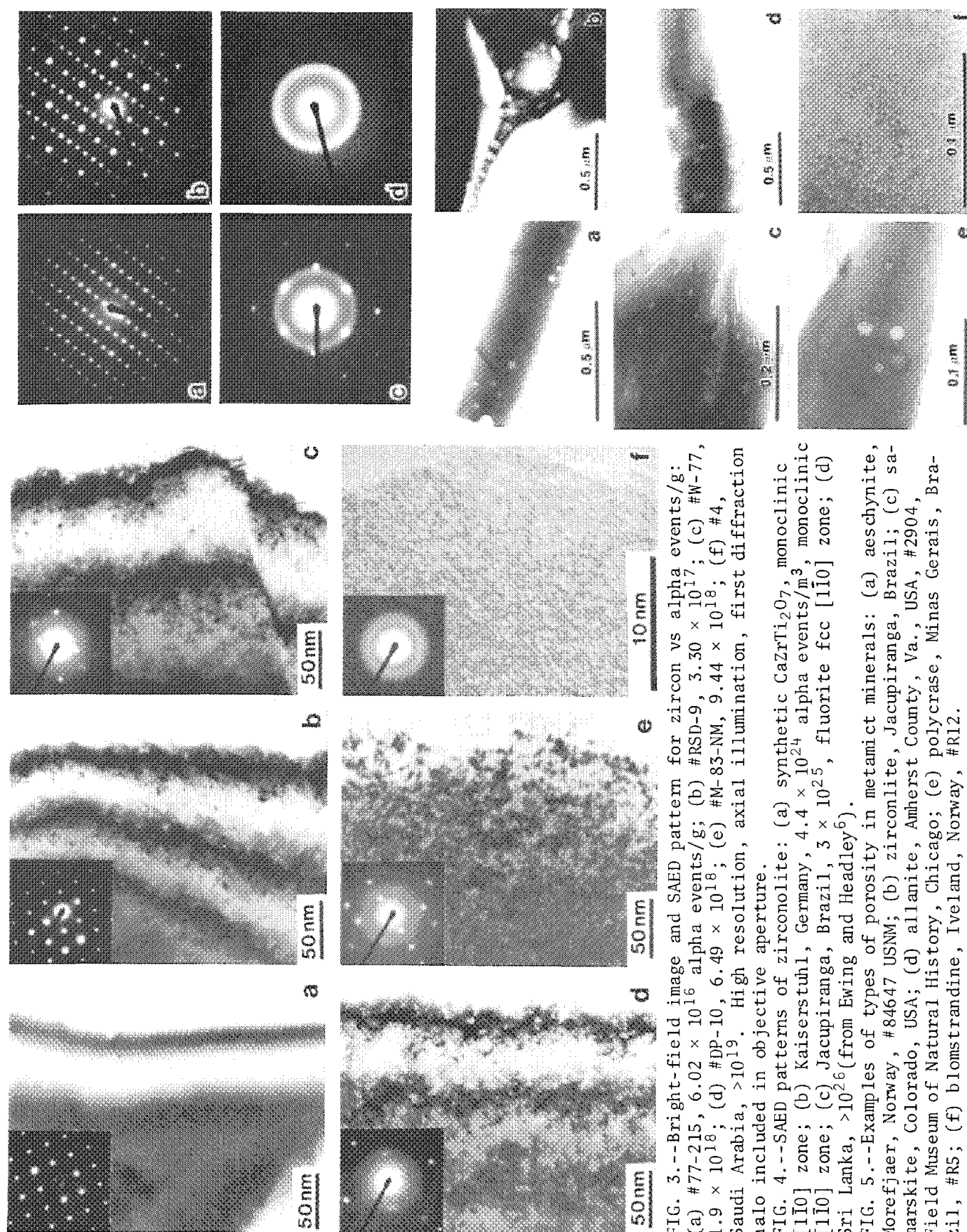


FIG. 3.--Bright-field image and SAED pattern for zircon vs alpha events/g: (a) #77-215,  $6.02 \times 10^{16}$  alpha events/g; (b) #RSD-9,  $3.30 \times 10^{17}$ ; (c) #W-77,  $1.9 \times 10^{18}$ ; (d) #DP-10,  $6.49 \times 10^{18}$ ; (e) #M-83-NM,  $9.44 \times 10^{18}$ ; (f) #4, Saudi Arabia,  $>10^{19}$ . High resolution, axial illumination, first diffraction halo included in objective aperture.

FIG. 4.--SAED patterns of zirconolite: (a) synthetic  $\text{CaZrTi}_2\text{O}_7$ , monoclinic [110] zone; (b) Kaiserstuhl, Germany,  $4.4 \times 10^{24}$  alpha events/ $\text{m}^3$ , monoclinic [110] zone; (c) Jacupiranga, Brazil,  $3 \times 10^{25}$ , fluorite fcc [110] zone; (d) Sri Lanka,  $>10^{26}$  (from Ewing and Headley<sup>6</sup>).

FIG. 5.--Examples of types of porosity in metamict minerals: (a) aeschynite, Morefjaer, Norway, #84647 USNM; (b) zirconolite, Jacupiranga, Brazil; (c) samarskite, Colorado, USA; (d) allanite, Amherst County, Va., USA, #2904, Field Museum of Natural History, Chicago; (e) polycrase, Minas Gerais, Brazil, #R5; (f) blomstrandine, Iveland, Norway, #R12.

## HIGH-RESOLUTION TRANSMISSION ELECTRON MICROSCOPY OF MICROLITE FROM THE HARDING PEGMATITE, TAOS COUNTY, NEW MEXICO

G. R. Lumpkin and R. C. Ewing

Microlite, ideally  $\text{NaCaTa}_2\text{O}_6\text{F}$ , is the Ta-rich end-member of the pyrochlore group (Fd3m,  $Z = 8$ ). It is one of the major accessory minerals of the Harding pegmatite (1300 m.y. old), where it formed during late magmatic and early hydrothermal phases of crystallization. Analyzed samples contain <0.1 to 11.0 wt%  $\text{UO}_3$  and range from highly crystalline to completely metamict.<sup>1</sup> Calculated alpha-recoil doses range from  $<10^{15}$  to  $4 \times 10^{17}$  alpha-events/mg (<0.1 to ~50 displacements per atom, dpa). X-ray diffraction analyses indicate that the fully metamict state is reached at ~3.2 wt%  $\text{UO}_3$ , corresponding to a dose of  $10^{17}$  alpha-events/mg (17 dpa). We have employed high-resolution transmission electron microscopy (HRTEM) and energy-dispersive spectroscopy (EDS) to characterize the transition from the crystalline to the metamict state.

### *Experimental*

Samples were ground in acetone and deposited onto holey carbon films supported by copper grids. Thin edges of grains were examined using a JEOL 2000FX TEM operated at 200 kV. HRTEM images were taken at 410 000 $\times$  or 500 000 $\times$  with use of axial illumination. Images were recorded with the electron beam perpendicular to [111] or (110). Selected area diffraction (SAD) patterns were calibrated with a polycrystalline gold film. EDS was performed with a TRACOR TN-5500. A 10nm beam was used and spectra were acquired for 300 s live time (5-10% dead time). Analyses were calculated by a standardless metallurgical thin film procedure with k-factors derived from microlite standards.

### *Results*

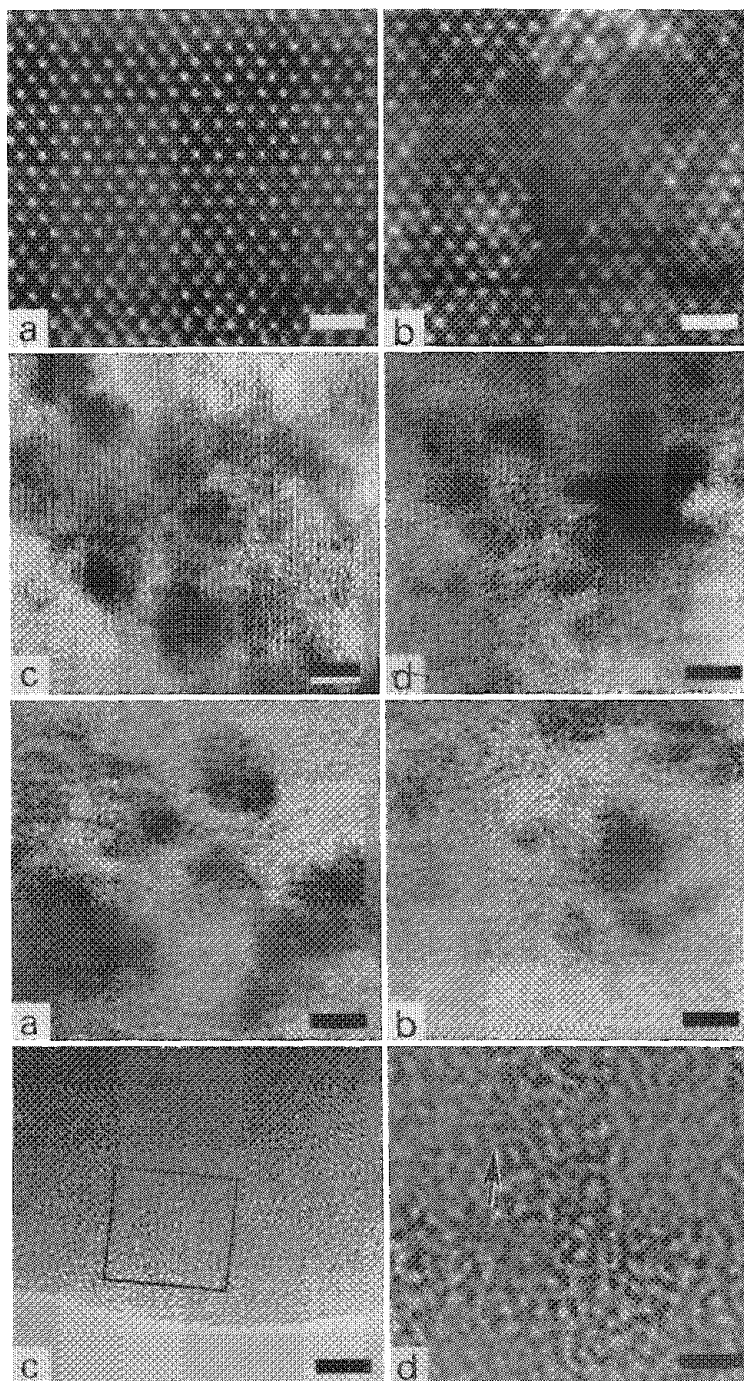
The structure of microlite can be described as an octahedral framework in which (111) planes consist of sheets of octahedra with the hexagonal tungsten bronze (HTB) topology. Three- and six-member rings of the HTB layers are aligned to form small and large channels parallel to [110]. Figure 1(a) shows a (110) HRTEM image of sample 147 in which the bright spots probably correspond to the large channels. HRTEM images of sample 147 taken normal to [111] display 0.6 nm (111) fringes that correspond to HTB layers. Such images often show 0.3nm (222) fringes. Microlite 147 contains <0.1 wt%  $\text{UO}_3$  and has an alpha-event dose of  $<10^{15}$   $\alpha$ /mg.

Effects of increasing uranium content are shown in Figs. 1(b)-(d), 2(a)-(d), and 3(a)-(d). At 0.9-1.0 wt%  $\text{UO}_3$  ( $3 \times 10^{16}$   $\alpha$ /mg), sample 149 exhibits mottled diffraction contrast and disrupted lattice periodicity within isolated, 1-3nm areas (Figs. 1b,c). With 1.5 wt%  $\text{UO}_3$  ( $6 \times 10^{16}$   $\alpha$ /mg), aperiodic areas increase in abundance and fine scale mosaic textures are observed (Fig. 1d). The mosaic pattern consists of 1-5nm crystalline domains having lattice misorientations of several degrees. At this point, diffuse rings appear on SAD patterns (Fig. 3b). With a uranium content of 2.5 wt%  $\text{UO}_3$  ( $9 \times 10^{16}$   $\alpha$ /mg), sample 288 clearly shows regions of coexisting crystalline and aperiodic microlite (Fig. 2a). The SAD pattern (Fig. 3c) exhibits prominent diffuse rings. At 2.9 wt%  $\text{UO}_3$  ( $10^{17}$   $\alpha$ /mg), the mosaic texture is lost and "islands" of crystalline microlite are left within an aperiodic matrix (Fig. 2b). When 3.6 wt%  $\text{UO}_3$  ( $10^{17}$   $\alpha$ /mg) is reached, no lattice fringes were seen in HRTEM images and only diffuse rings appear in SAD patterns (Fig. 3d). With 8.9 wt%  $\text{UO}_3$  ( $4 \times 10^{17}$   $\alpha$ /mg), sample 153 exhibits an aperiodic, random network structure in HRTEM images taken at thin edges of grains (Fig. 2c). The images also show that nanometer-sized fragments of the original structure persist beyond the saturation level of alpha-recoil damage

---

The authors are at the Department of Geology, University of New Mexico, Albuquerque, NM 87131. This work was supported by the U.S. Department of Energy, Office of Basic Energy Sciences, grant DE-FG04-84ER45099. The electron microscopy was completed in the Electron Microbeam Analysis Facility of the Department of Geology at the University of New Mexico.

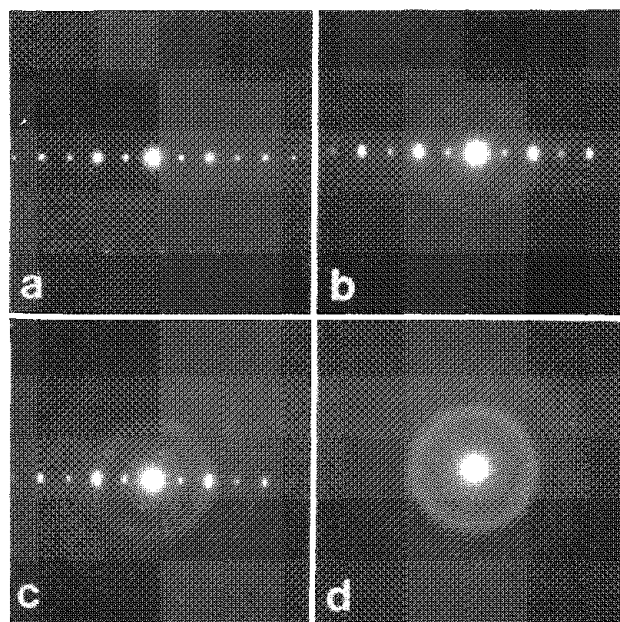




**1** FIG. 1.--HRTEM images showing progressive structural damage to microlite at low-to-moderate uranium content. (a) Microlite 147, <0.1 wt%  $\text{UO}_3$ ,  $<10^{15}$   $\alpha/\text{mg}$ , (110) orientation, bar = 2 nm. (b) Sample 149, 0.9 wt%  $\text{UO}_3$ ,  $3 \times 10^{16}$   $\alpha/\text{mg}$ , (110) orientation, bar = 2 nm. (c) Sample 149, 1.0 wt%  $\text{UO}_3 = 3 \times 10^{16}$   $\alpha/\text{mg}$ , [111] orientation, bar = 5 nm. (d) Sample 149, 1.5 wt%  $\text{UO}_3$ ,  $6 \times 10^{16}$   $\alpha/\text{mg}$ , [111] orientation, bar = 5 nm.

FIG. 2.--HRTEM images showing structural damage in microlite at moderate to high uranium content. (a) Sample 288, 2.5 wt%  $\text{UO}_3$ ,  $9 \times 10^{16}$   $\alpha/\text{mg}$ , [111] orientation, bar = 5 nm. (b) Sample 288, 2.9 wt%  $\text{UO}_3$ ,  $10^{17}$   $\alpha/\text{mg}$  [111] orientation, bar = 5 nm. (c) Microlite 153, 8.9 wt%  $\text{UO}_3$ ,  $4 \times 10^{17}$   $\alpha/\text{mg}$ , bar = 5 nm. (d) Enlargement of area outlined in (c), bar = 2 nm, arrow indicates possible fragment of original structure.

**2** FIG. 3.--SAD patterns corresponding to HRTEM images in Figs. 1 and 2. (a) Sample 149, Fig. 1(c). (b) Sample 149, Fig. 1(d). (c) Sample 288, Fig. 2(a). (d) Sample 153, Fig. 2(c).



**3**



(Fig. 2d). Similar images have been observed from amorphous areas of bismuth-implanted silicon.<sup>2</sup> The pattern of random contrast observed in Fig. 2(c) and (3) closely resembles calculated images of amorphous arsenic.<sup>3</sup> The SAD pattern of sample 153 has diffuse rings at 0.298 nm and 0.180 nm, from which mean interatomic distances of 0.343 nm and 0.207 nm are calculated.<sup>4</sup> These values are approximately 5% lower than the mean M-M distance of 0.364 nm and the mean M-O distance of 0.223 nm calculated for the microlite structure based on the mean cation radii of sample 153.<sup>5</sup>

In addition to the results described above, we found rare polycrystalline grains with 5 wt%  $\text{UO}_3$  in sample 149. Crystallite dimensions are on the order of 5-20 nm (Fig. 4a). Triple junctions are common, which shows that the texture resulted from recrystallization of initially metamict microlite. Since all attempts to recrystallize microlite with the electron beam have failed, we tentatively ascribe the texture to low-temperature, natural annealing. Some of the crystallites exhibit both ordered and disordered intergrowths on (111) with a 0.4nm phase (Fig. 4b). Extra spots on the SAD pattern are consistent with the tetragonal tungsten bronze (TTB) structure type; however, 0.4nm lattice fringes could result from either the TTB or the HTB structure type.

### Conclusions

The transition from the crystalline to the metamict state in microlite from the Harding pegmatite can be summarized as follows: (1) At <0.1 wt%  $\text{UO}_3$  ( $<10^{15}$   $\alpha/\text{mg}$ , <0.1 dpa), isolated alpha-recoil tracks have little effect on SAD patterns and are difficult to observe in HRTEM images. (2) At 0.9 wt%  $\text{UO}_3$  ( $3 \times 10^{16}$   $\alpha/\text{mg}$ , 3 dpa), isolated alpha-recoil tracks are observable as 1-3nm areas of disrupted lattice periodicity. (3) When 2.5 wt%  $\text{UO}_3$  ( $9 \times 10^{16}$   $\alpha/\text{mg}$ , 13 dpa) is reached, alpha-recoil tracks overlap, yielding coexisting areas of crystalline and metamict microlite. Prominent diffuse rings occur in SAD patterns. (4) The fully metamict condition is attained at 2.9-3.6 wt%  $\text{UO}_3$  ( $1-2 \times 10^{17}$   $\alpha/\text{mg}$ , 15-19 dpa). Beyond this point, HRTEM images exhibit a random network structure. SAD patterns consist of diffuse rings which result from M-M and M-O distances within the random network. These results contradict the conclusion by Ringwood<sup>6</sup> that structures that have been rendered "metamict" are still essentially crystalline and do not resemble the highly disordered structure of glass.

### References

1. G. R. Lumpkin et al., "Mineralogy and radiation effects of microlite from the Harding pegmatite, Taos County, New Mexico," *American Mineralogist* 71: 569-588, 1986.
2. J. Narayan (personal communication).
3. L. A. Bursill et al., "Computer simulation and interpretation of electron microscopic images of amorphous structures," *J. Phys. Chem.* 85: 3004-3006, 1981.
4. H. P. Klug and L. E. Alexander, *X-ray Diffraction Procedures*, New York: Wiley, 1974.
5. B. C. Chakoumakos, "Systematics of the pyrochlore structure type, ideal  $\text{A}_2\text{B}_2\text{X}_6\text{Y}$ ," *J. Solid State Chem.* 53: 120-129, 1984.
6. A. E. Ringwood, "Disposal of high-level nuclear wastes: A geological perspective," *Mineralogical Magazine* 49: 159-176, 1985.

FIG. 4.--HRTEM images of polycrystalline microlite, Sample 149, ~5 wt%  $\text{UO}_3$ . (a) Typical microstructure showing grains in (110) and [111] orientations, bar = 5 nm. (b) Unusual intergrowth of microlite and a tungsten bronze structure type with 0.4nm fringes, bar = 5 nm.

## THE USE OF MICROTOMED THIN SECTIONS FOR THE ANALYSIS OF GEOLOGICAL MATERIALS WITH AUGER ELECTRON SPECTROMETRY

G. P. Meeker and R. H. Fleming

Auger electron spectrometry is a widely used technique in microelectronics and metallurgy. In recent years microbeam Auger instruments have become available that permit chemical analysis with submicron lateral resolution. Major and minor concentrations of elements, including light elements such as B, C, N, and O, can be routinely measured with good precision and accuracy by use of appropriate standards. Unfortunately, the maximum Auger electron escape depth ( $<50 \text{ \AA}$  in most materials) precludes the use of conductive surface coatings, which are typically much thicker. This disadvantage makes the technique impractical for the analysis of bulk dielectrics, including most geological materials. Although techniques for x-ray microanalysis of light elements with both solid-state and wavelength detectors have improved dramatically in the last few years, many problems still exist with regard to sensitivity and quantitative analysis. Auger microprobe analysis could be a viable alternative or supplement to x-ray microanalysis provided that the problems with electrical charging can be overcome.

In the microelectronics analytical laboratory thin films of dielectric materials such as  $\text{SiO}_2$  and  $\text{Si}_3\text{N}_4$  on conducting substrates are routinely analyzed by Auger spectrometry with no deleterious effects from electrical charging. Only when the dielectric layer is thicker than approximately  $7000 \text{ \AA}$  does charging become a problem. This finding suggests that ultrathin sections of geological or other dielectric materials coated on the back with a conductive coating such as Au or Pd could be analyzed by Auger spectrometry. The sample thickness required ( $<1 \text{ }\mu\text{m}$ ) can be obtained by ultramicrotomy. Although traditionally used for sectioning biological tissues, the technique is used by materials analysts for sectioning many hard and brittle materials. It is the purpose of this work to evaluate the performance of Auger microprobe analysis on dielectric specimens prepared by ultramicrotomy.

### *Experimental*

The samples chosen for this study are Illinois #6 (PSOG 1098) coal and Murchison meteorite matrix, both of which contain substantial amounts of C and O and minor amounts of N. Submillimeter grains of each sample were mounted in Spurr epoxy resin. No attempt was made to vacuum impregnate the samples because of the likelihood of contamination. The samples were then microtomed to thicknesses of a few hundred  $\text{\AA}$  and a few thousand  $\text{\AA}$ , respectively, for the coal and meteorite. Sections were placed on TEM grids and sputter coated with Au. The subsequent Auger analyses were performed on the back (uncoated) side of the samples through the grid openings.

Auger electron energy spectra and elemental maps were obtained with a JEOL JAMP-10 scanning Auger microprobe equipped with a secondary electron detector and a KEVEX 7000 x-ray microanalyzer, which controls both Auger and x-ray analytical functions. The system also utilizes a differentially pumped ion gun for in situ etching and depth profiling. Spectra were obtained at a primary electron accelerating voltage of 10 kV with currents of 10-100 nA. Auger elemental maps were obtained with a focused probe at currents of 3-10 nA. The pressure in the analyzing chamber was kept below  $1 \times 10^{-8}$  Torr. All surfaces were sputter cleaned with  $\text{Ar}^+$  before analyzing.

### *Results*

The sample of Illinois #6 coal yielded flat 200-500  $\mu\text{m}$ -diameter sections for analysis. It was found that some damage, in the form of a few long tears, occurred to the sections during sputter coating and subsequent  $\text{Ar}^+$  ion etching prior to Auger analysis. Figure 1 is a representative Auger electron energy spectrum from a portion of the coal sample.

---

Authors Meeker and Fleming are at Charles Evans & Associates, 301 Chesapeake Dr., Redwood City, CA 94063.

The spectrum shows the presence of C and O with small amounts of Si and N. All Auger transition peaks are at the correct energies, which indicates that the sample did not electrically charge during the analysis. After the spectrum was obtained the sample was examined for electron-beam damage; no damage was observed. Figure 2 is a spectrum obtained from the epoxy resin adjacent to the sample. This spectrum shows the presence of C, O, and N. An estimate of the approximate relative atomic concentrations of these elements in the resin is 80%, 20%, and <1%, respectively. Again, no electron-beam damage was observed at the point of analysis. Figure 3 is an Auger map of the relative O concentrations in a  $25 \times 20 \mu\text{m}$  area of the sample. The lateral resolution in the image is on the order of  $8000 \text{ \AA}$ . The light regions show areas of relatively high O concentrations. Spectra were obtained at points A (Fig. 1) and B (Fig. 4) in Fig. 3. The spectrum from point B shows the presence of Al and Si in addition to C and O. The shape of the low-energy side of the C peak suggests that K (243 eV) may also be present. Because of the much higher O to C ratio in area B along with the presence of Al, Si, and probably K, it is reasonable that the O-rich regions in Fig. 3 represent mineral-rich (clay) seams in the coal.

The Murchison meteorite sample proved to be very difficult to section. This problem was expected, due to the fine grain size and the extreme differences in hardness of the matrix constituents, and because the sample was not vacuum impregnated. Only two of ten sections contained analyzable areas. Figure 5 is a secondary-electron image of a section of the meteorite matrix. The width of the finder grid bar is approximately  $20 \mu\text{m}$ . The roughness of the surface is clearly visible in the image, which suggests that much of the material was not sectioned but was merely smeared across the surface. A spectrum of a point on the surface is presented in Fig. 6 showing the presence of S, C, O, Si, Mg, and Fe. Some Au may also be present from the sputter coating procedure. Figure 7 is a spectrum from a second area on the sample surface showing the presence of C, O, Mg, and Si. Small peaks representing Cu and Rh are due to electron or x-ray scattering from the grid. In both meteorite spectra the relatively high intensity of the C peak suggests that epoxy resin may have contaminated the surface of the sample.

### Conclusions

The above data demonstrate that Auger microprobe analysis and scanning Auger microscopy with submicron resolution can be performed on ultrathin sections of samples which in bulk form would be extremely difficult if not impossible to analyze. The samples show no indication of electrical charging during analysis, and no electron-beam damage was observed. Some damage was observed from sputter coating and ion etching. The meteorite sample was extremely difficult to section, but this difficulty may be in part due to the fact that the sample was not vacuum impregnated. Since the distribution of C is of major interest in carbonaceous chondrite meteorites, any attempt to analyze such specimens will require some method of labeling the epoxy resin with a tracer element or finding some other embedding medium that will not compromise the results.

No attempt was made to quantitate any of the results. However, it should be possible to obtain quantitative information from this type of analysis by the use of standards of similar materials prepared in the same manner as the sample to be analyzed.

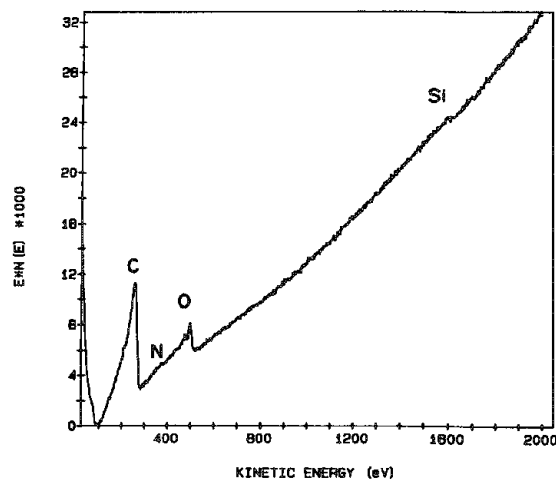


FIG. 1.--Auger electron energy spectrum of ultrathin section of Illinois #6 coal. C, O, Si, N, and Ar (at 211 eV) from  $\text{Ar}^+$  sputter cleaning are detected.

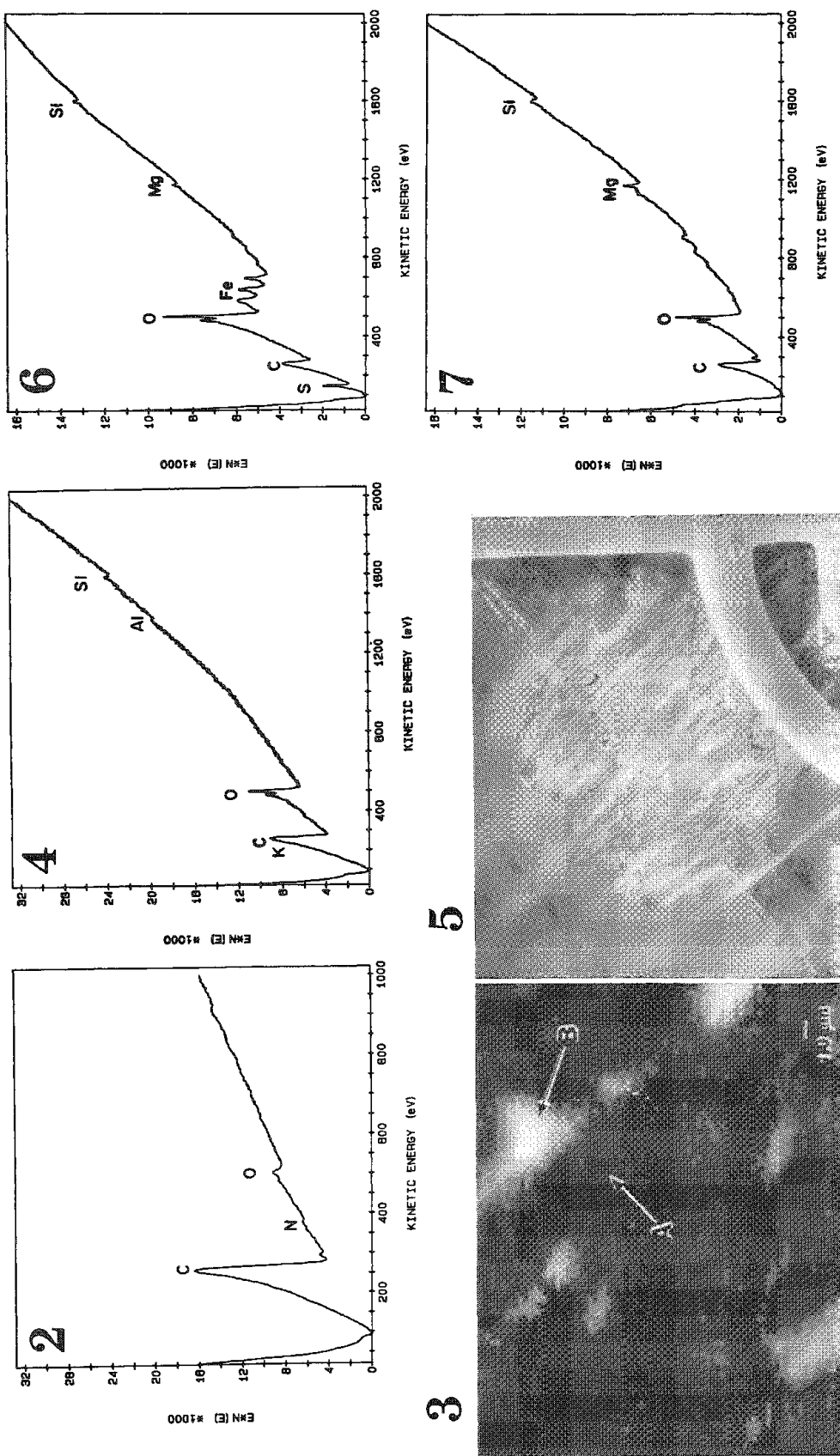


FIG. 2.--Auger electron energy spectrum of Spurr epoxy resin showing presence of C, O, and N. Approximate O/C ratio of this resin is 0.25. N is probably less than 1 at.%.  
 FIG. 3.--Scanning Auger electron image of O in Illinois #6 coal. Light areas indicate regions of high O concentration. Survey spectra were obtained from points A (Fig. 1) and B (Fig. 4). Oxygen-rich regions appear to be clay seams (see text).  
 FIG. 4.--Auger electron energy spectrum from point B in Fig. 3 showing presence of C, O, Al, Si, and probably K at 243 eV. Higher O/C ratios (cf. Fig. 1) and Al, K, and Si signals suggest presence of clay minerals.  
 FIG. 5.--Secondary-electron image of meteorite matrix thin section. Grid bar ~20  $\mu$ m wide. Note rough texture of surface, which indicates that much of the material was not sectioned, but smeared across surface.  
 FIG. 6.--Auger electron energy spectrum of portion of Murchinson meteorite matrix ultrathin section. Spectrum shows presence of C, S, O, Fe, Mg, and Si. C contamination from epoxy resin may be present.  
 FIG. 7.--Auger electron energy spectrum of grain in meteorite matrix ultrathin section showing presence of C, O, Mg, and Si. Some of C signal may be from epoxy embedding medium, and Cu (916 eV) and Rh (298 eV) signals are from finder grid.

## ELEMENTS Cu THROUGH Ge: COSMOCHEMICAL SIGNIFICANCE AND MICROANALYSIS IN METEORITES

Alfred Kracher and M. L. Pierson

Electron probe microanalysis of elements heavier than Ni in meteorites involves in most cases low-level detection and special counting strategies. With such techniques, Ge, Ga, and other not-too-rare elements can be used as geochemical tracers for fractionation processes that are as yet poorly understood. For example, the microdistribution of Ge in metal grains can be used to test the hypothesis that melting along the Fe-Ni-S peritectic was involved in the formation of winonaites and IAB irons.

### *Geochemistry*

Meteorites have undergone less geological processing than most terrestrial rocks, and cosmic element abundances generally control the composition of their major minerals. The cosmic abundance curve falls off steeply for elements heavier than Ni. Except for unusual assemblages like refractory inclusions in carbonaceous chondrites, very few elements with  $Z > 28$  (Cu, Zn, Ga, Ge, and perhaps Se) occur in high enough concentrations to be detected by microprobe analysis. These are also the heaviest elements whose K lines can be detected by conventional crystal spectrometers.

An example that illustrates the analytical problems and the practical usefulness of detecting these elements is the analysis of Ge in metal grains of the Allan Hills A77081 meteorite. The partition coefficient of Ge between solid metal and melt depends strongly on the concentrations of nonmetallic elements (S,P,C) in the melt. If A77081 contains metal associated with eutectic melting as well as unmelted metal, it should be possible to distinguish the two components on the basis of their Ge contents. Most metal in A77081 is kamacite ( $\alpha$ -Fe,Ni; typical composition in weight percent: Fe 92.5, Co 0.45, Ni 7.0).

### *Analytical Conditions and Problems*

The critical excitation potential for the Ge K series of 11.1 kV requires high acceleration voltages to achieve a high peak/background ratio (PBR). However, some of the metal grains are very small (10  $\mu\text{m}$  and less), and it is difficult to avoid beam penetration into underlying phases. We used 25 kV at 0.2  $\mu\text{A}$  sample current on pure Fe, and 100 to 300 s counting times. The unfavorable spectrometer geometry ( $2\theta = 36.3^\circ$ ) causes a high background near the Ge  $K\alpha$  peak, which is not linear. The effect of changing the width of the variable detector slit on the peak/background ratio was investigated. Count rate and PBR for various slit settings were fitted to the relationship

$$\text{PBR} = (\text{count rate})^{-n}$$

If exponent  $n$  were greater than unity, closing the slit would lower the detection limit, even though the count rate decreases. However, it was experimentally found that for a practically useful range of slit settings  $n = 0.4$ , so that a fully open slit resulted in the best counting strategy. Pure metal standards were used for Fe, Co, Ni, and Ge. A chip of Landes meteorite (6.31% Ni, 414 ppm Ge) was used as a secondary standard to validate the analyses.

Because nearly 1 million counts are acquired during 300 s with the spectrometer set to Ge  $K\alpha$ , the software has to be safeguarded against storage overflow. Taking alternate counts of 100 s each on background and peak, and repeating them until a significant result is obtained, has several advantages: (a) grains that have significant amounts of Ge are counted for shorter times, which makes for more efficient use of instrument time; (b) bias due to slow drift is largely eliminated; and (c) if necessary, background counts can be taken at several different positions to determine the background shape.

---

The authors are at the Department of Earth Sciences, Iowa State University, Ames, IA 50011. This work was supported by NASA grant NAG 9-112.

Monitoring the bulk composition of metal grains is difficult because of very high deadtimes for the Fe and Ni  $K\alpha$  lines at these high beam currents. Energy-dispersive analysis (EDS) can be used if the Si(Li) detector can be operated at an acceptably low deadtime. Since our detector is not retractable, a small aperture machined from an Al disk was mounted in front of it. Since the samples were not analyzed for Al, fluorescence from the aperture was of no importance. An alternate way of analyzing for Fe, Co, and Ni is the use of higher-order lines on the crystal spectrometers. Use of third-order  $K\alpha$  lines on an ADP crystal yielded acceptable count rates and also provided better separation of Co  $K\alpha$  from Fe  $K\beta$  than for first-order lines.

Various runs under these conditions gave detection limits between 70 and 120 ppm Ge, which is adequate for the samples analyzed. Counting times up to 1 h have been used previously,<sup>1</sup> which lowers the detection limit to 20 ppm. However, for the number of data points required in this study such long counting times would have been unacceptable.

### *Results*

In addition to the common, homogenous "normal" kamacite, A77081 contains small metal grains with lower Ni and Ge, and higher Co. These grains are always associated with troilite (FeS). Although the textures of Ni-poor and Ge-poor metal suggest formation from a eutectic melt, the low-Ni contents cannot be reconciled with a simple partial melting model.<sup>2</sup> The implications of this result are discussed in more detail elsewhere.<sup>3</sup>

### *Alternate Methods*

Proton probe microanalysis (PIXE) should provide a considerable improvement in sensitivity over electron-probe analysis. Since the trace elements discussed here have  $K\alpha$  energies higher than those of the major elements, nonspecific absorbers can be employed to filter the strong x-ray lines from elements present in high concentrations. Therefore elements heavier than Fe can be detected with high sensitivity by PIXE. The electron microprobe study reported here provided the preliminary information that will make it possible to identify the most promising samples for future PIXE work.

### *References*

1. J. I. Goldstein, "Distribution of germanium in the metallic phases of some iron meteorites," *J. Geophys. Res.* 72: 4680-4696, 1967.
2. A. Kracher, "The evolution of partially differentiated planets: Evidence from iron meteorite groups IAB and IIICD," *Proc. Lunar Planet. Sci. Conf.* 15 (*J. Geophys. Res.* 90): C689-C698, 1985.
3. A. Kracher, "Microdistribution of germanium in the Allan Hills A77081 winonaite," *Lunar and Planetary Science XVII*: 446-447, 1986.

## AUTOMATION OF MINERAL IDENTIFICATION FROM ELECTRON MICROPROBE ANALYSES

D. G. W. Smith

As in most areas of science and technology, the computer has made an enormous impact in the area of microanalysis. The most recent electron microprobes offer computer control of virtually the entire instrument and provide a broad range of software for qualitative and quantitative analysis as well. Computer hardware and software have also recently made inroads into the imagery capabilities of the instruments. We even see the beginning of built-in facilities for monitoring the performance and health of an instrument, via special diagnostics packages. This paper describes computer software that has been adapted to permit the automatic identification of minerals from electron microprobe analyses.

Earth scientists working in various areas of specialization including petrology (igneous, metamorphic, and sedimentary), economic geology, ore mineralogy, mineral exploration and beneficiation, geochemistry, meteoritics, and crystallography, are routinely faced with a need for rapid mineral identification. Techniques used have ranged from the recognition of physical properties in hand specimens to sophisticated and computerized techniques such as x-ray diffractometry and optical reflectance measurements. Most professional mineralogists are capable of recognizing, at the most, a few hundred minerals in hand specimens or under the petrographic microscope. To identify the remaining minerals (nearly 4000 in total), the mineralogist has traditionally turned to x-ray diffraction techniques. However in recent years the convenience of the energy-dispersive spectrometer has proved more and more seductive, so that many mineralogists now turn first to this instrument to obtain compositional constraints. Sometimes these constraints are sufficient to leave no doubt about an identity. However, frequently they are not, and a number of possibilities remain, many of which may not even be recognized, especially if the analyst is constrained by a widely dispersed database, time demands, etc.

Notwithstanding these reservations, it is intrinsically possible to use chemical composition systematically and automatically in accurately delineating possible mineral identities, provided that the necessary information about the composition of recognized minerals is available. The difficulties that must be surmounted to achieve this end in practice include the sheer number of different possibilities, the variable compositions of natural minerals, the common complexity of mineral compositions (some minerals may contain significant amounts of more than 30 elements), and the fact that certain light elements cannot be, or are not normally, determined in electron microprobe analysis (i.e., H, Li, Be, B, C, O, and F).

To some degree, the extent of compositional variations in natural minerals can be calculated from a formula. However, as may be seen from Table 1, the general formula for the common mineral hornblende gives rise to a very wide range of calculated compositions. Unless specific restraints are placed on the various generalized substitutions, this lack of precision plagues attempts at calculating realistic compositions. Although the procedure may be useful in the absence of other data, what are needed are real analytical data for a wide range of samples of each natural mineral. These data should be from samples that embrace, as far as is possible, the complete range of normal substitutional variations. Such data have recently become available in a database described by Smith and Leibovitz.<sup>1</sup> This database contains information for nearly 4000 mineral species, groups, and varieties, including real analytical data for more than 3300 of them. The remaining few hundred minerals are at the present time represented by compositional data calculated from formulas. In addition to compositional information, data have been stored for more than 20 other parameters, although not all minerals have data for all these fields. Data for a particular mineral can be formatted in index card form. A typical card showing the fields for the various parameters is represented in Fig. 1.

---

The author is at the Department of Geology, University of Alberta, Edmonton, Alberta, Canada T6G 2E3. Part of this work has been supported financially by the Natural Sciences Engineering Research Council of Canada.

age. 1 completed mineral data display

Record: 245 Name: BIOTITE Date: 14:01:15 FEB 27, 1986

Formula: K(Mg,Fe)3(Al,Fe3+)Si3O10(OH,F)2

Symmetry: Monoclinic Space Group: Cm JCPDS: 2-0045 Dispersion: R>V,V>R

Type: SILICATES Year First Described: Samples: 43 Generals: 3 Total Samples: 43

El	Wt Min	Wt Ave	Wt Max	Std Dev	At Prop	Coord	a	b	c	Alpha	Beta	Gamma
O	39.053	42.116	44.668	1.317	23.382*			5.300	5.300	90.000	90.000	90.000
Si	15.468	17.009	19.745	0.976	5.379		5.300	7.250	17.650	90.000	95.000	90.000
Fe	6.906	15.341	26.161	3.930	2.440			9.200	30.000		100.000	
Al	6.256	9.522	10.860	1.177	3.135		n(alph)	n(beta)	n(gamm)	Density	VHN	MOH
K	5.438	7.113	8.160	0.611	1.616		1.555	1.589	1.590	2.7		2.0
Mg	0.048	5.399	8.112	1.867	1.972		1.594	1.641	1.646	3.071		2.5
Ti	0.108	1.597	3.165	0.749	0.296		1.625	1.696	1.696	3.4		3.0
F	0.000	1.020	5.020	1.407	0.477*		R(470)	R(546)	R(589)	R(650)	2V(gam)	OAP
Rb	0.000	0.661	1.692	0.802	0.069						155.0	/(O10)
Cl	0.000	0.565	1.110		0.142*						177.167	
Na	0.000	0.439	1.981	0.428	0.170						180.0	
Cs	0.000	0.419	0.419		0.028		C(alph)	C(beta)	C(gamm)	d-vals		
H	0.067	0.387	0.586	0.112	3.413		Gy Y1	D Br	D Br	10.1		
Ca	0.000	0.334	1.172	0.337	0.074		Br Gn	D Gn	D Gn	3.37		
Li	0.000	0.307	0.883	0.318	0.393		Br	D Br Rd	D Br Rd	2.66		
Ba	0.000	0.167	0.663	0.224	0.011		L Br	Y1	Y1	2.45		
Mn	0.000	0.143	0.519	0.124	0.023					2.18		
N	0.000	0.134	0.134		0.085							
V	0.000	0.031	0.070		0.005							
P	0.000	0.023	0.044		0.007							
S	0.000	0.020	0.020		0.006							
C	0.000	0.014	0.014		0.010							
Cr	0.000	85 ppm	0.012		0.001							
Ni	0.000	50 ppm	70 ppm		0.001							
Co	0.000	30 ppm	35 ppm		0.000							
Zr	0.000	30 ppm	40 ppm		0.000							
Ga	0.000	19 ppm	20 ppm		0.000							
Sr	0.000	7 ppm	7 ppm		0.000							

102.782 43.134

Collection number(s):

Polymorphs:

Remarks: 2M polytype belongs to space gp. C2/c and 3T to C3(1)12 or C3(2)12.

Occurrence: Biotite schist. Dark brown biotite pegmatite-like lens in oligoclase-quartz-biotite gneiss. Low grade garnet-mica schists. Medium grade garnet-mica schists. Regionally metamorphosed biotite plagioclase hornfels. Muscovite-biotite-microcline-quartz schists. Biotite-staurolite-garnet-mica schists, staurolite zone. Biotite-kyanite gneiss. Sillimanite-bearing pyralisite-biotite-oligoclase-quartz gneiss. Cordierite-biotite hornfels: schists at contact with spodumene pegmatite. (and others).

Location(s): Chokolowska valley, Tatra Mountains, Poland. Morar, Inverness-shire; Carn Chuinneag-Inchbae region, Ross-shire; Cairnmore of Carsphairn, Kirkcudbrightshire; Glen Esk, Angus; Bellhelvie, Aberdeenshire (Scotland). Lakeview, Calif. Woodson, Calif. Rubideaux, Calif., Alboroto, San Juan district, Col., (U.S.A.). Mourne Mountains, N.Ireland. N.Nigeria. Seto, Ogawa-mati, Nakoso City, Fukushima Prefecture; Kaiya, Tabilo-mua, Gosaisyo-Takanuki District; Tenayokyo, Simoina-goni, Nagano prefecture, (Japan). (and others).

FIG. 1



Although much other information has been included, emphasis has been placed on compositional information in attempting to match an unknown mineral with those in the database. A special facility has been included that permits compositional information produced by a microprobe data reduction program to be entered directly into the MINIDENT mineral identification software. At the present time, the output of EDATA2 is directly compatible with the MINIDENT software. This program was chosen because it is capable of processing simultaneously and in an integrated fashion both energy- and wavelength-dispersive microprobe data and because EDATA2 is the program used in practice in the laboratory where MINIDENT was developed. Output from any such electron microprobe data processing program could be made with MINIDENT with only very minor modifications being required.

The programs in the package offer two distinct approaches to mineral identification. The procedure MATCH lists all minerals in the database for which the range of possible concentrations of major elements includes those determined for the test sample. If the sample lies outside the range in the database for any given mineral, even very slightly, that possibility will be rejected. This procedure stands in contrast to the alternative procedure IDENTIFY, which lists minerals that have the overall greatest similarity to the test sample. Mismatches do not result in outright rejection but instead incur "demerit points." The 20 minerals with the least number of demerit points are listed by the program as the most promising for further investigation.

The group of earth scientists who commonly face the most difficult mineral identification tasks are probably those dealing with ore deposits. Not only do unusual minerals frequently appear in the assemblages but alterations, secondary replacements, etc., often make the assemblages fine grained and extremely complex. Microbeam techniques are virtually essential to solve the problems of both textural relationships and identities. Because of their rather poor spatial resolution, x-ray diffraction techniques are often inadequate, as are also the techniques of accurate reflectance and microindentation hardness measurement. The application of MINIDENT to the interpretation of a rare-metal deposit was described by Smith and De St. Jorre.<sup>3</sup>

One can also envisage a useful role for MINIDENT in the automated modal analysis of rocks and other material by the electron microprobe. Procedures have been previously described by Keil<sup>4</sup> and Albee et al.<sup>5</sup> Modal analysis is usually rather time-consuming and is therefore normally carried out unattended and automatically at periods of low work pressure, e.g., overnight. During a run, the instrument may frequently encounter points that do not correspond to the mineral identities assigned by the user when the program was initiated. Although such data are usually discarded, additional useful information might result if analyses were obtained and compared to the compositional data in MINIDENT. Such a procedure could be carried out either during the modal analysis or subsequently.

As an illustration of the potential of MINIDENT in this general area, the phases in a mineralogically rather complex rock, a camptonite, have been analyzed by energy-dispersive techniques and the results processed by the MATCH and IDENTIFY procedures of MINIDENT. Table 2 summarizes these results. The names underlined are the identities of the minerals as determined from a mixture of optical, x-ray, and microanalytical data. In each case, the analytical data were compared with those for nearly 4000 minerals at present in the database.

MINIDENT was developed on a mainframe computer, an AMDAHL 580/FF, which has a cycle time of about 23 ns. Typical running times range between about 0.1 and 3.0 s of CPU time, depending on whether the MATCH procedure or the more time-consuming IDENTIFY procedure is being used. At present the MINIDENT identification and database management software uses about 400 Kbytes of memory and the database itself a further 12 Mbytes. However, the "compiled" database, which is required for identification purposes, presently occupies only about 4 Mbytes. It should certainly be possible to run MINIDENT on a state-of-the-art microcomputer equipped with a 10Mbyte hard disk drive. The production of such a version is currently being investigated.

## References

1. D. G. W. Smith and D. P. Leibovitz, "MINIDENT: A data base for minerals and a computer program for their identification," *Can. Mineral.* (in press).
2. D. G. W. Smith and C. M. Gold, "EDATA2: A FORTRAN IV program for processing wavelength- and/or energy-dispersive electron microprobe analyses," *Microbeam Analysis--1979*, 273-278.

3. D. G. W. Smith and L. de St. Jorre, "The MINIDENT data base: Examples of applications to the Thor Lake rare-metal deposits," Extended Abstr., 14th General Mtg., Internal. Mineral. Assoc. Stanford, Calif., 1986.

4. K. Keil, "Mineralogical modal analysis with the electron x-ray analyzer," *Amer. Mineral.* 50: 2089-2092, 1965.

5. A. L. Albee et al., "Quantitative analysis of petrographic properties and of mineral compositions with a computer-controlled energy-dispersive system," *Proc. 8th Intern. Cong. X-ray Optics & X-ray Microanal.*, 1977, 526-537.

TABLE 1.--Extreme concentration ranges calculated for hornblende.

Formula:  $[(Ca,Na,K)_{2-3}(Mg,Fe^{2+},Fe^{3+},Al,Ti,Mn)_5Si_6(Si,Al)_2O_{22}(OH,O,F,Cl)_2]$

	Ca	Na	K	Mg	Fe	Al	Ti	Mn	Si	O	H	F	Cl
Wt.% low	0.0	0.00	0.00	0.00	0.00	0.00	0.00	0.00	16.13	33.62	0.00	0.00	0.00
Wt.% high	14.17	8.65	13.88	15.71	29.97	23.99	26.85	29.63	28.95	49.61	0.26	4.87	8.72

TABLE 2.--Match and Identify outputs from MINIDENT.

1	2	3	4	5
<u>ALBITE</u>	OLIGOCLASE	ANORTHOCLASE	JADEITE	ALKALI FELDSPAR
LABRADORITE	BYTOWNITE	<u>PLAGIOCLASE</u>	MIZZONITE	ANDESINE
OLIGOCLASE	ANDESINE	ANORTHOCLASE	<u>PLAGIOCLASE</u>	ALBITE
<u>BIOTITE</u>	PHLOGOPIITE	LEPIDOMELANE	SURINAMITE	KAERSUTITE
PERISTERITE	OLIGOCLASE	<u>ALBITE</u>	ANORTHOCLASE	JADEITE
<u>KAERSUTITE</u>	FERROPARGASITE	BASALTIC-HORNBLende	TSCHERMakITE	HASTINGSITE
<u>SPHENE</u>	ISTISUITE	SAPPHIRINE	JEFFREYITE	KAERSUTITE
<u>TITANAUGITE</u>	FASSAITE	SALITE	AUGITE	DIOPSIDE
<u>ACTINOLITE</u>	AUGITE	<u>HORNBLende</u>	CLINO FERROSILITE	TREMOLITE
<u>QUARTZ</u>	TRIDYMITe	OPAL	SILHYDRITE	COESITE
FRANKLINITE	PARTRIDGEITE	<u>MAGNETITE</u>	ULVOSPINEL	MAGNESIOFERRITE
<u>ILMENITE</u>	PARTRIDGEITE	PSEUDOBROOKITE	FRANKLINITE	UM-107
<u>CHLORAPATITE</u>	HYDROXYLAPATITE	WILKEITE	WHITLOCKITE	CARBONATE-HYDROXYLAPATITE
MARCASITE	<u>PYRITE</u>	SMYTHITE	GREIGITE	PYRRHOTITE
<u>BARITE</u>	PARTRIDGEITE	FRANKLINITE	HYALOTERITE	CERPHOSPHORHUTTONITE

Notes: 1, 2, 3, 4 & 5 refer to the 5 most likely identities, i.e., those minerals having the highest matching indices as listed by the IDENTIFY procedure (see text). Bold print indicates the most likely mineral listed by the MATCH procedure (see text). In each case, 3741 minerals were considered. Underlined identities are those determined on the basis of optical properties. UM indicates unnamed mineral. These are listed by number in the data base. Some unlikely minerals may appear in the lists because, at the present time, the only compositional information present for them in the data base is calculated from generalised formulae. This gives a wide latitude in possible compositions (see table 1).

## ADVANCEMENTS IN NUCLEAR MICROPROBE TRACE ELEMENT ANALYSIS

P. S. Z. Rogers, C. J. Duffy, and T. M. Benjamin

The Los Alamos nuclear microprobe system has progressed from an instrument development effort to an analytical applications tool. Compositionally complex, fine-structured, thick-target samples can now be analyzed routinely for up to 76 elements by the proton-induced x-ray emission (PIXE) technique. However, the absolute accuracy of such analyses has not been previously assessed. To illustrate the expected accuracy of both individual and average results, we report detailed analysis of two very different types of standards: NBS standard reference material #610, which nominally contains 500 ppm of 61 elements in a glass matrix, and two Cl carbonaceous chondrites, Orgueil and Ivuna.

### *Software*

Recent development efforts at the Los Alamos nuclear microprobe have focused on improvement of the computer software needed to obtain quantitative analyses through deconvolution of the PIXE spectra. Design of the microprobe beam line, sample chamber, and data acquisition instrumentation has been described previously,<sup>1</sup> and this hardware has remained essentially unchanged. Briefly, data reduction is based on calculations using extensive literature data available for the basic physical interactions that occur as bombarding particles lose energy and produce x rays in a thick target.<sup>2</sup> The x rays are absorbed by the sample, and by filters placed between the sample and Si(Li) detector. As a recent improvement in the data treatment, the efficiency of the Si(Li) detector has been modeled, based on a nominal thickness of 3 mm.<sup>3</sup> These calculations yield the relative intensities of the x-ray lines for each element in that particular matrix. Combined with an independent calibration of the amplifier gain and offset, the peak width dependence of the detector, and the assumption of a Gaussian peak shape, the relative intensity calculations result in a sample-dependent envelope of lines for each element. The PIXE spectrum is then fit to these envelopes so that only one fitting parameter per element, concentration, is required. The PIXE method is so sensitive that accurate fitting requires that the peak envelopes contain contributions from up to 9 K lines and 15 L lines.

One advantage of this "envelope calculation" approach is that the spectrum fitting procedure is linear. A dramatic improvement in ease of use of the fitting routine was realized recently when inequality constraints were added to the least squares program. Element concentrations and spectrum background are constrained from taking negative values, so that all elements with any lines in the region of fit can be automatically included in the fit. The procedure will return only positive concentrations, as well as assign detection limits for elements that are not present in the spectrum. The need for operator interaction in spectrum fitting is greatly reduced by this method.

A second advantage is that, assuming the relative x-ray production cross sections and other data are accurate, the relative concentrations of the elements obtained from the spectrum fit are also quantitatively accurate. Concentrations of all elements in the spectrum can be obtained through reference to a single element that can be analyzed, for example with an electron microprobe, or can be determined from mineral stoichiometry. This approach eliminates the need for trace element standards, which are not available for many elements, are hard to synthesize, and are not generally homogeneous on the micron scale. The absolute accuracy of this approach, which depends on errors in the relative intensities, the filter thickness, and the peak and background models used in the fit, is illustrated below for two very different standard materials.

---

The authors are in the Isotope and Nuclear Chemistry Division of Los Alamos National Laboratory, Los Alamos, NM 87545. They gratefully acknowledge the assistance of D. S. Burnett in providing the carbonaceous chondrite samples and assisting in the data acquisition. This work was supported by the USDOE Office of Basic Energy Sciences under Geochemistry project KC-04-03-02; and by an IGPP grant, Nuclear Microprobe Trace Element Analysis for Geologic Materials (T. M. Benjamin).

### *NBS Standard Reference Material #610*

Reference material #610 contains 61 elements, at nominal concentrations of 500 ppm, in a Ca/Na/Al silicate matrix. The resulting PIXE spectrum is extremely complex, as shown in Fig. 1. This spectrum was taken in 43 min with 8 nA of 3MeV protons focused to a 20 $\mu$ m spot and an 80.675mg/cm<sup>2</sup> Al filter in addition to the standard 20.335mg/cm<sup>2</sup> Be filter required to prevent backscattered protons from entering the Si(Li) detector. An integrated current of 16.71  $\mu$ C was obtained at 16.5% dead time. We also took a similar spectrum of exactly the same spot, using a 13.117mg/cm<sup>2</sup> Al filter, with 4 nA of beam current in a count time of 46 min, and obtained 7.27  $\mu$ C at 17.7% dead time.

The purpose of the 80mg/cm<sup>2</sup> Al filter is to reduce counts entering the detector from low-energy x rays and thereby enable an increase in beam current and greater sensitivity for elements with high-energy x rays. As shown in Table 1, the two-fold increase in beam current obtained with this approach has halved the uncertainty for the elements Ru-Sb (x-ray energy >19 keV) and reduced the error for elements Rb-Mo and U (x-ray energy >13 keV). (Uncertainties listed in Table 1 result primarily from counting statistics errors, but they also contain contributions from the fitting error, compounded by the uncertainty in the element used as the concentration reference.) The trade-offs for use of a thick filter are complete loss of information, through filter attenuation, for elements whose x-ray lines are below 6 keV and greatly increased counting statistics error for elements with lines between 6 & 8 keV (Mn-Cu and La-Hf). Another side effect of this approach is that the fitting routine returns nonsensically high concentrations (coupled with even higher uncertainties) for La, Ce, and Pr. This behavior occurs because only minor-intensity, severely attenuated L lines for these elements are found above 6 keV. In fact, the absolute number of counts represented by the La concentration is less than one, in a region of the spectra where counting statistics errors are at least  $\pm 5$  counts. Therefore, the abnormally large concentrations reported for these elements are an artifact of fitting insignificant variations in the number of counts per channel in this region of the spectrum, and they should be considered meaningless.

Results of the two differently filtered analyses are interesting to compare because any differences should be due primarily to inaccuracies in the spectrum fitting procedure. The other source of a difference in the two analyses would be an error in the determination of the filter thicknesses; however, we have minimized this source of error by using previously characterized filters and by double checking the Ca K $\alpha$ /K $\beta$  peak ratio, which should be extremely sensitive to the filter thickness, in the 13.117mg/cm<sup>2</sup> Al filter spectrum. For example, a 1% error in the thickness of the 13.117mg/cm<sup>2</sup> filter would result in a 20% error in the Ca K $\alpha$ , a 5% error in the Ca K $\beta$ , and a negligible error above 8 keV. Of course, an error in the energy calibration would also cause inaccuracies in the fitting of both spectra. In this case, the energy calibration was obtained from the spectrum of a diopside glass sample, doped with Zn, Ge, Br, and Ag to provide well-resolved peaks over a wide energy range, and run just prior to the NBS standard. The excellent agreement between the calculated spectrum, drawn as the uppermost solid line in Fig. 1, and the experimental data (vertical dashes give  $\pm 1\sigma$  counting statistics) show the high quality of the spectrum fitting model.

The weighted mean of the ratio of the thin and thick filter analyses, calculated as  $\bar{x} = (\sum x/\sigma^2)/(\sum 1/\sigma^2)$  where  $x$  is the measured ratio, is given in Table 2 as  $1.00 \pm 0.01$ , showing excellent agreement. In Table 2 the uncertainty in the mean has been calculated as  $\sigma_s = 1/\sqrt{\sum (1/\sigma^2)}$ . Note that calculation of  $\sigma_s$  does not include any uncertainty in the reference values, and therefore  $\sigma_s$  is underestimated. The average ratio of the PIXE analyses to the NBS certified concentrations is perfect ( $1.00 \pm 0.02$ ) for the thin filter but off by 5% for the thick filter ( $1.05 \pm 0.02$ ). The uncertainty in the sample distribution is also given in the last column, calculated as  $\sigma_d = \sqrt{\sum [(x - \bar{x})^2/\sigma^2]/\sum (1/\sigma^2)}$ . These values provide a better estimate of the expected error in a single analysis and are of the order of  $\pm 10\%$ .

### *C1 Carbonaceous Chondrites*

The C1 carbonaceous chondrites are the primary source of the solar-system elemental abundances, and as such have been extensively analyzed by a variety of techniques.<sup>4</sup> They provide an excellent reference material for testing the accuracy of PIXE results, because of the wide range of elemental concentrations and the presence of many elements at or below the ppm level. They also provide a type of spectrum-fitting problem different from

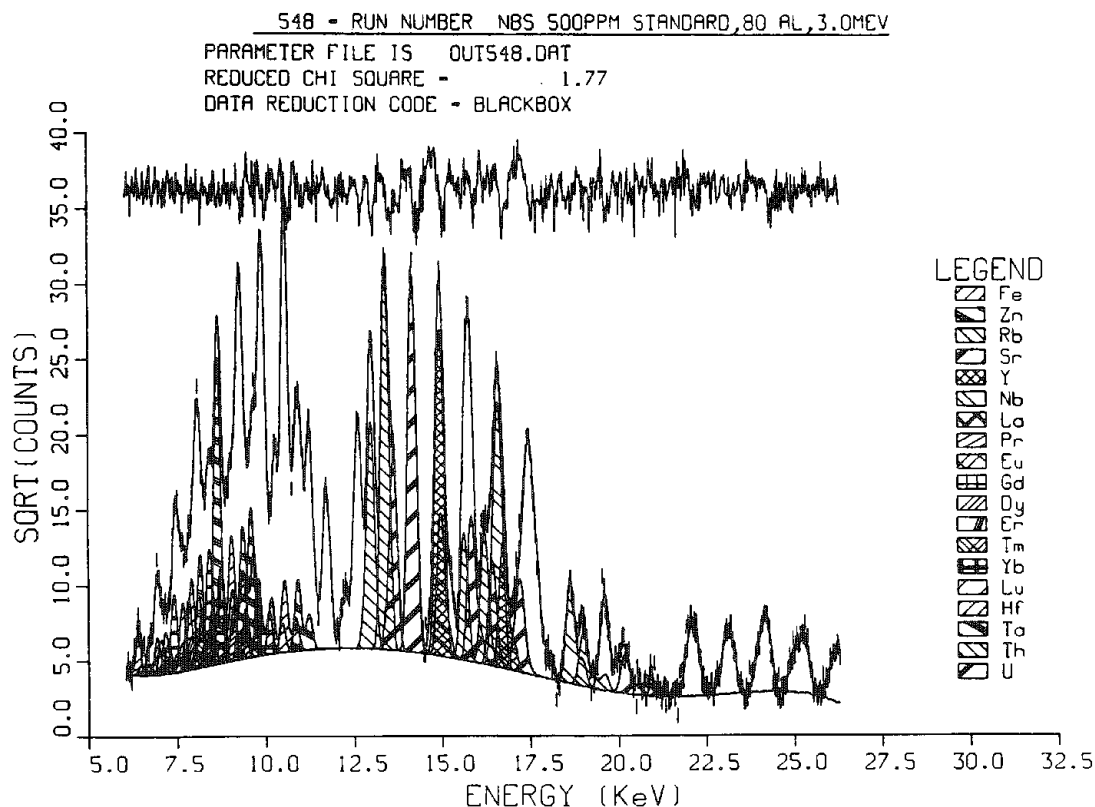


FIG. 1.--PIXE spectrum of NBS SRM #610, showing peak envelopes for fifteen highest concentration elements. Envelopes for 48 additional elements are superimposed to obtain fit to experimental data. Upper horizontal line is magnified plot of residual.

NBS #610. NBS #610 contains a large number of elements, all present at about the same high concentration. In the CI carbonaceous chondrites, the K lines of even trace elements are prominent in the PIXE spectra, and their peaks overlaid essentially all of the less intense L lines. Our analysis of these spectra has yielded minimum practical detection limits for the elements with K lines, but has also shown that the fitting procedure does not adequately treat the weak L lines.

Spectra for three homogenized and pressed samples of each of two CI carbonaceous chondrites, Orgueil and Ivuna (provided by D. S. Burnett, Caltech), were obtained with 200nA beams of 3.0MeV protons and approximately 4mm<sup>2</sup> spot sizes. Spectra were filtered by a thick, 106.909mg/cm<sup>2</sup> Al filter and 20.335mg/cm<sup>2</sup> Be. To determine minimum practical detection limits, 8h count times were used to obtain between 3000 and 5300μC integrated charge at 5 to 25% deadtime. Results for the six analyses are given in Tables 3 and 4.

As noted before, the spectrum-fitting model assumes Gaussian peak shapes. That is an oversimplification, because large peaks show obvious low-energy tails due primarily to Compton scattering and incomplete charge collection in the detector. The spectrum-fitting model is currently being improved to include this effect; however, for the present analyses only the low-energy region above 8.4 keV has been fit in order to avoid the low-energy tails on the Fe and Ni Kα peaks. Even so, results for Dy through W are probably affected by the low-energy tail on the Ni Kβ and are meaningless. Elements Sb through Tb have no major lines in the region of fit, and thus are not included in Tables 3 and 4. The remaining elements from Re through U have weak L lines that, because of the less than 1 ppm concentrations involved, should not be detectable. For example, the most favorable case for in these samples for detection of an L line overlaid by a K line involves a K/L ratio of roughly 100:1. (The average ratio is about 300:1.) In the ideal case, the fitting program should return small concentrations with large uncertainties for these elements. However, as can be seen in Tables 3 and 4, the calculated uncertainties do not seem

TABLE 1.--NBS SEM 610-500 ppm glass.

Concentrations-ppm (K-Lines)						Concentrations-ppm (L-Lines)					
Element	NBS*	PIXE (13.117 mg/cm <sup>2</sup> Al)		PIXE (80.675 mg/cm <sup>2</sup> Al)		Element	NBS*	PIXE (13.117 mg/cm <sup>2</sup> Al)		PIXE (80.675 mg/cm <sup>2</sup> Al)	
		Conc.	1 $\sigma$	Conc.	1 $\sigma$			Conc.	1 $\sigma$	Conc.	1 $\sigma$
19 K	(461)	0	1229			52 Te	X	0	564		
20 Ca	(85760)	87722	2037			53 I		0	173		
21 Sc	X	306	100			55 Cs	X	555	114		
22 Ti	(437)	455	32			56 Ba	X	973	99		
23 V	X	489	21			57 La	X	814	64	28098	67684
24 Cr	X	489	15			58 Ce	X	631	59	6641	26199
25 Mn	485	433	17	347	1461	59 Pr	X	510	48	2137	10790
26 Fe	458	499	15	656	205	60 Nd	X	594	35	0	6170
27 Co	(390)	417	15	356	126	62 Sm	X	613	29	0	1148
28 Ni	458.7	446	14	354	54	63 Eu	X	751	50	838	972
29 Cu	(444)	462	13	413	27	64 Gd	X	545	25	138	521
30 Zn	(433)	489	14	484	16	65 Tb	X	601	28	401	423
31 Ga	X	473	14	445	14	66 Dy	X	419	27	253	210
32 Ge	X	438	12	444	11	67 Ho	X	526	24	303	190
33 As	X	340	11	341	10	68 Er	X	542	38	614	126
34 Se	X	114	6	117	7	69 Tm	X	532	22	488	134
35 Br		0	5	0	5	70 Yb	X	592	33	699	106
37 Rb	425.7	446	15	452	10	71 Lu	X	491	21	469	70
38 Sr**	515.5	515.5	11.5	515.5	7.7	72 Hf	X	490	25	468	57
39 Y	X	472	17	462	11	73 Ta	X	446	27	509	53
40 Zr	X	443	20	448	13	74 W	X	464	22	423	42
41 Nb	X	469	20	452	12	75 Re	X	0	24	22	29
42 Mo	X	423	19	421	12	76 Os		0	15	13	21
44 Ru		0	7	0	4	77 Ir		5	20	60	21
45 Rh		6	11	11	6	78 Pt		16	16	24	21
46 Pd		0	8	9	5	79 Au	(25)	13	11	24	10
47 Ag	(254)	280	27	234	13	80 Hg	X	0	20	0	18
48 Cd	X	275	33	265	16	81 Tl	(61.8)	70	10	69	8
49 In	X	490	50	446	25	82 Pb	426	417	18	413	14
50 Sn	X	471	61	419	31	83 Bi	X	382	20	335	17
51 Sb	X	345	92	344	48	90 Th	457.2	502	25	552	18
						92 U	461.5	434	21	463	14
Reduced X <sup>2</sup>						3.04					
						1.78					

\* Values are certified unless in parentheses; X's signify that NBS claims that the element is nominally present at 500 ppm.

\*\* Sr chosen for internal standard. All concentration values obtained by normalization, Sr uncertainty included in all standard deviations. Note that results would be essentially unchanged had Ca, readily measured by electron microprobe, been chosen as the internal standard.

TABLE 2.--Assessment of the data.

	Ratio		Number of elements	Weighted Average	$\sigma_s$	$\sigma_d$
	Conc 13.117/conc 80.675					
A	Conc 13.117/NBS certified		43**	1.003	0.012	0.077
B*	Conc 13.117/NBS estimated		7	.999	0.014	0.076
C*	Conc 13.117/NBS cert+est		8	1.057	0.014	0.047
D*	Conc 80.675/NBS certified		15	1.028	0.010	0.068
E*	Conc 80.675/NBS estimated		7	1.046	0.015	0.088
F*	Conc 80.675/NBS cert+est		6	1.029	0.026	0.11
G*	Conc 80.675/NBS cert+est		13	1.042	0.013	0.089

\* Assumes 0 uncertainty in NBS values; this underestimates  $\sigma$ , resulting in somewhat uncertain values of the listed averages and  $\sigma_d$  while underestimating  $\sigma_s$ .

\*\* Excludes La.

nearly large enough. We do not know at this time what factors are responsible for the low error estimates. For this reason, the L line elements, except for Pb, have not been considered further.

Tables 5 and 6 give the weighted averages of the concentration results for the K line elements and Pb. Also included are uncertainties in the averages, calculated as for the NBS #610 sample. Since detection limits are nominally assigned at the  $2\sigma$  level, the information in column four can also be interpreted as showing half the minimum practical PIXE detection limits for the low-concentration elem The detection limits are then of the order of 0.1 to 0.5 ppm, showing excellent potential sensitivity for the PIXE method. Elements for which the ratio of the two uncertainties is ten or greater (Cu, Zn, Ge, Se, Mo, and Sr) suggest sample heterogeneity. The ratio of the weighted average concentration to the accepted reference concentration (shown in the seventh columns) is close to  $1 \pm 2\sigma$  for most, but not all, the elements. The weighted averages of the ratios are  $1.02 \pm 0.01$  and  $1.008 \pm 0.004$ , showing excellent average agreement between the analyses and the reference values. However, the uncertainty in the sample distribution (0.12 for Orgueil and 0.07 for Ivuna) is a better measure of the error to expect in a single measurement.

TABLE 3.--Elemental analysis for Orgueil.

Element		Concentrations in ppm					
		Orgueil**	Conc.	$\sigma_s$	Conc.	$\sigma_s$	Conc.
28	Ni*	11000	11000	29	11000	20	11000
29	Cu	112	104.0	6.7	289.0	5.1	128.3
30	Zn	308	326.9	2.7	327.0	1.8	188.4
31	Ga	10.1	10.3	1.0	10.27	.68	11.01
32	Ge	32.2	38.48	.64	36.10	.40	31.26
34	As	1.91	2.60	.43	1.55	.28	2.01
34	Se	18.2	21.90	.42	19.87	.27	17.55
35	Br	3.56	4.17	.33	4.00	.21	2.86
37	Rb	2.30	2.54	.18	2.48	.12	1.438
38	Sr	7.91	9.03	.13	7.69	.10	8.290
39	Y	1.50	1.36	.15	1.092	.096	1.231
40	Zr	3.69	4.27	.12	4.075	.093	3.798
41	Nb	.250	.38	.10	.178	.080	.336
42	Mo	.920	1.03	.11	1.296	.087	1.013
44	Ru	.714	.44	.13	.78	.10	.741
45	Rh	.134	.02	.15	.24	.12	.05
46	Pd	.557	.26	.18	.46	.14	.58
47	Ag	.220	0	.22	.21	.18	.43
48	Cd	.673	.97	.29	.61	.23	.12
49	In	.0778	.48	.37	0	.32	.30
50	Sn	1.680	.86	.55			
66	Dy	.242	0	145	212	97	245
67	Ho	.054	0	65	42	42	122
68	Er	.160	0	30	0	20	26
69	Tm	.022	47	23	0	14	0
70	Yb	.166	0	14	12.7	8.9	13.5
71	Lu	.0243	0	10	0	6.1	1.6
72	Hf	.119	0	6.2	4.0	4.1	0
73	Ta	.017	5.0	4.1	8.8	2.6	8.6
74	W	.089	0	3.4	11.0	2.1	13.1
75	Re	.0369	0	2.0	0	1.3	0
76	Os	.699	1.3	1.8	2.8	1.1	1.31
77	Ir	.473	2.7	1.6	2.2	1.0	2.62
78	Pt	.953	3.8	1.6	5.2	1.0	4.29
79	Au	.145	1.8	1.0	1.67	.65	.70
80	Hg	.390	0	1.1	.04	.70	.68
81	Tl	.143	1.65	.61	1.49	.39	1.00
82	Pb	2.430	2.47	.48	3.64	.30	2.42
83	Bi	.111	.24	.50	0	.32	0
90	Th	.0286	0	.32	0	.25	0
92	U	.0081	0	.28	.20	.21	0

\*Normalized to Orgueil Ni value given Anders and Ebihara (1982).

\*\*Orgueil values from Anders and Ebihara (1982).

## Conclusions

The primary advantage of the PIXE technique is the ability to analyze rapidly a large number of elements simultaneously at the ppm level. As shown in the analysis of the NBS standard #610, the spectrum fitting procedure can deconvolute even extremely complex spectra with individual peak fitting errors of 10 to 30 ppm (3 to 8% of the actual concentrations) and with absolute accuracy that is  $\pm 7$ -10% for an individual analysis and nearly perfect on average. Long count time analyses of two CI carbonaceous chondrites give the same results and further show that minimum practical detection limits, in complex thick targets, for the PIXE technique are about 0.1 to 0.5 ppm.

## References

1. T. M. Benjamin et al., "Development and application of the Los Alamos nuclear microprobe: Hardware, software, and calibration," *Microbeam Analysis--1985*, 235-240.
2. P. S. Z. Rogers et al., "Geochemical applications of nuclear microprobes," *Nuclear Instruments and Methods* B3 231: 671-676, 1984.
3. D. D. Cohen, "A radially dependent photopeak efficiency model for Si(Li) detectors," *Nuclear Instruments and Methods* 178: 481-490, 1980.
4. E. Anders and M. Ebihara, "Solar-system abundances of the elements," *Geochim. et Cosmochim. Acta* 46: 2363-2380, 1982.

TABLE 4.--Elemental analysis for Ivuna.

		Concentrations in ppm					
Element		Conc.	$\sigma_s$	Conc.	$\sigma_s$	Conc.	$\sigma_s$
28	Ni*	11000	21	11000	19	11000	33
29	Cu	96.8	4.7	101.2	4.3	116.1	8.1
30	Zn	209.5	1.8	286.6	1.7	298.7	2.7
31	Ga	8.18	.69	9.09	.64	12.42	.98
32	Ge	32.28	.43	33.73	.39	32.70	.58
33	As	1.80	.29	2.62	.26	.41	.40
34	Se	19.22	.29	19.33	.26	18.09	.38
35	Br	3.97	.23	5.40	.21	6.52	.31
37	Rb	1.26	.12	1.73	.11	2.62	.17
38	Sr	7.461	.094	7.60	.091	8.296	.098
39	Y	1.29	.10	1.380	.092	1.30	.14
40	Zr	3.507	.086	3.931	.085	3.593	.092
41	Nb	.171	.074	.366	.073	.223	.080
42	Mo	.924	.079	3.069	.084	1.125	.083
44	Ru	.598	.092	.917	.092	.57	.10
45	Rh	.03	.11	.09	.11	.18	.12
46	Pd	.34	.13	.48	.12	.53	.14
47	Ag	.11	.15	.51	.16	.25	.18
48	Cd	.26	.20	.38	.20	.98	.24
49	In	.23	.26	.10	.29	.12	.32
50	Sn	3.17	.39				
66	Dy	109	97	0	89	1091	151
67	Ho	0	43	0	39	29	59
68	Er	0	20	0	18	2	30
69	Tm	0	15	1	14	0	20
70	Yb	13.7	9.3	7.0	8.6	0	13
71	Lu	0	6.4	0	6.0	10.2	9.0
72	Hf	0	4.1	0	3.7	25.2	5.5
73	Ta	9.4	2.7	10.6	2.5	5.0	3.9
74	W	10.3	2.2	11.3	2.1	39.4	3.2
75	Re	0.5	1.4	1.7	1.3	0	1.9
76	Os	3.3	1.2	1.9	1.1	4.9	1.6
77	Ir	2.7	1.1	4.0	1.0	4.0	1.5
78	Pt	4.4	1.1	4.17	.99	6.9	1.5
79	Au	1.80	.69	1.81	.64	.75	.95
80	Hg	.26	.74	0	.69	1.7	1.0
81	Tl	.94	.41	1.83	.38	1.96	.56
82	Pb	2.04	.31	2.57	.32	4.05	.34
83	Bi	0	.34	0	.31	0	.45
90	Th	0	.23	0	.23	0	.25
92	U	0	.20	.05	.20	0	.19

\*Normalized to Orgueil Ni value given Anders and Ebihara (1982).



TABLE 5.--Concentration averages and ratios for Orgueil.

Element	Weighted Average (ppm)	$\sigma_s$ (ppm)	$\sigma_d$ (ppm)	$\frac{\sigma_d}{\sigma_s}$	Concentration Ratio**	$\sigma_s$
28 Ni*	11000	12				
29 Cu	181.5	3.1	100	33	***1.621	.028
30 Zn	257.8	1.1	85	80	***.837	.0036
31 Ga	10.63	.40	.45	1.1	1.052	.040
32 Ge	34.10	.24	3.5	14	***1.059	.0075
33 As	1.93	.17	.43	2.6	1.010	.089
34 Se	19.03	.16	1.96	12	***1.046	.0088
35 Br	3.50	.13	.73	5.6	.983	.037
37 Rb	1.964	.070	.65	9.2	.854	.030
38 Sr	8.232	.060	.60	10	***1.041	.0076
39 Y	1.199	.058	.11	2.0	.799	.039
40 Zr	4.000	.056	.23	4.1	1.084	.015
41 Nb	.290	.048	.10	2.2	1.16	.19
42 Mo	1.118	.052	.16	3.1	1.215	.057
44 Ru	.689	.061	.16	2.7	.965	.085
45 Rh	.110	.071	.12	1.7	.82	.53
46 Pd	.467	.084	.15	1.8	.84	.15
47 Ag	.25	.11	.21	1.9	1.14	.50
48 Cd	.48	.14	.41	3.0	.71	.21
49 In	.24	.19	.23	1.2	3.1	2.4
82 Pb	2.88	.18	.71	3.9	1.185	.074

Weighted average of the ratio is 1.022 with  $\sigma_s = .011$  and  $\sigma_d = .12$

\*Normalized to Orgueil Ni value given Anders and Ebihara (1982).

\*\*Normalized to Orgueil (Anders and Ebihara, 1982).

\*\*\*Too heterogeneous to be included in average.

TABLE 6.--Concentration averages and ratios for Ivuna.

Element	Weighted Average (ppm)	$\sigma_s$ (ppm)	$\sigma_d$ (ppm)	$\frac{\sigma_d}{\sigma_s}$	Concentration Ratio**	$\sigma_s$
28 Ni*	11000	12				
29 Cu	101.4	3.0	7.5	2.5	.905	.27
30 Zn	260.0	1.1	50	44	***.844	.0036
31 Ga	9.37	.42	1.9	4.4	.928	.042
32 Ge	33.00	.26	.81	3.1	1.025	.0081
33 As	1.90	.17	.99	5.7	.995	.089
34 Se	19.04	.17	.59	3.4	1.046	.0093
35 Br	5.10	.14	1.2	8.4	1.433	.039
37 Rb	1.720	.073	.59	8.0	.748	.032
38 Sr	7.768	.054	.44	8.0	.982	.0068
39 Y	1.331	.061	.053	.9	.887	.041
40 Zr	3.683	.051	.23	4.5	.998	.014
41 Nb	.256	.044	.10	2.4	1.02	.18
42 Mo	1.669	.047	1.2	25	***1.814	.051
44 Ru	.702	.055	.19	3.6	.983	.077
45 Rh	.096	.065	.074	1.1	.72	.49
46 Pd	.448	.075	.096	1.3	.80	.13
47 Ag	.284	.094	.21	2.3	1.29	.43
48 Cd	.49	.12	.36	2.9	.73	.18
82 Pb	2.82	.19	1.0	5.5	1.160	.078

Weighted average of the ratio is 1.0078 with  $\sigma_s = .0042$  and  $\sigma_d = .067$ .

\*Normalized to Orgueil Ni value given in Anders and Ebihara (1982).

\*\*Normalized to Orgueil (Anders and Ebihara, 1982).

\*\*\*Too heterogeneous to be included in average.

## EDS MICROANALYSIS APPLIED TO THE STUDY OF THE PYRITE COMPLEX ORE FROM RIO TINTO, HUELVA (SPAIN)

F. A. Calvo, J. M. Guilemany, J. M. Gómez de Salazar, A. Ureña, and A. Aguilar

Controversy about the genesis of stratiform sulfide deposits has been a constant among researchers<sup>1-3</sup> and continues to the present day. Hydrothermal, direct magmatic, and exhalative-sedimentary hypotheses have been proposed; the last one seems to be the most widely accepted at present. Various authors<sup>4-6</sup> have believed in each of these hypotheses as the appropriate one for the Rio Tinto pyrite complex ore.

Because the knowledge of the ore microstructure is of the greatest importance for metallurgical treatment and genesis studies, samples from Rio Tinto (under gossan zone) have been examined by SEM (scanning electron microscopy) and analyzed by the EDS (energy-dispersive x-ray spectrometry) technique.<sup>7</sup>

### *Experimental*

A JEOL JSM-35-C scanning electron microscope with a KEVEX 7077 microanalyzer and a ZAF-MAGIC-V data correction system were used. Work conditions were: 25 kV, work distance 39 mm, preset 150 s, reference current 400-450  $\mu$ A, take-off angle 35°. Johnson and Matthey mineral samples were used as analysis standards. Almost 100 EDS microanalysis were made and some backscattered-electron (BSE) images were obtained.

### *Results*

Minerals pyrite ( $\text{FeS}_2$ ), quartz ( $\text{SiO}_2$ ), chalcopyrite ( $\text{Cu}_2\text{S}\cdot\text{Fe}_2\text{S}_3$ ), galena ( $\text{PbS}$ ), sphalerite ( $\text{ZnS}$ ), arsenopyrite ( $\text{FeAsS}$ ), covellite ( $\text{CuS}$ ), enargite ( $3\text{Cu}_2\text{S}\cdot\text{As}_2\text{S}_3$ ), stannine ( $\text{Cu}_2\text{S}\cdot\text{FeS}\cdot\text{SnS}_2$ ), tetrahedrite [ $5\text{Cu}_2\text{S}\cdot 2(\text{Cu}, \text{Fe}, \text{Zn})\text{S}\cdot 2\text{Sb}_2\text{S}_3$ ], cassiterite ( $\text{SnO}_2$ ), and anglesite ( $\text{PbSO}_4$ ) have been identified. Idiomorphic pyrite appears as a major phase with the remainder allotriomorphic phases (Fig. 1). Arsenopyrite and cassiterite also appear idiomorphic (Figs. 2 and 3).

Solid solutions induce nonstoichiometry in all phases, as can be seen from the averaged metal percentages (Table 1). The presence of strange elements is remarkable in sphalerite, galena, covellite, enargite, stannine, and tetrahedrite.

Intracrystalline chalcopyrite and stannine often appear in sphalerite as a result of a solid-state precipitation (Fig. 4). Minor phases such as covellite, enargite, and anglesite are shown in Figs. 5 and 6.

### *Conclusions*

1. Rio Tinto pyrite complex ore is derived from a sulfide massive mineralization where pyrite, chalcopyrite, galena, sphalerite, arsenopyrite, covellite, enargite, stannine, tetrahedrite, cassiterite, and anglesite are present.

2. Covellite, cassiterite, and anglesite are clearly derived from a percolating phenomenon due to the action of meteoric water over the under gossan zone from which the samples were taken.

3. Idiomorphic crystals of pyrite and arsenopyrite, allotriomorphology of the remainder phases, exsolution textures (solid-state precipitation), and nonstoichiometry point to melt (magma) solidification as the direct origin of this ore.

---

Authors Calvo, Gómez de Salazar, Ureña, and Aguilar are at the Departamento de Metalurgia, Facultad de Ciencias Químicas, Universidad Complutense de Madrid, 28040 Madrid, Spain; author Guilemany is at Departamento de Metalurgia, Facultad de Química, Universidad de Barcelona, 08028 Barcelona, Spain.

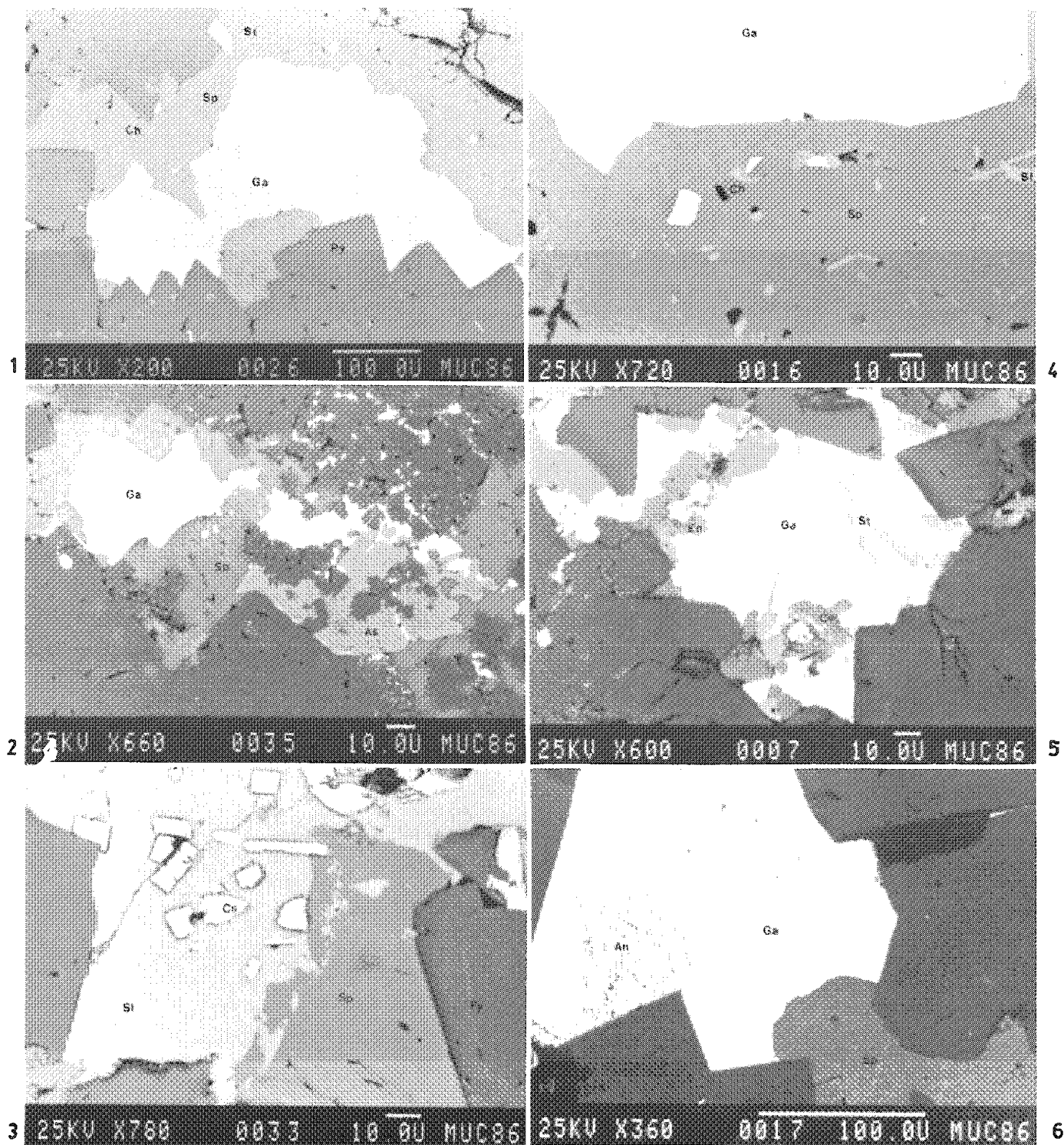


FIG. 1.--Idiomorphic pyrite and other allotriomorphic phases.  
 FIG. 2.--Idiomorphology of arsenopyrite  
 FIG. 3.--Idiomorphology of cassiterite.  
 FIG. 4.--Intracrystalline chalcopyrite and stannine in sphalerite.  
 FIG. 5.--Alteration phases: covellite.  
 FIG. 6.--Alteration phases: anglessite

## References

1. R. L. Stanton, *Ore Petrology*, New York: McGraw-Hill, 1972.
2. A. M. Evans, *An Introduction to Ore Petrology*, Oxford: Blackwell Scientific Publications, 1980.
3. F. A. Calvo and J. M. Guilemany, "Structure and composition of complex pyrite ore from Sotiel (Huelva)", *Microbeam Analysis--1983*, 65-69.
4. A. R. Kinkel Jr., "Observations on the pyrite deposits of the Huelva District, Spain, and their relation to volcanism," *Economic Geology* 57: 1071-1080, 1962.
5. D. Williams, "Further reflections on the origin of the porphyries and ores of Rio Tinto, Spain, *Inst. Min. Metallurgy Bull.*, 1962, 265-266.
6. *Síntesis geológica de la faja piritica del SO de España*, Madrid: Colección Memorias del Instituto Geológico Minero, 1982, vol. 98.
7. J. I. Goldstein et al., *Scanning Electron Microscopy and X-ray Microanalysis*, New York: Plenum Press, 1981.

TABLE 1

PHASE	STOICH. % wt.	ACTUAL AVERAGED % wt.	SOLID SOLUTION ELEMENTS AVERAGED % wt.	
PYRITE	Fe 46.6	46.4		
CHALCOPYRITE	Fe 30.4 Cu 34.6	30.7 34.1		
SPHALERITE	Zn 67.0	68.4	Fe 3.2	Cu 0.7
MARMATITE	Zn 52.0 Fe 15.0	59.2 14.4	Cu 0.9	
GALENA	Pb 86.6	85.9		
ARSENOPYRITE	As 46.0 Fe 34.3	44.7 34.6		
STANNINE	Fe 13.0 Cu 29.5 Sn 27.6	12.0 32.0 22.9	Zn 3.1	
TETRAHEDRITE	Fe Cu Zn Sb	5.9 38.5 2.8 28.1		
TETRAHEDRITE with Ag	Fe Cu Zn Ag Sb	3.8 38.5 8.8 4.8 23.4		
ENARGITE	Cu 48.3 As 19.1	48.1 20.4	Fe 1.2	
CASSITERITE	Sn 78.6	78.7		
ANGLESSITE	PbO 73.6	73.5		

## A STUDY OF APATITE OF GRANITOID BY SIMS

Yong Kang Liu, Shi Tao Zhou, Yu Quan Zhang, and Jen Fu Yu

A series of fluorapatites of granitoid in Xizhang (Tibet) have been analyzed by SIMS. After study of the distribution of rare-earth elements (REE) in them, information about the evolution of that geological body was obtained.

### *Method of Measurement*

All the REE mass spectra are obtained under the same analyzing condition by CAMECA IMS-300. As a first choice, a mineral in which the REE content is too low to be determined is selected, so that the REE can be considered to be blank in it. Then the REE mass spectra in apatite are compared with the blank mineral. Last, the isotopes of REE in apatite are determined against a reference standard.

### *Results*

Normalized by chondrite, the analysis data have been drawn in a diagram in which the REE distribution curves of apatite are accompanied by the curves of its host rock. Some results are as follows:

1. There are two clear depletions of Ce and Eu in apatite.
2. Compared with granitoid the right-hand part of the curve of apatite is more even. Obviously, during the formation of the granitoid body the heavy REE are relatively concentrated in apatite.
3. As is well known, each granite belonging to a different genetic type shows its characteristic REE distribution curve. In our study, the REE distribution curves between apatites and granites exhibit a certain relationship, so that the apatite can be used as a "fingerprinter" mineral to indicate the formation environment of the geological body.

---

Authors Liu, Zhou, and Zhang are at the Institute of Geochemistry of the Academia Sinica, Guiyang, Guizhou Province, People's Republic of China; author Yu is at the Measurement and Technic Research Institute of Shanghai, Shanghai, People's Republic of China.



## Special Biological Symposium Honoring T. A. Hall: Frontiers of Biological Microanalysis

### CAPABILITIES AND LIMITATIONS OF MICROPROBE METHODS IN BIOLOGY

T. A. Hall

A major objective of microprobe methods in biology has been the determination of the local concentrations of chemical elements within tissues. The capabilities of several microprobe methods are compared, with particular attention to electron-probe x-ray microanalysis.

It is argued that only cryopreparative techniques (or possibly the use of wet cells?) can provide specimens where the elemental distributions are fairly free of preparative artifacts. We review the usefulness (and hazards) of cryoprotective agents to facilitate quench-freezing.

For quantitative microanalysis, the use of standards is complicated by beam damage. If standards are used under low-dose conditions, there is no need to match specimen composition closely, but in high-resolution studies it may be preferable to aim at a similar degree of beam damage in specimen and matched standard.

One always wants to improve analytical spatial resolution. With frozen-dried specimens, high-resolution studies have proved feasible. The ultimate limit may be the elemental displacements inherent in dehydration. With frozen-hydrated specimens (essential for the analysis of matrix-free fluid spaces), beam damage may preclude high-resolution studies. One should be able to reduce the electron-beam dose needed for high-resolution analysis by using electron signals instead of the x-ray continuum for mass normalization, and perhaps by using EELS rather than characteristic x rays in very thin specimens.

---

The author's address is 49 Owlstone Road, Cambridge, England CB3 9JH.

## PROTON MICROSCOPY

G. J. F. Legge

The ideal analytical microscope would simultaneously

- (i) generate a high-contrast picture of surface morphology,
- (ii) generate a high-contrast picture of internal morphology,
- (iii) identify each atom in the specimen and its location, and
- (iv) measure other properties of the atoms (isotopic mass) or of the specimen (crystallinity) as they vary through the specimen area and depth.

Thus depth information is required as well as lateral information and this information is required for light elements as well as heavy ones. Each atom in the specimen would be probed once and only once in order to gain this information. Therefore the data-collection system would need to be 100% efficient. All this information would be collected without damage to the specimen or, if there were damage, it would be minimal and known. All information would be permanently recorded and could be quantitatively interrelated. In the face of such a formidable list of requirements naturally all our instrumentation will fail and in general we must resort to the use of several microanalytical instruments to collect a small part of the above information. Within the limits of present development, the many techniques available to the scanning proton microprobe (SPMP) enable it to make significant contributions in all the above areas of information.

### *The Scanning Proton Microprobe*

The SPMP makes use of accelerator technology, both atomic and nuclear techniques of analysis, and extensive data-handling circuitry and software to achieve its versatility. It is particularly suited to tackling problems that call for nondestructive trace elemental microanalysis multielemental quantitative imaging, and nondestructive depth profiling--problems for which the electron microprobe (EMP) and (sputter) ion microprobe (IMP) are less suited. Many of the techniques available are similar or analogous to those of the EMP or IMP--energy-dispersive and wavelength-dispersive x-ray spectroscopy (EDS and WDS), secondary-electron microscopy, and scanning transmission ion microscopy (STIM). The last technique may be used with energy loss or scattering contrast and with bright or dark field microscopy. A second group of techniques has nuclear associations--Rutherford backscattering (RBS) and forward scattering (RFS), nuclear-reaction analysis and channeling contrast microscopy (CCM)--all of which can be used for nondestructive depth profiling. Present limits are about 1  $\mu\text{m}$  for lateral resolution in elemental microanalysis and 0.3  $\mu\text{m}$  in STIM, about 4 nm in depth resolution, and about 1 ppm in elemental sensitivity. The first group of techniques is of most use in biological or medical and geological or mineralogical studies; the second group (which may be employed simultaneously) is of most use in light element detection and in the analysis of materials, including metals and semiconductors. In this paper emphasis is placed on the biological and medical applications, though all the above techniques are covered.

### *Proton-induced X-ray Emission*

In an earlier review of the SPMP it was pointed out that the cross section for ionization of target atoms by protons and electrons of the same velocity is similar but the protons, being much more energetic, have much greater penetrating power and, being much heavier, are less widely scattered.<sup>1</sup> In practice an EMP must operate with an electron-beam velocity greater than the orbital velocity of any electron to be ionized, whereas the greater mass of the proton enables the SPMP to operate at somewhat lower velocities. However, the ionizing interactions for the two beams are comparable. In biology and medicine

---

The author is in the Microanalytical Research Centre of the School of Physics, The University of Melbourne, Parkville, Victoria, Australia 3052.



thin specimens are customarily used. Both electron and proton beams generate secondary electrons that may be used for imaging the surface of the specimen; here the electron beam, with its generally superior focus, is capable of much better spatial resolution. On the other hand, the resolution for elemental maps depends on scattering and the SPMP is capable of maintaining a resolution of 1  $\mu\text{m}$  in a biological specimen more than 10  $\mu\text{m}$  thick. The possibility of utilizing thick specimens is important in the analysis of trace elements because the count rates are so low; this is one area in which the SPMP is of major use. The x-ray bremsstrahlung continuum from deceleration of the heavy protons is negligible and that from the secondary electrons is confined predominantly to low energies, so that the SPMP achieves a peak-to-background ratio which is typically three orders of magnitude better than that of the EMP for EDS of heavy elements.

### *Specimen Preparation*

The preparation of biological specimens for examination in the SPMP is similar to that for examination in the EMP--cryofixation, followed by cryosectioning and freeze drying. The development of these techniques for the SPMP was based on the earlier development of such techniques for the EMP by Ted Hall, whose advice was invaluable.<sup>2</sup> The fabrication and use of strong nylon foils for specimen support also followed the recipe of Hall used by the Cambridge Laboratory.<sup>3</sup> The much greater sensitivity of the SPMP leads to even greater concern over the possibilities of contamination during the preparation of specimens and their foils and in the drying procedure. To date no work on the SPMP has been done with frozen hydrated specimens, but this technique must be developed soon because problems are already being encountered with the loss or movement of lumen content during freeze drying--a problem familiar to EMP users.<sup>4</sup> The relatively poor contrast and lack of morphological information in the secondary electron image of an unstained freeze-dried biological section is a problem for both instruments and the technique of serial sectioning with the staining or freeze drying of alternate sections has been needed for some SPMP studies.

### *Imaging*

A recent review by Hall and Gupta of biological work with the EMP discusses many of the techniques needed and illustrates the good contrast possible even in hydrated sections with STEM imaging.<sup>5</sup> The SPMP is equipped with optical microscopes, but contrast in unstained freeze-dried semithin specimens is poor. Secondary-electron imaging of the surface is used and lately the imaging resolution has been improved to 0.3  $\mu\text{m}$  with STIM.<sup>6</sup> However, this technique is still in the developmental stage. The thickness of the specimens used guarantees that each transmitted particle will have several ionizing interactions in its passage through the specimen, most likely with matrix atoms. Hence the energy loss is a measure of local specimen thickness or density. Scattering events are rarer, involve the nucleus of the scattering atom, and are elastic in nature. Such scattering is known as Coulomb or Rutherford scattering and at extreme forward angles involves no measurable energy loss. With both elastic nuclear scattering and inelastic electronic nondeflecting interactions occurring independently, STIM imaging in four modes is possible--bright field or dark field with energy-loss contrast or scattering contrast.

### *Rutherford Scattering and Light-element Analysis*

Although many analytical problems can be solved with no more than the information obtained from the relative peak heights in x-ray spectra, in many cases an absolute measurement is required and therefore some knowledge of the specimen thickness. The technique of normalizing EDS spectra to the bremsstrahlung background developed by Hall for EMP work was utilized successfully for SPMP work.<sup>7</sup> However, the bremsstrahlung background is much lower in the proton instrument than it is in the electron instrument and an alternative technique is available. Although Rutherford scattering is an elastic process, in the laboratory frame of reference there is an energy exchange between the proton and the target nucleus. The energy of the scattered proton then depends on the angle of scattering and the mass of the target nucleus. At backward angles the energy spectrum of protons scattered from a biological specimen of several microns thickness shows well-resolved peaks associated with oxygen, nitrogen, and carbon, and at forward angles a peak associated with hydrogen is well resolved.<sup>8</sup> Thus it is possible to measure directly the major constituents

of the specimen matrix. As that can be done for any feature simultaneously with the collection of x-ray data on heavier elements, the local specimen thickness can be determined and all elemental concentrations normalized to dry mass and corrected for x-ray absorption and x-ray production cross-sectional dependence on beam energy. This technique is comparable to EELS but the peaks in the proton spectra are resolved for specimens that would be much too thick for EELS measurements.

#### *Depth Profiling and Channeling*

The technique of Rutherford backscattering is frequently used with the SPMP for the purpose of measuring a heavy-element distribution in a light-atomic-mass matrix.<sup>9</sup> A microbeam of alpha particles is generally employed and the scattered particle loses energy on entering and leaving the specimen. Consequently this energy loss is a measure of depth of the scattering nucleus beneath the specimen surface. Such a technique is ideal for the depth profiling of heavy dopant elements in semiconductors with a depth resolution limit of about 4 nm. The method can be extended to depth profile the crystallinity of the surface by aligning the beam with a crystal axis by means of a 2-axis goniometer.<sup>10</sup> Such techniques have been used extensively in work with semiconductors and metals but have not yet been used in biology with its very different surface problems.

#### *Nuclear Reaction Analysis and Isotope Analysis*

The light elements can also be detected and depth-profiled by the detection of nuclear reaction products. Such reactions are highly selective of a particular isotope and are very sensitive. The major problem with such work is that cross sections for these reactions are generally low compared to those for elastic scattering or x-ray production, which must restrict the practical resolution of any elemental mapping. The major call for light elemental depth profiling is in the metals industry and the first SPMP to be established has since devoted a major part of its work to this area.<sup>11,12</sup> An example of applications to biology is the depth profiling of fluorine in bone.<sup>13</sup> In this case the depth profile was achieved by line scanning of a section and gamma rays from the reaction  $^{19}\text{F}(p,\alpha\gamma)^{16}\text{O}$  were detected.

#### *Total Quantitative Scanning Analysis*

Throughout this paper the proton microprobe is referred to as a scanning proton microprobe in order to emphasize the mode of operation generally adopted in this laboratory. It relies on the use of a technique known as total quantitative scanning analysis, in which a computerized data collection system records the position and energy of every detected event generated by a continuously moving beam spot.<sup>14</sup> This technique and its advantages have been discussed in the earlier review.<sup>1</sup> It avoids the inefficiency of standard scanning techniques, insures that all data are quantitative and interrelatable, and minimizes possible specimen damage. A single example is given here.<sup>15</sup> A thin blood smear on a thin nylon foil was snap-frozen in liquid-nitrogen-cooled isopentane and freeze dried. Isolated erythrocytes were scanned and their total spectral information was recorded as three-dimensional blocks of data. One such block of data from a single scanning operation is used to generate the set of intensity plots of Fig. 1. These plots show the distributions of several elements in the erythrocyte. The hydrogen was measured with forward scattering of the proton beam, the carbon with backward scattering, and the other elements with proton-induced x rays. All distributions were measured simultaneously without any windows on the energy spectra collected being set. All have the characteristic biconcave shape (necessarily shown here as uniconcave). If elemental concentrations are required, the carbon distribution can be used to normalize the other elemental distributions. In this case the spatial resolution was about 1.5  $\mu\text{m}$  and the distributions were smoothed with a Gaussian 0.5  $\mu\text{m}$  wide in both lateral directions before plotting.

The above technique of data collection also records all events in time sequence and gives a complete history of the analysis. The mass loss measurements of Hall and Gupta,<sup>16</sup> who recorded changes in bremsstrahlung, can therefore be extended to the automatic measurement of all elemental losses down to intervals of 1 s or less as a standard procedure during microanalysis.<sup>17</sup>

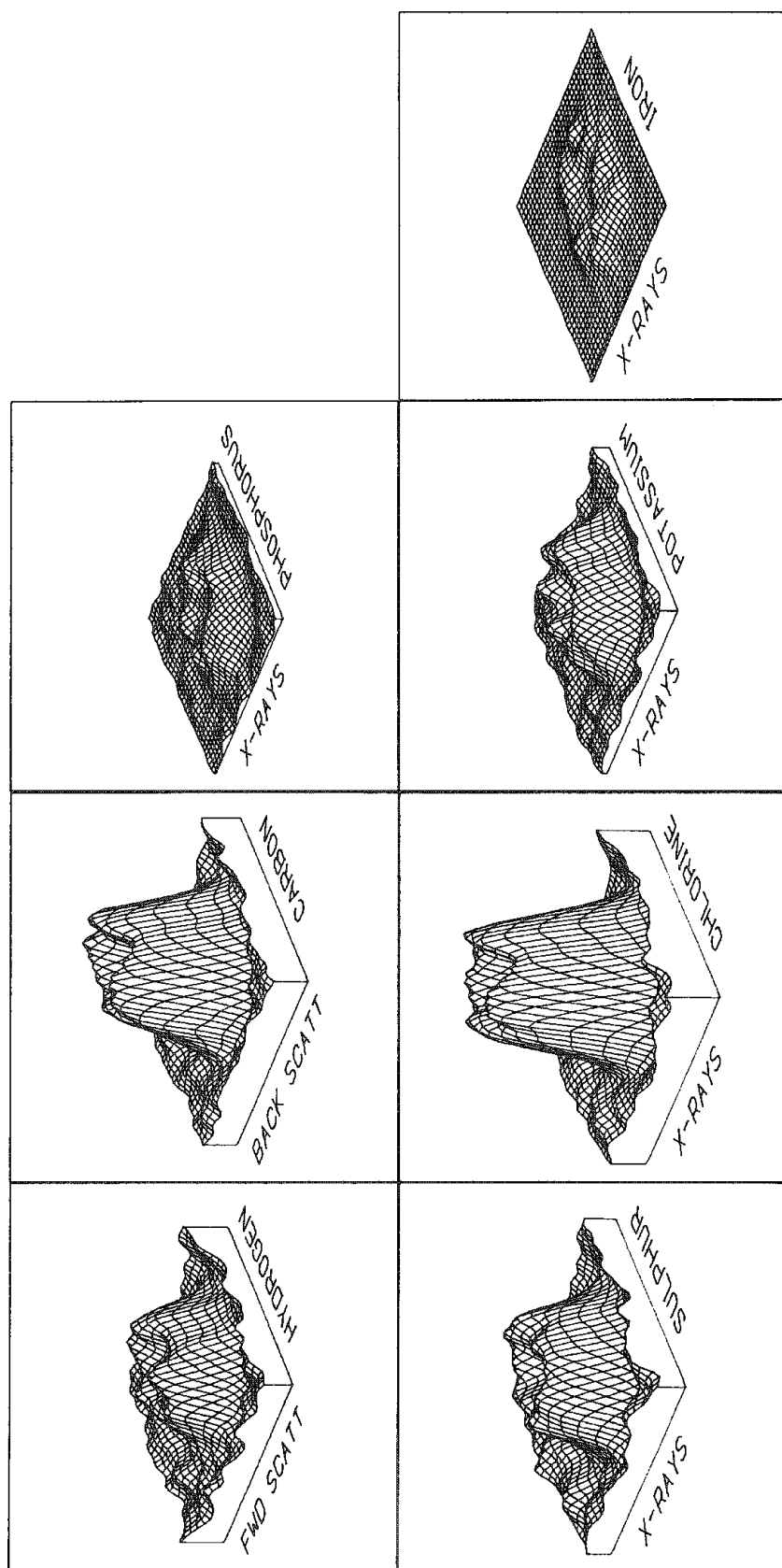


FIG. 1.--Elemental intensity plots of erythrocyte in snap-frozen freeze-dried thin blood smear on thin nylon foil. Erythrocyte was scanned with 150pA beam of 3MeV protons focused to  $1.5\text{ }\mu\text{m}$  and scanned over area of  $10 \times 12\text{ }\mu\text{m}$  for 2 h.<sup>15</sup> Data on all elements were collected simultaneously for forward scattering (for hydrogen), backscattering (for carbon), and EDS (for heavier elements). All data were smoothed with 2-dimensional Gaussian (FWHM =  $0.5\text{ }\mu\text{m}$ ) before being plotted.

## Conclusion

The SPMP currently has a resolution limit of 1  $\mu\text{m}$  for analytical work but there is essentially no diffraction limit and a resolution of 100 nm should be achievable with accelerator improvements and ion source developments. It is a versatile instrument, particularly suited to trace elemental and quantitative analysis. Some of these quantitative methods have been described more fully in a recent paper.<sup>18</sup> The development of these techniques owes much to the earlier work of Ted Hall with electron probes. We are indebted to him also for our preparation techniques and for advice and assistance on numerous other matters associated with elemental microanalysis.

## References

1. G. J. F. Legge, "The scanning proton microprobe," *Microbeam Analysis--1980*, 70.
2. T. A. Hall, "Biological x-ray microanalysis," *J. Microsc.* 117: 145, 1979.
3. P. Echlin and R. B. Moreton, "The preparation of biological materials for x-ray microanalysis," in T. Hall, P. Echlin, and R. Kaufmann, Eds., *Microprobe Analysis as Applied to Cells and Tissues*, London: Academic Press, 1974, 159.
4. R. B. Moreton, P. Echlin, B. L. Gupta, T. A. Hall, and T. Weis-Fogh, "Preparation of frozen hydrated tissue sections for x-ray microanalysis in the scanning electron microscope," *Nature* 247: 223, 1974.
5. T. A. Hall and B. L. Gupta, "The localization and assay of chemical elements by microprobe methods," *Quarterly Review of Biophysics* 16(3): 279, 1983.
6. G. J. F. Legge et al., "Microbeam imaging at micron and submicron resolution," *Nucl. Instr. and Meth.* B15: 669, 1986.
7. T. A. Hall and P. Werba, "Quantitative microprobe analysis of thin specimens: Continuum method," in W. C. Nixon, Ed., *Electronic Microscopy and Analysis*, London: The Institute of Physics, 1971, 146.
8. G. J. F. Legge, C. D. McKenzie, and A. P. Mazzolini, "The Melbourne proton microprobe," *J. Microsc.* 117: 185, 1979.
9. R. A. Brown et al., "MeV helium microbeam analysis: Applications to semiconductor structures," *Mat. Res. Soc. Symp. Proc.* 48: 403, 1985.
10. S. A. Ingarfield et al., "Semiconductor analysis with a channeled helium microbeam," *Nucl. Instr. and Meth.* 191: 521, 1981.
11. J. A. Cookson, A. T. G. Ferguson, and F. D. Pilling, "Proton microbeams, their production and use," *J. Radioanalyt. Chem.* 12: 39, 1972.
12. J. W. McMillan, F. C. W. Pummery, and P. M. Pollard, "Experience in the use of the Harwell nuclear microprobe," *Nucl. Instr. and Meth.* 197: 171, 1982.
13. G. E. Coote and R. J. Sparks, "Fluorine concentration profiles in archaeological bone," *N.Z. J. Archaeol.* 3: 21, 1981.
14. G. J. F. Legge and I. HAMMOND, "Total quantitative recording of elemental maps and spectra with a scanning microprobe," *J. Microsc.* 117: 201, 1979.
15. P. M. O'Brien and G. J. F. Legge, "Elemental microanalysis of individual blood cells," *Biol. Trace Element Res.* (in press).
16. T. A. Hall and B. L. Gupta, "Beam-induced loss of organic mass under electron-microprobe conditions," *J. Microsc.* 100: 177, 1974.
17. G. J. F. Legge and A. P. Mazzolini, "Elemental microanalysis of biological and medical specimens with a scanning proton microprobe," *Nucl. Instr. and Meth.* 168: 563, 1980.
18. A. P. Mazzolini, C. K. Pallaghy, and G. J. F. Legge, "quantitative micromanalysis of Mn, Zn and other elements in mature wheat seed," *New Phytol.* 100: 483, 1985.

## X-RAY FLUORESCENCE WITH SYNCHROTRON RADIATION

K. W. Jones, B. M. Gordon, A. L. Hanson, J. G. Pounds, and George Schidlovsky

X-ray fluorescence (XRF) has long been used to make measurements of trace-element concentrations in biological materials with very high sensitivity. It has not been previously possible to work with micrometer spatial resolutions because of the relatively low brightness of x-ray tubes. This situation is much improved by use of synchrotron storage-ring x-ray sources, since the brightness of the synchrotron source is many orders of magnitude higher than is obtained with the most intense tube sources. These intense sources open the possibility of the use of the XRF technique for measurements with resolutions of approximately cellular dimensions. Developments in the synchrotron source and associated optical components over the next ten years should result in at least an order-of-magnitude improvement in resolution. A description of a current research project at Brookhaven which uses synchrotron radiation-induced x-ray emission (SRIXE) is presented to illustrate a specific application of the method in biology. (The acronym SRIXE is used in analogy to PIXE, which refers to proton- (or particle-) induced x-ray emission.) The example is chosen from the biological area, but obviously SRIXE can be more widely applied.

Our SRIXE research is conducted on the X-26 bending-magnet beam port at the National Synchrotron Light Source (NSLS). Two separate facilities will be available. The second, at present being fabricated, uses a monochromator and an ellipsoidal focusing mirror to produce an image of the x-ray source of approximately  $60 \times 180 \mu\text{m}$ . Imperfections in the mirror will result in aberrations about the focused spot. Thus, a pinhole will be required to produce a clean image  $10 - 30 \mu\text{m}$  in diameter.

The target area for the white light beam line is shown in Fig. 1. The experiment must be carried out in a shielded enclosure (hutch) to protect personnel from exposure to the x rays. The x rays are transported to the hutch through a beam line which is isolated from the storage ring by a  $254\mu\text{m}$  beryllium window. The window modifies the x-ray spectrum, but eliminates the necessity to make measurements in a vacuum. A second  $254\mu\text{m}$  beryllium window is used in the hutch to separate a gas target region, used for atomic physics work, from the beam line vacuum. The photon intensity is monitored by a gas-filled ion chamber with  $7.5\mu\text{m}$  Kapton windows before and after stepper-motor-driven collimating slits, which can be closed to  $10\mu\text{m}$  size. The photon beam is brought out into the laboratory air, helium, or vacuum, for final use. The samples are mounted on stepper-motor-driven x-y-z stages which can be adjusted in  $1\mu\text{m}$  steps. The sample can be mounted in a controlled wet environment if desirable. A ZnS scintillator screen is used to position the beam quickly by use of a microscope-TV sample-viewing system. Further measurements are then made relative to that fiducial mark.

Knowledge of the energy spectrum of the x rays is obtained by calculation from the basic theory of synchrotron radiation. Figures 2 and 3 show the results obtained from such a calculation for our white-light beam line. We have done the calculation for an area of  $1 \text{ mm}^2$  located in the plane of the beam and with a beam current of 1 mA. Since the NSLS is now operating with currents of around 150 mA at injection, the values shown in Fig. 2 can be used to estimate sensitivities for trace-element determinations in a given sample area. Sensitivities for trace element detection can be estimated and measured and are in the region of 10 to a few hundred parts per billion (PPB), depending on the exact assumptions made regarding detectors and x-ray energy spectrum.<sup>1</sup>

In biology, the interaction of toxic and essential elements is of considerable importance in elucidating the mechanism of action of toxic elements in biological systems. It

---

The authors are at Brookhaven National Laboratory (Department of Applied Science), Upton, NY 11973. Development of the x-ray microprobe technology is supported by the Processes and Techniques Branch, Division of Chemical Sciences, Office of Basic Energy Sciences, Office of Basic Energy Sciences, U.S. Department of Energy under Contract DE-AC02-76CH00016; application to biomedical problems is supported by the NIH as a National Biotechnology Resource under Grant RR01838-02.

is necessary to characterize and understand these interactions at the cellular level, as interactions in particular cells may be obscured by the surrounding matrix when conventional bulk chemical analyses are used for trace element determinations. SRIXE is ideal for investigating the interaction between lead, a nonessential element of considerable health significance, and Ca, Fe, Cu, and Zn in brain and other target tissues for lead toxicity. Many brain structures are 0.01 to 1 mm in at least one dimension and have a complex topography. These structures are exceedingly difficult to dissect for conventional analyses, yet sections are easily prepared from frozen whole rodent brains. The full surface of the section is available for visual inspection, and the selected brain structure can be identified and its trace element content measured. The trace element content of the cerebellum is heterogeneous at the microscopic level. The molecular cell layer, the granule cell layer, and the fiber tracts have a characteristic trace-element content which can be related to the biochemical function of these structures. Figure 4 illustrates SRIXE trace element spectrum for a selected region of the cerebellum. The spatial resolution is 50  $\mu\text{m}$ . The characterization of trace elements in these structures provides the framework for investigating the role of trace element interactions in neurobiology and disease processes.

## References

1. See the summary given by A. L. Hanson et al., "Mapping of trace elements with photon microprobes: X-ray fluorescence with focused synchrotron radiation," *Microbeam Analysis--1985*, 227-229, and references cited there.

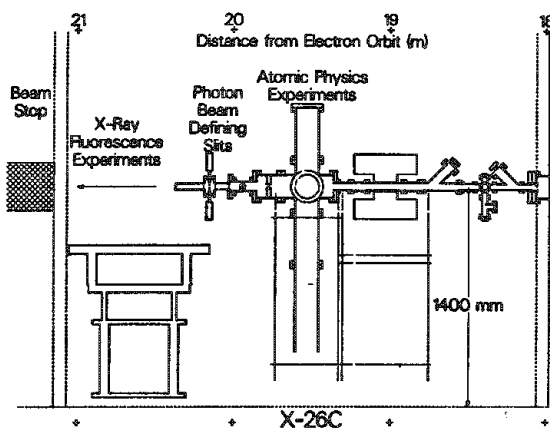


FIG. 1.--Experimental enclosure.

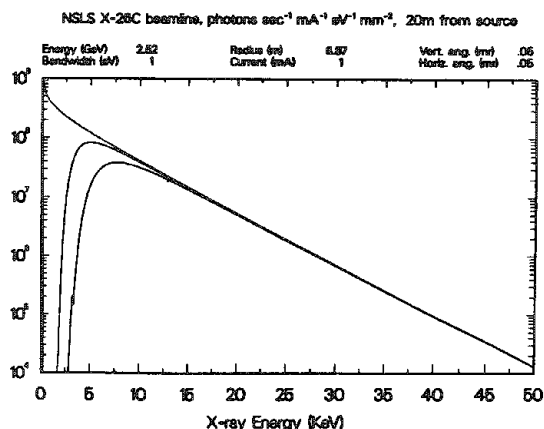


FIG. 2.--Energy spectrum of photons for unfiltered beam (top), atomic physics beam (middle), and x-ray fluorescence beam (bottom); parameters listed above.

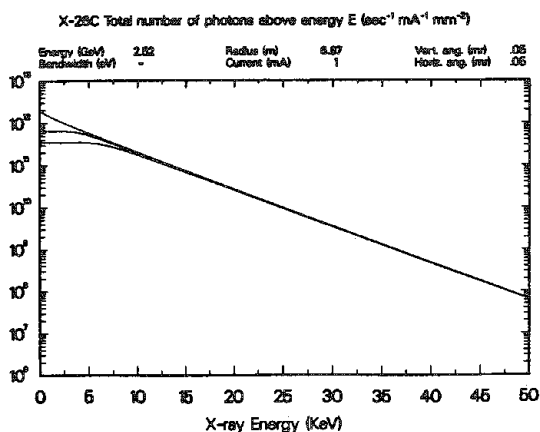


FIG. 3.--Total number of photons/ $\text{mm}^2\text{-mA}$  with energy above E, 20  $\mu\text{m}$  from electron orbit.

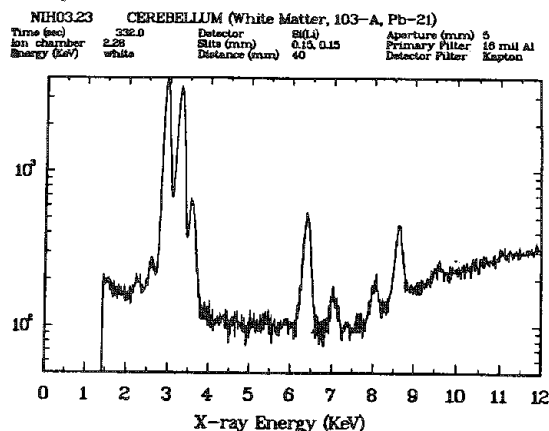


FIG. 4.--SRIXE spectrum from 20 $\mu\text{m}$  section of rat cerebellum; 150 $\mu\text{m}$  spot beam size was used.

## THE PRESENT STATE OF LASER MICROPROBE MASS ANALYSIS (LAMMA) AS APPLIED TO BIOMEDICAL SAMPLES

R. Kaufmann

Although the potential benefits and advantages of laser microprobe mass analysis (LAMMA) have been recognized for some time, the advent of this technique in practical analytical work did not occur before 1978, when the first instrument (LAMMA 500, Leybold-Heraeus) became commercially available. Since that time the technique has matured and gained much acceptance in various analytical fields such as biomedical microprobe analysis, material sciences, organic mass spectrometry, and environmental research.

At present the total number of original reports comes close to 500, including several excellent reviews and survey papers.<sup>1-5</sup> Besides the classical LAMMA 500 instrument primarily used for biomedical work and the LAMMA 1000 version devoted to bulk analysis, other instruments became commercially manufactured such as the LIMA<sup>®</sup> instrument (Cambridge Consultants Ltd.), combining facilities for either transmission or reflection type of geometry.

The present review concentrates on the use of LAMMA in biomedical specimens. Since practically all relevant results have been obtained on LAMMA 500 instruments so far, LAMMA is used throughout as a notation for the technique in general.

### *Basic Principle and Instrumentation*

In principle a laser microprobe consists of an impulse laser and an optical microscope which is used to image the specimen and to focus the incident laser beam onto a selected spot of interest. The interaction of laser light with the solid-state matter strongly depends on irradiance and may cover classical absorption at the low-irradiance end to the formation of a physical plasma at irradiances above  $10^6 \text{ Wcm}^{-2}$ . Usually, theoretical approaches dealing with laser-induced ion formation are based on so-called local thermodynamic equilibrium (LTE) models, which have been also applied to the ion formation process in SIMS. However, for the practice of laser microprobe analysis it has become customary to distinguish between two rather different modes of ion formation:

1. nonthermal laser desorption (LD) as a "soft" surface ionization process at irradiances of  $D \leq 10^8 \text{ Wcm}^{-2}$  and
2. thermal volume evaporation and ionization (laser pyrolysis) at  $D \geq 10^8 \text{ Wcm}^{-2}$ .

Since ion formation occurs in any case during the very short interval ( $\sim 15 \text{ ns}$ ) of the laser impact ( $\lambda = 264 \text{ nm}$ , frequency-quadrupled YAG laser) one can advantageously combine such a laser probe with a time-of-flight (TOF) mass spectrometer. Typical performance data are given in Table 1. A schematic representation of the LAMMA 500 instrument in a version especially updated for biomedical specimen is shown in Fig. 1. This instrument incorporates a UV (250nm) transillumination system which gives sufficient structural information even from unstained tissue sections; in addition, the useful magnification of the optical microscope could thus be improved by a factor of at least 2.5.

### *Quantitative Analysis*

In the present state of the technique and with the lack of a theory unifying all physical effects of ion formation, quantitative analysis is difficult, at least for absolute quantitation. Attempts at quantitation were based on either theoretical grounds (LTE model) or on empirical approaches such as relative sensitivity coefficients (RSC). However, accuracy and precision have remained rather limited so far, except for special cases in which working conditions could be carefully controlled beyond the usual limits.

---

The author is at the Physiological Institute, Department of Clinical Physiology, University of Düsseldorf, Moorenstr. 5, D-4000 Düsseldorf, Federal Republic of Germany.

TABLE 1.--Typical performance data of the LAMMA 500 instrument.

Analytical information		Atomic and/or molecular composition	
Analytical technique		TOF-MS	
Mass range		Typical 1-500 amu (up to 5000 amu attained)	
Mass resolution		$M/\Delta M \approx 800$	
Sensitivity	relative	1-10 ppmW	
	absolute	$10^{-10}$ - $10^{-20}$ g	
(element analysis)			
Detectable elements		All	
Isotopic discrimination		Yes ( 3% SD)	
Lateral resolution (analytical)		0.5-1 $\mu$ m	
Imaging		LM ( $\pm$ ) UVM +	
Sample thickness		0.1-2 $\mu$ m	
Scan or mapping facility		( + )	
Quantitation	relative	+	
	absolute	( + )	

However, in biomedical specimens one aims more often than not at the measurement of concentration gradients, profiles, or ratios rather than at absolute numbers. Since reproducibility can attain  $\pm 10\%$  RSD under favorable conditions for element analysis and  $\pm 3\%$  RSD for isotopic ratio measurements, this form of quantitation can be quite successful, particularly in repetitive biological structures such as red blood cells.

#### Biomedical Applications

The total number of published LAMMA work on biomedical specimens has reached more than 100 titles and cannot be covered within the space available for this abstract. However, it may be worthwhile to outline the "gravity centers" of applications where LAMMA has obviously overcome limitations (of sensitivity and selectivity) imposed by other techniques (mainly EPXMA or ion probe analysis). That appears to apply especially for microprobing of trace elements such as Li, F, Mg, Al, Ca, Mn, Fe, Cu, Pb with a remarkable predominance of Al- and Ca-related problems such as chronic hemodialysis, Alzheimer's disease, concret formation, and Ca turnover in sensory organs.

The other advantageous aspect of LAMMA analysis is the rather short cycle time (typically 10-20 s) for performing one duty cycle. Thus, "chemical histograms" can be obtained from larger populations of biological microentities such as bacteria, spermatozoa, blood cells, and so on. Histograms extending over several hundred individual analyses can be easily collected in a reasonable period of time. This approach has been successfully exploited for example by Lindner and Seydel to characterize the physiological state of bacteria<sup>6</sup> or by Kaufmann and Nachev to determine the distribution statistics of intracellular cations in human red blood cells.<sup>7</sup>

The applications of LAMMA as a special technique in mass spectrometry analysis (especially of thermally labile or nonvolatile organic compounds) has meanwhile also become an established approach in analytical chemistry, in competition with (for example) thermal spray ionization, FAB, or SNMS. In some special cases, in situ microprobing of organic constituents present in biomedical samples could also be successfully achieved, which would concern the possibility of detecting characteristic molecular signals from the compound itself (e.g., lichexanthone in microlichen<sup>8</sup> or glyceollin in soybean specimens<sup>9</sup>) as well as the approach of introducing an atomic label (e.g., F) into the molecule to be checked for.<sup>10</sup>

#### References

1. R. Kaufmann, "Laser microprobe mass analysis (LAMMA): Current state of the art with special emphasis on biomedical applications," *Microbeam Analysis--1982*, 341-357.
2. R. Kaufmann, "Laser microprobe mass spectroscopy (LAMMA) of particulate matter," in K. R. Spurny, Ed., *Physical and Chemical Characterization of Individual Airborne Particles*, Chichester: Ellis Horwood (in press).
3. F. Hillenkamp, "Laser desorption technique of nonvolatile organic substances," *Int. J. Mass Spec. Ion Phys.* 45: 305-313, 1982.
4. P. Schmidt, "Localization of trace elements with the laser microprobe mass



analyzer (LAMMA)," *Trace Elements in Medicine* 1: 13-20, 1984.

5. A. H. Verbueken, F. J. Bruynseels, and R. E. van Grieken, "Laser microprobe mass analysis: A review of applications in the life sciences," *Biomedical Mass Spectrometry* 12: 438-463, 1985.

6. B. Lindner and U. Seydel, "Results on taxonomy and physiological state of bacteria derived from laser-induced single cell analysis," *J. Physique, Colloque C2*, suppl. No. 2, C2-565-C2-568, 1984.

7. R. Kaufmann and C. Nachev (unpublished results).

8. A. Mathey, "LAMMA: New perspectives for lichenology?" *Fresenius Z. anal. Chem.* 308: 249-252, 1981.

9. P. Moesta, U. Seydel, B. Lindner, and H. Griesebach, "Detection of glyceollin on the cellular level in infected soybean by laser microprobe mass analyses," *Z. Naturforsch.* 37C: 748-751, 1982.

10. R. Kaufmann, H. J. Heinen, M. Schurmann, and R. Wechsung, "Recent advantages of laser microprobe mass analysis (LAMMA) as applied to biological and engineering specimens," *Microbeam Analysis--1979*, 63-72.

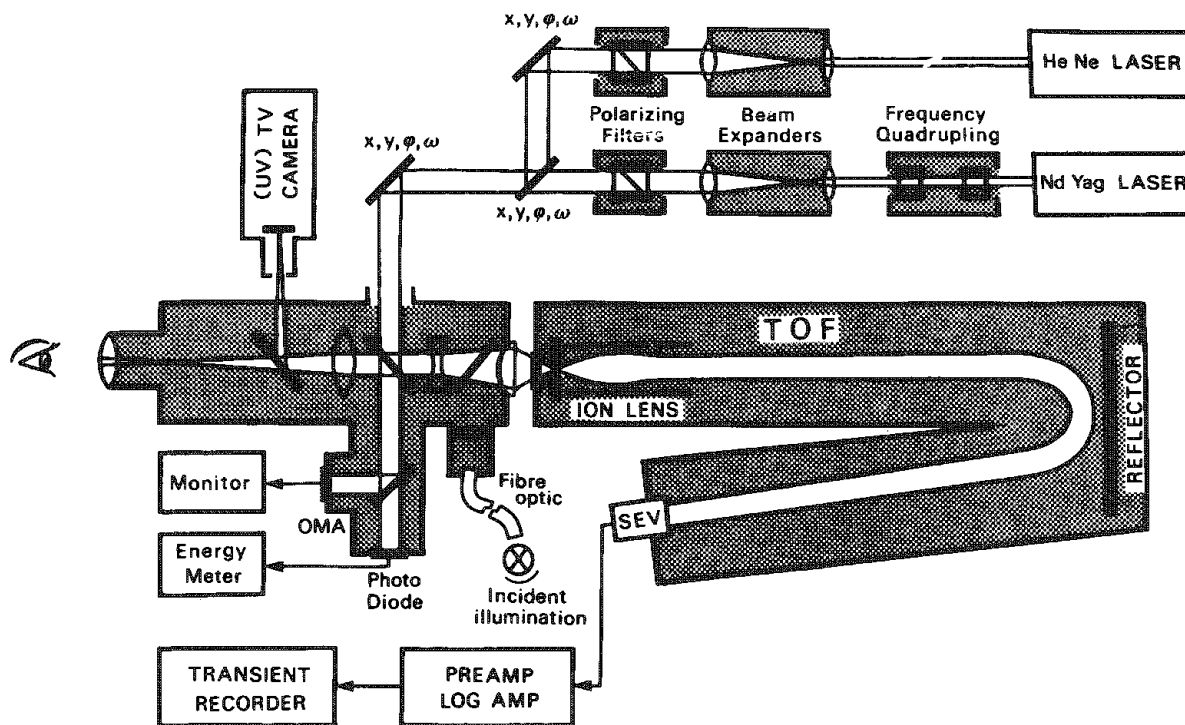


FIG. 1.--Schematic representation of modified LAMMA 500 instrument.

## PHOTOELECTRON IMAGING

O. H. Griffith and G. F. Rempfer

Photoelectron imaging involves subjecting the specimen to ultraviolet light and imaging the emitted electrons.<sup>1,2</sup> Since the specimen itself is the source of electrons, an electron gun is not used. There are several ways in which photoelectron images can be formed. The method with the highest resolution is photoelectron microscopy (PEM, also called photoemission electron microscopy). In a photoelectron microscope the electrons are accelerated and then focused by an electron-lens system similar to that of a transmission electron microscope (TEM). PEM is the electron optical analog of fluorescence microscopy, and shares with it the advantage of imaging an emission signal against a darker background (i.e., a form of dark-field microscopy).

### *Methods*

The photoelectron microscope used in this work is diagrammed in Fig. 1. Light from two short arc mercury xenon lamps is reflected off a highly polished anode and focused on the biological specimen. The UV light illuminates an area much larger than the area imaged at any one time in the PEM, and no scanning is involved. The specimen is located on the cathode of the PEM and is maintained at a high negative potential ( $\sim 30$  kV) so that the emitted electrons are at first accelerated in the cathode-anode gap and then imaged by the objective, intermediate, and projector lenses of the electron-optical system. The final image is formed on a fluorescent screen and fiber-optically coupled to an image intensifier and TV camera, or alternatively on a photographic film. This instrument and the electron lenses are described elsewhere.<sup>3,4</sup>

Specimen preparation for photoelectron microscopy involves growing or placing the sample on a conductive substrate and then fixing and dehydrating (or freezing) the specimen before inserting it into the PEM and evacuating the column. No stains and no metal or carbon coatings are necessary. The uncoated biological specimens are viewed directly in the photoelectron microscope.

### *Results and Discussion*

A representative photoelectron micrograph of a tissue culture cell is shown in Fig. 2. The specimen is a human foreskin fibroblast. The photoelectron image is formed from natural photoemission from the cell surface. We find that the photoelectron yield from cells and other biological specimens is sufficient for images to be formed without any special treatments or coatings. The photoemission from the surface is greater than that from the substrate so that the cell appears bright against the background. Visible in Fig. 2 are the nucleus N, two nucleoli n, and fine detail on the cell surface (including some pits which are probably artifacts of dehydration). These features are visible primarily because of topographic contrast, to which PEM is very sensitive. PEM is a surface technique; internal structures, such as the cytoskeleton and nucleus, are not seen except where they induce topography in the cell surface. Cells that are not well spread may have too much topography for PEM where image detail is lost on the steep slopes. In this sense, PEM is complementary to scanning electron microscopy (SEM), which exhibits poor contrast for fine details on flat cells but has no difficulty with rounded-up cells. Photoelectron images have been obtained of photosynthetic bacteria, thin sections, several types of cultured cells, viruses, and partially condensed DNA.<sup>5</sup>

### *Immunophotoelectron Microscopy*

A recent advance in photoelectron imaging is the use of photoelectron labels to identify specific proteins on cell surfaces and cell organelles.<sup>6,7</sup> The strategy is outlined

Author Griffith is at the Institute of Molecular Biology, University of Oregon, Eugene, OR 97403; author Rempfer is at the Department of Physics, Portland State University, Portland, OR 97207. They are pleased to acknowledge the work of their colleagues Drs. G. Bruce Birrell, Karen K. Hedberg, Mr. Douglas L. Habliston, and Mr. Walter P. Skoczylas. This work was supported by PHS grant CA11695 from the National Cancer Institute and by a grant from the M. J. Murdock Charitable Trust.

in Fig. 3, which shows the analogy between this approach (immunophotoelectron microscopy) and immunofluorescence microscopy. In both cases, monoclonal or polyclonal antibodies are tagged with labels and allowed to bind to specific sites (antigens). In immunofluorescence, the labels are fluorescent dyes, whereas in immunophotoelectron microscopy, the most useful labels are silver-enhanced colloidal gold particles.<sup>8</sup> Since colloidal gold is gaining popularity in SEM, TEM, and optical microscopy, immunolabeling provides a convenient method of comparing results from several different imaging experiments.

An example of immunolabeling is shown in Fig. 4, in which part of a detergent-opened marsupial kidney epithelial cell was double-labeled for microtubule visualization by both immunofluorescence (inset) and immunophotoelectron microscopy. A few of the many labeled microtubules that can be identified in both micrographs are indicated by white arrowheads. There are several differences between the two micrographs. First, the labeled fibers appear much smaller in the photoelectron micrograph, even though the magnification is approximately twice that of the fluorescence micrograph. This feature is the result of the higher resolution of photoelectron microscopy; the fibers are imaged at closer to their true dimensions. A second difference is that sample topography is also seen in the photoelectron micrograph, which allows the simultaneous visualization of labeled and unlabeled structures (e.g., the nucleus and unlabeled cytoskeletal elements indicated by black arrowheads in Fig. 4).

### Summary and Future Directions

The characteristics of PEM are (1) material contrast based on photoelectron quantum yield; (2) a high sensitivity to fine topographical detail due to the effects of the microfields at the specimen surface on the photoelectrons, which are emitted with very low kinetic energies; (3) a theoretical resolution limit of about 5 nm without correction of aberrations; (4) high surface specificity because of very short escape depths of the photoelectrons; and (5) relatively low specimen damage compared with electron-beam methods.

Looking toward the future, the trends in photoelectron imaging in biology are likely to be quite different from the trends in microelemental analysis. PEM and fluorescence microscopy probe the outermost electrons of atoms and molecules, whereas SEM and TEM involve core electrons as well. Thus, PEM and fluorescence microscopy are not techniques for determining elemental analysis. Their strength is in identifying the distribution on antigenic sites. Many cellular components have similar elemental composition. Biological diversity is made possible by rearrangements of a few elements to generate a large number of different proteins, lipids, nucleic acid sequences, and polysaccharides. One can recognize these subtly different structures by combining the contrast of photoemissive labels with the biological specificity of antibodies in the immunophotoelectron microscopy technique. The dimensions of proteins are typically in the range of a few nm to 10 nm, so that single-protein resolution is within the capability of photoelectron microscopy.

### References

1. O. H. Griffith and G. F. Rempfer, "Photoelectron imaging: Photoelectron microscopy and related techniques," in R. Barer and V. E. Cosslett, Eds., *Advances in Optical and Electron Microscopy*, London: Academic Press (in press), 1986, vol. 10.
2. O. H. Griffith and G. F. Rempfer, "Photoelectron imaging in cell biology," *Ann Rev. Biophys. Chem.* 14: 113-130, 1985.
3. O. H. Griffith, G. F. Rempfer, and G. H. Lesch, "A high vacuum photoelectron microscope for the study of biological specimens," *SEM/1981 II*, 123-130.
4. G. F. Rempfer, "Unipotential electrostatic lenses: Paraxial properties and aberrations of focal length and focal point," *J. Appl. Phys.* 57: 2385-2401, 1985.
5. O. H. Griffith, K. K. Nadakavukaren, and P. C. Jost, "The potential role of photoelectron microscopy in the analysis of biological surfaces," *SEM/1984 II*, 633-644.
6. G. B. Birrell, D. L. Habliston, K. K. Nadakavukaren, and O. H. Griffith, "Immunophotoelectron microscopy: The electron optical analogue of immunofluorescence microscopy," *Proc. Natl. Acad. Sci. USA* 82: 109-113, 1985.
7. O. H. Griffith and G. B. Birrell, "Photoelectron microscopy," *Trends in Biochemical Sciences* 10: 336-339, 1985.
8. G. B. Birrell, D. L. Habliston, K. K. Hedberg, and O. H. Griffith, "Silver-enhanced colloidal gold as a cell surface marker for photoelectron microscopy," *J. Histochem. Cytochem.* 34: 339-345, 1986.

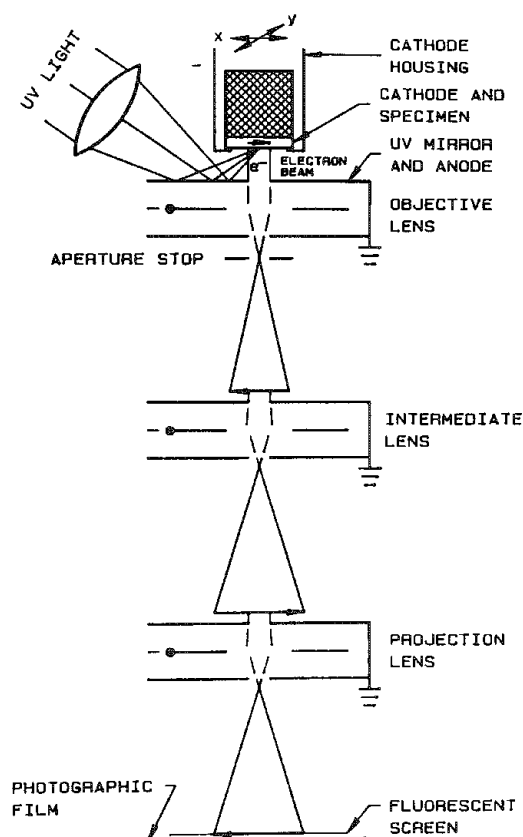


FIG. 1.--Schematic diagram of photoelectronic microscope. Electron lenses can be electrostatic (as shown here) or magnetic.

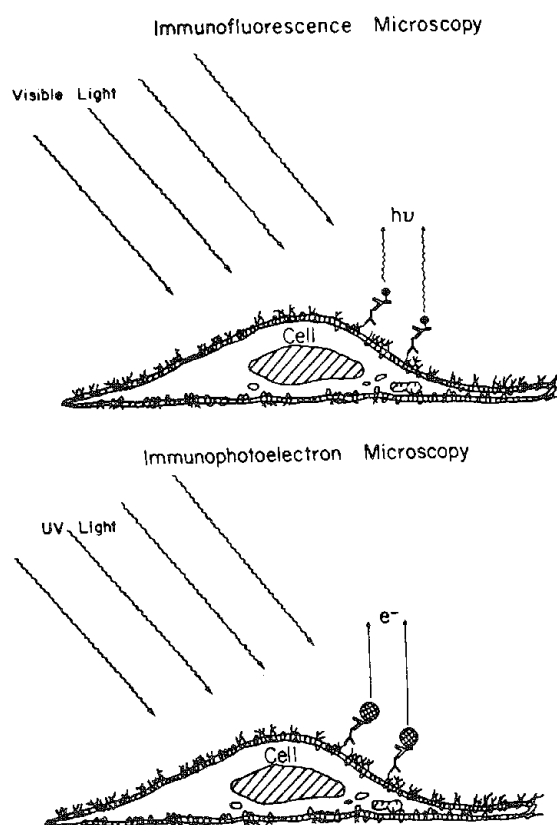


FIG. 3.--Schematic comparison of immunofluorescence experiment (top) with corresponding immunophotoelectron experiment (bottom).



FIG. 2.--Photoelectron micrograph of cultured normal human fibroblasts. Cells were grown on conductive glass disks, removed from culture medium, washed with isotonic buffer, and exposed to glutaraldehyde-containing fixative prior to dehydration through graded series of ethanol-water solutions, Freon 113 and vacuum drying from Freon 113. N is cell nucleus, n are nucleoli.

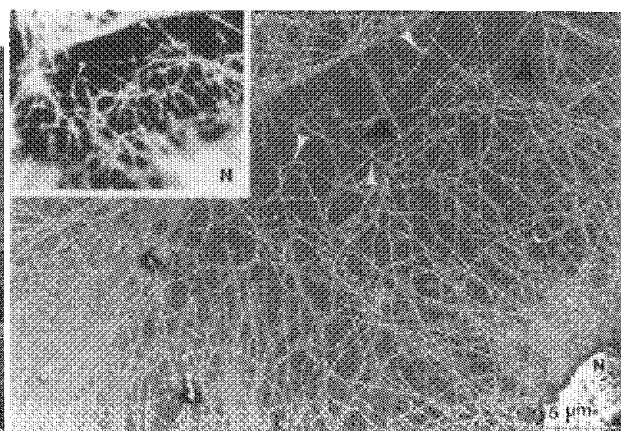


FIG. 4.--Partial view of detergent-opened marsupial kidney epithelial cell (cell line PtK2) labeled for both immunofluorescence and immunophotoelectron visualization of microtubules. Three-step labeling was used: first antibody bound to microtubules, second antibody (recognizing first antibody) carried fluorescent rhodamine molecule, and third antibody (recognizing second antibody) was bound to 20nm colloidal gold marker. N is cell nucleus.

## QUANTITATIVE COMPOSITIONAL MAPPING OF BIOLOGICAL CRYOSECTIONS

C. E. Fiori

Cryo-techniques of biological specimen preparation have been shown to be the best for preserving the location of the constituent chemical elements so that they are as representative of the material in its living condition as is possible. However, when using one of the conventional electron signals such as brightfield, darkfield, or secondary electron, we frequently find that it is difficult or impossible with cryo-prepared specimens to locate the structures we wish to examine. Often, only an image showing the distribution of one or more of the analyte elements (which are usually present at low concentrations) permits us to identify the various biological structures in the specimen.<sup>1,2</sup> Using this method, we analyze every point in a given region of a specimen (i.e., create an image) and then, a posteriori, extract the chemical information we require from the locations in the x-ray image of interest to us. This strategy is very different from that generally used for microanalysis. At first glance, such a procedure seems inefficient and brute force. However, in many situations that is not the case, and in other situations there is no alternative. The purpose of this communication is to discuss such an approach to analysis as practiced in our laboratory at NIH and to comment on several of the procedures that can be used to form quantitative elemental maps.

### *Discussion*

In the first step of any quantitative microprobe analysis of a single point on any type of specimen we extract a deadtime and background-corrected intensity from the raw x-ray counts from the specimen (or a reference standard). We then perform certain mathematical corrections that account for specimen and standard matrix effects. It is obvious that a similar procedure may be applied to x-ray "images." Indeed, many of the same correction procedures are applied and only the details of the application are different. X-ray microanalysis can be performed in many different ways in the various electron columns used in our field: the electron-beam x-ray microanalyzer, the analytical scanning electron microscope, and the analytical electron microscope. We restrict our discussion here to quantitative imaging in a scanning transmission electron microscope (STEM) equipped with an energy-dispersive x-ray detector (EDS).

X-ray data obtained from cryosections can be converted to elemental information in several ways. We shall limit the discussion to describing an application of the "Hall" procedure.<sup>3-5</sup> This powerful algorithm exploits the fact that by counting characteristic x rays, we obtain a measure of the number of analyte atoms present in the volume of target excited by the electron beam. By counting continuum x rays we obtain a measure approximately proportional to the product of the average atomic number and the mass thickness of the excited volume. If the average atomic number of the target is known, the continuum signal gives a measure of target mass thickness. In the ratio of a characteristic signal to a continuum signal, the factors that affect both signals equally cancel. Since, in the usual energy-dispersive x-ray analysis system, the two signals are recorded simultaneously, the effects of the recording time and incident probe current cancel. This procedure is widely used in biological applications for thin targets (<200 nm) in the scanning electron microscope and microprobe and analytical electron microscope. The required first step in using the procedure is to extract from the x-ray spectrum signals that are proportional to the number of generated characteristic x rays for each of the elements being determined.

In the usual procedure of forming an x-ray image with an energy-dispersive spectrometer system, two channels of the multichannel analyzer are defined as limits such that the channels in between include slightly more than one-half the height of an x-ray peak of the analyte. Whenever an x ray is detected and its resulting voltage pulse falls between the limits specified by these channels, a single pulse is sent to the display CRT to form a

---

The author is at the National Institute of Health (Division of Research Services), Bethesda, MD 20205.

single "dot" of light. Any x-ray photon within the energy of interest, whether a characteristic or continuum x ray from the specimen, or continuum from a grid bar or the specimen holder, is processed since there is no way to tell one from the other.

In this x-ray "dot" map technique we move the electron beam over the face of the recording oscilloscope in synchronism with the beam over the specimen surface. The synchronous beams are displaced by having horizontal and vertical velocity components  $v_x$  and  $v_y$  imparted to them;  $v_x$  is typically 500-2000 times  $v_y$ . The direction in which the velocity component is greater is commonly called the line direction and the other direction is called the frame direction. When the beam reaches the end of a line on the oscilloscope it is inhibited from producing light and moved to the beginning of the next line, and the scan is repeated. When an x-ray photon selected for mapping is detected from a location on the specimen, a bright dot appears at the corresponding location on the CRT. The dots comprising the image can be stored photographically; each dot saturates the film. Since the usual photographic film is capable of approximately 15 shades of gray from black to white the dot map technique considerably underutilizes the capability of the film. Variations in the x-ray production and hence the analyte concentration can only be deduced from variations in the spatial distribution of the dots. It would be extremely difficult to perform accurately the series of algebraic operations required in the Hall procedure on x-ray data stored in this fashion.

A method alternative to continuous-beam rastering is discrete rastering, accomplished with what is usually called a "digital scan generator." In this technique  $v_x$  and  $v_y$  are not constant but remain zero for a finite period of time and then the beam is rapidly stepped to the next point. The displacements along the line direction are equal. When the end of the line is reached, the beam is moved back to the beginning of the line and displaced one step along the frame axis with the step size equal to the line step. Each point in the image at which the beam dwells is called a "pixel." For x-ray imaging purposes it is common to use between 128 and 512 points along the "line" and the same number of lines in the "frame."

Discrete rastering is convenient for application with the digital computer. Since the area on the specimen surface is scanned point by point, in computer memory we can define this matrix of points as a two-dimensional array. If the beam remains at any given pixel long enough for a given beam current, beam voltage, and specimen type, it is probable that many pulses will be generated during the dwell time. These pulses can be counted and the value of the count stored along with the pixel coordinates. With appropriate circuitry the counts in this array can be displayed at the appropriate coordinates on the CRT, with the brightness at each point proportional to the number of counts. We shall call such a display an x-ray intensity map (to distinguish it from the x-ray dot map). With an intensity map, we can not only fully utilize the gray scale of photographic film, we can also perform powerful mathematical operations on these "images."

Procedures that accomplish removal of the continuum contribution to x-ray EDS spectra can be classified into one of two categories: modeling or filtering. Background modeling consists of measuring a continuum energy distribution (or calculating it from first principles) and combining it with a mathematical description of the detector response function. The resulting function is then used to calculate an average background spectrum that can be subtracted from the observed spectral distribution. Background filtering ignores the physics of x-ray production, emission, and detection; the background is viewed as an undesirable signal to be removed by modification of the frequency distribution of the spectrum by digital filtering or Fourier transform methods.

In our application we use a filtering procedure developed at NIH.<sup>6</sup> In this procedure the average effect of the continuum is highly suppressed and a dead-time correction is performed by which the pixel dwell time is caused to be the EDS system "live time." A signal for each measured x-ray peak is provided at the end of each pixel dwell period that is proportional to the number of detected characteristic x rays for each analyte.

There has been considerable discussion about the best energy at which to measure the continuum signal for the Hall procedure.<sup>7-8</sup> The choice involves a consideration of statistics (there is more continuum signal at low photon energies); instrumental effects (where is there a minimum of spectral artifacts, overlaps, effects of scattered electrons, etc.); and physics (how accurate are the physical expressions used in the algorithms?). We integrate over an approximately 100eV window centered at any peak-free region between about 1.2 and 1.6 keV in energy. This energy range is a good compromise choice since it contains

a minimum component of continuum radiation originating from the relatively thick support grid and specimen holder.

The acquisition phase of a Hall-corrected quantitative "image" consists of scanning over a chosen area of the specimen and storing in computer memory, at each pixel, a single real valued number (due to background and deadtime correction of the signals) for each of the chosen x-ray peaks and the single integer valued number obtained from the approximately 100eV-wide low-energy window. We now have in the computer memory several elemental "images" and a single continuum "image" all simultaneously acquired from a single pass over some region of specimen surface.

Since the "Hall" procedure requires the use of "standards," we must have already acquired or must now acquire spectra from our standard reference material(s). The reference material(s) and spectra must satisfy the usual criteria observed in any "Hall" type of analysis. The same continuum and deadtime correction algorithm as applied at each pixel in the image is applied to each "reference" spectrum and the corresponding information is extracted. As always, it is good practice to average the information obtained from several different readings from any given standard.

The "images" can now be converted into useful chemical information, by use of the "Hall" algorithm, in two ways. The first involves the creation of a new "image" for each element of interest, such that pixel intensity is linearly proportional to elemental concentration. This procedure is useful if one can assume that the average atomic number is approximately constant over most of the field of view. If one cannot make this assumption, then the image must be broken into discrete regions which are treated separately.

The calculation is made in a manner analogous to a point-mode analysis, except it is done at all pixels. After the calculation is made the numbers must be adjusted to fit into the allowable display range. This range is usually one computer "byte" (or 8 bits) which corresponds to 256 levels of brightness; level 0 is full black and level 255 full white (or full red, green, or blue if a color display is used). A complication occurs in those parts of the image which have a mean zero concentration of analyte. A mean of zero implies that half the pixels have negative values. We would like to be able to assign the "zero" regions of an image to the darkest gray of the gray scale, i.e., "black." The observer can immediately interpret a region of dominant black as having no analyte. However, by this assignment we essentially "clip" the negative values since there is no shade of gray to assign to them. The net result of neglecting the negative values is to "bias" the regions that do not contain analyte to a mean which has a positive value. The greater the original variance the greater this biased mean. An alternative procedure is to set the minimum pixel intensity in the entire image to be black. The latter method of setting the brightness scale of background-corrected images requires the author of the micrograph to identify regions that are "zero" with some symbol on the micrograph or comment in the figure caption. The observer must then be able to interpret certain gray levels as representing zero and negative values but numerical information is not compromised and the possibility of introducing artifacts is reduced.

There is a simple but powerful method that can be used to remove the average effect of the classic potassium  $K\beta$  to calcium  $K\alpha$  overlap. The method requires obtaining a background and deadtime-corrected image for both these elements. The "image" for calcium is really an image of calcium plus potassium. Since the ratio of potassium  $K\alpha$  to  $K\beta$  is well known, we multiply each pixel in the potassium image by this ratio and subtract the result from each corresponding pixel in the "calcium" image. It is sometimes advantageous to nearest-neighbor-smooth the potassium image before the procedure. After the average effects of the overlap have been removed from the calcium image we then proceed with the "Hall" correction.

The second way the background and deadtime corrected "images" can be converted into useful chemical information by the "Hall" algorithm is to perform the correction not at every pixel but on chosen regions. This approach requires some hardware device such as a mouse, light pen, or digitizing tablet to permit the user to "draw" a boundary around the object of interest. The computer is then instructed to sum all the pixels in the region and divide through by the number of pixels. The Hall correction is then applied to this single number.

When a high-magnification image of a low-concentration analyte is created, spatial drift becomes a limitation owing to the long acquisition time required. The answer is to take a series of short acquisition time images, apply an offset bias to the X and Y

deflection coils to remove the drift between each image, and then add together all the separate images. It is useful to record, along with the low-concentration analyte, a high-concentration analyte or an electron signal such as dark field. Between any two successive images we can calculate the amount of drift correction required for the next image by examining whichever of the signals best reveals the morphology. The comparison can be done by eye or mathematically either in real space or frequency space.

### References

1. S. B. Andrews, R. D. Leapman, D. M. D. Landis, C. E. Fiori, and T. S. Reese, "Elemental distribution in rapid-frozen cerebellar cortex," *J. Cell. Biol.* 99: 424a, 1984.
2. S. B. Andrews, R. D. Leapman, D. M. D. Landis, C. E. Fiori, and T. S. Reese, "Rapid freezing and quantitative elemental imaging in neurobiology," *Proc. Microscopic Soc. Canada* 12: 24-25, 1984.
3. D. J. Marshall and T. A. Hall, in Castaing, Deschamps, and Philibert, Eds., *X-ray Optics and Microanalysis*, Paris: Hermann, 1966, 374.
4. T. A. Hall et al., in T. D. McKinley, K. F. J. Heinrich, and D. B. Wittry, Eds., *The Electron Microprobe*, New York: Wiley, 1966, 805.
5. T. A. Hall, "Problems of the continuum-normalization method for the quantitative analysis of sections of soft tissue," in C. Lechene and R. R. Warner, Eds., *Microbeam Analysis in Biology*, New York: Academic Press, 1979.
6. C. E. Fiori, C. R. Swyt, and K. E. Gorlen, "Continuum correction of x-ray images in scanning electron column instruments," *Microbeam Analysis--1984*, 179.
7. C. E. Fiori, C. R. Swyt, and J. R. Ellis, "A critique of the continuum normalization method used for biological x-ray microanalysis in the analytical electron microscope," in A. D. Romig, J. I. Goldstein, and D. C. Joy, Eds., *Introduction to Analytical Electron Microscopy*, New York: Plenum Press, 1986.
8. C. E. Fiori, C. R. Swyt, and J. R. Ellis, "The theoretical characteristic to continuum ratio in energy-dispersive analysis in the analytical electron microscope," *Microbeam Analysis--1982*, 1982, 57-71.



## QUANTITATIVE ELECTRON ENERGY LOSS SPECTROSCOPY AND ELEMENTAL MAPPING IN BIOLOGY

R. D. Leapman

The aim of this paper is to survey the current state of electron energy loss spectroscopy (EELS) and the related technique of EELS mapping in applications to biology. After outlining some basic principles we shall consider the achievements in the field thus far. We shall then discuss certain fundamental limitations and make a few projections for the future.

### *Basic Principles*

EELS is a complementary technique to energy dispersive x-ray spectroscopy (EDXS) in being sensitive to the light elements ( $Z < 11$ ) that can be difficult to measure by x rays. That is because primary ionization events can be detected in energy losses of the fast electrons,<sup>1,2</sup> whereas in EDXS only a fraction of the excited atoms produce x rays especially for low-atomic-number elements where the fluorescence yield is small. In addition, the collection efficiency for EELS is high since the inelastically scattered electrons are concentrated in the beam direction and a large fraction enters the spectrometer. In comparison only a small fraction (<1%) of the isotropically emitted characteristic x rays can be collected by a silicon detector.

The main limitation in EELS sensitivity is due to the background that underlies the core edges. This background arises from excitation of less tightly bound electrons in the sample. In biological specimens important elements like calcium are normally present at the 100 ppm level or lower, so that very small signal-to-background ratios are often encountered. Therefore it is crucial to optimize the signal-to-noise ratio and to develop accurate procedures for removing the background intensity. With this purpose much effort has been devoted to improving spectrometer performance and its coupling to the microscope via postspecimen optics. In the analytical electron microscope (AEM), the energy loss spectrum is usually produced by means of a magnetic sector spectrometer. Scattered electrons are dispersed as a function of energy at the spectrometer slit and one can record the spectrum serially by ramping the magnet excitation or by applying a voltage offset to the spectrometer drift tube. Electrons transmitted through the slit are detected as single pulses by a scintillator and photomultiplier tube. In recent years highly efficient parallel detection systems have been developed to record many spectral channels simultaneously.<sup>3-5</sup> These devices require postspectrometer electron optics and light optics to image the energy loss spectrum on a two-dimensional array (e.g., SIT vidicon tube) or on a one-dimensional photodiode array (e.g., a reticon). An enormous improvement in the signal-to-noise ratio has already been demonstrated with such an arrangement.<sup>6</sup>

It has now become possible not only to obtain information from a point in the sample but also to obtain elemental distributions. Two competing approaches have been developed, one in the scanning transmission electron microscope (STEM) or the AEM,<sup>7-11</sup> the other in the energy-filtering transmission electron microscope (EFTEM).<sup>12,13</sup> In the STEM a focused electron probe can be digitally scanned across a sample and spectral data acquired around one or more core edges from each pixel sequentially. In the EFTEM the image is formed in parallel by adjustment of an energy filter (e.g., Castaing-Henry spectrometer) situated after the specimen to select one energy loss at a time. The spatial resolution in the EFTEM is limited mainly by the performance of the objective lens and by chromatic aberration, whereas in the STEM resolution is limited by the minimum useful probe size and hence by gun brightness, so that a field-emission source is generally required for resolution less than 5 nm in the STEM. The EFTEM is often operated with a microampere current on the sample compared with a nanoampere probe in the STEM. However, these advantages of the

---

The author is at the National Institutes of Health, Bethesda, MD 20892. He wishes to thank his colleagues C. E. Fiori, K. E. Gorlen, and C. R. Swyt for their help in developing the computer system and software with which the experimental data were collected. He is also indebted to R. L. Ornberg (NIH) and A. F. Boyne (University of Maryland) for providing samples.

EFTEM may be offset by important features of the STEM. First, the EELS signal in the STEM may be detected as single electron pulses that can be fed into a digital counter and then into a computer-controlled data-acquisition system. Data from several channels can be acquired at each pixel, so that it is possible to achieve a precise and accurate background subtraction. Second, in the STEM several different signals can be acquired simultaneously such as the EDXS signal providing information about heavier elements and ions, and the annular dark field elastic signal giving information about sample morphology. Third, parallel detection of the spectrum is possible in STEM but not in EFTEM mapping; the STEM is therefore the method of choice for beam-sensitive samples. Finally, in STEM it is easy to stop the probe on the sample and record a spectrum from a particular region where the elemental concentration may be too low to image. In the EFTEM it is more difficult to obtain spectra from small sample areas since an aperture rather than a probe defines the region of interest.

### *State of the Art*

*Sample Preparation.* Ultracryomicrotomy of quick-frozen tissue or cells is the preferred method of sample preparation since it is the only approach that has been shown to preserve ionic distributions.<sup>14</sup> The main difficulty is cutting thin enough sections since detection limits for EELS deteriorate rapidly due to plural inelastic scattering as the sample thickness approaches the total inelastic mean free path (approximately 50 nm for 100 keV beam energy). Thin cryosections are prepared as for EDXS analysis. They may be cryotransferred and subsequently dried in the microscope sample chamber or dried externally. In order to measure distributions of nondiffusible elements, such as sulfur in protein and phosphorus in nucleotides, it appears feasible under some conditions to use freeze-substituted and plastic-embedded samples (or freeze-dried and embedded). However, one should avoid staining these preparations with compounds that can interfere with the EELS analysis. The advantages of embedded sections include the easier recognition of morphology, less plural scattering because of thinner samples, and less variation in thickness on a fine scale (something that seems inevitable in cryosections due to drying).

*Quantitation.* Methods for quantifying electron energy loss spectra are now well established, though accuracy is often no better than 10%.<sup>15</sup> In biological applications we are often interested in the ratio of two elemental concentrations that can be determined by measurement of the ratio of areas under their core edges after the background has been subtracted. This quantity must be normalized by the inverse ratio of the respective partial ionization cross sections.<sup>16,17</sup> Errors can be in part attributed to discrepancies between the cross sections calculated from atomic models and the near-edge shape, which is influenced by chemical bonding effects. Further errors are introduced by inaccurate estimation of the collection geometry. A possible approach for avoiding some of these problems involves the use of standards (often not appealing to the physicist). For example, if we are interested in ratios of nitrogen/phosphorus, it is relatively easy to record spectra from adenosine triphosphate (ATP) deposited on a carbon film. This method has the potential advantage of canceling mass-loss effects in the unknown sample, although effects of irradiation on different samples are variable. When the sample thickness becomes comparable with the total inelastic mean free path, it is helpful to recover the single scattering distribution of the spectrum. One method involves a Fourier deconvolution<sup>18</sup> of the background-subtracted core loss signal by the low loss spectrum. Figure 1 shows this procedure applied to the spectrum recorded at 200keV beam energy from a secretory granule in a cryosection of adrenal chromaffin (epinephrine-secreting) cells.<sup>19</sup> The upper spectrum represents the raw data after background subtraction below the carbon K edge (285 eV). The lower spectrum is after deconvolution and shows removal of superimposed plasmon peaks and the increase in signal/background for the nitrogen K edge at 400 eV. Quantitation of such spectra yields a nitrogen/phosphorus ratio of  $5.0 \pm 0.5 : 1$  and suggests that only 33% of the nitrogen atoms can be accounted for by ATP, which is known to be a major granule component (assuming mass loss is negligible).

*Detection Limits.* The sensitivity of EELS depends on many factors relating to the sample and to the instrumentation. Certain elements such as calcium, which has a sharp resonance at the  $L_{23}$  edge, are favorable for EELS analysis, whereas potassium ( $L_{23}$  edge) has a severe overlap with carbon (K edge) and is therefore difficult to detect. Other biologically important elements suitable for EELS include C, N, O, P, and S. Detection

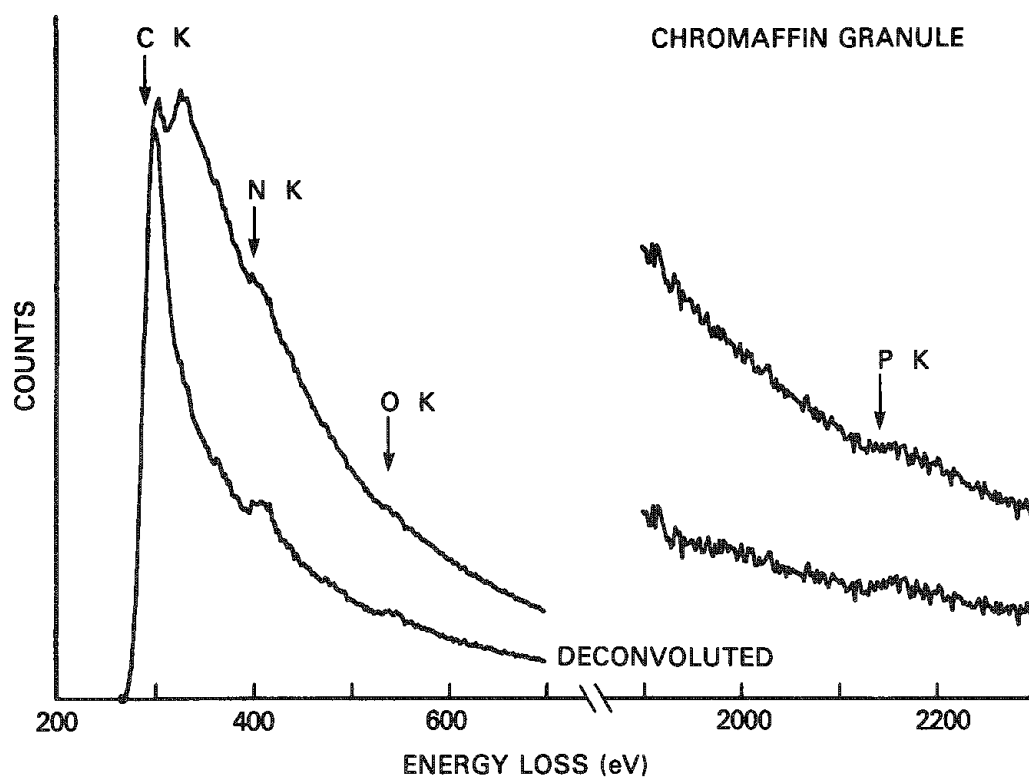


FIG. 1.--Energy loss spectrum recorded at 200keV beam energy from secretory granule in cryo-section of quick-frozen cultured bovine adrenal chromaffin cells. Upper curve is raw data after background subtraction below C K edge. Lower curve is deconvoluted to remove plural scattering. C, N, O, and P K edges are observed. Estimated value of N/P =  $5.0 \pm 0.5$  based on ATP standard and averaged over ten granules.

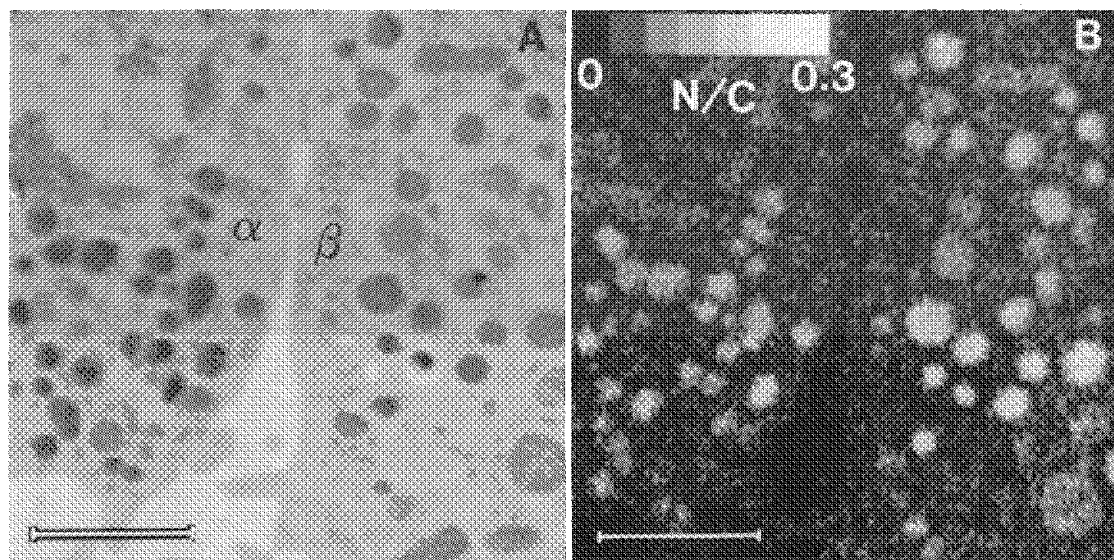


FIG. 2.--(A) Bright field STEM of quick-frozen, freeze-dried, and embedded rat Islet of Langerhans showing regions of alpha and beta cell; bar = 1  $\mu$ m. (b) N/C ratio map with calibrated intensity scale. Image histogram yields N/C = 0.23 in secretory granules, which do not appear to be penetrated by plastic.

limits clearly depend on the probe current, acquisition time, and detector efficiency, and on how the background estimation is performed. The highest sensitivity yet reported has been achieved by Shuman et al. for calcium.<sup>6</sup> These authors utilize a SIT vidicon camera coupled by a phosphor to record the spectrum in parallel around the Ca  $L_{2,3}$  edge. By using a second difference method to remove channel-to-channel gain fluctuations in the detector array, Shuman et al. were able to demonstrate a sensitivity of approximately 1 millimole per kilogram.

*Elemental Mapping.* The recent development of computer-controlled data acquisition for the AEM<sup>7-11</sup> permits an accurate EELS background determination at each pixel in an image. For example, the system developed by Gorlen et al.<sup>11</sup> consists of a 200 keV AEM interfaced to a dedicated acquisition processor (satellite computer) and a larger host computer that can reduce data dynamically. The satellite computer communicates with the host via a direct-memory access link. The satellite controls the x-y scan of the beam, the spectrometer electrostatic deflection, and a fast counter that measures the photomultiplier pulses. Simultaneous acquisition of x-ray maps and dark-field images is also possible. Resulting data are transferred to disk and can be loaded into an image display system with four  $512 \times 512 \times 8$ -bit image planes. This system also supports basic image processing capabilities such as addition, division, smoothing, and contrast enhancement. For EELS image acquisition, the counts are accumulated in several channels below and above an edge (typically 10 in all). An inverse power law<sup>8,11,12</sup> is used to extrapolate and then subtract the pre-edge background by means of a linear least squares fit.

Figure 2 shows a "ratio map" of the nitrogen/carbon distribution from a thin section of rapidly frozen, freeze-dried, and embedded rat Islet of Langerhans.<sup>21</sup> A factor of 1.2 has been applied to correct for the thin 10nm Formvar support film. The mean N/C ratio in the beta cell secretory granules was found to be  $0.23 \pm 0.01$ , which is close to the value of 0.241 for the protein insulin, known to be a major component of the beta cell granule. The embedding plastic did not appear to penetrate the granule cores in this preparation. The total dose on the sample, maintained at  $-80^\circ\text{C}$ , was about  $10^4 \text{ e}\text{\AA}^{-2}$ . The nitrogen/sulfur ratio in the beta granules of  $11.2 \pm 1.0$ , determined from point analyses, is also close to the value for pure insulin, which has an unusually high sulfur content. This result provides direct evidence that the beta granule core is composed almost entirely of the insulin. The nitrogen/sulfur ratio in the alpha cell (known to contain glucagon) is found to be much higher and reflects a difference in elemental composition between the two proteins.

One important point that has been clearly demonstrated by EELS mapping in the STEM is that a reasonable model for the pre-edge background must be used. In general one finds a two-parameter fit more satisfactory than simply taking the difference between the post- and pre-edge images.<sup>22</sup> The well-known inverse-power law for the background ( $AE^{-r}$ ) can be successfully applied, where  $E$  is energy loss. If the parameters  $A$  and  $r$  are each allowed to vary, then changes in background shape due to plural scattering or compositional differences are taken into account. A two-parameter fit could also be applied in the EFTEM especially if data were recorded electronically by means of a SIT vidicon.<sup>23</sup>

#### *Some Fundamental Limitations*

In STEM elemental mapping, the sequential nature of data acquisition limits the dwell time available per pixel. For example, a  $128 \times 128$  pixel image recorded in 30 min only allows 100 ms per pixel. It therefore becomes clear that even with a highly optimized detection system low (millimolar) levels of calcium cannot be mapped successfully. EELS imaging is probably better applied to the more abundant elements from which biological molecules are composed, i.e., C, N, O, P, and S, and sometimes Ca if the concentration is high enough (as in mineralizing cells). Radiation damage with concomitant mass loss is an important limitation for energy loss spectroscopy and mapping at higher spatial resolution. Thus, if nitrogen atoms are to be detected at 1 nm resolution at a concentration of 3%, the required dose is estimated to be in excess of  $10^6 \text{ e}\text{\AA}^{-2}$ . Under these conditions mass loss and structural degradation are inevitable,<sup>24</sup> even if the sample is maintained at low temperature. In order to overcome this problem one must average EELS data over many identical structures and hence achieve relatively low-dose conditions ( $<100 \text{ e}\text{\AA}^{-2}$ ). For example, estimation of the attainable signal/noise suggests that low-dose, high-resolution mapping of regular two-dimensional arrays of reconstituted membrane should prove

feasible. In such an experiment it is envisaged by Engel et al.<sup>25</sup> that low-dose EELS maps of the phosphorus and nitrogen distributions at 1 nm resolution could be averaged over some  $10^4$  unit cells. The resulting maps could provide information about localization of phospholipid (P) and protein (N) components of the membrane.

### *Conclusions and Projections for the Future*

Adequate sample preparation methods are a prerequisite for performing any useful microanalysis on biological samples. Frequently quick-freezing and cryosectioning are essential if the spatial distribution of elements in a cell is to be preserved. However, because of plural inelastic scattering, the mass-thickness of a cryosection is often too large for optimum EELS at 100 keV beam energy. Therefore it is likely in the future that intermediate voltage (200-400keV) AEMs will see more use for biological applications. On the other hand, EDXS analysis is generally optimized at lower beam energies since the ionization cross section is greater and less spurious x-ray background radiation is generated in the spectrum. These conditions produce some conflict if both techniques are to be used together. In addition to higher beam energy there will be a demand for brighter sources so that smaller structures can be probed, within the limits imposed by radiation damage. The ideal instrumentation might feature a beam energy of 300 keV, a field emission source, and a mechanically stable cold stage to minimize mass loss. Optimized mapping in the STEM will be performed by processing of an array of spectral data collected in parallel at each pixel. It is also probable that refined techniques will be developed for processing data in the EFTEM, such as more elaborate methods for subtracting the pre-edge background.

Finally, applications of EELS are expected to involve both measurement of low elemental concentrations (e.g., calcium) from single points in the sample, and also the acquisition of chemical maps over extended regions in order to learn about distributions of biological molecules. If such studies are to be performed at higher resolution, low dose averaging procedures are necessary.

### *References*

1. D. B. Wittry, R. P. Ferrier, and V. E. Cosslett, "Selected area electron spectrometry in the transmission electron microscope," *Brit. J. Appl. Phys.* D2: 1767-1773, 1969.
2. M. S. Isaacson and D. E. Johnson, "The microanalysis of light elements using transmitted energy loss electrons," *Ultramicroscopy* 1: 33-52, 1975.
3. D. E. Johnson, K. L. Monson, S. Csillag, and E. A. Stern, "An approach to parallel detection electron energy loss spectrometry," *Analytical Electron Microscopy--1981*, 205-209.
4. H. Shuman, "Parallel recording of electron energy loss spectra," *Ultramicroscopy* 6: 385-396, 1981.
5. R. F. Egerton, "Parallel-recording systems for electron energy loss spectroscopy (EELS)," *J. Electron Microsc. Tech.* 1: 37-52, 1984.
6. H. Shuman, P. Kruit, and A. P. Somlyo, "Quantitative electron energy loss spectroscopy of low concentrations of calcium in carbon containing materials," *Microbeam Analysis--1983*, 247-251.
7. J. M. Butler, F. Watari, and A. Higgs, "Simultaneous collection and processing of energy filtered STEM images using a fast digital data acquisition system," *Ultramicroscopy* 8: 327-334, 1982.
8. C. Jeanguillaume, M. Tencé, P. Trebbia, and C. Colliex, "Electron energy loss chemical mapping of low Z elements in biological sections," *SEM/1983 II*, 745-756.
9. P. Rez and C. Ahn, "Computer control for x-ray and energy loss line profiles and images," *Ultramicroscopy* 8: 341-350, 1982.
10. K. E. Gorlen, L. K. Barden, J. S. Del Priore, C. E. Fiori, C. C. Gibson, and R. D. Leapman, "A computerized analytical electron microscope for elemental imaging," *Rev. Sci. Instrum.* 55: 912-921, 1984.
11. R. D. Leapman, C. E. Fiori, K. E. Gorlen, C. C. Gibson, and C. R. Swyt, "Combined elemental and STEM imaging under computer control," *Ultramicroscopy* 12: 281-292, 1984.
12. F. P. Ottensmeyer and J. W. Andrew, "High resolution microanalysis of biological specimens by electron energy loss spectroscopy and by electron spectroscopic imaging," *J. Ultrastruct. Res.* 72: 336-348, 1980.

13. H. Shuman and A. P. Somlyo, "Energy-filtered transmission electron microscopy of ferritin," *Proc. Nat. Acad. Sci. USA* 79: 106-107, 1982.
14. A. V. Somlyo, H. Shuman, and A. P. Somlyo, "Elemental distributions in striated muscle and effects of hypertonicity: Electron probe analysis of cryosections," *J. Cell Biol.* 74: 828-857, 1977.
15. R. F. Egerton, "Principles and practice of quantitative electron energy loss spectroscopy," *Microbeam Analysis--1982*, 43-53.
16. R. F. Egerton, "K-shell ionization cross sections for use in microanalysis," *Ultramicroscopy* 4: 169-179, 1979.
17. R. D. Leapman, P. Rez, and D. F. Mayers, "K-, L-, and M-shell generalized oscillator strengths and ionization cross sections for fast electron collisions," *J. Chem. Phys.* 72: 1232-1243, 1980.
18. C. R. Swyt and R. D. Leapman, "Plural scattering in electron energy loss (EELS) microanalysis," *SEM/1982* I, 73-82.
19. R. D. Leapman and R. L. Ornborg, "Low atomic number imaging of cells by electron energy loss spectroscopy," *Proc. 41st Ann. Meet. EMSA*, 1983, 590-591.
20. C. Jeanguillaume, P. Trebbia, and C. Colliex, "About the use of electron energy loss spectroscopy for chemical mapping of thin foils with high spatial resolution," *Ultramicroscopy* 3: 237-242, 1978.
21. A. F. Boyne (to be published).
22. R. D. Leapman and C. R. Swyt, "Electron energy loss imaging in the STEM: Systematic and statistical errors," *Microbeam Analysis--1983*, 163-167.
23. F. P. Ottensmeyer, "Electron energy loss analysis and imaging in biology," *Proc. 42nd Ann. Meeting. EMSA*, 1984, 340-343.
24. M. Isaacson, D. Johnson, and A. V. Crewe, "Electron beam excitation and damage of biological molecules: Its implication for specimen damage in electron microscopy," *Radiation Res.* 55: 205-224, 1973.
25. A. Engel, R. Reichelt, and R. D. Leapman (to be published).

## FRONTIERS OF SECONDARY ION MASS SPECTROMETRY IN BIOLOGICAL ANALYSIS

Margaret Burns

Secondary Ion Mass Spectrometry has been used for biological microanalysis for many years but we now stand at the beginning of a new road of discovery due to rapid technical developments in the field.

### *Current Technique*

Details of the technique of SIMS and applications to biological problems can be found in several excellent reviews.<sup>1-4</sup> The principle is that a specimen is bombarded by a primary ion beam and secondary ions are produced from the sample surface which are a function of the composition of that surface. Mass spectrometric detection of secondary ions provides a background-free signal with isotopic resolving power. Depending on bombardment conditions, elemental or higher-molecular-weight ions are produced.<sup>5</sup>

The ideal instrument for analysis of cellular biological problems would have the following specifications: Lateral and depth resolution of 20 Å; minimum concentration detection limits in the micromole to picomole range; quantitative analysis over 4 decades of concentration; mass resolution of 10 000 or better; mass detection limits up to 10 000 daltons; equal sensitivity for all elements; analysis in the hydrated state; direct imaging capabilities; resolution of isotopes; resolution of ionized and bound species.

The commercial instrument most utilized to date has been the Cameca IMS300, or the second-generation IMS3f. What are the specifications of this instrument and limitations of the technique in comparison to an ideal instrument?

*Lateral resolution.* In the direct-imaging instrument, lateral resolution is determined by the ion optics, not by the primary-beam size. The resolution available in the direct-imaging instrument is approximately 0.1 to 1 µm, depending on the local elemental concentration. For cellular biological problems, submicron localization capacity for subcellular organelles would be desirable.

*Depth resolution.* The depth resolution depends on mixing of the sample surface during the collision cascade, and can be less than 100 Å in nonbiological systems. An actual value for biological specimens has not been reported.

*Quantitation.* Quantitative standards down to levels of 0.1 µmole have been reported for lithium, an element with favorable ion yields, and a dynamic range of 3 to 4 decades.<sup>6</sup> Due to different ionization probabilities, the detection limits vary greatly from element to element. Most of the particles sputtered from the specimen surface are not ionized.

*Mass resolution.* Mass resolution of 10 000 is currently available, more than adequate for resolution of elemental from most polyatomic interferences. For analysis of organic species, high mass resolution is needed to distinguish alternative structures of unknowns.

*Mass detection limits.* For elemental analysis, masses of up to 300 can be analyzed, within the range of elements of interest. For organic mass spectra, larger mass ranges are desirable.

*Hydrated material.* A limitation for water-bathed soft tissue is that the vacuum requirements ( $10^{-8}$  Torr) currently limit analysis to dehydrated specimens.

*Direct imaging.* Currently available.

*Isotopic resolution.* Currently available with high mass resolution.

*Ionized vs bound elements.* One of the most interesting aspects of biological systems is the ability of ions to initiate cellular events. The capacity to distinguish free from bound ions in the specimens would be very useful. Since the sputtering process itself involves ionization, it seems unlikely that this desideratum could be achieved.

---

The author is in the Department of Ophthalmology, School of Medicine, University of California, Davis, CA 95616. This work was supported in part by a Research to Prevent Blindness Research Manpower Award.

## Future Techniques

Several techniques have been developed or are under development that promise to meet the specifications of the ideal instrument.

*High-resolution SIMS instrument.* The development of high brightness liquid metal primary ion sources has resulted in a scanning ion microprobe with 200Å map resolution for a 40keV Ga<sup>+</sup> beam.<sup>7</sup> As usual, increased resolution has a trade off in sensitivity. This instrument is also capable of imaging total secondary ions, or secondary electrons to generate topographic maps of the specimen being analyzed.

*Analysis of hydrated samples.* The development of a cryogenic sample stage for the Cameca IMS3f<sup>8</sup> offers the possibility of examining diffusible ions and structures closer to the native state. The sputtering process of SIMS forms its own thin section, so that (unlike in electron microprobe analysis) if the sample can be frozen in the vitrified state, bulk samples can be analyzed. It remains to be seen whether new analytical challenges are generated by the frozen hydrated state.

*Quantitation.* Ion images contain localized information on ion emission (and ion content) which requires translation into numerical data to be of meaning to the biologist. Digital imaging systems have been developed based on camera-acquired image<sup>9,10</sup> and resistive anode encoders,<sup>11</sup> and need quantitative applications to biological problems. Quantitation is subject to the unknown existence of matrix effects, induced by differential sputtering<sup>12</sup> or difference in ion yield,<sup>13</sup> and must be examined for the specific problem. Ionization techniques for sputtered neutral ions<sup>14</sup> would obviate matrix effects, but at the price of losing localized information.

*Chemical information.* Under low-dose bombardment conditions ("static SIMS"), information about the parent ions in specimens have been known for some time. The development of a time-of-flight SIMS instrument<sup>15</sup> with a mass resolution up to 13 000 (50% valley) and mass detection up to ca 5000 m/z has been reported to detect as little as  $1 \times 10^{-15}$  moles of peptides.<sup>16</sup> It has been used to detect a single amino acid mutation in aliphatic peptides separated by HPLC. The difficulties of translating this type of static SIMS analysis with high spatial resolution "dynamic" SIMS imaging conditions is discussed by Linton.<sup>4</sup>

## Conclusions

New technical developments promise increased spatial resolution, the ability to examine hydrated material, quantitative information from ion images, reduced matrix effects, and chemical information. Each of these developments requires evaluation in terms of operating conditions and potential artifacts in application to biological problems. Although each improvement is bought at the cost of sensitivity or localized resolution, we have the opportunity to select new modes of analysis appropriate to the problem at hand. To paraphrase Gilbert and Sullivan, "Let the application fit the instrument."

The next mission for those involved in SIMS instrumentation is to engage the biological community by solving important, nontrivial problems with the techniques at hand.

## References

1. M. S. Burns, "Secondary ion mass spectrometry," in P. Echlin, Ed., *Analysis of Organic and Biological Surfaces*, New York: Wiley, 1983, 259-283.
2. A. R. Spurr, "Application of SIMS in biology and medicine," *Scanning*, 1980, 97-109.
3. S. Duckett and P. Galle, "The application of analytical ion microscopy (secondary ion mass microanalysis) to the study of normal and pathological neural tissue," in *Metal Ions in Neurology and Psychiatry*, New York: Alan Liss, 1985, 345-366.
4. R. Linton, *Biological Microanalysis Using SIMS: A Review*, SIMS-V, Springer-Verlag, 1986 (in press).
5. A. Benninghoven, "Organic secondary ion mass spectrometry," SIMS-IV, 1983, 342-356.
6. M. S. Burns-Bellhorn and D. M. File, "Secondary ion mass spectrometry (SIMS) of standards for analysis of soft biological tissue," *Anal. Biochemistry*, 1979, 213-221.
7. R. Levi-Setti, G. Crow, and Y. L. Wang, "Progress in high resolution scanning ion microscopy and secondary ion mass spectrometry imaging microanalysis," *SEM/1985*, 535-551.
8. M. T. Bernius, S. Chandra, and G. H. Morrison, "Cryogenic sample stage for the Cameca IMS3f ion microscope," *Rev. Sci. Instrum.* 56: 1347-1351, 1985.



9. S. R. Bryan, W. S. Woodward, D. P. Griffis, and R. W. Linton, "A microcomputer based digital imaging system for ion microanalysis," *J. Microscopy* 138: 15-28, 1984.
10. S. Chandra, W. C. Harris, and G. H. Morrison, "Distribution of calcium during interphase and mitosis as observed by ion microscopy," *J. Histochem. Cytochem.* 32: 1224-1230, 1984.
11. R. W. Odom, B. K. Furman, C. A. Evans, C. E. Bryson, W. A. Peterson, M. A. Kelly, and D. H. Wayne, "Quantitative image acquisition system for ion microscopy based on the resistive anode encoder," *Anal. Chem.* 55: 574-578, 1983.
12. R. W. Linton, M. E. Farmer, P. Ingram, J. R. Sommer, and J. D. Shelburne, "Ultrastructural comparison of ion beam and radiofrequency plasma etching effects on biological tissue sections," *J. Microscopy* 134: 101-112, 1984.
13. M. S. Burns, "Observations concerning the existence of matrix effects in SIMS analysis of biological specimens," SIMS-V, Springer-Verlag, in press, 1986.
14. H. Oechsner, "Secondary neutral mass spectrometry by postionization in a low pressure high frequency plasma," SIMS-V, Springer-Verlag, in press, 1986.
15. P. Steffens, E. Niehuis, T. Frieze, D. Greifendorf, and A. Benninghoven, "A new time-of-flight instrument for SIMS and its application to organic compounds," SIMS-IV, Springer-Verlag, 1984, 404.
16. A. Benninghoven, E. Niehuis, D. Greifendorf, D. VanLayen, and W. Lange, "Analytical application of a high performance TOF-SIMS," SIMS-V, Springer-Verlag, in press, 1986.

## FIELD-ION TOMOGRAPHY

J. A. Panitz

Field-ion tomography is a nondestructive, point-projection imaging technique that uses the field-ion microscope to visualize biological molecules in three dimensions.<sup>1,2</sup> Before imaging, a species of interest is deposited from aqueous solution onto the highly curved apex of a metallic needle known as a field-emitter "tip." A reliable deposition technique has been developed for this purpose.<sup>3,4</sup> One can evaluate the deposition procedure by rotary shadowing a tip with tungsten and viewing its profile in the transmission electron microscope.<sup>5</sup>

A FIT image of an unstained biological molecule is generated by covering of the tip apex with the molecule of interest and encasing the molecules within an immobile layer of amorphous benzene ice. The amorphous ice layer is prepared by placing the tip in ultrahigh vacuum, cooling it to a temperature below 20 K, and then condensing a precise quantity of benzene vapor onto the tip apex.<sup>6</sup> When a positive potential is applied to the tip, an electric field is established at its apex. At a field strength of  $\sim 30$  V/nm, the benzene layer begins to field-desorb—a sublimation process that erodes the layer at cryogenic temperatures in a controlled fashion and produces  $C_6H_6^+$  ions.<sup>7</sup> The ions accelerate almost radially from the tip apex and produce a highly magnified image of the ice layer several centimeters from the tip on a high-gain imaging detector. As the ice layer desorbs, molecules embedded within the layer are uncovered. As a molecule is exposed, a dark region appears in the image. This region changes in size and shape as the ice layer recedes. The contour of a dark region in a FIT image reflects the contour of a molecule defined by its intersection with the surface of the remaining layer of ice. A FIT image, integrated over time, contains a continuous series of contours that reflect the three-dimensional shape of the molecule. The three-dimensionality inherent in the image can be enhanced by a simple digital processing algorithm.<sup>8</sup>

The magnification of a FIT image is  $\sim D/1.5R$ , where  $D$  is the distance between the tip and the detector, and  $R$  is the radius of the tip.<sup>1</sup> For  $R = 300$  nm and  $D = 4.5$  cm, the image magnification is  $\sim 100\,000\times$ . The magnification can be changed by changing the distance between the tip and the detector. A magnification of several million times is usable because drift and vibration of the tip are not magnified during imaging.

The resolution of a FIT image can be calculated.<sup>1</sup> If diffraction effects are ignored (because of the small De Broglie wavelength of an ion), the resolution is  $R_0(\text{nanometers}) + 0.0282(RT/F)^{1/2}$ , where  $R_0$  is the spatial extent of ionization,  $R$  is the tip radius in nanometers,  $T$  is the tip temperature in degrees Kelvin, and  $F$  is the field strength in volts/nanometer. Figure 1 shows the calculated resolution of a FIT image as a function of tip radius and temperature for amorphous benzene or water ice. The calculation in Fig. 1 assumes that  $R_0(\text{benzene}) = 0.74$  nm,  $R_0(\text{water}) = 0.28$  nm,  $F(\text{benzene}) = 27$  V/nm, and  $F(\text{water}) = 46$  V/nm.

Figure 2 is a composite image of several unstained biological molecules imaged by field-ion tomography.<sup>9-11</sup> From similar images we have concluded that FIT imaging at 20 K with benzene can accurately depict the size and the shape of an unstained biological molecule at a resolution of about 2 nm, for tips less than 300 nm in radius.

### *Future Directions*

We are trying to extend FIT imaging to much larger species. Our goal is to obtain high-resolution three-dimensional images of unstained receptor molecules embedded within a cell membrane, and antibody molecules attached to them. Toward this end, we are developing a procedure for placing pieces of a cell membrane onto tips that are several microns in radius. A quick-freezing technique will embed the membrane within a layer of amorphous water ice on the tip surface. The tip is transferred into the cold stage of our microscope (cooled to 20 K) under liquid nitrogen. In this way, FIT images will be obtained

---

J. A. Panitz is a visiting research professor of molecular biophysics at The University of New Mexico School of Medicine, Department of Cell Biology, Albuquerque, NM 87131.

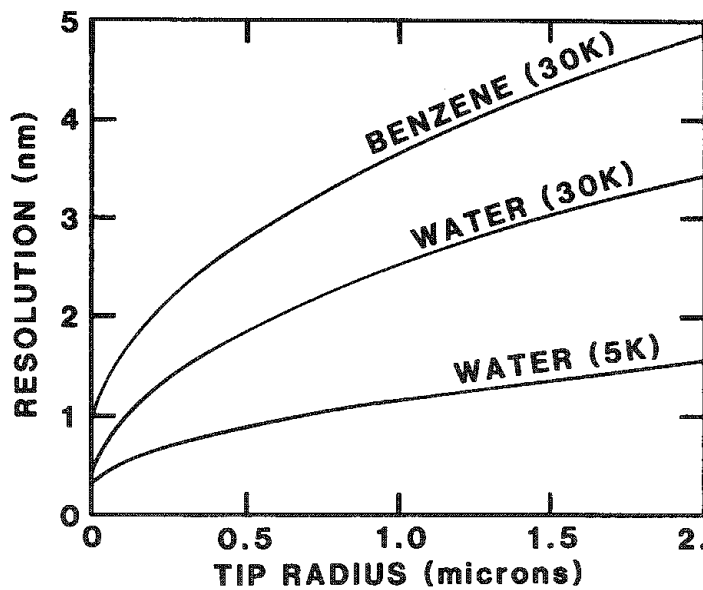


FIG. 1.--Calculated resolution of field-ion tomographic image.

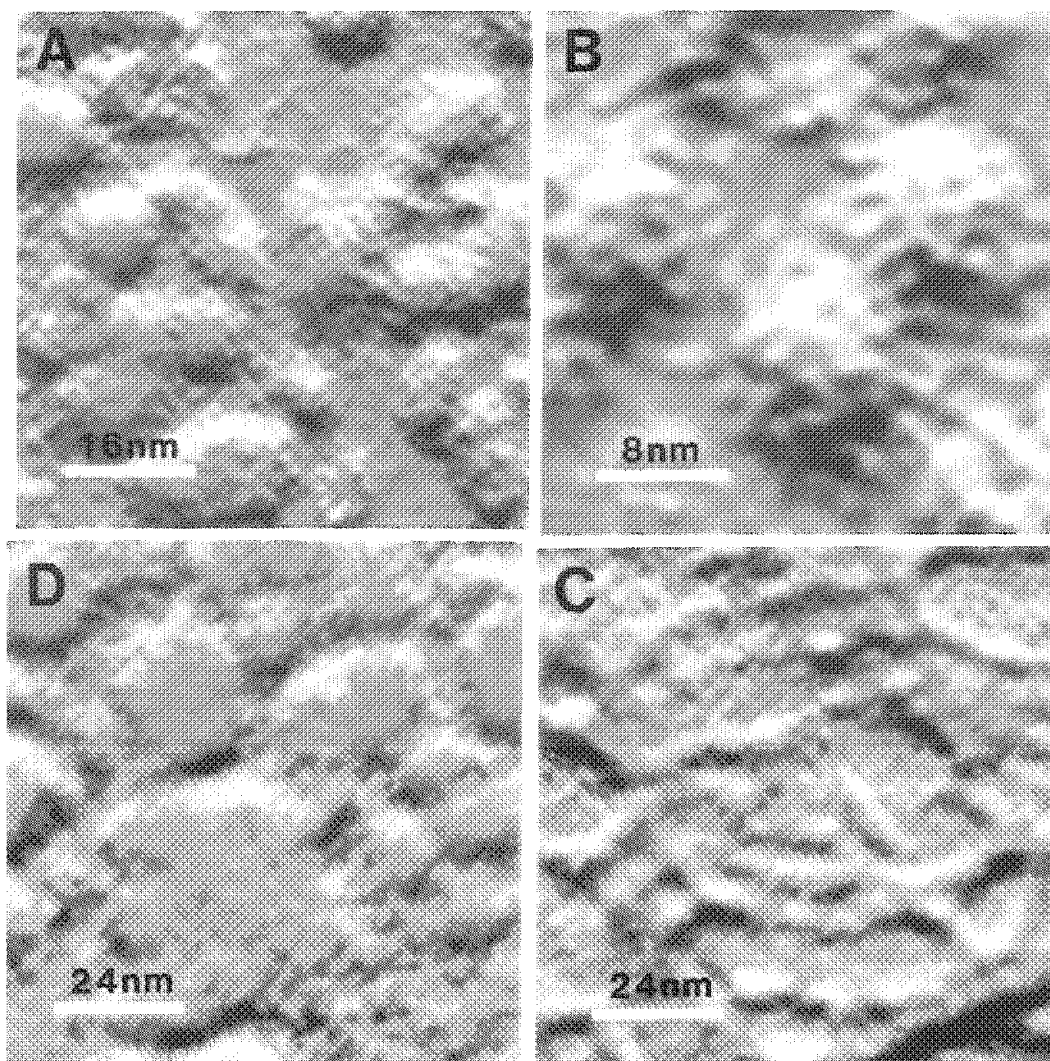


FIG. 2.--Field-ion tomographic images of unstained biological molecules: (A) ferritin clusters, (B) ferritin molecules, (C) DNA (poly GC), (D) hemocyanin (*Busycon canaliculatum*).

without drying the membrane or exposing it to high vacuum for an extended period of time. The first FIT image is obtained by field-desorbing the ice layer frozen at the time the membrane was deposited onto the tip apex. Additional images are obtained by spraying water vapor onto the cold tip to recoat the membrane surface with an amorphous layer of ice. Drying artifacts should be minimal because the membrane will be exposed to high vacuum for less than 1 min--essentially the time required to obtain a FIT image and reform a layer of ice. The conformation of receptor molecules embedded in the membrane should be preserved by tightly bound water, and the low tip temperature maintained since membrane deposition. We hope to analyze the chemical composition of a receptor molecule, and map the chemical composition of the membrane surface on a subnanometer scale. This ambitious program is being implemented by combining FIT imaging with the analytical capabilities of the imaging atom-probe.<sup>7,12,13</sup>

## References

1. J. A. Panitz, "Point-projection microscopy of macromolecular contours," *J. Microsc.* 125: 3-23, 1982.
2. J. A. Panitz, "Point-projection microscopy," in P. Echlin, Ed., *The Analysis of Organic and Biological Surfaces*, New York: Wiley, 1984, 171-190.
3. J. A. Panitz et al., "A deposition technique for the imaging and analysis of protein interaction with metal and semiconductor surfaces," *J. E. M. Techn.* 2: 285-292, 1985.
4. J. A. Panitz, "Biomolecular deposition on multiple field-emitter tips," *Rev. Sci. Instrum.* 56: 572-574, 1985.
5. J. A. Panitz and D. G. Bear, "A procedure for increasing the contrast of biological species in edge-projection TEM," *J. Microsc.* 138: 107-110, 1985.
6. G. L. Fowler and J. A. Panitz, "Retractable capillary closer," *Rev. Sci. Instrum.* 55: 1507-1508, 1984.
7. J. A. Panitz, "Isothermal ramped field-desorption of benzen from tungsten," *J. Vac. Sci. Technol.* 16: 868-874, 1979.
8. D. C. Ghiglia and M. D. Flickner, "Technique for conveying three-dimensionality from a sequence of image level slices," *Optics Letters* 7: 116-118, 1982.
9. J. A. Panitz, "Point-projection imaging of unstained ferritin clusters," *Ultramicroscopy* 7: 241-247, 1982.
10. J. A. Panitz and D. C. Ghiglia, "Point-projection imaging of unstained ferritin molecules on tungsten," *J. Microsc.* 127: 259-264, 1982.
11. J. A. Panitz, "Direct visualization of unstained nucleic acids on a metal substrate," *Ultramicroscopy* 11: 161-166, 1983.
12. J. A. Panitz, "High field techniques," in R. L. Park and M. Lagally, Eds., *Methods of Experimental Surface Physics* 22, New York: Academic Press, 1985, 349-423.
13. J. A. Panitz, "Imaging atom-probe mass spectroscopy," in S. G. Davison, Ed., *Progress in Surface Science*, Oxford: Pergamon Press, 1978, vol. 8, 219-262.

## QUANTITATIVE ELECTRON PROBE ANALYSIS IN BIOLOGY

A. P. Somlyo, A. V. Somlyo, M. Bond, and H. Shuman

The most general aim of biological electron probe x-ray microanalysis (EPMA) is to determine quantitatively the subcellular compartmentalization and transport of elements as they are found in vivo: in the cytoplasm, in cellular organelles, and in extracellular spaces. This process requires preparatory techniques that preserve the physiological distribution throughout dissection, tissue preparation, and transfer to the electron microscope, as well as a sufficiently accurate and sensitive method for extracting quantitative information from x-ray spectra. In this communication we review some of our previous work and outline requirements for specimen preparation and quantitation, with particular emphasis on the validation of EPMA results by independent methods. A major contribution to quantitative EPMA was made by T. E. Hall, who proposed the method of quantitating ultrathin specimens by relating concentrations to the characteristic/continuum x-ray ratio.<sup>1</sup> Without this approach<sup>1-3</sup> the application of EPMA to biology would have been probably less reliable and certainly much more laborious.

### *Preparatory Techniques*

Rapid freezing followed by cryoultramicrotomy is the only reliable method for the preservation of the in vivo distribution of diffusible elements. We have found freezing by propelling tissues into subcooled Freon 22 most convenient for physiological experiments in which relatively large tissues (up to 500  $\mu\text{m}$  in diameter) have to be frozen in various functional states.<sup>4-7</sup> Subcooling the cryogen and propelling the tissue enhances the contact of the two surfaces and reduces the slowing of freezing rate by nucleate boiling. It is not possible to overemphasize the importance of gentle dissection and preparatory conditions such as oxygenation and control of tissue temperature. Certain organs (e.g., liver) can be frozen in vivo with clamps containing melting Freon<sup>8,9</sup> or by other methods.<sup>10</sup> Inappropriate or careless preparatory methods can cause cell damage and abnormalities in the composition of cells and their organelles prior to freezing, such as increases in cell sodium and cell calcium, followed by the accumulation of mitochondrial calcium granules.<sup>11,12</sup> Such compositional abnormalities should not be erroneously attributed to elemental translocations during freezing, cryoultramicrotomy, or specimen transfer to the electron microscope. Cryoultramicrotomy at low temperatures ( $-130^{\circ}\text{C}$  and below) causes no detectable melting or elemental translocations, and low-temperature glues such as toluene can be used to reorient tissues requiring specific orientation in the cryoultramicrotome.<sup>13</sup>

Ultrathin cryosections placed on thin carbon films are generally transferred to vacuum evaporators while still at liquid-nitrogen temperature. Following drying at or below  $-80^{\circ}\text{C}$  at  $10^{-6}$  Torr,<sup>4,5,13</sup> they can be carbon coated and transferred to the electron microscope or for safe storage in carefully sealed dessicators. Carbon coating can protect sections from rehydration and elemental translocation even during direct exposure to aqueous gels.<sup>14</sup> We shall not deal here with special cases requiring the use of frozen hydrated specimens, such as analyses of the aqueous lumen of secretory epithelia (see, for example, Refs. 15 and 16).

### *Quantitative Analysis: Measurement of Calcium in the Presence of Potassium*

Quantitative analysis is based on the linear relationship between the characteristic/continuum x-ray ratio and elemental concentrations in thin specimens.<sup>1-3,17</sup> A potentially important source of error in the quantitation of the biologically important element, calcium, is due to the overlap of the generally small Ca  $K\alpha$  with the potassium  $K\beta$  peak, which

---

The authors are at the Pennsylvania Muscle Institute, University of Pennsylvania School of Medicine, Philadelphia, PA 19104. This work was supported by grant HL15835 to the Pennsylvania Muscle Institute and Training Grant HL07499.

can introduce a significant error in the quantitation of calcium<sup>2,17</sup> if there is a change in the detector calibration (position of the centroid or resolution) between the acquisition of the computer-stored reference and collection of a given experimental spectrum. The errors in the measurement of cytoplasmic Ca in the presence of high concentrations of potassium can be significant, even in laboratories adhering to the obligatory calibration of energy-dispersive x-ray detectors to within 1 eV. However, one can eliminate<sup>17-19</sup> such measurement errors by including the first and second derivatives of the potassium peaks in the multiple least-squares fit of the spectrum, and calcium can be measured in ultrathin cryosections with an accuracy of 300  $\mu\text{mol/kg}$  dry wt.<sup>8,20-22</sup>

### *Reliability and Independent Validation of EPMA Results*

The computer-fitting routines used for quantitative EPMA can be validated with homogeneous standards, such as proteins containing covalently linked elements,<sup>2</sup> carefully prepared (homogeneous) films or cryosections of solutions with albumin or gelatin,<sup>17,23</sup> or polymers.<sup>2,24-27</sup> However, *biological* EPMA requires not only correct quantitation<sup>1-3,17</sup> (for review, see Ref. 27), but also evidence that changes in elemental concentration and distribution do not occur prior to analysis. Therefore, the validity of both preparatory and quantitative techniques must be independently established to insure that EPMA can reliably answer important questions that are not answerable with, and cannot be verified by, other methods. In Table 1, we have collected some of our results and a limited sampling from the literature in which elemental concentrations measured with EPMA have been compared with the results of other methods. The examples are limited to experiments in which tissues were rapidly frozen, cryosectioned, and dried outside the microscope and transferred, with normal care to avoid rehydration, into the electron microscope. The table shows that quantitative EPMA of thin sections is in excellent agreement with results of other methods. The most stringent criterion for maintaining composition at high resolution is that imposed by small compartments and cell boundaries. Examples of EPMA results showing preservation of such boundaries and the *in vivo* composition of small domains are shown in Table 2. Indeed, one of the earliest cell physiological applications of EPMA was to determine the monovalent ion content of the terminal cisternae of the sarcoplasmic reticulum of skeletal muscle. Contrary to the interpretation of earlier ion flux studies conducted on whole muscles, the results of EPMA showed that the Na and Cl content of these organelles resembled that of the cytoplasm, rather than the extracellular space.<sup>4,6</sup> This conclusion was subsequently confirmed when the ion fluxes were repeated on single-muscle fibers to eliminate the various sources of error associated with compartmental analysis of fluxes in whole muscle. Similarly, measurements of calcium release from the terminal cisternae of skeletal muscle during contraction were subsequently confirmed with the use of calcium-sensitive dyes.<sup>57</sup> Most recently, estimates of the  $\text{K}^+$ -permeability of the sarcoplasmic reticulum based on EPMA<sup>6,28</sup> were confirmed by  $\text{K}^+$ -flux measurements in skinned single muscle fibers.<sup>29</sup>

### *Radiation Damage*

The potential errors induced by radiation damage or contamination in quantitative EPMA are well known<sup>2,27</sup> and can be reduced in modern microscopes having a "good" vacuum. Nevertheless, for doses commonly used in EPMA, an organic mass loss of approximately 20% is generally unavoidable. Much higher losses, such as total mass loss indicated by perforation of the specimen,<sup>30,31</sup> can occur secondary to the deposition of ice and etching of the specimen. Such ice deposition, associated with the use of cold stages, can be avoided if the cold stage temperature is kept at a level at which the vapor pressure of ice is above the residual water vapor pressure in the microscope column. In addition to insuring suitable vacuum in the electron microscope, this goal can be best accomplished with the use of a residual gas analyzer interfaced at the region close to the specimen.

### *Quantitative X-ray Mapping*

It is possible to determine the distribution of elements in qualitative x-ray maps (for review, see Ref. 32). Elements that occur at very high concentrations can be visualized with a simple x-ray map displaying the number of x-ray counts in the energy window containing the x rays emitted by the element of interest. A more quantitative approach is required for determining the distribution of elements occurring at lower concentrations.

TABLE 1.--Comparison of total elemental concentrations determined by EPMA and by other methods.

Tissue	Element	Concentration mmol/kg dry wt±SEM	Ref #
Erythrocytes			
		EPMA	Other: Method*
(i) human	Ca	0.2±0.3	0.03 AA
	Na	38±2	33±0.4 AA
	K	314±9	268±1.5 AA
	Cl	141±5	132 Chem.
(ii) rat	Na	15±1	14±0.5 AA
	K	341±4	378±24 AA
FROG SKELETAL MUSCLE			
(i) whole fiber	K	431±8	411 NAA
(ii) I band	K	510±7	516 NAA, ILM
I band (increase) during tetanus	Ca	3.5±0.1	3.9 CM
(iii) I band in skinned fibers	Ca	9.0±1	9 Cal
LIVER	Mg	16±2	15.8 Cal
	P	31±1	31.5 Cal
	K	422±6	362±10 AA
(i) whole cell	Ca	3.4±0.5	3.2±0.5 AA

Method\* AA = Atomic Absorption Spectroscopy

Chem = Chemical Analysis

NAA = Neutron Activation Analysis

ILM = Interference Light Microscopy

CM = Computer Modelling, based on free Ca<sup>2+</sup> measurements and Ca binding affinities of troponin and parvalbumin

Cal = Calculated value, based on known stoichiometry of thin filaments

\* A.V. Somlyo and A.P. Somlyo (unpublished)

\*\* M. Bond (unpublished)

+ P. Ferrari, A.P. Somlyo and A.V. Somlyo (unpublished)

TABLE 2

A. MICRODOMAINS IN FREEZE-DRIED CRYOSECTIONS				
Tissue/ Structure	Diameter of microdomain ( $\mu$ m)	Element	Concentration (mmol/kg dry wt±SEM)	Ref
MICRODOMAIN (N) SURROUND (N)				
Terminal cisternae of SR (frog skeletal muscle)	0.1	Ca	117±3.2 (229)	6
tetanus			48±1.3 (222)	
			(TC)	
			(cyto)	
Vacuoles (sickled RBC/s)	0.1	Ca	35±6.5 (15)	22
			(vacuole)	
			(cyto)	
Junctional SR (guinea pig portal vein)	.05-0.1	Ca	28.2±2.6 (81)	43
			(SR)	
			(cyto)	
B. ELEMENTAL BOUNDARIES IN FREEZE-DRIED CRYOSECTIONS				
Extracellular space vs. cytoplasm				
Tissue	Distance between probed regions ( $\mu$ m)	Element	Extracellular concentrations (mmol/kg dry wt)	Intracellular concentrations (mmol/kg dry wt)
Guinea pig portal vein (15 min in 20mM La <sup>3+</sup> soln)	0.2-1.0	La	108±70.6 (92)	1.1±4.16 (200)
Rabbit portal vein (Na-loaded, then 3 hr in 0 Na, Li soln)	0.2-5.0	Na	21.1±4.1 (19)	951±27.6 (11)

Such quantitative information can be produced by x-ray mapping, if the spectrum collected from each pixel is processed in a manner analogous to that used in point-mode analysis. Obviously, good counting statistics require rather long dwell times. Furthermore, a high brightness source, such as a field-emission gun, is required to form small probes needed for high spatial resolution. We have used this approach to map the calcium content (approximately 30 mmol/kg dry wt) of the cell wall of *E. coli*.<sup>33</sup> Practical application of this approach will require methods that correct for specimen drift over the very long collection times involved in mapping large areas at high resolution.

### Conclusion

There is now a large body of independent evidence, only some of which could be reviewed here, showing that the results of quantitative EPMA of ultrathin cryosections can reliably measure the *in vivo* composition of cells and organelles. The ultimate test of any new biological technique is whether it can provide significant new information that is not otherwise attainable. In our (perhaps slightly biased) view, EPMA has also met this test, and biological results obtained with EPMA have been reviewed elsewhere in detail.<sup>27,30,34-39</sup>

EPMA played a uniquely pivotal role in determining the low endogenous Ca content of mitochondria in a variety of cells and in the demonstration that, in most eukaryotic cells, it is the endoplasmic reticulum and not the mitochondria that regulates cytoplasmic  $\text{Ca}^{2+}$  (see, for example, Refs. 8, 20, and 40; reviewed in Refs. 41 and 42). Drawing further upon our own experience, EPMA was instrumental in determining the composition of the sarcoplasmic reticulum (SR) in resting and in contracting muscle, and significantly enhanced our understanding of excitation-contraction coupling in smooth<sup>12,32,43,44</sup> and in striated muscle.<sup>6,28,45,46</sup> Other salient results of biological EPMA include the clarification of cellular pathways in secretory and transporting epithelia,<sup>16,27,38,47,48,54</sup> and direct measurements of the ionic changes that occur during illumination in vertebrate photoreceptors.<sup>20</sup> The EPMA results showing the low Ca content of the outer segment in normal vertebrate retinal rods contributed to the demise of the " $\text{Ca}^{2+}$ -theory of visual transduction."<sup>20,49</sup> We anticipate that EPMA will play an increasing role in determining the dynamics of intracellular transport between cytoplasm and cell organelles in a variety of systems.

### References

1. T. A. Hall, "The microprobe assay of chemical elements," A. G. Oster, Ed., *Physical Techniques in Biological Research*, New York: Academic Press, 1971, vol. 1, 151-267.
2. H. Shuman et al., "Quantitative electron probe microanalysis of biological thin sections: Methods and validity," *Ultramicroscopy* 1: 317-339, 1976.
3. H. Shuman et al., "Theoretical and practical limits of ED X-ray analysis of biological thin sections," *SEM/1977* I, 663-672.
4. A. V. Somlyó et al., "Elemental distributions in striated muscle and effects of hypertonicity: Electron probe analysis of cryosections," *J. Cell Biol.* 74: 828-857, 1977.
5. A. V. Somlyó and J. Silcox, "Cryoultramicrotomy for electron probe analysis," in C. Lechene and R. Warner, Eds., *Microbeam Analysis in Biology*, New York: Academic Press, 1979, 535-555.
6. A. V. Somlyó et al., "Calcium release and ionic changes in the sarcoplasmic reticulum of tetanized muscle: An electron probe study," *J. Cell Biol.* 90: 557-594, 1981.
7. H. Plattner and L. Bachmann, "Cryofixation: A tool in biological ultrastructural research," *Internatl. Rev. Cytology* 79: 237-303, 1982.
8. A. P. Somlyó et al., "The calcium content of mitochondria and endoplasmic reticulum in liver rapidly frozen *in situ*," *Nature* 314: 622-625, 1985.
9. A. V. Somlyó et al., "Direct measurements of intracellular elemental composition utilizing a new approach to freezing *in vivo*," *Proc. 43rd EMSA*, 1985, 10-13.
10. T. B. Pool et al., "Evaluation of preparative method for x-ray microanalysis of soft tissues," *Cytobios* 28: 17-33, 1980.
11. A. V. Somlyó et al., "Electron probe analysis and cryoultramicrotomy of cardiac muscle: Mitochondrial granules," *Proc. 33rd EMSA*, 1975, 532.
12. A. P. Somlyó et al., "Electron probe analysis of vascular smooth muscle: Composition of mitochondria, nuclei and cytoplasm," *J. Cell. Biol.* 81: 316-335, 1979.



13. R. D. Karp et al., "Cryoultramicrotomy: Evidence against melting and the use of a low temperature cement for specimen orientation," *J. Microsc.* 125: 157-165, 1982.
14. J. R. J. Baker and T. C. Appleton, "A technique for electron microscope autoradiography (and x-ray microanalysis) of diffusible substances using freeze-dried fresh frozen sections," *J. Microsc.* 108: 307-315, 1976.
15. J. A. T. Dow et al., "X-ray microanalysis of elements in frozen-hydrated sections of an electrogenic K<sup>+</sup> transport system: The posterior midgut of tobacco hornworm (*Manduca sexta*) *in vivo* and *in vitro*," *J. Membrane Biol.* 77: 223-241, 1984.
16. B. L. Gupta and T. A. Hall, "The x-ray microanalysis of frozen-hydrated sections in scanning electron microscopy: An evaluation," *Tissue and Cell* 13: 623-643, 1981.
17. T. Kitazawa et al., "Quantitative electron probe analysis: Problems and solutions," *Ultramicroscopy* 11: 251-262, 1983.
18. D. J. McMillan et al., "Experience with multiple-least-squares fitting with derivative references," *Microbeam Analysis--1985*, 137-140.
19. J. McD. Tormey, "Improved methods for x-ray microanalysis of cardiac muscle," *Microbeam Analysis--1983*, 221-228.
20. A. P. Somlyo and B. Walz, "Elemental distribution in *Rana pipiens* retinal rods: Quantitative electron probe analysis," *J. Physiol.* 358: 183-195, 1985.
21. M. Bond et al., "Total cytoplasmic calcium in relaxed and maximally contracted rabbit portal vein smooth muscle," *J. Physiol.* 357: 185-201, 1984.
22. V. L. Lew et al., "Compartmentalization of sickle cell calcium in endocytic inside-out vesicles," *Nature* 315: 586-589, 1985.
23. A. Warley et al., "X-ray microanalysis of HeLa S3 cells," *J. Cell Biol.* 60: 217-229, 1983.
24. N. Roos and T. Barnard, "Aminoplastic standards for quantitative x-ray microanalysis of thin sections of plastic-embedded biological material," *Ultramicroscopy* 15: 277-286, 1984.
25. B. S. Weakley et al., "Phosphorus standards for the electron probe x-ray microanalysis of ultrathin tissue sections," *J. Microsc.* 118: 471-476, 1979.
26. D. M. R. Harvey et al., "The preparation of calibration standards for sodium, potassium and chlorine analyses by analytical electron microscopy," *J. Microsc.* 118: 143-152, 1980.
27. T. A. Hall and B. L. Gupta, "The localization and assay of chemical elements by microprobe methods," *Quarterly Rev. Biophys.* 16: 279-339, 1983.
28. T. Kitazawa et al., "The effects of valinomycin on ion movements across the sarcoplasmic reticulum in frog muscle," *J. Physiol.* 350: 253-268, 1984.
29. P. M. Best and C. W. Abramcheck, "Potassium efflux from single skinned skeletal muscle fibers," *Biophys. J.* 48: 907-913, 1985.
30. H. Shuman and A. P. Somlyo, "Quantitative electron probe microanalysis of biological thin sections: Methods and validity," *Ultramicroscopy* 1: 317-339, 1976.
31. H. Shuman and A. P. Somlyo, "Electron probe x-ray analysis of single ferritin molecules," *Proc. Natl. Acad. Sci. USA* 73: 1193-1195, 1975.
32. A. P. Somlyo, "Compositional mapping in biology: X-rays and electrons," *J. Ultrastruct. Res.* 83: 135-142, 1985.
33. C.-F. Chang et al., "Electron probe analysis, x-ray mapping and electron energy loss spectroscopy of elemental distribution in *Escherichia coli* B," *Proc. 42nd EMSA*, 1984, 570-571.
34. R. B. Moreton, "Electron probe x-ray microanalysis: Techniques and recent applications in biology," *Biol. Rev.* 56: 409-461, 1981.
35. T. A. Hall, "Biological x-ray microanalysis," *J. Microsc.* 117: 145-163, 1979.
36. T. E. Hutchinson and A. P. Somlyo, Eds., *Microprobe Analysis of Biological Systems*, New York: Academic Press, 1981.
37. C. P. Lechene and R. R. Warner, Eds., *Microbeam Analysis in Biology*, New York: Academic Press, 1979.
38. M. M. Civan, *Epithelial Ions and Transport: Application of Biophysical Techniques*, New York: Wiley, 1983.
39. T. E. Hutchinson, "Determination of subcellular elemental concentration through ultrahigh resolution electron microprobe analysis," *Internatl. Rev. Cytology* 58: 115-157, 1979.

40. A. P. Somlyo et al., "Mitochondrial calcium and cellular electrolytes in brain cortex frozen *in situ*: Electron probe analysis," *Biochem. Biophys. Res. Commun.* 132: 1071-1978, 1985.
41. A. P. Somlyo, "Cellular site of calcium regulation," *Nature* 308: 516-517, 1984.
42. P. F. Baker, "Intracellular signalling: GTP and calcium release," *Nature* 320: 395, 1986.
43. M. Bond et al., "Release and recycling of calcium by the sarcoplasmic reticulum in guinea pig portal vein smooth muscle," *J. Physiol.* 355: 677-695, 1984.
44. D. Kowarski et al., "Calcium release by norepinephrine from central sarcoplasmic reticulum in rabbit main pulmonary artery smooth muscle," *Proc. Natl. Acad. Sci. USA* 82: 5231-5235, 1985.
45. T. Yoshioka and A. P. Somlyo, "The calcium and magnesium contents and volume of the terminal cisternae in caffeine-treated skeletal muscle," *J. Cell Biol.* 99: 558-568, 1984.
46. A. V. Somlyo et al., "Electron probe x-ray microanalysis of post-tetanic Ca and Mg movements across the sarcoplasmic reticulum *in situ*," *J. Biol. Chem.* 260: 6801-6807, 1985.
47. K. T. Izutsu et al., "Elemental analysis of labial glands in cystic fibrosis," *Microbeam Analysis--1984*, 277-280.
48. R. Rick et al., "Intracellular electrolyte concentrations in the frog skin epithelium: Effect of vasopressin and dependence on the Na concentration in the bathing media," *J. Membrane Biol.* 78: 129-145, 1984.
49. G. H. Gold, "Plasma membrane calcium fluxes in intact rods are inconsistent with the 'calcium hypothesis'," *Proc. Natl. Acad. Sci. USA* 83: 1150-1154, 1986.
50. V. L. Lew et al., "Compartmentalization of sickle cell calcium in endocytic inside-out vesicles," *Nature* 315: 586-589, 1985.
51. J. L. Junker et al., "Electron probe analysis of sodium and other elements in hypertrophied and Na-loaded smooth muscle," *Circ. Res.* 54: 254-266, 1984.
52. R. M. Bookchin and V. L. Lew, "Progressive inhibition of the Ca pump and Ca:Ca exchange in sickle red cells," *Nature* 284: 561-563, 1980.
53. J. Funder and J. O. Wieth, "Potassium, sodium, and water in normal human red blood cells," *Scand. J. Clinical Invest.* 18: 167-180, 1966.
54. S. B. Andrews et al., "The distribution of intracellular ions in the avian salt gland," *J. Cell Biol.* 96: 1389, 1983.
55. A. L. Hodgkin and P. Horowicz, "Movements of Na and K in single muscle fibers," *J. Physiol.* 145: 405-432, 1959.
56. A. F. Huxley and R. J. Niedergerke, "Measurement of the striations of isolated muscle fibres with the interference microscope," *J. Physiol.* 144: 403-425, 1958.
57. S. M. Baylor et al., "Calcium release and sarcoplasmic reticulum membrane potential in frog skeletal muscle fibres," *J. Physiol.* 344: 625, 1983.
58. T. Kitazawa et al., "Calcium and magnesium binding to thin and thick filaments in skinned muscle fibres: Electron probe analysis," *J. Muscle Research Cell Motility* 3: 437-454, 1982.
59. J. Kleineke and H-D. Soling, "Mitochondrial and extramitochondrial  $\text{Ca}^{2+}$  pools in the perfused rat liver," *J. Biol. Chem.* 260: 1040-1045, 1985.

## QUANTITATIVE ELEMENTAL CHARACTERIZATION OF CULTURED HEART CELLS BY ELECTRON PROBE X-RAY MICROANALYSIS AND ION-SELECTIVE ELECTRODES

Ann LeFurgey, Shi Liu, Melvyn Lieberman, and Peter Ingram

To clarify the complex relationships between cell structure and ion transport, one must define (a) the total ion and water content within cells, (b) the distribution of this content among cell types comprising the tissue, (c) the distribution of ions and water among intracellular compartments and cytoplasm, and (d) the activity of the various ions in the several cellular compartments.<sup>1</sup> Of the available techniques for measuring elemental or ionic composition in cells, electron probe x-ray microanalysis (EPXMA) provides the spatial resolution necessary to sample regions as small as sarcoplasmic reticulum or mitochondria and as large as a single cell or groups of cells. Thus, EPXMA can measure not only the total (free and bound) amount of an element (ion) within various cell types, but also the elemental compartmentation within individual cells. Ionic activity can be determined directly by insertion of ion-selective microelectrodes (ISME) into living cells to provide complementary information by use of an established physiological technique.

In our studies of ion transport in heart cells, we have applied the techniques of EPXMA and ISME to cultured embryonic chick heart cells. This model system can be used advantageously for such determinations because (1) it facilitates experiments which affect only the cells of interest and eliminates secondary effects that in an animal model compromise the function of the cardiovascular system; and (2) cells can be grown with variable geometries which reduce ionic diffusion limitations for physiological measurements and promote cryopreservation which is so rapid that ionic translocation does not occur prior to EPXMA. In addition, utilization of both EPXMA and ISME methods in the same preparation provides unique experimental data appropriate for direct comparisons of ionic activity with elemental concentration and also for evaluation of problems particular to each technique.

### *Materials and Methods*

*Cell Culture.* For x-ray microanalysis, aggregates of cardiac muscle cells were obtained as described by Ebihara et al.<sup>2</sup> For ion-selective microelectrode analysis, growth-oriented heart cells (polystrands) were prepared according to the method of Horres et al.<sup>3</sup> Briefly, muscle-enriched cells from 11-day-old embryonic chick hearts were used to seed agar-coated culture dishes containing small openings (20  $\mu$ m) or nylon monofilament (20  $\mu$ m OD) contained within silicone rubber growth chambers.<sup>3</sup> The cultures were incubated for 3 or 4 days at 37 C in a humidified chamber containing 4%CO<sub>2</sub> and 96% air.

*Cryopreservation.* On day 3 or 4 the cultures were observed by light microscopy and small, 50-100 $\mu$ m spontaneously beating aggregates chosen for rapid freezing. Individual aggregates were withdrawn from the medium into a pipette attached to a syringe and placed on a cryomicrotome specimen stub precoated with a drop of 20% gelatin solution. The aggregate on the specimen stub was rapidly plunged into liquid nitrogen-cooled liquid propane and then stored under liquid nitrogen. Average time from withdrawal of the aggregate from the culture dish to freezing was <20 s. Frozen aggregates from each experiment were then processed either by freeze substitution for examination by transmission electron microscopy (TEM) to determine the quality of quick freezing,<sup>4</sup> or by cryosectioning at -120 C and freeze drying prior to EPXMA.

*X-ray Microanalysis.* All analyses were performed on freeze-dried cryosections  $\sim$ 1000 Å thick, in a scanning transmission electron microscope (JEOL 100CX-II TEMSCAN) equipped with a 30mm<sup>2</sup> Si(Li) energy-dispersive x-ray detector and microcomputer system (Tracor Northern 5500) and a liquid nitrogen-cooled low-background cryotransfer stage (Gatan 626). X-ray spectra were obtained from selected cell compartments at -120 C by use of a small raster at 100 000 to 150 000 magnification with specimen tilt of 30°; beam current,  $\sim$ 1 nA;

---

Authors LeFurgey, Liu, and Lieberman are at the Department of Physiology, Duke University, Durham, NC 27710; author Ingram is at Research Triangle Institute, Research Triangle Park, NC 27709. The work was supported by NIH grants HL28280, HL27105, and HL17670, and the Walker P. Inman Fund.

and accelerating voltage, 80 kV. Standards were prepared according to the methods of Shuman, Somlyo, and colleagues,<sup>5</sup> and quantitation was performed by the Hall continuum normalization method<sup>6</sup> with the peak centroid shift correction of Kitazawa et al.,<sup>7</sup> as implemented by McMillan et al.<sup>8</sup>

*ISME.* Ion-selective microelectrodes were drawn from Omega dot borosilicate glass tubing (1 mm OD, 0.5 mm ID). Electrodes were silanized by exposure to hexamethyldisilazane vapor at 200 C for 15 min.<sup>9</sup> K electrodes were filled with Corning 477317 ion exchange resin and 0.5M KCl. Cl electrodes were filled with Corning resin 477913 and 0.1M KCl. Na electrodes were filled with the neutral carrier Fluka 71176, and 0.1M NaCl. Electrodes were calibrated according to the method of Dagostino and Lee.<sup>10</sup> The selectivity ratio for the electrodes were as follows: K, K:Na 50:1; Na, Na:K 50:1 and Na:Ca 1:2; Cl, Cl:HCO<sub>3</sub> 25:1. The outputs from voltage and ion-sensitive microelectrodes were led into a conventional configuration of buffer and differential amplifiers and a variable low-pass filter. Data were analyzed from records obtained using both magnetic tape and oscillographic chart recorders.

### *Results and Discussion*

*EPXMA.* Figures 1(a) and (b) show comparative EPXMA spectra from cytoplasm and mitochondria of control heart cell aggregates. Quantitative results, expressed as millimoles per kilogram dry weight, are shown in Table 1 for cytoplasmic and mitochondrial compartments. The contents of Na, Mg, P, S, Cl and K in mitochondria were lower on a dry weight basis than in paired regions of the cytoplasm. However, the greater number of x-ray continuum counts obtained (with identical analysis conditions) in mitochondria ( $1921 \pm 207$  SEM), as compared to the adjacent cytoplasm ( $806 \pm 155$  SEM), indicates that the mitochondria were less hydrated originally. The K:Na ratio in mitochondria and cytoplasm of control heart muscle cells is approximately 10 to 1, consistent with bulk measurements made on whole cells by atomic absorption spectrophotometry.<sup>11</sup> Quantitative evaluation of Ca measurements obtained by EPXMA is currently in progress; however, no sequestration of Ca has been found in mitochondria, which confirms indirect biochemical measurements in which FCCP-releasable calcium was used as an indicator of calcium sequestered by mitochondria.<sup>12</sup> Cytoplasmic calcium is qualitatively variable, which suggests that some x-ray probes include sarcoplasmic reticulum, a site of possible high calcium accumulation.

*ISME.* Resting steady-state levels of intracellular Na, K, Cl activity obtained from polystrands at 37 C are summarized in Table 2. K concentrations calculated from the activity measurements are consistent with values calculated from chemical and isotopic analysis of the same preparation (see Table 3). K measured in mitochondria by EPXMA compares favorably with ISME cytoplasmic K values and total (cell) K chemical measurements; however, K measured in cytoplasm by EPXMA is consistently higher than the other values. If a uniform water distribution is assumed for all cell compartments, then total cell K, converted from dry-weight EPXMA measurements to wet weight, is also higher (Table 3). EPXMA continuum readings, as mentioned, suggest that cytoplasm is more hydrated than mitochondria. The technique of zero-loss EELS measurements and imaging for directly determining water content of intracellular organelles is currently being developed; this method should allow accurate conversion of dry weight to wet weight for each compartment.<sup>13</sup>

Similar calculations for Na concentration indicate that values obtained with ISME are lower than those obtained either by chemical/isotope analyses and EPXMA. Presently, the cause for the experimental differences are unresolved. Cl concentration calculated from Cl activity is higher than the calculated values obtained from either coulometric/isotope analyses<sup>14</sup> or EPXMA. In this case, the value for Cl activity could overestimate the true activity because liquid ion-exchange chloride-electrodes respond to other anions.<sup>15</sup> However, HCO<sub>3</sub> interference can be ruled out as a possible contributing factor because upon its removal chloride activity decreases by only 1-2 mM.<sup>16</sup>

Similar comparisons of EPXMA and ISME values for ionic activity, content, and distribution have been made in cultured skeletal muscle.<sup>17</sup> Literature comparisons of ionic activity with concentration have been also made in myocytes, based on data obtained by various laboratories in similar but more structurally complex preparations.<sup>18</sup> However, in many instances the geometry and mass of more complex tissue preparations make measurements by either one or the other technique impossible. The cultured heart cell model can provide new and unique data because both techniques are applied in parallel in the same

preparation. These preliminary EPXMA results for ionic content and distribution, obtained in conjunction with ISME measurements of ionic activity in cultured cardiac cells, demonstrate the feasibility of studying mechanisms of heart cell ion transport under basal conditions and those simulating ischemic injury.

## References

1. A. D. C. MacKnight, "Comparison of analytic techniques: Chemical, isotopic and microprobe analysis," *Fed. Proc.* 39: 2881-2887, 1980.
2. L. Ebihara et al., "The initial inward current in spherical clusters of chick embryonic heart cells," *J. Gen. Physiol.* 75: 437-456, 1980.
3. C. R. Horres et al., "Growth orientation of heart cells on nylon monofilament," *J. Mem. Biol.* 34: 313-329, 1977.
4. J. R. Sommer et al., "Side bridge geometry after quick freezing of stimulated and unstimulated frog skeletal muscle fibers," *Proc. 41st Mtg EMSA*, 1983, 464-465.
5. H. Shuman et al., "Quantitative electron probe microanalysis of biological thin sections: Methods and validity," *Ultramicroscopy* 1: 317-339, 1976.
6. T. Hall, "Biological x-ray microanalysis," *J. Microscopy* 117: 145-163, 1979.
7. T. Kitazawa et al., "Quantitative electron probe analysis: Problems and solutions," *Ultramicroscopy* 11: 251-262, 1983.
8. D. J. McMillan et al., "Experience with multiple-least-squares fitting with derivative references," *Microbeam Analysis--1985*, 137-140.
9. R. Y. Tsien and T. J. Rink, "Neural carrier ion-selective microelectrodes for measurement of intracellular free calcium," *Biochim. Biophys. Acta* 599: 623-638, 1980.
10. M. Dagostino and C. O. Lee, "Neural carrier  $\text{Na}^+$ - and  $\text{Ca}^{2+}$ -selective microelectrodes for intracellular application," *Biophys. J.* 40: 199-207, 1982.
11. E. Murphy et al., "Coupled sodium-calcium transport in cultured chick heart cells," *Am. J. Physiol.* 250: C442-C452, 1986.
12. E. Murphy et al., "Calcium elevation in cultured heart cells: Its role in cell injury," *Am. J. Physiol.* 245: C316-C321, 1983.
13. D. Kopf, et al., "Mass thickness images of frozen hydrated sections," this volume.
14. D. Piwnica-Worms et al., "Transmembrane chloride flux in tissue-cultured chick heart cells," *J. Gen. Physiol.* 81: 731-748, 1983.
15. C. M. Baumgarten, "An improved liquid ion exchange for Cl-selective microelectrodes," *Am. J. Physiol.* 241: C258-C263, 1981.
16. S. Liu, *Electrophysiological Studies of Transmembrane Coupled Ion Movements in Cultured Chick Heart Cells*, Thesis, Duke University, 1986.
17. H. Acker et al., "Comparative measurements of potassium and chloride with ion-sensitive microelectrodes and x-ray microanalysis in cultured skeletal muscle fibers," *In Vitro* 21: 45-48, 1985.
18. T. von Zglinicki et al., "Fast cryofixation technique for x-ray microanalysis," *J. Microscopy* 141: 79-90, 1986.

TABLE 1.--Elemental concentrations in cytoplasm and mitochondria of cultured embryonic chick heart cells as determined by EPXMA.

	mmol/kg dry weight						
	Na	Mg	P	S	Cl	K	Ca*
Mitochondria (n = 25)	78.3±8.8	43.2±3.5	457.6±15.0	202.2±5.9	92.7±13.6	727.8±6.0	-
Cytoplasm (n = 27)	113.3±14.5	77.9±7.4	611.3±28.7	212.1±11.1	107.8±18.2	1055.3±48.8	-

n = number of raster probes (500 s) obtained from each region; values are mean ± S.E.M.

\* Processed spectra gave data with unacceptable negative values.

TABLE 2.--Resting intracellular ionic activities in cultured heart cells.

	Na	K	Cl
$a_x^i$ (mM)	$6.2 \pm 0.2$	$103.0 \pm 1.3$	$26.7 \pm 1.9$
$[X]_i$ (mM)	8.4	140	37
n	20	57	13

Values for ionic activities are mean  $\pm$  S.E.M.

$[X]_i$  means  $a_x^i/0.736$ , assuming intracellular activity coefficient is equal to extracellular activity coefficient.

TABLE 3.--Summary of intracellular concentrations of sodium, potassium, chloride, and calcium in cultured embryonic chick heart cells.

Method	mM			
	Na	K	Cl	Ca
Electron probe x-ray microanalysis*	19	175	19	-
Ion-specific microelectrodes	8	140	37	-
AA-Chemical analysis	16	119-137	-	1.8-3.7
Isotope analysis	18	140	25	-
Coulometric analysis	-	-	25	-

\*Conversion from EPXMA dry weight (mmol/kg dry wt) measurements made within intracellular compartments (mitochondria, cytoplasm) to wet weight (mmolar) values for total cell contractions is based on:

1. Total cell water content equals 8.4  $\mu$ l/mg protein; 1 mg protein equals 1.54 mg dry weight; therefore there is 5.46  $\mu$ l H<sub>2</sub>O/mg dry weight.
2. Mitochondrial volume fraction is assumed to be ~30%.
3. Elemental content in the nucleus is assumed to be the same as in the cytoplasm.
4. Water distribution among intracellular compartments is assumed to be uniform.

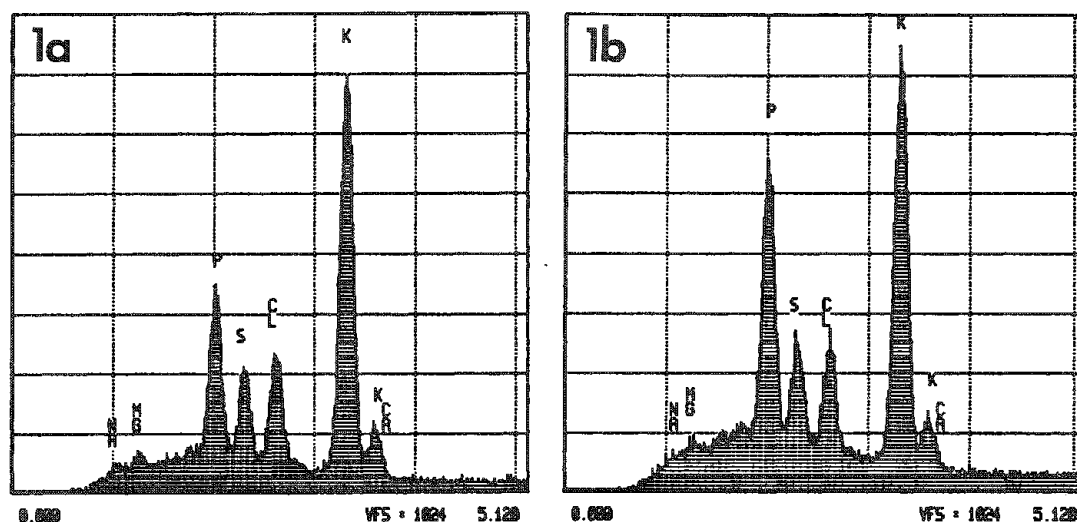


FIG. 1.--EPXMA spectrum from (a) cytoplasm and (b) mitochondrion of cultured heart cell.

## REGULATION OF TRANSEPITHELIAL Na TRANSPORT AS REVEALED BY ELECTRON-MICROPROBE ANALYSIS

Roger Rick, Adolph Dörge, and Klaus Thureau

Quantification of the intracellular ion concentrations in transporting epithelia is a prerequisite for detailed elucidation of the individual transport mechanisms involved. Unfortunately, chemical or radiochemical analyses, which have been often employed to measure the intracellular ion concentrations in epithelia, generally provided inconsistent and conflicting data, in part because these techniques measure only mean values for all epithelial cells, comprising cells with possibly different transport functions. Moreover, it has been shown that chemical analyses, at least in the intact skin, yield too high intracellular Na concentrations and too low K concentrations, mainly because of an underestimate of the extracellular space.<sup>1</sup> Some of the difficulties involved in accurately estimating the extracellular space can be overcome by use of isolated epithelia in which the size of the extracellular space is drastically reduced.

During recent years two new methods have been increasingly applied for measuring intracellular ion concentrations in transporting epithelia: ion-selective microelectrodes and electron-microprobe analysis. Impalement with ion-selective electrodes yields intracellular activities; electron microprobe analysis measures the total chemical concentration of an ion, irrespective of binding or activity state. The two methods have different limitations, advantages, and disadvantages, and should be therefore considered as complementary rather than alternative techniques. Ion-selective electrodes allow the recording of temporal changes in the ion concentration, whereas electron-microprobe analysis yields concentration 'frozen' at only one point in time. On the other hand, when performed on sufficiently thin sections in a scanning transmission or conventional transmission EM, electron-microprobe analysis provides a much better spatial resolution, even down to sub-cellular structures. This feature is of particular importance in histologically complex epithelia composed of different cell layers or cell types with possibly different transport functions.

### Methods

Energy-dispersive x ray microanalysis was performed on freeze-dried cryosections in a scanning electron microscope (Cambridge S150) to which an Si(Li) solid-state x-ray detecting system (LINK) was attached. The cryosections were obtained from specimens snap-frozen in a liquid propane/isopentane mixture at -196 C. Sections 1  $\mu\text{m}$  thick were cut at -90 C in a modified Reichert cryoultramicrotome (OmU 3) and freeze-dried at -80 C and  $10^{-6}$  Torr in a custom-made freeze-dryer based on a turbomolecular pumping unit (Balzers). The measuring conditions were 20 kV acceleration voltage and between 0.2 and 0.5 nA beam current (determined in a Faraday cup at the level of the specimen). During analysis small areas of between 0.1 and 5  $\mu\text{m}^2$  of the section were scanned for 100 s. The emitted x rays were analyzed in the energy range from 0 to 20 keV comprising the  $K\alpha$  lines of the biologically relevant light elements Na, Mg, P, S, Cl, K, and Ca. Quantification of the cellular element concentrations and cellular dry weight was achieved by a comparison with an internal standard. The standard was obtained by covering of the specimen immediately prior to freezing with a thin layer of an albumin solution. The albumin standard solution contained an extracellular composition of electrolytes and 20g/100g solution bovine serum albumin (Behringwerke, Marburg). A detailed description of the methods has been given previously.<sup>2-5</sup>

The experiments were performed on isolated abdominal skins of *Rana temporaria* and *Rana esculenta* (Stein, Lauingen). Several pieces (up to four) obtained from one skin were incubated in Ussing-type chambers in which short-circuit current, transepithelial potential difference, and skin conductance were continuously monitored. The normal bathing solution was NaCl Ringer containing 2.5 mM bicarbonate. After appropriate incubation under various

---

Author Rick is at the Department of Physiology and Biophysics, University of Alabama at Birmingham; authors Dörge and Thureau are at the Department of Physiology, University of Munich.

experimental conditions, the skin pieces were quickly removed from the chambers and snap-frozen by plunging into the liquid coolant.

### *Results and Discussion*

According to the model proposed by Koefoed-Johnson and Ussing,<sup>6</sup> transepithelial Na transport involves two different transport steps. Na influx into the epithelial cell across the apical membrane is thought to be passive, driven by an inwardly directed electrochemical gradient, whereas Na extrusion across the basolateral membrane is assumed to be active, directly coupled to an energy-providing metabolic reaction. The model predicts that the Na concentration of the cells participating in transepithelial transport, usually referred to as the Na transport compartment, should vary according to the activity of the individual transport steps. However, chemical or radiochemical analysis of the intracellular Na concentration in transporting epithelia such as frog skin or toad urinary bladder often failed to show the expected behavior, which lends some support to the view that Na may take a noncellular transport route.<sup>7</sup> Ussing himself entertained the possibilities that actually only a small fraction of the epithelial cell is engaged in transepithelial transport<sup>8</sup> or that Na transport proceeds along specialized intracytoplasmic structures.<sup>9</sup>

To determine which of the various epithelial cell types in a histologically complex epithelium such as the frog skin are actually engaged in transepithelial Na transport, we measured the intracellular electrolyte concentration using electron microprobe analysis. Figure 1 shows a scanning transmission electron micrograph of a freeze-dried cryosection of the frog skin epithelium as used for x-ray microanalysis. The epithelial layers from the outside to the inside are stratum corneum, stratum granulosum, spinosum, and germinativum. The homogeneous layer adhering to the outer surface of the epithelium corresponds to the layer of albumin standard solution with which the skin was coated immediately prior to freezing.

As shown in Fig. 2, a typical cellular distribution of Na and K was observed under control conditions in all layers of the multilayered epithelium, except in the outer cornified layer. The data are displayed as mean intracellular concentrations, since for small cations such as Na and K no significant differences between the nuclear and cytoplasmic concentration values were detectable. After inhibition of the Na pump by the reversible ouabain analog DH-ouabain, the Na concentrations in all living cell layers were increased by about 100 mmol/kg w.w., and the K concentrations showed an equivalent drop (Fig. 2). Since such a Na/K exchange may also occur in cells not participating in transepithelial transport, we further tested whether the Na originates mainly from the outer bathing medium, as is to be expected only for transporting cells. For this purpose we abolished the apical Na influx by adding amiloride to the outer bath. As shown in Fig. 2, the Na increase after DH-ouabain was completely abolished, which suggests that all epithelial layers participate in transepithelial Na transport. It is further shown that after wash-out of DH-ouabain, the intracellular Na and K concentrations return to values almost identical with control.

The behavior of the Na concentration confirms the two-barrier concept of Koefoed-Johnsen and Ussing.<sup>6</sup> Moreover, the results shown in Fig. 2 provide a direct proof for a syncytial organization of the epithelium. Since the paracellular shunt pathway between the cells is sealed at the level of the stratum granulosum,<sup>10</sup> only this cell layer can directly communicate with the outer medium. The observed Na influx from the outer bath into deeper-lying epithelial layers can therefore only be explained if the several epithelial layers are interconnected. However, the syncytial Na transport compartment does not comprise all the epithelial cells. The stratum corneum obviously represents a layer of dead cells, exchanging their electrolytes freely with the outer bathing medium. Further exceptions are the mitochondria-rich cells<sup>11</sup> and the cells of the mucous and seromucous glands, which seem to be involved in the Cl secretion elicited by beta-agonists.<sup>12</sup>

The rate of transepithelial Na transport in the frog skin as well as in other high-resistance epithelia is controlled by a variety of hormonal and nonhormonal factors. Electron-microprobe analysis of intracellular electrolytes can provide further information regarding the mechanism of action of modulators of transepithelial transport. A finding from a recent study on the effect of vasopressin<sup>13</sup> may serve to illustrate this point. In the frog skin as well as other tight epithelia the antidiuretic hormone vasopressin is known to stimulate transepithelial Na reabsorption. Figure 3 shows the effect on the intracellular concentrations of Na and K when the Na transport was stimulated by arginine



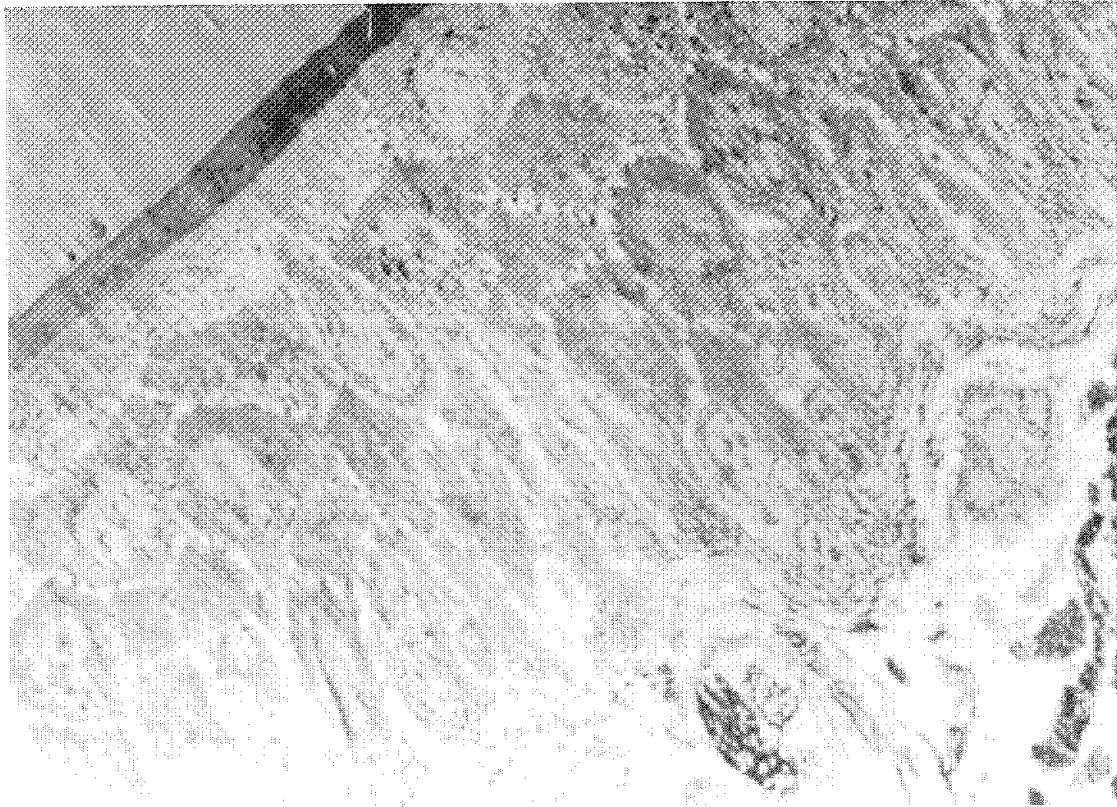


FIG. 1.--Freeze-dried cryosection of frog skin epithelium.

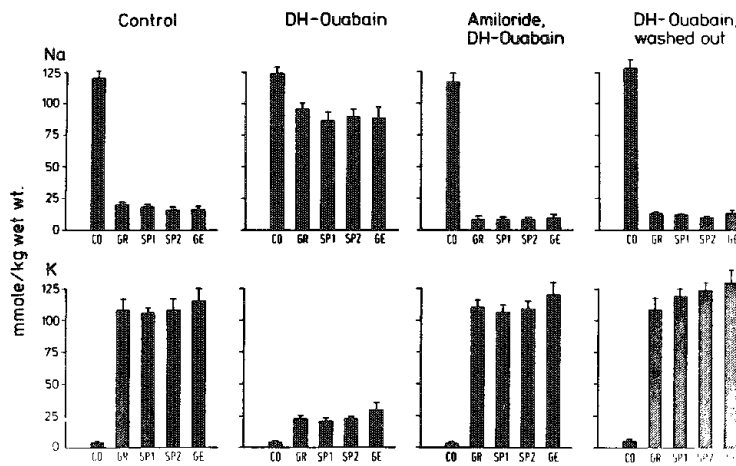


FIG. 2.--Na and K concentrations in epithelial layers of frog skin in control, after DH-ouabain ( $10^{-4}$  M, 60 min), after additional application of amiloride ( $10^{-4}$  M), and after wash-out of DH-ouabain (60 min). Layers are: stratum corneum (CO), granulosum (GR), superficial and deeper spinosum (SP1, SP2), and germinativum (GE). Modified from Rick et al.<sup>20</sup>

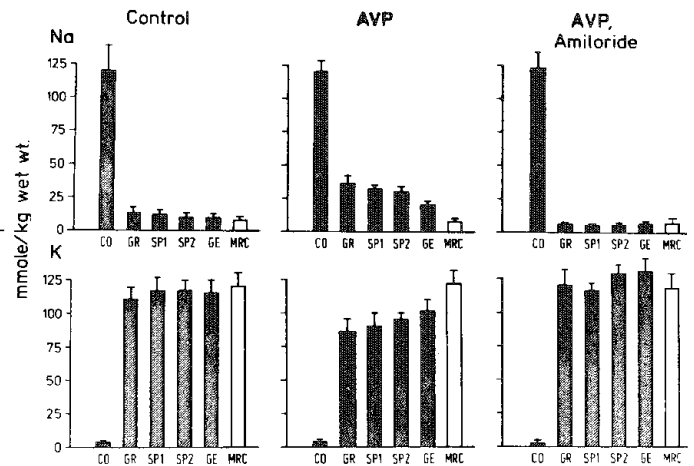


FIG. 3.--Na and K concentrations in epithelial layers and in mitochondria-rich cells (MRC) of frog skin in control, after AVP (150 mU/ml, 45 min), and after subsequent additional application of amiloride ( $10^{-4}$  M). From Rick et al.<sup>20</sup>

vasopressin (AVP) to about 250% of the control value. Again with the exception of the mitochondria-rich cells, a marked increase in the Na concentration and an about equivalent drop in the K concentration can be observed in all epithelial cells. The vasopressin-induced changes could be completely abolished by additional application of amiloride. The Na concentration under this condition was even lower than in control. Under all three experimental conditions no significant changes in the Cl concentration were observed.

The increase in the Na concentration suggests that vasopressin stimulates transepithelial Na transport primarily by increasing the apical Na influx. In fact, if combined with measurements of the apical membrane potential obtained in the same preparation,<sup>14</sup> a 3-5 fold increase in the apical Na permeability can be calculated. However, the data do not rule out the possibility of an additional effect on the active transport step. Indeed, in further experiments we obtained some evidence for a pump stimulation by vasopressin.<sup>13</sup> In addition to vasopressin, we investigated the natriferic action of isoproterenol and aldosterone. In all cases we observed a significant, amiloride-inhibitable increase in the intracellular Na concentration in the syncytium cells, which suggested that these hormones also stimulate Na transport by a primary increase in the apical Na permeability.

The stimulation of the Na pump observed after vasopressin need not necessarily be a direct effect of the hormone. It is conceivable that the enhanced pump activity is secondary to changes in the intracellular ion composition. Indeed, further experiments designed to answer this question provided some evidence that the stimulation of the pump is caused by the transient increase in the intracellular Na concentration.<sup>13</sup> A similar effect on the pump was also observed after inhibition of the active transport step by the reversible ouabain analog DH-ouabain. After the wash-out of the inhibitor, the intracellular Na concentration falls below the control value (Fig. 2). This result might also be influenced by a Ca-mediated inhibition of the apical Na influx,<sup>15,16</sup> assuming that the Ca inhibition outlasts the Na increase. However, at this point during the wash-out the short circuit current already exceeded the control value, which would exclude this inhibition as the only explanation for the lower Na value. The above findings suggest that the activity of the Na pump is being regulated, whether directly or indirectly, by the intracellular Na concentration.

The intracellular Na concentration may also play a role in regulating the apical Na permeability.<sup>17,18</sup> A negative feedback between the intracellular Na concentration and the apical Na permeability might account for the observed saturation of transepithelial Na transport with increasing Na concentrations in the outer bath.<sup>19</sup> The physiological significance of such a feedback mechanism may lie in the maintenance of constant intracellular Na concentrations in the transporting epithelial cells. At least in the frog skin epithelium, this goal seems to be achieved. Figure 4 shows the intracellular Na concentration and the short-circuit current (SCC) as a function of the external Na concentration.<sup>13</sup> The circles give the mean Na concentration in the transport syncytium and the triangles the value for the outermost living cell layer, the stratum granulosum. The intracellular Na concentration follows essentially the same curve as the transepithelial transport rate measured by the short-circuit current (squares), demonstrating that the saturation of transepithelial Na transport is due to a downregulation of the apical Na permeability rather than to a limited transport capacity of the pump. Over a large range of external Na concentrations the intracellular Na concentration is virtually independent of the outer Na concentration, which suggests a threshold-like control of the apical Na influx. As the intracellular Na exceeds a certain set value, the Na permeability of the apical membrane is downregulated until the Na concentration again reaches subthreshold values.

## References

1. A. D. C. Macknight and A. Leaf, "The sodium transport pool," *Am. J. Physiol.* 234: F1-F9, 1978.
2. A. Dörge, R. Rick, K. Gehring, and K. Thureau, "Preparation of freeze-dried cryosections for quantitative x-ray microanalysis of electrolytes in biological soft tissues," *Pflügers Arch.* 373: 85-97, 1978.
3. R. Bauer and R. Rick, "Computer analysis of x-ray spectra (EDS) from thin biological specimens," *X-ray Spectrom.* 7: 63-39, 1978.
4. B. Jehl, R. Bauer, A. Dörge, and R. Rick, "The use of propane/isopentane mixtures for rapid freezing of biological specimens," *J. Microsc.* 123: 307-309, 1981.

5. R. Rick, A. Dörge, and K. Thureau, "Quantitative analysis of electrolytes in frozen dried sections," *J. Microsc.* 125: 239-247, 1982.
6. V. Koefoed-Johnsen and H. H. Ussing, "The nature of the frog skin potential," *Acta Physiol. Scand.* 42: 298-308, 1958.
7. M. Cereijido and C. A. Rotunno, "Fluxes and distribution of sodium in frog skin: A new model," *J. Gen. Physiol.* 51: 280-289, 1968.
8. C. L. Vôte and H. H. Ussing, "Some morphological aspects of active sodium transport," *J. Cell. Biol.* 36: 625-638, 1968.
9. C. L. Vôte, K. Møllgaard, and H. H. Ussing, "Quantitative relationship between active sodium transport, expansion of endoplasmic reticulum and specialized vacuoles ('scalloped sacs') in the outermost living cell layer of the frog skin epithelium (*Rana temporaria*)," *J. Membrane Biol.* 21: 273-289, 1975.
10. D. Erlij, "Salt transport across isolated frog skin," *Phil. Trans. Roy. Soc. Lond.* B262: 69-89, 1971.
11. R. Rick, A. Dörge, E. von Arnim, and K. Thureau, "Electron microprobe analysis of frog skin epithelium: Evidence for a syncytial sodium transport compartment," *J. Membrane Biol.* 39: 313-331, 1978.
12. J. W. Mills, K. Thureau, A. Dörge, and R. Rick, "Electron microprobe analysis of intracellular electrolytes in resting and isoproterenol-stimulated glands of frog skin," *J. Membrane Biol.* 86: 211-220, 1985.
13. R. Rick, C. Roloff, A. Dörge, F. X. Beck, and K. Thureau, "Intracellular electrolyte concentrations in the frog skin epithelium: Effect of vasopressin and dependence on the Na concentration in the bathing media," *J. Membrane Biol.* 78: 129-145, 1984.
14. W. Nagel, "Effects of antidiuretic hormone upon electrical potential and resistance of apical and basolateral membranes of frog skin," *J. Membrane Biol.* 42:99-122, 1978.
15. S. Grinstein and D. Erlij, "Intracellular calcium and the regulation of sodium transport in the frog skin," *Proc. Roy. Soc. London* B202: 353-360, 1978.
16. A. Taylor and E. E. Windhager, "Possible role of cytosolic calcium and Na-Ca exchange in regulation of transepithelial sodium transport," *Am. J. Physiol.* 236: F505-F512, 1979.
17. E. A. C. MacRobbie and H. H. Ussing, "Osmotic behavior of the epithelial cells of frog skin," *Acta Physiol. Scand.* 53: 348-365, 1961.
18. D. Erlij and M. W. Smith, "Sodium uptake by frog skin and its modification by inhibitors of transepithelial sodium transport," *J. Physiol. (London)* 228: 221-239, 1973.
19. L. B. Kirschner, "On the mechanism of active sodium transport across the frog skin," *J. Cell. Comp. Physiol.* 45: 61-87, 1955.
20. R. Rick, A. Dörge, E. von Arnim, J. Weigel, and K. Thureau, "Properties of the outer and inner barriers to transepithelial Na transport: An electron microprobe analysis," in A. D. C. MacKnight and J. P. Leader, Eds., *Epithelial Ion and Water Transport*, New York: Raven Press, 1981, 117-125.

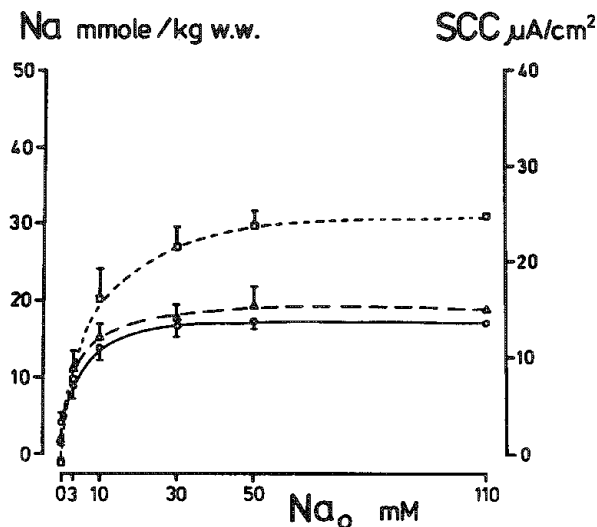


FIG. 4.--Dependence of intracellular Na concentration and short-circuit current (SCC) on Na concentration in outer bath ( $Na_o$ ). Na was replaced with choline. For further explanation see text. Modified from Rick et al.<sup>13</sup>

## CHARACTERIZATION OF SUBCELLULAR ELEMENTAL DISTRIBUTION CHANGES OCCURRING CONCOMITANT WITH MAMMALIAN SPERM DEVELOPMENT

Katy Colonna and G. Oliphant

Capacitation and the acrosome reaction constitute two stages of development necessary for mammalian sperm to acquire the ability to fertilize an ovum. Associated with these physiological changes is a dynamic and specialized ionic microenvironment that surrounds the sperm as they progress toward maturation. Evidence has suggested that the capacitation and the acrosome reaction are mediated by a complex coordinated series of ionic fluxes.<sup>1</sup> However, insufficient knowledge does not permit speculations concerning the relationships between the ionic milieu and the maturing sperm cell. Potential relationships cannot be discerned until the intracellular ionic milieu is examined. Energy-dispersive x-ray microanalysis was used to analyze changes in the subcellular distributions of Na, P, S, Mg, Cl, K, Ca, and Zn accompanying the capacitation and acrosome reaction of mammalian sperm. The data obtained provide direct evidence for changes in the subcellular elemental distribution and the degree of plasma membrane permeability occurring concomitant with the capacitated and acrosome reacted stages of sperm cell development.

### *Experimental Protocol*

*Cell Preparation.* All sperm were obtained from mature New Zealand White rabbits. Ejaculated, capacitated, and acrosome-reacted sperm were prepared as described in the protocol of Oliphant and Eng.<sup>2</sup> To prepare the sperm for analysis by EDS, 50 nanoliters of the sperm solutions were micropipetted onto frozen carbon and Formvar-coated copper slot grids. The grids were plunged directly into liquid nitrogen. The liquid nitrogen bath was mechanically stirred so as to minimize temperature gradients. After freezing, the sperm were vacuum evaporated, carbon coated, and stored in an evacuated dessicator until the time of analysis.

*System Analysis.* All analyses were performed on a Hitachi H-600 equipped with a STEM attachment. X rays were collected on a 30mm<sup>2</sup> Si(Li) crystal. EDS spectra were displayed on an EG&G Ortec EEDSII computer-based multichannel analyzer and processed for quantification on a FDP11-44. Sperm were analyzed in seven anatomically specific probe sites for each of eight elements. A software package was prepared that

- (1) removed contributions to the spectrum by the support film;
- (2) stripped a modeled background from the spectrum;
- (3) calculated the net number of counts in each peak of interest;
- (4) calculated the average bremsstrahlung on the modeled background;
- (5) corrected the net peak counts for variations in x-ray fluorescent yield, ionization cross section, atomic weight, relative detector efficiency, and K fraction of the total yield; and
- (6) Normalized to varying mass-density by calculating a correct peak background ratio for each element of interest.

One-way analysis of variance (ANOVA) was used to estimate the relative contribution of variations within and between groups. The null hypothesis was tested by the F-statistic and interpreted by Duncan's Multiple Range Test. Construction of least-squares regression curves demonstrated patterns in intracellular ionic distributions. Only significance levels less than or equal to 0.01 are reported.

---

The authors are in the Department of Anatomy and Cell Biology, University of Virginia School of Medicine, Charlottesville, VA 22908. This research was supported by NIH grant HD08573.

## *Results and Discussion*

Statistical analysis of the spectral data revealed several very consistent patterns of subcellular compositional changes. Concomitant with capacitation was a significant increase in nuclear Na, nuclear and midpiece-associated Cl, acrosomal, nuclear and midpiece-associated Ca, midpiece-associated P, and acrosomal and midpiece-associated Zn. Elemental decreases were observed in nuclear K and principal piece-associated Zn. Mg levels remained constant and no significant changes were observed. The subcellular elemental changes associated with capacitated cells were very similar to those observed in acrosome-reacted cells. Differences between the two maturational stages exists only in the midpiece-associated Ca, nuclear Na, and P levels. Acrosome reacted cells showed a decrease in nuclear Na and P and an increase in midpiece-associated Ca.

Many investigators have demonstrated a potentially integral role for Na in the facilitation of capacitation and the acrosome reaction. Evidence stemming from examination of the acrosome reaction in sea urchin sperm has shown that a rise in intracellular pH and an efflux of  $H^+$  occur concomitant with the acrosome reaction.<sup>3</sup> An acidic pH may prevent premature activation of proteolytic zymogens in the organelle. The uptake of  $Na^+$  may serve to facilitate or electrically balance the  $H^+$  efflux, which in turn increases the intracellular pH level. The significant increase in nuclear Na observed when capacitated and acrosome-reacted cells are compared to ejaculated cells appears to be consistent with this earlier evidence. The slight but significant increase in Cl concentrations may be due to the electrical gradient established by the large influx of  $Na^+$ .

Mammalian sperm have been shown biochemically and cytochemically to have  $Na^+, K^+$  activated ATPase activity on the plasma membrane. As a means to reestablish ionic gradients, the  $Na^+, K^+$  ATPase pump may be activated following the acrosome reaction. Although no increase in K was observed, the slight loss in intracellular Na may be indicative of the pump's activation.

There has been substantial evidence linking the movement of  $Ca^{+2}$  to capacitation and the acrosome reaction. Evidence has linked a high regional concentration of Ca with the promotion of membrane fusion and the activation of proteolytic zymogens.<sup>4</sup> The permeability of the plasma membrane to cations increases with a rise in intracellular pH. The increase in acrosomal and nuclear Ca observed in the EDS data appears to be consistent with these findings. Evidence has also suggested that a majority of the  $Ca^{+2}$  uptake accompanying the acrosome reaction is mitochondrial. The EDS data indicate a substantially greater increase in Ca uptake in the midpiece region of the acrosome reacted cells than in the capacitated cells.

Substantially lower levels of Zn were found to be associated with the principal piece of both capacitated and acrosome-reacted sperm than with ejaculated cells. Earlier investigations have linked the presence of Zn with immature chromatin-thiol and protein-thiol complexes.<sup>5</sup> Zn reversibly binds chromatin-thiol and protein-sulfhydryl complexes and temporarily prevents the oxidation of free sulfhydryls to disulfide linkages. Formation of disulfide cross linkages facilitates chromatin condensation in the nucleus and confers structural stability to the accessory fibers of the principal piece. Decreased levels of Zn in both the nucleus and principal piece of the capacitated and acrosome reacted cells suggests the existence of condensed nuclear chromatin and protein cross linkages in the accessory fibers. Mature, fully motile capacitated and acrosome reacted cells contain much lower levels of Zn than do their relatively immature and functionless counterparts (data to be submitted).

Changes in subcellular Mg levels did not occur during either the capacitated or acrosome reacted states. The absence of a change indicates that changes in plasma membrane permeability were specific to particular ions. It also indicates that the plasma membrane remained intact during the preparation of the cells. If cell damage had occurred, a non-specific leakiness of the plasma membrane would have resulted.

## *Conclusion*

The critical role that ion transport exerts in the control of mammalian cell metabolism and proliferation is becoming increasingly evident. The information obtained with EDS clearly demonstrates that changes in the subcellular elemental distribution and plasma membrane permeability are specific to both particular ions and particular stages of sperm cell maturation. The information obtained with EDS has provided further characterization of the

dynamic intracellular ionic milieu and thus another step in the definition of the developmental changes occurring in mammalian sperm cells.

#### References

1. M. Cantino, R. W. Schackmann, and D. E. Johnson, "Changes in subcellular elemental distributions accompanying the acrosome reaction in sea urchin sperm," *J. Exp. Zool.* 226: 255, 1983.
2. G. Oliphant and L. A. Eng, "Collection of gametes in laboratory animals and preparation of sperm for *in-vitro* fertilization," in L. Mastroianni and J. D. Biggers, Eds., *Fertilization and Embryonic Development in Vitro*, New York: Plenum Publishing Co., 1981, 11-26.
3. R. W. Schackmann, R. Christen, and B. M. Shapiro, "Membrane depolarization and increased intracellular pH accompany the acrosome reaction of sea urchin sperm," *PNAS* 78: 6066, 1981.
4. S. Meitzel and S. Mukerji, "Proacrosin from rabbit epididymal spermatozoa: Partial purification and initial biochemical characterization," *Biol. Reprod.* 13: 83, 1975.
5. H. I. Calvin, C. C. Yu, and J. M. Bedford, "Effects of epididymal maturation, zinc (II) and copper (II) on the reactive sulfhydryl content of structural elements in rat spermatozoa," *Exp. Cell Res.* 81: 333, 1973.

## QUANTITATIVE ELECTRON PROBE X-RAY MICROANALYSIS AND FLAME ATOMIC ABSORPTION SPECTROSCOPY OF HUMAN MONONUCLEAR BLOOD CELL MAGNESIUM

G. R. Hook, J. M. Hosseini, R. J. Elin, and C. E. Fiori

Magnesium (Mg) is an essential element required for a wide variety of biochemical, cellular and physiological processes.<sup>1</sup> Mg deficiency may develop in various clinical conditions including alcoholism, diabetes mellitus, malabsorption syndromes, diuretic therapy, extensive parenteral fluid administration, and low Mg diets.<sup>2</sup> Hypomagnesemia is inversely correlated with cardiovascular disease, tetany, and seizures.<sup>2</sup> The normal adult 70kg male contains approximately 24 g of Mg, of which approximately 60% is in bones, 39% is in cells, and 1% is in plasma and extracellular fluid. It is therefore not surprising that plasma Mg is a poor indicator of Mg status (except in severe Mg depletion) and that total body Mg status has been difficult to assess.

The Mg concentration of peripheral mononuclear blood cells (MBC) may be a good indicator of total body Mg status.<sup>3,4</sup> Peripheral MBC are a heterogeneous population composed of approximately 80% lymphocytes (both T and B) and 20% monocytes, but the composition can vary significantly among individuals and with disease states. Monocytes have approximately twice the volume of lymphocytes and the volumes can change due to disease. The Mg concentration of MBC and cell size are unknown.

Recently, we developed an energy-dispersive electron probe x-ray microanalysis (EPMA) method to quantitate Mg concentration in individual whole lymphocytes grown in culture.<sup>5</sup> In this paper, we determine and compare the Mg concentration of MBC from normal adult volunteers using EPMA and flame atomic absorption spectroscopy (FAAS).

### Methods

Whole blood was collected from 10 adult volunteers of both sexes in sodium heparin to prevent clotting. The blood was washed three times ( $700 \times g$  for 10 min) in isotonic, pH 7.4 buffered saline glucose (BSG) with 1% bovine serum albumin to remove platelets. Peripheral MBC were separated from the remaining blood by an arabinogalactan (Stractan) discontinuous density gradient method described previously.<sup>6</sup> The conventional Ficoll-Hypaque density gradient method was not used to isolate MBC because the Hypaque contaminated the cells with sodium and iodine (not shown). The isolated MBC were washed twice in isotonic, pH 7.4, ammonium nitrate ( $\text{NH}_4\text{NO}_3$ ) prior to analysis with EPMA or FAAS (Fig. 1).

For EPMA, MBC were spray deposited on large-area thin-film supports, air dried, and carbon coated (Fig. 2) as described previously.<sup>5</sup> Thirty individual cells from each donor were analyzed by EPMA. The EPMA was calibrated with lithium borate glass microspheres with known Mg concentrations obtained from the National Bureau of Standards.<sup>7</sup> The electron-beam raster was adjusted so that an individual cell or microsphere was circumscribed by the scanned area. Cells and microspheres were analyzed with a 35keV beam. Cells were analyzed with a  $2.0 \times 10^{-8}$  A beam and microspheres were analyzed with a  $2.0 \times 10^{-9}$  A beam as measured by a Faraday cup. The Mg concentration was determined from the ratio of Mg peak-to-local continuum x-ray intensities<sup>8,9</sup> from a cell and the standard. The Mg peak-to-local continuum x-ray counts were measured within a fixed-size energy window (190 eV wide) that contained all observed Mg x-ray counts. The spectra were filtered by a weighted average smooth and the continuum under the measured peak was estimated by a linear interpolation between one channel on each side of the peak. The local continuum x-ray counts were the integrated counts within the measured region. The net Mg x-ray counts were calculated by subtraction of the local continuum x-ray counts from the Mg peak-plus-continuum x-ray counts. The Mg peak-to-local continuum x-ray intensity ratio was calculated by division of the net Mg x-ray counts by the local continuum x-ray counts.

---

Author Hook is at the Surgical Neurology Branch, authors Hosseini and Elin are at Clinical Pathology, and author Fiori is at Biomedical Engineering and Instrumentation Branch, National Institutes of Health, Bethesda, MD 20892.

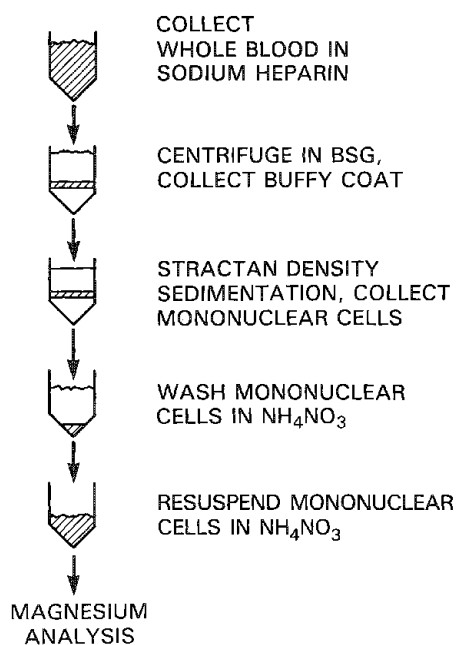


FIG. 1.--Method for isolation of MBC.

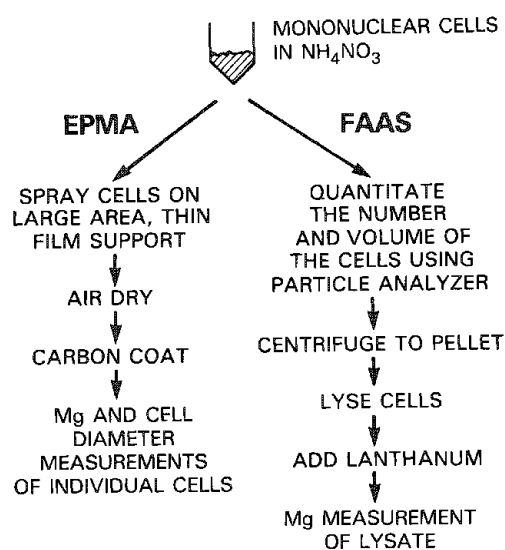


FIG. 2.--Comparison of EPMA and FAAS Mg methods for determination of MBC Mg concentration.

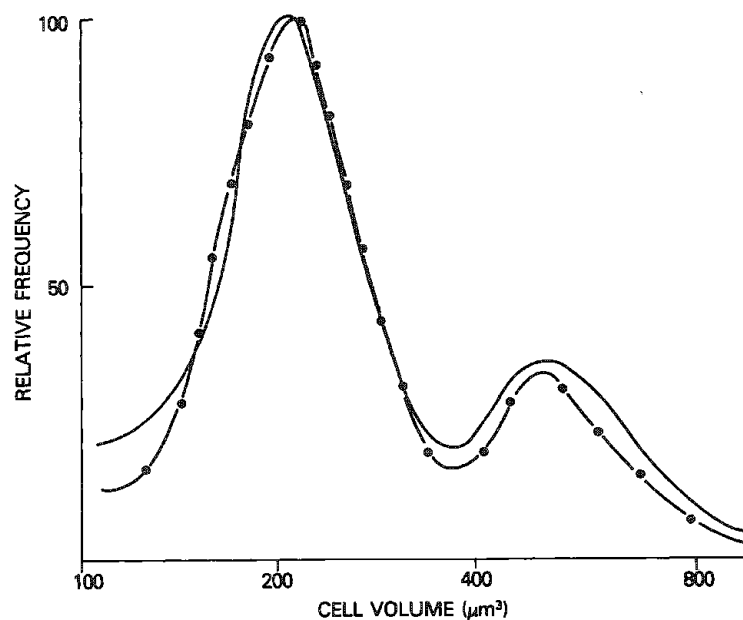


FIG. 3.--Cell volume ( $\mu\text{m}^3$ ) vs relative frequency for MBC. Bimodal distribution is composed of lymphocytes (smaller volume) and monocytes (larger volume). Cells washed in  $\text{NH}_4\text{NO}_3$  (—) or BSG (---) have same relative frequency distribution. Relative frequency is number of cells of given size divided by number of cells of mode size multiplied by 100.

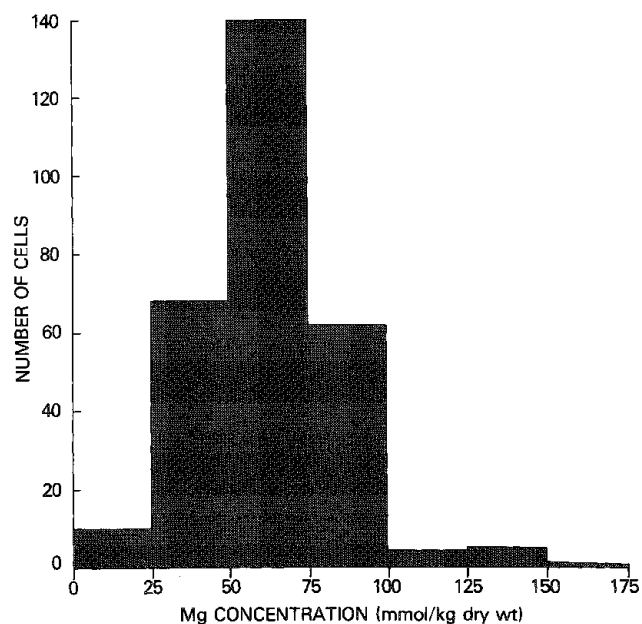


FIG. 4.--Histogram of Mg concentration of individual MBC from all donors.



Individual cell diameters were measured from a scanning transmission electron image to correlate cell size and Mg concentration. A Cameca microprobe equipped with a Tracor Northern 5500 energy-dispersive x-ray analyzer system were used for EPMA.

For FAAS, MBC were counted and sized by means of a cell size analyzer and pelleted by centrifugation; the supernate was then removed and the cells were lysed in 0.01M saline by sonication (Fig. 2). The Mg concentration in the lysate was determined in lanthanum by FAAS. The Mg concentration of the MBC was calculated from the total Mg in the lysate and total cell volume. The Mg concentration for the dry weight of MBC was calculated from the Mg concentration of MBC by assuming a cell density of 1.09 g/ml and 78% water content.<sup>10</sup> One sample from each donor was analyzed by FAAS. An Instrumentation Laboratory Video 22 was used for FAAS and a Particle Data Celloscope 80xy was used to count and size the MBC.

## Results

The volume of MBC had a bimodal distribution (Fig. 3). The cells with a small volume were primarily lymphocytes and the cells with a larger volume were primarily monocytes. The ratio of lymphocytes to monocytes varied among donors. The mean Mg concentrations of MBC obtained by EPMA and FAAS were  $64.0 \pm 14.3$  and  $52.2 \pm 13.8$  mmol/kg dry weight, respectively. No significant difference was found between the means by paired sample t test (Table 1). The distribution for the Mg concentrations among the MBC appeared to be normally distributed (Fig. 4). No trend was found between the Mg concentration of MBC and cell diameter (Fig. 5). Figure 6 shows a typical EPMA spectrum obtained from a MBC.

## Discussion and Conclusion

Two different analytical methods, EPMA and FAAS, determined the same Mg concentration of the MBC. The MBC Mg concentrations we determined were between the values previously reported by Ryan et al. (43.0 mmol/kg dry weight)<sup>3</sup> and Negandank (79.0 mmol/kg dry weight).<sup>10</sup> Monocytes are larger than lymphocytes and therefore the Mg content (weight per cell) of monocytes is expected to be greater than lymphocytes. Since Mg content is a function of cell volume but cell Mg concentration is independent of cell volume, it is obvious that MBC Mg concentration rather than Mg content should be determined.

## References

1. J. K. Aikawa, *Magnesium: Its Biological Significance*, Boca Raton, Fla.: CRC Press, 1981.
2. M. S. Seelig, *Magnesium Deficiency in the Pathogenesis of Disease*, New York: Plenum, 1980.
3. M. P. Ryan et al., "The effect of diuretics on lymphocyte magnesium and potassium," *Acta Med Scand. (Suppl.)* 647: 153-161, 1980.
4. L. Cohen and R. Kitzes, "Magnesium sulfate and digitalis-toxic arrhythmias," *J. Am. Med. Assoc.* 249: 2808-2810, 1983.
5. G. Hook et al., "A sample preparation for quantitative determination of magnesium in individual lymphocytes by electron probe x-ray microanalysis," *J. Microsc.* 141: 69, 1986.
6. J. M. Hosseini et al., "Comparison of two separation techniques for the determination of blood mononuclear cell magnesium content," *J. Am. Col. Nutr.* 4: 361-368, 1983.
7. C. E. Fiori and D. H. Blackburn, "Low Z glass standards for biological microanalysis," *J. Microsc.* 127: 223-226, 1982.

TABLE 1.--Human peripheral blood mononuclear cell Mg concentrations determined by EPMA and FAAS (mmol/kg dry weight).

Donor	EPMA	FAAS
RE	51.3 $\pm$ 8.2	36.7
GH	46.1 $\pm$ 16.5	34.2
JR	50.2 $\pm$ 16.5	63.6
MR	68.9 $\pm$ 19.9	63.2
JL	65.3 $\pm$ 8.9	49.3
SS	64.0 $\pm$ 20.6	68.4
DB	74.0 $\pm$ 12.2	54.0
DG	95.0 $\pm$ 34.7	32.3
PB	56.3 $\pm$ 13.8	58.7
RS	62.0 $\pm$ 13.7	63.0
Mean	64.0 <sup>a</sup>	52.2 <sup>a</sup>
Standard Deviation	14.3	13.8
Coefficient of variation	22%	26%

<sup>a</sup>No significant difference between the means ( $p > 0.1$ ) by paired-sample t test.

8. J. A. Small et al., "The production and characterization of glass fibers and spheres for microanalysis," *SEM/1978*, 445-454.
9. P. Statham and J. Pawley, "A new method for particle x-ray microanalysis based on peak to background measurements," *SEM/1978*, 469-478.
10. W. Negandank, "Ionic and volume maintenance in human lymphocytes," *Physiol. Chem. Physics Med. NMR* 16: 3-20, 1984.

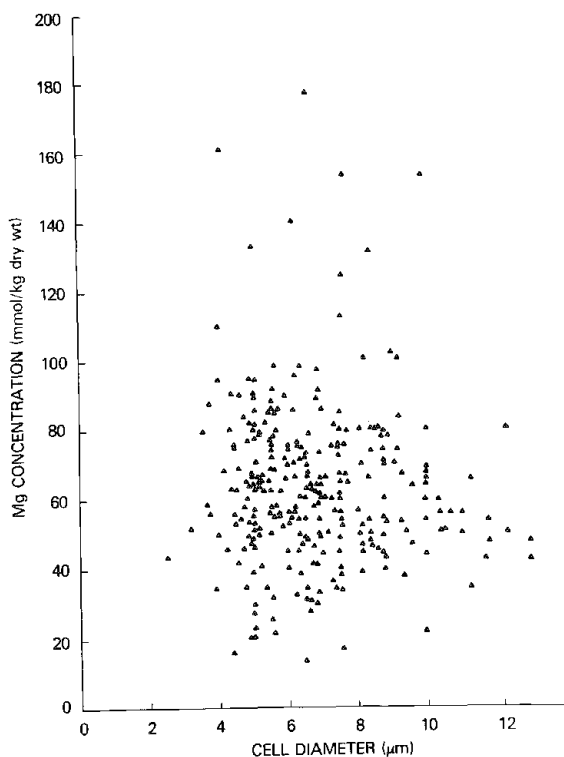


FIG. 5.--Mg concentration of MBC (mmol/kg dry wt) plotted as function of cell diameter (μm). No significant trend is found.

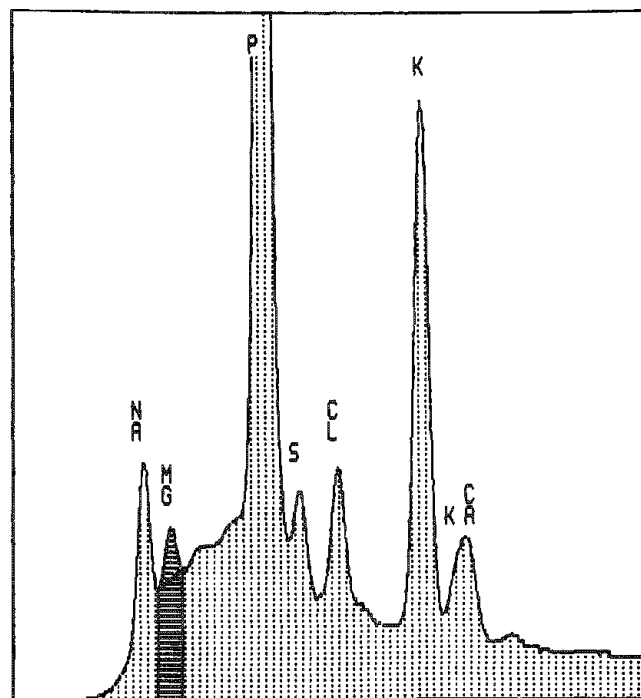


FIG. 6.--Typical EPMA spectrum obtained from analysis of individual MBC. Sodium (Na), magnesium (Mg), phosphorus (P), sulfur (S), chlorine (Cl), potassium (K), and calcium (Ca) are detected. Mg characteristic peak and local continuum x-ray intensities are marked.

## X-RAY MICROANALYSIS OF SECRETORY CELLS

G. M. Roomans

Exocrine glands secrete a mixture of proteins, water, and ions. In many glands, the ionic composition of the final secretion is not equal to that of the primary secretion produced in the acini, due to ductal reabsorption or ductal secretion of ions. Therefore, analysis of local ion concentrations at various levels in the gland is necessary in the study of ion transport mechanisms in a particular gland. X-ray microanalysis may, by itself or in combination with other analytical techniques, provide such information. This paper reviews our studies on calcium distribution in exocrine glands and other secretory cells.

Our motive in studying exocrine glands by means of x-ray microanalysis stems from our interest in the disease cystic fibrosis (CF). CF is a generally lethal, inborn, hereditary disease that affects 1 in 2000 to 4000 newborns in the Caucasian population. The main clinical signs of the disease are recurrent airway infections associated with abnormally viscous mucus, and pancreatic insufficiency. Although the molecular basis of the disease is still unknown, it is suspected that a faulty regulation of ion and water transport in exocrine glands (and probably also in other epithelial cells) is a central factor in the disease. In particular abnormalities in calcium<sup>1</sup> or chloride<sup>2,3</sup> transport or distribution have been implicated. We have mainly studied calcium distribution in some secretory cells of CF patients and in exocrine glands of animal models of CF (the chronically reserpinized rat,<sup>4</sup> the chronically isoproterenol-treated rat, and the chronically pilocarpine-treated rat<sup>5</sup>), as well as in related experimental animal models.

### *Materials and Methods*

Bronchial biopsies were, after informed consent, obtained during bronchoscopy from adult CF patients and controls (patients with chronic bronchitis). Fibroblast cultures were initiated from skin biopsies from CF patients or from healthy controls.

Rats (Sprague-Dawley, 200 g) received a daily intraperitoneal injection with reserpine (0.5 mg/kg body weight, bw), isoproterenol (5 mg/kg bw), or pilocarpine (50 mg/kg bw) for seven days. In some studies the animals received a single dose of reserpine (0.5 mg/kg bw) or isoproterenol (160 mg/kg bw) and tissue samples were taken at various points in time within a 24h period.

Chronic metabolic acidosis was induced in rats by substitution of a solution of 0.6 g/l ammonium chloride for the normal drinking water for 7 days. To induce metabolic acidosis, the animals received 100 mmol/l sodium bicarbonate solution for 2 weeks.

Fibroblast cultures were rinsed with cold ammonium chloride solution to remove the culture medium, frozen in liquid nitrogen, freeze-dried, coated with carbon, viewed in the secondary mode, and analyzed at 20 kV. Bronchial biopsies were frozen in Freon 13 sub-cooled with liquid nitrogen and freeze-substituted for three weeks in dry diethyl ether at -80 C, embedded in epoxy resin, sectioned on a dry knife, examined in the scanning transmission (STEM) mode, and analyzed at 100 kV. Small pieces of rat salivary glands were frozen in Freon 13; thick (16µm) cryosections for analysis at the cellular level were cut at -20 C on a conventional cryostat, mounted on a carbon specimen holder, freeze-dried, and analyzed in the SEM mode at 20 kV.<sup>6</sup> For analysis at the subcellular level, thin cryosections were cut on an LKB Ultratome III with CryoKit at about -100 to -120 C; these sections were placed on Formvar film-covered copper grids, freeze-dried in the cryochamber, covered with a second film, and analyzed in the STEM mode at 80 kV. All analyses were performed with a Kevex 7000 energy-dispersive spectrometer system mounted on a JEOL 100C electron microscope with scanning attachment.

---

The author is at the Department of Ultrastructure Research, University of Stockholm, Biology E4, S-10691 Stockholm, Sweden. This study was supported by grants from the Cystic Fibrosis Research Trust, the Swedish National Association against Heart and Lung Diseases, the Swedish Association for Cystic Fibrosis, and the Medical Research Council.

Quantitative x-ray microanalysis of thin sections was carried out with the continuum method of Hall<sup>7</sup> after correction for the extraneous background.<sup>8,9</sup> Quantitative analysis of thick cryosections was carried out by a comparison of the peak-to-local background ratio of specimen and standard.<sup>10</sup> As standards, cryosections of a gelatin/glycerol matrix containing known amounts of inorganic salts were used.<sup>11</sup> In the analysis of cell cultures, only semiquantitative analysis could be carried out, owing to the presence of the Teflon substrate on which the cells were grown.

## Results

X-ray microanalysis of cultured fibroblasts of CF patients showed that these cells have abnormally high calcium levels compared to control fibroblasts. Similarly, the calcium concentration in goblet cells from bronchial epithelium of CF patients was higher than that in goblet cells of controls (Table 1).

TABLE 1.--Calcium concentrations in secretory cells and secretory granules measured by x-ray microanalysis.

	absolute concentration	% of control
CF patients:		
fibroblasts	not det.	183
goblet cells	67 ± 3	231
animal models:		
chronic reserpine:		
submandib. acinar cells	103 ± 6	239
--mucous granules	158 ± 16	227
parotid acinar cells	3 ± 1	15
chronic isoproterenol:		
submandib. acinar cells	94 ± 11	219
--mucous granules	207 ± 13	296
parotid acinar cells	14 ± 2	70
--zymogen granules	20 ± 3	48
chronic pilocarpine:		
submandib. acinar cells	77 ± 7	179
--mucous granules	97 ± 9	138
single reserpine:		
submandib. acinar cells	126 ± 19	293
--mucous granules	211 ± 14	301
single isoproterenol:		
submandib. acinar cells	84 ± 6	195
--mucous granules	133 ± 10	190
acidosis:		
submand. acinar cells	61 ± 5	142
alkalosis:		
submand. acinar cells	64 ± 6	149

Absolute concentration given in mmol/kg dry weight, mean and s.e.m. The table is based on previous publications<sup>12-15</sup> and unpublished data.

"not det.": not determined (see Materials and Methods).

Increased calcium levels were also found in the submandibular acinar cells of rats treated chronically with reserpine, isoproterenol, or pilocarpine (Table 1). Analysis of mucus granules and concurrent studies of gland ultrastructure showed that this increase

was due to two factors: (1) an increase of the relative mucus content of the cell--in normal cells most of the intracellular calcium is contained in the mucus granules; and (2) an increase of the local calcium concentration in the mucus. A single injection with isoproterenol resulted in complete depletion of cellular mucus; after about 8 h, mucus was again visible in the cells and at 24 h the cells were filled with calcium-rich mucus. A single injection with reserpine resulted after about 4 h in an increase of the relative mucus content of the cell as well as of the cellular calcium levels; the newly synthesized mucus had a higher calcium content than normal mucus (Table 1).<sup>12,13</sup> Increased calcium levels were also found in acinar cells of the submandibular gland of acidotic rats. In this case, however, the local calcium content of the mucus was normal and the increase in cellular calcium could be explained by the increase in relative mucus content of the cell.<sup>14,15</sup> Similar results were obtained with alkalotic rats (Table 1).

In the parotid gland, however, chronic reserpine and isoproterenol treatment resulted in a decrease of the cellular calcium levels. The zymogen granules (the main pool of intracellular calcium<sup>13,16</sup>) were decondensated and had an abnormally low calcium and sulfur concentration.

### Discussion

Both in fibroblasts and in goblet cells of CF patients the increase in calcium must reflect an increase in bound calcium, since this forms the bulk of the cellular calcium. Conclusions about free calcium concentrations cannot be made on the basis of x-ray microanalysis. In both cell types, it can be assumed that calcium is mainly localized to the secretory macromolecules. The elevated calcium levels in CF goblet cells could be associated with an elevated calcium content of the tracheobronchial secretions in these patients<sup>1</sup> and thus be of clinical significance. However, this result must be interpreted with caution since the goblet cells are not the only source of calcium in tracheobronchial secretions, and the contribution of the submucosal glands may be more important.

The study of the "animal models" for CF shows that an increase in the calcium concentration of the secretory cells (at the cellular level) can be mediated by two separate mechanisms: (1) accumulation of mucus, and (2) increased calcium binding by intracellular mucus. We have shown that accumulation of intracellular mucus is associated with a decreased response to  $\beta$ -adrenergic stimulation.<sup>13</sup> This response can be measured by a determination of the cellular calcium concentration (as a measure of cellular mucus content) after stimulation of mucus secretion by isoproterenol. We have not been able to pinpoint the cause of the increased calcium binding by the intracellular mucus in the submandibular acinar cells after chronic reserpine or isoproterenol treatment or after a single dose of these substances. Since we could show that all these treatments resulted in metabolic acidosis of the submandibular acinar cells,<sup>17</sup> we studied an animal model with "pure" acidosis. However, neither acidosis nor alkalosis induces increased calcium binding to intracellular mucus.<sup>15</sup> On the other hand, acidosis could contribute to the observed decreased responsiveness to stimulation and thereby to intracellular accumulation of mucus.

Since the effect of chronic reserpine or isoproterenol treatment on the calcium content of the parotid acinar cells is the reverse of that seen in the submandibular gland, it appears likely that the changes in calcium levels in the gland cells are mainly due to changes in the nature of the secretory macromolecules. This and other evidence<sup>15</sup> has led us to believe that the changes in cellular calcium, certainly in the animal models, and therefore possibly also in the human disease, may be secondary to the basic defect in CF.

### References

1. S. Katz et al., "The calcium hypothesis of cystic fibrosis," *Cell Calcium* 5: 421-440, 1985.
2. P. M. Quinton, "Chloride impermeability in cystic fibrosis," *Nature* 301: 421-422, 1983.
3. M. R. Knowles et al., "Abnormal ion permeation through cystic fibrosis respiratory epithelium," *Science* 221: 1067-1070, 1983.
4. J. R. Martinez et al., "The chronically reserpinized rat as a possible model for cystic fibrosis: II. Composition and cilioinhibitory effects of submaxillary saliva," *Pediat. Res.* 9: 470-475, 1975.
5. J. Sturgess and L. Reid, "The effect of isoprenaline and pilocarpine on (a) bron-

chial mucus-secreting tissue and (b) pancreas, salivary glands, heart, thymus, liver and spleen," *Brit. J. Exp. Path.* 54: 388-403, 1973.

6. R. Wroblewski et al., "Electron probe X-ray microanalysis of human muscle biopsies," *Histochemistry* 55: 281-292, 1978.

7. T. A. Hall et al., "The use of thin specimens for X-ray microanalysis in biology," *J. Microsc.* 99: 177-182, 1973.

8. B. L. Gupta and T. A. Hall, "Quantitative electron probe X-ray microanalysis of electrolyte elements within epithelial tissue compartments," *Fed. Proc.* 38: 144-153, 1979.

9. G. M. Roomans, "Quantitative X-ray microanalysis of thin sections," in M. A. Hayat, Ed., *X-ray Microanalysis in Biology*, Baltimore: University Park Press, 1980, 401-453.

10. G. M. Roomans, "Quantitative electron probe X-ray microanalysis of biological bulk specimens," *SEM/1981 II*, 344-356.

11. G. M. Roomans and L. A. Sevéus, "Preparation of thin cryosectioned standards for quantitative microprobe analysis," *J. Submicrosc. Cytol.* 9: 31-35, 1977.

12. R. M. Müller et al., "Effects of reserpine and isoproterenol on elemental distribution in submandibular gland of rat," *Acta Physiol. Scand.* 123: 383-391, 1985.

13. R. M. Müller and G. M. Roomans, "X-ray microanalysis of exocrine glands in animal models for cystic fibrosis," *SEM/1985 IV*, 1583-1601.

14. G. M. Roomans and A. Bardoñ, "Effect of metabolic acidosis on acinar cells of rat submandibular gland," *Res. Commun. Chem. Pathol. Pharmacol.* 46: 155-158, 1984.

15. G. M. Roomans, "Calcium and cystic fibrosis," *SEM/1986 I*, 165-178.

16. G. M. Roomans and X. Wei, "X-ray microanalysis of resting and stimulated rat pancreas," *Acta Physiol. Scand.* 124: 353-359, 1985.

17. A. Bardoñ et al., "Glycolytic enzymes in the submandibular gland of reserpine-treated rats," in J. R. Martinez and G. J. Barbero, Eds., *Animal Models for Cystic Fibrosis: The Reserpine-treated Rat*, San Francisco: San Francisco Press, 1985, 155-164.

## ANALYTICAL ELECTRON MICROSCOPY OF SECRETION RELATED ELEMENTAL DISTRIBUTIONS

K. T. Izutsu and D. E. Johnson

We are continuing studies of the function of secretory cell systems using Analytical Electron Microscopy (AEM). The purpose of this presentation is to summarize results of these studies and to discuss both the limitations and the potential of AEM for this application.

The specimen-preparation methods used involve cryofixation, cryosectioning, and freeze drying and have been described in detail, as have been the methods of quantitative energy-dispersive x-ray analysis used.<sup>1</sup> The physiological phenomena under study include normal secretion function in rat salivary glands and the pathophysiological function of human salivary glands in cystic fibrosis (CF).

In the rat salivary gland studies, the elemental concentrations measured indicated several statistically significant differences between secretory granules, cytoplasm, and nuclei of resting acinar cells. Cytoplasm and nuclei had significantly higher concentrations of Na, Mg, P, Cl, and K, and lower concentrations of S and Ca than secretory granules. The only significant differences between cytoplasmic and nuclear concentrations were that S was lower and K was higher in nuclei.

Following pilocarpine-induced secretion, quantitative analyses showed secretory granule levels of Na increased ten-fold, S by 18%, and Cl by 66%. Cytoplasmic and nuclear Na concentrations increased by over sixfold and sevenfold, respectively; and cytoplasmic and nuclear K concentrations decreased by about 30% and 35%, respectively. Cytoplasmic Ca increased by 56%. Analyses of elemental concentration differences between organelles showed two salivation-related changes. Whereas cytoplasmic and nuclear Ca and P concentrations were not significantly different from one another in resting acinar cells, they were significantly different in salivating cells, with Ca lower and P higher in the nucleus.

X-ray microanalysis of freeze-dried human labial gland cryosections revealed that Na concentration was doubled and the Ca/S concentration ratio was decreased in secretory granules of labial glands from patients with cystic fibrosis (CF) when compared with glands from normal subjects. Other results suggested that the decrease in the Ca/S concentration ratio resulted from an increase in S concentration. These findings imply that mucous granules in labial saliva showed a CF-related increase in Na and S content, and such changes would be expected to affect the rheology of the mucus after exocytosis. In contrast with a previous study in human parotid glands, no evidence was found for CF-related changes in cytoplasmic or nuclear Na, K, and Ca concentrations.

For the majority of the questions being asked in these studies, the practical limitations of AEM are not significant. Specimen-preparation techniques preserve morphology and elemental distributions to at least the spatial resolution obtainable with a hot-filament electron source. Specimen contamination can be made negligible through both clean vacuums and clean specimens. Radiation damage (principally mass loss of matrix atoms) is significant but can be monitored and corrections can be made. Overall, the situation is one in which most specimens contain more high-resolution elemental distribution data than can be analyzed in an EDS/hot-filament AEM. Most questions being asked, however, are answerable with such a system and for those situations requiring higher resolution, the field-emission STEM is of course available.

### References

K. T. Izutsu et al., "Electron microprobe analysis of human labial gland secretory granules in cystic fibrosis," *J. Clin. Invest.* 75: 1951-1956, 1985.

Author Izutsu is with the Departments of Oral Biology and Oral Medicine, author Johnson with the Center for Bioengineering, University of Washington, Seattle, WA 98195. The work was supported by NIH Grant R01DE06373.

## X-RAY MICROANALYSIS OF RAT PAPILLARY MUSCLE

M. E. Cantino, L. E. Wilkinson, E. Wang, and D. E. Johnson

The direct measurement of calcium sequestration in terminal cisternae of frog skeletal muscle<sup>1</sup> has demonstrated the value of the electron microprobe in the study of calcium regulation in striated muscle. Since a number of inotropic agents may act via changes in the amount of calcium stored in junctional sarcoplasmic reticulum (JSR), there is great interest in similar measurements in cardiac muscle. Recent reports have described such measurements in guinea pig and rabbit papillary muscles.<sup>2,3</sup> Because the role of the sarcoplasmic reticulum in regulation of cardiac output may be species-dependent, we have been investigating subcellular elemental distributions in rat ventricular papillary muscles, where the sarcoplasmic reticulum is thought to play a relatively major role.<sup>4</sup> In this report, we describe the methods we have developed to isolate, freeze, and analyze rat ventricular papillary muscles, and we present preliminary data showing subcellular elemental distributions in relaxed muscles.

Large (400-500g) rats were sacrificed and the hearts were quickly removed and placed in a perfusion chamber. Cylindrically shaped papillary muscles were removed from the right ventricle and transferred to a second chamber, where they were mounted between a fixed hook and a force transducer. The muscle length was adjusted for maximum tension and the muscles were stimulated at 0.2 Hz until the twitch tension stabilized (30 to 60 min). The stimulus was then shut off and the muscles were frozen within 1 min in one of two ways. In early experiments, the muscles were raised out of the bath and frozen between the jaws of liquid-nitrogen-cooled, copper-clad pliers. More recently, we have designed a muscle holder compatible with an Emtex Fast Freeze device. The holder contains a force transducer and fixed hook, between which the muscles were mounted, stretched, and stimulated. Just prior to freezing, the bath was removed, and the muscles, still connected to the transducer, were dropped onto a liquid helium-cooled block. In this way continuous tension measurements could be made up to the point of freezing.

The frozen tissue was mounted on cryomicrotome chucks with a low-temperature glue and longitudinally sectioned on a Sorvall MT2B cryomicrotome at -100 C. Cryosections on carbon-coated, Formvar-covered grids were vacuum freeze-dried overnight and stored in a desiccator thereafter. Electron probe microanalyses were performed in the STEM mode in a JEOL 100C with a Link AN10000 analytical system. Rasters were 100-300 nm on a side, and beam currents were 1-5 nA. The analyses were made at room temperature in four subcellular regions: A-band, I-band, mitochondria, and JSR.

Potassium to chlorine concentration ratios were high in mitochondria (10:1) and in myofibrillar regions (7:1). These findings, along with measured twitch tensions, indicate that the tissue was healthy at the time of freezing. Calcium was frequently found in electron-dense sites adjacent to T-tubules (presumed to be JSR). Calcium levels in such sites varied widely, ranging from 4 to 32 mmol/kg dry wt. They were on average significantly higher than those found in mitochondria ( $1 \pm 2$  mmol/kg dry wt), A bands ( $3 \pm 4$  mmol/kg dry wt) or I bands ( $3 \pm 4$  mmol/kg dry wt). The large variation in JSR Ca content may be largely due to the sampling of profiles of various sizes within the section. We are currently analyzing samples frozen in the presence of an extracellular marker (Cobaltic EDTA) to assess the contribution of T-tubular calcium in JSR measurements.

### References

1. A. V. Somlyo et al., "Calcium release and ionic changes in the sarcoplasmic reticulum of tetanized muscle: An electron probe study," *J. Cell Biol.* 90: 557-594, 1981
2. M. F. Wendt-Gallitelli and R. Jacob, "Rhythm-dependent role of different calcium stores in cardiac muscle: X-ray microanalysis," *J. Mol. Cell Cardiol.* 14: 487-492, 1982.
3. E. S. Wheeler-Clark and J. McD. Tormey, "Redistribution of subcellular electrolytes accompanying the increased myocardial contractility produced by low Na," *Microbeam Analysis --1985*, 116-118.
4. D. M. Bers, K. D. Philipson, and G. A. Langer, "Cardiac contractility and sarcolemmal calcium binding in several cardiac muscle preparations," *Am. J. Physiol.* 240: H576-583, 1981.

The authors are with the Center for Bioengineering, University of Washington, Seattle WA 98185. The work was supported by NIH Grants HL31962 and HL31444.



## ELEMENTAL CONCENTRATIONS OF THYMOCYTES IN VIVO AND IN VITRO

Alice Warley

Previous studies have shown that the thymus atrophies in rats rendered diabetic by the drug streptozotocin.<sup>1</sup> We wish to understand why atrophy occurs and to elucidate the effect that this occurrence has on immune function in the diabetic animal. Many aspects of immune function are commonly studied *in vitro* and there is a need to relate the *in vitro* findings to function *in vivo*. The techniques of cryoultramicrotomy and x-ray microanalysis can be used to study elemental content *in vivo* and allow comparison to be made with isolated cells *in vitro*. However, earlier studies on isolated thymocytes gave results in which the elemental concentrations appeared too high.<sup>2</sup> Further studies on isolation methods have been carried out and the results are reported here.

### *Methods*

Male CSE Wistar rats (weight 250 g) were killed under chloroform anaesthesia and small pieces of the thymus gland were excised rapidly and frozen onto silver stubs by being plunged into Freon 22 cooled by liquid nitrogen. The method for preparing thymocytes in suspension has been described previously.<sup>2</sup> After isolation the thymocytes were resuspended in Hepes buffered RPMI 1640 medium and incubated at  $1 \times 10^6/\text{ml}$  for 1 h. After incubation the cells were harvested by centrifugation, the pellet was resuspended in 0.1 ml medium, and cells were taken up in a haematocrit centrifuge tube. The tubes were sealed and centrifuged at 10 000 g for 90 s. The portion of the tube containing the pellet was scored and snapped off, the tube was inverted, and the cells were extruded onto silver stubs and frozen as for the tissues. This method for concentration of the cells is similar to that described by Masters et al.<sup>3</sup>

Cryosections were cut at -65 to -70 C in a cryoultramicrotome and freeze dried and coated before analysis. Analysis was performed in a AEI EMMA-4 electron microscope fitted with a Link systems 860 series 2 energy-dispersive detection system. Analysis was carried out for 100 s at 60 kV and 4 nA beam current with a circular probe diameter 0.5  $\mu\text{m}$ . Spectra were processed and quantitative information obtained by use of the Quantem/FLS program; this program is described in Gupta and Hall.<sup>4</sup> Full details of the analytical and quantitative procedures are given in Kendall et al.<sup>2</sup>

### *Results and Discussion*

The appearance of freeze-dried sections of tissue thymocytes and thymocytes in suspension are shown in Figs. 1(a) and (b), respectively. Elemental concentrations of thymocytes in tissues and in suspension are shown in Table 1. For tissues the results are pooled analyses of thymocytes from the cortical region of the thymus of 4 animals shown in Table 2; the values for isolated thymocytes represent pooled results from 3 different animals. The results presented here are in contrast to those reported previously for mouse thymocytes, in which very high levels of Na and Cl were recorded in the isolated cells. Thus the procedures adopted here, incubation of the cells to allow recovery from the isolation procedure and high speed centrifugation of the cell pellet to remove excess medium, result in elemental concentrations in the isolated cells that are closer to the values found in tissue thymocytes. There are still some differences between the pooled values for the tissues and the isolated cells, mainly in the concentrations of Cl in both nucleus and cytoplasm, and the concentration of S in the nucleus. However, in this case the higher values of Cl are found in the tissue rather than the isolated cells. All the differences can be ascribed to variation in elemental concentrations that we have seen between tissue thymocytes from the different animals (Table 2). The results for Na and

---

The author is in the Division of Anatomy, United Medical and Dental Schools, St. Thomas's Campus, Lambeth Palace Road, London, England SE1 7EH. This work was supported by the Sir Jules Thorn Charitable Trust.

TABLE 1.--Concentration of elements (mean  $\pm$  SE, mmoles/kg dry weight) in thymocytes in tissues and in suspension; n = number of observations, P values refer to level of significance between corresponding values in tissues and in suspension.

	n	Na	Mg	P	S	Cl	K
<b>Nuclei</b>							
Tissues	99	91 $\pm$ 8	29 $\pm$ 4	868 $\pm$ 27	126 $\pm$ 5	220 $\pm$ 12	676 $\pm$ 19
Suspensions	63	66 $\pm$ 7	36 $\pm$ 2	980 $\pm$ 36	100 $\pm$ 4	135 $\pm$ 6	655 $\pm$ 21
P		<0.05	ns	<0.05	<0.001	<0.001	ns
<b>Cytoplasm</b>							
Tissues	90	64 $\pm$ 6	35 $\pm$ 3	526 $\pm$ 21	140 $\pm$ 7	194 $\pm$ 10	498 $\pm$ 20
Suspensions	49	72 $\pm$ 8	26 $\pm$ 5	613 $\pm$ 28	128 $\pm$ 7	135 $\pm$ 8	528 $\pm$ 19
P		ns	ns	<0.05	ns	<0.001	ns

TABLE 2.--Elemental concentrations (mmoles/kg dry weight, mean  $\pm$  SE) in nucleus (N) and cytoplasm (C) of thymocytes from the cortical region of rat thymus; n = number of observations.

Animal		n	Na	Mg	P	S	Cl	K
2	C	20	92 $\pm$ 15	14 $\pm$ 9	391 $\pm$ 32	204 $\pm$ 16	218 $\pm$ 18	383 $\pm$ 33
	N	21	152 $\pm$ 22	29 $\pm$ 7	728 $\pm$ 53	162 $\pm$ 11	226 $\pm$ 26	606 $\pm$ 43
8	C	22	63 $\pm$ 8	41 $\pm$ 4	647 $\pm$ 57	157 $\pm$ 10	175 $\pm$ 12	626 $\pm$ 54
	N	22	91 $\pm$ 9	40 $\pm$ 5	988 $\pm$ 69	148 $\pm$ 5	187 $\pm$ 10	779 $\pm$ 44
11	C	24	55 $\pm$ 10	48 $\pm$ 6	531 $\pm$ 37	116 $\pm$ 39	279 $\pm$ 15	518 $\pm$ 30
	N	27	69 $\pm$ 10	38 $\pm$ 4	962 $\pm$ 48	105 $\pm$ 7	316 $\pm$ 17	705 $\pm$ 35
13	C	24	53 $\pm$ 11	35 $\pm$ 6	525 $\pm$ 26	95 $\pm$ 6	105 $\pm$ 7	459 $\pm$ 21
	N	25	48 $\pm$ 10	36 $\pm$ 4	823 $\pm$ 33	89 $\pm$ 6	119 $\pm$ 6	630 $\pm$ 27

Cl in the isolated thymocytes were less variable between animals and results for all elements fell within the ranges of concentrations for elements that were found in tissue thymocytes in the individual animals.

It is interesting to compare the results presented here with those published by other authors for isolated thymocytes. Averdunk estimated concentrations of 32 mM Na and 103 mM K in mouse thymocytes by use of radioactive tracer studies;<sup>5</sup> Iverson, again with the use

of tracers, estimated concentrations of Na, K, and Cl of 30, 177, and 43 mM, respectively, in isolated rat thymocytes.<sup>6</sup> We estimated the water content of the isolated rat thymocytes using <sup>51</sup>CrEDTA as a marker for extracellular space and found a water content of 73%. If the average values for nucleus and cytoplasm in Table 1 are used and the dry weight concentrations converted to molar concentrations, the values for the isolated thymocytes are 25 mM Na, 218 mM K, and 50 mM Cl, and those for tissue thymocytes are 28 mM Na, 217 mM K, and 77 mM Cl. The values for Na and Cl in the isolated thymocytes correspond well with those of Iverson. In both tissues and suspensions the values of K are higher. That may be because higher concentrations of K are recorded in the nucleus, in which we are measuring heterochromatin; if K is bound to the heterochromatin then averaging the values for nucleus and cytoplasm may bias the result toward a higher value for K.

### Conclusions

These results show that when suitable isolation procedures are used, isolated thymocytes are obtained that closely resemble their tissue counterpart in elemental composition. Because isolated thymocytes can be easily separated into subpopulations, it should be possible to use information derived from the isolated thymocytes to clarify events occurring in the thymus in vivo in both normal and diseased animals.

### References

1. K. Chatamra et al., "Atrophy of the thymus in rats rendered diabetic by streptozotocin," *Horm. Metabol. Res.* 17: 630-632, 1985.
2. M. D. Kendall et al., "Differences in apparent elemental composition of tissues and cells using a fully quantitative x-ray microanalysis system," *J. Microsc.* 138: 35-42, 1985.
3. S. K. Masters et al., "Preparative techniques for freezing and freeze sectioning macrophages for energy dispersive X-ray microanalysis," *SEM/1979 III*, 97-110.
4. B. J. Gupta and T. A. Hall, "Electron probe x-ray microanalysis," in P. F. Baker, Ed., *Techniques in Cellular Physiology*, County Clare, Ireland: Elsevier/North Holland Scientific Publishers Ltd., 1982, 1-52.
5. R. Averdunk, "Early changes of 'leak flux' and the cation content of lymphocytes by concanavalin A," *Biochem. Biophys. Res. Comm.* 70: 101-109, 1976.
6. J. G. Iverson, "Unidirectional K fluxes in rat thymocytes stimulated by concanavalin A," *J. Cell Physiol.* 89: 267-276, 1976.

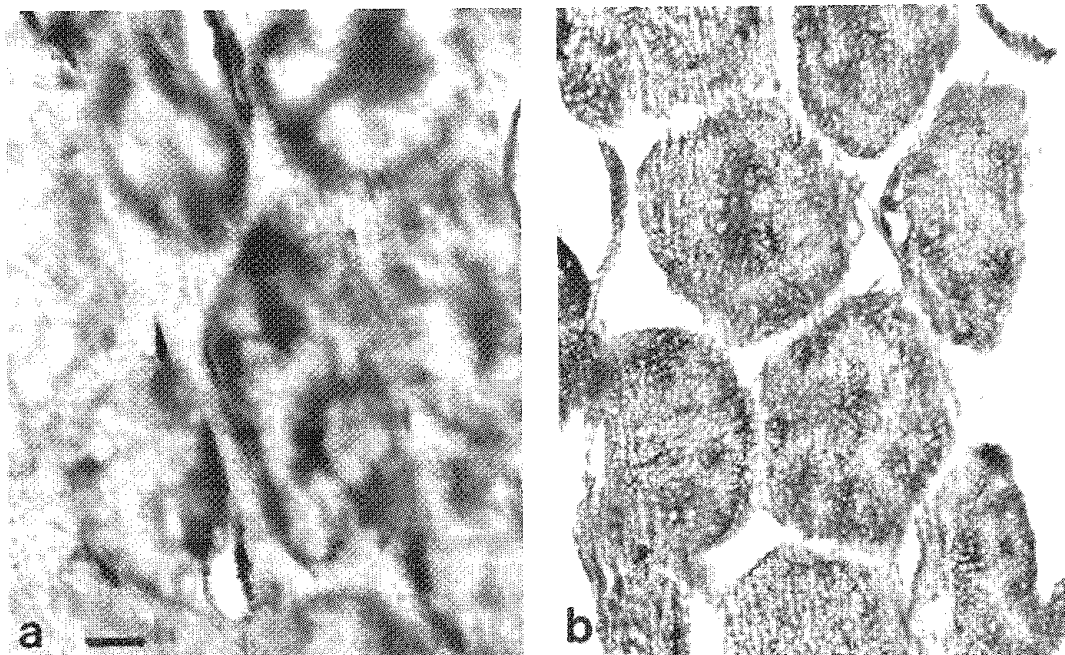


FIG. 1.--Freeze dried frozen sections of (a) tissue thymocytes and (b) thymocytes in suspension; marker = 1  $\mu$ m.



## CRYOULTRAMICROTOMY

H. K. Hagler

The preparation of biological materials for analytical electron microscopy requires the use of techniques that preserve diffusible elements in situ and offer good morphology of subcellular structures. Cryoultramicrotomy has become the method of choice to meet these requirements. There are basically three steps involved: rapid freezing of tissue or cells, cutting of ultrathin sections, and transfer of the sections to the microscope for analysis. There have been and continue to be many misunderstandings about cryoultramicrotomy to the point that it is often treated as more art than science. We present some of the basic principles of the process and how the same principles learned from routine plastic thin sectioning apply to cryoultramicrotomy. Some new data regarding rehydration artifacts that can be seen in sections improperly freeze dried are presented along with the use of a cryotransfer stage as a way to avoid these artifacts.

The use of rapid cryofixation for good structural preservation is an absolute requirement for the performance of cryoultramicrotomy of biological tissues. The demonstration by McDowell et al.<sup>1</sup> that pure vitrified water can be sectioned easily and without devitrification as determined by electron diffraction studies on the hydrated sections has been a major step in the understanding of the sectioning process. The cryofixation step determines the basic material properties of the biological tissue. In general if tissue is frozen vitreously, it will be very uniform and easy to section.<sup>2</sup> As the ice crystals become larger, the biological material becomes progressively more difficult to section. The ice becomes a primary variable that must be controlled so that cryoultramicrotomy may be done on a routine basis. The material properties of the frozen specimen (quality of the freeze) are just as important for cryoultramicrotomy as a well-cured plastic block is for ultramicrotomy. The size of the ice formed during freezing will determine the primary sectioning properties of biological tissue. In general, tissue which has amorphous and/or cubic ice can be sectioned at much colder temperatures and with better results than can tissue containing large hexagonal ice. The distribution of ice size across the block face influences the way the tissue behaves during sectioning. A specimen that is well frozen on the edges and poorly frozen in the middle will have a gradient in material properties that can make sectioning difficult.

Even though ultrathin frozen sections are generally cut at a temperature between -80 and -160 C, the basic principles of good ultramicrotomy must be followed. The cutting of sections introduces artifacts that are commonly seen with all types of sectioning, namely compression, knife marks, tearing, and chatter. Chatter is most frequently attributed to the coupling of external vibrations into the microtome, a block face that is too wide, a dull knife, or inappropriate choice of clearance angle for the knife. Chatter need not be an inherent part of cryoultramicrotomy, just as it is not inherent with routine ultrathin plastic sectioning. Chatter can usually be eliminated if the same guidelines as are used in routine plastic sectioning are followed. Tearing can be minimized in the frozen thin section by use of good-quality glass knives as described by Griffiths,<sup>3</sup> or by use of high-quality glass or diamond knives. Compression is generally manifested by high-frequency lines parallel to the knife edge. It results in a reduction of the dimension in the direction of sectioning and an increase in the section thickness.<sup>2</sup> Compression is generally 30% or greater in the dry sections that are used for analytical microscopy and this distortion should be considered when the dimensions of structures in dry-cut sections are measured.

---

The author is at the Department of Pathology, University of Texas Health Science Center at Dallas, 5323 Harry Hines, Dallas, TX 75235-9072. The collaboration of L. M. Buja and D. Bellotto is gratefully acknowledged. The work was supported in part by the National Institutes of Health Ischemic Heart Disease Specialized Center of Research grant HL17669.

In general the fully hydrated thin section cannot withstand the beam currents necessary for x-ray microanalysis.<sup>4</sup> Most groups use a freeze-drying procedure to improve the specimen stability and permit ultrastructure to be easily visualized in brightfield images, either scanning transmission or conventional transmission mode. In the past most groups were concerned only with the removal of water from the tissue; hence freeze-drying procedures were developed. With the recent availability of cryotransfer stages it is now apparent that the stability of the lipid in tissues has to be considered as well.<sup>5</sup> If conventional external freeze-drying is accomplished by slowly warming of the sections to room temperature, the lipid content may be sufficient to melt and destroy the morphology and elemental distribution within the section. Equally important, though more subtle changes in elemental concentrations and distributions can occur with rehydration of sections by exposure to atmosphere, such as transfer from a carbon coater to a dessicator, or from the dessicator to the electron microscope. Even when the sections are transferred to the microscope stage using a dry nitrogen-filled glovebox, and rapid introduction of the stage into the electron microscope, small but significant redistribution of Cl has been demonstrated.<sup>6</sup> New data regarding the changes which can be seen in tissue with moderate to severe dehydration can be shown.

Cryoultramicrotomy can be routinely and reproducibly applied to biological tissue if the basic principles of cryofixation, cryoultramicrotomy, and freeze-drying are followed. The technique has become less of an art and more of a science as a result of the advances that have occurred during the past five years. This valuable technique will yield new biological insights through the use of hydrated sections for the analysis of molecular structure and freeze-dried sections for physiological and pathophysiological correlation with data obtained by analytical electron microscopy.

#### References

1. A. W. McDowall, J-J. Chang, R. Freeman, J. Lepault, C. A. Walter, and J. Dubochet, "Electron microscopy on frozen hydrated sections of vitreous ice and vitrified biological samples," *J. Microsc.* 131: 1-9, 1983.
2. J-J. Chang, A. W. McDowall, J. Lepault, R. Freeman, C. A. Walter, and J. Dubochet, "Freezing, sectioning and observation artefacts of frozen hydrated sections for electron microscopy," *J. Microsc.* 132: 109-123, 1983.
3. G. Griffiths, "Selective contrast for electron microscopy using thawed frozen sections and immunocytochemistry," in J. P. Revel, T. Barnard, and G. H. Haggis, Eds., *The Science of Biological Specimen Preparation for Microscopy and Microanalysis*, AMF O'Hare, Ill.: SEM Inc., 1984.
4. K. Zierold, "Contrast of biological cryosections in scanning transmission electron microscopy," *J. Microsc.* 140: 65-71, 1985.
5. H. K. Hagler and L. M. Buja, "Effect of specimen preparation and section transfer techniques on the preservation of ultrastructure, lipids and elements in cryosections," *J. Microsc.* 141: 311-317, 1986.
6. J. McD. Tormey (personal communication).

## BIOLOGICAL ABSORPTION-EDGE IMAGING WITH SYNCHROTRON RADIATION

B. J. Panessa-Warren

Synchrotron radiation provides a high-intensity stable x-radiation source that permits the investigator to tune or select a desired bandwidth or wavelength of emitted photons. By use of monochromators, the incident synchrotron radiation can be accurately tuned to provide a high-intensity beam of monochromatic x rays for exposure. X rays in the soft x-ray region (1-10nm wavelength) have inherent properties that permit high-resolution imaging of hydrated, unstained, and dried biological materials without the high dosage and specimen-beam interactions associated with the heat and mass-loss damage of electron microscopy.<sup>1,2</sup> Soft x rays interact with biological materials predominantly by the photoelectric effect, and the strength of the interaction is characterized by the sum of the individual atomic cross sections.<sup>3</sup> "Typical photoelectric cross sections are characterized by a steep energy dependence interrupted by absorption edges whose locations are characteristic of each element."<sup>3</sup> The absorption of incident x rays by a biological specimen depends on the energy (wavelength) of the incident radiation, the sample thickness, and the atomic-number composition of the specimen. In areas of high atomic number or greater specimen thickness, the incident x rays have greater difficulty penetrating the specimen and a greater probability of absorption. In areas of the specimen that are thin, or composed of lower-atomic-number constituents, the incident x rays have a greater probability of penetrating the sample. By putting an x-ray detector on the underside (opposite side of the tissue from the x-ray beam) of the specimen, the transmitted x rays can be detected and a soft x-ray image formed.<sup>4</sup> These images vary according to the type of detector used. A polymer or x-ray resist can be spun uniformly onto a substrate and the biological specimen placed on top of the x-ray resist. During the x-ray exposure the biological material faces the x-ray beam.<sup>4</sup> The x rays transmitted through the specimen damage the underlying resist causing chain scission or crosslinking in the polymer.<sup>3</sup> Following the removal of the biological tissue, the resist is chemically developed, or etched, to reveal an atomic number/thickness map of the original tissue. Polymethylmethacrylate (PMMA) is the x-ray resist most frequently used for this type of soft x-ray contact microscopy. With photons of the wavelengths just below the carbon absorption edge (at 4.36 nm) and with a dosage of  $10^4$  J/g, PMMA offers a resolution of 5 nm.<sup>1,5</sup>

The resultant contact replica when coated with a thin layer of metal (to increase thermal and electrical conductivity, durability, and electron-scattering capabilities) can be mounted on a grid or specimen support and viewed by transmission<sup>6</sup> or scanning<sup>7,8</sup> electron microscopy. Although this technique offers high-resolution ultrastructural micrographs, the use of a polymer as an x-ray detector presents some artifacts and limitations (for quantification, ultrahigh resolution, interpretation, handling, etc.). Soft x rays transmitted through a biological specimen can also be detected by a flow-proportional counter and the sample may be displayed as a computer-generated real-time image.<sup>3</sup> This real-time detection and quantification of the transmitted x rays is done with a scanning x-ray microscope developed by the laboratory of Prof. Janos Kirz at SUNY, Stony Brook. Here the biological sample is scanned with a submicron spot of monochromatic x rays. The radiation dose delivered to the wet specimen is minimized by exposure of the sample to a small area of x rays at any given time and by use of an efficient detector with the less efficient optics positioned upstream from the specimen.<sup>9,10</sup> With this type of detection system quantification of the transmitted x rays is possible, which thus provides a way to interpret accurately (pixel by pixel) absorption-edge images. Unlike contact x-ray microscopy, the resolution possible with the x-ray scanning microscope is only approximately 0.19  $\mu\text{m}$ .<sup>10</sup>

---

The author is in the Department of Allied Health Resources, SUNY Health Sciences Center, Stony Brook, NY 11794. She wishes to acknowledge the help and sincerely appreciated advice offered by Drs. J. Kirz, H. Rarback, R. Rosser, and the staff at the National Synchrotron Light Source, and to thank Dr. M. Dewey and his staff for providing the isolated muscle preparations.

### *Inherent Characteristics of Soft X-ray Microscopy*

Because of the inherent differences between the soft x rays and other forms of radiation used for biological microscopy, soft x rays offer some distinct advantages. Transmission electron microscopy (TEM) is characterized by the elastic and inelastic scattering of electrons under high vacuum ( $10^{-5}$  to  $10^{-9}$  Torr) in a metal-stained, relatively thin (50-200nm-thick) section of biological materials. Multiple scattering effects limit the thickness of the biological specimen. The electron scattering cross section varies slowly with atomic number and necessitates the use of heavy-metal stains to increase electron scattering, which in turn increases contrast. Because the specimen must be viewed in a vacuum and withstand the heat and atomic effects of the electron beam, fresh tissue must be specially prepared by chemical, physical, and/or cryo-techniques which may all produce artifacts and limit the validity of the data obtained. The difficulty in achieving adequate contrast from unstained biological samples becomes even more complicated if the sample in question must be viewed while it is suspended in water or buffer, because the electron scattering cross section for endogenous water and organic matter are nearly the same.

Soft x rays interact with biological materials in quite a different manner without multiple scattering effects. Because x rays have a mean free path of several millimeters in air, specimens can be viewed at atmospheric pressure. Since image contrast is the result of differential x-ray absorption by the specimen, unstained and hydrated samples can be clearly imaged. When x-ray wavelengths between the oxygen K and carbon K absorption edges (2.3 to 4.4 nm) are used for exposures, biological samples suspended in aqueous matter appear as if the water were transparent or nonexistent.<sup>2,7,9</sup> Figure 1(a) shows a transmission electron micrograph of a uranyl acetate negatively stained preparation of isolated *Limulus* paramyosin and myosin filaments. The filaments, prepared in the laboratory of Prof. Maynard Dewey at SUNY, Stony Brook, were homogenized from *Limulus* telson levator muscle and isolated by differential centrifugation, dialyzed overnight against a relax buffer containing EDTA(4 C), and resuspended in a low KCl Tris buffer at pH 7.4-7.5. The paramyosin paracrystal and myosin filaments are readily identifiable. Under soft x-ray contact microscopy using a wet cell to maintain the filaments in an aqueous buffer, and a broad band of radiation for exposure (2.3 to 4.4 nm) generated from a carbon-rich plasma,<sup>11</sup> the same isolated muscle filament preparation appears quite similar to the TEM image. The paramyosin and myosin filaments are comparable (Fig. 1).

### *Absorption-edge Microscopy*

By exploiting the high resolution and contrast mechanism characteristics of soft x rays and also taking advantage of the abrupt changes in the absorption coefficient of a particular element as a function of the x-ray wavelength due to atomic resonances and absorption edges, one can achieve a new type of atomic number mapping. Absorption-edge imaging involves the exposure of a sample to two x-ray wavelengths straddling a specific absorption edge or resonance. To demonstrate how differently soft x-ray replicas may appear when the same sample is exposed to two different but neighboring x-ray wavelengths, the same isolated muscle filament preparation imaged in Fig. 1 was divided into two aliquots and exposed to 3.1 and 3.5nm monochromatic x rays at the U15 beamline at Brookhaven National Laboratory (National Synchrotron Light Source). Figure 2 shows x-ray replicas with filamentous structures decorated with numerous globular prominences. The edge of the exposure area is flat and reveals no specimen replication (Fig. 2a). In the x-ray exposure area numerous decorated filaments can be seen. At higher magnification an occasional clean filament is evident (arrow, Fig. 2b). Since the exposure was made with x rays at the nitrogen absorption edge, the globular decoration artifact may represent imaging of the Tris buffer (which has a high nitrogen content) in which the filaments were bathed. Figure 3 shows x-ray replicas exposed to x rays at the calcium  $L_{II}$  absorption edge. Although the same *Limulus* muscle filaments were exposed, none can be seen in the two micrographs (Fig. 3). By dialyzing with EDTA, one finds that these samples have virtually no bound calcium, so that there is no clear imaging of any structures with Ca  $L_{II}$  x rays.

To identify clearly sites of calcium localization in such a sample, x-ray exposures would have to be made specifically above and below the Ca  $L_{II}$  absorption edge. Even then, with the contact microscopy technique for imaging, one could only estimate visually where the Ca imaging has occurred. To make absorption-edge imaging into a technically accurate



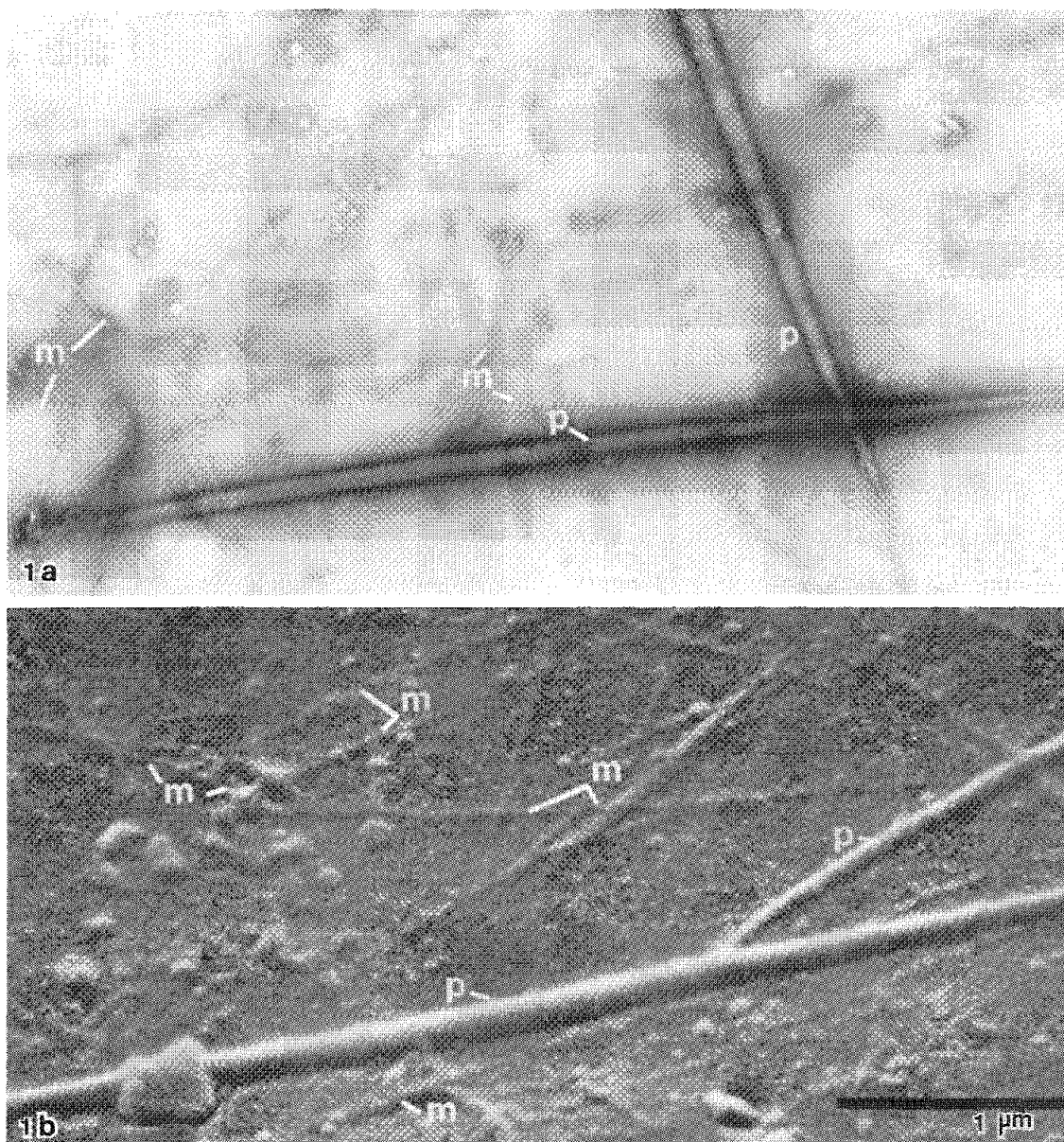


FIG. 1.--(a) TEM of paramyosin (p) and myosin (m) filaments negatively stained with uranyl acetate; 80 kV. (b) X-ray contact micrograph of p and m filaments, suspended in buffer in wet cell during 60ns exposure to broadband radiation (2.3-4.4nm wavelength) from pulsed plasma source; SEM 30 kV, 40° tilt.

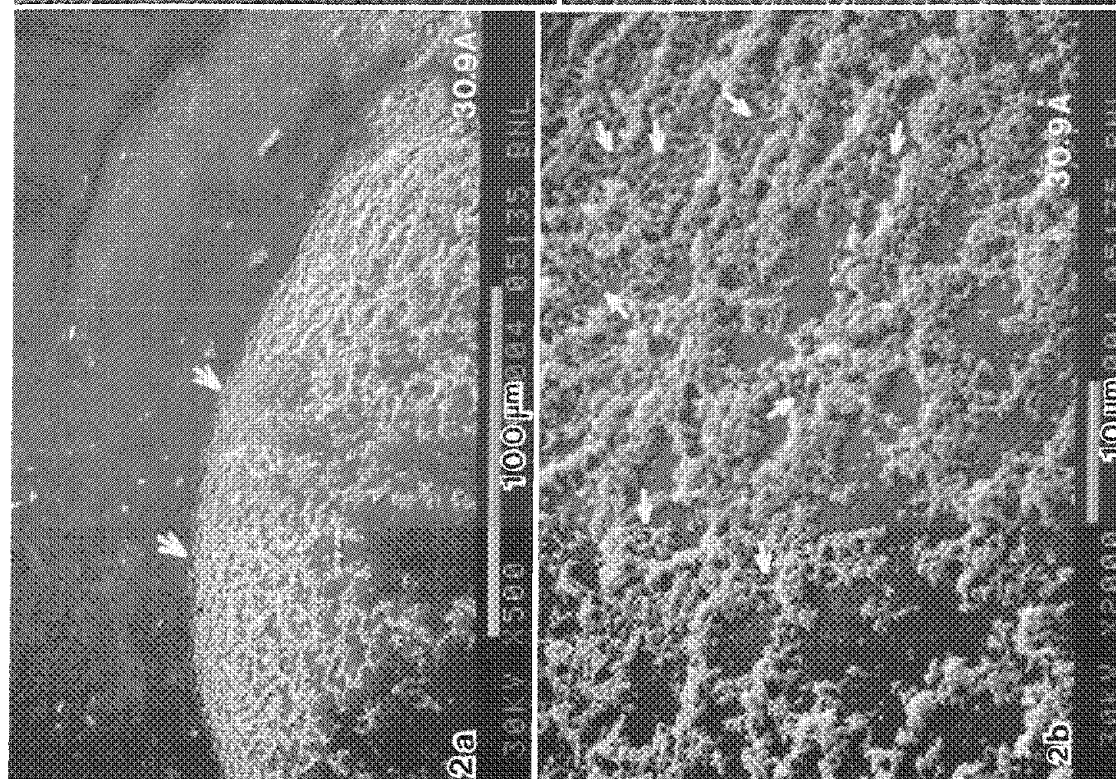


FIG. 2.--(a) Muscle-filament preparation imaged with 3.09nm monochromatic synchrotron radiation. Areas not exposed to x rays showed no specimen replication. Regions directly exposed to x rays at N absorption edge reveal filamentous structures (arrows). SEM 30 kV, 74° tilt. (b) At higher magnification some muscle filaments are visible (arrows), but globular artifact decorates most filaments (possibly imaging of Tris buffer). SEM 30 kV, 74° tilt.

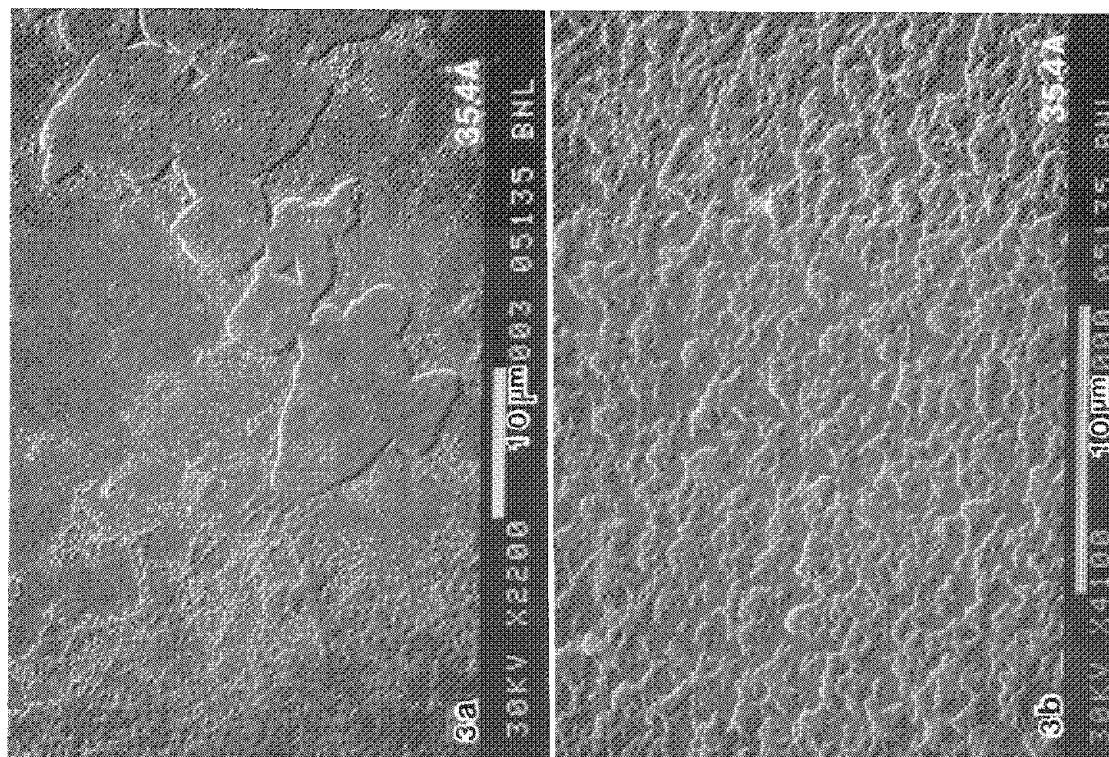


FIG. 3.--(a) X-ray replica of *Limulus* muscle filament preparation exposed to 3.54nm Ca L<sub>II</sub> x rays. No filaments can be seen. SEM 30 kV, 74° tilt. (b) At higher magnification some vague structures are evident in Ca L<sub>II</sub> x-ray replica, but no filaments could be found. SEM 30 kV, 74° tilt.

method, it is better to abandon the contact microscopy polymer detectors and collect and digitize the transmitted x rays with a flow-proportional counter.<sup>12</sup> Kenney, Kirz, Rarback, and colleagues at Stony Brook<sup>10,13</sup> have collectively demonstrated the usefulness of the scanning x-ray microscope for quantitative calcium mapping of CaF<sub>2</sub> test specimens and human cranium fragments analyzed by absorption-edge-induced changes in x-ray transmission. Glutaraldehyde-treated chips of human cranium were embedded in plastic, sectioned, and exposed to 3.55 and 3.58 nm x rays. The number of transmitted x rays detected per pixel for each image were stored, subtracted from one another, and displayed as an image of the calcium distribution. To convert the absorption edge images into quantitative calcium maps requires the calculation of background x-ray events, wavelength stability of the monochromator, etc. Although absorption-edge imaging with polymer detectors offers high spatial resolution and x-ray replicas that are easy for biologists to interpret, the methodology is still too primitive for clear analytical determinations of specific elemental localizations to be made or to quantify elemental content. The scanning x-ray microscope, on the other hand, can offer accurate quantification of elements in biological unstained and/or hydrated sections. However, this method can only offer a maximum resolution of 0.19  $\mu\text{m}$  at this time. It would seem that the best solution would be to use contact microscopy with soft x rays for high-resolution imaging of the specimen. Both broadband imaging for maximum detail (wavelengths between 2.3 and 4.4 nm) and monochromatic absorption-edge imaging could be used for good spatial studies. And for quantitative determinations identical sections or preparations could be analyzed by scanning transmission x-ray microscopy.<sup>10</sup>

## References

1. J. Kirz and D. Sayre, "Soft x-ray microscopy of biological specimens," in S. Doniach and H. Winick, Eds., *Synchrotron Radiation Research*, New York: Plenum Press, 1980, 277-322.
2. D. Sayre, J. Kirz, R. Feder, D. M. Kim, and E. Spiller, "Potential operating region for ultrasoft x-ray microscopy of biological materials," *Science* 196: 1339-1340, 1977.
3. J. Kirz and H. Rarback, "Soft x-ray microscopes," *Rev. Sci. Instrum.* 56: 1-13, 1985.
4. B. J. Panessa-Warren and J. B. Warren, "Determining biological fine structure by differential absorption of soft x-rays," *Ann. N. Y. Acad. of Sciences* 302: 350-367, 1980.
5. A. Neureuther, "Microlithography with soft x-rays," in Ref. 1, pp. 223-275.
6. R. Feder, J. Costa, P. Chaudari, and D. Sayre, "Improved detail in biological soft x-ray microscopy: Study of blood platelets," *Science* 212: 1398-1400, 1981.
7. B. Panessa, G. Coleman, R. McCorkle, and J. B. Warren, "A wet-cell for high resolution imaging of hydrated biological specimens," *Scanning* 4: 21-26, 1981.
8. B. Panessa-Warren, "Biological applications of x-ray contact microscopy," in G. Schmahl and D. Rudolph, Eds., *X-ray Microscopy*, Berlin: Springer-Verlag, 1984, 268-278.
9. J. M. Kenney, *Elemental Analysis Using a Scanning Transmission X-ray Microscope*, Ph.D. Thesis, Department of Physics, SUNY, Stony Brook, 1985.
10. J. Kenney, C. Jacobsen, J. Kirz, and H. Rarback, "Absorption microanalysis with a scanning soft x-ray microscope: Mapping the distribution of calcium in bone," *J. Microscopy* 138: 321-328, 1985.
11. R. McCorkle, J. Angilello, G. Coleman, R. Feder, and S. La Placa, "Flash x-ray microscopy," *Science* 205: 401-402, 1979.
12. M. Howells, J. Kirz, D. Sayre, and G. Schmahl, "Soft x-ray microscopes," *Synchrotron Radiation Res.* 6, *Physics Today* 1985, 2-11.
13. C. Jacobsen, J. Kenney, J. Kirz, R. Rosser, and H. Rarback, "Scanning microscopy with soft x-rays," *Proc. 43rd EMSA*, 1985, 594-595.

## WATER MEASUREMENT IN BIOLOGICAL TISSUE

R. R. Warner, N. E. Morgan, T. A. Eby, M. C. Myers, and D. A. Taylor

The ability of the electron microprobe or analytical electron microscope (AEM) to measure water in subcellular volumes of tissue is seldom emphasized, but it is a unique capability with an important future. We have used this instrumentation to obtain the first experimentally measured water profile across skin. Currently we are developing a new procedure for measuring water content that is based on densitometry of STEM images.

The microprobe and AEM are generally regarded as instruments for measuring elemental concentrations, but in biological analyses these instruments also routinely record sample dry weight. Usually dry-weight measurements are incidental to the primary biological study;<sup>1</sup> only occasionally have they been as important as elemental determinations.<sup>2</sup> Since a dry-weight measurement can be converted to water content, and since there are fundamental biological studies for which water content is the major scientific focus, it is surprising that there has been so little interest in the use of electron-beam instruments to measure water. A good example of a scientific field that could benefit from this technology is dermatology. Water uniquely affects physical properties important to the function and appearance of human skin, and maintaining an appropriate water content in the outer skin layers (stratum corneum) is of clinical and cosmetic concern. Many techniques have been developed to measure water in skin, including techniques based on sonic, electrical, thermal, mechanical, topographical, and spectroscopic measurements. Generally these techniques have measured water content within poorly defined regions of skin<sup>3</sup> and with a few exceptions have provided only qualitative indications of changes in water content. As a consequence, major questions concerning the barrier to water loss and the nature of defects in dry or pathologically altered skin remain unanswered. Of existing methods, the electron-beam instruments offer unique opportunities for absolute quantitation of water in subcellular volumes. Techniques for quantifying water content using these instruments have been developed by Hall,<sup>4-6</sup> Rick,<sup>7,8</sup> and the Ingrams.<sup>9,10</sup> We have used a modified version of the Rick technique to investigate the water barrier in skin. Limitations of this technology, primarily with respect to speed, have prompted us to investigate a new procedure for water measurement based on densitometry of STEM images. Our techniques for measuring water in skin are described in this paper.

### *Water Gradient of Skin Obtained by the Rick Technique*

The Rick technique for measuring water content is based on the constant proportionality between the x-ray continuum and dry mass in a thin specimen.<sup>4</sup> The sample dry mass fraction  $F_d$  is determined from continuum measurements on freeze-dried cryosections, and water content (grams water/total grams tissue) is then given by  $1 - F_d$ . We believe the Rick quantitation procedures for calculating  $F_d$  should not be used for samples with extreme mass heterogeneity such as that found in skin. For this tissue we use the following alternative equation<sup>11</sup>:

$$\frac{1}{F_d} = \frac{C_d^{II} G_d^I}{C_d^I G_d^{II}} \left[ \frac{1}{F_d^{II}} - \frac{p_d^{II} - p_w}{p_d^{II}} \right] + \frac{p_d^I - p_w}{p_d^I}$$

where  $p_d$  is the density of the sample dry mass,  $p_w$  is the density of ice,  $C$  is a continuum x-ray count,  $G$  is a term describing the atomic number dependence of continuum generation,<sup>6</sup> the subscripts  $d$  and  $w$  denote "dry mass" and "water (ice)," respectively, and the superscripts  $I$  and  $II$  denote sample and standard, respectively. Mass loss during analysis is

---

Authors Warner, Morgan, and Eby are at Miami Valley Laboratories, Procter and Gamble Co., Cincinnati, OH 45257; author Taylor is at Sharon Woods Technical Center, Procter and Gamble Co., Cincinnati, OH 45241; author Myers is at Norwich Eaton Pharmaceuticals, Norwich, NY 13815.

of particular concern and is carefully monitored.<sup>12</sup> The Rick technique fundamentally requires application of a standard of known water content (known dry mass) to the tissue prior to freezing. Such a standard cannot be applied to skin without altering the water content of the outer cell layers. To address this problem, we are developing a toluene-based standard that can be applied at very low temperatures to the previously frozen tissue. In the interim we are using the deeper living cells of skin as an internal standard. With this approach, we have produced semi-quantitative results that provide new insight into the function of skin. Figure 1 shows the averaged dry mass profile and corresponding water profile across skin. A significant finding is the dramatic discontinuity in water concentration that occurs at or slightly below the stratum corneum layer. This discontinuity suggests that the barrier to water loss begins in a region slightly beneath the stratum corneum and involves a partitioning process. A morphological feature coinciding with the water discontinuity is the presence of a lipid-enriched intercellular domain produced by the cellular secretion of "lamellar bodies."<sup>13</sup> A water discontinuity below the stratum corneum would effectively isolate the stratum corneum from the rest of the body, and water loss could be governed not so much by diffusion as by solubility.

#### *Water Content Measured by Densitometry*

The electron microscope has long been used to measure the mass of biological particles,<sup>14</sup> and its extension to the measurement of water content should be straightforward. Of the several ways it could be done, we have chosen to use STEM images combined with microdensitometry. A STEM image of a cryosectioned, freeze-dried sample is photographed on the instrument CRT with positive/negative Polaroid film. The negative is placed in a densitometer and the water content is determined from light transmission. In the STEM mode there is a large range in image contrast under operator control that can complicate standardization of the densitometric process. The need to reproduce the brightness and contrast settings on the microscope exactly can be avoided by use of samples with a peripheral dry mass standard. The standard provides an intrinsic photometric calibration for each image and the conversion factor for calculating water content. It is then only necessary to insure that limitations of specimen thickness or film response are not exceeded. As in our discussion of the Rick technique, quantitative results must await the development of a dry-mass standard that can be applied to the skin surface. The primary advantages of this densitometric technique over previous techniques are: (1) a decrease in sample damage from the electron beam due to the lower currents that can be used, (2) an improvement in resolution and visibility inherent in the photographic negative, and (3) an increase in the speed of data collection by orders of magnitude due to the simultaneous nature of data collection inherent in a photograph. An example of a single dry-mass profile across skin obtained by this technique is shown in Fig. 2. There is an obvious similarity between the results obtained with the Rick technique (Fig. 1, right) and the densitometric technique.

#### *Summary*

The electron microprobe and analytical electron microscope have a unique ability to measure water quantitatively in subcellular volumes. We used this capability to determine the water profile across human skin. Similar studies promise to expand the understanding of skin function and dysfunction. In our studies, specimen dry mass was determined from x-ray continuum measurements obtained sequentially at individual points, a very slow and tedious procedure. Since the dry mass distribution across the entire thickness of the skin epithelium can be captured in a single photograph, water content measurements could be greatly aided by a photometric/densitometric approach. Our initial efforts in developing a densitometric technique for measuring water content are encouraging.

#### *References*

1. R. Rick, A. Dörge, A. D. C. Macknight, A. Leaf, and K. Thurau, "Electron microprobe analysis of the different epithelial cells of toad urinary bladder," *J. Membrane Biol.* 39: 257-271, 1978.
2. R. Rick, A. Dörge, U. Katz, R. Bauer, and K. Thurau, "The osmotic behavior of toad skin epithelium (*Bufo viridis*)," *Pflügers Arch.* 385: 1-10, 1980.
3. A. Triebkorn, M. Gloor, and F. Griener, "Comparative investigations on the water



content of the stratum corneum using different methods of measurement," *Dermatologica* 167: 64-69, 1983.

4. T. A. Hall, "The microprobe assay of chemical elements," in G. Oster, Ed., *Physical Techniques in Biological Research*, New York: Academic Press, 1971, 2nd ed., vol. 1A, 157-275.

5. T. A. Hall, "Problems of the continuum-normalization method for the quantitative analysis of sections of soft tissue," in Lechene and Warner, Eds., *Microbeam Analysis in Biology*, New York: Academic Press, 1979, 185-208.

6. T. A. Hall and B. L. Gupta, "EDS quantitation and application to biology," in Hren, Goldstein, and Joy, Eds., *Introduction to Analytical Electron Microscopy*, New York: Plenum Press, 1979, 169-197.

7. A. Dörge, R. Rick, K. Gehring, and K. Thureau, "Preparation of freeze-dried cryosections for quantitative x-ray microanalysis of electrolytes in biological soft tissues," *Pflügers Arch.* 373: 85-97, 1978.

8. R. Rick, A. Dörge, K. Gehring, R. Bauer, and K. Thureau, "Quantitative determination of cellular electrolyte concentrations in thin freeze-dried cryosections using energy dispersive X-ray microanalysis," in Lechene and Warner, Eds., *Microbeam Analysis in Biology*, New York: Academic Press, 1979, 517-534.

9. M. J. Ingram and F. D. Ingram, "Electron microprobe calibration for measurement of intracellular water," *SEM/1983 III*, 1249-1254.

10. F. D. Ingram and M. J. Ingram, "Intracellular hydration measurement with freeze-dried, plastic-embedded biological soft tissue," *Microbeam Analysis--1983*, 229-230.

11. R. R. Warner, "Water content from analysis of freeze-dried thin sections," *J. Microsc.* (in press).

12. M. C. Myers and R. R. Warner, "A routine procedure for monitoring sample mass during microanalysis," *Microbeam Analysis--1985*, 129-131.

13. G. F. Odland, "A submicroscopic granular component in human epidermis," *J. Invest. Dermatol.* 34: 11-15, 1960.

14. G. F. Bahr and E. Zeitler, "The determination of the dry mass in populations of isolated particles," *Laboratory Investigation* 14: 217-239, 1965.

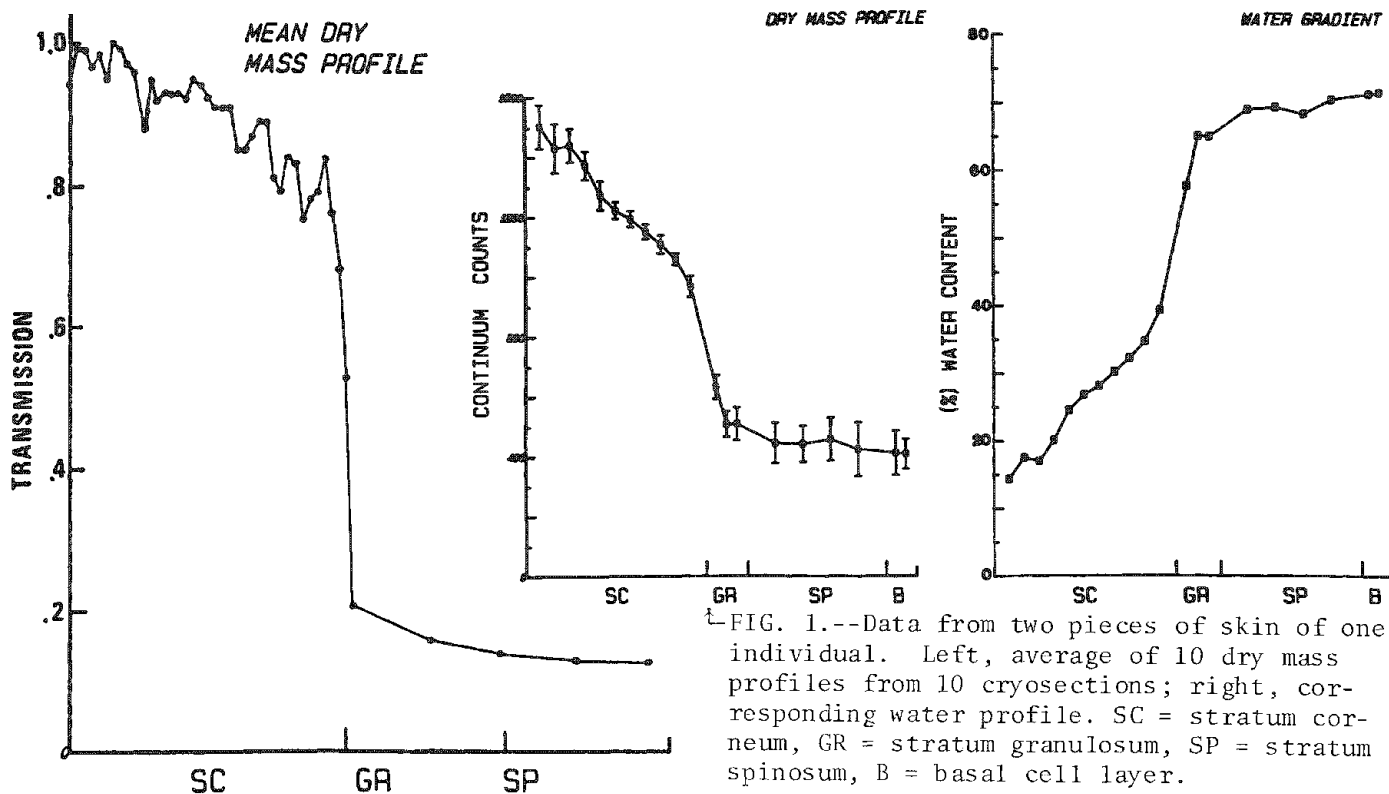


FIG. 1.--Data from two pieces of skin of one individual. Left, average of 10 dry mass profiles from 10 cryosections; right, corresponding water profile. SC = stratum corneum, GR = stratum granulosum, SP = stratum spinosum, B = basal cell layer.

FIG. 2.--Densitometric recording of single dry mass profile from STEM image of cryosection analyzed in Fig. 1. Y axis is in arbitrary units (transmission); X axis legend same as for Fig. 1.

## MASS THICKNESS IMAGES OF FROZEN-HYDRATED AND FREEZE-DRIED SECTIONS

D. A. Kopf, Ann LeFurgey, L. A. Hawkey, B. L. Craig, and Peter Ingram

Since variations have been demonstrated in the degree of hydration between mitochondria and cytoplasm,<sup>1</sup> accurate conversion of dry weight measurements made within such intracellular compartments by x-ray or EELS microanalysis to wet weight values requires in situ measurement of water content. Valid comparisons with other physiological measurements made on living cells, such as ionic activity determined with ion-selective microelectrodes,<sup>2</sup> depend predominantly on the accuracy of this conversion. Mass thickness measurements can also be determined from the elastic signal in STEM, or from the inelastic spectrum in STEM or CTEM.<sup>4</sup>

In general, the weight per unit area  $w$  results in a decrease in the detected transmitted current  $I$  given by Beer's law:

$$I = I_0 \exp(-w/\lambda)$$

where  $I_0$  is the incident current and  $\lambda$  is the extinction coefficient, representing all processes that remove electrons from the detection apparatus. With  $w$  expressed in units of  $\text{g}/\text{cm}^2$ ,  $\lambda$  is the inverse of the total effective cross section for all these scattering processes.

Zeitler and Bahr<sup>3</sup> demonstrated that useful measurements of  $w$  could be obtained from photometry of conventional bright-field micrographs, if the extinction coefficient could be adjusted (via selection of objective aperture) so as to map the elastic scattering range of the specimen to the relatively narrow density range of photographic film. Mass standards with similar scattering properties were used to determine the extinction coefficient for each objective aperture. Mass can also be determined from the elastic signal in STEM, or from the inelastic spectrum in STEM or CTEM.<sup>4</sup>

The inelastically unscattered "zero-loss" signal is conveniently obtained with an electron spectrometer in either CTEM or STEM. The mass thickness is:

$$w = \lambda \ln(I_{z1}/I_0)$$

where  $I_{z1}$  is the zero-loss current through the specimen and  $I_0$  is the zero-loss current through a hole. In CTEM imaging with no objective aperture, if the contrast vanishes at focus (as is the case for thin frozen hydrated sections), elastic scattering does not contribute to the extinction coefficient and  $\lambda$  can be calculated from the mean free path for inelastic scattering in the material, which gives roughly  $1.5 \times 10^{-5} \text{ g}/\text{cm}^2$  at 100 kV for organic materials. In this special case specimen mass thickness can be determined without the use of standards. One can make spot measurements in the image mode from areas as small as 1-2 nm in diameter by lifting the screen after centering the feature of interest and allowing the image to fall onto the entrance aperture of the spectrometer. Mass measurements corresponding to several times the mean free path are possible. In principle the hydrated masses could be measured directly from the various cellular compartments, although the low contrast in the hydrated state makes identification of the structures difficult, and examination cannot proceed indefinitely in the hydrated state due to the gradual loss of water under the electron beam.

One can overcome this problem by forming an image from the zero-loss signal, storing it in computer memory, and performing the analysis later. The hardware used has been described previously.<sup>5</sup> X and Y ramps are fed into the image scanning coils though the low-

---

Author Kopf is with the Department of Anatomy, Duke University Medical Center, Durham, NC 27710; authors LeFurgey, Hawkey, and Craig are with the Department of Physiology, Duke University Medical Center; author Ingram is with the Research Triangle Research Institute, Research Triangle Park, NC 27709. The work was supported by grants NSF PCM 8306638, NIH HL 17670, HL 27105, and AM 26816, and a research gift from the R. J. Reynolds Industries.

dose attachment on a Philips EM 420, and the image is scanned across the spectrometer aperture. The zero-loss electrons are counted for each pixel. Up to a  $4096 \times 4096$  image is transferred to a VAX 11/750 through a 9600-baud line. The mass-thickness map is then generated and viewed on a digital image memory. In this manner the contrast can be enhanced, and structures can be identified from micrographs taken after subsequent freeze-drying to determine the precise location of the compartments of interest. The mass thickness is then read directly by positioning of a cursor, or integrals over small areas can be performed.

A test using 126nm polystyrene latex spheres showed a spherical mass projection and the correct thickness based on the 122nm inelastic mean free path in polystyrene at 100 kV (Fig. 1).



FIG. 1.--Experimental (left) and theoretical (right) thickness maps of 126nm-diameter polystyrene latex spheres (Dow Chemical LS-052-A). Measured central sphere mass thickness corresponds closely with sphere diameter when normalized by mean free path in polystyrene of 122 nm at 100 kV, after correction for 7.5nm carbon support film.

Initial application of this technique has been made on hydrated and freeze-dried sections of a suspension of kidney proximal tubules or cultured embryonic chick heart cells, prepared as previously described.<sup>2,6</sup> The hydrated sections are transferred into the microscope by a cryotransfer stage (Gatan 626) maintained at 110 K or below during transfer and analysis. Figure 2(a) demonstrates a bright-field electron micrograph of a hydrated section of cultured heart cells; and Fig. 2(b) shows the corresponding section after freeze-drying in the microscope. Although little structure is apparent in the hydrated image, mitochondria and cytoplasmic features are visible in the freeze-dried image, together with a lacy appearance characteristic of ice crystal damage during freezing. Figures 2(c) and (d) show the mass thickness maps obtained from the scanned zero-loss images; Figs. 2(e) and (f) are histograms of the mass thickness distribution over the sections. Average mass thickness for this hydrated section was  $3.9 \times 10^{-5}$  g/cm<sup>2</sup>, and for the freeze-dried section  $1.8 \times 10^{-6}$  g/cm<sup>2</sup>, when corrected for the 34nm ( $6.8 \times 10^{-6}$  g/cm<sup>2</sup>) carbon support film.

The areas analyzed must be viewed in orthogonal projection, as many frozen hydrated sections do not lie flat on the support film or contain areas that are tilted to the view (Fig. 3). In such cases the mass thickness projection must be corrected by the cosine of the tilt angle.

Figure 4 demonstrates how the technique has been used in freeze-dried sections to measure mass thickness of regions such as mitochondria, cytoplasm, and nucleus. In this section of a kidney proximal tubule cell, the mitochondria are apparently twice the mass thickness of the nucleus or regions of the cytoplasm, which suggests that the initial water content of the mitochondria was less than that of the other regions.<sup>1,2</sup> This possibility can be effectively verified in sections examined sequentially in the hydrated and freeze-dried states as described above.

These preliminary results suggest that it will be feasible to make mass thickness measurements from selected intracellular compartments before and after removal of cell water by freeze drying. The same freeze-dried section and intracellular regions can then be analyzed by x ray or EELS to determine elemental content. The ratio of the mass thickness in the intracellular regions, frozen hydrated and freeze dried, will be used to convert element content in mmols/kg dry weight to wet weight values (mmolar). Such a means of conversion will facilitate the physiological interpretation of quantitative data from both electron probe x-ray microanalysis and electron energy loss spectroscopy.



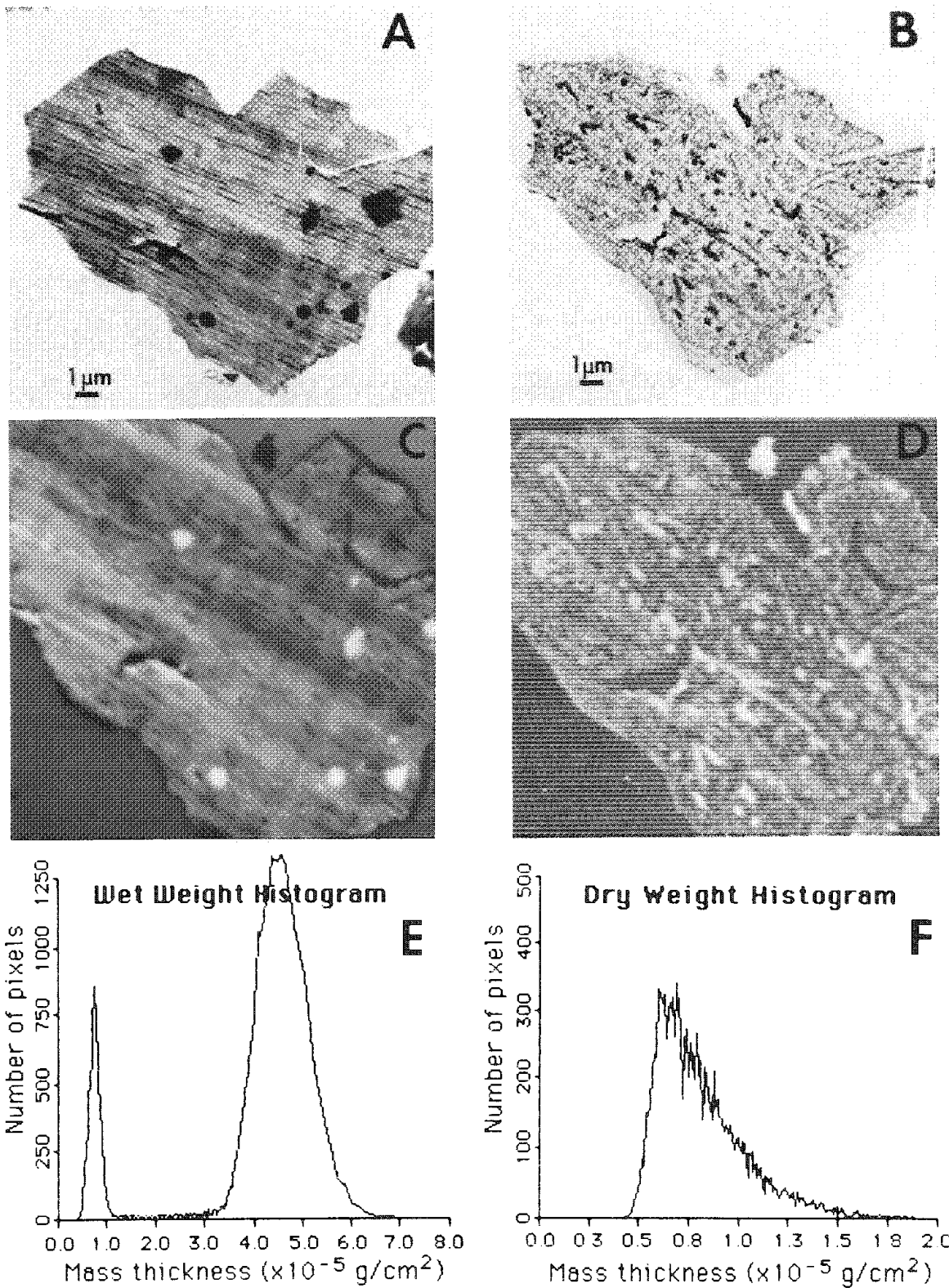


FIG. 2.--Transmission electron micrograph (TEM) of frozen hydrated section of cultured heart cell (A) and TEM of same section following freeze drying (B). Freeze drying was accomplished by gradual warming of cryotransfer stage to 310 K over 2.5 h. Before and after freeze drying, zero-loss images were scanned as described in text. Mass thickness maps of frozen hydrated (C) and freeze-dried (D) sections were generated from zero-loss images. Histograms (E, F) show range of mass thickness in each image.

## References

1. A. V. Somlyo et al., "Calcium release and ionic changes in the sarcoplasmic reticulum of tetanized muscle: An electron probe study," *J. Cell Biology* 90: 577-594, 1981.
2. A. LeFurgey et al., "Quantitative elemental characterization of cultured heart cells by electron probe x-ray microanalysis," this volume.
3. E. Zeitler and G. F. Bahr, "A photometric procedure for weight determination of submicroscopic particles: Quantitative electron microscopy," *J. Appl. Phys.* 33: 847-853, 1961.
4. R. D. Leapman et al., "Mass thickness determination by inelastic scattering in microanalysis of organic samples," *Analytical Electron Microscopy--1984*, 83-88.
5. D. A. Kopf, "An EELS acquisition peripheral for a superminicomputer," *Proc. 43rd Mtg. EMSA*, 1985, 148-149.
6. A. LeFurgey et al., "Reduction of potassium in kidney proximal tubules to aid in electron probe x-ray microanalysis of calcium," *Proc. 43rd Mtg. EMSA*, 1985, 474-475.

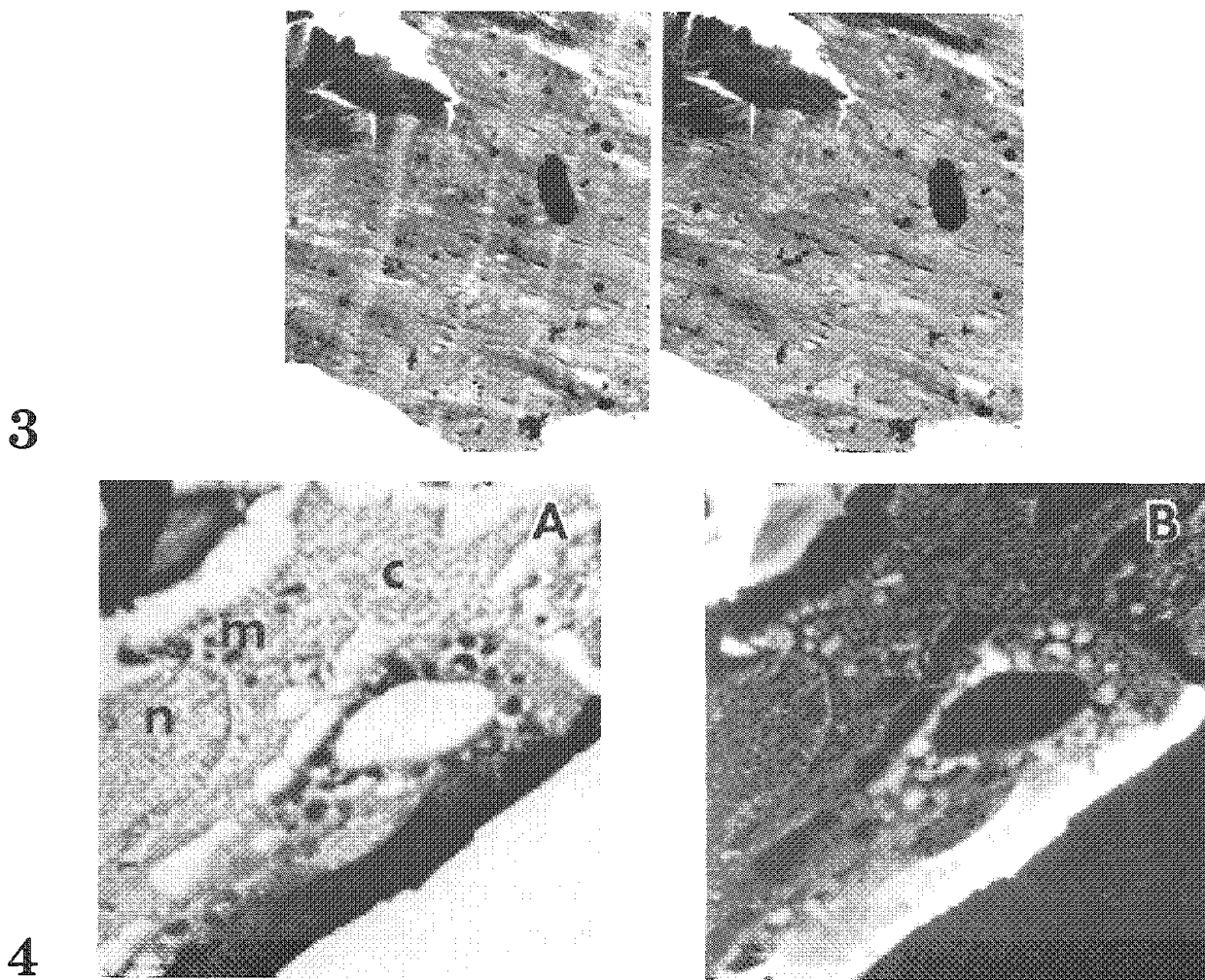


FIG. 3.--Stereo pair of frozen hydrated section of kidney proximal tubule cell. Surface topography is such that very few areas are orthogonal to electron probe. Misleading mass measurements are obtained from tilted areas. Full horizontal scale, 15  $\mu\text{m}$ ; tilt,  $\pm 10^\circ$ . FIG. 4.--Zero-loss image (A) and generated mass thickness image (B) of freeze-dried section of kidney proximal tubule cell. M = mitochondria, N = nucleus, C = cytoplasm. Mass thickness of mitochondria is roughly twice the mass thickness of nucleus or cytoplasm.

## THE DISTRIBUTION OF ELEMENTS IN DEVELOPING ROOTS OF *LEMNA MINOR* L.

Patrick Echlin and T. L. Hayes

Low-temperature x-ray microanalysis has been used to measure local concentrations of seven elements in two major tissue types along the length of the roots of *Lemna minor* L. Duck-week plants consist of a flat green floating blade or frond that functions as a leaf. From the underside of each frond, one or more long adventitious roots hang down into the water. These roots are green in the apical region and have a well-developed root cap. At present it is uncertain whether these roots are actively involved in the transport of minerals from the water to the frond or whether they have a more passive role in acting as a keel for the floating fronds.

### *Experimental*

Plants were grown as described previously<sup>1</sup> in a medium containing 2mM[K<sup>+</sup>] and [Cl<sup>-</sup>]; 0.5mM[P], 0.2mM[Mg<sup>++</sup>], [Ca<sup>++</sup>], and trace amounts of [Na<sup>+</sup>]. Roots 20 mm long were removed and prepared for low-temperature microscopy and analysis by the techniques and equipment described by Echlin et al.<sup>1</sup> Samples were maintained in a fully frozen-hydrated state throughout preparation, examination, and analysis by the use of the AMRAY Biochamber and associated microscope cold stage. The spectra were analyzed by the peak-to-background (P/B) ratio method of Statham and Pawley<sup>2</sup> and frozen hydrated standards were made from solutions of salts mixed with colloidal graphite and a cryoprotectant.<sup>3</sup> Analysis was carried out on approximately 1700 different cells from about 80 fracture faces taken from various regions along the length of the root. Although we have data from each of the ten cell types shown in Fig. 1 (and described in more detail in Ref. 1), for this study we have combined the data from different cell types into two major tissue regions. The results from xylem and phloem cells have been combined into a category called vascular tissue, and the results from the three cortical layers plus the epidermis have been combined into a category called cortical tissue. Data from the endodermis and the root cap have not been included in this study. The vascular tissue is usually associated with the long-distance transport processes in plants, whereas the cortex serves as an intermediary in the mineral uptake process.

### *Results and Discussion*

The results of these analyses are shown in Tables 1 and 2. Note that the values are the same for both the cortical and vascular tissue in the first region, 0.75  $\mu$ m from the root tip, where the cell types remain undifferentiated. The sectors 75-200 and 200-300  $\mu$ m are regions of active cell division and the vascular tissue is clearly differentiated from the cortex. The sector 300-1000  $\mu$ m is a region of cell elongation and at 2500  $\mu$ m the root is no longer surrounded by the root cap. The remaining sectors at 8, 10, and 15 mm are at different positions away from the root tip. There is very little difference in the concentration of Na<sup>+</sup>, Mg<sup>++</sup>, S, Cl, and Ca<sup>++</sup> between the vascular tissue and the cortical tissue along the whole length of the root. This result shows that no particular part of the root is involved in the preferential uptake of these elements and that any uptake is for local use only rather than for transport to other regions of the plant. The P and K<sup>+</sup> values are higher in the undifferentiated vacuolate regions of the first 75  $\mu$ m of the root and in the regions of cell elongation beyond the regions of cell division. The values for these two elements are lower in the region of cell division between 75 and 300  $\mu$ m. Although there is considerable variation in the concentration of P and K<sup>+</sup> between the vascular and cortical tissues, our studies show that there is a progressive increase in K<sup>+</sup> in the vascular tissue along the length of the root. No such relationship is seen

---

Patrick Echlin is at the Department of Botany, University of Cambridge, Cambridge, England, CB2 3EA; T. L. Hays is at Donner Laboratory, University of California, Berkeley, CA 94720.

TABLE 1.--Concentration of seven elements in the vascular tissue at various regions along the roots of *Lemna minor*.

VASCULAR TISSUE							
From Root tip ( $\mu\text{m}$ )	Na	Mg	P	S	Cl	K	Ca
0 - 75	25 (4.2)	22 (3.7)	268 ( 7.6)	39 (1.4)	14 (1.1)	263 ( 4.3)	6 (1.2)
75 - 200	26 (1.6)	23 (1.0)	213 ( 9.7)	28 (1.3)	16 (0.6)	109 ( 8.0)	10 (0.6)
200 - 300	25 (1.3)	22 (1.0)	153 ( 8.3)	23 (1.0)	14 (0.6)	109 ( 6.7)	12 (1.0)
300 - 1 000	26 (2.7)	24 (2.1)	156 (15.7)	22 (1.8)	15 (1.3)	146 (14.8)	13 (1.2)
2 500	44 (4.8)	48 (2.4)	358 (17.0)	49 (3.1)	12 (4.2)	170 (11.2)	31 (3.4)
8 000	25 (4.6)	22 (3.7)	268 ( 7.5)	39 (1.4)	14 (1.4)	263 ( 5.9)	6 (1.2)
10 000	42 (5.0)	40 (2.8)	152 (11.2)	-	-	318 ( 9.7)	54 (1.9)
15 000	34 (6.1)	18 (4.9)	29 ( 6.0)	-	-	78 (11.8)	13 (2.1)

Values in mM/Kg F.W. (S.E. of mean)

TABLE 2.--Concentration of seven elements in the cortical tissue at various regions along the roots of *Lemna minor*.

CORTICAL TISSUE							
From Root Tip ( $\mu\text{m}$ )	Na	Mg	P	S	Cl	K	Ca
0 - 75	-	-	-	-	-	-	-
75 - 200	27 (2.3)	27 (2.1)	242 (20.4)	29 (2.6)	15 (1.5)	188 (23.0)	12 (1.2)
200 - 300	21 (1.9)	18 (1.3)	69 ( 8.2)	14 (1.2)	16 (1.1)	63 ( 3.8)	12 (1.3)
300 - 1 000	39 (9.4)	16 (4.2)	358 (15.7)	30 (2.8)	21 (3.0)	51 ( 4.1)	16 (3.6)
2 500	48 (4.4)	58 (3.7)	480 (15.2)	7 (3.3)	16 (1.7)	88 ( 4.8)	41 (2.4)
8 000	37 (3.1)	35 (2.9)	143 (20.2)	39 (4.6)	15 (3.8)	150 (23.0)	29 (3.0)
10 000	43 (7.7)	46 (4.3)	186 (29.2)	-	-	306 (28.0)	41 (3.4)
15 000	34 (6.2)	15 (2.3)	136 ( 3.1)	-	-	153 (15.0)	7 (2.3)

Values in mM/Kg F.W. (S.E. of mean)

for P and the values for P and K<sup>+</sup> between the vascular tissue and the cortex show too much variation to allow any firm conclusions to be drawn regarding the significance of the local concentration of these two elements.

Potassium is the major counter cation in duckweed fronds and our present study supports our earlier work,<sup>4</sup> which showed evidence for the transport of this element in the xylem tissue, the major long-distance mineral transport system of vascular plants. As far as the other elements are concerned, our present studies show that mineral uptake from the surrounding aqueous medium is primarily for local use only and that there is little throughput to other parts of the plant. In this respect it suggests that the root of *Lemna minor* functions primarily as a passive keel rather than a major absorptive organ.

### Conclusion

Low-temperature x-ray analytical studies suggest that there may be local [K<sup>+</sup>] uptake by the root and subsequent transport of the element to the aerial parts of the plant, but

the uptake of other elements is for local use only. These findings are discussed in relation the possible function of the adventitious roots of *Lemna minor*.

#### References

1. P. Echlin, C. E. Lai, and T. L. Hayes, "Low-temperature x-ray microanalysis of the differentiating vascular tissue in root tips of *Lemna minor* L.," *J. Microscopy* 126: 285, 1982.
2. P. J. Statham and P. J. Pawley, "A new method for particle x-ray microanalysis based on peak to background measurements," *SEM/1978 I*, 469.
3. P. Echlin, T. L. Hayes, and M. McKoon, "Analytical procedures for bulk frozen-hydrated biological tissues," *Microbeam Analysis--1983*, 243.
4. P. Echlin, C. E. Lai, and T. L. Hayes, "The uptake and distribution of potassium in roots of duckweed (*Lemna minor* L.) as measured by low temperature x-ray microanalysis," *Proc. 40th Ann. Meetg. EMSA*, 1982, 408.

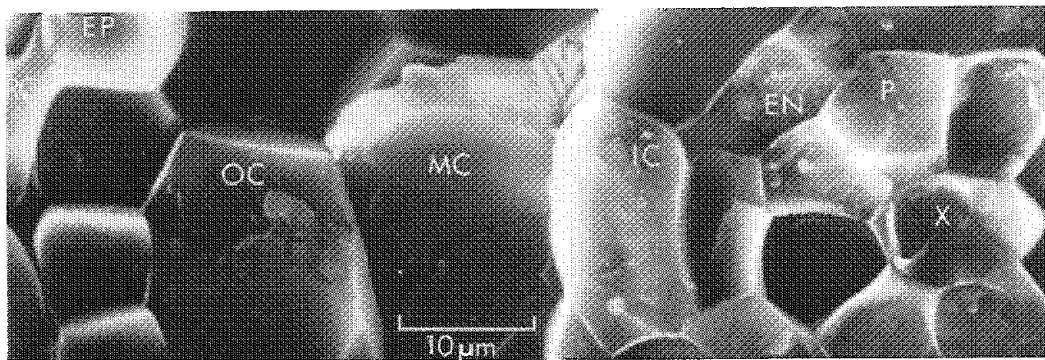


FIG. 1.--Portion of frozen-hydrated fracture face across root of *Lemna minor*. RC = root cap, EP = epidermis, OC = outer cortex, MC = middle cortex, IC = inner cortex, EN = endodermis, P = phloem, X = xylem.

## LOCALIZATION OF POTASSIUM IN *NICOTIANA* LEAVES AT FIVE STAGES OF GROWTH

S. Edith Taylor and Patrick Echlin

Low-temperature x-ray microanalysis techniques are used to measure diffusible elements in bulk frozen-hydrated cells. In our previous study the method of low-temperature x-ray microanalysis was fully described and shown to be useful for measurement of a number of elements within cells of tobacco leaves at the ripe and senescent stages of growth.<sup>1</sup> Other studies have shown the importance of potassium in plant cells: e.g., maintenance of cell turgor, stomatal action, and as a charge-balancing cation for organic acids.<sup>2-4</sup> Due to the importance of potassium in plant cells there was a need to extend the previous study to include other stages of leaf growth.

### *Experimental Procedures*

*Nicotiana tabacum* L. cv. Coker 319 was grown in the Philip Morris greenhouse from April to September. Leaves were harvested from the 6th to 12th nodes (counting from the first true bottom leaf). The leaves picked from the juvenile, mature, ripe, senescent, and old-growth stages were different in size, color, and turgidity. The juvenile leaves were approximately one quarter the size of the mature leaves that were fully grown. The ripe leaves had yellow margins and a yellow-green color in the lamina. Senescent leaves were yellow except for the main vascular tissue. Old leaves were pale yellow or almost white, in some cases blotched with brown necrotic areas. The old leaves appeared less turgid than the other leaves from younger growth stages. Sample preparation techniques were the same as in our previous study.<sup>1</sup>

The standardized conditions used to collect the x-ray spectra are described in Ref. 1. In the present experiments the counting time was increased from 100 to 200 s livetime to increase the signal to noise ratio. A  $6\mu\text{m}^2$  raster was placed on fully hydrated fracture faces of the individual cells. The raster was placed primarily on the vacuole region of the cells with the exception of some palisade cells, where the measurements included a portion of the cell wall, a consequence of the fracturing process, which occurred *between* the palisade cells but *through* the other cell types.

Measurements were taken from twenty leaves at each of the five stages of growth. The cell types were each measured three or four times within each leaf. Data from replications of cell types within the same leaf were averaged to reduce the cell to cell variation, which reduced  $n$  from 60 to less than 20. The data were then subjected to an analysis of variance by use of the software BMDP2V.<sup>5</sup>

### *Results*

In the histogram showing the means of the potassium concentrations of each cell type at the five stages of growth (Fig. 1), the ordinate represents the percentage concentration in g/kg of fresh weight in the analyzed microvolume. The abscissa represents the four cell types in the five growth stages. The standard error of the means of each cell type is shown for each cell type. The sample number  $n$  of leaves is given below each growth stage. The number  $m$  of measurements for each cell type in each growth stage is also listed. The error bar indicates the inherent variability of the leaves. An analysis of variance indicated that there were significant differences in the mean  $\text{K}^+$  concentrations between the growth stages and cell types.

The mean values for  $\text{K}^+$  concentrations will be discussed for each cell type at the five stages of growth. Comparisons of mean  $\text{K}^+$  concentration will be made between the stages of growth. When examining the means one must take into account the variation due

---

Author Taylor is at the Philip Morris Research Center, Box 26583, Richmond, VA 23261; author Echlin is at the Department of Botany, University of Cambridge, Cambridge, England, CB2 3EA. The authors would like to acknowledge the support of E. Thomas, of G. West for growing the plants, and of Dr. D. Ennis for help in the statistical analysis of the data.

to inhomogeneity of the leaves, particularly in the juvenile and mature stages of growth.

When the  $K^+$  concentrations are compared among cell types in the juvenile stage, there is a noticeable variation in the means. The  $K^+$  concentrations are not significantly different in the upper and lower epidermal cells. The  $K^+$  concentrations in the palisade and spongy mesophyll cells are also not significantly different and are lower than the epidermal cells. The lower epidermal cells have a small overlap with the palisade cells due to leaf variation, but overall the  $K^+$  concentration is lower in the palisade cells.

The potassium concentrations in the cell types at the mature stage also vary. The spongy mesophyll cells have a higher  $K^+$  concentration than the palisade cells but are not significantly different from the upper and lower epidermal cells. The palisade cells have a lower  $K^+$  concentration than the upper and lower epidermal cells. The upper and lower epidermal cells are not significantly different in  $K^+$  concentration. When these cells are compared to the juvenile cells, it can be seen that the spongy mesophyll cells increase in  $K^+$  concentration from the juvenile to the mature stages of growth. The other cell types have no significant differences between the two growth stages.

In the ripe stage the potassium concentrations are not significantly different between the cell types. When cells from ripe leaves are compared with cells from the juvenile and mature leaves the potassium concentrations are lower in the upper epidermal cells, but the other cell types are not substantially different.

In the senescent stage the upper epidermal cells have a lower  $K^+$  concentration than the other cells. For palisade, spongy mesophyll, and lower epidermal cells, the  $K^+$  concentrations are not significantly different. When the senescent stage is compared to the earlier growth stages the mean concentration of potassium decreases at senescence. This trend continues into the old stage, where the  $K^+$  concentrations decrease in cell types.

### Discussion

A general trend emerged from examining the data in Fig. 1. The  $K^+$  concentration is higher in the juvenile and mature stages than in the senescent and old stages. During the period of leaf development, potassium has been shown to regulate cell expansion,<sup>6</sup> which appears to be the reason for the higher  $K^+$  in the juvenile stage. It may be possible that higher potassium concentrations are required to maintain full turgor in the juvenile and mature stages of growth. Water measurements taken from similar leaves at the five stages of growth showed the water content decreased as the leaves aged.<sup>7</sup> Our microanalysis data show the decrease in  $K^+$  concentration with leaf growth stage, particularly in the senescent and old stages. Other studies have shown that potassium may be readily exported from older leaves to young, developing leaves on the plant.<sup>8,9</sup> Differences in the potassium concentration between the cell types at a given stage of growth may indicate that turgor is not the same in all the cell types. The decrease in concentration of  $K^+$  seems to be an indication of senescence in tobacco leaves. In the old stage the leaves are visibly less turgid, so that it is not surprising to find less potassium present.

### Conclusion

Differences in  $K^+$  concentration exists in tobacco leaves between the early and later stages of growth. The decrease in  $K^+$  in the senescent and old growth stage correlated with the decrease of water in the leaves at those stages.

### References

1. P. Echlin and S. E. Taylor, "The preparation of bulk frozen-hydrated vacuolate plant tissue," *J. Microscopy* 141: 329-348, 1986.
2. U. Zimmerman, "Physics of turgor and osmoregulation," *Annual Review of Plant Physiology* 29: 121-148, 1978.
3. M. G. Penny and D. J. F. Bowling, "A study of potassium gradients in the epidermis of intact leaves of *Commelina communis* L. in relation to stomatal opening," *Planta* 119: 17-25, 1974.
4. F. B. Salisbury and C. W. Ross, Eds. *Plant Physiology*, Belmont, Calif.: Wadsworth, 1978, 62.
5. W. J. Dixon et al., Ed. *BMDP Statistical Software*, Berkeley: University of California Press, 1985, 359-388.

6. K. Mengel and E. A. Kirkby, "Potassium in crop production," *Advances in Agronomy* 33: 59-110, 1980.
7. P. Echlin (private communication).
8. R. D. Graham and A. Ulrich, "Retranslocation of potassium in *Beta vulgaris* L. under conditions of low sodium supply," *Australian J. Plant Physiology* 1: 387-396, 1974.
9. H. Greenway and M. G. Pitman, "Potassium retranslocation in seedlings of *Hordeum vulgare*," *Australian J. Biological Science* 18: 235-247, 1965.

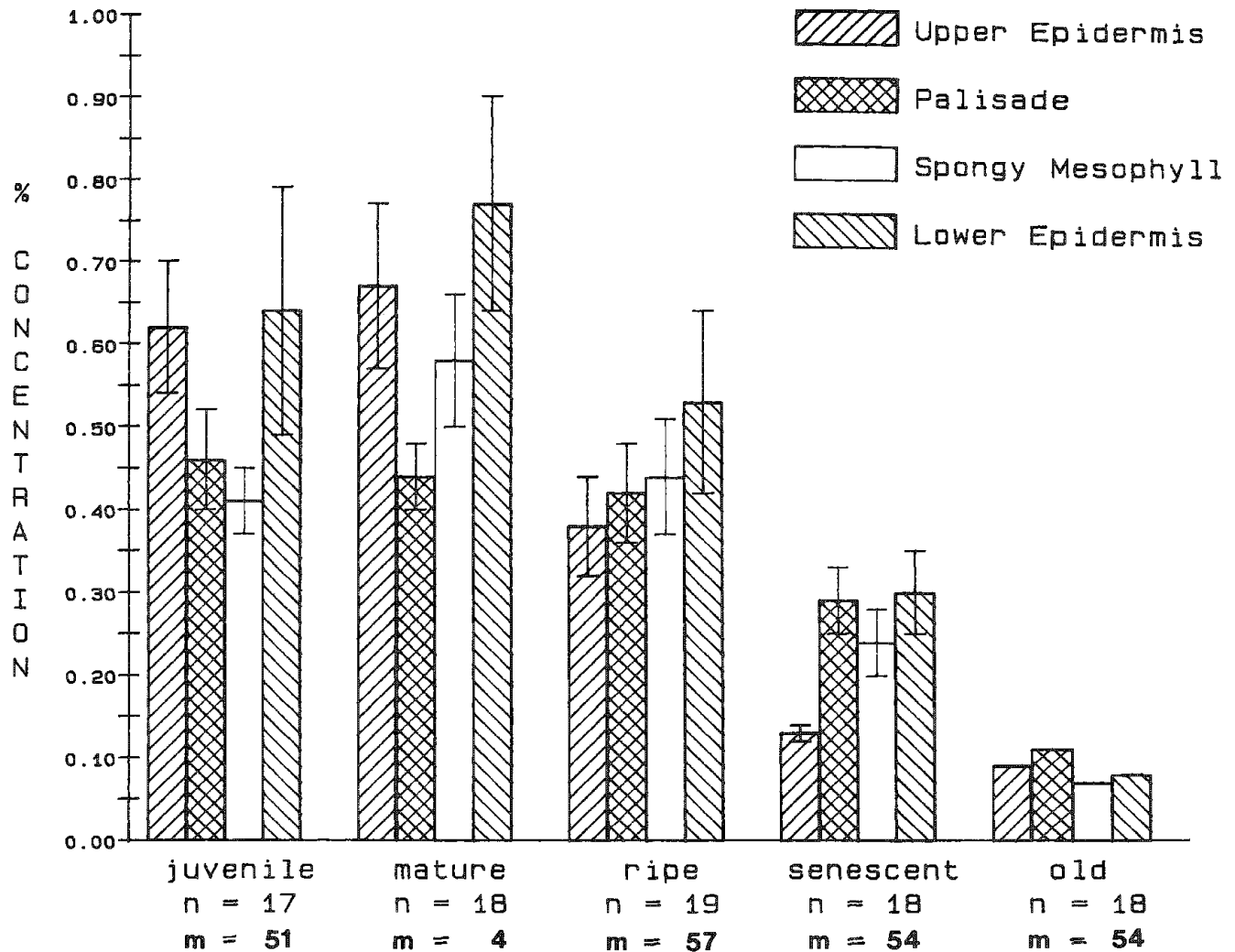


FIG. 1.--Potassium concentrations vs growth stage.



## New Instrumentation and Techniques in Electron Microscopy

### RECENT DEVELOPMENTS IN HITACHI TEM

S. Isakozawa and M. Kubozoe

Recent trends in science and technology are moving toward smaller and finer areas. In semiconductor materials, for example, researchers are working on building required materials from an atomic structure level in submicron areas. In biomedical fields, researchers are trying to resolve molecular structures of cells and tissues. As research objects become smaller and smaller, the role of electron microscopes grows increasingly important in its viewing and analytical capabilities. Applications of the electron microscope are expanding more widely than ever before. For these diversified applications, we have developed various types of electron microscopes ranging from 100 kV to 1 MeV.

#### 1MeV TEM

Figure 1 is a block diagram of the H-1250ST. This instrument has a maximum accelerating voltage of 1250 kV. To reduce high-voltage ripple to an absolute minimum, the high-voltage generator and accelerator are housed in two separate pressure vessels and are connected by a high-voltage resistor cable. STEM is one of the primary operation modes of this instrument. The 1MeV STEM has the following unique advantages:

1. greatly reduced specimen beam damage,
2. observation capability of thick specimens,
3. improved spatial resolution and enhanced signal-to-background noise ratio in the EELS mode.

#### 300kV UHR TEM

Ultrahigh-voltage microscopes have many inherent advantages such as higher resolving power, higher EELS performance, thicker specimen observations, etc. However, instrument size significantly increases as the operating voltage increases. This dimensional increase can cause many associated problems, including the construction of the room housing the instrument.

The H-9000 is a compact ultrahigh-resolution (UHR) microscope that can be installed in an ordinary laboratory room without sacrifice of the many advantages of ultrahigh-voltage microscopes.

Figure 2 is a general view of the H-9000. The instrument is 2.68 m high, which is just about the same as conventional 200kV microscope. It has three illumination lenses and five magnification lenses. The objective lens has spherical aberration  $C_s = 0.9$  mm and chromatic aberration  $C_c = 1.5$  mm. Figure 3 is a structure image of a diamond (111) recorded with the H-9000. The H-9000 has a theoretical resolution of 0.19 nm, which is clearly demonstrated by Fig. 3.

#### 200kV Analytical TEM

When the optimum balance of TEM resolution and analytical capability is considered, the optimum cost performance is given at an accelerating voltage of 200 kV. We have a 200kV ATEM (the H-800) in our product line (Fig. 4). The H-800 accommodates an ultrathin-window EDX detector in addition to the usual Be-window EDX detector (take-off angle  $68^\circ$ ). The ultrathin-window (UTW) detector permits analysis of light elements such as carbon. The UTW detector has no critical limitations in specimen thickness that may be required for EELS. It also has a good S/N ratio so that normal elemental analysis can be performed better and quicker with UTW than with EELS.

---

The authors are at the Naka Works of Hitachi Ltd., Katsuta, 312 Japan.

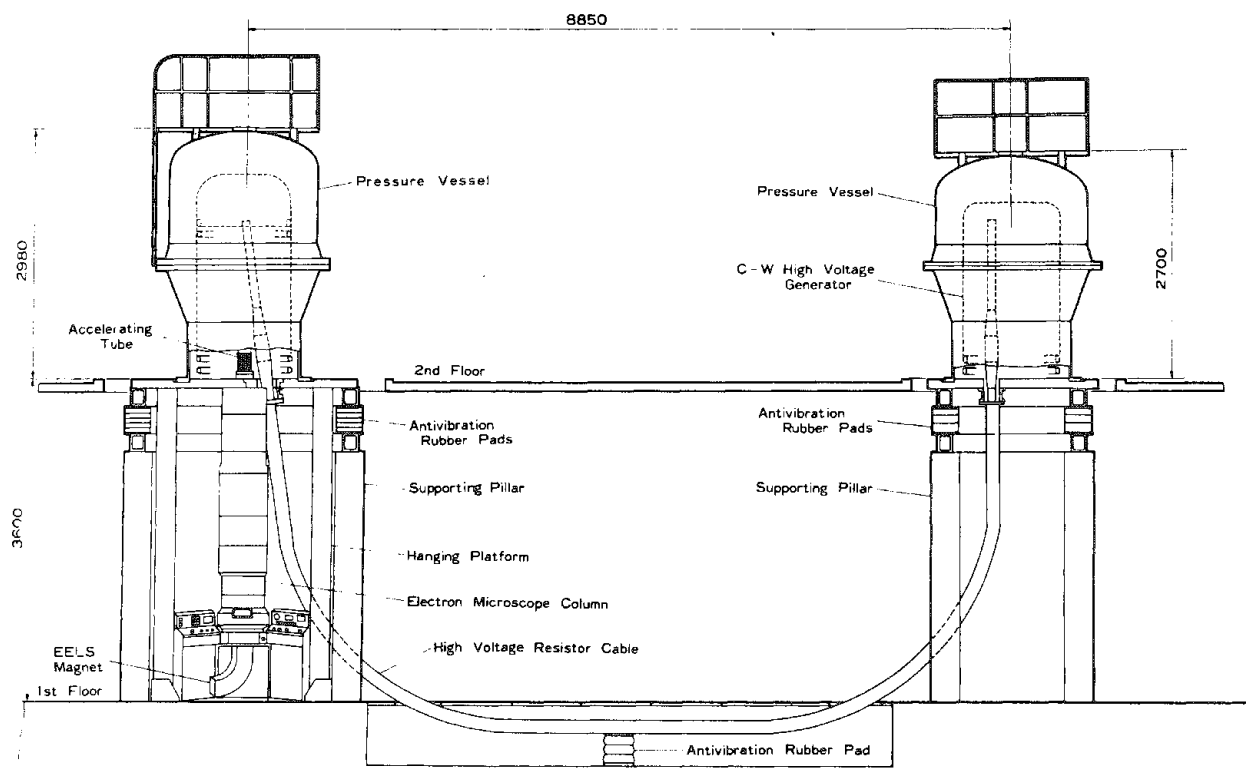


FIG. 1.--General view of H-1250ST high-voltage STEM.

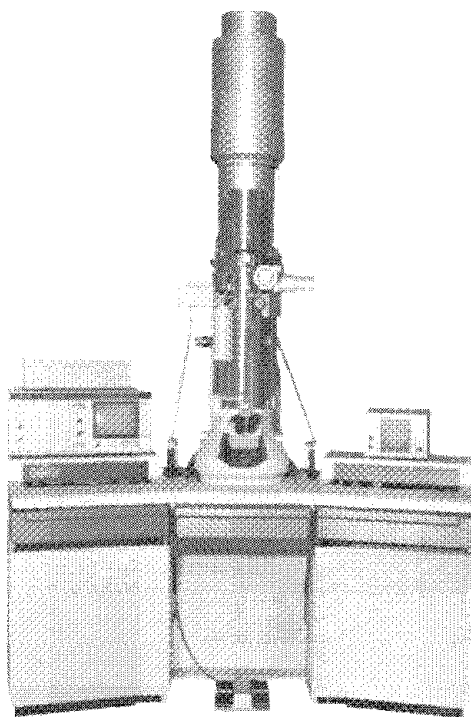


FIG. 2.--General view of H-9000.

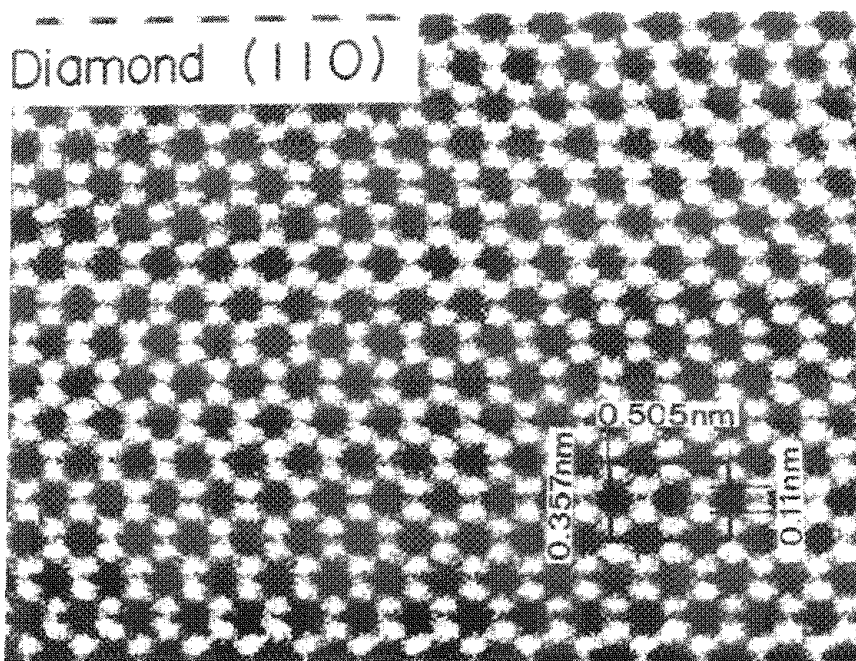


FIG. 3.--Structure image of diamond (110). (Courtesy of Prof. H. Fujita, Osaka University.)

### 125kV Integrated TV-TEM

Most biological research does not require high accelerating voltage of 200 kV and above. For this type of application, we have the H-7000, which has an integrated TV system (Fig. 5). A high-sensitivity TV camera is built in and normal TEM operation such as focusing and image recording can be done with a help of the TV image on a CRT monitor. There is a separate image filing system utilizing an optical disk recorder that records TV camera images.

In addition, we have also developed TEMs with a field-emission electron source, as introduced at Symposium E during the EMSA 1986 meeting.

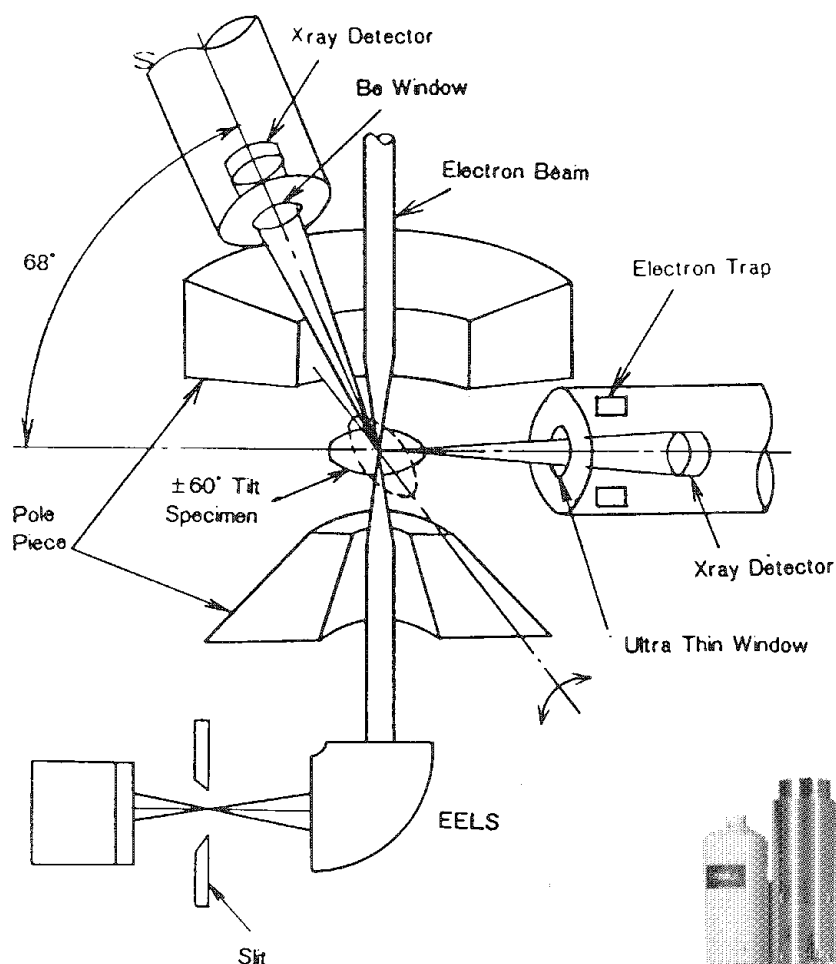


FIG. 4.--EDX dual detector system

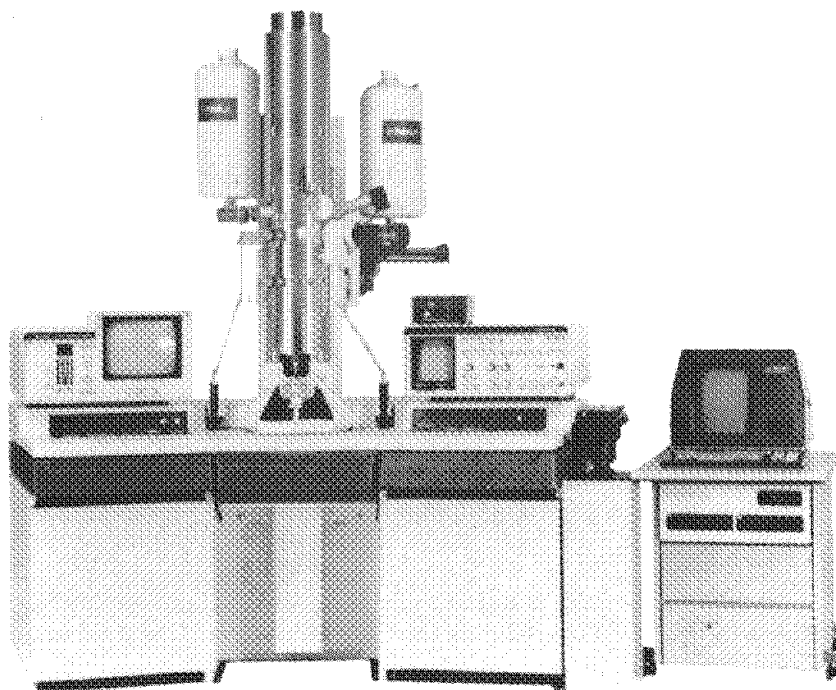


FIG. 5.--General view of H-7000.

## UNATTENDED IMAGE ANALYSIS OF MULTIPLE SAMPLES IN THE SEM

R. M. Edwards, Jozef Lebieczik, and Garvin Stone

The analysis of many microscopic features (particles, fibers, inclusions, etc.) is so tedious that statistically meaningful results are seldom obtained unless an automated system is used. A fully automated system for size and chemical characterization of microstructures has been assembled that uses a scanning electron microscope (SEM), an energy-dispersive spectrometer (EDS), and an image analyzer (IA). In the course of developing and using the fully automated SEM/EDS/IA system, three levels of unattended image analysis have been devised:

- Level 1: 12 h unattended analysis of a single sample
- Level 2: multiple-sample unattended analysis (12 h unattended) for up to nine samples
- Level 3: fully automated multiple-sample unattended analysis with more than one magnification value; analysis at two different magnifications permits evaluation of feature size ranges covering 5 orders of magnitude

The fully automated system has operated successfully for as long as 48 h. It is routinely used for characterizing the size and elemental composition of contaminants from several samples over 14h periods. Unattended image analysis systems hold great promise for opening up new areas and applications of general feature analysis. At the extremes of sparsely populated samples in a large area and highly populated samples requiring many measurements, unattended image analysis systems are absolutely necessary. They also reduce or eliminate the time and tedium previously imposed on laboratory scientists and quality-assurance technicians.

### *Basic SEM Image Analysis*

Three SEM/EDS/IA systems have been assembled that correspond to the three levels of unattended operation identified above. The level 3 system was implemented first, the level 1 system last. Figure 1 shows an image analysis system that has been successfully applied to automatic analysis of features since 1974.<sup>1</sup>

The computer is generally an integral part of the EDS unit and, with the right software, provides the program capability for flexible and repetitive operations. The SEM provides the images to be analyzed for features. The digital scan generator allows the computer to position the electron beam; the threshold selector returns image data at the beam's position. The backscatter-electron (BSE) image is generally evaluated to extract feature physical characteristics of size (area, width, length), position, and shape.<sup>2</sup> X-rays generated as a result of the electron beam impinging on a feature provide a means to identify features chemically.<sup>2,3</sup>

The number of features that can be analyzed by the basic image analyzer without operator intervention is limited to one frame; then the operator can position the sample to another field of view, adjust the focus, correct for instrumentation drift, and instruct the analyzer to evaluate another frame. To collect large quantities of data, the constant presence and attention of an operator is required. An operator cannot be reasonably expected to continue to give the same high level of attention to detail indefinitely. Unattended image analysis systems capable of operating without human assistance are required for large sample populations.

In addition to being a stable system for 12 h, a flexible and practical unattended system must:

- (1) be stabilized with automatic compensation of instrumentation drift,
- (2) include automatic focus,

---

Authors Edwards and Lebieczik are at LeMont Scientific Inc., 2011 Pine Hall Drive, State College, PA 16801; author Stone is at IBM General Products Division, San Jose, CA 95193.

- (3) contain provisions to continue analysis after a detected component failure is corrected without losing any previously obtained data,
- (4) be capable of relocating to unique features identified during the unattended operation to permit verification and interactive identification of complex features, and to features whose presence triggers a critical conclusion concerning the sample,
- (5) accept several conditions for terminating analysis of a sample--number of frames, number of particles, and number of particles of a certain chemistry and/or size.

#### *Level 1: 12h Unattended*

Figure 2 presents the expansion of the Fig. 1 system to the Level 1 unattended classification with the addition of stage automation, threshold stabilization, and remote control of the SEM automatic focus functions.

*Stage Automation.* SEM stage automation has been implemented in two ways: (1) with stage translation along the X and Y axes of a specimen holder (X-Y stage), and (2) with stage rotation about the center of the specimen holder and translation along either the X or Y axis (R- $\theta$  stage). The choice of automation depends on the capabilities of the SEM stage and application requirements. If the entire surface of a sample is to be searched, X-Y stage automation is required. For evaluation of large or numerous samples, R- $\theta$  stage automation, which utilizes the limited space of an SEM sample chamber more efficiently than X-Y stage automation, is required. X-Y automation can handle samples that are half as big as the SEM chamber in each translation axis. R- $\theta$  automation can handle samples equal to one dimension of the SEM chamber and up to two-thirds of the SEM chamber in the direction of the stage-translation axis. However, R- $\theta$  stage automation precludes the efficient full coverage search of an entire sample.

Present programming permits 50% of a sample to be searched with R- $\theta$  automation and avoids overlapping areas of analysis. Basic stage control permits the computer to position additional frames for analysis in a simple preselected pattern (Fig. 3). Short-term unattended operation has been achieved with the addition of simple-stage automation on many SEM/EDS/IA systems.

*Threshold Stabilization.* SE and BSE signals to the threshold selector unit can drift away from the initially set level and thus distort image data. The threshold stabilization unit compensates for this drift via an analog signal-processing technique and maintains the threshold setting even when the incident beam intensity changes by as much as 50%. This unit also contains circuitry to warn the computer if the average sample current drops to zero, which usually means a failed SEM filament. When this state is detected, the unattended analysis software suspends analysis and sounds an alarm. Once the condition is corrected, the software reanalyzes the frame during which the failure was detected and then continues with the remainder of the unattended analysis.

*Focus Control.* Two approaches to automatic focus have been implemented. The first approach, taken with the Hitachi HS-520 SEM, was to provide computer activation of the automatic focus sequence available by means of the SEM microprocessor controls (Fig. 2). Automatic focus using the HS-520 controls consists of activating the automatic brightness, focus coarse, and focus fine controls through a remote-control module between the computer and the HS-520 control panel. These automatic functions for optimizing brightness and focus have become available on SEMs only recently.

For focus automation on older SEMs, the second approach is to control the SEM objective lens electronics directly from the imaging computer (Fig. 4). This approach requires somewhat more hardware and software in the imaging computer, but it also yields a quality of focus measurement not available when SEM controls are remotely activated (Fig. 2). If poor focus quality is detected, alternate focusing algorithms are automatically tried from the imaging computer. A failure to focus (no features, charging, or any similar problem) is detected and dealt with by preprogrammed requirements (enter alarm state and wait for operator assistance, or log frame identification where focus failed and proceed with remainder of analysis).

Addition of stage automation, threshold stabilization, and automatic focus raises the system to the Level 1 unattended classification. The software sophistication for this level is such that the system can still be implemented on a dual floppy-disk computer

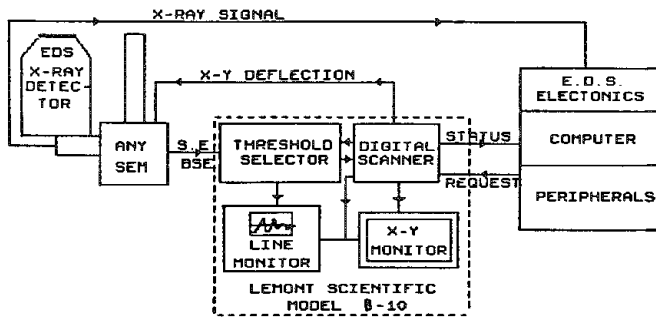


FIG. 1.--SEM image analysis system.

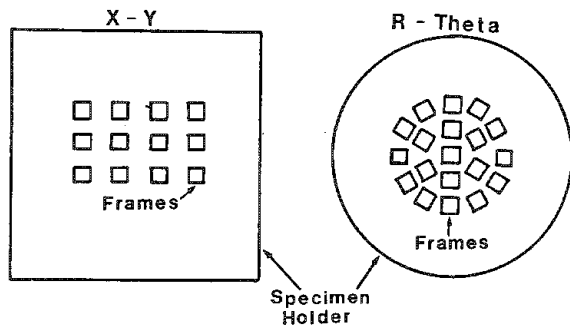


FIG. 3.--Basic stage control patterns.

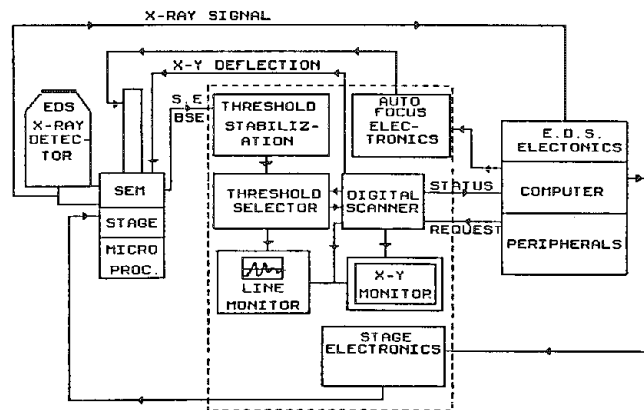


FIG. 4.--Unattended SEM image analysis system with auto-focus electronics.

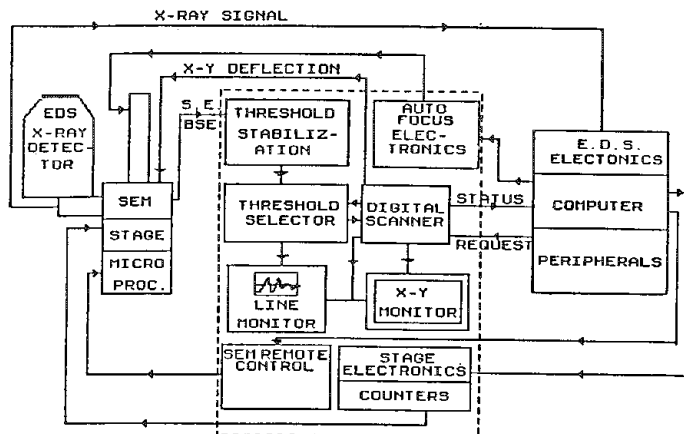


FIG. 5.--Multiple sample SEM image analysis system.

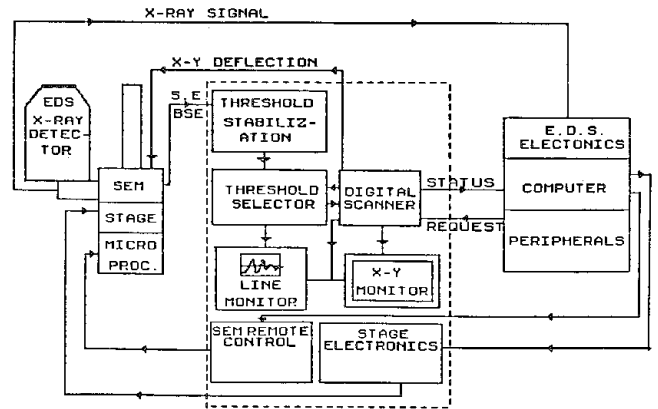
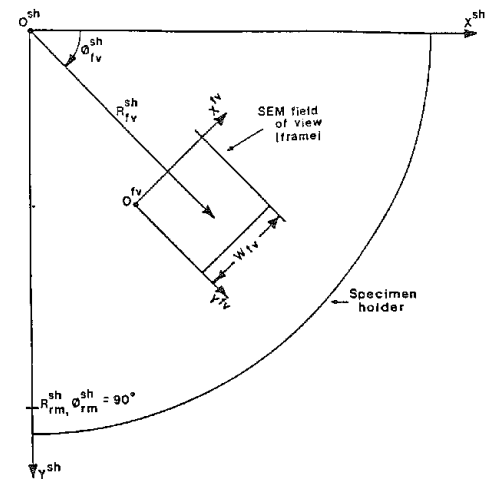


FIG. 2.--Unattended SEM image analysis system with SEM remote control.



The superscript "sh" refers to a coordinate system with origin ( $0^{sh}$ ) at the center of rotation of the specimen holder with  $X^{sh}, Y^{sh}, R^{sh}$  and  $\theta^{sh}$  directions as shown above. The field of view (frame) coordinate system has the origin ( $0^{fv}$ ) at the upper left corner of the SEM display with  $X^{fv}$  and  $Y^{fv}$  direction as shown above. (Coordinates without superscript refer to the frame coordinate system).

$R^{sh}_{fm}$  = Radial coordinate to a registration mark in the sh coordinate system ( $\theta^{sh}_{fm} = 90^\circ$ ).

$W_{fv}$  = Width of a frame.

$R^{sh}_{fv}$  = Radial coordinate to the center of a frame in the sh coordinate system.

$\theta^{sh}_{fv}$  = Theta coordinate to the center of a frame in the sh coordinate system.

FIG. 6.--Specimen holder and frame coordinate system.

system provided the number of frames to be analyzed is under 1000 and fewer than approximately 7000 features are analyzed (2000 features with chemical identification based on 32 EDS elements).

### *Level 2: Multiple Sample Unattended*

Advance to the Level 2 classification requires the addition of some hardware and a major portion of software.

*Additional Hardware.* The additional hardware includes step counters to keep track of the number of steps the stage is moved, either manually or by the computer (Fig. 5). When properly initiated, the stage counters thereafter contain the location of the currently viewed frame relative to a defined coordinate system.

*Additional Software.* Much software is needed to permit operator definition of sample locations and individual sample stage control patterns within a frame location scheme provided by the stage step counters. A coordinate system is chosen so that all samples, frames, features, and individual pixels on a feature can be defined and relocated, within the limitations of mechanical repeatability of the stage and electronic repeatability of the SEM and digital scan generator.

In R- $\theta$  stage automation, the center of the specimen holder (and center of rotation) is chosen as the origin and an X-Y coordinate system is selected (Fig. 6). With respect to an observer in the defined specimen-holder coordinate system, stage translation and rotation appears as if the SEM is being translated and rotated above a specimen holder fixed in space.

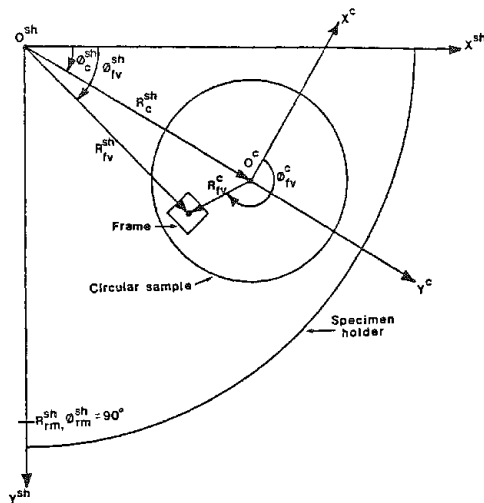
To initiate the hardware stage step counters, the operator positions a registration mark inscribed on the specimen holder to the center of a frame, each time a new specimen holder is mounted. Once initiated, the computer knows the position of the currently displayed frame regardless of complexity of subsequent stage movement under manual or computer control; and since it also knows magnification, the computer can calculate the coordinate of any currently displayed pixel in reference to the specimen-holder coordinate system.

To define the location of a circular sample mounted on the specimen holder, the operator identifies the location of three points on the circumference of the sample by any combination of stage movement and cursor movement to a pixel within a frame. A coordinate system in the sample frame of reference is chosen with the positive Y axis congruent with the ray from the center of the specimen holder to the center of the sample (Fig. 7). Rectangular samples are defined by the operator's identification of any three corners on the sample.

To study spatial variations within a sample, the operator may divide a sample into sections. Circular samples may be divided into radial or  $\theta$  sections. Once the operator has identified the sample locations and optional sectioning of the samples, a graphics display presents a drawing of the specimen-holder geometry (Fig. 8). For each section of each sample, the operator specifies the number of frames to be analyzed and whether they are to be equally spaced or randomly selected (random but not overlapping). Example stage control patterns for R- $\theta$  automation are space filling (approximate full sample coverage), line of frames, or a cross pattern (Fig. 9).

The determination of frame coordinates and spacing to get the desired number of frames is an iterative process. A pattern of frame locations in the specimen holder coordinate system must be translated to positions in the sample coordinate system and then tested against sample and section boundaries. If a particular spacing does not yield the desired number of frames, a different spacing is tried. This iterative process can be quite time consuming when many frame locations are possible (as there are at high magnification). Fortunately, once computed, frame locations are stored in a disk file and can be reused for subsequent projects, provided the operator has developed a system of mounting samples in approximately the same locations relative to the registration mark. The graphics display of specimen holder and sample geometry indicates the frame locations to be analyzed on each sample. Before launching an unattended analysis, the operator can select a stage position test to preview each frame to be analyzed. In this way he can verify that all frames to be analyzed will indeed land on a sample.

Figure 10 depicts the overall scenario of multiple sample unattended image analysis after sample and frame locations are identified. As each frame is analyzed, individual



The superscript "c" refers to a coordinate system with origin ( $O^c$ ) at the center of a circular sample with  $x^c, y^c, R^c$  and  $\theta^c$  directions as shown above. See Specimen Holder and Frame Coordinate System for the (sh) coordinate system.

- $R_c^{sh}$  = Radial coordinate to the center of a circular sample in the sh coordinate system.
- $\theta_c^{sh}$  = Theta coordinate to the center of a circular sample in the sh coordinate system.
- $R_{fv}^c$  = Radial coordinate to the center of a frame in the c coordinate system.
- $\theta_{fv}^c$  = Theta coordinate to the center of a frame in the c coordinate system.

FIG. 7.--Circular sample coordinate system relative to specimen holder coordinate system.

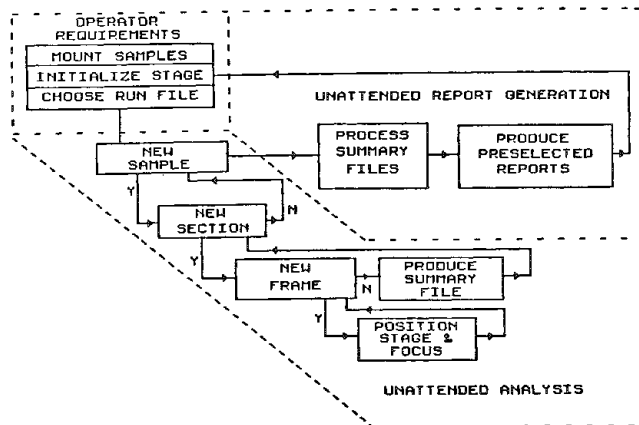


FIG. 10.--Multiple sample SEM image analysis scenario.

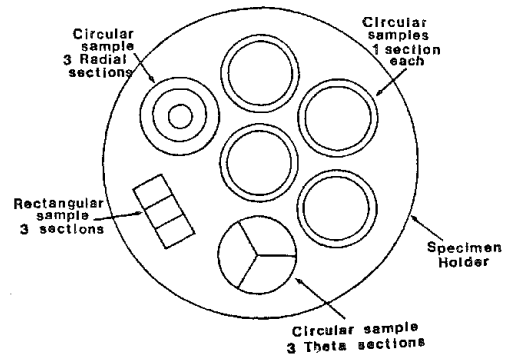


FIG. 8.--Multiple sample set-up.

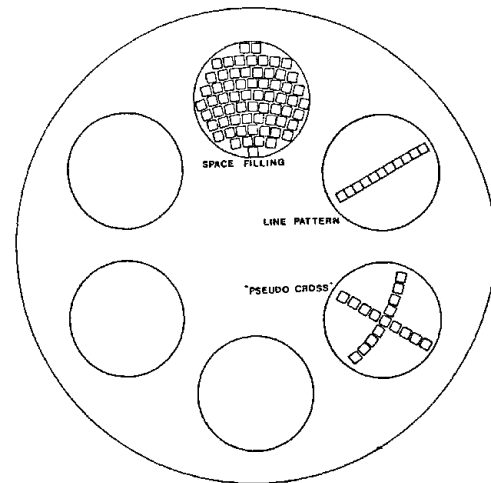


FIG. 9.--Approximate stage control patterns at magnification 50x on 1-in.-diameter samples.

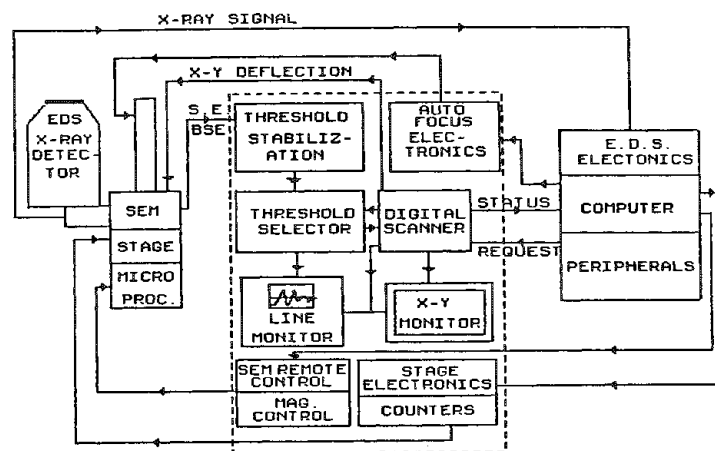


FIG. 11.--Fully automated SEM image analysis system.



feature data are saved in disk files. Upon completion of the analysis of all frames within a section of a sample, a summary disk file is generated that contains total particles within chemical classifications, measurement histogram data, and other tabular data. Summary files are created in order to permit fast algebraic operations between groups of data. For example, the addition of the results from two sections is accomplished by addition of the results contained in the section summary files, not by reprocessing the individual feature data.

Upon completion of the analysis of all sections and all samples, a special program named SUMARY is activated which first adds the results from all section summary files of a sample to create a summary file for each sample. The SUMARY program then processes and reports the analysis results by performing one or more of the following preselected operations:

1. Report the results in any summary file.
2. Normalize the results in a summary file to total sample area or by an operator-supplied constant.
3. ADD or SUBtract the results of any summary file.
4. Produce a chemical-category report versus selected sample section summary files (versus sample position).

The Level 2 multiple-sample unattended classification is achieved with the addition of a great deal of software. An operator can direct a duplicate unattended analysis by mounting samples in approximately the same location, initiating the stage to the registration mark, and instructing the system to use a specific-run parameter file. The multiple sample level of unattended operation cannot function on a dual-floppy-disk system, and is only minimally functional on a 10 Megabyte (Mb) disk system. A 20Mb disk system is recommended.

### Level 3: Fully Automated

For the Level 3 unattended classification, an additional control loop must be available to enable automatic change of magnification, so as to cover a wider size range of features or to analyze different samples at different magnifications (Fig. 11). This mode of operation has been implemented only with the Hitachi SEM; it is not suited to older SEMs.

When multiple magnification analysis is selected, the operator also specifies stage control patterns and number of frames for each magnification in each section of all samples.

Figure 12 shows the overall scenario of fully automated SEM image analysis. It includes the additional loop over preselected magnification values. When unattended operation is launched, the software first directs the analysis at low magnification within a section, then analyzes at higher magnifications before proceeding to the next section. For each section at each magnification, a summary file is created. At the end of all analyses the SUMMARY program merges the results obtained at various magnifications to yield the total results for each section.

The Level 3 fully automated unattended system is currently implemented with up to five preselected magnification values. Since the digital scan generator has a resolution of  $4096 \times 4096$  pixels, features with size ranges spanning five orders of magnitude can be analyzed with only two magnification values; more than two are more likely to be used to evaluate samples with different characteristics than because more than five orders of magnitude are wanted.

### Implementation of Unattended Systems

Three unattended SEM image analysis systems have been assembled with slightly different equipment configurations; each roughly corresponds to a level:

1. The Level 1 unattended system uses a Vickers Nanolab 7 SEM, KEVEX 7500 EDS, and a LeMont DA-10 with autofocus controlled from the imaging computer. (Installed in 1985.)

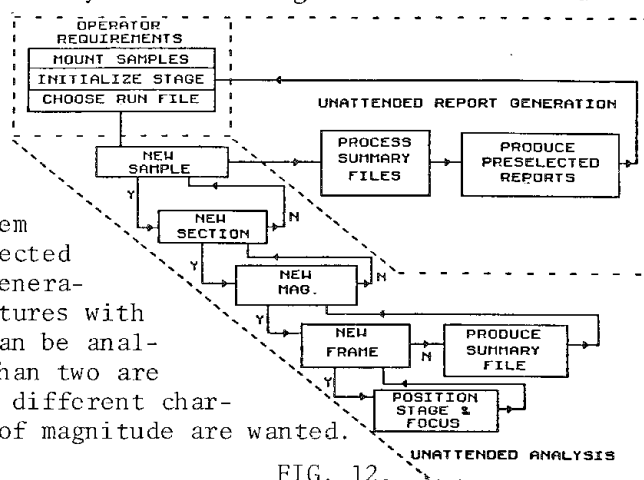


FIG. 12.

2. The Level 2 multiple-sample system uses an ETEC Auto Scan SEM, KEVEX 8000 EDS, and a LeMont DB-10 image analysis system. (Installed in 1984.)

3. The Level 3 fully automated system uses a Hitachi HS-520 SEM, KEVEX 800 EDS, and a modified LeMont DA-10 image analysis system. (Installed in 1983.)

The fully automated SEM image analysis system has successfully operated fully automated for as long as 48 h and is routinely used for size and chemical characterization of contaminants from two samples with 200 fields analyzed per sample over 14h periods. During the 48h operation six samples were analyzed with 200 frames analyzed for each sample. These analyses included EDS x-ray acquisitions of up to 25 s per feature.

Unattended performance has been successfully implemented and has been adopted as a routine method for evaluating large sample populations. To quantify performance in terms of a rate of features analyzed is difficult because the rate depends on the following conditions of the analysis:

- (1) type of data collected (with or without x-ray data)
- (2) SEM operating conditions and overall signal-to-noise ratio of the secondary or backscatter electron image
- (3) size range of features to be analyzed
- (4) feature shape complexity
- (5) measurement precision requirements
- (6) feature loading (features per unit area on the sample)

When EDS x-ray data are collected for each feature, the collection time per feature is usually the most influential condition controlling overall rates of feature analysis.

### *Conclusion*

Three levels of unattended image analysis have been described: (1) 12h unattended (single sample), (2) multiple sample unattended, (3) fully automated multiple sample/multiple magnification unattended. Unattended image analysis systems are essential in two extremes of general feature analysis: (1) sparsely populated samples where a large area is to be searched at high magnification for a handful of features, and (2) highly populated samples where a large quantity of measurements is to be performed. Specific applications which can be addressed include:

- (1) air and water solid pollutants or contamination
- (2) gunshot residue search and analysis
- (3) inclusions in steel
- (4) geological samples including mineralogy

Unattended analysis systems reduce or eliminate the time and tedium previously imposed on laboratory scientists and quality-assurance technicians and make possible the following modes of operation.

1. Parallel processing of large quantities of samples by a single operator is possible.
2. Large areas or large numbers of features may be screened automatically for some specific feature such as an asbestos fiber or any other needle in a haystack without operator fatigue or lack of attention.
3. The system can pre-screen thousands of features just to locate the few that must be analyzed manually for a final report (gunshot residue, for example) in cases where the analysis must be very extensive or a proof of discovery of a special feature is required.
4. In the SEM, at the maximum scan generator resolution, the system is capable of locating, analyzing, and registering features that are not even visible on the viewing CRT of the SEM since all viewing CRTs have resolutions around 500-1000 lines (pixels per line).

### *References*

1. M. F. Hoover et al., "Automated characterization of particulates and inclusions," *Microbeam Analysis--1975*, 54A-54B.
2. D. L. Johnson, "Automated SEM characterization of particulate inclusions in biological tissues, *SEM/1983* III, 1211-1228.
3. L. E. Stettler et al., "Particle contents of human lung," *Proc. EMSA* 1985, 116-119.

## ADVANCED VACUUM SYSTEM FOR ANALYTICAL ELECTRON MICROSCOPY

G. S. Venuti

Recent technological advancements such as significantly improved power supply stability and polepiece design, as well as increased accelerating voltage all contribute to the primary objective of scanning electron microscope (SEM) design: higher resolution. Similarly, the advent of analytical electron microscopy (AEM) has also expanded the scope of applications to include energy-dispersive spectrometry, wavelength-dispersive spectrometry, and electron probe analysis. Specimen contamination and damage have become increasingly problematic as SEMs are used as analytical instruments. In an effort to minimize contamination and etching, and thereby benefit from these advances, cleaner and more efficient vacuum systems are required.

A high-energy beam of electrons used for electron microscopy and microanalysis can have significant impact on the specimen. Beam damage is usually more severe in organic and biological specimens<sup>1</sup> and it has been reported by numerous authorities that this damage ranges from loss of organic material<sup>2</sup> and removal of volatile elements to significant hydrocarbon contamination<sup>3,4</sup> and etching. Hydrocarbon contamination can, by absorbing radiation, decrease x-ray intensities, thereby degrading analysis. This effect is much more noticeable during light-element analysis.

Although specimen cooling<sup>5-7</sup> has been shown to reduce mass loss considerably, specimen cooling itself can create problems. If the microscope's vacuum system is not generally free of hydrocarbon contaminants, the cooled specimen can then act as a contamination trap, causing further complications. It is therefore advantageous not only to reduce the pressure<sup>8</sup> in the specimen chamber but also to insure that the vacuum system itself is not a source of contamination.

This paper describes the achievement of excellent vacuum levels, high pumping speeds, reduction of the water vapor partial pressure,<sup>9</sup> and, most important, the total elimination of vacuum system-induced contamination<sup>10</sup> through the replacement of the original vacuum pump with an Air Products low-vibration cryopump.

### *Original Vacuum System*

A Cameca Camebax-MBX combined scanning electron microscope and microprobe, consisting of three Cameca wavelength-dispersive (WDS) spectrometers and a single energy-dispersive spectrometer (EDS), was chosen for modification. The SEM (Fig. 1) had been designed and installed with a fully automated vacuum system that included all the necessary safety and control devices. The vacuum system consisted of a 700 liter/s diffusion pump, a water-cooled baffle, a liquid nitrogen trap, a vacuum ballast tank, and two 12m<sup>3</sup>/h mechanical water pumps.

The elimination of all vacuum system-induced contamination, meaningful pressure reductions, and a substantial lowering of the present partial pressure of water vapor would significantly improve the microprobe's analytical capabilities. The advantages vs the disadvantages of major vacuum systems are shown in Table 1. Of these systems, only the cryopump is totally contaminate free; it also reduces substantially the water vapor partial pressure<sup>11</sup> because of its high intrinsic pumping speed for water vapor, approaching the theoretical limit.

### *Vacuum System Testing and Modification*

Prior to the modification, the diffusion pump system was evaluated. Testing determined that the existing primary vacuum gauge, chosen by Cameca and located directly on top of the pumping stack, was correctly indicating and recording specimen chamber pressures. The maximum obtainable vacuum levels using the diffusion pump were evaluated

---

Author Venuti is president of Venuti Associates, Boston, Mass.

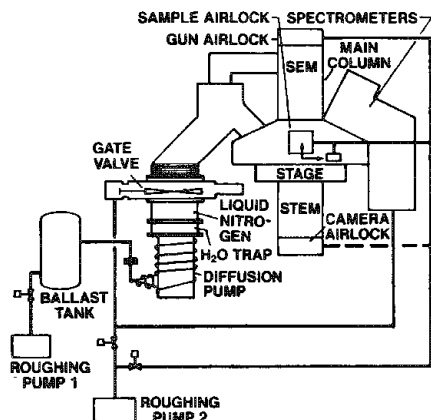


FIG. 1.--Original Cameca SEM.

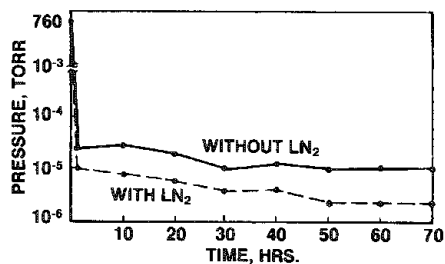


FIG. 2.--Diffusion-pump vacuum levels.

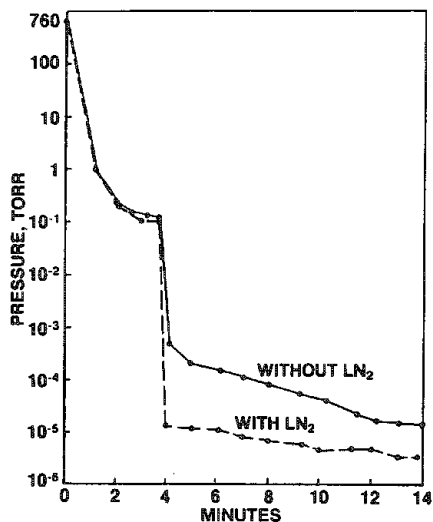


FIG. 3.--Initial diffusion-pump vacuum levels.

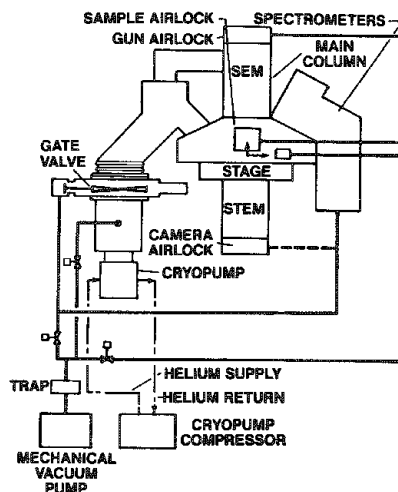


FIG. 4.--Modified Cameca SEM.

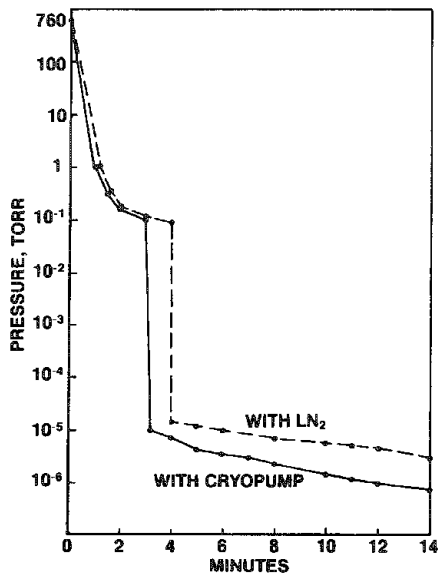


FIG. 5.--Vacuum levels: diffusion pump vs cryopump.

TABLE 1.--Pumping systems comparison.

Low-vibration Cryopump

ADVANTAGES

Requires no continuous forepumping  
 No LN<sub>2</sub> required  
 Highest pumping speeds for all gases  
 Contamination free  
 High throughput  
 Pumps dangerous gases  
 No moving parts exposed to vacuum chamber  
 Field maintainable  
 Cost comparable with turbo pump  
 Low maintenance intervals  
 (10 000 h)

DISADVANTAGES

Regeneration required  
 Longer initial startup times  
 Vertical installation only

Turbomolecular Pumps

ADVANTAGES

No LN<sub>2</sub> required  
 Fast initial startup  
 Horizontal or vertical installation

DISADVANTAGES

Lower pumping speeds than cryopump for water  
 and hydrocarbons  
 Potential for oil backstreaming from roughing  
 pump or bearings  
 Requires continuous forepumping  
 Frequent bearing maintenance  
 Cost comparable with cryopump  
 Potential self-destruction if particle falls  
 into turbine blades  
 Vibration must be considered  
 Splinter shield recommended but does decrease  
 net pumping speeds  
 Not contamination free

Diffusion Pumps

ADVANTAGES

Low initial cost  
 No vibration

DISADVANTAGES

Requires LN<sub>2</sub> to prevent contamination  
 and to pump condensables  
 Restricted to vertical mounting  
 Requires continuous forepumping  
 Lower pumping speeds than cryopump  
 Potential for catastrophic failures  
 Oil creep problem can be significant  
 Not contamination free

Ion Pumps

ADVANTAGES

Requires no continuous forepumping  
 No LN<sub>2</sub> required  
 No vibration  
 Contamination free

DISADVANTAGES

Low throughput  
 Gas re-emission, memory effects  
 High cost  
 Difficult to start  
 Strong magnetic field  
 Electrical isolation required for some  
 applications  
 Extremely heavy  
 Not field maintainable

and are shown in Fig. 2, which shows baseline pressure readings over several days of continuous pumping with and without LN<sub>2</sub> in the primary trap.

The final series of tests involved pumpdown cycles from atmosphere to high vacuum, obtaining normal operating conditions of  $5 \times 10^{-6}$  Torr with and without LN<sub>2</sub> in the primary trap. These test results are shown in Fig. 3.

After the entire microprobe was cleaned by standard ultra-high vacuum procedures,<sup>12-14</sup> a low-vibration cryopump (Air Products and Chemicals Model AP-6LV) was installed in place of the diffusion pump. With the diffusion pump replaced by the cryopump, the LN<sub>2</sub><sup>15</sup> trap and the water baffle were no longer required, as these items were used on the original vacuum system to prevent oil backstreaming from the diffusion pump. Their use in preventing backstreaming had the adverse effect of reducing the diffusion pump's pumping speed by approximately 40%. Fig. 4 shows the modified system.

*Vacuum System Data*

The performance of the modified vacuum system is shown in Fig. 5. This graph compares an average pumpdown cycle of the diffusion pump system with that of the Air Products

low-vibration cryopump. After 70 h, the final recorded vacuum levels were  $5 \times 10^{-6}$  Torr for the diffusion pump, with  $\text{LN}_2$  baffle and water trap; and  $1 \times 10^{-7}$  Torr for the cryopump. Though clearly the superior vacuum source, the cryopump was not available for use on vibration-sensitive equipment such as the microprobe until the development of the Air Products low-vibration cryopump. Its successful use on SEMs is well documented.<sup>16</sup> In this installation and numerous others, including dual-pumped transmission electron microscopes, no detectable vibrational interference has been recorded when the Air Products low-vibration cryopump was used.

### Conclusions

Successful installations of the low-vibration cryopump in the disciplines of electron beam microscopy and microlithography now include Hitachi SEM Models S570 and S800, and TEM Models H600 and S800. JEOL installations include TEM Models 100CX, 200CX, and 1200EX, and SEM Model 35C; ISI Microscopes SEM installations include Models SS-40 and IC-130.

Microlithography, ion beam, and x-ray lithography all use and benefit from cryopumping. Residual gas analysis studies at a number of user sites has clearly shown the benefits of cryopumping through the significant reduction of hydrocarbons, improved vacuum levels, and substantial reductions of water vapor partial pressures, all of which contribute to the growing acceptance of this technology.

In consideration of the on-going programs, cryopumping should help achieve new goals in microanalysis and electron microscopy.

### References

1. M. S. Issacon, *Ultramicroscopy* 4: 193, 1979.
2. J. Hren, in Hren, Goldstein, and Joy, Eds., *Introduction to Analytical Electron Microscopy*, New York: Plenum Press, 1979, 481-505.
3. P. Echlin, "Contamination in the scanning electron microscope," *SEM/1975*, 679.
4. D. E. Miller, "Vacuum techniques and contamination measurements," *SEM/1978 II*, 513.
5. T. A. Hall, in C. Lechene and R. R. Warner, Eds., *Microbeam Analysis in Biology*, New York: Academic Press, 1979, 185.
6. T. Tomita, Y. Harada, H. Watanabe, and T. Ethoh, *Ninth Intern. Congress on EM* 1: 114, 1978.
7. J. J. Hren, E. J. Jenkins, and E. Aigeltinger, *Proc. 35th Ann. Meeting EMSA*, 1977, 66.
8. J. Wall, J. Bitter, and J. Hainfield, *Proc. 35th Ann. Meeting EMSA*, 1977, 558.
9. H. Shuman, *Ultramicroscopy* 1: 317, 1976.
10. C. Boiziau, J. P. Duraud, C. LeGressus, and D. Massignon, *SEM/1983 IV*, 1525-1534.
11. J. Hren, in Hren, Goldstein, and Joy, Eds., *Introduction to Analytical Electron Microscopy*, New York: Plenum Press, 1979, 494-497.
12. T. L. Lamont Jr., in G. L. Weissler and R. W. Carlson, Eds., *Vacuum Physics and Technology*, New York: Academic Press, 1979, 491-497.
13. L. Holland, L. Laurenson, and M. J. Faulkner, *Japan J. Appl. Phys.* 12: 1468, 1973.
14. R. J. Elsey, *Vacuum* 25: 299, 347, 1975.
15. N. Yoshimura, H. Hirano, S. Norioka, and T. Etoh, *J. Vac. Sci. and Tech.* A2-1: 61, 1984.
16. G. S. Venuti, "Use of vibration isolated cryopumps to improve electron beam instrument operating efficiencies," *SEM/1983 IV*, 1555-1562.

## AN ELECTROMAGNETIC/ELECTROSTATIC DUAL CATHODE SYSTEM FOR ELECTRON BEAM INSTRUMENTS

J. G. Bradley, D. B. Wittry, J. M. Conley, and A. L. Albee

For the last eight years a miniaturized, light weight, low-power scanning electron microscope and x-ray analysis system for spaceflight applications has been under development at the California Institute of Technology and the Jet Propulsion Laboratory (JPL).<sup>1,2</sup> This instrument, known as the Scanning Electron Microscope and Particle Analyzer (SEMPA) instrument, has recently been proposed for NASA's Mariner Mark II Comet Rendezvous/Asteroid Flyby (MMII CRAF) mission for launch in the 1990s.<sup>3</sup> During the CRAF mission, the spacecraft will rendezvous with a comet near aphelion and will reconnoiter in the vicinity of the comet for about three years. During that interval it is proposed that SEMPA will sample the dust leaving the comet surface at least 50 times and spend a total of about 1000 h doing imaging and x-ray analysis of collected dust. The long duration of the CRAF mission places great demands on the reliability of its scientific instrument packages.

In particular, for SEMPA, the durability and reliability of the x-ray detector and cathode systems are of primary concern. Conventional lithium drifted silicon [Si(Li)] x-ray detectors require near-liquid-nitrogen temperatures for operation. Such temperatures would be excessively difficult and costly to achieve on the CRAF mission. As a result it has been necessary to examine uncooled x-ray detectors (e.g., mercuric iodide) and special Si(Li) detectors. Initial studies of mercuric iodide detectors in the SEMPA research prototype instrument make them appear quite promising.<sup>4,5</sup> Recent research on specially designed, partially cooled Si(Li) detectors, by ourselves and others,<sup>6,7</sup> show promise also.

We have recently been addressing the cathode concerns with an examination of appropriate cathode types and methods for achieving cathode redundancy. For the vacuums achievable in SEMPA and the stability requirements of quantitative x-ray analysis, only W and LaB<sub>6</sub> are practical cathode materials. The limited life of W cathodes at useful operating temperatures would require using 10 to 20 in the instrument to achieve 1000 h of operating time, whereas direct-heated LaB<sub>6</sub> cathodes have been demonstrated to function well for far in excess of 1000 h in the research prototype SEMPA. Thus a single LaB<sub>6</sub> cathode could provide all the necessary operating life. However, no matter what the cathode design and how carefully made, there remains the possibility of unexpected premature failure of a cathode due to, for instance, mechanical shock to the spacecraft or undetected defects. It is prudent then to have at least two cathodes in the instrument that can each provide the 1000 h of operation.

We have considered two ways of providing redundant cathodes. One way would be to provide a shuttle or carousel arrangement that would mechanically place either of two cathodes on the electron optical axis. This system is certainly achievable, but would probably be rather heavy and expensive, and have its own reliability concerns. The alternative is a system that has two fixed cathodes and uses electromagnetic and/or electrostatic fields to direct the electron beam to the electron optical axis. Such a system has been tested in the research prototype SEMPA.

### *Design Concept*

The concept of the tested system is illustrated schematically in Fig. 1. The area labeled A, B, and C represent the polepieces of the three independent electromagnets. The two cathodes, with Wehnelts, are located 8 mm on either side of the microscope geometric

---

Authors Bradley and Conley are at the Jet Propulsion Laboratory, California Institute of Technology, Pasadena, CA 91109; author Albee is at California Institute of Technology, Pasadena, CA 91125; author Wittry is at the University of Southern California, Los Angeles, CA 90089. The contributions of J. Hill and V. Taylor for electronic and mechanical design and construction are greatly appreciated. The research described in this paper was carried out by the Jet Propulsion Laboratory, California Institute of Technology, under a contract with the National Aeronautics and Space Administration.

axis. The Wehnelt tips are 5 mm from the top of the magnet assembly, which also acts as the anode. The electron trajectory from one cathode is indicated. The electrons undergo a sigmoid deflection in being brought to the electron optical axis. The design radius of curvature of the trajectories is 107.75 mm and the deflection angles are each  $15.19^\circ$ . The magnet field necessary to deflect the 15keV electrons in the 107.75mm radius through the homogeneous fields is only about  $3.8 \times 10^{-3}$  Tesla (38 Gauss), so that the magnet yokes are thin and light.

The symmetric double deflection system was chosen for this dual cathode assembly because of the special focal properties obtained. Analysis shows that, in optical terms, an image of the effective electron source is formed above the magnet assembly near the apparent position of the effective source. The relationship between the source and its image are shown in Fig. 1. The effective electron source is the electron-beam crossover between the Wehnelt and magnet structure. The sideways displacement of the beam in the magnet makes the effective source seem to be positioned on the geometric centerline at nearly the same height above the magnets (the lower dot in Fig. 1). The image of the effective source is formed well above the magnets on the centerline (the upper dot in Fig. 1). However, this focusing of the beam at a different height introduces significant astigmatism into the beam because, in fact, the refocusing occurs only in the direction perpendicular to the magnetic field. Thus the condenser and objective lenses must simultaneously focus two apparent electron sources (line sources) located at different heights. It would clearly be impossible to focus these two sources to a single round spot without the action of the stigmation focusing elements in the system.

Another desirable feature of the symmetric deflection is that, to first order, it makes the transverse positions of the electron sources independent of electron beam energy. Thus small amounts of drift in cathode bias or drift in the 15kV power supply should have a minimal effect on resolution and not "smear" the images.

### *Experimental System*

Figure 2 shows the dual cathode system as it was constructed and tested in SEMPA. All magnetic components were machined from Carpenter 49 iron-nickel alloy and then hydrogen annealed for maximum permeability. Heat-treated Carpenter 49 has a high permeability that aids considerably in reducing fringe fields that could increase aberrations or prevent transmission of the electron beam through collimating apertures. The entrance face and exit faces of the assembly are Carpenter 49 Herzog shunts which further control fringe fields. The magnet core at each polepiece are wound with 300 turns of #34 polyester/polyimide-insulated wire. The resistance of the series connection of the coil pair on each magnet is about 30 ohms so that the 25 mA necessary to achieve  $3.8 \times 10^{-3}$  Tesla is readily available from integrated operational amplifiers. During normal operation, the coil temperatures rise  $\sim 20^\circ\text{C}$  due to the excitation current.

Coarse alignment of the cathode system is achieved by rotation and translation of the header holding the dual cathodes on its O-ring vacuum seal. Fine alignment in one direction is achieved by adjustment of magnetic field strengths. In the direction parallel to magnetic field lines, fine alignment is achieved by the application of potentials up to  $\pm 150$  V to the electrically isolated magnet polepieces. Because the magnet gaps are only 3 mm, potentials of  $\pm 150$  V provide substantial deflections.

### *Results*

In practice the dual cathode system has proved quite easy to use. Initial beam finding is done by driving the electrostatic and one magnetic deflection excitation in synchronization with the visual cathode-ray-tube scan, so that an "image" of the cathode emission pattern can be seen if the fields are only approximately correct and the beam is passing through the anode aperture (and the SEM column is aligned so that electrons reach the sample). Then manual electrical controls are used to center the beam and the scan drive is disconnected. There are only small beam-position drifts due to initial power supply and magnet warmup. After coarse alignment to transmit the beam from one cathode, the beam from the second cathode can be obtained without any header realignment.

Overall the dual cathode system has performed well and, as expected, has been convenient to use and does not measurably degrade the imaging performance of SEMPA. The sample imaging resolution has been the same as for the single on-axis cathode (approaching 40 nm edge



to edge) although a large stigmation correction is necessary. Tests show that the two apparent crossed-line images created by the magnet system are 0.23 mm apart vertically at the standard 15mm working distance. The magnetically refocused line image is above the other, as expected. If the overall condenser-objective demagnification is the design value of 125, that corresponds to a separation of  $\sim 29$  mm in the apparent sources above the condenser lens. Calculation indicates the sources should be  $\sim 9$  mm apart. The cause of this  $\sim 3\times$  discrepancy may be smaller than expected demagnification, or the focusing action of field boundaries and inadvertent field inhomogeneities. More tests are expected to resolve the question.

Future development of this dual cathode system at JPL may include combining magnets A and B to reduce complexity and use of controlled inhomogeneous magnetic fields and shaped electrodes to minimize the astigmatism.

The beam position is, as expected, quite insensitive to cathode voltage changes. The small sensitivity present may be due to changes in the angle at which the beam enters the optical system.

Although this dual cathode system has been designed for a special SEM application, it could prove valuable in other applications where cathode reliability is critical; for example, in electron-beam lithography, Auger analysis, and microfocus x-ray sources.

### References

1. R. K. Hart, A. L. Albee, A. A. Finnerty, and R. Frazer, "A mini-electron microscope and particle analyzer for space applications," *SEM/1981 I*, 96-104.
2. J. M. Conley, J. G. Bradley, C. E. Giffin, A. D. Tomassian, and A. L. Albee, "Development of a miniature scanning electron microscope for in-flight analysis of comet dust," *Microbeam Analysis--1983*, 177-182.
3. The Solar System Exploration Committee, *Planetary Exploration Through the Year 2000*, Washington, D.C.: U.S. Government Printing Office, No. 033-000-00882-1, 1983.
4. J. S. Iwanczyk, A. J. Dabrowski, G. C. Huth, J. G. Bradley, J. M. Conley, and A. L. Albee, "First use of a mercuric iodide ( $\text{HgI}_2$ ) energy-dispersive x-ray detector in a scanning electron microscope," *SEM/1984 I*, 9-14.
5. J. S. Iwanczyk, A. J. Dabrowski, G. C. Huth, J. G. Bradley, J. M. Conley, and A. L. Albee, "Low energy x-ray spectra measured with a mercuric iodide energy dispersive spectrometer in a scanning electron microscope," *IEEE Trans. NS-33*: 355-358, 1986.
6. N. W. Madden, J. M. Jaklevic, J. T. Walton, and C. E. Wiegand, "A high-resolution Si(Li) spectrometer with thermoelectric cooling," *Nucl. Instr. and Meth.* 159: 337-338, 1979.
7. N. W. Madden, G. Hanepen, and B. C. Clark, "A low power high resolution thermoelectrically cooled Si(Li) spectrometer," *IEEE Trans. NS-33*: 303-305, 1986.

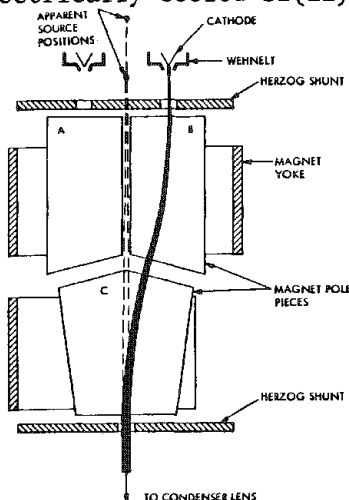


FIG. 1.--SEMPA dual-cathode system showing electron trajectories (dark ribbon) and two apparent source positions.

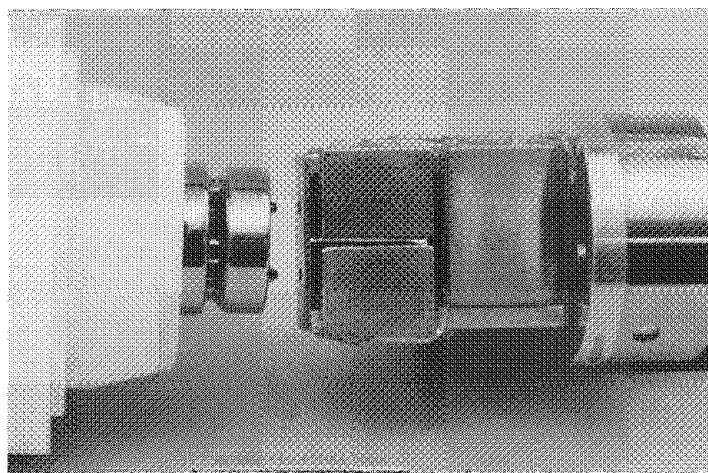


FIG. 2.--SEMPA dual-cathode system: left, ceramic vacuum header with two cathodes and conical Wehnelts attached; right, system of three magnets mounted on condenser lens.

## Electron Microprobe Quantitation and Automation

### A GENERAL EQUATION FOR PREDICTING X-RAY INTENSITIES FROM STRATIFIED SAMPLES IN THE ELECTRON MICROPROBE

Rod Packwood

The mean depth of penetration of 10kV electrons into low-atomic-number materials is of the order of  $5 \times 10^{-5}$  cm, which is more than the thickness of some components in LSI (large scale integrated circuit) devices in common use in the electronics industry. These devices cannot be analyzed in the microprobe in the ordinary way. However, an extension of the Gaussian  $\phi(\rho z)$  model may overcome the difficulties that the conventional microprobe experiences with compositional stratification of the analysis volume.

#### Primary Excitation

The depth distribution  $\phi(\rho z)$  of electron-excited x-ray production has been measured experimentally on a number of elements, at different accelerating potentials and x-ray energies. It is a ratio and is measured relative to a thin film of the same material.

In 1979 the author found that when  $\ln[\phi(\rho z)]$  was plotted against  $(\rho z)^2$ , the square of the mass thickness, extensive straight lines were obtained. The only exception was the near-surface region where transient behavior was observed. Essentially all published  $\phi(\rho z)$  showed the same behavior.

These findings imply that  $\phi(\rho z)$  can be represented by a function of the general type

$$\phi(\rho z) = \gamma_0 \exp(-\alpha^2 \rho z^2) - (\gamma_0 - \phi_0) \exp(-\alpha^2 \rho z^2 - \beta \rho z) \quad (1)$$

i.e., a Gaussian centered at the surface of the sample and modified at small  $\rho z$  by a "capacitor charging" function.<sup>1</sup>

To calculate the observed intensity,  $\phi(\rho z)$  must be multiplied by an x-ray absorption factor and integrated over all values of  $\rho z$ :

$$I_{\text{obs}} = C_A \int_0^{\infty} \phi(\rho z) \exp(-\chi \rho z) d(\rho z) \quad (2)$$

where  $\chi = \mu \csc \theta$  as usual and  $C_A$  is the concentration of the element of interest.

For a semi-infinite sample we have as a result

$$I_{\text{obs}} = C_A \frac{\sqrt{\pi}}{2} \left[ \gamma_0 \exp(\chi/2\alpha)^2 \operatorname{erfc}(\chi/2\alpha) - (\gamma_0 - \phi_0) \exp\left(\frac{\beta + \chi}{2\alpha}\right)^2 \operatorname{erfc}\left(\frac{\beta + \chi}{2\alpha}\right) \right] \quad (3)$$

where  $\operatorname{erfc}(\chi)$  is the complementary error function given by

$$\operatorname{erfc}(\chi) = 1 - \operatorname{erf}(\chi) \quad (4)$$

For the general case of a layer inside a sample extending from mass depths,  $\delta'$  to  $\delta$ , the observed intensity can be shown<sup>2</sup> to be given by

$$I_{\text{obs}} = C_A \frac{\sqrt{\pi}}{2} \exp[-\delta'(\chi' - \chi)] \left\{ \gamma_0 \exp(\chi/2\alpha)^2 \left[ \operatorname{erf}\left(\alpha\delta + \frac{\chi}{2\alpha}\right) - \operatorname{erf}\left(\alpha\delta' + \frac{\chi}{2\alpha}\right) \right] - (\gamma_0 - \phi_0) \exp\left(\frac{\beta + \chi}{2\alpha}\right)^2 \left[ \operatorname{erf}\left(\alpha\delta + \frac{\beta + \chi}{2\alpha}\right) - \operatorname{erf}\left(\alpha\delta' + \frac{\beta + \chi}{2\alpha}\right) \right] \right\} \quad (5)$$

where  $\chi'$  is the x-ray absorption in the material covering the buried layer.

By putting  $\delta' = 0$  and  $\delta = \infty$  we have the formula for a semi-infinite sample. Setting  $\delta' = 0$  gives the x-ray intensity from a surface deposit of thickness  $\delta$ ; and setting  $\delta = \infty$  gives the intensity from a substrate covered by  $\delta'$  of material with absorption factor  $\chi'$  (Fig. 1).

The author is with the Physical Metallurgy Research Laboratory, Department of Energy, Mines, and Resources, 568 Booth Street, Ottawa, Ont., Canada K1A 0G1.

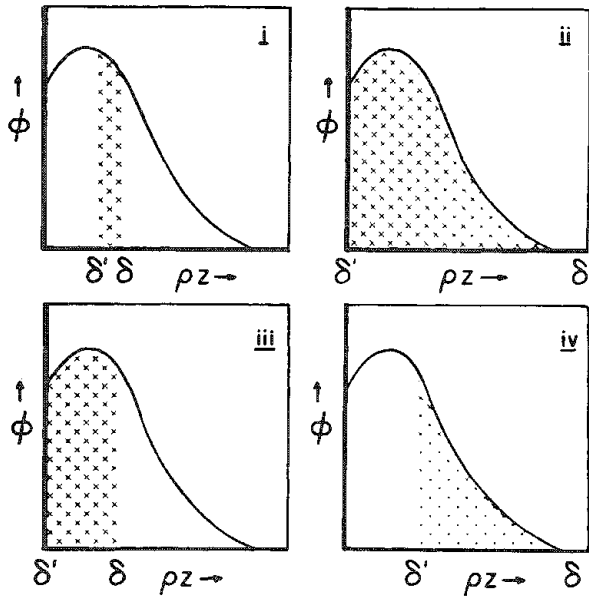


FIG. 1.--Signal volumes for particular values of  $\delta'$  and  $\delta$ : (i) buried layer  $\delta'$  to  $\delta$ , (ii) regular sample, (iii) surface layer  $\delta$ , (iv) substrate covered by layer  $\delta'$ .

K, L, or M spectral series.  $\phi_0$  and  $\beta$  are the variables most affected by the changing Z for layered versus unlayered samples; their variation with  $\delta$  and  $\delta'$  has yet to be determined. However, a simple linear weighting based on a scale length of  $1/2\alpha$  is a reasonable starting point and gives for a sample with surface layer  $\delta$ ,

$$\bar{\beta} = \delta(2\alpha)\beta_{\text{matrix}} + [1 - \delta(2\alpha)]\beta_{\text{layer}} \quad (10)$$

$$\text{and } \bar{\phi}_0 = \delta(2\alpha)\phi_{0\text{matrix}} + [1 - \delta(2\alpha)]\phi_{0\text{layer}} \quad (11)$$

In other words, a layer of thickness  $\delta = 1/2\alpha$  behaves in this approximation as a semi-infinitely thick sample.

### Fluorescence

This correction is both complicated and small, and not strongly dependent on  $\phi(\rho z)$ . The form in which this correction is often employed has, among many terms, two containing  $(U_0 - 1)^{1.67}$  and also one of the form  $f_A(\chi_A)$ . The latter is simply an approximation for  $f_B(\chi_A)$ , which can now be calculated with some confidence from the new  $\phi(\rho z)$  equation. The  $(U_0 - 1)^{1.67}$  terms arise from Cosslett and Thomas<sup>3</sup> and give an empirical value for an integral involving the ionization cross section from 1 to  $U_0$ . The approximation only saves one factor, so that the original may just as well be used; i.e.,  $(U_0 \ln U_0) - U_0 + 1$ . In turn, the assumptions made in deriving the latter equation can also be reexamined (see, for example, Reed<sup>4</sup>). The logarithmic integral functions that result from using the Bethe retardation law can be evaluated by computer.

Incorporating the improved  $\phi(\rho z)$  formulation into the main part of the fluorescence integral is not as easy as might be hoped. The correction is in two parts and considers separately the effect of radiation going (i) downward and (ii) upward. Part (i) presents little trouble; the ionization distribution function is separable and can be simply included as an approximation in terms of complementary error functions. This first term is also likely to be the major part of the correction, which is just as well because in the second part (ii) the form of  $\phi(\rho z)$  must be used explicitly and as a consequence the approximation term, multiplied by other terms, would have to be integrated.

To avoid this difficulty  $\phi(\rho z)$  can be represented by a series of exponential terms in the manner of Cross and Birks,<sup>5</sup>

The functional variations in the parameters  $\gamma_0$ ,  $\phi_0$ ,  $\alpha$ , and  $\beta$  are approximately as follows:

$$\gamma_0 \approx 10\pi \frac{U_0}{U_0 - 1} \left[ 1 + \frac{10}{\ln U_0} (U_0^{-0.1} - 1) \right] \quad (6)$$

$$\phi_0 \approx 1 + 2.7\eta \left[ 1 - \exp\left(\frac{1 - U_0}{2}\right) \right] \quad (7)$$

$$\alpha \approx \frac{4.5 \times 10^5}{E_0^{0.75}} \cdot \frac{Z - 1.3}{Z} \left(\frac{Z}{A}\right)^{0.5} \cdot \left\{ \frac{\frac{Z}{A} \ln \left[ \frac{1.166}{J} \left( \frac{E_0 + E_c}{2} \right) \right]}{E_0^2 - E_c^2} \right\}^{0.5} \quad (8)$$

$$\beta \approx 0.4\alpha Z^{0.6}; U_0 = E_0/E_c; J \approx 1.15 \times 10^{-3}Z \quad (9)$$

where Z and A are the atomic number and atomic weight,  $\eta$  the electron backscatter coefficient, and  $E_0$  and  $E_c$  are the accelerating potential and critical excitation potential, respectively. For  $\gamma_0$  the ionization cross section used is  $Q(U) \propto U^{-0.9} \ln U$ ; the exact form may vary with

$$\phi(\rho z) = \gamma_0 \exp(-\sigma \rho z) - (\gamma_0 - \phi_0) \exp[-(\sigma + \beta) \rho z] \quad (13)$$

where  $\sigma \approx 3/2\alpha$  and the other symbols have their usual meanings.

For the case of a surface layer the method of Cox et al.<sup>6</sup> can be followed--with modifications where necessary as in the previous remarks. The other cases can be handled if the results for a normal sample are combined with that from a layer in the same fashion as in the derivation for the primary electron generated radiation.

### Conclusion

An analytical solution has been developed for the problem of the x-ray intensity observed in the microprobe from compositionally stratified samples. This solution definitely holds for the case of relatively small differences in atomic number. For large differences between layer and substrate the appropriate coefficients are some weighted mean of the individual values for two semi-infinite solids of composition equal to that of the layer material and the substrate material, respectively.

### References

1. R. H. Packwood and J. D. Brown, "Concerning x-ray production and quantitative analysis," *Microbeam Analysis--1980*, 45-48.
2. R. H. Packwood and K. S. Milliken, "A general equation for predicting x-ray intensities from stratified samples in the electron microprobe," CANMET Report PMRL 85-25(TR), May 1985.
3. P. Duncumb, 1957 Ph.D. thesis, University of Cambridge, reported by M. Green and V. E. Cosslett, "The efficiency of production of characteristic x-radiation in thick targets of a pure element," *Proc. Phys. Soc.* 78: 1206, 1961.
4. See, for example, S. J. B. Reed, *Electron Microprobe Analysis*, Cambridge: Cambridge University Press, 1975, 209-211.
5. J. W. Criss and L. S. Birks, "Intensity formulae for computer solution of multicomponent electron probe specimens," in T. D. Kinley et al., Eds., *The Electron Microprobe*, New York: Wiley, 1966, 217-236.
6. M. G. C. Cox et al., "A characteristic fluorescence correction for electron-probe microanalysis of thin coatings," *J. Phys.* D12: 1441-1452, 1979.

## UNIVERSAL EPMA CORRECTION PROCEDURE NOW IN SIGHT

V. D. Scott and G. Love

One obtains quantitative electron-probe microanalysis data usually by taking the ratio  $k$  of characteristic x-ray intensities emitted from specimen and appropriate standard (often the pure element) and multiplying it by correction factors (sometimes amounting to more than 100%) to account for differences in electron scattering, x-ray generation, absorption, and fluorescence between specimen and standard. Over the years a number of correction procedures have been proposed. Most are based on the use of a curve depicting the manner in which the intensity of generated x rays varies with depth in the sample, the  $\phi(\rho z)$  curve (Fig. 1). The size and to some extent the shape of this curve depends on sample composition, incident electron energy, and x-ray line energy. Once an analytical expression incorporating these parameters is formulated, it may be used for developing equations which, with the addition of an x-ray fluorescence factor, can be applied to convert  $k$  values into elemental weight concentrations  $c$ . However, the production of a truly universal correction procedure has proved to be elusive because it is not easy to derive an analytical expression for  $\phi(\rho z)$  that adequately covers the wide range of specimen materials and instrumental operating conditions met in practice.

One approach to the problem, essentially theoretical, is to consider the physical processes involved in electron-induced x-ray emission. The method was pursued by Philibert,<sup>1</sup> and although his final equation for  $\phi(\rho z)$  proved satisfactory only for the construction of an absorption correction  $A$ , it worked well on a number of systems when refined<sup>2</sup> and combined with atomic number  $Z$ <sup>3,4</sup> and fluorescence  $F$ <sup>5,6</sup> corrections; i.e.,  $k = cZAF$ . This particular ZAF model remains in common use today despite the fact that the absorption component appears to limit its usefulness for ultralight-element work.<sup>6</sup> Attempts to overcome this deficiency have been made,<sup>7,8</sup> but without a great deal of success.<sup>9</sup>

An alternate and purely empirical approach to producing an analytical expression for  $\phi(\rho z)$  is based on the similarity of the actual shapes of  $\phi(\rho z)$  curves for a wide range of conditions. Hence a curve-fitting exercise is feasible provided that adequate experimental data are available. One suggestion<sup>10</sup> was that the shape could be represented by a Gaussian profile with the center displaced along the  $\rho z$  axis, although Packwood and Brown<sup>11</sup> later decided that it was better described by centering the Gaussian profile at the surface and modifying it close to the  $\phi(\rho z)$  axis. Love and Scott, in their empirical treatments, chose to apply the atomic-number correction separately since then it would be unnecessary to model exactly the  $\phi(\rho z)$  curve. Their first effort<sup>12</sup> assumed a rather crude rectangular profile, but subsequently they opted for a quadrilateral shape<sup>13</sup> which more closely followed the form of a  $\phi(\rho z)$  curve.

It is the quadrilateral model that is examined in the present paper. After an evaluation of its potential for the construction, in principle, of an absorption correction, it is assessed with reference to microanalysis measurements obtained at various electron-probe voltages and specimen tilt angles. Finally, with the use of a large accumulation of microanalysis data, the universality of the quadrilateral model is further tested and then compared with some other proposed correction methods.

### *The Quadrilateral Model*

The assumed quadrilateral shape ABC is shown superimposed upon a typical  $\phi(\rho z)$  curve in Fig. 1. The point A is positioned on the  $\phi(\rho z)$  axis, at the value for the surface ionization function  $\phi(0)$ ; point B represents the peak of the  $\phi(\rho z)$  curve, with coordinates given by  $\rho z_m$  and  $\phi(m)$ ; C, with coordinates  $(\rho z_r, 0)$ , is positioned close to the x-ray range.

Now the absorption factor  $f(\chi)$  is given by the ratio of total emitted x rays divided by the total generated x rays, which expressed mathematically is

---

The authors are at the School of Materials Science, University of Bath, Claverton Down, Bath, England BA2 7AY. The research was supported by SERC and AERE Harwell.

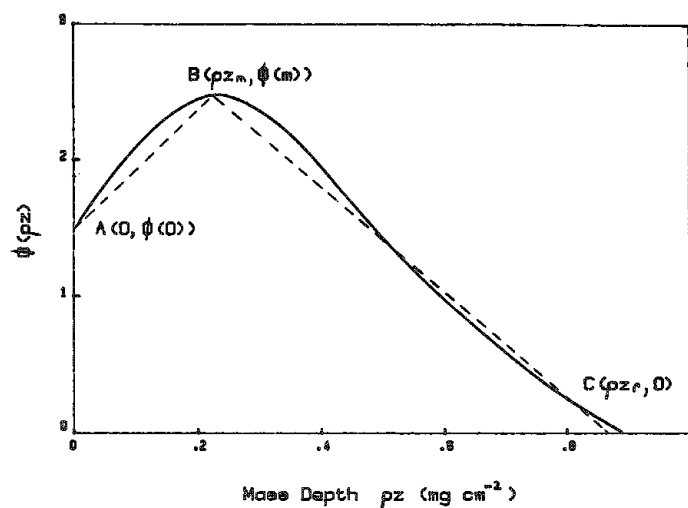


FIG. 1.--  $\phi(\rho z)$  curve for Al  $K\alpha$  radiation in aluminum matrix; probe voltage, 20 kV; --- quadrilateral representation.

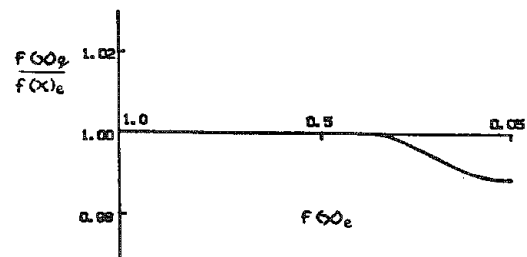


FIG. 2.--Ratio  $f(\chi)_q/f(\chi)_e$  plotted as function of  $f(\chi)_e$ ; where ratio is unity, quadrilateral model may be judged to be operating perfectly.

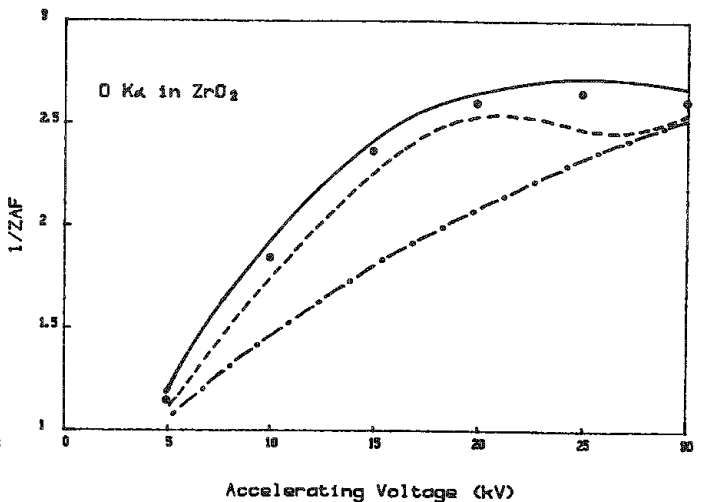
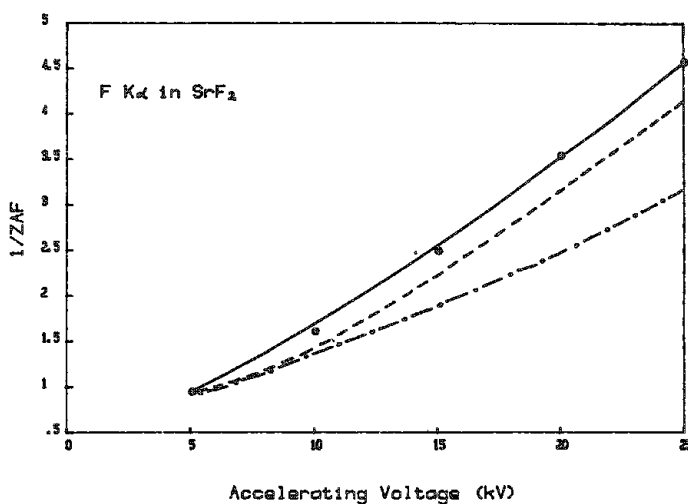
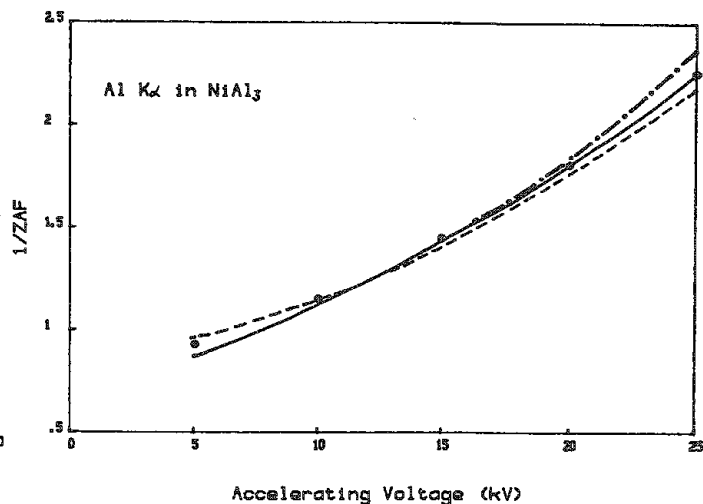
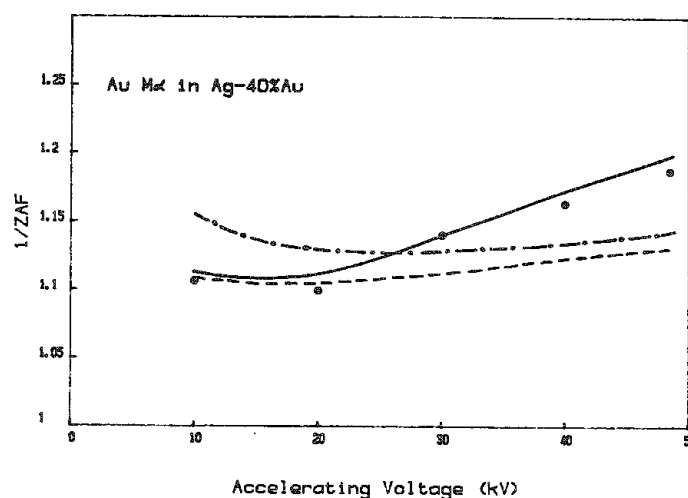


FIG. 3.--Reciprocal of ZAF ( $\equiv c/k$ ) plotted against accelerating voltage; ● experimental measurements, — quadrilateral, --- Bastin, -.- Philibert.

$$f(\chi) = \frac{\int_0^{\infty} \phi(\rho z) \exp(-\chi \rho z) d(\rho z)}{\int_0^{\infty} \phi(\rho z) d(\rho z)}$$

where  $\chi = (\mu/\rho) \operatorname{cosec} \psi$ ,  $\mu/\rho$  is the mass absorption coefficient, and  $\psi$  is the x-ray take-off angle. Substitution of the quadrilateral parameters for  $\phi(\rho z)$  into this equation gives

$$f(\chi) = 2\{(\rho z_R - \rho z_m)(\rho z_m + h\rho z_R)\chi^2\}^{-1} \{[-\exp(-\chi\rho z_m) + h \exp(-\chi\rho z_R) + \chi(\rho z_R - \rho z_m) - h + 1] + [\exp(-\chi\rho z_m)(\rho z_R - h\rho z_R) + h\rho z_R - \rho z_R] \rho z_m^{-1}\} \quad (1)$$

where  $h = \phi(m)/\phi(o)$ . This expression may appear unwieldy but it is readily computed; the reader is referred to Sewell et al.<sup>14</sup> for further details.

Next we have to produce equations for  $h$ ,  $\rho z_m$ , and  $\rho z_R$ , but before doing so, it is worth confirming that this simple quadrilateral shape is adequate for constructing an accurate absorption correction applicable to a range of absorbers.

#### *Preliminary Assessment of Quadrilateral Model*

The method adopted is to compare experimental values  $f(\chi)_e$  for the absorption factor with those predicted by the model,  $f(\chi)_q$ . Thus, when the model is working accurately, the ratio  $f(\chi)_q/f(\chi)_e$  will be unity, whereas a ratio of less than unity indicates overcorrection and vice versa.

The ratio is plotted against  $f(\chi)_e$  in Fig. 2 from tracer results<sup>15</sup> obtained on aluminum at 20 keV, although any such data may be used for this purpose. The closeness of the ratio to unity shows that the quadrilateral model is satisfactory and accurately represents  $f(\chi)$  over a wide range of absorption, from  $f(\chi) = 1.0$  (no absorption) to  $f(\chi) = 0.05$  (95% absorption). And so we can now turn our attention to obtaining the  $\phi(\rho z)$  data needed for constructing equations for  $h$ ,  $\rho z_m$ , and  $\rho z_R$ .

#### *$\phi(\rho z)$ Data*

We have used a combination of experimental  $\phi(\rho z)$  results obtained from tracer measurements and from Monte Carlo calculations. The dual approach was considered necessary because:

- (i) it was impracticable to produce sufficient data by the tracer method that covered the range of electron energies and target materials needed here; and
- (ii) the accuracy of Monte Carlo methods was considered doubtful, especially for low electron energies and higher-atomic-number elements, where scattering cross sections deduced by the Born approximation are less valid.<sup>16</sup>

Details of the tracer experiments are given elsewhere.<sup>15</sup> The majority of Monte Carlo calculations were carried out on a simplified scattering model,<sup>17</sup> after it was first established that the model gave results comparable with those computed by use of a more rigorous program.<sup>18</sup> When the Monte Carlo data were compared with the tracer results, it was found that they modeled the shape of the  $\phi(\rho z)$  curve fairly well. However, calculated values for  $\phi(m)$  were slightly higher than those given by the tracer experiments, particularly at low electron energies, and this factor was taken into account when the equation for  $h$  was developed.

#### *Formulation of Analytical Expressions*

Here we shall outline the principle of the method only; detailed derivations are given elsewhere.<sup>14</sup>

As regards the parameter  $h$ , tracer results showed that it could be expressed as  $h = a_1 - a_2 \exp(-a_3 U_0^x)$ , where  $a_1$ ,  $a_2$ ,  $a_3$ , and  $x$  are constants for a particular element and  $U_0$  is the overvoltage ratio. Further analysis of experimental data gave  $a_1 = 2.2 + 1.88 \times 10^{-3}Z$ ,  $a_3 = 0.01 + 7.19 \times 10^{-3}Z$ ,  $a_2 = (a_1 - 1)\exp a_3$ , and  $x = 1.29 - 1.25\eta$ , where  $Z$  is the atomic number and  $\eta$  the electron backscatter coefficient as given in Love and Scott.<sup>12</sup>

Turning next to  $\rho z_m$ , we chose to express it in terms of the mean depth of x-ray gene-

ration ( $\overline{\rho z}$ ) and, using our experimental  $\phi(\rho z)$  data, obtained,  $\rho z_m = \overline{\rho z}(0.29 + bZ^{0.5})$ , where  $b = 0.622 + 0.433U_0^{-0.2}$ . An equation for  $\overline{\rho z}$  was now needed and, using an earlier idea, we related it to the electron range  $\rho s_m$ , for which an equation was already available:<sup>19</sup>

$$\rho s_m / \overline{\rho z} = 2.4 + 0.07Z + (1.04 + 0.48\eta) / \ln U_0$$

Finally,  $\rho z_r$  was related to both  $\rho z_m$  and  $\overline{\rho z}$  by the definition

$$\overline{\rho z} = \frac{\int_0^\infty \phi(\rho z) \cdot \rho z \, d(\rho z)}{\int_0^\infty \phi(\rho z) \, d(\rho z)}$$

which, after substitution for  $\phi(\rho z)$ , gave

$$\overline{\rho z} = \frac{1}{3} \frac{\rho z_m^2 + h\rho z_r^2 + h\rho z_m \rho z_r}{\rho z_m + h\rho z_r} \quad (2)$$

### *The Specimen Tilt Factors*

Tracer experiments and Monte Carlo calculations were carried out for specimen tilt angles of 30° and 50°. As with the normal incidence data, the Monte Carlo method was found to model the shape of the  $\phi(\rho z)$  curve fairly well but not the height of the peak.<sup>20</sup> However, since we now express the quadrilateral parameters as ratios  $\rho z_\beta / \rho z_{90}$ ,  $h_\beta / h_{90}$ , etc., where  $\beta$  is the angle between the beam direction and the specimen surface, such differences can be ignored. Our method is outlined below; a more detailed description is given in Sewell et al.<sup>20</sup>

When the experimental data were plotted as  $\rho z_\beta / \rho z_{90}$  vs  $\sin \beta$ , the points were found to lie on a straight line, essentially independent of probe voltage and target material. Least-squares analysis gave the following equation:

$$\overline{\rho z}_\beta = \overline{\rho z}_{90} (0.291 + 0.708 \sin \beta)$$

As regards  $\rho z_m$ , we again chose to represent it in terms of the mean depth, i.e., the ratio  $\rho z_m / \overline{\rho z}$ ; our results indicated a  $\sin^2 \beta$  dependence according to

$$(\rho z_m / \overline{\rho z})_\beta = (\rho z_m / \overline{\rho z})_{90} (1.18 \sin^2 \beta - 0.18)$$

The relationship between  $h$  and  $\beta$  was more difficult to establish since  $h$  values were affected by probe voltage. The following equation was first confirmed:

$h_\beta = h_{90}(b_1 + b_2 \sin^2 \beta)$ , where  $b_1$  and  $b_2$  depend upon the overvoltage ratio  $U_0$ ; further analysis gave  $b_1 = 0.44 + 0.56 U_0^{-2/3}$  and  $b_2 = 0.56 - 0.56 U_0^{-2/3}$ .

Finally,  $(\rho z_r)_\beta$  was obtained from Eq. (2) by substitution of  $(\overline{\rho z})_\beta$ ,  $(\rho z_m)_\beta$ , and  $h_\beta$ .

### *The ZAF Correction Routine*

In the following evaluation we have combined the quadrilateral absorption model with the atomic number correction of Love et al.<sup>20</sup> and the characteristic fluorescence correction of Reed.<sup>5</sup> Continuum fluorescence has not been included since previous experience indicated that this factor would not amount to more than 1% in most cases. With regard to mass absorption coefficients, the formulas<sup>21</sup> derived from Heinrich's tabulation<sup>22</sup> were used for x-ray energies above 2 keV (K radiations from elements above silicon) and the data of Henke et al.<sup>23</sup> for radiations below 2 keV. When we dealt with multicomponent specimens the complete formula for the mean depth  $\overline{\rho z}$  was weight averaged [i.e.,  $\sum c_i \overline{\rho z}_i$ , but with the equations for  $h$ , etc., the terms were averaged individually].

### *Evaluation of Universal Correction Procedure*

In the first part of the evaluation, the performance of the correction routine is assessed with respect to the effect of incident electron energy. Then the model is tested by use of microanalysis results obtained on tilted specimens. The final part of the evalua-



tion utilizes an extensive collection of microanalysis data produced in a number of different laboratories.

### *Effect of Voltage*

Four systems were chosen for study, ranging in mean atomic number but all involving measurements of relatively highly absorbing x radiation: Au M $\alpha$  in Ag-40%Au ( $\mu/\rho = 1211$ ), Al K $\alpha$  in NiAl<sub>3</sub> (2036), F K in SrF<sub>2</sub> (6009), and O K in ZrO<sub>2</sub> (12285). The microanalysis measurements, plotted as a function of probe voltage, are shown as points in the series of diagrams (Fig. 3). Units along the vertical axis are expressed as  $c/k$  (i.e.,  $1/ZAF$ ), since this method of plotting gives an indication of the magnitude of the correction factor needed; for example, a  $c/k$  value of 1.0 means that no ZAF correction factor is needed, whereas 2.0 indicates a factor of 100%. The continuous line gives data predicted by our universal correction procedure, which in every instance may be seen to give results lying close to the experimental points, mostly within a few percent relative. The steepness of a curve is indicative of substantial differences in absorption between specimen and standard and, even with measurements of fluorine in SrF<sub>2</sub> (Fig. 3c), where the correction factor is as high as several hundred per cent, the correction model is still working satisfactorily. Note that the oxygen measurements in ZrO<sub>2</sub> (Fig. 3d) show a maximum  $c/k$  value around 25 kV and then a slight decrease at higher probe voltages. That is because the standard used (Al<sub>2</sub>O<sub>3</sub>) is a fairly high absorber for oxygen radiation. In other words, at higher kV the "thin-film criterion"<sup>24</sup> was being approached such that x rays were being collected mainly from surface regions of both specimen and standard and, consequently,  $c/k$  was tending towards a constant value.

### *Effect of Specimen Tilt*

As with the work described in the previous section, the systems selected for study were heavily absorbing materials to make the test as rigorous as possible. The results are again presented as  $c/k$  values. Comparison of microanalysis measurements with data predicted by the universal correction procedure (continuous line) shows (Fig. 4) that there is good agreement for all tilt angles up to 50° at these probe voltages (10, 15, and 20 kV). The decrease in the magnitude of the correction factor as samples are tilted toward the detector is due mainly to two factors--a progressive increase in the x-ray take-off angle and the greater confinement of x rays to regions of the surface--both of which reduce the amount of absorption.

For comparison purposes, an alternate method for dealing with tilted specimens, which consists of simply replacing  $\chi$  by  $\chi \sin \theta$  in the equation for  $f(\chi)$ , has been examined. The data are plotted (broken line) in Figure 5 as the ratio  $k'/k$ , where  $k'$  refers to the predicted x-ray intensity ratio from specimen and standard. Thus, when the model corrects properly,  $k'/k = 1$ ; whereas  $k'/k > 1$  indicates undercorrection and vice versa. It may be seen that large errors are incurred that increase substantially with tilt angle and approach 7 or 8% at a beam energy of 20 keV.

The continuous line in Fig. 5 refers to our method of incorporating the tilt factor into equations for  $\phi(0)$ , etc., which is clearly a more satisfactory treatment of the problem.

### *Overall Performance*

An effective way of testing a correction procedure is to determine how well it performs when applied to a large and wide-ranging collection of microanalysis measurements. We have used a database containing 554 results as listed in Sewell et al.<sup>14</sup> Essentially, they were derived from an earlier collection,<sup>25</sup> after some doubtful results were subtracted and some new ones were inserted. In addition, some new ultralight-element data on oxide and fluorides (94 results) were produced; they are treated separately in order to differentiate between the model's performance on heavy-element and light-element systems.

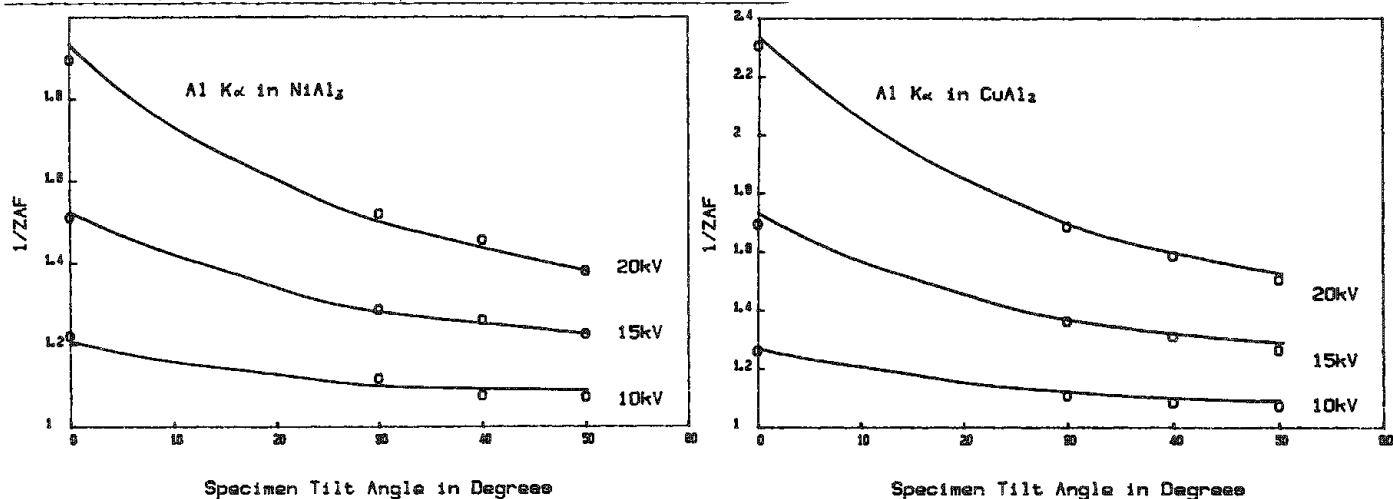
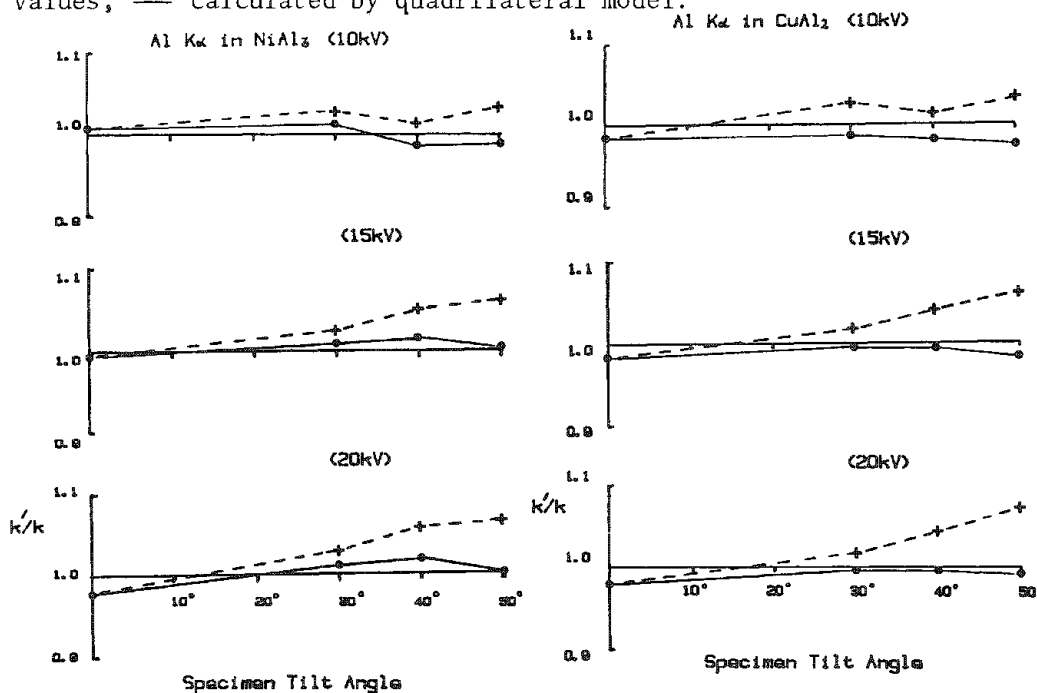
From the values of  $k'/k$ , the RMS errors were calculated. For the heavier elements ( $Z > 10$ , 554 measurements), the RMS error was found to be 2.9%. Bearing in mind that the original microanalysis measurements probably contained ~2% error the correction model is working as well as can be expected. When applied to ultralight elements ( $Z < 10$ , 94 measurements), the universal correction procedure appeared to be slightly less satisfactory, with an RMS error of 4.8%.

TABLE 1.--Correction models evaluated.

Model	Atomic number correction	Absorption correction	Fluorescence correction
Love-Scott	Love et al. <sup>8</sup>	Quadrilateral	Reed <sup>5</sup>
Established	Duncumb and Reed <sup>3</sup>	Philibert <sup>1</sup>	"
Bastin	Bastin et al. <sup>26</sup>	Bastin et al. <sup>26</sup>	"

TABLE 2

Model	Percentage RMS errors	
	Elements Z > 10	Ultralight elements Z < 10
Love-Scott	2.9	4.8
Established	4.8	16.5
Bastin	3.7	7.0

FIG. 4.--Reciprocal of ZAF ( $\equiv c/k$ ) plotted against specimen tilt angle; o experimental values, — calculated by quadrilateral model.FIG. 5.--Ratio  $k'/k$  vs specimen tilt angle; --- obtained by  $\chi \sin \beta$  approximation and quadrilateral model for normal electron beam incidence, — calculated by quadrilateral method incorporating tilt correction.

### Comparison with Other Correction Models

Before we conclude, it is instructive to draw comparisons between our universal correction procedure and two alternative models.

First, the procedure said in the second paragraph of this paper to be in common use ("established method") is tested. This procedure contains the Philibert absorption model and we have combined it with the atomic-number correction of Duncumb and Reed<sup>5</sup> and the fluorescence factor given by Reed.<sup>5</sup> We could have chosen instead the Philibert and Tixier<sup>4</sup> atomic-number correction, but our experience shows it makes little difference to the final result. For reasons given earlier, methods which involve essentially modifications<sup>7,8</sup> to the Philibert absorption correction are not examined.

Second, the recent empirical approach of Bastin et al.<sup>26</sup> is evaluated. This is a development of the Packwood and Brown<sup>11</sup> curve-fitting method, which uses an adjusted Gaussian profile to represent the  $\phi(\rho z)$  curve. The model provides a combined atomic number and absorption correction to which we have added Reed's fluorescence correction (Table 1).

It would have been interesting to examine the treatment of Pouchou and Pichoir,<sup>27,28</sup> especially since data predicted by their model appear to show excellent agreement with experimental  $\phi(\rho z)$  profiles. Unfortunately, the method could not be assessed here because the requisite equations were not given by the authors.

The RMS errors listed in Table 2 were obtained when the two correction methods were applied to the microanalysis databases. With regard to the heavier elements, the Bastin model shows considerable improvement over the established method, with an RMS error of 3.7% compared with 4.8%, but it is not as good as our universal correction procedure (RMS error 2.9%). Turning to the ultralight-element data, the Bastin model again performs more satisfactorily than the established method with RMS errors of 7.0% and compared with 16.5%, but fails to match the universal correction procedure with its significantly smaller RMS error of 4.8%.

Data predicted by the two correction models are plotted in Fig. 3 as a function of voltage for the four systems referred to above (Ag-40%Au, NiAl<sub>3</sub>, SrF<sub>2</sub>, and ZrO<sub>2</sub>). With regard to Au M $\alpha$  data on Ag-40%Au (Fig. 3a), neither model describes the voltage dependence accurately, although Bastin's model seems to function adequately at the lower probe voltages, up to 20 kV. However, their performance with respect to Al K $\alpha$  radiation in NiAl<sub>3</sub> (Fig. 3b) appears to be satisfactory. With the two most heavily absorbing systems (F K in SrF<sub>2</sub> and O K in ZrO<sub>2</sub>), the established procedure is seriously overcorrecting (up to 50%) except at the very lowest probe voltages,  $\sim$ 5 kV. Bastin's method performs rather better on these two systems but still overcorrects, especially at the higher voltages.

### Concluding Remarks

We have developed a correction procedure for quantitative electron-probe microanalysis based on new tracer measurements and Monte Carlo calculations. It has been tested and shown to work well for a wide range of systems, including those containing ultralight elements, and to perform satisfactorily at various probe voltages and specimen tilt angles. It is clearly superior to the established correction method and also outperforms the recent procedure introduced by Bastin et al. We consider that our new method can be regarded as a truly universal solution to the problem of quantitative electron-probe microanalysis.

### References

1. J. Philibert, "A method for calculating the absorption correction in electron probe microanalysis," in H. H. Pattee, V. E. Cosslett, and A. Engstrom, Eds., *X-ray Optics and X-ray Microanalysis*, New York: Academic Press, 1963, 379-392.
2. K. F. J. Heinrich, "The absorption correction model for microprobe analysis," in *Trans. 2nd Nat. Conf. on Electron Probe Microanalysis*, Boston: Electron Probe Analysis Society of America, 1967, paper 7.
3. P. Duncumb and S. J. B. Reed, "The calculation of stopping power and backscatter effects in electron probe microanalysis," in K. F. J. Heinrich, Ed., *NBS Spec. Publ. 298*, Washington: U.S. Department of Commerce, 1968, 133-154.
4. J. Philibert and R. Tixier, "Some problems with quantitative electron probe

microanalysis," *ibid.*, 13-34.

5. S. J. B. Reed, "Characteristic fluorescence corrections in electron probe microanalysis," *Brit. J. Appl. Phys.* 16: 913-926, 1965.

6. G. Love, M. G. C. Cox, and V. D. Scott, "Assessment of Philibert's absorption correction models in electron probe microanalysis," *J. Phys.* D8: 1686-1702, 1975.

7. W. Reuter, "The ionisation function and its application to the electron probe microanalysis of thin films, in G. Shinoda, K. Kohra, and T. Ichinokawa, Eds., *X-ray Optics and Microanalysis*, Tokyo: Tokyo University Press, 1972, 121-130.

8. J. Ruste and C. Zeller, "Correction d'absorption en micro-analyse," *C. R. Acad. Sci.* 284(B): 507-510, 1977.

9. G. Love, "Evaluation of ZAF methods" in V. D. Scott and G. Love, Eds., *Quantitative Electron-Probe Microanalysis*, Chichester: Ellis Horwood Ltd., 1983, 226-230.

10. D. B. Wittry, "Resolution of electron probe microanalyzers," *J. Appl. Phys.* 29: 1543-1548, 1958.

11. R. H. Packwood and J. D. Brown, "A Gaussian expression to describe  $\phi(\rho z)$  curves for quantitative electron probe microanalysis," *X-ray Spectrom.* 10: 138-146, 1981.

12. G. Love and V. D. Scott, "Evaluation of a new correction procedure for quantitative electron-probe microanalysis," *J. Phys.* D11: 1369-1376, 1976.

13. G. Love, D. A. Sewell, and V. D. Scott, "An improved absorption correction for quantitative analysis," *J. de Physique*, Colloque C2, supplement au no. 2, 21-24, 1984.

14. D. A. Sewell, G. Love, and V. D. Scott, "Universal correction procedure for electron-probe microanalysis: II. The absorption correction," *J. Phys.* D18: 1245-1267, 1985.

15. D. A. Sewell, G. Love, and V. D. Scott, "Universal correction procedure for electron probe microanalysis: I. Measurement of x-ray distributions in solids," *ibid.* D18: 1233-1243, 1985.

16. H. E. Bishop, *Electron Scattering and X-ray Production*, Ph.D. thesis, University of Cambridge, 1966.

17. G. Love, M. G. C. Cox, and V. D. Scott, "A simple Monte Carlo method for simulating electron solid interactions and its application to electron-probe microanalysis," *J. Phys.* D10: 7-23, 1977.

18. R. L. Myklebust, D. E. Newbury, and H. Yakowitz, "NBS Monte Carlo electron trajectory calculation program," in K. F. J. Heinrich, D. E. Newbury, and H. Yakowitz, Eds., *NBS Spec. Publ. 460*, Washington: U.S. Department of Commerce, 1976, 105-125.

19. G. Love, M. G. C. Cox, and V. D. Scott, "A versatile atomic number correction for electron-probe microanalysis," *J. Phys.* D11: 7-22, 1978.

20. D. A. Sewell, G. Love, and V. D. Scott, "Universal correction procedure for electron-probe microanalysis: IV. The specimen tilt correction," *ibid.* (to be published).

21. G. Springer and B. Nolan, "Mathematical expression for the evaluation of x-ray emission and critical energies and of mass absorption coefficients," *Canad. J. Spectrosc.*, 134-138, 1976.

22. K. F. J. Heinrich, "X-ray absorption uncertainty," in T. D. McKinley, K. F. J. Heinrich, and D. B. Wittry, Eds., *The Electron Microprobe*, 1966, 296-377.

23. B. L. Henke, P. Lee, T. J. Tanaka, R. L. Shimabukuro, and B. K. Fujikawa, "Low-energy x-ray interaction coefficients: Photoabsorption, scattering and reflection," *Atomic Data and Nuclear Data Tables* 27: 1-145, 1982.

24. P. Duncumb and D. A. Melford, "Quantitative applications of ultra soft X-ray microanalysis," in R. Castaing, P. Deschamps, and J. Philibert, Eds., *X-ray Optics and Microanalysis*, Paris: Hermann, 1966, 240-254.

25. G. Love, M. G. C. Cox, and V. D. Scott, "Assessment of Bishop's absorption correction model in electron-probe microanalysis," *J. Phys.* D9: 7-13, 1976.

26. G. F. Bastin, F. J. J. Van Loo, and H. J. M. Heijligers, "Evaluation of the use of Gaussian  $\phi(\rho z)$  curves in quantitative electron probe microanalysis: A new optimisation," *X-ray Spectrom.* 13: 91-97, 1984.

27. J. L. Pouchou and F. Pichoir, "Extension des possibilités quantitatives de la microanalyse par une formulation nouvelle des effets de matrice," *J. de Physique*, Colloque C2, supplement no. 2, 17-20, 1984.

28. J. L. Pouchou and F. Pichoir, "Un nouveau modèle de calcul pour la microanalyse quantitative par spectrométrie de rayons X: Partie 1. Application à l'analyse d'échantillons homogènes," *La Recherche Aérospatiale* no. 3: 167-192, 1984.

## COMPARISON OF ALGORITHMS FOR X-RAY MASS ABSORPTION COEFFICIENTS

K. F. J. Heinrich

Before computerized data evaluation in microprobe analysis became commonplace, x-ray mass absorption coefficients (MAC) were presented in tables.<sup>1-3</sup> In small computers, it is preferable to store algorithms for the calculation of MACs.<sup>4,5</sup> Frequently, algorithms are also used for the energies of lines and edges; however, that may lead to errors due to misplacement of lines with respect to the edges of the absorber.

Although MACs can be obtained from theory,<sup>1,6,7</sup> the procedures used at present are all based on empirical fits, with the assumption that a good approximation to MACs can be obtained by

$$\mu = C\lambda^n = C(12397/E)^n \quad (1)$$

in which  $\lambda$  is the wavelength of the absorbed radiation (Å),  $E$  its energy (eV), and  $C$  and  $n$  are parameters that vary with the atomic number of the absorber and change abruptly across absorption edges, but are otherwise independent of the photon energy. It is also commonly assumed that  $C$  for each region within edges varies smoothly with the atomic number  $Z$ , although it is more reasonable to postulate that the atomic cross section, and hence  $C.A$ , will vary smoothly with  $Z$  ( $A$  = atomic weight).

However, the exponential model embodied in Eq. (1) is a poor approximation, especially at lower photon energies. The deviations from this equation may cause significant errors in the estimates of MACs, particularly at energies slightly above absorption edges.

The limitations of previous models for MACs are reduced in a procedure called MAC24, based on the following steps:

1. The energies of the absorption edges (K to N1) and the most important x-ray lines are read from a random access file.
2. The MACs are calculated by a modified model:

$$\mu = C(12397/E)^n \cdot \{1 - \exp[(b - E)/a]\} \quad (2)$$

In this equation, the parameters  $C$ ,  $n$ ,  $a$ , and  $b$  are estimated from experimental data where obtainable, and elsewhere, especially at energies below 1000 eV, from the compilations of Henke<sup>7</sup> and Veigele.<sup>6</sup> Quadratic fits are obtained for the variation of  $C.A$ ,  $a$  and  $b$  with the atomic number of the absorber, and of  $n$  with photon energy, for each of the regions separated by the absorption edges.

In the energy region above 1000 eV, for which the previous techniques were established, this model fits reliable experimental data better than previous models, and the error of the estimations should be in general smaller than 5%. The better fit of Eq. (2) also permits extension of the procedure to energies as low as 180 eV for most elements; hence the absorption for C, N, O, and F K emissions can also be estimated, although with a larger uncertainty. The accuracy of the MACs obtained by MAC24 depends mainly on the availability and quality of measured data or calculated estimates used in the fit. As further measurements or better calculations become available, it will be easy to update the procedure.

The fitting and the graphic work were performed on a small (64K) computer; COMAL 3 was the language used. The graphic and numeric data presentation modes developed with the method provide an efficient way of comparing algorithmic models with experimental or theoretical values, or one model with another (Figs. 1 and 2).

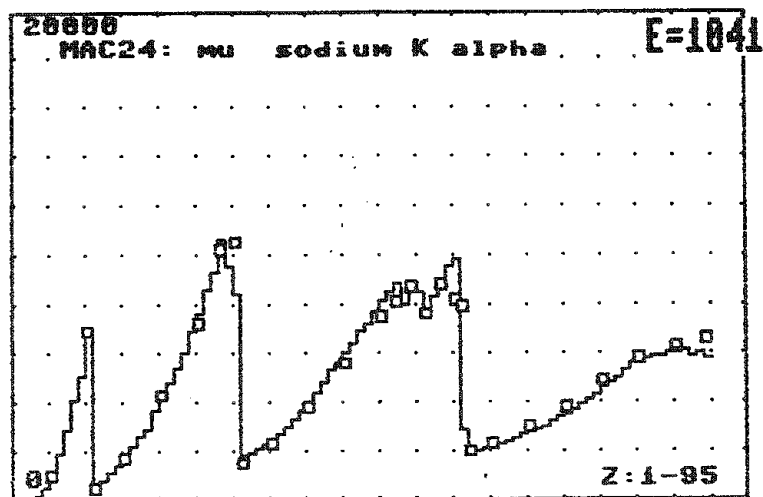


FIG. 1.--Mass absorption coefficients from program MAC24 (continuous), and data from Henke<sup>7</sup> (empty squares), for Na K $\alpha$  radiation.

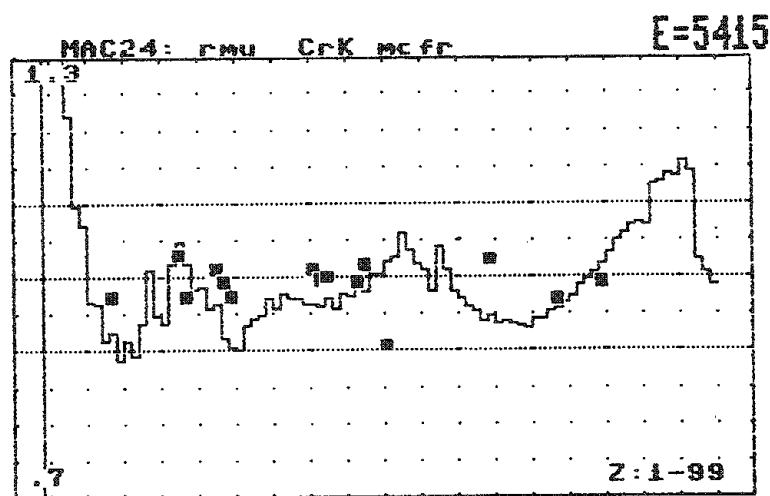


FIG. 2.--Ratio of mass absorption coefficients from FRAME and from MAC24, and experimental data by Hon<sup>9</sup> (full squares), for Cr K $\alpha$  radiation.

#### References

1. L. V. Birks, *Electron Probe Microanalysis*, New York: Wiley, 1971, Appendix 1.
2. K. F. J. Heinrich, in T. D. McKinley et al., Eds., *The Electron Microprobe*, New York: Wiley, 1966, 296.
3. R. Theisen, *Quantitative Electron Microprobe Analysis*, Berlin: Springer Verlag, 1965.
4. J. Z. Frazer, Report SIO 67-29, Institute for the Study of Matter, University of California at San Diego, La Jolla, CA 92093, 1967.
5. H. Yakowitz, R. L. Myklebust, and K. F. J. Heinrich, *NBS Technical Note 796*, National Bureau of Standards, Gaithersburg, Md., 1973, Table D.
6. W. S. Veigele, *Atomic Data* 5: 51, 1973.
7. B. L. Henke and E. S. Ebisu, *Adv. X-ray Anal.* 17: 150, 1974.
8. K. F. J. Heinrich, *Proc. 11th Internat. Conf. X-ray Optics and Microanalysis*, London, Ont. (in preparation).
9. R. Hon, 1968 (personal communication).

## ASPECTS OF QUANTITATIVE MICROANALYSIS OF LIGHT ELEMENTS BY EDXS

P. J. Statham

If it is assumed that the well-documented (see, for example, Ref. 1) problems of sample preparation, contamination, method of correction for matrix effects, and accuracy of mass absorption coefficients will be eventually overcome, precision and accuracy for microanalysis of light elements by energy-dispersive x-ray spectrometry (EDXS) will then be governed by reproducibility of detector response and statistics of spectrum processing. The problem areas peculiar to EDXS are mainly those of

- (1) backscattered electrons and light entering the detector;
- (2) contamination of detector, e.g., by ice or hydrocarbons;
- (3) detection of small photon signals buried in electronic noise;
- (4) signal degradation (peak tailing, bias, and low energy "spur");
- (5) overlap of peaks by other peaks and the noise "tail."

Topics 1 and 2 have been discussed at length in earlier papers and no further mention will be made save to note that materials such as  $\text{MgF}_2$  with one peak just above the O K edge are particularly useful for revealing the presence of ice by virtue of it causing a change in the F  $K\alpha$ /Mg  $K\alpha$  intensity ratio (M. Jones, personal communication). The remaining subjects are discussed in some detail.

### *Electronic Noise and Detectability*

The step at the preamplifier output due to the arrival of a low-energy photon (e.g., B  $K\alpha$ ) may be barely distinguishable from the fluctuations due to noise; as a result, the accumulated spectrum shows a peak overlapped strongly by the tail of a noise distribution.<sup>2</sup> Perhaps the first convincing demonstration of boron detection by EDXS was achieved with proton excitation of a polished boron specimen,<sup>3</sup> but probably the first record of boron detection in a conventional SEM was many years later<sup>2</sup> and was followed soon thereafter by demonstrated detection of a beryllium peak from a foil sample.<sup>4</sup> The last two successes could be attributed primarily to the use of a special low-noise "tetrode" FET and a time-variant pulse processor with excellent "1/f" noise performance.<sup>5-7</sup> It is convenient to define a simple quality factor for assessing performance. The "peak-to-valley" ratio P/V (the ratio of the count in the peak channel to that in the valley between peak and noise tail) is suitable, as it increases with any improvement in electronic noise, detector resolution, or elemental sensitivity.<sup>8</sup> The P/V for Musket's proton-excited pure boron was 1.8, whereas the SEM-excited boron from LaB6 (32% B) gave P/V = 1.9 and the beryllium foil gave P/V = 1.1 for Be.

### *Charge Collection*

The signal from a single photon is "degraded" if not all the liberated charge is collected. In this case, a count is added to the spectrum somewhere lower than the correct channel and after many photons have been recorded, the overall result is a peak with a low-energy tail corresponding to degraded events. Since charge loss is generally worse for photons absorbed near the detector surface, very low-energy peaks can have a tail so large that it forms the majority of the observed peak, which is therefore at too low an energy in the spectrum. This effect has been understood in qualitative terms for some time,<sup>9</sup> but recent papers have made attempts to quantify and suggest mechanisms for charge loss.<sup>10,11</sup> Although peak tailing, bias, and nonlinearity do not present any insoluble problems for subsequent mathematical treatment, a shift to lower energy exacerbates overlap with the noise distribution and thus reduces P/V.

After a series of developments, summarized elsewhere,<sup>8</sup> a proprietary production

---

The author is with Link Systems Limited, Halifax Road, High Wycombe, Bucks, England HP12 3SE.

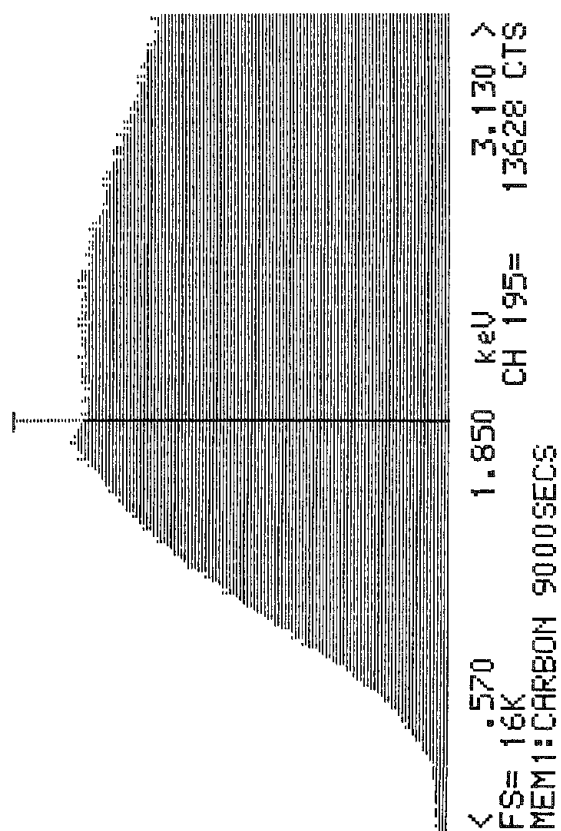


FIG. 1.--Spectrum from pure carbon at 20 kV.

Noise

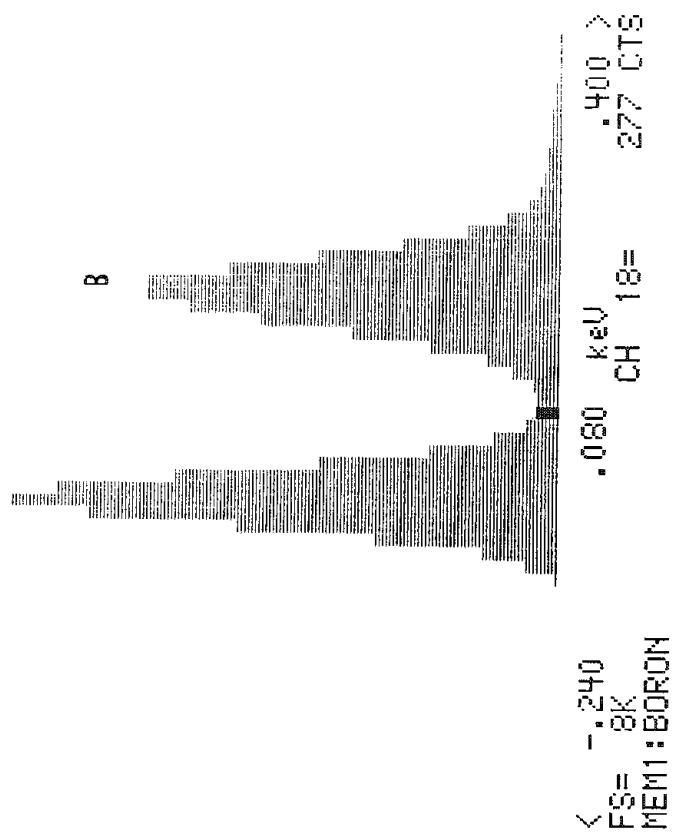


FIG. 3.--Current best-performance spectra from metals in SEM. P/V for boron is 20; for beryllium, 2.1.

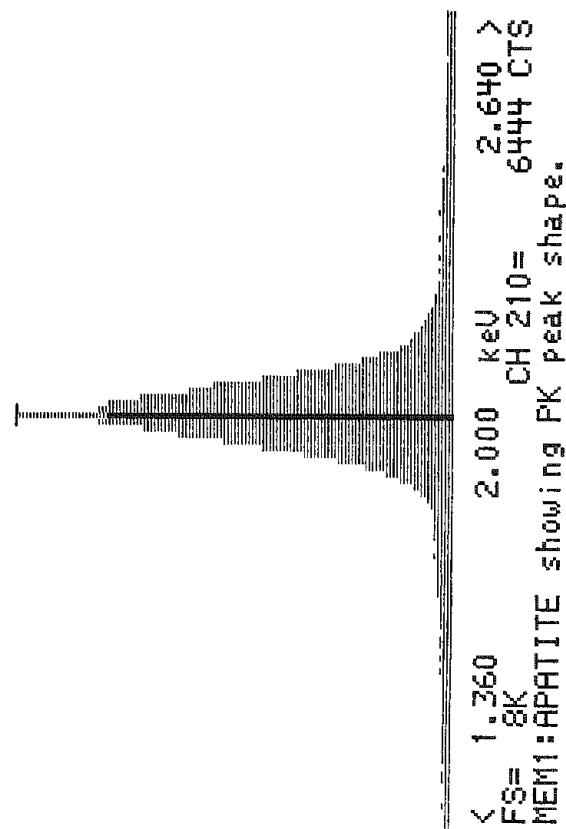


FIG. 2.--P K $\alpha$  peak from spectrum of apatite at 20 kV.

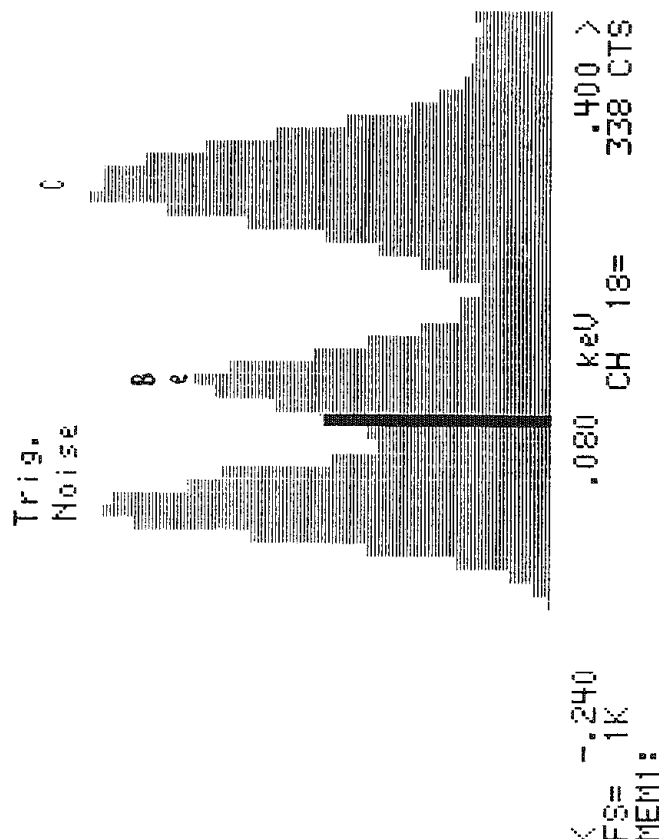


FIG. 3.--Current best-performance spectra from metals in SEM. P/V for boron is 20; for beryllium, 2.1.



process ("series E") was designed for detectors so as to improve charge collection and noise performance to counter the above limitations. Measurements on a spectrum of an Fe-55 source are routinely employed and three parameters are normally calculated in our laboratories: (1) the ratio of the peak height at Mn K $\alpha$  to that of the residual background level at 1 keV (P/B); (2) the percentage of counts that fall in the energy region between the escape peak and the start of the Mn K $\alpha$  peak (TAIL), and (3) the percentage of events from zero energy to just above the Mn K $\alpha$  peak that fall outside the Mn K $\alpha$  peak (DEGRADED). With these definitions, the average performance of series-E detectors can be quantified.

1. P/B is increased to > 10 000 (previously 1000-2000)
2. TAIL is normally below 0.15% (previous detectors gave ~0.4%)
3. DEGRADED percentage is now <2% (previously around 5%)

Figure 1 shows an example of early "series-E" detector performance on a spectrum from pure carbon, where the step at the Si K edge (an indicator of the transition layer of poor charge collection) is considerably smaller than has sometimes been reported.<sup>10</sup> Furthermore, the spectrum of apatite from the same detector (Fig. 2) shows a well-formed P K $\alpha$  peak with virtually no low-energy tail in contrast to earlier spectra.<sup>12</sup> The best results that have been obtained so far with such a detector are shown in Fig. 3 where a P/V of 20 has been achieved on boron metal and a P/V of 2.1 from a Be foil.

### *Spectrum Processing*

Calculations of 3 $\sigma$  detection limits based on spectra from bulk samples acquired in around 2 min have suggested state-of-the-art performance of around 4% for B and 25% for Be,<sup>4</sup> but the full spectrum-processing method should be considered to assess realistic capabilities for practical analysis. One approach has been described in detail,<sup>13</sup> where the noise tail, low-energy "spur," and bremsstrahlung background are modeled and then subtracted from the spectrum before the peaks are fitted. However, no mention is made of escape peaks, which present some special problems because of the surface nature of the phenomenon. If a photon is absorbed at depth  $x$  and this event involves the production of a Si K $\alpha$  photon, the probability that it will escape through the surface is

$$P \propto \int_0^{\pi/2} \sin \theta \exp(-\mu \rho x \sec \theta) d\theta \quad (1)$$

where  $\mu$  is the mass absorption coefficient for Si K $\alpha$  x rays in silicon and  $\rho$  is the density of silicon. If this integral is evaluated as a function of  $x$  as shown in the top curve of Fig. 4, it is clear that the escape peak will be derived from incoming photons which are absorbed close to the detector surface. In particular, if the depth distribution for absorption of S K $\alpha$  incident photons is applied to this function, the distribution of photoelectric events that give rise to the S K $\alpha$  escape peak is seen to be almost the same as that for those contributing to a phosphorus peak (Fig. 4). In other words, any charge collection defects evident on a peak from P K $\alpha$  should also be apparent on the escape peak for S K $\alpha$ . The clean escape peak in Fig. 5 is thus further evidence of the charge collection properties of the detector that produced the P K $\alpha$  peak in Fig. 2. In the case of a detector with poorer charge collection, the escape peak would be shifted toward lower energy and show tailing, so that conventional methods of escape peak stripping would be inadequate.

In the present study, problems of peak overlap and background have been tackled by use of the "filtered-least-squares" approach to spectrum treatment.<sup>14</sup> A spectrum with a noise peak alone is stripped from spectra of single elements to prepare a set of standard spectra; these spectra are individually filtered before fitting by least-squares to a filtered specimen spectrum. This procedure avoids explicit calculation of both the bremsstrahlung and the "spur," and the inclusion of a filtered noise peak profile compensates for the noise tail. To avoid any dependence on accuracy of "ZAF" corrections, tests have been performed by accumulation of known mixes of standard spectra by dwelling for set intervals on different standards. For example, a 50% B, 50% C spectrum was simulated by counting for 100 s on a boron standard followed by 100 s on a carbon standard (Fig. 6). The spectrum processing for this spectrum gave B:  $47.0 \pm 4.9\%$ , C:  $49.1 \pm 0.5\%$ , where the

concentrations were calculated by ratioing to the appropriate standard and standard deviations were calculated during processing.<sup>14</sup> A simulated 30% B, 60% C spectrum gave B:24.0  $\pm$  3.6%, C:61.4  $\pm$  0.4% and a 10% B, 90% C spectrum gave B:2.4  $\pm$  3.9%, C:90.5  $\pm$  0.5%. This last result shows the boron to be below the 3 $\sigma$  detection limit which, at around 12%, is much higher than the value of 4% quoted above. However, that merely serves to demonstrate that precision is adversely affected by overlap from nearby peaks and that statistical calculations must be based on realistic practical conditions.<sup>15</sup> To emphasize this point further, note that when derivative spectra were included to cope with drift<sup>16</sup> the standard deviation for boron increased to 6.4% in "payment" for the insensitivity to peak shift! It is clearly of benefit to have a system with automatic drift compensation,<sup>6</sup> so that further correction is unnecessary and such loss of precision is avoided.

Despite the notes of caution, these results are all within the bounds of statistical variation and indicate that quantitative analysis is feasible for major concentrations of light elements even in the presence of severe peak overlap. Prospects will be even better when the sort of performance exhibited by Fig. 3 becomes routinely available.

### References

1. G. F. Bastin and H. J. M. Heijligers, *Microbeam Analysis--1985*, 1.
2. P. J. Statham, *J. Microscopy* 130: 165-176, 1983.
3. R. G. Musket, *Nuclear Instrum. & Meth.* 117: 385, 1974.
4. P. J. Statham, *J. de Physique* 45 (coll. C2, suppl. 2): C2-175, 1984.
5. C. E. Cox and K. Kandiah, "The dependence of low frequency noise of JFETs on device parameters and operating conditions," *Proc. 6th Intern. Symp. Noise in Physical Systems*, NBS, 1981.
6. K. Kandiah, A. J. Smith, and G. White, "A pulse processor for x-ray spectrometry with Si(Li) detectors," *Proc. 2nd ISPRA Nucl. Electron. Symp.*, Stresa, Italy (*IEEE Trans. Nucl. Sci.*, Oct. 1975).
7. J. Llacer and D. F. Meier, *Nucl. Instrum. & Meth.* 142: 597, 1977.
8. P. J. Statham, "Progress in instrumentation for EDX detection of light elements," *Proc. ANRT*, Paris (in press).
9. J. M. Jaklevic and F. S. Goulding, *IEEE Trans.* NS-18: 187, 1971.
10. A. J. Craven et al., *EMAG--1985*, Inst. Phys. Conf. Ser. No. 78, 189.
11. D. C. Joy, *Microbeam Analysis--1985*, 342.
12. P. J. Statham, *J. Microscopy* 123(1): 1-23, 1981.
13. G. Love, et al., *Microbeam Analysis--1984*, 191.
14. P. J. Statham, *Anal. Chem.* 49: 2149, 1977.
15. P. J. Statham, *Microbeam Analysis--1982*, 1.
16. T. Kitazawa et al., *Ultramicroscopy* 11: 251-262, 1983.

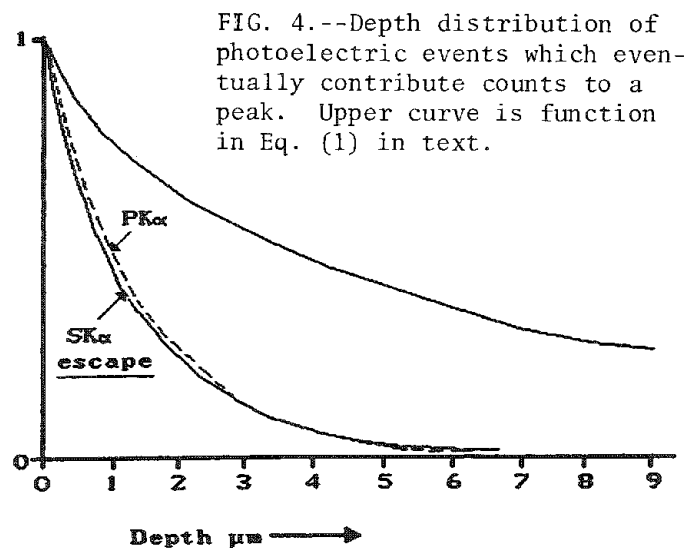
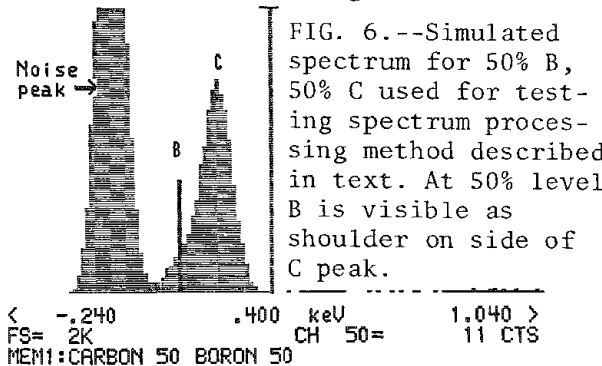
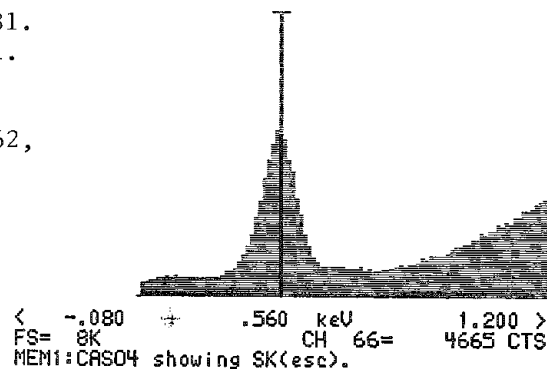


FIG. 4.--Depth distribution of photoelectric events which eventually contribute counts to a peak. Upper curve is function in Eq. (1) in text.



## QUANTITATIVE ELECTRON-PROBE MICROANALYSIS OF BORON IN SOME BINARY BORIDES

G. F. Bastin and H. J. M. Heijligers

On previous occasions<sup>1-3</sup> we have shown that quantitative wavelength-dispersive analysis of very light elements such as carbon is possible with an accuracy comparable to that in the analysis of much heavier elements. However, several demands have to be met in order to achieve this accuracy. The most important requirement is that the effects of peak shifts and especially peak shape alterations be taken into account, which means that in principle all intensity measurements should be carried out in an integral fashion. We have demonstrated that the necessary effort can be considerably reduced by the use of so-called Area/Peak Factors (APFs), which represent the ratio between the true integral (or area) k-ratio and the peak k-ratio for a given compound with respect to a given standard and for a given spectrometer. Once such a factor is known subsequent measurements can simply be performed on the peak again and multiplication by the appropriate APF will yield the correct integral k-ratio.

Once reliable integral k-ratios are available it is up to the matrix correction program to convert them into correct concentrations. However, that is possible only if a set of accurate and consistent mass absorption coefficients (mac's) is available, in conjunction with an adequate program, of course. According to our experience a 1% change in the mac can produce a 1% change in the results for very light elements. Because it is unlikely that the mac's for very light element radiations<sup>4</sup> have anywhere near that accuracy, we shall have to be satisfied at present with statements on the performance of correction programs in conjunction with the particular set of mac's used. On the other hand, if sufficient intensity measurements are available over a wide range of accelerating voltages and a wide range of systems, it is possible to test existing sets of mac's on their consistency and to propose better values where necessary.<sup>1-3</sup>

In the present paper we discuss the preliminary results of our work on boron, which was performed on 27 binary borides distributed over 17 systems. Despite additional measuring problems,<sup>2</sup> we finally achieved a relative root-mean-square error of approximately 6.2% over 180 measurements between 4 and 30 kV. Considering the extreme conditions encountered in both the measurements as well in the matrix correction procedure (e.g., extreme overvoltage ratios) this result must be regarded as remarkable.

### *Experimental*

The majority of the 27 borides (ranging from B<sub>4</sub>C to UB<sub>4</sub>) were prepared by arc-melting in our own laboratory. Independent chemical analysis of the boron content could not be carried out because most samples were two- or more phased, due to losses of boron which occurred during melting. However, a fair proportion of the borides are line compounds, and others have relatively narrow composition ranges (within a few per cent relative to the stoichiometric composition). In the remaining cases microscopical evidence such as presence of second phases, together with microprobe analysis of the metal lines, was used to fix the composition.

The APFs relative to an elemental boron standard were determined by scanning of the spectrometer (JEOL Superprobe 733, lead-stearate crystal, take-off angle 40°) very slowly in steps of 0.05 mm (0.01788 Å) from 164 mm (58.66 Å) to 214 mm (76.54 Å). In each interval counts were accumulated during 10 s and subsequently transferred to successive channels of a multichannel analyzer (TRACOR Northern, TN 2000). After completion the spectra were stored on floppy disk. During the measurements, an air-jet<sup>1-3</sup> was used to prevent contamination. Previous experience with carbon indicated that the APFs were essentially independent of accelerating voltage; hence, all measurements were carried out at 10 kV only. The stored spectra were processed to obtain the net (background subtracted) integral and peak intensities the ratios of which simply yielded the APFs. Finally, large

---

The authors are at the Laboratory for Physical Chemistry, University of Technology, P. O. Box 513, NL-5600 MB Eindhoven, The Netherlands.

numbers (at least 50) of peak k-ratios were measured at each accelerating voltage for each boride, in some low-absorbing systems between 4 and 30 kV, in others up to 15 kV. These values were multiplied by the appropriate APFs to yield the true integral k-ratios. A total number of 180 accurate integral k-ratios were thus collected.

### *Results and Discussion*

During the integral measurements it was soon discovered that an additional problem arises in the analysis of boron. There are two types of borides:

1. The first group behaves quite similar to the carbides, insofar that only peak shifts and peak shape alterations regardless of the crystallographic orientation of the specimen can be observed. In this case the peak shape alterations can be successfully dealt with by a single and unambiguous APF. Figure 1 shows a few examples of the emission profiles of some members of this group. It is apparent that most of these spectra contain more than one component. One of the nicest examples to demonstrate the need for integral measurements is perhaps BN with its two pronounced satellites which definitely belong to the B K $\alpha$  emission spectrum. The introduction of an APF equal to 1.198 (Table 1) accounts for the presence of these components, which would clearly go unnoticed in a peak intensity measurement.

TABLE 1.--Area/Peak Factors for some borides relative to elemental boron. (Borides represented here do not show peak shape alterations with crystallographic orientation due to polarization effects in B K $\alpha$  emission peak.)

Boride	APF	Structure
B <sub>4</sub> C	1.014	Rhombohedral
BN	1.198	Hexagonal
AlB <sub>12</sub>	1.008	?
Fe <sub>2</sub> B	1.242	Tetragonal
Co <sub>2</sub> B	1.015	Tetragonal
CoB	1.186	Orthorhombic
Ni <sub>2</sub> B	1.059	Tetragonal
LaB <sub>6</sub>	0.898	Cubic
UB <sub>4</sub>	1.028	Tetragonal

2. The second group presents an additional problem in that pronounced peak shifts and shape alterations can be observed depending on crystallographic orientation of the specimen. Both can be seen even within a single crystal of the specimen, merely by rotation of the specimen in a plane perpendicular to the electron beam.<sup>2</sup> Typical peak shifts of 1 m $\mu$  (0.385 Å) are quite common. Apart from these peak shifts, however, a simultaneous variation in peak shape is observed with the narrowest peak and the highest peak intensity at the shortest wavelength; and conversely, the broadest peak and the lowest peak intensity is found at the longest wavelength. A typical representative of this group is TiB with a variation in APF from 0.690 at 67.53 Å to 0.835 at 67.76 Å. The origin of these phenomena must be sought in the presence of polarized components<sup>5</sup> in the emitted x radiation, which can be partly filtered out by the lead-stearate crystal. This filtering action is optimal when the angle of incidence of the x rays on the analyzer crystal is 45°; by sheer coincidence this angle is 42.5° in our spectrometer. Although the presence of polarized components can be expected in all noncubic compounds,<sup>5</sup> only approximately 50% of the investigated borides show these effects.

In general, a sawtooth-like behavior of APF with atomic number of the metal partner was found that is similar to what is found in the carbides<sup>1-3</sup>: the lowest values (down to 0.67) were always found in strong boride formers like Ti and Zr, and the highest values in less stable boride formers like Ni (e.g., up to 1.30 for NiB). These figures underline once more the necessity for integral measurements in ultra-light element analysis.

As a direct consequence of the polarization phenomena one has the choice either of measuring the variation of APF with observed peak position for each compound, or of doing

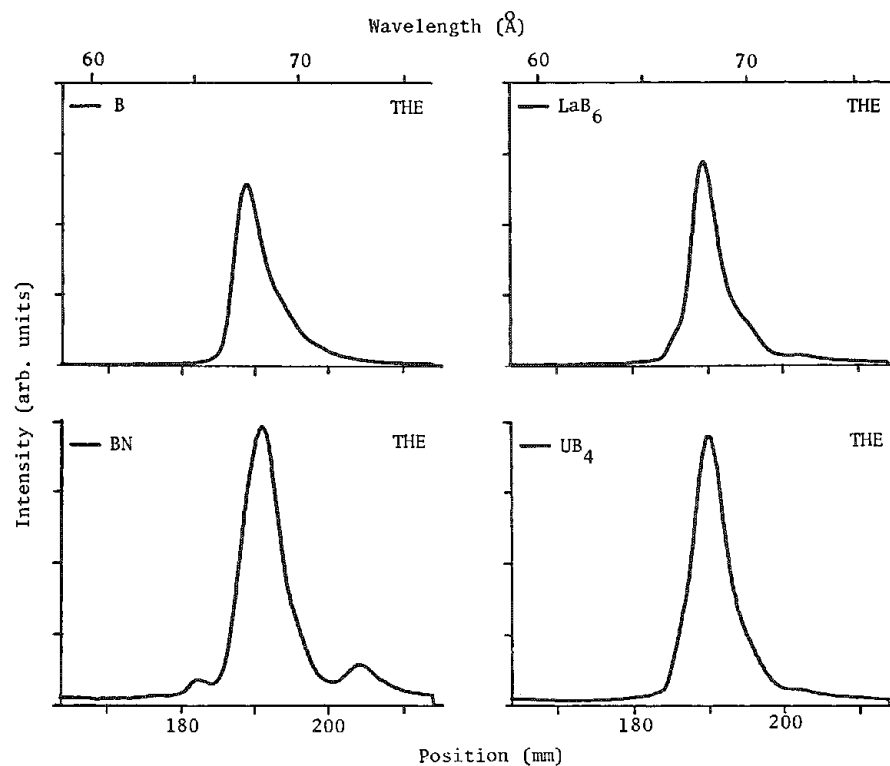


FIG. 1.--Boron  $K\alpha$  spectra emitted by some binary borides in comparison with that of elemental boron. Experimental conditions: 10 kV, 300 nA, lead-stearate crystal.

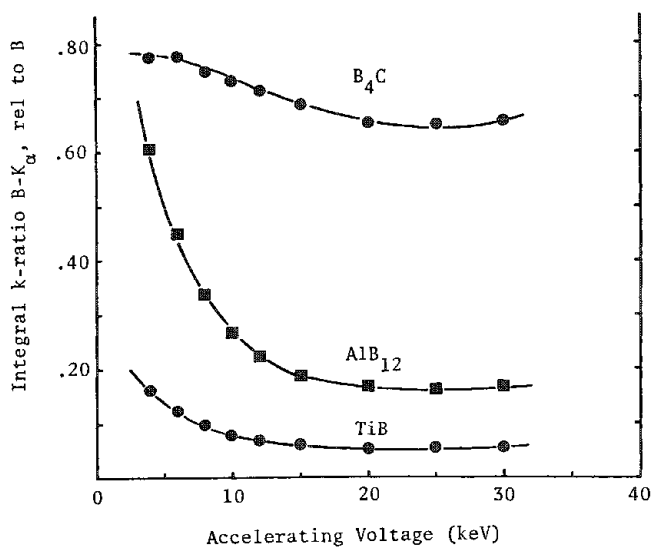


FIG. 2.--Integral k-ratios for three borides relative to elemental boron.  $TiB$  shows pronounced polarization phenomena; the others do not.

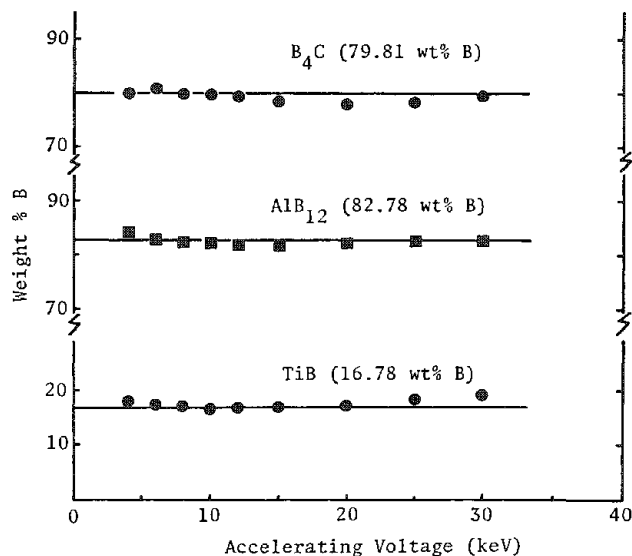


FIG. 3.--Corrected results for the three borides in Fig. 2 according to adapted version of our Gaussian  $\phi(\rho z)$  program. Mass absorption coefficients according to Henke:<sup>4</sup> B  $K\alpha$  in B 3350; B  $K\alpha$  in C 6350; B  $K\alpha$  in Al 64 000; B  $K\alpha$  in Ti 15 300.

each measurement in an integral fashion. We have chosen in favor of the first option and established the variation of APF with peak position for 14 borides. In the subsequent peak intensity measurements care has to be taken to carry out a new peak search for each new crystal in the specimen. After multiplication by the APF appropriate to the observed peak position, the correct integral k-ratio is again obtained.

Figure 2 shows the results of the integral intensity measurements for  $B_4C$  and  $AlB_{12}$ , as representatives of the first, and TiB as a representative of the second group. It is obvious that in spite of the experimental difficulties in the measurements, especially in the case of TiB, highly consistent sets of data can indeed be obtained, even for an extreme light element like boron.

Finally, matrix correction was carried out using a Gaussian  $\phi(\rho z)$  program based on modifications of the original approach of Packwood and Brown.<sup>6</sup> Our usual version<sup>1-3</sup> of this program had to be adapted to the very extreme conditions encountered in the analysis of boron. This adapted version was found capable of dealing with these extreme conditions shown in Fig. 3. In general Henke's<sup>4</sup> mac's were found quite satisfactory with a few exceptions: among other things, the value for Zr is obviously too high. According to 6 current correction programs, the use of Henke's value leads to corrected concentrations of more than 100% too high at 30 kV.

As stated before, an overall rms value of 6.2% could be obtained. In fact, the rms values for each set of measurements were generally much better, with typical values of less than 1% up to 6% in an exceptional case. Some borides, however, notably the Ni borides, seem to exhibit an abnormal low emission of B K $\alpha$  x-rays, leading to corrected concentrations of approximately 0.85 times the nominal concentrations. This result may be perhaps related to typical features in the chemical bond in these compounds. Work to this effect has recently been started in cooperation with experts in this field.

In summary, we may state that it is apparently possible not only to measure boron sufficiently accurately but also to perform accurate matrix correction, which demonstrates that accurate quantitative analysis of boron is possible. More details of the present work will be supplied in future publications.

### References

1. G. F. Bastin and H. J. M. Heijligers, "Quantitative electron-probe microanalysis of carbon in binary carbides," *Microbeam Analysis--1984*, 291.
2. G. F. Bastin and H. J. M. Heijligers, "Quantitative electron-probe microanalysis of very light elements," *Microbeam Analysis--1985*, 1.
3. G. F. Bastin and H. J. M. Heijligers, "Quantitative electron-probe microanalysis of carbon in binary carbides," *X-ray Spec., Part I and II*, 1986, in press.
4. B. L. Henke et al., "Low energy x-ray interaction coefficients: Photoabsorption, scattering and reflection," *Atomic Data and Nuclear Data Tables* 27: 1-144, 1982.
5. G. Dräger and O. Brümmer, "Polarized x-ray emission spectra of single crystals," *Phys. Stat. Sol.* B124: 11, 1984.
6. R. H. Packwood and J. D. Brown, "A Gaussian expression to describe  $\phi(\rho z)$  curves for quantitative electron probe microanalysis," *X-ray Spec.* 10: 138, 1981.

## CONTINUUM RADIATION PRODUCED IN PURE-ELEMENT TARGETS BY 10-40keV ELECTRONS: AN EMPIRICAL MODEL

J. A. Small, S. D. Leigh, D. E. Newbury, and R. L. Myklebust

In analytical techniques based on the measurement of the ratio between characteristic and continuum x rays, a critical step in the quantitative analysis is the accurate determination of the continuum radiation.<sup>1,2</sup> The intensity of the continuum  $I_v$  is a function of the atomic number of the target  $Z$ , the energy of the continuum x rays  $E_v$ , and the energy of the incident electrons  $E_0$ .

The work described in this paper was initiated for two reasons. First, it was observed that significant deviations, greater than 200% relative, were observed between continuum values predicted by various equations in the literature and experimental data generated from a wide number of pure-element targets.<sup>3,4</sup> Second, in the development of an analytical scheme based on peak-to-background measurements it was necessary to determine continuum intensities from elements for which experimental measurements are not possible, such as oxygen and chlorine.<sup>1,2</sup> Because of these limitations, we decided to generate a comprehensive database experimentally and determine an empirical expression for continuum emission by modeling the data.

The data set used in this study consisted of approximately 4100 continuum x-ray intensity values. The targets used in the study were opaque to the electron beam and consisted of 44 pure elements ranging in atomic number from  $Z = 4$  to  $Z = 92$ . Beam energies of 10, 15, 20, 25, 30, 35, and 40 keV were investigated for this study.

The modeling of continuum x-ray production was done on generated x-ray intensities; i.e., the intensity per unit of electron flux produced within the target. The experimental intensities were selected so that they were free of characteristic and escape peaks as well as other major spectral artifacts.<sup>5</sup> The calculation of the generated continuum x-ray intensities from experimental x-ray intensities required correcting the data for absorption of x-rays by the target material and the detector, electron backscatter loss, and anisotropic x-ray generation. No corrections were made for the escape of Si x rays from the detector, incomplete charge collection, and the absorption of x rays in the 20nm-thick carbon coat on the sample.

The final equation represents an empirical fit to experimental data and does not include a geometric efficiency term. The calculated continuum intensities are in units of photons/coulomb-Δ energy. As a result, the coefficients of  $M$  and  $B$  in Eq. (1) will have different numerical values for different detectors.

Our basic approach in developing a parametric empirical model to describe the data was to employ graphical methods to analyze the data by plotting various portions of it in 2-, 3-, and 4-D representations. For this work  $I_v$  was consistently used as the dependent variable. The 2-D plots referenced above refer to plots of  $I_v$  vs  $Z$  at constant  $E_v$  and  $E_0$  or plots of  $I_v$  vs  $E_v$  at constant  $Z$  and  $E_0$ . The 3-dimensional plots are  $I_v$  vs  $Z$  and  $E_v$  at constant  $E_0$  with  $E_0$  as the fourth dimension. These plots could then be fit in an iterative fashion with models suggested by the observed shapes. The modeling was done with the DATA-PLOT program.<sup>6</sup> The 2-D plots were modeled first. The information from the fits run on the 2-D plots was then combined to model the 3- and 4-D surfaces. A more detailed discussion of the modeling procedure will appear elsewhere.<sup>7</sup>

The formulation of the final equation is based on three observations:

The first observation is that it is necessary to transform the experimental intensity values (i.e., the dependent variable) for variance stabilization before modeling is possible. In addition to transforming the dependent variable  $I_v$ , we found it useful for modeling purposes to transform the independent variables  $E_v$ ,  $E_0$ , and  $Z$  as well. After considering various power transformations between 0.5 and 0, with 0 corresponding to a square-root transformation, we finally settled on a consistent use of the log throughout. The log transformation gives a generally smoother, more linear transformation of the 3-D subsurfaces and consistently yields structure in the 2-D plots that can be modeled. The main objective in transforming the dependent and independent variables is to simplify the shapes of the 2- and 3-D projections of the 4-D surface used for fitting. The ideal situ-

---

The authors are at the National Bureau of Standards, Gaithersburg, MD 20899.

then be used to develop an equation describing the untransformed intensities.

The second observation is that the family of lines of  $\ln I_v$  vs  $Z^c[(E_0/E_v) - 1]^d$  representing the various  $E_v$  values at a given  $E_0$  value coalesced into a single straight line at unique values of  $c$  and  $d$ , with the values of maximum coalescence being  $c = 1.0$  and  $d = 1.0$ , respectively. An exponent value of 1.0 supports Kramers's formulation for the independent variable rather than power transformations proposed by other workers.<sup>4,8</sup> That does not imply a verification of Kramers's "law," only the form of his independent variable. In our work, the relation between  $\ln I_v$  and  $\ln \{Z[E_0/E_v] - 1\}$  is a straight-line function containing both a slope and intercept, which are functions of  $E_0$ .

The third observation is that the fitted slopes and intercepts from the 7 linear functions relating to  $\ln I_v$  to  $\ln \{Z[E_0/E_v] - 1\}$  at each value of  $E_0$  are themselves highly linear in  $E_0$  but only after the experimental intensities for anisotropic x-ray generation are corrected by means of Monte Carlo calculations.<sup>9</sup> After straight lines are fitted to the slope and intercept curves, the final model can be expressed in photons/coulomb-per 10eV energy window as:

$$\ln I_v = \frac{M}{10^5} \left\{ \ln \left[ Z \left( \frac{E_0}{E_v} - 1 \right) \right] + B \right\} \quad (1)$$

where  $M = 0.0060E_0 + 1.047$ ,  $B = -0.032E_0 + 5.799$ , and the uncertainties in the  $M$  and  $B$  coefficients, expressed as  $3\sigma$  ranges, are:

$$\begin{aligned} M &= 0.0060 \pm 0.0007 \\ &\quad 1.047 \pm 0.018 \\ B &= -0.032 \pm 0.004 \\ &\quad 5.799 \pm 0.011 \end{aligned}$$

Equation (1) is not a restatement of Kramers's relation, but does confirm the utility of Kramers's variable (overvoltage times atomic number) and the use of exponents of unity on the  $Z$  and  $[E_0/E_v] - 1$  factors in that variable. However, Eq. (1) goes beyond Kramers by including an additional multiplicative factor and additive term, linear in beam energy, which make it a global model for continuum intensity over the range of  $E_0 = 10$ -40 keV, which Kramers's relation is not.

The performance of Eq. (1) in predicting the experimental intensity over all ranges of  $E_0$  and  $E_v$  is shown in Fig. 1(a), which is a histogram of the deviations between experimental and predicted intensity values, normalized to experimental values, in untransformed space. This plot shows a symmetrical distribution centered around zero error with 63% of the values falling between  $\pm 10\%$  relative error. The performance of Kramers's equation, which models the data substantially better than other "global" equations, is shown in Fig. 1(b). This plot shows a significantly poorer fit to the data, with almost 50% of the values exceeding 50% relative error; and we have incorporated an energy dependence into Kramers's "constant," fitting a separate constant for each  $E_0$ , without which Kramers's model produces even larger errors when the entire data set is fitted.

The new relation, given by equation 1, can be summarized as follows:

$\ln I_v$ , with  $I_v$  adjusted for anisotropy effects, is linear in  $\ln \{Z^c[(E_0/E_v) - 1]^d\}$ , and the fitted line parameters are linear in beam energy.

This relation incorporates the well-known-Kramers's variable  $Z^c[(E_0/E_v) - 1]^d$  into a global model used for predicting generated continuum intensities over a wide range of accelerating voltages 10-40 keV, atomic numbers 4-92, and x-ray energies 1.5-20 keV. It was determined from the mathematical modeling of an extensive data set that includes a broad range of  $E_0$ 's and  $E_v$ 's and a majority of the pure-element targets usable in electron-beam instruments. It is designed for calculating continuum intensities in analytical procedures, such as those requiring peak-to-background measurements, where the direct measurement of the continuum intensities is impracticable. Error histograms for different ranges of atomic number indicate that the relationship systematically underestimates the intensities for beryllium, boron, and carbon. The reason for this discrepancy is not currently understood. In general, under normal analysis conditions, relative errors smaller than 20% can be expected for intensities calculated with this equation.



## References

1. J. A. Small, K. F. J. Heinrich, C. E. Fiori, R. L. Myklebust, D. E. Newbury, and M. F. Dilmore. *Scanning Electron Microsc.* 1: 445, 1978.
2. P. J. Statham and J. B. Pawley, *ibid.*, p. 469.
3. H. A. Kramers, *Phil. Mag.* 46: 836, 1923.
4. D. G. W. Smith and C. M. Gold, *X-ray Spect.* 4: 149, 1975.
5. C. E. Fiori, R. L. Myklebust, and D. E. Newbury, *Microbeam Analysis in Biology*, 1979, 225.
6. J. J. Filliben, *Comp. Graphics* 15: 199, 1981.
7. J. A. Small, S. D. Leigh, D. B. Newbury, and R. L. Myklebust, "Modeling of electron-induced bremsstrahlung emission from solid targets" (in preparation).
8. T. S. Rao-Sahib and D. B. Wittry, *Proc. 6th Intern. Conf. X-ray Optics and Microanal.*, 1972, 131.
9. R. L. Myklebust, D. E. Newbury, and H. Yakowitz, *NBS Special Publication 460*, 1979, 105.

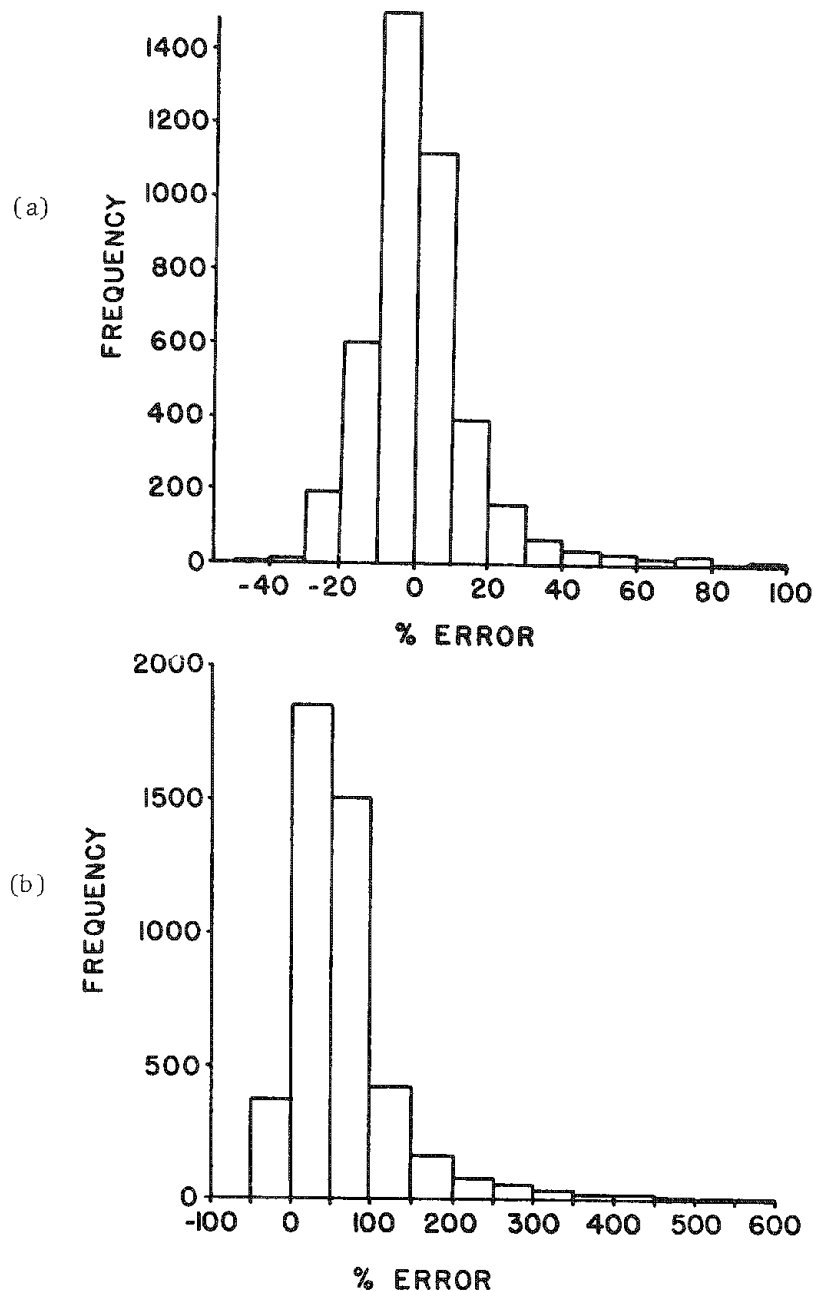


FIG. 1.--Error histograms comparing (a) empirical model, (b) Kramers's equation to data.



## ON THE POTENTIAL APPLICATIONS OF ARTIFICIALLY STRUCTURED MATERIALS FOR X-RAY MICROANALYSIS

A. D. Romig Jr.

A new class of materials known as artificially structured materials (ASMs) has recently received a great deal of attention and has become the subject of substantial research efforts in the solid state physics and materials science communities.<sup>1</sup> These materials are artificially structured on the atomic scale and exhibit properties uniquely different from those found in naturally occurring or conventionally processed materials. Recent advances in high-vacuum-deposition techniques have made these materials possible, since the manufacture of ASMs requires very clean environments and the capability to deposit layers with thicknesses ranging from fractions of 1 nm to a few nanometers. ASMs have been made from semiconductors, metals, metal-semiconductor combinations, and metal-nonmetal combinations. The ASMs produced by layering high atomic number (Z) metals and low-Z nonmetals or metals have unique x-ray interaction properties in that they can be used to produce normal-incidence x-ray mirrors. The objective of this paper is to review this new class of materials, with special emphasis on the high-Z/low-Z multilayer materials; describe applications for these materials currently in use for microanalysis; and suggest future applications that should be considered by the x-ray microanalysis community.

### *Structure and Properties of Artificially Structured Materials*

There are several structural types of ASMs, distinguished by the crystallographic correspondence between the layers (Fig. 1).<sup>1,2</sup> The first type are the incoherent multilayers, in which the interface between the layers is totally incoherent. The materials used to produce each layer may both be crystalline, or one but not both of the two materials may be amorphous. The ASMs that have been used for x-ray optics applications belong to this class. The second category are the compositionally modulated materials (CMM), or in the case of an all-metal system, compositionally modulated alloys (CMA), which have no discrete layer interfaces but rather a sinusoidal variation in composition through the thickness of the film. The final category are the artificial superlattices (AS) in which the composition changes abruptly at the layer interface although the interface exhibits some degree of coherence.

The properties of each category of ASM are unique; the specific properties depend on the type of ASM and the materials used to form the layers. Since it is not the objective of this paper to review ASMs in detail, a thorough review of the materials that fall into this category is not warranted. However, for the sake of completeness, and to give the reader an appreciation of the extent of the technology, a brief review of specific types of ASMs developed to date is appropriate.

*Semiconductors.* Semiconductors are the most widely studied ASM materials. Those of highest structural quality have been produced from semiconductors, the category of ASMs most likely to have a major economic impact in the near future. One very interesting subset of the semiconductor ASMs are the strained layer superlattices (SLS).<sup>3</sup> The materials used in each layer have significantly different lattice parameters, but the layers are coherent, which induces significant strain in the lattice. The strains interact with and alter the electronic structure of the material and produce semiconductors with properties far different from those of the pure materials used for each individual layer. Among the materials used to produce this type of ASM are Si-SiGe, GaAs-GaAsP, InSb-GaSb and GaAs-InAs.<sup>1</sup>

*High-Z/Low-Z Multilayers.* This category of ASM, the focal point of the current paper, is interesting because of the way in which they interact with x rays.<sup>11-15</sup> These materials have been used successfully to produce normal incidence x-ray mirrors with reflectivities

---

The author is with Sandia National Laboratories, Albuquerque, NM 87185. This work was performed at Sandia National Laboratories, supported by the U.S. Department of Energy under contract De-AC04-76DP00789.

exceeding 60%. As described below, the technology to produce these materials is well established and the principles of x-ray interactions with these materials are well understood.<sup>16-17</sup> As such, the author believes that it is appropriate to consider the development of applications of these materials for use in electron-column and x-ray beam instruments. The first application of these materials to x-ray microanalysis, as high-efficiency Bragg diffracting crystals for long-wavelength x rays in wavelength-dispersive spectrometers, is already commercially available.<sup>18,19</sup>

### *Processing and Characterization of Artificially Structured Materials*

Several deposition techniques have been used to produce ASMs, including the high-Z/low-Z multilayers. These techniques have recently been reviewed in detail by Falco and Schuller.<sup>2</sup> Briefly, these deposition techniques are thermal and electron-beam evaporation, molecular-beam epitaxy (MBE), ion sputtering, and chemical vapor deposition (CVD). MBE produces the layers with the greatest accuracy and finest surface finish. The requirements for semiconductor ASMs are the most stringent, and MBE is the technique of choice to produce these materials. MBE does not produce metallic superlattices or high-Z/low-Z multilayers with the same precision as it does semiconductors. In fact, for these materials evaporative and sputtering processes produce final structures comparable to those produced by MBE. Fortunately, the level of perfection required to produce the desired properties in metallic superlattices or high-Z/low-Z multilayers is not as great as that required for semiconductors. As a consequence, most metallic superlattices and high-Z/low-Z multilayers are not produced by MBE, but rather by a more economical evaporation or sputtering process.<sup>16</sup> As will be illustrated later, the control of layer thickness in high-Z/low-Z multilayers is critical, requiring in situ measurement of deposited layer thickness. X-ray reflection techniques, and more recently ellipsometry, have been used to monitor and control layer thickness.<sup>16</sup>

### *Fundamentals of X-ray Optics*

X rays, like other forms of electromagnetic radiation, can be reflected from solid surfaces under the appropriate conditions. In general, there are two types of mirrors which can be used to reflect electromagnetic radiation: single-interface mirrors and transparent-multilayer mirrors.

Single-interface mirrors are the type most commonly encountered. The standard metalized glass mirror used to reflect visible light is a single-interface mirror. These mirrors utilize a highly absorbing material that attenuates the incident radiation over a depth of less than one integral wavelength, and a surface finish comparable to the wavelength of the incident radiation. A highly polished metal satisfies these criteria for electromagnetic radiation in the visible-light range and therefore can be used for a normal-incidence mirror. However, no materials are known which satisfy these criteria for electromagnetic radiation in the 0.1-10nm range (x rays and high-energy ultraviolet). X rays with wavelengths less than 1 nm typically penetrate several micrometers into a material; softer x rays and ultraviolet rays in the 1-10 nm range may penetrate up to 100 nm. It is thus not possible to produce efficient single-interface normal-incidence mirrors for x rays and hard ultraviolet rays. The best single-interface mirror can reflect x rays with a wavelength of 5 nm at an efficiency of less than 0.01%. At shorter wavelengths, the reflectivity decreases with wavelength with a fourth-order power law.<sup>11</sup>

Although it is not possible to reflect x rays at normal incidence from single interface mirrors, they can be reflected at grazing or glancing incidence, as was first demonstrated by Compton in 1922.<sup>17</sup> Grazing-incidence reflection is actually a familiar phenomenon. The reflection of visible light at oblique incidence from the surface of a pool of water is an example of glancing-incidence reflection. (The same phenomenon is responsible for the total internal reflection of light in an optical fiber.) In the case of visible light, total internal reflection is possible since the oblique angle of incidence is still relatively large due to the significant difference in the refractive index of the glass relative to air or a vacuum. However, the refractive indexes for x rays in a solid material and in a vacuum are almost identical. Consequently, the grazing angle is very small. The grazing angle, in degrees, would have to be of the order of the 0.01 of the wavelength of the x ray measured in nanometers. Total internal reflection of x rays is therefore not possible. However, total external reflection from planes, large hemispheres, or hyperbolas

of revolution is possible. Such grazing incidence x-ray mirrors are used as beam splitters for synchrotron lines and in astronomical x-ray telescopes.<sup>17</sup> Grazing-incidence mirrors would be of little use in x-ray microanalysis or electron-beam instruments because they are physically large and suffer from a number of severe aberrations, especially astigmatism, spherical aberration, and coma.<sup>17</sup>

The second type of mirrors are the transparent multilayer mirrors. These mirrors reflect electromagnetic radiation at any angle of incidence, including normal incidence. However, each mirror reflects efficiently only over a very small range of wavelengths. Such mirrors can be used not only to reflect electromagnetic radiation, but also to discriminate wavelengths. Mirrors of this type are made for optical light from layers by different dielectrics. These mirrors are wavelength selective and reflect wavelengths only over a narrow range (i.e., they reflect only a certain color of visible light). Such mirrors reflect electromagnetic radiation because a small amount of the incident wave is reflected at each interface. If the layers are properly spaced, the components reflected from each interface add through constructive interference and result in significant total reflection. To work efficiently, the layer spacing must be carefully controlled and the layer materials must be chosen so that there is sufficient penetration through enough layers to produce significant total reflection. Optical multilayer mirrors have been produced for many years, but it is only recently, through the development of advanced deposition techniques, that multilayer x-ray mirrors with reflectivities in excess of 60% have been produced.

#### *Normal-incidence X-ray Mirrors*

Normal-incidence x-ray mirrors are made with high-Z/low-Z multilayer materials. A small amount of the incident wave is reflected at each high-Z/low-Z layer interface. The reflection is from the high-Z material, with the low-Z materials acting as spacers to separate the high-Z reflecting surface. If the layer spacing is proper, the reflected components add through constructive interference. Although a detailed mathematical description is not appropriate, it is instructive to consider the fundamental aspects of the reflection of x rays by multilayer materials.

If the reflectivity of an x ray from a single interface  $r$  is approximately 0.01% (0.0001) (corresponding to a reflected amplitude of  $r = 0.01$ ), then to obtain a total reflectivity of 1, 100 reflecting interfaces would be required. Generalizing this calculation yields an estimate for the minimum number  $N_{\min}$  of layer pairs (2 interfaces per pair) required to produce unit reflectivity,

$$N_{\min} = 1/(2r) \quad (1)$$

However, to obtain high total reflectivities it is not sufficient simply to build a mirror with the number of layers calculated from Eq. (1). The x rays are absorbed in the medium, and if the absorption is sufficient, they do not penetrate through a sufficient number of layers to produce the desired total reflectivity. For an ideal case in which the thickness of the layer pair is the integral wavelength, the maximum number of periods  $N_{\max}$  that can contribute to the reflectivity is given by

$$N_{\max} = \frac{1}{2\pi k} \quad (2)$$

where  $k$  is the average absorption coefficient for the multilayer.<sup>11</sup> The variation of  $N_{\min}$  and  $N_{\max}$  with wavelength for Re-C and Ni-C is shown in Fig. 2.<sup>11</sup> Over certain ranges of wavelength, these mirrors exhibit high reflectivities (Fig. 3).<sup>11</sup> Both materials show a high reflectivity, greater than 40%, for x rays with wavelengths greater than the carbon K edge (4.48 nm). High reflectivities, greater than 30%, are also observed for wavelengths shorter than 2 nm and 1.4 nm for Re-C and Ni-C, respectively. At certain wavelengths, the reflectivities for these mirrors exceeds 50%. For very short wavelengths (< 1 nm), the reflectivities can approach 100%, since the x rays are not efficiently absorbed in the multilayer materials. However, for good normal-incidence reflectivities of short-wavelength x rays, a large number of multilayers, precisely deposited, is required.

The quality of the finish of the mirror surface and the interfaces between the layers

must be good. To obtain ideal performance, the surface finish of each layer must be better than  $1/20$  of the incident x-ray wavelength.<sup>16</sup> Further, the surface finish of the substrate must be better than 1 nm, RMS.<sup>19</sup> These surface constraints highlight the need for very precisely controlled deposition processes.

Successful normal-incidence x-ray mirrors have been manufactured at several laboratories.<sup>11,19</sup> Mirrors tuned to reflect x rays with wavelengths ranging from 0.05 to 30 nm have been constructed and tested.<sup>16,21</sup> However, most of the mirrors made to date have been planar. Barbee and Underwood described a spherical mirror tuned to 4.48 nm used for x-ray imaging, which they produced by depositing the multilayer on a silicon wafer bent into a spherical shape.<sup>21</sup> Ferris manufactured high-Z/low-Z multilayer toroidal strips possessing a slight radius of curvature for use as a focusing Bragg crystal.<sup>19</sup> Complex geometries, such as parabolas and hyperbolas of revolution, have not been manufactured.

#### *Current Applications of Normal-incidence X-ray Mirrors in Electron-column Instruments*

High-Z/low-Z multilayer mirrors have been made from several material combinations including Ni-C, W-C, Re-C, ReW-C, Mo-Si, and W-Si. Which multilayer combination is chosen for a given application depends primarily on the wavelength of the x ray to be reflected.

Several manufacturers have produced x-ray mirrors as replacement Bragg diffracting crystals for wavelength-dispersive spectrometry.<sup>18,19</sup> Used in this configuration, the mirrors are usually referred to as x-ray dispersive mirrors. The multilayers become, in essence, a Bragg crystal with an artificially controlled d spacing. W-Si multilayers are used to diffract the K lines of O and N; W-C multilayers are used to diffract the K lines of C and B. The advantage of the artificial multilayers over conventional diffracting crystals lies in their efficiency. For example, a properly tuned W-C multilayer will yield peak diffracted intensities 3 to 4 times greater than those obtained from conventional lead stearate crystals.<sup>19</sup>

#### *Future Potential Uses of Normal-incidence X-ray Mirrors in X-ray Microanalysis*

A number of interesting future applications of x-ray mirrors for use in x-ray microanalysis and electron-column instruments exist. All the applications that come to mind require the production of a mirror with focusing capability. The difficulty in constructing such devices will be in manufacturing the focusing mirror with the proper geometry.

One possibility is the use of a parabolic mirror in the electron microprobe or scanning electron microscope to focus long-wavelength x rays from light elements onto a detector. Such a mirror would have a very large angle of collection, which would greatly increase the measured x-ray count rate. The reflected x rays could be focused onto a conventional proportional counter, thus avoiding the development of a new detector system. If properly configured, such a mirror could also be focused onto a thin-window energy-dispersive spectrometer (UTW-EDS) and so allow the acquisition of all x rays simultaneously. Since low-Z elements have low fluorescence yields, the number of measurable x rays is always smaller than desirable. The use of such a mirror would not increase the total production of x rays, but would allow more of the x rays generated in the sample to be counted and improve the total counts, and so reduce the elemental detectability limit and improve the statistics of analysis.<sup>23</sup> X-ray line interference would be avoided since the mirrors would selectively reflect only the wavelength of x ray for which it was tuned, which would allow for elemental discrimination.

The parabolic mirror might also be used to collect x rays in the analytical electron microscope (AEM) in a similar way. Wavelength-diffracting crystals have not found much use in AEMs owing to their inherent low efficiency, mechanical complexity, and geometrically constrained small collection angle. However, a parabolic mirror properly designed and used in conjunction with a proportional counter or UTW-EDS may provide a means for light-element analysis superior to conventional UTW-EDS or electron energy loss spectroscopy (EELS). In a more complicated design, various mirrors could be used to focus selectively the x ray of interest onto the proportional counter or UTW-EDS.

In a totally different application, focusing optics could perhaps be used to produce a micro x-ray fluorescence (XRF) instrument. Beam size in the XRF is currently limited by slits and apertures. For high spatial resolution, a small aperture is required. Although spatial resolution is improved, the resulting low x-ray count rate has serious detrimental statistical consequences. Perhaps focusing optics could be used to reduce the incident

beam diameter without a loss in incident x-ray intensity. Such a device could have excellent lateral spatial resolution. Spatial resolution in the depth direction would not be improved since only the sample, not the XRF unit, limits the depth of x-ray penetration into the sample.

### Summary

The objective of this paper has been to review the current technology of ASMs, with specific emphasis on the high-Z/low-Z multilayers used in normal-incidence x-ray mirrors. Much of the recent work has not been formally presented to the microanalysis community and therefore many of its members are unaware of this body of technology. Perhaps the material and suggestions made in this paper will encourage the community to consider what applications these new materials may have in x-ray microanalysis. This laboratory plans to pursue some of the ideas presented here, and it is hoped that these studies as well as those undertaken at other laboratories may lead to a new and useful class of electron optical/x-ray microanalytical devices.

### References

1. *Report of Artificially Structured Materials*, report to the National Research Council by the Panel on Artificially Structured Materials, Washington: National Academy Press, 1985.
2. C. M. Falco and I. K. Schuller, "Artificial metallic superlattices," in G. W. Crabtree and P. Vashishta, Eds., *Novel Materials and Techniques in Condensed Matter*, New York: Elsevier, 1982, 21-34.
3. J. M. Gibson and L. R. Dawson, Eds., *Layered Structures, Epitaxy, and Interfaces*, Materials Research Society Symposia Proceedings, vol. 37, 1985.
4. A. L. Greer and F. Spaepen, "Diffusion," in L. L. Chang and B. C. Giessen, Ed., *Synthetic Modulated Structures*, New York: Academic Press, 1985, 419-485.
5. I. K. Schuller and C. M. Falco, "Superconducting properties of metallic heterostructures," *Synthetic Metals* 5: 205-216, 1983.
6. I. Banerjee and I. K. Schuller, "Transition temperatures and critical fields of Nb/Cu superlattices," *J. Low Temperature Physics* 54: 501-518, 1984.
7. A. F. Jankowski and T. Tsakalakos, "The effect of strain on the elastic constants of noble metals," *J. Phys.* F15: 1279-1292, 1985.
8. A. Kueny, M. Grimditch, K. Miyano, I. Banerjee, C. M. Falco, and I. K. Schuller, "Anomalous behavior of surface acoustic waves in Cu/Nb superlattices," *Phys. Review Lett.* 48: 166-170, 1982.
9. W. M. C. Yang, T. Tsakalakos, and J. E. Hilliard, "Enhanced elastic modulus in composition-modulated gold-nickel and copper-palladium foils," *J. Appl. Phys.* 48: 876-879, 1977.
10. D. W. Goodman, "Kinetics of hydrogen absorption by chemically modified Pd(110)," *Surface Sci.* (accepted for publication).
11. E. Spiller, "Multilayer x-ray mirrors, a first step toward the custom design of new materials properties," Proc. 1985 Fall Meeting of the Materials Research Society (to be published).
12. E. Spiller, "Low-loss reflection coatings using absorbing materials," *Appl. Phys. Lett.* 20: 365-367, 1972.
13. J. H. Underwood and T. W. Barbee Jr., "Synthetic multilayers as Bragg diffractors for x-rays and extreme ultraviolet: Calculations of performance," in D. T. Attwood and B. L. Henke, Eds., *Low Energy X-Ray Diagnostics*, New York: American Institute of Physics, 57: 170-178, 1981.
14. N. M. Ceglio, "The impact of microfabrication technology on x-ray optics," *ibid.*, pp. 210-222.
15. B. Vidal and P. Vincent, "Metallic multilayers for x-rays using classical thin film theory," *Appl. Optics* 23: 1794-1801, 1984.
16. A. Dhez, *J. Micros.* 138: 267, 1985.
17. J. H. Underwood and D. T. Attwood, "The renaissance of x-ray optics," *Physics Today*, April 1984, 44-52.
18. D. J. Bleu, Electron Microprobe Technologies Corporation, Valencia, Calif. (personal communication).

19. D. Ferris, Energy Conversion Devices, Troy, Mich. (personal communication).
20. F. E. Fernandez and C. M. Falco, "Sputter deposited multilayer V-UV mirrors," *Proc. Condensed Matter Div. European Physical Society* (to be published).
21. T. W. Barbee and J. H. Underwood, "Solid Fabry-Pérot etalons for x-rays," *Optics Comm.* 48: 161-165, 1984.
22. J. I. Goldstein, D. E. Newbury, P. Echlin, D. C. Joy, C. E. Fiori, and E. Lifshin, *Scanning Electron Microscopy and X-ray Microanalysis*, New York: Plenum Press, 1981.

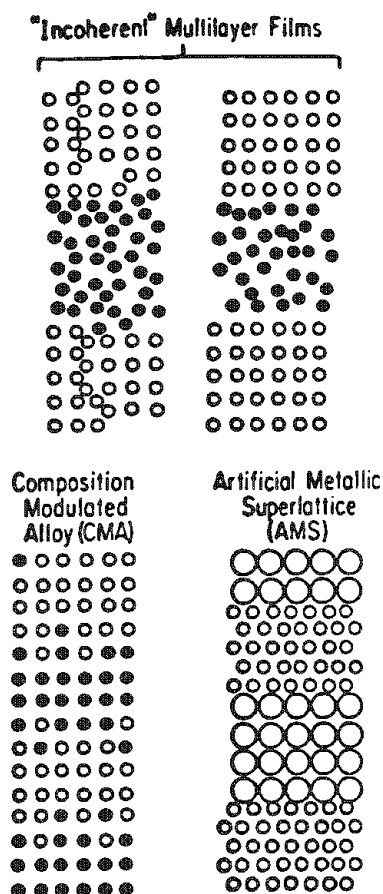


FIG. 1.--Degrees of structural order of artificially structured materials. (Courtesy of C. M. Falco.<sup>1,2</sup>)

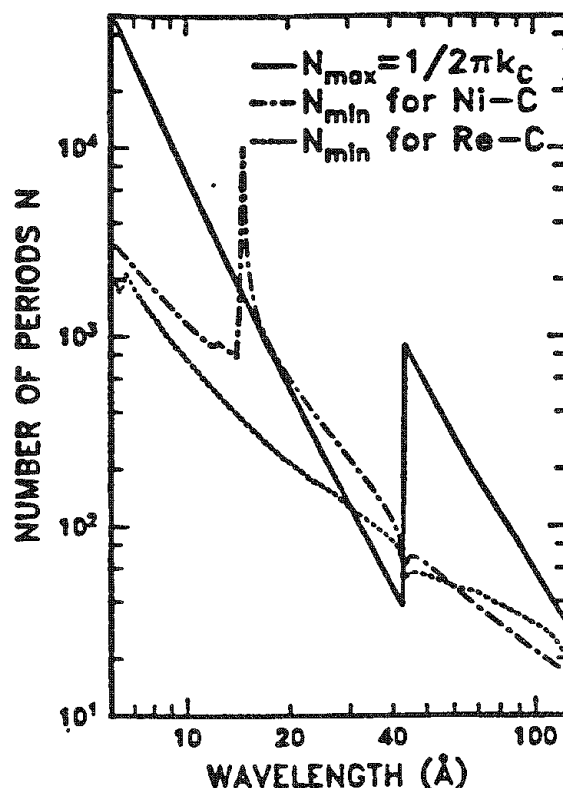


FIG. 2.--Maximum number  $N_{\max}$  of layer pairs possible in multilayer with carbon spacer layer due to absorption of carbon; and minimum number  $N_{\min}$  in Ni-C and Re-C system required for reflectivities that approach 1. (From Spiller.<sup>11</sup>)

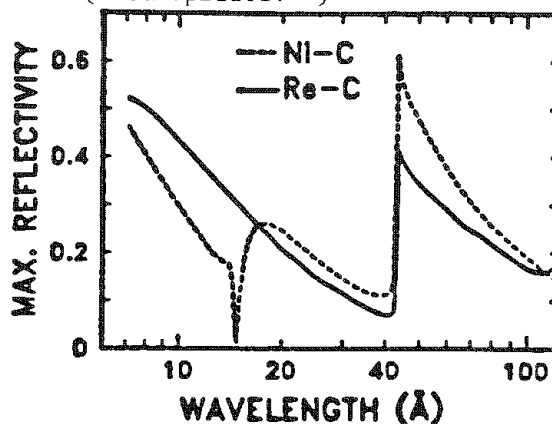


FIG. 3.--Maximum reflectivity obtainable with periodic Ni-C and Re-C multilayers for normal incidence; large number of layer pairs; and smooth, sharp (perfect) layer interfaces. (From Spiller.<sup>11</sup>)



## ALKALI METAL LOSS IN GLASS FROM A CHARACTERIZING ELECTRON PROBE

T. M. Walker and D. G. Howitt

Quantitative analysis of light elements by electron-probe techniques is often complicated by diffusion and desorption processes that accompany the irradiation. During microanalysis, beam currents as low as  $100 \mu\text{A}/\text{cm}^2$  can cause significant depletion in regions close to the surfaces of a material. In sodium silicate glasses, the damage results from an ionization process that can lead to electron stimulated desorption (ESD) or diffusion into the bulk. In other materials, such as the refractory metal carbides, it is thought that displacement events are possible. Regardless of the mechanism, the effects of the damage are similar: compositional changes occur within the interaction volume of the specimen, and these changes are reflected in the x-ray and electron signals that are collected.

The response of glass to electron irradiation has been the subject of several studies; in particular, the depletion of alkali species close to the surfaces has been well characterized. However, the process that leads to the surface depletion is still not understood. The first in a series of models for glass was proposed by Lineweaver.<sup>1</sup> According to his model,  $\text{Na}^+$  is attracted into the bulk by an electrostatic charge set up by the incident electrons that come to rest in the specimen. The charge should therefore accumulate at a depth comparable with the maximum electron penetration, yet this phenomenon has never been observed directly. This simple model is of course only qualitative and cannot be considered a complete description, since the desorption of sodium from the surfaces has been observed by mass spectrometry. A quantitative model must therefore consider electron-stimulated desorption from the surfaces, as well as the variety of enhanced diffusion mechanisms that are capable of transferring material away from the probe.

The contributions to surface depletion by the mechanisms of diffusion and desorption can be modeled by use of finite-element methods to solve the differential equations governing this effect. The calculations are done in much the same way as the calculations for heat flow in complicated geometries. The case of a thin, cylindrical foil characteristic of a uniformly irradiated transmission electron microscope (TEM) specimen has already been investigated by Howitt et al.,<sup>2</sup> who set up a grid as shown in Fig. 1. Using polar coordinates, they modeled a three-dimensional wedge one radian in circumference in two dimensions to account for the mass transfer away from the irradiated region. The number of excited species created by the irradiation in a particular element is the product of the beam current, local atomic density, and cross section for ionization. Since the excited species can have properties distinctly different from the unirradiated species, both species are considered to move independently at rates governed by different diffusion coefficients. The desorption effect is taken into account at the surfaces of the specimen in the same way as excitation, by use of the desorption cross sections for the top and bottom surfaces. To account for enhanced diffusivity in the irradiated matrix, the diffusion coefficients must reflect the formation of vacancies due to irradiation. The measured diffusion coefficients are therefore multiplied by  $[\exp(-\Delta G/kT) + F]/\exp(-\Delta G/kT)$ , where  $G$  is the activation energy for vacancy formation,  $F$  is the fraction of vacant sites,  $k$  is the Boltzmann constant, and  $T$  is the absolute temperature. Such calculations have shown that even for extremely large values of the desorption coefficient, the loss of sodium in thin foils cannot be accounted for without matrix diffusion, because of the slow transport of sodium to the surface. This result may indicate that an enhanced diffusion of all species within the probe region must occur, or that the radiation effect is more substantial than the decomposition to form oxygen defects suggests.<sup>3</sup>

The modeling of bulk specimens differs from that of thin foils in several important respects. First, the relative contribution of desorption occurs only at one surface, which essentially cuts the desorption effect in half. In addition, the energy of excita-

---

The authors are at the Department of Mechanical Engineering, University of California, Davis, CA 95616.

tion events change substantially as the electrons penetrate the sample. There is also the possibility of substantial charge accumulation at the end of the electron range, and the likelihood of field effects.

The modeling of bulk specimens is also complicated by the geometry, because the interaction volume is no longer cylindrical but pear shaped. On the other hand, the detection of low-Z elements in the SEM is facilitated, because of the increased efficiency of collection and of the improved signal-to-noise ratios, especially when wavelength-dispersive spectrometers are used.

### Experimental

High purity soda-silica glass (21.95%Na<sub>2</sub>O, 78.08%SiO<sub>2</sub>) was obtained from the National Bureau of Standards. The glass was prepared into samples by slicing cylindrical sections 1 cm in diameter. For the SEM evaluation, the sections were thinned to a thickness of approximately 2 mm and mounted by means of thermoset resins on a standard aluminum Cambridge stub. The specimens were then coated with a thin layer of carbon to prevent charging during electron bombardment.

The high-soda glass specimens were irradiated in a Cambridge SEM at 20 kV at Microspec Corp. in Fremont, Calif. The Na x-ray signal was recorded with the Microspec WDX-2A wavelength-dispersive spectrometer. The time-dependent sodium signal was recorded for various current densities, by simple adjustment of the area rastered at constant beam current. A beam current of approximately 4.5 nA was used in the experiment.

### Results

The normalized sodium signal versus time and the accumulated sodium signal versus time for four different current densities is shown in Figs. 2 and 3, respectively. At low currents densities (0.3 mA/cm<sup>2</sup>), the initial depletion is slow and takes almost 1 min for a detectable drop in the Na signal. At high current densities (>1 mA/cm<sup>2</sup>), however, the initial decrease in the Na signal is rapid and consistent with previous experimental observation.

The surface depletion is not limited to the rastered area (Fig. 4). This graph shows the surface depletion as measured from the probe center. The sample was originally irradiated at 32 000 $\times$  magnification for 10 min (a current density of approximately 20 mA/cm<sup>2</sup>). At this high electron flux, Na surface concentrations were reduced to 15% of their original bulk concentrations. The interesting result is that the adjacent area was also depleted in Na, as we found by scanning out in steps and taking Na counts for short intervals (<15 s). The bulk concentration was not restored until  $\sim$ 40  $\mu$ m from the probe center. The damage is not confined to a local area and it is evident that a substantial amount of diffusion occurs in the unirradiated material, which indicates that a large sampling volume is necessary to model the depletion accurately.

### References

1. J. L. Lineweaver, *J. Appl. Phys.* 34: 1786, 1963.
2. D. G. Howitt, W. A. P. Nicholson, W. P. Jones, and B. E. Launder, *Inst. Phys. Conf. Ser.* No 78, Chap. 8, 1985, 293.
3. J. F. DeNatale and D. G. Howitt, "Nuclear instruments and methods," *Phys. Res. B*1: 489-497, 1984.

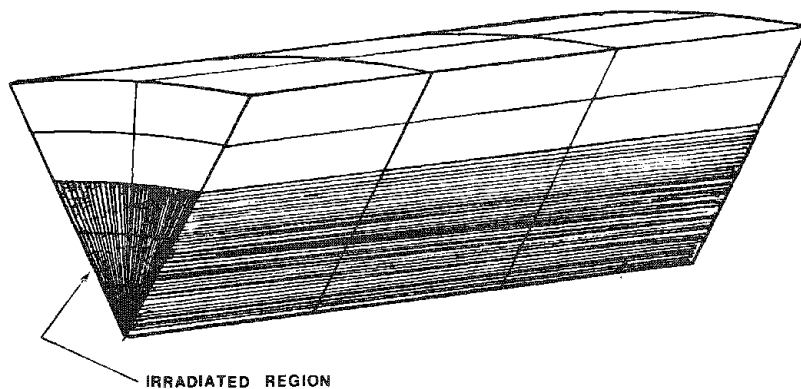


FIG. 1.--Geometry of computer-modeled foil.

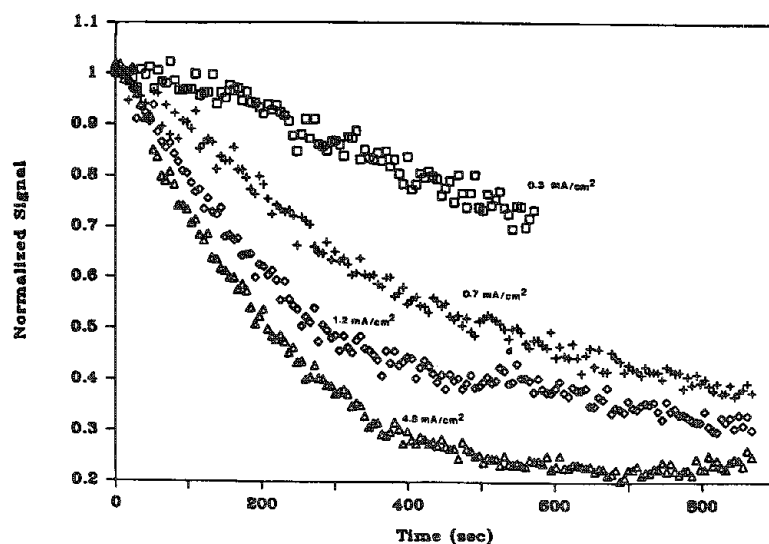


FIG. 2.--Normalized sodium signal vs time.

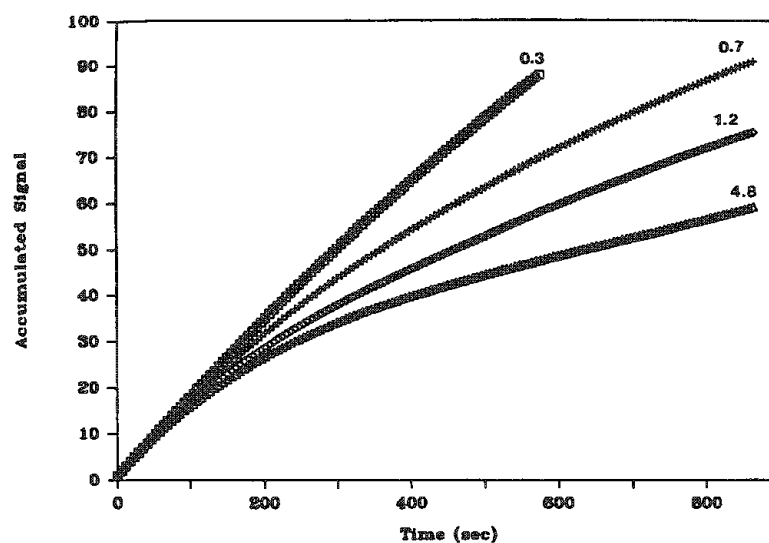


FIG. 3.--Accumulated sodium signal vs time.

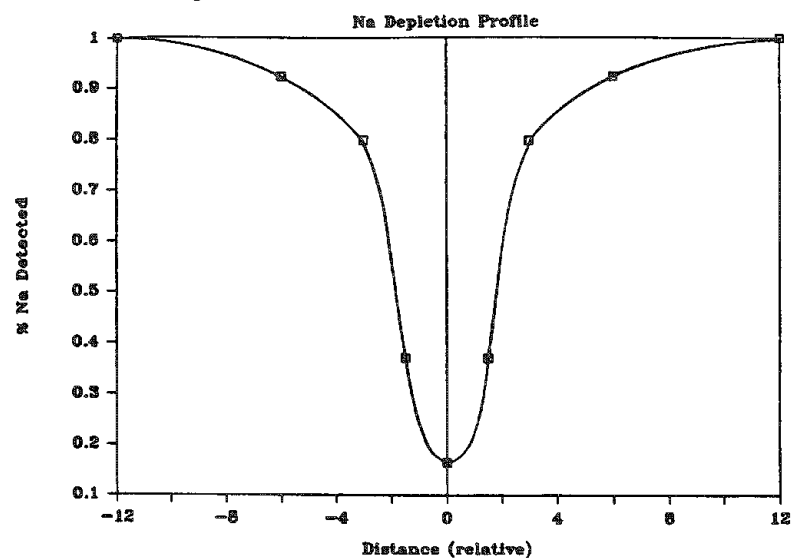


FIG. 4.--Sodium depletion profile as function of distance from probe; 12 relative distance units equal 40  $\mu\text{m}$ .

## THE DEVELOPMENT OF EPMA QUANTITATIVE ANALYSIS IN CHINA

Yong Kang Liu

### *General Situation*

MARK IIA, made by Cambridge Instrument Co. in England in 1964, was the first commercial instrument imported into China. Up to now, about 160 sets of EPMA and SEM with WDX or EDX are being used in all provinces of China, except Tibet. As for microbeam analysis, EPMA is still used as the major method.

### *Calibration Methods*

The calibration procedures for quantitative analysis are the same as abroad. Among them ZAF is the usual method, and the BA method is available for analyzing oxide, silicate, and any nonconductor material, especially for mineral content. Moreover, the Monte Carlo method is still studied by some for thin-membrane samples and special problems.

Two effects, density effect and crystal-direction effect, influence the precision of quantitative analysis and was first proposed by us: the C K $\alpha$  intensity in the synthetic B-diamond is 34% higher than in glassy carbon, and x rays emitted from [111] and [100] of B-diamond exhibit different intensities.

In China, a rather rational method has been suggested for specimens bearing Fe mineral to calculate the content of Fe<sup>2+</sup> and Fe<sup>3+</sup>.

### *Standard Preparation*

As is well known, if the standard matches with the specimen in composition and structure, quantitative analysis is simplified and the results are more precise. Therefore, in recent years, much attention has been paid by CEMS and the Microbeam Analysis Committee of CSMPG to the work of standard preparation.

---

The author is at the Institute of Geochemistry of the Academia Sinica, Guiyang, Guizhou Province, People's Republic of China.

## Materials Applications

### THE INITIATION OF PITTING CORROSION IN MARTENSITIC STAINLESS STEELS

W. R. Cieslak, R. E. Semarge, and F. S. Bovard

The form of localized corrosion known as pitting often initiates preferentially at microstructural inhomogeneities. The pit-initiation resistance is therefore controlled by the characteristics of the initiation sites rather than by the bulk material composition. This investigation correlates the pit-initiation resistance, as measured by critical pitting potentials, with preferred pit-initiation sites for three martensitic stainless steels. Pit-initiation sites are determined by secondary electron (SE) and backscattered electron (BSE) imaging, and energy-dispersive and wavelength dispersive spectrometries (EDS and WDS) with a scanning electron microscope (SEM) and an electron probe micro-analyzer (EPMA).

#### Experimental Procedure

Table 1 lists the bulk compositions of the three stainless steels. They were precipitation-strengthened by solutionizing for 1 h, quenching in oil, aging in a salt pot at 500 C for 1 h, and quenching in water. We prepared samples for corrosion testing by resistance welding a stainless steel wire to the back face, mounting in Maraglas™ resin, and grinding the face to a 600 grit SiC finish. Electroplating tape, used to mask off all but a 0.5cm<sup>2</sup> area, provided a low incidence of crevice corrosion at the edge of the exposed area.

We determined critical pitting potentials by a potentiodynamic polarization technique. We performed this technique (Fig. 1) by first cathodically polarizing the sample from  $E_{corr1}$  down to -1.0 V (referenced to Saturated Calomel Electrode, SCE) using a 1.0mV/s scan rate, then reversing the scan through  $E_{corr2}$  back up to -0.1 V (SCE). Cathodic polarization is commonly employed to provide a uniform starting condition for all samples. Anodic polarization was continued from -0.1V at 0.5mV/s until pitting occurred. The electrolyte was 1.0M NaCl + 0.5M Na<sub>2</sub>SO<sub>4</sub> solution at 30 C. A minimum of five replicate tests were performed.

Pitting for EPMA analysis was created galvanostatically with a 10s scan from 0.1 to 1 mA/cm<sup>2</sup>, followed by a 140s hold at 1 mA/cm<sup>2</sup>. Galvanostatic control tends to enable a greater number of pits of more uniform size to initiate than does potentiostatic control. A finer metallographic polish was used on these samples to allow observation of microstructural details. After being removed from the electrolyte, the samples were rinsed under running water and in methanol. Occasionally, adherent corrosion products remained around the pits. However, pitted samples could not be cleaned ultrasonically because this procedure would cause the collapse of the latticework of covered pits.

The pitted samples were analyzed with a Cameca MBX EPMA equipped with a Tracor Northern EDS detector and a LeMont

TABLE 1.--Alloy compositions (wt%).

	17-4 PH	13-8 Mo	Custom 450
Cr	16.78	12.79	15.01
Ni	3.91	8.35	6.65
Mo	<0.01	2.06	0.65
Cu	3.6	0.01	1.6
Al	<0.01	1.07	0.02
Nb	0.29	0.06	0.63
Si	0.50	0.04	0.36
Mn	0.32	0.06	0.34
C	0.039	0.038	0.043
N	0.031	0.002	0.014
P	0.018	0.009	0.016
S	0.0042	0.0029	0.0044
O	0.0070	0.0013	0.0022

The authors are at Division 1842 and 1822, Sandia National Laboratories, Albuquerque, NM 87185. This work was supported by the U.S. Department of Energy under Contract DE-AC04-76DP00789.

Scientific BSE system. The samples were initially examined in the BSE imaging mode which allowed ease of location of pits and inclusions in the bulk metal matrix through optimization of contrast and brightness. After location of corrosion pits, EDS spectra were first obtained. WDS measurements were then made (15 kV, 22 na, 20a maximum count time, 1 $\mu$ m effective beam diameter) in an effort to discriminate any overlapping elemental energies such as Mo and S and also to verify the presence of carbon and oxygen. Finally, a set of photomicrographs including SE, BSE, and elemental distribution (EDPM) was taken for each stainless steel sample to document the pitting site morphology and chemistry.

### Results and Discussion

The 500 C aging treatment does not affect pitting resistance, as shown by the critical pitting potentials in Table 2. This implies that the finely dispersed precipitates do not influence pit initiation and that no major alloying element segregation occurred (as might be expected for the temperature and time of the treatment). PH 13-8 Mo is more resistant to pit initiation than the other two alloys and 17-4 PH is the least resistant. It is not clear whether this ranking might be expected based on bulk alloy compositions (Table 1). Chromium and Mo have long been known as the most effective alloying elements in promoting pitting resistance<sup>1,2</sup> and more recently the positive effect of N, in solid solution, has been established.<sup>3,4</sup> However, the presence of soluble sulfide inclusions can considerably lower the critical pitting potential.<sup>5-9</sup> Therefore, interpretation of critical pitting potentials requires knowledge of the preferred sites for pit initiation.

TABLE 2.--Critical pitting potentials (mV vs SCE).

	Solutionized Only		500 C Age	
	Average	Std deviation	Average	Std deviation
13-8 Mo	260	19	247	20
C 450	162	15	170	34
17-4 PH	0	14	23	21

The 17-4 PH contains stringers of mixed oxide and sulfide inclusions (Fig. 2). The oxides contain primarily Al and the sulfides are rich in Mn. The pits (arrows) initiate only at sites containing sulfur, as was noted by Szklarska-Smialowska,<sup>5</sup> because oxide inclusions are not soluble or conductive. Each pit grows by undercutting the surface to follow the sulfide boundary (Fig. 3), thereby creating the latticework typical of a covered pit.

The pit morphology in Custom 450, like that in 17-4 PH, is typical of initiation at inclusions. However, the inclusions are much less numerous and do not form stringers. Examination by EPMA revealed no manganese sulfides, which are the most soluble and therefore most effective pit initiators of the commonly observed sulfides.<sup>6</sup> The lack of manganese sulfides is consistent with the higher critical pitting potential for Custom 450 than for 17-4 PH. This difference illustrates that the inclusion content and pitting susceptibility may be significantly different even in two materials with similar impurity concentrations. Residual elements in the vicinity of the pits in Custom 450 include Cu, Nb, C, and trace S. Like oxides, carbides are generally considered innocuous for pit initiation, except in the case of Cr carbides surrounded by matrix Cr depletion. Nb carbides are therefore not expected to act as preferred sites for pit initiation. Because only trace amounts of S are present with the Cu at the pits in the Custom 450, the pit initiation sites cannot be positively identified as sulfide inclusions. Further EPMA investigations are underway to identify the Cu-rich sites.

The most resistant alloy tested, PH 13-8 Mo, exhibits a pit morphology considerably different from that of the other two alloys (Fig. 4). The pits were not associated with any inclusions. Therefore, the lack of soluble inclusions is the reason for the superior pitting resistance of the PH 13-8 Mo.

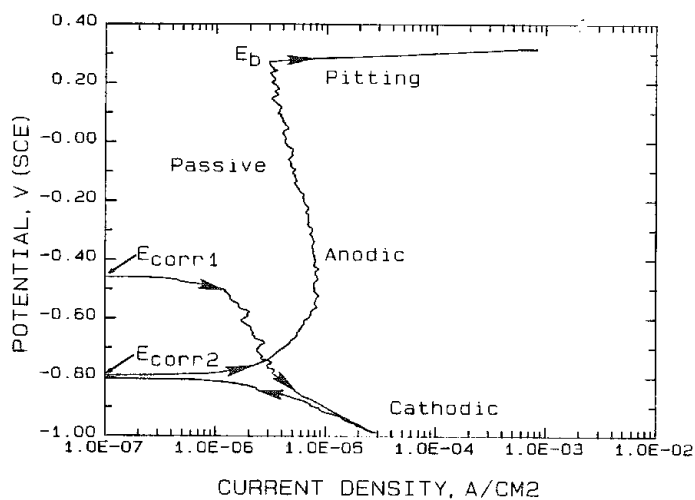
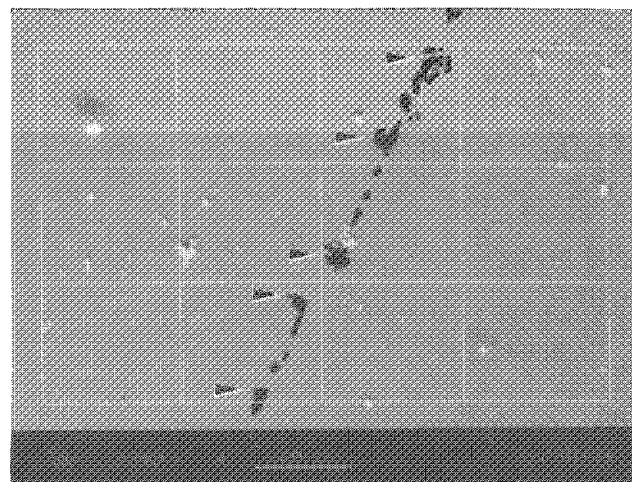
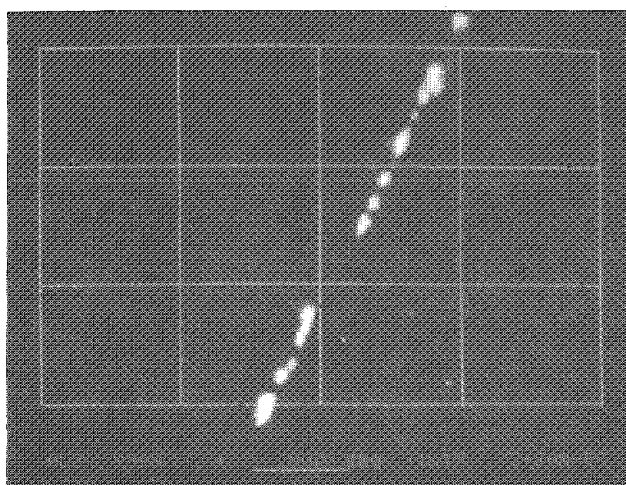


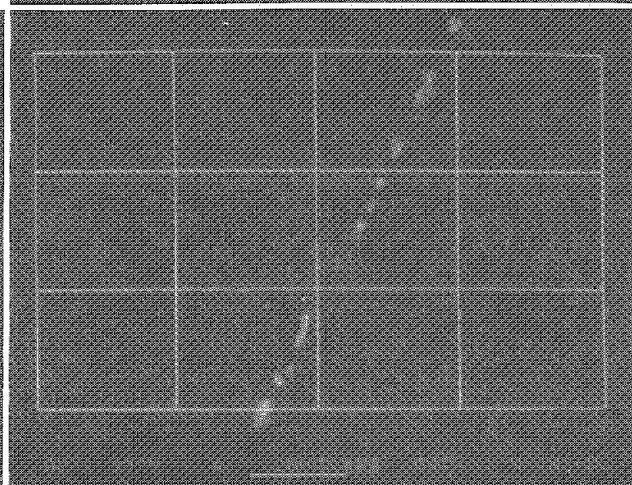
FIG. 1.--Example of determination of critical pitting potential for alloy PH 13-8 Mo by potentiodynamic polarization technique.



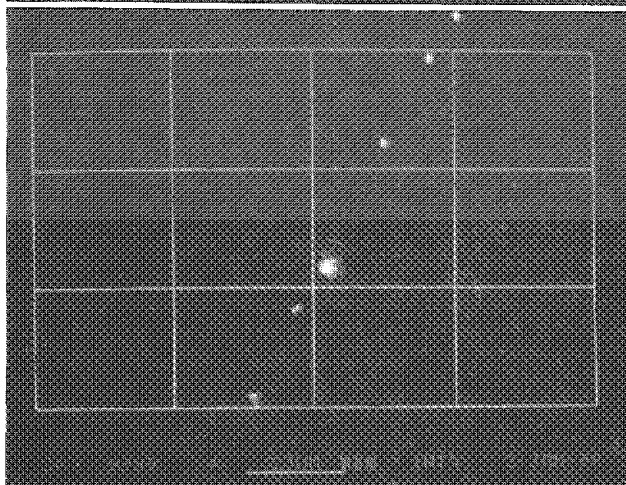
(a)



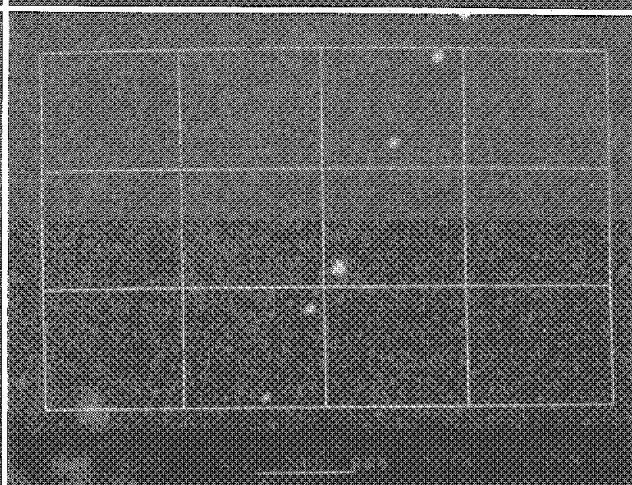
(b)



(c)



(d)



(e)

FIG. 2.--Microprobe analysis of pitting along inclusion stringer in alloy 17-4 PH. (a) SEM photomicrograph, arrows indicate corrosion pits; (b) elemental distribution photomicrograph (EDPM) for Al; (c) EDPM for O--note correlation of O with Al in (b); (d) EDPM for S--note correlation of S with pits in (a); (e) EDPM for Mn--note correlation of Mn with S in (d).

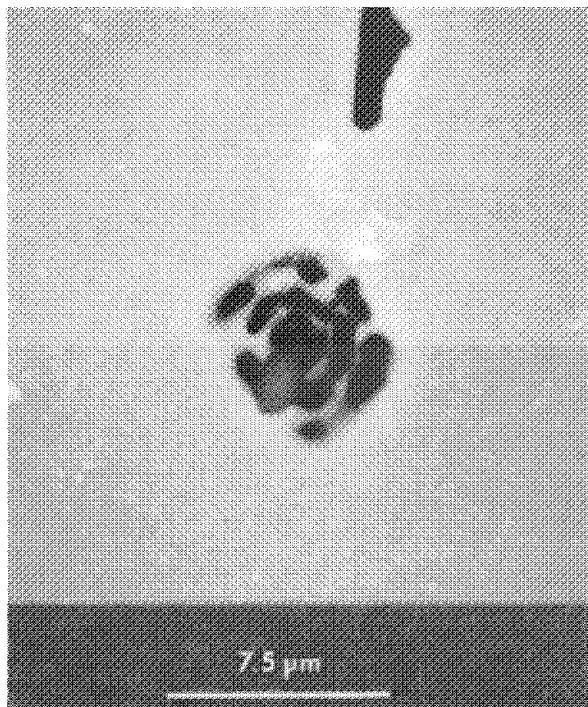


FIG. 3.--Higher-magnification SEM photomicrograph showing detail of centermost pit in Fig. 2.

#### Conclusions

1. The resistance to pit initiation of three martensitic stainless steels has been correlated with alloy inclusion content, as follows:
  - a. The most susceptible alloy, 17-4 PH, suffers pitting at soluble Mn-rich sulfide inclusions.
  - b. Custom 450 is more resistant than 17-4 PH and suffers pitting at sites containing Cu, Nb, C, and trace S.
  - c. The most resistant alloy, PH 13-8 Mo, is free of inclusions that initiate pitting.
2. Heat treatment of these steels for precipitation strengthening does not influence resistance to pit initiation.

#### References

1. J. M. Kolotyrkin, "Pitting corrosion of metals," *Corrosion* 19: 261t-268t, 1968.
2. A. P. Bond and E. A. Lizlovs, "Anodic polarization of austenitic stainless steels in chloride media," *J. Electrochem. Soc.* 115: 1130-1135, 1968.
3. P. E. Manning, "Comparison of several accelerated tests for the determination of localized corrosion resistance of high performance alloys," *Corrosion/82*, NACE meeting, Houston, Paper No. 176, March 1982.
4. R. Bandy and D. Van Rooyen, "Pitting resistant alloys in highly concentrated chloride media," *Corrosion* 39: 227-235, 1983.
5. Z. Szklarska-Smialowska, "Influence of sulfide inclusions on the pitting corrosion of steels," *Corrosion* 28: 388-396, 1972.
6. G. Wranglen, "Pitting and sulphide inclusions in steel," *Corrosion Science* 14: 331-349, 1974.
7. G. S. Eklund, "Initiation of pitting at sulfide inclusions in stainless steel," *J. Electrochem. Soc.* 121: 467-473, 1974.
8. P. E. Manning, D. J. Duquette, and W. F. Savage, "The role of sulfide inclusion morphology in pit initiation of several 300 Series stainless steels," *Corrosion* 36: 313-319, 1980.
9. A. J. Sedriks, "Role of sulphide inclusions in pitting and crevice corrosion of stainless steels," *International Metals Reviews* 28: 295-307, 1983.

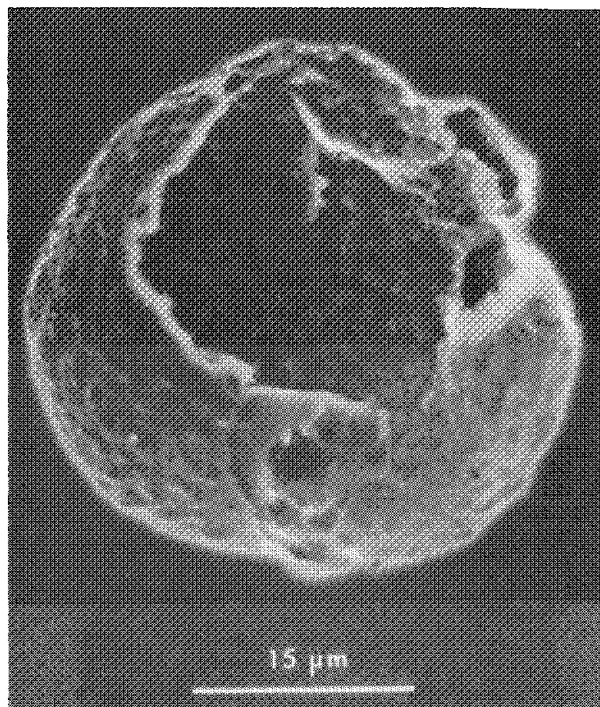


FIG. 4.--SEM photomicrograph showing open hemispherical pit morphology in alloy PH 13-8 Mo, typical of pitting not initiated at inclusions.



## CHARACTERIZATION OF RESIDUES FROM A ZINC PLANT

R. Lastra Q.

Metallurgical wastes of various compositions are generated at various stages of operation in a zinc extraction plant. These residues still contain significant quantities of zinc, lead, and copper. The recovery of these valuables could be of economic significance. As an aid in determining possible process routes for their treatment, a detailed knowledge of the minerals or phases present is required.

### *Jarosite*

Separation of iron from zinc in zinc leaching circuits is usually done by jarosite precipitation in which iron and other impurities are rejected. Composition of jarosite is expressed by  $MFe_3(SO_4)(OH)_6$  where  $M = K^+, Na^+, NH_4^+, Ag^+, \frac{1}{2}Pb^{+2}, H_3O^+$ ; etc.<sup>2</sup> Also it appears<sup>3</sup> that divalent ions such as  $Cu^{+2}$  and  $Zn^{+2}$  may partially replace  $Fe^{+3}$  in the jarosite lattice, producing small but unwanted losses.

The jarosite residue as received was a reddish brown bulk material. Chemical analysis was determined by atomic absorption (AA) and yielded 7.24%Zn, 38.76%Fe, and 1.61%Pb. Size analysis by cyclosizer showed that nearly 90% of the material is  $<10 \mu m$ . X-ray diffraction (XRD) patterns of the cyclosizer products were obtained and the two main crystalline phases were identified: sodium jarosite,  $NaFe_3(SO_4)_2(OH)_6$ ; and zinc ferrite,  $ZnFe_2O_4$ . It was found that the fraction  $\geq 15.2 \mu m$  carried higher proportions of  $ZnFe_2O_4$ . However, AA analysis showed that the  $\geq 8.2 \mu m$  fraction still carried 67% of the zinc contained in the original sample.

Knowing that zinc ferrite shows a paramagnetic behavior it was then decided to determine the magnetic profile of the fraction  $\geq 15.2 \mu m$  by use of a Frantz isodynamic separator. The division of the jarosite residue into a series of products obtained by their different behavior under magnetic field provided a powerful tool for further characterization of the sample, since these Frantz products were less complex than the original residue. Table 1 provides the results of the magnetic separation, together with the XRD intensities in counts per second, of the strongest peak of the two main components. From Table 1 it is possible to see that the zinc ferrite concentration in the magnetics increases as the current increases, up to 250 mA, where the ratio  $I_{100}ZnFe_2O_4:I_{100}Na \text{ jarosite}$  is 40:1. After this point, the magnetics show increasing amounts of jarosite up to 500 mA, where the product is almost only Na-jarosite. Therefore, there are two distinct magnetic products: zinc ferrite and Na jarosite; their corresponding magnetic susceptibilities are  $7.61 \times 10^{-3}$  and  $1.03 \times 10^{-3}$  SI units, respectively. The nonmagnetic of 600 mA contained both zinc ferrite and Na jarosite as minor constituents.

*SEM of the 250mA Magnetic Product.* Figure 1 illustrates the type of particles most frequently encountered. The average EDS Zn/Fe ratio in this type of particles was around 0.6, which suggest that these particles are indeed zinc ferrites. Copper is present mainly at low concentrations; the EDS Cu/Fe ratio most then encountered was around 0.07. Previous studies with zinc ferrites in copper smelter dusts<sup>1</sup> have shown that the amount of copper in the zinc ferrites plays an important role in their magnetic susceptibilities and may increase it to 0.75 SI units when the EDS Cu/Fe ratio is around 0.9.

*SEM of the 500mA Magnetic Product.* Figure 2 shows the typical particles found in this product. Their morphology and EDS peak counts are characteristic of the jarosites. It was possible to find in them variable minor amounts of Cu, Zn, As, and Pb. X-ray mapping for these elements showed an even and intimate distribution in all particles. This result is in agreement with Dutrizac's findings<sup>3</sup> and suggest that these elements are incorporated in the jarosite lattice.

---

The author is a Ph.D. student at the Mining and Metallurgical Department of McGill University, 3450 University Street, Montreal, Canada H3A 2A7.

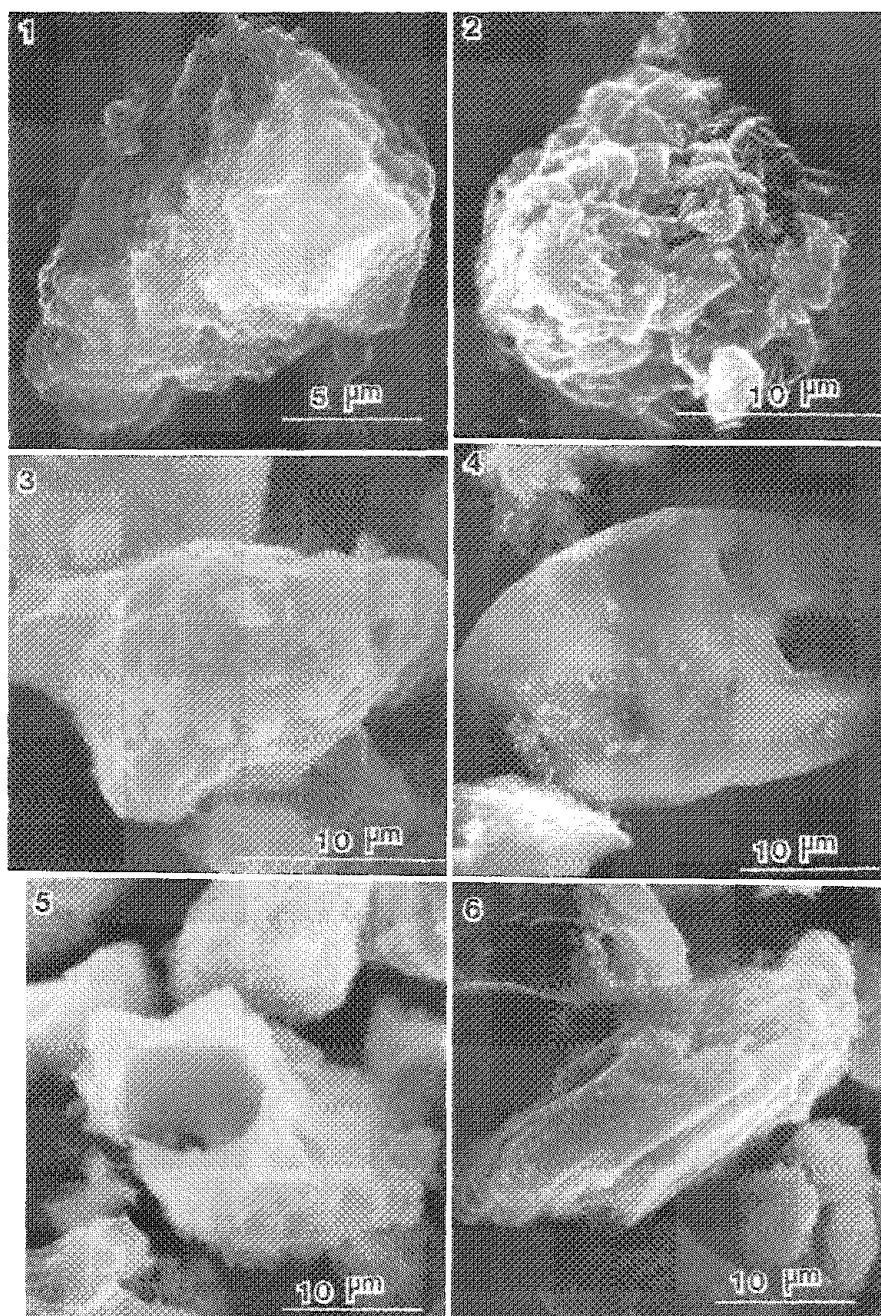


FIG. 1.--EDS peak ratios (EDSPR) to Fe are: Fe 1.0, Zn 0.62; Cu 0.07.  
 FIG. 2.--EDSPR to Fe: Fe 1.0, S 0.11, Cu 0.09, Zn 0.02, Na 0.00109.  
 FIG. 3.--EDSPR to Zn are: Zn 1.0, Fe 0.03, S 0.1.  
 FIG. 4.--EDSPR to Sn are: Sn 1.0, Si 0.03, Cu 0.01, Zn 0.01, Fe 0.01, S 0.0004.  
 FIG. 5.--EDSPR to Si are: Si 1.0, Zn 0.77, Fe 0.32, Cu 0.16, S 0.14, Pb 0.14, Al 0.07.  
 FIG. 6.--EDSPR to Si are: Si 1.0, Al 0.76, K 0.37, Zn 0.31, Fe 0.16, Cu 0.06.

TABLE 1.--X-ray diffraction intensities of two strongest peaks for the two most abundant phases in Frantz products.

Frantz Product	ZnFe <sub>2</sub> O <sub>4</sub> I <sub>100</sub> [cps]	Na-jarosite I <sub>100</sub> [cps]	I <sub>100</sub> ZnFe <sub>2</sub> O <sub>4</sub> I <sub>100</sub> Na-jarosite
Magnetic of 50 mA	981	90	11.0
Mag. of 200 mA	927	80	11.6
Mag. of 250 mA	1133	28	40.0
Mag. of 300 mA	605	136	4.0
Mag. of 400 mA	737	172	4.0
Mag. of 450 mA	77	448	0.2
Mag. of 500 mA	-	560	--
Mag. of 550 mA	-	452	--
Mag. of 600 mA	-	264	--
Final NON--MAG.	84	84	--

*SEM of the Nonmagnetic Product of 600 mA.* The most abundant particles in this product gave large EDS Si counts, which indicated the presence of SiO<sub>2</sub>.

A large variety of other particles were found in this product. Figure 3 shows a particle with EDS counts indicating zinc sulfide. Figure 4 presents a particle with large Si and Sn contents. The presence of Sn is not surprising since the Kidd Creek ore body contains tin-bearing minerals.<sup>4</sup> Figure 5 shows the remains of a once-locked particle: the Zn-S-O compound (either oxide, sulfate, or sulfite) was readily dissolved but the base-metal silicate remains insoluble. Finally, Fig. 6 shows a particle with morphology and composition typical of the alkali-feldspar family: (KNa)AlSi<sub>3</sub>O<sub>8</sub> with minor amounts of Zn, Fe, and Cu. The alkali-feldspar family occurs in the county rock of the Kidd Creek ore body.<sup>4</sup>

#### *Silver-lead Residue (SLR)*

This is the solid residue after three stages of sulfuric acid leaching, with some of those leaching stages being performed at -90 C. The residue was studied in a way similar to that used for the jarosite residue. Its determined AA analysis gave 9.80%Zn, 11.72%Fe, 7.94%Pb, and 0.60%Cu. Size analysis by cyclosizer gave 85% < 8.2 μm.

The SLR was separated into products according to their magnetic behavior using a Frantz apparatus. XRD of these Frantz products showed zinc ferrite to be the major mineral phase in the magnetics separated at 50 to 500 mA. However, the richest zinc-ferrite product was that of 300 mA. The determined magnetic susceptibility for the zinc ferrite in the SLR was 0.00501 SI units.

*SEM of the 50mA Magnetic Product.* This is the first magnetic product of the Frantz series. Two main morphologies were found. Figure 7 shows the most abundant type of particles; their EDS peak counts indicate zinc ferrite. The second most abundant type of particles is seen in Fig. 8; they show large Fe counts but also large Pb and S counts together with some Zn and Cu counts. An automated search-match program of the XRD pattern of this magnetic product identified the presence of ZnFe<sub>2</sub>O<sub>4</sub> and PbCS<sub>3</sub>.

*SEM of the 300mA Magnetic Product.* Figure 9 shows the most abundant type of particles in this product. The large EDS counts of Fe and Zn indicate a zinc ferrite particle. The wt% ratio for Zn/Fe for these particles is ~0.47 (determined by ZAF-corrected EDS analysis), which suggests that some Zn has been leached out. The corresponding ratio for Cu/Fe is only ~0.03, which agrees with the low magnetic susceptibility of the zinc ferrite in the

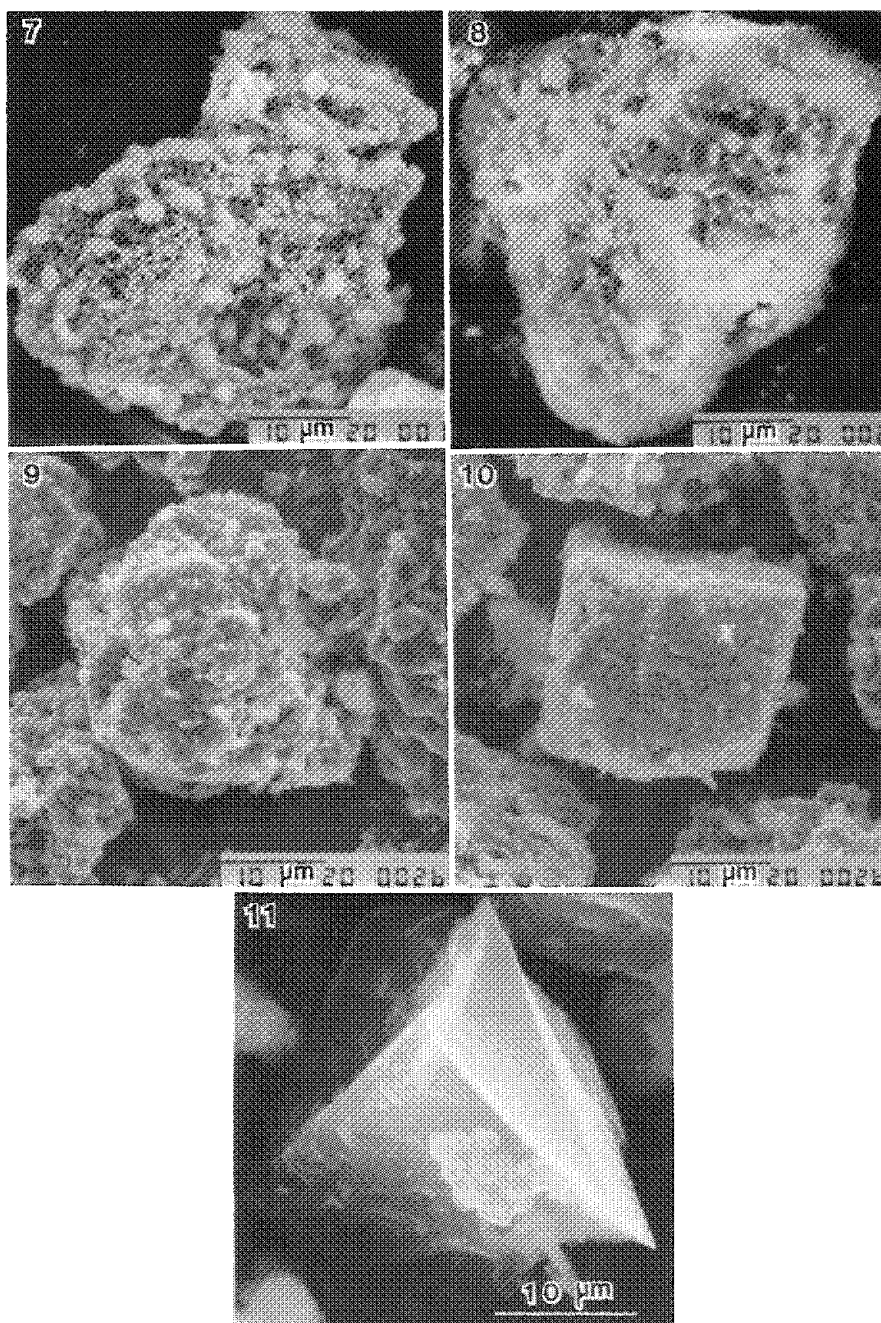


FIG. 7.--EDSPR to Fe are: Fe 1.0, S + Pb 0.15, Zn 0.14, Cu 0.01  
 FIG. 8.--EDSPR to Fe are: Fe 1.0, S + Pb 1.04, Zn 0.12, Cu 0.03.  
 FIG. 9.--EDSPR to Fe: Fe 1.0, Zn 0.19, S + Pb 0.09, Cu 0.01.  
 FIG. 10.--EDSPR to Fe: Fe 1.0, Zn 0.02, Cu 0.01.  
 FIG. 11.--EDSPR to Si: Si 1.0, Fe 0.11, Cu 0.14, Zn 0.08, Mn 0.05.

SLR. The particle in Fig. 9 also shows small amounts of Pb-S compounds.

In this product it was possible to find particles of hematite (see Fig. 10) and of  $\text{MnO}_2$ . The presence of  $\text{MnO}_2$  is explained as an excess of the added in the first leaching steps to reduce the undesired concentration of ferrous iron.<sup>5</sup>

*SEM of the 600mA Nonmagnetic Product.* Most of the particles in this product suggest the presence of  $\text{SiO}_2$ ; Fig. 11 shows an example. Also it was possible to find particles with large Si counts and appreciable Cu, Fe, and Zn counts. Together with strongly angular features, that suggest the existence of base-metal silicates.

An automated search-match program was used further to identify the XRD patterns of the various magnetic and nonmagnetic products of jarosite and SLR. The success of the search program depends heavily on a provided list of known elements. Therefore, the results obtained by SEM-EDS were used to give a partial list of elements present in the products. The results of this automated search-match program confirmed the existence of the suggested phases by SEM-EDS and also added the presence of few other phases.

### Conclusions

1. The evidence collected by SEM and XRD showed that jarosite residue is made up of the major abundant phase ( $\% > 10$ ) of Na jarosite, with some small quantities of Zn, Cu, As, and Cu incorporated in the crystal lattice; the medium abundant phases ( $10 > \% > 1$ ) are zinc-ferrite associated with copper ferrite in small variable amounts and  $\text{SiO}_2$ ; and other phases encountered in small proportions ( $\% < 1$ ), which in order of abundance are feldspars, ZnS, FeS,  $\text{Cu}_5\text{FeS}_4$ ,  $\text{Cu}(\text{Fe},\text{Sn})_2\text{S}_{3.9}$ , and Cu-Zn-Fe-Sn silicates.

2. The collected evidence showed that the silver lead residue were found to be, as the most abundant phases ( $\% > 10$ ),  $\text{ZnFe}_2\text{O}_4$ ,  $\text{Fe}_2\text{O}_3$ , and  $\text{SiO}_2$ ; as medium abundant phases ( $10 > \% > 1$ ),  $\text{SnO}_2$ ,  $\text{PbCS}_3$ ,  $\text{PbFe}_6(\text{SO}_4)_4(\text{OH})_{12}$ , ZnS, and  $\text{CuS}_2\text{Sb}$ ; and as minor abundant phases ( $\% < 1$ ),  $\text{MnO}_2$ , FeS,  $\text{Cu}_3\text{FeS}_4$ ,  $\text{Fe}_9\text{S}_8$ , S, and  $\text{Cu}_2\text{FeSnS}_4$ .

### References

1. R. Lastra et al., "Characterization and separation of a Cu-smelter dust residue," *Can. Met. Quart.* (in press).
2. J. E. Dutrizac et al., "A mineralogical study of the jarosite phase formed during the autoclave leaching of zinc concentrate," *Can. Met. Quart.* 23: 147, 1984.
3. J. E. Dutrizac, "The behavior of impurities during jarosite precipitation," in R. G. Bautista, Ed., *Hydrometallurgical Process Fundamentals*, New York: Plenum Press, 1984, 125.
4. A. Matulich et al., "The ECTSTALL story," The Geology Department, CIM Bulletin, 1974, 56-58.
5. D. K. A. Donyina, "Treatment of Cottrell dusts at the Kidd Creek plant," Professional Development Seminars, Department of Mining and Metallurgical Engineering, McGill University, 1985.

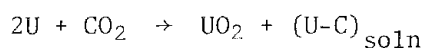
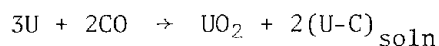
## A RELATIVELY INERT MATERIAL FOR CASTING URANIUM AND URANIUM ALLOYS

L. R. Walker, C. E. Holcombe, W. M. Swartout, and K. A. Thompson

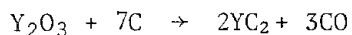
Uranium and uranium alloys are typically induction melted in graphite crucibles under vacuum;<sup>1</sup> but because of the chemical reactivity of the metal and the alloy constituents with graphite, crucibles must be protected with a nonreactive coating. Over the years several metal oxides have been used as protective coatings with varying degrees of success.<sup>2</sup> A material that resists chemical reactivity, that is not wetted by the uranium or alloys, reduces carbon contamination, and is heat conductive would be a desirable alternative to the carbon crucibles with protective coatings.<sup>3</sup> In this study a new material produced by Fansteel, Tribocor 532N,<sup>4</sup> is examined as a possible replacement for graphite. It has many desirable features such as good heat conductivity and easy toolability; it has been found to be fairly unreactive to uranium and two other alloys that were studied, although one alloy did show some interaction. The result of this study indicates a high potential for this new material.

Both uranium and its alloys react with carbon at elevated temperatures. Because low carbon content in the metal and narrow concentration ranges in the alloys are required to produce the desired properties, carbon contamination must be held to a minimum. Carbon dissolves in the uranium metal, then reacts to form insoluble carbides of the metal and of the alloy constituents. Several coatings have been used to reduce the carbon pickup from the graphite crucible during melting and casting. Figure 1 shows the average carbon increase as a function of temperature for several different coatings. Two of these coatings are currently being used at the Oak Ridge Y-12 Plant. Zirconia is used at temperatures below 1250 C (uranium metal), and yttria is used for temperatures greater than 1250 C but less than 1450 C (uranium alloys).

Carbon contamination occurs in many ways. If the protective coating breaks down for any reason, direct reaction of uranium and its alloys with the carbon crucible can occur. More indirect sources of carbon also exist. Although the melt occurs in a vacuum, water and oxygen from inleakage react with the hot graphite crucible to form carbon monoxide (CO) and carbon dioxide (CO<sub>2</sub>), which are strongly gettered by uranium. The reactions with uranium occur as follows:



Some dissolved carbon remains, but the remainder reacts with uranium and/or the alloy constituents to form carbides, which deplete the alloy of the alloying constituent. Other possible sources of CO and CO<sub>2</sub> exist; these gases might have been absorbed on the uranium or the alloy before being placed in the vacuum. In addition, they can be generated by other reactions, such as the following reaction of the protective yttria coating at high temperatures with the graphite crucible:<sup>5</sup>



A similar reaction occurs with the zirconia coating.

At moderate temperatures, these coatings adequately protect the graphite crucibles. However, even the yttria coating (which allows the least amount of carbon pickup) yields a significant increase in carbon pickup at temperatures above 1450 C. In addition, these protective coatings when applied as a mold wash might suffer from an inadequate application, cracking during loading, or thermal cracking. Any of these failures would result in the

---

The authors are at Martin Marietta Energy Systems, Inc., Y-12 Plant, Oak Ridge, TN 37831. The work was performed for the U.S. Department of Energy under Contract DE-AC05-84OR21400.

direct reaction of the melt and the crucible. These effects cause the carbon level to increase in the uranium or its alloys, interfering with reuse of the scrap for direct remelting, casting, or alloying. Therefore, a better method of reducing the carbon level is desirable.

The recognition of this need has led to the testing and development of a noncarbon furnace.<sup>3,6</sup> Materials such as tungsten or castable concretes of yttria, zirconia, or tantalum carbide are being tested, but each has some undesirable characteristics. A new material of interest is Tribacor 532N,<sup>4</sup> which is an alloy of 50 wt% niobium, 30 wt% titanium, and 20 wt% tungsten. The alloy can be formed, welded, machined, or otherwise fabricated as any other refractory metal alloy. Once the desired shape is achieved the alloy is nitrided at elevated temperatures to produce a complex titanium-niobium nitride-rich layer on the surface. Tests by the manufacturer show that the depth of the nitride layer can be controlled by the time and temperature at which the alloy is nitrided. This nitride layer forms a protective ceramic coating, giving the material some qualities of both a refractory metal and a ceramic. Additionally, the manufacturer states that the surface can be renitrided if the layer becomes depleted, which would increase the part's effective lifetime.

### *Experimental*

The Tribacor 532N crucibles were fabricated with 2mm-thick walls, 13 mm in diameter and 13 mm high. Uranium or uranium alloys were added, followed by heating to 1500 C at 6 C/min in vacuum, held at that temperature for 15 min, then cooled at a rate of ~40 C/min. The crucibles were mounted metallographically and cross-sectioned normal to the height for electron microprobe analysis. Uranium and three uranium alloys, uranium-6 wt% niobium (U-6Nb), uranium-2 wt% niobium (U-2Nb), and uranium-0.75 wt% titanium (U-0.75Ti), were heat treated in the above manner in unprotected Tribacor 532N crucibles. In addition, U-2Nb and U-0.75Ti were heat treated in yttria-coated Tribacor 532N crucibles and U-0.75Ti was heat treated in a zirconia-coated Tribacor 532N crucible.

Six of the seven melts appeared nonwetting from a visual inspection. The remaining melt, U-0.75Ti in an uncoated crucible, appeared wetted, but a distinct boundary is still visible at the interface. The U-0.75Ti alloy was the only sample for which the crucible and melt were mounted together; the others were mounted separately because the uranium and the alloys were unattached to the crucible.

### *Results*

Electron microprobe analyses were performed to determine qualitatively whether a reaction occurred at the crucible-metal interface and to determine the reaction products, if formed. Figure 2(a) is a backscattered electron (BSE) image of the contact surface of the U-6Nb alloy and the uncoated crucible. The image shows a layer lower in average atomic number than the matrix along the surface. Figure 2(b) shows the elemental x-ray maps for this same area, which identifies this layer as a mixture of uranium, carbon, and nitrogen. A similar layer was also found on the crucible and indicates that the melt released by fracturing the formed layer. An examination of the contact surfaces of the uranium metal and the U-2Nb in the uncoated crucibles showed similar layers and indicated essentially the same type of behavior.

Figure 3(a) is the BSE image of the contact surface of the U-0.75Ti alloy and the uncoated crucible. The image shows a nonuniform attack of the crucible, with the uranium alloy penetrating the surface to depths of 50  $\mu$ m. Figure 3(b) is the elemental x-ray map of the same area and shows the alloy surrounding a phase rich in titanium and nitrogen. Noticeably absent in this image is a carbon-rich material (the carbon x-ray map is not shown because no significant amount of carbon was present) and the exclusion of niobium from the titanium nitrides surrounded by the melt. Also, there is some indication of a uranium/niobium phase and a uranium/nitrogen phase.

Figure 4 shows two BSE images of the contact surfaces of the U-0.75Ti alloy and the yttria-coated crucible (the alloy separated from the crucible and was mounted separately). The images indicate an intact layer of yttria between the crucible and the melt (top portion of Fig. 4(b), probably separated from the crucible during mounting), with no apparent mixing of the crucible elements with the alloy. This result is in contrast with the melt for the uncoated crucible. Therefore, the coating has protected the crucible from reacting with the U-0.75Ti alloy. Similar results were found for the other coated crucibles. The



titanium/carbon inclusions on the edge of the melt (bottom portion of Fig. 4a) are not uncommon for this alloy. A portion of these carbides are from previous alloying procedures, whereas new carbides are formed from residual gasses and the reaction with the carbon-based binder used in the yttria wash. The surface-area ratio of the coating to the volume of melt is fairly high for this test, which results in an increase of carbides.

Because carbon and nitrogen are very difficult to quantitate by use of only pure-element standards and because serious overlaps exist between the uranium  $N_6O_4$  with the carbon  $K\alpha$  and between the titanium  $LL$  with the nitrogen  $K\alpha$ , no rigorous attempt was made to determine the actual quantitative compositions. Table 1 lists the various phases examined and shows the k-ratios for the elements. The k-ratios for U-0.75Ti and the uncoated crucible indicate some interaction of crucible elements with the uranium alloy, particularly in the form of inclusions of titanium and nitrogen that have been depleted of niobium, along with uranium/nitrogen inclusions. Noticeably absent is the uranium/carbon/nitrogen layer found in the other melts. Also absent are titanium carbides which are normally found in this alloy.

Some interaction was also seen for the niobium alloys, but to a much lower extent. The presence of titanium in the niobium carbide inclusions suggests that titanium was released from the Tribocor 532N as the uranium/carbon/nitrogen layer was formed, then was concentrated in the niobium inclusions. If this process also occurred in the titanium alloy and the pure uranium, the increase in titanium level would be below the detection limit of these analyses without the concentrating effect of the niobium inclusions. Further work would be necessary to determine whether such an increase is occurring. The two niobium alloy melts as compared with the uranium melt have a lower carbon-to-nitrogen ratio in the inclusions and in the thin layer. The niobium is a better getter for carbon and reduces the amount available for the uranium carbide inclusions.

### Summary

In the uranium, U-2Nb, and the U-6Nb melts in uncoated crucibles, no significant deterioration of the crucible was observed. For U-0.75Ti in an uncoated crucible, some reaction did take place, but this was a worst-case scenario. The ratio of alloy to the crucible surface area was low, which would not be true in a typical full-scale melt. In addition, the coated crucibles indicate no interaction between the melts and the crucible. Further work is indicated to determine whether low concentrations of crucible materials are dissolving in the uranium or in its alloys. Whether these small levels would interfere with the desired qualities of the uranium or its alloys would also have to be considered, but two of the constituents of Tribocor 532N, niobium and titanium, are already used in uranium alloys.

The Tribocor 532N appears to be an excellent candidate for vacuum-induction melting of uranium and uranium alloys. The material offers the following advantages:

- little reaction at melt temperatures, even as an uncoated substrate;
- compatibility with conventional crucible/mold coatings;
- good high-temperature strength and thermal shock resistance;
- vacuum stability and rejuvenation possibilities;
- good fabricability; and
- susceptibility in induction furnaces.

Additional work on the material for noncarbon furnace use is in progress.

### References

1. In J. L. Cadden, N. C. Jessen Jr., and P. S. Lewis Jr., "Melting of uranium alloys," *Preprint Y-DA-5323*, Union Carbide Corp. Nuclear Div., Oak Ridge Y-12 Plant, Dec. 28, 1973.
2. J. W. Koger, C. E. Holcombe, and J. G. Banker, "Coatings on graphite crucibles used in melting uranium," *Thin Solid Films* 39: 297, 1976.
3. N. C. Jessen Jr., C. E. Holcombe, and A. B. Townsend, "Application of metal oxide refractories for melting and casting reactive metals," *Proc. Sixth International Vacuum Metallurgy Conference*, San Diego, American Vacuum Society, 1980, vol. 3.



4. P. F. Ziegler and J. J. Rausch, "Tribacor 532N: A new material for environments involving wear and corrosion," *A. S. Metals International Conference on Surface Modifications and Coatings*, 1985, 1-9.

5. J. B. Condon and C. E. Holcombe, "Kinetics of yttria-carbon reaction," *High Temperature Science*, 79-95, 1984.

6. C. E. Holcombe, D. R. Masters, and W. A. Pfeiler, *Carbon-free Induction Furnaces*, U.S. Patent 4,550,412, 24 October 1985.

TABLE 1.--Listing of k-ratios of the various elements found in the uranium and uranium alloys after heating at 1500 C for 15 min in coated and uncoated Tribacor 532N crucibles.

melt	phase	U	Nb	Ti	W	N	C
Uranium	matrix	0.99	<0.002	<0.002	<0.001	<0.005	0.02
	U rich incl.	0.92	<0.002	<0.002	<0.001	0.04	0.06
	Ti/Nb/C incl.		none found				
	U/N/C interface	0.88	<0.002	<0.002	<0.001	0.05	0.06
U-2Nb	matrix	0.95	0.02	<0.002	<0.001	<0.005	0.01
	U rich incl.	0.88	<0.002	<0.002	<0.001	0.07	0.02
	Nb rich incl.	0.05	0.77	0.03	<0.002	<0.005	0.06
	U/N/C interface	0.88	<0.002	<0.002	<0.002	0.06	0.02
U-6Nb	matrix	0.90	0.06	<0.002	<0.002	<0.005	0.01
	U rich incl.	0.89	<0.002	<0.002	<0.002	0.07	0.02
	Nb rich incl.	0.002	0.85	0.02	<0.002	<0.004	0.04
	U/N/C interface	0.89	<0.002	<0.002	<0.002	0.07	0.02
U-0.75Ti	matrix	0.96	0.008	0.005	<0.002	<0.005	0.01
	U in react. zone	0.96	0.009	0.004	<0.002	<0.005	0.01
	2nd phase, reac. zone	0.88	<0.002	0.002	<0.002	0.09	0.01
	Ti/N incl. in melt	0.003	0.006	0.78	<0.002	0.14	0.01
	Ti/N at interface	0.001	0.01	0.78	<0.002	0.15	0.02
U-2Nb Y <sub>2</sub> O <sub>3</sub>	matrix	0.94	0.02	<0.002	<0.001	<0.005	0.01
	U rich incl.	0.88	0.001	<0.002	<0.001	0.04	0.03
	Nb rich incl.	0.05	0.79	0.002	<0.001	<0.005	0.05
U-0.75Ti Y <sub>2</sub> O <sub>3</sub>	matrix	0.98	<0.001	0.006	<0.001	<0.001	0.01
	Incl. interface	0.006	<0.001	0.75	<0.001	0.01	0.12
	Incl. matrix	0.003	<0.001	0.79	<0.001	0.003	0.15
U-0.75Ti ZrO <sub>2</sub>	matrix	0.97	<0.001	0.006	<0.001	<0.001	0.01
	Incl. interface	0.01	<0.001	0.74	0.001	0.01	0.13
	Incl. matrix	0.003	<0.001	0.76	<0.001	0.01	0.15

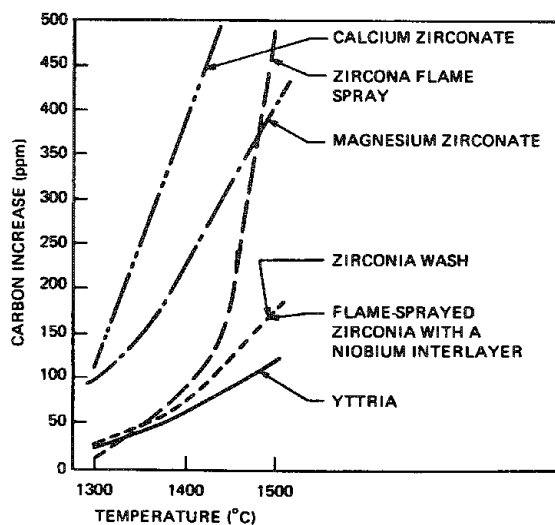


FIG. 1.--Carbon uptake by uranium in graphite crucibles with various coatings.

FIG. 2.--Digital images of U-6wt%NB melted at 1500 C for 15 min in Tribocor 532N crucible. Left, elemental x-ray maps; right, backscattered electron image.

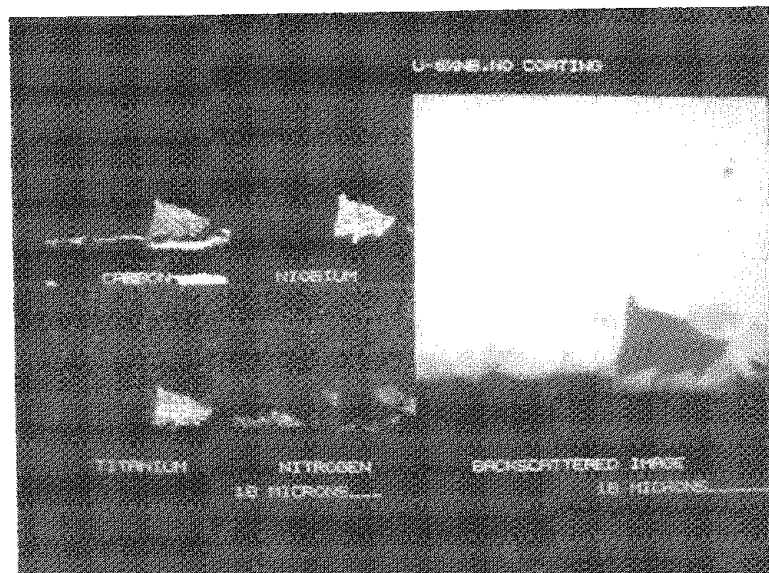


FIG. 3.--Digital images of U-0.75wt%Ti melted at 1500 C for 15 min in Tribocor 532N crucible. Left, elemental x-ray maps; right, backscattered electron image.

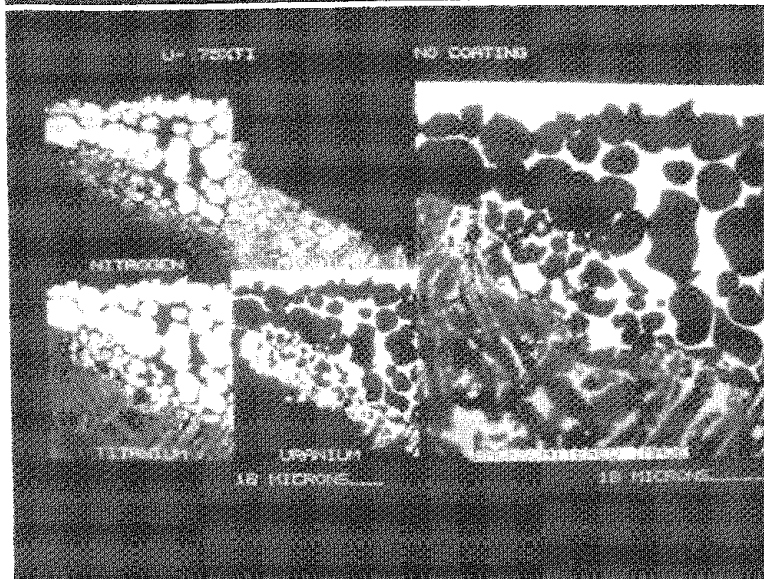
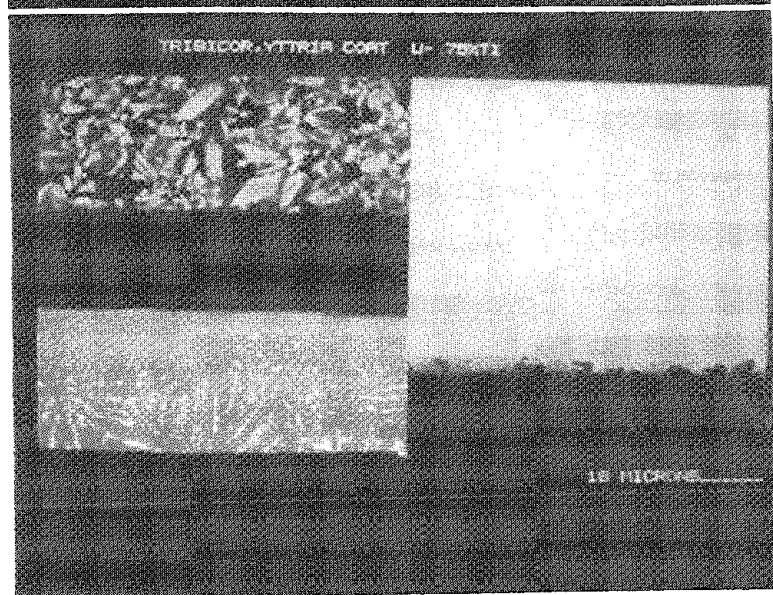


FIG. 4.--Digital backscattered electron images of U-0.75wt%Ti melted at 1500 C for 15 min in yttria-coated Tribocor 532N crucible. Left, crucible; right, melt.



## IN SITU STEM STUDIES OF THE INTERACTION BETWEEN MOLYBDENUM DISULFIDE AND OXYGEN

R. T. K. Baker and R. D. Sherwood

We have extended the capabilities of the scanning transmission electron microscope to enable us to study gas-solid reactions at high magnifications as they occur. This result has been accomplished by modification of the specimen chamber of a JEOL 200 CX TEM/STEM microscope to accommodate an environmental cell and specimen heating holder. With this arrangement, it is possible continuously to observe changes in the appearance of the specimen as it undergoes reaction and also perform in situ chemical analysis of particular features of interest. This paper discusses the use of the technique to investigate the structural and chemical changes that accompany the reaction of molybdenum disulfide when heated in oxygen.

Molybdenum disulfide ( $\text{MoS}_2$ ) is one of several transition metal sulfides used as catalysts for removing sulfur compounds from petroleum feedstocks.<sup>1</sup>  $\text{MoS}_2$  is a layered compound with hexagonal symmetry in the basal plane. Despite its importance, it is only in recent years that efforts have been made to understand the origin of its catalytic activity.<sup>2</sup> Early work by Bahl and co-workers<sup>3</sup> indicated that oxidation took place at edges and steps, and at defect sites on molybdenum disulfide crystals. Chianelli and co-workers<sup>4</sup> later confirmed these findings and further demonstrated that if metal was introduced onto molybdenum sulfide, the metal particles would tend to collect at edge sites on the surface during reaction. In the present work we have been able to observe directly the attack of edges and the creation and expansion of pits in the basal plane as molybdenum disulfide single crystals were heated in oxygen. Furthermore, it has been possible to correlate these dynamic events with structural and chemical changes obtained from in situ selected area electron diffraction analysis.

### *Experimental*

The key feature of the technique is the environmental cell, which was built by Gatan, Inc., to a design similar to that described in Ref. 5. Figure 1 is a schematic cross section of the specimen chamber region of the electron microscope. The cell A is permanently located at the center of the objective lens and positioned so that the pre-aligned apertures B and C fall on the electron optical axis. The specimen heating holder D, also Gatan design, can be inserted and withdrawn as desired through "O" ring seals in the cell as in a conventional specimen holder. On insertion into the microscope, the specimen holder seats against the conical end of the left-hand specimen translate. Gas enters the microscope via a duct around this mechanism and contacts the specimen at the region E. Gas exits through the apertures into the differential pumping ports G and thence to a Balzers (110 liter/min) turbo-molecular pump backed by a Balzers Duo 12 mechanical pump. With this arrangement, it is possible to work at a pressure of 2 Torr hydrogen or 15 Torr oxygen in the environmental cell and at the same time maintain a vacuum of  $10^{-6}$  Torr in the electron-gun region. Gas is introduced into the reaction region via a metering valve and the pressure is measured by a thermocouple gauge in the duct leading to the cell.

Transmission specimens (< 50 nm thick) of molybdenum disulfide were prepared from natural molybdenite (originating from Froland, Norway) by the same cleaving procedure used for obtaining thin sections of graphite.<sup>6</sup> These specimens were picked up from a clean water surface on stainless steel microscope grids and mounted into the heating stage. Finally, the whole assembly was inserted into the microscope specimen chamber, and the cell evacuated before gradually heating up to 625 C in the presence of 3 Torr oxygen. The behavior is monitored via closed-circuit television observations of the viewing screen.

---

The authors are at Corporate Research Science Laboratories, Exxon Research and Engineering Company, Annandale, NJ 08801.

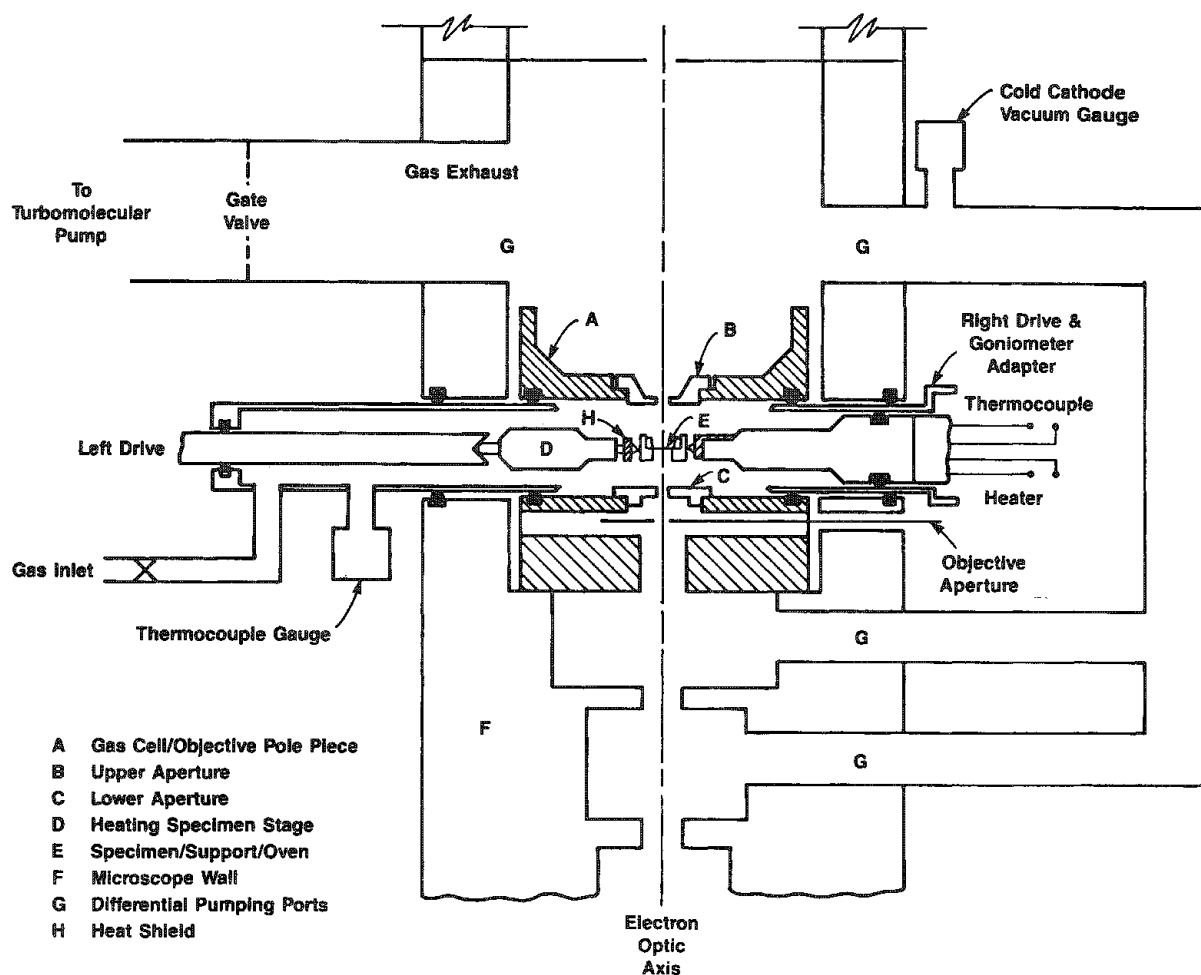
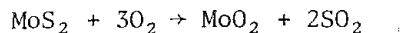


FIG. 1.--Schematic diagram showing cross section of gas cell and heating stage.

### Results

The first signs of reaction were observed at 315C when tiny crystallites and needle-like structures started to form at the edges of the molybdenum disulfide crystals. When the temperature was raised to 415 C, these structures slowly transformed into more compact shapes, some of them globular in outline. These structures increased in size by consuming material from the substrate and causing edges to recede. Figure 2 is a sequence taken from the TV monitor showing this oscillating type of action, which became more pronounced at higher temperatures. Selected area diffraction at these conditions showed the presence of  $\text{MoO}_2$ , which suggests that under these conditions the oxidation of the sulfide is proceeding by the following reaction:



A survey of the basal plane showed that particles with similar characteristics were also being generated in these regions at the expense of the substrate, which tended to become progressively thinner as the reaction proceeded. Globular particles located on the basal plane exhibited mobility at 415 C; however, when they came into contact with edges, they lost this characteristic. It was significant that during this time Moiré fringes remained static, indicating that the action was taking place layer by layer rather than by bulk transformation of the  $\text{MoS}_2$  structure.

At 450 C it was evident that some of the particles on the basal plane were undergoing a rearrangement in shape from the globular form to a thin faceted morphology, change that was accompanied by a loss in particle mobility. Following this action, the particles

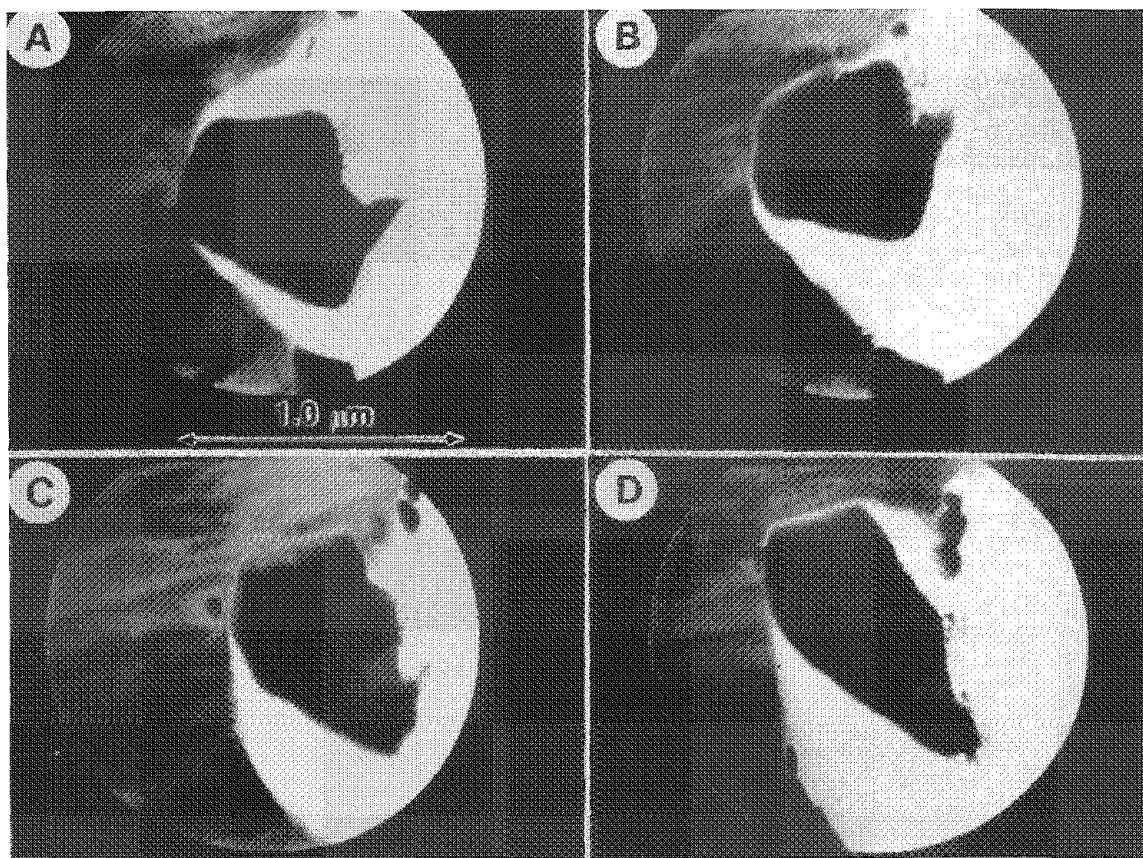


FIG. 2.--Sequence showing erosion of MoS<sub>2</sub> edge regions and simultaneous growth of MoO<sub>2</sub> particles.

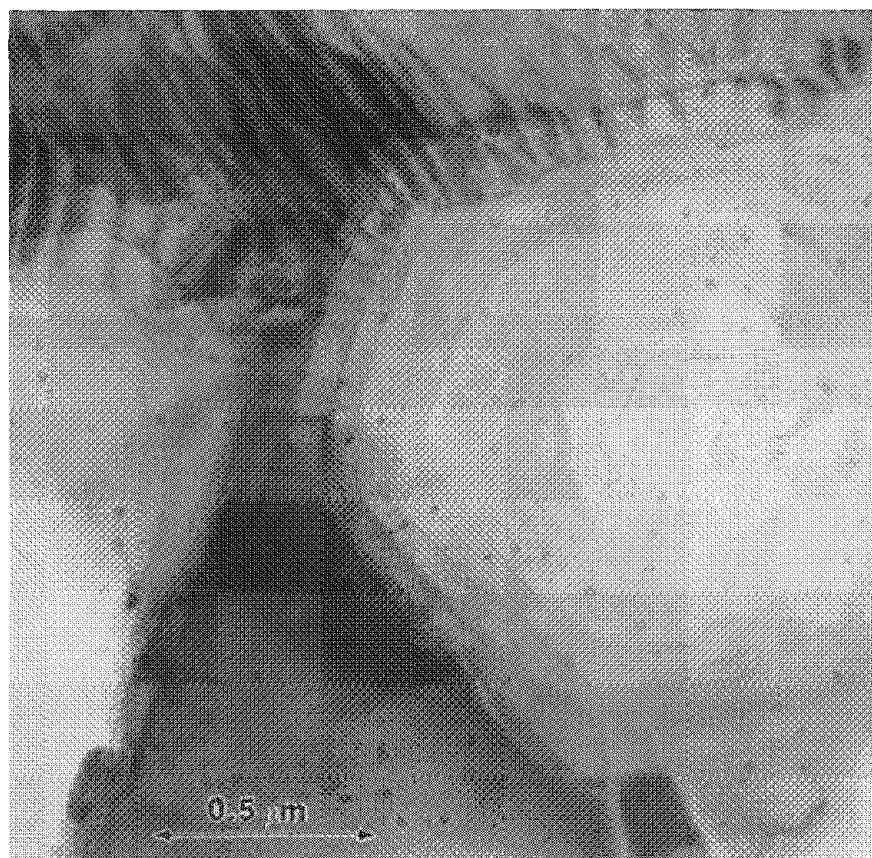
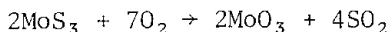


FIG. 3.--Formation of pit in basal plane of MoS<sub>2</sub> crystal.

would contract to their original globular geometry, leaving behind the imprint of a shallow pit with dimensions identical to that of the particles in their spread condition. On continued reaction the width and depth of the pits increased as did the size of the particles associated with them, which suggests that material was being transported from the substrate to the particles. We believe that the pits are formed at point defects, probably vacancies, in the basal plane. Figure 3 is a micrograph taken at room temperature after the reaction showing the extensive development of a pit. During cooling to room temperature the particle originally associated with this pit has migrated away or possibly fragmented into many smaller entities.

Examination of the characteristics of many pits showed that there was no definite relationship between the width and depth of a given pit. However, it was evident that the sides of the pits were aligned in a preferred orientation with respect to the MoS<sub>2</sub> crystallographic structure and that they expanded radially in a very uniform manner as the reaction proceeded.

As the temperature was raised to 525 C, the rates of both edge recession and pit expansion increased. Also, at this stage many of the large globular particles on the basal plane were observed to exhibit some fascinating transformations. Large needle-shaped structures were produced from the globules via an extrusion process. In general, the needles were parallel-sided and ranged in length from 1 to 2 μm; the size depended directly on that of the globule from which they were derived. A further example of metastable behavior was the observation that diamond-shaped particles producing pits would frequently transform to globules. Selected area electron diffraction examination at 525 C showed the appearance of a new phase, MoO<sub>3</sub>, which was present in a lower concentration than the major components, MoO<sub>2</sub> and MoS<sub>2</sub>. However, as the temperature was progressively raised to 625 C, the concentration of MoO<sub>3</sub> reached a level comparable to that of MoO<sub>2</sub>, which suggests that the rate of the alternative reaction pathway



was becoming significant. Furthermore, it was evident that the majority of particles were diminishing in size, consistent with the fact that MoO<sub>3</sub> undergoes sublimation under these conditions.<sup>7</sup>

### Summary

We have demonstrated that oxidation of molybdenum disulfide takes place preferentially at edged and point defects on the basal plane. It appears that the reaction proceeds by two pathways: conversion to MoO<sub>2</sub> predominates at low temperatures and formation of MoO<sub>3</sub> becomes significant at high temperatures, with intermediate metastable oxides playing some role.

### References

1. C. Weisser and S. Landa, *Sulfide Catalysts: Their Properties and Applications*, Oxford: Pergamon Press, 1973.
2. R. R. Chianelli, "Catalysis by transition metal sulfides," in J. P. Bonnelle et al., Eds., *Properties and Catalysis by Non-Metals*, D. Reidel Publishing Co., 1983, 361-378.
3. C. R. Bahl, E. L. Evans, and J. M. Thomas, "The identification of some properties of point defects and non-basal dislocations in molybdenite surfaces," *Proc. Roy. Soc. A306*: 53, 1968.
4. R. R. Chianelli, A. F. Ruppert, S. K. Behal, B. H. Kear, A. Wold, and R. Kershaw, "The reactivity of MoS<sub>2</sub> single crystal edge planes," *J. Catal.* 92: 56, 1985.
5. J. R. Porter, D. S. Tucker, P. R. Swann, B. Kraus, S. Mehta, and C. A. Anderson, "The performance of the Gatan environmental cell in the JEOL 200CX," *Analytical Electron Microscopy--1984*, 9.
6. R. T. K. Baker and P. S. Harris, "Controlled atmosphere electron microscopy studies of graphite gasification," *Carbon* 11: 25, 1973.
7. G. V. Samsonov, *The Oxide Handbook*, New York: Plenum Press, 2d ed.



## OXIDATION KINETICS OF Pb-Sn EUTECTIC SOLDER FILMS BY AES ANALYSIS

G. Di Giacomo

Lead-tin solders are widely used in the electronic and semiconductor industries to interconnect components. These solders tend to form a chemically protective film of tin oxide (predominantly SnO at temperatures below 200 C). The tin oxide film forms preferentially to lead oxide and thus covers the alloy surface even when the tin content is of the order of less than 10%. The oxidation is diffusion controlled as the tin must diffuse to the surface from beneath to be oxidized.<sup>1 5</sup>

The presence of an oxide film also affects the electric and thermal contact resistance of the solder. To quantify these effects (chemical, electrical, and thermal), one must know the oxidation kinetics of the solders with respect to the environment so that they can be related to the material's performance.

Auger Electron Spectroscopy (AES) is an effective analytical approach to determining the average oxide film thickness through depth profiles of oxygen and tin concentration.

### *Objectives*

1. To study by AES the oxidation of Eutectic Pb-Sn solder in air and within "hermetic modules" where the oxygen permeates at a small finite rate.
2. To develop a model describing the oxidation kinetics as a function of temperature and permeation rate and projecting the results to field conditions.

### *Experimental*

The experiment was conducted with copper films, about  $\frac{1}{4}$  mm thick and 1 cm<sup>2</sup>. They were electroplated with 0.05 mm of Pb-Sn eutectic solder and reflowed at 220 C. The solder reacted with copper and formed Cu-Sn intermetallics at the interface. The films were uniform and showed a smooth surface. Twenty films were prepared for this experiment. Ten of them were exposed to 160 C for 500 h and the other ten to 125 C for a maximum of 2000 h. The films were removed from the test chambers at intervals and analyzed by AES to determine the oxide thickness as a function of time. Figures 1-4 show typical intensity profiles of oxygen and tin. From the profiles, the average oxide thickness was estimated on the basis of the sputtering rate and time, and the use of the oxygen/tin profile intersection as reference. The amount of oxygen reacted is calculated from the oxide thickness assuming SnO is predominant.

In addition, two films were sealed within "hermetic" modules having leak rates  $3.3 \times 10^{-7}$  and  $2.5 \times 10^{-6}$  cm<sup>3</sup>(ATM)/s and exposed at 160 C for 500 h as done with open films. The results show that the average films oxidation rates in air at 160 and 125 C are  $\sim 0.6$  and  $\sim 0.07 \text{ \AA/h}$ , respectively.

Figures 5 and 6 show plots of average oxide thickness versus time, from which an activation energy of 21 kcal/Mol was derived. Within the modules, the oxidation rates for  $2.5 \times 10^{-6}$  and  $3.3 \times 10^{-7}$  cm<sup>3</sup>(ATM)/s leakers were lower as expected, since oxidation depends on the oxygen ingress rate, which affects the oxygen partial pressure within the module cavity. The partial pressure is the result of two competing rates, the ingress rate and the rate of reaction at the film surface.

Based on the kinetics of chemical oxidation, the rate of oxidation is proportional to the oxygen partial pressure and inversely proportional to the thickness of the film. Assuming an average oxidation rate, a model was developed to calculate the oxygen level within the module as a function of leak rate (through the seal), time, and temperature, and to project the results to field conditions. The oxide film thicknesses calculated by the model for the two leakers are in good agreement with the measured values (Table 1), which serves to verify the model at the given levels of hermeticity. The validity of the model therefore extends from hermetic to completely open, at which the basic oxidation

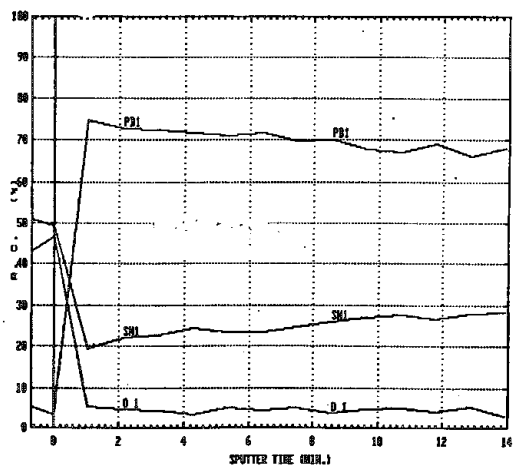


FIG. 1.--Time zero (control).

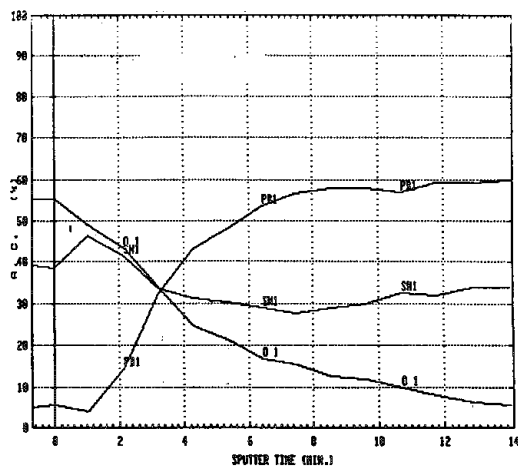


FIG. 2.--160 C, 376 h, sputter rate 2 nm/min.

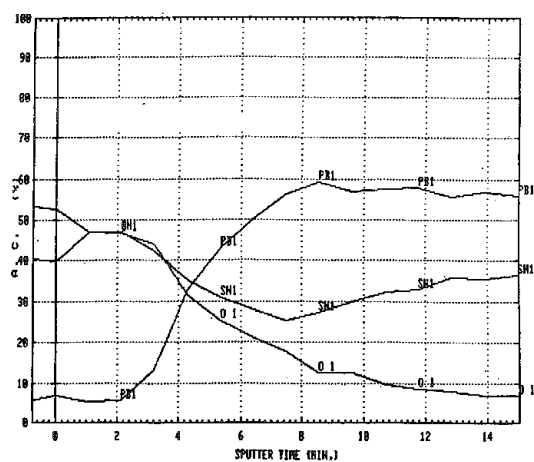


FIG. 3.--160 C, 500 h, sputter rate 2 nm/min. FIG. 4.--160 C, 1000 h.

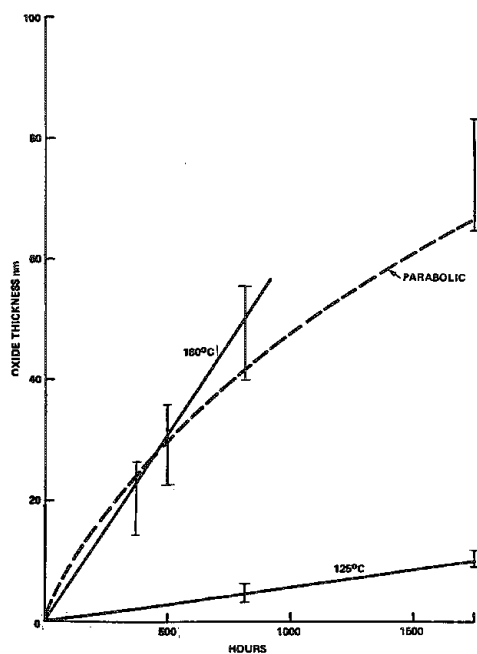
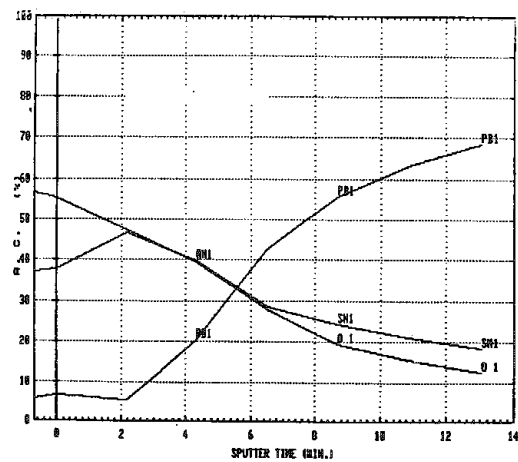


FIG. 5.--Oxide thickness vs time at two temperatures,

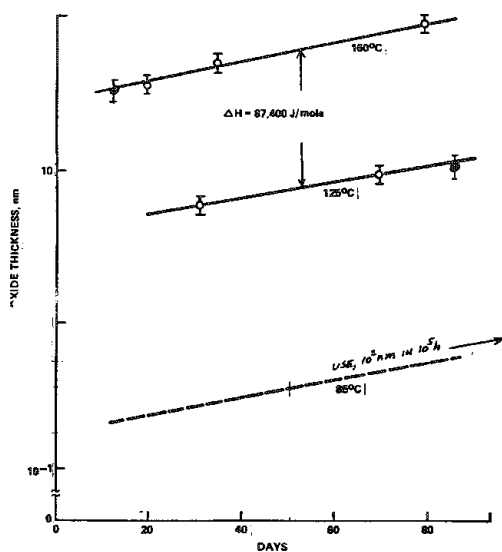


FIG. 6.--Activation energy and projection to use condition.



TABLE 1.--Oxidation results for known leak Rates.

Leak Rate cm <sup>3</sup> (ATM)/s	Oxide Thickness (A)	
	Calculated	Measured
$3.3 \times 10^{-7}$	95	100
$2.5 \times 10^{-6}$	365	350

kinetics were determined.

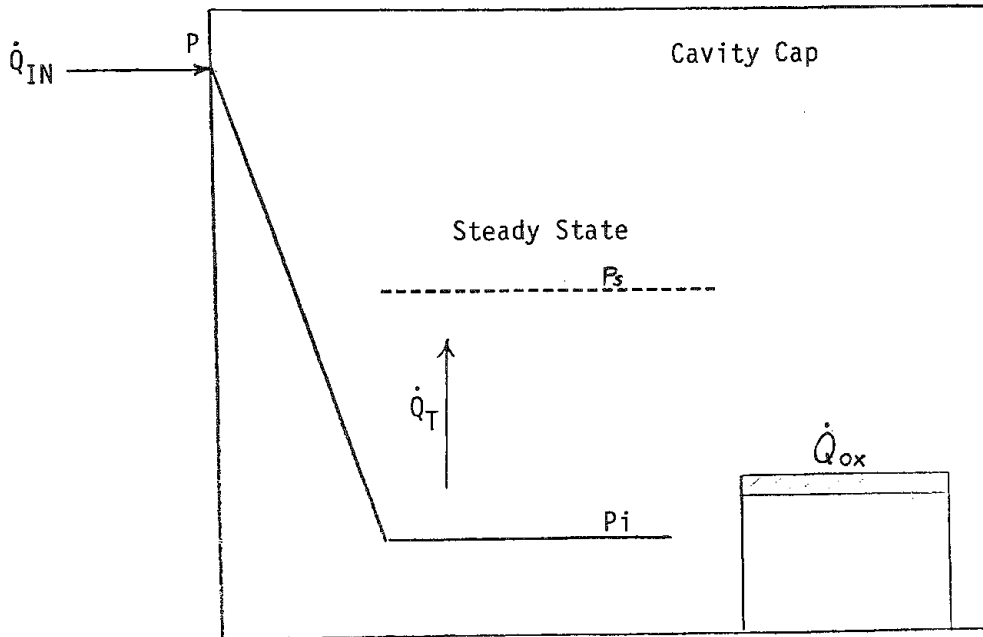
### Models

In the module interior, the oxidation of the film takes place in two periods, transient and steady state. The first is the period during which the amount of oxygen within the module cavity increases at a rate  $\dot{Q}_T$  since the ingress rate  $\dot{Q}_{IN}$  exceeds the oxidation rate  $\dot{Q}_{OX}$ . The ingress rate is proportional to the O<sub>2</sub>-partial pressure difference between outside and inside, and the oxidation rate is assumed to be proportional to the internal partial pressure  $P_i$ . At steady state,  $\dot{Q}_{IN} = \dot{Q}_{OX}$  and  $\dot{Q}_T = 0$ .

The model is developed on the basis that the rate of oxygen into the module equals the rate at which it is used in the oxidation process plus the rate at which it is accumulated in the cavity:

$$\dot{Q}_{IN} = \dot{Q}_{OX} + \dot{Q}_T \quad (1)$$

which is illustrated in the diagram below:



where  $\dot{Q}_{IN} = L(P - P_i) = r(P - P_i)$ ;  $\dot{Q}_{OX} = \rho A \dot{R} P_i = m P_i$ ;  $\dot{Q}_T = \sigma V \dot{P}_i$ ;  $\sigma$  = oxygen density (gas) per cm Hg;  $L$  = oxygen ingress rate, cm<sup>3</sup>(ATM)/s;  $\rho$  = oxygen density in oxide film based on SnO, g/cm<sup>3</sup>;  $A$  = oxide film area, cm<sup>2</sup>;  $V$  = module cavity, cm<sup>3</sup>; and  $\dot{R}$  = linear oxidation rate per cm Hg, cm/s.

From Eq. (1), the solution for the internal pressure is

$$P_i = \frac{rp}{m + r} \left[ 1 - \exp\left(-\frac{m + r}{\sigma V} t\right) \right] \quad (2)$$

from which

$$\dot{Q}_{OX} = m P_i = \frac{mrp}{m + r} \left[ 1 - \exp\left(-\frac{m + r}{\sigma V} t\right) \right] \quad (3)$$

The oxide film thickness  $d_{OX}$  can be expressed by

$$d_{OX} = \frac{\dot{R}rp}{m+r} \left\{ t - \frac{\sigma V}{m+r} \left[ 1 - \exp \left( - \frac{m+r}{\sigma V} t \right) \right] \right\} \quad (4)$$

$$\text{where } m = 9.2 \times 10^{-16} \exp \left[ \frac{-20880}{R} \left( \frac{1}{358^\circ K} - \frac{1}{T} \right) \right] \quad (5)$$

The oxide film thicknesses calculated from Eq. (4) for  $2.5 \times 10^{-6}$  and  $3.3 \times 10^{-7}$   $\text{cm}^3(\text{ATM})/\text{s}$  are in good agreement with the measured values shown in Table 1. Since  $m \ll r$  at ambient temperature, the oxidation process is not controlled by hermeticity for leak rates as low as  $10^{-7}$   $\text{cm}^3(\text{ATM})/\text{s}$ , except at high temperature (160 C), when the specific oxidation rate  $m$  becomes comparable or greater than the specific leak rate  $r$  ( $\text{g/s} \cdot \text{cm Hg}$ ). Figures 7 and 8 show calculated oxide thicknesses versus time at various levels of hermeticity for 85 and 160 C, respectively, assuming the module is filled with inert gas initially. The graphs illustrate the point that under normal temperature conditions, a leak rate of  $10^{-7}$   $\text{cm}^3(\text{ATM})/\text{s}$  produces the same oxidation as in the open ambient. Likewise, at 160 C, a leak rate of  $10^{-5}$   $\text{cm}^3(\text{ATM})/\text{s}$  is equivalent to the open environment whereas  $10^{-7}$  is effective in reducing the oxidation rate.

### Conclusions

Oxidation kinetics for Pb-Sn eutectic solder have been developed on the basis of oxygen and tin AES intensity profiles and known sputter rates.

A model has been derived as a function of temperature, time, and leak rate to project the rates to field conditions.

Predictions are in good agreement with the oxidation results in terms of Auger intensity, which has provided validation for the model.

At steady state, the oxidation rate does not depend on the leak rates  $\sim 10^{-7}$   $\text{cm}^3/\text{s}$  at temperatures  $\sim 85$  C for films  $\sim 1$   $\text{cm}^2$ . Outside these limits, the oxidation rate is controlled by the ingress rate of oxygen.

### References

1. R. J. Bird, "Corrosion-resistant lead-indium and lead-tin alloys: Surface studies by photo-electron spectroscopy (ESCA)," *Metal Science J.* 7, 1973.
2. S. K. Sen, S. Sen, and C. L. Bauer, "Determination of the oxidation states of tin by Auger electron spectroscopy," *Thin Solid Films* 82: 157-164, 1981.
3. C. L. Lau and G. K. Wertheim, "Oxidation of tin: An ESCA study," *J. Vac. Sci. Technol.* 15(2), 1978.
4. Y. Okamoto, W. J. Carter, and D. M. Hercules, "A study of the interaction of Pb-Sn solder with  $\text{O}_2$ ,  $\text{H}_2\text{O}$ , and  $\text{NO}_2$  by ESCA and AES," *Applied Spectroscopy* 33(3), 1979.
5. S. C. Britton and K. Bright, "An examination of oxide films on tin and tinplate," *Metallurgia*, Oct. 1957, 163-170.
6. N. D. Tomashov, "Theory of corrosion and protection of metals," in *The Science of Corrosion*, London: Macmillan, 1966.

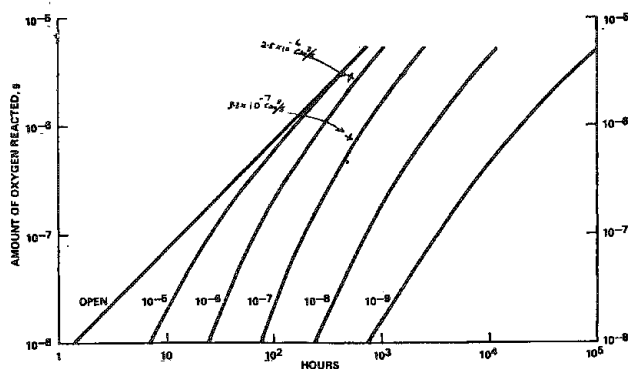


FIG. 7.--Amount of oxygen reacted vs time for various leak rates at 160 C calculated with model.

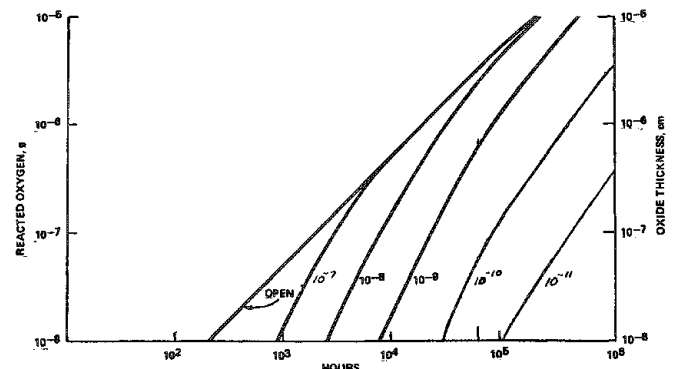


FIG. 8.--Amount of oxygen reacted vs time for various leak rates at 85 C calculated from model.

## LOW-VOLTAGE, HIGH X-RAY SPATIAL RESOLUTION MICROANALYSIS OF ALUMINUM ZINC

J. J. Friel

Al-Zn corrosion-resistant coatings consist of separate Al-rich and Zn-rich regions that are not easily analyzed with an electron microprobe because of their small size and the effects of atomic number and absorption. The microstructure and corrosion properties of these coatings have been reviewed by Friel and Townsend,<sup>1</sup> but quantitative analysis of the phases has always been difficult. An alloy of 55 wt% Al in Zn when applied as a hot-dipped coating on steel solidifies into cored Al-rich dendrites surrounded by Zn-rich interdendritic regions. The dendrites are usually about 5  $\mu\text{m}$  in diameter, but the interdendritic regions are often less than 3  $\mu\text{m}$ . A typical accelerating voltage for transition metal analysis in which K-lines are used would be 20 kV, but under such conditions it is not possible to analyze each phase separately, nor to quantify the Al/Zn composition gradient across a dendrite. Besides, analyses at 20 kV tend to total more than 100% because more than one phase is contained within the excited volume. Atomic number and particularly absorption effects are also significant. For example, absorption of the Al  $K\alpha$  line by Zn requires a correction factor of 1.8. However, if the accelerating voltage on the microprobe is lowered, the analytical volume decreases significantly, and the effects of absorption are minimized. Moreover, if a suitable Al-Zn mixed standard can be prepared, all the matrix corrections approach unity and uncertainties in such things as the mass absorption coefficient or electron backscattering correction factor are reduced.

### *Experimental*

A sample of an Al-Zn coating on sheet steel was mounted and polished in cross section in a Cu diallyl phthalate conductive mounting medium and analyzed with a JEOL 733 electron probe microanalyzer located at Lehigh University. The probe was operated at 5, 10, and 20 kV, at 20 nA beam current. At 5 and 10 kV, the Al  $K\alpha$  and the Zn  $L\alpha$  lines were used with the TAP crystal. At 20 kV, the Zn  $K\alpha$  line was used with the LIF crystal, and all the data were corrected on-line by the method of ZAF. Quantitative profiles were obtained by moving of the beam across the sample in steps of approximately 0.25  $\mu\text{m}$ , which is roughly of the order of the beam diameter. An Al-Zn standard consisting of Al with 8.3 wt% Zn was melted, homogenized at 500 C for 144 h, and then air cooled. The alloy composition was determined wet chemically and checked for homogeneity with the microprobe.

### *Results and Discussion*

*Effect of Accelerating Voltage.* Analyses of the center of Al-rich dendrites containing about 30 wt% Zn are given in Table 1 for incident beam voltages of 20, 10, and 5 kV. The spot size for each voltage at a beam current of 20 nA was calculated in accordance with the method reviewed by Goldstein et al.<sup>2</sup> These spot sizes vary from 190 to 320 nm; therefore, as voltage is decreased to minimize x-ray volume, beam size is increased if current is held constant. If current is decreased to maintain the smallest possible spot size, counting times increase and carbon contamination becomes a problem with a low-energy primary beam.

The electron range for each voltage was calculated for an alloy of 30 wt% Zn in Al according to the equation of Kanaya and Okayama.<sup>3</sup> The x-ray generation ranges of Andersen and Hasler are also listed.<sup>4</sup> Of course, the actual x-ray sampling volume is smaller than the generation range, primarily owing to absorption of these relatively soft x rays. Furthermore, the ranges are those that would be produced by an infinitesimally small beam. Therefore, the real x-ray resolution will be the beam radius plus some value less than the x-ray generation range. Table 1 shows that a resolution of about 1  $\mu\text{m}$  is possible at 10 kV with use of the Zn  $L\alpha$  line. Considerably better resolution can be obtained at 5 kV as

---

The author was formerly at the Homer Research Laboratories of Bethlehem Steel Corp., and is now with Princeton Gamma-Tech, Princeton, NJ 08540. The assistance of Mr. James Kerner of Lehigh University with the microprobe analyses is gratefully acknowledged.

TABLE 1.--Electron probe analyses of Al-Zn at various accelerating voltages.

E <sub>o</sub> (kV)	I (nA)	Spot Size (nm)	Line	(Z)	(A)	(F)	(ZAF)	WT%	X-ray Range ( $\mu$ m)	Electron Range ( $\mu$ m)	Standard
20	20	190	Al-K	0.979	1.818	0.999	1.782	72.87	2.9	3.5	Al
			Zn-K	1.091	0.998	1.000	1.090	30.18	2.2		Zn
			TOTAL 103.04								
10	20	250	Al-K	0.968	1.269	1.000	1.229	70.13	0.9	1.1	Al
			Zn-L	1.091	0.973	0.991	1.053	29.59	0.9		Zn
			TOTAL 99.71								
			Al-K	0.977	1.182	1.000	1.155	70.57	0.9	1.1	Al <sub>8</sub> Zn
			Zn-L	0.978	1.012	1.009	0.999	29.78	0.9		Al <sub>8</sub> Zn
			TOTAL 100.35								
5	20	320	Al-K	0.954	1.077	1.000	1.028	70.31	.25	0.3	Al
			Zn-L	1.114	0.990	0.994	1.122	29.45	.25		Zn
			TOTAL 99.75								
			Al-K	0.962	1.062	1.000	1.022	71.93	.25	0.3	Al <sub>8</sub> Zn
			Zn-L	0.963	1.004	1.008	0.974	28.65	.25		Al <sub>8</sub> Zn
			TOTAL 100.58								

long as the count rate is adequate and the vacuum is very clean. However, imaging is poor at 5 kV on an instrument not designed for low-voltage operation. A 2 $\mu$ m interdendritic region of essentially pure Zn was analyzed at 20 kV. The analysis reported 10 wt% Al in Zn, and a total of 111%. Repetition of this analysis at 10 kV resulted in less than 1% Al and 99% Zn.

*Effects of Atomic Number and Absorption.* The analyses in Table 1 do not represent exactly the same analytical point, but they were chosen at various points along the centerline of an Al-rich dendrite. The most significant of the matrix effects was absorption of Al x rays by Zn because of the large excited volume at 20 kV. This factor was reduced from 1.8 to 1.3 at 10 kV. Reducing the voltage to 5 kV resulted in no factor exceeding 1.1. By use of a mixed standard consisting of Al with 8.3 wt% Zn, the effects of Z, A, and F were reduced to below 7% at 5 kV, and 18% at 10 kV. Thus the uncertainty in any of the factors should not significantly degrade precision.

#### Conclusion

A potential of 10 kV produced high-quality analyses of Zn-rich regions that were less than 2  $\mu$ m across and revealed composition gradients across Al-rich dendrites. Although a 5kV potential could theoretically produce a much smaller analytical volume, this improvement would have to be achieved at a smaller spot size and therefore less beam current. Under these conditions, counting times were found to increase and generate an unacceptable level of

carbon contamination. This problem plus the poor backscattered electron imaging at 5 kV dictated the use of 10 kV. Furthermore, the use of an Al<sub>8</sub>Zn mixed standard considerably reduced the level of uncertainty in the atomic number and absorption corrections. By careful choice of analytical conditions, it was possible not only to analyze the as-solidified structure in Al-Zn but also to examine any changes after corrosion.

#### References

1. J. J. Friel and H. E. Townsend, "Corrosion resistance of zinc and zinc aluminum alloy coatings," *Sheet Metal Industries* 60: 506-507, 1983.
2. J. I. Goldstein et al., *Scanning Electron Microscopy and X-ray Microanalysis*, New York: Plenum Press, 1981.
3. K. Kanaya and S. Okayama, "Penetration and energy-loss theory of electrons in solid targets," *J. Phys.* D5: 43-58, 1972.
4. C. A. Andersen and M. F. Hasler, "Extension of electron microprobe techniques to biochemistry by the use of long wavelength x-rays," in R. Castaing et al., Eds., *4th Intl. Cong. on X-ray Optics and Microanalysis*, Paris: Hermann, 1966, 310-327.

## Cu-Nb COMPOSITE WIRE STRENGTH: AN ELECTRON MICROSCOPE STUDY

F. C. Laabs, A. R. Pelton, and W. A. Spitzig

Cu-Nb composite wires formed by an in situ fabrication process<sup>1</sup> demonstrate phenomenal increases in strength with corresponding increases in drawing strains,  $n = (\ln A_0/A)$ , (where  $A_0$  is the original, and  $A$  is the final transverse area of the wire).<sup>2</sup> The purpose of this study was to identify those microstructural parameters or mechanisms involved in the strengthening process.

### *Experimental Procedure*

In situ composite wires were prepared by rod rolling a 2 $\mu$ m-diameter as-cast Cu-20vol%Nb ingot to  $\frac{1}{2}$  in. and subsequently wire drawing through successively smaller dies to a smallest diameter of 0.0062 in. Representative wires were tested and examined between drawings and tested with a model 1125 Instron for mechanical property studies and a Zeiss-Axiomat optical microscope, a Cambridge S-200 SEM with thin-window EDS, and a JEOL-100CX TEM for structural studies.

### *Results and Discussion*

The as-cast ingot contains Nb dendrites whose arms have  $\langle 100 \rangle$  orientations which on being drawn form into long ribbon-like filaments that exhibit a  $\langle 110 \rangle$  texture.<sup>3</sup> Figure 1 shows the Nb dendrites in the as-cast material. The strength vs  $\ln(A_0/A)$  behavior of the resulting wires is shown in Fig. 2.

The shape and distribution of the resulting filaments in the wires were examined by optical microscopy ( $\eta = 0-7$ ). Scanning microscopy was used for wires with  $\eta = 0-12$ . Standard metallographic mounting techniques were utilized for both optical and scanning microscopy. A moderate etch composed of 27% $H_2O_2$ , 27% $H_3PO_4$ , 46% $H_2O$  was used to enhance surface relief for optical examinations. Surface preparation for scanning microscopy included a Cu-Nb etch of 20% $H_2SO_4$ , 20% $HF$ , 2% $HNO_3$ , 58% $H_2O$  to remove surface deformation between each of the mechanical polishing steps. The final polish was followed by a light Cu etch composed of 55% $H_2PO_4$ , 25% $CH_3COOH$ , 20% $HNO_3$ . Figure 3(a) shows a typical longitudinal SEM micrograph. From the longitudinal examinations it was observed that as  $\eta$  increased the Nb filaments assumed a more lamellar-like distribution, becoming thinner and having less tadpole-like features as part of the filament (Fig. 3b). Figures 3(c) and (d) show the corresponding transverse distributions of these same wires.

Examination of the fracture surfaces resulting from tensile testing shows a cup/cone type ductile fracture for the lower values of  $\eta$ ; however, at higher values of  $\eta$  ( $\eta \geq 11$ ), the overall fracture occurred by a shear mechanism (Fig. 4).

TEM studies indicate relatively large numbers of dislocation tangles which coalesce into cell walls at lower strains. Above  $\eta = 6-7$ , the dislocation boundaries sharpen and dynamic recovery (Nb) and recrystallization (Cu) occurs.<sup>4</sup> Thus, the observed high strengths at larger  $\eta$  values are due primarily to filament size and spacing.

### *References*

1. R. Roberge, in S. Foner and B. B. Schwartz, Eds., *Superconductor Materials Science: Metallurgy, Fabrication, and Applications*, New York: Plenum, 1981, 394.
2. J. Bevk, J. P. Harbison, and J. L. Bell, *J. Appl. Phys.* 49: 6031-6038, 1978.
3. C. C. Cheng, F. C. Laabs, A. R. Pelton, and J. D. Verhoeven, *Proc. Ann. EMSA Meeting* 43: 200, 1985.
4. A. R. Pelton, F. C. Laabs, and W. A. Spitzig (submitted to *Frontiers in Materials Science*).

The authors are at Ames Laboratory, Iowa State University, Ames, IA 50011. This work was done at Ames Laboratory, which is operated for USDOE by Iowa State University, under Contract W-7405-Eng-82 with the Office of Basic Energy Sciences.

FIG. 1.--SEM micrograph of as-cast Cu-20

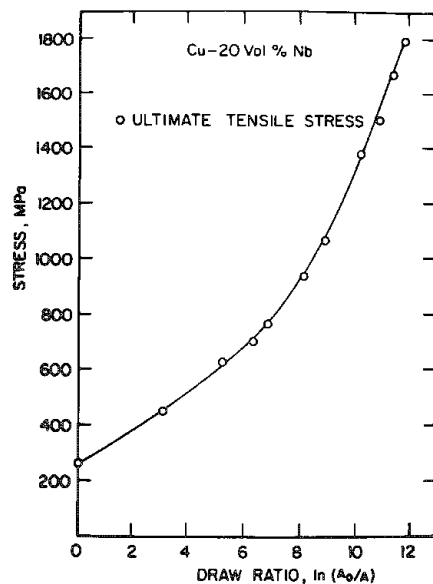
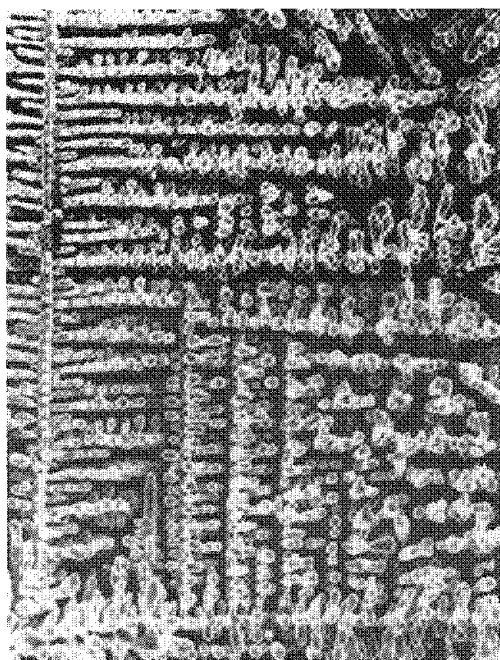


FIG. 2.--Strength of Cu-20 v/o Nb wire as function of draw ratio.

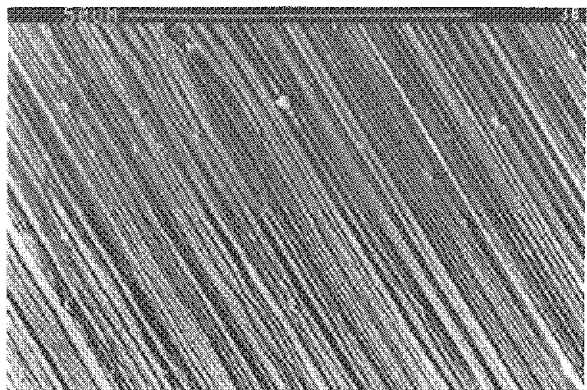
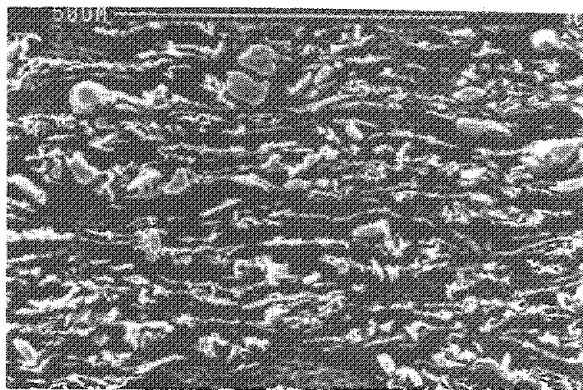
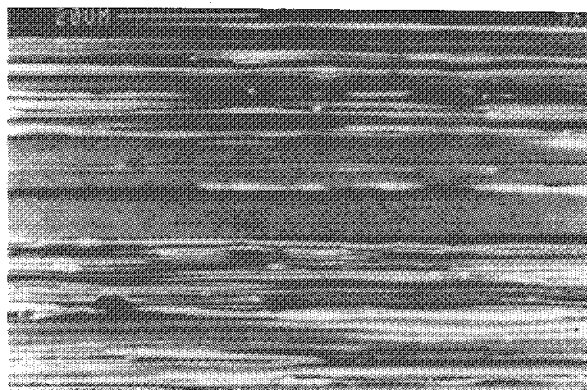


FIG. 3.--Longitudinal section through Cu-20 v/o Nb composite wire, (A)  $\eta = 5.3$ , (B)  $\eta = 11.1$ ; transverse section through Cu-20 v/o Nb composite wire, (C)  $\eta = 5.3$ , (D)  $\eta = 11.1$ .

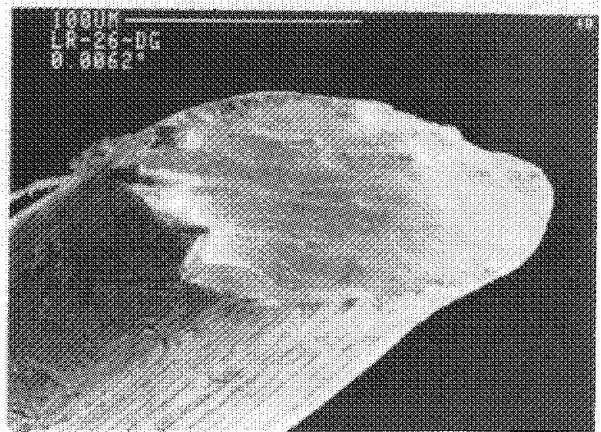
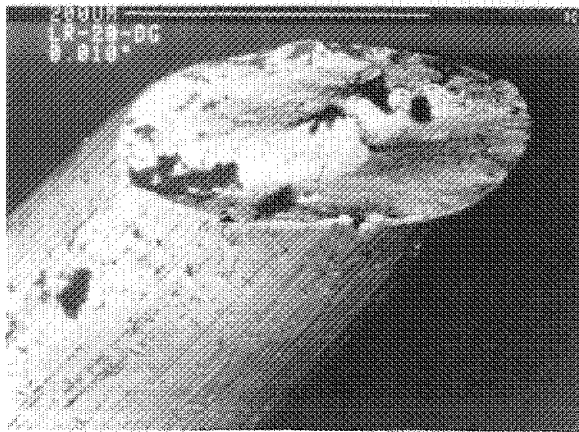
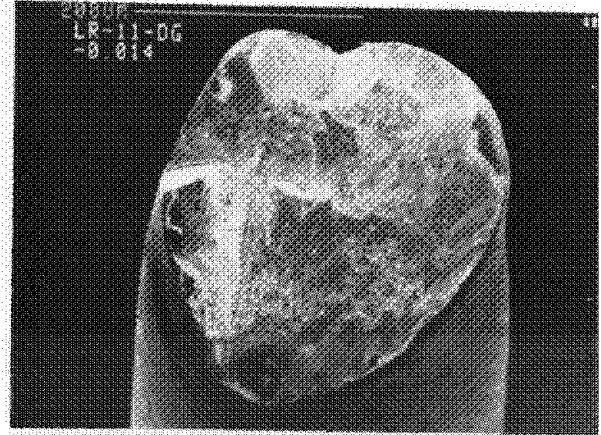
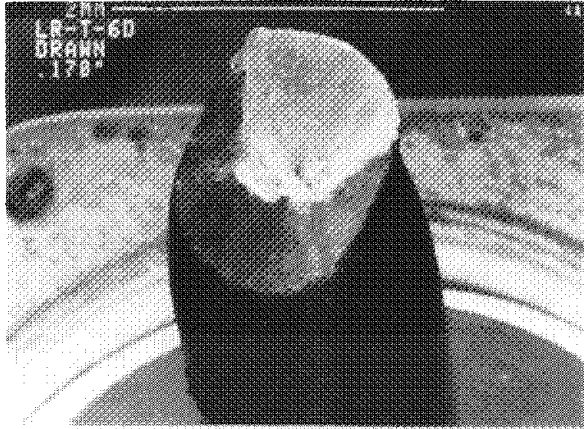


FIG. 4.--Tensile fracture of Cu-20 v/o Nb: (A)  $\eta = 5.3$ , (B)  $\eta = 10.4$ , (c)  $\eta = 11.0$ , (D)  $\eta = 11.9$ .



## FRACTURE OBSERVATION IN POLYMER SYSTEMS USING SEM

C. C. Garrison

A polymer testing stage (PTS) that allows observation of fracture in bulk samples by SEM is described. Examples are drawn from several filled polymer systems and it is shown that the results correlate with results from commercial testing systems. Combined with data from other test methods, PTS observations help elucidate fracture mechanisms and so improve understanding of failure and of polymer systems.

The primary advantages of the PTS over other SEM stages described in the literature<sup>1</sup> are high load capability and versatility in the types of tests that can be performed. Force transfer from outside the SEM to the PTS is achieved through hydraulic fluid, allowing loads up to 1250 lb to be achieved. This method has been reported by researchers working on metals,<sup>2,3</sup> but previous work in polymers was performed by use of mechanical advantage which provides lower loads. The PTS was designed to be flexible in application of its load as well. Grips have been fitted for tension, three-point bend, four-point bend, and driven-wedge tests. Many more types of grips are possible with design and machining being performed as need arises.

Figure 1 shows the PTS in a three-point bend setup. All materials of construction are nonmagnetic to avoid possible field problems. Four-point bend and driven-wedge setups are similar to the setup shown in Fig. 1. The springs over the shoulder bolts help maintain even pressure distribution in the hydraulic cylinders during early stages of a test when the load on a sample is small. In tension testing, the springs, loading nose, and support span are removed, and tensile grips are inserted in each half of the frame. The hydraulic cylinders apply the load by pushing one half of the frame away from the half in which the cylinders are mounted. This half is also affixed to the SEM stage, which allows positioning of the PTS under the electron column by means of the SEMs X and Y stage motors.

### Results

The first experiment performed with the PTS was a three-point bend on a unidirectional graphite-fiber reinforced (GFR) epoxy. Equivalent samples were cut from the same sheet and run under the same loading conditions with the PTS and an MTS Systems Corporation servohydraulic load frame. A stroke rate of 0.05 in./min on the load frame produced a load-vs-deflection plot with two discontinuities before catastrophic failure at 449 lb. The discontinuities occurred at 379 and 414 lb; the first was just a deflection in the curve and the second showed a small plateau. A videotape was made of this experiment performed on the PTS. The stroke rate was much slower and no event was observed near 380 lb. The event depicted in Fig. 2 occurred at 412 lb, corresponding to the second event observed on the MTS load frame. Only three video frames are presented from this event, which covered 10 frames (approx. 1/3 s) when played back frame by frame. The total sequence consisted of the easily visible dark crack appearing near the loading nose, a slower crack propagating at 45° from the direction of the loading nose, and finally a delamination on the side of the specimen opposite the loading nose. The catastrophic failure occurred at a load of 438 lb with the PTS.

The above example illustrated unstable crack propagation. Figure 3 gives results from a stable crack propagation. Here another sample of GFR was put under a three-point bend load. However, a prenotch in the fiber direction allowed the observation of a slowly propagating shear crack and the deformed region ahead of the crack tip (Fig. 3). This micrograph shows the beginnings of hackle formation ahead of the crack tip. More hackles imply a higher crack surface area and greater dissipation of energy in the cracking process.

A problem-solving case was chosen for the last example. Flake glass filled polyurethane was being tested in a Reaction Injection Molding (RIM) application, but the mechanical testing results were not what was expected and there was some question as to how well the polyurethane was adhering to the glass. The results of a single edge notched tension

test are shown in Fig. 4. This experiment was also videotaped and the glass could be observed falling out of the urethane. This led to investigations of glass surface treatments and an eventual solution to the problem.

It has been shown that data obtained from the PTS can be correlated with data obtained from other mechanical testing systems. This correlation allowed direct observation of fracture phenomena associated with specific events in stress-strain plots. The PTS also functioned as a valuable problem-solving tool.

#### References

1. S. Bandyopadhyay, *J. Mater. Sci. Letters* 3: 39-43, 1984.
2. Andrew Nagy, J. B. Campbell, and D. L. Davidson, *Rev. Sci. Instrum.* 55: 778-782, 1984.
3. D. W. Cameron and D. W. Hoepfner, *Closed Loop*, Winter 1985, pp. 3-9.

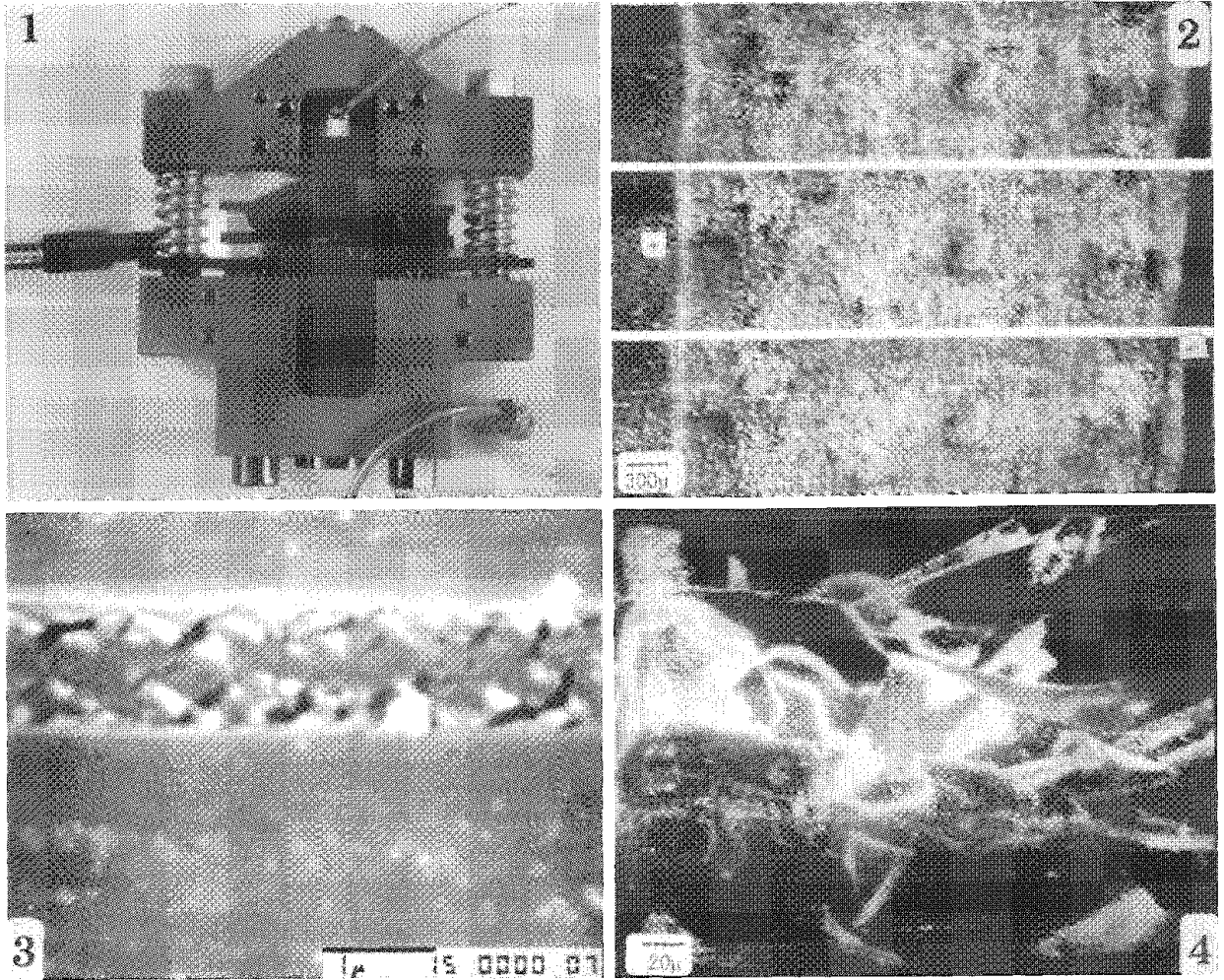


FIG. 1.--PTS with three-point bend specimen.

FIG. 2.--Unstable crack in GFR. Initiation and delamination are arrowed.

FIG. 3.--Deformation ahead of tip of shear crack in GFR.

FIG. 4.--Crack tip in single edge notched tension of flake glass filled polyurethane.

## PIXE ANALYSIS OF SOLDERS ON ANCIENT GOLD ARTIFACTS WITH A NUCLEAR MICROPROBE

Michel Piette, Guy Demortier, and Franz Bodart

An inexpensive personal computer is used to pilot the mechanical displacement of the target sample into the proton beam of a nuclear microprobe. It allows the simultaneous collection of a maximum of 128 images during scans up to  $40 \times 40$  steps in less than 90 min. A selection of applications on gold jewelry artifacts permits the confirmation of previous conclusions on the possibility that cadmium can have been used in antiquity to obtain brazing alloys for the workmanship of goldsmiths.

### *Experimental*

Narrow beams ( $2 \mu\text{m}$  in diameter) of an ion microprobe are obtained by a set of strong focusing magnetic quadrupoles. Atomic and nuclear techniques (PIXE, PIGE, RBS, etc.) may be simultaneously used to obtain quantitative analysis of a great variety of chemical elements with a high spatial resolution.

The images shown in this paper have been obtained by PIXE for measuring the relative concentration of Au, Ag, Cu, and Cd in ancient gold artifacts. Their characteristic x rays emitted during the irradiation procedure are analyzed by an Si(Li) energy-dispersive detector.

Relative concentrations of elements are obtained by comparison with reference material containing at least all the elements present in the studied sample. Matrix effects are taken into account.<sup>1</sup>

The data-acquisition system is based on an Olivetti M24 microcomputer (IBM PC compatible). This microcomputer controls the mechanical displacement of the sample (with a reproductibility better than  $2.5 \mu\text{m}$  even after a displacement of centimeters), the collection of x-ray spectra, and, if necessary, the counting of information from other detectors (gamma ray, charged particles, secondary electrons, integration of the incident proton beam). It also draws the images (concentration maps with 64 gray levels), adds or subtracts different images (e.g., background subtraction), normalizes them with respect to one particular image (e.g., instantaneous beam current) or shows correlation between elements, draws binary or ternary phase diagrams, and performs many other functions. At present it can collect 128 simultaneous images (each  $40 \times 40$  analyzed points). Typical collecting rate is 5-10 s per analyzed point. The images on gold artifacts shown below were collected less than 2 h. No other nondestructive method of microanalysis can give the amount of information in the same time.

Two of the main advantages are the low cost (microcomputer + interfaces + ADC for less than \$10 000) and its flexibility (multidetector). Considering that all the images are collected simultaneously, we can be sure that they are *superposable*. The full description of the acquisition system is given elsewhere.<sup>2</sup>

### *Applications to the Study of Solders on Ancient Gold Artifacts*

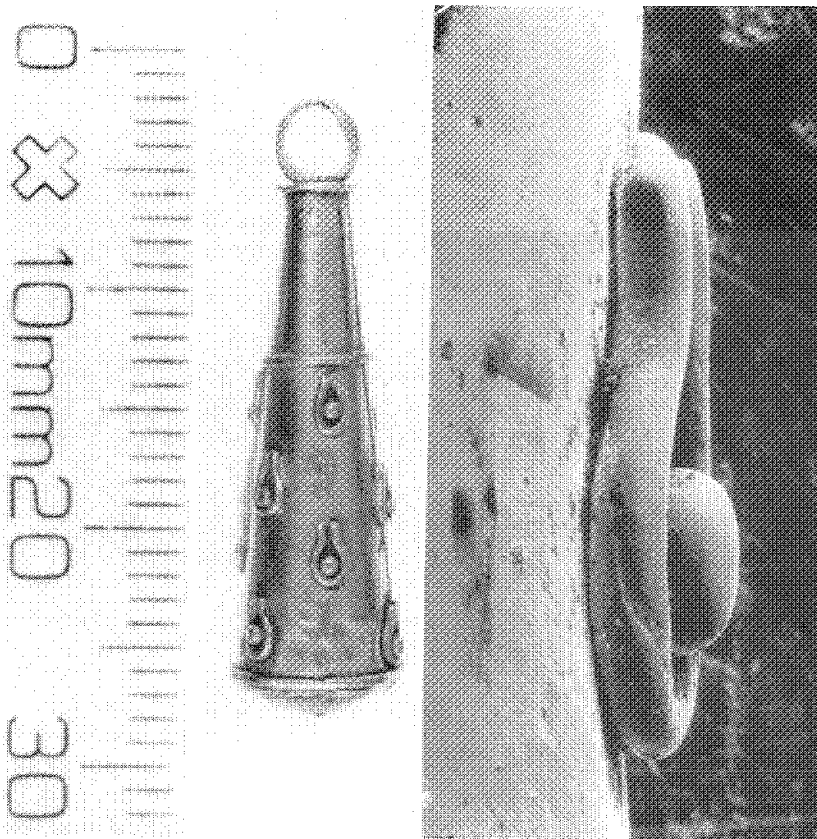
As discussed in previous papers,<sup>1,3,4</sup> ancient procedures for the soldering of gold artifacts may be recognized by the study of local relative concentrations of Cu, Ag, Au, and sometimes Cd. These elements are quantitatively analyzed by PIXE; the characteristic X-ray lines used are Cu  $K\alpha$ , Au  $L\beta$ , Ag  $K\alpha$ , and Cd  $K\alpha$ .

Figure 1(a) represents a conical finial (2nd cent.) often used at both ends of open necklaces of Hellenistic and Roman jewelry. Figure 1(b) is an electron micrograph of the simple decorative motive (wire shaped in horseshoe surrounding a little sphere of gold). The total length of the motive is 2.3 mm. Figure 2 summarizes the results of comparative compositions in Cu, Au, and Ag with a microbeam of protons ( $20 \times 20 \mu\text{m}^2$ ).

Regions such as "h" indicate that the incident beam reaches a hole in the irregular

---

The authors are at L.A.R.N., Facultés Universitaires Notre-Dame de la Paix, 22 Rue Huzet, B-5000 Namur, Belgium.



(a)

(b)

FIG. 1.--(a) Conical finial of open necklace, Roman, 2nd cent. A.D.; (b) electron micrograph of detail.

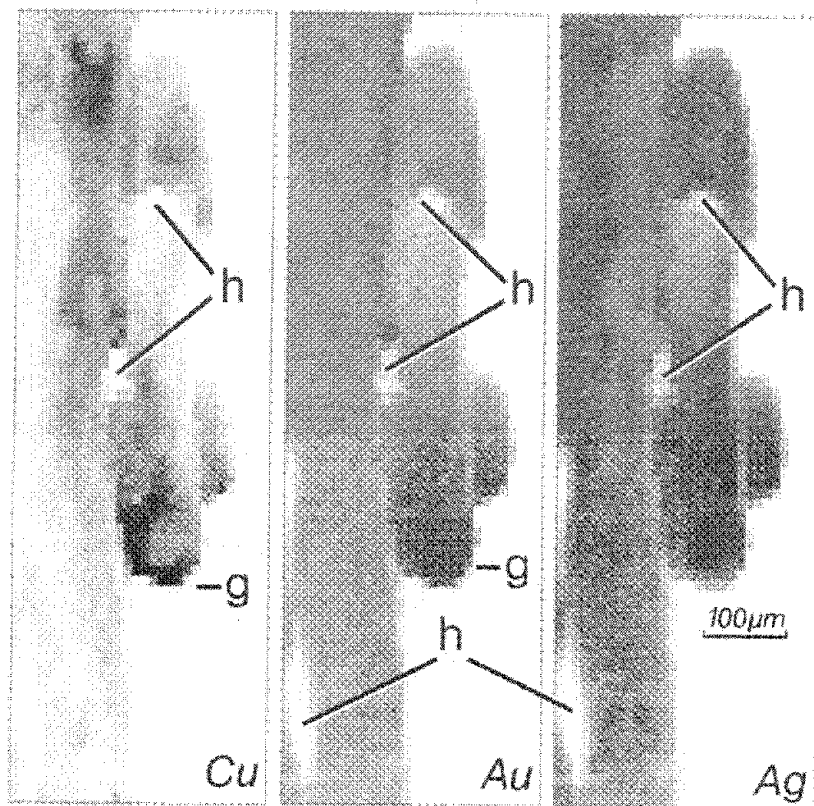


FIG. 2.--Copper, gold, and silver images obtained by PIXE microprobe (beam size  $20 \times 20 \mu\text{m}^2$ , steps of  $50 \mu\text{m}$  in both directions).

surface: no x-ray signal can reach the detector. In the region of the solder of the horse-shoe on the main conical body, one observes a significant increase of Cu with a low decrease of Ag and nearly no variation of Au. The soldering of these decorative elements may have been done by a process of diffusion of finely powdered copper at a temperature of about 900 C.<sup>5</sup> This process is similar to that used by Etruscan goldsmiths as rediscovered in 1933 by L. Littledale of the British Museum.<sup>6</sup> The apparent increases of Cu and Au (less evident for Au) in region "g" may be partially due to a geometrical effect: in that particular region the incident proton beam interacts with the material at grazing incidence. There, the absorption of low-energy x rays is lower than elsewhere and enhancement of the x-ray signals of copper and gold is expected relative to nonaffected signals from Ag.

Figure 3 represents a small hollow sphere (8.5 mm in diameter) found in Lebanon with other more prestigious artifacts (6th cent.): it may be part of a necklace. Motives such as roses, pairs of disks and little granulations are soldered by a brazing procedure, as can be visually observed under a magnifying glass.

Figure 4 obtained during scans by steps of 150  $\mu\text{m}$  (beam size: 50  $\mu\text{m}$ ) illustrates the general repartition of Cu, Au, Ag, and Cd. The scanned area is  $3 \times 6 \text{ mm}^2$ . Regions indicated by "s" concern proton impacts for which the x-ray detector is in the shadow of predominant elements; regions indicated by "a" concern "accidents" in the collection of results. Data of the figures collected at each impact for an identical time of irradiation were corrected for the fluctuations of the beam current, which is measured simultaneously. The data simply indicate irregularities of the irradiated surface. Cu K $\alpha$  and Au L $\beta$  data are specially sensitive to problems of casual geometries, but Ag K $\alpha$  data are less sensitive to these geometrical effects. Cd appears only in the region of the brazing of the disks on the hollow sphere and of granulations on the disks. Figure 5 illustrates a detail of a scan in a particular region indicated in Figure 4(d) (10  $\mu\text{m}$  proton beam by steps of 25  $\mu\text{m}$  in an area of  $750 \times 1000 \mu\text{m}^2$ ). Each elemental concentration of Ag, Cu, and Cd is divided by that of Au so that geometrical accidents are eliminated: the Ag distribution (Fig. 5a) is nearly uniform, but Cu and Cd distributions (Figs. 5b and c) specially typify the region of the solder. Their correlation offers the main criterion to assert that the cadmium brazing is probably of ancient origin (Fig. 5d).<sup>1,4</sup> The region "m" corresponds to a greater mobility of Cd during the brazing procedure.<sup>7</sup>

The rediscovery of one possible process used by ancient goldsmiths for the fabrication of brazing alloys containing cadmium has been recently discussed.<sup>1,4</sup> Results obtained by the nuclear microprobe confirm these previous results. Ternary diagrams of Cu, Ag, and Cd that can be extracted from Fig. 5 indicate that the soldering on the artifact had not been done with commercial soldering alloys. Observations by a scanning electron microprobe indicate that the surface of all parts of the jewel reflects no trace of modernity.<sup>8</sup>

### Conclusions

The use of a personal computer to plot and to extract significant results from mechanical scans on the irregular surface of gold artifacts may be more rapid than conventional electron microprobes if a large number of elemental compositions is necessary. Illustration of performances on the analysis of the composition of solders on gold jewelry artifacts of archaeological interest allows the rapid identification of the soldering procedure used by the goldsmiths and the clarification of the criteria to distinguish modern from ancient brazing procedures.

### References

1. B. Van Oystaeyen and G. Demortier, *Nucl. Instr. and Methods* 215: 299-313, 1983.
2. M. Piette and F. Bodart (to be published).
3. G. Demortier, *Gold Bulletin* 17: 27-38, 1984.
4. A. Boullar, C. Vermeyen-Moor, Z. Gabelica, and G. Demortier, *Calorimétrie et Analyse Thermique* 15: 179-188, 1984.
5. A. Thouvenin, *Revue Archéologique de l'Est et du Centre-Est* (France) 24: 11-68, 1973.
6. H. A. P. Littledale, British patent 415 181, 1936.
7. G. Demortier and T. Hackens, *Nucl. Instr. and Methods* 197: 223-236, 1982.
8. M. Lecaille (CARME, La Teste, France), private communication.



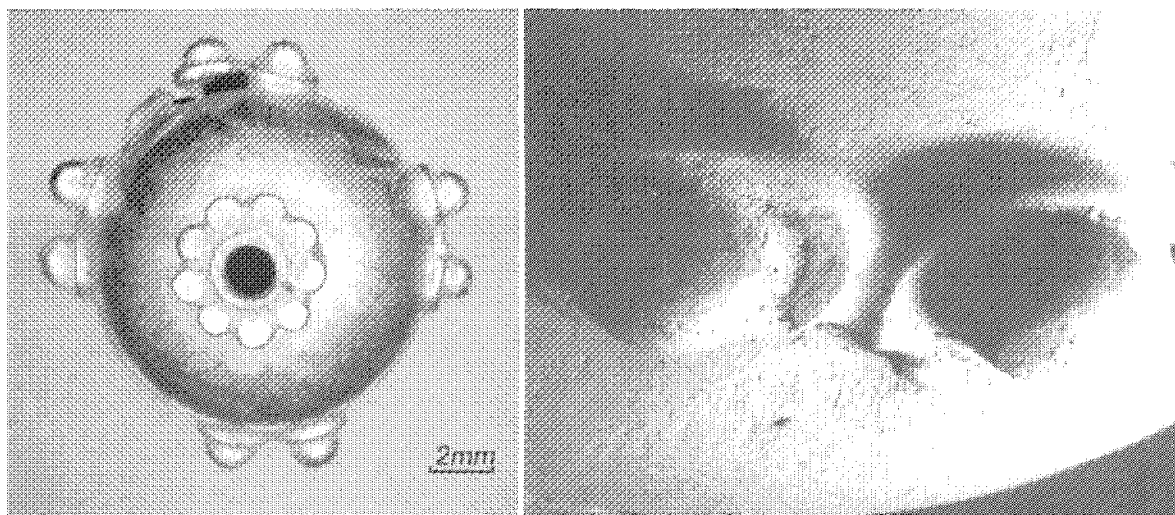


FIG. 3.--(a) Gold sphere decorated with disks and granulations (Byzantine, 6-7th cent. A.D.); (b) electron micrograph of detail.

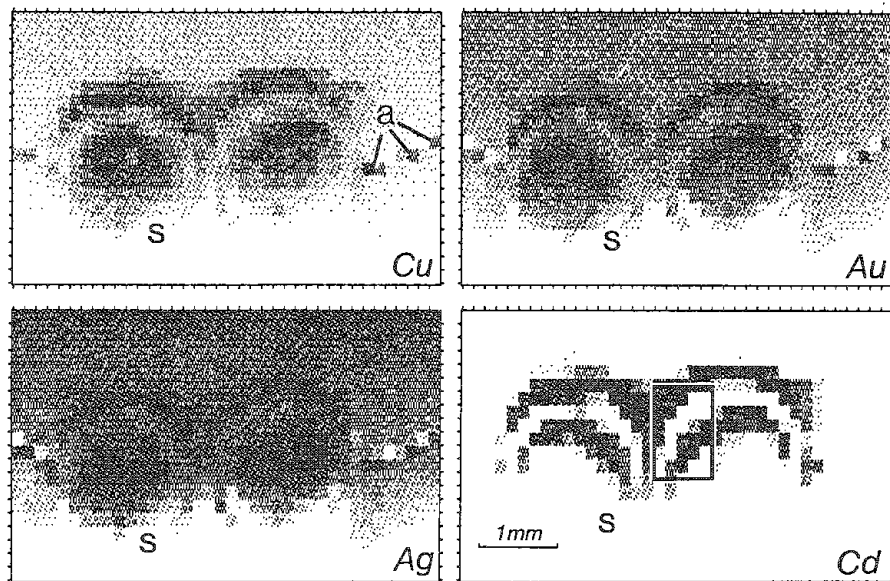
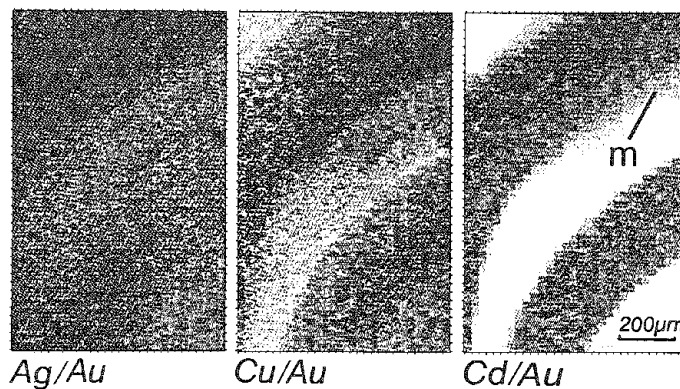


FIG. 4.--Copper, gold, silver, and cadmium images obtained by PIXE microprobe (beam size  $50 \times 50 \mu\text{m}^2$ , steps of  $150 \mu\text{m}$  in both directions). Limits of narrow scans in Fig. 4(d) are illustrated in Fig. 5.

FIG. 5.--Ag/Au, Cu/Au, and Cd/Au images obtained by PIXE microprobe (beam size  $10 \times 10 \mu\text{m}^2$ , steps of  $25 \mu\text{m}$  in both directions).



## CHARACTERIZATION OF OXIDE SCALE FORMED ON INCOLOY 800 TUBES IN THE MOLTEN SALT ELECTRIC EXPERIMENT (MSEE)

J. J. Stephens, R. E. Semarge, and R. W. Bradshaw

Solar energy receivers utilizing molten nitrate salts as a heat transfer fluid have been under development at Sandia National Laboratories for several years.<sup>1,2</sup> When used with a properly sized storage system, the molten nitrate salt serves as a buffer against cloud transients that can interrupt the electric power production of a central receiver. In particular, systems employing a salt mixture of 60 NaNO<sub>3</sub>-40 KNO<sub>3</sub> (wt%) have been used in receivers made of Incoloy 800 tubing with maximum operating temperatures in the range 550 to 600 C. Previous laboratory studies have evaluated the corrosion of Incoloy 800 due to the 60 NaNO<sub>3</sub>-40 KNO<sub>3</sub> mixture during steady-state operation of a thermal convection loop,<sup>3</sup> as well as static exposure during slow strain rate tensile testing.<sup>4</sup> The results of these studies indicated that the oxide scales that formed were relatively complicated multilayer films. The present investigation is aimed at characterizing the oxide scales formed during actual operation of the 5MW (thermal) MSEE receiver which was operated at the Solar Central Receiver Test Facility from January 1984 to July 1985. This receiver saw approximately 1000 h of operation under actual power production conditions. Combined wavelength-dispersive x-ray analysis and x-ray diffraction of the oxide scales formed on tubes cut from this receiver has shown the oxide scales to have a spinel structure, with an outer layer rich in Fe, Mg, and Si, and an inner layer rich in Ni and Cr.

### *Experimental*

The MSEE receiver utilized a serpentine flow design with 18 vertical tube banks, consisting of 16 tubes per bank. The tubes were made of Incoloy 800, drawn to an outside diameter of 3/4 in. and a wall thickness of 0.065 in.; each tube was 11.5 ft long. The nominal chemical composition<sup>5</sup> of Incoloy 800 is shown in Table 1. Tubes were cut from three specific horizontal locations in the receiver: (1) the high-temperature salt outlet bank, (2) the mid-receiver tube bank, and (3) the low-temperature salt inlet bank. Specimens for scanning electron microscopy and electron probe microanalysis were cut from both the top and the middle of each of the tubes in the above three locations. The specimens were nickel plated (electrolytic process) on both inside and outside diameters, and mounted in epoxy. The mounts were ground through 600 grit SiC, and subsequently polished with 30, 6, and 1  $\mu$ m diamond paste. In addition, a 1 in. OD Incoloy 800 tube specimen from the thermal convection loop apparatus,<sup>3</sup> which had been mounted (without nickel plate) in epoxy along with a concentric 0.75 in. OD steel tube for edge retention, was polished as described above. All micrographs presented herein are of as-polished, unetched surfaces.

TABLE 1.--Nominal chemical composition of Incoloy 800 (wt.%). (Source: average of 5 production heats from Ref. 5.)

C	Mn	Si	Ti	Al	Cu	Cr	Ni	S	P	N	Fe
0.05	0.8	0.2	0.4	0.3	0.5	19.7	32.5	0.003	0.007	0.015	Bal.

Authors Stephens and Semarge are with Sandia National Laboratories, Albuquerque, NM 87185; author Bradshaw is with Sandia National Laboratories, Livermore, CA 94550. This work was supported by the U.S. Department of Energy under contract DE-AC04-76DP00789. The authors gratefully acknowledge the assistance of R. G. Tissot in performing the x-ray diffraction analysis. Metallographic assistance was provided by A. J. Romero, and R. D. Lujan assisted in obtaining high-magnification SEM micrographs.

Electron probe microanalysis was performed by a Cameca MBX EPMA equipped with a Tracor Northern EDS detector and a LeMont Scientific BSE system. EDS spectra were obtained for several areas of the oxide scale present on the inside diameter of the tubes. WDS measurements were also obtained from these areas (15 kV, 20 nA, 20 s maximum count time, 1  $\mu$ m effective beam diameter) to aid in elemental identification. Sets of photomicrographs, including secondary electron (SE) images, backscattered electron (BSE) images (compositional mode), and elemental distributions (EDPM) were taken at a magnification of 800 $\times$  for each specimen. The analyzing crystals were set to  $K\alpha$  lines for each EDPM. Higher magnification (3000 $\times$ ) SE/BSE pairs of the oxide scales were taken to determine whether any finer fluctuations in composition in the oxide scale was present. These latter micrographs were obtained with a Hitachi S-500 SEM operated at 25 kV.

X-ray diffraction was utilized in an attempt to determine the structure of the various oxide phases present. Tube sections were cut in half, then flattened in a vise, with care taken not to abrade the oxide scale. Diffraction patterns were obtained for both the bare oxide scale and following the careful polishing of the scale on 600 grit SiC paper. A Siemens D500 automated powder diffractometer was used with monochromatic Cu  $K\alpha$  radiation, operated at tube settings of 40 kV, 30 mA. Data were collected digitally with an LSI-1170 computer equipped with a Daco MP interface.

### Results and Discussion

*Tubes from Low-temperature Regions.* No detectable oxide scale was found on the tube specimen taken from the low-temperature salt inlet (tube #3). Mounted specimens indicated a minor amount of surface pitting, up to 4  $\mu$ m deep. The observations for tube #3 indicate that the operating temperature in this part of the receiver was probably in the range of 400-500 C, where oxide growth kinetics would be sluggish and some intergranular pitting is expected.<sup>3</sup>

*Tubes from High-temperature Regions.* Oxide scales approximately 15-20  $\mu$ m thick were found on the tube specimens from both the high temperature salt outlet (tube #1) and the middle bank of the receiver (tube #2). Figure 1 shows a BSE image and companion EDPM's for a specimen taken from the center of tube #1, and is representative of both tubes. Inspection of these micrographs indicates that the oxide scale is composed of two major components. The outer part of the scale is rich in Fe, Mg, and Si, which corresponds to the dark-gray and black regions on the backscattered image, consistent with the relative concentrations of the light elements Mg and Si. The inner part of the scale is rich in Ni and Cr, along with minor amounts of Fe and Mn. This inner phase is lighter in the backscattered image (Fig. 1a). A higher magnification SE/BSE pair for the same specimen is shown in Fig. 2. Note that a variation in Mg and Si concentration is readily apparent

TABLE 2.--Lattice parameter for selected transition metal spinels.<sup>6</sup>

Phase	Lattice Parameter (nm)
$Fe_3O_4$	0.8394
$FeCr_2O_4$	0.8377
$MgFe_2O_4$	0.836
$MnCr_2O_4$	0.8437
$NiCr_2O_4$	a= 0.8248
	c= 0.8454

from Fig. 2(b), corresponding to the dark-gray and black regions in the outer oxide. Point analyses of the outer oxide scale indicated a variation in Mg from 2 to 5 wt%. Figure 2 also indicates a significant amount of porosity in the outer, darker phase which was filled by the nickel plate. Finally, there are finger-like areas of intrusion of the darker oxide phase into the inner oxide phase, which is also apparent from inspection of the Mg map in Fig. 1(b).

X-ray diffraction patterns (Fig. 3) were obtained for a specimen immediately adjacent to the specimen shown in the above figures. Patterns from both the original scale and with 12  $\mu$ m removed indicate the major peaks in both patterns correspond to a

spinel structure. The lattice parameter of the spinel in the patterns was found to be 0.835 nm. That is comparable to the lattice parameters for the various transition metal spinels listed in Table 2.<sup>6</sup> Figure 3 also shows the line positions for  $Cr_2O_3$  and  $NiO$ ; it



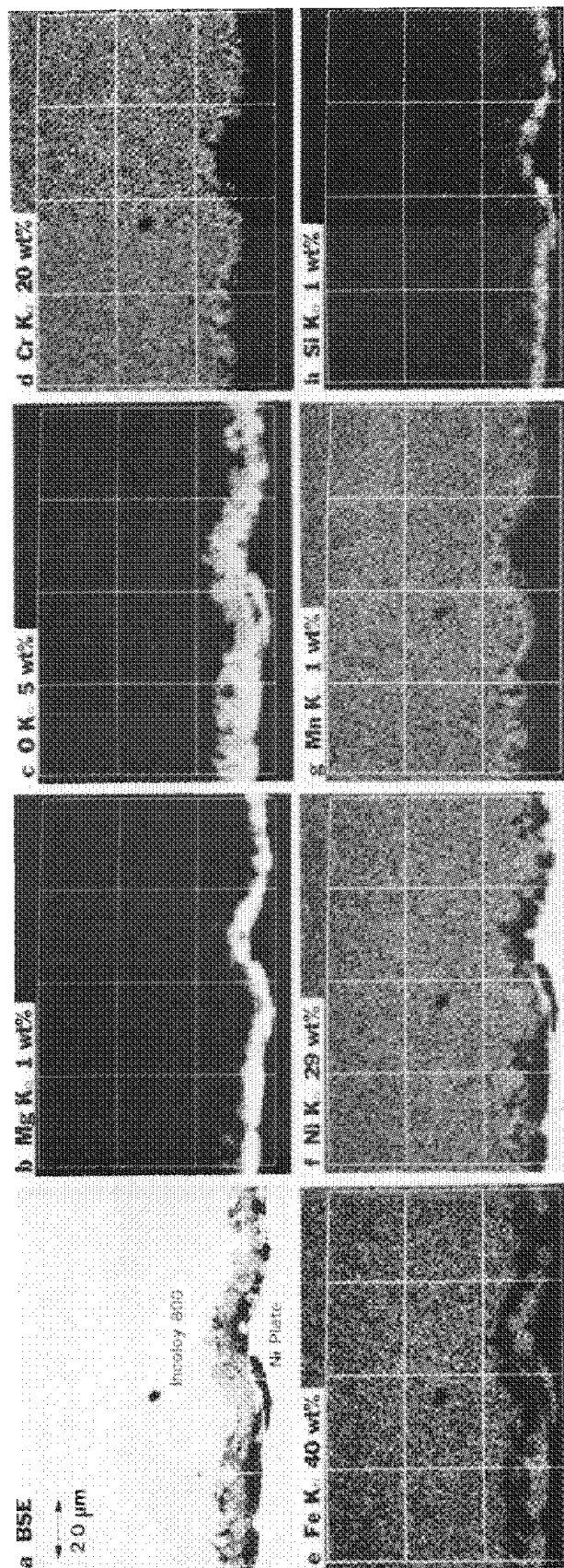


FIG. 1.--Oxide scale and base metal of inside diameter of center of Tube #1 from MSE. (a) Backscattered electron image. EDPMs: (b) Mg, (c) O, (d) Cr, (e) Fe, (f) Ni, (g) Mn, (h) Si.

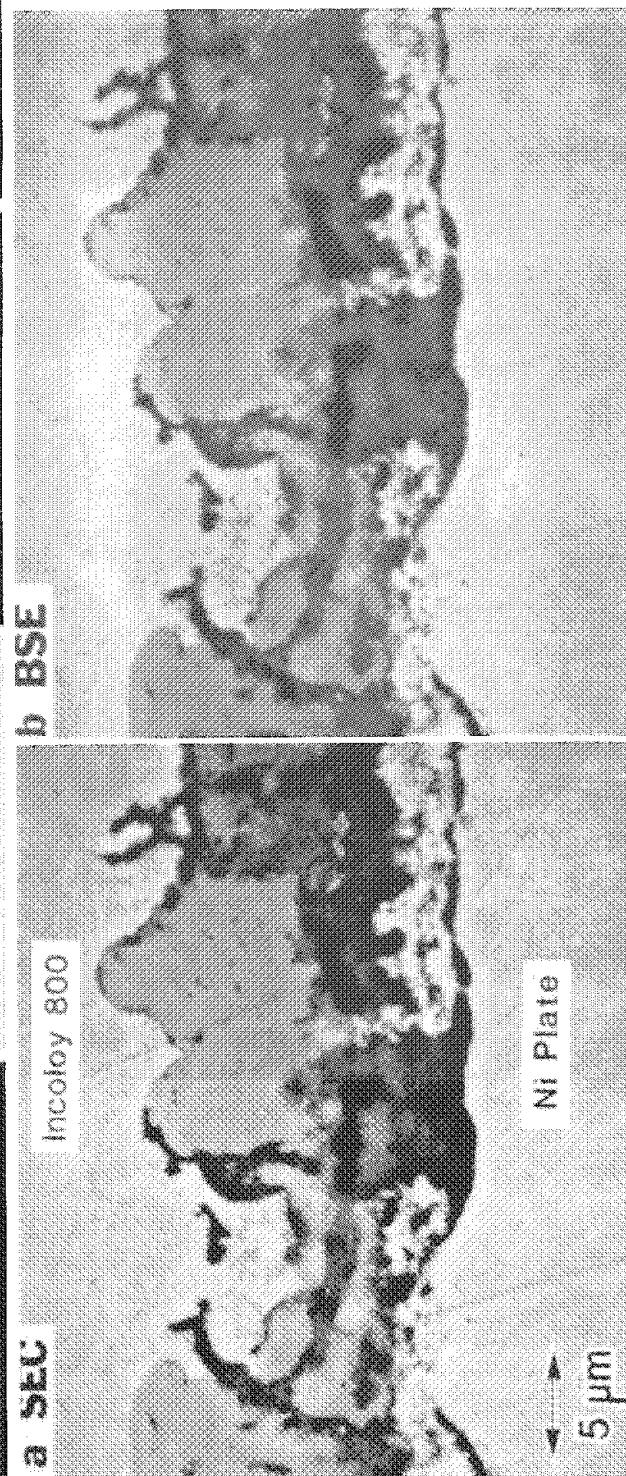


FIG. 2.--Higher-magnification detail of specimen shown in Fig. 1. (a) Secondary electron image; (b) backscattered electron image.

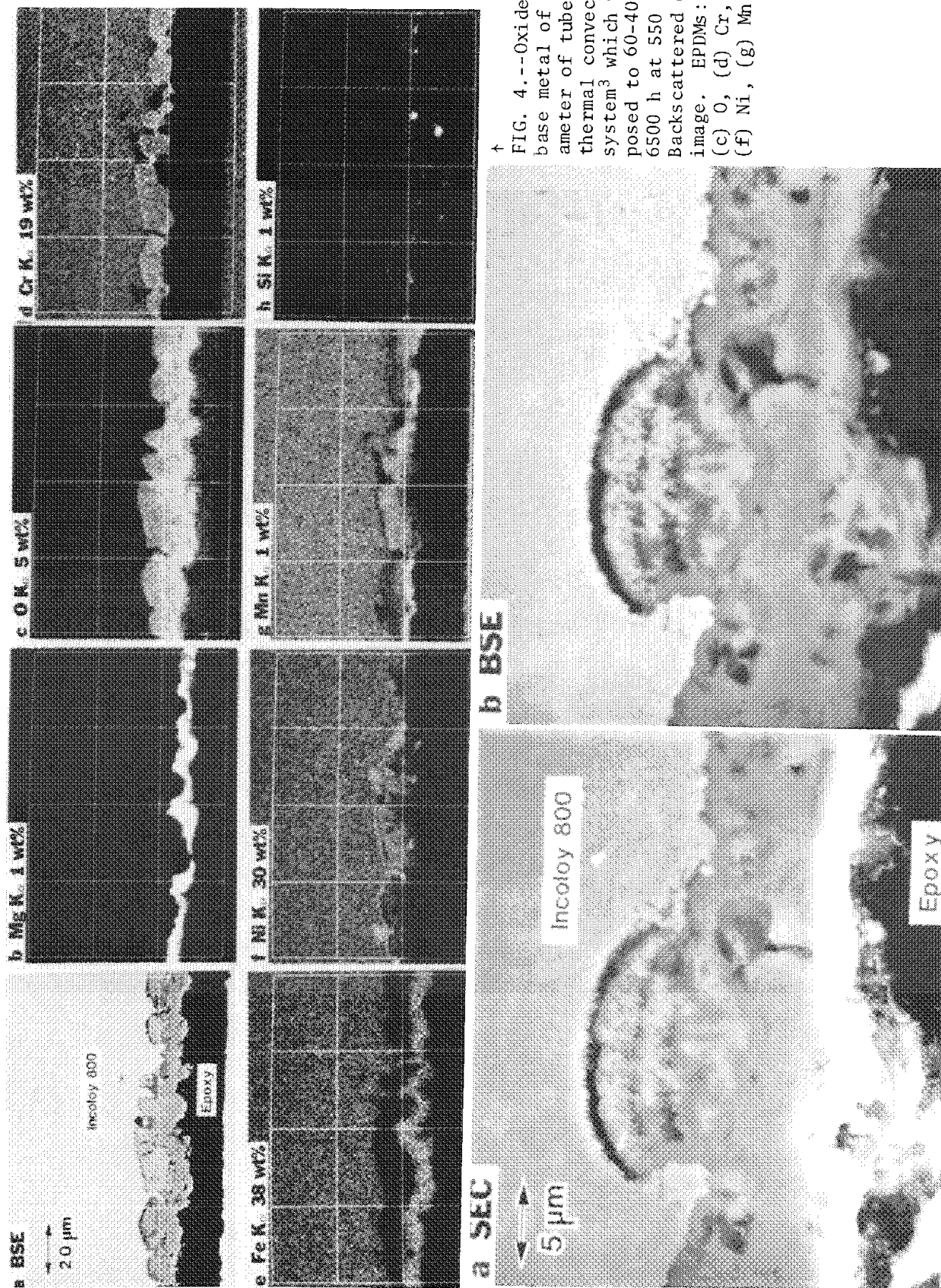


FIG. 5.--Higher-magnification detail of specimen shown in Fig. 4. (a) Secondary electron image; (b) backscattered electron image.

FIG. 4.--Oxide scale and base metal of inside diameter of tube from thermal convection loop system<sup>3</sup> which was exposed to 60-40 salt for 6500 h at 550 C. (a) Backscattered electron image. EPDMs: (b) Mg, (c) O, (d) Cr, (e) Fe, (f) Ni, (g) Mn, (h) Si.

is evident that the majority of the oxide scale has a spinel structure. No shift in angular positions was observed in the spinel lines as material was removed; if any changes in lattice parameter of the spinel occur, they are rather small ( $<0.01$  nm).

Inspection of Table 1 indicates that Mg is not present in the Incoloy 800; this element must be incorporated into the oxide spinel from the molten salt. Chemical sampling and analysis of the salt were performed during operation of the MSEE receiver.<sup>7</sup> Inspection of these results indicate that the concentration of Mg in the salt was initially 4 ppm, increased to 8 ppm during operation of the receiver, and declined to 2 ppm during the final months of operation. It is remarkable that such a low concentration of Mg in the salt can lead to significant amounts of Mg in the oxide scale. The presence of the Mg in the scale is regarded as fairly innocuous: incorporation of Mg into the scale implies that proportionately less metal atoms must diffuse from the matrix to form a protective scale.

*Tubes from Thermal Convection Loop Experiment.* A section of Incoloy 800 tubing from a laboratory thermal convection loop study<sup>3</sup> exposed to the flowing 60-40 salt mixture at 554 C for 6500 h was examined. A series of EDPMs in Fig. 4 allow us to compare the oxide scale formed under isothermal conditions with those in the MSEE. The outer oxide scale is rich in Fe and Mg, but little Si is evident. The inner oxide scale is rich in Cr and Ni, along with a significant amount of Mn. Close inspection of Fig. 4 reveals a depletion layer of Fe which is accompanied by relative enrichment of Cr in the Incoloy 800 just inside the inner oxide layer. A higher magnification SE/BSE pair (Fig. 5) indicates that the outer oxide scale is fairly dense and homogeneous, but that there is finer mixing of oxide phases within the inner oxide.

Comparison of Figs. 1 and 4 reveal that both tubes formed Fe and Mg rich outer scales but the amount of Si is greater in the MSEE scale. The inner scale on both tubes is rich in Ni and Cr, but the thermal convection loop specimen exhibits larger concentrations of Mn. A comparison of the respective O maps indicates that the concentration of O within the scale is much more uniform in the MSEE tube. The map for O in the thermal convection loop tube (Fig. 4c), along with the BSE image (Fig. 4a), suggests a range in oxide stoichiometry within the inner scale, ranging between  $M_2O_3$  and  $M_3O_4$ . Inspection of Figs. 2 and 5 leads one to suspect that the oxide scales formed under actual thermal transient operation tend to be more porous than under isothermal laboratory conditions. This suspicion must be tempered with the fact that we are comparing tubes in the MSEE which saw only about 1000 h service with tubes from laboratory equipment which saw about six times as much service.

### *Summary and Conclusions*

Examination of the scales formed inside Incoloy 800 tubes of the MSEE receiver indicate that two major oxide layers are present. The outer layer is rich in Fe, Mg, and Si; the inner layer is rich in Ni and Cr, with some Mn present. The structure of the oxide scale is predominantly spinel, with a lattice parameter comparable to many of the transition metal spinels. The Mg is not originally present in the tubes and is found as an impurity in the receiver salt mixture.

Combined electron-probe microanalysis and SEM on an Incoloy 800 tube specimen from the thermal convection loop study<sup>3</sup> indicates the presence of two major layers in the oxide scale. The outer scale is rich in Fe and Mg; the inner layer is rich in Cr, Ni, and Mn. As in the MSEE receiver, Mg is present in the oxide scale due to Mg impurities in the salt.

### *References*

1. R. W. Carling et al., *Molten Nitrate Salt Technology Development*, Status Report, SAND 80-8052, Sandia National Laboratories, 1980.
2. T. R. Tracey, *Advanced Central Receiver Power System, Phase II*, Final Report, vol. 2, MCR-81-1707, Sandia Contract 18-6879C, May, 1981.
3. R. W. Bradshaw, *A Thermal Convection Loop Study of Corrosion of Alloy 800 in Molten  $NaNO_3$ - $KNO_3$* , SAND82-8911, Sandia National Laboratories, 1983.
4. S. H. Goods, "The mechanical properties of alloy steels in molten sodium-potassium nitrate salts," in M. F. Rothman, Ed., *High Temperature Corrosion in Energy Systems*, Metallurgical Society of AIME, 1985, 643-657.
5. J. C. Lippold, "An investigation of HAZ cracking in alloy 800," *Welding J.*

(Research Supplement), 1983, 1s.

6. F. S. Galasso, *Structure and Properties of Inorganic Solids*, New York: Pergamon Press, 1970, 225-231.

7. A. B. Quakenbush, *MSEE Salt Sampling*, 1985 Status Report, Olin Chemical Corp., Lake Charles, La., December, 1985.

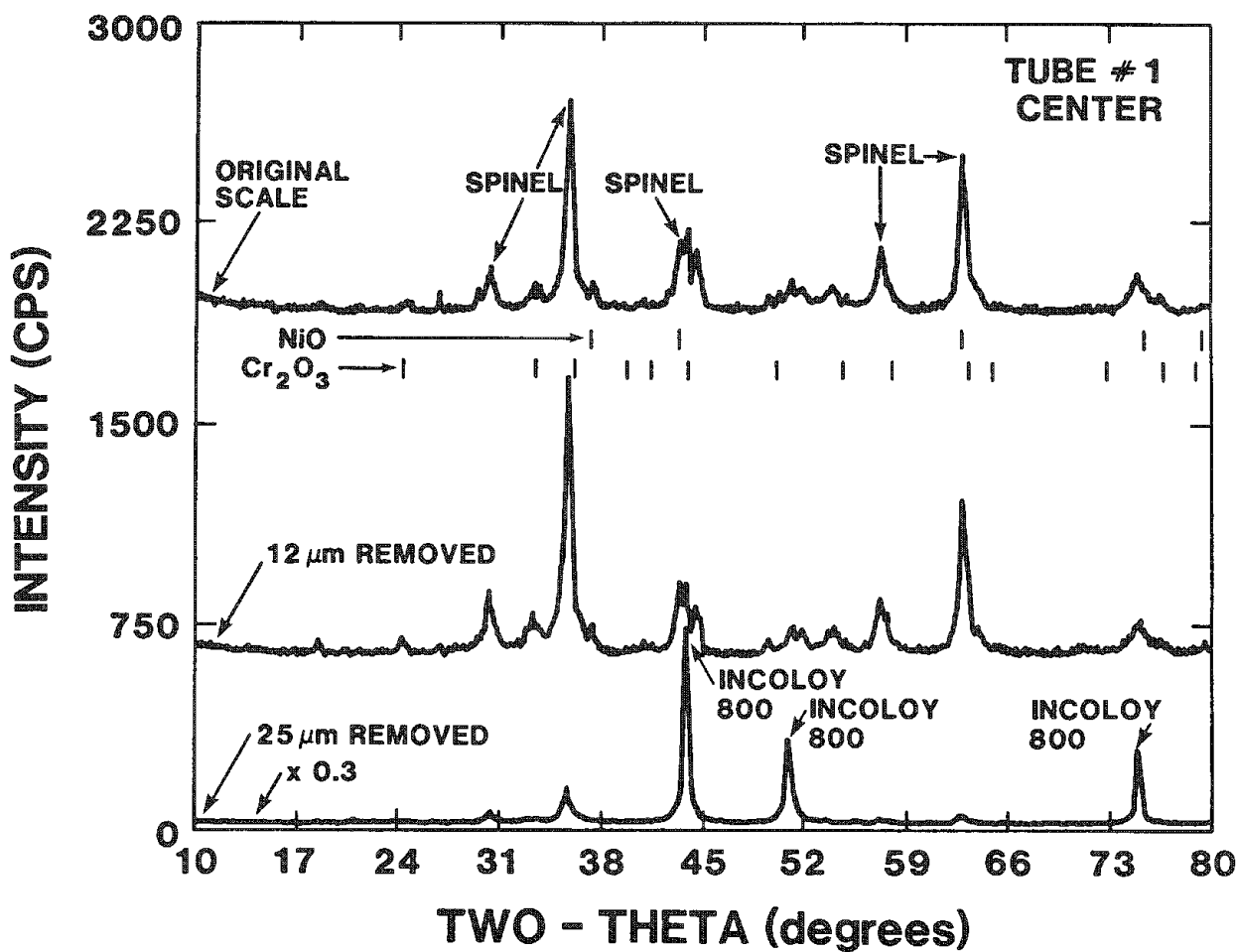


FIG. 3.--X-ray diffraction patterns of inside diameter of specimen from center of Tube #1. Patterns for original scale, 12  $\mu\text{m}$  removed and 25  $\mu\text{m}$  removed. Peak positions corresponding to spinel structure ( $a = 0.835 \text{ nm}$ ) and Incoloy 800 are noted. Angular peak positions for NiO and  $\text{Cr}_2\text{O}_3$  are shown. Note that intensity for 25  $\mu\text{m}$  removed pattern is 0.3 times labeled intensity scale.

## Special Atom-Probe Field-Ion Microscopy Symposium

### ATOM-PROBE FIELD ION MICROSCOPY

M. K. Miller

The atom-probe field-ion microscope (APFIM) is a very powerful instrument for microstructural and chemical analysis down to the atomic level of a wide range of materials. The principles of the instrument are quite distinct from the conventional electron-optical based microscopes.

#### *The Instrument*

A schematic diagram of a state-of-the-art atom probe is shown in Fig. 1. The ultra-high-vacuum (UHV) shell has four distinct instruments incorporated into one system. The Field-Ion Microscope (FIM) is the heart of the system, where high-resolution images of the specimen are obtained.<sup>1-3</sup> The Atom Probe, where the chemical analysis is performed, is the combination of a FIM and a time-of-flight mass spectrometer. Modern atom probes incorporate an energy-compensating electrostatic lens in the mass spectrometer to improve mass resolution. The Imaging Atom Probe (IAP) is a variant of the atom probe, where the distribution of one element is obtained over the specimen surface. The Pulsed Laser Atom Probe (PLAP) is another variant of the instrument, developed primarily for semiconducting materials, where surface atoms are removed from the specimen by laser-assisted field evaporation.<sup>4</sup>

#### *Field-Ion Microscopy*

The principle of the FIM is shown in Fig. 2. The cryogenically cooled needle-shaped specimen is placed a few centimeters from a screen. A trace of imaging gas, usually neon or helium, is admitted into the UHV system and a positive voltage is slowly applied to the specimen. At a certain voltage, dependent on the sharpness of the specimen, the image of the specimen is formed by the radial projection of the ionized gas atoms onto the channel plate and phosphor screen assembly. If the voltage is raised further, the surface atoms of the specimen become ionized and field evaporated. By taking a series of field-ion micrographs after small amounts of material have been field evaporated one obtains a true three-dimensional representation of the microstructure. As different phases generally exhibit slightly different contrast<sup>5</sup> in field-ion micrographs (Fig. 3), the morphology of complex interconnected microstructures or the size and number density of small precipitates can be measured precisely. Other microstructural features such as grain boundaries can also be analyzed (Fig. 4).

#### *Chemical Analysis in the Atom Probe*

The relationship between the field-ion microscope and the atom probe is shown in Fig. 5. The small hole in the channel plate and screen assembly serves as the entrance aperture to the time-of-flight mass spectrometer. This aperture is the central region of the dark area in the center of the field-ion micrographs. The effective size of this aperture can be varied to suit the type of analysis, by adjusting the distance of the channel plate and phosphor screen assembly from the specimen. A typical range would be from single atom up to approximately 4 nm in diameter. To make a chemical analysis of a specific area, such as a precipitate, the specimen is rotated until the image of that area falls over the aperture. The surface atoms are then removed by pulsed field evaporation and those that pass through the aperture are analyzed in the mass spectrometer. The identity of each atom is determined by accurate measurement of the flight time  $t$  between its removal from the surface of the specimen by the field evaporation pulse and its arrival at the

---

The author is at the Metals and Ceramics Division, Oak Ridge National Laboratory, Oak Ridge, TN 37831. The research was sponsored by the Division of Materials Sciences, U.S. Department of Energy, under contract DE-AC05-849R21400 with Martin Marietta Energy Systems, Inc.



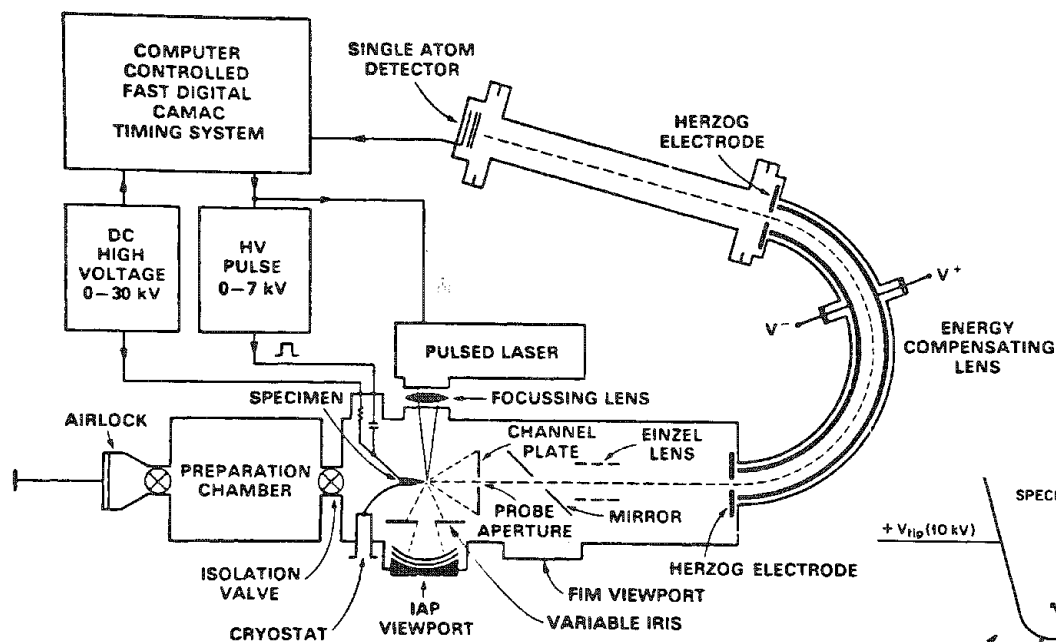


FIG. 1.--Schematic diagram of an atom probe.

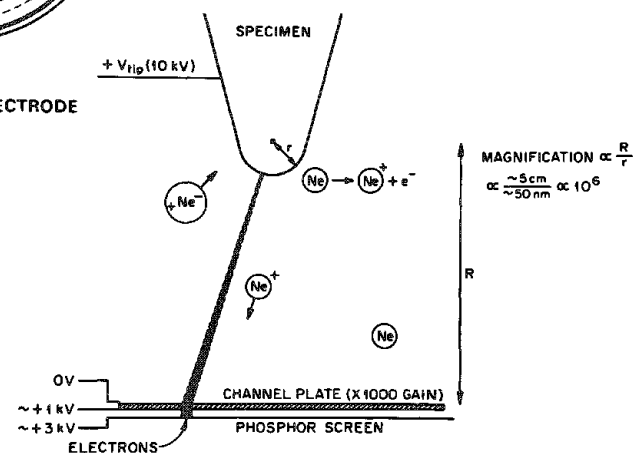


FIG. 2.--Principle of the field-ion microscope.

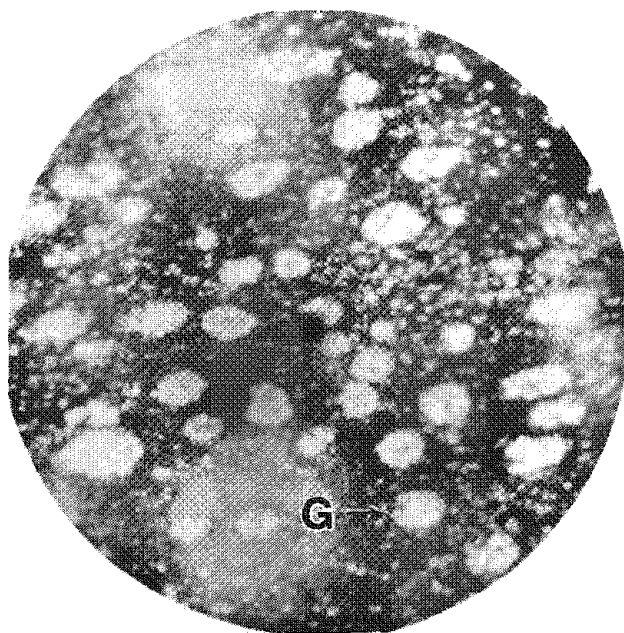


FIG. 3.--Field-ion micrograph of a cast primary coolant pipe steel from a nuclear reactor showing small roughly spherical G-phase precipitates (arrowed) after thermal aging for 7500 h at 400 C.

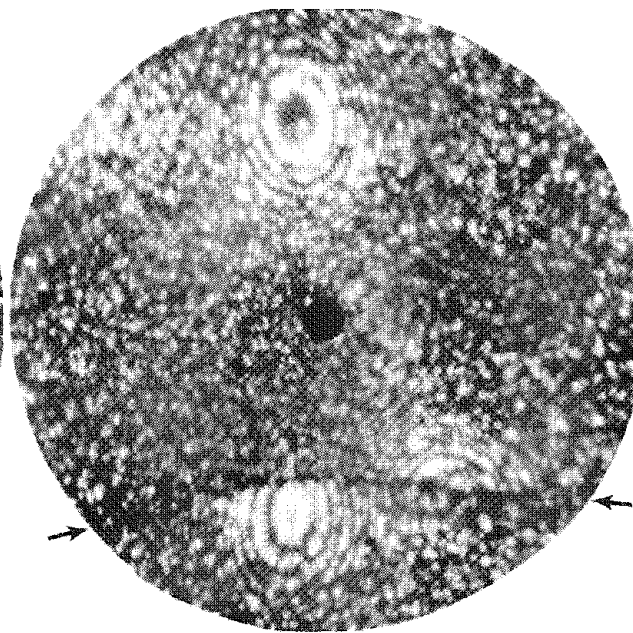


FIG. 4.--Field-ion micrograph of a grain boundary in a silicon whisker.

single-atom detector at the end of the mass spectrometer. The mass-to-charge ratio ( $m/n$ ) is given by

$$m/n = \text{constant}(V_{\text{dc}} + V_{\text{pulse}})(t^2/d^2)$$

where  $d$  is the distance traveled in the mass spectrometer, and  $V_{\text{dc}}$  and  $V_{\text{pulse}}$  are the standing voltage on the specimen and the voltage of the HV pulse, respectively. In the PLAP a laser pulse is substituted for the high-voltage pulse. This cycle is executed and monitored by the computer-controlled digital timing system shown in Fig. 1. By a repetition of this process a cylinder of atoms whose volume is defined by the effective area of the probe aperture and the amount of material field evaporated is analyzed until a statistically significant number of atoms is collected. There is no restriction in the mass range that can be analyzed with this technique. Modern atom probes, with energy compensating types of mass spectrometers, have sufficient mass resolution to separate completely adjacent isotopes of all elements in their normal mass-to-charge states.

One of the unique types of analysis that can be performed in the atom probe is single-atom analysis. This type of analysis is generally used to identify a segregant to boundaries such as shown in Fig. 6. In this micrograph an antiphase boundary in rapidly solidified  $\text{Ni}_3\text{Al}$  is decorated with bright spots. The bright spots were identified as boron atoms by correlation of the atom that produces the bright spot in the image with the atom that is caught in the mass spectrometer when it is field evaporated.

The atom probe may also be used to analyze layered or ordered type microstructures with atomic precision to determine the degree of order and the substitution behavior of solutes. An example of an analysis in a hafnium-containing  $\text{Ni}_3\text{Al}$  ordered alloy is presented in Fig. 7. In this type of analysis the probe aperture is positioned to collect atoms from an ordered plane such as 001 in this example. The specimen is then field evaporated and the atoms from sequential layers are collected. Each time a nickel atom is collected one step is plotted horizontally and each time an aluminum is collected one step is plotted vertically. The horizontal portions of this diagram are therefore the pure nickel planes, and the portions with a  $45^\circ$  slope are the mixed nickel and aluminum planes. The degree of order is determined from the slope of each plane. The substitutional behavior of additional elements is determined by observing in which layer the solute evaporates. In this case the hafnium prefers to be in the mixed layer and not the pure nickel layer; therefore, as all nickel sites are identical, the hafnium must have a preference for the aluminum sites.

The composition of a region is directly determined by a count of the number of atoms of each element that is present in the cylinder of atoms collected from that region. In addition to measuring the composition of selected regions such as precipitates, the composition variations as a function of distance can also be determined. A composition profile normal to the 001 plane through the  $\text{L1}_2$  ordered structure of  $\text{Ni}_3\text{Al}$  is shown in Fig. 8 to demonstrate the atomic resolution of the technique. The alternation between the pure nickel layers and the mixed 50% nickel and 50% aluminum layers of this ordered structure is clearly evident. Composition profiles through modulated microstructures, or as a function of distance from a boundary or a precipitate, are conducted in the same way. Small trajectory aberrations in the path of the atoms to the detector limit the minimum size of analysis to approximately 1 nm.

### *The Imaging Atom Probe*

In this variant of the atom probe,<sup>5</sup> a single-atom detector is placed relatively close to the specimen without an intervening imaging device. The IAP can be used in three modes. When the detector is operated at low gain and in the presence of an imaging gas, a field-ion image is obtained on the detector, although with a restricted field of view compared to the normal FIM image. If the detector is run at high gain and without any image gas present, a mass spectrum of the entire imaging surface of the specimen can be obtained for each field evaporation pulse. In the third mode the distribution of a selected element is observed on the detector over the entire imaging field of view. A schematic diagram of this "gated" mode is shown in Fig. 9. This mode exploits the fact that different elements take different times to reach the detector. The detector is off for most of the time, except during the arrival time of the selected element, when it is operated at

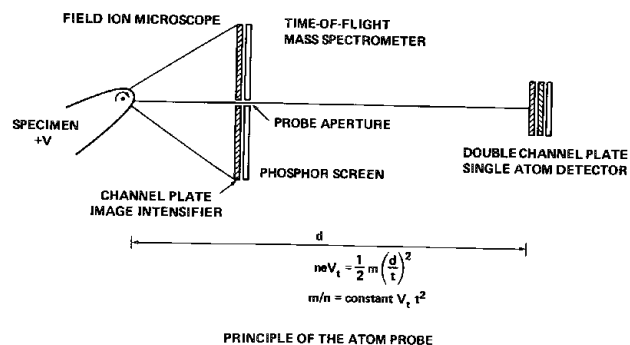


FIG. 5.--Principle of atom probe.

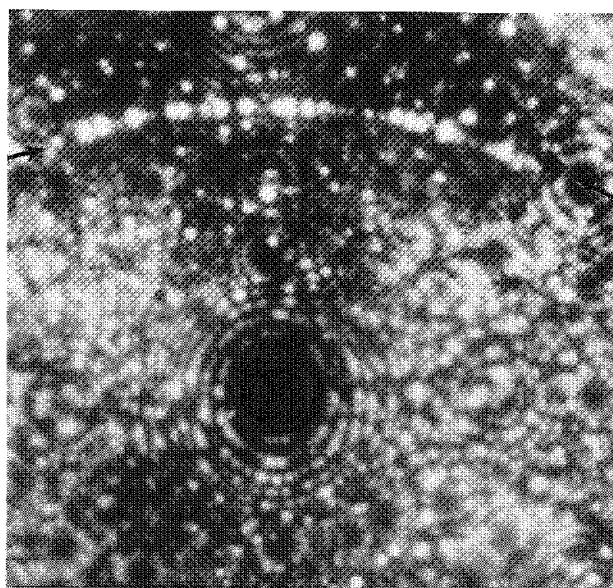


FIG. 6.--Field-ion micrograph of boron-decorated antiphase boundary in rapidly solidified  $\text{Ni}_3\text{Al}$ . Each bright spot on APB is single boron atom.

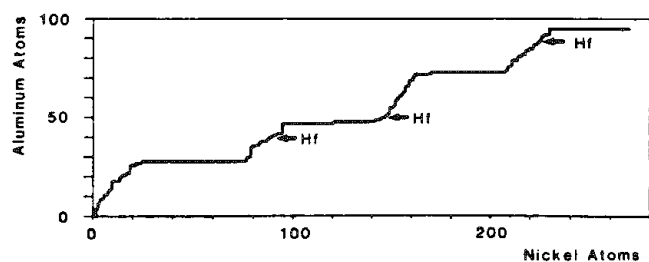


FIG. 7.--Ladder diagram of 001 plane in  $\text{Ni}_3\text{Al}$  alloy containing 1% hafnium. (Hafnium is located in mixed Ni + Al layer.)

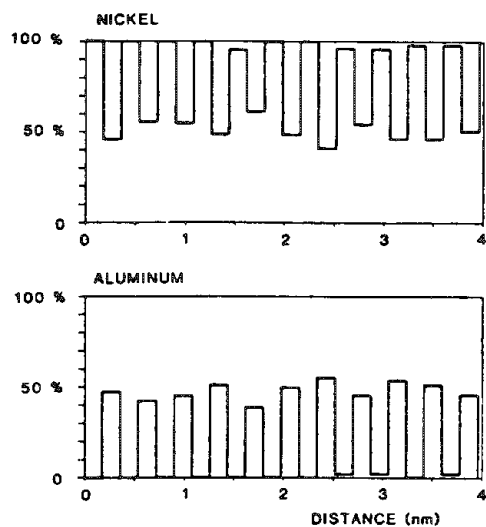


FIG. 8.--Composition profile along 001 direction in  $\text{Ni}_3\text{Al}$  showing atomic resolution of technique. Each composition measurement is 0.18 nm apart and alternating pure nickel and mixed Ni + Al planes are clearly resolved.

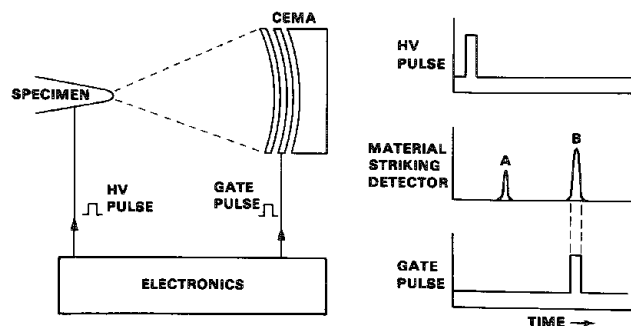


FIG. 9.--Principle of imaging atom probe.



full gain. Therefore, each atom of the selected element is seen as a single dot on the detector. The position of the spots on the detector provides the distribution of the selected element. An example of the beryllium distribution in a triaxially modulated two-phase microstructure is shown in Fig. 10. The two phases are imaged as the areas where there are high and low densities of spots. In this microstructure the spacing of the two phases was measured to be 4.3 nm.

#### References

1. E. W. Mueller and T. T. Tsong, *Field-ion Microscopy*, New York: Elsevier, 1969.
2. K. M. Bowkett and D. A. Smith, *Field-ion Microscopy*, Amsterdam: North Holland, 1970.
3. R. G. Forbes, "Seeing atoms: The origin of local contrast in field-ion images," *J. Phys.* D18: 973-1018, 1985.
4. G. L. Kellogg and T. T. Tsong, "Pulsed-laser atom-probe field-ion microscopy," *J. Appl. Phys.* 51: 1184-1193, 1980.
5. J. A. Panitz, *Progress Surf. Sci.* 8: 219, 1978.

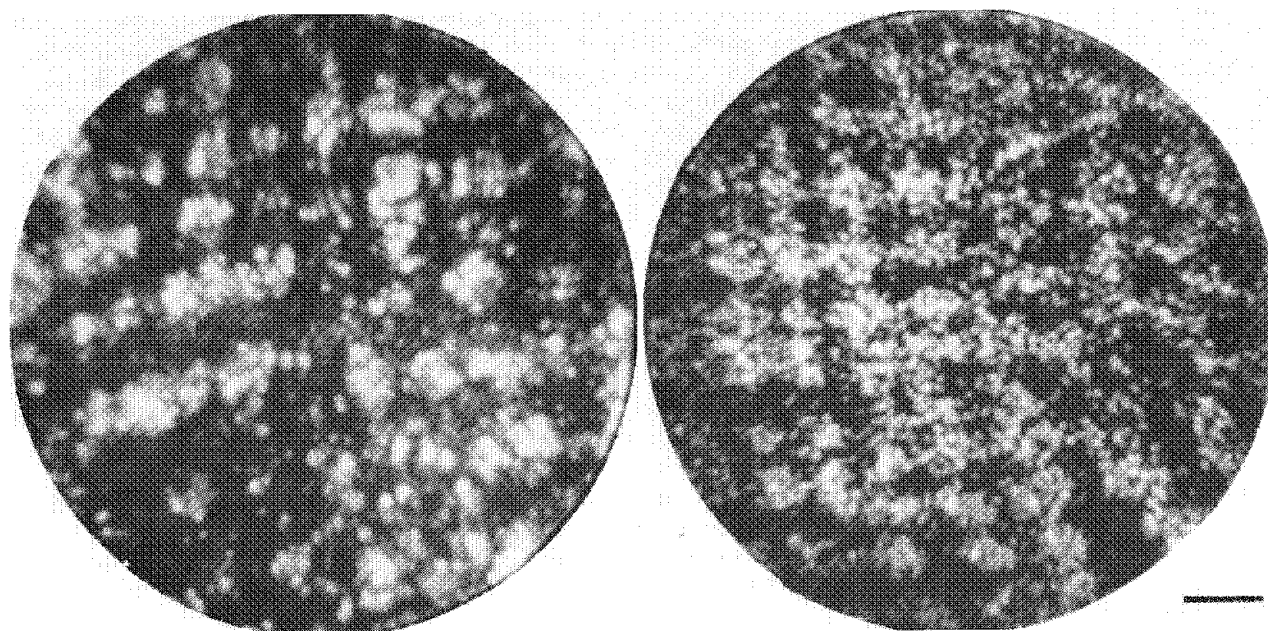


FIG. 10.--IAP field-ion micrograph and the Be distribution in a triaxially modulated microstructure. (Fe-25 at% Be alloy aged 20 min at 400 C.) Bar = 5 nm.

## CHEMISTRY ON AN ATOMIC SCALE OF SOLID-STATE PROCESSES

D. N. Seidman

The atom-probe field-ion microscope has been used to study several fundamental solid-state phenomena that are difficult or impossible to study by conventional microanalytical techniques: (a) the diffusivity of  $^3\text{He}$  in perfect tungsten crystals, (b) the diffusivity of 200eV  $^1\text{H}_2^+$  ions implanted in tungsten at 29 K, (c) radiation-induced precipitation on a subnanometer scale in fast-neutron irradiated tungsten (rhenium) alloys, and (d) solute-atom segregation in two-dimensional phase transitions at stacking faults in cobalt (niobium) and cobalt (iron) alloys. The primary results and physical interpretations for each of these phenomena are presented and discussed.

### *Experimental*

All the atom-probe field-ion microscope (FIM) experiments were performed with an atom probe described previously.<sup>1-3</sup> This atom probe is equipped with a liquid-helium-cooled goniometer stage, a specimen exchange device, and a specially designed differentially pumped low-energy (50 to 3keV) gas ion-beam system for in situ irradiation of an FIM specimen.<sup>3</sup> The atom probe is controlled by a Data General Nova microcomputer, which controls the pulse frequency and measures the TOFs and steady-state and pulse voltages. In addition, the microcomputer is employed for online analysis of the experimental data.

### *Diffusivity of $^3\text{He}$ Atoms in Perfect Tungsten Crystals*

The diffusivity of  $^3\text{He}$  atoms in perfect crystals of tungsten has been studied by the atom-probe technique.<sup>4</sup> Tungsten FIM specimens were implanted in situ with 300eV  $^3\text{He}^+$ , to a fluence of  $3 \times 10^{15}$  ions  $\text{cm}^{-2}$ , at specimen temperatures that ranged from 60 to 110 K. The  $^3\text{He}^+$  ion beam was analyzed magnetically and the ion source was connected to the atom probe through a differentially pumped aperture. At an implantation energy of 300 eV *no* radiation damage was produced by the implanted  $^3\text{He}$  atoms. Thus, the state of a tungsten specimen after an implantation consisted of  $^3\text{He}$  atoms with an initial depth distribution that was determined solely by the range profile of the low-energy ions.<sup>5</sup> Isothermal annealing experiments between 90 and 110 K were employed to study the kinetics of recovery of the implanted  $^3\text{He}$  atoms; at 60 K the  $^3\text{He}$  atoms are immobile. These data, in combination with a suitable diffusion model, were used to determine the diffusivity  $D_{\text{He}}(T)$  and enthalpy change of migration of  $^3\text{He}$  atoms  $\Delta h_{\text{He}}^m$  in tungsten. The quantity  $D_{\text{He}}(T)$  is given by the Arrhenius expression  $D_{\text{He}}(T) = 5.4 \times 10^{-3} \exp[-0.28(\text{eV}/kT)] \text{ cm}^2\text{s}^{-1}$ . The value of  $\Delta h_{\text{He}}^m$  for  $^3\text{He}$  is approximately the same as for  $^4\text{He}$  atoms (0.24-0.32 eV) in tungsten.<sup>6</sup> This result shows that the diffusive behavior of helium in tungsten can be described in a classical way.  $D_{\text{He}}(T)$  is considerably smaller, at the same temperature, than the diffusivities of self-interstitial atoms<sup>7,8</sup> or  $^1\text{H}$  atoms.<sup>9</sup>

### *Diffusivity of 200eV $^1\text{H}_2^+$ Ions Implanted in Tungsten at 29 K*

The atom-probe technique was used to study the low-temperature diffusive behavior of hydrogen ( $^1\text{H}$ ) in tungsten.<sup>9</sup> Tungsten FIM specimens were implanted in situ with 200eV  $^1\text{H}_2^+$  ions at a specimen temperature of 29 K. The specimens were analyzed chemically on an atomic scale, via the atom-probe technique, during the controlled pulse field evaporation of the (110) planes. No hydrogen events were detected at depths below the surface that corresponded to the calculated mean projected range of either  $^1\text{H}$  or  $^1\text{H}_2$ . The mean projected ranges were calculated by use of a modified version of Biersack's and Haggmark's Monte

---

The author is at the Department of Materials Science and Engineering, Northwestern University, Evanston, IL 60201-9990. He wishes to thank his co-workers Drs. J. Amano, A. S. Berger, T. M. Hall, R. Herschitz, A. T. Macrander, A. Wagner, and M. Yamamoto for their important contributions to the atom-probe FIM effort at Cornell University. This research was supported by the National Science Foundation and the U.S. Department of Energy.

Carlo program called TRIM (transport of ions in matter). The experimental results set a lower bound of  $(1-10) \times 10^{-18} \text{ cm}^2\text{s}^{-1}$  on the diffusivity of hydrogen ( $^1\text{H}$ ) in tungsten at 29 K. This extremely high value, when compared with the value extrapolated from  $\sim 1100 \text{ K}$  on an Arrhenius plot, suggests strongly that the diffusion of hydrogen in tungsten should be described by a nonclassical model. In addition, experiments were performed that demonstrated the adsorption of hydrogen on the surface of tungsten FIM tips (initially cleaned atomically by field evaporation) from the ambient pressure in the FIM.<sup>10</sup>

#### *Radiation-induced Precipitation on a Subnanometer Scale*

The phenomena of radiation-induced precipitation and segregation have been investigated in W-10 at.% Re and W-25 at.% Re alloys, with the atom probe FIM.<sup>11,12</sup> The W-10 at.% Re alloy is subsaturated with respect to the solvus line of the primary solid solution ( $\beta$  phase), whereas the W-25 at.% Re alloy is supersaturated with respect to the same solvus line. The specimens had been irradiated in the Experimental Breeder Reactor II to a fast-neutron fluence of  $\sim 4 \times 10^{22} \text{ neutrons cm}^{-2}$  ( $E > 0.1 \text{ MeV}$ ) at 575, 625, and 675 C, which corresponds to 8.6 displacements per atom (dpa) and an average displacement rate, for the two-year irradiation time, of  $1.4 \times 10^{-7} \text{ dpa s}^{-1}$ . The results of the present investigation show a very significant alteration of the microstructure of both alloys as a result of the fast-neutron irradiation. In the case of the W-10 at.% Re alloy coherent, semicoherent, and possibly incoherent precipitates with the composition  $\sim \text{WRe}$  and a disk-shaped morphology --one or two atomic planes thick--were detected at a number density of  $\sim 10^{16} \text{ cm}^{-3}$  and a mean diameter of 57 Å. For the W-25 at.% Re alloy coherent, semicoherent, and incoherent precipitates with the composition  $\sim \text{WRe}_3$  were detected; the precipitates' number density is  $\sim 10^{17} \text{ cm}^{-3}$  with a mean diameter of 40 Å. None of the  $\sim \text{WRe}$  precipitates or the  $\sim \text{WRe}_3$  coherent precipitates was associated with either line or planar defects or with any impurity atoms. Therefore, a true homogeneous radiation-induced precipitation occurs in these alloys. The semicoherent  $\text{WRe}_3$  precipitates were associated with  $^4\text{He}$  atoms; that is, these precipitates may have been heterogeneously nucleated. In the W-25 at.% Re alloy a two-dimensional  $\text{WRe}_3$  phase has been observed at a grain boundary.

A physical argument is presented for the nucleation of  $\text{WRe}$  or  $\text{WRe}_3$  precipitates in the vicinity of displacement cascades produced by primary knock-on atoms. It is suggested that in both cases the first step in the nucleation of a precipitate is due to the formation of tightly bound mobile mixed dumbbells, which react to form an immobile di-rhenium cluster. Possible sequences of point-defect reactions, which can lead to either  $\text{WRe}$  or  $\text{WRe}_3$ , have been detailed.<sup>11,12</sup> The further growth of a cluster ( $\text{WRe}$  or  $\text{WRe}_3$ ) into a precipitate is most likely driven by the *irreversible* vacancy: self-interstitial atom annihilation reaction, as suggested by Cauvin and Martin.<sup>13</sup> Point-defect mechanisms for all the other observations have also been considered.<sup>11,12</sup>

#### *Solute-atom Segregation and Two-dimensional Phase Transitions at Stacking Faults*

Solute-atom segregation effects to individual stacking faults in Co-0.96 at.% Nb and Co-0.98 at.% Fe alloys have been investigated with the atom-probe FIM.<sup>14-15</sup> The composition of individual stacking faults (SFs) has been directly measured in the range 450-575 C. The diameter of the analyzed cylinder of alloy was  $\sim 30-50 \text{ Å}$ . It was shown that the solute concentration falls off very quickly with distance--within less than 4 Å--from the plane of the SF in both alloys. And it is suggested that solute-atom segregation effects of SFs have been observed in both alloys. After correction for the matrix contribution to the chemical analyses, the Nb concentration in the SFs in the Co-0.96 at.% Nb alloy is greater than the bulk concentration by factors of 30, 12, and 7 at annealing temperatures of 450, 525, and 575 C. The corrected Fe concentration in the SFs in the Co-0.96 at.% Fe alloy is greater than the bulk composition by factors of 10, 6, and 4 at the annealing temperatures 450, 550 and 575 C. There are small solute-rich fluctuations (5-20 Å in diameter) whose compositions differ significantly from the Co-0.96 at.% Nb alloy. Together with the experimental observations that at 450 C the SF composition is close to that of  $\text{Co}_2\text{Nb}$ , these fluctuations suggest that in addition to solute-atom segregation we have evidence for a first-order phase transition with the plane of the SF. Small solute-rich fluctuations ( $\sim 20 \text{ Å}$  in diameter) have also been observed in the Co-0.98 at.% alloy at 550 and 575 C. Recently, we have obtained an electron-diffraction pattern from SFs in the Co(Nb) alloy which exhibits superlattice reflections around each of the

reflections from the hexagonal-close packed matrix; the superlattice reflections exhibit 6-fold symmetry and are consistent with the two-dimensional structure  $\text{Co}_2\text{Nb}$ .<sup>16</sup>

### Conclusions

The atom-probe FIM has been used to obtain unique chemical information on an atomic scale, which has helped to yield important information about solid-state processes.

### References

1. T. M. Hall, A. Wagner, and D. N. Seidman, *J. Phys.* E10: 884, 1977.
2. A. Wagner, T. M. Hall, and D. N. Seidman, *J. Nucl. Mater.* 69/70: 693, 1978.
3. J. Amano and D. N. Seidman, *Rev. Sci. Instrum.* 50: 1125, 1979.
4. J. Amano and D. N. Seidman, *J. Appl. Phys.* 56: 983, 1984.
5. J. Amano, A. Wagner, and D. N. Seidman, *Phil. Mag.* A44: 177 and 199, 1981.
6. A. Wagner and D. N. Seidman, *Phys. Rev. Lett.* 42: 515, 1979.
7. R. M. Scanlon, D. L. Styris, and D. N. Seidman, *Phil. Mag.* 23: 1439, 1971.
8. K. L. Wilson and D. N. Seidman, *Radiat. Eff.* 27: 67, 1975; D. N. Seidman, K. L. Wilson, and C. H. Nielsen, *Phys. Rev. Lett.* 35: 1041, 1975.
9. A. T. Macrander and D. N. Seidman, *J. Appl. Phys.* 56: 1623, 1984.
10. A. T. Macrander and D. N. Seidman, *Surf. Sci.* 147: 451, 1985.
11. R. Herschitz and D. N. Seidman, *Acta Metall.* 32: 1141, 1984.
12. *Ibid.*, p. 1155.
13. R. Cauvin and G. Martin, *Phys. Rev.* B23: 3322 and 3333, 1981.
14. R. Herschitz and D. N. Seidman, *Scripta Metall.* 16: 849, 1982.
15. R. Herschitz and D. N. Seidman, *Surf. Sci.* 130: 63, 1983.
16. R. Herschitz and D. N. Seidman, *Acta Metall.* 33: 1547, 1565, 1985.
17. A. Brokman, D. N. Seidman, and F. Schapink (to be published, 1986).

## ATOM-PROBE STUDY OF SEMICONDUCTORS AND CONDUCTING POLYMERS

Osamu Nishikawa

The application of atom-probe (A-P) has been extended to various materials. The validity of the A-P analysis of compound semiconductors was exhibited by the introduction of a pulsed laser and a combined A-P of a linear flight path type, an energy-focusing deflected flight path type, and an imaging type. The applicability of the A-P to a conducting polymer, polypyrrole, was examined. The study successfully demonstrated that the A-P can clarify its oxidation process and reveal the nonuniform distribution of oxygen and dopants in atomic dimension.

The unique capability of the atom-probe (A-P)<sup>1,2</sup> is the atom-by-atom and atomic layer-by-layer mass analysis of various materials, including metals, semiconductors, and organic materials. Thus, one of the most suitable applications for the A-P is the analysis of surfaces and interfaces where structures and compositions change abruptly in a few atomic layers. The studies of Si-W,<sup>3</sup> Si-Ni,<sup>4,5</sup> and Al-GaAs<sup>6</sup> interfaces clarified the abrupt change of compositions, the epitaxial growth of the silicides, and the formation process of an AlAs layer. However, since the A-P analysis often gives erroneous compositions,<sup>7</sup> a combined A-P of a straight flight path type, an energy focusing deflected flight path type, and an imaging type was constructed. Another attempt is the introduction of a pulsed laser.<sup>8</sup> The validity of the pulsed laser A-P was examined by analysis of the Al-GaAs interfaces and comparison of the result obtained by the conventional voltage-pulse A-P.

Mass analysis of organic materials by conventional techniques is rather impractical: for example, Auger electron spectroscopy (AES) cannot detect the major element of the polymer, hydrogen, and secondary ion mass spectroscopy (SIMS) utterly destroys structures composed of light elements such as H, N, and C. Thus, the application of the A-P to conducting polymers was welcome because it was realized that the ordered field evaporation<sup>9</sup> of polymers would proceed by breaking weak bonds in the polymer, and the analysis of the desorbed fragment ions of the polymer would provide the information on the binding states in the polymer. The study was found to be unexpectedly rewarding because it clarified the oxidation process of polypyrrole (PP) and the nonuniform distribution of oxygen and dopants in atomic dimensions for the first time.

### *Combined Atom-Probe*

Figure 1 shows a schematic diagram of the combined A-P with two flight paths, straight and deflected. The straight path is 1.2 m long and terminated by a chevron detector 75 mm in diameter. The other flight path is deflected by the Poschenrieder type electrodes<sup>1,2,10</sup> and is 2.5 m long. One section of the outer deflector electrode, 70 × 177 mm, is cut open and the W wires, 0.3 mm in diameter and spaced parallel 3 mm apart, effectively fill the open section of the electrode. The tip-to-screen distance can be changed from 50 to 125 mm. Since the maximum acceptance angle to the probe hole is as wide as 5.7° and the chevron detector at the end of the deflected flight path has a large open area ratio (more than 70% instead of the conventional ratio of 50%), more than 200 ions are detected from one atomic layer of the (011) plane of the W tip with the tip radius of 45 nm. The mass resolution of the deflector type A-P is lowest for the minimum tip-to-screen distance but is barely high enough to discriminate the W isotopes and is significantly higher than that of the straight type.

In order to accept the ions in the wide acceptance angle the 178mm-high outer and inner deflector electrodes are set 100 mm apart. The top and bottom of the deflector space are partitioned by two sets of 22 concentric stainless steel wires at the potentials

---

The author is at Department of Materials Science and Engineering of the Graduate School at Nagatsuta, Tokyo Institute of Technology, 4259 Nagatsuta, Midori-ku, Yokohama 227, Japan.

FIG. 1.--Schematic diagram of combined atom probe.

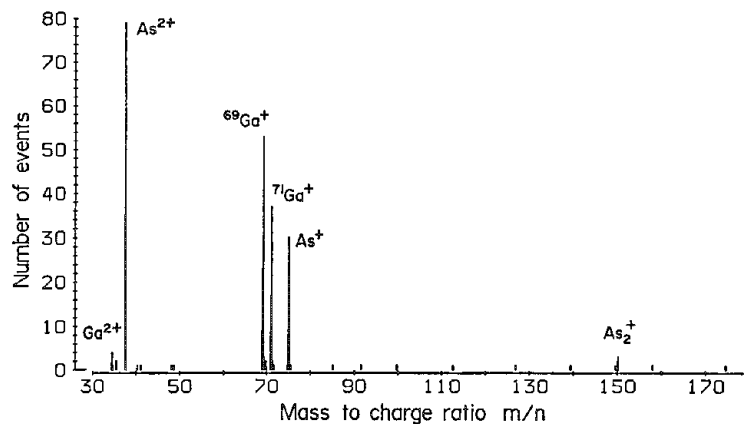
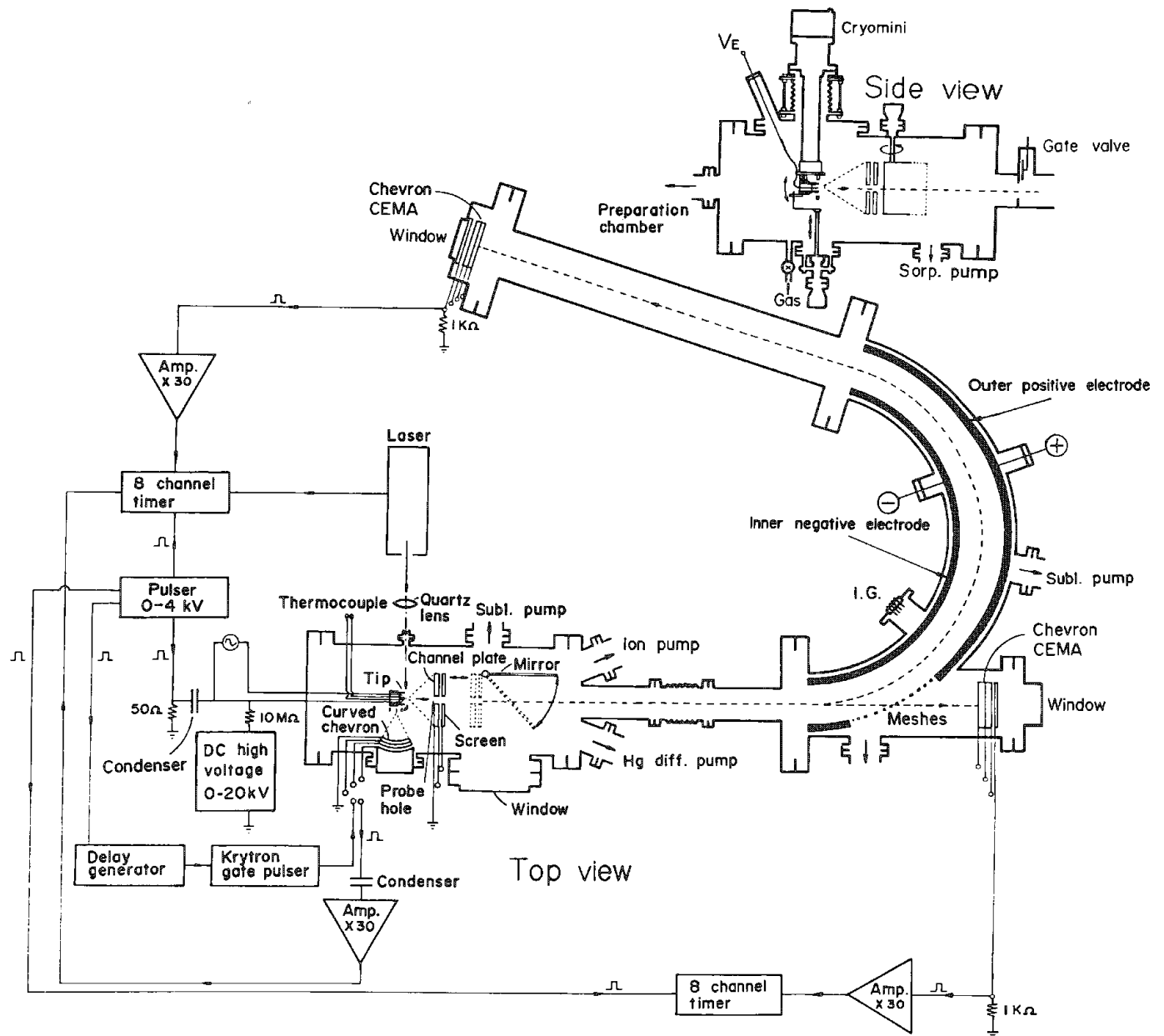


FIG. 2.--Mass spectrum of GaAs obtained by operation of combined A-P as deflector type. Ratio of number of Ga ions to that of As ions is 1.02:1, close to stoichiometric composition. Tip voltage  $V_t$  (sum of pulse and dc voltages) is 6.24 kV; pulse fraction (ratio of pulse voltage to  $V_t$ ) is as low as 13.5% to pass low-energy ions.

proportional to the deflector voltages to reduce the distortion of the electric field in the deflector space by the grounded metal plates encasing the electrodes.

The instrument can be operated as an imaging A-P if the specimen tip is rotated by  $90^\circ$  and is directed to the curved chevron. The flight path of this A-P is 11.8 cm. This A-P also serves as a pulsed-laser A-P by irradiation of the tip through a quartz window. The peak power of the laser is 200 kW and the pulse width is 0.8 ns.

### *Compound Semiconductors*

The mass analysis of GaAs and GaP by a voltage-pulse deflector type A-P tends to provide As- and P-rich compositions.<sup>7</sup> The cause of the erroneous compositions can be attributed to the significant attenuation of pulse voltages during travel through a semiconductor tip. Thus the effective pulse voltage at the tip apex is lower than the applied voltage and evaporated ions fly slower than ions fully accelerated by the total applied voltage. The masses of such slow ions appear to be heavier than the true masses and these ions fail to pass through the deflected flight path because the voltages of the deflector electrodes are set for the applied voltage. The advantage of the straight A-P is that it allows us to estimate effective pulse voltages from mass shifts; e.g., 95% and 75% of the applied pulse voltages for Zn-doped GaAs with the resistivity of  $3 \times 10^{-3} \Omega \cdot \text{cm}$  and for S-doped GaP with  $3 \times 10^{-2} \Omega \cdot \text{cm}$ , respectively. Furthermore, mass spectra obtained by the straight A-P showed that many Ga atoms are preferentially evaporated immediately after the evaporation of nearby As atoms and accelerated at a voltage as low as the dc voltage applied to the tip. Since these slow ions cannot pass through the deflected flight path, the deflector voltages were lowered to the attenuated pulse voltage. Then the fraction of the pulse voltage (the ratio of the effective pulse voltage to the sum of the pulse and dc voltages) was lowered to approximately 10%, which is close to the range of the full transmission of ions through the deflector. Figure 2 is the mass spectrum of GaAs analyzed by the A-P with a deflected flight path. The ratio of the numbers of the Ga and As ions detected is 1.02:1 and close to the stoichiometrically expected composition.

### *Pulsed Laser*

Since only dc voltages are applied to a specimen tip, the pulsed-laser A-P requires no adjustment of the deflector electrode voltages. However, the laser beam heats up the tip surface for a few nanoseconds<sup>11,12</sup> and promotes the formation of clusters of nonmetallic atoms.<sup>13,14</sup> The clusters get smaller as the dc voltage rises and the laser power is reduced. The apparent composition of compound semiconductors also changes with laser powers because temperature rise by the laser beam promotes the thermal evaporation of the elements with a high vapor pressure, such as As and P, and activates the surface diffusion of elements with a low melting temperature, such as Ga, to the tip shank. Thus the tip voltage and the laser power must be optimized to yield the stoichiometrically expected composition (Fig. 3).

Al-GaAs interfaces were analyzed by optimization of the laser power. After the deposition of a thin Al layer on the GaAs tip at 20 K, the tip was heated for 40 s at 800 K and then the pulsed-laser A-P analysis proceeded. Al and As were detected alternately, which indicated the formation of an AlAs layer by the Al-Ga exchange reaction (Fig. 4). Surprising differences in the results of the voltage-pulse A-P analysis<sup>6</sup> are the detection of one or two atomic layers of Ga at the interface between the AlAs layer and the substrate GaAs and that of Al atoms in the substrate GaAs. The cause of the Ga layer formation and the Al diffusion into GaAs are under investigation at present.

### *Polypyrrole*

A-P specimens are sharp needles with a tip radius of less than 100 nm; it is extremely difficult to make such a fine PP tip. Thus, a thin PP film was electrochemically deposited on a Pt tip. The electrolyte solution is acetonitrile containing 0.05 M pyrrole monomer and 0.1 M tetraethylammonium-perchlorate [TEAPC:  $(\text{C}_2\text{H}_5)_4\text{NClO}_4$ ], which provides  $\text{ClO}_4^-$  anions as a dopant. In order to dope  $\text{BF}_4^-$ , acetonitrile containing 0.01 and 0.1 M pyrrole monomer with 0.01 and 0.1 M tetraethylammonium-tetrafluoroborate [TEAFB:  $(\text{C}_2\text{H}_5)_4\text{NBF}_4$ ], respectively, was used.

After the deposition of a PP layer, the tips were exposed to air to oxidize the layer

FIG. 3.--Variation of mass spectra and ratio of number of P atoms detected  $N_P$  to that of Ga atoms  $N_{Ga}$  with tip voltage and laser power. (a) Fraction of reduced evaporation voltage by laser  $L_f$  is 55% of evaporation voltage of GaP;  $N_P$  is larger than  $N_{Ga}$ . (b)  $L_f$  is 34%; tip voltage is increased to compensate  $L_f$  reduction;  $N_P/N_{Ga}$  is close to stoichiometric ratio. (c)  $L_f$  is 21%;  $N_P$  is significantly smaller than  $N_{Ga}$ .

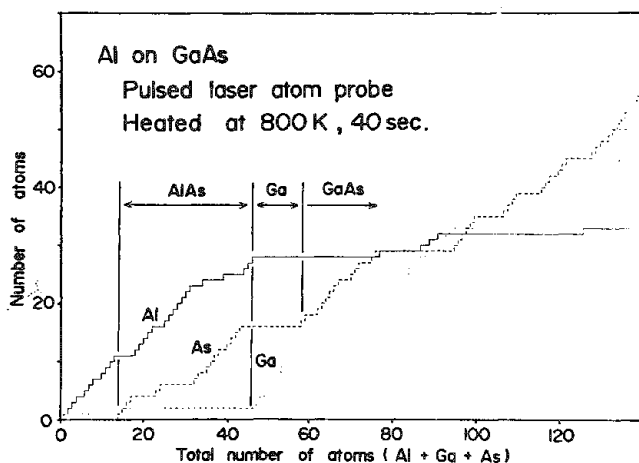
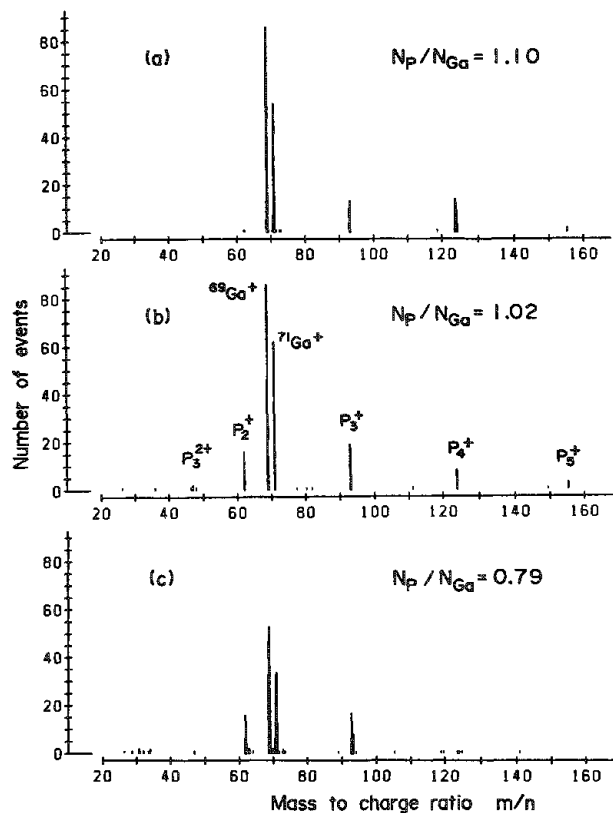


FIG. 4.--Detection sequence of field-evaporated ions from Al-deposited GaAs. Abscissa is total number of detected ions, ordinate is number of Al, Ga, and As ions plotted respectively in order of detection. Variation of composition is indicated by horizontal lines. Tip voltage is 2.8 kV,  $L_f$  is 20%. Average number of ions detected from one atomic layer is about 10.

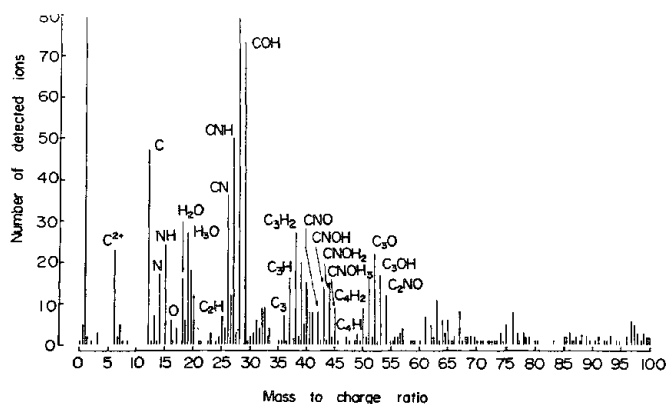


FIG. 5.--Mass spectrum of polypyrrole film exposed to air for 1 day.



from 1 day to 3 months. Then the tip was mounted in the A-P with the background pressure of  $3 \times 10^{-8}$  Pa and the tip temperature was maintained at or below 100 K during the A-P analysis.

Many  $H^+$ ,  $C^{2+}$ , and  $C^+$  ions were detected from a tip exposed to air for 1 day (Fig. 5). The other mass peaks are identified as the fragments of PP, such as  $NH^+$ ,  $CN^+$ ,  $CNH^+$ ,  $CO^+$ , and  $COH^+$ . The tip exposed to air for 3 months exhibited a completely different spectrum (Fig. 6). Few H atoms were found in fragment ions, but the number of oxygen atoms is as large as that of C atoms. Satellite mass peaks beside the major peaks indicate the detection of ions containing a heavier C isotope,  $^{13}C$ , and doubly charged fragment ions. The fragment ions designated in Fig. 6 are deduced from the assumption that the ideal PP structure (Fig. 7a) would change to the fully oxidized structure if H is replaced by O (Fig. 7b). Closed lines designate the fragments without breaks in strongly bound double bonds. Dots represent unpaired electrons by the formation of C-O bonds. Many fragment ions of Fig. 5 contain O and H, which may suggest that oxygen breaks into the C-H bond, forming a C-O-H bond (Fig. 7c) at the initial stage of oxidation, and then detaches an H atom from the bond.

As the A-P analysis proceeds to the deeper section, the number of H atoms increases and finally an unoxidized section (Fig. 5) is uncovered. The thickness of the fully oxidized layer in the 3-month exposure is found to be approximately 60 nm.

The detection of a large number of oxygen atoms even from the fresh PP layer of Fig. 5 suggests that a PP layer is highly vulnerable to oxidation and is oxidized during the formation of a PP layer.<sup>15</sup> The distribution of oxygen and doped atoms are found to be nonuniform. The detailed study is in progress.

### Conclusion

The present study successfully demonstrated that the combined A-P and the pulsed-laser A-P are indispensable for the analysis of compound semiconductors. However, the study also indicates that care must be taken in the adjustment of deflector voltages, laser power, and tip voltages. The study also showed that A-P has the unparalleled capability of analyzing organic materials such as PP in atomic dimensions. It is expected that extensive study of polymers with A-P will clarify not only the structure and composition but also the hidden relation between the conductivity, distribution of dopants, and polymerizing conditions.

### References

1. E. W. Müller, "The atom-probe field ion microscope," in A. W. Czanderna, Ed., *Methods of Surface Analysis*, Amsterdam: Elsevier Scientific Publishing Co., 1975, 329-378.
2. O. Nishikawa, K. Kurihara, M. Nachi, M. Konishi, and M. Wada, "Performance of the new high mass resolution time of flight atom probe," *Rev. Sci. Instrum.* 52: 810-818, 1981.
3. O. Nishikawa, Y. Tsunashima, E. Nomura, S. Horie, M. Wada, M. Shibata, T. Yoshimura, and R. Uemori, "Atom-probe study of the early stage of silicide formation: I. W-Si system," *J. Vac. Sci. Technol.* B1: 6-9, 1983.
4. O. Nishikawa, E. Nomura, M. Wada, Y. Tsunashima, S. Horie, M. Shibata, T. Yoshimura, and R. Uemori, "Atom-probe study of the early stage of silicide formation: II. Ni-Si system," *J. Vac. Sci. Technol.* B1: 10-14, 1983.
5. O. Nishikawa, M. Shibata, T. Yoshimura, and E. Nomura, "Atom-probe study of silicide formation at Ni/Si interfaces," *J. Vac. Sci. Technol.* B2: 21-23, 1984.
6. O. Nishikawa, O. Kaneda, M. Shibata, and E. Nomura, "Atom-probe study of Al-Ga exchange reaction at Al-GaAs interfaces," *Phys. Rev. Lett.* 53: 1252-1255, 1984.
7. O. Nishikawa, H. Kawada, Y. Nagai, and E. Nomura, "Erroneous composition of GaAs mass-analyzed by atom-probes," *J. de Physique* C9: 465-470, 1984.
8. G. L. Kellogg and T. T. Tsong, "Pulsed-laser atom-probe field ion microscopy," *J. Appl. Phys.* 51: 1184-1193, 1980.
9. E. W. Müller and T. T. Tsong, *Field Ion Microscopy: Principles and Applications*, New York: American Elsevier Publishing Co., 1969.
10. W. P. Poschenrieder, "Multiple-focusing time-of-flight mass spectrometers: Part II. TOFMS with equal energy acceleration," *Intern. J. Mass Spectrom. Ion Phys.* 9: 357-373, 1972.
11. G. L. Kellogg, "Determining the field emitter temperature during laser irradiation

in the pulsed laser atom probe," *J. Appl. Phys.* 52: 5320-5328, 1981.

12. H. F. Liu and T. T. Tsong, "Numerical calculation of the temperature evolution and profile of the field ion emitter in the pulsed-laser time-of-flight atom probe," *Rev. Sci. Instrum.* 55: 1779-1784, 1984.

13. T. T. Tsong, "Formation of multiatomic cluster ions of silicon in pulsed-laser stimulated field desorption," *Appl. Phys. Lett.* 45: 1149-1151, 1984.

14. O. Nishikawa, E. Nomura, M. Yanagisawa, and M. Nagai, "Pulsed-laser atom-probe study of Si, GaAs and GaP," *J. de Physique* (in press).

15. T. A. Skotheim, M. I. Florit, A. Melo, and W. E. O'Grady, "Ultrahigh-vacuum in situ electrochemistry with solid polymer electrolyte and x-ray photoelectron spectroscopy studies of polypyrrole," *Phys. Rev.* B30: 4846-4849, 1984.

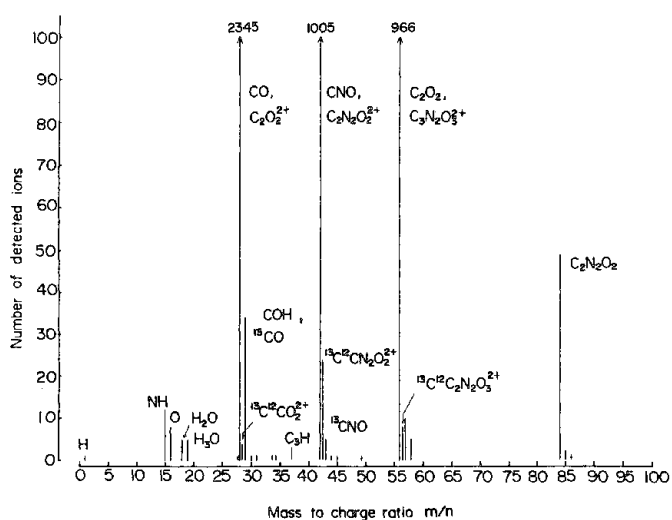


FIG. 6.--Histogram of first 4600 ions detected from 3-month-old PP film. Only four major mass peaks are seen. Spectrum changed to one similar to Fig. 5 after detection of another 2000 ions, which shows that thickness of fully oxidized layer is approximately 60 nm, assuming that analyzing section is deepened 1 nm by detection of 100 ions.

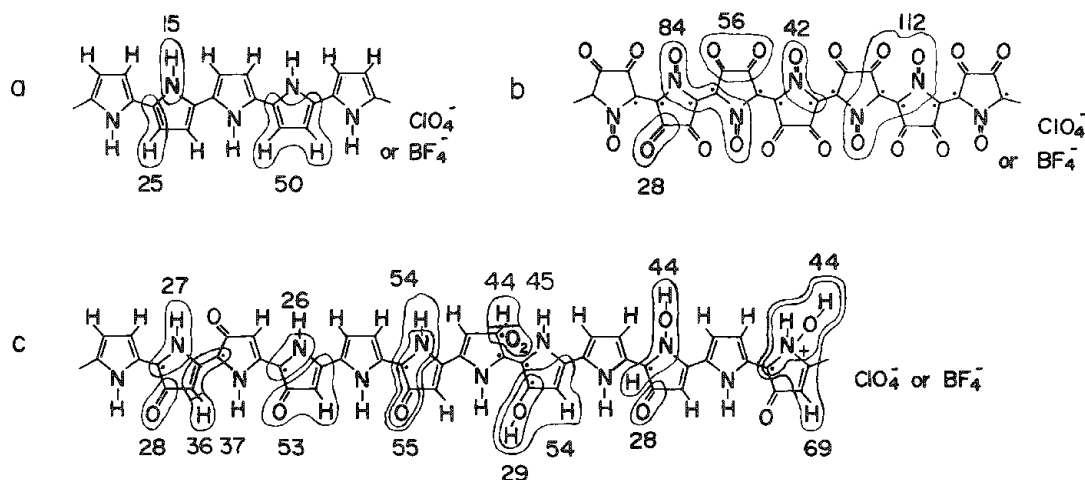


FIG. 7.--Structure of polypyrrole and possible fragments. (a) Nonoxidized ideal PP. (b) Fully oxidized PP. (c) PP at initial stage of oxidation. Closed lines indicate fragments induced by mass spectra, dots represent unpaired electrons by formation of C=O bonds.

## PHASE TRANSITION STUDIES THROUGH FIELD-ION MICROSCOPY

O. T. Inal, H.-r. Pak, and M. M. Karnowsky

Field-ion microscopy and x-ray diffraction analyses on solution treated, quenched, and annealed ternary alloy consisting of 40 a/o Pd, 35 a/o Ag, and 25 a/o Cu seem to suggest that water quench is not rapid enough to suppress phase separation. The only transformation observed in further annealing of this alloy is continued phase growth and the introduction of ordering in one of the resultant phases. No evidence of spinodal decomposition is observed, in contrast to the assumption of earlier work on this alloy. Based on the electron microscope observations of the earlier work (a fine modulated structure and the associated satellite reflection spots), a spinodal decomposition was proposed to have taken place followed by a discontinuous transformation to an ordered alloy. The microhardness results, structural features, and resistance behavior observed in the earlier study is explained here in light of the present observations.

The resistance survey of the initial study shows a rapid increase at the interval of room temperature to 493 K and an anomalous behavior within the interval of 493 K to 803 K, but above 803 K the change in resistance with temperature of anneal is seen to be linear. Therefore, annealing treatments were given to quenched alloys at 403 K and 673 K, for various durations, followed by field-ion microscopy and x-ray diffraction analyses of the field-emission tips to elucidate further the structure features observed.

The ternary alloy was solution treated, as in the initial study, at 1133 K for 1 h and water quenched, rolled into wire form amenable to field-ion imaging, followed by a second solution treatment at 1133 K for 4 h and quenched in water. The wires were then etched to a fine end form, previous to and following the annealing treatments, and the imaging was made in a pure neon atmosphere at liquid nitrogen temperature. The x-ray diffraction analyses were made by the Debye-Scherrer powder diffraction technique (35 kV, 25 mA) with a camera diameter of 225 mm and an exposure time of 6 h for each sample.

Field-ion micrographs exhibiting the structures observed are shown in Figs. 1(a) through (f) and the results of the x-ray diffraction analyses, as well as the findings of the initial study, are listed in Table 1.

The field-ion micrograph of Sample I exhibits two different phases (Fig. 1a), which is confirmed by the x-ray data, which indicate the presence of two phases of quite similar lattice constants with one showing partial preferred orientation and the other one revealed by slightly broadened lines. No satellite spots in the Debye-Scherrer lines were observed and the field ion micrograph suggests that if spinoidal decomposition is present, the modulation wavelength has to be greater than 100 nm, an order of magnitude greater than the value computed in the earlier study. The suggestion here seems to be that the satellite spots observed in the diffraction pattern of the earlier study exhibit the presence of the second phase rather than a spinodal composition.

The sample annealed at 403 K for 72 h exhibits a structure (Fig. 1b) similar to that of the quenched alloy, consistent with x-ray diffraction analysis and the TEM data of the earlier study (Table 1), which obviously suggests that 403 K is too low a temperature to induce further transformation.

The alloy annealed at 673 K for 1 h is seen (Table 1) to exhibit an additional phase (of small amount, ~10 v/o), possibly silver-rich as suggested by its lattice constant<sup>2</sup> and revealed by very broad lines. The field-ion micrograph of this sample (Fig. 1c) is seen to exhibit two phases with one still containing the slip traces of the previous two alloys.

Sample IV, annealed at 673 K for 2 h (Fig. 1d), is observed to contain the initial two phases of Sample I, with the Ag-rich phase of Sample III missing in this anneal, possibly because phases in small amounts might not be recorded by both x-ray diffraction and

---

Authors Inal and Pak are at the New Mexico Institute of Mining and Technology, Socorro, NM 87801; author Karnowsky is at Sandia National Laboratory, Albuquerque, NM 87185.

TABLE 1.--Phase transition studies through field-ion microscopy.

Treatments following sol. solu. formation	X-ray Diffraction	Field-Ion Microscopy	Prev. Work <sup>(1)</sup>	Physical Property with Increased time at temperature <sup>(1)</sup>	
				Hardness	% change in resistance
I water quench	two clearly separated fcc phases: a) $a_0 = 3.898 \pm 0001 \text{ \AA}$ b) $a_0 = 2.840 \pm 0005 \text{ \AA}$ phase (a) shows partial preferred orientation phase (b) shows broadened lines indicating texturing	two definitely different phases one showing insufficient anneal in the form of slip traces (Figure a)	Extremely fine modulated structure; satellite spots in the electron diffraction pattern possibly suggesting spinoidal decomposition	neither property unusual	
II 403K-72 hrs	structure unaltered by the	smaller tip radius, i.e. higher-magnification exhibiting the slip traces more vividly; otherwise structure unaltered (Figure b)	no discernible structural change	no change	slight change up to 20 hrs and remains constant
III 673K-1 h4	3 fcc phases are present a) $a_0 = 3.898 \pm 0002 \text{ \AA}$ b) $a_0 = 3.840 \pm 0005 \text{ \AA}$ c) $a_0 = 3.96 \pm 001 \text{ \AA}$ phase (b) shows slightly broadened lines; phase (c) shows very broad lines and is in small amount.	two phases with one phase still exhibiting a striation revealing slip traces i.e. still insufficient anneal. (Figure c)	modulated structure of two phases developed in quench is seen to coarsen.	hardness peak at 4 hrs and then becomes constant	tremendous drop in resistance up to 20 hrs and then levels off
IV 673K-2hrs	two phases with lattice constants a) $a_0 = 3.898 \pm 0002 \text{ \AA}$ b) $a_0 = 3.840 \pm 0005 \text{ \AA}$ phase (c) of sample III is not exhibited	two phase structure persistent (Figure d)	coarsening of modulated structure	hardening peak at 4 hrs and then becomes	tremendous drop in resistance up to 20 hrs and then levels off
V 673K-8hrs	two phase structure a) $a_0 = 3.98 \text{ \AA}$ very badly developed preferred orientation and large crystallite size b) $a_0 = 3.82 \text{ \AA}$	definite ordering exhibited in the form of a well defined spiral (Figure e & f)	limited appearance of a discontinuous phase within one of the two phases present	ditto	ditto
VI 673K-24 hrs	two phases of equal amount are present a) $a_0 = 3.985 \pm 0001 \text{ \AA}$ b) $a_0 = 2.981 \pm 0005 \text{ \AA}$ this is an ordered structure with superlattice lines exhibited. CsCl type structure is seen to develop	better developed order with an ordered protruding phase in the matrix	discontinuous structure, consisting of two phases, is seen to consume the whole structure. One phase is ordered.	ditto	ditto
VII 673K-72 hrs	3 phases present a) $a_0 = 3.840 \text{ fcc}$ with preferred orientation b) $a_0 = 2.984 \text{ \AA bcc}$ c) $a_0 = 2.985 \text{ \AA fcc}$ quenching strains no longer exhibited	well developed ordered phase in the form of bacon slices in the matrix	no structural change	ditto	ditto

field-ion microscopy. The coarsening of the modulated structure at this stage, suggested by the earlier study, cannot be supported by the present data.

The alloy annealed at 673 K for 8 h shows the first discrepancy between field-ion microscopy and x-ray diffraction analyses. X-ray diffraction (Table 1) shows the reappearance of the Ag-rich phase and the presence of the initial two phases, but the field-ion micrograph exhibits an ordered structure (Figs. 1c and f) at 90° different orientations of the tip.

This difference could be due to the localized nature of the ordered region, as suggested by the earlier study as a "limited appearance of a discontinuous phase." The microhardness peak observed and the large decrease in resistance recorded in the earlier study, it is now believed, support that ordering is indeed the main transformation observed in this alloy.

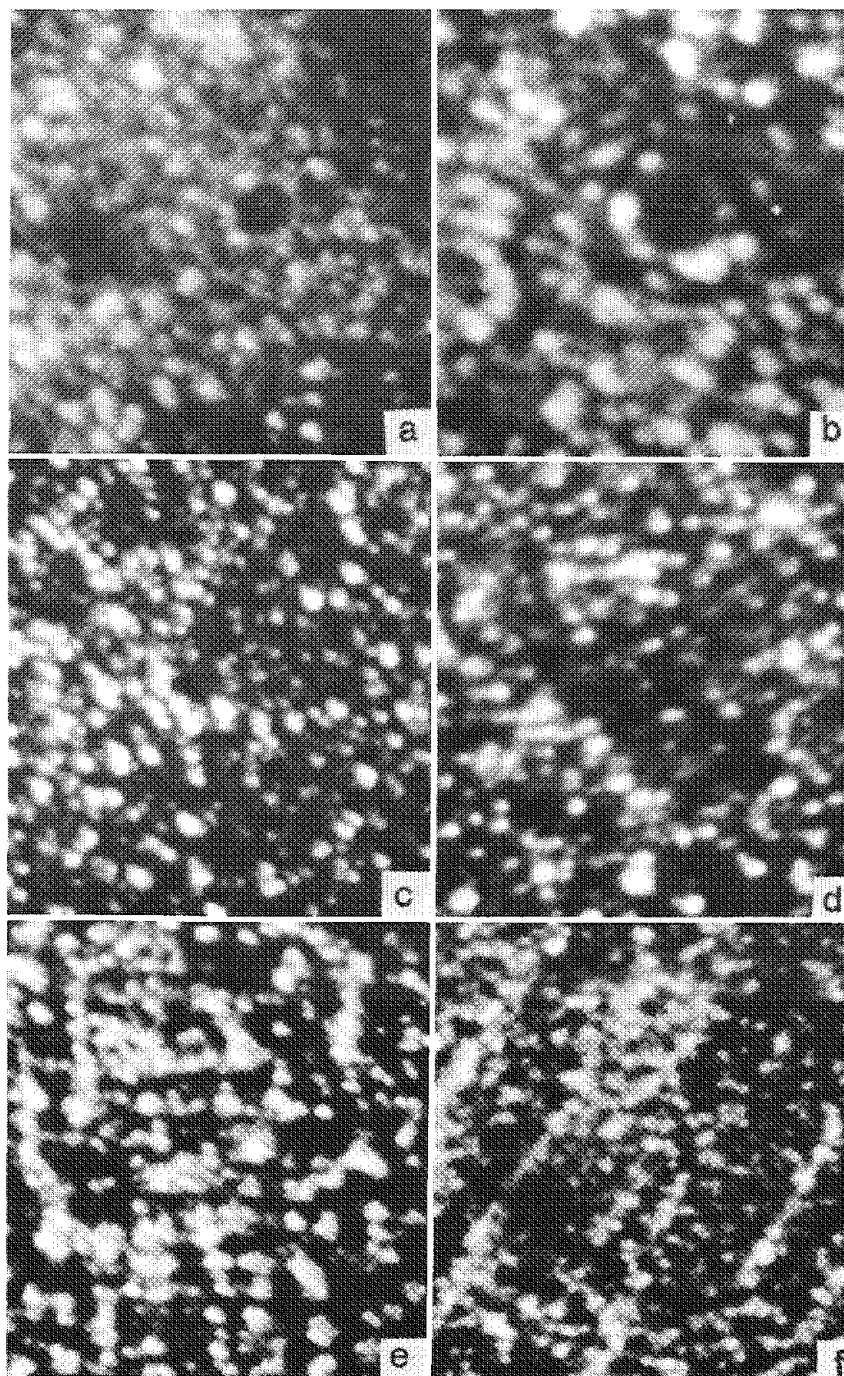


FIG. 1

The alloy annealed at 673 K for 24 h is revealed by a more developed ordered phase in a matrix, as shown in Fig. 1(g), whereas the x-ray diffraction data (Table 1) show an ordered phase, pertaining to a CsCl type of structure, along with the Ag-rich phase. This information is also consistent with the TEM data of the earlier study where the "discontinuous phase" is seen to be further developed.

Sample VI, annealed at 673 K for 72 h, consists of a Cu-rich phase, a Ag-rich phase, and the ordered phase; the field-ion micrograph of this sample exhibits (Fig. 1h) a well-ordered phase formed in a bacon-slice configuration within the matrix phase.

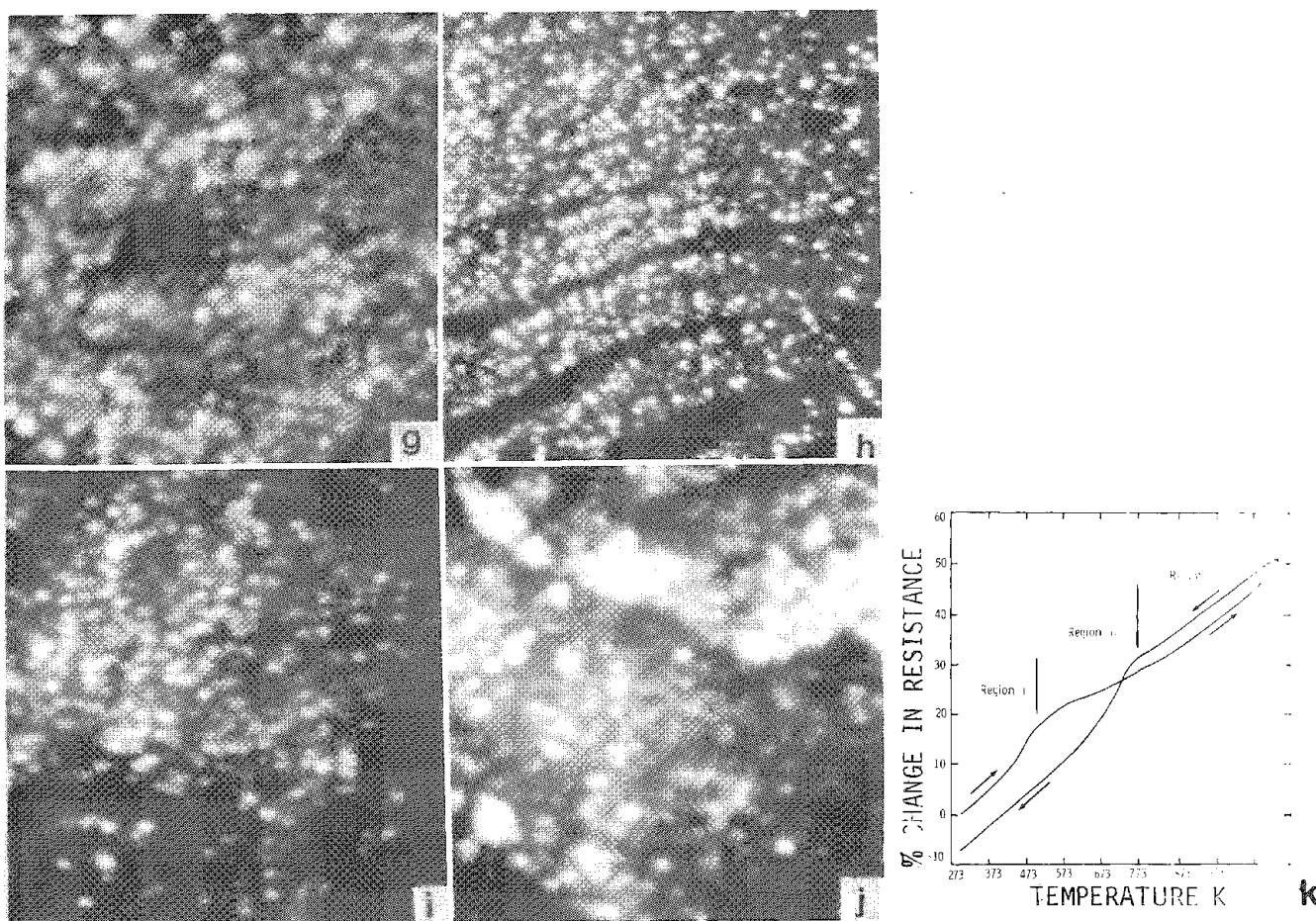
An alloy annealed at 873 K for 24 h (Figs. 1i and j) exhibit a Cu-rich and a Ag-rich phase in the x-ray diffraction and the field-ion micrograph contains two phases; thus both modes of studies showing the break-up of the order. Since this temperature is beyond the region of anomalous resistance behavior exhibited in Fig. 1(k), it is consistent with the earlier study and is also expected from energy considerations.

Our x-ray diffraction studies show an important discrepancy with the TEM data of the previous work. The main discrepancy is that no evidence of satellite peaks was observed in the diffraction patterns of as-quenched specimens, whereas the reported electron diffraction spots show satellite spots even around transmitted spots. Further studies are needed for clarification, currently being undertaken through field-ion and transmission electron microscopy. Also to be included is atom probe imaging to delineate the species of image spots observed in the field-ion microscopy.

#### References

1. M. M. Karnowsky, *J. Mat. Sci.* 13: 2339, 1978.
2. W. B. Pearson, *A Handbook of Lattice Spacing and Structure of Metals Alloys*, New York: Pergamon Press, 1958, 281.

FIG. 1 (Cont'd)



# FIM/IAP DEPTH PROFILING OF NITROGEN-IMPLANTED FIELD EMITTERS

S. D. Walck and J. J. Hren

Very little data are available for the ranges of low-energy (<40 keV) ions into metals; conventional analytical techniques such as secondary ion mass spectrometry (SIMS), nuclear reaction analysis (NRA), and Rutherford backscattering (RBS) suffer from a limited spatial resolution for the shallow depths. Although it is not widely recognized outside the FIM community, the atom probe and imaging atom probe are superb for compositional depth profiling. With an imaging gas present, depth resolutions of one atomic plane are expected. The imaging atom probe (IAP) has several advantages over the conventional atom probe (AP) for profiling: (1) it offers a larger area of analysis ( $10^2$ - $10^3$  larger), (2) crystallographic effects are minimized, (3) a complete mass spectrum is collected with each pulse, and (4) all atoms within the probed volume will strike the detector. However, there are two disadvantages in using the IAP. The IAP employs an extremely short flight distance ( $\sim 0.15$  m) as compared to the AP ( $\sim 1$  m) and mass resolution suffers accordingly. Therefore, systems must be chosen such that the mass-to-charge ratios are sufficiently resolved temporally. The other disadvantage is the difficulty in the determination of ring collapses under UHV conditions (i.e., no imaging gas present). In the AP an increase in signal occurs when the edge of a ring sweeps by the probe hole. This periodic increase corresponds to the collapse of a ring and can be used to assign the depth scale. In the IAP, distinguishing between an increase in signal and an increase due to a voltage increase is difficult because the signal from one set of planes is small compared to that coming from the entire probed surface. A method has been developed for determining the depth scale of a specimen by relating the volume probed to the integrated signal of the matrix.<sup>1</sup> This procedure was used to depth profile 5 keV  $N^+$  implanted nickel specimens. When  $N^+$  is implanted into tungsten, the rings can be distinguished, allowing for ring counting. The results of these profiles are also presented for comparison to those of the nickel.

In the IAP, if all the atoms within the detected area strike the detector and the detector efficiency is constant, the integrated signal should be proportional to the number of atoms contained within the probed volume. In turn, the number of atoms is simply related to the volume probed by the specimen density. This integrated signal is easy to measure, since it is simply the cumulative matrix signal from the spectra collected. Furthermore, the accumulated spectra approximate an integration because field evaporation can be controlled very precisely and the collapse of one set of planes is made to occur over several spectra. The tip geometry assumed is a conical shank with a spherical cap which joins the shank tangentially. With this model, the radius of curvature  $R$  is given as

$$R = (h + l_0) (\sin \alpha) / (1 - \sin \alpha) = (h + l_0) K_\alpha \quad (1)$$

where  $\alpha$  is the shank half-angle,  $h$  is the distance probed from the interval surface, and  $l_0$  is the distance from the initial surface to the apex of the cone. The volume probed  $V$  is found to be,

$$V = \frac{\pi}{3} [K_\alpha^2 \sin^2 \alpha - K_\alpha^3 (1 - \cos \beta)^2] (h^3 + 3 h^2 l_0 + 3 h l_0^2) \quad (2)$$

where  $K_\alpha$  is defined in Eq. (1) and  $\beta$  is the subtended viewing half-angle (equal to  $20^\circ$  for our system). The tip geometrical parameters  $\alpha$  and  $l_0$  are measured from TEM micrographs. A proportionality constant between the volume and the cumulated matrix signal is found by ring counting a calibration sample that has not been implanted, and is then used with Eq. (2) to find the depth as a function of the cumulative matrix signal.

---

Author Walck is at the Department of Materials Science and Engineering, University of Florida, Gainesville, FL 32611; author Hren is at the Department of Materials Engineering, North Carolina State University, Raleigh, NC 27695. This work was sponsored by the U.S. Department of Energy under contract DE-FG05-84ER45172.



Figure 1 shows a typical cumulative  $N^+$  versus depth profile for a Ni specimen implanted with 10 keV  $N_2^+$  to a fluence of  $1.8 \times 10^{16} N^+/cm^2$ . As can be seen a surface  $N^+$  peak is detected within the first few Ångstroms. The S curve, which is expected, suggests a Gaussian profile is absent. The curve levels off when  $N^+$  is no longer present. This curve is contrasted with that for W implanted to a fluence of  $7.5 \times 10^{15} N^+/cm^2$  (Fig. 2) found by the ring-counting method. The surface  $N^+$  peak is still present. However, two peaks can be seen, at approximately 2 nm and 10 nm. The first can be attributed to the expected implantation depth, and the second to channeling down the [011] direction of the specimen's axis. The lack of a well-defined  $N^+$  peak is not understood, but it is probable that only a fraction of the nitrogen at the surface is being evaporated as nickel is removed. The tungsten system can be made to behave like the nickel system by lowering of the pulse fraction (the ratio between the pulse amplitude and applied dc voltage). Future work is directed toward understanding this phenomenon in order to obtain accurate profiles of implanted species. Range data for various energies are available.

### References

1. S. D. Walck, T. H. Büyüklımanlı, and J. J. Hren, *Proc. 32nd Intern. Field Emission Symp.*, Pittsburgh, 1985.

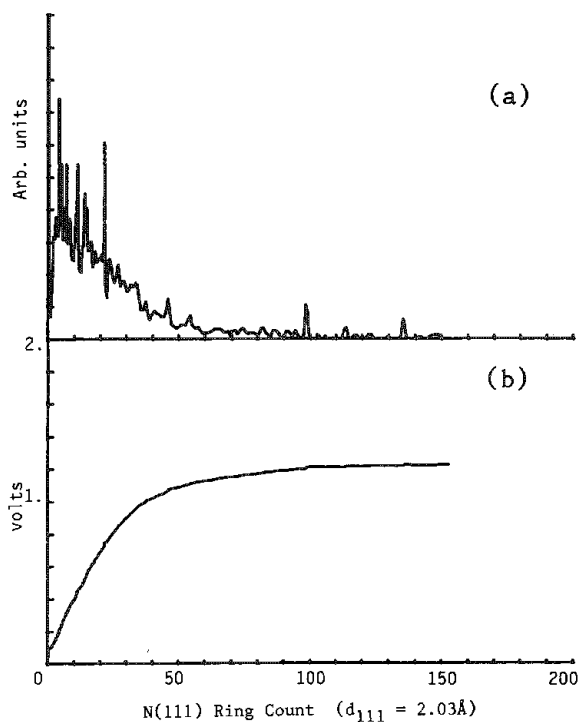


FIG. 1.--IAP profile of 10keV  $N_2^+$  implanted into Ni to fluence of  $1.8 \times 10^{16} N^+/cm^2$ . (a) 3-point numerical derivative of (b) cumulative  $N^+$  signal vs Ni(111) ring collapses. Initial surface  $N^+$  peak is off scale in (a). Depth scale calculated from Eq. (2).

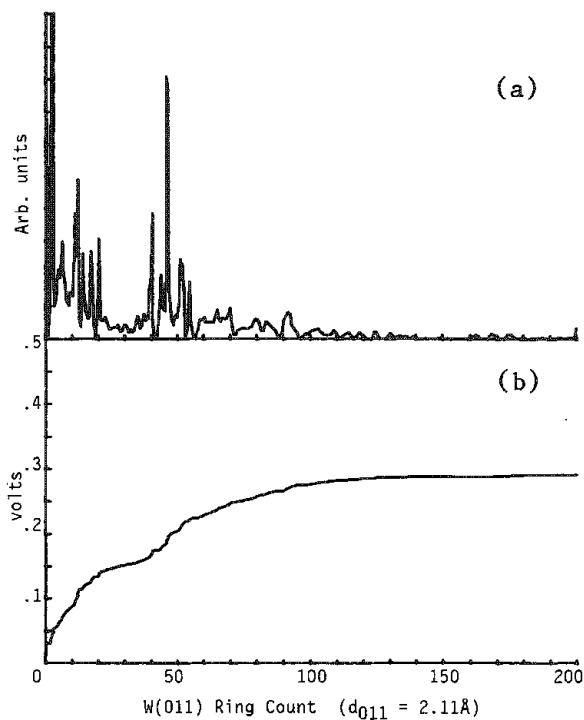


FIG. 2.--IAP profile of 10keV  $N_2^+$  implanted into W to fluence of  $7.5 \times 10^{15} N^+/cm^2$ . Note presence of channeled peak at approximately 95 Å. Depth found by counting (011) ring collapses.



## APPLICATIONS OF ATOM PROBE FIELD-ION MICROSCOPY TO SEGREGATION AND CLUSTERING STUDIES IN MATERIALS SCIENCE

M. G. Burke and S. S. Brenner

Numerous structure/properties investigations in materials science have been concerned with the phenomenon whereby small microstructural changes have dramatically altered the mechanical behavior of materials. It is thought that even monolayer segregation can exert a considerable effect on material properties. Thus, there is a continuing desire for higher spatial resolution quantitative microanalysis to study such segregation. The Atom Probe Field-Ion Microscope (APFIM) is a uniquely powerful analytical instrument that not only permits quantitative microanalysis on an atomic scale, but is also not subject to the limitations of other analytical techniques regarding elemental detectability.

The applications of APFIM are constantly increasing as new materials problems are found to be amenable to study using this technique.<sup>1</sup> The great advantages of APFIM in terms of elemental detectability and spatial resolution indicate that APFIM is the ultimate technique for microchemical characterization on an atomic scale. The technique has some limitations: specimen preparation (particularly for nonmetals) may be difficult, specimen fracture resulting from the high fields imposed for field-evaporation may occur before the analysis is completed, and the sampling of specific microstructural features is difficult due to the small amount of material that is analyzed at the tip of the needle-shaped specimen. This last problem, which may involve considerable experimental effort, can be significantly alleviated by combining APFIM with conventional or analytical electron microscopy for specimen pre-selection. Indeed, the combined techniques of APFIM and TEM have been shown synergistically to extend the applicability of each technique.<sup>2,3</sup>

It is not the intent of this paper to describe the operation of an APFIM; for more detailed information concerning the instrument and technique, the reader is referred to publications by Brenner and Miller,<sup>4</sup> Wagner,<sup>5</sup> and Bowkett and Smith.<sup>6</sup> Rather, some recent advanced applications of APFIM research into segregation and clustering phenomena in materials science will be described.

### *Segregation in Metals and Alloys*

*Grain Boundary Segregation in Ferrous Alloys.* The segregation of very dilute solute elements in ferrous alloys has been the subject of numerous atom probe investigations. One solute of particular interest because of its often deleterious effect on mechanical properties is phosphorus. Temper embrittlement and premature intergranular fracture have been observed in phosphorus-bearing alloys and have been frequently postulated to be associated with the segregation of phosphorus to various microstructural features. There have been two approaches to the study of phosphorus segregation in ferrous alloys. Investigators have been primarily concerned with the characterization of the microstructure of the degraded alloy or with why certain additions alleviate the problem.

The extent of grain boundary phosphorus segregation in an Fe 0.04% P alloy was examined by Sakurai et al.<sup>7</sup> The investigation analyzed a single grain boundary after a series of in situ aging treatments at successively higher temperatures. The results of their study confirmed Auger results that phosphorus segregates to grain boundaries at temperatures below 600 C, and showed that the phosphorus enrichment was restricted to the region close to the boundary.

More recently, Möller et al.<sup>8</sup> have examined the distribution of phosphorus segregation in Fe-Mo-P and Fe-Mo-P-C alloys to determine the beneficial role of Mo in reducing the phosphorus embrittlement of steels. Analysis of the aged alloys showed that no precipitates or Mo-P clusters were formed in the absence of carbon indicating that there is no direct interaction between Mo and P as has been suggested. However, a strong interaction between phosphorus and the numerous small (2-4nm) Mo<sub>2</sub>C precipitates that were formed in

---

The authors are at the Department of Materials Science and Engineering, University of Pittsburgh, Pittsburgh, PA 15261.

the Fe-Mo-P-C alloy was observed. Atom probe analysis revealed that P was not contained in the carbides, but a significant enrichment of P was measured in the ferrite that surrounded the  $\text{Mo}_2\text{C}$  precipitates. It is interesting that this phosphorus enhancement was not found exactly at the carbide/matrix interface, as is illustrated in Fig. 1, which is an evaporation sequence diagram from the atom probe analysis through the carbide and into the adjacent matrix. Each layer in this diagram represents one (110) atom layer or a depth of 0.202 nm.

In Fig. 2, an example of a grain boundary analysis in an Fe-C-0.3Cu alloy is presented.<sup>9</sup> The field-ion images of the alloy at different intervals in the atom probe analysis are shown with the experimentally measured carbon and copper concentration profiles through the ferrite. Carbon segregation to the grain boundary is clearly evident, as compared to the copper concentration, which is unchanged from the boundary to the matrix. The carbon segregation did not embrittle the boundaries, and thus this effect cannot be observed by Auger analysis which is useful for intergranularly embrittled materials.

*Grain Boundary Segregation of Boron.* Modern nickel-base alloys and some stainless steels are especially formulated to include a small amount of boron in order to improve mechanical properties, but the mechanism by which boron effects such improvements is still far from clear. Although boron has been postulated to effect improvements in SCC and hot ductility properties by segregating to grain boundaries, conventional analytical techniques present considerable experimental difficulties in the detection and quantification of light elements such as boron. In contrast, the APFIM is ideally suited to investigate problems such as the grain boundary segregation of boron. Indeed, a number of studies of boron segregation in a variety of alloy systems have been reported in the literature.<sup>10,15</sup>

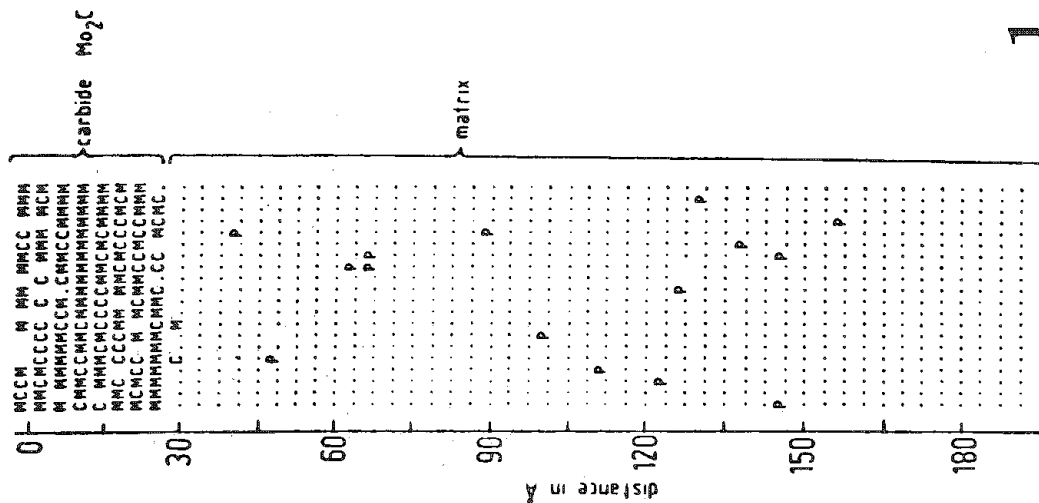
Grain boundary enrichment of boron content in 316L austenitic stainless steel was characterized by Karlsson et al,<sup>10</sup> who reported a grain boundary boron content of ~1.5 at.% in an alloy of 0.004% nominal composition. In nickel-base alloys, Delargy and Smith<sup>11</sup> detected boron in grain boundary  $\text{M}_{23}\text{C}_6$ -type carbides in the alloy IN939. These results suggested that the precipitates should be in fact considered to be  $\text{M}_{23}(\text{CB})_6$  type. Furthermore, significant segregation of boron was also observed at the MC/gamma interfaces in this alloy.

Current research efforts at the University of Pittsburgh and Oak Ridge National Laboratory involve the study of the segregation of boron in nickel aluminide alloys. Because the beneficial effect of boron has been associated with grain-boundary segregation, structures containing a large number of grain boundaries, both melt-spun ribbons<sup>12,13</sup> and splat-quenched alloys,<sup>14,15</sup> have been analyzed by APFIM. Enhanced boron concentrations in the grain boundary regions have been reported in both investigations. An example of boron segregation measured at a grain boundary in the melt-spun NI 24at% Al 0.24at% B alloy is presented in Fig. 4.<sup>13</sup>

*Segregation to Second Phases in Ferrous Alloys.* In addition to grain boundaries, second phases can become preferential locations for the enhancement of solute concentrations. The enhancement can be caused by differential solubility effects or can be due to the lowering of surface and/or strain energies. The APFIM has become an important tool in investigating the exact mode of such segregation. In studies similar to those of segregation to grain boundaries, the APFIM investigations have concentrated not only the location of primary segregants, but also on the influence of secondary elements on such segregation. Systems such as Fe/TiC/Sb,<sup>16,17</sup> Fe-MoN-(Sb,P),<sup>18</sup> 2.25 Cr-1Mo steels,<sup>19</sup> pearlitic steel,<sup>20,21</sup> and Pd-modified 4150 steel<sup>22</sup> have been studied by APFIM.

Brenner and Myers<sup>16</sup> examined Fe FIM specimens that had been ion-implanted with Ti, C, and Sb. Atom probe evidence for the trapping of Sb by TiC precipitates was obtained; moreover, large numbers of defects associated with ion-implantation were observed in the field-ion images. This aspect of precipitate segregation was continued in the research by Pillar, Miller, and Brenner.<sup>17</sup> Using conventionally prepared Fe-Ti-C-Sb alloys, the influence of Sb upon TiC precipitation and coarsening was studied. APFIM analyses of TiC precipitates revealed that an enrichment of Sb (up to 7 times the average concentration) occurred at the TiC/ferrite interface and into the surrounding ferrite. A field-ion micrograph depicting an analyzed TiC precipitate is presented in Fig. 3. The results of their investigation indicated that the segregation of Sb may be controlled by both chemical and strain effects.

The study of antimony and phosphorus segregation in Fe-Mo-N alloys by Brenner and Walck<sup>18</sup> highlighted the influence of MoN precipitates on segregation. Through atom probe

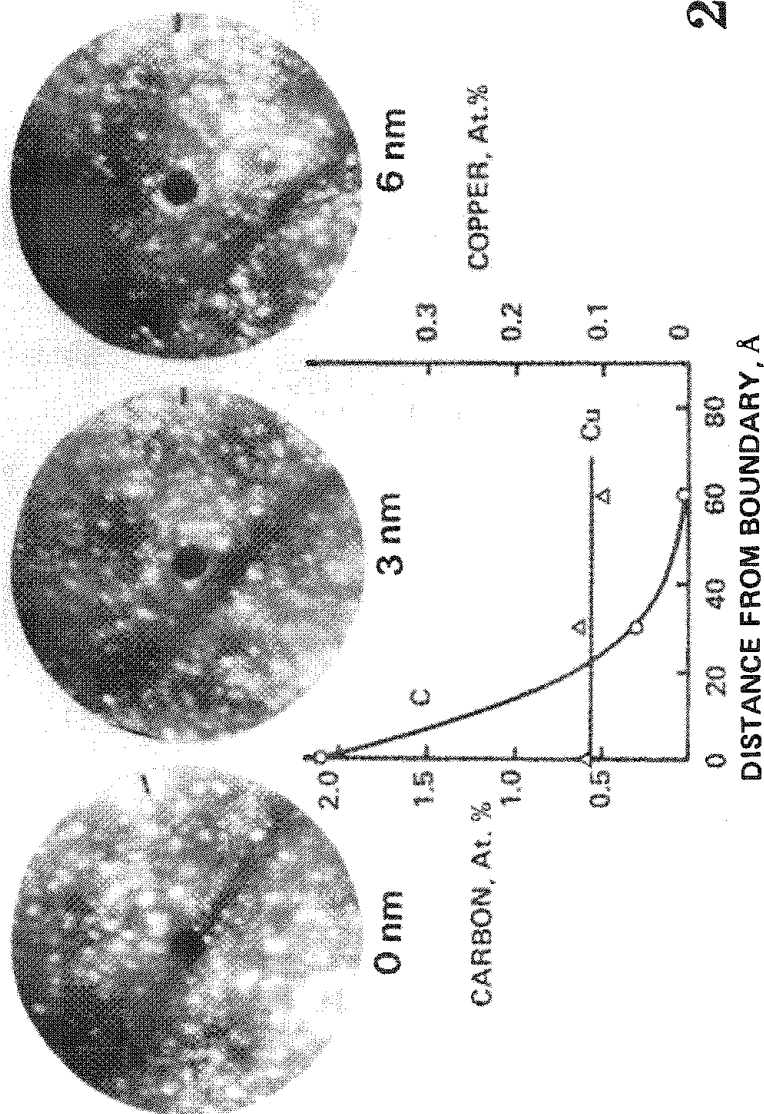


1

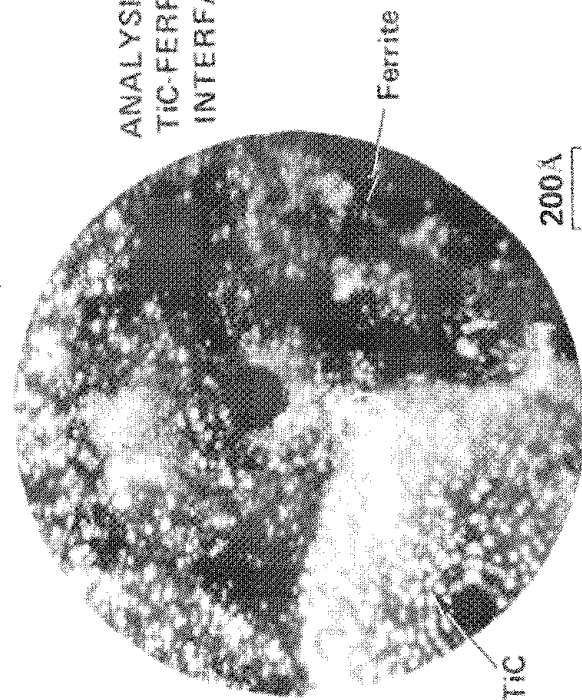
FIG. 1.--Evaporation sequence diagram through  $\text{Mo}_2\text{C}$  precipitate into adjacent ferrite matrix, showing phosphorus enrichment. (M = molybdenum, P = phosphorus, C = carbide, • = iron.)

FIG. 2.--Field-ion micrographs of grain boundary in Fe-Cu alloy with corresponding microchemical data from atom probe analysis. Note C enrichment at grain boundary.

FIG. 3.--Field-ion micrograph of TiC precipitate in ferrite.



2



200 Å

3

ANALYSIS OF  
TiC-FERRITE  
INTERFACE

analysis, Sb was found to segregate to the interfaces of the MoN precipitates. A significant observation was that the degree of precipitate coherence did not affect the extent of segregation. However, the phosphorus-containing (0.2 and 0.4 at.% P) alloys behaved differently. Atom probe analysis of the MoN precipitates showed that the nitrides contained ~4 to 6 at.% P, and segregation to the nitride/ferrite interface was not observed.

Careful APFIM analysis of a Mo/Cr-rich  $M_2C$  carbide in a tempered 2.25 Cr-1 Mo steel revealed the presence of boron at the carbide/ferrite interface even though the boron content of the alloy was in the ppm range.<sup>19</sup> Silicon enrichment in the vicinity of cementite has been observed in APFIM studies of tempering.<sup>20,21,23</sup> The results were interpreted in terms of the diffusion of silicon away from the ferrite/ $M_3C$  interface and the retardation of the growth and coarsening of the cementite.

Microstructural and microchemical changes in a tempered 4130 steel containing palladium were examined by Miller et al.<sup>22</sup> In the Pd-modified alloy, Pd segregation to ferrite/ferrite lath boundaries was observed in addition to the formation of Pd-Mn precipitates. Figure 5 shows a field-ion micrograph of such a lath boundary in the Pd-modified 4130 steel and the measured Pd concentration on the boundary and at various locations away from the boundary.

The extent of hydrogen trapping at carbide interfaces has been of great theoretical interest in the area of hydrogen embrittlement. By ion-implanting an Fe-TiC alloy with deuterium, Spitznagel et al.<sup>24</sup> were able to measure an enhanced deuterium concentration at the TiC/ferrite interface. Although the experimental aspects of this study presented some problems, the APFIM has been shown to be capable of quantitative analysis of deuterium in alloys. The potential clearly exists for additional APFIM experiments to confirm theoretical speculation in this and other similar areas.

### *Clustering in Ferrous Alloys*

Solute segregation in alloys is associated with specific microstructural features such as boundaries and second-phase interfaces. Clustering of solute atoms is generally more homogeneous, but may also be associated with defects. It is usually a precursor to the precipitation process. Solute clusters are difficult to detect, even by field-ion microscopy, because of their small size and the minimal contrast, if any, associated with such features. However, their effect on material properties can be significant, either in terms of alloy hardening or embrittlement. The atom probe can readily detect such clusters if their number density is sufficiently large ( $>10^{14} \text{ cm}^{-3}$ ). The presence of solute clusters in a material is determined by extensive random-area atom probe analysis and subsequent re-analysis of the chemical data. In this respect, the evaporation sequence diagrams provide important information concerning local depletions or enrichments of various solutes.

Atom probe field-ion microscopy has provided direct evidence of solute clustering in iron-base alloys. APFIM data from the analyses of Fe-Ni-C martensites<sup>20,23,25</sup> has revealed that carbon clustering occurs during room temperature aging. Such clustering precedes the precipitation of epsilon carbide.<sup>23</sup> Carbon atoms have also been shown to segregate to dislocations.<sup>26</sup> Using an imaging atom probe, Chang et al. demonstrated that the carbon content in an Fe-C alloy was enhanced in the vicinity of the dislocation core.<sup>26</sup> The solute atmosphere was approximately 3-4 nm from the core. However, not all dislocations were observed to be associated with solute atoms.

*Irradiation-induced Clustering in RPV Steel Weld Metal.* Significant progress in the study of irradiation damage and embrittlement has also resulted from the application of APFIM. Irradiation-induced segregation and clustering occur on a scale which is below the spatial resolution of conventional electron-optical techniques. The APFIM not only provides structural information concerning voids and defects, it also permits quantitative microchemical composition within the clustered regions. Using APFIM, Miller and Brenner<sup>27</sup> demonstrated for the first time that irradiated A302B monitor material contained fine copper clusters and precipitates. Examination of irradiated and unirradiated copper-bearing RPV steel welds by Burke and Brenner<sup>28</sup> also revealed the presence of nickel and manganese in the copper-rich clusters. In Fig. 6, an evaporation sequence diagram through a cluster in a 0.66 Ni-0.3 Cu - 1.0 Mn steel is presented. Clearly, APFIM provides information with respect to microstructural changes occurring during irradiation which is essential to materials evaluation and development in the nuclear power industry.

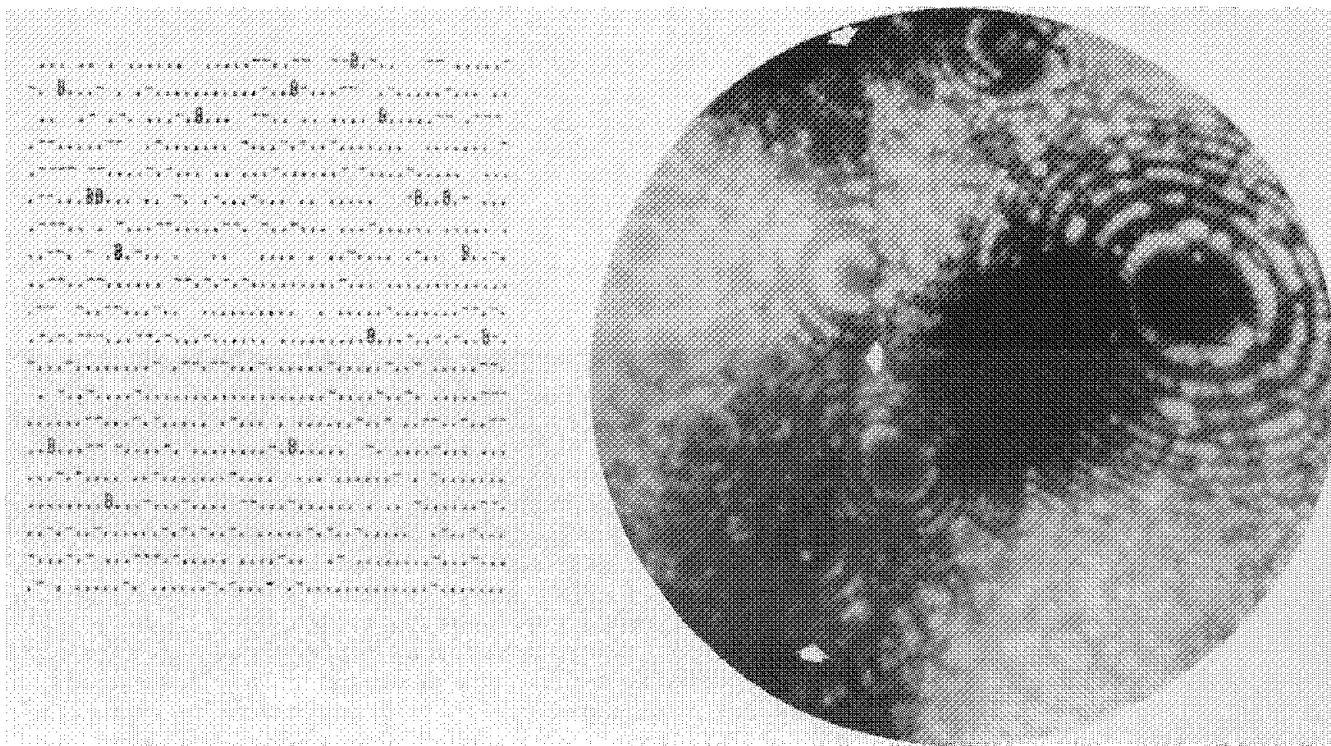


FIG. 4.--Analysis from Ni-24Al-0.24B specimen containing grain boundary (arrow).

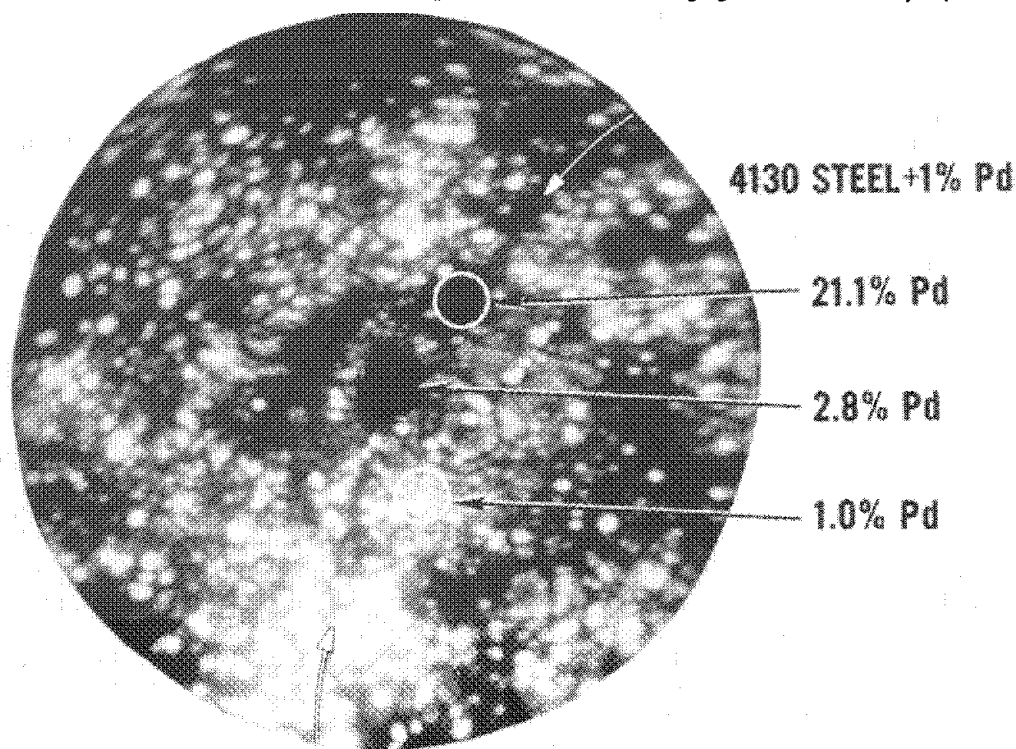


FIG. 5.--Field-ion micrograph of Pd-decorated lath boundary in Pd-modified 4130 steel. Pd content as determined by APFIM at various locations is indicated on micrograph.

## Electronic Materials

The considerable interest in the interfacial structure and properties of compound semiconductors has prompted several APFIM investigations.<sup>29,33</sup> Specifically, research has been conducted into the nature of Ni-GaAs and Al-GaAs interfaces. Also, chemical fluctuations in compound semiconductors have been studied by APFIM because of the deleterious effects associated with nonuniform structures. The atom probe's unique capability of quantitative analysis on an atomic scale is well suited to the characterization of the structures.

By depositing a thin Ni film on a GaAs FIM specimen, Wada et al.<sup>29</sup> were able to study the effect of aging temperatures (500 and 600 C) on the Ni-GaAs interface. The existence of two intermediate interfacial layers was confirmed by atom probe analysis of the transition region between the Ni and the GaAs substrate: first, a Ni-As region ( $\text{Ni}_5\text{As}_2$ ); and second, a  $\text{Ni}(\text{AsGa})_2$  zone adjacent to the GaAs.

In a study of AlGaAs interfaces, Nishikawa et al.<sup>30</sup> were interested in the compositional variations at heterojunction interfaces and the effect of dopants on interdiffusion. Al was deposited on Zn-doped and Si-doped [011] GaAs. Aging temperatures from 150 to 900 K were examined. Mixed layers were observed to form between the Al and GaAs substrate. They concluded that Zn doping promoted the Al-Ga exchange reaction. In addition, the As content of the Al-As mixed layer was observed to increase with aging temperature, approaching the stoichiometric AlAs at 900 K. The important result of this APFIM investigation was that the Al-GaAs and AlAs-GaAs interfaces are atomically sharp.

A modification of the conventional (DC pulse) atom probe, namely the pulsed laser atom probe, has been successfully employed by Cerezo et al.<sup>31</sup> and Grovenor et al.<sup>32</sup> to study fluctuations of Al in GaAlAs layers. They have shown that the Al concentration can vary significantly in thick MOCVD layers. Pulsed laser atom probe analysis has also been applied to the examination of the  $\text{SiO}_2/\text{Si}$  interface<sup>33</sup> and has provided evidence for the existence of an interfacial SiO layer approximately 0.5 nm thick.

## Summary

Recent applications of APFIM have provided significant contributions in the areas of grain boundary segregation, segregation to second phases, clustering in metals and alloys, and in the detection of interfacial chemical inhomogeneities and compositional fluctuations in electronic materials. The unique capability of APFIM to detect and measure even monolayers of light elements make APFIM a powerful tool for microstructural characterization. Experimental difficulties associated with the sampling of small volumes can be alleviated through specimen preselection using TEM. The range of applications for APFIM is constantly increasing to meet the demands of materials technology.

## References

1. S. S. Brenner, *Surface Science* 70: 427, 1978.
2. K. Stiller, L. E. Svensson, P. R. Howell, Wang Rong, H. O. Andren, and G. L. Dunlop, *Acta Met.* 32: 1457, 1984.
3. M. K. Miller, M. G. Burke, and S. S. Brenner, *J. Microscopy* 139: 41, 1985.
4. S. S. Brenner and M. K. Miller, *J. Metals* 35: 54, 1983.
5. R. Wagner, *Field-Ion Microscopy*, Berlin: Springer-Verlag, 1982.
6. K. M. Bowkett and D. A. Smith, in S. Amelinckx et al., Eds., *Field-Ion Microscopy: Defects in Crystalline Solids*. Amsterdam: North Holland, 1970, vol. 2.
7. T. Sakurai, Y. Kuk, H. J. Grabke, A. K. Birchenall, and H. W. Pickering, *Proc. 27th International Field Emission Symposium (IFES)*, University of Tokyo, 1980, 334.
8. R. Möller, S. S. Brenner, and H. J. Grabke, *Scripta Met.* (in press).
9. S. S. Brenner and M. K. Miller, *Proc. 40th EMSA*, 1981.
10. L. Karlsson, H. O. Andren, and H. Norden, *Scripta Met.* 16: 297, 1982.
11. K. Delargy and G. D. W. Smith, *Met. Trans.* 14A: 1771, 1983.
12. S. S. Brenner, D. D. Sieloff, and M. G. Burke, *Proc. 32nd IFES 1985 (J. de Physique)*, in press.
13. S. S. Brenner, D. D. Sieloff, and M. G. Burke, *1986 AIME Conference*.
14. M. K. Miller and J. A. Horton, in Ref. 12.
15. M. K. Miller and J. A. Horton, in Ref. 13 (submitted for publication in *Scripta Met.*

16. S. S. Brenner and S. M. Myers, Ref. 7, p. 219.
17. J. Pillar, M. K. Miller, and S. S. Brenner, *Proc. 29th IFES*, Stockholm, 1982, 473.
18. S. S. Brenner and S. D. Walck, Ref. 7, p. 328.
19. M. K. Miller, P. A. Beavan, and G. D. W. Smith, *Surface and Interface Analysis* 1: 149, 1979.
20. M. K. Miller and G. D. W. Smith, *Metal Science* 11: 249, 1977.
21. L. Chang and G. D. W. Smith, *Proc. 31st IFES (J. de Physique)*, 1984, C9-397.
22. M. K. Miller, S. S. Brenner, and M. G. Burke, *Met. Trans.* (accepted for publication).
23. M. K. Miller, P. A. Beavan, G. D. W. Smith, and S. S. Brenner, *Proc. Int'l. Conf. Solid-Solid Phase Transformations*, AIME, 1982, 863.
24. J. A. Spitznagel, S. S. Brenner, M. K. Miller, and W. J. Choyke, *J. Nuclear Materials* 122: 252, 1984.
25. L. Chang, A. Cerezo, G. D. W. Smith, M. K. Miller, M. G. Burke, S. S. Brenner, K. A. Taylor, T. Abe, and G. B. Olson, *Proc. 31st IFES (J. de Physique)*, 1984, C9-409.
26. L. Chang, S. J. Barnard, and G. D. W. Smith, *Proc. 30th IFES*, University of Pennsylvania, 1983, 97.
27. M. K. Miller and S. S. Brenner, *Res. Mechanica* 10: 161, 1984.
28. M. G. Burke and S. S. Brenner, in Ref. 12.
29. M. Wada, H. Kita, and O. Nishikawa, Ref. 21, C9-471.
30. O. Nishikawa, O. Kaneda, M. Shibata, and E. Nomura, Ref. 21, C9-459.
31. A. Cerezo, C. R. M. Grovenor, and G. D. W. Smith, *J. Microscopy* (in press).
32. C. R. M. Grovenor, A. Cerezo, and G. D. W. Smith, *Proc. 1985 MRS Meeting*, Boston, 1985 (in press).
33. C. R. M. Grovenor, *ibid.*

# SEQUENCE OF ARRIVAL OF IONS AT DETECTOR

C = Copper

M = Manganese

\* = Nickel

+ = Molybdenum

S = Silicon

. = Iron

```

.....M.....S.....M.....M
.....M.....M.....
.....M.....
.....+S.....
.....
C...+.....M.....M.....
.....M.....
.M...S.....M.M...S...M...SC..M.
O.....M.....M.....+...SM.....M.....S.O.
.M.....M.M.S...M.M.....O...M.....M
..SS.SM...CM.....S..MSM+.....SM..+..SS..
SM...SM.....M+.....C.S.....S.M...O.....
OMM..M..M.M.S..C.....M.M.M.O..M...S.....OC..
.....M.....M...S.MS.M.C.O.C.S.....L..M.....
.C.O... ..OC.S.M..... ..SM..C.S..+..OM..M
..O.O.M.O.SC.....O.C.....S..SM.C.....C.....M.O...+
...S...+..S...+M.C...M.....O...O...M+...
.S.....M.....S.....SM.....M..+.....
..M..O.....
.....M.....
.....M..M+.....
..+.....
.....M.....M.....
.....M.....M.....M.....
.....O.. ..+.....O.....
.....M.....M.....
.....S.....

```

FIG. 6.--Evaporation sequence diagram from APFIM analysis of irradiated Cu-bearing weld containing Cu-Ni-Mn-rich cluster.



## APFIM STUDIES OF PHASE TRANSFORMATIONS

M. K. Miller

The atom-probe field-ion microscope (APFIM) has proved to be a very effective instrument for the study of phase transformations in many metallic systems. The atom-probe field-ion microscope provides a technique for direct observation and quantification of important microstructural and chemical features of the transformation such as the three-dimensional morphology of the evolving phases, the wavelength and spatial extent of the solute-rich regions, the sharpness of the interface between the phases, and the changes in composition of the coexisting phases. The atomic spatial resolution of the instrument permits the earliest stages of phase transformations to be investigated experimentally. The unrestricted mass range permits the location and quantification of all elements, including the light elements such as carbon and boron, to be determined. In this paper a summary of some of the types of information relating to phase transformations that may be obtained with the atom probe is outlined.

### *Characterization of the Morphology*

The morphology of a microstructure is determined in the field-ion microscope (FIM) section of the atom probe. This section of the instrument is where high-resolution images of the specimen are obtained.<sup>1</sup> A field-ion micrograph of an iron-chromium alloy that was aged within a low-temperature miscibility gap is shown in Fig. 1. The phase separation is evident by the presence of some darkly imaging and some brightly imaging regions in the micrograph. Phase identification is determined from the composition measured by atom-probe microchemical analysis of the differently imaging regions. The dark regions were shown to be the chromium-enriched  $\alpha'$  phase and the bright regions the iron-rich  $\alpha$  phase by this technique.

Each field-ion micrograph is a high-resolution view of the surface of the specimen. The technique of field evaporation enables the surface of the specimen to be removed and thus exposes successive layers of the microstructure.<sup>1</sup> Field-ion microscopy and field evaporation is performed with the specimen at cryogenic temperatures; therefore, no surface migration or diffusion occurs. The amount of material removed from the surface of the specimen can be controlled and quantified with better than atomic precision. This ability permits a complete three-dimensional model of the microstructure to be constructed. The morphology of the darkly imaging  $\alpha'$  phase was revealed by this technique to be in the form of roughly spherical particles. The morphological interpretation of more complex or relatively coarse microstructures is generally performed by video recording of the field-ion image during an extensive field evaporation sequence over many thousands of atomic layers.

The size of a precipitate is not generally measured from its extent in a field-ion micrograph because of differences in local magnification between the precipitate and the surrounding matrix. Instead, the size is determined with atomic precision from the persistence of the image of the precipitate through a field-evaporation sequence by a count of the number of atomic layers of material removed.

The field-ion microscope is also particularly suitable for interpreting the morphology of fine scale microstructures that contain high volume fractions of a second phase. Field-ion micrographs of an isotropic two-phase microstructure and a crystallographically aligned two phase microstructure<sup>2</sup> are compared in Figs. 2 and 3, respectively. Both the dark imaging chromium-enriched  $\alpha'$  phase and the brightly imaging iron-rich  $\alpha$  phase (Fig. 2) were found to be fully interconnected in field-evaporation sequences. The triaxially modulated microstructure was found to consist of a macrolattice of the brightly imaging

---

The author is at the Metals and Ceramics Division, Oak Ridge National Laboratory, Oak Ridge, TN 37831. The research was sponsored by the Division of Materials Sciences, U.S. Department of Energy, under contract DE-AC05-84OR21400 with Martin Marietta Energy Systems, Inc.



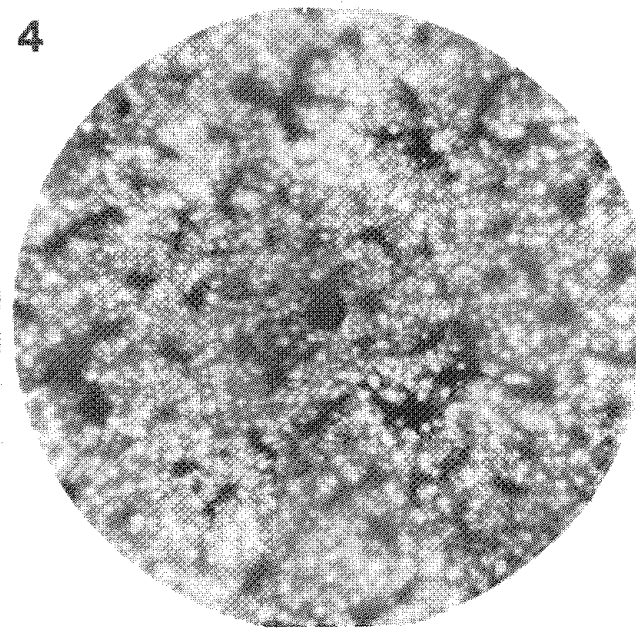
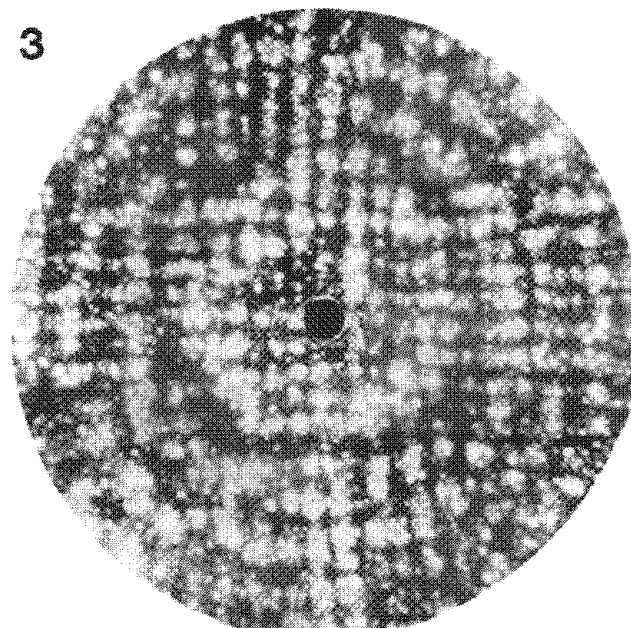
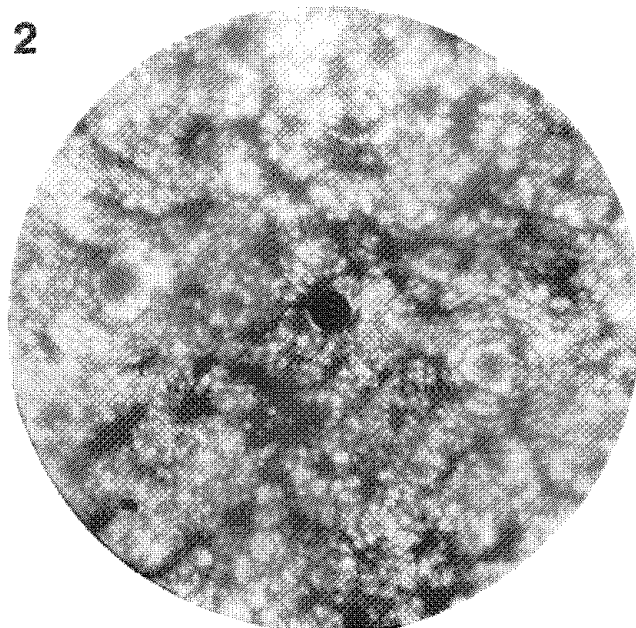
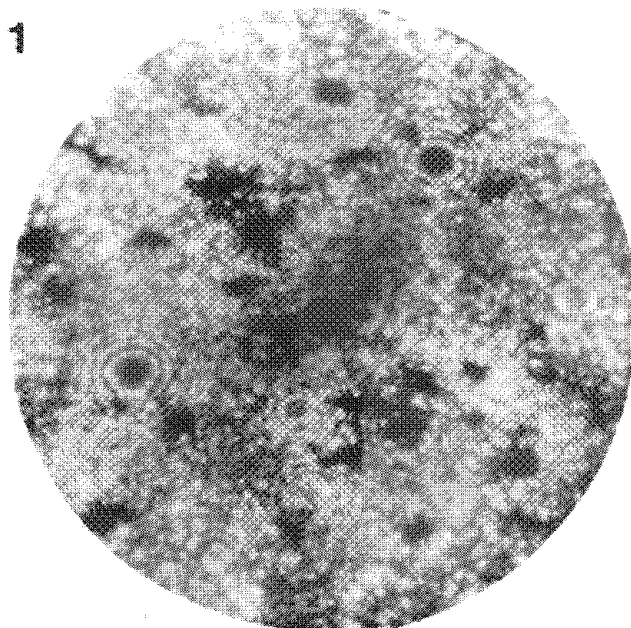


FIG. 1.--Field-ion micrograph of Fe- 24% Cr aged 485 h at 540 C showing isolated darkly imaging chromium-enriched  $\alpha'$  precipitates.  
 FIG. 2.--Field-ion micrograph of fully interconnected isotropic two-phase microstructure in Fe- 32% Cr aged 10 000 h at 470 C.  
 FIG. 3.--Field-ion micrograph of triaxially modulated two-phase microstructure in Fe- 25% at% Be aged 20 min at 400 C. The spacing of the composition modulations was measured from the micrograph to be 4.3 nm.  
 FIG. 4.--Field-ion micrograph of Fe- 28.5% Cr- 10.6T Co alloy aged 192 h at 525 C showing isotropic interconnected two-phase microstructure of chromium-enriched  $\alpha'$  and iron-rich  $\alpha$  phases.

iron-rich  $\alpha$  phase embedded in continuous darkly imaging beryllium-enriched B2 ordered phase.<sup>2</sup> In this micrograph the three orthogonal sets of composition modulations are revealed as the horizontal, vertical, and circular dark bands of the beryllium-enriched phase. The image interpretation of these type of microstructures in the TEM is very complex because of the many factors that contribute to image formation.<sup>3,4</sup>

The periodicity of a modulated microstructure can be measured from the linear intercept of one phase in the field-ion micrograph, since the local magnification effects are cancelled out. However, the determination of the wavelength of the modulations from the FIM micrographs must take account of the effects of the orientation of the modulations in the specimen and the projection of the curved FIM specimen surface.<sup>3</sup> When these effects are taken into account, the FIM results are in good agreement with results from measurements of the spacing of sidebands in electron diffraction patterns in identically aged material.<sup>5</sup> A field-ion micrograph of a ternary Fe-Cr-Co alloy that was aged deep within the low-temperature miscibility gap is shown in Fig. 4. A comparison of the distance between adjacent regions of the chromium-enriched  $\alpha'$  phase in this material, or wavelength, measured by the linear intercept method from both FIM and TEM micrographs, is shown in Fig. 5 for a series of various isothermal aging times.<sup>6</sup> The two sets of measurements are in excellent agreement.

#### *Characterization of Composition Fluctuations in the Microstructure*

The atom probe may be used to obtain composition information in addition to the visual data from the field-ion micrographs. One determines the composition by collecting and identifying all the atoms that pass through the entrance aperture to the mass spectrometer during pulsed field evaporation.<sup>1</sup> This aperture is the dark area in the center of the field-ion micrographs (Fig. 1). In this way a cylinder of material defined by the effective area of the aperture and the amount of material field evaporated is analyzed. The composition is directly determined by a count of the number of atoms of each element in the analyzed volume. This method allows the composition of a selected region, such as a precipitate, or the composition variations as a function of distance to be determined. An example of a composition profile through the modulated microstructure of the Fe-Cr-Co ternary alloy aged within the miscibility gap is shown in Fig. 6. The alteration between the chromium-enriched  $\alpha'$  and iron-rich  $\alpha$  phase is evident. The sharpness of the interface region between the two phases can also be estimated from these profiles. The composition of the  $\alpha'$  phase determined from a series of similar composition profiles reveals that the chromium level increases during aging until steady-state conditions are achieved (Fig. 7).

The characteristic distances can also be measured directly from the composition profiles. This alternative method can be used where the contrast between the phases in the micrograph is less well defined, such as in the very early stages of decomposition where the composition differences between the phases is small. The mean intercept  $\lambda$  and the thickness  $\tau$  of the chromium-enriched  $\alpha'$  phase are plotted in Fig. 8. Both characteristic distances increase with aging time, although there is a distinct difference in the behavior of these two parameters. The volume fraction of the  $\alpha'$  phase is simply the ratio of these two distances,  $\tau/\lambda$ . As aging progresses the volume fraction of the  $\alpha'$  decreases until the compositions of the two phases reach their steady state values. The time exponent (given by the gradient of the  $\lambda$  curve) and hence the coarsening kinetics determined from these data indicated that this Fe-Cr-Co system does not observe conventional LSW type coarsening under these aging conditions.<sup>7</sup>

The composition profiles can also be subjected to statistical analysis to characterize the microstructure further. One method is to perform autocorrelation analysis of the composition profiles (Fig. 9). In this type of analysis the composition of blocks of atoms are compared to see if any deviation from random behavior is observed. The presence of the first and second maxima,  $k_1$  and  $k_2$ , indicates that the specimen has a periodic modulated microstructure. The wavelength of the modulations is determined from  $(k_2 - k_1)d$ , where  $d$  is the distance between each composition measurement. The wavelengths determined from a series of autocorrelation analyses of the composition profiles of the aged Fe-Cr-Co alloy are shown in Fig. 10. The wavelengths determined from the autocorrelation, the composition profiles, and the FIM and TEM micrographs are in excellent agreement. The position of  $k_0$ , the first minimum in the autocorrelation, is an indication of the extent of the phase. In a random alloy no statistically significant peaks appear in the

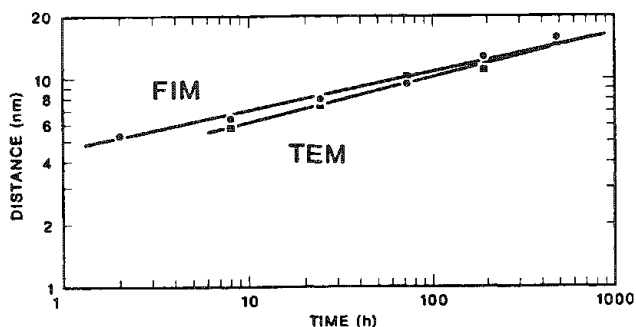


FIG. 5.--Comparison of periodicity of isotropic microstructure in Fe- 28.5% Cr- 10.6% Co isothermally aged at 525 C measured from FIM and TEM micrographs.

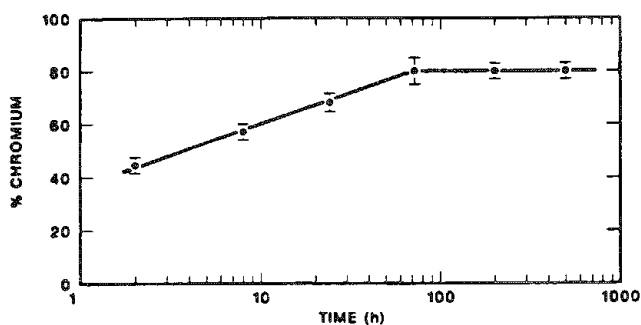


FIG. 7.--Variation in composition of chromium-enriched  $\alpha'$  phase determined from composition profiles. Fe- 28.5% Cr- 10.6% Co isothermally aged at 525 C.

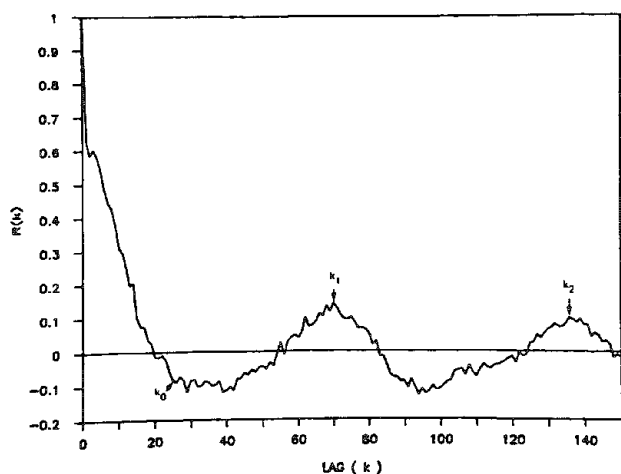


FIG. 9.--Example of autocorrelation analysis of composition profiles. Fe- 28.5% Cr- 10.6% Co isothermally aged at 525 C.

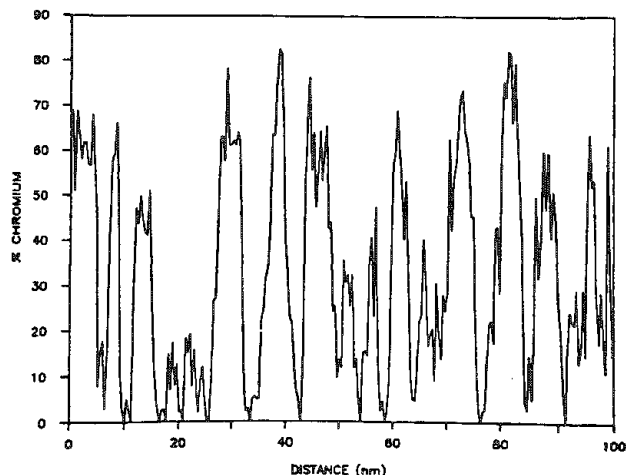


FIG. 6.--Atom probe composition profile through two-phase modulated microstructure in Fe- 28.5% Cr- 10.6% Co aged 192 h at 525 C.

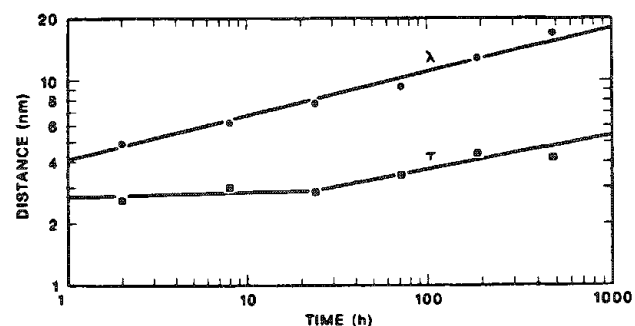


FIG. 8.--Mean intercept,  $\lambda$ , and thickness,  $\tau$ , of chromium-enriched  $\alpha'$  phase determined from composition profiles. Fe- 28.5% Cr- 10.6% Co isothermally aged at 525 C.

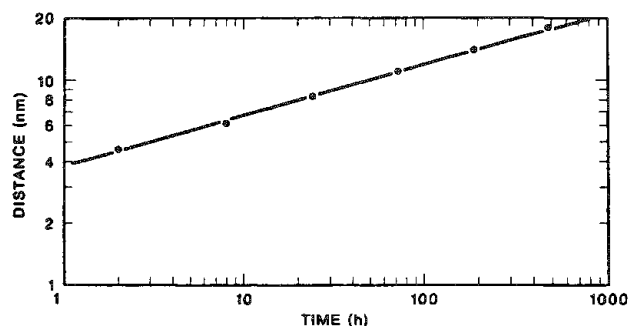


FIG. 10.--Wavelength of chromium-enriched  $\alpha'$  regions determined from autocorrelation analysis of composition profiles. Fe- 28.5% Cr- 10.6% Co isothermally aged at 525 C.

autocorrelation function and  $k_0$  is not observed. Similar types of statistical analyses can also be used to detect and measure the extent of clustering, the initial stages of phase separation, and cosegregation of solutes in a matrix.

#### References

1. M. K. Miller, "Atom-probe field ion microscopy," *Microbeam Analysis--1986*, 343.
2. M. K. Miller, S. S. Brenner, M. G. Burke, and W. A. Soffa, "Atom probe field-ion microscopy studies of triaxially modulated microstructures in Fe-Be alloys," *Scripta Met.* 18: 111-116, 1984.
3. M. G. Burke and M. K. Miller, "A comparison of TEM and APFIM to the interpretation of modulated microstructures," *Proc. 43rd Ann. Mtg. EMSA*, 1985, 70.
4. M. K. Miller, M. G. Burke, and S. S. Brenner, "Morphological interpretation of modulated microstructures," *J. de Physique* C9: 239-244, 1984.
5. M. K. Miller, M. G. Burke, and S. S. Brenner, "Measurement of characteristic wavelengths in modulated microstructures by field-ion microscopy," *J. Microscopy* 139: 41-47, 1985.
6. M. K. Miller, L. L. Horton, and S. Spooner, "Characteristic distance measurements by AP, TEM and SANS," *J. de Physique* C2: 409-412, 1986.
7. S. S. Brenner, P. P. Camus, M. K. Miller, and W. A. Soffa, "Phase separation and coarsening in Fe-Cr-Co alloys," *Acta Met.* 32: 1217-1227, 1984.

## THE APPLICATION OF APFIM TO EARLY STATE DECOMPOSITION OF THE SUPERALLOY NIMONIC PE16

Werner Wagner, Wilfried Hein, H. P. Degischer, R. P. Wahi, and Heinrich Wollenberger

The development of highly stressed materials in metallurgy shows the general trend to a decrease of the size scale of dispersed second phases. This trend is reflected in results reported in the literature in recent years, which illustrate the importance of detailed information on early decomposition stages with precipitate particles in the interesting size range of a few nanometers.<sup>1</sup> To observe and analyze such small particles, Field-Ion Microscopy (FIM) combined with Atom-Probe (AP) has been developed to a particularly powerful method and is now successfully applied to various alloy systems.<sup>2</sup> However, the limited specimen volume of FIM investigations has the consequence that the attainable range of precipitate size and density is restricted. Furthermore, it turns out that even with the high resolution of FIM there are uncertainties in how to rate data obtained for extreme conditions. These restrictions have suggested the combination of APFIM with complementary experimental techniques, predominantly conventional Transmission Electron Microscopy (TEM) and Small Angle Neutron Scattering (SANS). We applied this combination successfully to various binary and ternary alloys, such as CuCo,<sup>3</sup> CuNiFe,<sup>4-6</sup> and NiAlTi.<sup>7</sup> The present paper reports APFIM investigations on the commercial alloy Nimonic PE16, supplemented by TEM and SANS results. The aim of the paper is to demonstrate that APFIM can be successfully applied to a commercially available multicomponent alloy. The APFIM data are found to be consistent with the corresponding TEM and SANS results, with overlapping sensitivity ranges for the several techniques. It becomes obvious that the range of reaction parameters of the present investigation could not have been covered by any one of the methods alone.

### *Experimental*

Nimonic PE16 is a NiFeCr-based superalloy intended for high-temperature applications. It is strengthened by precipitates of the L1<sub>2</sub>-ordered  $\gamma'$  phase Ni<sub>3</sub>(Al,Ti). For the present investigation, commercial rod material was used (Table 1). TEM and SANS specimens were directly sliced from the rods. For FIM specimens, wires 0.2 mm in diameter were drawn. All specimens were solution treated for 1 h at 1313 K, water quenched to room temperature, and finally annealed at temperatures between 773 and 1113 K. The final preparation of TEM and FIM specimens was done by electropolishing.

### *Results and Discussion*

FIM micrographs imaged with Ne at a temperature around 70 K clearly resolve the  $\gamma'$  precipitates as brightly imaging areas (Fig. 1), for average precipitate radii of  $\bar{R} = 4$  nm and above (Fig. 1b) as well as for those below 1 nm (Fig. 1a). We note that the limit for quantitative TEM analysis is reached for  $\bar{R} < 5$  nm. The FIM micrographs confirm the TEM results of spherical shape and random spatial arrangement of the precipitates. In Ni-based alloys one frequently observes that initially randomly dispersed spheres change to cubes with preferential alignment along  $\langle 100 \rangle$ .<sup>8</sup> In PE16 no such change in morphology occurs over the entire investigated range of precipitate sizes, which reflects the distinctly small lattice mismatch of the  $\gamma'$  phase in PE16. The precipitate sizes were determined from FIM images during continuous field evaporation by counting of the evaporated atomic layers while a precipitate is visible. Results of precipitate size analysis are given in Fig. 2, along with size distributions determined from TEM. Figure 2 shows that FIM still measures precipitates with radii of 0.5 nm, significantly beyond the visibility limit of TEM. The analysis reveals the size distribution function as given for the diffusion-controlled Ostwald-ripening,<sup>9</sup> starting from the smallest precipitates resolved.

---

The authors are at the Hahn-Meitner-Institut für Kernforschung Berlin, Glienicke Str. 100, D-1000 Berlin 39, Federal Republic of Germany. Author Degischer is now at the Österreichisches Forschungszentrum Seibersdorf, A-1082 Wien, Austria.

The atom probe allows the determination of the composition of both phases with a spatial resolution of about 2 nm (projected spot size). The measured composition for the homogenized alloy and for the  $\gamma'$  phase and the  $\gamma$  matrix of the decomposed alloy are given in Table 1. The ratio Al/Ti > 1 for the homogenized alloy is not found in  $\gamma'$ , where the Ti content exceeds the Al content. This result is in agreement with measurements by Mangen et al.,<sup>10</sup> whereas microchemical analysis of  $\gamma'$  extractions by Windsor et al.<sup>11</sup> reveal an excess of Al in  $\gamma'$  precipitates.

TABLE 1.--Nominal composition of the homogenized alloy (manufacturer's specification) and atom probe results of the homogenized and decomposed alloy (in at.%).

	Ni	Fe	Cr	Al	Ti	Mo	Si
Nom. homog.	42	34	17.6	2.38	1.47	1.9	
homog.	45.6±0.9	32.3±0.7	15.6±0.5	2.5±0.2	1.53±0.16	1.87±0.18	0.79±0.12
AP $\gamma$	44.6±1.1	34.2±0.9	16.7±0.7	1.42±0.19	0.36±0.10	2.1±0.2	0.63±0.13
$\gamma'$	64.4±1.3	5.8±0.4	3.8±0.3	10.0±0.5	12.8±0.6	2.1±0.2	1.11±0.17

The most relevant kinetic parameter, "average precipitate size," is shown in Fig. 3, in which the results obtained from the several techniques are combined. The FIM and TEM data were directly derived from the measured individual size distributions; the SANS data were determined by fitting of the calculated structure function for a dispersion of spheres to the measured patterns. For these calculations, the FIM and TEM results on composition, size distribution, and spatial arrangement were used, which reduces the number of unknown parameters for the SANS calculations significantly and therefore allows a precise and reliable analysis.

Figure 3 reveals that in PE16 over the entire investigated range the radii follow the  $t^{1/3}$  dependence expected for Ostwald ripening.<sup>9</sup> The precipitate size distribution shows the corresponding shape from the very beginning (Fig. 2). Further, the SANS analysis reveals constant volume fractions and a proportionality between average precipitate size and average interparticle distance, which indicates that in PE16 the Ostwald ripening begins before the particles have reached an average radius of 1 nm. This result is in accordance with calorimetric measurements, which indicate very fast nucleation in this material.<sup>12</sup> Segregation seems to be completed when the sample reaches the aging temperature.

The results of the present investigation have some impact on concepts for industrial heat treatments, in particular when a structure of fine dispersed precipitates is required. Moreover, the results should permit the improvement of model descriptions of the decomposition in PE16, since the behavior of precipitates in the size range between 1 and 10 nm can be now considered. This information is particularly important for high-temperature fatigue and irradiation studies.

#### References

1. P. Haasen et al., Eds., *Decomposition of Alloys: The Early Stages*, Proc. 2nd Acta-Scripta Conf., Sonnenberg, New York: Pergamon Press, 1984.
2. P. Haasen, *Metall. Trans. A16*: 1173, 1985.
3. W. Wagner, J. Piller, H. P. Degischer, and H. Wollenberger, *Z. Metallkunde* 76: 693, 1985.
4. J. Piller, W. Wagner, H. Wollenberger, and P. Mertens, in Ref. 1, 1984, 156.
5. R. P. Wahi and J. Stajer, in Ref. 1, 1984, 165.
6. W. Wagner, R. Poerschke, and H. Wollenberger, in Ref. 1, 1984, 170.
7. W. Hein, W. Wagner, H. Wollenberger, and D. Juul Jensen, *Proc. 5th Risø Intern. Symp. Metallurgy and Materials Science*, Risø National Laboratory, 1984, 279.

8. A. J. Ardell and R. B. Nicholson, *J. Phys. Chem. Solids* 27: 1793, 1966.
9. C. Wagner, *Z. Elektrochemie* 65: 581, 1961.
10. W. Mangan, H. Schäfer, and E. Nembach (to be published in *Mater. Sci. and Engineering*).
11. C. G. Windsor, V. S. Rainey, P. K. Rose, and V. M. Callen, *J. Phys.* F14: 1771, 1984.
12. H. P. Degischer et al. (to be published).

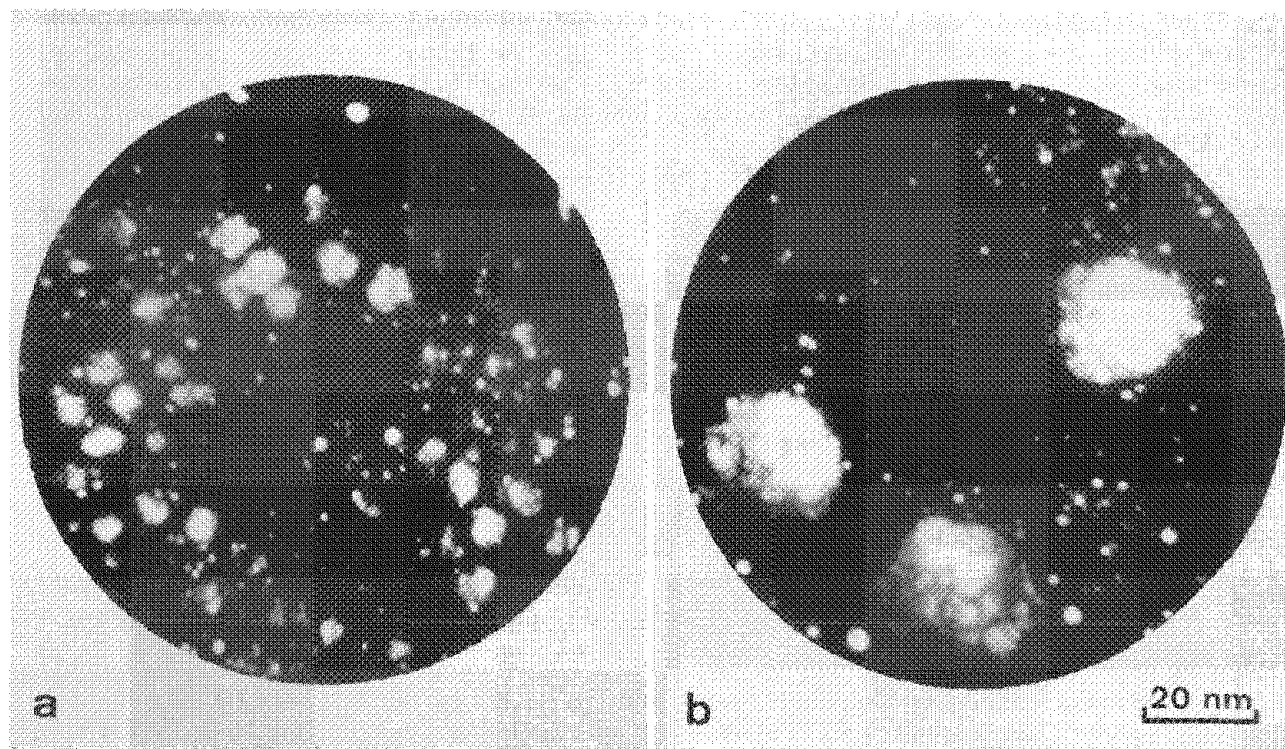


FIG. 1.--FIM micrographs of  $\gamma'$  precipitation in Nimonic PE16: (a) 973 K/6 min,  $\bar{R} = 0.9$  nm; (b) 1073 K/6 min,  $\bar{R} = 4.0$  nm. (Note that bright imaging precipitates appear overmagnified.)

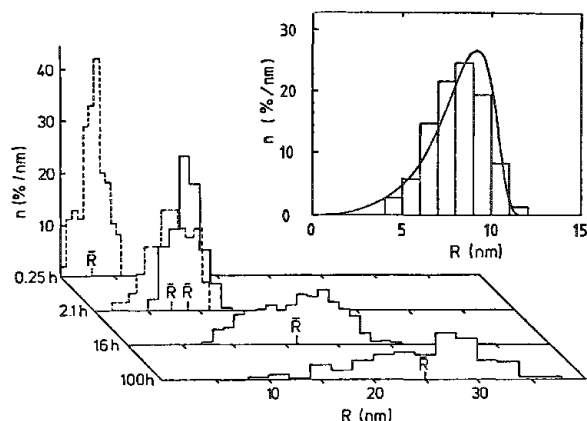


FIG. 2.--Size distribution of  $\gamma'$  precipitates in PE 16 aged at 1073 K, measured with FIM (---) and TEM (—). Insert compares measured size distribution with theoretical size distribution of diffusion-controlled Ostwald ripening.

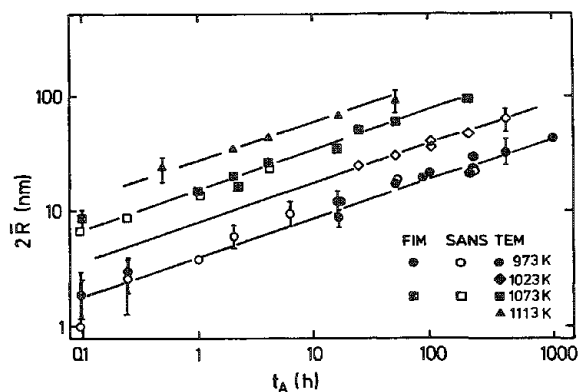


FIG. 3.--Average size of  $\gamma'$  precipitates in Nimonic PE16 against annealing time for various annealing temperatures, combining SANS, TEM, and FIM results. Lines are drawn with 1/3 slope.



## APFIM STUDY OF ANTIPHASE AND GRAIN BOUNDARIES IN $\text{Ni}_3\text{Al}$

J. A. Horton and M. K. Miller

$\text{Ni}_3\text{Al}$  is an ordered intermetallic material and is potentially useful for high-temperature applications. Unlike in most alloys, the yield stress of  $\text{Ni}_3\text{Al}$  actually increases with an increase in temperature. Unfortunately, pure  $\text{Ni}_3\text{Al}$  exhibits a brittle intergranular fracture and consequently low ductility. However, doping  $\text{Ni}_3\text{Al}$  with boron improves the mechanical properties; it can result in room temperature ductilities up to 50% and a completely transgranular failure.<sup>1</sup>

Auger electron spectroscopy (AES) has shown that boron segregates to the boundaries that can be made to fail intergranularly and that no embrittling agents are found on fracture surfaces of pure  $\text{Ni}_3\text{Al}$ .<sup>2</sup> Atom-probe field-ion microscopy (APFIM) is an excellent technique to study the structure and chemistry of "good" boundaries, especially for light elements such as boron.

Results from this study have shown that boron segregates to both grain boundaries and antiphase boundaries (APB) and that a thin phase is usually present at the grain boundaries in rapidly solidified  $\text{Ni}_3\text{Al}$ .

### *Experimental Procedure*

The alloy used in this investigation had a composition of Ni-24 at.% Al-0.24 at.% B.<sup>1</sup> The material was rapidly solidified into wire form by the Pendant Drop Melt Extraction method, which produced a grain size of about 1 to 4  $\mu\text{m}$ .<sup>3</sup> Specimen preparation followed standard techniques. A full description of the ORNL atom probe has been presented elsewhere.<sup>4</sup>

### *Results and Discussion*

The ductilizing effect of the boron additions to  $\text{Ni}_3\text{Al}$  is not altered by rapid solidification.<sup>5</sup> The fracture surface of the rapidly solidified material used in this investigation and broken in tension at room temperature exhibited a completely transgranular failure (Fig. 1). The microstructure of the rapidly solidified material and a description of the solidification process has been presented previously.<sup>6</sup> This microstructure (Fig. 2) consists of networks of antiphase boundaries (APB), usually with a small domain size near the center of the grains and a larger domain size adjacent to the grain boundaries. The small-domain regions solidify first and are nickel enriched, but reach the  $\text{Ll}_2$  ordered phase field at a lower temperature than the large domain regions. These latter regions solidify last, are aluminum enriched, and reach the  $\text{Ll}_2$  phase field at a higher temperature, which allows the domains to grow to a larger size.

APFIM and TEM analyses in the matrix indicated no evidence of precipitation.<sup>7</sup> Atom-probe analyses of the matrix showed measured boron compositions ranging from 0.07 to 0.2 at.%. As expected from the TEM characterization, aluminum levels measured in the atom probe ranged from 22 to 26 at.%, with 26% Al present in regions adjacent to grain boundaries. The long-range order parameter as measured from ladder diagrams was approximately 0.97.<sup>8</sup> The  $\text{Ll}_2$  order was maintained up to the edge of grain boundaries.

Field-ion micrographs of both grain and antiphase boundaries showed that most were decorated with bright spots. Single-atom analysis identified the bright spots as boron atoms, which shows that boron is indeed segregated to "good" grain boundaries and also to APBs. In addition, the presence of a distinct phase along most grain boundaries was observed. The thickness of this boundary phase varied from 0.4 to 1.2 nm. Although both the boundary phase and bright spots were usually present concurrently, that was not always the case. Some boundaries exhibited very few bright spots.

---

The authors are at the Metals and Ceramics Division, Oak Ridge National Laboratory, Oak Ridge, TN 37831. The research was sponsored by the Division of Materials Sciences, U.S. Department of Energy, under contract DE-AS05-84OR21400 with Martin Marietta Energy Systems, Inc.



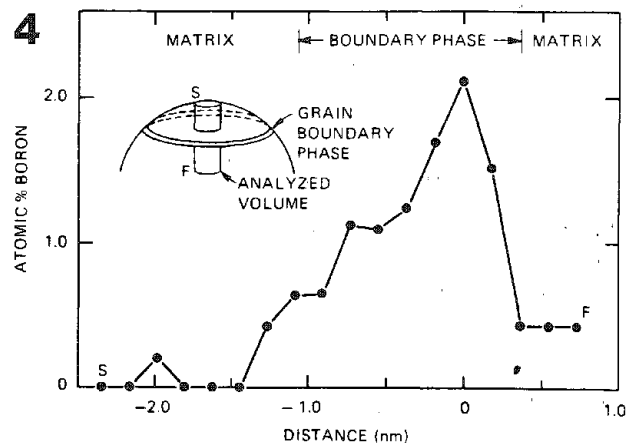
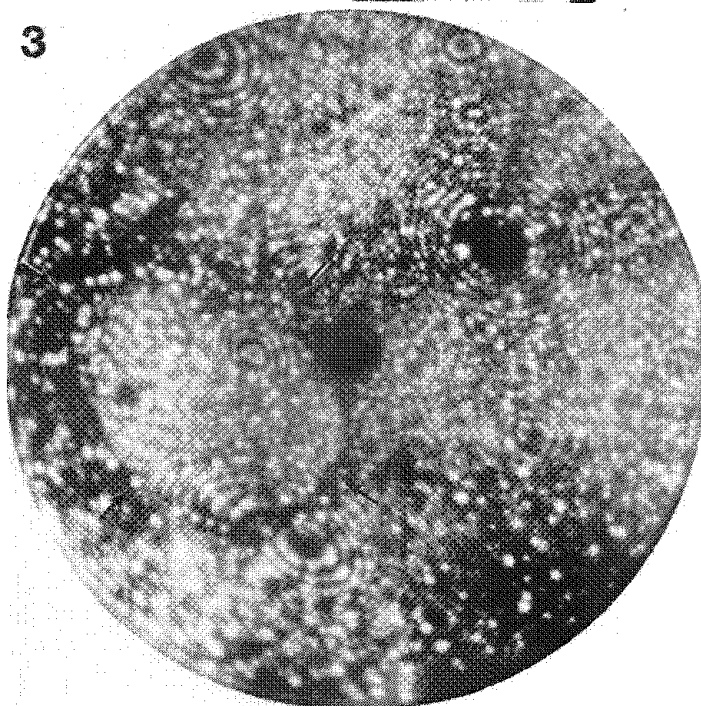
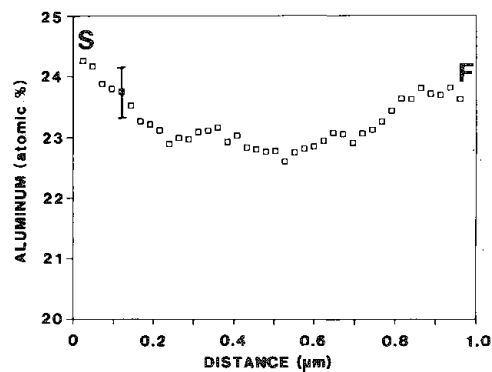
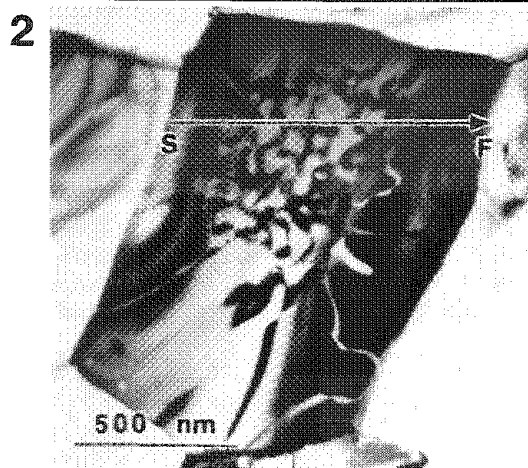
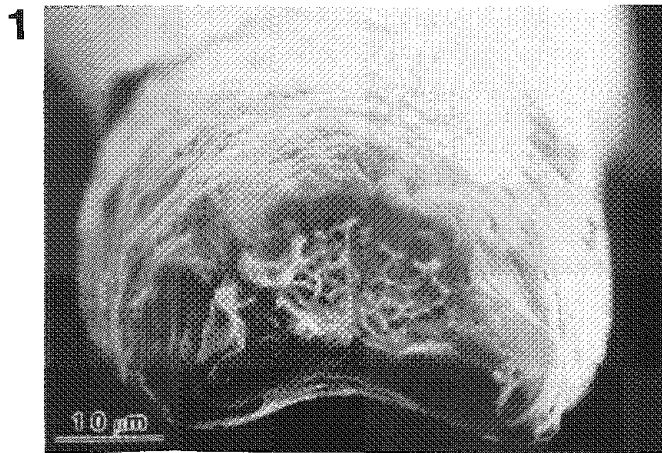


FIG. 1.--Fracture surface of Ni-24 at.% Al-0.24% B rapidly solidified wire showing 100% transgranular failure.  
 FIG. 2.--TEM micrograph and corresponding x-ray energy-dispersive spectroscopy (EDS) line scan showing APB structure and aluminum enrichment near grain boundaries.  
 FIG. 3.--Field-ion micrograph of grain boundary and composition profile for boron normal to and through boundary phase.

Several of the grain boundaries analyzed were normal to the axis of the FIM specimen. The intersection of these boundaries with the hemispherical end cap of the specimen produces a circular appearance (Fig. 3). The area within the circle is the image of the last remnant of a grain which is at the apex of the specimen. This boundary orientation is ideal for a composition depth profile normal to the boundary plane. As evaporation proceeds, the grain boundary shrinks in diameter. The probe aperture, which determines the area of analysis, was positioned in the center of the top grain for the depth profile. After the last of the top grain was field evaporated, the area left in the center of the image was the grain boundary phase, which exhibited a large number of bright spots. By a visual count of planes on a nearby pole during evaporation, the thickness of the boundary phase was determined to be  $1.2 \pm 0.2$  nm. The composition profile for boron through this boundary is shown in Fig. 3. The peak boron level was 2 at.% and the apparent thickness of the boundary phase, as ascertained on the depth profile, agrees well with the thickness determined visually from the field ion image during the actual evaporation. The aluminum level was constant at approximately 26 at.% throughout this profile. Atom-probe analyses of other grain boundary phases indicated boron levels up to 5 at.%.

Two additional examples of boron segregation are presented in Figs. 4 and 5. An APB normal to the specimen axis is shown in Fig. 4. Note the sharp delineation of the row of boron atoms on this boundary. The boron coverage, as measured from the lineal fraction of the boron in the micrographs, was approximately 5% of a monolayer. No precipitation was observed on the APBs. Figure 5 shows two grain boundaries, one with a few isolated boron atoms and a small precipitate located at a slight kink in the boundary. On the other grain boundary in Fig. 5 a more extensive boundary phase was present. The boron atoms were distributed throughout the thickness of the grain boundary phase, in contrast to the APB in Fig. 4. Some isolated boron atoms were also observed on grain boundaries where no separate phase existed locally.

In this study boron has been shown to segregate both to APBs and grain boundaries. A common feature of the two types of boundaries is the presence of aluminum-aluminum nearest neighbors that are not present in the  $Al_2$  matrix. Since APBs are otherwise perfect material with little associated strain, boron may have an affinity for aluminum-aluminum nearest neighbors. It has also been shown that, even with near-boundary compositions of 26 at.% Al, boron still segregates to and ductilizes the grain boundaries. In contrast, normally processed alloys with 26% aluminum are not effectively ductilized by boron additions. One mechanism proposed to explain the ductilizing effect of boron relies on boundaries that are more accommodating to slip in material with boron than in material without boron.<sup>9</sup> The boundary phase, especially if it is disordered fcc, could allow dislocations to more easily reorient and thereby allow more accommodation of slip.

## References

1. C. T. Liu, C. L. White, and J. A. Horton, *Acta Metall.* 33: 213-229, 1985.
2. C. L. White, R. A. Padgett, C. T. Liu, and S. M. Yalisove, *Scripta Metall.* 18: 1417-1420, 1984.
3. R. E. Maringer and C. E. Mobley, *Wire Journal*, Jan. 1979, p. 70.
4. M. K. Miller, *J. de Physique* C2: 493-498, 499-504, 1986.
5. C. C. Koch, J. A. Horton, C. T. Liu, O. B. Cavin, and J. O. Scarbrough, in R. Mehrabian, Ed., *Rapid Solidification Processing Principles and Technologies III*, Washington, D.C.: National Bureau of Standards, 1983, 264.
6. J. A. Horton and C. T. Liu, *Acta Metall.* 33: 2191-2198, 1985.
7. J. A. Horton and M. K. Miller, *J. de Physique* C2: 209-214, 1986.
8. M. K. Miller, this volume.
9. E. M. Schulson, T. P. Weihs, I. Baker, H. J. Frost, and J. A. Horton, *Acta Metall.* (in press).

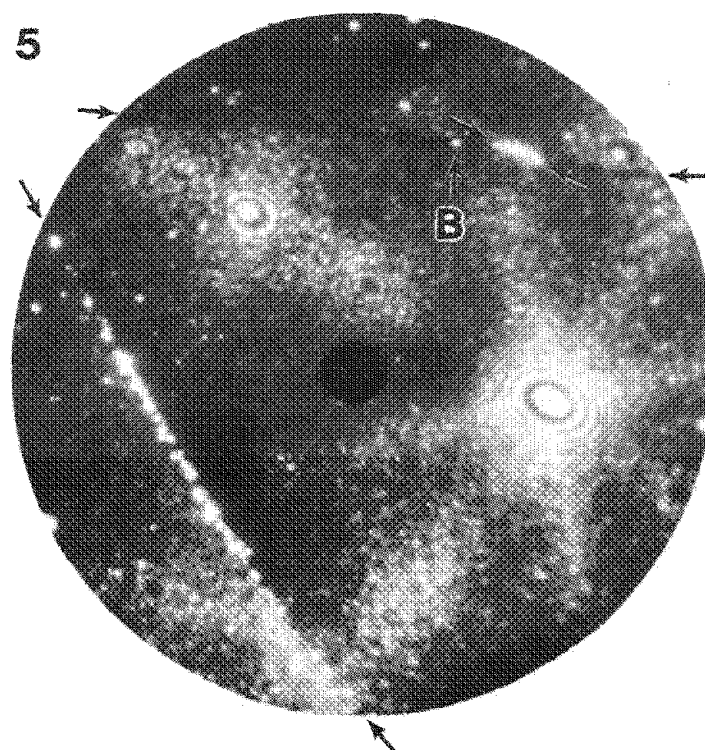
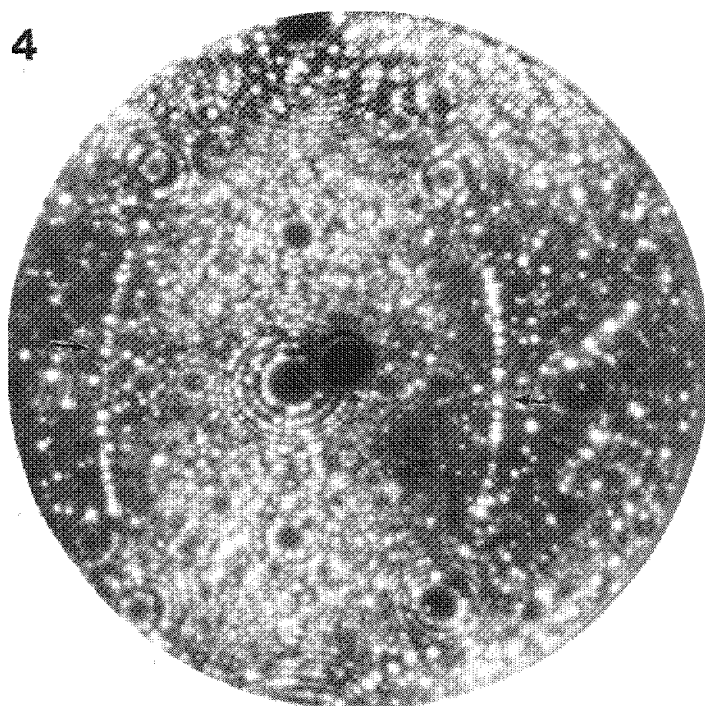


FIG. 4.--Field-ion micrograph of APB with boron atoms in narrow row on boundary.  
 FIG. 5.--Field-ion micrograph of two grain boundaries showing segregation and boron-enriched boundary phases.

## A DIRECT VIEW OF ATOMIC INTERACTIONS AND DIFFUSION ON METALS

John D. Wrigley and Gert Ehrlich

Thirty years after its invention by Erwin Müller,<sup>1</sup> the field-ion microscope is no longer unique in its ability to reveal solid surfaces with atomic resolution. During the past decade, electron microscopic methods have progressed to the stage where they provide some information about surfaces on the atomic level.<sup>2</sup> More recently, scanning tunneling microscopy has begun to yield a wealth of data about structural features of crystal surfaces on a scale of angstroms.<sup>3</sup> Despite these advances in other observational techniques, the field-ion microscope is still alone in yielding quantitative data about the behavior and properties of individual metal atoms and clusters on metals.

Basic to such quantitative measurements has been the ability of the field-ion microscope to pinpoint the location of a single atom deposited on a surface, which in turn has led to a reliable distance scale. This capability is illustrated in Fig. 1, from the work of Fink, showing an atom that has been evaporated onto a (211) plane of tungsten.<sup>4</sup> The adatom is visible, as are the lattice atoms that form the boundaries of the plane; but the atomic arrangement of the (211) plane itself, which is suggested by the hard-sphere model, is not apparent in the image. Nevertheless, the binding sites for the adatom can readily be mapped out. The surface is warmed until the atom begins to jump from one site to another; on this particular plane, movement occurs along the close-packed rows of lattice atoms seen in the model. After a heating interval, the surface is cooled and the location of the atom is determined from a field-ion image. Repetition of this process then yields a map of the locations where the adatom has been found. It is clear from the data in Fig. 2 that position assignments can be made quite reproducibly. The atom sightings are all closely clustered around a limited number of sites, comparable to the estimated number of lattice atoms in that particular row. Even though the lattice structure has not been directly imaged, we now have a reproducible distance calibration.

In what follows we illustrate, with selected examples drawn from work in this laboratory, how this capability has been put to use in quantitative measurements of two related phenomena--the motion, as well as binding, of atoms and clusters on metals. As shown in the next section, information about interaction energies between an adatom and the lattice, as well as between several adatoms, can be derived from observations of the spatial distribution in an equilibrium ensemble. In the last section, we present examples of studies in which the rate of redistribution of atoms over different sites is used to derive data about transport on surfaces.

### *Atomic Interactions*

A basic question about atoms on a crystal is their strength of binding at different sites on a surface. Given the ability to identify individual binding sites, it is also possible to determine which sites are preferred by adatoms and hence to estimate the relative binding energy at different positions on a crystal terrace. Consider the sites in one channel on W(211), modeled in Fig. 1. These sites are not all equivalent; binding of an adatom at the center of a channel should be different from those at sites close to the edge of the plane, where the number of near lattice atoms is lower. This difference can be readily checked. In an equilibrium system, the probability  $P_i$  of finding site  $i$  occupied, as compared to the occupation probability  $P_0$  for a reference site, is just

$$P_i/P_0 = \exp(-F_i/kT) \quad (1)$$

The relative binding energy can therefore be deduced from observations of the distribution

---

Authors Wrigley and Ehrlich are at Coordinated Science Laboratory, University of Illinois, Urbana, IL 61801. The work was supported by NSF under Grant DMR-84-20751. The authors are indebted to Drs. H.-W. Fink and Kaj Stolt for the use of some as yet unpublished material.

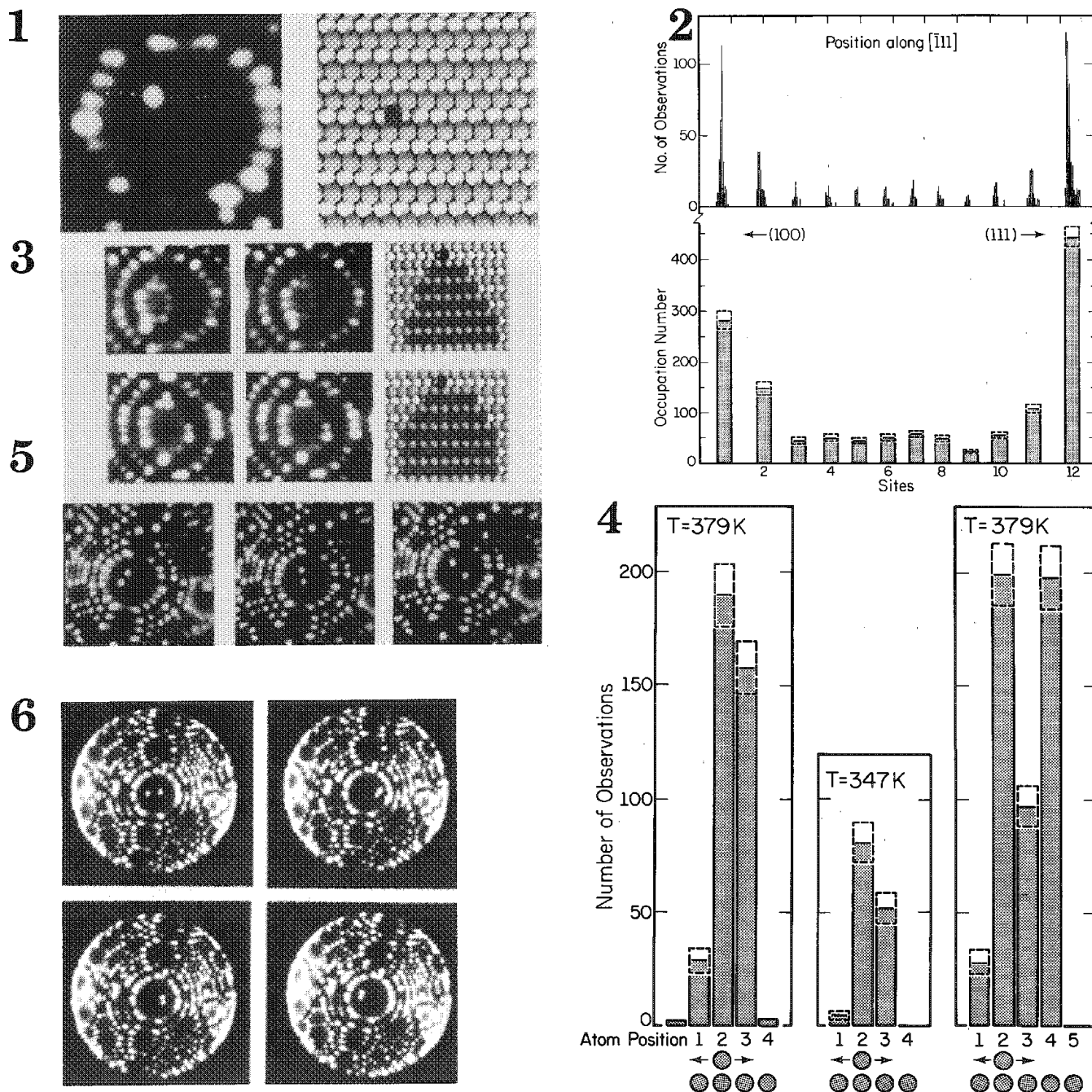


FIG. 1.--Field-ion image of W(211) with single rhenium atom on it (left), compared with hard-sphere model (right). Adatom locations after diffusion have been superposed (in white) on micrograph.<sup>4</sup>

FIG. 2.--Equilibrium distribution of single tungsten atom on W(211) at 363 K.<sup>4</sup> Actual adatom locations are recorded at top, revealing 12 binding sites. Distribution over binding sites is shown at bottom.

FIG. 3.--Rhenium overlayers on W(211); layer at top has four edge sites, layer at bottom has five.<sup>5</sup> Field ion micrographs show Re adatom in various edge positions; models suggest layer geometry.

FIG. 4.--Equilibrium distribution of Re adatom over edge positions at rhenium overlayers.<sup>5</sup>

FIG. 5.--Two rhenium adatoms, separated by an empty channel on W(211), after warming for 90 s at 289 K. (Photographs courtesy K. Stolt.)

FIG. 6.--Formation of rhenium dimer on W(211). Two rhenium atoms in adjacent channels (top left) have combined into dimer (top right) after warming to 375 K for 3 s. Continued heating displaces dimer as a unit. (Photographs courtesy K. Stolt.)

of atoms over the different kinds of sites, provided the system has been heated to temperatures at which the atom can sample the different environments. Such measurements are shown in Fig. 2 for tungsten atoms on W(211).<sup>4</sup> It turns out that, contrary to the view fairly standard in theories of crystal growth, atoms prefer to be close to the ends of the channels rather than in the center; that is, binding is stronger toward the ends. Similar effects have been observed for rhenium and silicon atoms, but there are detailed chemical differences that deserve more study.

This general technique can be applied to examination of atom binding at more complex surface features. Shown in Fig. 3 are rhenium layers on W(211) with 4 and 5 edge sites, respectively.<sup>5</sup> A single rhenium adatom has been used both to establish the number of sites and to map out their occupation probability. The relative binding energy of the adatom again surprises. At a layer with 4 edge sites, binding is strongest at the center sites. However, it appears from Fig. 4 that for an edge with 5 sites, the equilibrium distribution, and therefore the binding, has a minimum at the central site. There are not yet enough data to establish trends in binding varying with the structure of the substrate or the chemical nature of the adatom. However, it is clear that quantitative binding energy measurements for single adatoms at different surface features are quite feasible.

The same idea of measuring the distribution of adatoms in an equilibrium system is also useful in looking at interactions between adatoms, that is, in exploring cohesion in clusters. In Fig. 5, a single rhenium atom has been deposited in each of two channels of W(211), separated by an intervening empty channel. Are there interactions between the two adatoms; and if so, how strong are they? Provided the atoms are properly equilibrated, the probability  $P(R)$  of being at a separation  $R$  is given by

$$P(R) = C_R P_0(R) \exp[-F(R)/kT] \quad (2)$$

and depends exponentially on  $F(R)$ , the free energy of interaction.  $P_0(R)$  is just the likelihood of finding a separation  $R$  between noninteracting atom pairs, and  $C_R$  insures normalization.

Observations of the pair distribution function  $P(R)$  can therefore be used to estimate the strength of interactions as a function of the distance. Such measurements have been made, and suggest that when an empty row separates the two adatoms, the interplay between them is negligible.<sup>6</sup> Obviously the distance between the atoms is greater than the range of sensible interactions. When two atoms are placed in neighboring rows, to explore effects at smaller separations, the situation changes, as is evident in Fig. 6.<sup>7</sup> Attractive forces between atoms in adjacent rows are so strong that when two atoms in their individual rows get to within one lateral spacing of each other, they combine to form a cluster.<sup>8,9</sup> These entities are so stable near room temperature that it has only been possible to measure the equilibrium pair distribution function for small separations. Nevertheless, the energetics of these clusters have been thoroughly explored. The dimers can exist in two states, easily distinguished from one another in Fig. 6. In the straight configuration the atoms in adjacent rows are aligned next to each other; in the staggered configuration, they are offset by one spacing. From the relative probability of these states at different temperatures, it has been possible to derive an internal energy difference of 0.06 eV between them.<sup>7</sup> At high temperatures, the dimers occasionally dissociate, as in Fig. 7. The temperature dependence of the equilibrium constant between bound and dissociated dimers gives a dissociation energy of 0.16 eV in the usual way. In short, the ability to determine the location of individual atoms at the surface has made it possible to achieve a reasonably detailed view of the strength and range of atomic interactions.

This approach is by no means limited to simple, essentially one-dimensional surfaces such as W(211), or to interactions between only two adatoms. Mapping of binding sites in a fairly dense, two-dimensional plane such as W(110) is shown in Fig. 8.<sup>10</sup> The distance calibration achieved in this way has made it feasible to measure the distribution of distances between two rhenium atoms, equilibrated on W(110). From a comparison of this distribution, in Fig. 9, with a Monte Carlo simulation for two noninteracting atoms, it is evident that interactions are repulsive out to fair distances ( $\sim 8 \text{ \AA}$ ).<sup>8,11</sup> With such repulsive interactions we expect difficulties in forming larger clusters. However, that is not the case! As seen in Fig. 10, rhenium trimers do form, and have been shown stable to dissociation.<sup>10</sup> From observations of the equilibrium between trimers and single atoms, the binding in trimers has been estimated at  $\sim 0.25 \text{ eV}$ . It appears that on W(110) the cohesion of rhenium trimers, and of larger clusters as well, rests upon many-atom interactions.



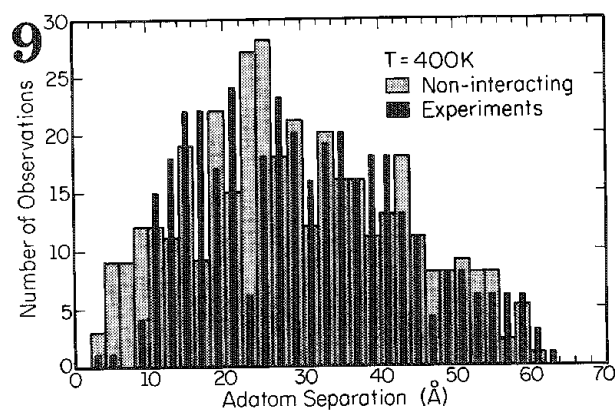
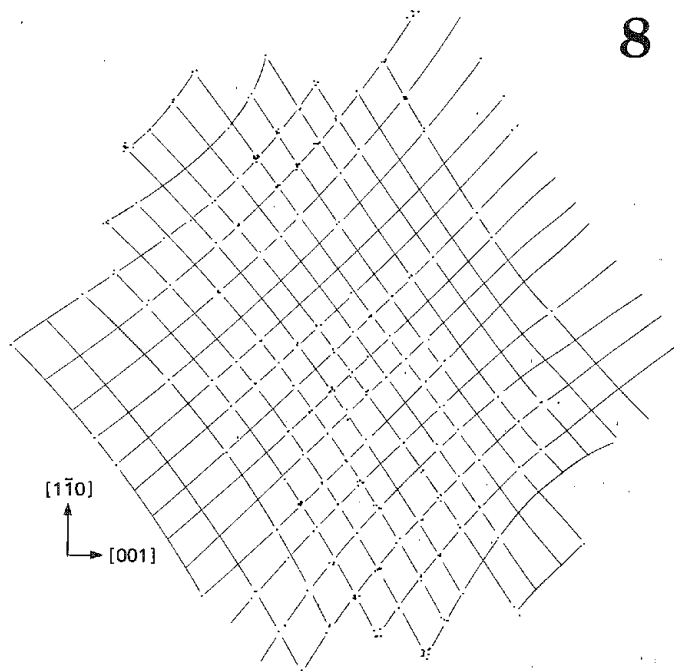
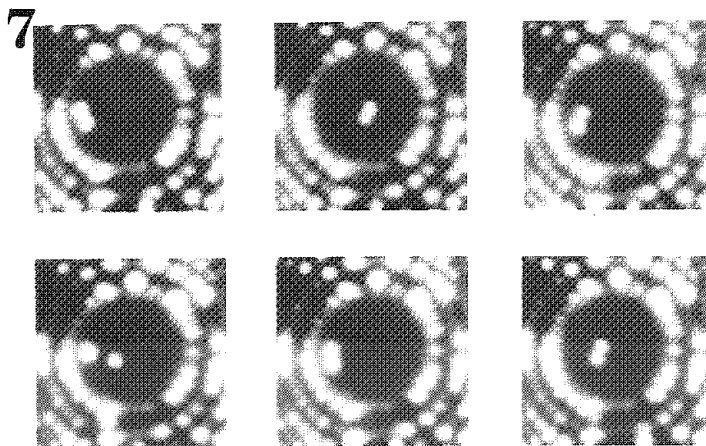


FIG. 7.--Dissociation of rhenium dimer on W(211) after 3 s heating intervals at 392 K.<sup>7</sup>  
 FIG. 8.--Mapping of sites on W(110) by observation of single Re adatom after diffusion at 380 K.<sup>10</sup> Points indicate observed atom positions.  
 FIG. 9.--Distribution of separations between two Re adatoms on W(110).<sup>10</sup> Equilibration intervals: 20 s at 400 K.

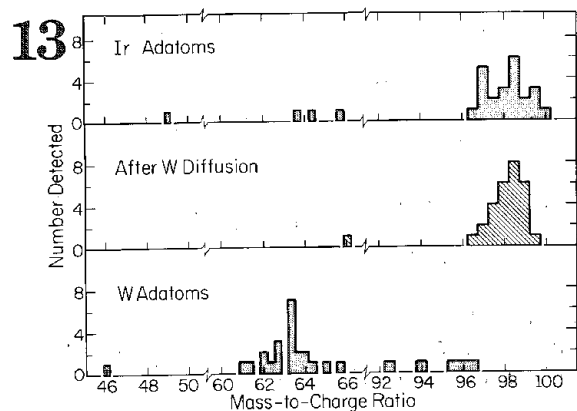
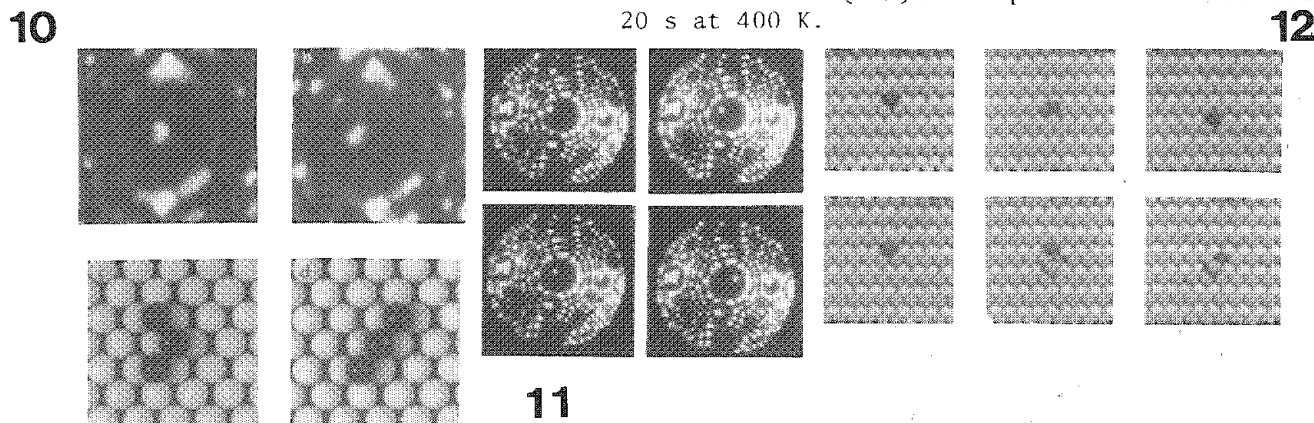


FIG. 10.--Different configurations of rhenium trimers on W(110).<sup>10</sup> Hard-sphere models in (c) and (d) suggest atomic arrangement in field-ion micrographs (a) and (b).  
 FIG. 11.--Diffusion of single Re atom on W(211). Migration takes place during 30s interval at 351 K, between observations at ~20 K. (Photographs courtesy K. Stolt.)  
 FIG. 12.--Models of possible mechanisms for cross-channel motion on Ir(110).<sup>18</sup> Top: Adatom hopping over atom rows. Bottom: Diffusion through replacement of lattice atom by adatom.  
 FIG. 13.--Atom probe examination of cross-channel diffusion.<sup>18</sup> Top and bottom: calibration runs. Atoms analyzed without prior heating of Ir(110) substrate. Center: Atoms analyzed after cross-channel motion.

In closing this section, two things must be stressed. First, for the sake of clarity, we have concentrated on one system, rhenium on tungsten, for which much has already been done. However, the same techniques are applicable to a wide range of substrates and adatoms, and it now is just a matter of exploring these in order to establish a larger basis of experience. Second, in the studies reviewed here, the system was equilibrated in the absence of applied fields. Imaging is always done at low temperatures, under conditions where the act of observation can be shown to have no perceptible effect on the atom distribution. These results are therefore indicative of atomic properties in an ordinary thermal environment.

### *Atomic Motion*

In the previous examples an equilibrium spatial distribution was achieved by allowing atomic migration over the surface. This process is itself of considerable interest, not only for its contributions to material transport on solids, but also as an indicator of atomic interactions. It turns out that the ability of the field-ion microscope to locate individual atoms on a metal also makes it possible to study quantitatively the details of diffusion processes.<sup>12</sup> Consider a single atom on a one-dimensional plane; the mean-square displacement  $\langle \Delta x^2 \rangle$  during a time  $t$  is, according to Einstein, given by

$$\langle \Delta x^2 \rangle = 2Dt = 2D_0 t \exp(-E_D/kT) \quad (3)$$

Here  $D$  is the diffusivity,  $E_D$  an activation energy for atomic jumps, and  $D_0$  a prefactor.<sup>12</sup> As was noted above, distances are readily derived from measurements with the field-ion microscope. By repeated observations before and after allowing diffusion to occur at some elevated temperature  $T$ , as for example in Fig. 11, the mean-square displacement and therefore the diffusion parameters are immediately accessible. In principle, atomic motion can also be observed continuously; however, in practice, field effects then make an unequivocal interpretation difficult.

A great deal of information about atomic motion has already been derived in this way. How, for example, do we know that atomic movement is really random? For random motion the mean-square displacement should vary linearly in time as prescribed by Eq. (3). Measurements indicate that this requirement is indeed satisfied.<sup>13</sup> In such random walks, the geometry of the substrate can be expected to have a profound effect, and that expectation has also been verified. Not only are the diffusion barriers different on differently oriented crystal planes, but the preferred directions for diffusion also differ. These quantitative results on the surface diffusion of atoms have been previously reviewed.<sup>12</sup> Here we should like to emphasize the depth to which it has been possible to probe these phenomena, by citing selected examples.

Consider how atoms really move on a surface. On W(211) as well as on Rh(110), diffusion always is along close-packed rows of surface atoms.<sup>14</sup> On Pt(110) and Ir(110), however, that is not true.<sup>15,16</sup> In fact, motion across the rows predominates on the latter. How does this occur? Cross-channel motion has been envisioned as taking place in two different ways illustrated in Fig. 12: either by jumping across the channel walls, or else by a replacement mechanism (in which an adatom pushes a lattice atom into the adjacent channel and takes its place in the channel wall). Which of these schemes provides a better description of the actual diffusion? That has been established by looking at the movement of tungsten on Ir(110), but to do so an additional capability, namely mass discrimination, was necessary.

If the hopping mechanism is appropriate, then the atom that appears in an adjacent channel after diffusion should be tungsten. If the replacement mechanism is favored, then an iridium atom should be seen adjacent to the original channel after diffusion.<sup>16</sup> In the atom probe,<sup>17,18</sup> it is a straightforward matter to distinguish between iridium and tungsten atoms; that is shown by the calibration runs in Fig. 13, in which atoms deposited on the surface were time-of-flight analyzed without any prior heating. When a tungsten atom is placed on Ir(110) and cross-channel diffusion is brought about by heating, analysis of the atom that appears in the adjacent channel always indicates that it is iridium. Mass analysis also reveals a tungsten atom in the top layer of the substrate after cross-channel motion.<sup>16</sup> These observations establish that on Ir(110) motion occurs by a replacement process; the original adatom, tungsten, goes into the lattice and a



lattice atom continues the diffusion. So far there is no evidence for such a diffusion process on other types of planes.

Even without mass analysis, detailed diffusion events can be closely examined if full advantage is taken of the spatial information provided by field-ion microscopic methods. Diffusivities can always be derived from the mean-square displacement, in accord with Eq. (3); that is, from the second moment of the distribution function governing displacements. However, the entire distribution can be measured, and the additional information is critical when we look at diffusion processes that depend upon several different jump rates. That has proved to be the case in the examination of surface clusters, the behavior of which is of considerable interest in its own right.

Clusters formed by association of several atoms show surprising mobility. How does that come about, and how is the diffusivity related to individual atom jumps and to interactions between the adatoms? As an example of what can be done, consider the movement of heterodimers on a two-dimensional surface, the (110) plane of tungsten. The possible atomic jumps that may contribute to cluster motion are shown schematically in Fig. 14.<sup>19</sup> Two different intermediate configurations are illustrated: horizontal intermediates, in which the cluster is oriented along [001]; and those in which the dimer is vertical, oriented along [110]. The interatomic spacing for the latter is larger than for the horizontal intermediate; its energy is therefore likely to be higher and it should provide a less favorable path for diffusion.<sup>19,20</sup> This presumption can be readily checked. For motion via horizontal intermediates, the orientation of the dimer at any position on the surface is fixed by the starting orientation, as indicated in Fig. 15. Only when a transition to a vertical intermediate occurs is an element of randomness introduced. An additional capability is again needed to analyze the motion--the ability to discern orientations. In dimers made up of one silicon and one metal atom, the atoms appear separated by a nearest-neighbor distance, and the silicon end can be distinguished from the metal the field at which the metal atom is imaged is considerably higher than that at which the silicon appears in view.<sup>21</sup> The orientation of the dimer W-Si has been studied on W(110), and at low temperatures no reorientation is found after diffusion.

With this result established, it is clear that motion occurs via horizontal intermediates and can be described in terms of the four jump rates in Fig. 14. Dimers are never observed in the intermediate state, hence rates  $b$  and  $d$  must be much larger than the inverse rates  $a$  and  $c$ . To describe diffusion of W-Si quantitatively therefore requires knowledge of two rates  $a$  and  $c$ , but measurements of the mean-square displacement only define the overall diffusivity. The additional information necessary for quantitative evaluation of both jump rates can be derived from the displacement distribution. For an assumed set of jump rates, this distribution can be worked out, either through Monte Carlo simulation or from statistical reasoning.<sup>19</sup> The jump rates describing the behavior of W-Si are then estimated by minimizing the differences between the predicted distribution and the experimental measurements, as in Fig. 16. In this way, it has been for example established that in W-Si, silicon jumps more readily than the metal atom. It is of interest to note that the dimer is much more mobile than either, a behavior suggestive of particularly strong interactions between the adatoms in the cluster. Even more complicated cluster motions have been successfully handled by the techniques outlined here, which is indicative of the great power of the field-ion microscope to provide detailed quantitative information about kinetic events on solids.

### Summary

In this briefest of surveys, only a few studies of atomic motions and interactions have been cited. They are intended to demonstrate the ability of field-ion microscopic methods to derive quantitative information about atomic events on metals under ordinary thermal conditions. So far, measurements have been done on a very limited number of systems. However, a wide range of materials can be examined by these techniques, and this extension to a range of materials will constitute the next important stage in gaining a better understanding of interfacial phenomena.

### References

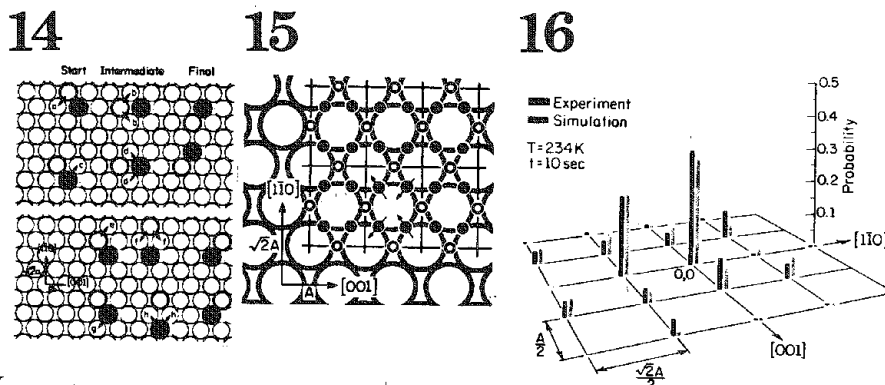
1. E. W. Müller and T. T. Tsong, *Field Ion Microscopy, Principles and Applications*, New York: American Elsevier, 1969.

2. M. S. Isaacson et al., "The study of adsorption and diffusion of heavy atoms on light element substrates by means of the atomic resolution STEM," *Ultramicroscopy* 1: 359-376, 1976.
3. G. Binnig and H. Rohrer, "Scanning tunneling microscopy," *Helv. Phys. Acta* 55: 726-735, 1982.
4. H.-W. Fink and G. Ehrlich, "Lattice steps and adatom binding on W(211)," *Surf. Sci.* 143: 125-144, 1984.
5. H.-W. Fink and G. Ehrlich, "Atom binding at overlayers: Re on W(211)," *Surf. Sci.* (in press).
6. W. R. Graham and G. Ehrlich, "Direct measurement of the pair distribution function for adatoms on a surface," *Phys. Rev. Lett.* 32: 1309-1311, 1974.
7. K. Stolt et al., "Thermodynamics of surface clusters: Direct observations of  $\text{Re}_2$  on W(211)," *J. Chem. Phys.* 69: 1151-1161, 1978.
8. D. W. Bassett, "Observing surface diffusion at the atomic level: II. Adatom clusters," in V. T. Binh, Ed., *Surface Mobilities on Solid Materials*, New York: Plenum Press, 1983, 83-108.
9. T. T. Tsong, "Direct observation of interactions between individual atoms on tungsten surfaces," *Phys. Rev. B* 6: 417-426, 1972.
10. H.-W. Fink and G. Ehrlich, "Pair and trio interactions between adatoms: Re on W(110)," *J. Chem. Phys.* 81: 4657-4665, 1984.
11. T. T. Tsong and R. Casanova, "Direct measurement of pair energies in adatom: Adatom interactions on a metal surface," *Phys. Rev. B* 24: 3063-3072, 1981.
12. D. W. Bassett, "Observing surface diffusion on the atomic level; I. Single atoms," in V. T. Binh, Ed., *Surface Mobilities on Solid Materials*, New York: Plenum Press, 1983, 63-82.
13. G. Ehrlich and F. G. Hudda, "An atomic view of surface self-diffusion: Tungsten on tungsten," *J. Chem. Phys.* 44: 1039-1049, 1966.
14. G. Ayrault and G. Ehrlich, "Surface self-diffusion on an fcc crystal: An atomic view," *J. Chem. Phys.* 60: 281-294, 1974.
15. D. W. Bassett and P. R. Webber, "Diffusion of single adatoms of platinum, iridium and gold on platinum surfaces," *Surf. Sci.* 70: 520-531, 1978.
16. J. D. Wrigley and G. Ehrlich, "Surface diffusion by an atomic exchange mechanism," *Phys. Rev. Lett.* 44: 661-663, 1980.
17. E. W. Müller et al., "The atom probe field ion microscope," *Rev. Sci. Instr.* 39: 83-86, 1968.
18. J. D. Wrigley Jr., *Surface Diffusion by an Atomic Exchange Mechanism*, Ph.D. thesis, University of Illinois, Urbana-Champaign, 1982.
19. J. D. Wrigley and G. Ehrlich, "Two-dimensional random walks of diatomic clusters," *J. Chem. Phys.* (in press).
20. D. W. Bassett, "Migration of platinum adatom clusters on tungsten (110) surfaces," *J. Phys. C* 9: 2491-2503, 1976.
21. J. D. Wrigley and G. Ehrlich, "Direct observation of diffusion for metal-silicon complexes on W(110)," *Abstract Bulletin 32nd International Field Emission Symposium*, Wheeling, W. Va., 1985.
22. J. D. Wrigley and G. Ehrlich, "Atomic jump rates in heteroclusters," *J. Vac. Sci. Technol.* (in press).

FIG. 14.--Schematic of heterodimer jump processes in diffusion on bcc(110).<sup>19</sup> Top: horizontal intermediates. Bottom: vertical intermediates.

FIG. 15.--Center-of-position grid for heterodimers moving via horizontal intermediates. Arrows indicate allowed orientation of dimer.<sup>19</sup>

FIG. 16.--Distribution of W-Si over W(110) after 10 s at 234 K, compared with simulations.<sup>22</sup>



## SURFACE REACTIONS INVESTIGATED BY FIELD DESORPTION

J. H. Block, Norbert Kruse, and Gunter Abend

Since Hugh S. Taylor<sup>1</sup> introduced the concept of active sites and Georg-Maria Schwa developed the "adlineation theory,"<sup>2</sup> many attempts have been made to understand the topochemistry of heterogeneous catalysis. Particular discussions have been devoted to the particle size effect, the observation that particles with diameters smaller than, say, 20-50 Å differ in specific catalytic activity or selectivity from large particles. There are several reactions with extensive "structure sensitivity," like hydrogenolysis of ethane or like the ammonia synthesis.<sup>3</sup> Other reactions, like various hydrogenation reactions, have been found "structure insensitive." Different models are developed to explain the structure sensitivity. Van Hardefeld and Hartog,<sup>4</sup> for example, discussed five-fold coordinated metal surface atoms or "B<sub>5</sub> sites" as particularly active centers. The experimental basis for this model was the specific infrared-active molecular nitrogen chemisorption. For another case, the ammonia synthesis, Boudart<sup>5</sup> postulated active C<sub>7</sub> sites, surface atoms of an iron crystal with seven nearest neighbors. Evidence for this conclusion was based on a site-specific surface magnetic anisotropy of Fe crystals supported by MgO, which were investigated by Mössbauer spectroscopy. The statistical population of these active sites was supposed to depend on particle size. The correlation between structure sensitivity and coordination number of a surface site is based on the existence of perfect crystal lattices even in small particles.

As pointed out recently,<sup>6</sup> these correlations must be questioned, since small particles are unlikely to be perfect in the sense of having exactly the right number of neighbors of a regular geometric lattice.<sup>7</sup>

In most of the examples studied by indirect methods, the association of a specific catalytic property and the particular coordination number of an active surface site is still uncertain. The displacement of such surface sites into new crystallographic positions, due to catalytic reactions, at unexpected low temperatures is discussed below.

One of the methods that permits us to image surface sites and chemisorption structures in a direct way is field ion microscopy and mass spectrometry. A field emitter can be considered as a catalyst particle with a half cone 100-1000 Å in diameter, which exposes surface lattice atoms in well-defined geometry with identified coordination number. In field electron and field ion microscopy the surface face and surface site specificity of chemisorption can be investigated. One advantage--compared to work on single crystal planes--is the simultaneous presence of all the equilibrium planes and many high index planes at the emitter specimen. Thus, preferential chemisorption can be envisaged in one experiment. In addition, this method is very sensitive to morphological alterations of a catalyst due to chemisorption or surface reaction. After displacement of relatively few lattice atoms, new morphologies, which belong to a certain system, are visible. Field desorption in combination with mass spectrometric methods permits the identification of chemical composition, and with pulse techniques kinetic data can be evaluated.

In this contribution we describe investigations on surface plane- and surface site-specific reactions and discuss the problems involved; in particular, the influence of the high electrostatic field on chemical interactions at solid surfaces.

### *Experimental*

Field electron and field ion microscopy have been applied in combination with Pulsed Field Desorption Mass Spectrometry (PFDMS), as described in detail elsewhere.<sup>8</sup> It differs from a normal atom probe in the following manner. Fast negative field pulses (amplitudes up to 20 kV, rise times ~100 ns, repetition rates up to 100 kHz) are applied to a counter electrode mounted at distances of 0.1 mm in front of a field emitter. Adsorbed species

---

The authors are at the Fritz-Haber-Institut der Max-Planck-Gesellschaft, Faradayweg 4-6, D-1000 Berlin 33, Federal Republic of Germany. Support by the Deutsche Forschungsgemeinschaft, Sfb 6/81, for part of the work is gratefully acknowledged.

are field desorbed, and the chemical nature of the ions is determined by time-of-flight measurements. Between the pulses, an arbitrary field, usually zero, can be maintained. A channel plate with a probe hole is mounted at the entrance of the flight tube, so that the orientation of the tip can be observed. Temperatures are measured by a thermocouple spot-welded to the base of the emitter tip.

The general procedure for providing kinetic data of surface processes in PFDMS is illustrated in Fig. 1. While the field emitter surface is continuously dosed by the gaseous reactant, adsorption takes place only in the field-free reaction interval  $t_R$  between two pulses. At the end of this interval the adsorbed layer is desorbed by a field pulse. If the layer is completely removed by each pulse the measured ion intensity directly represents the surface concentration within the monitored area before the pulse.

By variation of  $t_R$  (usually in the time range 100  $\mu$ s to 10 s) both the kinetics of adsorption and the thermal equilibration of the adlayer are examined. For short times, supply from the gas phase is insufficient to achieve a steady surface concentration. The field pulses interrupt the adsorption process, and the amount of material accumulated on the surface at this instant is thus measured. For long times (compared with the mean lifetime) a dynamic adsorption thermal desorption equilibrium is established. Then the surface concentration remains constant with increasing  $t_R$ , and consequently the ion intensity does not increase any further. Assuming the adsorption process to proceed with a constant sticking probability and thermal desorption to obey first-order kinetics the mean lifetime can be measured as the value of  $t_R$  at which the  $[1 - (1/e)]$  level of the equilibrium coverage is reached.

In another kind of experiment, energy distributions of field ions and appearance energies have been determined. The measurements were carried out in few cases with the help of quadrupole mass filters, in most cases by use of a 60° magnetic sector field mass spectrometer of the Inghram type equipped with a field ion source.<sup>9,10</sup> The ion beam was either focused on the entrance slit, for performing mass spectrometric investigations; or was displayed by an image intensifier (channel plate and luminescent screen) that could be positioned in front of the entrance slit. Thus, the condition of the emitter surface could be observed by field-emission patterns. Measurements of the appearance energy of field ions were performed by the analysis of their kinetic energies with a retarding energy analyzer. The retarder system was located behind the magnetic sector field and in front of the electron multiplier, about 150 cm from the emitter. The central retarder electrode was connected to the emitter potential via an additional potential source that could be scanned. The onset appearance energy values  $A_E$  were obtained from the maximum ion kinetic energy in the integral energy distribution. The measurements were performed with an accuracy of  $\pm 0.1$  eV. Differential energy distributions were measured (less accurately, within  $\pm 0.5$  eV), by utilizing the energy dispersion of the magnetic sector field and sweeping the tip voltage at a constant magnetic field.

#### *Microscopic Observation of Morphological Changes During Surface Reactions*

One of the first observations of morphological alterations due to surface gas interactions was published by Brill.<sup>11</sup> Field electron microscopy studies in connection with problems of the  $\text{NH}_3$  synthesis revealed an increase of the size of Fe(111) planes after nitrogen adsorption and subsequent annealing at 673 K. One of the conclusions from this experiment was that (111)-planes of iron display pronounced interaction with nitrogen. Recent mechanistic studies on the ammonia synthesis reaction confirmed this conclusion. The nitrogen activation--although in form of dissociative chemisorption--proceeds fastest at the (111)-plane and is the rate-determining step of the reaction toward  $\text{NH}_3$ . Field-emission studies with molybdenum showed that (111) planes are preferable in nitride formation, when nitriding is performed with ammonia.<sup>14</sup>

Morphological structure variation during a real catalytic reaction has been investigated by McCabe and Smith.<sup>15</sup> A Pt-Rh field emitter was part of a catalyst bed in the oxidation of  $\text{NH}_3$  to nitric acid. With the aid of field ion microscopy, atom-probe analysis, and electron microscopy it was found that under oxidizing conditions Rh-enriched oxide layers are formed. Corrosion of the surface is due to gas phase transport of  $\text{PtO}_2$ . From these observations a model could be deduced for morphological changes, which are due to the gradient of the  $\text{O}_2$  chemical potential within pores and grooves.

Another catalytic reaction was studied by Kellogg.<sup>16</sup> The catalytic oxidation of CO at

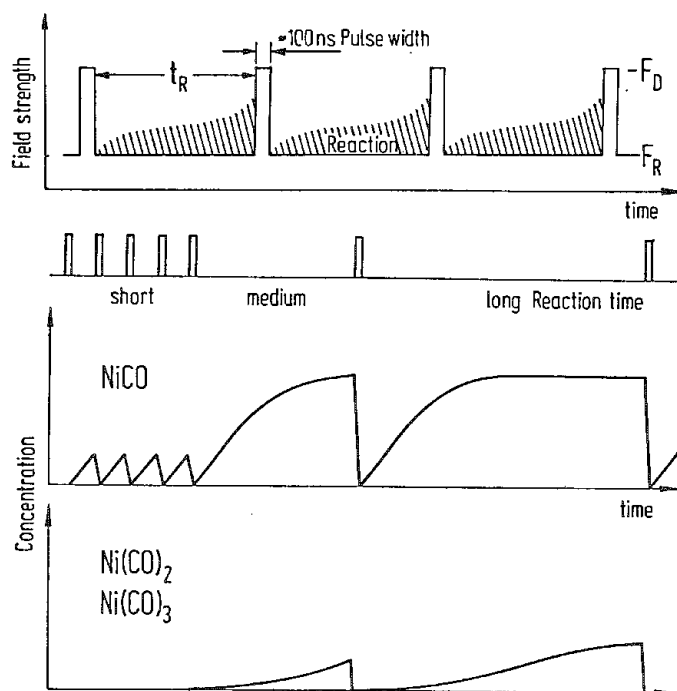


FIG. 1.--Evaluation of kinetic data from field pulse desorption.  $F_R$  and  $F_D$  are reaction and desorption field strengths, respectively. Development of surface coverage is shown for nickelcarbonyl, as discussed later. (a) Time scheme of desorption pulses; (b) development of surface coverage.

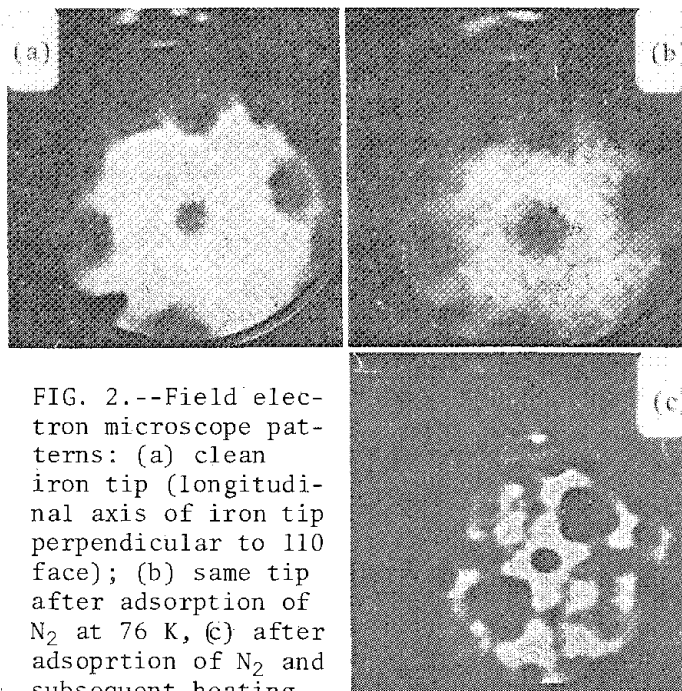


FIG. 2.--Field electron microscope patterns: (a) clean iron tip (longitudinal axis of iron tip perpendicular to 110 face); (b) same tip after adsorption of  $N_2$  at 76 K, (c) after adsorption of  $N_2$  and subsequent heating at ca 400 C for  $\sim 3$  s.

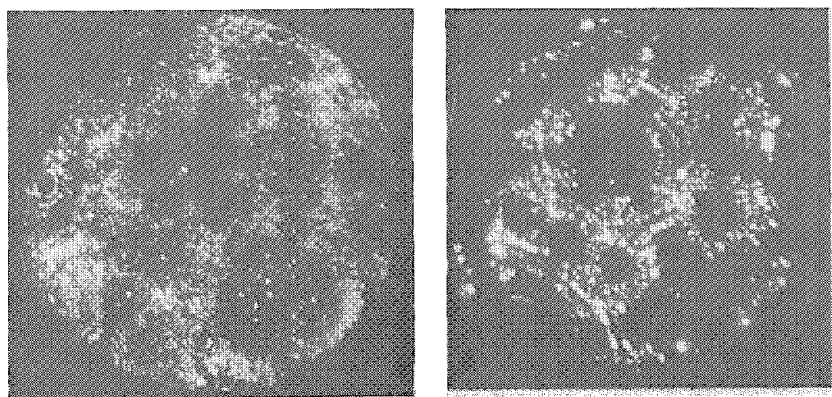


FIG. 3.--(a) Field ion image of clean, nearly hemispherical nickel single crystal at 80 K,  $F = 30.8$  V/nm, image gas: neon. Radius of crystal calculated from central (111) area:  $\sim 650$  Å, orientation about [311]. (b) The same nickel single crystal at 80 K, image gas neon, after 23h reaction time in CO,  $p = 1.3$  mbar at 373 K.

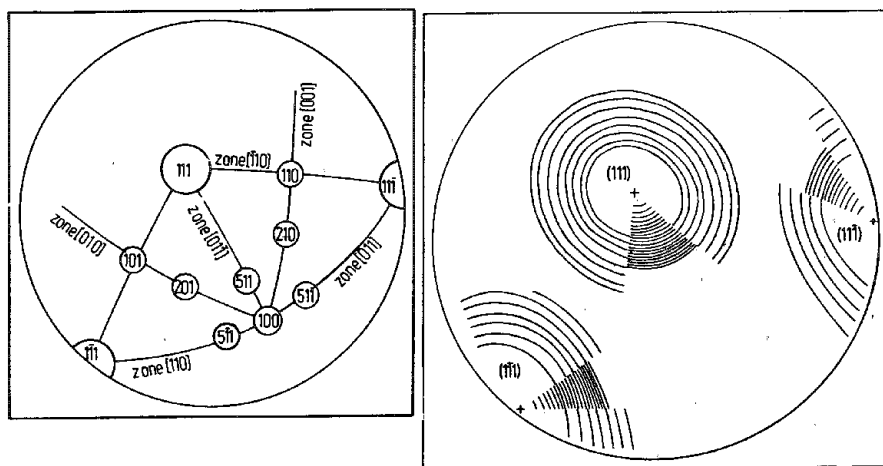


FIG. 4.--(a) Map of planes appearing on intermediate state. (b) Rings around {111} poles taken from original micrographs. Ring systems within small sectors are from initial state images.

an Rh-emitter is poisoned at higher  $O_2/CO$  ratios owing to the formation of inactive rhodium oxide. For an active catalyst and with stoichiometric mixtures of reactive gases, changes in surface morphology were found to differ from ordinary thermal faceting. At temperatures of 550-600 K an enlargement of the  $\{111\}$  and  $\{11\bar{1}\}$  planes was significantly greater than that produced by thermal treatment in vacuum. It was also observed that the circular  $\{100\}$  plane changes shape into rectangular appearance. These structural changes are still not understood in detail.

#### *The Reaction of CO with Ni*

Field ion microscopic studies by Schmidt, Block, and Becker<sup>17</sup> have revealed details of the topochemistry of the reaction of nickel and carbon monoxide toward nickel tetracarbonyl:



Figure 3(a) shows an ion micrograph of the clean nickel crystal field evaporated in neon at 80 K. The middle part shows the relatively broadly extended system of  $\{111\}$  layers. The step height of one layer is equal to the lattice step height, as can be demonstrated by comparison of ion images with ball models. Slightly to the right in the lower part are the layers of the  $\{100\}$  plane. The transient areas between the central  $\{111\}$  and the peripheral  $\{111\}$  and  $\{100\}$  planes are subdivided neatly up to very high index planes. The crystallographic orientation can be compared in Fig. 4.

The surface structure in Fig. 3(b) was obtained after the crystal was under field-free reaction with CO at 1.3 mbar pressure for 23 h at 373 K. In comparison to the initial state of the nickel crystal, there were conspicuous alterations of the crystal shape after reaction with CO. This form will be called the intermediate state, which has the following features:

1. Areas of the  $\{111\}$  planes were increased.
2. At half angles between the central  $\{111\}$  and the peripheral  $\{111\}$  planes there were  $\{110\}$  planes flanked by  $\{210\}$ , and  $\{100\}$  flanked by  $\{511\}$ , respectively. The small top layer of the  $\{100\}$  plane showed within a cross a quadratic form in  $\langle 110 \rangle$  orientation. The planes mentioned above are mapped in Fig. 4(a).
3. The number of rings around the  $\{111\}$  poles was reduced compared with the initial state (Fig. 4b).

The features that characterize the intermediate state can be observed after relatively short times of reaction, for instance 10-20 min; they were only more pronounced after reaction times of many hours.

The map of planes of the original crystal and the main features after the reaction are illustrated in Figs. 4(a) and (b).

The structural phenomena can be interpreted by the theory of crystal growth introduced by Kossel and Stranski. The rate of dissolution of a lattice is controlled by the detachment of lattice elements from the half-crystal position. Such sites can be found at an open atom chain of certain planes. The removal of a lattice element from such a surface site represents the most frequent, repeatable step within the dissolution process. The dissolution form of a crystal displays those planes on the surface which have the greatest dissolution velocities. The dissolution of a sphere-shaped single crystal always has a final dissolution form that is bounded by only one kind of planes having the fastest dissolution velocity. Predictions of the dissolution form of a crystal can be made if one knows the equilibrium form, which is the state of the crystal where the surface free energy is at a minimum under the conditions of the system. The growth form consists of the slowest growing planes, the dissolution form of the fastest removed planes. Thus, by cutting off the corners of the equilibrium form, one obtains the dissolution form.

The dissolution of Ni is due to the chemical reaction with CO. As a result, the equilibrium form in the Ni/CO system differs from that of pure Ni, where the equilibrium form planes  $\{111\}$ ,  $\{100\}$ , and  $\{110\}$  appear, having the approximate extension  $\{111\} > \{100\} > \{110\}$ . For the equilibrium form in the Ni/CO system, when specific data for heats of CO adsorption are considered, one would expect that the extension of the  $\{111\}$  planes is at least markedly reduced, favoring the  $\{100\}$  and  $\{110\}$  planes. On such an equilibrium form all corners are of the same kind, namely  $1x\{111\} + 1x\{110\} + 1x\{100\}$ . Cutting off these corners results in an intermediate dissolution form which applies to the inter-

mediate state of the crystal without surface reaction. In Fig. 4(b) a particular structure is displayed with planes such as (111), (100), (110), (210), (511), which allows more extensive conclusions toward the sites reacting with CO. Whereas all the planes except {111} have been found small in size, the {111} planes themselves were considerably expanded during reaction with CO. According to the theoretical concept, therefore, the detachment from  $\langle 110 \rangle$  atom chains of the {111} planes must occur considerably faster than from other atomic entities of the surface. From this fact the conclusion can be drawn that the final dissolution form is an octahedron, {111}. Crystallographic consequences of this process require that the top layer atom chains of the (100) plane are no longer confined within a circle, but within a correctly  $\langle 110 \rangle$  oriented square. Several further structural elements of a final octahedron can be located in Fig. 3(b). The edges of the octahedron develop along the region of {210} and {110} planes; the corners of the octahedron develop in the center of the {100} planes.

The experimental observation of reduced ring densities around the {111} poles in the intermediate state can be also explained as due to the dissolution process. According to the interpretation of field ion images, a wider ring system means that the step heights on the surface are increased. As is seen in Fig. 4(b), diatomic or higher step heights were formed. Such an increase in step heights is usually considered as a so-called coarsening of the crystal. According to the theory of the dissolution process, it is a consequence of different reaction velocities. A preferable dissolution of Ni atoms of the (111) plane in the  $\langle 110 \rangle$  direction can explain all these structural observations.

From the energetic point of view, half crystal positions of the (100) and the (111) planes are identical in bond energies. The preferential dissolution of atoms in the (111) plane is due to kinetic processes and has been investigated by PFDMS. From these results it may be concluded that lattice nickel atoms are removed in the form of dicarbonyl or tricarbonyl intermediates. It will be shown that this process proceeds fastest at half-crystal positions of a  $\langle 110 \rangle$  atom chain of a (111) plane.

#### *Pulsed Field Desorption Measurements*

The reaction between Ni and CO was studied with the time-of-flight mass spectrometer described previously. Three different subcarbonyls,  $\text{NiCO}^+$ ,  $\text{Ni}(\text{CO})_2^+$ , and  $\text{Ni}(\text{CO})_3^+$ , are found during the reaction of CO ( $4 \times 10^{-6}$  to  $3 \times 10^{-2}$  Pa) with the nickel surface at specimen temperatures between 270 and 380 K, as described in detail in Ref. 18. The respective molecular subcarbonyls are products of a consecutive surface reaction. This conclusion can be drawn from the time dependence of the surface concentration of  $\text{Ni}(\text{CO})_2$  and  $\text{Ni}(\text{CO})_3$ , as seen in Fig. 5. It is known<sup>19</sup> that absorbed CO forms compression structures on low-index nickel planes at higher coverage. For our experimental conditions, the formation of a compression structure coincides with the appearance of the subcarbonyls  $\text{Ni}(\text{CO})_2$  and  $\text{Ni}(\text{CO})_3$ . During the desorption pulse,  $\text{Ni}^+$  and  $\text{Ni}^{++}$  also are observed (omitted in Fig. 5), which indicates a field evaporation process initiated by the field pulses.

Figure 5 describes surface species originating from the chemisorbed layer ( $\text{CO}_{\text{ad}} + \text{NiCO}$ ) and those from a surface reaction [ $\text{Ni}(\text{CO})_2$ ,  $\text{Ni}(\text{CO})_3$ ]. Under the conditions chosen in our experiments, the chemisorbed layer is desorbed only partly by each pulse. However, the reaction products  $\text{Ni}(\text{CO})_2$  and  $\text{Ni}(\text{CO})_3$  are completely desorbed, so that the number of ions per pulse is equal to the number of corresponding neutral species. Division of the experimental intensities by the size of the monitored area (9.5 nm<sup>2</sup>, containing 150 surface sites) leads to the displayed concentration data.

Important conclusions can be drawn from Fig. 5. At reaction times  $t_R < 1$  ms, the main portion of the measured intensity consists of species originating from the chemisorbed layer ( $\text{CO}_{\text{ad}} + \text{NiCO}$ ). Since this layer is only partly desorbed by each pulse, refilling of the emptied sites is already finished after 1 ms at  $3 \times 10^{-4}$  Pa. The slope of the intensity at  $t_R < 1$  ms indicates a first-order CO pressure dependence. Once the chemisorbed layer is saturated, at  $t_R \approx 1$  ms, measurable amounts of  $\text{Ni}(\text{CO})_2$  and  $\text{Ni}(\text{CO})_3$  are formed. Both species reach a constant concentration level at nearly the same time, i.e.,  $t_R \approx 10$  ms. There is obviously a considerable time lag in the formation of  $\text{Ni}(\text{CO})_2$ , whereas the forward reaction toward  $\text{Ni}(\text{CO})_3$  proceeds rather quickly.  $\text{Ni}(\text{CO})_4^+$  is not observed during these measurements. The formation of gaseous  $\text{Ni}(\text{CO})_4$  is not expected for thermodynamic reasons at  $p_{\text{CO}} = 3 \times 10^{-4}$  Pa. From the initial slope of the  $\text{Ni}(\text{CO})_2$  concentration, the rate of

formation of this species is calculated to be  $10^{-2}$  molecules per site per second. The constant concentration level of  $\text{Ni}(\text{CO})_2$  and  $\text{Ni}(\text{CO})_3$  at  $t_R > 10$  ms reflects a balance of formation, forward, and backward reactions.

The pressure dependence of  $\text{NiCO}^+$  reaches zero order at  $P_{\text{CO}} > 5 \times 10^{-5}$  Pa ( $T = 295$  K); at  $P_{\text{CO}} > 10^{-4}$  Pa the pressure dependence of  $\text{Ni}(\text{CO})_3^+$  formation is steeper than the formation of  $\text{Ni}(\text{CO})_2^+$ . Thus, the relationship of the rates  $r$  of formation of subcarbonyls,

$$r_{\text{Ni}(\text{CO})_1} > r_{\text{Ni}(\text{CO})_2} > r_{\text{Ni}(\text{CO})_3}$$

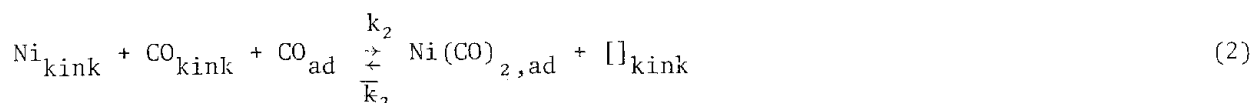
is valid only at pressures  $P_{\text{CO}} \leq 10^{-2}$  Pa. No conclusions can be drawn for rate-determining steps at higher pressures in the formation of nickeltetracarbonyl.

In the temperature dependence the intensities of all species show the same tendency, i.e., the intensities first increase slightly at low temperatures ( $T > 270$  K), then reach a maximum at  $T \approx 330$  K and decrease rapidly at higher temperatures. This behavior is explained by increasing reaction rates at  $T < 330$  K and increasing thermal instability above these temperatures. Thus, the reaction is kinetically controlled at lower temperatures, and thermodynamically at higher temperatures.

From the experimental data, the following reaction scheme can be derived. Reversible adsorption ( $T < 420$  K) with an initial sticking coefficient of nearly unity leads to adsorption states that differ from surface  $[]_{\text{ad}}$  and kink sites  $[]_{\text{kink}}$ .



Field-ion microscopic studies<sup>17</sup> show that kink site nickel atoms are removed from the lattice. The field dependence of intensity shows that the  $\text{Ni}(\text{CO})_2$  and  $\text{Ni}(\text{CO})_3$  are mobile surface species; from Fig. 5 it follows that  $\text{Ni}(\text{CO})_2$  has a long incubation time with a relatively fast subsequent formation of  $\text{Ni}(\text{CO})_3$ . These results are in agreement with a mechanism



and a consecutive step



(The  $[]_{\text{kink}}$  of step 2 need not be necessarily reproduced.) Accordingly, the rate of formation has a steeper  $P_{\text{CO}}$  dependence for  $\text{Ni}(\text{CO})_3$  than for  $\text{Ni}(\text{CO})_2$ , as observed. From the time dependence (Fig. 5) and the pressure dependence, it also follows that  $\text{Ni}(\text{CO})_2$  and  $\text{Ni}(\text{CO})_3$  are only formed after a certain surface coverage has been established, i.e., when the compression structure of CO on Ni is reached. At  $T < 380$  K and  $10^{-5}$  Pa  $< P_{\text{CO}} < 10^{-2}$  Pa the transfer of nickel lattice atoms from  $\text{Ni}_{\text{kink}}$  sites into adsorbed  $\text{Ni}(\text{CO})_2$  is the rate determining step. At  $T > 420$  K, CO is known to decompose, which causes poisoning of the carbonyl reaction. On macroscopic crystal surfaces with a limited amount of kink sites, the generation of these kink sites can be rate determining. From these considerations, it is not surprising that literature data on reaction rates<sup>20</sup> differ by orders of magnitude. For a quantitative rate evaluation, the factors discussed above have to be taken into account.

The formation of surface carbonyls has been observed for many other metals; in a recent investigation<sup>21</sup> kinetic data for the formation of ruthenium carbonyls have been established. They differ from those for nickel, since the tetracarbonyl  $\text{Ru}(\text{CO})_4$  is observed, but shows a field-induced decomposition.



## *Effects of High Electric Fields on Surface Reactions Investigated by Field Desorption*

The transformation of neutral surface species into desorbing ions in the presence of an extremely high electrostatic field represents a process that may involve bond cleavage, fragmentation of ions, association reactions, ion molecule reactions, and other field effects. The identification of the original surface species from detected ionic structures is possible only if these processes are understood.

The PFDMS method can measure field effects on chemical reactivity, since the reaction field  $F_R$  may be scanned continuously. Intermolecular interactions prior to the ionization step are frequently influenced by electric fields. As is to be demonstrated in the present communication, not only the product distribution of a chemical reaction, but also the energy distribution of field ions can elucidate electric field effects on reaction mechanisms.

In a series of experiments the reaction of sulfur molecules  $S_2$  from the gas phase in the physisorbed layer of a sulfidized tungsten or platinum emitter was investigated, with the following observations.<sup>22,23</sup> After a desorption pulse the tip surface is free of adsorbed molecules. A new layer starts to accumulate from continuously impinging molecular beam of  $S_2$  (density  $2 \times 10^{15} S_2 \text{ cm}^{-2} \text{ s}^{-1}$ ). Reactions between adsorbed molecules occur, and a certain concentration of intermediates and products builds up. The next desorption pulse removes and analyzes this layer. The longer the reaction time, the more the reaction proceeds toward the steady state, the thermodynamically stable modification of sulfur. Figure 6 shows the relative abundance of the various  $S_x^+$  ions desorbed after the reaction times indicated. At increasing reaction times the intermediates ( $S_4/S_5$  and  $S_6/S_7$ ) decrease, and the most stable product,  $S_8$ , becomes predominant. At very long times larger  $S_x$  also are found in small portions. These measurements were performed at 300 K and with low reaction fields; a definite influence of the reaction field strength was not yet seen. These data indicate subsequent reaction steps toward the formation of the energetically favored  $S_8$ . Sulfur molecules  $S_x$  ( $x \geq 5$ ) are ring molecules.

The qualitative observation of the steady adsorbed sulfur layer formed under the influence of a high reaction field,  $F_R$ , yields a completely different mass spectrum. Adjustment of the amplitude of the desorption pulses at such a low level that only a few percent of the impinging sulfur is desorbed establishes a steady state of the adsorbed layer. A mass spectrum taken during a 9h period is presented in Fig. 7. The relative abundances in Fig. 7 reflect the differences in the ion desorption probabilities, as well as the concentrations of the  $S_x$  species. Ionization probabilities increase from  $S_2$  to  $S_7$ . Beyond  $S_{22}$  a few more signals were seen below the noise level.

In this measurement the reaction field was as high as possible, just below the onset of ion formation, about 80% of the desorption field. Under these conditions surprisingly large amounts of high  $S_x$  ( $x > 8$ ) are present in the adsorbed layer.

The low field-desorption rate allows the formation of a multilayer. The high reaction field strength prevents the  $S_x$  molecules from forming rings, and stabilizes large chain molecules. These chain molecules with up to 22 sulfur atoms are field stabilized due to polarization forces. They extend some 50 to 80 Å in the field direction perpendicular to the surface. These field-induced polymerization reactions may lead to whisker growth, as observed by Beckey<sup>24</sup> with substances such as benzonitrile.

## *Appearance Energies of Sulfur*

With the aid of the retarding grid analyzer, energy distributions of various sulfur molecules were measured, as described in detail in Refs. 23,25. During these experiments appearance energies of  $S_2$ ,  $S_5$ ,  $S_6$ ,  $S_7$ , and  $S_8$  molecules were investigated in the first case for molecules entering the ionization zone from the gas phase. In the second case only  $S_2$  molecules were supplied and  $S_5$ ,  $S_6$ ,  $S_7$ , and  $S_8$  were formed as intermediates in a surface reaction. The appearance energies of gaseous  $S_x^+$  are compared with those of corresponding  $S_x^+$  produced from  $S_2$  by surface reactions. The appearance energies of the gas phase  $S_x^+$  ions are determined by the respective ionization potentials. The ionization energy for a gaseous  $S_x$  is provided by the external field. The tunneling distance, at constant field strength, increases with the ionization energy. The deficit in the origin's potential of the ion is measured as deficit in kinetic energy. From the onset in energy distribution and the resulting appearance energies the ionization energy can be derived.

The reaction of  $S_2$  toward  $S_x$  in the adsorbed layer leads to excited intermediates in

the activated complex of the reaction. These intermediates determine the high energy onset in energy distribution of  $S_X^+$  from the adsorbed layer. These appearance energy values for field-desorbed ions are remarkably smaller than those of the gas phase ions in spite of the theoretical consideration that the heat of condensation should enlarge the  $A_E$ , as is shown in the last column of Table 1.

TABLE 1.--Comparison of ionization potential I with  $A_E$  of various sulfur molecules.

Species	I[eV]	Gas	Field Desorption	
		$A_E$ exp[eV]	$A_E$ exp[eV]	$A_E$ theoret.*[eV]
$S_2$	$9.36 \pm 0.05$	$9.33 \pm 0.1$		
$S_5$	$8.6 \pm 0.05$	$8.1 \pm 0.3$	$7.75 \pm 0.5$	8.65
$S_6$	$9.00 \pm 0.03$	$8.94 \pm 0.1$	$8.25 \pm 0.15$	9.59
$S_7$	$8.67 \pm 0.03$	$8.50 \pm 0.1$	$7.35 \pm 0.15$	9.26
$S_8$	$9.04 \pm 0.03$	$8.97 \pm 0.1$	$8.35 \pm 0.15$	9.84

\*Theoretical values (theoret.) are obtained by the addition of the heat of condensation of sulfur species to  $A_E$  gas and thus describe data for the ground state of  $S_X$  species.

In all experiments known so far surface compounds displayed higher energy deficits than corresponding gas molecules, on account of surface interaction energies. In the present case, surface compounds with lower energy deficits were detected for the first time. The discrepancy amounts approximately to 1-1.5 eV, which is in the same direction and order of magnitude as is to be expected for the difference in ionization potentials of sulfur ring and chain molecules.

This example demonstrates how appearance energy values can yield information on activated complexes of surface reactions.

#### *Field-dependent Reaction Rates*

The classical experiments by Bergmann, Eigen, and De Maeyer<sup>26</sup> on chemical relaxation effects due to electrical field pulses clearly demonstrated field effects on chemical kinetics in the homogeneous phase. In field-emitter experiments several observations indicate field-enhanced reaction rates, for instance during oxidation reactions of metals and semiconductors.

Okuyama<sup>27</sup> found an increase of the oxidation rate of molybdenum single crystal emitters at 1000-1200K with negatively as well as with positively charged surfaces. The application of a negative field high enough to induce field electron emission resulted in the formation of a thin oxide layer at the tip apex. The oxide layer exhibited a range of roof-like structures at its surface and was confirmed by electron diffraction to be monocrystalline molybdenum tri-oxide. In positive fields evidence was obtained that oxide crystallites grow selectively on the Mo {100} planes.

Very extensive field effects have been observed during the oxidation of silicon.<sup>28</sup> The field-free interaction of  $O_2$  with the Si surface has been investigated by observing the hydrogen field ion images. When the cleaned Si surface was exposed to  $O_2$  ( $\sim 10^{-5}$  Torr, 3000 L) at temperatures  $T < 573$  K, only a limited disorder due to oxidation was produced. The Si-surface could be recovered by field evaporation of only a few surface layers. At tip temperatures  $T > 673$  K thick oxide layers were formed. After partial field evaporation, the Si substrate is represented by a dark region surrounded by the bright ion

projection of the Si/SiO<sub>2</sub> interface. Further field evaporation results in the appearance of an elemental silicon pattern, which after removal of one or two additional monolayers shows an ordered structure. These observations indicate only slow oxidation rates of Si at  $T < 573$  K, in agreement with the literature. Observations are also in agreement with suggestions that the transitions from the bulk SiO<sub>2</sub> to single crystal Si is abrupt and includes only one or two monolayers of disordered Si.

The oxygen interaction at a Si surface is largely influenced by an electrical field. At a field of  $1 \text{ V/\AA}$ , surface oxide layers are readily grown within few seconds even at  $T = 80$  K. The oxidized surface gives a homogeneous image brightness over the whole surface from the beginning of the exposure. This result suggests that oxidation occurs homogeneously without crystallographic preferences.

#### *Field-induced Desorption Products*

As usual in mass spectrometric investigations, the correlation of the observed ions with their original neutral species requires calibration. In field desorption, field-induced surface structures or collision processes cause further complications. Molecular ions can be observed that have no neutral counterparts. For example, proton-attached parent molecular ions are frequently formed.

One example is the formation of  $\text{H}_3^+$ -ions from hydrogen adsorption layers during field desorption, a process that does not occur during field-free ion formation, for instance with SIMS. Detailed studies<sup>28</sup> have shown that the  $\text{H}_3^+$  ions are formed by a field-induced surface reaction with a neutral  $\text{H}_3$  precursor state, which has a linear upright position on the field emitter surface and a lifetime  $\tau$  of  $10 \text{ } \mu\text{s} < \tau < 300 \text{ } \mu\text{s}$ .

Other field-induced processes are less well understood. For instance, Ai and Tsong<sup>30</sup> report the field-induced formation of  $\text{NH}_3$  from nitrogen and hydrogen atoms. Experiments on 20 transition metals gave evidence for such a reaction only on Fe and Co; its mechanism is unknown.

Extended research work will be required if a deeper insight into field-induced chemical reactivity is to be found.

#### *References*

1. H. S. Taylor, *J. Phys. Chem.* 30: 145, 1926.
2. G.-M. Schwab, *Zeitschr. physik. Chem.* B1: 385, 1928.
3. M. Boudart, in G. C. Bond, P. B. Wells, and F. C. Tompkins, Eds., *Proc. of the Sixth Intern. Congress on Catalysis*, London: The Chemical Society, 1976, 1.
4. R. van Hardefeld and F. Hartog, *Adv. Catal.* 22: 75, 1972.
5. M. Boudart, H. Topsøe, and J. A. Dumensie, in E. Dranglis and R. Jaffee, Eds., *The Physical Basis for Heterogeneous Catalysis*, New York: Plenum Press, 1975, 337.
6. G. C. Bond, *Surf. Sci.* 156: 967, 1985.
7. O.-L. Pérez, D. Romen, and M. J. Yacamán, *J. Catal.* 79: 240, 1983.
8. J. H. Block and A. W. Czanderna, in *Methods and Phenomena*, Amsterdam: Elsevier, 1975, 379.
9. N. Ernst and J. H. Block, *Surf. Sci.* 126: 397, 1983.
10. J. H. Block, *Ber. Bunsenges. Phys. Chem.* 86: 852, 1982.
11. R. Brill, E. L. Richter and E. Ruck, *Angew. Chemie* 79: 905, 1967.
12. G. Ertl, *Sci. Engin.* 21: 201, 1980.
13. M. Grunze, in D. A. King and D. P. Woodruff, Eds., *The Chemical Physics of Surfaces and Heterogeneous Catalysis*, Amsterdam: Elsevier, 1982, IV, 143.
14. G. Bergeret and M. Abon, *Surf. Sci.* 93: L143, 1980.
15. A. R. McCabe and G. D. W. Smith, *Proc. 8th Intern. Congress on Catalysis*, Weinheim: Verlag Chemie, 1984, IV, 73.
16. G. L. Kellogg, *Surf. Sci.* (in press).
17. W. A. Schmidt, J. H. Block, and K. A. Becker, *Surf. Sci.* 122: 409, 1982.
18. D. B. Liang, G. Abend, J. H. Block, and N. Kruse, *Surf. Sci.* 126: 392, 1983.
19. J. C. Tracy, *J. Chem. Phys.* 56: 2736, 1972.
20. P. de Groot, M. Coulon, and K. Dransfeld, *Surf. Sci.* 94: 204, 1980.
21. N. Kruse, ECOS-8 (to be published in *Surf. Sci.*).
22. D. L. Cocke, G. Abend, and J. H. Block, *J. Phys. Chem.* 80: 524, 1976.
23. G. Abend, R.-G. Abitz, and J. H. Block, in L. Neel, Ed., *Non-linear Behaviour of*

*Molecules, Atoms and Ions in Electric, Magnetic or Electromagnetic Fields*, Amsterdam: Elsevier, 1979, 261.

24. H. D. Beckey, in *Principles of Field Ionization and Field Desorption Mass Spectrometry*, Oxford: Pergamon Press, 1977.

25. R.-G. Abitz, Ph.D. Thesis, Freie Universität Berlin, 1978.

26. K. Bergmann, M. Eigen, and L. De Maeyer, *Ber. Bunsenges. Phys. Chem.* 67: 819, 1963.

27. F. Okuyama, *Surf. Sci.* 67: 109, 1977.

28. T. Sakata and J. H. Block, *Proc. 29th Intern. Field Emission Symp.* in Göteborg, A82, Stockholm: Almqvist and Wiksell, 1982, 135.

29. N. Ernst and J. H. Block, *Phys. Rev.* B29: 7092, 1984, and references therein.

30. C. Ai and T. T. Tsong, *Surf. Sci.* 138: 339, 1984.

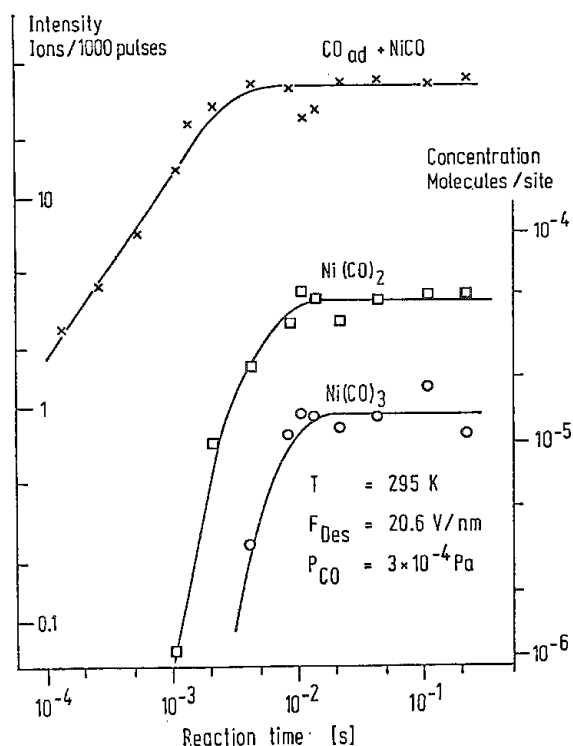


FIG. 5.--Surface concentration of nickel subcarbonyls as function of reaction time  $t_R$ , monitored at an area of about 150 surface sites (impingement rate  $\sim 450$  CO/s).

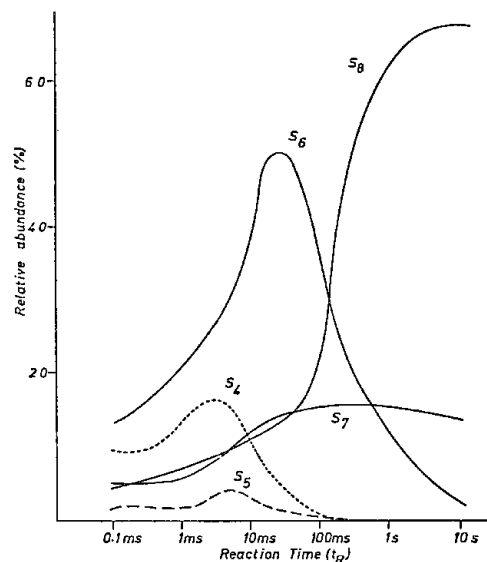


FIG. 6.-- $S_x^+$  desorbed from sulfide-covered tungsten tip at room temperature; tip radius, 400 nm.

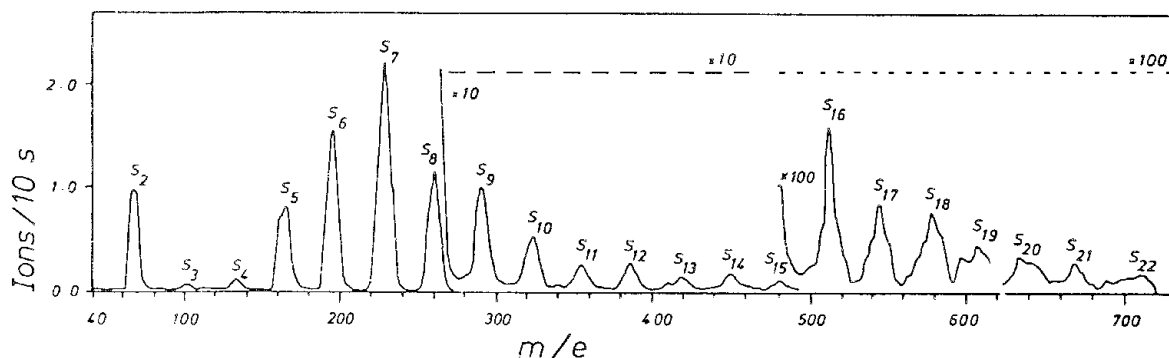


FIG. 7.--Mass spectrum of field-desorbed species from liquid-like physisorbed layer of sulfur on sulfide-covered tungsten tip at room temperature, under continuous impact of molecular  $S_2$  beam. Reaction field is 80% of desorption field strength, pulse repetition rate is 10 kHz. Due to the large pulse width (500 ns), signals are broadened toward longer flight times (i.e., higher masses).

## FIELD-ION MICROSCOPE OBSERVATIONS OF SURFACE SELF-DIFFUSION AND ATOMIC INTERACTIONS ON PT

G. L. Kellogg

The unique attributes of the field ion microscope permit direct observations of the surface diffusion of individual atoms on perfectly defined surfaces.<sup>1-4</sup> In this study the diffusion of Pt atoms on the Pt (110) plane was investigated. The motivation for the study stemmed from our recent field ion microscope observations of the reconstruction of the Pt (110) plane.<sup>5</sup> This plane is a channeled surface consisting of close-packed rows of atoms separated by a distance of 3.92 Å. We found that the unreconstructed Pt surface transformed to a surface consisting of alternate missing rows of atoms at temperatures above 300 K. These results confirmed the controversial "missing row" model proposed to explain the (1x2) diffraction patterns observed in Low Energy Electron Diffraction.<sup>6</sup> The fact that the transition was observed for small clusters of atoms suggested that the reconstruction involves surface diffusion and is driven by strong attractive interactions between atoms within a surface channel and repulsive interactions between atoms in adjacent channels. In an attempt to observe these interactions, we are now carrying out an investigation of surface self-diffusion on the Pt (110) plane. The investigation involves studies of the diffusion of single atoms and the interaction of two or more atoms deposited on the (110) plane. Studies of single-atom diffusion of Pt on Pt (110) have been previously reported by Bassett and Webber<sup>7</sup> and, where appropriate, the findings of this study are compared to their results.

### *Experimental*

The experiments were performed in an all-metal field ion microscope pumped by a liquid-nitrogen-trapped oil diffusion pump and a liquid-nitrogen-cooled titanium sublimation pump. After extensive vacuum processing, which included at least three bakeouts at 230 C, the background pressure with the tip cooled and the diffusion pump valved-off was  $4-5 \times 10^{-11}$  Torr. The sample tip was prepared from 0.005 in.-diam. polycrystalline Pt wire and sharpened in a mixture of molten NaNO<sub>3</sub> and NaCl. The tip was cleaned in situ by a combination of neon ion bombardment and field evaporation. The sample temperature was controlled and monitored with the use of the resistive heating method discussed in the literature.<sup>1-4</sup> Neon purified by diffusion through a vycor glass bulb was used for the imaging gas. The field ion microscope images were intensified with an internal channel-plate assembly cleaned by both electron and ion bombardment. The Pt adatoms were supplied from deposition coils made from 0.005 in.-diam. Pt wire. The coils and support loops were extensively outgassed as a part of the vacuum processing procedure.

The experimental procedure used in this study followed closely those introduced by Ehrlich and Hudda<sup>8</sup> and discussed in several review articles.<sup>1-4</sup> The tip was cleaned as discussed above and Pt atoms were deposited onto the (110) plane at 78 K. At this temperature the adatoms were immobile. We then induced the atoms to migrate by turning off the imaging voltage and raising the temperature of the tip. The heating interval used in the present investigation was 45 s. After the heating interval, the tip was cooled to 78 K and the surface re-imaged to determine the new location of the adatom. In the single-atom diffusion experiments, this procedure was repeated a number of times to determine the atom's mean square displacement.

The collection and analysis of data were semi-automated. The field ion images were photographed with a RCA model TC1005 video camera and stored on a JVC model 6060U video recorder. A home-built microprocessor was used to control the alternate application of the imaging voltage, heating of the tip, and starting and stopping of the video recorder. The analysis of the recorded images consisted of marking the position of the atom with a

---

The author is at Sandia National Laboratories, Albuquerque, NM 87185. This work was supported by the U.S. Department of Energy under contract DE-AC04-76DP00789.

cursor generated by a x-y digitizer which transmitted the coordinates of the atom to a microcomputer. Actual displacements of the atom were calibrated from the known spacings along and across the  $[1\bar{1}0]$  channels.

### Results

Surface diffusion of single Pt atoms on the Pt (110) plane was detected at temperatures above 250 K. Figure 1 shows a series of field ion microscope images that illustrates the diffusion of Pt on Pt (110). Between each photograph, the tip was heated to 273 K for 45 s. As indicated in the photographs, the atom migrates across, as well as within, the surface channels along the  $[1\bar{1}0]$  direction. This behavior, which was observed previously by Bassett and Webber,<sup>7</sup> is quite different from that found for surface diffusion on other channeled surfaces. On W (211) or Pt (311), for example, the migration is one-dimensional, i.e., the atom is confined to a single surface channel.<sup>1-4,7</sup> Experimental evidence has been reported which indicates that cross-channel diffusion actually involves an exchange mechanism; i.e., the a surface atom next to the adatom moves into the adjacent channel and the adatom takes its place.<sup>9</sup>

A detailed analysis of our diffusion data indicates that cross-channel diffusion and in-channel diffusion occurs with about equal probability. The mean square displacement for diffusion in each direction was measured at four temperatures in the range 253-281 K. The data, plotted in Arrhenius form, are shown in Fig. 2. A least-squares analysis of the data yields activation energies for surface diffusion of  $0.72 \pm 0.07$  eV for in-channel diffusion and  $0.69 \pm 0.07$  eV for cross-channel diffusion. Within the limits of experimental uncertainty, the activation energies are the same. These values are slightly lower than those reported by Bassett and Webber,<sup>9</sup> but still within the experimental errors. The Arrhenius prefactors, sometimes called the "diffusivity," are obtained from the intercepts of the plots. The diffusivities obtained from Fig. 2 are  $3 \times 10^{-4}$  and  $6 \times 10^{-4}$  cm<sup>2</sup>/s for cross-channel and in-channel diffusion, respectively.

To examine atomic interactions on the Pt (110) surface, two Pt atoms were deposited and allowed to diffuse at 264 K until they encountered each other. When this encounter occurred, the atoms formed a close-packed dimer within a given channel of the surface. Once formed, the dimer was very stable. An attempt to determine the bond strength by measurement of the dissociation probability of the dimer as a function of temperature was made. Unfortunately, the bond was so strong that dissociation was not detected, even when the sample temperature was raised to 335 K. An interesting observation was made at this temperature. Without any additional adatoms present on the plane, the dimer grew into a chain of atoms along the surface channel. Our present explanation for this behavior is that substrate surface atoms next to the dimer (or the end of the chain) make a displacement to the end of the chain and the remainder of the atoms in the row move to fill the vacancy. Clearly, more experiments are required to verify this mechanism. Thus, although no quantitative information on the bond strength could be obtained, these observations obviously indicate a very strong attractive interaction between atoms at their close-packed separation within a channel.

The formation of a missing row structure on Pt (110) suggests that, in addition to a strong attractive interaction between atoms in the same channel, there is a repulsive interaction between atoms in adjacent surface channels. The ideal experiment to identify a repulsive interaction between two atoms in adjacent channels would be to deposit an adatom in two adjacent channels and observe their diffusion. A repulsive interaction would be reflected in a decrease in the number of observations at the closest separations. However, because diffusion on the (110) plane is not confined to a single channel, this experiment was not possible. We did obtain qualitative evidence for such a repulsive interaction by depositing 5-10 atoms on the surface and observing their subsequent interaction during diffusion at 280 K. In every case the atoms formed chains along the surface channels, but the chains never formed next to each other in adjacent channels. This observation indicates that once a chain of atoms forms in a given channel, atoms in adjacent channels experience a repulsive interaction.

### Summary

Platinum atoms diffuse on the Pt (110) plane at temperatures above 250 K. Cross-channel and in-channel diffusion occurs with nearly equal probability. Evidence for a

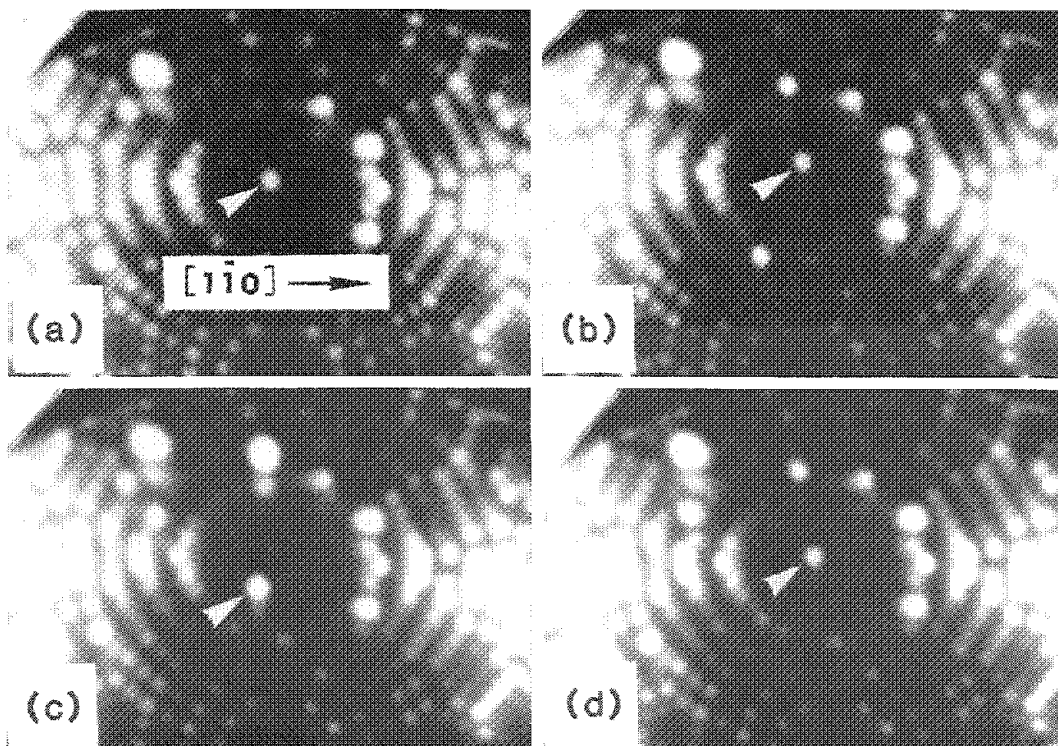


FIG. 1.--Series of field ion micrographs showing diffusion of single Pt atom on Pt(110) plane. Atom migrates across as well as in  $[1\bar{1}0]$  channels.

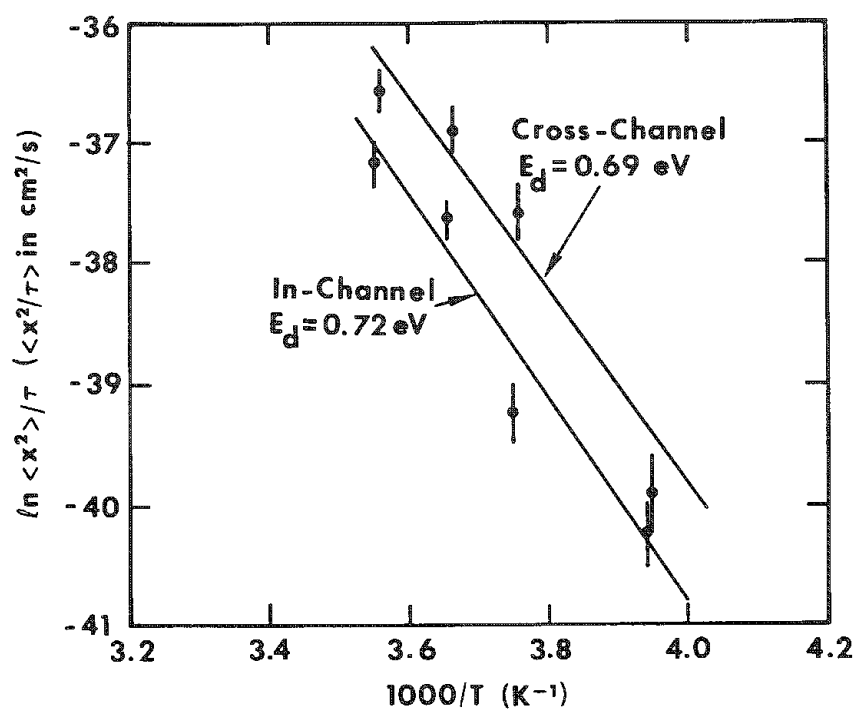


FIG. 2.--Arrhenius plots for diffusion of Pt on Pt(110). Activation energy for cross-channel and in-channel diffusion are the same within experimental uncertainty.

strong attractive interaction between Pt atoms at their closest separation within a given channel of the Pt (110) plane was found. However, because dissociation of the atoms could not be induced, the actual bond strength could not be measured. The rearrangement of deposited atoms at 280 K also suggested a repulsive interaction between atoms in adjacent channels. These interactions are just the type expected to produce the observed "missing-row" reconstruction of the Pt (110) plane. Further experiments have been initiated on the Pt (311) plane to obtain quantitative interatomic potentials between Pt atoms on channeled Pt surfaces.<sup>10</sup> The (311) plane is similar to the (110) plane in that it consists of close-packed chains of atoms; the only difference is that the spacing between rows is somewhat larger (4.62 Å). Since diffusion on the (311) plane is one-dimensional, the diffusion of atoms in adjacent channels can be studied in detail to determine whether a repulsive interaction exists between atoms at the separation distance.

### References

1. G. Ehrlich and K. Stolt, *Ann. Rev. Phys. Chem.* 31: 603, 1980.
2. D. W. Bassett, in V. T. Binh, Ed., *Surface Mobilities on Solid Materials*, New York: Plenum, 1983, 63.
3. T. T. Tsong and P. L. Cowan, *CRC Critical Reviews of Solid State Materials Science* 7: 289, 1978.
4. G. L. Kellogg, T. T. Tsong, and P. L. Cowan, *Surface Sci.* 70: 485, 1978.
5. G. L. Kellogg, *Phys. Rev. Lett.* 55: 2186, 1985.
6. See, for example, J. C. Campuzano, A. M. Lahee, and G. Jennings, *Surface Sci.* 152/153: 68, 1985, and references therein.
7. D. W. Bassett and P. R. Webber, *Surface Sci.* 70: 520, 1978.
8. G. Ehrlich and F. G. Hudda, *J. Chem. Phys.* 44: 1039, 1966.
9. J. D. Wrigley and G. Ehrlich, *Phys. Rev. Lett.* 44: 661, 1980.
10. G. L. Kellogg, *J. de Physique* (in press).



## THEORY OF SURFACE STRUCTURE DETERMINATION BY FIELD-ION MICROSCOPY: COMPARISON WITH SCANNING TUNNELING MICROSCOPY

D. R. Kingham

For many years field-ion microscopy<sup>1</sup> (FIM) was the only known means of directly viewing the structure of a surface on the atomic scale. Scanning tunneling microscopy (STM) developed by Binnig et al.<sup>2</sup> is now known to have similar capabilities and has attracted much attention recently because of its versatility and remarkable resolution of surface topography. FIM may not have the versatility of STM, but it can provide similar information about surface structure with potentially better resolution.<sup>3</sup>

### *Surface Imaging in the Field-Ion Microscope*

The first images of individual atoms of a metal surface by FIM were reported 30 years ago.<sup>1</sup> The microscope is simple and direct in operation, but theoretical understanding of field-ion image formation has been incomplete.<sup>4</sup> In particular, there has been some disagreement over the relative importance of the two main factors that can influence local image contrast: (i) the electron tunneling probability for field ionization, and (ii) the local concentration of imaging gas atoms.

This disagreement has now been resolved by some calculations of Homeier and Kingham,<sup>5</sup> which are supported by independent work of Bono and Good.<sup>6</sup> This work shows that variations in the electron transition rate constant may be sufficient to explain the observed contrast in the field-ion microscope. The significance of this is that it indicates the similarity of FIM and STM: both techniques rely on an electron tunneling mechanism to give information on surface structure on the atomic scale.

### *Contrast in the Field-ion Microscope Compared to the Scanning Tunneling Microscope*

A comparison of contrast in FIM and STM has been made by Kingham and Garcia<sup>3</sup> using a three-dimensional electron tunneling model. The model is essentially the same in both cases. The probe (imaging gas) position in FIM is determined by the critical distance for field ionization, whereas in the STM it is variable. The comparison is made on the assumption that the STM tip follows the locus of the critical surface for field ionization, whereas in the STM it is variable.

For the Au (110) 2x1 surface the ratio of field ion currents from a point directly above a protruding surface atom and above a point half way between two such atoms is 10.7 for helium imaging gas. The comparable figure for STM is only 2.0 assuming a probe tip 3 Å in radius. For a typical (100) face of a bcc or fcc crystal the He FIM contrast is calculated to be 1.53 and the figure for STM is very close to 1 indicating that STM is unlikely to reveal the structure of such a weakly corrugated surface, whereas FIM might be able to do so.

The advantages of FIM are that the probe is small and reproducible (an inert gas atom), but it suffers from the disadvantages of requiring both a highly curved sample and a strong electric field.

However, STM has the advantage of versatility, with the disadvantage of probe preparation being awkward and not easily reproducible. It is ironic that the problem of probe preparation for STM can be solved by preparation and characterization of the probe in a field-ion microscope.<sup>7</sup>

### *Digital Imaging in Field-ion Microscopy*

One of the most exciting recent developments in FIM has been the computer-aided measurement of FIM intensities reported by Witt and Muller.<sup>8</sup> With this technique they are able to image atoms in the normally dark areas of FIM patterns; that is, in the central

areas of high index planes, where the surface structure is least distorted by the electric field. They used a video intensity digitizing system, but the technology exists to replace the channelplate and conventional FIM imaging screen with an array detector with single ion counting capability to give a direct digital image in place of a conventional field-ion micrograph. Such a digital image could be used in the determination of the corrugation of the charge density above a surface and hence the elucidation of the precise positions of surface atoms.

### *Summary*

Field-ion microscopy and scanning tunneling microscopy both rely on an electron tunneling process between an atomic scale probe and the surface being studied. Although it lacks the flexibility of STM, FIM has remarkable and as yet unrealized potential for determining surface structures.

### *References*

1. E. W. Muller and K. Bahadur, *Phys. Rev.* 103: 624, 1956.
2. G. Binnig, H. Rohrer, C. Gerber, and E. Weibel, *Appl. Phys. Lett.* 49: 57, 1982; *Phys. Rev. Lett.* 50: 120, 1983.
3. D. R. Kingham and N. Garcia, *J. de Physique* 45: 119, 1984.
4. R. G. Forbes, *J. Phys.* D18: 973, 1985.
5. H. H. H. Homeier and D. R. Kingham, *J. Phys.* D16: 1115, 1983.
6. S. Bono and R. H. Good, *Surface Sci.* 134: 272, 1983.
7. H. W. Fink, Proc. 32nd Intern. Field Emission Symposium, 1985 (to be published in *J. de Physique*).
8. J. Witt and K. Muller, *ibid.*
9. T. Schiller, U. Weigmann, W. Kessel, and J. H. Block, *ibid.*

## Analytical Electron Microscopy

### CBED POINT GROUP ANALYSIS OF THIN PRECIPITATES IN METALLIC SYSTEMS

J. M. Howe and Mehmet Sarikaya

Point and space group analysis were performed on thin  $\gamma'$ -precipitates in Al-15 wt% Ag alloy by CBED. It was found that different results can be obtained related to the symmetry elements of the precipitates depending on the analysis performed by following the procedures stated in the literature. Comparative analyses using a pure  $\alpha$ -titanium standard demonstrate that the limited thickness of the plate-shaped precipitates is responsible for the varied results. The space group of the precipitates in the present system were determined to be  $P6_3/mmc$ , and it is suggested here that a preferred method should be used for point and space group determination of thin precipitates.

#### *Experimental*

An Al-14.92 wt% Ag (both 99.99% pure) alloy was used in this work. After the initial solution heat treatment at 550 C, samples were subjected to aging at 350 C for 30 and 120 min. The  $\gamma'$ -precipitates were extracted from the matrix by use of a 5% NaOH solution.<sup>1</sup> The precipitates were dispersed in  $CH_3OH$  solution and deposited on a carbon film for TEM observations. Disk-shaped 3.0mm-diameter specimens of Ti, which were initially annealed to a full  $\alpha$ -phase microstructure, were twin-jet electropolished in a solution of 25%  $HNO_3$ /75%  $CH_3OH$  at -35 C under 50 V potential and 50 mA current conditions. All CBED experiments were performed with a Philips 400 AEM fitted with free-lens control unit for the adjustment of C2L current, which allowed incident electron probe diameters down to 100 Å with convergence angles up to 300 mrad in the TEM mode. This system increased the ease of tilting experiments and was continuously used to change the diameter of the diffraction disks, which were made to barely touch each other on each recorded pattern.<sup>2</sup> Both 300 $\mu$ m and 100 $\mu$ m C2L apertures and 450 and 280mm camera lengths were used to record the ZOLZ disks and FOLZ circle, respectively. A double tilt, liquid nitrogen cooled specimen holder (GATAN) was used (-180 C) to reduce contamination and thermal diffuse scattering in the specimen and produce sharper HOLZ lines.

#### *Results and Discussions*

In analyzing the diffraction group and, hence, the point group, of a crystal, Buxton et al.<sup>3</sup> make use of zone axis (z.a.) patterns with the C2A displaced to special points to reveal the symmetry features. A "special position" may be a Bragg position ( $0_B$ ) from the transmitted beam and the symmetry elements can be extracted from the dark field (DF) disk. Tanaka et al.,<sup>4,5</sup> on the other hand, introduce a slightly different approach, which uses the details within all the disks in a single or a pair of symmetric-many-beam (SMB) patterns to obtain the diffraction group.

In the present study, these procedures were used initially to determine the point and space groups of  $\gamma'$ -precipitates in an Al-Ag alloy, which was prepared in two different growth conditions. In this paper, a summary of some of the important points is presented. A detailed analysis appears in Refs. 1 and 6.

In using these techniques for the analysis of thin precipitates, problems arise due to the thinness of the precipitates, which limits the contrast and eliminates some of the symmetry features from the patterns. This is mostly apparent, for example, in the diffraction patterns given in Fig. 1, which were taken from the extracted  $\gamma'$ -precipitates. Although the thinness of the precipitates causes the disappearance of any symmetry details in the bright-field (BF) disk in Fig. 1(b), the whole pattern (WP) in Fig. 1(a) and the first-

---

Author Howe is at the Metallurgical Engineering and Materials Science, Carnegie-Mellon University, Pittsburgh, Pa.; author Sarikaya is at the Department of Materials Science and Engineering, University of Washington, Seattle, WA 98195. The authors are grateful for the discussions with Dr. R. Gronsky during the progress of this work and they are thankful to Dr. G. Thomas for the use of the TEM facility at the University of California at Berkeley.

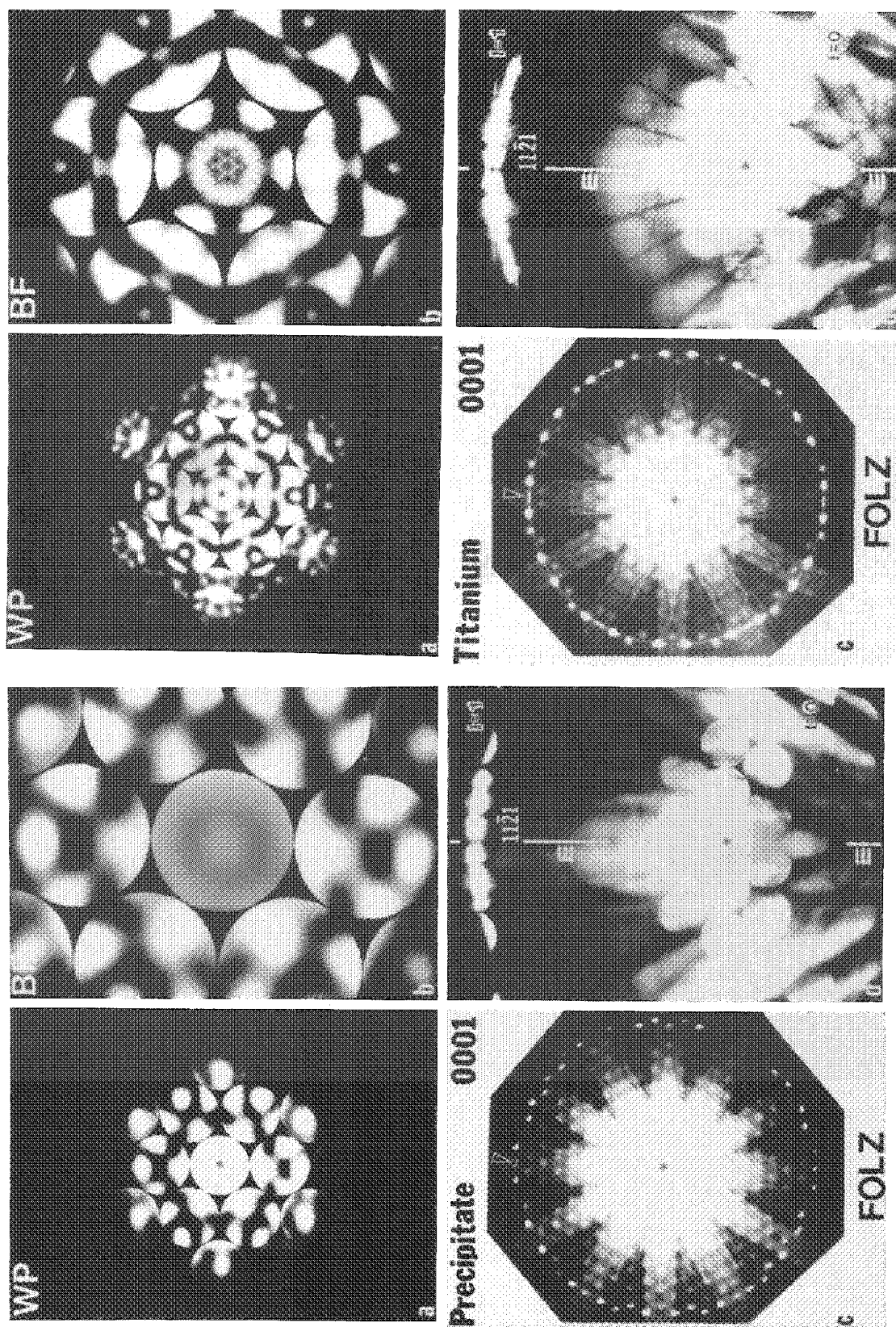


FIG. 1.--CBED patterns from extracted  $\gamma'$ -precipitate in [0001] orientation revealing (a) 6mm symmetry of intensity distribution in FOLZ disks; (b) absence of contrast detail within BF disk due to insufficient thickness of precipitate; (c) 6-fold symmetry of FOLZ; (d) G-M line in 1121-type FOLZ reflection at Bragg position. In all patterns, position of optic axis is indicated by asterisk.

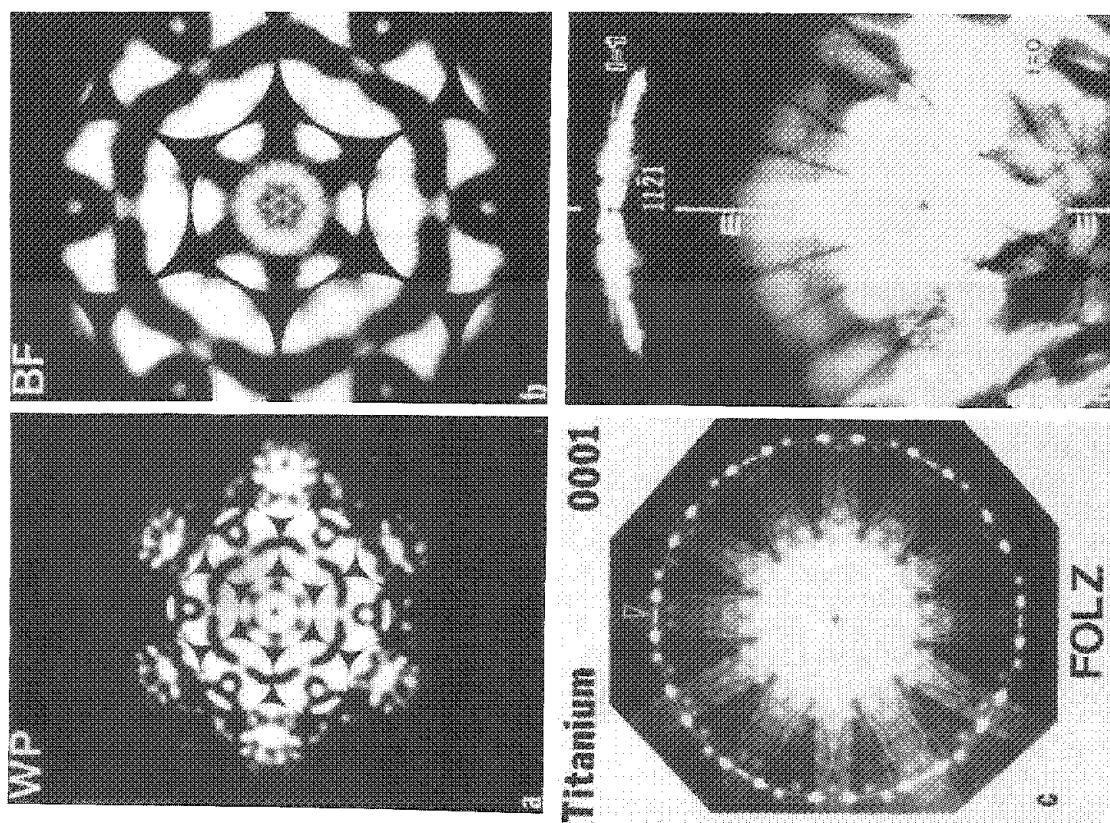


FIG. 2.--CBED patterns from  $\alpha$ -titanium in [0001] revealing (a) 6mm symmetry of intensity fringes within FOLZ disks; (b) detail in BF disk; (c) 6-fold symmetry of FOLZ; (d) G-M line in 1121-type FOLZ reflection at Bragg position.

order Laue zone (FOLZ) ring in Fig. 1(c) both display 6mm symmetry. These patterns can be compared directly with the same series of patterns acquired from the  $\alpha$ -titanium sample, as shown in Fig. 2. From the above symmetry elements and with reference to the tables,<sup>3</sup> the diffraction group for the  $\gamma'$ -precipitate can be determined as either 6mm or 6mm1<sub>R</sub>.

In continuing the search for the correct diffraction group, and therefore for the point group, further analyses were performed by the outlined procedures.<sup>3</sup> Figure 3 presents a series of  $\pm g$  and tilted-illumination (TI) patterns which may be directly compared with the patterns for the  $\alpha$ -titanium samples in Fig. 4. In Figs. 3(a) and (b), the  $\bar{1}010$  and  $10\bar{1}0$  disks clearly display only m symmetry and they are related by a 180° rotation, rather than by a translation operation. This finding reduces the possibility for the diffraction group to 6mm and 6mm1<sub>R</sub> is eliminated. If the Tanaka et al. 6-beam pattern is used, as given in Fig. 3(c), a different result is obtained. Although the detail within some of the disks in the SMB pattern is slightly distorted due to bending of the precipitate during the electron beam radiation, the 2020 disk clearly displays 2mm symmetry. The 0000 and four remaining disks all have m symmetry, where the mirror lines intersect the center of the 2020 disk. Thus, comparison with the SMB patterns in Tanaka et al.<sup>4</sup> indicates that the diffraction group for the precipitate is 6mm1<sub>R</sub> and not 6mm, which is the same as the findings for  $\alpha$ -titanium as given in Fig. 4(c). Reference to the Buxton et al.<sup>3</sup> tables identifies the point group of the precipitate as 6/mmm. Therefore, the two different methods, i.e., Buxton et al.<sup>3</sup> and Tanaka et al.,<sup>4,5</sup> yield two different point groups for the same precipitate. Since the Steeds and Vincent<sup>7</sup> method for point group determination also relies on the comparison of the intensity distributions between the  $\pm g$  and  $-g$  disks or in a DF disk, the result is the same as the Buxton et al. method.<sup>3</sup> The centro-symmetry versus thickness results<sup>1</sup> for  $\alpha$ -titanium, analyzed in a  $[1\bar{1}02]$  z.a. orientation, show that a loss of translational symmetry between  $\pm g$  and  $-g$  disks can occur in thin specimens due to their limited thickness along the electron beam direction. Therefore, it is likely that this effect is responsible for the 180° rotational symmetry observed between the  $\bar{1}010$  and  $10\bar{1}0$  disks in Figs. 3(a) and (b), particularly since no HOLZ lines are present in the patterns and the precipitate is too thin for strong dynamical diffraction to occur. Consequently, it is probable that the precipitate has the higher-symmetry diffraction group given by the SMB pattern in Fig. 3(c), and that its point group is 6/mmm.

In summary, the Tanaka et al.<sup>4,5</sup> method for diffraction group determination by SMB CBED patterns indicates less sensitivity to the thickness of the specimens than the Buxton et al.<sup>3</sup> and Steeds and Vincent<sup>7</sup> procedures. Therefore, the former method is preferred for the point group determination of thin precipitates extracted from a metallic matrix, with thicknesses on the order of a few extinction distances. Since HOLZ interactions are stronger, the  $\pm g$  test for the examination of the centro-symmetry is the most reliable when tested in low symmetry zone axes. In the current study, after the thorough tests for the absence of forbidden (AOF) reflections,<sup>8-11</sup> it was found that the  $\gamma'$ -precipitates have a space group of P6<sub>3</sub>/mmc for both 30 min and 120 min aging (at 350 C) conditions.

## References

1. M. Howe, M. Sarikaya, and R. Gronsky, to be published in *Acta Cryst.* (1986).
2. M. Sarikaya and G. Thomas, *Microbeam Analysis--1984*, 97-104.
3. B. F. Buxton, J. A. Eades, J. W. Steeds, and G. M. Rackham, *Phil. Trans. Roy. Soc. London* A281: 171-194, 1976.
4. M. Tanaka, R. Saito, and H. Sekii, *Acta Cryst.* A39: 357-368, 1983a.
5. M. Tanaka, H. Sekii, and T. Nagasawa, *Acta Cryst.* A39: 825-837, 1983b.
6. J. M. Howe and R. Gronsky, *Ultramicroscopy* 18: 83-90, 1985.
7. J. W. Steeds and R. Vincent, *J. Appl. Cryst.* 16: 317-324, 1983.
8. J. Gjønnes and A. F. Moodie, *Acta Cryst.* 19: 65-67, 1965.
9. P. Goodman, *Acta Cryst.* A31: 804-810, 1970.
10. P. Goodman and H. J. Whitfield, *Acta Cryst.* A36: 219-228, 1980.
11. *International Tables for X-ray Crystallography*, Vol. 1, Birmingham, England: Kynoch Press, 1976, 487-489.

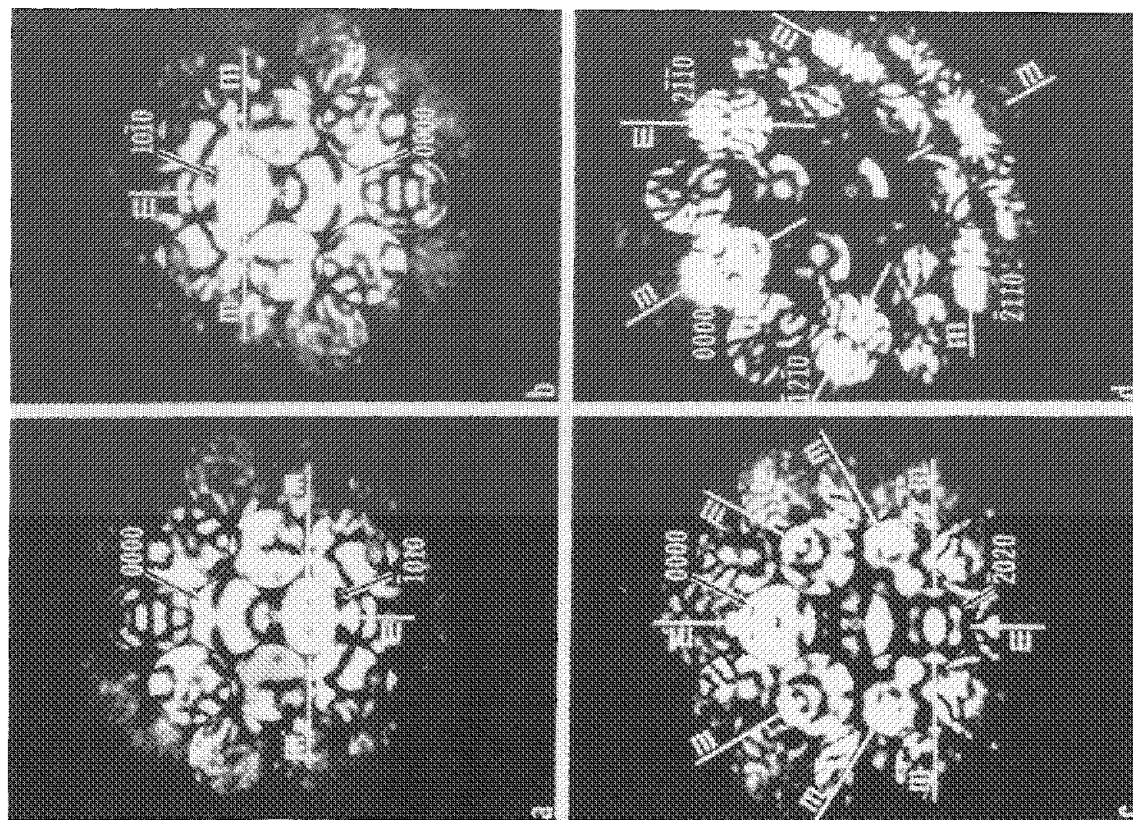


FIG. 3.--CBED patterns from extracted  $\gamma'$ -precipitate in [0001] orientation presenting (a) and (b) single mirror line and  $180^\circ$  rotational symmetry between  $10\bar{1}0$  and  $1010$  disks, respectively; (c) mirror lines in 6-beam pattern with  $10\bar{1}0$  centered on optic axis; (d) symmetric excitation of  $1\bar{1}20$  and  $2\bar{1}\bar{1}0$  reflections with mirrors in all  $11\bar{2}0$  (and  $10\bar{1}0$ ) type disks spaced at  $30^\circ$  intervals.

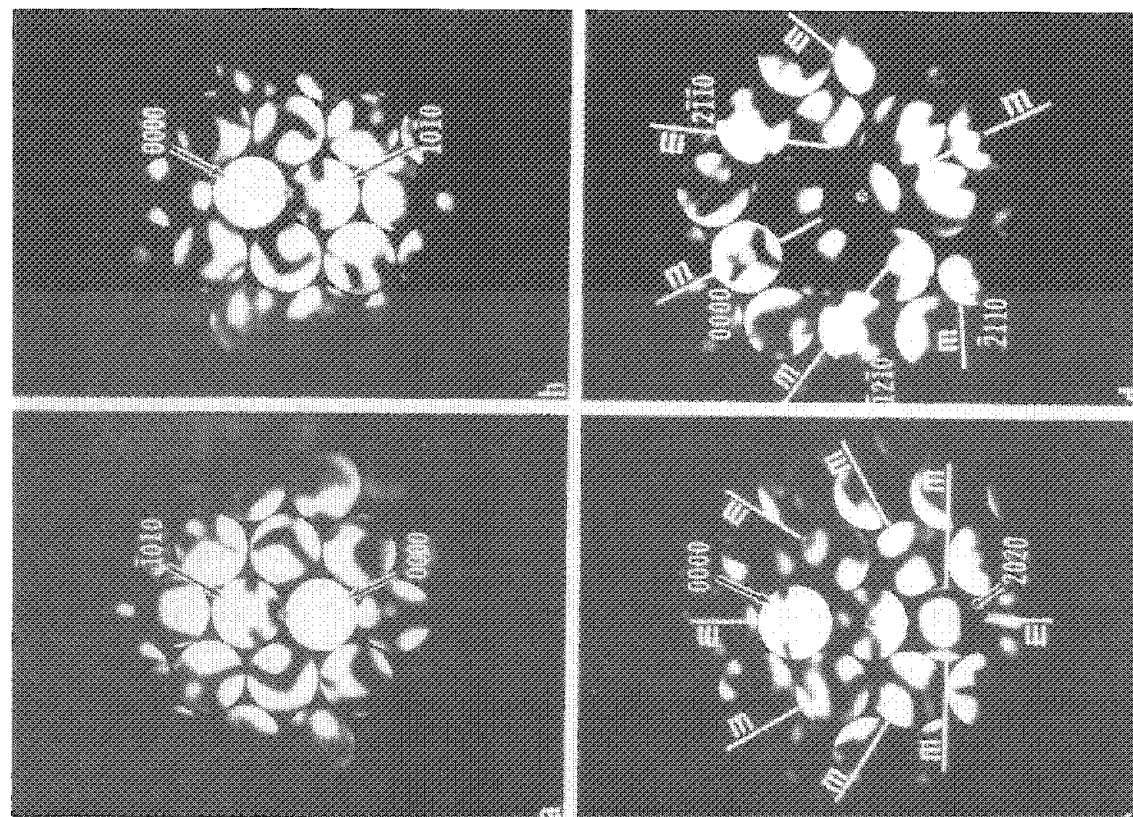


FIG. 4.--CBED patterns for  $\alpha$ -titanium in [0001] orientation showing (a) and (b) 2mm symmetry within  $10\bar{1}0$  and  $10\bar{1}0$  disks located at Bragg positions, respectively; (c) mirror lines in 6-beam pattern with  $10\bar{1}0$  reflection centered on optic axis; (d) symmetric excitation of  $1\bar{1}20$  and  $2\bar{1}\bar{1}0$  reflections with mirror lines in all  $11\bar{2}0$  (and  $10\bar{1}0$ ) type disks spaced at  $30^\circ$  intervals.

## DIGITAL CBED PATTERNS COLLECTED BY EELS

P. M. Budd, P. J. Goodhew, and S. H. Vale

Digital information from electron diffraction patterns is now easily obtainable with the coupling of the multichannel analyzer computer system to the STEM unit of a TEM/STEM.<sup>1</sup> The availability of an EEL spectrometer as well as a STEM detector permits the collection of the pattern over a range of acceptance angles and enables the resolution to be optimized for the pattern of interest. In this paper we discuss the parameters involved and compare the EELS and STEM detectors with respect to obtaining interpretable digital data from CBED patterns.

### *Experimental Procedure*

The experiments were carried out on a Philips EM 400TEM/STEM with a VG ELS80 spectrometer and a LINK Systems AN10000 computer coupled to the STEM unit. The CBED pattern was set up normally on the TEM so that the TEM was image coupled to the EELS. The pattern was then scanned across either the STEM detector or EELS entrance aperture by use of post-specimen deflection coils. For both the STEM detector and EELS the camera length could be varied to optimize the resolution, and the EELS also offered the choice of four entrance apertures (1, 2, 4, and 8 mm in diameter).

A program has been developed in conjunction with LINK Systems to allow the collection of a line profile through a CBED pattern to give on-line thickness values.<sup>2</sup> Line profiles were collected for various camera lengths and EELS entrance aperture diameters.

### *Results and Discussion*

It is well known that for STEM or EELS

$$\text{Angular resolution} \geq \frac{\text{Detector aperture}}{\text{Camera length}}$$

Since the diameter of the detector is fixed for the STEM, the upper limit on resolution is determined by the largest camera length available. However, for EELS both the entrance aperture and camera length can be varied, which provides a greater range of values of resolution. Also, since the STEM detector is positioned considerably above the EELS, one obtains a maximum camera length of  $\sim 2000 \text{ mm}^{-1}$  for the STEM and  $\sim 6500 \text{ mm}^{-1}$  for the EELS. The best resolution obtainable is  $\sim 0.75 \text{ mrad}$  for the STEM and  $\sim 0.15 \text{ mrad}$  for the EELS.

The angle subtended by a disk in a CBED pattern is  $\sim 10 \text{ mrad}$ ; the better the resolution the more thickness fringes can be distinguished in the diffracted disk.

Figure 1 shows two line profiles collected at the same position in the diffracted disk of an aluminum CBED pattern with the STEM detector and the EEL spectrometer. In this case the angular resolution was approximately the same for both, since the camera lengths and entrance apertures were approximately the same. As expected, the two traces give similar information with respect to the number of fringes and their spacings. However, when the camera length is increased by a factor of three for the EELS, with a corresponding change in angular resolution, the pattern obtained in Fig. 2 is obtained. The original STEM pattern is also included for comparison; it can be seen that the same fringe spacing determinations could be determined in each case. Therefore, both techniques have sufficient resolution for an on-line thickness determination to be carried out with the program on the LINK Systems computer.<sup>2</sup> However, if the profile from the EELS in Fig. 2 is examined more closely, Kikuchi lines through the diffracted disk can be distinguished. Measurements of the widths of these lines indicate an angular resolution of  $\sim 0.2 \text{ mrad}$ , which is close to the limit of the resolution obtainable with the EELS for the collection of a

---

Authors Budd and Goodhew are at the Department of Materials Science and Engineering, University of Surrey, Guildford, England GU2 5XH; author Vale is at LINK Systems Ltd., Halifax Road, High Wycombe, Bucks, England HP12 3SE.



CBED pattern.

To conclude, therefore, although the STEM has proved capable of giving adequate resolution for on-line thickness determinations, the EELS has the capacity of superior angular resolution. The EELS also has the added advantage of energy filtering the electron diffraction patterns. It is these advantages that may allow collection of CBED patterns by EELS on-line to give other information that may be interpreted, e.g., relative lattice parameters and changes in symmetry.

### References

1. James Bentley, G. L. Lehman, and A. T. Fisher, "Structural characterization by intensity measurements of electron diffraction patterns," *Analytical Electron Microscopy--1984*, 143-146.
2. P. M. Budd and P. J. Goodhew, "On line analysis of electron diffraction information," *Proc. EMAG 85*, Inst. Phys. Conf. Ser. 78, 55-59.

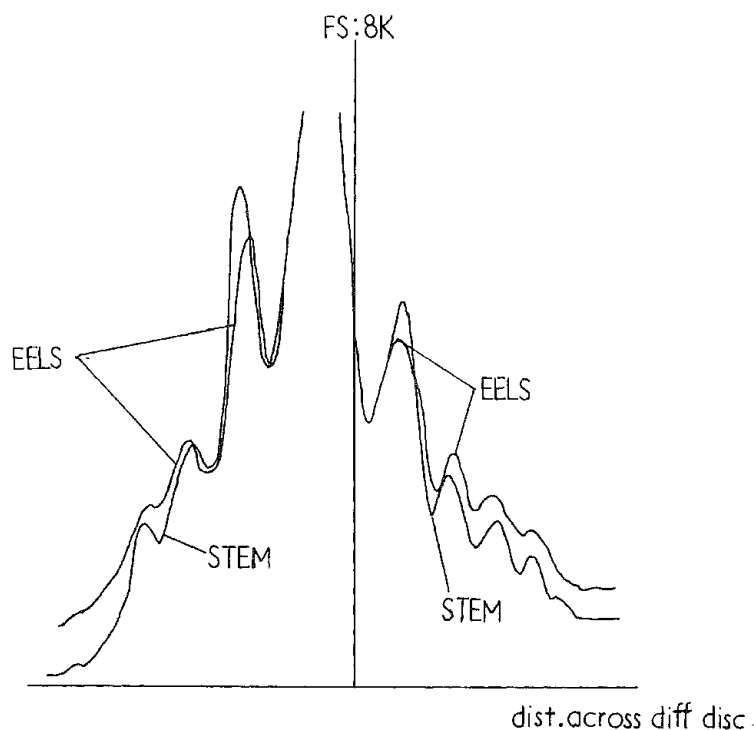


FIG. 1.--Comparison of line profiles collected with STEM and EELS of same camera lengths and detector apertures.

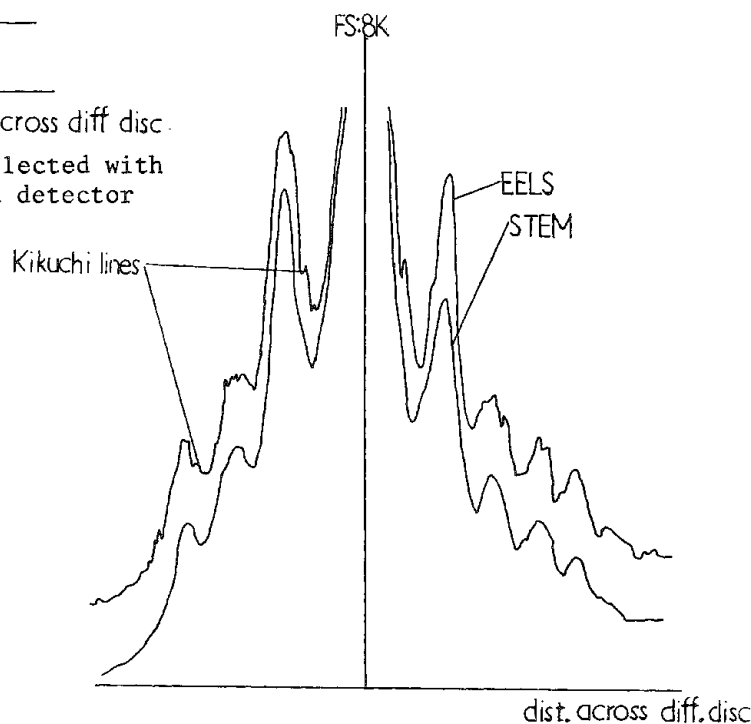


FIG. 2.--Comparison of line profiles collected with EELS at camera length of  $6500 \text{ mm}^{-1}$  compared to  $2000 \text{ mm}^{-1}$  for STEM with same detector aperture.



## PUSHING TOWARD THE LIMITS OF DETECTABILITY IN ELECTRON ENERGY LOSS SPECTROSCOPY

Pieter Kruit

There is no theoretical lower limit for the mass fraction one can detect with electron energy loss spectroscopy, and the theoretical lower limit for the detectable number of atoms is one. If the experimentalist has the patience to wait, at some point in time the signal in his or her energy spectrum will outgrow the statistical noise of the background. Theoretical considerations on the signal rate and the signal-to-background ratio lead us to believe that even this patience can stay within reasonable limits: Isaacson speaks of only a few minutes needed to detect a single iron atom in a 1000 pixel map,<sup>1</sup> and only a 100 s to detect a mass fraction of  $10^{-5}$  for any element in a carbon matrix.<sup>2</sup> Yet in reality, only a few papers have reported the detection of clusters as small as 20 atoms,<sup>3,4</sup> and the measurement of a mass fraction of  $10^{-4}$  is a real exception.<sup>5</sup> Many of the electron energy loss spectrometers in the field are not even used for the detection of small clusters or small mass fractions, but only for identification of the presence of those low-Z elements which cannot be detected by an x-ray microanalysis system. Why is there such a large discrepancy between the theoretical possibilities and the daily reality in the laboratories? In this field of research 100 s data accumulation time is not unusual. Two possible causes remain: because of shortcomings of the instrumentation, the statistics of the information is not as good as theoretically derived; or the information is buried under nonstatistical noise. This paper deals with both problems for the case of a scanning transmission type of microscope. Detection limits in energy-filtered imaging are not discussed. After a short look at the equations for counting statistics, the optimal conditions of the several parts in the microscope is discussed with emphasis on the detector. A detector with parallel collection capability is very necessary for a high information rate, but is also a source of nonstatistical noise. Some methods to eliminate this noise are discussed.

### Counting Statistics

Following Isaacson and Johnson<sup>2</sup> and accepting the criterion for detectability that the signal is at least  $3\times$  the statistics of the background, the minimum detectable mass fraction (MMF) within a measuring time  $\tau$  is:

$$\text{MMF} = 3 \frac{[\sum_j (\eta_B)_j (\sigma_B)_j]^{\frac{1}{2}}}{\eta_p \sigma_p} \frac{1}{(I\tau)^{\frac{1}{2}}} \frac{\exp(\rho T \sigma_0/2) \exp(-\rho T \eta_p \sigma_p)}{(\rho T)^{\frac{1}{2}}} \quad (1)$$

where  $(\eta_B)_j$  is the collection efficiency for the  $j$ -th type of background whose cross section is  $(\sigma_B)_j$ ,  $\eta_p$  is the collection efficiency of the characteristic events whose cross section is  $\sigma_p$ ,  $I$  is the total current in the probe,  $\rho$  is the average mass density of the sample and  $T$  the thickness, and  $\exp(-\rho T \sigma_0)$  is the probability that a background electron is not removed from the beam through a second scattering event. For the purpose of this paper Eq. (1) is simplified to:

$$\text{MMF} = 3 \frac{\sigma_B^{\frac{1}{2}}}{\sigma_p} \frac{1}{\eta^{\frac{1}{2}}} \frac{1}{(J\tau)^{\frac{1}{2}}} \frac{1}{(\frac{1}{4}\pi d^2 T \rho)^{\frac{1}{2}}} \quad (2)$$

in which  $\sigma_B$  is now a total cross section for background events and  $\eta$  is the collection

---

The author is at the Department of Applied Physics, Delft University of Technology, Lorentzweg 1, NL-2628 CJ Delft, The Netherlands. The material presented in this paper is a result of work done with H. Shuman and A. P. Somlyo at the Pennsylvania Muscle Institute. The author gratefully acknowledges their guidance and contributions.

efficiency which is assumed to be about equal for all processes. For samples that are thinner than the total mean free path of the electron, the exponentials disappear from Eq. (1) to yield Eq. (2). The current  $I$  is replaced by  $\frac{1}{4}\pi d^2 J$ , in which  $d$  is the diameter of the probe and  $J$  is the current density in the probe. Equation (2) is essentially the same as used by Cazaux.<sup>6,7</sup> Several authors have analyzed the cross sections  $\sigma_B$  and  $\sigma_p$  and the collection efficiency  $\eta$  quantitatively.<sup>2,8</sup> In this paper the equation is only used to demonstrate the effect of different instrumental solutions.

The relation between minimum detectable mass fraction and minimum detectable mass (MDM) is demonstrated in Fig. 1, where the MMF is set out along the vertical axis and the total exposed mass  $\frac{1}{4}\pi d^2 T \rho$  along the horizontal axis. Certain values for the MDM form diagonal lines in the diagram: for the detection of  $6.6 \times 10^{-23}$  g of calcium (1 atom) one can either expose a mass of  $10^{-18}$  g and detect an MMF of  $6.6 \times 10^{-5}$ , or expose a mass of  $10^{-21}$  g and detect an MMF of  $6.6 \times 10^{-2}$ . Every measurement can now be represented by a point in the diagram, and the influence on the MMF and MDM of every parameter in Eqs. (1) and (2) by a line. Point A stands for a result of Bourret,<sup>3</sup> point B represents a measurement of Shuman et al.,<sup>5</sup> "smaller probe 1" shows the effect of a smaller probe with the current changing according to Eq. 3, and "smaller probe 2" stands for a smaller probe at constant current. The effect of using a thicker or thinner sample is more complex: a very thin sample leads to a small MDM, but Eq. 1 shows that there is an optimum thickness for the MMF which is about equal to the total mean free path of the electrons in the sample.

#### *Electron Source, Accelerating Voltage, and Illumination Optics*

In an optimized probe-forming system, if we neglect the effect of diffraction and chromatic aberration, the current in the probe can be expressed as:

$$I \approx 2d^{8/3} C_s^{-2/3} B_{chr} U \quad (3)$$

where  $d$  is the diameter of the probe,  $C_s$  the coefficient of spherical aberration of the objective lens,  $U$  the accelerating voltage, and  $B_{chr}$  the chromatic brightness of the source. The relation between  $B_{chr}$  and the often used brightness  $B$  is given by  $B_{chr} = B/U$ . The first conclusion that can now be drawn is that increasing the accelerating voltage of the microscope is definitely advantageous for the minimum detectable mass. The smaller scattering angle enables a higher detection efficiency, and according to Eq. (3), the probe current increases. The disadvantage is a loss of signal caused by the decrease of the cross sections. For the minimum detectable mass fraction, only the smaller scattering angle plays a role, because the probe size is of no importance, and in this situation the smaller cross section can be compensated for by a thicker sample, which is convenient anyway. An extra effect of high accelerating voltage is that the cross section of the background often decreases more than the signal cross section.<sup>9</sup>

When Eq. (3) is combined with Eq. (2), it follows that  $MDM \propto d^{2/3}$ , so that it is always advantageous to use a smaller probe in minimizing the detectable mass, even if the current goes down with  $d^{8/3}$ . In many microscopes the smallest size is still determined by instabilities of the beam or by drifts of the specimen holder, especially if measurement times are in the order of minutes. Moreover, delocalization puts a theoretical limit on the minimum probe size: Electrons can inelastically scatter on atoms that are not within the probe! A rule of thumb is that for a characteristic loss of  $\Delta E$  at primary energy  $E_0$ , a probe smaller than  $d_L$  does not improve the results,<sup>10,11</sup> with

$$d_L = \frac{\lambda E_0}{\pi \Delta E} = 0.4 \frac{\sqrt{E_0}}{\Delta E} \text{ [nm]} \quad (4)$$

The fact that the probe current is directly proportional to the chromatic brightness of the source is responsible for everyone's wish for a field-emission gun: an FEG has a chromatic brightness in the order of  $5 \times 10^3$  A/cm<sup>2</sup> sr eV, whereas a tungsten thermionic source has  $B_{chr} \approx 10$  A/cm<sup>2</sup> sr eV. A LaB<sub>6</sub> source can reach a  $B_{chr} \approx 50$  A/cm<sup>2</sup> sr eV. Brightness is of course not the only criterion for comparing sources. For MMF and for filtered imaging the total current can be important: At spot sizes larger than 100 nm a

thermionic source provides a larger total current than an FEG. For microanalysis the energy width of the gun is only important if the intrinsic features of the studied core edges are narrow, like the white lines in many  $L_{23}$  edges. Generally, the energy width does not determine the MMF or MDM.

#### *Pre-spectrometer Optics*

Each double-focusing magnetic spectrometer has an object plane that is imaged on the detector plane. The energy resolution is determined by the size of the crossover in this object plane and, through the spectrometer aberrations, by the opening angle in the object plane. Thus, for a desired energy resolution, the size of the crossover and the opening angle into the spectrometer must be optimized. Pre-spectrometer optics makes it possible. In the spectrometer object plane, there can either be an image of the sample or a diffraction pattern of the sample (magnification coupling and diffraction coupling, respectively). For the maximum detection efficiency the mode of coupling makes no difference.<sup>12</sup> A second-order-corrected spectrometer can have an energy resolution

$$\Delta E \geq 1.3 \frac{1}{\partial x / \partial E} (M_S^3 A_3 \alpha^3 d^3)^{1/4} \quad (5)$$

where  $\partial x / \partial E$  is the dispersion,  $M_S$  the magnification of the spectrometer, and  $A_3$  the third-order aberration of the spectrometer;  $\alpha$  and  $d$  are the opening angle and the size of the spectrometer object, respectively. Given an energy resolution,  $\alpha d$  is then limited. For example, a spectrometer with  $\partial x / \partial E = 4 \text{ } \mu\text{m/eV}$ ,  $M_S = 1.25$ , and  $A_3 = 1.5 \text{ m}$  gives:

$$\alpha d \leq 30 \Delta E^{3/4} \text{ [mrad.}\mu\text{m]} \quad (6)$$

Because of Liouville's theorem this same restriction applies for the accepted scattering angle and the size of the object in the plane of the sample. The "size of the object in the plane of the sample" may be much larger than the probe size, because it includes the aberrations of the pre-spectrometer optics, mainly those of the objective lens. These aberrations are also a function of the scattering angle, so that Eq.(6) can often be read as a restriction on the accepted scattering angle and therefore on the detection efficiency of the system. If the pre-spectrometer optics are not adjusted correctly, the limitations will be more severe than suggested by Eq. (6).

#### *Spectrometer*

The detection efficiency of the spectrometer is a determining factor for the detectable limits. For a certain energy resolution, the aberrations limit the accepted angle and thus the detection efficiency, as discussed in the section above. From this point of view the type of the spectrometer (omega, dipole, or any other) is not important.

#### *Post-spectrometer Optics*

For a high detection efficiency a parallel detector is necessary. The dispersion of the spectrum must be matched to the size of the detector. A typical dispersion in the image plane of the spectrometer is  $4 \text{ } \mu\text{m/eV}$  and a typical size of a 1024-element detector array is 25 mm, which would give a best resolution of 8 eV, if no coupling optics are used. The set of lenses, quadrupoles, and deflectors becomes fairly complicated,<sup>13</sup> but can also be used for the formation of filtered images. For the discussion on detection limits it is worth noticing that long collection times sometimes call for a stabilization of the spectrum on the detector, which can be done for instance by a lock-in on the position of the zero-loss peak.<sup>14</sup>

#### *Parallel Detector*

In theory, one needs to measure only 2 or 3 channels in a spectrum in order to know the signal at the characteristic edge and the pre-edge background. So the gain in efficiency of using a parallel detector would only be a factor of 2 or 3. In practice 10 channels is the minimum and 100 channels is typical. If the shape of the signal and the background are already known, the large number of channels is just a matter of convenience.

If not, the large number is necessary for a correct background extrapolation under the signal peak. A second reason for the use of a parallel detector is the cancellation of beam-current fluctuations. Many systems for parallel collection are possible, but the following discussion will be restricted to criteria for a good detection system and its proper use.

The function of the detector is to get the statistical information that is present in the electron spectrum into the data storage. Usually this process implies an analog to digital conversion somewhere in the system. At that point, four requirements must be fulfilled:

1. Every electron in the energy-loss spectrum must be represented in the signal that is digitized (detective quantum efficiency).
2. The added noise from the readout electronic process and from the detector dark current must be less than the statistical noise.
3. The precision of the A/D conversion must be high enough to measure a signal of the size of the statistical noise.
4. The storage device in the detector must not saturate in between two consequent readouts.

The details and mathematics of these requirements are discussed in a recent paper by Shuman and Kruit.<sup>13</sup> If it is assumed that an electron from the spectrum is at some point represented by an amount of  $G$  electrons in the current pulse which is digitized,  $G$  can be called the gain of the detection system. Requirement (2) calls for a high gain:

$$G(TR_S)^{\frac{1}{2}} > (TR_D + \sigma_R^2)^{\frac{1}{2}} \quad (7)$$

where  $T$  is the time between A to D conversions,  $R_S$  is the signal rate,  $R_D$  is the dark rate, and  $\sigma_R$  is the readout noise. Requirement (3) also calls for a high gain:

$$G(TR_S)^{\frac{1}{2}} > N_{sat}/A \quad (8)$$

where  $N_{sat}$  is the saturation level of the detector and  $A$  is the number of steps of the digitizer. Note here that in order to preserve counting statistics, actual counting is not necessary! Requirement (4) sets a maximum for the gain:

$$GTR_S < N_{sat} \quad (9)$$

These restrictions are demonstrated in Fig. 2 for an available reticon system.

The general conclusion from these considerations is that a parallel detection system can preserve the counting statistics, but only in a limited range of signal rates. This range can be sufficiently enlarged if the detector has an adjustable gain.

At the moment there is a good deal of activity in parallel detectors. Several groups and companies are developing their own systems, some with one-dimensional arrays, others with two-dimensional arrays. The first criterion for all of them is that they must preserve counting statistics for a large range of signal rates.

#### *Data Processing and Spectrum Analysis*

Different elements of a parallel detector can have slightly different gains, for instance because they are of a different size. These differences can be of the order of a few percent, whereas for trace element detection the signal-to-background ratio might be less than 0.1%. Some kind of data processing has to be done before the spectrum can be analyzed. The spatial fluctuations can be reduced if the spectrum is divided by a normalization curve, which can be obtained by homogeneous illumination of the detector. This gain normalization is not totally correct if the intensity of the real spectra along one detector element is not the same as it was for the normalization spectrum. It is expected that the gain normalization is sufficient in the case of a two-dimensional array, where the individual elements are small enough to be illuminated homogeneously in all cases. However, a two-dimensional array calls for fast processing of two-dimensional images. If this direct normalization is impossible, several other solutions are available.<sup>13</sup> These solutions are all based on the use of a single detector element to record several channels

of the spectrum, by shifting of the spectrum over the detector. The preferred method is then to shift the spectrum many times over a distance of exactly one detector element. In the software the spectra are shifted back and added, so that the element-to-element gain variations are averaged. An alternative is to find the normalization curve from the spectral measurement itself. If two identical spectra are subsequently collected with a relative shift of exactly one element, the relative gain of neighboring detector elements is obtained by division of one spectrum by the other. A drawback of this method is that errors in the relative gain of two neighboring elements may accumulate for the determination of two elements which are far apart, because of the recursive nature of the method. A third method for reduction of element-to-element gain variations is subtracting in a straightforward manner two spectra that have been recorded with a small shift. The result is a first difference of the energy-loss spectrum that has a much higher signal-to-background ratio than the spectrum itself, so that the gain variations have a correspondingly smaller effect. It is possible to obtain a second difference spectrum in a similar fashion. An additional advantage of the first and second difference method is that small features are more easily identified in the spectrum, because the background is effectively subtracted. This effect is similar to that of a digital filter,<sup>15</sup> which is sometimes used for fast recognition of the presence of an element. The disadvantage is a loss of statistical information. If the characteristic feature is not narrower than the spectral shift (or the width of the digital filter), signal is subtracted from signal and lost forever.

The result of these efforts is that it has been shown possible to get information from a spectrum with as many as  $10^7$  electrons per channel, so that the ratio of statistics to background per channel is 0.03% (Fig. 3).

The next step in data processing is the quantification of the result. When we speak of detectable limits, quantification just means: is the element there or not? The huge background is clearly a problem here, because it is so easy to "recognize" the long-expected characteristic peaks in a small blip in that background! In order to determine the presence of characteristic signal in case the signal is distributed over several channels, it is best to perform a multiple regression fit to standards, as is known from x-ray analysis. The development of good procedures for this method is still in progress.

### *Coincidence Counting*

Clearly the problem with EELS is the large background in the spectrum. A decrease of this background can in principle be obtained by detection of the energy loss events in coincidence with x rays or Auger electrons. A recent experiment has shown that at the present state of the art, the use of coincidence between EELS and x ray for this purpose is very limited, mainly due to the low detection efficiency of x-ray detectors.<sup>16</sup> The further development of Auger analysis in electron microscopes might lead to new possibilities for coincidence measurements.

### *Conclusions and Outlook*

The practical limits of detectable mass fraction and total mass are at least an order of magnitude away from the theoretical possibilities. The reasons are all connected with experimental difficulties. In the best experimental set-up for a small MDM, clusters of 10-50 atoms are now detected. In the best set-up for a small MMF, a fraction of  $10^{-4}$  is measured. It may take some time before these values are generally obtained. In the meantime we can expect new developments in instrumentation: the combination of a bright electron source with a medium high voltage (300-400kV) microscope, post-spectrometer optics for easy conversion between spectral acquisition and filtered imaging, new parallel detector systems (probably two-dimensional arrays) that guarantee preservation of statistics, and perhaps most important, hardware and software for convenient processing of spectra and images.

### *References*

1. M. Isaacson and M. Utlaut, "On the chemical identification of individual atoms," *Proc. 37th Mtg. EMSA*, 1979, 524-525.
2. M. Isaacson and D. Johnson, "The microanalysis of light elements using transmitted energy-loss electrons," *Ultramicroscopy* 1: 33-52, 1975.

3. A. Bourret and C. Colliex, "Combined HREM and STEM-microanalysis on decorated dislocation cores," *Ultramicroscopy* 9: 183-190, 1982.
4. C. Colliex and P. Trebbia, "Performance and applications of electron energy-loss spectroscopy in STEM," *Ultramicroscopy* 9: 259-266, 1982.
5. H. Shuman et al., "Quantitative electron energy-loss spectroscopy of low concentrations of calcium in carbon containing matrices," *Microbeam Analysis--1983*, 247-251.
6. J. Cazaux, "Another expression for the minimum detectable mass in EELS, EPMA and AES," *Ultramicroscopy* 12: 83-86, 1983.
7. J. Cazaux, "Detection limits in Auger electron spectroscopy," *Surf. Sci.* 140: 85-100, 1984.
8. D. C. Joy and D. M. Maher, "Electron energy-loss spectroscopy: Detectable limits for elemental analysis," *Ultramicroscopy* 5: 333-342, 1980.
9. Y. Bando et al., "The usefulness of a 400 kV high resolution analytical electron microscope," *Ultramicroscopy* 18: 117-124, 1985.
10. C. Colliex, "An illustrated review of various factors governing the high spatial resolution capabilities in EELS microanalysis," *Ultramicroscopy* 18: 131-150, 1985.
11. M. Isaacson et al., "Determination of the nonlocalization of the inelastic scattering of electrons by electron microscopy," *Optik* 41: 92-96, 1974.
12. P. Kruit and H. Shuman, "The influence of objective lens aberrations in energy-loss spectrometry," *Ultramicroscopy* 17: 263-268, 1985.
13. H. Shuman and P. Kruit, "Quantitative data processing of parallel recorded electron energy-loss spectra with low signal to background," *Rev. Sci. Instrum.* 56: 231-239, 1985.
14. P. Kruit and H. Shuman, "Position stabilization of EELS spectra," *J. Electron Microscopy Technique* 2: 167-169, 1985.
15. J. Zaluzec, "Digital filters for application to data analysis in electron energy-loss spectrometry," *Ultramicroscopy* 18: 185-190, 1985.
16. P. Kruit et al., "Detection of x-rays and electron energy-loss events in time coincidence," *Ultramicroscopy* 13: 205-214, 1984.

FIG. 2.--Operation limits for a system with 14-bit ADC ( $A = 16384$ ),  $T = 8.5$  ms (for 512 elements that means 60 000 conversions/s),  $N_{\text{sat}} = 8.7 \times 10^7$  electrons.<sup>13</sup>

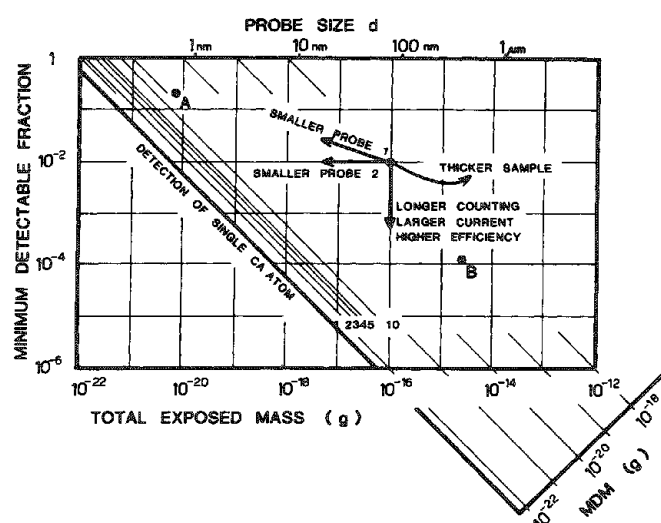


FIG. 1.--Influence of instrumental parameters on detection limits in EELS. Upper horizontal scale shows probe diameter connected with total exposed mass of lower horizontal scale for carbon film 10 nm thick.

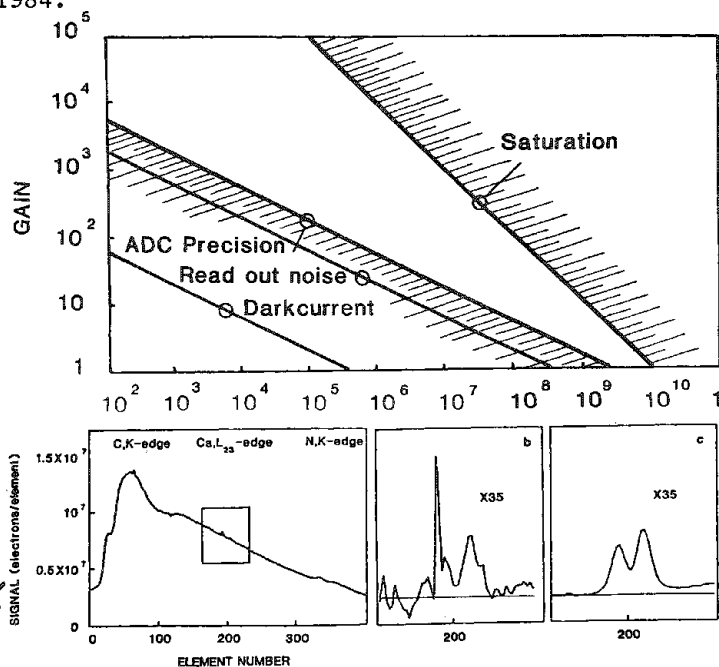


FIG. 3.--(a) Electron energy loss spectrum measured with parallel detector. (b) Detail from spectrum with smooth background subtracted. (c) Same detail but from spectrum consisting of sum of 59 shifted spectra, so that element-to-element gain variations are averaged.<sup>13</sup>

## ANALYSIS OF SEMICONDUCTOR EELS IN THE LOW-LOSS REGIME

M. K. Kundmann

The low-loss regime (0-100 eV) in electron energy-loss spectra has largely been ignored by the AEM community. This neglect is due to its complexity and the dominance of plasmons, collective excitations generally considered void of information for chemical microanalysis, in this region. However, the low-loss regime contains by far most of the inelastic events recorded in an energy-loss spectrum (ELS) and is of interest to those who must work with the low total signal levels inherent to micro-area (<10nm) analysis.<sup>1,2</sup> For many materials, low-loss core edges do occur, but they are often masked by strong plasmon peaks. In addition, multiple scattering further complicates the low-loss background. The  $\text{Al}_x\text{Ga}_{1-x}\text{As}$  spectrum in Fig. 1 is a typical example. These difficulties have prevented use of the relatively intense signal (compared to that of higher-energy edges) provided by low-energy edges.<sup>3</sup>

A method of analysis that overcomes the above difficulties and allows the structure of spectra such as that of Fig. 1 to be unraveled is described here. The method has been so far applied only to semiconductors, but is likely to be applicable to some metals as well. The analysis involves two steps, multiple scattering correction followed by plasmon-background modeling and subtraction. The validity of these procedures depends upon the experimental conditions under which spectra are collected; hence a brief description of the experimental set-up used to acquire spectra follows.

### *Experimental*

The instrumentation used consists of a Gatan 607 (serial) electron energy-loss spectrometer attached to a Phillips EM400 microscope retrofitted with a twin-lens objective. All spectra were collected at 120 kV in image mode with  $\sim 20,000\times$  magnification and a 1mm spectrometer aperture. No objective aperture was used, hence the collection angle was  $\sim 100$  mrad. Strong elastic scattering was avoided by tilting away from high-symmetry axes and exciting as few Bragg beams as possible. Specimens were prepared by standard grinding and ion-milling techniques.

### *Multiple Scattering Correction*

Methods for the removal of multiple scattering from the ELS are well documented in the literature.<sup>4,5</sup> However, the method used and the details of its implementation vary from one laboratory to the next. Since these details can significantly affect the final result, the actual procedures found to work best for this analysis are described below. Multiple scattering correction can only be accurately applied to data that have not had multiple scattering partially removed through use of a restricted collection angle. This is the motivation for operating without an objective aperture.

The basis of the correction procedure is complete logarithmic deconvolution.<sup>4</sup> For finite, discrete spectra comprised of  $N$  data points, the Fourier transform (FT)  $s^1$  of the normalized single-scattering probability distribution is given by

$$s_i^{-1} = \frac{\lambda}{Nt} \ln \left( \frac{S_m^i}{Z_m^i} \right), \quad i = 0, N-1$$

where  $\lambda$  is the mean free path for inelastic scattering,  $t$  is the specimen thickness,  $S_m$  is the FT of the measured ELS (not normalized)  $k$  and  $Z_m$  is the FT of the zero-scattering part of the measured ELS. The subscript  $i$  indicates the  $i^{\text{th}}$  element of the discrete FT.<sup>6</sup> In-

The author is at Lawrence Berkeley Laboratory, Bldg. 77G, University of California, Berkeley, CA 94720. He should like to thank his supervisor, Prof. Ron Gronsky, for his support and enthusiastic encouragement. He also thanks Dr. C. Ahn and Dr. K. Krishnan for helpful discussions and Dr. T. Sands for providing specimens. This work is supported by the U.S. Department of Energy (Materials Science Division) under Contract DE-AC03-76SF0098.

put to the algorithm can be simplified by direct calculation of  $S^1$ , the FT of the (non-normalized) single-scattering part of the measured ELS

$$S_i^{-1} = \frac{t}{\lambda} I_0 s_i^{-1} = \frac{Nt}{\lambda} Z_0^m s_i^{-1} = Z_0^m \ln \left( \frac{S_1^m}{Z_0^m} \right)$$

where  $I_0$  is the integral of zero-scattering counts contained in the measured ELS. Inverse Fourier transformation of  $S^1$  yields the ELS with multiple scattering removed.

Although this algorithm is simple, its straightforward application leads to noise and artifact oscillations in the final result. To minimize noise, the zero-scattering in the measured ELS is removed and replaced by a (discrete)  $\delta$ -function.<sup>5</sup> This procedure also simplifies the algorithm for  $S^1$  to

$$S_i^{-1} = Z_0^m \ln \left( 1 + \frac{\hat{S}_1^m}{Z_0^m} \right)$$

where  $\hat{S}^m$  is the FT of the measured ELS with zero-scattering removed. The spectrometer resolution function is not deconvoluted by this method, but due to the natural breadth of features in semiconductor low-loss spectra this is a small error. One obtains the modified input  $\hat{S}^m$  by fitting a hole-count zero-scattering peak to that of the measured ELS. The fit is subtracted and residuals are set to zero. The integral of the fit divided by  $N$  provides the value of  $Z_0^m$ . One avoids artifact oscillations by making the periodic extension of the measured spectrum (the implicit input to any discrete FT<sup>6</sup>) continuous, by extending the spectral range and appending a parabolic tail to the measured spectrum. The parabolic tail is chosen to match the slope and value of the spectrum in the last measured channel and to cross zero intensity with zero slope.

The final result of the multiple scattering correction procedure is shown for spectra from Si and  $\text{Al}_x\text{Ga}_{1-x}\text{As}$  in Figs. 2 and 3, respectively.

#### *Plasmon-background Modeling and Subtraction*

After removal of multiple scattering, the distinct components of a low-loss spectrum can be resolved. For most semiconductors, the dominant component is the bulk plasmon peak. This peak can be accurately modeled and removed by use of the dielectric response theory<sup>7</sup> of fast-particle energy loss in solids. According to this theory, the probability per unit time that a fast charged particle (initial energy  $E_0$ ) traversing a solid at velocity  $\vec{v}$  loses energy in the range  $\hbar\omega (= E)$  to  $\hbar(\omega + d\omega)$  and transfers momentum in the range  $\hbar\vec{q}$  to  $\hbar(\vec{q} + d\vec{q})$  is given by

$$P(\omega, \vec{q}) d\omega d\vec{q} = \frac{e^2}{\pi^2 \hbar^2 q^2} \text{Im} \left\{ \frac{-1}{\epsilon(\omega, \vec{q})} \right\} \delta(\omega - \vec{q} \cdot \vec{v}) d\omega d\vec{q}$$

where  $\epsilon(\omega, \vec{q})$  is the complex dielectric function of the solid and  $\delta(\omega - \vec{q} \cdot \vec{v})$  takes account of energy and momentum conservation. Since the collected spectra are integrated over scattering angle, it is the integral over momentum transfer,  $\vec{q}$ , that is required. This integral can be carried out because  $\epsilon(\omega, \vec{q})$  is practically constant and equal to  $\epsilon(\omega, 0) \equiv \epsilon(\omega)$  for the range of momentum transfers that contribute significantly to the low-loss inelastic scattering at 120 kV. The characteristic scattering angle  $\theta_{E_0} = E/2E_0$  indicates that typical momentum transfers in the low loss are  $\sim 10^6 \text{ cm}^{-1}$ . However,  $\epsilon$  only varies appreciably for  $|\vec{q}| \sim 10^8 \text{ cm}^{-1}$ , a typical Brillouin zone or Fermi wavevector. Factoring out  $\text{Im}\{-1/\epsilon(\omega)\}$  and integrating over  $d\vec{q}$  yields<sup>8</sup>

$$P(\omega) d\omega = \frac{2e^2}{\pi \hbar v} \text{Im} \left\{ \frac{-1}{\epsilon(\omega)} \right\} \ln \left( \frac{2E_0}{\hbar\omega} \right) d\omega$$

$P(\omega)$  is directly proportional to the observed single-scattering low-loss spectrum. For many semiconductors, a very good approximation to  $\epsilon(\omega)$  is<sup>9</sup>

$$\epsilon(\omega) = \epsilon_c + \frac{E_p^2}{(E_g^2 - E^2) - i\Gamma E}$$



where  $\epsilon_c$  is the core electron contribution to the dielectric constant,  $E_p$  is the free-electron equivalent plasmon energy of the valence electrons,  $E_g$  is an "average" band gap of the semiconductor, and  $\Gamma$  is the plasmon damping parameter, which roughly gives the plasmon peak width. Substitution of  $\epsilon(\omega)$  into the expression for  $P(\omega)$  yields the functional form used to model the semiconductor plasmon peak

$$I_p(E) = P \left( \frac{E}{\hbar} \right) = \frac{2e^2 \Gamma E_p^2}{\pi \hbar V \epsilon_c^2} \frac{E \ln(2E_0/E)}{[E_g^2 + (E_p^2/\epsilon_c) - E^2]^2 + \Gamma^2 E^2} = \frac{C_1 E \ln(2E_0/E)}{(C_2 - E^2)^2 + C_3 E^2}$$

This three-parameter functional form gives an excellent fit to semiconductor plasmon peaks as illustrated for Si and  $\text{Al}_x\text{Ga}_{1-x}\text{As}$  in Figs. 4 and 5, respectively. The small deviation below the main peak is due to Čerenkov and surface plasmon losses, which are not included in the above approximation of  $\epsilon(\omega)$ . These neglected excitations do not extend beyond the bulk plasmon peak and thus do not affect the extraction of edges. Figure 6 shows the result of subtracting the modeled plasmon peak from the low-loss  $\text{Al}_x\text{Ga}_{1-x}\text{As}$  spectrum. The Ga M<sub>IV,V</sub> (3d ionization) edge, although initially indiscernible, is cleanly extracted.

### Discussion

The preceding shows how complicated semiconductor low-loss spectra can be resolved into bulk valence plasmon and core ionization components. Although low-energy edges can apparently be cleanly extracted, it remains to be seen whether they are useful for microanalysis. Figure 7 shows some preliminary results in which the extracted edges from a pure GaAs specimen are compared to those of the  $\text{Al}_x\text{Ga}_{1-x}\text{As}$  specimen analyzed above. These spectra have been roughly normalized to their As edge integrals. From other information it is known that  $1 - x$  is greater than 0.5 for this specimen. However, that is not borne out by the ratio of Ga edges in Fig. 7. Another question worthy of pursuit is whether the precision with which the plasmon can be modeled might be harnessed to measure changes in the valence electron properties of inhomogeneous specimens. Since the plasmon model involves fundamental, rather than empirical, parameters, this would seem to be a good possibility.

### References

1. M. Scheinfein, A. Muray, and M. Isaacson, "EELS across a metal-insulator interface at sub-nanometer spatial resolution," *Ultramicroscopy* 16: 233, 1985.
2. O. L. Krivanek and Z. Liliental, "High resolution microanalysis of semiconductor interfaces," *Ultramicroscopy* 18: 355, 1985.
3. O. L. Krivanek and S. L. Fortner, "HREM imaging and microanalysis of a III-V semiconductor/oxide interface," *Ultramicroscopy* 14: 121, 1984.
4. D. W. Johnson and J. C. H. Spence, "Determination of the single-scattering probability distribution from plural-scattering data," *J. Phys.* D7: 771, 1974.

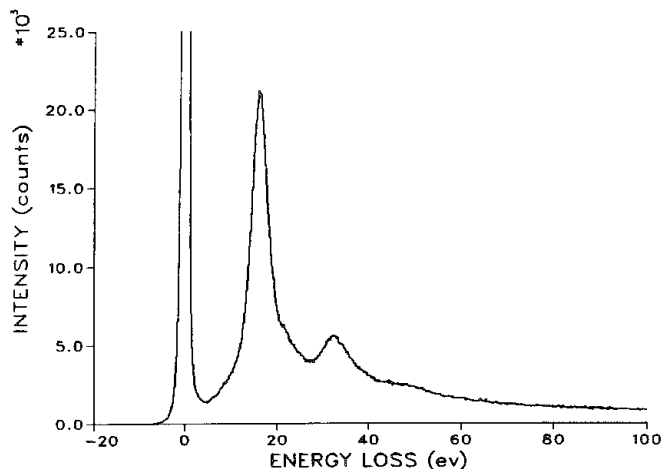


FIG. 1.--Low-loss EELS from  $\text{Al}_x\text{Ga}_{1-x}\text{As}$ ,  $x$  unknown.

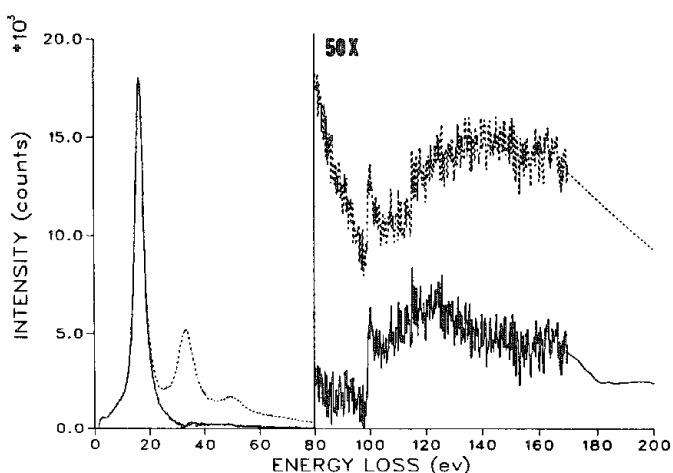
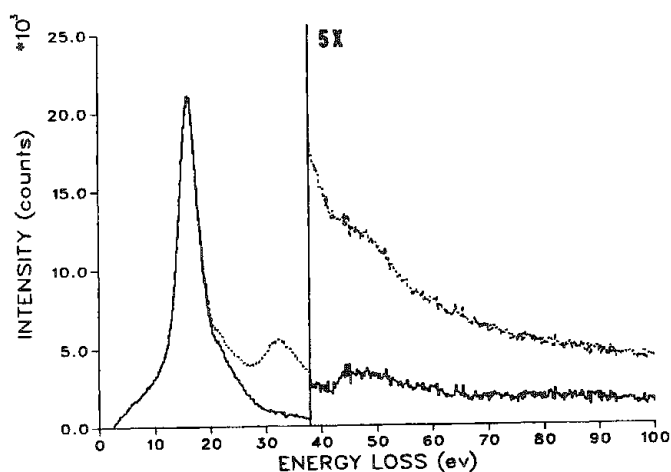
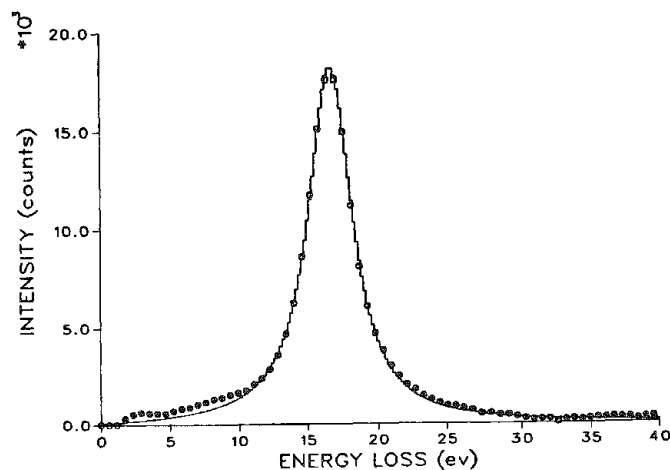


FIG. 2.--Dotted curve: measured ELS from crystalline Si, zero scattering removed; solid curve: extracted single-scattering ELS.

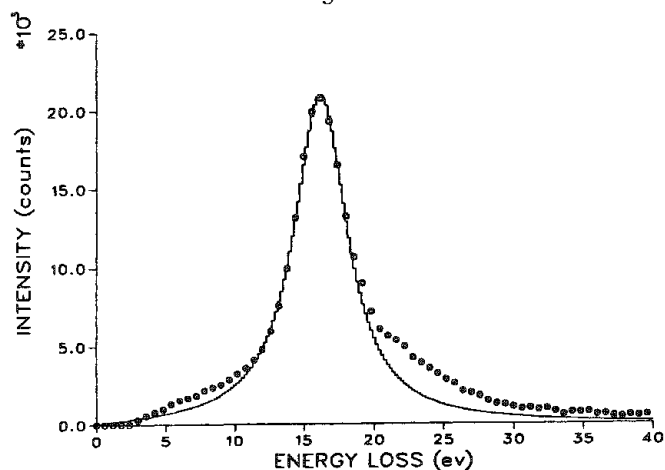
5. R. D. Leapman and C. R. Swyt, "Electron energy-loss spectroscopy under conditions of plural scattering," *Analytical Electron Microscopy--1981*, 164.
6. R. C. Gonzalez and P. Wintz, *Digital Image Processing*, Reading, Mass.: Addison-Wesley, 1977, 41.
7. D. Pines, *Elementary Excitations in Solids*, New York: W. A. Benjamin, 1963, 121.
8. H. Fröhlich, "Phenomenological theory of the energy loss of fast particles in solids," in W. Frank, Ed., *Max Planck Festschrift*, Berlin: Deutscher Verlag, 1958, 277.
9. H. Raether, *Excitation of Plasmons and Interband Transitions by Electrons*, Springer-Verlag, 1980, 1-33.



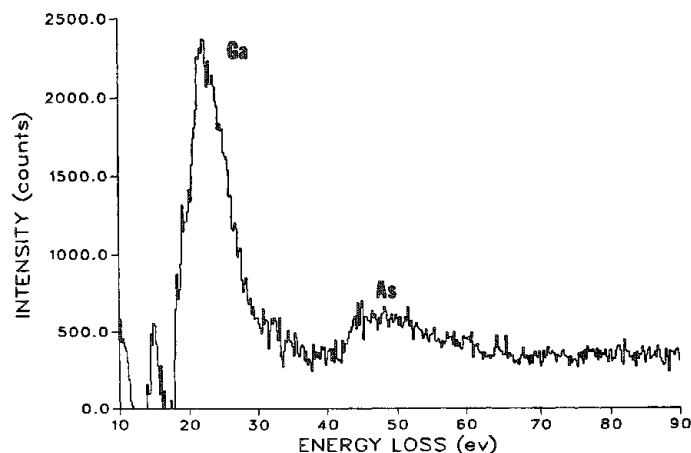
3



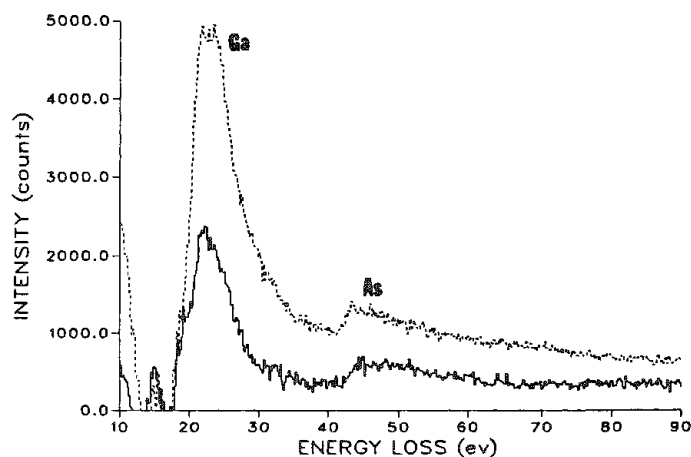
4



5



6



7

FIG. 3.--Dotted curve: measured ELS from MBE-grown  $\text{Al}_x\text{Ga}_{1-x}\text{As}$ , zero scattering removed; solid curve: extracted single-scattering ELS. FIG. 4.--Circles: experimental single scattering ELS; solid curve: fit to plasmon peak by use of  $P(\omega)$ . FIG. 5.--Dotted curve: experimental  $\text{AlGaAs}$  single-scattering ELS; solid curve: fit to plasmon peak by use of  $P(\omega)$ . FIG. 6.--ELS of Fig. 5 after plasmon fit subtraction. FIG. 7.--Edges extracted from GaAs (dotted) and  $\text{Al}_x\text{Ga}_{1-x}\text{As}$  (solid); normalized to As edges.

## WHITE LINES IN THE ELECTRON ENERGY LOSS SPECTRA OF 3d TRANSITION METALS

Peter Rez, W. G. Waddington, I. P. Grant, and C. J. Humphreys

The electron energy loss edges for the 2p excitation in the 3d transition metals are marked by two sharp peaks rather than the smoothly varying cusp or hump seen in other elements. These peaks are due to transitions from the 2p states which are split by spin orbit coupling to empty 3d states. The less deeply bound  $2p^{3/2}$  state gives rise to the first peak and is called the  $L_3$  excitation by spectroscopists; the other peak or  $L_2$  excitation arises from transitions from the  $2p^{1/2}$  state. As these peaks were first observed photographically in x-ray absorption spectroscopy, they appeared as white lines on the photographic film. Although counting techniques have superseded photographic recording, the name has remained.

There are twice as many  $2p^{3/2}$  states as the more deeply bound  $2p^{1/2}$  states, so it would be expected that the intensity of the first white line due to  $2p^{3/2}$  transitions is twice that of the second white line due to  $2p^{1/2}$  transitions. This ratio is not observed in practice<sup>1</sup>; the ratio varies from about 1:1 for elements such as calcium and scandium to about 3:1 for ionized copper.

Similar effects are seen in the energy loss spectra of the 3d ( $M_{4,5}$ ) edge in rare earth oxides<sup>2</sup> where the ratio of the  $3d^{5/2}$  ( $M_5$ ) peak to the  $3d^{3/2}$  ( $M_4$ ) peak is not 3:2 as expected from initial state occupation. In the rare earths the transitions are from a filled d orbital to the partially filled f states. Although there were some early observation of these anomalous ratios in the x-ray absorption spectroscopy<sup>3</sup> of the rare earths, it is only recently that the  $L_{2,3}$  edge in the transition metals has been studied by synchrotron radiation.<sup>4</sup> This study has led to a resurgence of interest in theoretical explanation of the effect.

The earliest work is based on an atomic multiplet approach due to Sugar<sup>5</sup> and was applied with some success to  $M_{4,5}$  edges in rare earth elements near the ends of the period. The allowed arrangements of the electrons in the d and f shells were tabulated and transition strengths calculated assuming that spin orbit and electrostatic interactions are perturbations on an essentially nonrelativistic Schrödinger equation. This method has been extended to the  $L_{2,3}$  excitations by Zaanen et al.<sup>6</sup> As there are many possible configurations in elements with half-filled shells it becomes difficult to consider all possible transitions.

An alternative approach to white line ratios has been developed by Mattheis and Deitz,<sup>7</sup> who used a relativistic LCAO method to calculate the energy bands. They leave the number of holes in the two bands associated with the spin orbit components as a parameter that can be fixed by accurate calculation of the Fermi level or by experiment.

### Theory

Our approach is in many ways similar to the atomic multiplet theory. We applied the multiconfiguration Dirac-Fock program of Grant et al.<sup>8</sup> to the calculation of  $L_3$  and  $L_2$  line strengths in the 3d transition metals. It is purely an atomic theory and takes no account of band-structure, molecular-orbital, or other solid-state effects. Possible changes in cation charge (which result in changes in d state occupation) are taken into account. This can be justified as a first approximation because the d wavefunctions are relatively localized and the d bands are quite narrow.

Unlike the atomic multiplet calculation the multiconfiguration Dirac-Fock program

---

Author Rez is at Arizona State University, Center for Solid State Science and Department of Physics, Tempe, AZ 85287; author Waddington is at the University of Oxford, Department of Earth Sciences, Parks Road, Oxford, England OX1 3PR; author Grant is at the University of Oxford, Department of Theoretical Chemistry, South Parks Road, Oxford, England; author Humphreys is at the University of Liverpool, Department of Metallurgy and Materials Science, P.O. Box 147, Liverpool, England L69 3BX.

FIG. 1.--Comparison of calculated spectra (dashed lines) with EELS Atlas experimental spectra (solid lines): (a)  $\text{Sc}^{3+}$  calculated,  $\text{Sc}_2\text{O}_3$  experimental; (b)  $\text{Cr}^{4+}$  calculated,  $\text{Cr}^{3+}$  experimental; (c)  $\text{Fe}^{3+}$  calculated,  $\text{Fe}_2\text{O}_3$  experimental; (d)  $\text{Ni}^{2+}$  calculated,  $\text{NiO}$  experimental.

$$L_3/L_2$$

FIG. 2.--Variation of white-line intensity ratio with d state occupation: calculated results,  $\Delta$  Sparrow et al.,<sup>14</sup>  $\nabla$  Leapman et al.,<sup>1</sup>  $\bullet$  EELS Atlas,<sup>2</sup>  $\diamond$  Miner and Rask.<sup>13</sup>

3d STATE OCCUPANCY

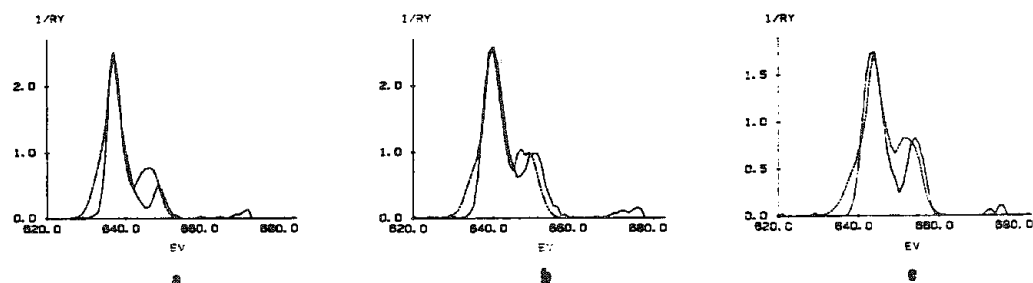


FIG. 3.--Comparison of calculated spectra (dashed lines) with spectra for Mn (solid lines) from Miner and Rask:<sup>13</sup> (a)  $\text{Mn}^{2+}$  in  $\text{MnO}$ , (b)  $\text{Mn}^{3+}$  in  $\text{Mn}_2\text{O}_3$ , (c)  $\text{Mn}^{4+}$  in  $\text{MnO}_2$ .

treats the electrostatic and spin orbit interactions as part of the Dirac formalism, so that there is no need to consider them separately by perturbation theory. It also generates all the possible configurations of spin up and spin down electrons in the partially occupied d shell automatically. As there can be many hundreds of possibilities for elements such as Cr and Mn with half-filled shells, this is a very convenient feature. Another significant difference is that we do not arbitrarily scale the electrostatic or spin orbit interactions to fit experiment.<sup>5,6</sup>

The line strengths were calculated by use of a program due to Dyal and Grant<sup>9</sup> and the lines were convoluted with a Gaussian representing life time and instrumental broadening for comparison with experiment. The main mechanism of life-time broadening is Auger recombination, which is usually of the order of 0.5 eV, much less than the instrumental broadening of about 1.5 eV for EELS atlas data.<sup>2</sup> For comparison of our calculated  $L_3$  and  $L_2$  profiles with experiment we have taken spectra from the EELS atlas.<sup>2</sup> These spectra were usually taken from oxides and so the transition metal cation is in a charged state. The background under the edge was first subtracted by use of the standard  $AE^{-r}$  fit, where A and r are arbitrary constants and E is the energy loss. The continuum contribution was then subtracted by fitting of the results of Hartree-Slater calculations<sup>10</sup> to a region 20-40 eV above the peak. Although the starting energy for the continuum contribution is to some extent arbitrary, that made less than 5% difference to the ratio of  $L_3$  and  $L_2$  line strengths.

## Results

The  $L_3$  and  $L_2$  lines calculated by the multiconfiguration Dirac-Fock program are compared with the experimental spectra in Fig. 1 for  $Sc^{3+}$ ,  $Cr^{4+}$ ,  $Fe^{3+}$ , and  $Ni^{2+}$ . The main trend to notice is the change in the  $L_3/L_2$  ratio from about 1:1 or less for  $Sc^{3+}$  in  $Sc_2O_3$  to over 3:1 for  $Ni^{2+}$  in  $NiO$ . The ratio of white-line heights is most closely related to the number of electrons in the d shell; the white-line ratios from these calculations and a number of experimental sources are plotted as Fig. 2. The disagreements among different experiments appear greater when the ratio is much more than 1 as the  $L_2$  peak has low intensity. Any line-height measurements therefore have a correspondingly greater error.

Results for  $Ca^{2+}$  in  $CaCO_3$  and  $Ti^{4+}$  in  $TiO_2$  are very similar to the result shown for  $Sc^{3+}$  in  $Sc_2O_3$ . In all cases the theoretical ratio is slightly greater than that observed experimentally and both the peaks are split into two components. This splitting is due to transitions to different molecular orbitals.<sup>11</sup> The spectrum for Cr (Fig. 1b) shows the correct white-line intensity ratio though the details of the calculated structure do not match the experimental result. There is some uncertainty in the charge state of Cr in the experiment; it is likely that in this case solid-state effects should also be taken into account in the calculation. Similar considerations apply in the result for  $Fe^{3+}$  (Fig. 1c), which is compared to the experimental result for  $Fe_2O_3$ . The results for  $Ni^{2+}$  show excellent agreement with the experimental results for Ni in  $NiO$ . Calculations for  $Co^{2+}$  and  $Cu^{2+}$  show similar agreement with experimental spectra. A complete tabulation of the results for white-line ratios for different charge states is given by Waddington et al.<sup>12</sup>

It is of some interest to determine whether the white-line ratios can be used to measure the charge state of the cation. In our calculations we found that the white-line ratio is only sensitive to charge for Cr and Mn which have half-filled d bands. In Fig. 3 the results of calculations for  $Mn^{2+}$  in  $MnO$ ,  $Mn^{3+}$  in  $Mn_2O_3$ , and  $Mn^{4+}$  in  $MnO_2$  are compared with the experimental data of Miner and Rask<sup>13</sup> at 4eV resolution. The decrease in white-line intensity ratio with increasing charge is apparent from both calculated and experimental spectra. The same sensitivity to charge is shown for calculated spectra for  $Cr^{3+}$  and  $Cr^{4+}$  for 3eV resolution given as Figs 4(a) and (b). For comparison purposes the individual lines making up these spectra are shown as Figs. 4(c) and (d).

## Conclusions

We have shown that multiconfiguration Dirac-Fock calculations of  $L_3$  and  $L_2$  white-line profiles in the 3d transition metals show good agreement with experimental results. This result confirms that the dominant effects determining white-line intensities are purely atomic. In particular, our calculations show the trend of increasing  $L_3/L_2$  ratio with

increasing d state occupation. We also show that for elements with half-filled d shells such as Cr and Mn the  $L_3:L_2$  white-line ratio is sensitive to cation charge. To predict the structure of the individual white-line components it will be necessary to take into account solid state or molecular orbital effects.

### References

1. R. D. Leapman, L. A. Grunes, and P. L. Fejes, *Phys. Rev.* B26: 614, 1982.
2. C. C. Ahn and O. L. Krivanek, *EELS Atlas*, ASU HREM Facility and Gatan, 1982.
3. C. Bonelle, R. C. Karnatak, and J. Sugar, *Phys. Rev.* A9: 1920, 1974.
4. J. Barth, F. Gerken, and C. Kunz, *Phys. Rev.* B28: 3608, 1983.
5. J. Sugar, *Phys. Rev.* A6: 1764, 1972.
6. J. Zaanen, G. A. Sawatzky, J. Fink, W. Speier, and J. C. Fuggle, *Phys. Rev.* 32B: 4905, 1985.
7. L. F. Mattheis and R. E. Deitz, *Phys. Rev.* B22: 1663, 1980.
8. I. P. Grant, B. J. McKenzie, P. M. Norrington, D. F. Mayers, and N. C. Pyper, *Comp. Phys. Comm.* 21: 207, 1980.
9. K. G. Dyall and I. P. Grant, *J. Phys.* B17: 1281, 1984.
10. R. D. Leapman, P. Rez, and D. F. Mayers, *J. Chem. Phys.* 72: 1223, 1980.
11. L. A. Grunes, R. D. Leapman, C. N. Wilker, R. Hoffmann, and A. B. Kunz, *Phys. Rev.* B25: 7157, 1982.
12. W. G. Waddington, P. Rez, I. P. Grant, and C. J. Humphreys (submitted to *Phys. Rev.*).
13. B. Miner and J. Rask (private communication).
14. T. G. Sparrow, B. G. Williams, C. N. R. Rao, and J. M. Thomas, *Chem. Phys. Lett.* 108: 547, 1984.

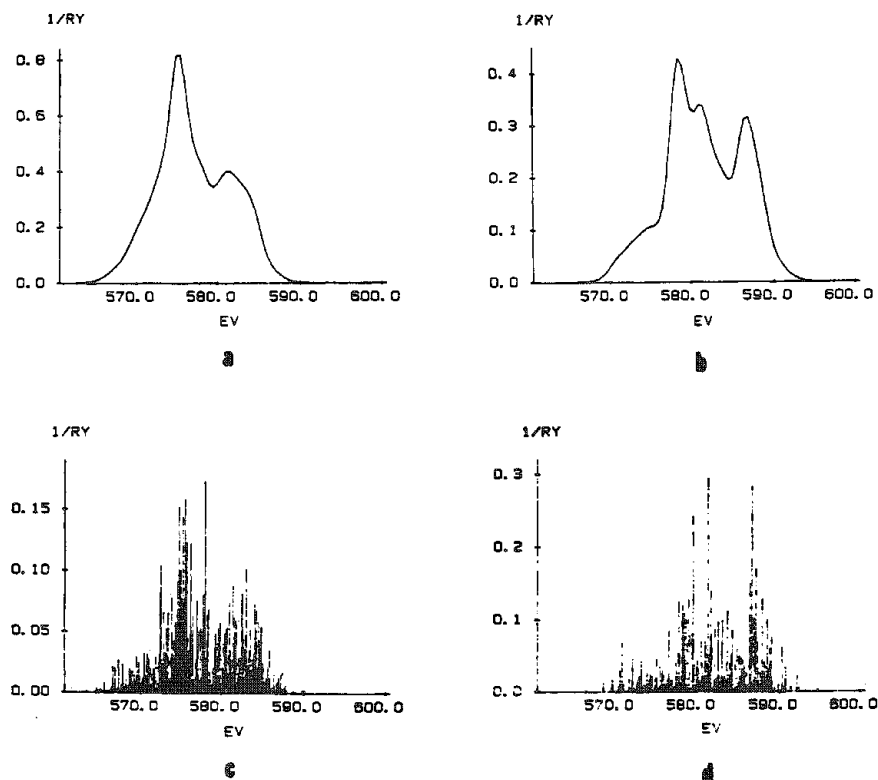


FIG. 4.--Calculated spectra for (a)  $Cr^{3+}$ , (b)  $Cr^{4+}$ ; calculated transitions for (c)  $Cr^{3+}$ , (d)  $Cr^{4+}$ .

# PROGRESS TOWARD PRECISE COMPOSITION DETERMINATION OF Al-Li ALLOYS BY ELECTRON ENERGY LOSS SPECTROMETRY

D-R Liu and D. B. Williams

Electron Energy Loss Spectrometry (EELS) has found wide application in quantitative microanalysis of light elements ( $Z \leq 10$ ) which are difficult to analyze with other techniques such as x-ray energy-dispersive spectrometry. The atomic ratio of two elements in a sample  $N_A/N_B$  can be obtained with the following formula:<sup>1</sup>

$$N_A/N_B = \{\sigma_K^{B(\beta, \Delta)} / \sigma_K^{A(\beta, \Delta)}\} \cdot \{I_K^{A(\beta, \Delta)} / I_K^{B(\beta, \Delta)}\} \quad (1)$$

where  $\sigma_K^{A(\beta, \Delta)}$  and  $\sigma_K^{B(\beta, \Delta)}$  are the partial ionization cross sections for K, L, or M electrons of the two elements, with a spectrometer acceptance semi-angle  $\beta$  and an integration window  $\Delta$ ;  $I_K^{A(\beta, \Delta)}$  and  $I_K^{B(\beta, \Delta)}$  are the corresponding signal counts obtained in the K, L, or M edge under the same conditions. The accuracy obtainable with this technique has always been of great concern, especially when one is dealing with problems in material science where a precise determination of composition can be critical to an unequivocal understanding of certain metallurgical phenomena (e.g., phase diagram determination). When the detection limit is not pursued, the influence of statistical fluctuations in the electron counts on the quantification will be small. Under these circumstances, the result then depends mainly on the nonstatistical aspects, i.e., the correct conditions for use of the quantitative formula, the extraction of values  $I_K^{A(\beta, \Delta)}$  and  $I_K^{B(\beta, \Delta)}$  from collected spectra, and the calculation of  $\sigma_K^{A(\beta, \Delta)}$  and  $\sigma_K^{B(\beta, \Delta)}$ . This paper reports the accuracy with which Li can be detected in two phases in the Al-Li alloy systems-- $\alpha$  Al-Li solid solution and  $\delta'$  nominally  $Al_3Li$ .

## Experimental

A specimen of composition Al-10.1 at% Li was solution treated at 565 C for 10 min and then direct quenched to the aging temperature of 295 C and held for 2 h to precipitate  $\delta'$ . After jet polishing in a perchloric acid and ethanol mixture (1:9), the specimen was examined in a Philips EM400T transmission microscope at an accelerating voltage  $E = 120$  kV. Spectra were collected (in TEM mode) from a through-thickness  $\delta'$  particle (Fig. 1) and the  $\alpha$  matrix, by use of a Gatan 607 magnetic prism spectrometer with a collection semi-angle  $\beta = 50$  mrad. Before collection of a spectrum was started, care was taken to insure that the specimen was oriented in a symmetrical Laue condition (i.e., many beam condition) to avoid any anomalous effects.<sup>2</sup>

## Results and Discussion

With increasing specimen thickness, the influence of multiple plasmon losses on the quantification procedure should be taken into consideration.<sup>3</sup> As demonstrated by the experiments on some specimens of known composition,<sup>4,5</sup> when the thickness of the specimen is comparable to the mean free path of the specimen material, the computed results with the above formula will deviate from the known result. The thicker the specimen is, the more deviation one would obtain. Therefore, it was considered necessary to deconvolute the collected spectra (shown in Fig. 2) before the extraction of signal counts of  $I_{Al}$  and  $I_{Li}$ . The deconvolution procedure we used is basically the same as the one developed by Egerton et al.<sup>6</sup> The deconvoluted results are shown in Fig. 3. For integration of the  $I_{Al}$  and  $I_{Li}$  signals, the energy windows were taken as  $\Delta = 15$  and 30 eV for the Li K edge and Al  $L_{23}$

---

The authors are in the Department of Materials Science and Engineering, Lehigh University, Bethlehem, PA 18015. This work is supported by the National Science Foundation under contract NSF-DMR-8400427. Provision of SIGMAK(L) and deconvolution programs by Dr. R. F. Egerton is gratefully acknowledged.

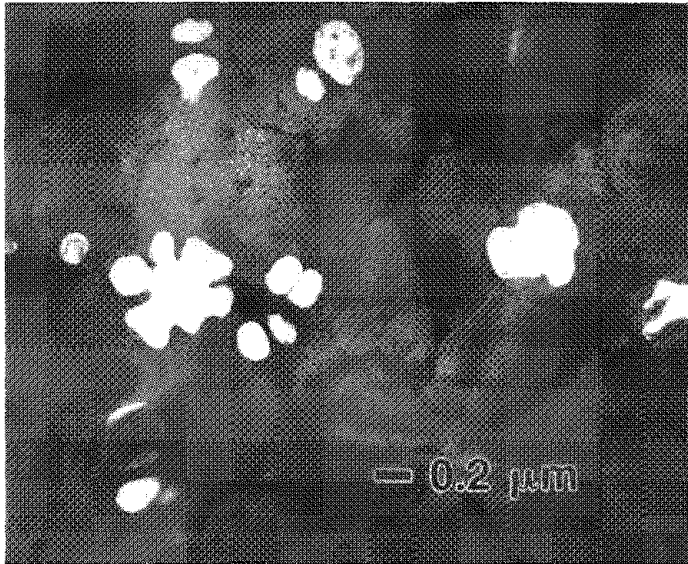


FIG. 1.--Centered dark-field image on  $\delta'$  superlattice reflection showing coarse, through-thickness  $\delta'$  particles in specimen of Al-10.1 at% Li aged at 295 C for 2 h.

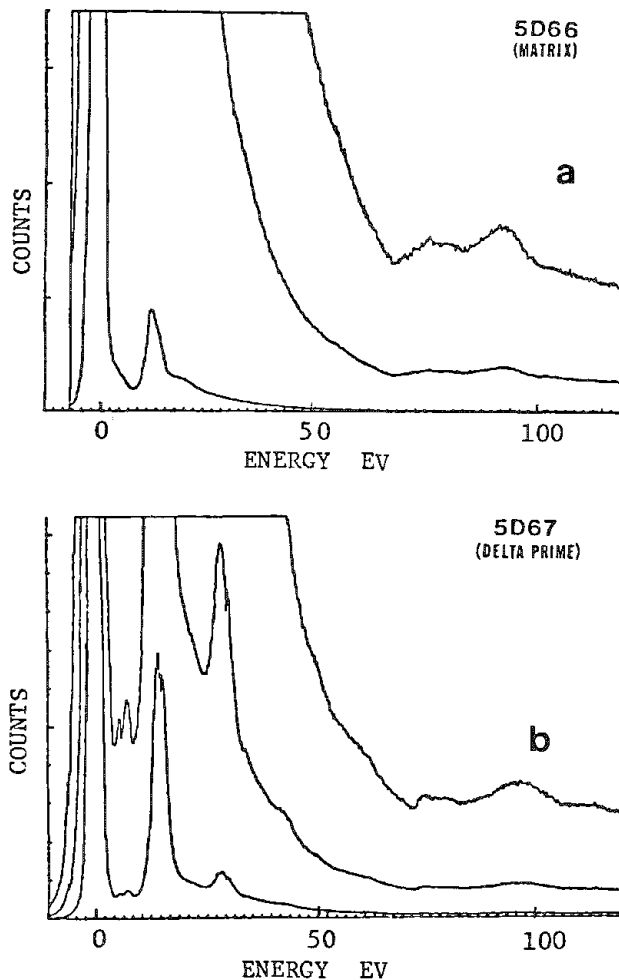


FIG. 2.--Spectra collected from  $\alpha$  phase matrix (marked 5D66) and from  $\delta'$  phase (marked 5D67). Displays show as-collected spectra and the same spectra with increasing gains ( $\times 24$  and  $\times 96$  for 5D66 as well as  $\times 8$  and  $\times 32$  for 5D67).

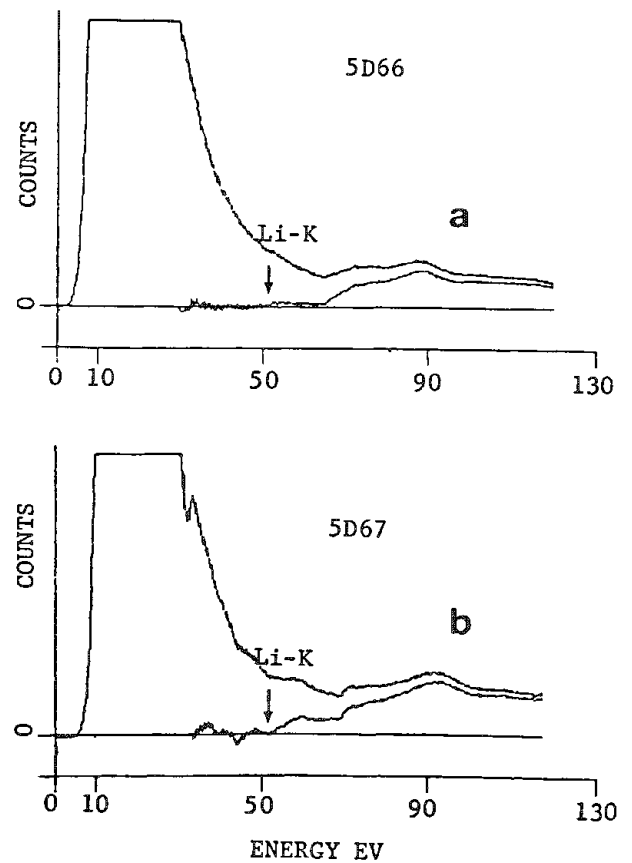


FIG. 3.--Deconvoluted spectra from (a) matrix and (b)  $\delta'$  particle. Li K edge without preceding background is also shown.



edge, respectively. In view of current uncertainties in the stoichiometry of the  $\delta'$  phase,<sup>7,8</sup> significant effort was expended to insure that best available values of the partial cross sections were obtained. A Fano plot approach is useful to check the results of cross section computations.<sup>9</sup> This approach predicts that the total cross section of an element must obey the following relation:<sup>10</sup>

$$\sigma_t E_n^2 U_n (6.51 \times 10^{-14} Z_n) = b_n \ln U_n + A_n \quad (2)$$

where  $\sigma_t$  is the total cross section of the K edge or  $L_{23}$  edge of an element,  $Z_n$  is the number of electrons in that shell,  $E_n$  is the corresponding core loss energy, and  $U_n = E_0^*/E_n$ , where  $E_0^*$  is the relativistically corrected primary energy of the incident electron beam. The total cross sections of the Li K edge and Al  $L_{23}$  edge at various primary energies were calculated from SIGMAK and SIGMAL programs, as shown by the crosses in Fig. 4. Clearly the SIGMAK and SIGMAL cross sections obey the Fano plot approach. The slopes of these plots,  $b_n$  and constants  $c_n$ , derived from intercepts  $A_n (= b_n \ln c_n)$  can be deduced as  $b(\text{Li}) = 0.763$ ,  $b(\text{Al}) = 0.688$ ,  $c(\text{Li}) = 2.04$ , and  $c(\text{Al}) = 0.714$  by a linear least-square fit. These results are within acceptable limits as summarized by Powell.<sup>10</sup> In addition, these theoretical values are in quite reasonable agreement with experimental cross-section results, as shown by the line in Fig. 4(b), which is based on Al  $L_{23}$  data from Leapman and Cosslett.<sup>10</sup> At  $E_0 = 120$  kV, the Leapman and Cosslett data give a total cross section 16% smaller than that calculated from SIGMAL. One may then expect that the partial cross section computation with SIGMAK(L) gives results with reasonable accuracy (about  $\pm 20\%$  or better) for Li K ( $\Delta = 15$  eV) as well as for Al  $L_{23}$  ( $\Delta = 30$  eV). Therefore the compositions of the matrix ( $\alpha$  phase) and the  $\delta'$  particle were calculated as 8.3 at% Li and 18.0 at% Li from Eq. (1).

The precision of the computed composition can be improved. The matrix ( $\alpha$  phase) compositions at various aging temperatures are well known<sup>11</sup> from various phase diagram determinations. This information can be used as an internal calibration standard for the partial cross section ratio in Eq. (1). In the present case, if the matrix composition aged at 295 C is Al-9.3 at% Li rather than the computed Al-8.3 at% Li, then the composition of the  $\delta'$  particle at the same temperature should be corrected to Al-19.8 at% Li, with its uncertainty now solely resulting from statistical aspects of the quantification procedure. One may assume that the main part of the statistical error in the calculated  $\delta'$  particle composition comes from the statistical uncertainty of the collected Li K edge signal counts in the matrix composition determination, because this has the smallest signal/noise ratio. The uncertainty in those counts is about  $\pm 3.5\%$  with a 99% confidence. The usual background extrapolation procedure enlarges this uncertainty value by  $\sim 3.5$  times.<sup>12</sup> Therefore the total error is  $\sim \pm 12\%$ . We may then state that the  $\delta'$  particle composition is Al-(19.8  $\pm$  2.4) at% Li.

This result is significant because currently there are two conflicting models of  $\delta'$  composition variation with temperature. Based on Small Angle X-ray Scattering (SAXS) data,<sup>13</sup>  $\delta'$  composition is observed to decrease below 25 at% Li with increasing temperature. Conversely, thermodynamic calculations<sup>14</sup> indicate that  $\delta'$  should retain its  $\text{Al}_3\text{Li}$  stoichiometric composition up to its disordering temperature of 570 C. Clearly these latest EELS data support the SAXS experiments.

### Conclusions

1. The precision of EELS quantification can be improved by deconvolution of spectra and correction to (or inspection of) partial cross section computations.
2. A calibration standard examined under diffraction and thickness conditions similar to the unknown specimen is the best approach to obtain accurate partial cross section values.
3. At 295 C the  $\alpha$  matrix has a composition of 9.3 at% Li, which when used as a standard permits the  $\delta'$  composition to be determined as 19.8  $\pm$  2.4 at% Li.

### References

1. R. F. Egerton, "Quantitative energy-loss spectroscopy," *SEM/1978* I, 13.
2. N. J. Zaluzec, "The influence of diffraction conditions on quantitative electron

energy loss spectroscopy," *Proc. 38th Ann. Mtg. EMSA*, 1980, 114.

3. A. P. Stephens, "Quantitative microanalysis by electron energy loss spectroscopy: Two corrections," *Ultramicroscopy* 5: 343, 1980.

4. N. J. Zaluzec, "The influence of specimen thickness in quantitative electron spectroscopy," *Proc. 38th Ann. Mtg. EMSA*, 1980, 112.

5. R. F. Egerton, "The range of validity of EELS microanalysis formulae," *Ultramicroscopy* 6: 297, 1981.

6. R. F. Egerton, B. G. Williams, and T. G. Sparrow, "Fourier deconvolution of electron energy-loss spectra," *Proc. Roy. Soc. A* 398: 395, 1985.

7. P. Sainfort and P. Guyot, "High spatial resolution STEM analysis of transition micro-phases in Al-Li and Al-Li-Cu alloys," *Phil. Mag.* A51: 575, 1985.

8. H. M. Chan and D. B. Williams, "Quantitative analysis of lithium in Al-Li alloys by ionization energy loss spectroscopy," *Phil. Mag.* B52: 1019, 1985.

9. D. R. Liu, "Application of Fano plot to electron energy loss spectroscopy in STEM," *Proc. 10th Intern. Cong. EM*, Hamburg, 1: 275, 1982.

10. C. J. Powell, "Cross sections for ionization of inner shell electrons by electrons," *Rev. Mod. Phys.* 48: 33, 1976.

11. D. B. Williams, "Microstructural characteristics of Al-Li alloys," in T. H. Sanders Jr. and E. A. Starke Jr., Eds., *Aluminum-Lithium Alloys*, AIME, 1981, 89.

12. R. F. Egerton, "A revised expression for signal/noise ratio in EELS," *Ultramicroscopy* 9: 387, 1982.

13. G. Cocco, S. Fagherazzi, and L. Schiffini, "Determination of the  $\delta'$  coherent miscibility gap in the Al-Li system by small angle x-ray scattering," *J. Appl. Cryst.* 10: 325, 1977.

14. C. Sigli and J. M. Sanchez, "Cluster variation calculation of stable and metastable equilibrium in Al-Li alloys," *Acta Metallurgica* (in press).

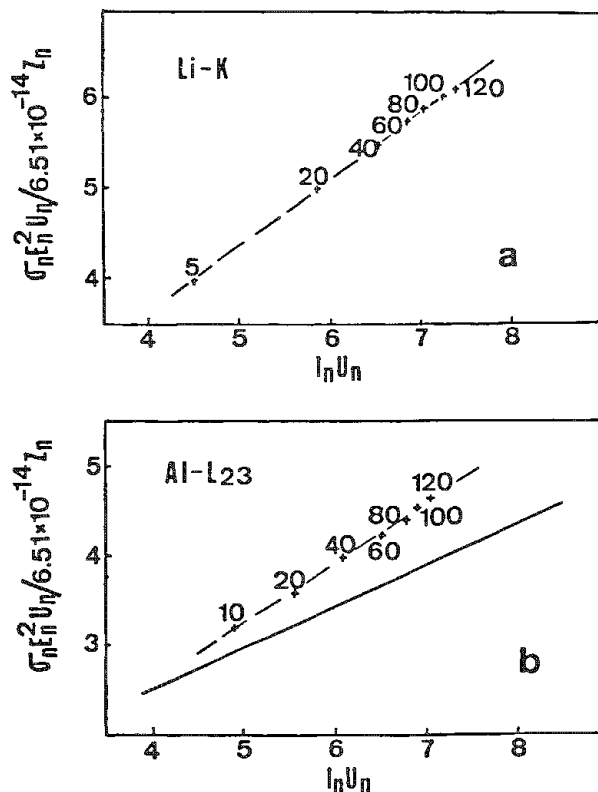


FIG. 4.--Fano plots. Crosses on dashed lines are computed from SIGMAK and SIGMAL programs (numbers stand for incident energy in keV). In (b) solid line is drawn with data from Leapman and Cosslett.<sup>10</sup>

## PRACTICAL METHODS FOR QUANTITATIVE AND FINE STRUCTURE ANALYSIS OF ENERGY LOSS SPECTRA

M. M. Disko

Electron energy loss spectra obtained by use of transmitted electrons provide a large amount of useful information with high spatial resolution if proper attention is devoted to various experimental effects and analytical methods. The literature abounds with detailed descriptions of the theory and application of electron energy loss spectroscopy (EELS) as incorporated in transmission electron microscopy (TEM).<sup>1,2</sup> A need exists for a description of some of the practical techniques routinely used in EELS experiments. Important parameters in EELS experiments, and how the selection of particular values of these parameters is influenced by the nature of the specimen and the type of EELS experiment (e.g., fine structure or quantitative information) are discussed.

Techniques described here are appropriate to  $\pi/2$  sector magnet analyzer spectrometer systems equipped with serial detection. This is the most common type of system currently used in TEM. Data were obtained with a Philips EM430 TEM (300 kV maximum accelerating voltage) equipped with a Tracor Northern 5500 multichannel scaler (MCS) and a Gatan 607 EELS system designed for accelerating voltages of 300 kV or less. Many of the techniques described here can also be applied to EELS studies performed with dedicated scanning transmission electron microscopes.

### *Experimental Parameters: Pre-specimen*

Figure 1 provides a partial list of experimental EELS variables that should be considered. The variables are grouped according to which of three devices (electron microscope, spectrometer, and MCS) are adjusted to control the corresponding variable. The selection of these variables ultimately involves a number of trade offs; e.g., improved energy resolution is inevitably accompanied by a reduction in current density. The search for an optimal set of parameters requires a systematic consideration of how the measured energy loss distribution depends on specific parameters. It should be possible to reproduce the results of a particular EELS experiment if all the Fig. 1 parameters are reported along with several additional details (e.g., diffraction conditions and specimen preparation). Methods for the determination of some of the parameters listed in Fig. 1 are discussed below.

Parameters  $E_0$ ,  $\alpha$ ,  $d$ , and  $I$  are determined by the operating conditions of the electron gun and condenser lens system. The energy resolution  $E$  measured by the EELS system is determined by the type of electron gun (LaB<sub>6</sub> in the EM430), beam current  $I$ , scattering angles  $\alpha$  and  $\beta$ , and aberration characteristics of the energy analyzer.<sup>3</sup> Best energy resolution (full width at half maximum of the zero loss peak) obtained so far with the EM430 plus Gatan 607 system was  $\sim 0.8$  eV at 100 kV and  $\sim 1.2$  eV at 300 kV (filament slightly undersaturated and zero bias in both cases). The energy spread of the electron beam incident on the specimen increases when either the filament temperature (thermal spread) or beam current (Boersch effect) are increased.<sup>4</sup> Probe current and size are governed by the choice of condenser aperture and spot sizes. Collection semi-angle  $\alpha$  is also controlled with the condenser aperture size. The angular beam disk radius measured in a convergent beam electron diffraction (CBED) pattern gives  $\alpha$ . Beam current at the specimen can be measured by use of a specimen holder equipped with a Faraday cup. The spectrometer drift tube in the Gatan 607 is electrically isolated from the microscope, so that with the sector magnet's field switched off the total current reaching the spectrometer can be measured. Beam currents measured by means of a Faraday cup at the specimen position were within 10% of those measured by the EELS drift tube for currents greater than  $10^{-11}$  A.

---

The author is with Exxon Research and Engineering Co., Route 22 East, Annandale, NJ 08801. Numerous discussions of EELS techniques with Drs. C. C. Ahn, R. F. Egerton, O. L. Krivanek, P. Rez, J. C. H. Spence, H. Shuman, J. Taftø, D. B. Williams, and N. Zaluzec are acknowledged.

### *Experimental Parameters: Specimen*

Efforts to optimize operating conditions involve experimentation with various combinations of  $d$ ,  $I$ ,  $\alpha$ , and  $\beta$  in order to obtain a "good" signal-to-noise ratio from a specimen region that is sufficiently thin to minimize multiple inelastic scattering effects (typically  $t < 100$  nm). It is not necessary to know the specimen thickness  $t$  accurately at the time of the experiment, but the negative effects that occur when  $t$  is too large must be recognized and minimized. Thus the crucial experimental parameter is often specimen preparation. Quite often the thickness can be minimized simply by selection of the inelastically scattered electrons from a localized thin region. Thin regions with small diameters can be isolated in either the diffraction (diffraction pattern on screen) or image (image on screen) modes of spectrum acquisition.<sup>3</sup> In diffraction mode, the spectrometer object is a low-magnification image of the specimen, so that the probe size is an effective means of obtaining localization. The spectrometer entrance aperture determines the specimen region sampled in image mode, so that high spatial resolution can be obtained with a defocused probe and high magnification. Diffraction mode is often advantageous because a low magnification ( $\sim 9000\times$ ) must be used in image mode to collect a large fraction of the inelastically scattered electrons. The use of such a low magnification requires repeated trips to higher magnification in order to locate the probe on the region of interest, followed by realignment at low magnification for optimal coupling to the spectrometer. Image mode can be advantageous when beam drift is excessive, or when very large ( $\beta > 20$  mrad) collection angles must be used because the spectrometer object is a demagnified diffraction pattern. Chromatic aberrations of the TEM lenses can lead to a large increase in the effective probe size when  $\beta$  is large.<sup>3</sup>

If it is assumed that a region of uniform thickness can be located, the energy loss spectrum provides a relative measure of thickness according to

$$t/\lambda_T = \ln(I_0/I_T) \quad (1)$$

which gives the thickness  $t$  as a fraction of the total inelastic mean free path  $\lambda_T$  in terms of the zero loss peak intensity  $I_0$ , and the total spectrum intensity after dark current removal  $I_T$ .<sup>5,6</sup> The use of Eq. (1) requires some care by the user. The mean free path  $\lambda_T$  is a function of the incident beam energy, range of scattering angles given by  $\alpha$  and  $\beta$ , specimen composition, and range of energy losses ( $E_{\min}$ ,  $E_{\max}$ ) that make up  $I_T$ .<sup>6</sup> Values of  $\lambda_T$  can be obtained by combination of the experimental  $\lambda_T$  with an independent measurement of thickness, such as two-beam interference, extinction contours, or thin film methods.<sup>5</sup>

### *Experimental Parameters: Post-specimen*

Collection semi-angle  $\beta$  is determined in image mode by the angular radius of the objective aperture. In diffraction mode,  $\beta$  is determined by the spectrometer entrance aperture diameter EA, camera length CL, physical distance from the projector lens cross-over to the spectrometer entrance aperture PD, and camera length PL for which the diffraction pattern magnification is 1 as  $2\beta = EA/\{CL[1 + (PD/PL)]\}$ . For Philips EM400 and EM430 microscopes and the Gatan spectrometer this gives simply  $\beta = [EA/(CL*2.2)]$ . The camera lengths and aperture sizes should be determined from CBED patterns obtained with both the condenser and diffraction lenses focused in a consistent manner. Large errors in  $\beta$  can occur in diffraction mode spectra if the lenses are not consistently focused as the camera length is changed. Thus,  $\beta$  is determined in diffraction mode by the camera length (microscope) and collection aperture (spectrometer). The shortest camera length supplied with the EM430 was 250 mm, which gives a maximum collection angle in diffraction mode  $\beta = 9.1$  mrad (largest EA = 5 mm). A switch was retrofitted to the EM430 to provide camera lengths down to 80 mm while in standard TEM mode.

Errors in the  $t/\lambda_T$  measurement given by Eq. (1) can occur if the spectrum is recorded under high-signal conditions for which the measured spectrum is distorted by the detection system.<sup>7</sup> Many EELS signal processing systems can acquire the high-intensity low-loss region in a voltage-to-frequency (V/F or analog) mode, and single electron pulse counting at higher energy losses. The article by Craven and Buggy provides a detailed

treatment of various signal-processing effects that introduce artifacts in spectra.<sup>7</sup> Distortions are minimized by spectrum acquisition in V/F mode with signal levels reduced so that no high-signal alarm occurs when the energy scan is turned off, and the zero loss peak is selected. Energy loss spectra shown in Fig. 2 were acquired with high-to-low (reversed) energy scans and all parameters held constant except for signal processing mode. The factor of 1685 used to scale the V/F spectrum to the pulse spectrum was obtained as part of the procedure for correcting dead-time effects.<sup>7</sup> This procedure yielded a constant dead time of 38 ns. For count rates below 1 MHz the pulse and V/F signals are identical, but at higher count rates the pulse signal is lower than the scaled V/F signal because of the finite response time of the detector.

Once the filament settings, image mode, probe characteristics, energy range, and scattering angles have been determined, the only remaining parameters involve the MCS-controlled dwell time per channel, number of sweeps, and energy position of the V/F to pulse signal processing transition channel. The best acquisition time depends on the stability of the entire system. Beam or specimen drift are always limitations when one is working with small probes. Many samples contaminate rapidly with amorphous carbon when stationary small probes are used. This contamination can be minimized by careful specimen preparation, specimen heating, or use of a liquid nitrogen cold stage. A fundamental constraint on acquisition time is the radiation damage rate.<sup>8</sup> A good procedure when working with samples that contain light elements is to monitor the light-element concentration by quantitative EELS over a wide range of radiation doses.<sup>9</sup> Short dwell times (<0.01 s/channel) often show problems due to either hysteresis of the sector magnet or scintillator afterflow. Slow dwell time scans sometimes enhance effects due to fluctuations in the filament emission. Drift of the energy zero position was found to be somewhat worse at 300 kV than at 100 kV for the EM430, so that shorter scans should be employed when calibration of the energy scale is important at 300 kV. A best average collection scheme was found to be a 100ms dwell time plus the use of software routines to shift manually and add successive scans if longer dwell times are required. The choice of V/F to pulse transition channel is dictated by the detector dead time effects discussed above.<sup>7</sup>

### *Qualitative Analysis*

Qualitative EELS analysis can be broadly divided into studies of either the low energy loss or core edge regions.<sup>2</sup> Low-loss studies require small  $\Delta E$  and minimum zero loss peak distortion. An important technique for low energy loss studies is to employ a reverse or high-to-low energy loss scan. The reason for the reverse scan is made clear by the low energy loss regions shown in Fig. 3 for a reactively sputtered  $\text{TiC}_{0.7}$  film.<sup>10</sup> Both spectra in Fig. 3 were obtained with  $E_0 = 100$  kV, V/F mode,  $\Delta E \approx 1$  eV,  $\alpha = 2.6$  mrad,  $\beta = 5.5$  mrad, channel separation = 0.2 eV, and dwell = 100 ms in a single sweep of 1024 channels that gave  $t/\lambda_T = 0.52$ . No alarm was sounded by the Gatan system when the Fig. 3 data were acquired, yet large qualitative differences between the forward and reverse scans are apparent at  $E < 10$  eV. Scintillator afterglow has caused the feature near 11 eV to be almost completely lost in the background for the low-to-high scan.

Deconvolution of the measured loss function is important for both low-loss and core edge fine structure studies. Two popular methods are used: the logarithmic method and the delta function ratio method.<sup>11</sup> Great care must be taken to correct for dead time or V/F saturation effects, and to remove the V/F to pulse gain change if the logarithmic method is used for core loss analysis. It is often easiest to use separate measurements of the low-loss and core edge regions and the ratio method. If applied correctly, these deconvolution procedures produce spectra which correspond to single inelastic scattering, and thus thickness effects are normalized when comparing spectra from different specimens.

General topics of importance in fine-structure studies include calibration of the energy axis, variations in  $\Delta E$  with increasing energy loss, and the effects of variations in scattering angles. Use of a voltage scan instead of the magnetic field ramp normally used to sweep the energy loss spectrum provides 0.05% or better absolute calibration for energy losses up to 1 keV. Degradation of energy resolution at large energy losses can be improved somewhat by careful spectrometer alignment. The use of parallel detection systems makes it possible to align and focus the spectrometer while observing low count rate core edges.<sup>12</sup> Finally, fine-structure experiments should be conducted with a

variety of scattering angle geometries and diffraction conditions whenever possible. The use of reasonably large ( $\beta > \theta_E = E/2E_0$ ) collection angles averages out effects that can distort spectra when very small ranges of momentum transfer (small off-axis  $\beta$ ) are selected.

### Quantitative Analysis

Quantitative EELS experiments begin with a search for a region where  $t/\lambda_T$  is significantly less than unity, followed by the selection of scattering angles that provide the best signal-to-background ratios for the core edges of interest. The criterion for the selection of  $\beta$  is normally that  $\beta$  should be somewhat larger than  $\theta_E$  for the core edge with the highest threshold energy.<sup>13</sup> A collection semi-angle of 10 mrad is normally quite good for edges with thresholds up to 1 keV at 100 kV; smaller collection angles can yield similar results at 300 kV. In cases where the signal level is weak, it is often best to take one scan complete with the zero loss peak for  $t/\lambda_T$  determination, followed by a pure pulse mode scan with the zero loss offset adjusted so that the high intensity zero loss region is avoided. This shift of the energy zero can be combined with a reverse scan in order to maximize the core loss signal and minimize detector saturation.

The accuracy of quantitative EELS experiments depends on a large number of parameters that have not yet been well characterized.<sup>13</sup> These parameters include specimen thickness, chemical variations of near edge fine structure, atomic cross sections, convergence correction, channeling-induced localization, and accelerating voltage. The use of accelerating voltages greater than 100 kV is expected to improve the quantitation accuracy because larger specimen thicknesses can be used before multiple scattering effects become important. Efforts are currently under way to investigate such effects.

### Conclusion

It is hoped that the topics discussed here will be useful for both novice and experienced EELS users. Techniques of EELS analysis are in a rapid stage of development, and very few procedures have been rigorously established. EELS users are strongly encouraged to consider the parameters listed in Fig. 1, and to make an effort to report these parameters in future publications. The further development of the EELS techniques will depend on the refinement of procedures for the systematic selection of these parameters, and the development of theoretical models that provide accurate results under typical experimental conditions. Parallel detection systems should greatly shorten the learning curve for mastering the variation of these parameters in order to improve data quality, and thus make possible the full utilization of EELS for the high spatial resolution characterization of chemistry and electronic structure.

### References

1. R. F. Egerton, "An electron energy-loss bibliography," *SEM/1983* I, 119-142.
2. C. Colliex, T. Moanoubi, M. Gasgnier, and L. M. Brown, "Near edge fine structures of EELS core loss edges," *SEM/1985* II, 489-512.
3. R. F. Egerton, "Effects of postspecimen optics on the performance of an electron spectrometer," *Analytical Electron Microscopy--1981*, 235-240.
4. L. Reimer, *Transmission Electron Microscopy*, Berlin: Springer-Verlag, 1984, 87-92.
5. R. D. Leapman, C. E. Fiori, and C. R. Swyt, *J. of Microscopy* 133: 239-253, 1984.
6. R. F. Egerton and S. C. Cheng, "Thickness measurements by EELS," *Proc. 43rd EMSA Meeting*, 1985, 398-399.
7. A. J. Craven and T. W. Buggy, "Correcting electron energy loss spectra for artefacts introduced by a serial data collection system," *J. Microscopy* 136: 227-239, 1984.
8. E. Zeitler, "Radiation damage in beam-sensitive material," *Inst. Physics Conf. Ser. 61 EMAG*, 1982, 1-6.
9. L. E. Thomas, "Microanalysis of light elements by simultaneous x-ray and electron spectrometry," *Analytical Electron Microscopy--1984*, 358-362.
10. J. Taftø, G. Rajeswaran, and T. Saulys, "Characterization of reactively sputtered titanium carbide films by analytical electron microscopy," in L. W. Hobbs, K. H. Westmacott, and D. B. Williams, Eds., *Materials Res. Soc. Symposia Proc.* 62: 1986 (in press).
11. R. F. Egerton, B. G. Williams, and T. G. Sparrow, "Fourier deconvolution of

energy loss spectra," *Proc. Roy. Soc.* A398: 395-404, 1985.

12. H. Shuman and Pieter Kruit, "Quantitative data processing of parallel recorded energy loss spectra with low signal to background," *Rev. Sci. Instrum.* 56: 231-239, 1985.

13. P. A. Crozier, J. N. Chapman, A. J. Craven, and J. M. Titchmarsh, "Some factors affecting the accuracy of EELS in determining elemental concentrations in thin films," *Analytical Electron Microscopy--1984*, 79-82.

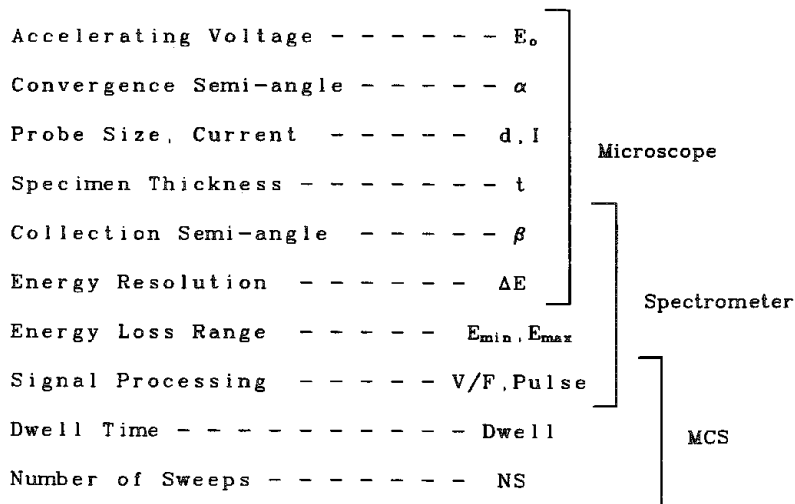


FIG. 1.--EELS experimental parameters and devices used to control them. (MCS denotes multi-channel scaler.)

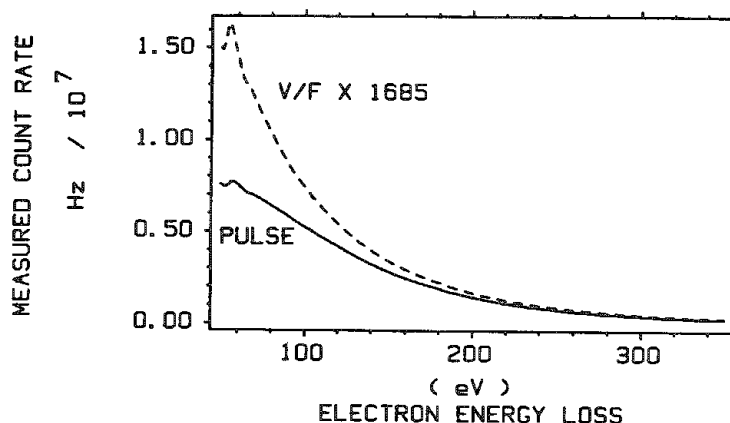


FIG. 2.--Comparison of energy-loss spectra of  $(Cr,Fe)_{23}C_6$  recorded with pulse and voltage-to-frequency (V/F) signal-processing modes. Dead-time distortion is apparent in pulse spectrum for count rates  $>1$  MHz.

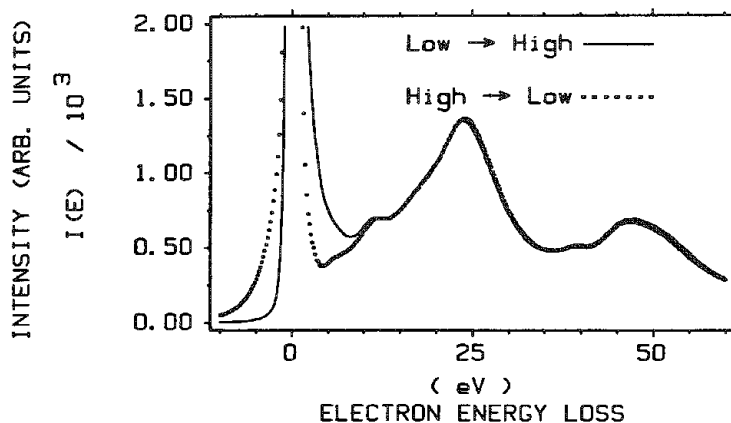


FIG. 3.--Forward (low- to high-energy loss) and reverse (high- to low-energy loss) scans of low-energy-loss region of TiC.

## MICROANALYSIS LIMITS ON THE USE OF ENERGY-DISPERSIVE X-RAY SPECTROSCOPY IN THE ANALYTICAL ELECTRON MICROSCOPE

C. E. Lyman

The attainment of high analytical sensitivity concurrent with high spatial resolution has been a goal of microanalysis since the early days of the electron microprobe. For the polished solid specimens analyzed in the microprobe, elemental sensitivity (or detectability limit) and spatial resolution were optimized by the employment of a 1  $\mu$ m electron beam, an accelerating voltage of 30 kV, and a wavelength-dispersive crystal spectrometer. The spatial resolution varies with probe size, voltage, and specimen material; however, an analytical sensitivity of about 100 ppm or 0.01 wt% Ni in Fe can be obtained under the above conditions.<sup>1</sup> For the thin specimens typical of the analytical electron microscope (AEM) with an energy-dispersive x-ray spectrometer (EDS), such an optimization depends on specimen thickness as well as probe size, voltage, and specimen material. Measurements and estimates of the sensitivity and spatial resolution for detecting one element in a solid solution or compound,<sup>2-4</sup> particles in foils,<sup>5</sup> particles on supports,<sup>6</sup> and elements segregated to grain boundaries<sup>7-11</sup> have been reported for 100 kV. Advances in instrumentation such as accelerating voltages of 300-400 kV, field-emission electron sources, and windowless EDS detectors are important steps toward increasing both spatial resolution and sensitivity in the AEM. The gains that these technological advances represent are not obvious ones since, in general, sensitivity degrades as the spatial resolution improves.

This paper suggests some criteria for evaluating present and future AEMs with regard to the simultaneous attainment of analytical spatial resolution and analytical sensitivity. Determination of spatial resolution and sensitivity in a standard manner for the case of one transition metal detected in another allows the analytical performance of different microscopes to be compared.

### *Spatial Resolution*

Electron scattering in the thin specimen causes a broadening  $b$  of the electron beam, which can be modeled either by Monte Carlo methods<sup>11-12</sup> or by an analytical expression that assumes single-scattering models.<sup>13-15</sup> Although the Monte Carlo methods are inherently more accurate, the single-scattering model is used here to permit comparisons. The single-scattering model<sup>14</sup> predicts:

$$b = 721 \frac{Z}{E_0} \left( \frac{\rho}{A} \right)^{1/2} t^{3/2} \quad (1)$$

where  $Z$  = average specimen atomic number,  $E_0$  = electron energy in keV,  $\rho$  = specimen density in g/cm<sup>3</sup>,  $A$  = specimen atomic weight, and  $t$  = specimen thickness in cm.

The spatial resolution of analysis  $R$  can be estimated if  $b$  is added to the electron-probe size  $d$  in quadrature:<sup>14</sup>

$$R = (d^2 + b^2)^{1/2} \quad (2)$$

It is difficult to measure the probe size  $d$ , especially when  $d < 10$  nm as is the case for field-emission AEMs where the probe size for analysis is usually about 1-5 nm. In that situation,  $d$  is often calculated or estimated.<sup>16</sup> The value for  $R$  calculated from Eq. (2) is used in Fig. 1 as the measure of spatial resolution.

Experimental measurement of the analytical spatial resolution  $R$  can be obtained from the apparent width of a step change in composition on a measured chemical profile across a sharp phase boundary.<sup>3</sup> Some fraction of this width, generally 90%, is taken as the

---

The author is in the Department of Materials Science and Engineering, Lehigh University, Bethlehem, PA 18015. The assistance of J. R. Michael and the Bethlehem Steel Corporation is gratefully acknowledged.



spatial resolution of analysis R. For relative comparisons of instruments under different conditions, this rather difficult measurement is avoided by use of Eqs. (1) and (2).

### *Analytical Sensitivity*

For straightforward comparisons of analytical sensitivity between different instruments it is useful to remove the geometrical complications of particles and grain boundaries and consider only the detectability of one element in another. The measurement of sensitivity to be used in this case is the minimum mass fraction (MMF), often called the detectability limit, which can be defined as the minimum weight fraction of a solute element detectable in a solid solvent matrix.<sup>2</sup> The characteristic x-ray intensity for the solute, above background, may be assumed to be statistically real at a 95% confidence level if the peak is greater than three times the standard deviation of the counts in the background under the peak. Combining this criterion with the Cliff-Lorimer equation<sup>17</sup> and assuming Gaussian statistics, Romig and Goldstein<sup>3</sup> showed that the detectability (in wt.%) of element B in element A may be expressed as

$$C_B(\text{MMF}) = \frac{3(2I_B^b)^{1/2}}{I_A - I_A^b} C_A k_{AB}^{-1}$$

where  $I_A^b$  and  $I_B^b$  are background intensities for elements A and B,  $I_A$  is the raw integrated intensity of peak A,  $C_A$  is the concentration of A (in wt.%), and  $k_{AB}^{-1}$  is the reciprocal of the Cliff-Lorimer k-factor  $k_{AB}$ . However, by expressing the Cliff-Lorimer equation as

$$\frac{C_A k_{AB}^{-1}}{I_A - I_A^b} = \frac{C_B}{I_B - I_B^b}$$

and substituting into Eq. (1), Michael<sup>4</sup> found the detectability limit for B to be

$$C_B(\text{MMF}) = \frac{3(2I_B^b)^{1/2}}{I_B - I_B^b} C_B \quad (3)$$

The value of  $C_B(\text{MMF})$  calculated from Eq. (3) is used in Fig. 1 as the measure of analytical sensitivity.

The detectability limit  $C_B(\text{MMF})$  is a minimum for the largest number of counts  $I_B$  and the largest peak-to-background ratio  $I_B/I_B^b$  as shown for solid samples by Ziebold:<sup>18</sup>

$$C_B(\text{MMF}) = K' [I_B (I_B/I_B^b) \tau]^{-1/2} \quad (4)$$

where  $I_B$  and  $I_B^b$  are measured on pure element B,  $\tau$  is the total counting time, and  $K'$  is a constant.

The value for  $C_B(\text{MMF})$  decreases as the volume analyzed increases. It also decreases as the electron dose  $D$  increases if the specimen experiences mass loss at high electron doses. Cazaux<sup>19</sup> proposed the following expression for  $C_B(\text{MMF})$  taking into account both the volume excited which increases with  $R$  and the electron dose:

$$C_B(\text{MMF}) = \frac{K''}{R} [(I_B/I_B^b) D]^{-1/2} \quad (5)$$

where  $I_B/I_B^b$  is for the pure element B,  $D = J_0 \tau$  where  $J_0$  is the current density on the specimen,  $\tau$  is the total counting time, and  $K''$  is a constant. Colliex<sup>20</sup> showed that Eq. (5) could be used to plot the spatial resolution  $R$  as a function of dose  $D$  and

indicated the limits imposed on the analysis by electron-beam damage of the specimen. For the comparisons in the present case, Eq. (5) is used assuming that no electron beam damage takes place in the metal specimen.

To extrapolate the performance from 100 to 300 kV of AEMs employing thermionic emitters, one may use the fact that the probe current is proportional to gun brightness, which is proportional to voltage. The increase in x-ray signal  $I_B$  from this effect outweighs the decrease due to the decrease in ionization cross section for the elements in the specimen. To extrapolate the field-emission results from 100 to 300 kV, the beam current was assumed<sup>21</sup> proportional to  $V^{3/4}$ . If we use the conventional term for peak-to-background ratio, i.e., P/B, Eq. (4) predicts that  $C_B(\text{MMF})$  will vary as  $(P^2/B)^{-1/2}$ , whereas Eq. (5) predicts a variation as  $(P/B)^{-1/2}$ . For the extrapolations of this paper, both values were calculated to give a range. Recent measurements<sup>22</sup> show that P/B can double from 100 to 300 kV. Nicholson et al. have demonstrated a gain in P/B at 100 kV by modifying the specimen stage area and employing a better x-ray collimator design.<sup>23</sup> These increases in P/B were included in the extrapolations.

### *Experimental*

Measurements of spatial resolution and detectability limit were made on an electro-polished foil of Fe-3.15 wt.% Ni. A 100kV Vacuum Generators HB-501 gun-lens field-emission STEM fitted with a Link Systems 30mm<sup>2</sup> windowless x-ray detector was used for measurements of Ni in Fe. Specimen thickness was determined by convergent-beam electron diffraction. X-ray counting continued until the FWHM of the Ni peak contained 11 000 counts. Counting times ranged from 100 to 1000 s depending on the specimen thickness. The probe size was estimated to be about 2 nm from the resolution of dark-field micrographs of small particles supported on carbon films.

Values for the spatial resolution of analysis were calculated from Eqs. (1) and (2). Values for  $C_{Ni}(\text{MMF})$  were obtained from equation (3). Estimates for expected improvements in performance at 300 kV were made by scaling of measured data from Eqs. (1), (2), (4), and (5).

### *Results and Discussion*

A plot that indicates the minimum detectable amount of one element in another at a particular spatial resolution may be used to evaluate the x-ray microanalysis performance of individual AEMs. Figure 1 shows the present data compared to previous work on other instruments.<sup>1,3,4</sup> Instruments that detect smaller amounts of solute (better sensitivity) from smaller excited volumes (better spatial resolution) are considered to have the better analytical performance. Data showing better sensitivity for the same instrument were from thicker specimen regions and thus exhibited poorer spatial resolution. Figure 1 also shows estimates for the improved performance expected at 300 kV.

Several points may be made about the data and predictions. Since the MMF is inversely related to the excitation volume, the sensitivity improves for larger electron probes and thicker specimens. Of course, for quantitative analysis the thin-film criterion<sup>13</sup> should not be violated. The improvement in detectability for the data of Michael<sup>4</sup> versus those of Romig and Goldstein<sup>3</sup> reflect an AEM designed to deliver more current into a 20nm probe size. Better vacuum at the specimen allowed counting times to be extended before contamination problems curtailed analysis. Although an increase from a 100kV to a 120kV beam brings a small improvement, the larger number of x-ray counts obtained with the newer instrument accounts for most of the difference in performance. These data are not necessarily linear on a log-log plot but are shown as such for convenience.

To be strictly correct, the electron beams used in all the studies shown in Fig. 1 should be of similar shape. Cliff and Kenway have shown that an extensive halo of electrons surrounds the central peak of the beam if the condenser aperture is too large to limit the spherical aberration of nonaxial electrons.<sup>24</sup> To minimize this effect, Cliff proposed that the probe size be  $d = 1.1C_s\alpha^3$ , where  $C_s$  is the spherical aberration coefficient of the probe-forming lens and  $\alpha$  is the semi-angle of the convergent beam.<sup>25</sup> A smaller condenser aperture reduces  $\alpha$  but it also reduces the probe current and thus causes the minimum detectability limit MMF to increase. For the data of Fig. 1 it is not known whether the electron beams were properly limited.

Improvements in both spatial resolution and sensitivity should be derived from the

change to a 300kV beam. An estimate of the expected improvement in MMF for a thermionic AEM operating at 300 kV with a 20nm probe size is shown in Fig. 1. However, the expected factor of 2 increase<sup>22</sup> in P/B for 300 kV over 100 kV is not always achieved in practice (see the paper by Williams in these proceedings). Another potential factor of 2 improvement in P/B might be obtained from the reduction of x-ray background in the specimen stage area if the polepieces and aperture mechanisms are covered with light metals and heavy-metal baffles are inserted in the detector collimator.<sup>23</sup> Since that has not yet been done on any intermediate-voltage instrument, the actual performance of current AEMs operating at 300 kV with thermionic sources is not likely to reach the shaded area predicted in Fig. 1. Not shown in the figure is the possibility that probe sizes smaller than 20 nm may contain 1 nA at 300 kV.

The significant improvement in spatial resolution for the 100kV field-emission AEM derives both from the smaller probe size and the increased current in the probe. The typical 1 nA required for microanalysis can be obtained at a 2nm probe size in the field-emission case, whereas this beam current usually requires a 20nm probe size in the thermionic AEM. This relatively large current for a 2nm probe allows analysis of thinner specimens, which means that the beam broadening can be smaller by an order of magnitude for the field-emission AEM.

The performance prediction for a field-emission AEM operating at 300 kV is also shown in Fig. 1. Even though the probe current increase with voltage is not as great as for the thermionic case,<sup>21</sup> the predicted performance of the 300kV field-emission AEM is significantly better than either the 300kV thermionic AEM or the 100kV field-emission AEM. Sensitivity improves by factors of 2-5, and spatial resolution improves by a factor of at least 2 at 300 kV.

Finally, these predictions neglect specimen drift, contamination, and electron-beam damage to the specimen. Drift compensation by computer control of analysis experiments appears feasible and is worth pursuing, especially to utilize the very high spatial resolution predicted for the 300kV field-emission AEM. Specimen contamination should not be a problem if the specimen is clean when it enters the microscope and if the specimen is kept in a  $<10^{-8}$  Torr environment during analysis. Electron-beam damage remains the only truly limiting factor for high-spatial-resolution microanalysis. For materials that can withstand the very high electron doses of the 300kV field-emission AEM, analysis may be as predicted in Fig. 1; materials that lose mass under these severe conditions can only be analyzed with worse sensitivity and/or worse spatial resolution than shown in Fig. 1.

### Conclusions

By determining the sensitivity and spatial resolution of x-ray microanalysis in a standard manner, the performance of various analytical electron microscopes may be compared. These performance figures, extrapolated to 300 kV, show significant advantages in operating at the highest voltage possible consistent with the maintenance of high peak-to-background ratios and acceptably low electron-beam damage of the specimen.

### References

1. J. I. Goldstein and H. Yakowitz, *Practical Scanning Electron Microscopy*, New York: Plenum Press, 1975.
2. D. C. Joy and D. M. Maher, *SEM/1977* I, 325.
3. A. D. Romig and J. I. Goldstein, *Microbeam Analysis--1979*, 124.
4. J. R. Michael, M.S. Thesis, Lehigh University, 1981. (Also reported in D. B. Williams, *Practical Analytical Electron Microscopy in Materials Science*, Mahwah, N.J.: Philips Electronic Instruments, 1984, 83.)
5. J. M. Titschmarsh et al., *Analytical Electron Microscopy--1984*, 64.
6. H. Dexpert et al., *Quantitative Microanalysis with High Spatial Resolution*, The Metals Society, 1981, 101.
7. E. L. Hall et al., *Phil. Mag.* A43: 1569, 1981.
8. P. Doig and P.E.J. Flewitt, *Met. Trans.* 13A: 1397, 1982.
9. J. R. Michael and D. B. Williams, *Met Trans.* 15A: 99, 1984.
10. A. J. Garratt-Reed, *SEM/1985* I, 21.
11. R. H. Geiss and D. F. Kyser, *Ultramicroscopy* 3: 397, 1979.
12. D. E. Newbury and R. L. Myklebust, *Analytical Electron Microscopy--1981*, 91.

13. J. I. Goldstein et al., *SEM/1977 I*, 315.
14. S. J. B. Reed, *Ultramicroscopy* 7: 405, 1982.
15. L. M. Brown, *J. Phys. Fl1*: 1, 1981.
16. L. E. Thomas, *Ultramicroscopy* 9: 311, 1982.
17. G. Cliff and G. W. Lorimer, *J. Microsc.* 103: 203, 1975.
18. T. O. Ziebold, *Anal. Chem.* 39: 858, 1967.
19. J. Cazaux, *Appl. Surf. Sci.* 20: 457, 1984-85.
20. C. Colliex, *Ultramicroscopy* 18: 131, 1985.
21. M. Troyon, *Proc. 8th European Congress on Electron Microsc.* 1: 11, 1984.
22. Y. Bando et al., *Ultramicroscopy* 18: 117, 1985.
23. W. A. P. Nicholson et al., *J. Microscopy* 125: 25, 1982.
24. G. Cliff and P. B. Kenway, *Microbeam Analysis--1982*, 107.
25. G. Cliff, *J. Microsc.* 130: RP3, 1983.

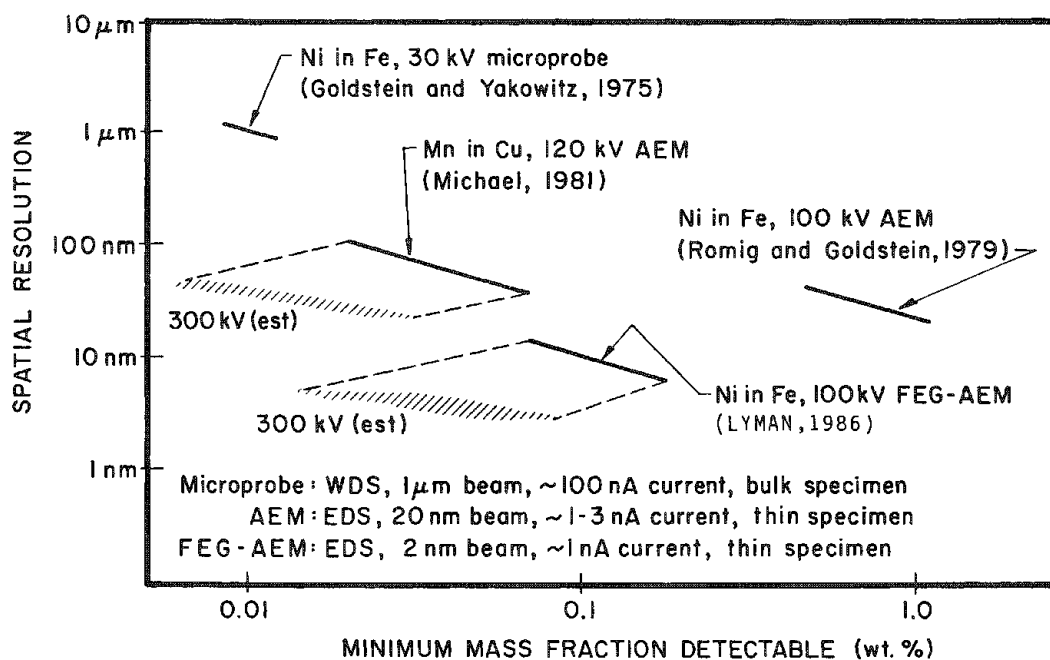


FIG. 1.--Spatial resolution vs elemental sensitivity in x-ray microanalysis. Data by Goldstein and Yakowitz,<sup>1</sup> Romig and Goldstein,<sup>3</sup> and Michael<sup>4</sup> are from instruments with thermionic sources. Data for present work are from field-emission analytical electron microscope. Extrapolations of data to 300 kV are shown as shaded areas.

## A HIGH-PURITY GERMANIUM X-RAY DETECTOR ON A 200kV ANALYTICAL ELECTRON MICROSCOPE

E. B. Steel

Theoretical predictions and preliminary experimental results are compared for high-purity germanium (HPGE) and lithium-drifted silicon [Si(Li)] x-ray detectors mounted on an analytical electron microscope (AEM). A germanium detector has several advantages and disadvantages when compared to the traditional Si(Li) x-ray detectors used on the AEM. The main advantage is the high detector efficiency over a large range of energies, which means that high-energy K lines can be analyzed. These high-energy K lines have several analytical advantages including high fluorescent yields, low continuum, small absorption corrections, and relatively few overlaps. The main disadvantages with the use of the high-energy K lines in analysis is the low ionization cross section. Two other problems with the HPGE are the poor efficiency below 3 kV and the large incomplete charge tails on the low-energy peaks.

### *Experimental*

A JEOL 200CX AEM with a zero-take-off-angle germanium detector and with a high-take-off-angle Be window Si(Li) detector was used to collect data for this paper. The window thicknesses were 13  $\mu\text{m}$  Be on the Si(Li), and 50  $\mu\text{m}$  Be on the HPGE. The detectors were connected to either a TN-2000 with a PDP-11 or a multiplexed Ortec 918 multichannel analyzer connected to a VAX 11/730.<sup>1,2</sup> NBS synthetic glasses, natural minerals, and pure metals were examined at an accelerating potential of 200 kV. The specimens were prepared as particles or sputtered films on thin carbon films supported by 200 mesh copper grids.

### *Advantages of the HPGE*

An AEM operating at an accelerating voltage of 200 kV is capable of exciting the K-line x rays of all known elements, but the sensitivity of the Si(Li) x-ray detectors mounted on these instruments decreases with increasing energy for the K-line x rays for elements heavier than approximately molybdenum ( $K\alpha = 17.44$  keV). This decrease occurs because the K-line x rays from these heavy elements pass through the Si(Li) detectors at high enough energy to cause little or no interaction. One way to overcome this problem is to use a detector made of a material that has more stopping power for these high-energy x rays. The HPGE detector has been used for many years to analyze the even higher-energy gamma rays. Figure 1 shows the relative efficiencies of an ultrathin window (UTW) and a Be-window Si(Li), and the HPGE for the K lines by atomic number. This figure shows the well-documented differences between the UTW and Be windowed Si(Li) detectors and also the HPGE detector at both the low and high energy ranges.<sup>3-5</sup> The 5.6mm-thick HPGE has an efficiency of more than 90% for the K-line x rays from the elements with atomic numbers from approximately 25 through 85. The Si(Li) detectors must rely on the observations of M- and L-line x rays for most elements above approximately atomic number 50.

Analysis with these high-energy K lines may have certain advantages over the analysis of L and M lines from the same elements. (1) The fluorescent yield is seen to be many times larger for the K lines than the L or M lines (Fig. 2). The yields were calculated with minor modifications from the data and equations published by Bambynek et al.<sup>6</sup> (2) The continuum has lower intensity at high energies, which improves the signal-to-noise ratio for the high-energy K lines. (3) The absorption correction is very low for these high-energy x rays in the thin specimens analyzed on the AEM and in most cases can be ignored. (4) The k-line spectra are relatively simple with reasonably well-known weights of lines. The M- and L-line x rays yield much more complex spectra with many more (often

---

The author is with the Center for Analytical Chemistry, National Bureau of Standards, Gaithersburg, MD 20899. He wishes to thank John Giles of Princeton Gamma-Tech, Inc., for his special attention in supervising the building of the experimental HPGE; and Barbara Thorne for writing the computer programs that run the MCA and the x-ray spectral manipulation.

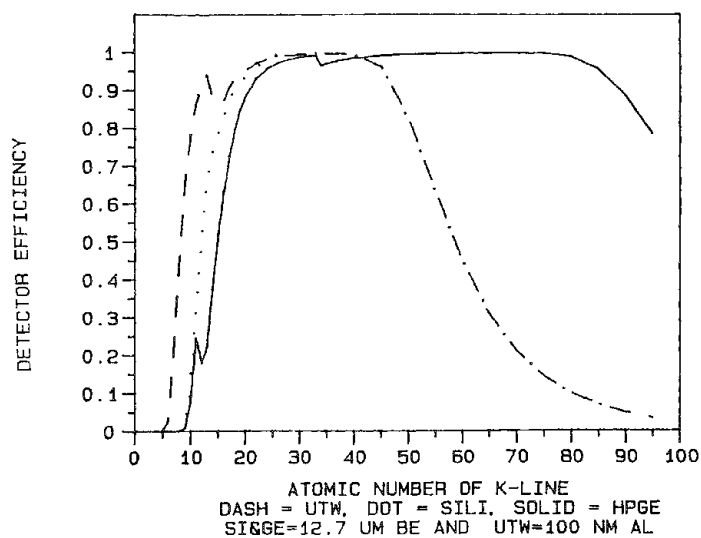


FIG. 1.--Detector efficiency for K lines.

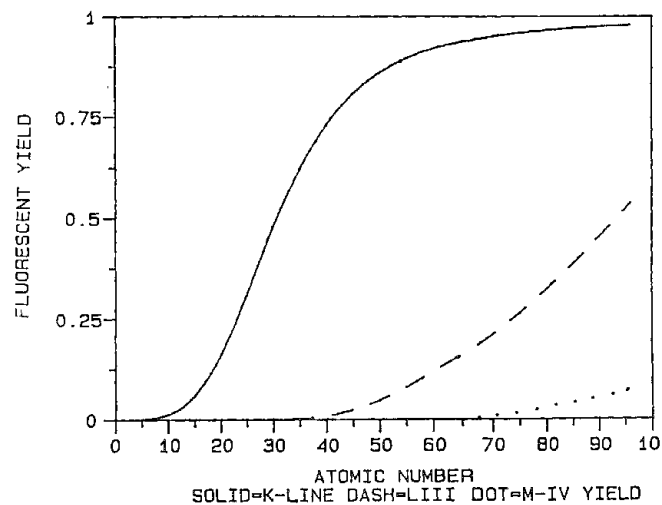


FIG. 2.--Fluorescent yield for K, L, and M lines vs atomic number.

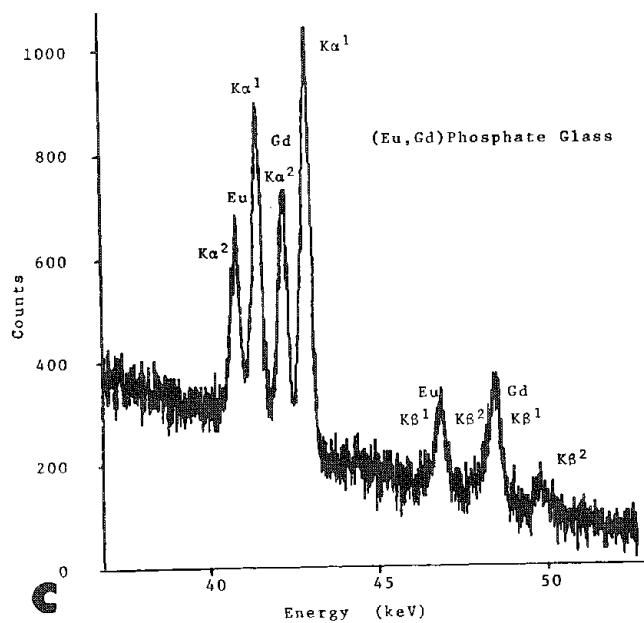
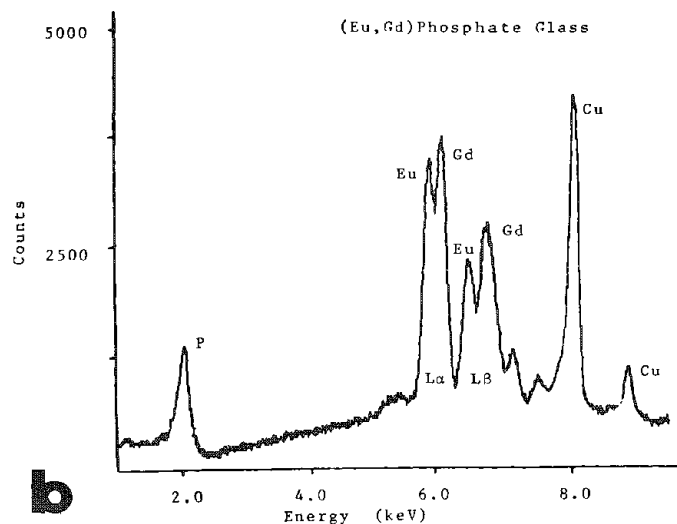
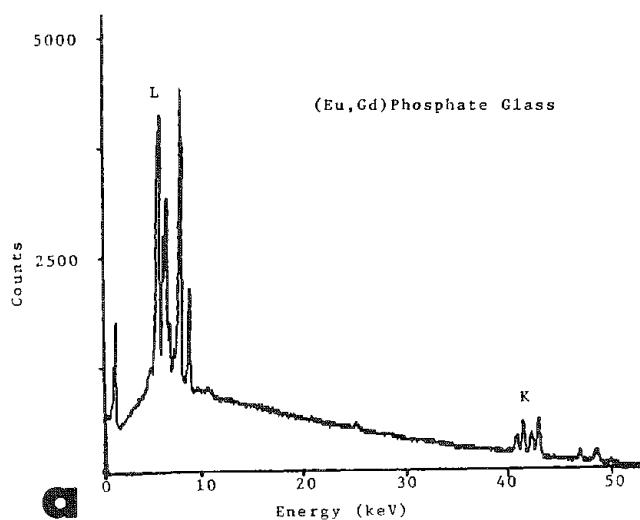


FIG. 3.--(a) HPGE x-ray spectrum of (Eu,Gd) phosphate glass; (b) enlarged low-energy region of spectrum in (a); (c) enlarged high-energy region of spectrum in (a).

overlapping) peaks than are seen for K lines. In addition, much less is known about the relative weights of these L and M x rays than for the K lines. Because of these problems with L- and M-line x rays, quantitation of heavy-element compositions can be difficult.

One example of an application of the HPGE is where the specimen has overlapping L-line x rays due to special combinations of high-Z elements or in combination with lighter elements. This situation is frequently encountered in the analysis of rare-earth elements. Figure 3 shows an x-ray spectrum of a rare earth phosphate glass prepared at NBS which contains Eu and Gd. Figure 3(a) shows the x-ray spectrum from 0 to 50 keV. Figure 3(b) shows the complex overlapping low energy x rays from 0 to 10 keV, and Fig 3(c) shows the well-resolved high-energy K lines of the rare-earth elements.

#### *Disadvantages of the HPGE*

The positive factors associated with the AEM x-ray analysis and HPGE are tempered by several problems. The chief difficulty is the behavior of the ionization cross section (Fig. 4). This figure shows that the cross section falls by a factor of ten from atomic number 50 to 96 at 200kV operation. This result was obtained from the equation of Powell for overvoltages greater than 4 and Gryzinski for lower overvoltages.<sup>7,8</sup> Discontinuities are observed at the transitions between these equations in the curves for each excitation voltage. Figure 4 also shows a rapid drop of many orders of magnitude in the ionization cross section for heavy elements when 100kV excitation is used. This drop suggests that it is not worth while trying to use a HPGE detector with an AEM operating at an excitation potential of 100 kV, but may be of use at the higher incident energies of 200 kV and more.

Figure 5 is an x-ray spectrum of a lead silicate glass collected on the HPGE. The full energy range from 0 to 80 keV is shown in Fig. 5(a). The relative intensities of the K, L, and M lines can be seen in further detail in Figs. 5(b) and (c). The effect of the reduced cross section for the Pb K x rays is shown by the relatively low intensity of these K x-ray peaks compared to the Pb L and M x-ray peaks. Figure 4 shows that these effects will be improved only by a factor of approximately two by an increase in voltage to 400 kV.

Figure 1 shows another disadvantage of the HPGE: the poor efficiency for the low-energy x rays from the elements with atomic number less than 20, controlled largely by the absorption in the Ge dead layer of the detector. Another factor that exacerbates the low-energy problem is the presence of large incomplete charge tails on the peaks in this region. Figure 3(b) shows a P peak with a large incomplete charge tail. These problems can be overcome by use of the Si(Li) detector for analysis of the low-energy x-ray lines.

#### *Conclusion*

An HPGE detector has been attached to an AEM and spectra have been taken of high-energy K-line x rays that cannot be efficiently detected with traditional Si(Li) detectors. The ability to detect these high-energy K lines has been shown to be useful for the analysis of elements for which significant overlap occurs in the L- and M-line peaks. To improve the low-energy efficiency, we plan to replace the 50 $\mu$ m Be window with a 13 $\mu$ m window on the HPGE. The full extent of the practical use of the HPGE will be determined by measurement of the peak-to-background ratio and relative intensities of the K, L, and M lines for various elements. This procedure will permit the quantitative calculation of sensitivity factors, cross sections, and detection limits for comparison with the qualitative observations made in this paper.

#### *References*

1. Certain commercial equipment, instruments, or materials are identified in this paper. Such identification does not imply that the materials or equipment identified are necessarily the best available for the purpose.
2. E. B. Steel, R. L. Myklebust, and A. A. Boll, *Microbeam Analysis--1985*, 151-152.
3. G. Cliff, D. M. Maher, and D. C. Joy, *J. Microscopy* 136: 219-225, 1984.
4. R. W. Fink, "Properties of silicon and germanium detectors for x-ray spectrometry," in K. F. J. Heinrich et al., Eds., *Energy Dispersive X-ray Spectrometry*, NBS Special Publication 604, 1981.
5. N. C. Barbi and D. B. Lister, "A comparison of silicon and germanium x-ray detectors," *ibid.*

6. W. Bambynek et al., *Rev. Mod. Phys.* 44: 763-813, 1972.
7. C. J. Powell, "Evaluation of formulas for inner-shell ionization cross section," in K. F. J. Heinrich et al., Eds., *Use of Monte Carlo Calculations in Electron Probe Microanalysis*, NBS Special Publication 460, 1976.
8. M. Gryzinski, *Phys. Rev.* 138: A336, 1965.

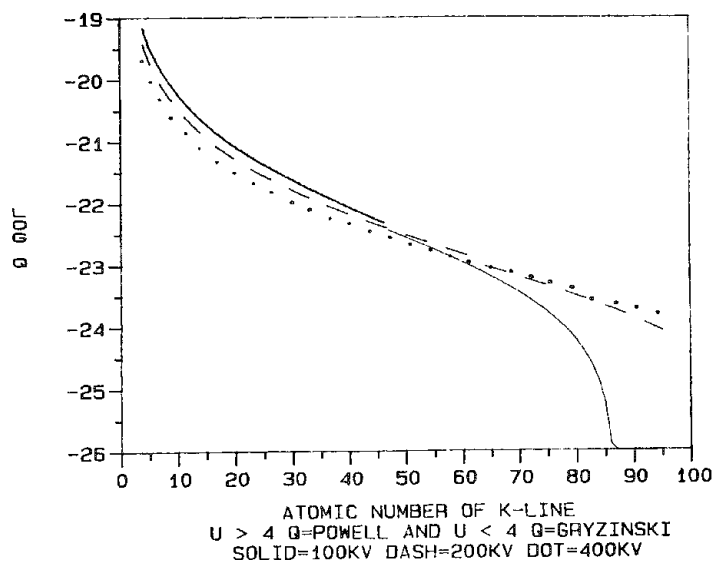


FIG. 4.--Log cross section (Q) for K lines at 100-400 kv.

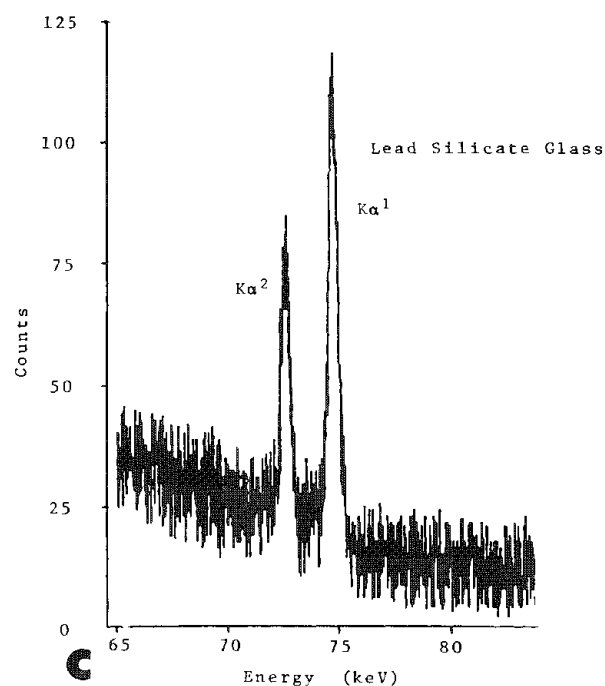
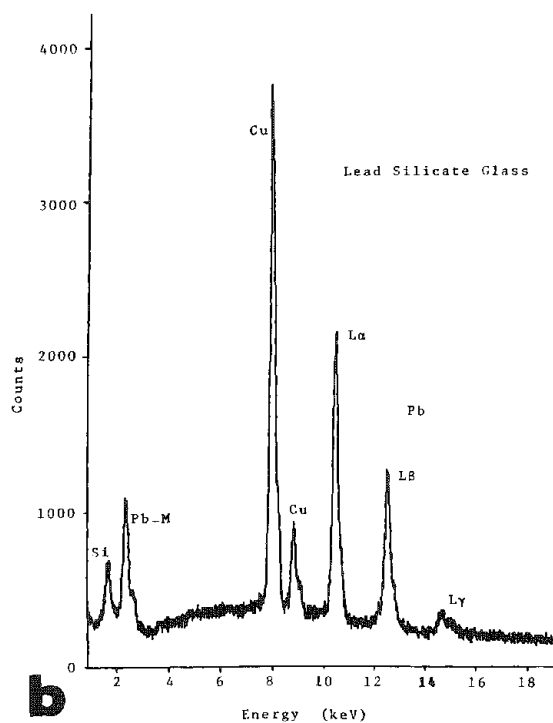
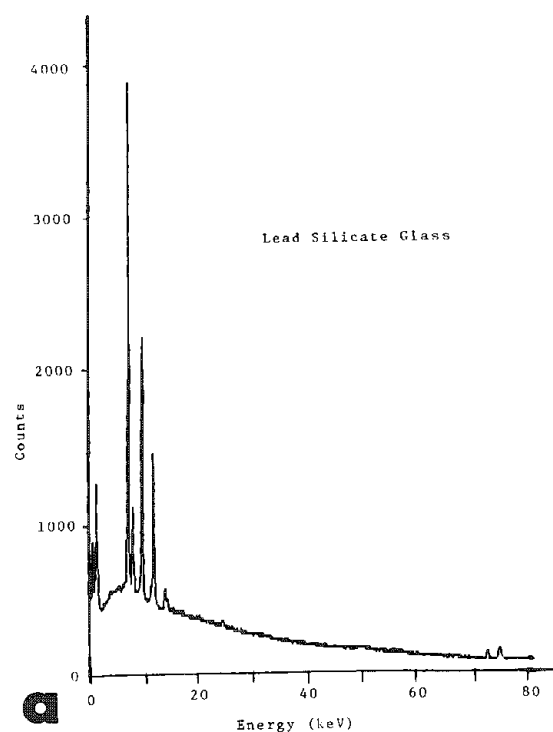


FIG. 5.--(a) HPGE x-ray spectrum of lead silicate glass; (b) enlarged low-energy region of spectrum in (a); (c) enlarged high-energy region of spectrum in (a).



## STANDARDIZED DEFINITIONS OF X-RAY ANALYSIS PERFORMANCE CRITERIA IN THE AEM

D. B. Williams

Progress in the development and performance of transmission and scanning electron microscopes has usually been measured in terms of the attainment of well-defined performance criteria. Typically, in the case of both TEM and SEM, image resolution has been the principal criterion. For TEMs the ability to resolve certain lattice planes and more recently, measurements of the objective lens transfer function, have been used. In the case of SEMs the resolution criterion has usually been the smallest discernible edge-to-edge spacing of Au islands on a carbon film. In contrast to these well-defined and easily measurable resolution criteria, there are no universally accepted criteria for x-ray microanalysis in the analytical electron microscope (AEM). The only criterion currently in use is the resolution of the x-ray energy-dispersive spectrometer (XEDS). This is defined as the full width half maximum (FWHM) of the Mn K $\alpha$  line generated by an Fe<sup>55</sup> source --when the x-ray detector is off the microscope! This resolution figure is not a function of the design of the AEM itself (although very high x-ray fluxes can degrade the resolution from the best values, ~145-155 eV). Therefore, universally accepted definitions are required for such important x-ray analytical functions as:

- (a) electron probe size, and minimum acceptable currents in specific probe sizes; these factors ultimately limit the spatial resolution of microanalysis and the detectability limit
- (b) the peak to background ratio, which governs the detectability limit
- (c) the "cleanliness" of the AEM column, which affects the peak-to-background ratio and introduces systematic errors into routine quantification

In the opinion of the author the absence of such criteria has slowed the development of AEMs with the best x-ray analytical performance. In the last decade, despite the many new AEMs on the market, there have been no major changes to the design of the specimen stage region, and the interface between the EDS and the AEM. In this paper, the problems of deciding on universally acceptable criteria for the performance of AEMs are discussed and some suggestions are made concerning suitable standard experiments that can be easily performed on an AEM. If some such criteria become widely acceptable, they could be incorporated into the AEM manufacturers' literature. That would stimulate competition and result in the development of succeeding generations of instruments showing improved performance.

### *Spatial Resolution of Microanalysis and Electron Probe Characteristics*

Spatial resolution  $R$  is the analytical analog of image resolution and therefore should be an ideal criterion for the performance of an AEM. Unfortunately, at present the specimen rather than the instrument remains the primary factor in determining spatial resolution. Until field-emission guns become more widely available, x-ray count rates from very thin samples will be insufficient to permit probe-limited microanalysis. With LaB<sub>6</sub> and W guns, sufficient x-ray counts for quantification can only be generated in specimens of such thickness that beam spreading  $b$  dominates the spatial resolution given by<sup>1</sup>

$$R^2 = d^2 + b^2, \text{ where } d \text{ is the probe diameter.}$$

Therefore, it is not yet considered feasible to propose a specific criterion for spatial resolution. Nevertheless, significant progress can be made if there are accepted definitions of (a) the electron probe size and (b) the minimum acceptable levels of current in a given probe size. Ultimately these two criteria will limit both spatial resolution and detectability limits at given spatial resolution, respectively.

In many current AEMs, it is possible to image the probe directly on the TEM screen.<sup>2</sup>

---

The author is in the Department of Materials Science and Engineering, Lehigh University, Bethlehem, PA 18015.

This capability is unique to STEMs and gives a direct record of the probe dimensions, the electron distribution, and any aberration<sup>3</sup> or misalignment problems. Microdensitometry across an image of the probe should permit determination of the full width at tenth maximum (FWTM) of the electron distribution. Since this dimension correlates with that containing 90% of scattered electrons, used widely in the definition of beam spreading,<sup>4</sup> it is proposed that FWTM should be used as the definition of probe size. (Currently calculations defining the FWHM are given by manufacturers.) Imaging the probe removes problems involved in either calculating the probe dimensions or indirect methods such as traversing the probe across knife-edge samples.<sup>2</sup> Direct measurement of the current in the probe should be performed in situ by a Faraday cup in the plane of the sample. Some typical examples of probe images are shown in Fig. 1 and the probe current data given in Table 1 are proposed as a base measurement for minimum acceptable currents from thermionic sources. Further details of the correlation between probe currents and probe images and comparison with nominal probe sizes are being published separately.<sup>5</sup> From Table 1 it is clear that the emission current (Wehnelt bias) is a critical factor in defining probe current (and therefore affecting probe size). There is no routine indication, however, on any TEM/STEM instrument, how to operate at optimum Wehnelt bias for maximum brightness.

#### *Peak-to-background Ratio (P/B)*

There are several definitions of P/B where P is the intensity in the characteristic peak above the background B. Based on x-ray analysis in the electron probe microanalyzer (EPMA), Reed<sup>6</sup> defined P/B as the number of counts in the channel at the center of the peak (minus the background contribution to the center channel), divided by the background contribution (Fig. 2a). Lifshin et al.<sup>7</sup> suggested an integrated P/B in which a certain region of interest is defined. In the limit, the full integrated peak value is divided by the full integrated background value (i.e., a "gross/net" approach available on commercial MCA systems) (Fig. 2b). The question of choosing a specific region of interest within the peak to "maximize" P/B was addressed by Sutfin and Ogilvie,<sup>8</sup> who reported an optimum sensitivity at 1.2 FWHM (Fig. 2c). This finding agrees with the work of Geller,<sup>9</sup> who showed a maximum in  $P^2/B$  at  $\sim 1.2$  FWHM. However, both these approaches ignore many of the counts in the peak.

In the EPMA, most analyses are a compromise between choice of optimum overvoltage and the minimization of spatial resolution, which results in use of accelerating voltages between 15 and 30 kV. The EPMA itself has little effect either on P (because of the limited voltage range) or on B (because the specimen is thick and there are no problems with post-specimen scatter). In contrast in AEMs, overvoltage effects are ignored in favor of high spatial resolution and P/B from maximum kV beams in the 100-400kV range. This fact in conjunction with the use of thin specimens giving significant post-specimen scatter means that the AEM itself invariably influences the P/B, particularly by contributing unknown intensity to B.

Both Nicholson et al.<sup>10</sup> and Fiori et al.<sup>11</sup> have endeavored to define P/B in an AEM. Nicholson et al.<sup>10</sup> chose a thin Co film and defined P/B in terms of a peak intensity integrated over 360 eV around the Co K $\alpha$  peak and a bremsstrahlung intensity in a 20eV channel under the peak (Fig. 2d). Fiori et al.<sup>11</sup> proposed integrating the peak over its full width (which makes the result independent of the EDS resolution) and choosing a 10eV bremsstrahlung channel (Fig. 2e). The 10eV width is argued as (a) being close to the natural x-ray line width and (b) a common setting on most commercial multichannel analyzer (MCA) systems.

This last definition therefore has the advantages of simplicity, and relevance to the actual x-ray generation characteristics. All that is now required is the choice of a standard specimen to measure P/B. The specimen should be robust, nonmagnetic, easily fabricated, stable (both in the beam and on the laboratory shelf), not subject to atmospheric corrosion, thin enough to show no absorption edge, and should have a well-defined K $\alpha$  peak not overlapping the K $\beta$  peak. In addition the film should be microcrystalline to avoid problems with coherent bremsstrahlung. An evaporated film of chromium <50 nm thick has these advantages. Figure 3(a) shows a typical Cr spectrum from such a film fabricated in a conventional (low-vacuum) evaporator onto a 5nm carbon film supported on a Cu grid.

It is critical in defining P/B to insure a reproducible method of determining P and B. A "gross/net" approach has the advantage of simplicity and only requires definition

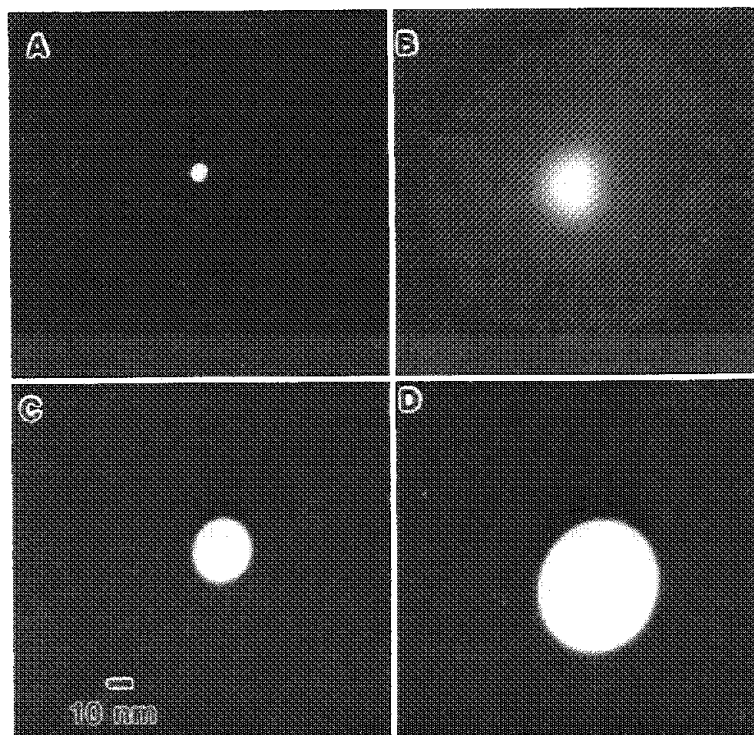


FIG. 1.--Images of electron probe recorded from TEM screen. Nominal probe size (FWHM) and  $C_2$  aperture size: (a) 2 nm, 70  $\mu\text{m}$ ; (b) 2 nm, 150  $\mu\text{m}$ ; (c) 10 nm, 70  $\mu\text{m}$ ; (d) 20 nm, 70  $\mu\text{m}$ . Compare nominal size with marker: 3 mm = 10 nm.  
Cursor: 0.000keV = 0 ROI (0) 5.000: 5.700-99950

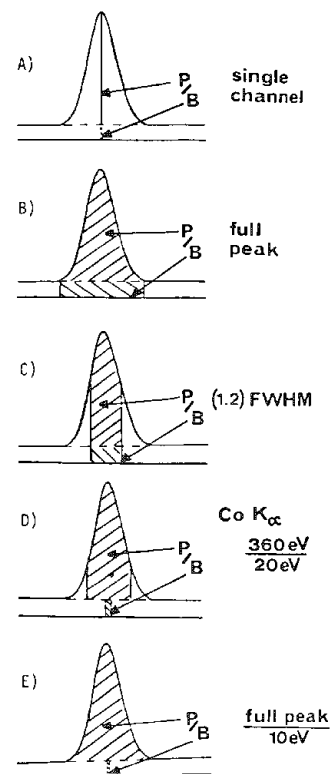


FIG. 2.--Various definitions of peak to background. (Definition E is used in this paper.)

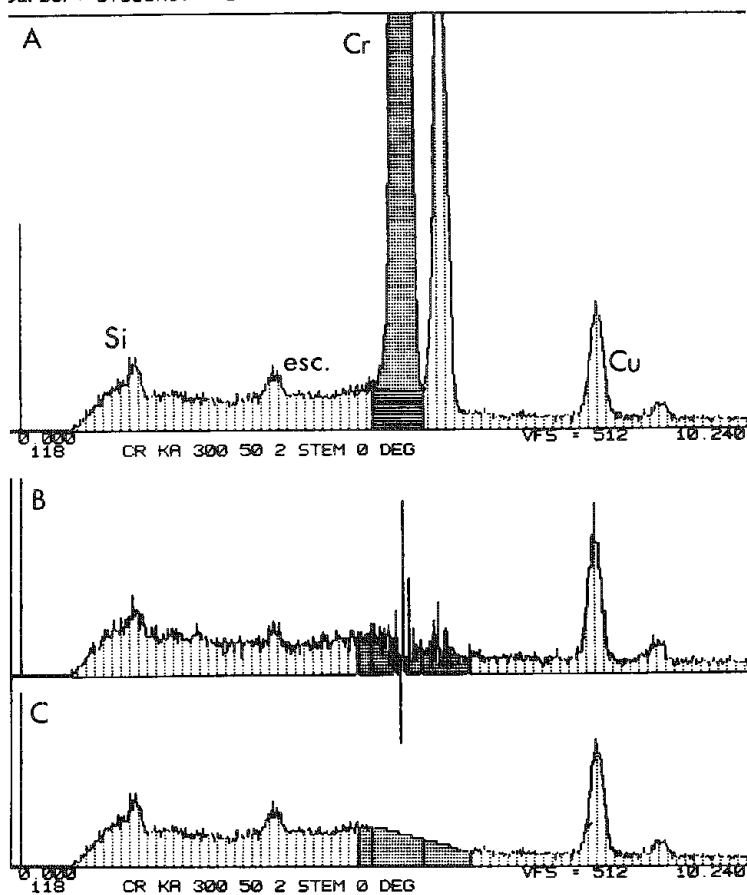


FIG. 3.--(a) Spectrum from thin Cr film with region of interest indicated from 5.0 to 5.7 kV. Cr escape peak is evident as well as Si contamination from evaporator. Cu  $K\alpha$  and  $K\beta$  peaks are from grid bar. Background intensity can be obtained by peak subtraction after least-squares peak fitting with library standard (b) or with specimen used as its own standard (c).

of a region of interest within the peak, which in this case comprises the full width of the Cr K $\alpha$  peak. A suitable integration window is 700 eV around the Cr K $\alpha$  maximum at 5.41 keV; i.e., from 5.0 keV to 5.7 keV, which incorporates any small incomplete charge collection tail. Values of B can be most reliably extracted by means of a digital-filter approach that is now widely available on commercial MCAs. Subtraction of the peak (after least-squares fitting to give  $\rho$ ) gives the background intensity (Fig. 3b). If necessary the spectrum can be used as its own library standard (Fig. 3c). This approach avoids problems with absorption edges, the background shelf, etc. A standard definition of P/B is thus: P = counts above background in the 700eV window comprising the Cr K $\alpha$  peak from 5.0 keV to 5.7 keV; B = average counts in a 10eV channel under the Cr K $\alpha$  peak (i.e., remaining counts in the 700eV window after peak subtraction, divided by 70, which is the total number of channels comprising the window). Table 2 shows data obtained from a thin Cr specimen in several AEMs, over a range of voltages, based on the Fiori et al.<sup>11</sup> definition of P/B.

The results of this experiment at 100 kV should be compared with the work of Fiori et al.,<sup>11</sup> which predicts  $P/B \approx 3000 \pm 1200$ , based on calculations using different ionization cross sections. Similarly, Nicholson et al.'s<sup>10</sup> value for Co at 100 kV is 2000, which when converted to a 10eV background channel and  $\sim 700$ eV width for the peak yields a value of  $P/B \approx 4000$ , i.e., toward the upper range of Fiori et al.'s<sup>11</sup> calculations. Clearly from Table 2 current commercial AEMs have room for significant improvement in P/B before they match either the theory<sup>11</sup> or the practical results of Nicholson et al.,<sup>10</sup> who substantially modified the stage region of their AEM and redesigned their EDS collimator.

#### *Cleanliness of the Microscope Column*

Substantial discussion on methods of "cleaning-up" the AEM column have been reported.<sup>12,13</sup> Generally the method involves use of a self-supporting disk sample which generates a high-energy K or L line ( $>15$ - $20$  keV) and a low-energy ( $<5$  keV) L or M line. The "in-hole" spectrum from such a sample permits discrimination of column-generated stray x-ray effects (high K/L, L/M ratio) from stray electron effects (low K/L, L/M ratio). Although specimens of Ag, Mo, and Au have all been used and many methods of defining the "hole count" problem have been reported, there is still no standard definition. A major problem is that the hole-count varies with distance from the hole edge, probe size, aperture size, kV, etc. Similarly, the hole-count/specimen-count ratio is a function of specimen thickness and is therefore not an ideal measurement of instrument performance. Nevertheless, it is still the best method for assessing column cleanliness, and it is proposed here that any acceptable definition should relate to typical microanalysis conditions. Thus, under any combination of instrument conditions and specimen thickness that generate  $\sim 10\,000$  counts in the K $\alpha$  peak of interest in  $\sim 100$  s live time, the same K $\alpha$  peak recorded with the beam in the hole for the same live time should be less than the background obtained when the beam was on the sample. The probe should be far enough away from the edge of the sample so that any beam tails do not touch the foil. A hole count and specimen spectrum obtained from a Mo disk sample under these conditions is shown in Fig. 4. This performance is acceptable because clearly the hole count would not seriously disturb any quantification.

Recently, Wood and Statham<sup>14</sup> reported a wide variation of Mo (full shell) L/K ratio from several AEMs, which was attributed to variations in spurious counts. It is considered, based on Fig. 4, that this cannot be the case. Differences in XEDS performance affect the L/K value. In particular, a large incomplete charge collection effect in the Mo L line region would raise the background "shelf" below the Mo L line energy and decrease the Mo L line intensity. Also, a wide variation in the detector thickness would give a variation in the Mo K intensity.

It was found that in instruments in which the hole count was acceptable (i.e., similar to Fig. 4) L/K values still varied from 1.8 to 4. This variation must be due to detector performance and not due to column-generated effects. Table 3 lists these data. Thus the Mo L/K ratio is a poor indicator of column cleanliness. A better definition is if the Mo K $\alpha$  hole count is less than the background intensity generated from the Mo specimen, as defined above. The Mo L/K ratio is perhaps a sensitive monitor of detector performance.

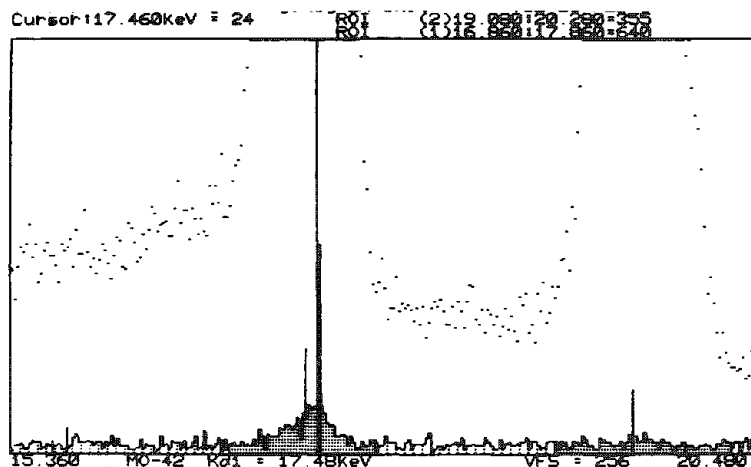


FIG. 4.--X-ray spectrum from thin area of Mo disk sample (dots) and corresponding hole count (solid spectrum) in region of Mo K $\alpha$  and K $\beta$  peaks. Hole count contributes less than one-tenth of *background* intensity obtained from sample during the same live time.

TABLE 1.--Probe current measurements as a function of probe size.

Calculated Nominal Spot Size (nm)		Measured Current (nA)	Calculated Nominal Spot Size (nm)		Measured Current (nA)
FWHM	FWTM		FWHM	FWTM	
100	183	15	40	73	1.4
50	92	7	24	43	0.2
20	36	1	14	25	0.05
10	18	0.3	6	11	0.01
5	9	0.1	2.6	4.7	0.002
2	4	0.03	1.4	2.5	
<u>Conditions</u>			<u>Conditions</u>		
kV = 120      C <sub>2</sub> = 50 $\mu$ m			kV = 100      C <sub>2</sub> = 50 $\mu$ m		
Source = W      STEM Mode			Source = LaB <sub>6</sub> Nanoprobe Mode		
Emission = 45 $\mu$ A			Emission < 5 $\mu$ A		
Courtesy Philips Electron Optics Publishing Group			Courtesy C. F. Klein		

TABLE 2.--P/B ratio defined at Cr K $\alpha$  peak ( $\pm 3\sigma$ ).

	100 kV	200 kV	300 kV
Instrument 1	2750 $\pm$ 300	3350 $\pm$ 300	3400 $\pm$ 300
Instrument 2	2650 $\pm$ 250	3200 $\pm$ 300	2200 $\pm$ 800
Instrument 3	1200 $\pm$ 150		
Instrument 4	1750 $\pm$ 75		
Instrument 5	2900 $\pm$ 300		
All measurements in STEM mode			
Instruments 1, 2, 5 specimen horizontal			
Instrument 3 specimen tilted 20°			
Instrument 4 specimen tilted 35°			

TABLE 3.--Mo L/K ratio--full shell intensities [(L<sub>1</sub> + L $\alpha$  + L $\beta$  + L $\gamma$ )/(K $\alpha$  + K $\beta$ )].

	100 kV	200 kV	300 kV
Instrument 1	1.95	1.54	1.42
Instrument 2	2.55	1.95	1.82
Instrument 3	4.20		
STEM mode			
L range 1.92-2.72 keV			
K range 16.86-17.86 keV			
K $\alpha$ range 19.28-20.28 keV			
K $\beta$			

### Summary

1. Spatial resolution performance criteria cannot be defined yet for all current AEMs. However, probe sizes defined as FWTM should be measured directly from the TEM screen where possible and total currents recorded by use of a Faraday cup in the column of the AEM.

2. P/B should be defined in terms of the characteristic intensity above background within a Cr K $\alpha$  peak integrated from 5.0 to 5.7 keV. Background counts should be averaged over an identical range and then divided by 70 to give those in a single 10eV channel as proposed by Fiori et al.; values at  $\sim$ 100 keV accelerating voltage should be in the range 3000-4000 in agreement with both theory and the best experimental results.

3. Column cleanliness is still best described in terms of the hole count as a fraction of the sample spectrum from a suitable specimen such as Mo. The Mo L/K ratio is more a measure of detector characteristics than column cleanliness.

### References

1. S. J. B. Reed, *Ultramicroscopy*, 1982, 7, 405.
2. D. B. Williams, *Practical Analytical Electron Microscopy in Materials Science*, Mahwah, N.J.: Philips Electronic Instruments, 1984, 34.
3. G. Cliff and P. B. Kenway, *Microbeam Analysis--1982*, 107.
4. J. I. Goldstein et al., *SEM/1977 I*, 315.
5. C. F. Klein et al., in "Intermediate voltage microscopy and its application to materials science," *Philips Norelco Reporter* (in press).
6. S. J. B. Reed, *Electron Microprobe Analysis*, Cambridge: Cambridge University Press, 1975, 144.
7. E. Lifshin et al., "X-ray spectral measurement and interpretation," in J. I. Goldstein and H. Yakowitz, Eds., *Practical Scanning Electron Microscopy*, New York: Plenum, 1975, 263.
8. L. V. Sutfin and R. E. Ogilvie, in J. C. Russ, Ed., *Energy Dispersion X-ray Analysis: X-ray and Electron Probe Analysis*, Philadelphia: ASTM, 1971, 197.
9. J. D. Geller, *SEM/1977 I*, 281.
10. W. A. P. Nicholson et al., *J. Microsc.* 125: 25, 1982.
11. C. E. Fiori et al., *Microbeam Analysis--1982*, 57.
12. J. I. Goldstein and D. B. Williams, *SEM/1978 I*, 427.
13. L. F. Allard and D. F. Blake, *Microbeam Analysis--1982*, 8.
14. J. E. Wood and P. J. Statham, *Microbeam Analysis--1985*, 354.

## BORON ANALYSIS WITH A WINDOWLESS X-RAY DETECTOR

P. M. Budd and P. J. Goodhew

The development of windowless x-ray detectors for TEMs has made light-element analysis of thin specimens routinely available in many laboratories. The presence of boron has been detected, at least in compounds with a relatively high concentration of the element.<sup>1</sup> However, our comparative studies of the boron content of a metallic glass using both WEDX and EELS<sup>2</sup> indicated that the intensity of the boron x-ray peak was lower than would be expected at first sight. The observed intensity was lower than could be accounted for in terms of absorption in either the detector or the specimen. Clearly the development of detectors suitable for boron is in its early stages and it is qualitatively useful even to have separated the boron peak from the low energy noise peak. In this paper we assess the outlook for quantitative analysis of samples containing boron.

### *Experimental*

All experiments were carried out using a LINK Systems LZ-5 detector with a rotatable turret carrying a conventional Be window and a hole for windowless analysis. The detector was mounted at an elevation of 7° above the specimen position on a Philips 400T microscope. All analysis was performed at 100 kV with the sample tilted a nominal 30° toward the detector.

Powdered samples of pure boron, TiB<sub>2</sub>, and TiO<sub>2</sub> were mounted on thin films of aluminum or on holey carbon films. Spectra were collected with the beam, of spot size 200 nm focused on to the edge of a particle. Care was taken to select only fairly thin regions, whose maximum thickness was estimated as 150 nm. The particles were in all cases on the same side of the support film as the detector.

### *Results and Discussion*

Spectra from pure boron particles lying on a thin aluminum film show that a substantial boron K peak can be obtained with excellent separation from the noise peak. The visibility of this peak is enhanced at high count rates (Fig. 1), since the magnitude of the system noise peak is essentially independent of count rate. Based purely on the statistics of this peak and its background, the minimum detection limit (MDL) for boron would be between 2 and 3 wt%. We would not expect the practical limit to be as low for several reasons. The effect of absorption in the specimen, which is often ignored in MDL calculations, is substantial in many cases and may be as high as a factor 2. The other major problem is the presence of carbon. The C K peak overlaps B K substantially for all likely detector resolutions and few microscope/sample configurations are both carbon free and contamination free. In principle, of course, the two peaks can be deconvoluted but in practice it is difficult to prepare a reproducible B K peak profile for fitting. A more reasonable estimate of the MDL for boron is 6-8 wt%, as the following analysis shows.

Spectra from TiB<sub>2</sub> particles, with a boron concentration of 31 wt%, appear to show a much lower boron signal compared to the noise peak (Fig. 2). The MDL based on the statistics of this peak is about 6 wt%, but this limit assumes there is no C K present, which is unlikely in practice.

The B K/Ti L ratio was also small, both for particles on holey carbon films and for those on aluminum films. It is difficult to attribute this result to absorption in the support film. There must be substantial absorption of B K in the compound specimen, although for the majority of the particles analyzed the absorption correction would not be larger than 1.5. Since the detector is quite sensitive to O K (K/O<sub>F</sub>e approximately 3), it might be thought sensible to compare the O K/Ti L ratio from Ti O<sub>2</sub> to the B K/Ti L ratio from Ti B<sub>2</sub>.

---

The authors are at the Department of Materials Science and Engineering, University of Surrey, Guildford, England GU2 5XH.

and thus obtain an indirect "k-factor" for boron. This procedure is difficult because of the small separation of the O K and Ti L peaks but a rough estimate indicates a B/O peak ratio of 19. The total factor by which the B signal from Ti B<sub>2</sub> would be expected to differ from the O signal from Ti O<sub>2</sub> is compounded of the x-ray production efficiency factor, the detector efficiency factor, the sample absorption factor, and the difference in concentrations factor. We can estimate these factors to be 2.5,<sup>3</sup> 4,<sup>3</sup> 1.1,<sup>4</sup> and 1.3, a total factor of 14.3. This result would therefore give an estimate of a "k-factor" for boron of ~45, which compares favorably with the estimate of 55 from our current work. Consideration of the B K/Ti K peak ratio also gives an estimate of the "k-factor" for boron since K<sub>TiFe</sub> is ~0.8 with absorption and concentration differences taken into account, an estimate for the "k-factor" for boron is ~50. Therefore the agreement between the results is good, which is surprising when the experimental setting-up procedure for the detector is considered, as we now show.

In some systems the sensitivity of a Si(Li) detector to very low energy x rays can vary with the slow discriminator setting.<sup>5</sup> We therefore collected a series of spectra at various settings of this discriminator. Figure 3 shows two spectra from the series. It is clear that the absolute intensity of the apparent boron K signal can be easily altered by a factor of 2 by relatively minor adjustments of the discriminator, which leave all other higher-energy peaks unaffected. The ratio of the noise peak to the boron peak rises as the discriminator setting is reduced but the two peaks remain clearly separated. However, since the oxygen peak is unaffected, the boron K/oxygen K ratio changes by a factor of as much as 2. It is clearly of great importance for quantitative analysis of boron that the discriminator setting is neither changed deliberately nor drifts between analysis sessions. Because of (1) the difficulty of establishing reproducible specimen and microscope conditions from day to day (or even from hour to hour), (2) the irregular shape of the powder particles, and (3) the problem of contamination build-up, it has not yet been possible to monitor the stability of the boron peak over long periods.

## References

1. N. Zaluzec, R. McConville, and A. Sandborg, "A comparison of XEDS and EELS with the use of conventional Be window and windowless Si(Li) detectors," *Analytical Electron Microscopy--1984*, 348-352.
2. N. R. Gregg, P. J. Goodhew, and P. M. Budd, "Boron redistribution during solidification," *Proc. EMAG 85*, Inst. Physics Conf. Series 78, 277-280, 1985.
3. L. E. Thomas, "Microanalysis of light elements by simultaneous x-ray and electron spectroscopy," *Analytical Electron Microscopy--1984*, 358-362.
4. B. L. Henke and E. S. Ebisu, "Low energy x-ray and electron absorption within solids," *Adv. X-ray Analysis* 17: 150-213, 1973.
5. P. J. Statham, "Prospects for improvement in EDX microanalysis," *J. Microscopy* 130: 165-176, 1985.

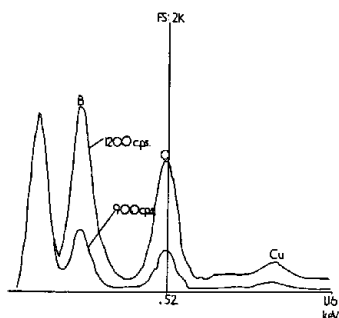


FIG. 1.--Comparison of spectra collected from pure B particles on Al film at different count rates.

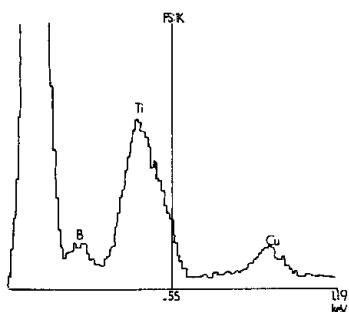


FIG. 2.--Spectrum collected from Ti B<sub>2</sub> showing B K and Ti L peaks.

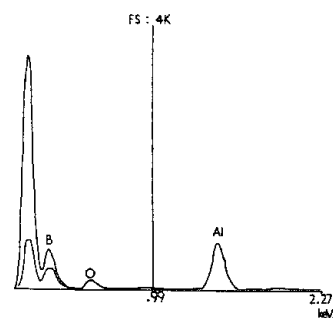


FIG. 3.--Comparison of spectra collected at various slow discriminator settings showing the variation in the B K and noise peaks.



## THIN-FILM ANALYSES OF SILICATE STANDARDS AT 200 kV: THE EFFECT OF TEMPERATURE ON ELEMENT LOSS

I. D. R. Mackinnon, G. R. Lumpkin, and S. B. Van Deusen

Current generation analytical electron microscopes (AEMs) provide powerful diagnostic techniques for microstructural and microchemical investigations of complex mineralogical systems.<sup>1</sup> Significant progress toward quantitative chemical analyses at submicron sizes has been possible due to the development of the "thin-film criterion" for which the intensity ratios  $I_{AB}$  of an unknown are directly related to element concentration ratios by an instrument-dependent  $k_{AB}$  factor determined with well-characterized standards.<sup>2,3</sup> Most determinations of  $k_{ZSi}$  factors in silicate systems have used standards from a wide variety of mineral classes in order to maximize the concentration range<sup>1,3</sup> and obtain a reasonably accurate value of the slope in  $C_Z/C_{Si}$  vs  $I_Z/I_{Si}$  plots. In order to reduce the relative error for major element determinations, care must be exercised in (a) the choice of standards, (b) the elimination of secondary x-ray absorptions and possible spurious peaks, (c) the calculation of peak intensities, and (d) the collection of statistically significant data sets. However, few statistical analyses on the reliability of thin-film determinations have been performed. A notable exception is the study by Blake et al.,<sup>4</sup> in which average ratios from up to 25 individual analyses were used to construct plots for the determination of  $k_{ZCa}$  for calcium-rich mineral systems. This study also demonstrates an effective method which may be used to assess the degree of heterogeneity of a mineral standard. Nord has also shown that accurate AEM analyses can be obtained for pyroxenes (a deviation of ~1.5 mole% endmember) using a 100nm probe at 200 kV.<sup>1</sup> In this study, we present preliminary data on a detailed statistical analysis of k-factor determination for a single class of minerals (amphiboles) which contain a wide range of element concentrations. These amphiboles are homogeneous, contain few (if any) subsolidus microstructures, and can be readily prepared for thin-film analysis. In the above-mentioned studies, element loss during the period of irradiation has been assumed negligible for the determination of k-factors. Since this phenomenon may be significant for certain mineral systems,<sup>5</sup> we also report on the effect of temperature on k-factor determination for various elements using small probe sizes (~20 nm).

### *Experimental*

The instrument used was a JEOL 2000FX AEM with an attached Tracor Northern TN-5500 energy-dispersive spectrometer (EDS) having an effective take-off angle of 68° when the sample is at zero degrees tilt (X and Y) in the eucentric plane of the objective lens. All samples were mounted in a Gatan double-tilt holder with Be inserts and an attached Faraday cup for beam-current measurements. The average beam current used for all determinations was 0.8 nA from a W hairpin filament operating at 200 kV. Nominal beam size in the TEM mode at the specimen using a LaB<sub>6</sub> filament is 20 nm (FWHM; JEOL specifications), although the use of a W filament probably increased the beam size to <30 nm. The line-of-sight distance from the sample to the Si(Li) detector was 31 mm. Window widths for all elements were set at 0.26 keV. A background subtraction routine using a fitted polynomial equation supplied by Tracor Northern was employed for all spectra. All AEM analyses were performed under the same lens conditions at a vacuum <2.0 × 10<sup>-5</sup> Pa. Sample thickness for all analyses was less than that at which x-ray absorption is considered significant for the general mineral system.<sup>1</sup> Low-temperature analyses were performed with a Gatan low-background, double-tilt cold stage using liquid nitrogen and a temperature controller with a precision of ±1 C.

---

Authors Mackinnon and Lumpkin are at the Department of Geology, University of New Mexico, Albuquerque, NM 87131; author Van Deusen is at Sandia National Laboratories, Albuquerque, NM 87185. This work was performed in the Electron Microbeam Analysis Facility in the Department of Geology and Institute of Meteoritics at UNM. Partial support from NASA and DOE is acknowledged.

Amphibole standards were obtained from a variety of sources including the Australian Museum (courtesy F. L. Sutherland, curator) and G. Cliff (University of Manchester; via F. J. M. Reitmeijer). These latter samples included cummingtonite, hornblende, and tremolite, all analyzed by the Minnesota Rock Analysis Laboratory. Two other amphiboles, richterite and hornblende, were analyzed with a fully automated JEOL 733 electron microprobe prior to preparation for thin-film AEM analysis. Conventional mineral standards and a full Bence-Albee correction procedure were used for the microprobe analyses of the richterite and hornblende standards shown in Table 1. These data were taken from a minimum of five points per sample, and estimated standard deviations (esd's) for each element oxide are given in parentheses. The cummingtonite, hornblende, and tremolite provided by G. Cliff were dispersed on holey carbon films on 200-mesh Cu grids; the other two amphiboles were ion-milled and placed on Be slot grids. For room-temperature AEM analyses of amphiboles, at least 30 individual analyses for collection periods of 300 s were obtained.

Extensive modifications to reduce system background in EDS spectra (see, for example, Ref. 6) were not necessary for this AEM as appropriate thick apertures and low-Z inserts were included in the off-the-shelf product. With the smallest size electron beam ( $\sim 2.5$  nm; LaB<sub>6</sub> filament), the total full scale counts (0 to 20 kV) for an "in-hole" test (beam positioned  $<100$  nm from a thin Au film) was 9 for a collection period of 200 s at 100 kV. This "in-hole" count rate compares with a value of 25 for a similar test performed on a modified JEOL 100 CX AEM in STEM mode with the EDS detector at the eucentric plane and the sample tilted at  $35^\circ$ .<sup>7</sup> An additional test to gauge the effect of "electron spray" in the sample chamber was performed. The full-scale integrated counts (0 to 20 kV) for thin-film analyses of crushed boron-carbide grains dispersed on a holey-carbon film on a 150-mesh Be grid averaged 145 for a 300s collection period. The total integrated counts in the Cu K $\alpha$  peak for this test was 5. Thus, contributions to EDS spectra from the AEM column were negligible. For thin-film analyses of the crushed amphibole grains, x rays from the Cu support grid were always apparent, though care was taken to insure the contribution was minimized.

### *Results and Discussion*

K-factors for Na, Mg, Al, K, Ca, and Fe have been determined by use of the five amphibole standards listed above. Additional data points for Na and Al have been obtained from the feldspar standard, Amelia albite, described below in the section on cold-stage analyses. Plots for the four elements Na, Al, Mg, and Ca are shown in Fig. 1, along with the value for  $k_{ZSi}$ , the straight-line intercept, and the correlation coefficient. The (0,0) data point has not been included in least-squares analyses of each element. For all elements except Na, the correlation coefficients for least-squares fits of the data points are greater than 0.95. The value for Na is 0.896 and the intercept value is 0.013. This slightly poorer value of the correlation coefficient may be due to an underestimate of the  $I_{Na}$  for richterite. For this sample, the complete set of 30 analyses were obtained with a very low count rate ( $<512$  counts full scale), which caused the Na peak to be poorly approximated by the background subtraction routine. Nevertheless, all six k-factors determined from these few amphibole standards are in good agreement with values obtained by other workers using different instruments<sup>1,3</sup> or using theoretical calculations.<sup>8</sup>

A study by McGill and Hubbard<sup>5</sup> using a thin specimen of Amelia albite showed that element loss during electron irradiation can be significant. At 100 kV and a beam diameter of 3  $\mu$ m, the apparent  $k_{NaSi}$  value increased dramatically (factors of 4 $\times$ ) with irradiation times up to 300 s. Plots of  $k_{NaSi}$  vs irradiation times were then extrapolated to  $t = 0$  to obtain an estimate of the actual  $k_{NaSi}$  value for beam-sensitive minerals. In these experiments, the beam current density was quite low compared with that available in current-generation instruments. In Fig. 2, we show a similar type of study on Amelia albite at 200 kV using a smaller probe size ( $\sim 20$  nm) and higher beam-current density. At room temperature ( $\sim 20$  C), both the Na and Al k-factors increase with irradiation time, though the relative increase for Al is not as rapid. This change in k-factor (for both elements) can be directly correlated with loss of crystalline structure by observation of diffraction phenomena (e.g., Kikuchi lines and higher-order diffraction spots).

For comparison, the same analyses performed at  $-150$  C are also plotted on Fig. 2 (open circles). For both elements, k-factors do not deviate significantly from the extrapolated  $t = 0$  value with irradiation time. This indicates that element loss is not significant

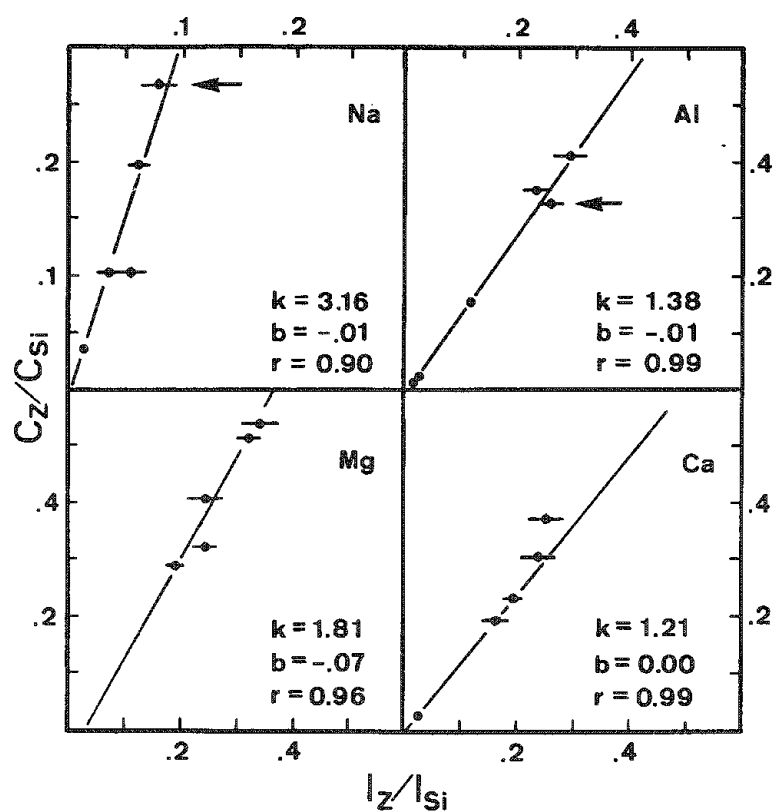


FIG. 1.--Concentration ratios vs intensity ratios for Na, Mg, Al, and Ca for five amphibole standards at  $\sim 20^\circ\text{C}$ . Data for Amelia albite at  $-150^\circ\text{C}$  are also included in Na and Al plots (arrows). Slope of least-squares linear fit is experimental  $k_{ZSi}$  value; intercept  $b$  and correlation coefficient  $r$  are also listed for each plot.

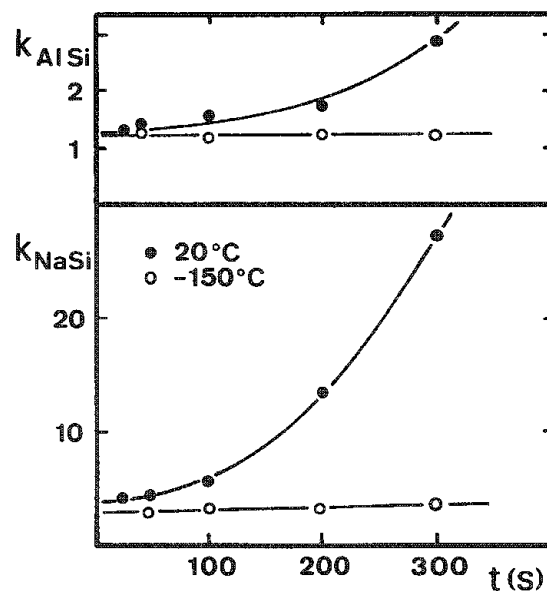


FIG. 2.--Observed  $k_{ZSi}$  values for Amelia albite as function of irradiation time and ambient temperature.

TABLE 1.--Electron microprobe analyses of two amphibole standards provided by Australian Museum: Richterite (Cat. No. D29299) from Langban, Sweden, and hornblende (Cat. No. 1144) from Verona, Ont. Estimated standard deviations shown in parentheses.

	Richterite		Hornblende	
SiO <sub>2</sub>	56.7	(.45)	46.7	(.18)
TiO <sub>2</sub>	0.00		0.75	(.04)
Al <sub>2</sub> O <sub>3</sub>	0.75	(.02)	6.20	(.08)
MgO	22.6	(.35)	11.1	(.13)
CaO	7.17	(.09)	6.63	(.06)
MnO	3.11	(.22)	0.97	(.02)
FeO	0.14	(.01)	18.5	(.22)
Na <sub>2</sub> O	3.66	(.07)	5.86	(.20)
K <sub>2</sub> O	1.15	(.05)	1.33	(.03)
F <sup>-</sup>	0.42	(.09)	1.76	(.24)
Cl	0.00		0.03	
	95.70		99.83	

at this low temperature, presumably because loss of crystallinity during irradiation is reduced significantly. In addition, these low-temperature results confirm the expectation<sup>5</sup> that extrapolation of higher temperature plots to  $t = 0$  will give a reasonable approximation to the real k-factor value for a given mineral system. In order to test the effectiveness of our room-temperature k-factor determinations using the amphibole standards, we also performed similar analyses on hornblende (Table 1) at -150 C. Table 2 shows intensity ratios for this hornblende at 20 C and -150 C. There is no significant difference (within 1 esd) in the intensity ratios calculated for any element at these two temperatures. Thus, element loss for this particular amphibole is negligible or, at least, it occurs at the same rate at both temperatures. However, a significant improvement in the value of the esd's associated with each element ratio can be observed for the lower temperature data. Furthermore, at a given temperature, we note that esd's of ion-milled samples are lower than those of crushed grains.

### Summary

A number of amphibole standards can provide a range of element concentrations suitable for reliable calculation of  $kZ_{Si}$  values without significant element loss during electron-beam irradiation. Element loss for albite is significant for irradiation times >25 s at 200 kV and ~20 C. If the sample is held at lower temperatures (150 C), element loss can be eliminated and reproducibility of calculated k-factors is enhanced.

### References

1. G. L. Nord Jr., "Analytical electron microscopy in mineralogy: Exsolved phases in pyroxenes," *Ultramicroscopy* 8: 109-120, 1982.
2. N. J. Zaluzec, "A beginner's guide to x-ray analysis in an analytical electron microscope: Part 1. Quantification k-factor and Si(Li) detector calculations," *EMSA Bulletin* 14: 67-75, 1984.
3. P. E. Champness et al., "Quantitative analytical electron microscopy of metals and minerals," *Ultramicroscopy* 8: 121-132, 1982.
4. D. F. Blake et al., "A statistical method for the analysis of quantitative thin-film x-ray microanalytical data," *J. Microscopy* 131: 249-255, 1983.
5. G. W. Lorimer, "X-ray microanalysis in the TEM," *Inst. Phys. Conf. Ser. No. 61*, 1982, 147-152.
6. L. F. Allard and D. F. Blake, "The practice of modifying an analytical electron microscope to produce clean x-ray spectra," *Microbeam Analysis--1982*, 8-20.
7. I. D. R. Mackinnon et al., "Microbeam analyses of stratospheric particles," *Microbeam Analysis--1985*, 291-297.
8. J. I. Goldstein et al., "Quantitative x-ray analysis in the electron microscope," *SEM/1977 I*, 315-324.

TABLE 2.--Comparison of intensity ratios for hornblende standard from Verona, Ont., at 20 and -150 C.

Z	$I_Z/I_{Si}$	
	20 C	-150 C
Na	0.054 (16)	0.061 (6)
Mg	0.185 (35)	0.190 (9)
Al	0.116 (10)	0.119 (2)
K	0.037 (10)	0.037 (2)
Ca	0.182 (15)	0.197 (8)
Mn	0.028 (6)	0.033 (2)
Fe	0.606 (58)	0.619 (21)

## IMPROVED SPATIAL RESOLUTION FOR EDX ANALYSIS WITH INTERMEDIATE VOLTAGES

K. Rajan, J. McCaffrey, P. B. Sewell, and G. L'Esperance

Improved spatial resolution for energy-dispersive x-ray (EDX) analysis using 300 kV instead of 100 kV incident electron energies is experimentally demonstrated. Comparisons are made with single scattering and Monte Carlo calculations for beam broadening.

It is a well-established fact the spatial resolution for EDX analysis for thin foils examined by analytical electron microscopy is ultimately limited by beam broadening. The dominant process causing beam spreading is elastic scattering by atomic nuclei. Almost all electrons contribute to x-ray production, and those scattered at the greatest angles define the effective width of the x-ray source. Irrespective of the approach to model this scattering, the basic prediction is that the extent of beam spreading is minimized with increasing incident voltage (for a given atomic number and sample thickness). The new class of intermediate-voltage microscopes provides an opportunity to achieve a higher spatial resolution for EDX analysis. This paper provides the initial results of a study to determine quantitatively the extent of beam broadening in a 300 kV analytical electron microscope.

### *Experimental Details*

In doing any beam broadening experiment we need a sharp interface that can be examined edge-on. The relatively few experimental studies of beam broadening described in the literature have tended to use naturally occurring boundaries,<sup>1</sup> although Hutchings et al.<sup>2</sup> have used artificially produced interfaces. For our study we used a cross-sectional sample of a Ge/Si bicrystal prepared by the molecular beam epitaxy technique. Such a system provides a configuration with an atomically sharp chemical discontinuity.

The experiments were carried out at 100 kV and 300 kV with a Philips 430 microscope operating in the STEM mode with a tungsten filament. A spot size of 7 nm was used. The beam divergence in STEM and during x-ray microanalysis was 20 mrad. The probe was held stationary for 100 s counting time and the Si and Ge x-ray counts were recorded. The experimental estimate of beam broadening was determined by measurement of the maximum distance from the interface where the element on the other side of the interface can first be detected.

### *Results and Discussion*

X-ray line traces were obtained at 100 kV and 300 kV from an area 1  $\mu\text{m}$  thick. Thickness measurements were made by convergent-beam diffraction. Strong dynamical diffraction conditions were avoided. The results for beam broadening in silicon are summarized in Table 1. It is clear that the increase in voltage does indeed offer a noticeable improvement in spatial resolution for EDX analysis.

TABLE 1.--Estimates of beam spreading in silicon.

Voltage (kV)	Beam spreading (nm)		
	Experiment	Single-scattering calculation	Monte Carlo calculation
100	260	250	240
300	100	85	160

Authors Rajan, McCaffrey, and Sewell are at National Research Council Canada (Division of Microstructural Sciences), Ottawa, Ont. K1A 0R8; author L'Esperance is at Ecole Polytechnique, Montréal, P.Q., Canada.

For comparison we have also listed beam broadening estimates made from the Reed single-scattering model<sup>3</sup> and Monte Carlo calculations.<sup>4</sup> We made the single-scattering calculation for the total 90% beam diameter at a given depth by adding the initial probe diameter and the beam broadening from the Reed model in quadrature. The Monte Carlo calculations provide a beam-broadening estimate based on the diameter of a cylinder containing 90% of the total x-ray production.

At 100 kV both the single-scattering and Monte Carlo calculations agree to give comparable results to experiment. However, at 300 kV, the two models deviate substantially from experimental results. In fact of the two, the Monte Carlo calculation shows a greater discrepancy from experiment at the higher voltage. These discrepancies may be a result of the values of the ionization cross sections used in the calculations and their validity at higher voltages. This deviation is at present being studied in more detail and the results will be reported in more detail elsewhere.<sup>5</sup>

### *Conclusions*

Spatial resolution for x-ray microanalysis is noticeably improved with intermediate-voltage microscopes. The present results suggest that further work is required in the modeling of beam broadening at higher voltages.

### *References*

1. I. P. Jones and M. H. Loretto, "Some aspects of quantitative STEM x-ray microanalysis," *J. Microscopy* 124: 3-13, 1981.
2. R. Hutchings et al., "Spatial resolution in x-ray microanalysis of thin foils in STEM," *Ultramicroscopy* 3: 401-405, 1979.
3. J. I. Goldstein et al., "Quantitative x-ray analysis in the electron microscope," *SEM/1977 I*, 315-324.
4. D. Joy, *Thin-film Monte Carlo Program*, Lehigh University AEM Course.
5. K. Rajan and P. B. Sewell, Eds., *Intermediate Voltage Microscopy and Its Application to Materials Science*, Mahwah, N.J.: Philips Electronics Instruments, Electron Optics Publ. Group (in press).

## Special Biological Symposium: Applications in Forensic Science

### HAIR COMPARISON IN THE SEM EDX BASED UPON INCREASED SULFUR INTENSITY ALONG THE LENGTH OF HAIR: EVIDENCE OF A "SULFUR PUMP"

Samarendra Basu

Based upon scanning electron microscopy with energy-dispersive x-ray analysis (SEM-EDAX), this laboratory has undertaken a preliminary research program to determine whether conventional microscopy tests for hair comparison can be significantly aided by the use of parameters derived from spatial variations of sulfur and other elements found in elevated amounts particularly at the root of scalp hairs of some individuals. The most interesting parameter to be reported here is the sudden rise in the uptake of sulfur within the endodermal portion of the hair root, which is followed by a gradual increase in the concentration of sulfur along the length of the hair shaft. The rate of incorporation of sulfur measured at the hair root ("sulfur index") varies remarkably from one individual to another. The observation infers the existence of a biochemical pump for sulfur within the hair root.

The difficulties associated with forensic hair comparison is that the hairs from various parts of an individual's scalp are rarely alike in terms of macroscopic and microscopic characteristics<sup>1</sup> and concentration distribution of several inorganic elements except sulfur.<sup>2,3</sup> The present research was undertaken with a view to obtaining corroborative parameters of hair comparison, based on the spatial variation of sulfur.<sup>4</sup> The consensus is that the consumption of sulfur by scalp hairs perhaps depends on physiological stress or body status. Sulfur is not only the major stable inorganic element (5 to 6% w/w) of scalp hairs,<sup>3,5</sup> it determines the increased stability of eukeratin fibers which constitute the hair structure almost entirely. Sulfur forms disulfide (-S-S-) cross linkages between cystine residues of adjacent peptide chains of eukeratin. The major question now is how S is incorporated into hair. The technical merit of superimposing an x-ray line scan on the image of the sample area has been determined elsewhere.<sup>4</sup> Seta et al.<sup>3</sup> have shown that S is more abundant in hair cuticle and cortex than in medulla. This finding would also serve as a reference for comparative assessment of the modes of distribution of other elements (e.g., copper)<sup>6</sup> in hair. These various methods have been used in a hair comparison test.

#### *Experimental*

Both plucked and combed natural (unpermed) hairs from the heads of several donors (total 14) were employed for studies of spatial variation of sulfur. The growth phases of plucked (anagen) hairs and combed (telogen) hairs were identified according to King et al.<sup>7</sup> Selected hairs (6 to 9 per head) were examined for elemental analysis before they were washed and also after their washing by successive rinses in cycles (20 min each), in three solvents: distilled water, diethyl ether, and acetone.<sup>4,7</sup> Only anagen (plucked) hairs that have had no prior indication of copper in them were soaked in a solution of  $\text{Cu}(\text{NO}_3)_2$  (pH 4.5) for incorporation of copper ions into these hairs.<sup>4,7</sup> The Cu uptake was maintained as measured after washing and drying of these hairs at about 0.6%, which has been encountered in some individual's hairs (cf. Maes and Pate<sup>7</sup>).<sup>4</sup>

Sample hairs, each cut to 15mm segments, were attached in known arrays on diluted rubber cement layers on a polished carbon planchet (diam. 13 mm). They were coated with evaporated carbon and then line-scanned along and across their length. Characteristic x-ray spectra and line scans were obtained under identical conditions of tilt (45°) and sample orientation, etc., for all hairs.<sup>2,3</sup> The integral x-ray counts due to S  $K\alpha$  were corrected for background radiation and then converted to intensities (cps). The x-ray line scanning studies were conducted by a careful application of the analog, or rate-meter (EDAX 352) approach,<sup>8</sup> with an x-ray analyzer (EDAX 707A) in an SEM (AMRAY 1000) at 20 kV electron potential.

---

The author is at New York State Police Crime Laboratory, Albany, NY 12226.

### *Characteristics of Absorbed Copper*

The hair topography starts to be smoother above the hair root and so the density effect due to variable absorption of an external element (e.g., copper ions) predominates on the hair shaft. The line scans of S across hair in this area are usually unvarying or dome shaped, depending on the local hair topography. Thus, sulfur distribution was relatively homogeneous (Fig. 1) across hair segments, whereas the absorbed copper ions had a variable distribution across the same segments (Fig. 1).

### *Characteristics of Sulfur*

A sudden increase in the S K $\alpha$  intensity (cps) takes place at a short distance above the proximal end of hair. This observation is represented in Fig. 2(A) in terms of x-ray spectra obtained on a telogen (combed) hair of an individual (solid). The S K $\alpha$  peak measured away from the papilla (the bulge of hair root) was about 5.5-fold more intense than the S K $\alpha$  peak obtained on the papilla (cf. curves a and b, Fig. 2A). The root of this individual's hair (unwashed) also contained Cl, K, and Ca. For an anagen hair of a second individual (Fig. 2B), which had mainly S and P at the root, the measured increment in the S K $\alpha$  intensity was only 1.6-fold for a distance of 100-200  $\mu$ m from papilla. The intensities of S K $\alpha$  and P K $\alpha$  were not affected by washing of those and other hairs. Among the elements that were variably removed due to washing were Na (not shown), Cl, and Ca. For combed (telogen) hairs the increase in the S uptake was rapid within the endodermal portion of the hair root. These hairs also represented an early saturation in the S K $\alpha$  intensity at a variable distance (0.25 mm to 1.5 cm) from the proximal end of the hair (cf. hair A, Fig. 3); whereas for plucked hairs (anagen) the uptake of S was rather slow within the hair root but increased gradually along the length of the hair shaft (cf. hair D, Sl, Fig. 3). Because the plucked hairs of the individuals did not indicate any saturation within the maximum examined distance (1.5 cm) from the root, the rate of incorporation of S was measured at the hair root ( $\Delta I_s/\Delta X$ ,  $x \geq 0$ ). This rate was as low as  $0.2 \times 10^3$  cpm/cm, or was high as  $30 \times 10^3$  cpm/cm. This rate, which was similar for both anagen and telogen hairs, will be termed "sulfur index" as it was apparently a characteristic of each donor (total 14).

### *A Laboratory Test on Hair Matching*

These characteristics of S and absorbed Cu (ions) were applied to a hair matching test consisting of four hairs (A, B, C, and D) collected from a rape scene and three control hairs, one from each of two suspects (Sus 1, Sus 2) and a victim (Vi) (Figs. 3 and 4). The hairs marked A, B, D, and Sus 1 contained their roots. The rest of hairs (C, Vi, and Sus 2) were only cut hair segments, having no attached root. Hairs D and Sus 1 were identified as anagen hairs, whereas hair A was a telogen hair. Hair B was unusually thick and had a strange structure. It had no characteristics that matched the other control hairs. Line scans of P at the root of hairs A, D, and Sus 1 and those due to Cu (hairs C, Vi) showed that these were endogenous (or strongly absorbed) elements as their line scans matched in shape with the line scans of sulfur. The presence of Ca was ignored because the element was found as deposits. A detailed analysis of these results has been given elsewhere.<sup>9</sup>

The combined data in Fig. 4 of "root elements," "shaft elements," and the measured "sulfur indices" at the root of hairs A, B, D, Sus 1, and Sus 2 (or Sl, S2) have shown that the hairs A, D, and Sus 1 matched each other in terms of those three parameters. The hairs C and Vi had only one parameter in common (i.e., copper in the hair shafts) and so no definite conclusion could be given about these two hairs and about the hair Sus 2. These two comparisons proved to be true (see bottom of Fig. 4) and this conclusion was strengthened when light microscopic features of hair color, pigmentation, medullation, structure, and cuticular trait, etc., were taken in account. The standard deviation in the measurements of the "sulfur index" of anagen vs telogen hairs was about 2% to 3% (cf. hair D vs hair Sus 1; hair A vs D, etc., Fig. 4).

### *Conclusion*

The conventional microscopy test for hair comparison can be significantly aided with the uses of S uptake and elemental data examined in the SEM-EDX.<sup>10</sup>



FIG. 1.--Line scans of S K $\alpha$  and absorbed Cu K $\alpha$  intensities (x rays) across washed hair segment. Bar = 20  $\mu$ m.

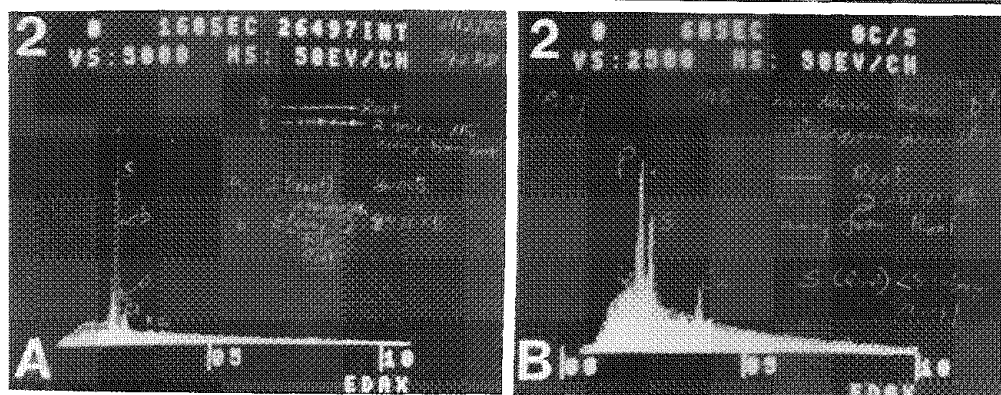
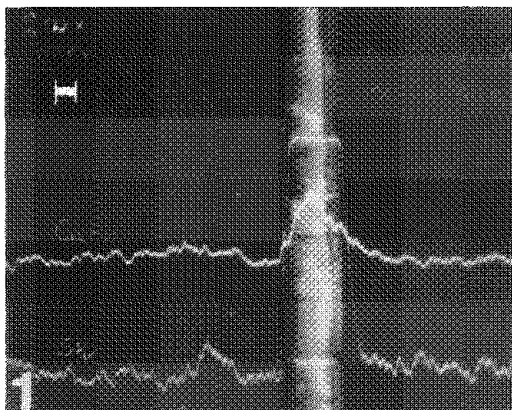


FIG. 2.--Characteristic x-ray spectra of telogen (combed) hair (A) and anagen hair (B) of two different individuals. Solid lines, spectra at bulge (papilla) of hair root; dotted lines, spectra 100-200  $\mu$ m away from papilla. (For S uptake of hair in B, see curve D in Fig. 3.)

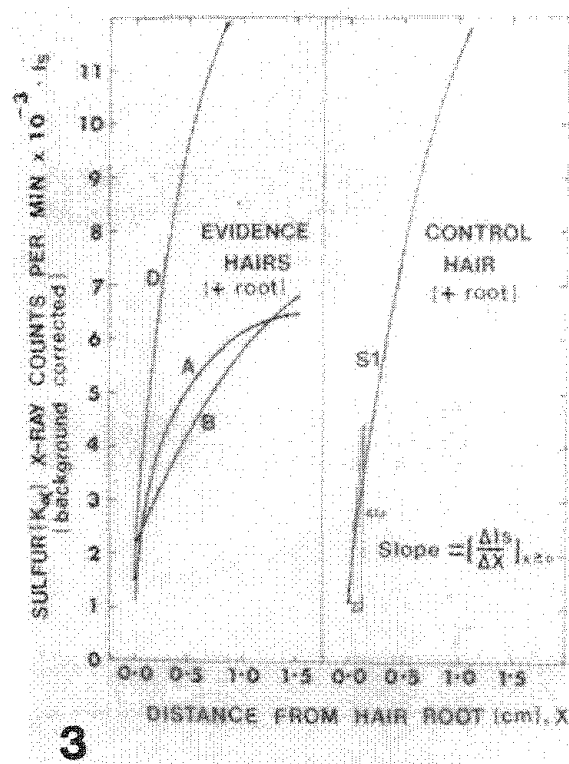


FIG. 3.--Spatial variation of S in scalp hairs in laboratory matching test. Clean unwashed hairs.

## References

1. B. D. Gaudette, "Forensic hair comparisons," *Crime Lab Digest* 12: 44-49, 1985.
2. S. Seta et al., "SEM/EDX analysis of inorganic elements in human scalp hairs with special reference to the variation with different locations on the head," *SEM/1982* I, 127-138.
3. S. Seta et al., "Quantitative investigation of sulfur and chlorine in human head hairs by energy dispersive x-ray analysis," *SEM/1979* II, 193-201.
4. S. Basu, "Spatial variation of sulfur and absorbed copper ions in human hair by x-ray line scanning," *Proc. 43 Mtg. EMSA*, 1985, 124-125.
5. E. S. West and W. R. Todd, *Textbook of Biochemistry*, New York: Macmillan, 1964.
6. D. Maes and B. D. Pate, "The spatial distribution of copper in individual human hairs," *J. Forensic Sciences* 21: 127-149, 1976.
7. L. A. King et al., "The morphology and occurrence of hair sheath cells," *J. Forensic Sci. Soc.* 22: 267-269, 1982.
8. J. C. Russ, "New methods to obtain and present SEM x-ray line scans," *EDAX Editor* 9: 3-7, 1979.
9. S. Basu, "Spatial variation of sulfur and absorbed copper ions in human hair by x-ray line scanning," in S. Basu and J. R. Millette, Eds., *Electron Microscopy in Forensic, Occupational and Environmental Health Sciences*, New York: Plenum (in press).
10. Supported by New York State Police. Figures 2B and 3 are reprinted from Ref. 9.

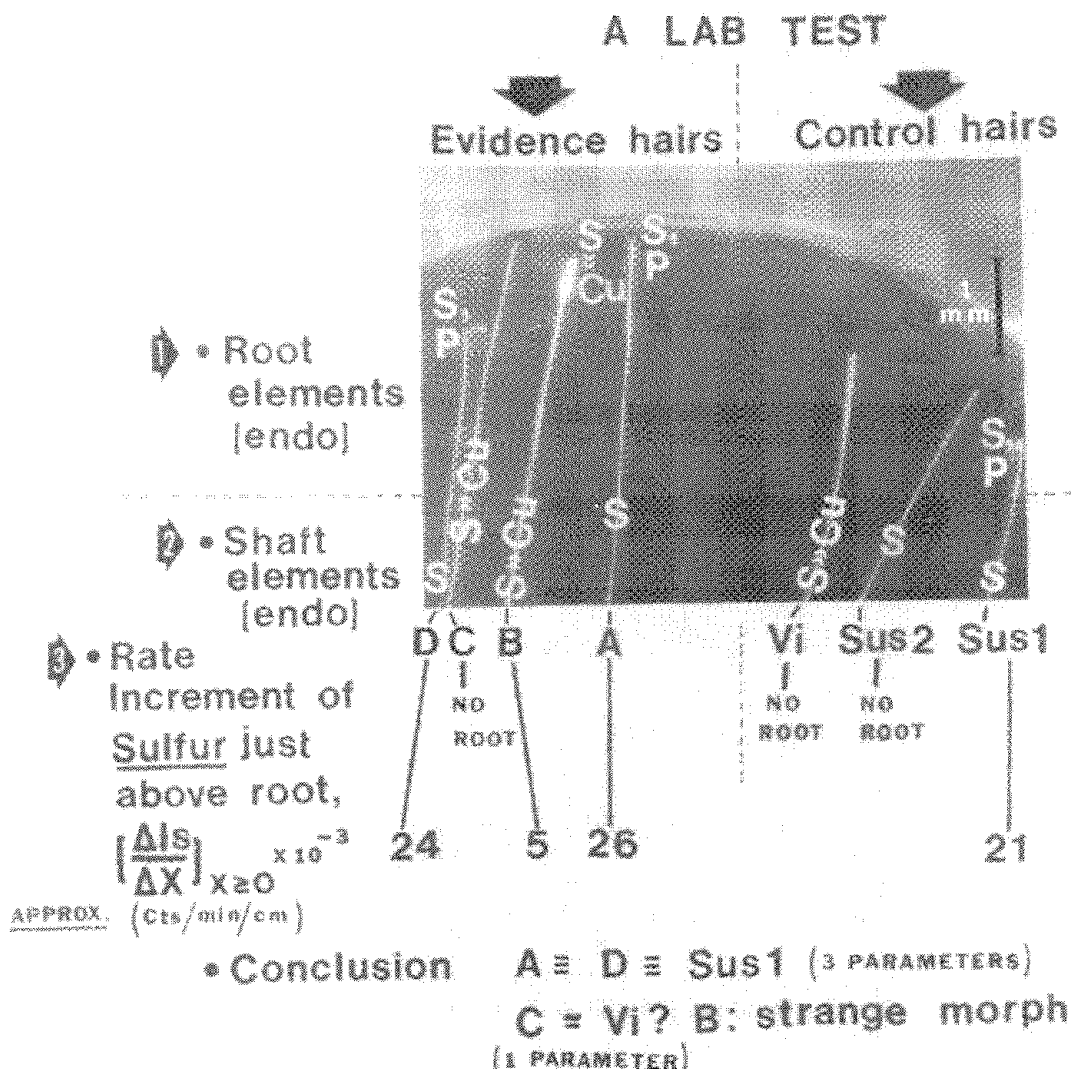


FIG. 4.--Hair comparison based on elemental parameters in laboratory matching test in Fig. 3.

## GUNSHOT RESIDUE ANALYSIS IN BULLET WOUNDS WITH THE SEM-EDX

Samarendra Basu

Of all techniques currently in use, scanning electron microscopy with energy-dispersive x rays (SEM-EDX) is the most definitive in testing for gunshot residues (GSR).<sup>1-4</sup> Testimony based on GSR analysis in the SEM-EDX has been accepted in courts of law. The present report is on a new application of the known characteristics of muzzle-blast GSR<sup>4,5</sup> to bullet wounds, which has assisted in reporting on the proximity of a bullet entrance wound from a discharged firearm. The method involves the uses of high-energy backscattered electrons and energy-dispersive x rays. The method is fast and provides positive identification of bullet wounds.

In the investigation of a shooting death the pathologist may find it difficult to determine the distance of a bullet entrance wound from a suspect firearm as it was discharged. Certain offensive conditions of the wound area may not permit discrimination between bullet entrance and bullet exit. Tissue scrapings from a wound are usually opaque to light. Even though reflected light is utilized to illuminate the specimen, the micron-size metallic GSR, each containing Pb, Sb, and Ba,<sup>1</sup> are hardly visualized. The GSR of muzzle-blast imbed into tissues at the wound, or they are obstructed from view by an overlay of contaminated blood. Obviously the nature of such a specimen also imposes a limitation on the use of secondary electrons in the scanning electron microscope. The conventional backscattered detection system (Everhart-Thornley arrangement), in which the collector screen is negatively biased to reject the low energy secondary electrons, is not adequate for a search of GSR in tissue scrapings. The required criteria for GSR identification are their condensate (molten) shape, size, and elemental composition (Pb, Sb, Ba).<sup>1-3</sup>

### *Experimental*

Tissue scrapings were collected from a wound with a surgical razor (scalpel) and then mounted on a "Glue-Lift"<sup>1,2</sup> disk ( $\frac{1}{2}$  in.-diameter polished carbon planchet with spread diluted rubber cement). The planchet was attached on top of an aluminum stub ( $\frac{1}{2}$  in.) and then examined at 20kV electron potential in the AMR 1000 SEM in conjunction with an x-ray analyzer (EDAX 707A). Whenever necessary the specimens were coated with evaporated carbon (thickness 20 nm) in vacuum to make them conductive to incident electrons. (Charging effects are usually negligible with grounded "Glue-Lift" disks.<sup>2-4</sup>) The search and identification of GSR were made with the use of backscattered electrons of high energy (>10 keV) and energy-dispersive x rays. The backscattered detector consisted of "quad" (four) semiconductor detectors mounted on the final polepiece<sup>6</sup> that surrounds the incident electron beam. The signal was processed for material contrast<sup>7</sup> or atomic contrast so that the embedded GSR in tissues are brighter than the surroundings due to lower-atomic-number elements.

When the bullet entrance was in close proximity (inches) of a discharged firearm, a dense distribution was found which consisted of irregular, and hollow GSR spheroids (diameters 0.5-18  $\mu$ m) and bullet residues (Pb). Additionally some of these GSR also contained elements of bullet coating (e.g., tin, copper, etc.) which arise due to the etching of the bullet. These are usual characteristics of muzzle-blast residues<sup>4</sup> (Fig. 1). If it was an exit wound, or if the shooting was from a certain distance (several feet), only bullet residues (Pb) would have been found.<sup>5</sup>

### *Conclusion*

The developed method provides positive identification of bullet wounds and has the potential to determine the approximate muzzle-to-wound distances.<sup>5,8,9</sup>

---

The author is at New York State Police Crime Laboratory, Albany, NY 12226.

## References

1. Samarendra Basu and Stark Ferriss, "A refined collection technique for rapid search of gunshot residue particles in the SEM," *SEM/1980 I*, 375-384, 392.
2. Samarendra Basu, "Formation of gunshot residues," *J. Forensic Sci.* 27: 72-91, 1982.
3. Samarendra Basu et al., "Suicide reconstruction by Glue-Lift of gunshot residue," *J. Forensic Sci.* 29: 843-864, 1984.
4. Samarendra Basu, "The mechanism of gunshot residue deposition and its probing characteristics to reconstruct shootings," *Proc. 43rd Mtg. EMSA*, 1985, 104-107.
5. M. Ueyama et al., "SEM/EDS analysis of muzzle deposits at different distances," *SEM/1980 I*, 367-374.
6. E. D. Wolf and T. E. Everhart, "Annular diode detector for high angular resolution pseudo-Kikuchi patterns," *SEM/1969*, 41-44.
7. H. Niedrig, "Physical background of electron backscattering," *Scanning* 1: 17-34, 1978.
8. S. Basu, "The mechanism of gunshot residue deposition and its probing characteristics to reconstruct shootings," in S. Basu and J. R. Millette, Eds., *Electron Microscopy in Forensic, Occupational, and Environmental Health Sciences*, New York: Plenum (in press).
9. Supported by New York State Police. Figs. 1A and B are reprinted from Ref. 8.

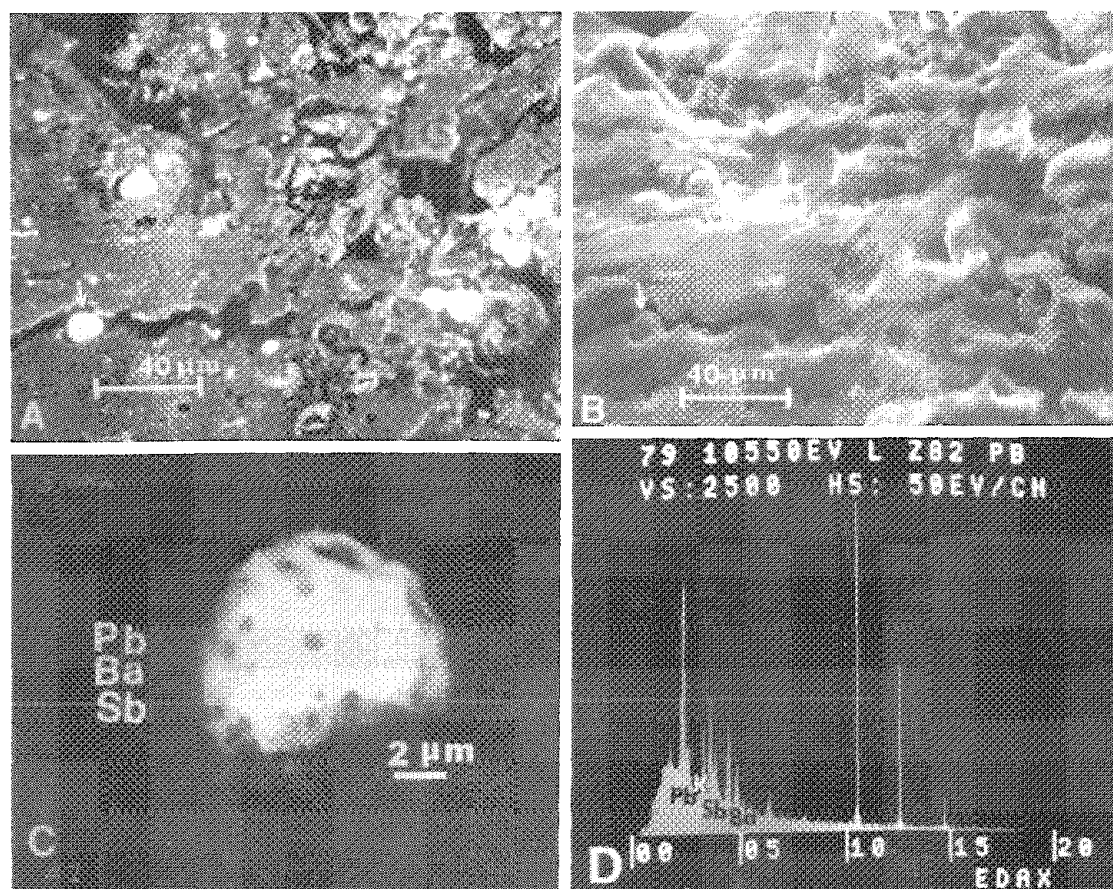


FIG. 1.--Tissue scraping containing embedded GSR. Backscattered electron image with annular solid-state detector (panel A) and secondary electron image (panel B) of same field of view at 500× magnification. Bright particles in panel A are irregular and regular GSR spheroids of muzzle blast.<sup>4</sup> Arrowhead in A and B shows a "GSR with holes" on it. See panel C for greater magnification (backscattered electron image) of this GSR and panel D for EDX spectrum of this GSR.

## SCANNING ELECTRON MICROSCOPY, FOURIER TRANSFORM INFRARED MICROSCOPE, AND THE LIGHT MICROSCOPE IN THE ANALYSIS OF PARTICULATE EVIDENCE IN THE CRIME LABORATORY

T. A. Kubic

In attempting successfully to prosecute individuals for committing crimes against persons and personal property, physical evidence is becoming increasingly important. Whether that is due to the growing mistrust of jurors for eyewitness testimony and confessions or court cases limiting the investigatory actions of police has not been shown. It is likely that it is a combination of the above along with the fact that jurors have been sensitized to the importance of physical evidence and feel that if conclusive scientific proof cannot be demonstrated then at least the "forensic people" should be able almost to prove the defendant's guilt.

The modern criminalist spends a considerable portion of his efforts in attempting to establish a common origin or association between person, places, things, or a mixture of the aforementioned. The weight that a statement of possible common origin or similarity of source has in proving a fact in issue depends on the specificity and discrimination power of the test or series of tests that the scientist employs.

A large portion of the samples submitted to the laboratory are microscopic in size but still require an extensive series of tests to be performed in order properly to characterize the exhibit. It is a decided advantage for any particular analytical technique to be nondestructive as well as fast and sensitive, and to have a high discrimination ability.

Many samples consist not only of inorganic and organic components but also possess morphological characteristics that are important to proper classification and evaluation.

The polarized light microscope (PLM), scanning electron microscope equipped with an energy-dispersive x-ray analyzer (SEM/EDS), and the Fourier transform infrared spectrophotometer equipped with a microscope (Micro FT/IR) are routinely employed singly or in combination by the Scientific Investigation Bureau of the Nassau County (N.Y.) Police Department. The examination of gunshot residue (GSR), man-made fibers, paint chips and smears, and other polymeric materials are conducted with the above instrumentation.

### *Instrumentation*

Stereo microscopes are employed to search for and retrieve evidence, document exhibits via photomicrography, and prepare samples. An AMRAY 1000A diffusion-pumped SEM with a solid-state backscatter quad detector, dual magnification and imaging, raster rotation, and gamma options is employed for high depth of field imaging and location of high-atomic-number elements.

When operated along with the EDAX 9100 energy-dispersive x-ray analyzer, the microscope serves as an electron-beam microanalyzer. Samples of predominantly organic composition can be analyzed by a number of high-sensitivity FT/IR methodologies employing beam condensers, attenuated total reflectance (ATR) and diffuse reflectance (DR) accessories on an Analect 6200 spectrophotometer. The most often used accessory is the Analect 515 infrared microscope, which enables the criminalist routinely to obtain high-quality spectra of samples 20  $\mu\text{m}$  in size.

Morphological determinations are made with an Olympus BHP polarized light microscope, and microfluorescence and adsorption studies are performed with an Olympus BH microscope coupled to a Farrand MSA microphotometer, with the data collected through an Anadata Smartface interface and processed with an Apple IIe employing Anadata software products.

Paint samples are routinely analyzed for vehicle composition employing the Analect microscope FT/IR followed by an EDS determination of elemental composition. Synthetic fibers lend themselves readily to generic analyses by FT/IR and SEM observations aid in manufacturer identification and type.

A number of transfer evidence example case studies employing the SEM, PLM, and FT/IR are available with descriptions of the data developed and the conclusions drawn from those data. Paint, fiber, and GSR studies can be presented.

Microbeam analysis employing electron, ultraviolet, visible, and infrared radiation is an integral part of the modern technology employed by today's crime laboratories in their efforts successfully to assist investigators in solving crimes and protecting society.

---

The author is with T. A. Kubic & Associates, Box 208, Greenlawn, NY 11740.

## Destructive Laser Microprobe

### LIMA ANALYSIS: QUANTIFICATION OF BINARY METALLIC SYSTEMS

Andy Harris and E. R. Wallach

The possibility of obtaining partially or fully quantitative analyses from laser-microprobes has been discussed both for inorganic<sup>1-3</sup> and organic<sup>4</sup> materials. In all cases, however, it is acknowledged that the results show a marked degree of scatter, which is a major hindrance. This paper sets out to quantify analysis of binary systems and hence examines the variability of data obtained from some elements and binary metallic systems. These results provide an insight into some of the causes of the apparent scatter. Data were obtained by use of a Cambridge Mass Spectrometry LIMA 2A instrument described elsewhere.<sup>5</sup>

#### *Elemental and Isotopic Analysis*

A single-crystal specimen of high-purity silicon was used for this work. Results were obtained at three laser powers, the lowest of which was just sufficient to produce a measurable mass spectrum for about half of the shots taken; the other powers were 45% and 65% greater. The incident laser power was measured by a light-sensitive diode and was nominally constant; in fact, a spread of about 6% about the mean was measured. From 100 mass spectra at each power, the total area beneath all the silicon isotope peaks in each mass spectrum and the isotopic ratios were recorded.

The isotopic ratios were found to be consistently incorrect. Further investigation showed that this systematic error was strongly and positively correlated with the area of the peak due to the most abundant isotope, silicon 28. The error was traced to the partial saturation of the ion detector for large final-dynode electron yields, as has been found by Simons with the LAMMA instrument.<sup>6</sup> An empirical correction for this effect, similar to that used by Simons although based on peak areas rather than peak heights, was necessary prior to further quantitative work.

The total silicon peak areas, which depend on the number of ions arriving at the detector and hence on the ion yield in the laser plasma (allowing for instrumental ion transmission), increased with increasing laser power. At the two higher laser powers, the distribution of the results was close to Gaussian. Reducing the power caused deviations from a Gaussian in both tails of the distribution, with more results occurring at greater than one standard deviation from the mean than would be expected. It was also found that the standard deviation decreased as a percentage of the mean with increasing laser power; a change from the medium to the highest laser power (an increase of 15%) halved the spread of the results from a  $2\sigma$  value of 50% to one of 25%. At the lowest laser power, just over half the laser-shots did not produce a spectrum and so a mean value is unrepresentative. The mode of the distribution is a much more representative average, and in this case is very close to zero. The shape of the distribution appears to be non-Gaussian: the tails are longer than for a Gaussian. This result may be explained by the very strong dependence of the ion yield on laser power at lower powers, which gives rise to a large change in ion yield for a relatively small change in laser power.

#### *Binary Metallic Alloys*

To extend the results obtained from silicon to more complex systems where differing elemental sensitivities contribute to the results, a 60wt% copper-40wt% nickel alloy was analyzed. The copper-nickel alloy was analyzed fifty times at each of an increasing series of laser powers. The original incident laser power is at present measured in arbitrary units but is assumed to be linear with power. The lowest power used was 600, at which about 60% of the spectra were measurable, and was increased in steps of 100. The spread of powers was reduced from the 6% quoted above to 3% by limiting accepted mass

---

The authors are at the Department of Metallurgy and Materials Science, University of Cambridge, Pembroke Street, Cambridge, England CB2 3QZ.



spectra to those obtained at measured powers within a preselected range.

The combined ion yield of copper and nickel was found to increase with laser power between 600 and 800, but above this power the yield began to decrease and had fallen to about half the 800 value at a power of 1100. This result is initially interpreted as being an instrumental effect caused by ions escaping from the extraction field at higher powers, probably due to increased ion kinetic energy. The spread of the results decreases markedly with increasing power: at 600 the  $2\sigma$  value is about 200%, at 700 it is 40%, and at 800 it is 15%. Above 800, it seems to remain at about 15-20%. As can be seen in Fig. 1, the results become closer to a Gaussian distribution as the average total area increases, particularly at a power of 800.

The area of the peaks corresponding to the individual elements show distributions very similar to those for the total ion yields but with slightly larger standard deviations, perhaps due to the smaller number of ions concerned. Application of simple error analysis allows the error in the sum of the average elemental ion yields to be calculated and compared with the value obtained by averaging the total areas of each result (the result discussed above). It is found that at powers of 600 and 700, the predicted value is lower than the actual. This is an indication that the copper and nickel yields are not independent of each other,<sup>7</sup> and Fig. 2(a) shows that at 600 there is indeed a strong correlation. The results are scattered about a line with a slope given by the average copper-to-nickel ratio for the results (in this case, 1.76). This correlation is not apparent for the results obtained at higher powers. However, that seems to be due to the spread of results along the line (the spread in total areas) being of similar magnitude to the scatter on either side of the line (interpreted as due to errors in peak area measurement, discussed later) rather than a lack of correlation. In contrast, no correlation between total area and copper-to-nickel ratio is observed.

The alloy has an actual copper-to-nickel ratio of 1.39 (in atomic percent). The average measured ratios all had spreads of about 40% and standard errors of about 2-4%. The variation of average ratio with power is shown in Fig. 2(b); the measured ratio reaches a minimum at a power of 900 and then appears to approach the actual value. This initial decrease in relative sensitivity to copper with increasing power is contrary to the generally expected trend toward more uniform sensitivities with increasing power.<sup>8</sup> However, application of the local thermodynamic equilibrium (LTE) model of plasma processes<sup>1,3,9</sup> to the copper-nickel system predicts just such a trend, although the actual sensitivities do not fit the model quite as well. This result shows that the LTE model can be useful in explaining general trends in laser-microprobe results.

### *Causes of Variability*

It has been shown that the relative amounts of copper and nickel remain approximately constant at constant laser power. Hence the variation in total ion yield seems primarily due to variations in the amount of material in the plasma, rather than any changes in the relative degree of ionization of the two elements. The amount of material in the plasma depends on the amount removed from the specimen surface by the laser-surface interaction. Thus it appears that the distribution of the total ion yields is due to the variation in the surface absorption of the incident laser energy. The Gaussian-like distribution of results suggests that the variation is due to some random variable, and it does seem likely that any surface feature causing changes in absorption will be randomly distributed across the surface. As the power is increased, the changes in absorption should become less important and hence the observed decrease in standard deviation of the results at higher powers is expected.

Analyses of specimens of brass with various surface finishes lead to similar conclusions. Four grades of surface finish were used, and a three-fold increase in the standard deviation of the results was found between an optically smooth surface and one prepared with a coarse grit. Investigation of the craters formed by the laser showed that the crater size was also more variable on the less-polished surfaces. Hence the amount of material removed would also be expected to be more variable, as was found.

Although most of the variation in the total ion yield can be attributed to variations in the absorption of laser energy by the surface, for a given laser power it appears that the relative ion yields of the two elements remain constant and independent of the total ion yield. This finding can be explained by reference to the LTE model, which predicts

that the relative ion yields depend only on the conditions in the plasma. Hence it seems that, for a given laser power, the conditions in the plasma are much the same for each shot. Thus the laser-surface interaction appears to be variable, but the laser-plasma interaction is quite constant. Accordingly, variations in the measured copper-to-nickel ratios are attributed to peak overlap in the mass spectrum and to additional variations in the multiplier saturation (i.e., even after the correction for this effect has been made). These results seem to hold for a metallic system, although extension to nonmetals may be problematic as the formation of clusters and negative ions frequently occurs.

### Conclusion

It has been shown that the spread in the results obtained from LIMA analysis of metals is primarily due to variations in the laser-surface interaction. The results seem to have distinct and reproducible distributions, with average values that are much more reproducible than an individual result. The measured relative ion yields for the individual elements seem to be constant for a particular laser power, although instrumental effects still give rise to variability. Overall, the application of a statistical approach utilizing numerous results appears to improve both quantification and the understanding of the technique considerably.

### References

1. M. J. Southon et al., *Microbeam Analysis--1985*, 310-314.
2. T. Mauney, *Microbeam Analysis--1985*, 299-309.
3. R. Kaufmann, *Microbeam Analysis--1982*, 341-358.
4. A. H. Verbueken et al., *Biomed. Mass Spec.* 12: 438-463, 1985.
5. M. J. Southon et al., *Vacuum* 34: 903-909, 1984.
6. D. S. Simons, *Intl. J. Mass Spec. Ion Proc.* 55: 15-30, 1984.
7. S. K. Muthu, *Probability and Errors*, Sangam Books Ltd., 1982.
8. T. Dingle and B. W. Griffiths, *Microbeam Analysis--1985*, 315-318.
9. P. K. Carroll and E. T. Kennedy, *Contemp. Phys.* 22: 61-96, 1981.

FIG. 1.--Smoothed distributions of total peak area (50 results) obtained from copper-nickel alloy showing variation with increasing laser power.

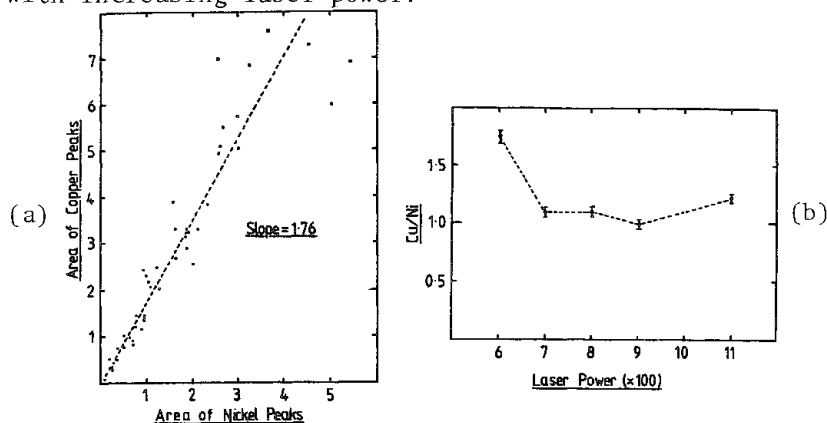
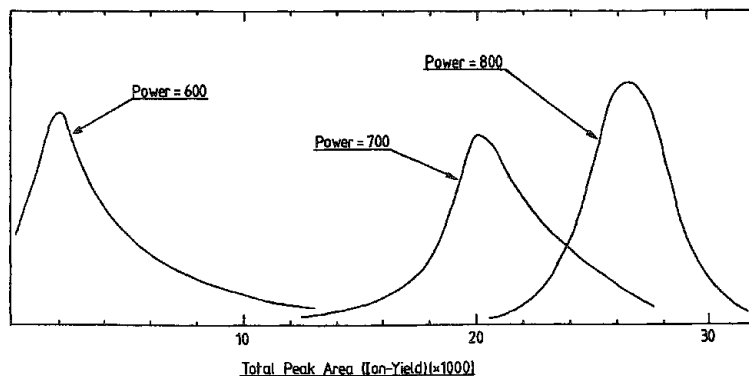


FIG. 2.--(a) Plot of area of copper peaks against area of nickel peaks obtained at a power of 600; (b) variation in mean copper-to-nickel ratio with laser power.



## LIGHT-ELEMENT ANALYSIS BY LIMA

V. L. Kohler, A. Harris, and E. R. Wallach

Routine microanalysis of light elements in bulk solids is not straightforward. Electron-beam microanalysis of light elements down to ppm levels can only be achieved with a wavelength-dispersive spectrometer, requiring sequential analysis, and even then is difficult. Auger electron spectroscopy is extremely sensitive to surface contamination and is very surface-specific, hence is of limited use in the routine microanalysis of bulk solids. Secondary-ion mass spectrometry (SIMS) is capable of detecting light elements but the large range of elemental sensitivities and production of molecular and multiply charged ionic species can be a problem. In contrast to these techniques, the laser microprobe<sup>1,2</sup> has many of the advantages of SIMS but data acquisition is more rapid; the probe has a lower range of elemental sensitivities, is less susceptible to matrix effects, and produces simple mass spectra. The technique does have disadvantages; in particular, the results have only moderate reproducibility, similar to SIMS.<sup>3</sup> This paper discusses the use of such an instrument (LIMA 2A, Cambridge Mass Spectrometry Ltd.) in measuring the concentrations of the light elements hydrogen, lithium, beryllium, boron, and carbon.

### *Hydrogen*

Established analytical methods for hydrogen, with the exception of SIMS, offer bulk analyses through reactive weight loss or pressure measurements rather than data related to specific microstructural features. The feasibility of LIMA for hydrogen analysis was tested by analysis of a series of aluminum-lithium specimens with well-characterized bulk hydrogen contents of the order of 1-3 ppm. The analyzed specimens were subsequently etched to correlate the mass spectra obtained with the microstructures. It was found that minimal hydrogen was present within the grains; most was present at grain boundaries and the specimen surfaces. Subsequent heat treatment under vacuum was used to purge the hydrogen from the specimens. It is interesting that the expected surface layers of adsorbed hydrogen were not found in the purged specimens, nor was any hydrogen found in the bulk or at grain boundaries.

It is not possible to apply the Local Thermodynamic Equilibrium model of plasma processes to quantify the hydrogen levels since the electron partition coefficient is undefined for this element; hence no theoretical working curve can be derived. However, it is possible to generate a working curve for quantification by the use of standards and this work is currently under way. This study confirms the suitability of LIMA for the qualitative analysis of hydrogen within materials, with the potential for quantitative analysis (with an estimated error of 10-15%).

### *Lithium*

Aluminum-lithium alloys are of increasing significance in the aerospace industry owing to their potential high strength-to-weight ratios. Traditional routes of fabrication (e.g., casting) suffer from problems arising from segregation of the alloying elements. Instead, rapid solidification is used as this process removes macrosegregation, reduces the extent of microsegregation, and enhances solute levels, and so provides alloys with high strengths at elevated temperatures.

LIMA was used to analyze gas-atomized rapidly solidified aluminum-lithium powder,<sup>5</sup> in order to determine the extent of segregation of the lithium and other alloying elements within the cells of the microstructure and across cell boundaries. Line analyses were carried out, on polished cross sections, of particles with an average diameter of 40  $\mu\text{m}$ . Each particle analyzed was then etched in order to correlate the mass spectra obtained

---

The authors are at the Department of Metallurgy and Materials Science, University of Cambridge, Pembroke Street, Cambridge, England CB2 3QZ. They acknowledge the work of Professor W. Jones Williams and David Kelland on beryllium.

with microstructure; this procedure was adopted to minimize any artifacts introduced by etching. It was found that there was significant partitioning of lithium to the cell walls with, on average, a cell-wall to cell-core ratio of 7 to 3. The major alloying elements, copper and iron, were also found to segregate to the cell boundaries. Duplication of this study with electron energy loss spectroscopy (EELS), another microanalytical technique capable of light-element analysis, was attempted. EELS requires the preparation of specimens of thinner than 30-50 nm in order to prevent multiple scattering of electrons, and hence production of specimens is difficult. Lithium detection is also complicated in EELS by the presence of plasmon peaks which obscure the lithium edge. Thus, in contrast to EELS, LIMA proved to be a simple and effective method for the detection of lithium segregation in small particles.

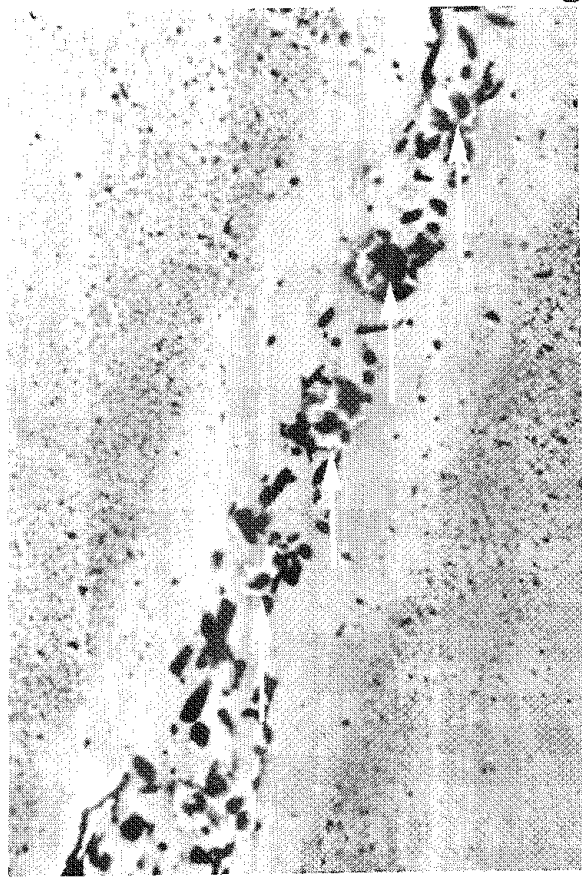
### *Beryllium*

This element is extremely toxic and exposure to it or its compounds can lead to chronic beryllium disease (CBD).<sup>6</sup> This disease exhibits symptoms similar to those shown in a wide range of diseases known by the nonspecific name granulomatous disease and typified by the formation of small granulomas within the body. In order to diagnose CBD unambiguously, it is necessary to detect beryllium within a tissue sample. However, the amounts of beryllium present are typically no more than 1-10 ppm by weight. Hence for bulk analysis, large samples are required and even then the beryllium may not always be detected owing to its low concentration.

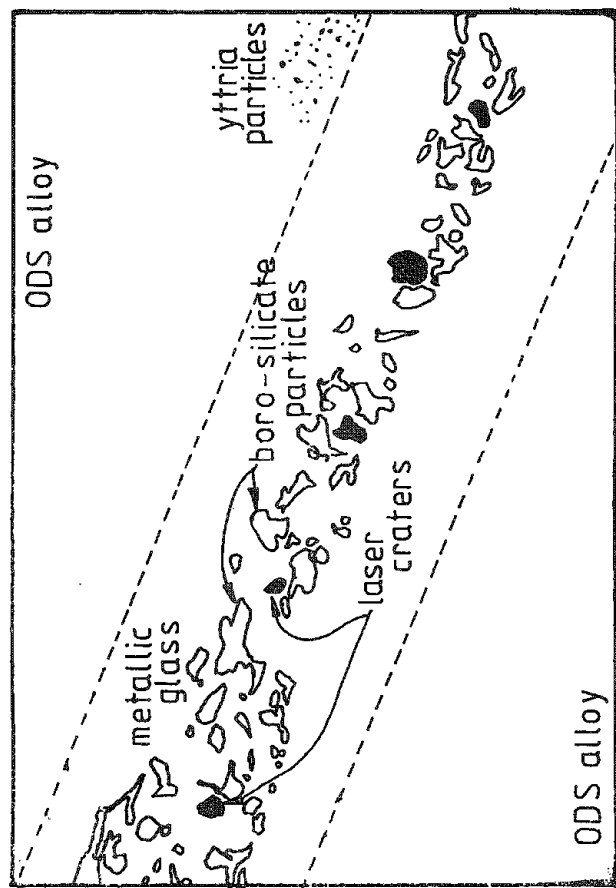
LIMA has been used to look for beryllium in a large number of histological specimens and the results have been compared with those obtained by other methods.<sup>7</sup> The specimens comprised 14 control cases where CBD had been confirmed by other methods and 5 cases of suspected CBD. In the controls, LIMA was able to detect beryllium in all cases; in the suspect cases LIMA was able to confirm CBD once, in agreement with the bulk analysis by spectroscopic methods. An added advantage of LIMA is that it shows that the beryllium is confined to specific regions of the tissue. The precise location of the beryllium-bearing tissue is important in the study of the onset and progress of the disease, as well as confirmation that the beryllium is the causative agent. The speed and simplicity with which samples can be handled means that LIMA is extremely useful in this field.

### *Boron*

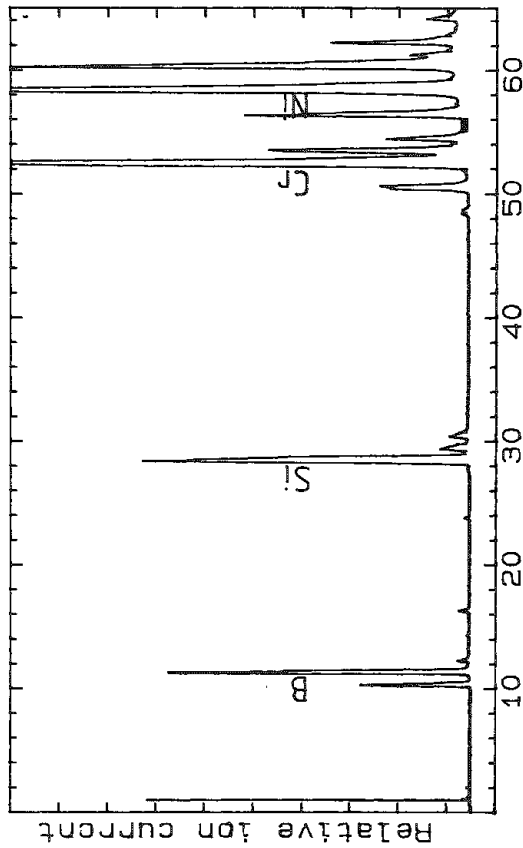
Materials to be used in gas-turbine engines require high-temperature strength and good resistance to creep during operation. To achieve these properties, solid-solution, precipitation, and dispersion hardening mechanisms must be incorporated into the design of the alloy. Conventional nickel-based superalloys can offer solid-solution and precipitation hardening, but the inclusion by conventional fabrication routes of a stable, uniformly distributed dispersoid phase has proved to be a problem. Accordingly, Oxide Dispersion Strengthened (ODS) superalloys, incorporating inert oxides, are produced by powder metallurgical methods with subsequent hot extrusion to consolidate the powder. Although this process achieves a suitable microstructure, the formation of intricate shapes, such as gas turbine blades, is limited by the extrusion operation. Half sections can be produced, and hence brazing is used to join the halves together without destruction of the homogeneity of the mechanically alloyed material. The brazing alloy is of composition similar to the ODS alloy and includes a melting-point depressant; in this study, a metallic glass containing 3wt% boron was chosen. LIMA showed that boro-silicates formed in the metallic glass filler during brazing. Diffusion profiles of boron away from the braze were quantified by use of a working curve derived from measurements of boron concentration in the original metallic glass. Figures 1(a) and (b) show a backscattered electron micrograph and schematic diagram of a brazed joint. The precipitates running down the center of the metallic glass (probably boro-silicates formed during brazing) and yttria particles in the ODS alloy appear dark due to atomic-number contrast. The craters, 3-5  $\mu\text{m}$  in diameter, created during LIMA analyses are indicated by arrows in Fig. 1(a). The spectra shown in Figs. 1(c) and (d) were obtained from a precipitate and an adjacent region of metallic glass; the boron depletion of the glass caused by the precipitate formation is obvious.



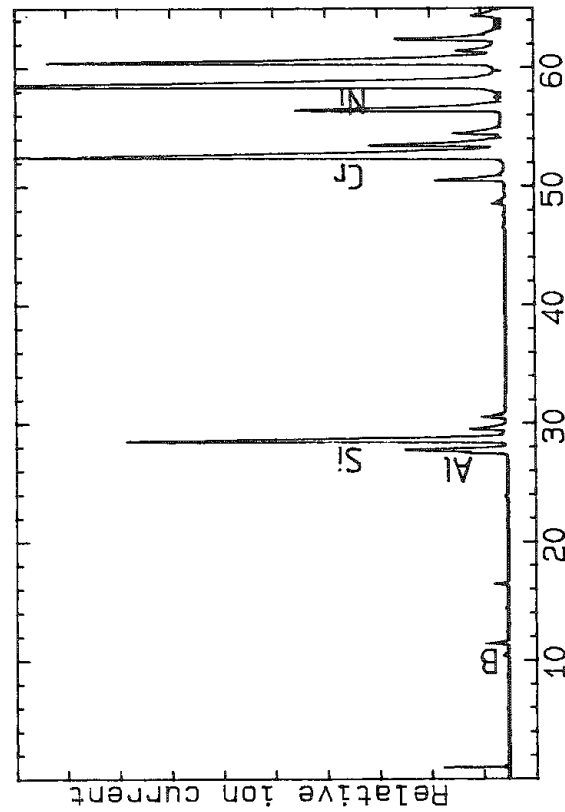
a.



b.



c.



d.

FIG. 1.--(a) Backscattered electron image of brazed joint; craters created by LIMA are shown by arrows. (b) Schematic diagram of brazed joint. (c) Mass spectrum obtained from precipitate in metallic glass. (d) Mass spectrum obtained from metallic glass adjacent to precipitate.

## Carbon

Properties of steels are strongly influenced by both the carbon content and its distribution in the microstructure. Surface hardness can be improved by alloying with carbon to a depth of a few hundred microns. This goal may be achieved by spraying of the surface with carbon and passage of a high-power laser beam over it to melt the surface region. The precise concentration of the carbon is determined by the speed with which the laser passes over the surface; a higher speed produces a smaller melt pool and a higher carbon concentration.

LIMA analysis has been used to quantify the increase in carbon concentration for melt zones produced at two different laser pass speeds on an EN56c steel (12wt% chromium and 0.2wt% carbon). Three melt zones were investigated with ten analyses per zone. The first two results (indicating carbon contents of  $0.5 \pm 0.1$  wt%) came from regions produced by the lower laser speed; these values agree well with the expected two- to three-fold increase in carbon concentration. A higher value ( $1.3 \pm 0.2$  wt% carbon) came from the third region and is consistent with a higher speed.

A further specimen was analyzed, but in this case the melt zone was markedly inhomogeneous; etching showed two distinct regions, one of which had an increased Vickers hardness. Two such melt zones were analyzed. The zone associated with a higher speed gave carbon contents of  $3.0 \pm 0.5$  wt% for the softer region, and  $0.7 \pm 0.1$  wt% for the harder region. The zone produced at the lower speed had values of  $1.0 \pm 0.2$  wt% and  $0.3 \pm 0.04$  wt%, respectively. Hence, for both speeds LIMA has shown that the harder region has about 20-30% of the carbon concentration of the softer region. This result is not as expected and may be attributed to poor mixing in the molten material and/or differential cooling rates. Since the differing regions were approximately 100  $\mu\text{m}$  wide, bulk analysis of carbon was not possible, and hence required a microanalytical approach such as LIMA.

## Conclusion

The above examples show that LIMA is capable of analyzing for low concentrations of light elements and that quantitative analysis is also feasible. In contrast to some of the other techniques available for light-element analysis, LIMA is shown to be rapid and very versatile (accepting both inorganic and organic materials), sample preparation is minimal, and the analyses can be correlated with microstructure.

## References

1. M. J. Southon et al., *Vacuum* 34: 903-909, 1984.
2. R. Kaufmann, *Microbeam Analysis--1982*, 341-358.
3. A. Harris and E. R. Wallach (this volume).
4. P. K. Carroll and E. T. Kennedy, *Contemp. Phys.* 22: 61-96, 1981.
5. R. A. Ricks et al., *Proc. 3rd Intern. Al-Li Conf.*, Oxford, 1985.
6. D. G. James and W. Jones Williams, *Sarcoidosis and Other Granulomatous Disorders*, Major Problems in Internal Medicine Series No. 24, Philadelphia: Saunders, 1983.
7. W. Jones Williams and D. Kelland (to be published).

## DETERMINATION OF ELEMENTAL RELATIVE SENSITIVITY FACTORS IN THE ANALYSIS OF GEOLOGICAL SAMPLES BY LIMS

Filippo Radicati di Brozolo

In this communication we describe a series of analysis performed by laser ionization mass spectrometry (LIMS)<sup>1</sup> on selected mineral standards. The purpose of this experiment was to test a set of experimental conditions which maximize reproducibility of the data and allow the calculation of relative sensitivity factors (RSF), valid for some broad mineral classes.

The minerals standards selected for this study were: two Na-rich clinopyroxenes from a diamond-bearing eclogite,<sup>2</sup> obtained from N. V. Sobolev (Novosibirsk, USSR); a plagioclase from Lake County, Oregon, extensively used as a geochemical reference; and an extra-terrestrial plagioclase from the Moore County achondrite.<sup>3</sup>

For this study, the laser ionization mass spectrometer (LIMA-2A, Cambridge Mass Spectrometry, Cambridge, England) was tuned for:

- (a) high laser power density,
- (b) low ion transmission, and
- (c) low electron multiplier gain.

High laser power irradiation is a necessary condition so that the ionization of all elements of interest is essentially saturated and matrix effects are minimized; conditions (b) and (c), low ion transmission and low electron multiplier gain, are necessary so that the signal can be maintained well within the region of linear response of the detection system.

The results obtained on the four standards are shown in Table 1 as RSFs. The RSF expression is

$$RSF = i_x^+ / j_y^+ \cdot [y] / [x] \cdot f_j^y / f_i^x$$

where  $i_x^+$  and  $j_y^+$  are the measured intensities of the  $i$ th isotope of the element of interest and of the  $j$ th isotope of the normalizing element, respectively;  $[y]$  and  $[x]$  are the known elemental abundances of the normalization element and the element sought, respectively; and  $f_i^x$  and  $f_j^y$  are the fractions of isotopes  $i$  and  $j$  in elements  $x$  and  $y$ . In this study, the normalizing isotope was  $^{28}\text{Si}$ , and consequently the RSFs are referenced to Si, e.g.,  $\frac{A_i}{A_{\text{Si}}} RSF$ .

Several observations can be made on the results. For any element, the calculated RSF are similar within one mineral class, e.g., clinopyroxenes or plagioclase, but vary from one class to the other, with the exception of Al. Elements Al and Mg in the clinopyroxene group, Al and Ca in the plagioclase group exhibit RSFs rather close to 1, which is another way of saying that the measured peak intensity ratios are close to the known elemental ratios. This result indicates that for these elements the amount of ionization is similar to that of Si.

Fe, Ca, and O in the clinopyroxene group and O in the plagioclase group have RSFs lower than unity, which indicates a lower degree of ionization relative to Si. Na has RSFs higher than unity in both groups, which indicates the opposite effect.

These preliminary results show that for at least some major elements, laser microprobe mass spectrometry can generate quantitative results, with relative uncertainties of elemental ratios typically in the range of 15 to 30%.

It is reasonable to expect that it will become possible to establish relative sensitivity factors valid for sufficiently broad classes of minerals, and thus make possible their application to quantitative analysis of geological materials by laser microprobe.

---

Author Radicati di Brozolo is at Charles Evans & Associates, 301 Chesapeake Dr., Redwood City, CA 94063. Special acknowledgment is due to Dr. Robert W. Odom of CE&A for helpful discussions.

TABLE 1.--Relative sensitivity factors, normalized to Si.

	Na-rich clinopyroxenes		Plagioclases	
	M-180	M-52	Moore County	Lake County
Al	$1.32 \pm 0.46^*$	$1.38 \pm 0.47$	$1.79 \pm 0.51$	$1.47 \pm 0.09$
Fe	$0.36 \pm 0.22$	$0.39 \pm 0.27$	-	-
Mg	$0.93 \pm 0.39$	$1.05 \pm 0.25$	-	-
Ca	$0.49 \pm 0.39$	$0.63 \pm 0.18$	$0.72 \pm 0.17$	$1.22 \pm 0.11$
Na	$5.9 \pm 2.2$	$6.51 \pm 1.20$	$2.01 \pm 0.54$	$4.12 \pm 0.38$
O	$0.56 \pm 0.19$	$0.21 \pm 0.06$	$0.10 \pm 0.06$	$0.12 \pm 0.03$

\*The errors are 1 standard deviation of the measured peak area intensity ratios.

#### References

1. C. A. Evans Jr. et al., "Microanalysis of bulk samples by laser-induced ion mass analysis," *Microbeam Analysis--1983*, 101-105.
2. N. V. Sobolev, *Deep Seated Inclusions in Kimberlites etc.*, Washington, D.C.: American Geophysical Union, 1977, 95.
3. C. J. Hostetler and M. C. Drake, "Quench temperatures of Moore County and other eucrites: Residence time on eucrite parent body," *Geochim. Cosmochim. Acta* 42: 517-522, 1978.

## LASER PROBING UNDER ATMOSPHERIC CONDITIONS FOR LASER IONIZATION MASS SPECTROMETRY

Akira Ishimori, Takashi Yamamoto, and Tadatoshi Yamada

Laser ionization mass spectrometry (LIMS) under atmospheric conditions has been investigated and a method is proposed in which the sputtering step is separated from the ionization step. In this method, a small fraction of a sample is sputtered by a pulsed laser beam, and introduced into a vacuum chamber. Neutral particles are ionized by nonresonant multiphoton ionization by a focused UV laser, and the resulting ions are analyzed by a time-of-flight (TOF) mass spectrometer. The problem with this method is the local pressure rise in the vacuum chamber when sputtered particles are introduced into it. A method of reducing the effects of the pressure rise on the mass spectrometer is discussed.

This paper describes the application of a laser ionization mass spectrometry technique to the analysis of the samples under atmospheric conditions. With this technique, the analysis of biological material or even living samples might become feasible without any treatment.<sup>1</sup>

### *Method*

An important aspect of the present approach is the separation of the sputtering step from the ionization step. The laser microbeam is adopted for sputtering because it can be used under atmospheric conditions--unlike other microbeams such as the electron or ion beam, which can be used only under vacuum conditions.

The principle of this method is shown in Fig. 1. A sample in the atmosphere is irradiated with a laser microbeam. Desorbed or sputtered particles are introduced into a vacuum chamber with air near the sample. The neutral particles are ionized by the other laser beam. The ions are analyzed by a TOF mass spectrometer.

### *Experimental Setup*

The problem with this method is the pressure rise in the ionization chamber caused by the air introduced in it, which causes much background noise and reduces the number of ions transferred to the detector. The combination of a nozzle with a high-speed shutter is adopted to reduce the volume of the air flowing into the chamber. Passing through the nozzle, sputtered particles with air form a supersonic molecular beam.<sup>2</sup> The head of the supersonic molecular beam is ionized to carry out the analysis before the effects of the pressure rise appear.

A schematic diagram of our experimental setup is shown in Fig. 2. The Q-switched Nd:YAG laser pulse (Holobeam 2660-1RQ, wavelength 1064 nm, 1 mJ/pulse, pulse width 200 ns) is used for sputtering. For nonresonant multiphoton ionization, shorter wavelengths are preferable.<sup>3</sup> The 4th harmonic beam from the custom-made Q-switched Nd:YAG laser (wavelength 266 nm, 6 mJ/pulse, pulse width 15 ns) is used here. A schematic diagram of the nozzle and the ionization chamber is shown in Fig. 3. The laser microbeam is focused on the surface of a sample through the nozzle. The ionization laser is focused just above the nozzle. The ions produced go into the TOF mass spectrometer through a hole centered on a mirror. The output of the electron multiplier is digitized at 8-bit resolution and 10 ns sampling time, and is stored in a digital memory of 2 kilowords. The registered signal is displayed on a CRT and/or an analog plotter, or is transferred to a microcomputer for further processing, such as averaging and integration. The ionization chamber is pumped by a diffusion pump and the TOF chamber is separately pumped by a turbo molecular pump.

The characteristic of the shutter, the behavior of the supersonic molecular beam, and the optimum time delay between lasers are being studied.

---

The authors are with Mitsubishi Electric Corporation, Central Research Laboratory, Amagasaki, Hyogo, 661 Japan.

## References

1. Reimer Holm et al., "Laser microprobe mass analysis of condensed matter under atmospheric conditions," *Analytical Chemistry* 56: 690--692, 1984.
2. D. M. Lubman, "Supersonic-beam technique improves resolution in time-of-flight mass spectrometer," *Laser Focus/Electro-optics* 20: 110-115, 1984.
3. C. H. Becker and K. T. Gillen, "Surface analysis by nonresonant multiphoton ionization of desorbed or sputtered species," *Analytical Chemistry* 56: 1671-1674.

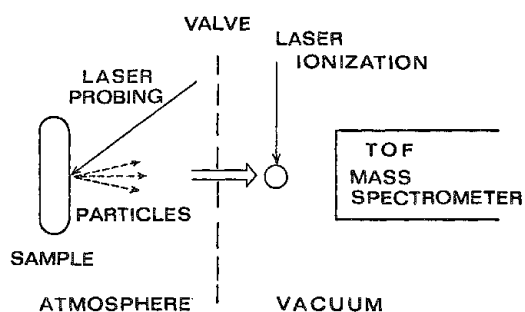


FIG. 1.--Separation of ionization step from sputtering step.

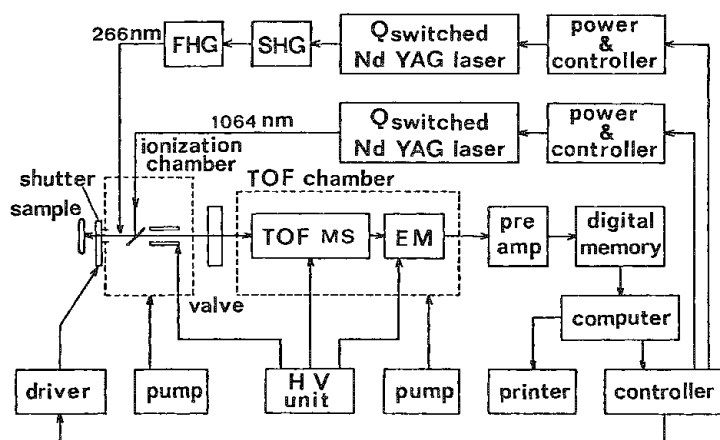


FIG. 2.--Experimental step.

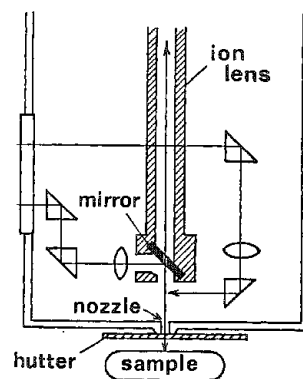


FIG. 3.--Schematic diagram of ionization chamber.



## LASER IONIZATION MASS ANALYSIS AT HIGH MASSES

Trevor Dingle, B. W. Griffiths, and S. J. Mullock

Laser microprobe mass analyzers typically use a time-of-flight analyzer to mass analyze the laser-produced ions. This type of mass analyzer has potentially significant advantages for the analysis of large organic molecules:

- (1) an "unlimited" mass range
- (2) a high transmission, "constant" over the mass range
- (3) "simultaneous" detection of all masses of the same sign of charge
- (4) short measurement time scale

In essence a time-of-flight mass analyzer has a high transmission efficiency compared with quadrupole mass filters or magnetic-electrostatic sectors and is inherently suited to a high mass detection. However, typically, time-of-flight analyzers lack the high mass resolution and mass accuracy achievable with, for example, commercial double focusing magnetic-electrostatic sector mass analyzers. Nevertheless, they have the potential for obtaining higher molecular weight measurements, albeit not necessarily with unit mass resolution. In this paper we describe the results of a series of preliminary experiments performed on an unmodified commercial laser microprobe mass analyzer, LIMA-2A (manufactured by Cambridge Mass Spectrometry Ltd.) that illustrate the potential advantages and problems using such an instrument for high molecular weight analyses.

### *Experimental*

One of the first necessities for high molecular weight analysis is that of providing suitable high mass markers for unambiguous mass identification. Cesium iodide is a high mass marker used in other mass spectrometry techniques such as Fast Atom Bombardment. Figure 1 shows a typical positive ion spectrum obtained from cesium iodide in LIMA. As can be seen, mass peaks up to around 3000 amu are obtained. The fall off in peak amplitudes with increasing cluster ion size was much reduced when the cesium iodide was placed on the sample holder in a solution of either water or glycerol. No systematic studies were performed on the matrix environment, but it is clear, as in Fast Atom Bombardment, that it can have a significant effect on the ion yield. It was found that use of cesium iodide to calibrate the mass scales yielded an accuracy within one mass unit on a given sample in the zero to 2000 amu mass range. In practice the mass accuracy is affected by the performance of the electronic circuits that digitize the transient signal from the ion detector. The transient recorder fitted to the LIMA, used for this work, has a maximum sampling rate of 60 MHz and 4096 time channels. Thus, if the maximum sampling rate is used, each time channel is just under 17 ns wide and the total time range is around 68  $\mu$ s. Relating this to ion flight times, the actual mass range detected would be approximately 0 to 250 amu. Larger mass ranges are obtained by a decrease in the transient recorder sampling rate. For example, a mass range of approximately 0 to 9000 amu can be attained at a 10MHz sampling rate. However, the sample time in each channel is now 100 ns which is greater than the flight time difference equivalent to 3 amu at around 5000 amu. Therefore, the mass resolution obtained in the time-of-flight analyzer at these mass numbers will not be unity. Clearly it would be advantageous to use a transient recorder, with say 32 000 time channels instead of the 4096 time channels available so that a high mass range (0-10 000 amu) can be covered with better time resolution.

The spectrum shown in Fig. 2 was obtained from Gramicidin S ( $C_{60}H_{92}N_{12}O_{10}$ ), which has a molecular weight of 1141.49. This cyclic decapeptide antibiotic readily gave molecular peaks with sodium and potassium attachments, in LIMA. Another spectrum in the same mass range is shown in Fig. 3. This is a spectrum of aluminum phthalocyanine chloride (APC), a

---

The authors are at Cambridge Mass Spectrometry Ltd., Cambridge Science Park, Milton Road, Cambridge, England, CB4 4FX.

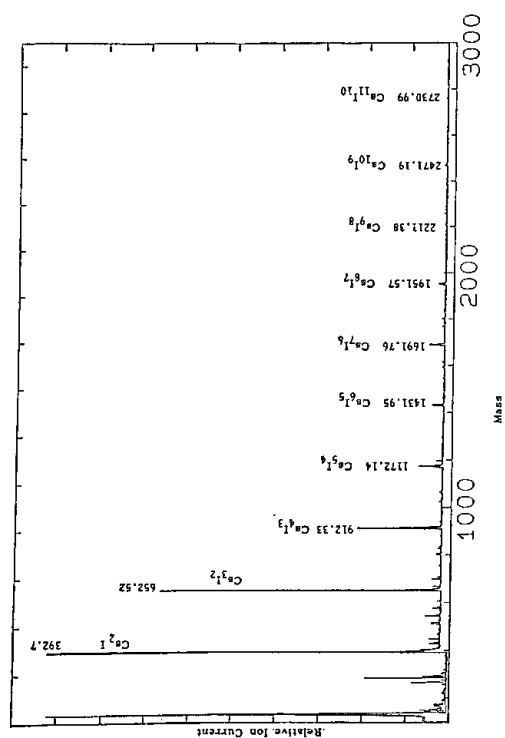


FIG. 1.--Cesium iodide (LIMA) positive ions.

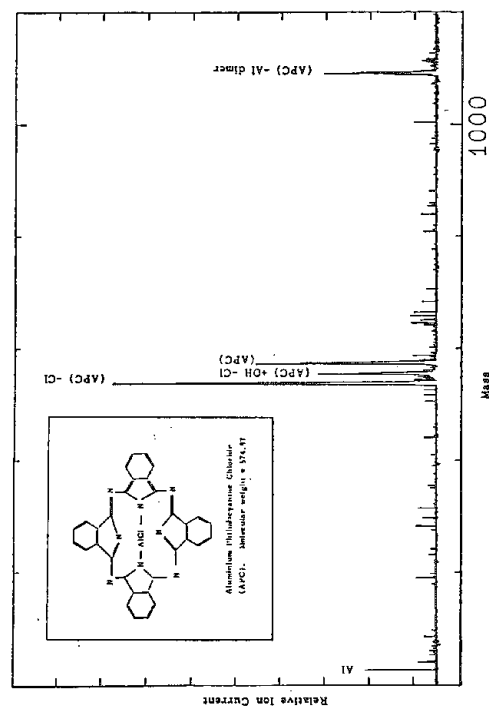


FIG. 3.--APC positive ions.

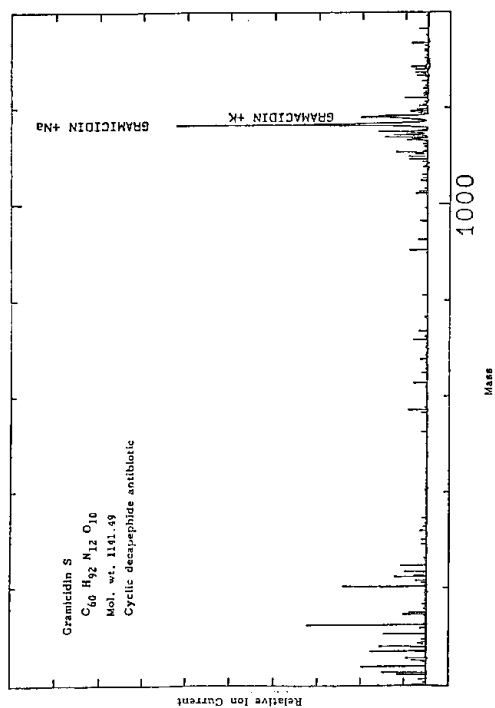


FIG. 2.--Gramicidin S cyclic decapeptide antibiotic.

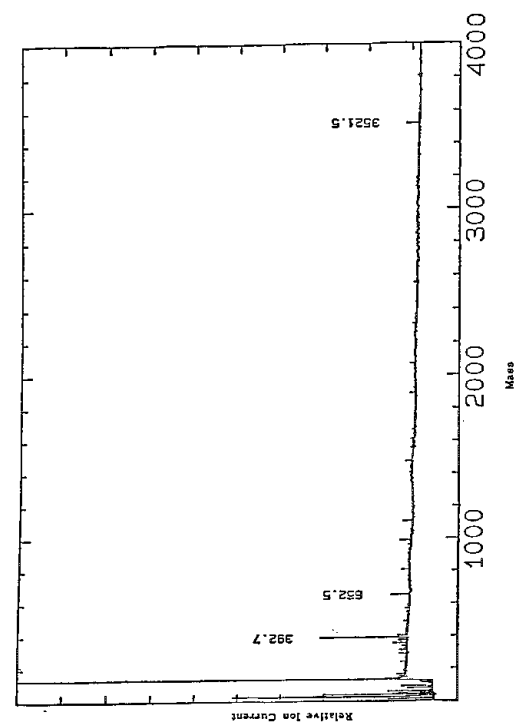


FIG. 4.--Insulin + CsI in glycerol.

dark-blue crystal soluble in benzyl alcohol. This particular material is difficult to ionize by other methods, whereas laser ionization produces the APC and the APC dimers as shown. It is not clear at present which aspects of the analysis procedure limit the high mass performance of LIMA. However, the contrast between the above results and measurements made on some other compounds of similar molecular mass, together with the matrix effects already mentioned, suggest that the ionization process itself is a very critical stage.

The ion detector used in the standard LIMA was a 17-stage Cu-Be dynode Venetian blind electron multiplier. In this set-up the ions are typically accelerated to around 6 kV onto the first dynode. As is well known, the ion-to-electron conversion efficiency of the first dynode depends on impact velocity. Thus, for large molecules the yield of ion electron conversion can drop significantly, and it would be advantageous to use a postacceleration ( $\sim 20$  kV) detector to reduce this effect. In practice, with use of the standard LIMA detector it does appear that sensitivity begins to diminish appreciably above 2000 amu. Nevertheless, we have been able to obtain preliminary spectra on a standard LIMA. Figure 4 shows a spectrum for oxidized insulin (mass  $3496 \pm 1$ ). This is a positive-ion spectrum of oxidized insulin mixed with cesium iodide in a glycerol matrix. Similarly, Fig. 5 shows a positive-ion spectrum of bovine insulin, a biological hormone of molecular weight 5780. Sodium chloride was added to this sample in an attempt to form an attachment ion. The mass scales on the insulin are in some doubt as we used no reference mass peaks; these figures are our best estimates. Also, at these mass numbers in a standard LIMA the results must be treated as in the sample preparation "with a little pinch of salt."

### Conclusions

There is no doubt that a LIMA type machine can be used for high mass analysis and it is reasonable to expect to see LIMA type machines with improvements in the detector and transient recorder that will be capable of working up to 20 000 amu. In addition, improvements in the sample vaporization and ionization method, such as postionization and pulsed extraction, could well lead to an increase in the range of high mass molecules that can be analyzed, as well as significant improvements in the mass resolution obtainable.

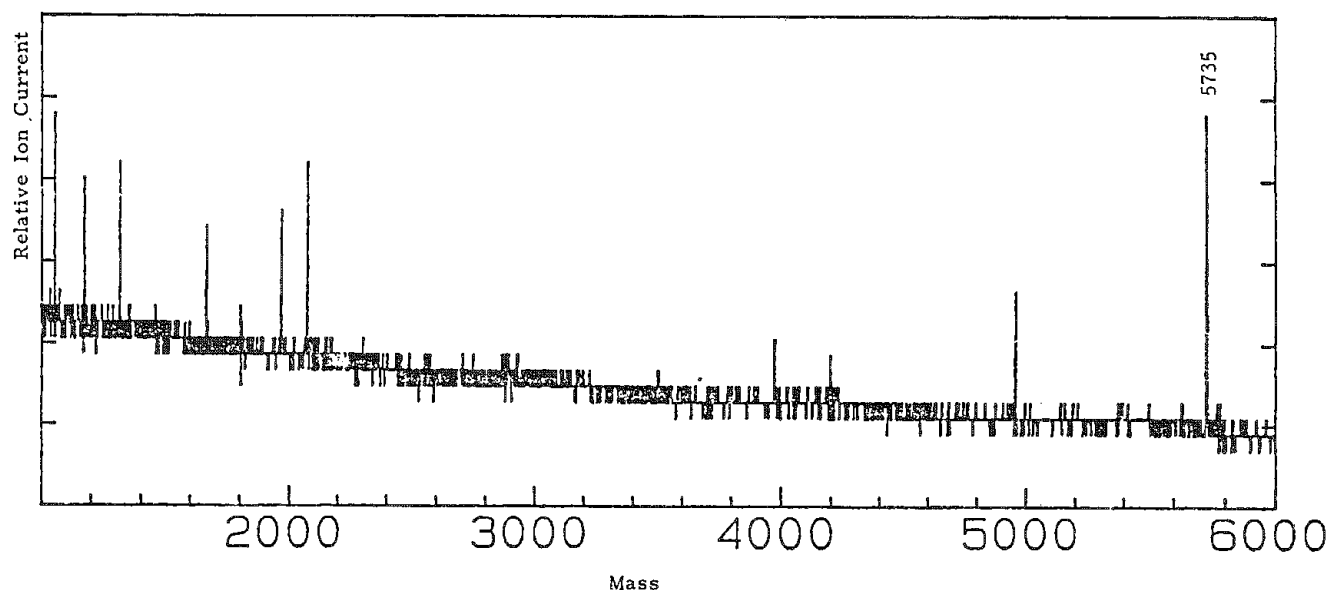


FIG. 5.--Insulin positive ions.



## Quantitative Image Processing and Analysis

### CHARACTERIZATION OF THE GEOMETRY OF MICROSTRUCTURES

R. T. DeHoff

Microstructures are geometrically peculiar; although we frequently view them as consisting of repeating geometric units, in a real microstructure no two features are in fact identical; although we treat them as collections of independent units, each operating independently, in fact the units all fit together to fill three-dimensional space, and their mutual interactions may dominate in determining the behavior of the aggregate.

Because microstructures are nonrepetitive and space filling, the geometric concepts that are most appropriate to their description with rigor are global, i.e., pertain to the structure as whole, rather than to individual features. Analogs of these global properties can be defined for individual features, but are not readily accessible to measurement. This paper briefly reviews these geometric descriptors and their quantitative estimation through the applications of stereological methods.

#### *Levels of Characterization*

The geometric state of a microstructure may be usefully described at three levels of characterization: the qualitative state, the quantitative state, and the topographic state.<sup>2</sup>

The *qualitative microstructural state* is a list of the features that exist in the structure. A complete list recognizes the space-filling nature of microstructures; units are typically polyhedra with curve faces, edges, and corners. Faces result from the incidence of two cells, edges from the incidence of three, and corners result where four cells meet in three-dimensional space. If the structure is a single-phase polycrystal, there is only one class of feature in each of these categories. In a two-phase ( $i + j$ ) structure, where incident cells may be labeled  $i$  or  $j$ , there are possible three kinds of interfaces, four kinds of triple lines, and five kinds of quadruple points; thus, fourteen kinds of features may exist in a two-phase structure. In a three-phase structure, 34 different kinds of features may exist; in a four-phase structure, there may be up to 69 features. Not all will be present in a given structure, so that the drawing up of a list of those that are present is potentially useful, and is a nontrivial task.

The *quantitative microstructural state* is described by a recognition that each of the feature classes identified in the qualitative state has associated with it one or more unambiguously definable geometric properties that may be assigned a numerical value. The most rudimentary of them are the topological properties, number of disconnected parts of the feature, and connectivity of multiply connected parts.<sup>1,3</sup> Most familiar of these properties are the measures of extent: volume fraction of three-dimensional features, surface area per unit volume of interfaces, and length per unit volume of lineal features.<sup>4,5</sup> In addition, measures that involve integrals of the local curvatures of features over their extent are also available,<sup>4-6</sup> and particularly useful in some applications.<sup>7,8</sup> If it is possible to determine values of these rigorously definable properties for individual features in the structure (volume, surface area, curvature integrals), then one may in principle evaluate distributions of these properties over the ensemble of features.<sup>9</sup>

The *topographic microstructural state* characterizes variations in these global property densities (e.g., volume, area, or length per unit volume of a feature) with position (gradients), orientation (anisotropies), or other features (associations with other specific features, feature clustering or ordering).

---

The author is at the Department of Materials Science and Engineering, University of Florida, Gainesville, FL 32611.

### *Stereological Measurements*

Images presented by microscopes are two dimensional; the real world microstructures they sample are three dimensional. Stereology is the body of mathematical relationships that provide the connections between the geometric properties of two-dimensional images and the properties of the three-dimensional microstructures that they sample. The classical stereological measurements are now well established, and include the following:

1. The point count (fraction of points in a random sample of points that lie inside phase *i*) estimates the volume fraction of phase *i*;  $\langle P_p \rangle = V_V$ .
2. The line intercept count (number of intersections that a unit length of a random line makes with interface *ij*) estimates the surface area of interface *ij* in unit volume;  $\langle P_L \rangle = S_V/2$ .
3. The area point count (number of points of emergence of lineal feature on unit area of sectioning plane) estimates the total length of lineal feature;  $\langle P_A \rangle = L_V/2$ .
4. The area feature count or area tangent count (number of closed loops of feature outline of class *ij*, or net number of tangents formed with these loops, observed in unit area of field viewed) estimates the integral mean curvature of *ij* interface;  $\langle N_A \rangle = \langle T_A \rangle/2 = M_V/2\pi$ .

Estimation of topological properties requires serial sectioning analysis.<sup>10</sup> Estimation of distributions of volume, area, or length also requires serial sectioning,<sup>9</sup> although methods abound in the literature for estimating size distributions if it is assumed that all the features are identical in shape.<sup>4,5</sup>

### *Transmitted Messages*

The simple equations of stereology relate geometric properties measured on plane sections to their three-dimensional counterparts. Many images observed in electron microscopy are not plane sections, but are projections through more or less thin slices of the three-dimensional microstructure. The part of the image that is due to intersections of the features with the top and bottom of the slice corresponds to information that would be obtained from a plane section. However, there are contributions to the projected image from features contained within the slice; further, some of these features may be more or less hidden from view by others in the slice. This added visual information contributes to the projected image in a way that depends on the slice thickness, the geometry of the features, and the distribution of the features in space. These contributions can be modeled but cannot be unambiguously estimated without geometric assumptions.

The most general model available for characterizing microstructure from projected images is that provided by Miles,<sup>11</sup> based on random set theory. The microstructure is constructed by distribution of a set of random points in space and then association with each of these points of a set or (three-dimensional feature) selected from a feature set generated by some physical process that is assumed to be operative, e.g., nucleation and growth of spherical particles. Miles's formalism provides equations that connect stereological measurements on the projected image to the geometrical properties of the feature set, and hence to the physical processes that generated the set.

Where it is feasible, perhaps the best strategy for analyzing projected images is to minimize the contributions from features inside the slice; in the limit, as these contributions approach zero, the complex stereology of transmitted images approaches the simple elegant relationships of plane section stereology.

### *Characterization and Image Analysis*

The classical relations of stereology contemplate the superposition of a grid of points or lines on each field, preferably live, under the microscope, and a manual count of the pertinent events that derive from the interaction of the grid with the features in the image. These measurements should be made directly on the microscope, as opposed to photographs or stored images, because it is desirable to sample the entire structure lightly, rather than to concentrate many measurements on a few fields.

The stereological measurements, or their equivalent, can be performed fully automatically with image-analyzing computers, or with appropriate software applied to digitized images provided by various modes of image formation. State-of-the-art image analyzers are

capable of sophisticated image processing, emphasizing user selected contrast or color ranges, responding to gradients in shading, employing geometric criteria (e.g., aspect ratio) for emphasizing features, and performing set operations (erosions, dilatations, skeletonizations<sup>12</sup>) to alter the structure as a precursor to analysis. Since the image is stored in memory as picture points with associated gray shade or color, image analysis can be implemented through virtually any algorithm that can be formulated for extracting numerical information.

In spite of these powerful potentials, unambiguous detection of the features of interest in an image remains a compromise; the operator can always find features that are erroneously detected. Sophisticated image processing routines may produce plausible pictures that are relatively unrelated to the original microstructure. The automatic instruments are not yet competitive with the human brain as a discriminator, particularly in biological applications, where the identification of a feature may involve context as well as geometric and shading factors.

The fundamental problem in image analysis is data reduction: information in a typical digitized image may contain from 60 000 to 4 million numbers (a gray shade or color for each point). This information is typically reduced to a handful of numerical values of selected geometric properties, or perhaps distributions of these values. It is thus crucial to the meaningful quantitative interpretation of microstructural behavior that we focus on the right set of geometrical properties. The global properties described earlier provide concepts that have unambiguous meaning for microstructures of arbitrary geometry, and are thus logical candidates for geometric characterization. The fact that these properties are precisely the ones that are accessible to stereological measurement is no accident, but rather attests to the fundamental importance of these measures. Whimsical deviation from the use of these measures, based on imagined or perceived simplifications in the form of microstructural features, will only continue to keep our materials science qualitative.

## References

1. F. N. Rhines, "Microstructology," *Pract. Metallog.*, 367-382, 1985.
2. R. T. DeHoff, "Topography of microstructures," *Metallography*, 71-91, 1971.
3. E. H. Aigeltinger and R. T. DeHoff, "Quantitative determination of the topological and metric properties during sintering of copper powder," *Met. Trans.*, 1853-1861, 1975.
4. R. T. DeHoff and F. N. Rhines, *Quantitative Microscopy*, New York: McGraw-Hill Book Co., 1968.
5. E. E. Underwood, *Quantitative Stereology*, Reading, Mass.: Addison-Wesley Press, 1970.
6. R. T. DeHoff, "Geometrical meaning of the integral mean surface curvature," in J. L. McCall, Ed., *Microstructural Science*, New York: Elsevier-North Holland Press, 1977, 331.
7. R. T. DeHoff, "Integral mean curvature and platelet growth," *Met. Trans.*, 1948, 1979.
8. C. V. Iswaran, A. H. Gokhale, and R. T. DeHoff, "On the usefulness of the integral mean curvature in the study of the kinetics of coarsening," *Met. Trans.*, 1389-1394, 1983.
9. Guoquan Liu, doctoral dissertation, University of Florida, 1984.
10. R. T. DeHoff, E. H. Aigeltinger, and K. R. Craig, "Experimental determination of the topological properties of microstructures," *J. Microscopy*, 69-85, 1972.
11. R. E. Miles, "On estimating aggregate and overall characteristics from thick sections by transmission microscopy," *Proc. Fourth Intern. Congress for Stereology*, NBS Spec. Pub. 431, Washington, D.C.: Government Printing Office, 1976, 1.
12. J. Serra, *Image Analysis and Mathematical Morphometry*, New York: Academic Press, 1981.

## LARGE-FIELD X-RAY COMPOSITIONAL MAPPING WITH MULTIPLE DYNAMICALLY FOCUSED WAVELENGTH-DISPERSIVE SPECTROMETERS

C. R. Swyt and C. E. Fiori

Wavelength-dispersive (WDS) digital x-ray images have two major advantages over those acquired by energy-dispersive techniques: no background correction for many samples and no artifacts due to peak overlaps. Besides the high beam current required, the main disadvantage of WDS x-ray imaging is the limited number of elements that can be imaged concurrently. This disadvantage has been exacerbated by the methods available when background subtraction is required and for very-low magnification images. We briefly discuss the principles of methods used for these two cases in our laboratory. The details of the computer program and implementation are not described because these are system dependent.

For very low elemental concentration, background correction may be achieved on a computer-acquired WDS digital image simply by subtracting pixel by pixel an off-peak image from an on-peak image. Both images may be acquired with the same spectrometer in sequence or, if geometric effects are not a problem, concurrently on two spectrometers, with the differing spectrometer efficiencies taken into account in the subtraction.<sup>1</sup> With the computer-controlled acquisition system in our laboratory,<sup>2,3</sup> it was possible to develop a program for our CAMECA MBX microprobe that allows acquisition of the background and elemental maps by the same spectrometer during a single pass over the specimen. For each image pixel, counts are accumulated for a selected time at two points on either side of the peak and at the peak spectrometer setting for the imaging wavelength. The averaged background counts and the peak counts are stored and the respective images can be displayed and subtracted by use of image processing software. Alternately, to minimize spectrometer movement and total acquisition time, the background data for a line in the scan may be acquired at only one off-peak setting after peak data for the line has been collected.

X-ray maps of sample areas greater than  $250 \times 250 \mu\text{m}$  are often useful and sometimes required, as with an unknown specimen. For large fields, defocusing of the WDS spectrometers caused by the changing x-ray source location results in variation of intensity in the image that confuses interpretation of the elemental distribution. The intensity distribution due to the defocusing can be modeled and a correction function applied to the image data.<sup>4</sup> However, for fields larger than about  $500 \mu\text{m}$  per side the method is inadequate because counts in some regions of the image may be near zero. One may avoid defocusing effects during acquisition either by moving the stage under a fixed beam or by focusing the spectrometer dynamically. Moving the stage has the advantage of allowing image fields not limited by the available minimum magnification, but stage motion control may not be fine enough for the smaller fields.<sup>5</sup> Dynamic focusing, as previously described,<sup>6</sup> has been limited to a single spectrometer. Briefly, the principle is to vary the crystal position so as to satisfy Bragg's law for the selected x-ray line at each beam position. This goal is accomplished by changing the crystal to x-ray source distance  $L$ , with movement on the Rowland circle. Since the distance  $L$  is usually calibrated in peak  $\sin \theta$  for an x-ray source on the electron optical axis, the apparent result is a change in Bragg angle  $\theta$ . For one-spectrometer focusing the linescan direction is oriented to minimize the change in spectrometer sensitivity along the line. For focusing of a vertical spectrometer the change in  $L$  is given by<sup>5</sup>

$$\Delta L = \Delta Y \sin B \quad (1)$$

where  $Y$  is the distance from the midpoint of the line scan for a raster centered on the optical axis and  $B$  is the x-ray take-off angle. For an inclined spectrometer the relationship is

---

The authors are at the National Institutes of Health, Bethesda, MD 20892.



$$\Delta L = \Delta Y / \tan \theta \quad (2)$$

Concurrent dynamic focusing of both vertical and inclined spectrometers is conceptually straightforward and easily achieved with computer-controlled digital x-ray imaging. As in the case of one-spectrometer dynamic focusing, the scan direction is oriented to minimize the change in spectrometer setting as a line is scanned, but equally offset from the preferred directions of both spectrometers. Digital x-ray images acquired without dynamic focusing to illustrate this scan orientation are shown in Fig. 1. The change in  $L$  required to satisfy Bragg's law at every point in the image can be written as a function of the  $x$  and  $y$  coordinates of the beam position, where  $x$  is in the linescan direction and  $y$  is in the raster-scan direction. For our application of this principle, the peak  $\sin \theta$  for the four extreme beam positions in the raster are determined at lowest magnification with a standard by stepping over the peak at each position. The coordinates and  $\sin \theta$  of each position are stored in a calibration file for the wavelength. From these the peak sine thetas for all beam coordinates in any size raster may be calculated from the following equation:

$$\sin \theta = \sin \theta_R + (CM/IM)[\Delta \theta_X \Delta XI + \Delta \theta_Y \Delta YI] \quad (3)$$

where  $\sin \theta$  is the peak value at coordinate  $(X,Y)$ ;  $\sin \theta_R$  is the value at the chosen reference position in the calibration raster;  $CM$  and  $IM$  are the calibration and image magnification, respectively;  $\Delta \theta_X$  and  $\Delta \theta_Y$  are the ratios of the change in  $\sin \theta$  to the change in coordinate from the calibration file along  $x$  and  $y$  respectively; and  $\Delta XI$  and  $\Delta YI$  are the steps from the reference position to the raster beam location in the  $x$  and  $y$  directions, respectively. Calibration files for a crystal may be generated for all elements within the diffracting range of the crystal by experimentally determining the  $\sin \theta$  calibration sets for a few selected x-ray lines encompassing the crystal range and interpolating. During computer-controlled acquisition the spectrometer is moved to the required  $\sin \theta$  for each beam coordinate in the chosen raster as calculated from Eq. (3).

The background images as well as the elemental images should be dynamically focused unless one is certain there are no beam positions in the raster for which a constant spectrometer setting is equivalent to a wavelength in a region of varying background shape or of another characteristic line. The "line mode" of peak-background imaging is most efficient with dynamic focusing since spectrometer slewing, and therefore total acquisition time, is minimized. Variations in intensity due to crystal imperfections and varying crystal-to-x-ray source distance may remain in the image. These variations may be removed by normalization of the specimen image by one from a uniform standard.

Two images acquired concurrently with dynamic focusing are displayed in Fig. 2. These images are of the same  $1 \times 1$  mm field shown in Fig. 1. The intensity distribution along the line across each image is overlaid on the image. These images illustrate that large-field digital x-ray images free of the intensity variations due to spectrometer defocusing may be acquired concurrently from more than one spectrometer by application of this rather simple dynamic focusing method. Used in conjunction with the peak-background image algorithm, it permits optimum use of the available spectrometers for low-magnification imaging of elemental distributions with concentrations near the detection limits.

### References

1. C. E. Fiori, C. R. Swyt, and K. E. Gorlen, "Continuum correction of x-ray images in scanning electron column instruments," *Microbeam Analysis--1984*, 179.
2. R. D. Leapman, C. E. Fiori, K. E. Gorlen, C. C. Gibson, and C. R. Swyt, "Combined elemental and structural imaging in a computer controlled electron microscope," *Proc. 41st EMSA*, 1983, 10.
3. K. E. Gorlen, L. K. Barden, J. S. Del Priore, C. E. Fiori, C. C. Gibson, and R. D. Leapman, "A computerized analytical electron microscope for elemental imaging," *Rev. Sci. Instr.* 55: 912, 1984.
4. R. L. Myklebust, R. B. Marinenko, D. E. Newbury, and D. S. Bright, "Quantitative calculations for compositional mapping techniques in electron probe microanalysis," *Microbeam Analysis--1985*, 101.

5. M. Mayr and J. Angeli, "Concentration mapping: A software package for the quantitative determination of two dimensional elemental distribution by an electron probe micro-analyser," *X-ray Spectrom.* 14: 89, 1985.

6. Instruction manual for Camebax Dynamic Focusing Device for X-ray Spectrometers, CAMECA, Courbevoie Cédex, France.

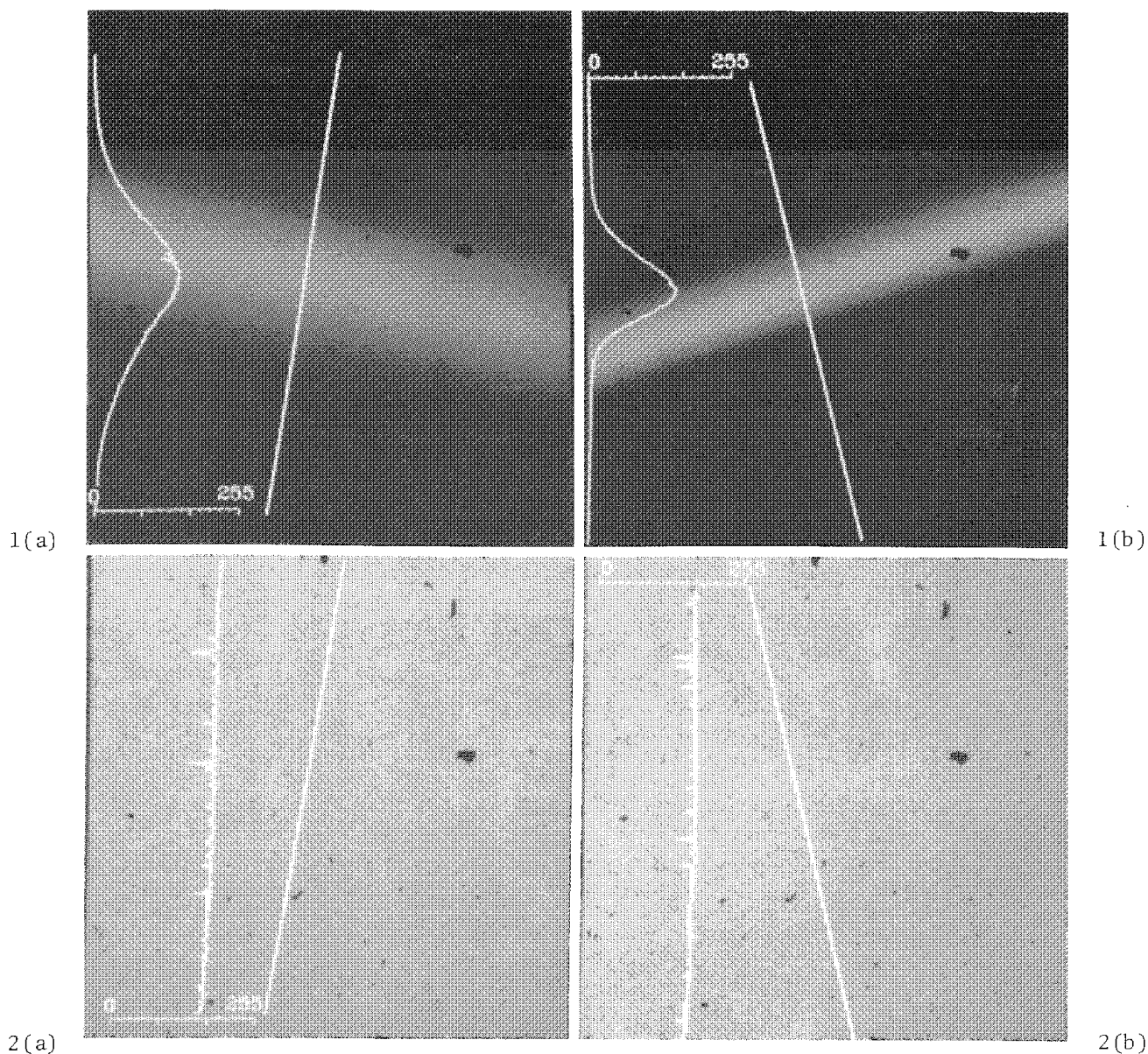


FIG. 1.--WDS digital x-ray images of  $1 \times 1$  mm field of pure Ti acquired with (a) vertical and (b) inclined spectrometers set to Ti  $K\alpha$  wavelength. Intensity rapidly falls to zero on either side of focusing band.

FIG. 2.--Concurrently acquired WDS x-ray images of same field as in Fig. 1, but with dynamic focusing of spectrometers.

## EVOLUTION OF AUTOMATED ELECTRON MICROSCOPY

R. J. Lee, J. S. Walker, and J. J. McCarthy

Automated electron microscopy has developed rapidly during the last decade. This paper reviews those developments from four perspectives: hardware, analysis, output, and results.

### *Hardware*

The development of automated systems interfaced to electron microscopes closely parallels developments in the microcomputer and minicomputer hardware. The early minicomputers used in some of the first automated systems seem slow when compared with today's high-speed, large-memory devices. The cost and physical size of memory has steadily decreased to permit ever larger storage arrays and increased sophistication in the software. Still missing is the development of sophisticated interfaces between microprocessors now used to control most electron microscopes and external computers. Programmable control functions will be increasingly important in the future if more sophisticated analysis schemes are to be developed.

### *Analysis*

The sophistication in analytical procedures available for automated electron microscopy also closely parallels the developments in speed and memory size available in the hardware. Originally, innovative real-time sizing algorithms were developed that performed a rudimentary particle sizing with little or no elemental data. The main goal of the original algorithms was to retain only the essential information about each feature. This approach was adopted by White, Lebedzik et al.,<sup>1</sup> because of the memory limitations of available hardware. Elemental data consisted of yes-no answers for the presence or absence of a particular element. Interfacing of a software-based EDS system with a digital beam-control system permitted sophisticated elemental analysis to be obtained and prompted extensive activity in the development of particle recognition or classification schemes.<sup>2,3</sup> Continued work in this area has seen mathematical procedures such as cluster analysis used to refine compositional classification systems on off-line mainframe computers. Lineal analysis techniques, complex particle analysis, and mineral association analyses have all been developed during the last few years. As the speed of the computers and the available memory increased, analysis of preprocessed stored images and multigraph level analyses have become available.

Virtually all the analysis programs in automated microscopy have tended to separate microscopists into two camps: those who take pictures or perform detailed characterizations of operator-selected features, and those who produce numerical data on the size, shape, abundance, and composition via operator-independent procedures. A new technique, which offers the promise of permitting the ultimate use of automated microscopy, has been termed microimaging.<sup>4</sup> Under this scheme a dual set of programs is operational. Computer controlled microscopy routines perform an automated panning function. The algorithms permit features with specific characteristics to be flagged, at which point a set of operator-controlled routines such as spot analysis, image processing functions, or x-ray mapping on the particular feature or area can be performed. The system then returns to the automated panning function, and continues to accumulate data on the entire sample until another feature of interest is encountered. The ultimate benefit of this approach is that it takes advantage of the benefits of the automated functions while permitting the microscopists to examine features of specific interest with the usual level of detail. This development has potential for being an important and standard function of future

---

Authors Lee and Walker are at Energy Technology Consultants, 350 Hochberg Road, Monroeville, PA 15146; author McCarthy is at Tracor Northern, Inc., 2551 West Beltline Highway, Middleton, WI 53562.

automated microscopic systems.

### *Output*

The output from automated microscopic analysis began with highly detailed results printed about the individual features examined. In effect, the information generated was so new and of such interest that the specific attributes of every particle or feature seemed important. Following that came the production of histograms, cumulative frequency, and statistical data. The introduction of tabular or summary results from the analysis was significant in permitting detailed comparisons of species abundance and their size distributions and relating them to properties. Recently a useful approach to examination of particle composition has been introduced via the use of ternary plotting functions, which are beneficial for examining trends in compositional clusters.<sup>5</sup> In the future, we can expect the data management and data processing software such as that available for personal computers to begin to impact the way we collect, store, and analyze the results from automated electron microscopy.

### *Results*

Given the extensive body of algorithms and the number of systems in use, published results seem remarkably scarce. Papers seem to be technique oriented rather than result oriented. There is a limited number of studies illustrating the use of automated electron microscopy in air-pollution studies, coal mineralogy, and quantitative metallography, as well as some biological problems. However, the conclusions or interpretation of data from these highly sophisticated systems does not seem to be keeping pace with the developments in technology. One wonders whether this is the result of a lack of standardization, the nature of the problems for which the systems are being used, the lack of training, or simply the natural time lag. In comparison with the electron microscope, we have not yet seen the extensive round-robin testing and evaluation which ultimately led to acceptance of the microprobe as an analytical tool in routine applications. We must establish the applications of the technology and validate them. Failure to do so will prevent the evolution of electron microscopy out of the fundamental research laboratory into quality control and production environments, where it can reach its ultimate potential.

A survey is now being carried out on the utilization of automated microscopy and an applications bibliography is being developed. The authors will make them available on request. We thank the manufacturers who participated in circulating the survey and developing the information base.

### *References*

1. M. R. Hoover, E. W. White, J. Lebedzik, and G. G. Johnson, "Automated characterization of particulates and inclusions by computer-controlled SEM/probe," *Microbeam Analysis*--1975, 54A.
2. J. J. McCarthy, "Application of a digital scan generator to EDS analysis," *Microbeam Analysis*--1979, 307-309.
3. R. J. Lee and J. F. Kelly, "Overview of SEM-based automated image analysis," *SEM/1980 I*, 303.
4. R. J. Lee, J. S. Walker, and J. J. McCarthy, "Microimaging: A link between microscopy image analysis and image processing," *Microbeam Analysis*--1985, 153.
5. J. S. Walker, R. J. Lee, and J. J. McCarthy, "Ternary representation of particle composition from SEM-EDS automated particle analysis: An application of object vector image analysis," presented at SEM (1984), manuscript available from authors.

## A TECHNIQUE FOR THE 3-D REPRESENTATION OF CARBON BLACK

P. J. Hood and D. G. Howitt

The assessment of the structure property relationships of dispersed media is far from straightforward when the dispersion is irregular. In the case of carbon black suspended in a polycarbonate matrix, for example, the electrical properties should be related to the connectivity of the individual chains of carbon spheres (Fig. 1), but conventional analysis in the TEM does not show any significant variation in structure between materials with very different properties.

In an attempt to assess more appropriately the structure of carbon black dispersions, we are developing a technique to distinguish the three-dimensional distribution of the component carbon spheres using transmission electron microscopy of thin specimens of material. The current technique for determining the 3D structure of such a system is to record electron micrographs over a range of angles and then to match the corresponding particles manually. The 3D position in space (relative to some fixed arbitrary point) can be calculated from the measured disparity  $r$  because the particles are at different depths  $d$ . Therefore, the particles in the thin specimen appear to be translated through a distance  $r = d \sin \theta$  when the specimen is tilted through an angle  $\theta$ . To obtain a representative measure of the characteristics of the dispersion a large number of particle locations must be determined. The manual correlation of the thousands of particles in a medium-density sample can be prohibitive. To solve this problem a computer program has been developed to measure the displacement between corresponding particles and to reconstruct their locations in the specimen. The carbon black system is ideal for the development of an automated 3D reconstruction program because the particles are of high contrast in the matrix and are of uniform density. The program takes advantage of current techniques in image segmentation and pattern recognition, and we have used artificial intelligence (AI) techniques to achieve the correlation.

Because of the immense size of these 3D images, the information necessary for the determination of material properties requires more than a graphical representation of the structure, such as for example those which can be obtained by stereo imaging. A 3D image that can be rotated and displayed from many different viewpoints is acceptable for qualitative analysis but, as will be shown later, the 3D image may not in fact be exactly calculated from a few projections, which is the case for this system. Calculations of the properties such as conductivity requires information about the relationships between particles, specifically how they are combined into chains and how far apart they are from each other. The final representation must therefore contain this information and be capable of being implemented into computer simulations. The 3D representation chosen for this program is built up of 3D blocks that contain information about the size, shape, and density of the particle (or group of particles), in addition to the neighboring 3D-blocks. With the information in this format, it is much easier to perform the calculations and interpret the data.

Current techniques in image processing make it straightforward to digitize the projections into 2D arrays of picture elements (pel). Each pel has an intensity that is directly related to the density contained in the column of space perpendicular to the projected plane. If each pel is simply used as a unit of information to correlate between projections, this correlation, and therefore the 3D solution, is not unique. The effect that gives rise to this phenomenon is known as aliasing. It occurs when more than one 3D configuration can give rise to the same pair of projections, as is apparent in the simple case shown in Fig. 2, where the two balls in space can be located in positions A or B and still yield the same pair of projections. If another projection were to be taken at a different angle, the balls could be placed in space uniquely, but as the problem becomes more complex, proportionally more projections are required and even a visually simple

---

The authors are at the Department of Mechanical Engineering, University of California, Davis, CA 95616.

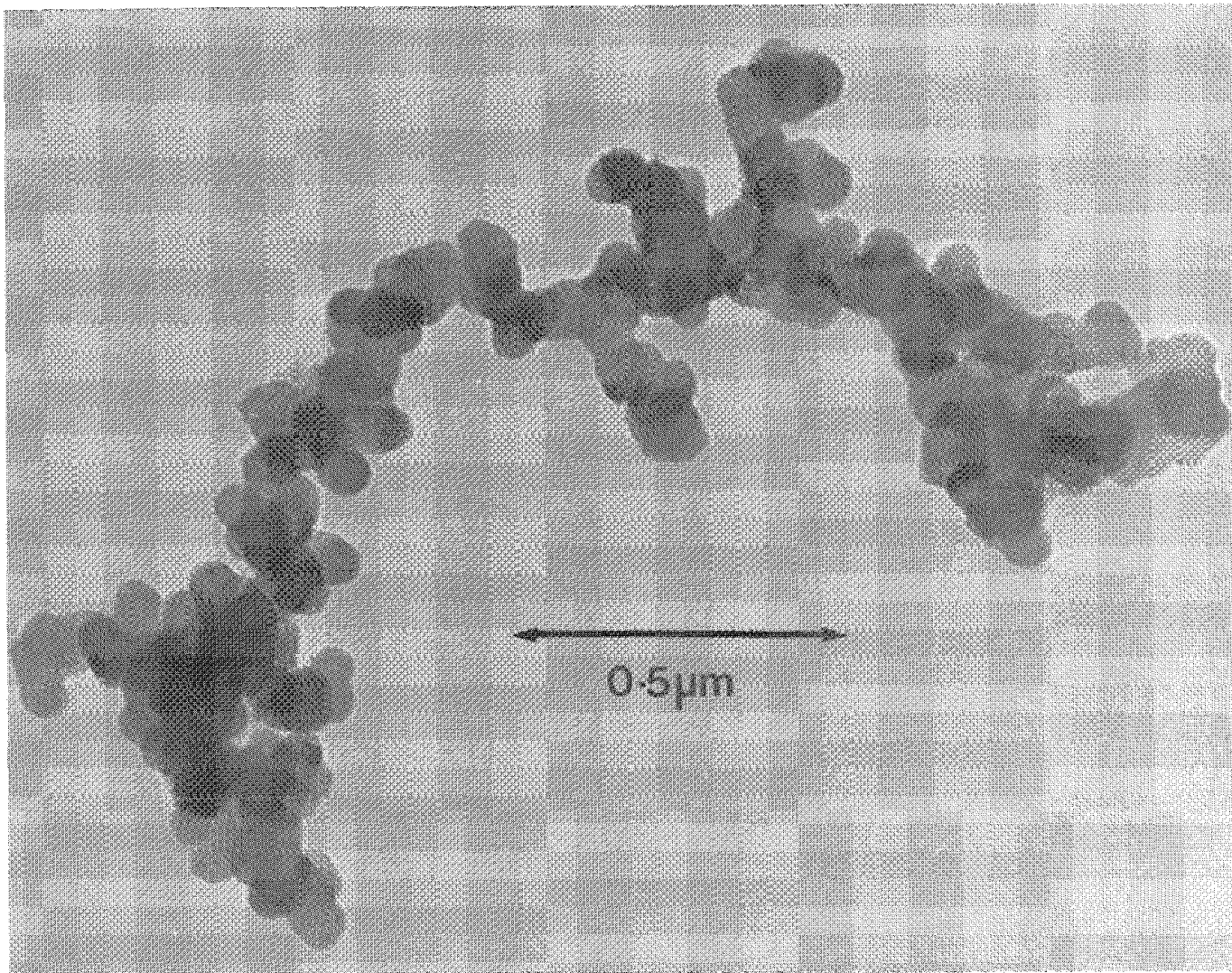


FIG. 1.--Carbon black chain dispersed in polycarbonate matrix.

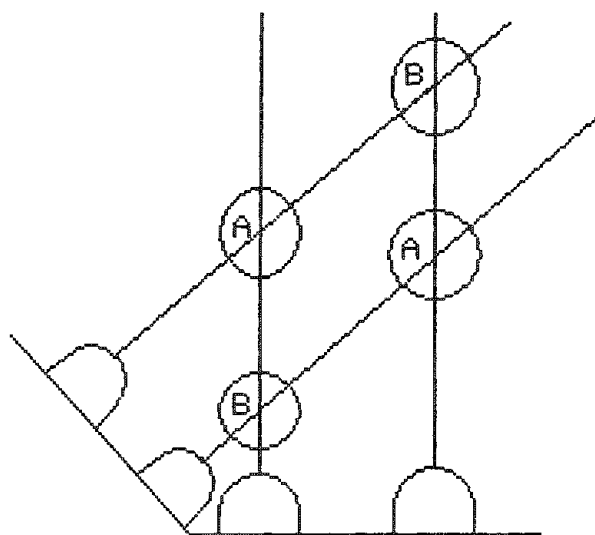


FIG. 2.--Similar projected pairs of spheres from two separate physical situations (A and B) resulting in aliasing.

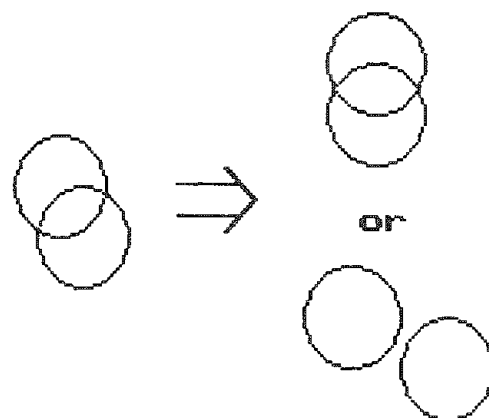


FIG. 3.--Two possibilities of transformation of two spheres in space.



image requires a continuum of projections to solve for the unique 3D structure. If a large number of projections is available, the structure may be solved in phase space by a Fourier method<sup>1,2</sup> or in real space by an algebraic method.<sup>1,3</sup> Neither technique, however, is possible with a wide range of applications (including carbon black) because of the imaging constraints of the TEM.

In the case of carbon black, and in most other systems, there is information apart from the intensity that can be used to optimize the correlation. Particles have shape, density variations, and positions relative to other particles. Although these relations change when the sample is tilted, the transformation is predictable. A simple example of the transformation is shown in Fig. 3, where two spheres initially overlap. When the sample is tilted, the projection transforms to either two spheres overlapping or two isolated spheres. In order to incorporate such information, one must isolate or segment the original projection into 2D blocks that can be described by data similar to those for the 3D blocks. The method of segmentation (whether it be edge detection, thresholding, or some other) can vary substantially as long as the resulting segments contain information that can be related to the transformations. Two simple examples of the segments possible in this system are shown in Fig. 4. The correlation of the segments is necessary for a unique solution, and since the segments can transform into each other, it is sensible to place similar segments into labeled groups or classes. The classes are used directly in the prediction of the transformation with the aid of a database; once the segmentation is complete, the segments are classified using a variation of the k-mean algorithm<sup>4</sup> to achieve the basis of correspondence.

In searching for corresponding segments, not all of the opposing projection needs to be searched because the axis and extent of rotation is known, as shown in Fig. 5. The vertical displacement in the "region of search" allows for initial image mismatch and segment transformations. It is helpful to solve first the simplest correlations (those in which there is only one possible correlation in the "region of search") and then to solve the more difficult correlations. As the correlations become increasingly difficult, the database comes to play a larger role. The database contains information about the transformations and, for aspects of the image where there is insufficient information to make a correlation, it must contain rules to infer structure by AI techniques. An example of a complex situation requiring the aid of AI is shown in Fig. 6, where a large block of particles could not be classified due to imaging constraints. By use of the known coordinates of connected chains, however, an inference can be made that the chains are connected through the unclassified region, although the exact description of how they are connected would not be known.

Once the correlations are made between 2D blocks, the 3D blocks are created from a weighted intensity sum of the contributing 2D blocks of each projection. The method involves a segmentation algorithm, the information for classification which is gathered from within segments, and a set of rules restrictive enough to reduce correlation aliasing.

## References

1. R. A. Crowther, D. J. DeRosier, and A. Klug, "The reconstruction of a three-dimensional structure from projections and its application to electron microscopy," *Proc. Roy. Soc. Lond.* A317: 319-340, 1970.
2. A. Engel and A. Massalski, "3D reconstruction from electron micrographs: Its potential and practical limitations," *Ultramicroscopy* 13: 71-84, 1984.
3. R. Gordon, R. Bender, and G. T. Herman, "Algebraic reconstruction techniques (ART) for three-dimensional electron microscopy and x-ray photography," *J. Theor. Biol.* 29: 471-481, 1970.
4. J. MacQueen, "Some methods for classification and analysis of multivariate data," *Proc. 5th Berkeley Sump. on Prob. and Stat.*, Berkeley: University of California Press, 1967.

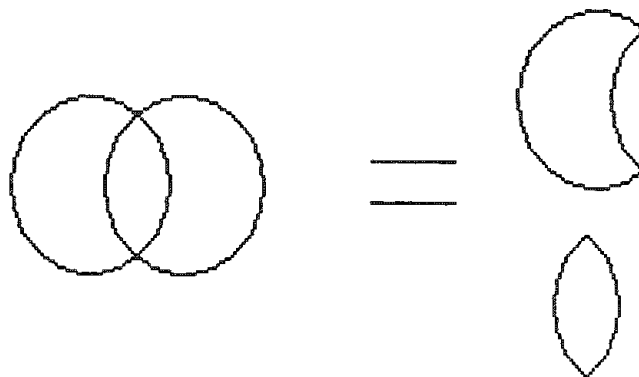


FIG. 4.--Segments resulting from two overlapping balls.

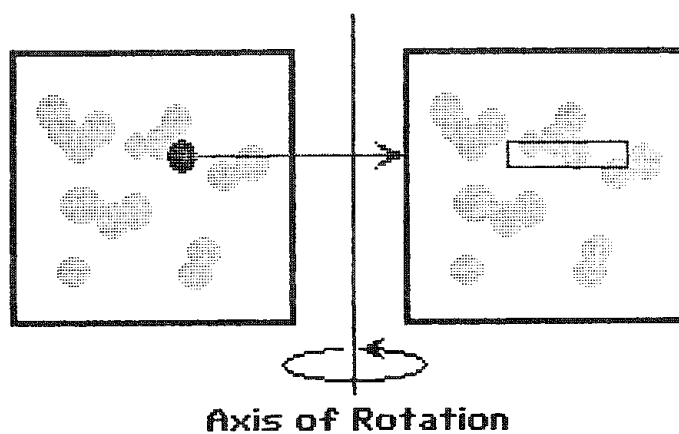


FIG. 5.--"Region of search," defined by rectangle, where tilted object must reside in second projection. Vertical range is result of image mismatch and segment transformation; horizontal range is restricted by thickness of specimen and angle of rotation.

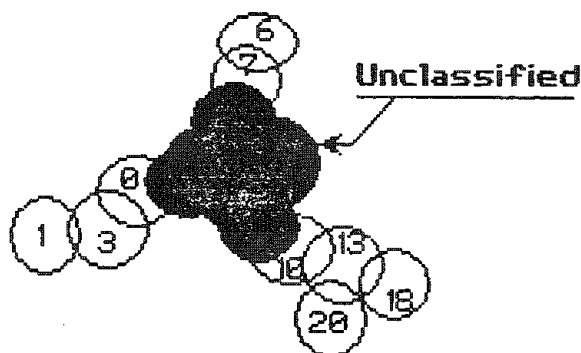


FIG. 6.--With numbers in spheres representing relative heights in specimen, an inference may be made that spheres are connected in some manner.



## QUANTITATIVE AND LOW-MAGNIFICATION MAPPING BY THE ELECTRON MICROPROBE

K. A. Thompson and L. R. Walker

In recent years the computer automation of the electron microprobe has allowed applications that would otherwise be impossible or too time consuming. This capability particularly applies to digital imaging of x-ray signals, which has many advantages over the traditional dot mapping. The need to surpass conventional dot mapping has led to the development at the Oak Ridge Y-12 Plant of a semiquantitative digital imaging technique, accomplished by correcting for a background, multiplying by a correction term, and displaying along with a concentration profile. This procedure can be quantitative in special cases, particularly for low-concentration elements in a uniform matrix. In addition, digital images can be accumulated by scanning the stage,<sup>1</sup> spectrometers,<sup>2</sup> and/or the electron beam. The procedure no longer limits images to relatively high magnifications, but allows low and very low magnifications to be recorded.

### *Instrumentation*

The electron microprobe is a Cameca Model MBX. It has an ultimate electron-beam resolution of 7 nm, although for x-ray mapping a lower resolution of  $\sim 1 \mu\text{m}$  is not uncommon. One energy-dispersive spectrometer (EDS) and three wavelength-dispersive spectrometers (WDS) allow the simultaneous analysis of several elements. One WDS spectrometer is inclined, which minimizes crystal defocus due to the specimen height. This spectrometer has four crystals that allow all elements with atomic numbers above lithium to be analyzed. Each of the other two spectrometers has two crystals. The stage has an x, y movement of  $50 \times 50 \text{ mm}$ , with a reproducible movement of  $1 \mu\text{m}$  under computer control.

The data system is a Tracor Northern 5500, which has an LSI 11/73 central processing unit (CPU), 4 Mbytes RAM, a 20 Mbyte hard disk, and 2 Mbytes floppy-disk storage capacity. Interfacing of the spectrometers and stage axis is handled through the TN1310 module. The data are displayed on a high-resolution color monitor from which photographs can be obtained. If higher resolution black and white images are desired, they can be transferred to the electron microprobe's cathode-ray tube (CRT).

### *Theory*

Quantitative elemental compositions are normally determined by positioning of the stage to the desired areas to be analyzed, use of the x-ray spectrometers to determine the intensity of the x-ray signals, subtraction of the background, comparison with standards, and application of a correction routine. Although this method can be used to obtain a two-dimensional (2-D) image of the elemental compositions, it would not be time efficient. The traditional method of x-ray mapping is to raster the electron beam across the sample and to form a white dot on the CRT whenever an x-ray signal is detected. This procedure adequately shows large changes in elemental composition.

Digital x-ray maps are desirable whenever a subtle difference exists for the elemental composition. X-ray maps are generated by rastering of the electron beam across the sample in a matrix fashion while the x-ray pulses detected for each element of the matrix (pixel) are counted. This type of image can be manipulated by a computer to enhance the desired features. Although quantitative information about the elemental composition is present, the typical byte storage limitation of 255 counts does not provide sufficient statistics. In order to increase the amount of quantitative information without increasing the amount of storage area, x-ray intensities are processed to a concentration which allows for sufficient counts to be accumulated without overrun of the byte storage capacity.

If the number of counts is increased by only an order of magnitude, concentration changes as low as 5% can be discerned, whereas features with obvious patterns stand out

---

The authors are at Martin Marietta Energy Systems, Inc., Y-12 Plant, Product Certification, Oak Ridge, TN 37831. The work was performed for the U.S. Department of Energy under Contract DE-AC05-84OR21400.

with as little as a 1% difference. In order to obtain more counts, either the signal rate must be increased or the acquisition time must be extended. Because it is advantageous to keep time to a minimum, higher signal rates can be obtained by use of the WDS and higher beam currents. The WDS has the added advantage of having a high peak-to-background ratio, which for many samples gives an insignificant background.

For cases where the background cannot be ignored, there are several methods of determination. The most accurate method is to take a second x-ray image of the same area with the WDS set for the background. Although this method would take twice as long, it is useful when extreme overlapping of different elemental peaks exists. A second possible solution would be to use a different WDS set for the background. This solution would eliminate the need for a second acquisition, but it could possibly introduce artifacts due to the different geometry. A third method to determine the background is to use the EDS,<sup>3</sup> assuming the count rate is not too high. For moderately high count rates the resolution would be degraded, but due to the normal linearity of the background, this degradation would not affect the results. The final method is to calculate the total background as a sum of all the elemental backgrounds, as described by the following equation:

$$B = \sum_{i=1}^N b_i k_i \quad (1)$$

where  $N$  is the number of elements present,  $k_1$  is the ratio of the x-ray intensity of the sample to a standard, and  $b_1$  is the ratio of the background to the peak for a standard. This method is a reliable estimate and is quick and simple.

Several correction routines are currently in use for calculating the composition from the  $k$  ratios, including ZAF<sup>4</sup> and PRZ.<sup>5</sup> For a computer system such as the TN 5500, several seconds are required to perform the correction. If the acquisition time for each pixel is of this order, then each pixel can be corrected while the next one is being acquired. In most cases, however, much shorter time periods are used, and some other form of correction is needed. For a simple binary system, a few calculations can be made at each limit of the range, and intermediate values can be assumed to be linear. If the range is too large for this method to be accurate, it can be broken down into smaller linear sections, or some other empirical method can be used, such as the hyperbolic approximation.<sup>6</sup> For multielement samples, similar schemes can be used, but they are more complicated. They are usually justified only if many similar samples are to be studied. Otherwise, uncorrected  $k$  ratios are usually considered adequate.

One remaining limitation of the WDS is the very small magnification range for which images can be accurately acquired. Because the typical lateral resolution is  $\sim 1 \mu\text{m}$ , magnifications higher than  $\sim 2000\times$  appear washed out. Images acquired at magnifications lower than  $\sim 1000\times$  suffer from defocusing of the WDS. Therefore, fewer counts are collected at the edges. One method to correct for it is to multiply the image by a normalizing image.<sup>7</sup> Although this correction appears very simple, the reduced counts would vary the statistics as the crystal becomes defocused. This effect would lend to washed-out edges, which is not satisfactory for the majority of cases.

Two methods of obtaining accurate low magnification x-ray images are to scan the spectrometers to keep them in focus<sup>1</sup> or to scan the stage.<sup>2</sup> The first method has the advantage of requiring the smallest amount of movement if only one element needs to be mapped. In order to produce multiple x-ray images simultaneously, each spectrometer would have to be scanned continuously to keep it in focus. Although this solution is possible, it is usually more desirable to keep their motion minimized to reduce wear. Also, each spectrometer has a preferred geometry for the raster orientation which would require only one movement for each line acquired of the 2-D image. If the two vertical spectrometers are  $18^\circ$  apart or if one inclined spectrometer is  $90^\circ$  apart from a vertical spectrometer, then they may share the same geometry. For the instrument described above, neither requirement is met.

Stage scanning is a fairly simple concept and has several advantages: the crystals are always in focus, multiple x-ray images can be acquired simultaneously, and very low magnifications can be obtained. The disadvantage is that a large amount of movement is required that causes more wear on the mechanical parts. That can be remedied by use of extra caution in keeping the friction points well lubricated. Other factors that must be dealt with

are sample tilt and sample shape. The tilt can be corrected by adjustment of the height periodically, assuming a flat surface and therefore a linear height correction which can be easily determined; for an irregular surface some other method can be used, such as scanning the height while monitoring a spectrometer to keep it in focus. The shape is mentioned to emphasize that some areas may be outside the desired area of analysis and can be ignored. Time should be spent only for the areas of interest.

### *Example*

Figure 1 shows low-magnification x-ray maps of gold and silver for a group of National Bureau of Standards (NBS) gold/silver standards. These maps were acquired simultaneously by scanning the stage, using Eq. (1) to determine the background, and using the hyperbolic approximation for the correction term mentioned earlier. The  $256 \times 256$  image was acquired in 2 h with a beam current of 100 nA, which necessitated dead-time corrections. Note the gray scales showing the concentrations of gold and silver, which usually appear in color to help visual determinations of actual concentrations. The concentrations of gold in the NBS standards as determined from the images are 100.0, 82.4, 60.0, 36.6, 19.3, and 0.0, which approach the actual concentrations of 100.0, 80.0, 60.0, 40.0, 20.0, and 0.0%.

This example shows a broad concentration range, which is always difficult to quantify accurately. Even use of ZAF corrections for each NBS standard calibrated against pure gold and pure silver yields values that vary as much as 2% from the actual concentrations. In addition to the concentration, the image's shape integrity is also demonstrated. These NBS standards are wires that were mounted in a rough rectangular grid. If the stage had not been scanning in a linear fashion, the image would be distorted. This feature was also verified by use of copper grids which initially hinted at a worn gear on the stage, which was subsequently replaced. This result demonstrates the importance of periodic checks of the stage linearity.

Figure 2 is a low-magnification x-ray map of niobium in a 6% niobium/uranium alloy. This map was acquired by scanning the stage in the same manner as was used for the NBS standards. This  $50 \times 400$  image was acquired in 12 h at a beam current of 300 nA, which necessitated dead-time corrections. The subtle bands in the sample show a relative percentage change of  $\sim 5\%$  and the dark splotches show a relative change of  $\sim 20\%$ . This example demonstrates two important points: only the area of interest was scanned and subtle changes are quite obvious when higher statistics are used; the total counts acquired for each pixel were  $\sim 600$ . If smaller changes in concentration are present, a higher beam current could be used to separate those features.

Figure 3 shows a quantitative line scan through this sample, for which a complete ZAF correction was used for each point. This type of linescan was originally used to determine the niobium distribution, but it was hard to interpret. The 2-D image describes the system with greater detail, showing the bands and splotches that might otherwise be missed. Comparisons of the ZAF determined line profile with the image concentrations also show the quantitativeness of the image.

### *Conclusion*

Low-magnification x-ray mapping can be extremely useful in determining large scale concentration changes. By scanning of the stage or the WDS, magnifications lower than  $\sim 1000\times$  can easily be studied. Besides being qualitatively informative, x-ray maps are also semi-quantitative and in many cases, quantitative. This type of information is applicable to many fields, and it is just starting to be used. Computer automation is allowing the microprobe applications to grow in areas that would otherwise be too tedious and time consuming. By allowing the computer to handle all aspects of data acquisition and control, periods of normal inactivity (nights and weekends) can be used to acquire data such as low-magnification x-ray maps.

### *References*

1. W. F. Chambers, "Digitally controlled x-ray mapping," *Microbeam Analysis--1981*, 43-44.
2. Yoshiaki Ono, et al., "High-speed wide area analysis by electron probe," *Microbeam Analysis--1985*, 145-147.

3. C. E. Fiori et al., "Continuum correction of x-ray images in scanning electron column instruments," *Microbeam Analysis--1983*, 179-185.
4. F. Schamber et al., "ZAF operation and program description version 10," *Internal Report*, Tracor Northern, 2551 W. Beltline Hwy., Middleton, WI 53562, 1977.
5. J. L. Pouchou and F. Pichoir, "'PAP'  $\phi(\rho z)$  procedure for improved quantitative microanalysis," *Microbeam Analysis--1985*, 104-106.
6. K. F. J. Henrich, *Electron Beam X-ray Microanalysis*, New York: Van Nostrand Reinhold, 1981.
7. R. L. Myklebust et al., "Quantitative calculations for compositional mapping techniques in electron probe microanalysis," *Microbeam Analysis--1985*, 101-103.

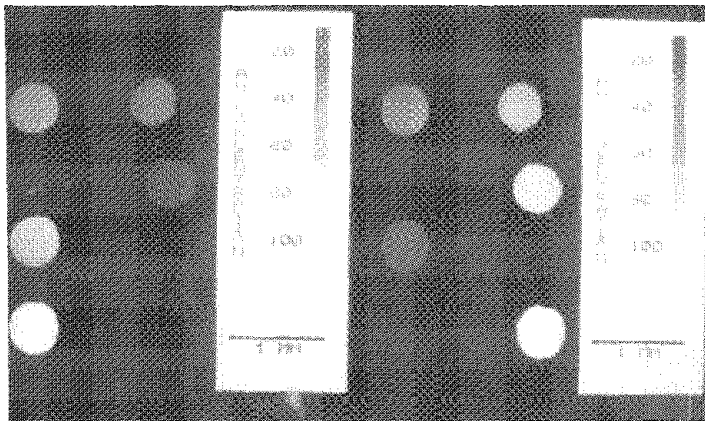


FIG. 1.--Low-magnification x-ray maps of gold and silver for array of NBS standards.

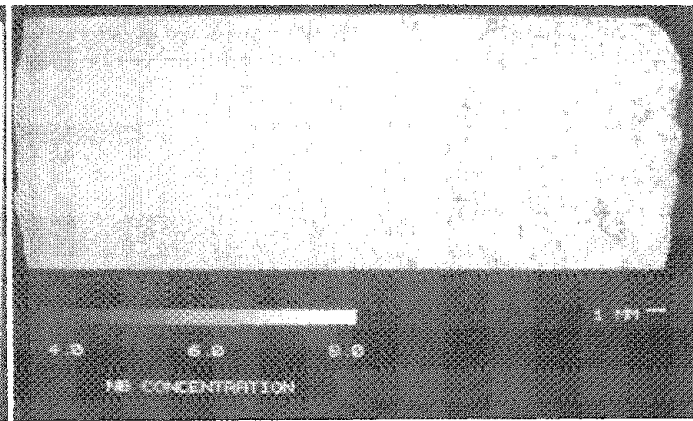


FIG. 2.--Low-magnification x-ray map of niobium for 6% niobium-uranium alloy.

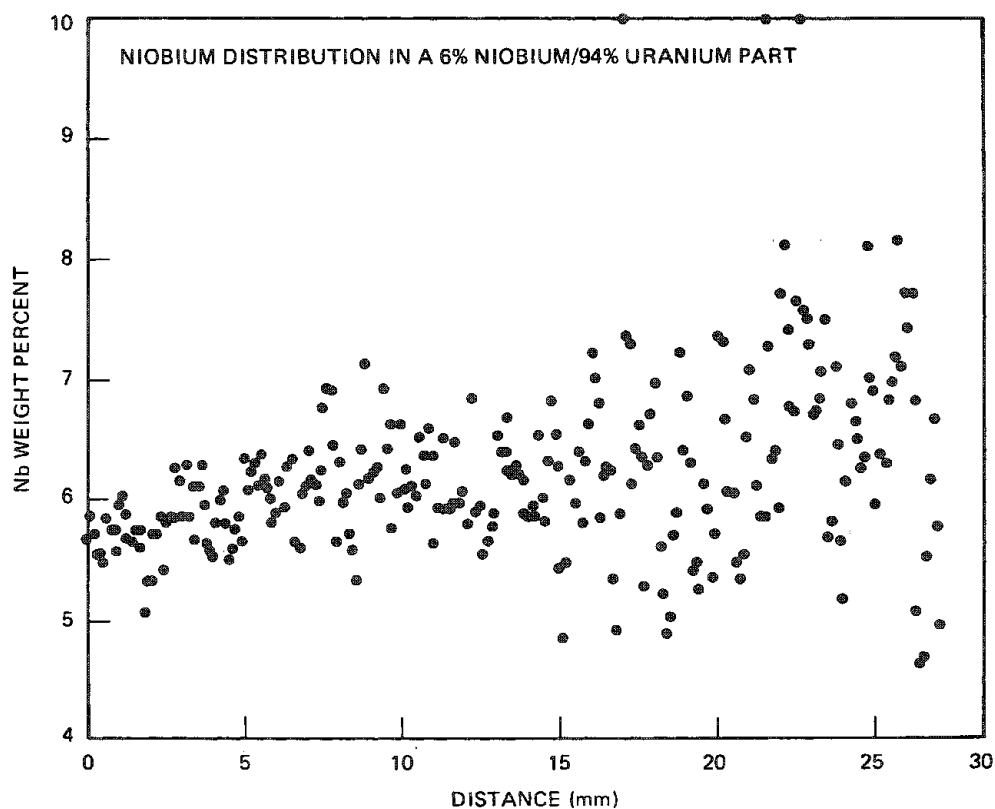


FIG. 3.--Linescan of niobium concentration (based on ZAF calculations) in 6% niobium-uranium alloy.

## DEFOCUS MODELING FOR COMPOSITIONAL MAPPING WITH WAVELENGTH-DISPERSIVE X-RAY SPECTROMETRY

R. L. Myklebust, D. E. Newbury, R. B. Marinenko, and D. S. Bright

Quantitative compositional mapping with the electron probe microanalyzer (EPMA) and wavelength-dispersive x-ray spectrometry provides a new and important mode of analysis.<sup>1-3</sup> The use of the wavelength-dispersive x-ray spectrometer (WDS) allows the elimination of most peak overlaps in complex specimens and provides access to trace compositional levels in a mapping mode, but in order to employ the WDS, a correction must be applied to the data to compensate for the effects of spectrometer defocusing. There are four methods to correct spectrometer defocusing: (1) fixed electron beam and fixed spectrometer position with stage scanning; (2) crystal rocking to move the focus position of the spectrometer in synchronism with the beam scan on the specimen; (3) "defocus mapping," in which a "standard map" is prepared under the same conditions as the unknown; and (4) "defocus modeling," in which the defocus map is calculated rather than measured directly.

In our previous work, we explored the use of the "standard map" for quantitative compositional mapping.<sup>2,4</sup> Although the standard map technique can provide accurate corrections for defocusing, there are significant drawbacks in practical application: (1) preparing the standard map requires scanning an area on each standard as large as that on the unknown, a time-consuming process. (2) Any defect in the standard (such as a scratch, hole, or inclusion) that affects the x-ray intensity appears as an artifact in the final compositional map of the unknown. Smoothing the standard map can compensate for these defects to some extent, but a defect larger than the smoothing kernel will still be noticeable. (3) Although the standard maps can be archived and readily scaled to changes in beam current or spectrometer efficiency, a new map is required for each new magnification and element. Defocus modeling can overcome several of these limitations and provide a more flexible approach to mapping.

### *Defocus Modeling*

The principle of defocus modeling is based on the observation that an x-ray area scan generated with a moving electron beam and a fixed spectrometer contains information equivalent to an intensity profile of an x-ray peak generated by scanning of the spectrometer while the beam is fixed on the specimen. This equivalence is illustrated in Fig. 1, where a peak scan has been obtained from an x-ray area scan as an intensity profile extracted perpendicular to the line of best focus. The asymmetry of the peak due to the presence of the  $K\alpha_1$  and  $K\alpha_2$  lines can be recognized in both scans. Thus, if we have a spectrometer scan across a peak, which consists of the intensity as a function of angular position, it should be possible to construct an equivalent "standard map." Moreover, it should be possible to construct the map for any magnification, given a sufficiently wide spectrometer scan.

The mathematical basis of this construction is illustrated in Fig. 2. The spectrometer is initially adjusted to set the ideal Bragg angle for x rays emitted when the beam is centered on the optic axis of the microprobe. The distance  $S_0$  from the specimen to the crystal at this point is given by

$$S_0 = 2R \sin \theta \quad (1)$$

where  $R$  is the radius of the spectrometer. From the point of view of the spectrometer crystal, the effect of scanning the beam on the specimen by a distance  $\Delta S$  from the optic axis is to cause an angular deviation  $\Delta\theta$  from the exact Bragg position. Since the spectrometer radius is of the order of 150 mm and the scan distance for a map at a low magnification of  $100\times$  is only 1 mm, the angle  $\Delta\theta$  can be accurately approximated as

$$\Delta\theta \approx \sin \Delta\theta = \Delta S/S_0 \quad (2)$$

---

The authors are at the Center for Analytical Chemistry, National Bureau of Standards, Gaithersburg, MD 20899.

In order to calculate a scan matrix (two-dimensional) from a spectrometer scan vector (one-dimensional), it is necessary to know the distance  $\Delta S$  of an arbitrarily chosen position (i,j) in the scan matrix from the position of the ideal focus line. If we know two points  $(X_1, Y_1)$  and  $(X_2, Y_2)$  on this line, which can be determined for each spectrometer from the raw intensity map of a standard or in many cases even from the intensity map of an unknown, then the distance  $\Delta S$  of another point  $(X_3, Y_3)$  from this line (which has a general form  $A \cdot x + B \cdot y + C = 0$ ) is given by

$$\Delta S = (-D \cdot X_3 + Y_3 - E) / \pm (D^2 + 1)^{1/2} \quad (3)$$

where  $D = (Y_2 - Y_1) / (X_2 - X_1)$  and  $E = Y_1 - D \cdot X_1$ . The sign of  $\Delta S$  indicates on which side of the focus line the measurement is taken. The distance  $\Delta S$  given by Eq. (3) has dimensions of matrix units: to translate it into a spatial dimension, one must calculate a scale factor which gives the linear distance between the points to which the beam is addressed on the sample. The scale factor SF can be expressed in terms of the magnification M, which is set on the scan generator of the EPMA automation system; the linear dimension L of the CRT scan display; and the number of points N in the scan line:

$$SF = L / (M \cdot N) \quad (\text{cm/matrix element}) \quad (4)$$

The deviation angle  $\Delta \theta$  from the Bragg angle can be found from Eqs. (2) to (4)

$$\Delta \theta = \Delta S \cdot SF / S_0 \quad (5)$$

The procedure to calculate a standard map is first to determine two points on the focus line in the matrix, which can be recognized in the intensity map of the unknown. For each point (i,j) in the standard matrix, the distance from the focus line is then calculated with Eq. (3). This matrix distance is converted into an angular deviation by means of Eq. (5), and the intensity that corresponds to this angular deviation away from the peak is determined from the spectrometer scan vector. The procedure is repeated until the standard map matrix is completed.

To test this procedure, a defocus map was generated by the modeling method and compared to a defocus map generated by the scanning method. Traces perpendicular to the line of best focus are compared in Figs. 3(a) and (b) for 170 $\times$  and 340 $\times$ . The agreement between the trace from the synthetic standard map and the trace from the experimental standard map is within  $\pm 2\%$  throughout the range.

Figures 3(a) and (b) illustrate two advantages of the defocus modeling method. First, a single peak scan was the basis for generating both synthetic standard maps at the two different magnifications. The defocus modeling technique is thus highly efficient since a single peak scan can be used to generate any magnification, including noninteger values. Archived peak scans can be used for subsequent mapping work with only a scaling factor applied to compensate for different electron doses or changes in spectrometer efficiency. Second, since the peak scan vector has relatively few channels compared to a standard map scan, the integration time of each channel can be increased by a factor of 10 without a significant time penalty. The statistics of the synthetic standard map can thus be made substantially better than the experimental standard map, which provides a direct benefit in the statistics of the final compositional map.

The principal disadvantage of the defocus modeling technique is the same as that which limits the standard map method. The fall in spectrometer efficiency at the extreme deflection of a low-magnification scan reduces the recorded count so that the statistics of the measurement become poorer. At a magnification of 150 $\times$ , this fall-off is approximately a factor of three, which is about the limit before the statistical problem becomes intolerable. Below this magnification, specimen stage scanning or crystal rocking are to be preferred.

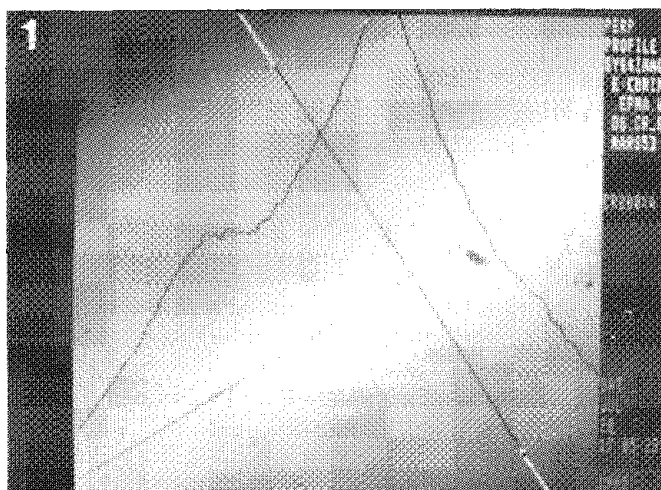
### Conclusions

Accurate standard maps can be synthesized from peak scans to provide defocus corrections in compositional mapping with wavelength-dispersive x-ray spectrometry. Only one peak scan of sufficient angular width is needed to generate a standard map appropriate to any magnification in the range covered. The modeling procedure is useful down to

magnifications of approximately 150 $\times$ , and is eventually limited by statistical considerations due to the fall-off in spectrometer transmission. The synthesized standard map can have better counting statistics than a conventionally scanned standard map because longer counting times per channel can be allowed when the peak scan is made.

### References

1. D. E. Newbury, "Compositional mapping of thick specimens," *Microbeam Analysis--1985*, 204-208.
2. R. B. Marinenko, R. L. Myklebust, D. S. Bright, and D. E. Newbury, "Wavelength-dispersive techniques for compositional mapping in electron-probe microanalysis," *Microbeam Analysis--1985*, 159,162.
3. R. L. Myklebust, R. B. Marinenko, D. E. Newbury, and D. S. Bright, "Quantitative calculations for compositional mapping techniques in electron probe microanalysis," *Microbeam Analysis--1984*, 101-103.
4. R. B. Marinenko, R. L. Myklebust, D. S. Bright, and D. E. Newbury, "Digital x-ray compositional mapping and 'standard map' corrections for wavelength-dispersive spectrometer defocusing," submitted to *J. Microscopy*.



2

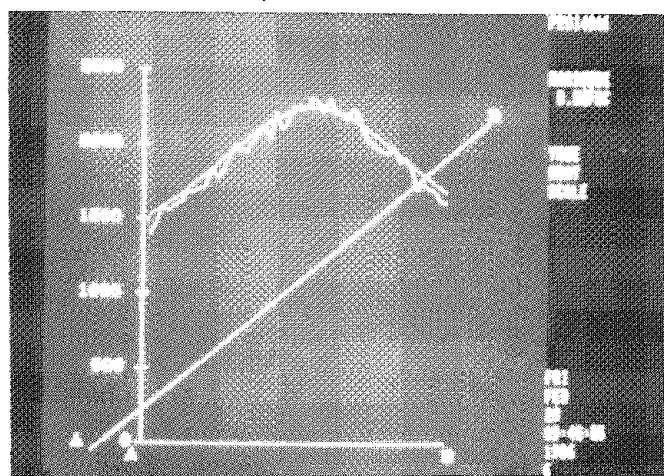
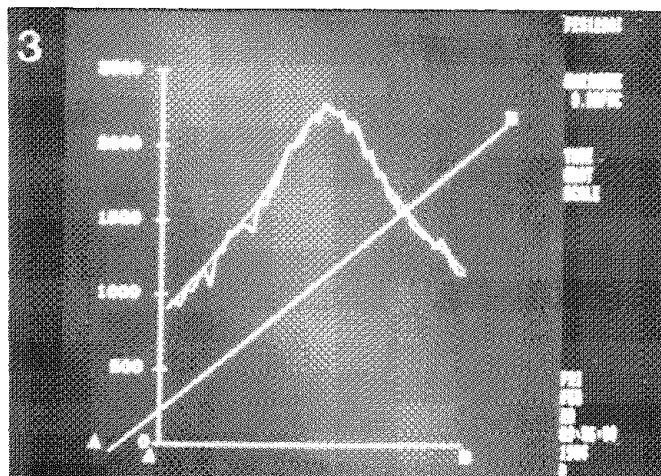
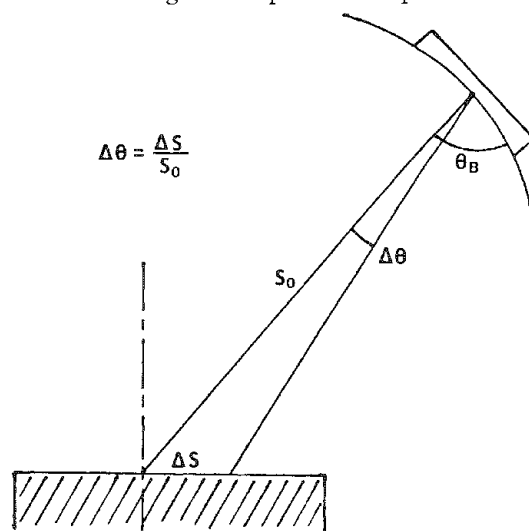


FIG. 1.--Standard map for Cr K $\alpha$  at 200 $\times$  magnification prepared by area scanning with intensity profile taken perpendicular to line of best focus. Note asymmetry of peak due to partial separation of K $\alpha_1$  and K $\alpha_2$ .

FIG. 2.--Relationship of scan deflection in plane of specimen to deviation from exact Bragg angle on peak.

FIG. 3.--Comparison of line traces perpendicular to line of best focus from synthetic standard map for FeK $\alpha$  mathematically constructed from peak scan with standard map constructed by area scanning on standard. Smooth curve = synthetic; irregular curve = area scan. Vector for line trace = AB. Magnification: (a) 170 $\times$ ; (b) 340 $\times$ .



## A MULTIFUNCTIONAL MINICOMPUTER PROGRAM PROVIDING QUANTITATIVE AND DIGITAL X-RAY MICROANALYSIS OF CRYOSECTIONED BIOLOGICAL TISSUE FOR USE BY THE INEXPERIENCED ANALYST

R. V. Heyman and A. J. Saubermann

Development of shared instrument and multi-user resource centers for biological x-ray analysis has presented several problems. Generally, it is not practical for each biologist who wishes to use x-ray microanalysis (XMA) for a specific biological question to become expert in technical aspects of XMA, and the reverse is just as impractical. One approach is to develop a working compromise by which a biologist would learn to operate the instrument in a limited fashion while using a computer program designed to proceed through a particular algorithm preselected for analysis. Such an approach would allow knowledgeable technical personnel to standardize operating conditions and allow users to perform analysis without having to study extensive computer manuals nor learning specialized computer commands. Therefore, a computer support program (or group of programs) suitable for use by inexperienced operators was required. These programs have been installed and are currently being used in our laboratory.

In general, such a program (or set of programs) should be easy to activate and use, and should lead the operator through all steps required by the analytical procedure. Furthermore, in our laboratory, the programs had to use less than 15 Kilobytes (Kb) of core memory; therefore, a modular approach was required.

### *Materials and Methods*

Program modules were written in Tracor Northern "Flextran" interpreter language, version 7T, and compiled for speed if necessary.<sup>1</sup> These programs were run on a PDP 11/23 computer interfaced with a TN 2000 energy-dispersive x-ray spectrometer (EDS) and a Spectra Chrome 512 color monitor. The EDS spectrometer was installed on an AMRay 1400T SEM. A logic diagram of the software package is shown in Fig. 1. Program execution begins when an operator loads and runs the start-up module. This module directs the operator to enter several operational parameters. Once these parameters have been entered, they are saved in a disk file and control passes to the main menu program. This module presents the operator with a list of options (Fig. 2). When an option is selected, control passes to the selected module. Operational parameters required by the particular module being run can now be retrieved from a disk file as needed. Upon completion, the module stores measurements it obtained in an appropriate data file and control is returned to the main menu.

### *Results*

Within the Microprobe Center nearly all analyses at present are being performed on frozen hydrated sections (0.5  $\mu\text{m}$  thick) or frozen dried sections (0.1-0.2  $\mu\text{m}$  thick) and are processed by continuum normalization methods.<sup>2-4</sup> Learning to use the program required minimal effort and competent technical assistance was always available to help if the need arose. One run through the program package was frequently all that was required. The fact that a whole series of different programs were being used was transparent to the user. No program user's manual was needed for either instruction or reference.

An example of a printout obtained from analysis of a cryosection of leech neuron is shown in Fig. 3; enough information is provided to permit a trained microanalyst to identify analysis artifacts. Results were stored in a user-generated and labeled file. This file could be sorted, by another module, and refiled into as many as 30 different groups. Basic sample population statistics were also provided by this module.

---

The authors are at the University of Texas Health Science Center, Microprobe Center, Houston, TX 77030. This work was supported in part by NINCDS Grant R01 NS21455-01A1.



## Discussion

All of our system requirements could not be met by any one program. Therefore, a modular programming approach was used. Reference data needed by the analytical procedure were stored in three disk files. Different aspects of the analytical procedure were divided into separate programs. Each program was written as a stand-alone module. An executive driving program, entitled Main Menu, acted as traffic director which loaded and ran each individual program when it was called. When an individual program had completed its task, the program loaded and ran the Main Menu.

This modular approach also had a major advantage in that it overcame our 15 Kb operational memory limitation. Each individual module was made small enough to fit in the limited computer memory available. Linkages were easily added to connect each module to the Main Menu and to connect the Main Menu to each module. The extra virtual memory thus available allowed the program to "talk" to the investigator with a series of understandable questions and receive (and error check) the relatively simple answers. No handbook of special commands was necessary because questions and required responses were self-evident. Program modifications were also very easy to perform; consequently, it would be easy to add any of the several approaches to biological specimen analysis to the main menu of options.<sup>5-7</sup>

Since most investigators requested analyses only of elements normally found in biological tissue (Na, Ca, P, K, S, Cl, and Mg), energy-window values for these elements were stored in the analysis programs and were set by the programs. Standards analyses are performed by the instrument operator on a timely basis. Results of these standard analyses were used to make a series of calibration curves, which were also stored in the analytical program. Therefore, the user need not be concerned with either of these very important details.

Because of its modular design, the program package could be easily adapted to other instruments; for example, the program package was adapted to a Cameca MBX Electron Microprobe equipped with a DEC PDP 11/34 computer and TN 2000 EDS spectrometer. The general approach to user training worked equally well with this instrument.

The algorithm normally used in this program package has been used extensively on a "point," i.e., limited raster area basis, and has been well documented and validated.<sup>3,4</sup> This algorithm has been adopted to a quantitative digital x-ray image program written by use of the general approach described by K. E. Gorlen et al. and is included as a series of self-directing modules within our program (Fig. 4).<sup>8</sup>

## Conclusion

A modular program package designed to permit inexperienced users an opportunity to analyze individual compartments they select, and lead them through analysis procedure, appears to provide a workable compromise for a multiuser biological x-ray microanalysis resource center.

## References

1. Printed copies of the program are available upon request from the authors. Flextran, Flextran compiler and libraries are copywritten software available from Tracor Northern, 2551 West Beltline Highway, Middleton, WI 53562, (608) 831-6511.
2. T. A. Hall et al., "The use of thin specimens for x-ray microanalysis in biology," *J. Microscopy* 99: 177-182, 1973.
3. A. J. Saubermann et al., "Applications of scanning electron microscopy to x-ray analysis of frozen-hydrated sections: I. Specimen handling techniques," *J. Cell Biology* 88: 257-267, 1981.
4. A. J. Saubermann et al., "Applications of scanning electron microscopy to x-ray analysis of frozen-hydrated sections: II. Analysis of standard solutions and artificial electrolyte gradients," *J. Cell Biology* 88: 268-273, 1981.
5. B. J. Gupta et al., "Electron microprobe and ion-selective microelectrode studies of fluid secretion in the salivary glands of *Calliphora*," *J. Exp. Biology* 72: 261-284, 1978.
6. R. Rick et al., "Quantitative analysis of electrolyte in frozen dried sections," *J. Microscopy* 125: 239-247, 1982.

7. Henry Shuman et al., "Quantitative electron probe microanalysis of biological thin sections: Methods and validity," *Ultramicroscopy* 1: 317-339, 1976.

8. K. E. Gorlen et al., "Computerized analytical electron microscope for elemental imaging," *Rev. Sci. Instruments* 55: 912-921, 1984.

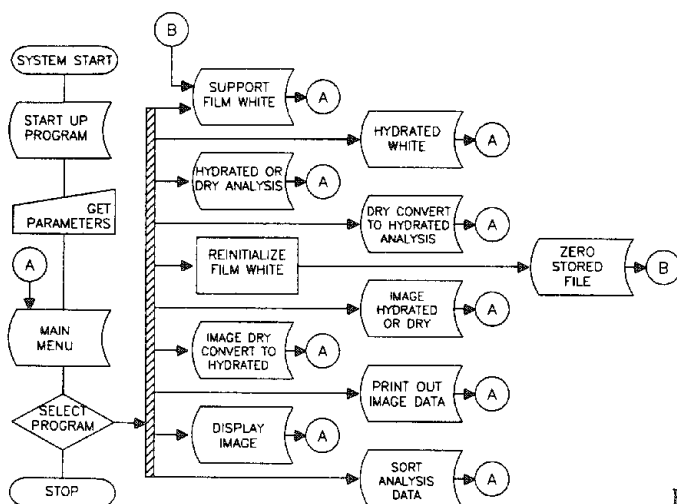


FIG. 1.--Logic diagram showing overall architecture of program modules.

1. Support film white radiation measurement
2. White radiation from hydrated areas
3. Process spectra from hydrated sections only
4. Process spectra from dried sections only
5. Process spectra from dried sections and convert to hydrated
6. Re-initialize support film white radiation
7. Raster spectra from hydrated section
8. Raster spectra from dried section
9. Raster spectra from dried section and convert to hydrated
10. Print raster results from disk
11. Plot (paint) raster data
12. Sort stored analysis data
13. Stop

FIG. 2.--List of options offered by Main Menu program module. Options reflect continuum normalization techniques commonly used in our laboratory.

NUMBER 15 N WHITE DRIED = 2870.7  
WHITE HYDRATED = 8410.0 % WATER = 65.86

	COUNTS	R-VALUE	MM/KG DWT	MM/KG WWT
NA	126.	0.0438	79.0	26.9
P	3358.	1.1697	540.8	184.6
S	1221.	0.4253	200.5	68.4
CL	342.	0.1191	64.7	22.1
K	2605.	0.9074	406.8	138.8
CA	1.	0.0003	0.1	0.0
MG	22.	0.0076	7.5	2.5
FE	1.	0.0000	0.0	-0.0

FIG. 3.--Example of computer printout of data obtained for leech neuron (frozen hydrated/converted from dried). Sufficient data are printed to permit experienced analysts to recognize analytical artifacts and systematic problems.

FIG. 4.--Example of fully quantitated image (64 x 64) of Na (mMole/kg dry weight) distribution in myelinated axons from rat sciatic nerve (courtesy of Dr. R. LoPachin, University of Houston). Mag 12K.

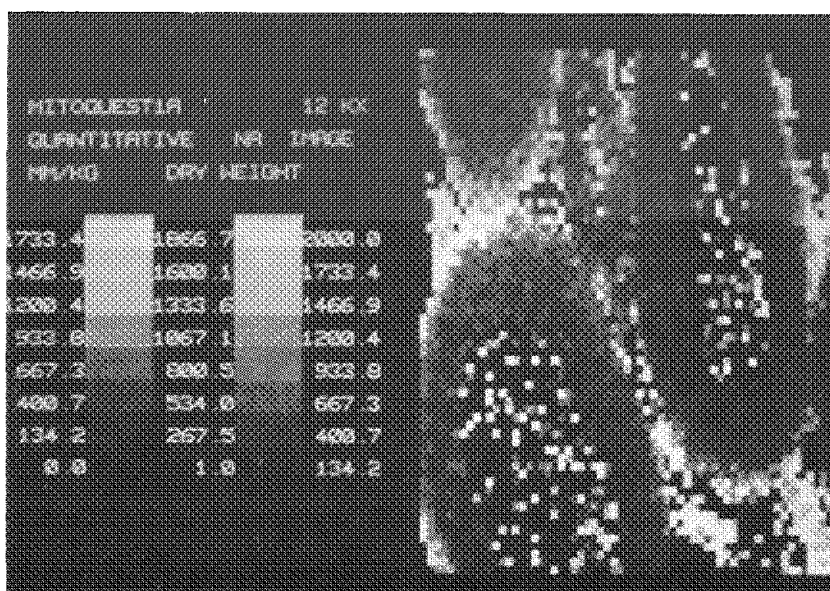


## IMAGE PROCESSING FOR THE LOCATION AND ISOLATION OF FEATURES

J. Christian Russ and John C. Russ

Many images, especially those acquired from electron microscopes, contain a significant amount of noise (random variation in the brightness of pixels within a single features or object). X-ray maps are perhaps the worst example of this problem. There may also be variations that are related to surface roughness or density fluctuations, but that one must ignore in deciding which pixels correspond to the image of an object. One method often used to smooth images and remove noise uses a low-pass filter. This can be done with a Fourier transform, but an equivalent and computationally simpler method uses local operators which calculate a weighted average of each pixel with its neighbors. Figure 1 shows some typical  $3 \times 3$  operators. (Larger ones,  $5 \times 5$ ,  $7 \times 7$ , or larger, can also be used, but the sequential application of small ones is usually a more efficient way to produce longer-range smoothing.)

$$\begin{array}{cc} \begin{array}{ccc} 1 & 1 & 1 \\ (a) & 1 & 1 & 1 \times (1/9) \\ 1 & 1 & 1 \end{array} & \begin{array}{ccc} 1 & 2 & 1 \\ (b) & 2 & 4 & 2 \times (1/16) \\ 1 & 2 & 1 \end{array} \end{array}$$

FIG. 1.--Typical smoothing operators. Each pixel is replaced by sum of each coefficient times corresponding pixel brightness, scaled down to original brightness range.

These smoothing operators are useful for reducing the visual noise in images to improve their appearance. When applied to images which contain features to be measured, they suffer from two important problems. First, discontinuities are especially smoothed so that the magnitude of the contrast change is reduced, which makes them more difficult to locate. Second, the location of these discontinuities may be shifted, so that features tend to change size depending on their relative brightness with respect to their surroundings (which may vary in different directions around the periphery).

A preferred method for smoothing image noise, often used in the field of satellite imagery, is called a "median filter." In this operation, each pixel and its neighbors are ranked in brightness order, and the median brightness value is stored in place of the original pixel brightness. The disadvantage of the median filter is that it cannot use a general-purpose routine that applies local operators to an image (smoothing, differentiation, texture extraction, and many other operations use a small array of values applied to each pixel and its neighbors<sup>1</sup>) and does not have an equivalent filter in transform space. On a gradually varying surface, or a uniform one with a small amount of noise, the median filter produces similar (or in some cases, better) noise reduction as a smoothing filter. But when edges or discontinuities are encountered, the median filter leaves the full step contrast intact, and does not shift the location of the discontinuity. This property allows it to be used recursively, and indeed it may be usefully repeated until no further change occurs. The median filter is also especially effective on images with "salt and pepper" noise, common in SEM images. Figure 2 shows an example in which the smoothing operator and median filter are compared.

### *Feature Outlining*

The vital step that must precede the measurement of features (objects) in an image is their isolation from each other and their surroundings. Fortunately one can often accomplish this step simply on the basis of pixel brightness, by setting upper and lower level discriminators to select a range of brightnesses that correspond to one class of objects. Automatic methods for determining the optimum levels for these discriminator settings are usually based on finding minima between peaks in the brightness histogram. Another ap-

---

Author J. Christian Russ is at the University of Michigan, Ann Arbor, MI 48109; author John C. Russ is at the North Carolina State University, Raleigh, NC 27695.

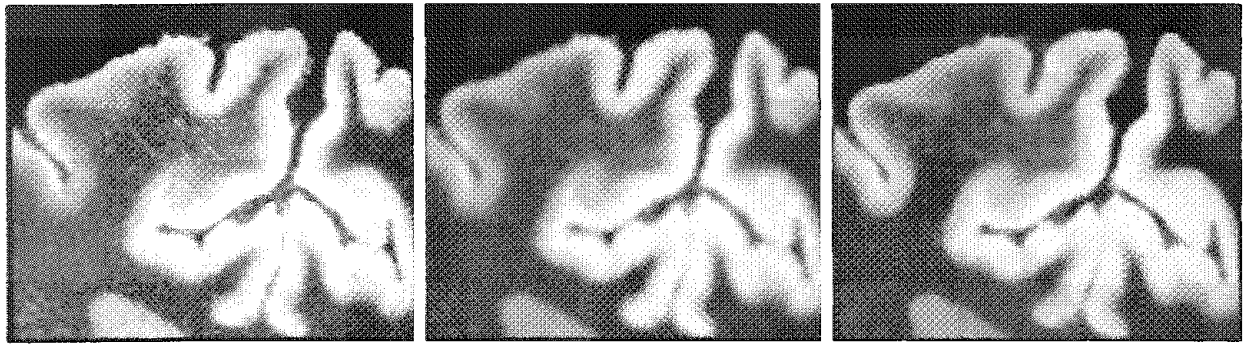


FIG. 2.--Noisy autoradiograph of cat brain: (a) original (portion enlarged to show individual pixels); (b) smoothed with local operator; (c) median filter applied.

proach is to find peaks in the histogram of pixels selected by (for example) the Laplacian described below, which selects boundary locations in the image. When images are complex, with many different classes of objects (many peaks), or they are close together, human setting by inspection is a far more sensitive and efficient method.

However, there are many images of interest in which a simple one-to-one relationship between brightness and type does not exist. That is especially true for images from the SEM, in which local surface inclination plays a major role in determining brightness. It is also true for most TEM images: for biological specimens, because the various tissue structures present are similar in density; for thin metal foils, because the brightness of different grains depends upon orientation. In these cases, an edge-finding algorithm is desirable, because if all of the edges around objects can be found, then discrimination between different classes of features can be performed using secondary criteria such as size, shape, and so on, rather than simply brightness.

The most common method for enhancing edges in an image is the application of a Laplacian operator,<sup>2</sup> which is equivalent to performing a Fourier transform on the image, applying a high-pass frequency filter (cutting off low frequencies), and then re-transforming the image. The most computationally efficient way to carry this operation out is with an operator that calculates a value for each pixel based on the brightness of the target pixel and its immediate neighbors. These operators may operate on  $5 \times 5$  or  $7 \times 7$  regions (including second- or third-nearest neighbors), but  $3 \times 3$  operators are shown here for illustration. The Laplacian is isotropic (within the constraints of a rectangular array of pixels) and "zero weighted" (that is, it returns a zero value for pixels in the middle of a flat, featureless region). The name is often extended to a similar operator in which a portion of the original brightness value is added in, as an aid to the operator in viewing the resulting image. Typical  $3 \times 3$  Laplacians are shown in Fig. 3.

1 -2 1	0 1 0	-1 -3 -1	0 -1 0
-2 4 -2	1 -4 1	-3 16 -3	-1 5 -1
1 -2 1	0 1 0	-1 -3 -1	0 -1 0
(a)	(b)	(c)	(d)

FIG. 3.--Typical  $3 \times 3$  Laplacian operators. Brightnesses for each pixel and its eight neighbors are multiplied by values shown and added. Result (either with a constant added to assure positive values, or the absolute value) is stored back in place of central pixel, for each pixel in image. Note that (d) is not zero weighted, but effectively averages difference image with original.

The advantage of the Laplacian is its simplicity, which allows it to be readily programmed into a small computer, or into an array processor in a minicomputer. The problem is that the high-pass filter increases the amount of noise in the resulting image. The Laplacian is especially sensitive to isolated points and line ends, which produce a larger response than edges. In many cases the noise overwhelms the desired edge information and the result is completely unsuitable for measurement purposes, even though the visually enhanced sharpness of edges (resulting from the increased relative contrast across discon-

tinuities) may improve the appearance of the image to the operator's eye. (Humans are good at ignoring noise in images.)

Edge-finding algorithms are of great importance in machine vision and robotics (to isolate objects so they can be identified and their orientation determined), as well as in satellite imagery to locate, identify, and count individual features. Some of the ones most appropriate for our needs are:<sup>2,3</sup>

*Roberts' cross*, evaluated as  $(E_x^2 + E_y^2)^{\frac{1}{2}}$  or  $|E_x| + |E_y|$  or  $\text{Max}(|E_x|, |E_y|)$  where the partial derivatives of brightness in two directions are estimated as  $E_x = P(x,y) - P(x+1,y+1)$  and  $E_y = P(x,y+1) - P(x+1,y)$ , where  $P$  is the pixel brightness. This operator is little used because it is rather susceptible to very high frequency (pixel to pixel variation) noise. However, it also yields the direction of edges as  $\tan^{-1}(E_x/E_y)$ .

*Sobel transform*, similar to Robert's cross but using 8 neighbors (as in Fig. 4) with  $E_x = N_2 + 2*N_3 + N_4 - N_6 - 2*N_7 - N_8$  and  $E_y = N_0 + 2*N_1 + N_2 - N_4 - 2*N_5 - N_6$ . The use of a  $3 \times 3$  kernel to get the partial first derivatives in two directions makes this relatively efficient to compute, and more immune to high-frequency noise than the Roberts' cross, but the methods for combining  $E_x$  and  $E_y$  are the same as shown above.

0 1 2

7 P 3

6 5 4

FIG. 4.--Indices used to identify neighbors of pixel P.

*Kirsch transform*, which achieves edge sensitivity in eight directions. (Human vision employs orientation detectors in at least 36 directions.) The calculated pixel value is  $\text{Max}[1, \text{Max}(E_0 \dots E_7)]$  where  $E_n = |5*(N_{n-1} + N_n + N_{n+1}) - 3*(N_{n+2} + N_{n+3} + N_{n+4} + N_{n+5} + N_{n+6})|$  and the indices are understood modulo 8.

*Median minus mean*, which creates a new image from the difference between the median-filtered image and one smoothed with a uniform filter (as in Fig. 1a, so that each pixel is replaced by the mean of itself and its neighbors). This method works well for high-contrast images, but performs poorly for low-contrast edges, and has some edge displacement problems.

*Laplacian-Gaussian or Log-Laplacian* edge detectors, which find the zero-crossing points of the second derivative (using a Laplacian operator) applied to the heavily smoothed

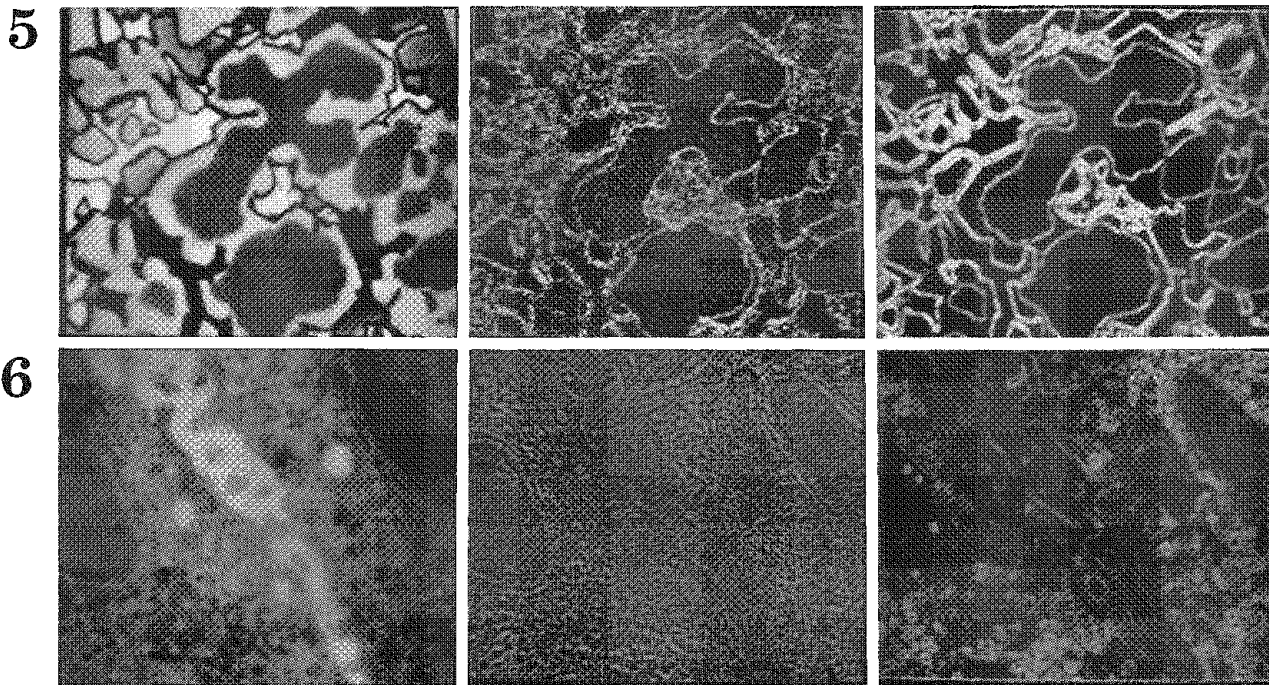


FIG. 5.--Light micrograph of four-phase metal alloy: (a) original, (b) high-pass Laplacian filter; (c) Sobel transform.

FIG. 6.--TEM image of kidney: (a) original, (b) Laplacian filter, (c) Kirsch transform.

(using a Gaussian smoothing operator) image or to the log of the brightness values. This approach suffers from sensitivity to noise (the method is especially sensitive to points, lines, and line ends, relative to edges), and displacement of edges because of the combined effects of the operators.

The first three methods provide not only the magnitude of edges and allow discrimination of the derived image to obtain feature outlines, but also the local edge direction. This information can be used to fill in gaps in the edges, by use of a Hough transform in which edge points "vote" for the local orientation of a line in proportion to their strength and distance from the line.

All these methods are less noise sensitive than the Laplacian. As an example, consider Fig. 5 (a light micrograph of a multiphase metal alloy), in which the several phases are well distinguished by their brightness (they can in fact be discriminated directly). Applying a Laplacian operator does show most, but not all of the edges present, at the cost of introducing considerable noise. The Sobel transform produces the desired outlines of the phases directly, with practically no noise at all.

A more difficult example is shown in Fig. 5 (a thin section of kidney imaged in the AEM with a video adaptor with single-crystal scintillator and CCD camera from Ernest F. Fullam, Inc.). Here, the contrast is much more subtle, and the features smaller and more similar in brightness. The Laplacian filter does not show most of the edges and causes noise to completely dominate the image, whereas the Kirsch transform nicely outlines the features present (even some that are rather difficult to see visually in the original image). The outlines can then be discriminated to obtain binary images, which may be filled, measured, and classified according to their size, integrated density, shape, or other stereometric parameters. These operations are described in an accompanying paper.

#### References

1. John C. Russ and J. Christian Russ, "Image processing in a general purpose micro-computer," *J. Microscopy* 135: 89, 1984.
2. W. K. Pratt, *Digital Image Processing*, New York: Wiley, 1978.
3. A. C. Rosenfeld and A. C. Kak, *Digital Picture Processing*, New York: Academic Press, 1982.

## AUTOMATIC EDITING OF BINARY IMAGES FOR FEATURE ISOLATION AND MEASUREMENT

John C. Russ and J. Christian Russ

As computers with enough memory and power to handle entire gray-scale images have become available, there has been a tendency to overlook the utility of binary images (in which each pixel is either "on" or "off"). However, in the fields of satellite imagery, machine vision (robotics), and stereology (using images from light or electron microscopes), it is generally necessary to isolate and locate objects ("features") before the brightness or color information from the pixels within each feature can be used for characterization or recognition, or the size and shape can be determined. It is with binary images that the isolation and measurement of features is best carried out.

Discrimination is usually based on the brightness of pixels in either an original image, or one processed as described in an accompanying paper. Automatic setting of discriminator levels based on the brightness histogram, or manual "trial and error" adjustment can be used. The binary image occupies less memory than the original gray image; it is further encoded to make the data more suitable for measurement.<sup>1</sup> Figure 1 summarizes the steps, from the gray image in which each pixel has a brightness value, to the binary image, to chord- or chain-encoded forms. In the chord-table form, the information is in the order in which scan lines intersect objects, whereas the chain-encoded form has the points around individual objects collected together to form outlines.

The as-discriminated binary image rarely delineates the various object outlines so perfectly that they can be accurately measured. Images may have noise (e.g., x-ray maps) or contrast variations (e.g., SEM images of rough surfaces) that cause some pixels in the interior of features to be left out, or pixels that are not part of objects to be set. Features may touch, which makes measurement difficult or impossible. Manual editing may be needed for complex images with features obscuring or overlapping others. This editing can be accomplished with user-interactive devices such as a mouse, to move a cursor over the screen image to connect or separate features, mark objects to be measured or ignored, and so forth. However, for speed and consistency automatic methods are preferred.

The first operation needed for binary images obtained with the SEM is often filling of holes. Figure 2 shows a typical SEM image of particles, in which the brightness of surfaces on the particles is brighter or darker than the substrate because of the inherent contrast mechanisms of the microscope. The edges are well defined, but the central holes must be filled in. The same operation is required when edge-detection has been used to define features, as described in an accompanying paper. Hole-filling can be considered as a series of logical steps: Invert the image, so that the background is selected. From each point where this meets the edge of the image, remove the scan chord and all chords it touches. This procedure leaves the image of the holes, which is ORed with the original image. Some consideration must be given to what constitutes touching chords or pixels. It is usual to treat pixels that touch as shown in Fig. 3 as part of the same object (this is called 8-connectedness, since each pixel has eight neighbors). However, it also means that the background is 4-connected (each pixel touches only its orthogonal neighbors, not diagonal ones).

Outlines of objects may be smoothed, small internal defects filled, stray noise in the image removed, or touching features separated, using plating and etching (also known as "propagation and shrinking" or "dilation and erosion"). Figure 4 shows examples of these operations. The method is simply to count the number of neighbors for each pixel which are on (for plating) or off (for etching). If this number exceeds a preset value (from 1 to 8), then the pixel is added (plating) or removed (etching) from the feature. This is a very rapid and effective method. Sequential application of these operations can produce smooth outlines with the approximate original feature areas. However, different results are obtained depending on the order used; etching followed by plating tends to open holes

---

Author John C. Russ is at the North Carolina State University, Raleigh, NC 27695;  
author J. Christian Russ is at the University of Michigan, Ann Arbor, MI 48109.







and separate touching features, whereas plating followed by etching tends to fill holes and merge disconnected portions of features.

Figure 5 shows an example, in which etching (to remove noise and separate touching features) has been followed by plating (to restore the size of the original features). The image is of lysosomes in a biological thin section viewed in the AEM. The staining method used has also darkened membranes which appear in the binary image, and some of the features touch. After editing, the isolated features may be counted and measured.

The logical combination of images is most often used when multiple signals from different detectors have been recorded (e.g., x-ray images from different elements).<sup>2</sup> Figure 6 shows a few of the possible combinations. However, such combination is also useful with multiple binary images obtained from the same original gray image, by use of different brightness criteria. Figure 7 shows an example, in which the dark pores are distinguished from other dark blemishes on the surface of a ceramic viewed in the SEM by ANDing the image with one obtained by selecting the whitest pixels (which mark the edges of the pores) and filling the outline.

Another powerful operation that can be performed on binary images allows study of the topology of objects. Skeletonization<sup>3</sup> (also known as a "medial axis transform") is a specialized form of etching, which leaves the central backbone of each shape. The number of loops, nodes, and branches can be counted to determine the genus of the shape, or they may be disconnected and their individual length and orientation measured. Figure 8 shows an example of this applied to a macroscopic specimen. The method is also applicable to dendritic phases in metals, biological structures, etc.

In some cases, editing of binary images can be used not only to prepare images for measurement, but also to perform the measurement. Figure 9 shows an example: in (a) three binary images from different phases (for instance imaged by their x-ray maps) are shown superimposed. By plating one of these and then ANDing the result with the original, the boundary images for combinations of phases gives the images shown in (c) and (d). The areas of these images, expressed as a ratio to the area of (a), gives the degree of contiguity between the phases, a measure of the probability that certain phases occur next to others.

ANDing of binary images with themselves after shifting by various distances in the X- and Y-directions also yields the areas of overlap images. Divided by the original image area, this set of auto-covariance values describes the anisotropy in the image. (The values decline much more slowly in directions in which the features in the image are elongated.)

These examples provide a few suggestive illustrations of ways that the automatic editing of binary images improves their correspondence to the features present in images and aids in the measurement of various stereological parameters that describe the three-dimensional objects to which they correspond, as described in an accompanying paper.

## References

1. John C. Russ, *Practical Stereology*, New York: Plenum Press, 1986.
2. J. Christian Russ and John C. Russ, "Enhancement and combination of x-ray maps and electron images," in *Microbeam Analysis--1984*, 161.
3. John C. Russ, "Implementing a new skeletonizing algorithm," *J. Microscopy* RP7, 1984.
4. Andrea G. Fabbri, *Image Processing of Geological Data*, New York: Van Nostrand-Reinhold, 1984.

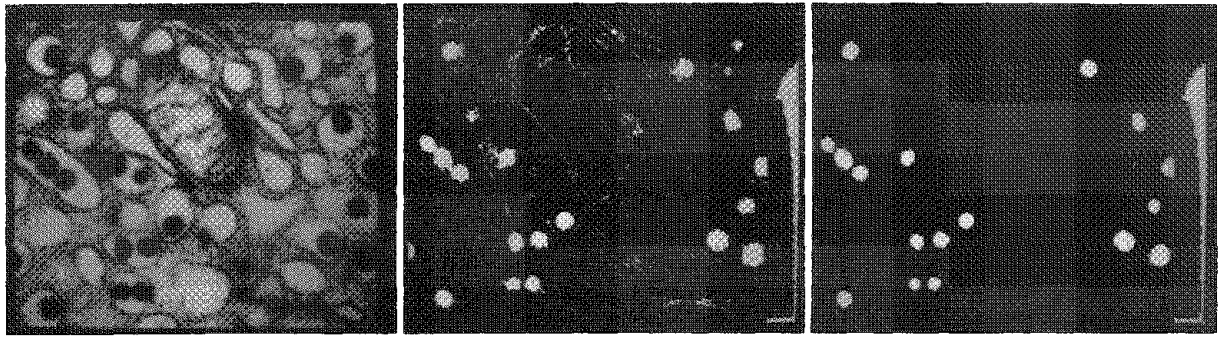


FIG. 5.--Application of etching and plating: (a) original gray-scale image; (b) discriminated binary image; (c) etched and plated to remove noise, smooth and separate features.

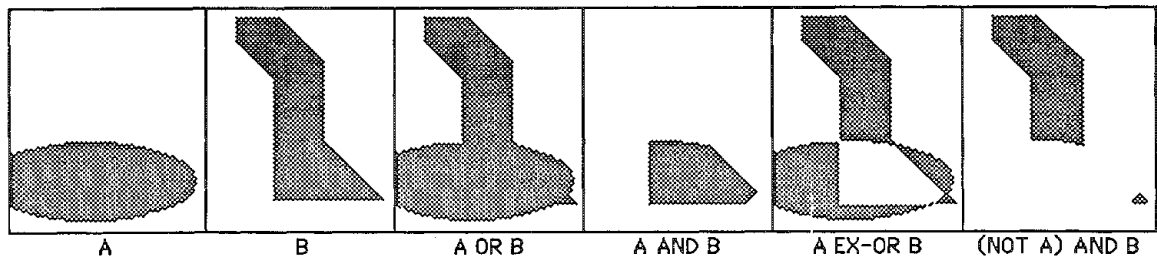


FIG. 6.--Some logical combinations of binary images, with use of OR, AND, Ex-OR, and NOT.

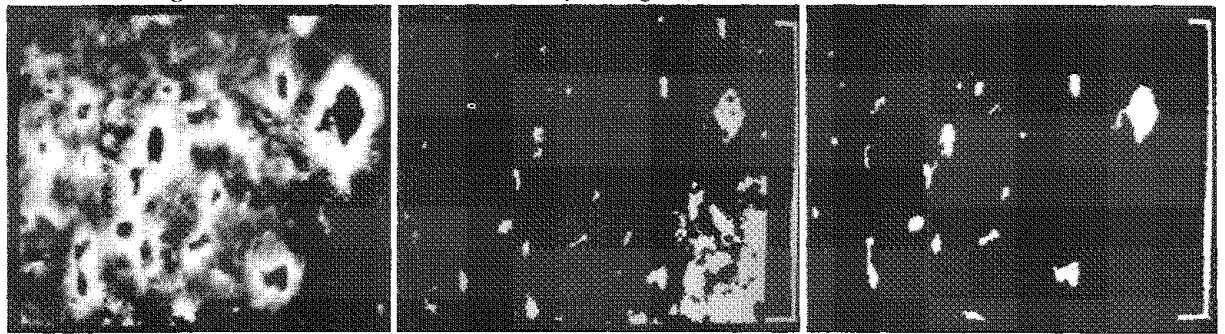


FIG. 7.--Surface of ceramic: (a) original SEM image, (b) dark pores and other surface discolorations; (c) pores obtained by ANDing (b) with filled binary image of white regions.

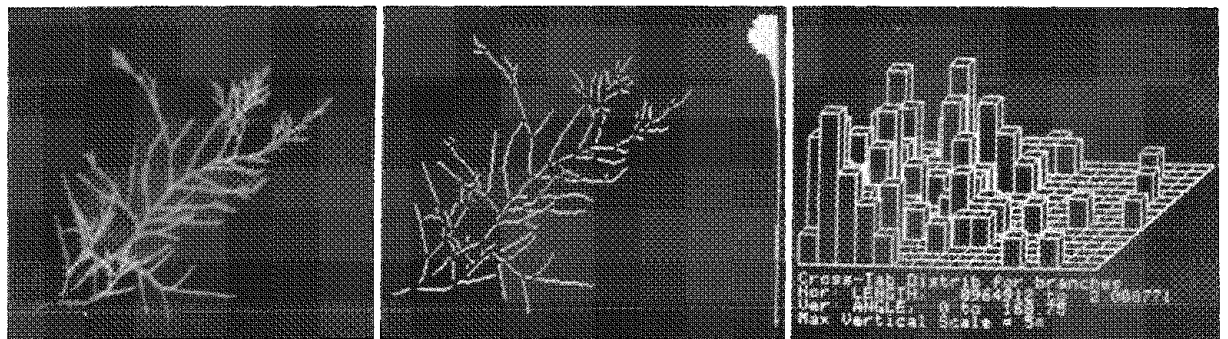


FIG. 8.--Image of cedar branch, its skeleton (with nodes disconnected), and histogram of length vs orientation for branches.

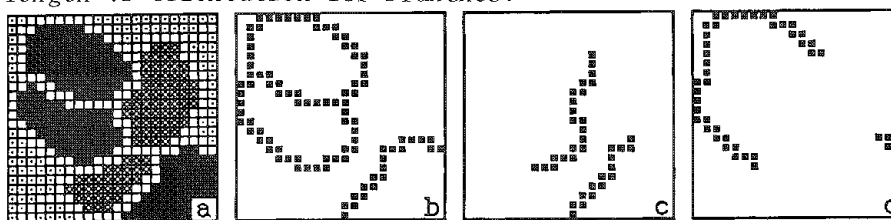


FIG. 9.--(a) Binary images of phases, (b) boundary of black phase, (c) and (d) common boundary with other phases present.

## SHAPE AND SURFACE ROUGHNESS CHARACTERIZATION FOR PARTICLES AND SURFACES VIEWED IN SEM

J. Christian Russ and John C. Russ

Because of its large depth of field, and the way in which image contrast is produced (which enhances edges), the SEM is usually the instrument of choice for the examination of specimens which have rough surfaces. However, comparison of different samples is difficult because few measurements are available to describe the parameters of shape or roughness.

Fundamentally, there are two sample types, which must be dealt with separately. Irregular shapes viewed in sections, such as phases within a metal, organelles, or membranes in tissues, or particles embedded in a matrix, show outlines on the section surface. It is clear that these outlines do not directly give the maximum dimensions of the feature, or even indicate the number of features present (Fig. 1). The second type of image, in which entire particles or other objects are observed in projection (either by being mounted on a substrate, or being viewed through a transparent medium), seems at first glance to tell us more about the actual size of the features. But this view can also hide information if there are concavities on the surface that are masked in the projection (Fig. 2). We present here methods to estimate quantitative roughness parameters for each type of image. These methods can be used to compare different samples to assess the probability that they have the same, or distinguishable roughnesses. The parameters also have use in machine vision and robotics, since the parameters are largely independent of object size or orientation and can be used for object recognition and identification.

Dimensionless parameters such as aspect ratio (the ratio of length, or longest dimension, to breadth or shortest dimension) and formfactor  $4\pi$  (area)/perimeter<sup>2</sup> (a value that is 1.0 for a circle, and decreases as features become more irregular) are used in an accompanying paper to characterize the shape of geometrical models used to estimate the surface and volume of particles. However, although such parameters may be useful to show differences in some cases, or to correlate systematic variations in shape with size, position, etc., they are insensitive to the scale of the roughness of feature outlines, as shown in Fig. 3.

One way to describe irregular shapes is to "unroll" the profile as a plot of radius (from the centroid) versus angle, and perform a Fourier analysis on the resulting curve.<sup>1</sup> Besides being computationally demanding, this approach has difficulty with shapes so irregular that the radius line may intersect the outline more than once. A new and very fruitful approach to descriptions of feature shape is the fractal dimension introduced by Mandelbrot.<sup>2</sup> To understand this approach it is useful to recognize that many objects examined in the SEM are "self-similar"; that is, as magnification is increased, the roughness and irregularity of the shapes remains the same. It is not meaningful to discuss the perimeter of such shapes, because as magnification increases, increasingly smaller details are resolved. A value for the perimeter can be determined by walking around the perimeter with a fixed stride length. As the stride length is reduced the perimeter increases and a plot of the perimeter vs. stride length can be made (Fig. 4). From the slope of this "Richardson" plot, the fractal dimension is 1.0 (the same as the Euclidean dimension for the boundary). As the irregularity increases, the fractal dimension increases as a measure of the roughness. Kaye has pointed out that many real objects have Richardson plots with several linear regions in different size regimes, corresponding to "structural" or "textural" features.<sup>3</sup>

One can determine the fractal dimension directly from a chain-encoded list of coordinates of the feature outline, by calculating the perimeter using all of the points and then repeating the operation with every second point, every third point, and so forth. This method is most appropriate when the feature outlines have been manually entered, for instance with a graphics tablet. For raster-scanned images, an alternate method<sup>4</sup> is to

---

Author J. Christian Russ is at the University of Michigan, Ann Arbor, MI 48109; author John C. Russ is at the North Carolina State University, Raleigh, NC 27695.

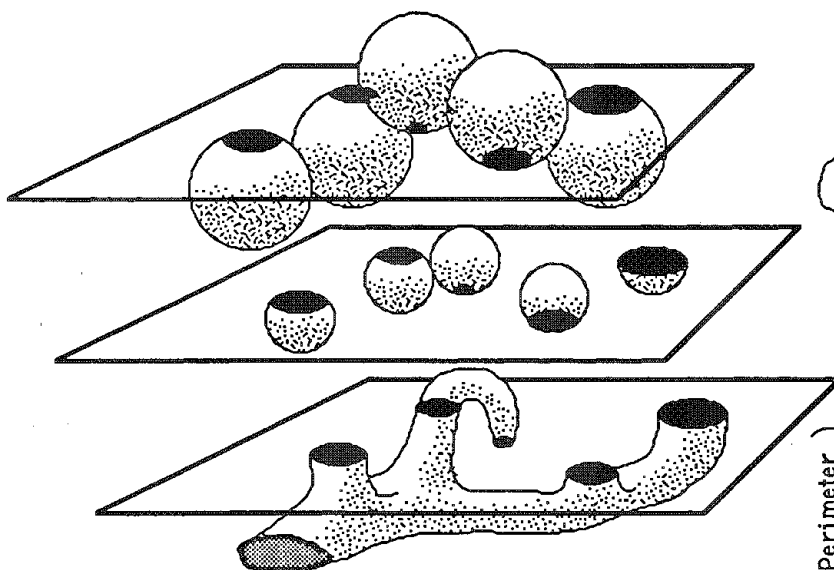


FIG. 1.--Identical planar sections through three-dimensional structures of various shapes and sizes.

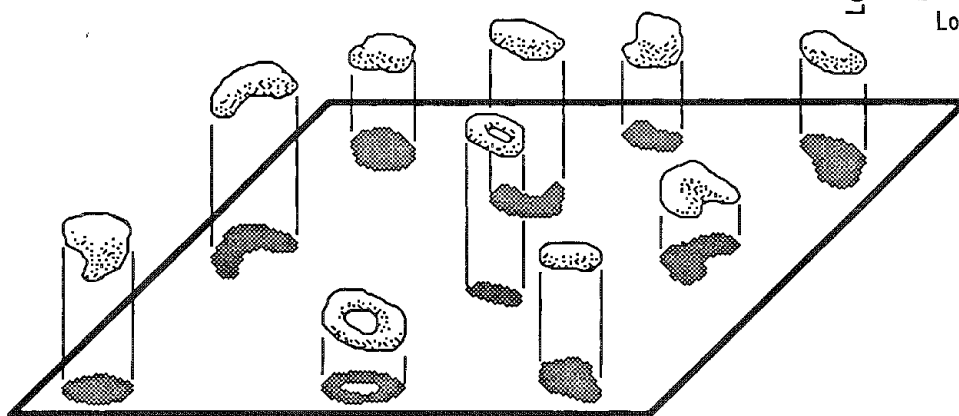


FIG. 2.--Particles on substrate or in transparent medium, with their shadow or projected images.

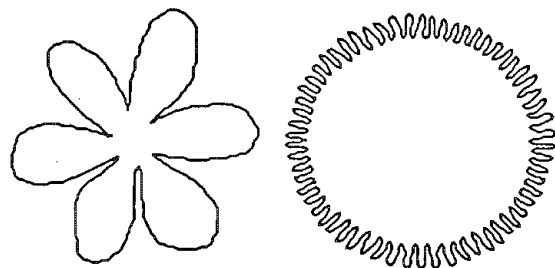


FIG. 3.--Two feature outlines with different roughnesses but similar formfactors.

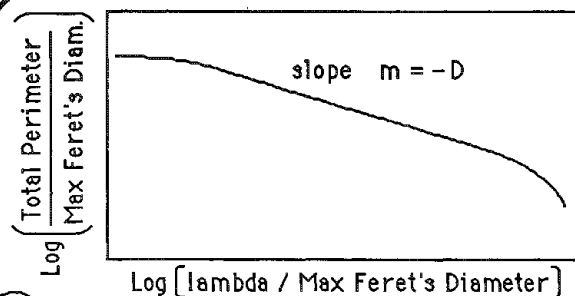
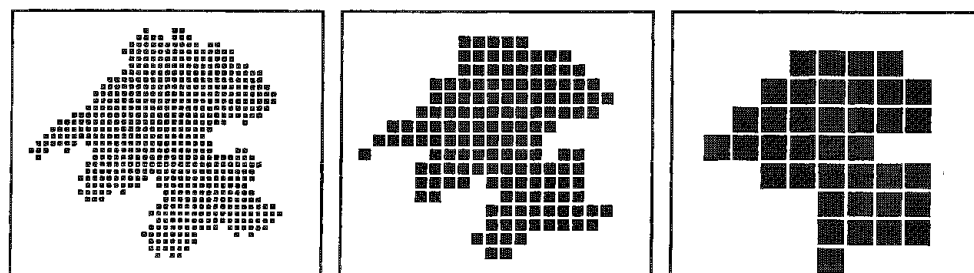


FIG. 4.--Richardson plot showing increase in perimeter of feature as stride length lambda is reduced. Over linear portion of plot, slope m gives fractal dimension D. Both perimeter and stride length are normalized with respect to maximum projected length (Feret's diameter) of feature outline.



Coarsening Rules: 

FIG. 5.--Repeated coarsening of image and recalculation of perimeter of feature outlines can be used to determine fractal dimension of raster-scanned images.

coarsen the binary pixels in steps, as shown in Fig. 5. The perimeter is determined by a summation of the lengths of sides of the polygon, and a Richardson plot is made from which the fractal dimension is obtained.

The same principles apply to surfaces as to outlines. A surface that is Euclidean (whose surface area does not increase as magnification increases) has a dimension of 2.0, and rough surfaces have higher fractal dimensions. In a few cases, surface areas are actually measured with stereoscopic techniques,<sup>5</sup> but in general we rely on the fact that sections through surfaces with a fractal dimension of the form 2.D will produce outlines with a fractal dimension 1.D, as shown in Fig. 6. (This surface was generated randomly using a computer program.<sup>4</sup>) Measuring the fractal dimension of the section outline enables the evaluation of the surface roughness.

For images of the type shown in Fig. 2, the outlines are shadows that tend to hide some of the irregularities in the surfaces. The fractal dimension D determined from the outline thus establishes a lower limit for the fractal dimension of the surface. Evaluation of a number of profiles may make it practical to estimate the actual surface fractal dimension, but in general the examination of surfaces in the SEM requires a more direct way to deal with the surface roughness.

One way to do that is to measure the variation in brightness as a function of distance on the image. Within each feature or object, the variation in brightness in the normal SEM secondary-electron image is a sensitive indicator of surface orientation. For other images, the variation can also be used with other interpretations (for instance for the backscattered electron image, it would indicate heterogeneity of composition). In the digitized and stored gray-scale image, the pixel brightnesses are available, and the previously determined object boundaries (as described in an accompanying paper) can be used as delimiters to control the summations shown below.

Haralick<sup>6</sup> has presented a set of fourteen parameters that can be determined from pixel brightness differences to characterize the texture of surfaces. These parameters include means, variance, entropy (based on the logarithm of mean difference over various distances), and moments of the brightness variation versus distance distribution. The parameters serve as identifiers of particular terrain in satellite photos. As originally presented, they determined texture information from the brightness differences between adjacent pixels, in each 45° direction. For features observed in the SEM, where the rotational orientation of features is randomized, we have found it more useful and computationally efficient to use differences only in orthogonal directions (which also avoids the problem that pixels are 40% farther apart along the 45° directions than along the X- and Y-directions), covering a range of distances within the boundaries of each object.

Figure 7 shows three examples of different fragments of gray-scale images (with a greatly reduced brightness range), and for each the table shows the number of pixel pairs a distance d apart with brightness difference b. From this frequency information, the mean and standard deviation of each column in the table can be used to construct the plots shown, for the mean brightness difference  $\mu_b$  between pixels a distance d apart.

Note that for image (a) the mean variation in brightness between adjacent pixels, or for that matter between pixels any distance apart within the feature, is greater than for image (b). On the other hand, for both (a) and (b) there is no significant trend of brightness difference with distance, as there is for (c). Both parameters are of potential use in characterizing the nature of the surface. The mean variation between adjacent pixels is called the *roughness*, by analogy to its visual interpretation by the microscopist. The slope of the  $\mu_b$ -vs-d plot (the correlation between brightness difference and scalar distance on the surface of the object) is called the *texture*, to suggest a patterned behavior that is influenced by scale.

Measurement of particles of varying degrees of roughness as evidenced by the fractal dimension of their perimeters (viewed in projection) shows a statistically significant correlation with these measures of surface irregularity. The parameters are also useful for comparison of surfaces on different samples, or different regions of one sample (for instance, to compare the roughness of fracture surfaces near their origin and elsewhere). The comparison is most straightforwardly made by use of an Analysis of Variance test on multiple sets of data points.

## References

1. J. K. Beddow, G. C. Phjilip, and A. F. Vetter, "On relating some particle profile characteristics to the profile Fourier coefficients," *Powder Technology* 18: 19, 1977.
2. B. B. Mandelbrot, *The Fractal Geometry of Nature*, New York: Freeman, 1983.
3. B. H. Kaye, "Multifractal description of a rugged fineparticle profile," *Particle Characterization* 1: 14, 1984.
4. J. C. Russ, *Practical Stereology*, New York: Plenum Press, 1986.
5. J. C. Russ, T. M. Hare, R. L. Christenson, T. K. Hare, and J. C. Russ, "Stereoscopic measurement of surface relief in tooth casts," *J. Microscopy* (in press).
6. R. M. Haralick, K. Shanmugam, and I. Dinstein, "Textural features for image classification," *IEEE Trans. SMC-3*: 610-621, 1973.

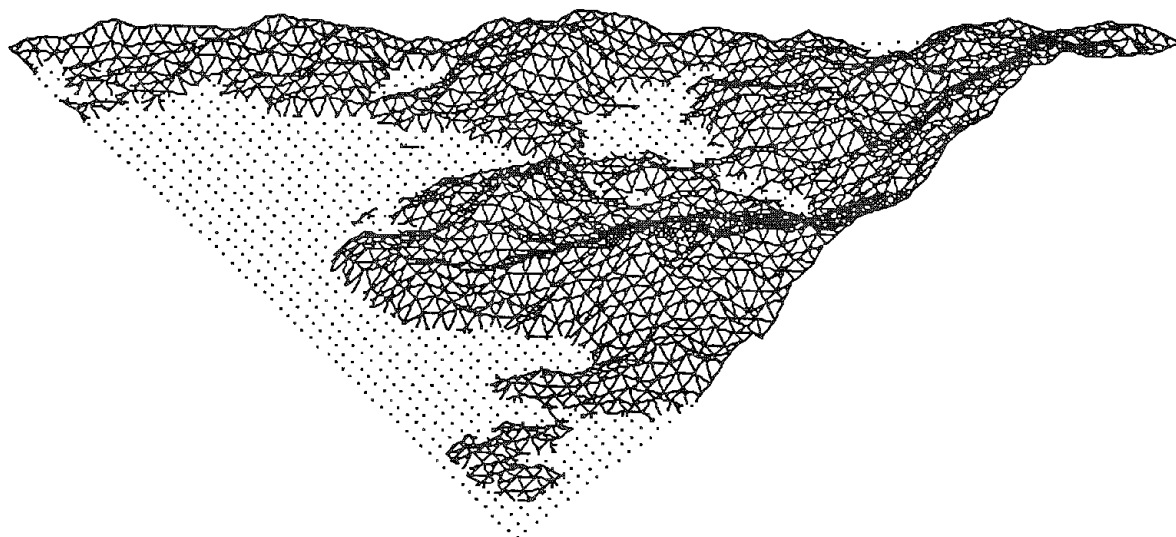


FIG. 6.--Rough surface with fractal dimension 2.18, and intersecting plane whose contour has fractal dimension of 1.18.

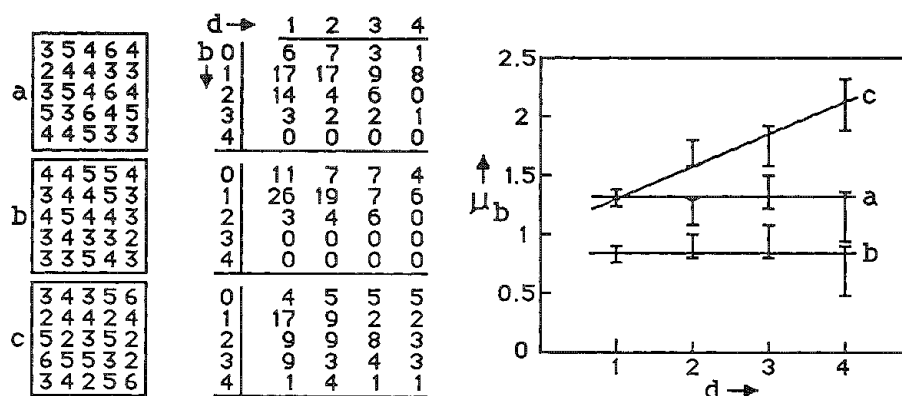


FIG. 7.--Variation in pixel brightness for three different images.

## MODELS FOR PARTICLE SHAPES VIEWED IN SEM PROJECTED IMAGES

John C. Russ and T. M. Hare

When particles are embedded or contained within a matrix, and are viewed in a section image in either the light or electron microscope, profiles are formed by their intersection with the plane of the section. From measurements of these profile dimensions (size and shape) it is possible to estimate statistically the size and shape distribution of the three-dimensional objects producing the intersection profiles. Stereological relationships for simple models, such as ellipsoids of revolution, are well established if the shape of the generating objects (for instance, the aspect ratio of an oblate or prolate ellipsoid) is assumed to be constant, with only the size changing. However, it is straightforward, at least in principle, to apply the same methods when the size and shape may both vary.

Simulation is used to construct objects of varying sizes and shapes, and to determine the size and shape of the profiles which would be observed. This is rarely practical if analytical expressions are used to compute the size and shape parameters, so computer methods (principally Monte Carlo sampling) are used to randomly orient and section the objects. The most common size and shape parameters are the area and aspect ratio, respectively, but one may also use other measures without changing the basic principles. Once the four-dimensional matrix of probabilities for observing any particular size and shape section profile from any size and shape three-dimensional object has been generated in this way, it is only necessary to invert the matrix and multiply it by the two-dimensional histogram of observed shapes and sizes, in order to determine the distribution of shapes and sizes of the objects that generated the intersection profiles. The principal practical difficulty with this method lies in the statistical uncertainties in the sparsely populated counting bins in the histogram, generally for the more extreme sizes and shapes. For several real applications, such as the characterization of oxide particles used in magnetic recording media, these uncertainties have required measuring from  $10^5$  to  $10^6$  particle profiles in order to describe the particles adequately.

When particles are examined in the SEM, they are not commonly viewed in section images. Instead they are often dispersed on a substrate, either directly (for instance with an aspirator to blow them onto an adhesive, where they are coated for conductivity) or indirectly (for instance by being floated on a liquid where surface tension may separate them, and from which they may be picked up on a surface dipped into and then withdrawn from the liquid; or by use of a more heroic method like mechanical dispersal in a eutectic wax, which is then spread onto the substrate and sublimated in a vacuum). When viewed in this way, the projected particle outlines are differently related to size and shape than for sections through the objects. Similar "shadow" outlines of objects may be obtained from light microscopes or the transmission electron microscope.

Although it may seem that the problem of characterizing the size and shape of the three-dimensional particles should be simpler in the case where the particle can be seen "whole," the opposite is actually the case. Several useful but inexact models can be employed to estimate the size of the three-dimensional objects (which are called "particles" here for simplicity). All are prone to strong bias if the particles are preferentially aligned on the substrate, or contain narrow but deep concavities that are not revealed on the projected outline images. They also produce systematic errors if the particles have strongly geometric shapes.

The most widely useful generalized shape for particle modeling is the ellipsoid of revolution. In specific cases where observation suggests that a particular shape such as a cylinder or platelet is a better match to the real objects, they may be used and the same type of analysis as shown here should be applied. The projected outline image can be measured to determine its area, perimeter, length (maximum Feret's diameter), and breadth

---

The authors are at the Analytical Instrumentation Facility, North Carolina State University, Raleigh, NC 27695-7916.

(minimum Feret's diameter). The fractal dimension of the outline may also be obtained, but it not considered here (see an accompanying paper describing its use in characterizing roughness of objects). As shown in Fig. 1, several additional parameters can be calculated from these measured values.

In particular, the "Width" is taken as the minor axis of an ellipse whose area and length (major axis) match those of the projected outline, and the "Curve length" is taken as half the measured perimeter. The Width gives a better estimate of the minor dimension of the outline than does the breadth, when the outline has any significant concavity in shape. The Curve length (or "Fiber length") is used to describe fibers of negligible width compared to their length. Various combinations of these parameters may be used to define ellipsoids of revolution (we confine ourselves to prolate shapes in the following comparisons) to model the three-dimensional particles. In the charts that follow, (L,W) identifies the model in which the major axis is the measured profile length and the minor axis is the calculated width, and (C,W) identifies the model in which the major axis is the calculated curve length and the minor axis is the calculated width. The (L,B) model (based on measured length and breadth) is similar to (L,W) for convex shapes, but somewhat inferior for concave ones.

The volume of the ellipsoid of revolution is  $\pi/6AB^2$ , where A and B are the major and minor axes. The calculated volume of the ellipsoidal model can be compared to the actual volume of geometric shapes taking into account the possible orientation of the particles, which produces different projected images. The graphs in Fig. 2 show the range of errors produced by these models for several simple geometric shapes, including regular polyhedra (tetrahedron, cube, octahedron and icosahedron) as well as cylinders and ellipsoids with length-to-diameter ratios ranging from 0.2:1 to 5:1.

Some trends are immediately apparent (and could be expected). The very angular shapes like the tetrahedron are not well modeled by the smooth ellipsoid of revolution. The trends suggest that the (L,W) model is most generally reliable, and the (C,W) model is superior for the long skinny shapes it was designed for. Even for such expectedly poor shape matches as approximating a short cylinder (which might correspond to a clay particle or other plate-like object) with a prolate ellipsoid, the results may be useful (in this case, an oblate ellipsoid would be much better). Also, there is a considerable range to the estimated volume, depending on the orientation of the generating particle. This is especially pronounced for cylinders, in which the orientation whose projected image is a circle hides all information about volume. In a random sample, these effects average out considerably.

Note that (L,W) model (and the L,B model) exactly predicts the correct result for ellipsoidal particles when the shadow image shows them at maximum elongation. On the average, this maximum projection is not seen and the observed aspect ratio is less than the maximum. If all orientations are equally likely, then the observed ratio (L/W) will be related to the three-dimensional ratio (A/B) by  $L/W = 1 + (\pi/4)(A - B)/B$ , which approaches 1 for a sphere (A = B) and approaches  $\pi/4(A/B)$  for long, thin objects (in agreement with the result of the Buffon needle problem).

Aspect ratio is a crude estimator of shape. In order to estimate the surface area of particles we require a more descriptive value, such as the "formfactor" defined as  $4\pi(\text{Area})/\text{Perimeter}^2$ . As indicated in Fig. 3, it is 1.0 for a circle and drops in value as the outline becomes more irregular. Division of the surface area of the ellipsoid of revolution used to estimate particle volume by this formfactor increases the surface area for rough particles so that a closer agreement with the actual surface area is obtained. The surface area of an ellipsoid of revolution with major and minor axes A and B is  $(\pi/2)(B^2 + AB \sin^{-1}(e)/e)$ , where  $e = (A^2 - B^2)^{1/2}/A$  is the eccentricity.

The plots in Fig. 4 show the error in the estimated surface area that results from use of this method, compared to the actual surface area for the same geometrical shapes used above. The results are actually better than for the volume. Again, the (L,W) model is most generally to be preferred, and the (C,W) model is good for long skinny shapes (and poor for oblate or disk shapes). The estimated surface area for ellipsoids is too high, because the model divides by the formfactor and thus overcorrects for shapes that are ideally smooth. For "real" particles that have some roughness, the formfactor correction is usually appropriate.

More elaborate geometrical models can be proposed to deal with specific types of particle shapes, but the simple ellipsoid model shown here produces useful estimates of



volume and surface area for a wide variety of real particles, from measurements on their projected image outlines as obtained with the SEM, for objects dispersed on a substrate.

L = Length (Max. Feret's Diam.)  
 B = Breadth (Min. Feret's Diam.)  
 W = Width ( $4 \text{ Area} / \pi \text{ Length}$ )  
 C = Curve Len. (Perim./2)

FIG. 1.--Measured and calculated size parameters discussed in text.

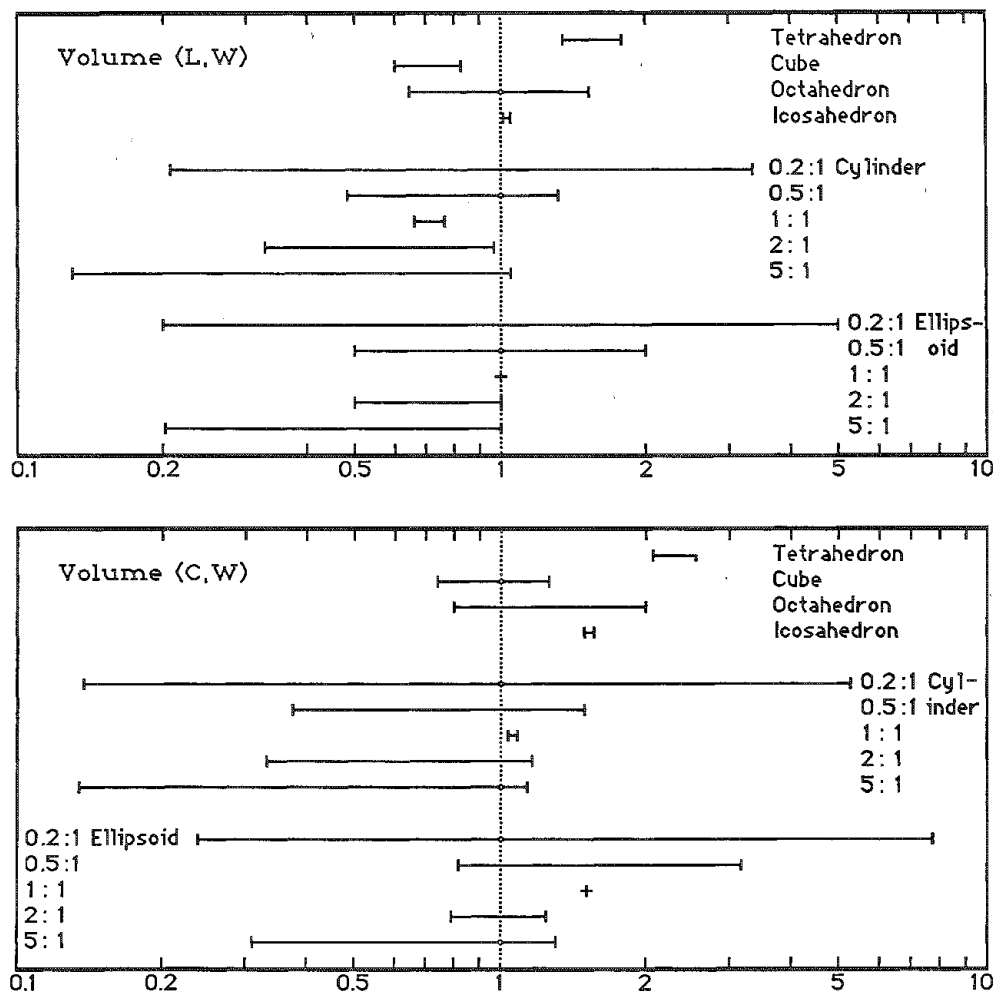
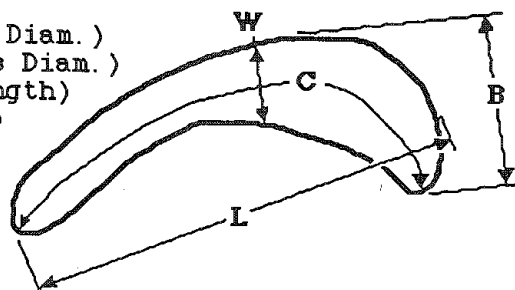


FIG. 2.--Ratio of estimated volume to actual, for variety of geometrical shapes, showing extremes of orientation.

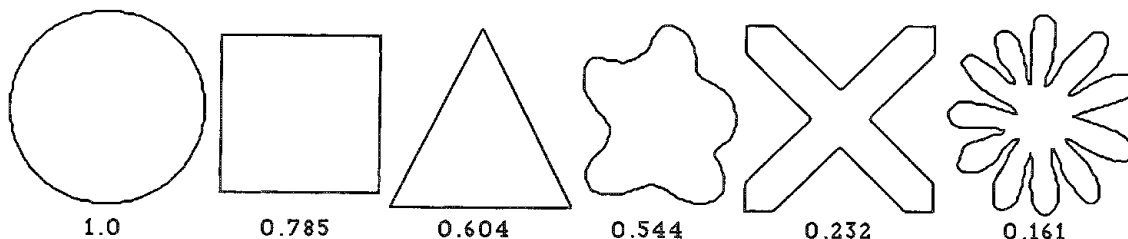


FIG. 3.--Formfactors for various shapes (see text).

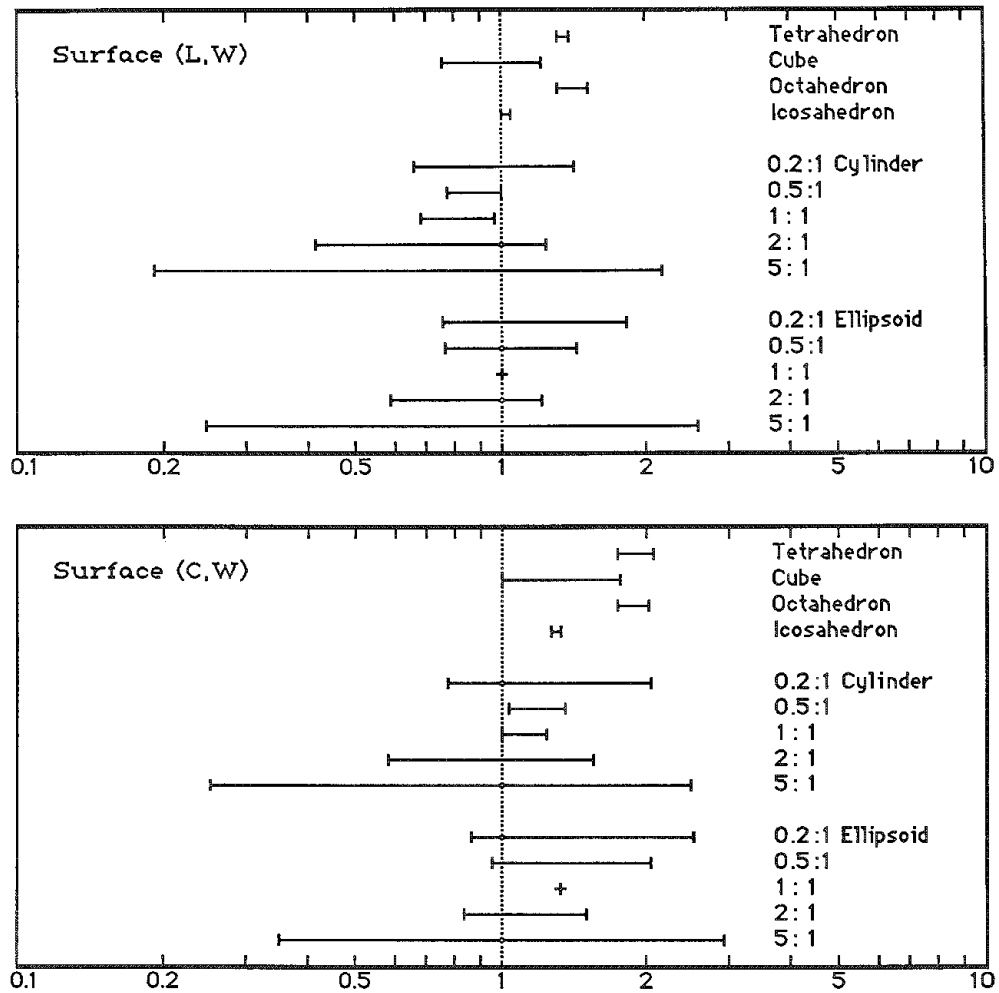


FIG. 4.--Ratio of estimated surface to actual, for variety of geometrical shapes, showing extremes of orientation.

## BRIGHT-FIELD IMAGE CORRECTION WITH VARIOUS IMAGE-PROCESSING TOOLS

D. S. Bright and E. B. Steel

Many microscopes, whether light or electron, have trouble maintaining uniform illumination across a field of view at the lowest magnification ranges, because the microscope optics and detectors are primarily designed for higher magnification viewing. A background or blank image, whether obtained on the instrument or generated from the image to be corrected, is employed in the two digital image-processing procedures to be described. The examples are of low-magnification images on a compound light microscope (LM) at approximately 40× and a scanning transmission electron microscope (STEM) at approximately 300×.

The first procedure allows LM or STEM bright-field images to be corrected for uneven background illumination and nonuniform detector sensitivity. To make the correction, the image is divided by a blank or background image, with appropriate filtering, and then the result is scaled. We use this procedure when enhancing the contrast or images for display, or when setting the threshold for automatically selecting objects of interest. The second procedure, which we have found useful for eliminating small-scale debris from an image, is to select small spots individually and replace them with the corresponding piece of the blank image.

### *Background Correction--LM*

The intensity of the blank image usually varies slowly with position. When the objects are thin or small enough, the blank image need not be taken on the instrument, but can be generated from the image itself by means of a maximum filter, which is similar to the median filter<sup>1</sup> and other smoothing operations. Each pixel of the resulting image is the maximum value (rather than the median or mean) of the original pixels in a square window around it.

The rationale for dividing an image by a blank image is the following. For each pixel,

$$I = L * A * S \quad (1)$$

where  $I$  is the pixel intensity,  $L$  is the illumination for that pixel,  $A$  is the fraction of radiation transmitted by the object, and  $S$  is the sensitivity factor of the detector.

With no sample present, the pixel intensity  $I_b$  for the blank image is

$$I_b = L * S \quad (2)$$

Dividing equation (1) by equation (2) gives:

$$A = I/I_b \quad (3)$$

$A$  is the desired intensity, to within a scaling factor, for the corrected image--one with even background illumination and uniform detector sensitivity.

Figure 1(a) is a transmitted light micrograph of asbestos fibers, which have low contrast, and is not contrast enhanced. Figure 1(b) is contrast enhanced, which makes the uneven background illumination noticeable. An attempt to set the threshold for this image (Fig. 1c)--that is, to select object pixels only by intensity--shows that the background at the edges is darker than objects at the center.

The blank image had some small spot like blemishes of its own, which corresponds to the detector sensitivity term  $S$  in Eqs. (1) and (2). The spots could have been retained in the blank image, but they were not because they were shifted slightly from the corresponding spots in this figure due to a slight change in the focusing optics. This shift had the effect of enhancing the edges of these spots in the corrected image. We thus

---

The authors are at the Center for Analytical Chemistry, National Bureau of Standards, Gaithersburg, MD 20899.

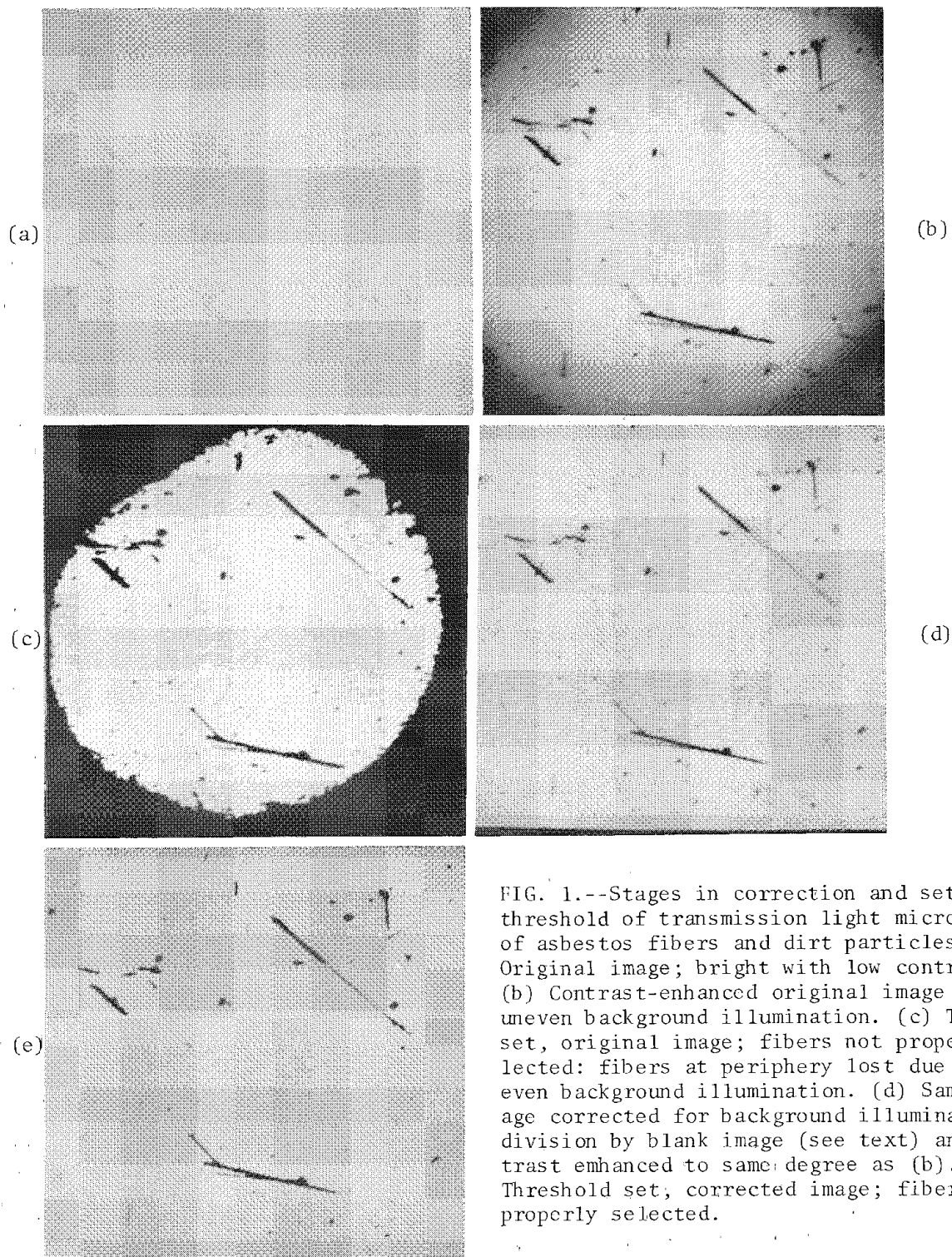


FIG. 1.--Stages in correction and setting of threshold of transmission light micrograph of asbestos fibers and dirt particles: (a) Original image; bright with low contrast. (b) Contrast-enhanced original image showing uneven background illumination. (c) Threshold set, original image; fibers not properly selected: fibers at periphery lost due to uneven background illumination. (d) Sample image corrected for background illumination by division by blank image (see text) and contrast enhanced to same degree as (b). (e) Threshold set, corrected image; fibers are properly selected.

corrected the image for background illumination by dividing it pixel by pixel, with a blank image from which the spots had been removed with a  $17 \times 17$  median filter.

Figure 1(d) shows the original image corrected with the filtered blank image, and enhanced identically to Fig. 1(b). The background intensity is now uniform, and one can select the fibers by setting the threshold (Fig. 1e).

#### *Background Correction--STEM*

Correction for background illumination by use of division by a blank image also works for STEM images. Figure 2(a) is a blank image, Fig. 2(b) is the uncorrected image of the sample, and Fig. 2(c) is the corrected image obtained when Fig. 2(b) is divided by Fig. 2(a). The division was confined to the disk region in Fig. 2(c), because the background illumination is very small outside this disk. The disk is defined by a nonadjustable aperture in the STEM system, which at low magnification keeps unscattered bright-field electrons at the edge of the image from reaching the electron detector. However, the edges outside the disk do contain scattered-electron or dark-field image information that causes very bright particles to be seen in the corrected image. The algorithm for correcting for the uneven illumination was therefore limited to the region within the disk.

#### *Spot Removal*

Optical microscope images of grain mounts often contain many very small spots that come from particles on the optics, slide, coverslip, and the specimen itself. These spots are often too small to be accurately analyzed on the light microscope and can be considered as "noise" or background to the actual particles being analyzed.

Figure 3(a) is a light micrograph of asbestos fibers and background spots. The photograph was intended to be made into a standard diagrammatic image with a calibrated fractional area of the image designated as fiber; it was thus desirable to remove the dirt spots from the photograph. Figure 3(b) has the spots to be removed marked with bullseyes. These spots were selected with a top-hat filter<sup>2</sup> with parameters adjusted to fit the majority of the darker dirt spots. The top-hat filter is again similar to the previously mentioned filters, except that it uses round windows and is gaited; that is, it acts as a thresholding operation. A disk-shaped window, corresponding to the top of a top hat, is centered on the pixel; an annular window, corresponding to the brim, is concentric to the top. A pixel in the resulting image has the same value as the corresponding pixel in the original image if the maximum value of the top pixels less the maximum value of the brim pixels is greater than a given threshold. Otherwise, the pixel in the resulting image has a value of zero.

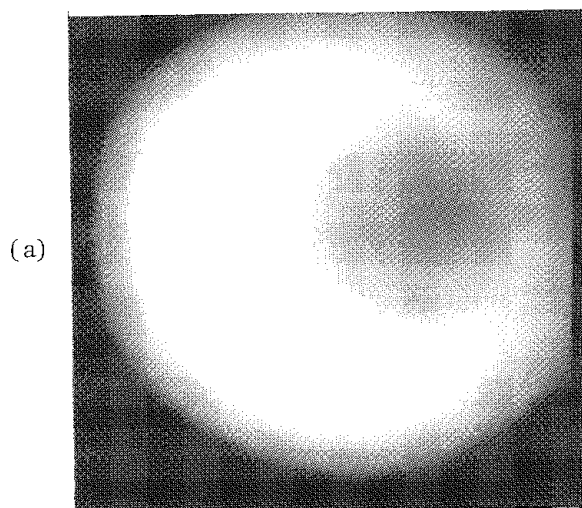
Figure 3(c) shows the original with the dirt spots of Fig. 3(b) removed by a masking operation that uses background levels obtained with the maximum filter. The background level used to fill in the removed spots was taken by the filter from the area immediately surrounding the spots. The imperfections in the image show the compromise taken when the parameters for the top-hat filter are chosen: few darker areas of the fibers were selected in error, and some small spots were missed.

#### *Conclusion*

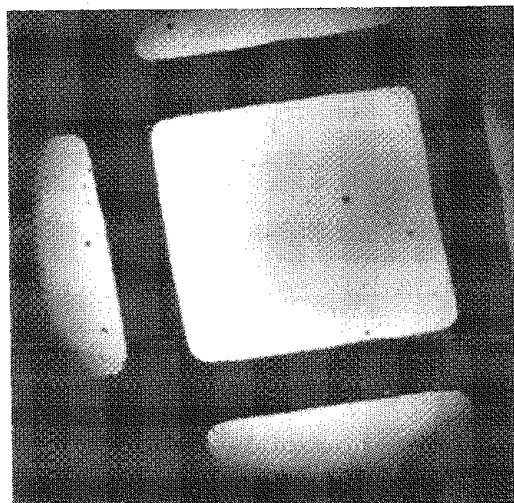
Blank or background images are useful for correcting images with uneven background and nonuniform detector sensitivity, and for removing small spots and blemishes. The image processing tools used in doing this are division, maximum filtering, median filtering, top-hat filtering, threshold setting, and masking.

#### *References*

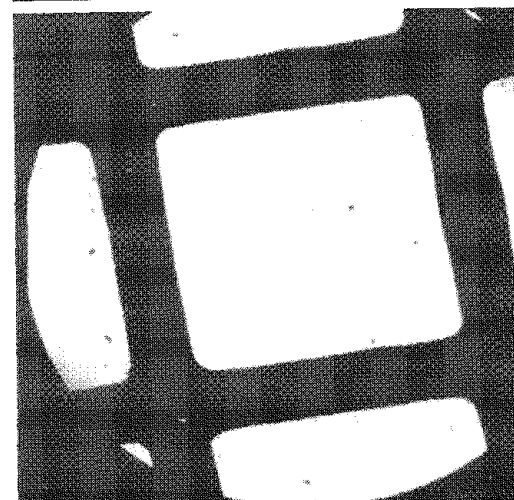
1. T. S. Huang, "A fast two-dimensional median filtering algorithm," *IEEE Trans. ASSP-27*: 13-18, 1979.
2. J. J. McCarthy and F. H. Schamber, "Least-squares fit with digital filter; A status report," in K. F. J. Heinrich et al., Eds., *Energy Dispersive X-Ray Spectrometry*, NBS Special Publication 604, U.S. Department of Commerce, 1981.



(a)

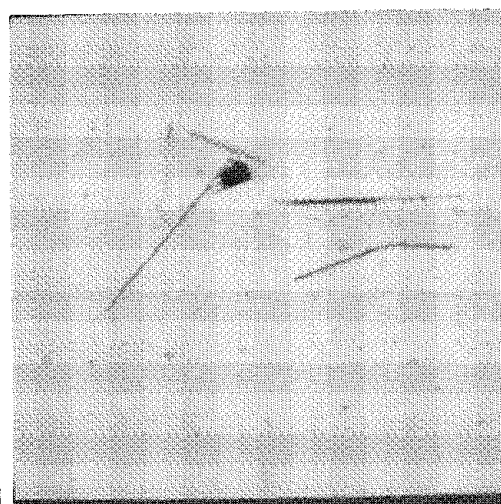


(b)

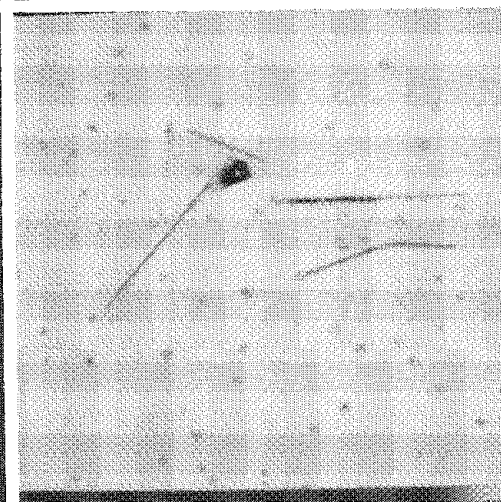


(c)

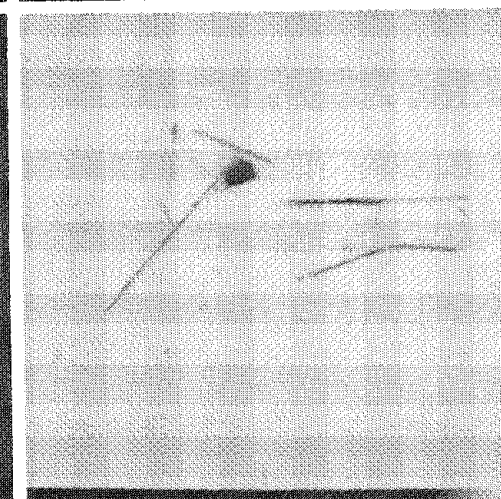
FIG. 2.--STEM image corrected for background illumination. (a) Background illumination or blank image. (b) Sample image. (c) Sample image corrected for background illumination by division by blank image.



(a)



(b)



(c)

FIG. 3.--Removal of dirt spots from light micrograph of asbestos fibers. (a) Sample image, corrected for background illumination as in Fig. 1. (b) Spots to be removed from image marked with bullseyes. (c) Image with spots removed.

## EUCLIDIAN DISTANCE MAPPING FOR SHAPE CHARACTERIZATION OF ALLOY GRAIN BOUNDARIES

D. S. Bright and D. E. Newbury

The quantitative physical description of microstructures<sup>1</sup> generally proceeds by the determination of characteristic spatial parameters to describe the structure. These measures include: one-dimensional parameters such as the mean grain boundary intercept length in single-phase materials, the mean-phase boundary intercept length in polyphase materials, or the perimeter of grains or discontinuous phase particles; area parameters, such as the surface area of a discontinuous phase particle; and volume parameters, such as the volume fraction which a phase occupies. In the course of examining two-phase microstructures such as that shown in Figs. 1(a) and (b), these simple spatial parameters were not adequate to follow the complex changes observed in the structure. In particular, the discontinuous phase showed the formation of string-like protuberances. In order to determine whether these structures were significant features for monitoring changes in the microstructure, a reliable measure was needed. It was necessary, then, for the measure to be sensitive to long, thin protuberances. It was also desirable for the measure not to be sensitive to the joining of two grains by a short bridge.

A measure that is sensitive to protuberances can be developed from the Euclidian distance map.<sup>2</sup> The distance map is constructed from the original image by the following sequence of operations. The range of possible intensities  $I$  of the image pixels is divided into two ranges, corresponding to the discontinuous grains  $I_g$  and the background of continuous phase  $I_b$ . Sets of adjacent grain pixels, each of which probably corresponds to a single grain, are shown with uniform intensity as in Figs. 1(c) and (d). Each pixel, with coordinates  $(x,y)$ , is labeled as either grain or background according to which intensity range the pixel intensity corresponds. Next, given a grain pixel at  $(x,y)$ , the image is searched for the nearest background pixel. If a circle is imagined to expand from the center of a grain pixel,  $(x,y)$ , then the center  $(v,w)$  of the first background pixel that the circle touches is the location desired. The radial distance  $R$  from  $(v,w)$  to  $(x,y)$ , in pixel width units, is the value stored at  $(x,y)$  in the distance map. If the pixel at  $(x,y)$  is a background pixel, zero is stored in  $(x,y)$  of the distance map. This process is repeated for all pixels in the image. An efficient algorithm developed by Danielsson has been employed in this work.

To illustrate how the distance map is used and why the measure derived from it works, we shall consider several diagrammatic shapes. Figure 2 shows a shape with a protuberance. The distance map for this shape is shown in Fig. 3 as a mesh plot where the height of the plot is proportional to the distance map, or to the radius of the circle centered at that point that just touches the edge of the shape. Note that the distance map has a point and a ridge that lie on the skeleton of the shape. The value or height of the distance map at any point on the skeleton indicates the width of the shape there; i.e., the radius of the circle centered on that point that just touches the edge on both sides of the point.

Peak and ridge points are selected with a function called 'ridge,' which returns the value of a pixel if it is greater than or equal to both upper and lower neighbors, or to both the left and right neighbors. 'Ridge' also looks two pixels out from the center pixel if necessary, as some ridges are two pixels in width. Ridge points, along with the outline for clarity, are shown for several shapes in Fig. 4. The average of this distance map for the ridge points of these shapes are in the 'Ridge Average' column in Table 1.

The perimeter in Table 1 is just a count of the pixels on the edge of the shape, where an edge pixel is adjacent on at least one of four sides to a background pixel.

In Fig. 4, shape b is the same as that of Figs. 2 and 3. Shape c is chosen to be relatively close to shape b in both area and perimeter, but has no protuberance. The ridge measure is sensitive to the protuberance of shape c, because the average contains many points along the ridge of the protuberance that have low values of the distance map, due to the relative narrowness of the protuberance.

---

The authors are at the Center for Analytical Chemistry, National Bureau of Standards, Gaithersburg, MD 20899.



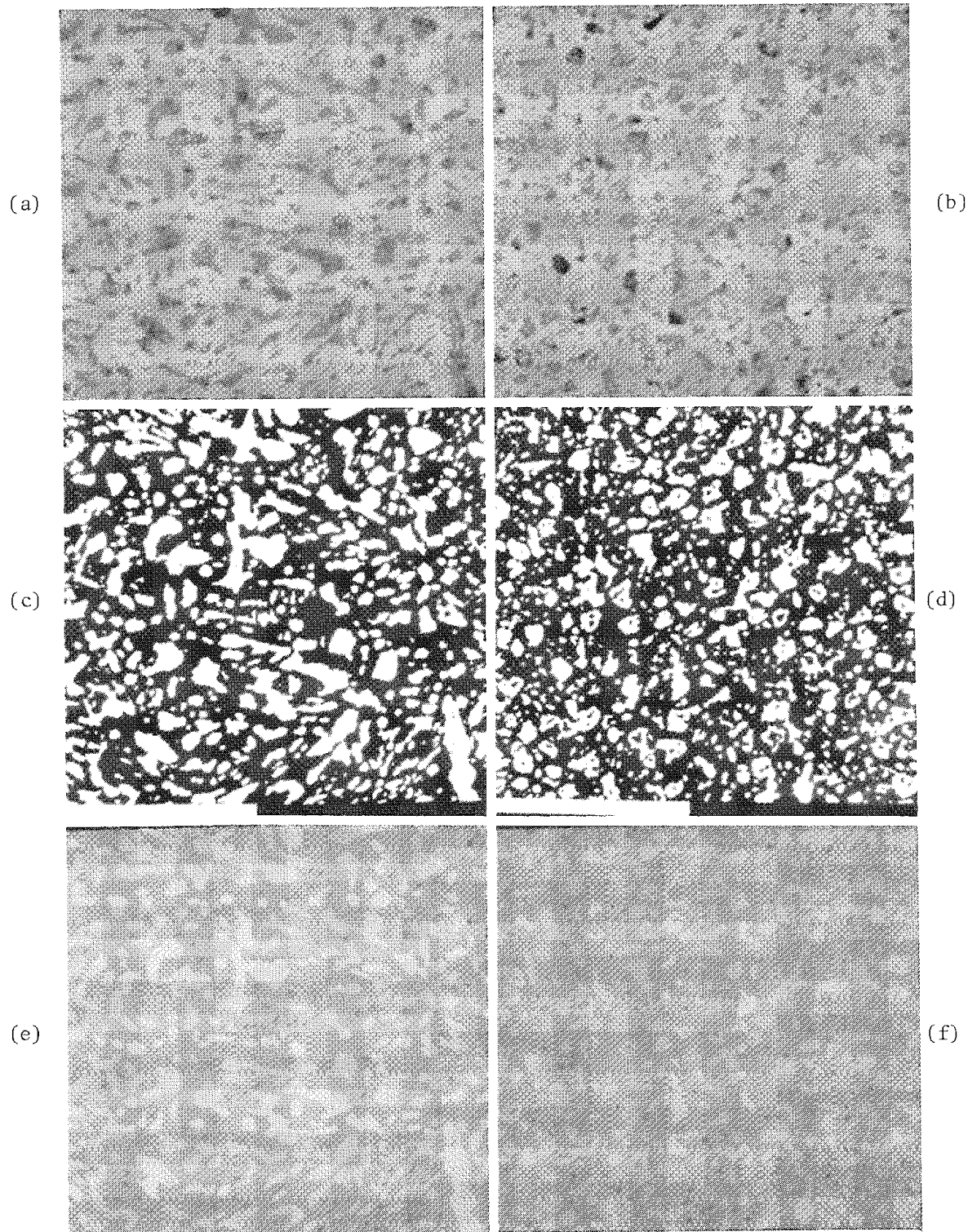


FIG. 1.--Light micrographs of polished surface of alloy. Left images are from one sample, right images from another: (a) and (b) originals; (c) and (d) with threshold set to show grains as white; (e) and (f) grains used in measurement calculations (Table 2) and comprising 90% of grain area shown as white and superimposed on original photographs.



Shape a, the disk, has only one ridge point, and a correspondingly great ridge average. Although the area/perimeter ratio is greater than shapes b or c by about 50%, the ridge measure differs by an order of magnitude. In comparison with shape a, shape c can be considered to have many small protuberances.

Shapes d and e illustrate that the ridge measure is not sensitive to joining two grains by a small bridge. That is desirable because grains are often separated by a narrow gap (Fig. 1), which can sometimes be opened or filled in with only a small change in the selection of the grain and background intensity ranges. Any analysis of grain sizes or shapes should be as insensitive to this selection as possible.

To characterize a sample, the measures are typically averaged over most of the grains in several images. For Figs. 1(e) and (f), and the results in Table 2, the smaller grains were not included in the measurement because there are many of them, they all have about the same rounded shape, and they account for only 10% of the grain area. Since the averages include broad ranges of sizes and shapes, they make the measures statistically less different between samples--an effect we wish to diminish. We prefer to use intensive measures (those that are independent of grain size) because the size distribution of these measures is narrower than that of the extensive measures (those that depend on grain size). From preliminary tests of images such as in Fig. 1, the ridge measure is more sensitive in distinguishing one sample from another than are other intensive measures that we have tried to date.

### References

1. R. T. DeHoff and F. N. Rhines, *Quantitative Microscopy*, New York: McGraw-Hill, 1968.
2. P. E. Danielsson, "Euclidian distance mapping," *Computer Graphics and Image Processing* 14: 227-248, 1980.

TABLE 1.--Various shape measures for diagrammatic shapes in Fig. 4.

Figure	Extensive measures			Intensive measures		Number of shapes
	Area (pixels)	Perimeter (pixels)	$\frac{\text{Area}}{\text{Perimeter}}$	$\frac{\sqrt{\text{Area}}}{\text{Perimeter}}$	Ridge average	
4(a)	80381	1276	63.0	0.222	160.0	1
4(b)	91027	2180	41.8	0.138	19.4	1
4(c)	92617	2020	45.8	0.151	31.4	1
4(d)	31585	816	38.7	0.154	32.4	2
4(d)	63170	1632	38.7	0.154	32.4	1
4(e)	63191	1628	38.8	0.154	32.4	1

TABLE 2.--Various shape measures for the light micrographs of Figs. 1(e) and (f).

Figure	Extensive measures			Intensive measures		Number of grains
	Area (pixels)	Perimeter (pixels)	$\frac{\text{Area}}{\text{Perimeter}}$	$\frac{\sqrt{\text{Area}}}{\text{Perimeter}}$	Ridge average	
1(e)	322	108	2.57	0.180	3.85	229
S.D. *	462	122	0.77	0.042	1.09	
1(f)	223	93	2.12	0.175	3.13	306
S.D. *	221	76	0.63	0.047	0.91	

\*S.D. = standard deviation.

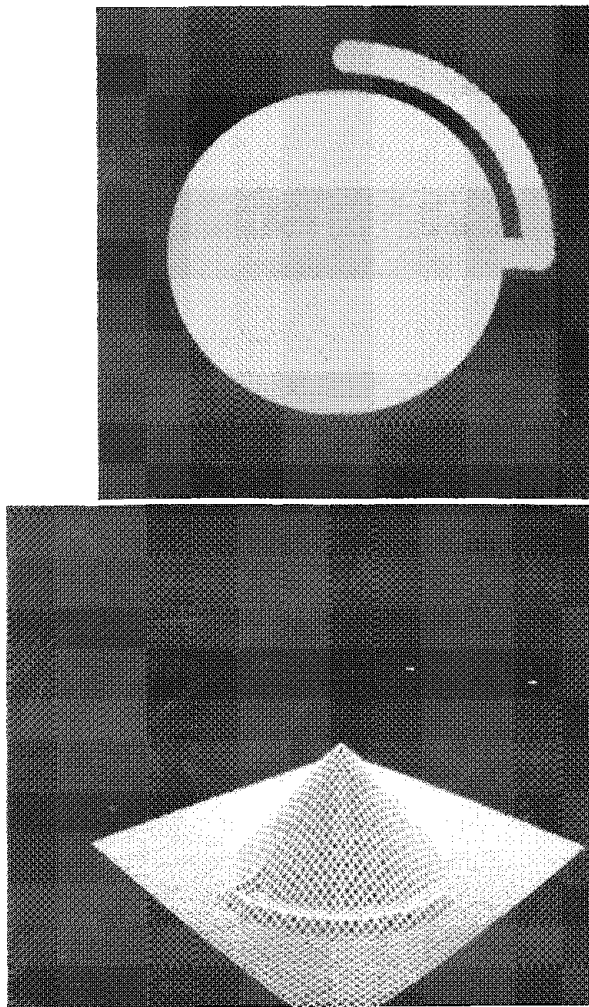
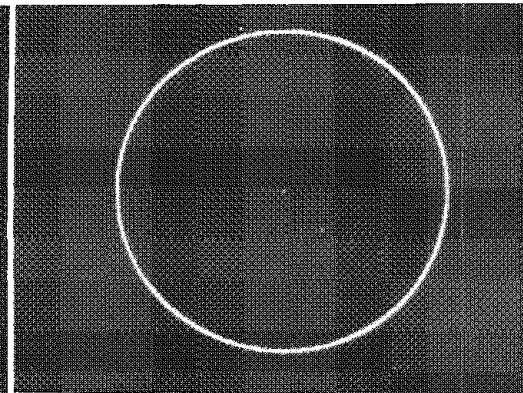
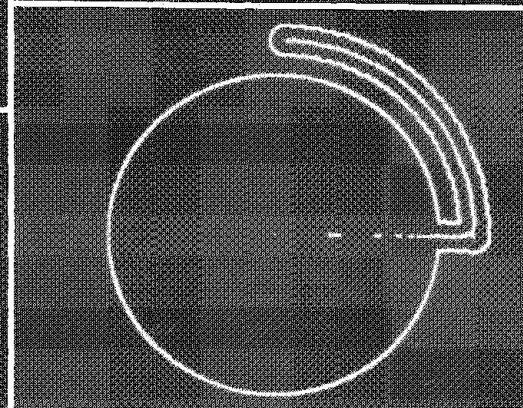


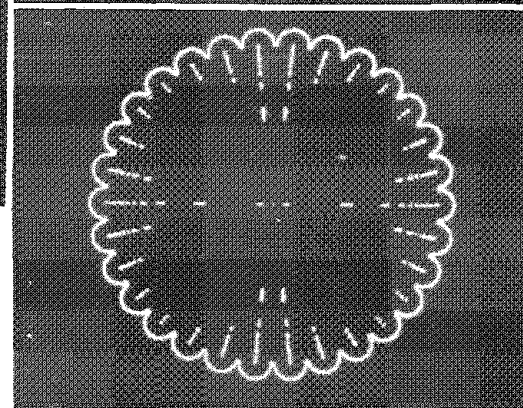
FIG. 2.--Diagrammatic shape representing grain with protuberance.  
 FIG. 3.--Distance map, shown as mesh plot, of shape in Figs. 2 and 4(b).  
 FIG. 4.--Ridge points and outlines for several shapes for comparison of measures shown in Table 1 (see text).



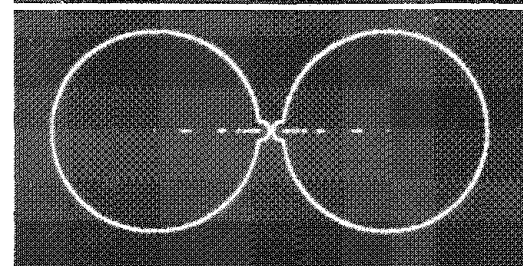
(a)



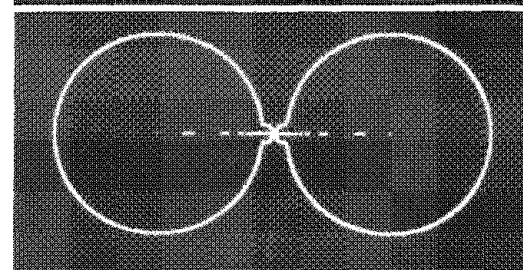
(b)



(c)



(d)



(e)

## Advances in Scanning Electron Microscopy

### DEVELOPMENT OF THE ULTRAHIGH-RESOLUTION SEM (S-900)

M. Sato, Y. Nakaizumi, I. Matsui, and K. Kanda

In response to customers' requirements for low-voltage operation with uncoated samples, ultrahigh-resolution (UHR) microscopy at high-voltage operation, and high accuracy/sensitivity elemental analysis, we have developed a UHR SEM with a guaranteed resolution of 0.8 nm in the secondary electron image (Fig. 1).

Figure 2 is a sectional view of the column. The electron-beam source is a cold field-emission electron gun. The objective lens is a strongly excited TEM type and the specimen is positioned between the upper and lower polepiece gap by means of a side entry holder. The secondary-electron detector is positioned above the upper polepiece of the objective lens and secondary electrons are collected with the aid of a magnetic field and a post-high-voltage field.

Figure 3 shows the theoretically calculated resolution of this instrument. At 30 kV it achieves 0.8 nm; at 1 kV, about 4 nm. Figure 4 is one of the UHR test results showing 0.8nm resolution. The specimen is evaporated Au-Pd particles. Figure 5 shows the vacuum system of the S-900. It is a complete dry pumping system. The electron gun is evacuated by three ion pumps differentially and the vacuum in the gun achieves up to  $10^{-7}$  Pa. The column uses metal gaskets for the most part with a minimum of O-rings. The specimen chamber is evacuated by a turbo molecular pump and the vacuum in the specimen chamber achieves of the order of  $10^{-5}$  Pa. The turbomolecular pump utilizes magnetically suspended bearings instead of conventional mechanical bearings. The magnetic bearings assure excellent reliability over a prolonged period.

Figure 6 is a resolution test micrograph of a backscattered electron image. It was recorded at 30 kV and at 300 000 $\times$ . The specimen is Pb-coated magnetic tape.

The S-900 can accommodate a backscattered-electron detector and an energy-dispersive x-ray spectrometer as options. The major specifications of the S-900 are: resolution, 0.8 nm (secondary-electron image); accelerating voltage, 1-30 kV; magnification, 150 $\times$  to 800 000 $\times$ ; specimen size, 20  $\times$  6  $\times$  2.4 mm (H) maximum.

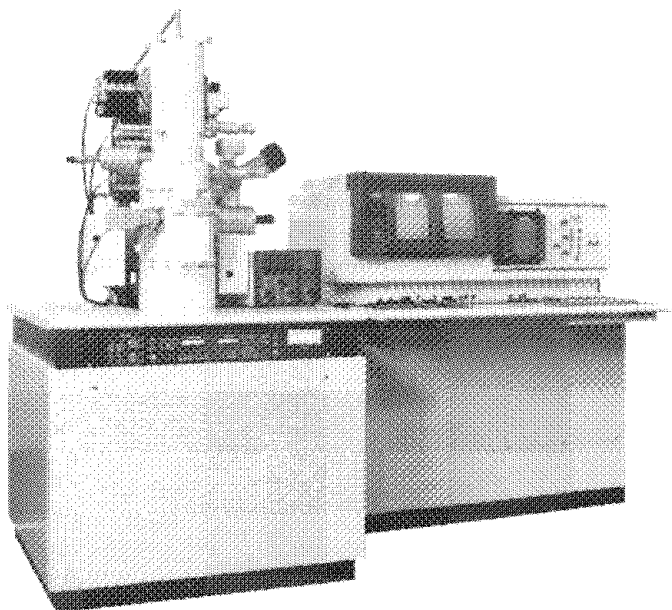


FIG. 1.--General view of S-900 SEM.

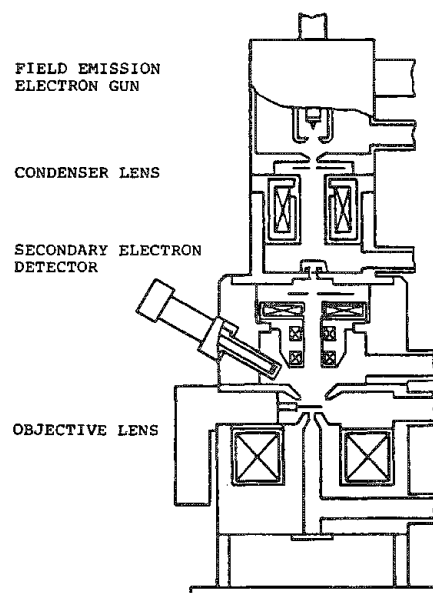


FIG. 2.--Sectional view of column.

The authors are at the Naka Works of Hitachi Ltd., Katsuta, 312 Japan.

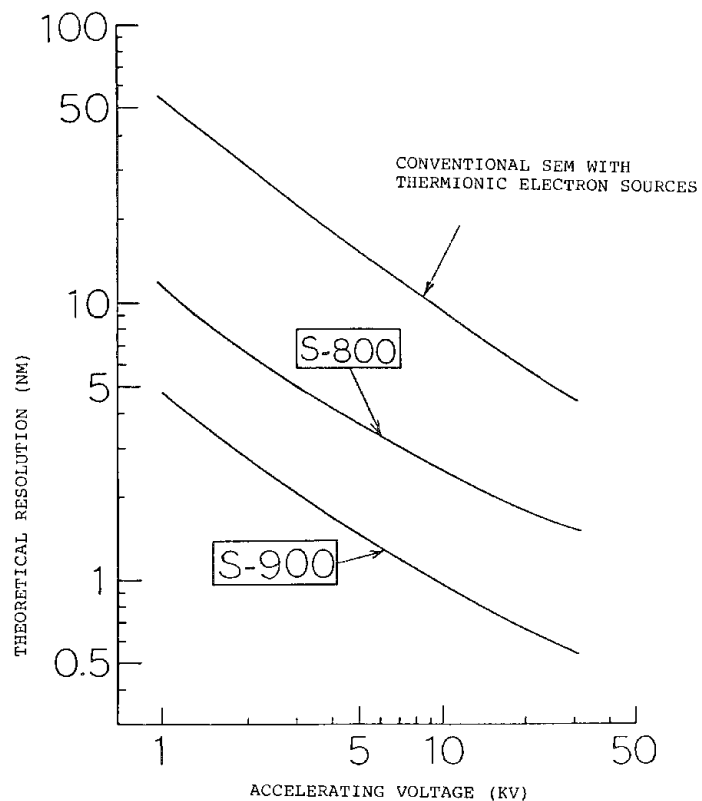


FIG. 3.--Theoretical resolution of S-900.

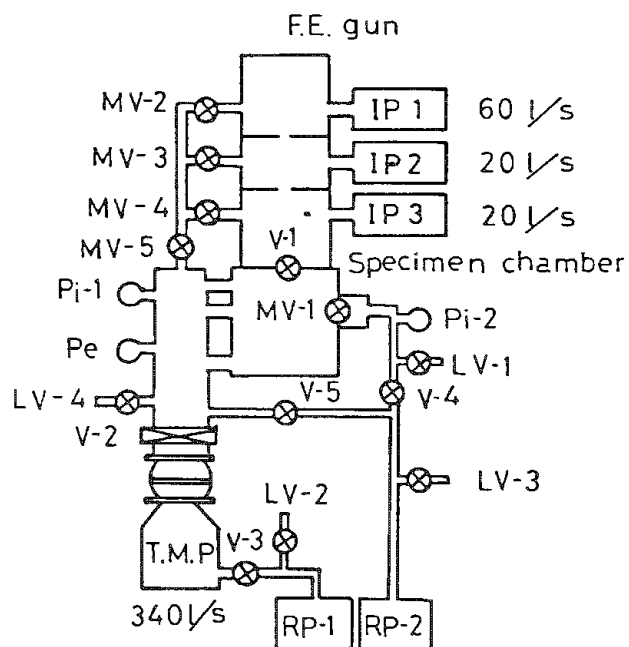


FIG. 5.--Vacuum system.

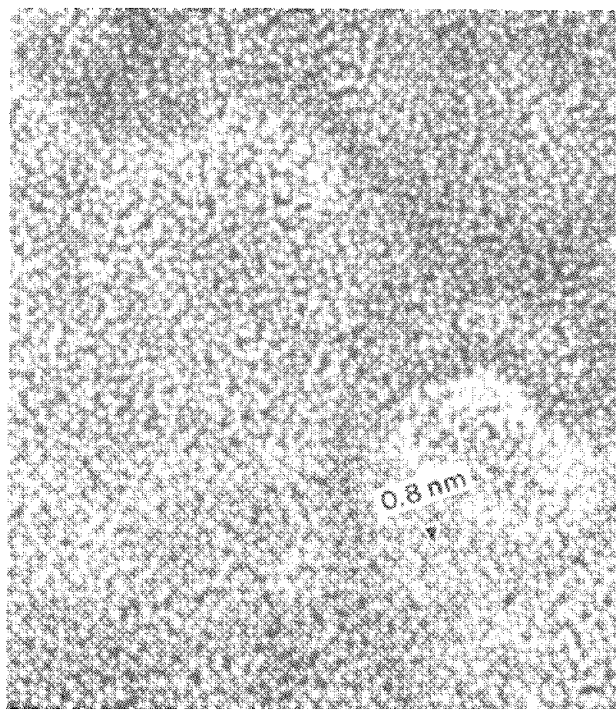


FIG. 4.--High-resolution test result. (Accelerating voltage, 30 kV; magnification, 300 000 $\times$ .)

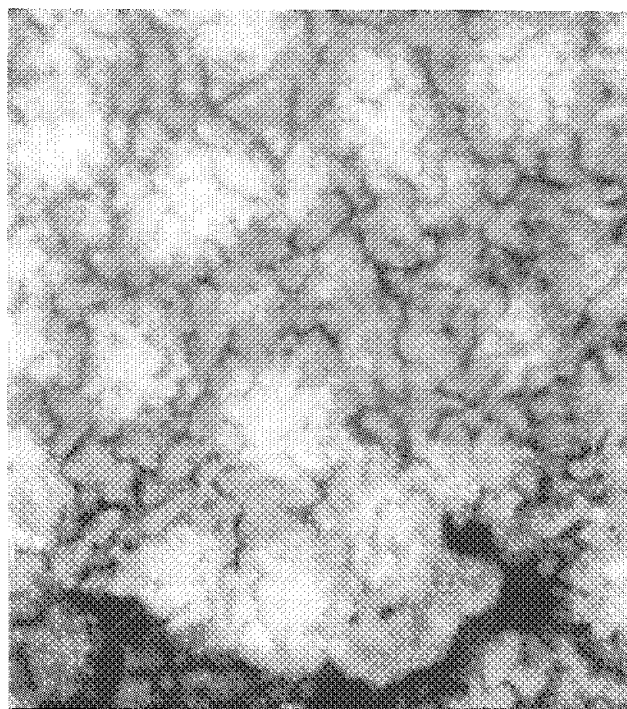


FIG. 6.--Backscattered-electron image. (Accelerating voltage, 30 kV; magnification, 300 000 $\times$ .)

## INTRODUCTION TO CHARGING EFFECTS OF INSULATORS BY INCIDENT ELECTRON BEAMS

J. Cazaux

The experimental evidence of charging effects of samples (giving rise to deflection of the incident beam, electric breakdown, migration of mobile ions, etc.) is well known when insulating materials (polymers, minerals, glasses, biological objects, etc.) are bombarded by electrons in electron microscopy (scanning: SEM scanning or conventional transmission: STEM or CTEM), electron probe microanalysis (EPMA), Auger spectroscopy (AES), and electron-beam lithography. Even though these effects are known qualitatively, to our knowledge no paper gives a global view of the macroscopic aspects of electron bombardment of insulators, independent of the specific technique used and of the specific sample investigated. The questions are: how can one characterize the electric field? where is it maximum? where is it zero? how can locations be changed by changes in the surrounding media (metallization), the incident spot size, or the thickness of the sample?

The present paper tries to fill this gap by use of simple electrostatic arguments. The analysis is applied to the most common situations and its predictions are compared to some selected published results obtained in EPMA, AES, SEM, CTEM, and STEM.

### *Sign of the Trapped Charges*

When an incident electron beam bombards an insulating material, it first causes the emission of secondary electrons (quantum yield  $\delta$ ) from a surface layer less than 50 nm thick. Next the incoming electrons penetrate deeper in the bulk ( $\sim 1 \mu\text{m}$ ), where they come at rest for a certain time (residence time  $\tau$ ) except a fraction  $\eta$  of them, which is back-scattered or (in thin samples) transmitted. That means that the sample is positively charged except when a thick insulating material ( $t > 50 \text{ nm}$ ) is bombarded by energetic electrons ( $E_n > 4 \text{ keV}$ ): in EPMA of bulk insulators the sample is negatively charged. For the sake of simplicity, we only consider here the field created by the majority charges ( $< 0$  or  $> 0$ ) having an axisymmetry around the normal to the surface (the  $z$  axis). Such a distribution  $\rho(r, z)$  is obtained by an incident electron beam normal to the surface; and we can deduce additional details by assuming that the charge distribution is uniform inside a cylinder of radius  $a$  (incident beam radius plus broadening due to scattering effects) and height  $d$  (thickness of the region where the majority charges are trapped).

### *Field Created in an Infinite Medium: Situation (a)*

From classical electrostatics, it can be shown that there is at least one point C inside the charge distribution where the electric field is zero. Around this point one can expect an accumulation (when the majority charges and the mobile ions have opposite signs) or a depletion region for the mobile ions of the dielectric medium. Not only cannot the electric field created by the trapped charges be considered to be uniform (as is often assumed in electromigration studies), but it changes direction along any straight line passing by point C and leads to the existence of other points at which the electric-field component (measured along this line) takes extreme values (see legend of Fig. 1 for a demonstration).

When the trapped charge distribution is assumed to be uniform inside a cylinder of radius  $a$  and height  $d$ , the evolution of  $F_z(0, z)$  and  $F_r(r, d/2)$  can be calculated.<sup>1</sup> The results are illustrated in Fig. 2 for two situations:  $d \ll a$  and  $d \gg a$ . The point C is (as expected) in the plane of symmetry ( $r = 0, z = d/2$ ) and for a given situation,  $F_z$  and  $F_r$  components reach comparable maximum values at the edges of the charge distribution.

### *Semi-infinite Sample: Situation (b)*

When the sample is very thick, the field in the dielectric is created by the true

---

The author is at the Laboratoire de Spectroscopie des Electrons, Faculté des Sciences, Université de Reims, BP 347, F-51062 Reims Cédex, France.

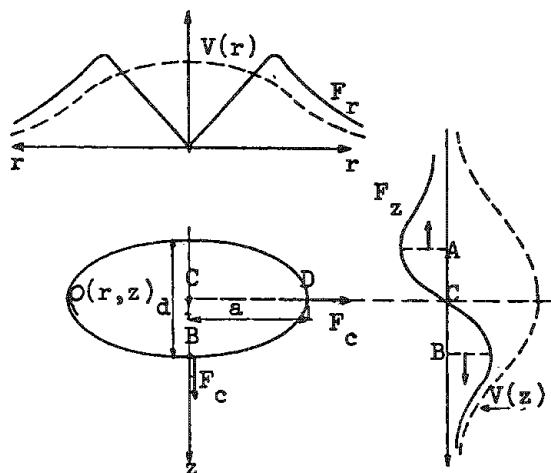


FIG. 1.--Electric field created by charge distribution that has axisymmetry in passing from  $-\infty$  to  $+\infty$  along  $z$  axis; electric potential  $V(0,z)$  is zero at infinity ( $\pm\infty$ ) and takes at least one extreme (max. or min.) value at a given point C. At that point  $F_z = -\partial V/\partial z = 0$  and  $F_r$  (radial component of  $F$ ) is always zero at any point on  $z$  axis (property of cylindrical symmetry). Thus,  $F = 0$  at point C and diverges (or converges if  $\rho < 0$ ) around it. Also,  $F = 0$  at  $\pm\infty$  along any line passing by C, which means that any component of  $F$  measured along this line, such as  $F_z(0,z)$ , takes at least one extreme value between C and  $-\infty$  and another between C and  $+\infty$ .

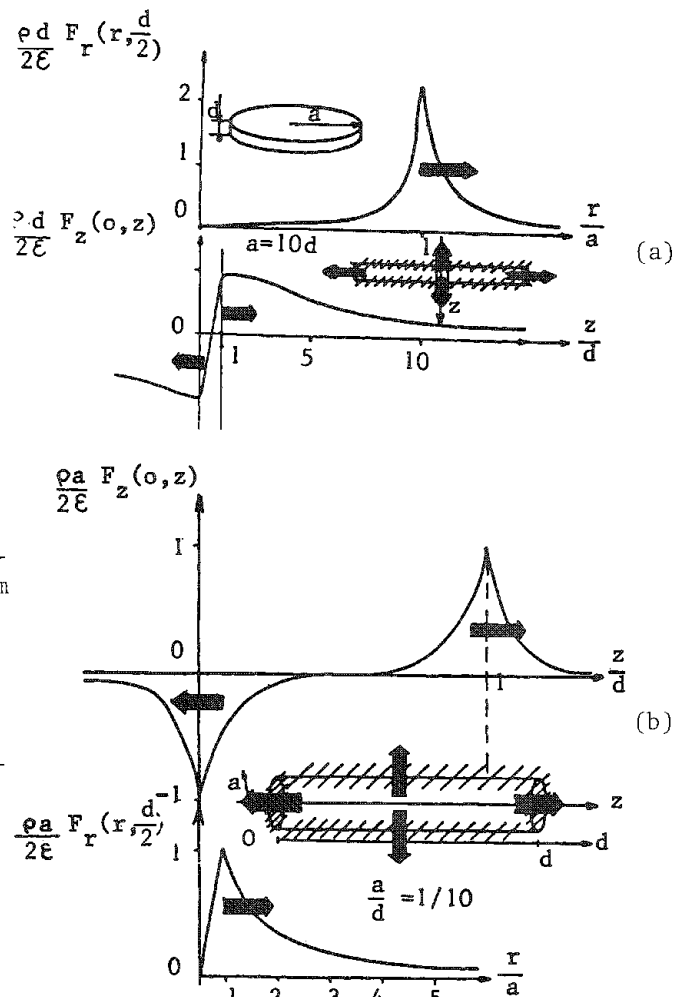
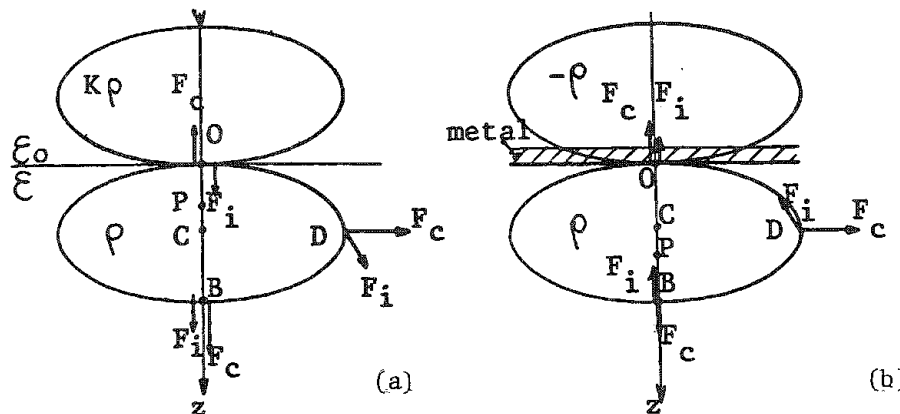


FIG. 2.-- $F_z(0,z)$  and  $F_r(r, d/2)$  components of electric field created by uniform charge distribution trapped inside cylinder of radius  $a$  and height  $d$  in an infinite medium, (a) for  $d \ll a$  and (b)  $d \gg a$ . Hatched areas represent region where  $F$  is maximum.

FIG. 3.--Effect of electric image associated with one interface. (a) Dielectric bounded by vacuum. Image weight  $K$  increases when  $\epsilon_r$  (rel. dielectric constant) increases. Relative to infinite medium, radial component  $F_r$  is reinforced and  $F_z$  is reduced around vacuum/dielectric interface.  $F_z$  becomes maximum close to end of charge distribution ( $z \approx d$ ) and P is shifted upward. (b) Dielectric covered by thin conducting film. Sign of image is opposite to sign of true charge distribution:  $-\rho$ . Its effect is independent of  $\epsilon_r$ .  $F_z(0,z)$  is now maximum at metal/dielectric interface. Relative to C, inversion point P is shifted downward ( $\overline{OC} < \overline{OP} < d$ ) and approaches end of real charge distribution when  $a$  is increased; see  $F_z(0,z)$  for  $z > d$  in Fig. 2 for (a)  $d \ll a$  and (b)  $d \gg a$ .



charge distribution  $\rho(r,z)$  and by one symmetric image  $K\rho(r,-z)$ , where  $K = (\epsilon - \epsilon_0)/(\epsilon + \epsilon_0)$  and  $\epsilon$  and  $\epsilon_0$  are the dielectric constants of the sample and of the surrounding medium, respectively.

When the insulator surface is bounded by a vacuum, it is clear (Fig. 3a) that the image reinforces the radial component  $F_r$ . The axial component  $F_z$  is also reinforced in the region where  $z > d/2$ , and it is reduced in the region where  $0 < z < d/2$ . That leads to a shift of the inversion point from C to a point P situated between the surface ( $z = 0$ ) and C. The influence of the image increases when the spot size increases ( $d \ll a$ ). OP is then nearly equal to  $OP \approx d/(\epsilon_r + 1)$ , or less (when the algebraic contribution of the minority charges is added).<sup>1</sup>

When the dielectric surface is covered by a thin conducting film (at zero potential), the electric field is zero outside the sample (as expected) and prevents the deflection of the incident beam. Nevertheless, inside the dielectric,  $K = -1$ ,  $F_r$  is reduced (it is zero at the metal/dielectric interface), but  $F_z$  is strongly increased relative to situation (a) at the same metal/dielectric interface where an electric breakdown can occur. Relative to point C, the inversion point P is now shifted closer toward the bulk and closer to the end of the real charge distribution when the incident spot size is increased (Fig. 3b and Ref. 1).

The above analysis can explain the decrease of the Auger signal of  $\text{Na}^+$  ions as well as the increase of the  $\text{K}^+$  ions signal because of the difference of their escape depth values  $\lambda$  relative to the position of the inversion point in the positively charged layer (Fig. 4a).<sup>2</sup>

The same analysis (but applied to the negatively charged region) explains the initial decay of the  $\text{Na}^+$  signal observed in EPMA by Borrom and Hanneman<sup>3</sup> followed by a strong increase occurring when the conducting layer is destroyed (Fig. 4b).

#### *Thin Foils: Situation (c)*

Relative to situation (a), we must now take into account the possible influence of the two series of electric images deduced from the real charge distribution (and then from each other) by symmetry with respect to the two plane interfaces limiting the dielectric foil. The weight of these images is  $K\rho$  and  $K_1\rho$  (and a combination of these values), where  $K_1 = (\epsilon - \epsilon_1)/(\epsilon + \epsilon_1)$  and  $\epsilon_1$  is the dielectric constant of the second surrounding medium.<sup>1</sup>

When the sample is an unsupported thin foil (thickness  $t$ ) bounded on the two sides by a vacuum ( $0 < K = K_1 < 1$ ), the radial component is reinforced by the effects of all the images. In STEM, ( $a \ll t, d$ ), the evolution of  $F$  is the same as that given in Fig. 2b). The evolution of  $F_r$  explains the radial migration of biological species stained by heavy metals salts.<sup>4</sup>

In CTEM ( $a \gg t, d$ ),  $F_r$  also takes noticeable values around  $r = a$  (Fig. 2a), which leads to a possible distortion of the sample through the tensile strength created by the Coulomb forces. Following Fourie<sup>5</sup> but using electrostatic (instead of electrokinetic) arguments, the fact that  $\partial F_r / \partial r$  is maximum for  $r = a$  can also explain the well-known contamination ring observed around the incident spot on the sample.

In SEM on a thin dielectric layer covering a bulk conducting (or doped silicon) substrate,  $F_r(r) = 0$  ( $K_1 = -1$ ) at the metal/dielectric interface or strongly reduced (relative to its value in an infinite medium) when  $K_1 < 0$ ; and so it is for an entrance surface covered by a thin metal film, where  $F_z(0,0)$  is maximum.  $F_z(0,z)$  always changes sign as one goes from the first toward the second interface, but the exact position of the inversion point P depends on the relative values of  $K$  and  $K_1$  and on the spot size. Figure 5 illustrates this analysis for a vacuum/ $\text{SiO}_2$ /Si system and a metal/ $\text{SiO}_2$ /Si system. These predictions are supported by the accumulation of mobile (+) ions observed at the two interfaces of a vacuum/glass/metal system (Fig. 6).<sup>6</sup>

#### *Charge Density-Beam Density Relationship*

The residence time  $\tau$  of the trapped charges is  $\tau = \epsilon/\gamma$ , but it takes quite different values according to whether the beam is turned off or not, because of the strong increase of the electrical conductivity  $\gamma$  under irradiation. This increase is due to many microscopic causes (beyond the scope of the present study) such as electron-hole pair creation during electron bombardment. If the residence time (under irradiation) is not very short,



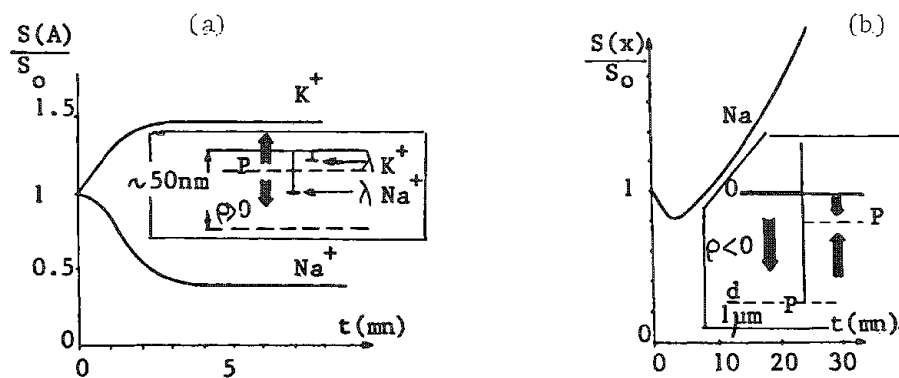


FIG. 4.--(a) Experimental change of signal from  $\text{Na}^+$  and  $\text{K}^+$  ions during Auger analysis of glasses.<sup>2</sup> Opposite behavior of ions with same sign can be explained as follows: inside positive layer  $F_z$  component changes direction at point P very close to surface [ $OP < d/(\epsilon_r + 1)$ , where  $d > 50 \text{ nm}$ ] and information depths for Na and K ions, respectively, obey  $\lambda_{\text{K}^+} < OP < \lambda_{\text{Na}^+}$  (see insert) because  $\lambda \propto E_K^{3/4}$  and  $E_K(\text{Na}) \approx 1000 \text{ eV}$ ;  $E_K(\text{K}) \approx 250 \text{ eV}$ . (b) Experimental change of  $\text{Na}^+$  signal in EPMA.<sup>3</sup> When sample is covered by thin conducting layer,  $F_z(0, z)$  is directed toward end of negative-charge region (see left-hand side of insert) and leads to decay of EPMA signal. When conducting layer is destroyed inversion point is shifted upward [ $OP < d/(\epsilon_r + 1)$ , where  $d \approx 1 \mu\text{m}$ ] and leads to signal increase because of shape of EPMA response function.<sup>1</sup>

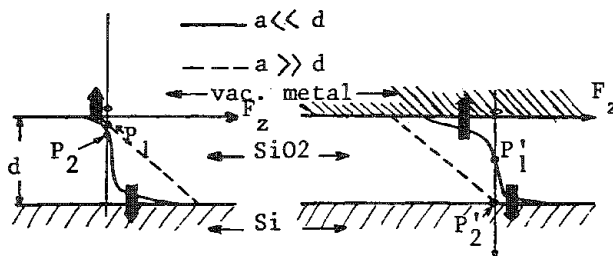


FIG. 5.-- $F_z(z)$  for two systems (vacuum  $\text{SiO}_2/\text{Si}$  and metal/ $\text{SiO}_2/\text{Si}$ ) and two experimental situations ( $t < d \ll a$  and  $a \ll t < d$ , high-resolution SEM);  $F_z$  is maximum at metal/dielectric interface and always changes sign as one goes from one interface to other.

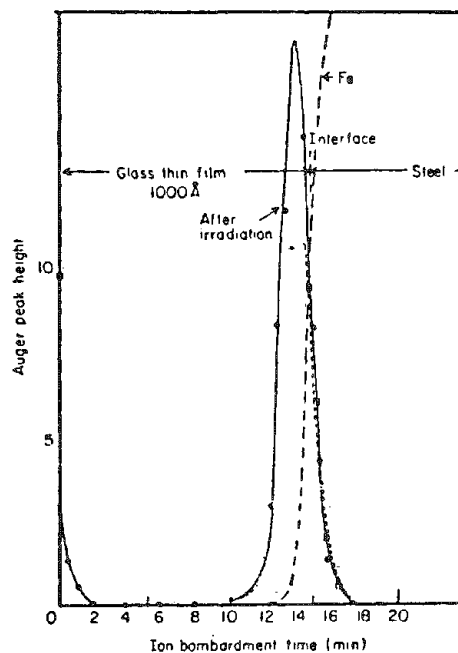


FIG. 6.--Experimental evidence of accumulation of  $\text{Na}^+$  mobile ions at the two interfaces.<sup>6</sup> (See legend of Fig. 5 for explanation.)



the maximum value of the electric field ( $\rho d/\epsilon \approx J_0 t/\epsilon$ ) reaches its disruptive value ( $10^7$  V/cm) in less than 0.1 s even when the beam density is very weak ( $J_0 \approx 1 \mu\text{A}/\text{mm}^2$ ). That means that either the breakdown value or the steady-state value ( $F_{2\text{max}} \approx \rho d/\epsilon \approx J_0 t/\epsilon$ ) are quickly attained under standard experimental situations. Fortunately the second situation is much more probable than the first because of the change of  $\gamma$  (and  $\tau$ ) under irradiation. For instance, polymer electrets such as teflon can be charged in few seconds and keep their charges for years.<sup>7</sup> That also means that even when the residence time (under irradiation) is very short, the electric field strength can take noticeable values.

### Conclusion

The electric images strongly influences the electric field  $F$  induced in insulators by electron bombardment. Nevertheless,  $F_z$ , the normal component of  $F$ , is at its maximum value at the metal/dielectric interface when the entrance surface is covered by a thin metal film.

$F_z(0,z)$  always changes direction as one goes from the surface into the bulk, leading to an accumulation (or a depletion if the majority charges and the mobile ions have the same sign) region for the mobile ions. This simple analysis is consistent with many experimental results that have remained unexplained until now. It can be generalized to charging effects of any kind of bombardment by charged particles.

We hope that it will be useful to define a strategy for reducing the disturbance due to charging effects. The next step is to take advantage of these effects in some specific applications as is done for electrets. Many other applications can be easily imagined.

### References

1. J. Cazaux, *J. Appl. Phys.* 59: 1418-1430, 1986.
2. M. Sfar et al., *J. Physique Sup. C2*: 375-377, 1984.
3. M. P. Borom and R. E. Hanneman, *J. Appl. Phys.* 38: 2406-2407, 1967.
4. R. M. Glasser, in J. J. Hren, J. E. Goldstein, and D. C. Joy, Eds., *Introduction to Analytical Electron Microscopy*, New York and London: Plenum Press, 1979, 423-436.
5. J. H. Fourie, "Electric field effects in contamination and electron beam etching," *SEM/1981 I*, 127-134.
6. F. Ohuchi et al., *Surf. Interf. Anal.* 2: 85-90, 1980.
7. B. Gross, G. M. Sessler, and J. E. West, *J. App. Phys.* 45: 2841-2851, 1974.

## THE CONTROL OF VACUUM-DEPOSITED ULTRATHIN FILMS

J. A. Trahan

The deposition of a thin metal film on electron microscopy specimens results in enhanced contrast of surface features and provides an electrically conducting surface to eliminate charging and deformation of the specimen. With the use of electron microscopes with high resolution comes the need for thinner films to coat the specimen so that the high resolving power of the microscope can be fully exploited. The thin film, whether deposited by sputtering or evaporation, must be as thin as possible and still be continuous and uniform. These requirements can be met by a thin-film deposition controller with a quartz crystal microbalance sensor. With this type of instrument, film growth can be monitored during the deposition to insure accurate results.

### *Theory*

The piezoelectric effect is the foundation of mass sensing by a piezoelectric quartz crystal resonator. Pierre and Jacques Curie observed in 1880 that when pressure is applied to a quartz crystal, an electrical potential is set up between the surfaces. Conversely, an applied voltage causes the crystal to oscillate.<sup>1</sup> The frequency of this oscillation is inversely proportional to the thickness of the quartz crystal.

In 1957 Sauerbrey's work<sup>2</sup> resulted in the theory that for small mass changes caused by the deposition of thin films on the quartz crystal, the frequency of oscillation decreases with added mass according to

$$M_f = M_q (f_c - f_q) / f_q$$

where  $M_f$  and  $M_q$  are the mass of the film and quartz crystal and  $f_c$  and  $f_q$  are the resonant frequency of the quartz crystal with and without the added film, respectively. From the film density  $d_f$ , we obtain the film thickness  $t_f$ :

$$d_f t_f = (d_q t_q / f_q) (f_c - f_q)$$

where  $d_q$  and  $t_q$  are the density and thickness of the quartz crystal. Since the above equation held only for small added mass, attempts were made to extend the usefulness of this formula to greater thicknesses. Studies by Lu and Lewis<sup>3</sup> show that for relatively thick films the acoustic impedance of the added film must be taken into account to relate added mass to the resulting frequency shift:

$$\tan(\pi f_c / f_q) = -(1/Z) \tan(\pi f_c / f_f)$$

where  $Z$  is the ratio of the acoustic impedance of quartz  $Z_q$  to the acoustic impedance of added film  $Z_f$ .

By use of this "Z-match method," as it is sometimes called, the usefulness of the quartz crystal as a microbalance can be extended to larger frequency shifts and thicker deposited films.

### *Discussion*

The quartz crystal resonator (QCR) has found widespread acceptance in many fields of science as a mass sensing device because of its accuracy and relative simplicity. With a QCR mass sensitivities in the range of picograms/cm<sup>2</sup> are possible,<sup>4</sup> and when it is used in conjunction with the correct formula to convert a change in frequency to added mass, the accuracy of the result is better than 3%.<sup>5</sup> In early experiments the mass load on the crystal had to be less than  $2 \times 10^{-3}$  g/cm<sup>2</sup> to achieve linearity. With the Z-match method the mass load can be increased to as much as  $50 \times 10^{-3}$  g/cm<sup>2</sup> with accurate results.<sup>6</sup>

The author is at Inficon Leybold-Heraeus, Inc., East Syracuse, NY 13057.

Use of a QCR for mass determination is not without limitations. Some of these limitations include no material selectivity, limited sensor life, and deviations caused by stress and temperature changes. The limited sensor life becomes a problem when the crystal fails to oscillate before the deposition process is complete, which normally occurs when the added mass causes a frequency shift too large for the crystal to bear. Since the sensor is not material selective, alloys cannot be accurately deposited without special geometric configurations of the deposition chamber.

Perhaps the greatest limitation is the sensitivity of the sensor to temperature changes. To overcome the problem of temperature dependence, various cuts of the quartz crystal have been tested. In virtually all commercially available instruments, crystals are cut along crystallographic lines called AT-cut. Such crystals are relatively insensitive to temperature changes at or near room temperature, and are less susceptible to mechanical stress and interfering modes of oscillation.<sup>7</sup> Other types of crystals include the BT-cut and Y-cut. The microprocessor-based thin-film deposition controller with a quartz crystal as the sensor is a very accurate instrument for determining the thickness of films in situ during the deposition. The basic operation of the instrument depends on the decrease in frequency of oscillation of the piezoelectric quartz crystal as mass is added; from this change in frequency, the rate of deposition and film thickness are calculated.

Not only can the instrument monitor changes in film thickness, it can also maintain a specified rate of deposition and automatically terminate the deposition when a final film thickness is reached. In addition, the instrument can be programmed to increase the source power slowly to prepare the source material for deposition before the actual deposition cycle begins (the "soak" period). When deposition begins the instrument maintains the user-programmed deposition rate by changing the power to the source automatically in a closed-loop fashion as needed. The desired rate is maintained until the user-programmed final film thickness is reached, at which time the instrument returns the source power to an idle phase. By use of these features, a completely automated deposition can be accomplished.

Among the programmable parameters in a thin-film deposition controller are power levels and time settings used to condition the source, density, and Z ratio of the material to be deposited, and a tooling factor. The tooling factor is the amount of evaporant to which the substrate (specimen to be coated) is exposed divided by the amount of evaporant to which the crystal is exposed. For example, if the crystal is positioned in the deposition chamber so that it is exposed to twice as much evaporant as the substrate being coated, the tooling factor is 0.5. Therefore, differences in geometric location of the crystal relative to the substrate can be accounted for. The density of the material being deposited must be programmed to enable the microprocessor to calculate a thickness value from the added mass. The Z ratio is a factor that corrects for the difference in acoustic impedance between the added film and the crystal itself.

The desired coating thickness on a substrate to be examined under an electron microscope is generally 1-10 nm to achieve film continuity as well as adequate resolution and contrast. Thin-film deposition controllers offered commercially can control the deposition rate down to 0.01 nm/s. When the deposition controller is pushed to its lower limit to yield the ultrathin continuous films needed in electron microscopy, many otherwise negligible factors become important: residual gas pressure, temperature of the substrate and crystal, and certain material-dependent factors. At higher residual gas pressure, film granulation is decreased and a thinner continuous film can be formed.<sup>8</sup> However, at higher background pressures unwanted errors in thickness readings are caused by the residual gas impinging on the crystal.

Changes in temperature affect the stability of the quartz crystal responses if it is used outside its temperature range specification. To overcome this problem, sensors are equipped with water-cooling lines to keep the crystal at a constant temperature. The temperature of the surface affects nucleation, film growth, and the ability of the evaporant to adhere to the surface without being re-evaporated. To minimize film growth differences, substrate and crystal must be maintained at comparable temperatures. Certain factors such as stress characteristics and the ability to form thin films without granulation are properties of the material being deposited and must be considered when a coating material is chosen.

Another method used to obtain lower rate control is to manipulate the density parameter. Since density is in the denominator of the conversion from added mass to calculated

thickness, a decrease in the programmed density by a factor of 10 results in a thickness readout of 1/10 of the actual thickness. For instance, with a density of  $8.93 \text{ g/cm}^3$ , the thickness readout resolution would be 0.1 nm. A change in the programmed density to  $0.89 \text{ g/cm}^3$  yields a thickness readout resolution of 0.02 nm.

The low sensor signal associated with low deposition rates dictates a lower limit for the rate set point. However, the crystal sensor can be positioned in the deposition chamber so that it is exposed to a much higher evaporant flux density than the substrate to be coated, which raises the signal and provides better rate control. If the crystal sensor is moved to a position where it is exposed to 4 times the evaporant flux density of the substrate and the tooling factor is left programmed at 1.0, an extra digit of thickness resolution is obtained. Of course, when the sensor is moved closer to the deposition source, the crystal becomes more susceptible to errors caused by thermal effects. Therefore, the sensor must be positioned to increase the rate control capability without the introduction of errors resulting from the source radiation.

The thermal shock on the quartz crystal when it is first exposed to the hot source causes instability and inaccuracy in thickness readings until the crystal stabilizes. The use of a substrate shutter can minimize this effect. After the source has been conditioned, the instrument can enter the deposit phase with the crystal exposed to the source and the substrate shuttered. In this way rate control and stability can be realized before the substrate is actually exposed to the deposition.

### Conclusion

The pertinent factors previously mentioned are interrelated in such a way that each cannot be optimized individually without a detrimental effect on the deposition as a whole. The choice of coating material may be the most important factor, because it dictates the temperature of the source and the process of nucleation, granulation, and film growth. Once this choice has been made, placement of the quartz crystal sensor can be selected to attain better control and a more desirable film. With proper adjustment of all the variables involved thin film deposition controllers with a quartz crystal microbalance can be used to obtain the very thin continuous films that are necessary in electron microscopy.

### References

1. A. W. Czanderna and C. Lu, in *Applications of Piezoelectric Quartz Crystal Microbalances*, Amsterdam: Elsevier, 1984, 2.
2. Chih-shun Lu, "Mass determination with piezoelectric quartz crystal resonators," *J. Science and Technology*, 1975, 578.
3. C. Lu and O. Lewis, *J. Appl. Phys.* 1972, 4385.
4. E. C. van Ballegooijen, Ref. 1, p. 151.
5. P. S. Burggraaf, "Deposition rate monitoring for thin film process control," *Semiconductor International*, October 1981, 4.
6. Chih-shun Lu, Ref. 2.
7. R. P. Riegart, "Getting the most from a quartz crystal monitor," *Research/Development*, 1968, 48.
8. L. Holland, in *Vacuum Deposition of Thin Films*, Fakenham, Norfolk, Gt. Britain: Cox & Wyman, 1956, 259.

## DYNAMIC OBSERVATION OF MAGNETIC DOMAINS IN IRON ALLOYS WITH HIGH-VOLTAGE SEM

Hiroshi Mase, Takashi Ikuta, and Ryuichi Shimizu

Observation of magnetic domains in ferromagnetic materials is very important in the analysis of their properties. Many methods have been utilized in such research. Power loss under an alternating magnetization field, so-called core loss, is very important for example in iron used in transformers cores. But the use of observation of domains for such analysis presents many difficulties.

Only two methods are available for the observation of domains in electric iron products: the colloid figure method and scanning electron microscopy (SEM) with the use of type-II magnetic contrast. The former has an advantage of simplicity, but cannot be used for dynamic observations, a great disadvantage in the analysis of core loss under alternating magnetization at line frequencies. On the other hand, we have techniques of dynamic observation by SEM, but we have had no way to observe periodic phenomena at line frequencies.

The authors have developed a new method for the SEM called "line-sampling stroboscopy,"<sup>1</sup> which enables the observation of periodic phenomena at low frequencies such as line frequencies. We have applied this method to the observation of magnetic domains in some kinds of electric iron. The results are presented below.

### *Experimental*

The mechanism of type-II magnetic contrast in the SEM is shown in Fig. 1. Incident electrons are deflected by a Lorentz force caused by magnetization in magnetic domains. If the direction of magnetization is perpendicular to the sheet plane, there appears a contrast in the backscattered-electron image for the domains of opposite directions of magnetization.

The use of high incident energy provides two advantages. One is that domains in silicon steel products can be seen with high energy. They are coated with forsterite films  $\sim 0.5 \mu\text{m}$  thick to reduce core losses by application of tensile stresses. With more than  $\sim 100 \text{ keV}$  we can get backscattered-electron signals through the coatings. The other advantage is the increase of magnetic contrasts.<sup>2</sup>

The principle of line-sampling stroboscopy is compared with conventional stroboscopy in Fig. 2. We can complete a whole line scan in a time shorter than the period of the phenomena at line frequencies. So we can take a whole line of the video signal for a dynamic observation of a certain phase instead of only one pixel as in the conventional way.

An electronic system specially designed for the operation<sup>3</sup> is attached to a commercial type 200kV SEM (JEOL JSEM-200B). Multiframe display<sup>1</sup> is also available with this system. The specimen holder with a magnetizing yoke is illustrated in Fig. 3. The incident and take off angles are set at  $45^\circ$  and  $60^\circ$ , respectively, to provide high contrast.<sup>2</sup>

### *Results*

High-permeability grain-oriented silicon steel sheet, Fe-Si 3wt%, 0.2 mm thick, oriented to (100)[001], is observed. An image without magnetization is shown in Fig. 4(a); dynamic images with magnetization at 60 Hz obtained by the line-sampling stroboscopy are shown in Figs. 4(b) and (c). Magnetization amplitudes are 2.17 T for (b) and 2.44 T for (c). The white and black stripes indicate stripe-shaped domains of opposite

---

Authors Mase and Shimizu are in the Department of Applied Physics, Osaka University, Suita, 565, Japan; author Ikuta is in the Department of Applied Electronics, Osaka Electro-communication University, Neyagawa, 572, Japan. They wish to acknowledge the support of Masao Yabumoto, Yukio Matsuo, and Tadao Nozawa at the R&D Laboratory III, Nippon Steel Co.

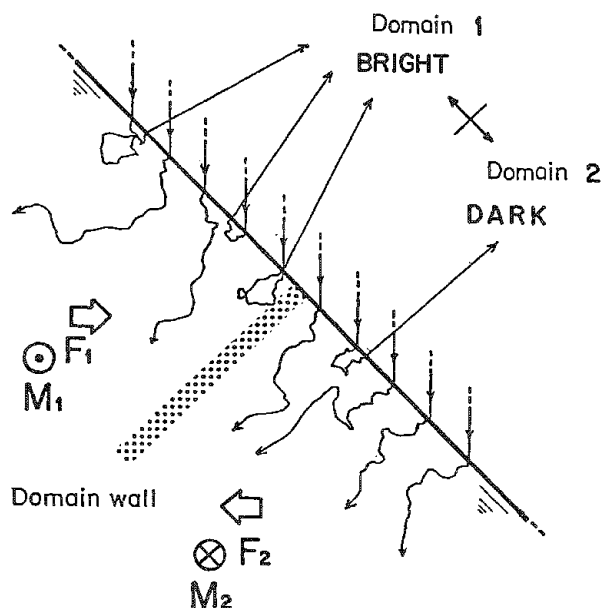


FIG. 1.--Mechanism of Type II magnetic contrast.

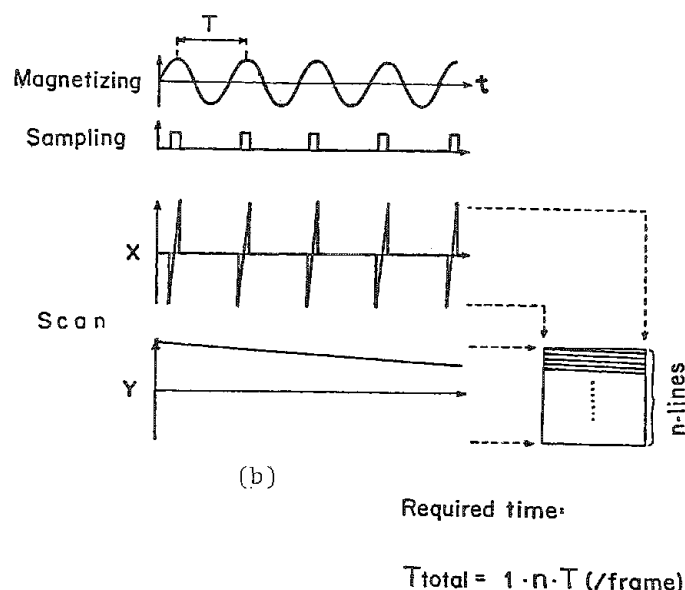
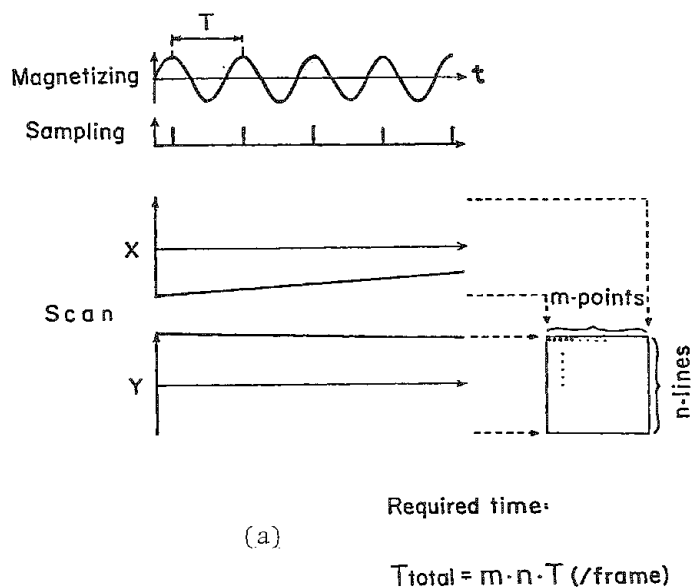


FIG. 2.--Comparison of two methods for dynamic observation for SEM: (a) conventional stroboscopy, (b) line-sampling stroboscopy.

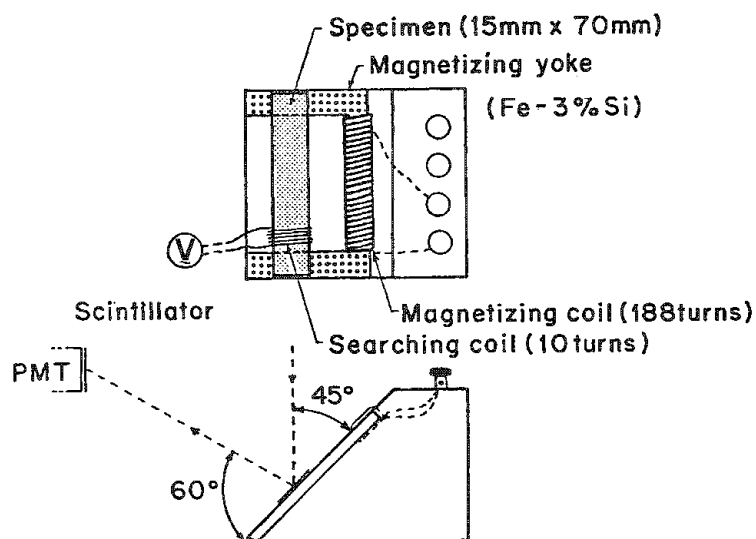


FIG. 3.--Scheme of specimen holder with magnetizing yoke. Amplitude of magnetization is monitored by induction of searching coil.

magnetization directions. There are some branch-shaped patterns in the dynamic images. But domains of such a shape do not really exist. We could see such patterns even without a vertical scan of the probe.

These results suggest that some stripe domains are divided or merged over a long period under strong magnetization. In Fig. 4(b), a black stripe was divided into two at the top, as shown by a branch-shaped domain pattern (point A). The stripe domains to the right of it then moved slowly to make the domain wall spacing uniform, which is shown as the change in the direction of stripes (area B). The branch-shaped pattern at point C indicates that two black stripes were merged into one there. When the stripe domains in area B had moved far enough and domain wall spacing became large, a division of a stripe domain appeared again in the same stripe domain with point A (point A'). As all the images were taken with a 50s vertical scan, this series of phenomena took place at a period of 25 s. In Fig. 4(c), the period becomes shorter ( $\sim 7$  s) under larger amplitude of magnetization.

Such phenomena are caused at some kinds of imperfections. The domain wall E did not move even when the stripe domain was divided at the point A or A', probably due to pinning of the wall caused by imperfections such as precipitations.

Recently, amorphous magnetic ribbons have become popular in electronics use. They have the great advantage of low core losses. But it is not easy to extend the conventional approach for the observations of magnetic domains to them because of their surface roughnesses and low permeabilities. An example of dynamic observation of domains in the commercial product is shown in Fig. 5. As can be seen, very complicated domain patterns often appear and the analysis of the phenomena is much more difficult than for grain-oriented silicon steel.

### Conclusion

The line-sampling stroboscopy is shown to be very useful for the observation of domain walls under alternating magnetization. Some nonperiodic phenomena have been observed with this technique, which may lead to a new approach to a more comprehensive understanding of core-loss mechanisms.

### References

1. R. Shimizu and T. Ikuta, *Appl. Phys. Lett.* 44: 811, 1984.
2. T. Yamamoto et al., *J. Phys.* D8: L113, 1975.
3. R. Shimizu et al., *J. Appl. Phys.* 58: 1606, 1985.

FIG. 4.--Magnetic domain images of grain-oriented silicon steel product: (a) without magnetization, (b) under magnetization of 2.17 T, (c) under magnetization of 2.44 T. Incident energy of primary electron is 150 keV. Numbers in (b) and (c) indicate phases of magnetization wave-forms (in degrees).

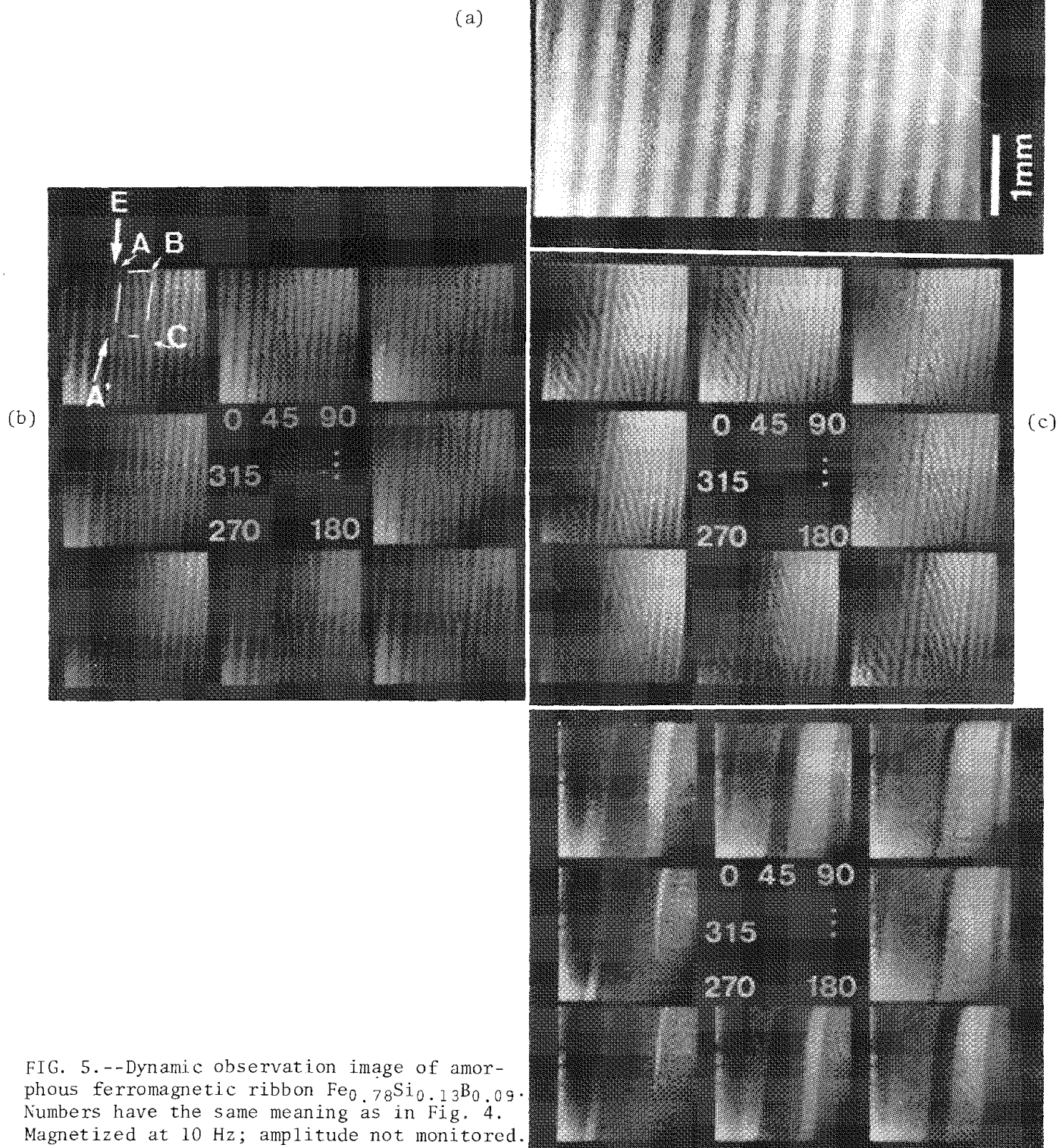


FIG. 5.--Dynamic observation image of amorphous ferromagnetic ribbon  $\text{Fe}_{0.78}\text{Si}_{0.13}\text{B}_{0.09}$ . Numbers have the same meaning as in Fig. 4. Magnetized at 10 Hz; amplitude not monitored.



## Special Biological Symposium: Microscopy and Pathology of Inhaled Toxicants

### ANALYTICAL ELECTRON MICROSCOPY AND PULMONARY TOXICOLOGY: AN OVERVIEW

V. L. Roggli and S. D. Greenberg

Technological advances in analytical electron microscopy have paved the way for new areas of investigation in pulmonary toxicology.<sup>1</sup> The high resolution of conventional transmission electron microscopy when combined with crystallographic data obtained through electron diffraction and chemical composition, as determined by energy-dispersive x-ray analysis (EDXA), allows the investigator conclusively to identify particles that are beyond the resolution of light microscopy. Secondary-electron and backscattered electron imaging with the scanning electron microscope enable one to detect inorganic particles within an organic matrix, and their composition may then be determined by EDXA. Thus routine histologic paraffin-embedded sections may be analyzed for particulate content, and the findings compared with the morphology of routinely stained sections.

Basic to the application of analytical electron microscopy in the study of pulmonary toxicology is a working knowledge of the lung's functional anatomy. The structural subunit of the lung is the secondary lobule; the functional subunit is the acinus. Each secondary lobule is up to 2 cm in greatest dimension and contains three to five acini. The alveolar wall is composed of four cells: Type I and Type II alveolar epithelial cells, capillary endothelial cells, and interstitial cells.<sup>2</sup> The pulmonary interstitial tissues include the visceral pleura, secondary lobular septa, bronchovascular bundles, and alveolar walls. The lung's two main defense mechanisms are clearance and phagocytosis. The former depends on the ciliated respiratory epithelium present in the bronchi and bronchioles, along with the mucous blanket secreted by the goblet cells and bronchial mucous glands.<sup>3</sup> The latter is performed largely by interstitial macrophages and free alveolar macrophages within the nonciliated alveolar ducts and alveoli. Lymphatic drainage of the lungs is also important in the removal of particulates. Lymphatic channels are present in the visceral pleura, bronchovascular bundles, and interlobular septa; however, there are no lymphatics within the alveolar septa or alveolar ducts. The normal turnover time of the lung's epithelial cells is less than 30 days. The Type II alveolar cell is the stem cell of the alveolar epithelium, and the Clara cell is the cell of origin of the bronchiolar epithelium.<sup>4,5</sup>

Analytical electron microscopy has been particularly useful in the investigation of diseases due to asbestos and other mineral fibers. Animal models of asbestos exposure have provided valuable information regarding deposition, clearance, and uptake of asbestos fibers. Short-term inhalation studies have indicated that in the lower respiratory tract, asbestos fibers impact primarily at bronchiolar and alveolar duct bifurcations, where they are either transported to the interstitial tissues by transepithelial migration or are phagocytized by the free alveolar macrophages.<sup>6</sup> Asbestos fibers directly activate complement, an activation that promotes accumulation of macrophages at the sites of fiber deposition. Autoradiographic studies have shown which cells in the various anatomic compartments are stimulated to divide as a result of exposure to fibers. Long-term inhalation studies using transmission electron microscopy with computer-assisted three-dimensional reconstruction and tissue analysis of asbestos content have probed into the relationship between fiber mass, numbers, and size on the one hand and tissue injury due to fiber deposition in the lower respiratory tract on the other. These studies have also shown that long fibers tend to be retained within the lung, whereas short fibers (<5 µm) are more readily cleared.<sup>7</sup>

Interesting findings have similarly resulted from investigation of fiber content in human lung tissues or sputum samples, with a variety of techniques used to extract the inorganic particulates from the organic matrix of the lung. Fibers of certain length and diameter tend to be coated with an iron-protein-mucopolysaccharide layer, probably as a

---

Author Roggli is at the Durham Veterans Administration and Duke University Medical Centers, Durham, NC 27710; author Greenberg is at the Baylor College of Medicine, Houston, TX 77030.

defense mechanism by phagocytic cells (i.e., macrophages) forming the so-called "ferruginous body." Analysis of ferruginous body cores by analytical electron microscopy has shown that virtually all bodies with a thin transparent core are nucleated on amphibole asbestos cores (which account for only 5-10% of asbestos used commercially).<sup>8</sup> The identification of ferruginous bodies isolated from human tissues with nonasbestos fibrous cores has confirmed the observation that not all ferruginous bodies are asbestos bodies. Conversely, asbestos fibers coated with calcium oxalate or calcium phosphate have been identified, so that not all asbestos bodies are ferruginous bodies. In addition, studies of asbestos content in human lungs have shown considerable regional variation in both asbestos body and uncoated fiber concentrations,<sup>9</sup> which may in turn be related to the distribution of pathologic changes within the lung.

Considerably less work has been reported for the nonfibrous particulates, with the possible exception of silica, and this area provides a fertile source of investigation in which analytical electron microscopy is used in combination with other analytical techniques. The particulate content of the human lung in health and in various diseases is just beginning to be explored by means of techniques such as automated image x-ray analysis and quantitative x-ray diffraction of lung-tissue digests. These complementary techniques provide a powerful tool for particle identification, since many nonfibrous particles can only be accurately classified when chemical composition and crystallographic structure are known.<sup>1</sup> The pulmonary toxicologist must keep in mind that the sizes and composition of particles retained in the lung may differ considerably from the size and composition of particles present in ambient air. Deposition in the lower respiratory tract of particles within a certain size range and differential clearance of particles of various chemical composition are important considerations in the ultimate pathologic response to dust inhalation. Experimental animal studies based on various models of exposure will provide valuable information regarding cell kinetics and turnover in response to particulate-induced injury, as well as a better understanding of pathogenetic mechanisms through the analysis of the effects of various chemical mediators of inflammation and tissue injury.

#### References

1. V. L. Roggli et al., "Inorganic particulates in human lung: Relationship to the inflammatory response," in W. S. Lynn, Ed., *Inflammatory Cells and Lung Disease*, Boca Raton, Fla.: CRC Press, 1983, 29-62.
2. E. J. Rosario et al., "The architecture of the alveolar wall: An ultrastructural study in man," *Cardiovasc. Res. Center Bull.* 12: 13-20, 1973.
3. C. W. M. Bedrossian et al., "Bronchial gland measurements: A continuing search for a yardstick," *Exper. Mol. Pathol.* 18: 219-224, 1973.
4. C. Kuhn, "The cells of the lung and their organelles," in R. G. Crystal, Ed., *The Biochemical Basis of Pulmonary Function*, New York: Marcel Dekker, 1976, 3-48.
5. N. M. Smith et al., "The Clara cell: A comparative ultrastructural study in mammals," *Am. J. Anat.* 155: 15-29, 1979.
6. A. R. Brody et al., "Chrysotile asbestos inhalation in rats: Deposition pattern and reaction of alveolar epithelium and pulmonary macrophages," *Am. Rev. Respir. Dis.* 123: 670-679, 1981.
7. V. L. Roggli et al., "Clearance and dimensional changes of crocidolite asbestos fibers isolated from lungs of rats following short-term exposure," *Environ. Res.* (in press).
8. A. M. Churg and M. L. Warnock, "Asbestos and other ferruginous bodies: Their formation and clinical significance," *Am. J. Pathol.* 102: 447-456, 1981.
9. A. Morgan and A. Holmes, "The distribution and characteristics of asbestos fibers in the lungs of Finnish anthophyllite mine-workers," *Environ. Res.* 33: 62-75, 1984.

## INHALATION OF ASBESTOS FIBERS INDUCES MACROPHAGE MIGRATION AND SUBSEQUENT INCORPORATION OF TRITIATED THYMIDINE BY EPITHELIAL AND INTERSTITIAL CELLS

A. Brody, L. H. Hill, and D. B. Warheit

Inhaled asbestos fibers cause interstitial lung disease in humans and animals.<sup>1</sup> Even though that has been known for decades, the biochemical and cellular mechanisms which produce the disease are not at all clear. In an animal model of asbestos-induced interstitial pulmonary fibrosis (i.e., asbestosis), using transmission and scanning electron microscopy in concert with biochemical techniques, we have shown that (1) inhaled asbestos fibers are deposited initially (Fig. 1) and are taken up by the epithelium at bifurcations of alveolar ducts;<sup>2</sup> (2) at these anatomic sites, a clear interstitial lesion develops within 48 h after a 1h exposure and persists for at least 5 mo;<sup>3</sup> (3) pulmonary macrophages are attracted to duct bifurcations through the activation of a complement-dependent chemotactic factor (Fig. 1);<sup>4</sup> (4) 20% of the asbestos originally inhaled is retained in the lung for at least 1 mo;<sup>5</sup> and (5) the retained fibers induce fibroblast injury with consequent production of intracellular microcalcifications and increased interstitial connective tissue.<sup>6</sup> In this report, we present the time course of appearance of the complement-dependent chemotactic factor and show that in the same time-frame there is a dramatic asbestos-induced incorporation of tritiated thymidine into epithelial and interstitial cells of the terminal bronchioles, proximal alveolar ducts, and alveolar duct bifurcations.

Exposure of rats and mice to chrysotile asbestos for 3 or 5 h produced a chemotactic factor for pulmonary macrophages. The factor, concentrated from proteins in lavaged lung fluids, was activated to maximum levels during the first 3 h of exposure, but the macrophage response in situ at duct bifurcations reached a maximum by 24 h post-exposure (Fig. 2). Neither the factor nor the macrophage response were detected 8 days after exposure (Fig. 2). Complement-deficient rats and mice exhibited a depressed macrophage response to asbestos exposure. The chemotactic factor, once activated, is stable after heating to 56 C and has a molecular weight of 14-18 kD. In addition, a quantitative assay for hemolytic complement (i.e., the CH50 assay for C5) in concentrated lavaged lung proteins showed high levels of C5 in sham-exposed animals (Fig. 2). In contrast, immediately after exposure and through the next 8 days, no C5 activity could be detected. Normal levels of C5 returned between 8 and 14 days post-exposure (Fig. 2). These data support the hypothesis that inhaled asbestos activates the 5th component of complement on alveolar surfaces, thus producing C5a, a known chemotactic factor for macrophages. Simultaneous with the activation of macrophage migration, there were 10 to 25-fold increases in the numbers of cells incorporating tritiated thymidine (<sup>3</sup>HTdr) at bronchiolar-alveolar junctions (Fig. 3). These increases were in the Clara cells of the terminal bronchioles and Type II cells of the alveolar surfaces (Fig. 3). Undifferentiated, fibroblast-like cells of the interstitium also incorporated <sup>3</sup>HTdr into DNA after asbestos exposure. Whether or not uptake of <sup>3</sup>HTdr is related to the migration of macrophages and/or secretion of mitogenic factors currently is under investigation.

### References

1. I. J. Selikoff and D. H. Lee, *Asbestos and Disease*, New York: Academic Press, 1978.
2. A. R. Brody et al., "Chrysotile asbestos inhalation in rats: Deposition patterns and reaction of alveolar epithelium and pulmonary macrophages," *Amer. Rev. Resp. Dis.* 123: 670-679, 1981.
3. D. B. Warheit et al., "Pulmonary macrophage accumulation and asbestos-induced lesions at sites of fiber deposition," *Amer. Rev. Resp. Dis.* 129: 301-310, 1984.
4. D. B. Warheit et al., "Inhaled asbestos activates a complement-dependent chemo-attractant for macrophages," *Lab. Invest.* 52: 505-514, 1985.

---

The authors are in the Laboratory of Pulmonary Pathobiology, National Institute of Environmental Health Sciences, Research Triangle Park, NC 27709.

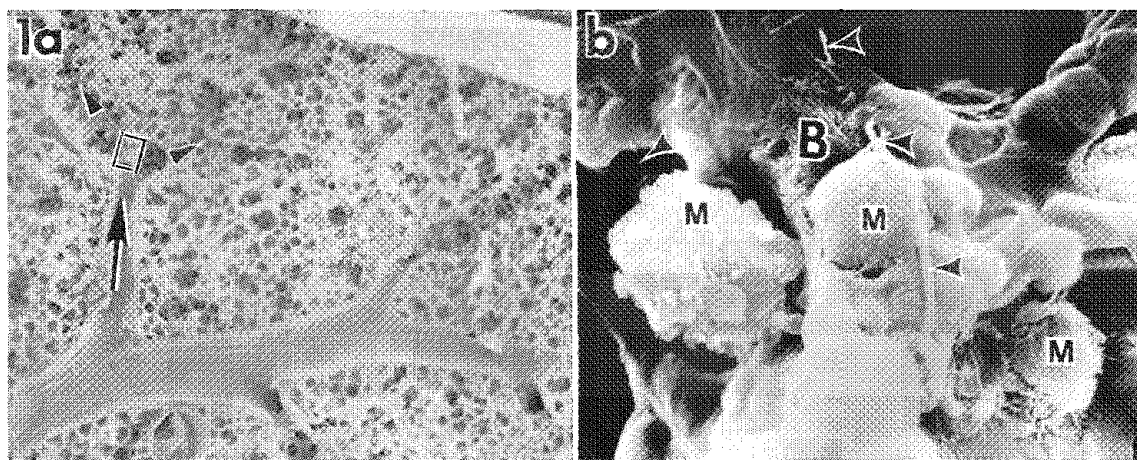


FIG. 1.--(a) SEM micrograph of rat lung tissue illustrating terminal bronchiole (arrow) which leads into alveolar ducts (arrowheads). (Region of first alveolar duct bifurcation is demarcated and magnified in b). (b) First alveolar duct bifurcation (B) is anatomic site where asbestos fibers (arrowheads) are initially deposited and where alveolar macrophages (M) are attracted by complement-dependent factor.

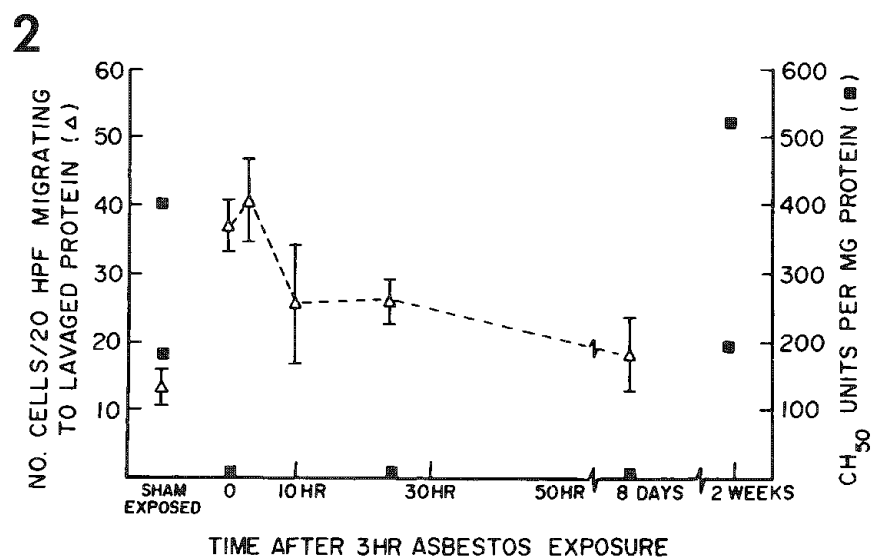


FIG. 2.--Proteins lavaged from lungs of rats were concentrated and tested for chemotactic activity (triangles). Little activity was found in sham-exposed animals, but during the 3h exposure and for several days thereafter, significant chemotactic activity was observed and was shown to be due to activation of C5a.<sup>4</sup> Accordingly, hemolytic assay for fifth component of complement (squares) shows high levels of available C5 in unexposed lavage fluids, but C5 is not detectable after C5a has been cleaved off by asbestos activation. Each data point represents mean value from lavaged protein pooled from at least 5 rats at each time point.

5. V. Roggli and A. R. Brody, "Changes in numbers and dimensions of chrysotile asbestos fibers in lungs of rats following short-term exposure," *Exp. Lung Res.* 7: 133-147, 1984.

6. A. R. Brody and L. H. Hill, "Interstitial accumulation of inhaled chrysotile asbestos fibers and consequent formation of microcalcifications," *Amer. J. Pathol.* 109: 107-114, 1982.

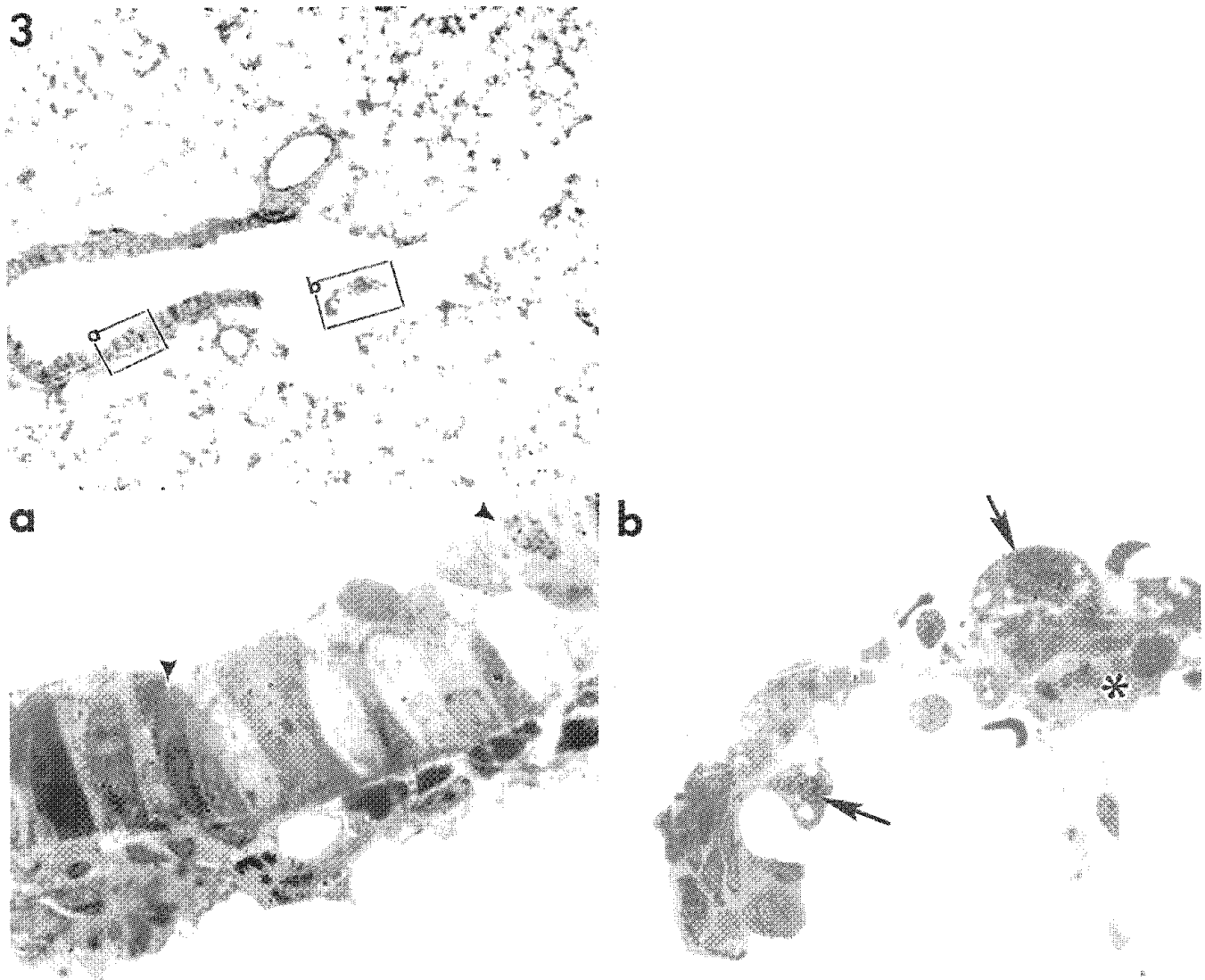


FIG. 3.--Increase in labeled cells after asbestos exposure: micrographs (a) and (b) are magnifications of corresponding regions in top micrograph. Rats injected with tritiated thymidine 4 h before sacrifice showed a dramatic increase in number of labeled cells between 19 and 48 h post exposure. Dividing cells identified were Clara cells of bronchioles (arrowheads), Type II cells (arrows), and interstitial cells (\*) of first alveolar duct bifurcations. Normal labeling patterns were found distal to bifurcation.

## COMPARISON OF SODIUM HYPOCHLORITE DIGESTION AND LOW-TEMPERATURE ASHING PREPARATION TECHNIQUES FOR LUNG TISSUE ANALYSIS BY TEM

J. A. Krewer and J. R. Millette

A wide variety of preparation techniques has been employed for analyses of particles and fibers in lung tissues. Wet digestion by sodium or potassium hydroxide, hydrochloric or nitric acid, hydrogen peroxide, enzymes, and sodium hypochlorite solutions have been tried, as well as ashing by high-temperature furnace and low-temperature oxygen plasma asher.<sup>1</sup> Two of these techniques which have seen recent application and are reportedly free of undesirable effects on inorganic fibers are the sodium hypochlorite digestion (SHD) and the low-temperature oxygen plasma ashing (LTA) technique.<sup>2,3</sup> In the present study we have examined the applicability and comparability of these two methods and the problems associated with them, as well as their effects on fiber and ferruginous body concentrations in adjacent human lung tissue sections.

### *Experimental*

Lung tissue samples were obtained from the Division of Biomedical and Behavioral Sciences, NIOSH, Cincinnati, Ohio. Formalin-preserved lung tissue from a subject exposed to vermiculite was found to contain a high concentration of amphibole fibers as well as numerous ferruginous bodies, and was used for the technique comparisons. In addition, freeze-dried homogenates of "urban" lung tissue were used to assess the applicability of the two techniques to varying tissue amounts and particle concentrations, to permit calculation of analytical sensitivity.

Selected tissue samples were digested by the sodium hypochlorite digestion techniques of Williams et al.,<sup>2</sup> except that readily available Clorox bleach (5.2% sodium hypochlorite) rather than Wright bleach (9.2% sodium hypochlorite) was used for the digestion. Tissue digestions were completed in 15 min or less in all cases. Replicate tissue samples were prepared following the low-temperature ashing procedure of Stettler et al.<sup>3</sup> The final steps for both techniques use carbon-coated filters prepared for transmission electron microscopy (TEM) on chloroform-saturated Jaffe wicks. Nuclepore 0.2µm polycarbonate filters (47 mm in diameter) were used for both techniques, and appropriate reagent blanks were prepared by subjecting empty sample vials to the complete procedures. Asbestos fibers counts never exceeded 2 fibers per 10 grid squares on the blanks.

Analyses of the samples were conducted on a Philips 400T TEM equipped with selected-area electron diffraction and energy-dispersive x-ray analysis capability (Tracor Northern Model 5400). For total fiber counts, a minimum of 100 fibers were counted and sized at 20 500× on three random TEM grids prepared from each filter. Ferruginous bodies were counted and sized at 5500× for 100 grid squares on 3 grids.

### *Results and Discussion*

Several studies have suggested that LTA techniques, though yielding a very residue-free preparation, may be responsible for fiber and ferruginous body breakup, due to tissue dicing and shrinkage of tissue during drying.<sup>4-7</sup> The SHD technique is believed to be less destructive to fibers and ferruginous bodies, but subject to organic interference, which can obscure small fibers. This problem has been noted even when sodium hypochlorite concentrations of up to 12.5% and solvent extractions to remove lipids were employed.<sup>6,8</sup>

Fiber concentrations and average fiber lengths and widths for amphibole fibers are given in Table 1 for four adjacent tissue sections prepared by the two methods. The variability in fiber concentrations includes differences between tissue sections as well as preparation techniques. Morgan and Holmes<sup>5</sup> noted that fiber concentrations in adjacent

---

The authors are at McCrone Environmental Services, Inc., 5500 Oakbrook Parkway, Suite 200, Norcross, GA 30093.

tissue blocks prepared by bleach digestion in their studies varied over nearly an order of magnitude. The concentrations in Table 1 are well within this range, which suggests that either method would yield usable fiber concentration data. Average fiber lengths do not clearly reflect fiber breakage for the LTA technique because the variation is large. Average fiber widths are comparable for both techniques.

The effect of the different techniques on ferruginous bodies is pronounced, as shown in Table 2. Although total ferruginous body concentrations again vary between tissue sections, the average length of ferruginous bodies in SHD preparations (29  $\mu\text{m}$ ) is double the length of bodies found in LTA preparations (14  $\mu\text{m}$ ). The concentration of bodies larger than 10  $\mu\text{m}$  and especially those larger than 20  $\mu\text{m}$  is higher in the tissue sections prepared by SHD (Fig. 1). Ferruginous bodies in SHD preparations commonly exhibited the well-known "clubbed" ends, and bodies in the LTA preparations were often fragments or obvious end pieces of larger bodies (Fig. 2), although for counting purposes these were considered ferruginous bodies.

Freeze-dried homogenates of human lung tissue were used to compare the amounts of tissue which could be prepared with the two techniques, which would avoid the calculation of wet/dry ratios that may be a source of error with the SHD technique.<sup>6</sup> It was found that the LTA technique could easily process 50 mg of dry tissue for deposition on a 47mm-diameter filter, but tissue weights greater than 10 mg resulted in increasing organic residue interference with the SHD technique. That was true even when the sodium hypochlorite digestion proceeded swiftly and apparently completely. The calculated one-fiber sensitivity for 10 grid squares in this case was in the range of  $1.6 \times 10^6$  fibers/g for the SHD technique and  $3.2 \times 10^5$  fibers/g for the LTA technique. The sensitivity of either method may not present a problem in working with high fiber levels, and obviously varies with tissue condition and type, yet the LTA technique could offer an advantage when one is dealing with the lung fiber concentrations found in persons not occupationally exposed to asbestos. For the detection and counting of ferruginous bodies at low magnification, the sensitivity of the two methods can be comparable, as these large structures are not likely to be obscured by moderate levels of organic residue. The LTA technique involves considerable time for drying and ashing the sample, but little time in actual preparation, whereas the SHD technique is "user-intensive" and depends more on technician experience to avoid complications at each step of the procedure. Considerable care must also be exercised in the preparation, storage, and filtration of the necessary reagents for the SHD technique.

### Conclusions

Both tissue preparation techniques can result in usable samples if properly carried out, and for fiber concentration analyses, the intra-lung variation may be greater than that found between methods. For analyses of ferruginous bodies, however, the SHD technique offers the advantage of a gentler digestion which preserves more bodies intact. For large-scale tissue surveys, the LTA technique would be more adaptable to a wide range of fiber concentrations and require less actual preparation time.

### References

1. F. D. Pooley, in Hans Weill and M. T. Warwick, Eds., *Occupational Lung Diseases--Research Approaches and Methods*, New York: Marcel Dekker, 1981, 189-235.
2. M. G. Williams Jr. et al., "A procedure for the isolation of amosite asbestos and ferruginous bodies from lung tissue and sputum," *J. Tox. Environ. Health*, 1982, 627-637.
3. L. E. Stettler et al., "Particle content of human lungs," *Proc. 43rd Annual Mtg. EMSA*, 1985, 116-119.
4. A. Morgan and A. Holmes, "The enigmatic asbestos body: Its formation and significance in asbestos-related disease," *Environ. Res.* 38: 283-292, 1985.
5. A. Morgan and A. Holmes, "The distribution and characteristics of asbestos fibers in the lungs of Finnish anthophyllite mine-workers," *Environ. Res.* 33: 62-75, 1984.
6. B. Glyseth et al., "Analysis of inorganic fiber concentrations in biological samples by scanning electron microscopy," *Scand. J. Work. Environ. Health* 7: 101-108, 1981.
7. B. Glyseth and R. Bannan, "Topographic and size distribution of asbestos bodies in exposed human lungs," *Scand. J. Work. Environ. Health* 7: 190-195, 1981.
8. A. J. Rogers, "Determination of mineral fibre in human lung tissue by light microscopy and transmission electron microscopy," *Ann. Occup. Hyg.* 28: 1-12, 1984.

TABLE 1.--Amphibole fiber concentrations in four adjacent tissue sections prepared by SHD and LTA techniques.

Sample	Fibers per g $\times 10^8$	95% CI	Avg.Length ( $\mu\text{m}$ )	Avg.Width ( $\mu\text{m}$ )
LTA #1	7.1	2.7	3.3	0.36
LTA #2	4.6	0.9	3.0	0.29
SHD #1	2.5	0.6	5.0	0.35
SHD #2	7.9	5.6	3.5	0.25

TABLE 2.--Ferruginous body concentrations in four adjacent tissue sections prepared by SHD and LTA techniques.

Sample	F.B. per g $\times 10^6$	95% CI	Avg.Length ( $\mu\text{m}$ )	Avg.Width ( $\mu\text{m}$ )
LTA #1	7.6	2.0	13.9	0.61
LTA #2	6.5	1.9	14.3	0.59
SHD #1	5.8	1.8	29.7	0.46
SHD #2	7.8	2.4	28.5	0.57

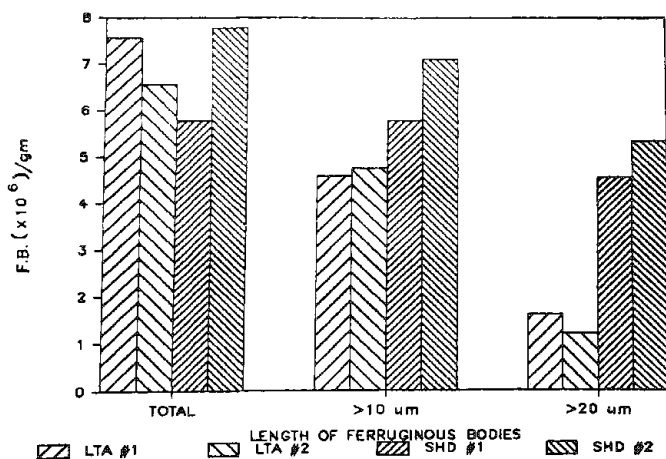


FIG. 1.--Ferruginous body lengths in adjacent tissue samples prepared by LTA or SHD.

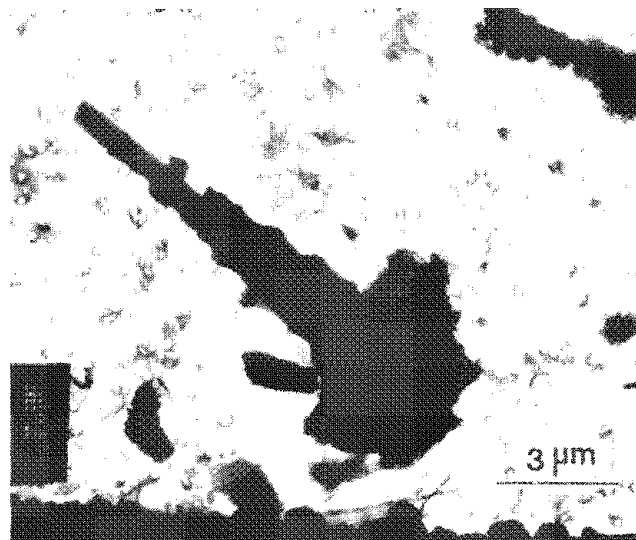


FIG. 2.--TEM micrograph of ferruginous body fragment in sample prepared by LTA.



## PARTICLE CONTENTS OF URBAN LUNGS: AN UPDATE

L. E. Stettler, S. F. Platek, R. D. Riley, D. H. Groth, and J. P. Mastin

Scanning electron microscopy (SEM) and energy-dispersive x-ray analysis (EDXA) have been used by many investigators to study the particle contents of human lungs. Much of this work has been performed on specimens with lung disease with the object of relating the composition and concentration of particles present in the lungs to the disease. With a few notable exceptions,<sup>1,2</sup> a major factor missing from past work have been data from typical "normal" lungs with which the analyses of the diseased lungs could be compared. Because of this paucity of data from typical lungs with no overt pneumoconioses, a study is being performed at NIOSH in which the particle contents of a large group of urban lungs from the Cincinnati area are being determined. Earlier preliminary reports from the analyses of 33, 35, and 48 of these lung specimens have been reported elsewhere.<sup>3-5</sup> An additional 27 lungs have now been analyzed. In this report, the data from all 75 lungs analyzed to date are summarized and discussed.

### *Sample Group*

A group of 100 lungs from residents of the Cincinnati urban area was collected in 1970-71. These specimens consisted of whole left lungs for each subject. These lungs were homogenized, freeze-dried, and have been extensively analyzed for trace metal contents by bulk analytical procedures.<sup>6</sup>

In 1984, when the current study was begun, lung homogenate samples for 92 of the original subjects remained. These 92 subjects were about evenly divided between men and women, blacks and whites. Ages ranged from 23 to 96 years, with a median age of 66 years. Thirty-seven of the subjects were nonsmokers; the remaining 55 were light to heavy users of tobacco. The range of occupations represented included foundry workers, machinists, farmers, salesmen, domestics, clerical workers, and homemakers. The subjects' deaths were from natural causes, mostly chronic degenerative conditions of advancing age. A hospital autopsy report and a personal/occupational/social history for each subject were available for analysis. Hematoxylin and eosin stained sections from the right lungs of approximately 80% of the subjects were also available for analysis.

### *Experimental Methods*

A small portion (0.1-0.2 g) of the freeze-dried lung homogenate for each subject was processed separately for microanalysis. This processing included low-temperature ashing of the specimen followed by sonication of the residue for 15 min in an ultrasonic bath, and finally filtration of an aliquot of the ash onto a 0.1µm pore size, 25mm-diameter Nuclepore® filter. A glassware blank was also prepared for each specimen. A complete description of the tissue processing procedure is given elsewhere.<sup>3-5</sup>

The filter preparations were analyzed in the SEM, which was equipped with a Kevex 7000 EDXA system and a LeMont Scientific DA-10 image analyzer using the backscattered electron image. For each specimen, a minimum of 1000 exogenous particles in a minimum of 20 randomly selected fields of view at a magnification of 1000× were sized and analyzed for 31 elements, with an x-ray spectrum acquire time of 5 s. Each analyzed particle was categorized by the image analyzer using a chemistry definition file which classifies the particles based on their major elemental components and their net fractional x-ray intensities. The list of elements analyzed and an extensive description of the chemistry definition file are given elsewhere.<sup>3</sup> Following completion of the x-ray analyses for each lung and its corresponding blank, the image analyzer calculated the net total exogenous particle concentration and concentration for each particle category from the particle density on the final filter preparation and the dry lung weight.

---

The authors are with the Division of Biomedical and Behavioral Science, National Institute for Occupational Safety and Health, Cincinnati, OH 45226.

## Results

The results for over 90 000 individual particle analyses performed for the 75 lungs analyzed to date are summarized in Table 1. The distribution of total exogenous particle concentrations for the 75 lungs is given in Fig. 1. The total concentrations for the three lungs in the  $>2300 \times 10^6$  particles/g category shown in Fig. 1 were 2306, 3009, and  $3127 \times 10^6$  particles/g.

TABLE 1.--Summary of exogenous particle data from 75 urban lungs.

Particle Type	Mean	Standard Deviation	Min.	Max.	Median
Total Exogenous (millions/g dry lung)	613	601	107	3127	417
% Silica	19.8	7.0	8.9	40.8	19.3
% Al Silicate	36.0	10.7	13.9	60.8	36.0
% Mg Silicate	2.3	2.8	0.0	17.1	1.4
% Iron Oxide-like	7.4	5.9	0.7	34.3	5.9
% Rutile-like	8.4	7.7	0.6	38.6	5.7
% Alumina-like	0.7	1.2	0.0	8.7	0.4
% Exog.-Endog. Comb.	7.5	7.3	0.6	35.6	4.7
% Silicon Rich	3.1	2.1	0.7	12.9	2.6
% Iron Rich	4.1	1.9	0.9	11.0	3.8
% Titanium Rich	2.7	1.0	0.4	5.9	2.6
% Other Al Silicates	1.3	0.6	0.0	3.1	1.2
% Alum. Rich	4.0	2.2	0.5	10.4	3.5
% Miscellaneous	2.7	1.2	0.6	7.7	2.5

The median circular area equivalent diameters for the analyzed exogenous particles ranged from 0.38 to 0.99  $\mu\text{m}$ . The distribution of these median diameters is shown in Fig. 2. In general, the median diameters for the major particle classes were similar to the overall total exogenous median diameter for each lung, with two major exceptions. Particles classified as rutile-like had median diameters consistently smaller than the overall exogenous median diameter for each lung. Particles classified as magnesium silicates generally had larger diameters than the overall exogenous median diameter.

The most frequently encountered particle species in the lung samples were those classified as aluminum silicates, silica, and rutile-like ( $\text{TiO}_2$ ). The percentage distributions for these three categories plus particles classified as iron oxide-like and magnesium silicates are shown in Figs. 3-7.

## Discussion

In terms of overall particle composition, all the analyzed lungs contained the same major particle types. Particles considered as individual entities, i.e., those classified as aluminum silicates, silica, rutile-like, iron oxide-like, magnesium silicates, and alumina-like, accounted for, on the average, 75% of the exogenous particle burden in the lungs. Particles in the remaining categories may be either individual species of unknown mineralogic identity or aggregates. Particles in the exogenous-endogenous combination category are thought to be either aggregates of exogenous and endogenous particles or exogenous particles coated with endogenous components, usually iron and phosphorus.

Aluminum silicates were the most frequently encountered species in 60 of the 75 lungs, the second most often seen category in 14 lungs, and the third most often seen category in the one remaining lung. These aluminum silicates typically fell into two major subclasses: those which also contained a peak for potassium and sometimes iron, and those which contained no peaks other than aluminum and silicon. The potassium-containing particles are most likely either mica or a feldspar. The "Pure" aluminum silicates are presumably kaolinite. Other common subclasses of the aluminum silicate category included particles which contained peaks for sodium and/or calcium. These particles, which were

seen in most lungs although at very low concentrations, are most likely plagioclase feldspars.

Particles classified as silica were the number one species in six lungs, the second most often encountered species in 48 lungs, and the third most often found in 16 lungs. Particles classified as rutile-like were the number one category in four lungs, the second most frequently seen species in three lungs, and the third-ranked particle in 23 lungs.

The data for the iron oxide-like and the exogenous-endogenous combination categories are very interesting. Particles classified as iron oxide-like were the number one category in two lungs; exogenous-endogenous combination particles were the most frequently seen particle type in three lungs. In most of the lungs having high iron oxide-like particle concentrations, there were correspondingly high concentrations of exogenous-endogenous combination particles. This result suggests to us that some of the iron oxide-like particles may be of endogenous origin. Of concern specifically are particles for which iron accounts for at least 90% of the total net x-ray intensity and also contain no phosphorus. These phosphorus-free, iron oxide-like particles have been arbitrarily classified as exogenous in the chemistry definition file used in this work. Churg and Wiggs<sup>2</sup> have considered such particles as endogenous.

The lungs thus far analyzed in this study are typical for subjects from an urban area who have terminal illnesses. However, there is a distinction between these urban lungs and normal lungs. These lungs are not normal since there are disease processes present in most of them. However, in most cases, these processes are typical considering the age and health of the subjects in question. In none of these lungs was there evidence of an overt pneumoconiosis.

A complete statistical analysis of the data obtained from these lung analyses has not been performed at this time. Statistical correlations, if any, between total exogenous particle concentrations and individual particle class concentrations with parameters such as age, smoking history, sex, and occupation (including dust exposure) will be determined when all 92 lung specimens have been analyzed.

Very little data concerning the exogenous particle concentrations in lungs with no pneumoconioses have been published. Recently, Churg and Wiggs<sup>2</sup> reported data on the mineral contents of 28 lungs, 14 with lung cancer and 14 controls. There was no history of occupational or other dust exposure for any of the 28 subjects. The average lung particle content determined by Churg and Wiggs for these lungs was  $525 \pm 369 \times 10^6$  particles/g of dry lung for the cancer subjects, and  $261 \pm 175 \times 10^6$  particles/g for the controls. The average lung particle content determined in this work is  $613 \pm 601 \times 10^6$  particles/g of dry lung. The fact that the overall average determined in this work is higher than that determined by Churg and Wiggs is not surprising, since a number of the subjects in this study were known to work in dusty environments. Furthermore, as was discussed earlier, phosphorus-free, iron oxide-like particles were considered exogenous in this work, whereas Churg and Wiggs considered such particles to be endogenous. The major particle types seen in both studies, however, were very similar; i.e., various silicates and silica.

### Conclusions

The mean exogenous particle concentration found in 75 lungs from the Cincinnati urban area was  $613 \pm 601 \times 10^6$  particles/g of dry lung, with a range of  $107\text{--}3127 \times 10^6$  particles/g. The particle compositions found in these lungs were very similar. Major particle types found include various aluminum silicates, silica, iron oxide, and rutile. When completed, the analysis data from the 92 lung sample group will serve as baseline data for lungs with no overt pneumoconioses against which the particle contents of diseased lungs can be compared.

### References

1. J. L. Abraham and B. R. Burnett, "Quantitative analysis of inorganic particulate burden *in situ* in tissue sections," *SEM/1983* II, 681-696.
2. A. Churg and B. Wiggs, "Mineral particles, mineral fibers, and lung cancer," *Environ. Res.* 37: 364-372, 1985.
3. L. E. Stettler et al., "Particulate concentrations in urban lungs," in J. Shel-

burne and P. Ingram, Eds., *Microprobe Analysis in Medicine*, New York: Hemisphere Publishing Corp. (in press).

4. L. E. Stettler et al., "Particle contents of human lungs," *Proc. 43rd Mtg. EMSA*, 1985, 116-119.

5. L. E. Stettler et al., "Particle contents of human lungs," in S. Basu and J. R. Millette, Eds., *Electron Microscopy in Forensic, Occupational, and Environmental Health Sciences*, New York: Plenum (in press).

6. D. V. Sweet et al., "Chemical and statistical studies of contaminants in urban lungs," *Am. Ind. Hyg. Assoc. J.* 39: 515-526, 1978.

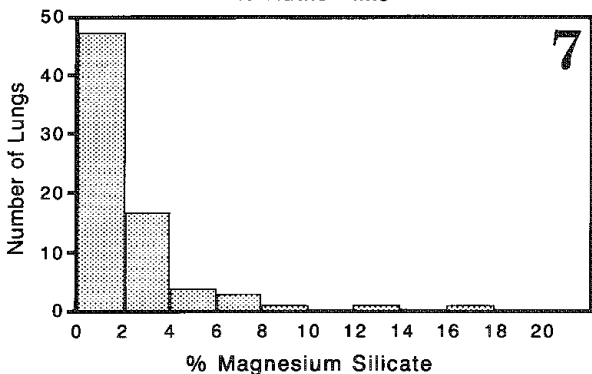
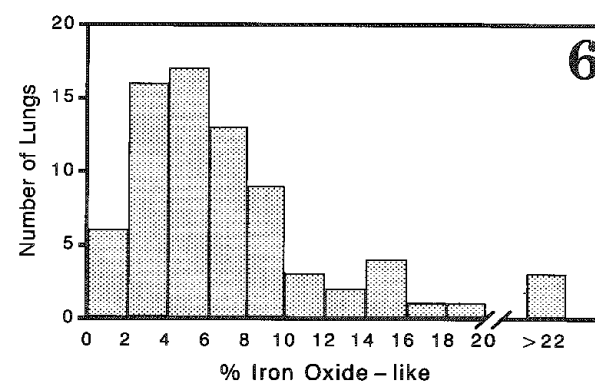
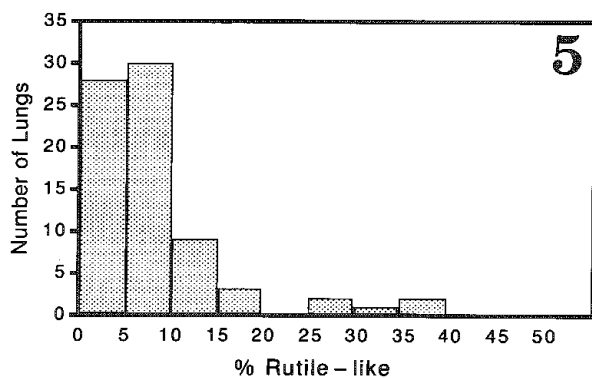
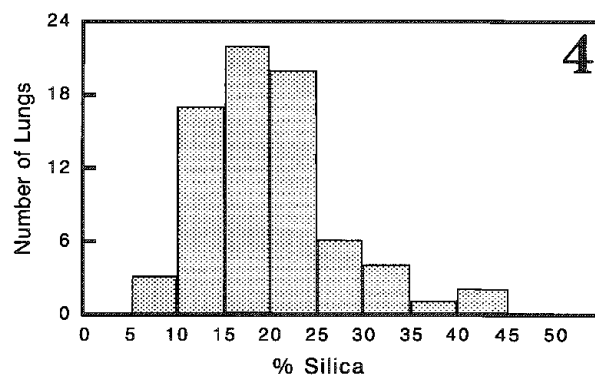
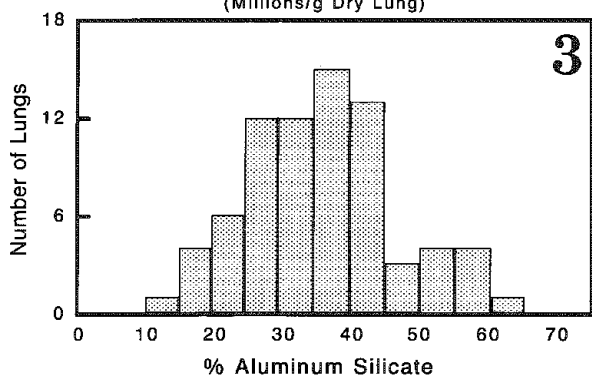
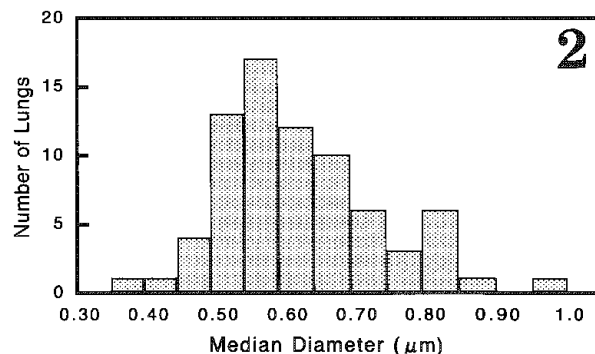
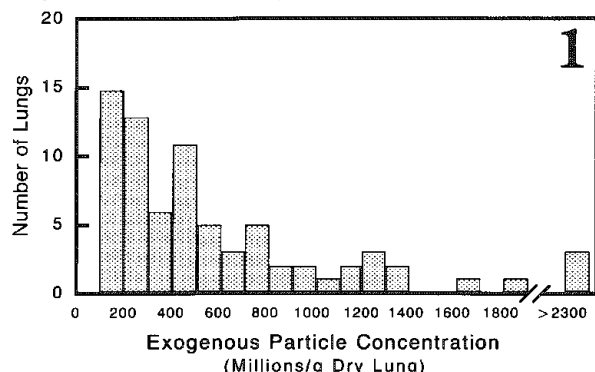


FIG. 1.--Total exogenous particle concentration distribution for 75 urban lungs.

FIG. 2.--Median circular area equivalent diameter distributions for exogenous particles for 75 urban lungs.

Percentage distributions for 75 urban lungs:

FIG. 3.--Aluminum silicate.

FIG. 4.--Silica.

FIG. 5.--Rutile-like.

FIG. 6.--Iron oxide-like.

FIG. 7.--Magnesium silicate.

## PARTICULATE ANALYSIS SAMPLES FROM AMOSITE WORKERS

R. F. Dodson

The Tyler Asbestos Workers' Program (TAWP) was established in 1974 by the National Cancer Institute. This program, as well as subsequent programs, has enabled The University of Texas Health Center at Tyler to maintain a continuing surveillance of a cohort of amosite asbestos workers.

The air quality to which the workers were exposed was quantified by several testing agencies and was found to have a high asbestos content.<sup>1</sup> Other dusty components to which the workers were exposed included man-made fibers, diatomaceous earth, and certain binding components.

Data obtained from the TAWP now include nearly 15 000 sputum specimens examined by light microscopy for both cytopathology and for the presence of ferruginous bodies. The findings have indicated that ferruginous bodies in sputum are a marker of significant exposure to amphibole asbestos.<sup>2</sup> However, the presence or absence of ferruginous bodies in sputum is highly variable, which indicates a high specificity but relatively low sensitivity.

Particulate analyses on sputum samples collected during the cytopathology screening facet of the program, or on lung tissue samples collected at surgical resection or autopsy, have been done by use of combined light and analytical electron microscopy techniques. Depending on the appropriateness for a given sample, the analysis included various digestion techniques and/or tissue sectioning.

Digestion techniques using the standard sodium hypochlorite bleach approach<sup>3</sup> are found to be of limited value for digesting sputum and to varying degrees in dissolving tissue due to the presence of organic components that often mask the particulates in the sample (Fig. 1).

Some sputa samples containing ferruginous bodies were collected from high-yield patients and embedded for thin sectioning (Fig. 2). Ultrastructurally, the cores of these bodies were confirmed to be of the amosite form. The thin-sectioned pellets also confirmed the presence of various particulates as well as uncoated asbestos fibers within the macrophages.

Lung tissue, treated with a modified bleach digestion procedure,<sup>4</sup> yielded preparations free of obscuring organic material, so that accurate quantitation of the particulate load was possible.

A wide diversity existed in ferruginous-body content between sample sites even when they were adjacent. A comparison of the "coated" fiber with the uncoated fiber burden from the same area confirmed the lack of any constant ratio. Furthermore, nonasbestos fibers existed in all of the tissue samples, in some cases in large numbers.

Since varying numbers of ferruginous bodies are nonanalyzable in any sample due to total surface coating, a study was carried out that involved removal of the coating with oxalic acid digestion<sup>5</sup> and characterization of the core material as to elemental as well as physical characteristics (Fig. 3).

The cores were found to be amosite asbestos comparable to the material used in the plant. Although length has been recognized as a factor in determining which fibers tend to become coated, width apparently also plays an important role as a criterion in these bodies, since many uncoated fibers of appropriate length but of very thin diameter were found in the samples.

Since tissue from two workers contained uncoated asbestos fibers of the appropriate length and number but undetected ferruginous bodies, it appeared that individual variance in the capability of forming ferruginous coatings exists in humans, as has been noted to exist in some animal specimens.

---

The author is at The University of Texas Health Center at Tyler (Department of Cell Biology and Environmental Sciences), Tyler, TX 75710.

## References

1. G. A. Hurst et al., "The Tyler Asbestos Program: I. A medical surveillance model and method," *Arch. Environmental Health*, 432-439, 1979.
2. J. W. McLarty et al., "The clinical significance of ferruginous bodies in sputa," *J. Occupational Medicine*, 92-96, 1980.
3. M. J. Smith and Bernard Naylor, "A method of extracting ferruginous bodies from sputum and pulmonary tissue," *American Journal of Clinical Pathology*, 250-254, 1972.
4. M. G. Williams et al., "A procedure for the isolation of amosite asbestos and ferruginous bodies from lung tissue and sputum," *J. Toxicology and Environmental Health*, 627-638, 1982.
5. R. F. Dodson et al., "Method of removing the ferruginous coating from asbestos bodies," *J. Toxicology and Environmental Health*, 959-966, 1983.

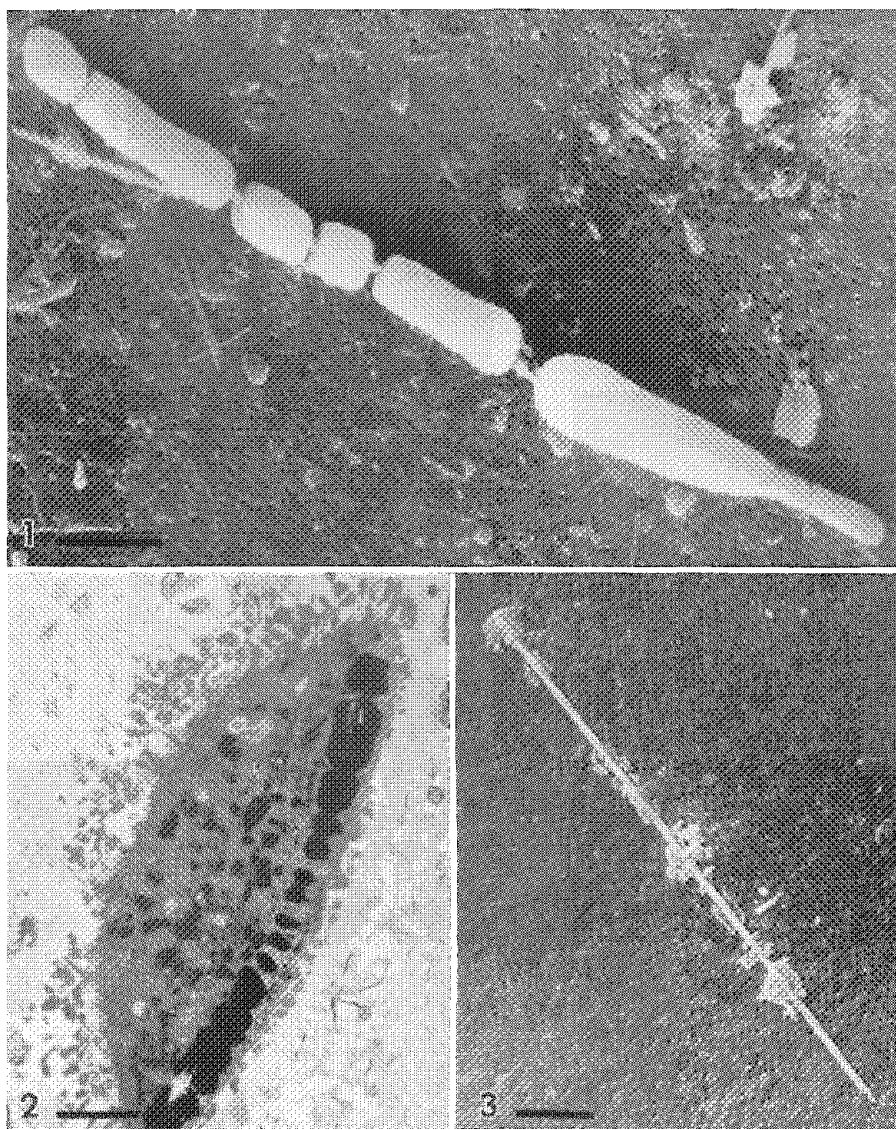


FIG. 1.--Ferruginous body and uncoated fibers from digested lung tissue from amosite worker (bar = 5  $\mu$ m).

FIG. 2.--Ferruginous body as seen within macrophage found in sputum of asbestos worker (bar = 1  $\mu$ m).

FIG. 3.--Asbestos core material from partially cleaned ferruginous body (bar = 5  $\mu$ m).

## THE ROLE OF FIBER NUMBER, SIZE, AND MASS IN ASBESTOS-INDUCED LUNG DISEASE

K. E. Pinkerton and V. L. Roggli

Inhalation of asbestos is known to cause pulmonary fibrosis.<sup>1</sup> However, the roles which fiber size and number play in the development of fibrosis are controversial. It has generally been accepted that long fibers ( $>10\text{ }\mu\text{m}$ ) are more injurious and thus, more fibrogenic than short fibers.<sup>2</sup> Recent work has suggested that short fibers ( $<10\text{ }\mu\text{m}$ ) can also cause fibrosis.<sup>3</sup> Furthermore, the amount of fibers by mass, regardless of size, may also be important in the fibrogenic response.

### *Materials and Methods*

To address these questions, Fischer 344 rats were exposed by inhalation to chrysotile fiber preparations of varying size distributions (Table 1). Exposure to asbestos ranged from 1 day (Jeffrey chrysotile only) to one year. Exposures were for 7 h per day, 5 days a week. Animals exposed for a single day were examined following one day and one year of recovery. Animals chronically exposed to asbestos were examined following 3 and 12 months of exposure and one year postexposure. The presence of asbestos in all regions of the lung was measured as the amount of silica in ashed lung tissue. The volume of asbestos in the alveolar region of the lungs was determined morphometrically by systematic sampling of micrographs containing fiber profiles photographed from random sites in the lungs.<sup>4</sup> The degree of pulmonary injury during and following fiber inhalation was determined by light and electron microscopic morphometry. The number, size, and mass of asbestos present in the lungs were determined (only for animals exposed to Jeffrey chrysotile) by the examination of fibers recovered from digested lung tissues using scanning electron microscopy.

### *Results*

As shown in Fig. 1, the chrysotile preparations used in this study demonstrated a similar degree of lung deposition following 3 months of exposure, but had different patterns of fiber deposition, retention, and/or clearance with progressive exposure. Asbestos within the alveolar regions of lung was noted following 3 months of exposure for all three preparations (Fig. 2); however, the long-term retention of asbestos (one year postexposure) within this region was significantly greater for Jeffrey and UICC B chrysotile than for Coalinga chrysotile. The primary difference between Coalinga chrysotile compared to the Jeffrey and UICC B preparations was a markedly greater diameter for fibers more than  $10\text{ }\mu\text{m}$  in length (Table 1). These thicker fibers are probably less likely to reach the alveolar airspaces. Differences in lung injury and fibrosis as noted by changes in the interstitial matrix volume were seen both during and following exposure to each fiber preparation (Fig. 3). These differences correlated well with the relative fiber burden in the lungs for each timepoint examined (Figs. 1 and 2). The presence of fibers was commonly associated with regions of marked collagen deposition (Fig. 4). Asbestos exposure for a single day followed by one year of recovery demonstrated that clearance of fibers from the lungs was most notable for fibers less than  $10\text{ }\mu\text{m}$  in length (Table 2). Expressed as an absolute number of fibers (calculated from Table 2), 90% of all fibers less than  $10\text{ }\mu\text{m}$  long were cleared, whereas less than 15% of fibers greater than  $10\text{ }\mu\text{m}$  in length were cleared during the postexposure year. However, numerous short fibers were also retained in the lung and were primarily found in the noncellular portions of the interstitium.

### *Conclusion*

Fiber number, size, and mass each appear to influence both the extent and degree of pulmonary fibrosis and are associated with the internalization of asbestos in the lung

---

The authors are at the Department of Pathology, Duke University Medical Center, Durham, NC 27710. This work was supported in part by a grant from the American Lung Association.

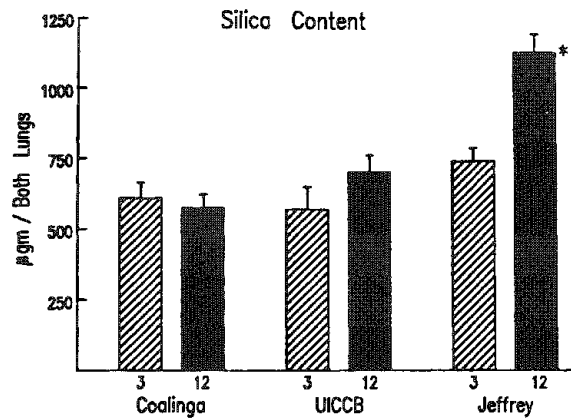


FIG. 1.--Silica content within alveolar and nonalveolar regions of both lungs following exposure for 3 months (hatched bars) and 12 months (black bars) to each type of chrysotile asbestos. Asterisk denotes statistically significant difference ( $p < 0.05$ ) from all other timepoints and treatment groups.

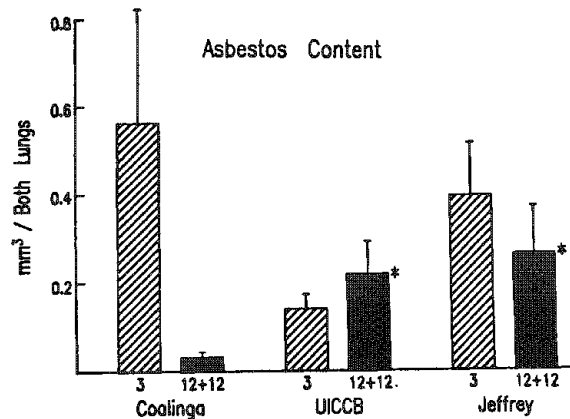


FIG. 2.--Asbestos fiber content within alveolar region of both lungs following exposure for 3 months (hatched bars) and 12 months after 1 year of exposure (black bars) to each chrysotile preparation. Asterisks denote  $p < 0.05$  compared to same timepoint for animals exposed to Coalinga chrysotile.

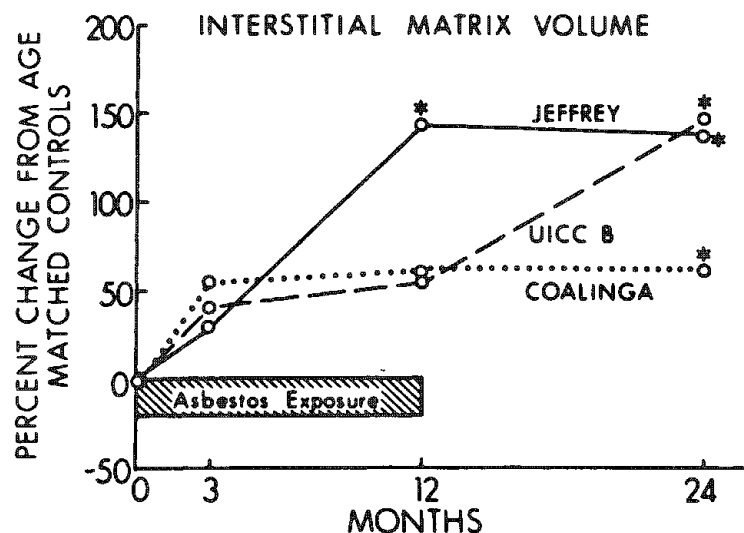


FIG. 3.--Changes in interstitial matrix volume expressed as percentage change from age-matched controls following exposure to each type of chrysotile asbestos. Asterisk denote  $p < 0.05$  compared to control value.



interstitium. The ranking of these parameters in relative importance for causing lung injury appear to be total mass of asbestos, fiber size, and fiber number.

#### References

1. I. J. Selikoff and D. H. Lee, *Asbestos and Disease*, New York: Academic Press, 1978.
2. A. J. Vorwald et al., "Experimental studies of asbestosis," *Archives Ind. Hyg. and Occup. Med.* 3: 1, 1951.
3. W. Klosterkotter, *Second International Conference of Biological Effects of Asbestos*, Dresden, 1968.
4. K. E. Pinkerton et al., "Fiber localization and its relationship to lung reaction in rats after chronic inhalation of chrysotile asbestos," *Am. J. Pathol.* 117: 484, 1984.

TABLE 1.--Chrysotile asbestos preparations.

Type	Chamber Concentration mass (mg/m <sup>3</sup> )	fiber #/cm <sup>3</sup>	Fiber Length (%)		Average Fiber Diameter (μ) per Fiber Length	
			<10μ	>10μ	<10μ	>10μ
Coalinga	7.76±1.46	2 000	65.9	34.1	0.36	2.03
UICC B	10.99±2.11	10 000	93.5	6.7	0.33	0.40
Jeffrey	11.36±2.18	10 000	92.0	8.0	0.29	0.39

TABLE 2.--Number, mass, and size of fibers in the lungs following exposure to Jeffrey chrysotile.\*

Exposure	Fiber #	Fiber Mass (ng)	Fiber Length (%)	
			<10μ	>10μ
1 day	2 300	0.24	95	5
1 day + 1 year air	400	0.05	74	26
12 months	170 000	14.75	76	24

\*All data are expressed per mm<sup>3</sup> of inflation-fixed lung.

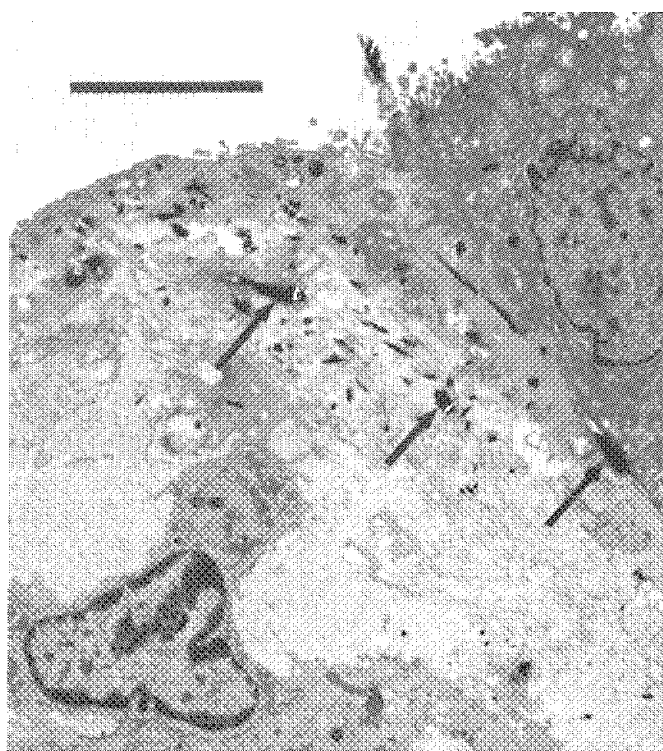


FIG. 4.--Electron micrograph from lungs of animal exposed to Jeffrey Mine chrysotile for 12 months. Numerous asbestos fibers (arrows) are present within collagenous interstitial matrix. Bar equals 5 μm.



## TOXICOLOGY OF OZONE INHALATION AS REVEALED BY ELECTRON MICROSCOPY

W. S. Tyler

Scanning (SEM) and transmission electron microscopy (TEM) have been especially useful in evaluating the respiratory tract responses to ozone. Just as ozone is often used as archetypical oxidant air pollutant, the methods used for EM studies of the reactions to ozone may be useful for studies of the reactions of the respiratory system to other vapors and gases. The objectives of this paper are: (1) to review some of the many EM techniques and principles that have been found useful for evaluation of the respiratory-tract responses to ozone, (2) to provide background and an introduction to the more specific and current papers that follow, and (3) to indicate some of the areas for future uses of EM in evaluating reactions of the lungs to vapors and gases.

### *Background and Principles*

The centriacinar ozone lesion was identified in early LM studies by Stokinger et al.<sup>1</sup> and Gross et al.<sup>2</sup> The focal nature of this lesion made impractical the use of "minced" tissue blocks for TEM and methods were developed to sample this site selectively. Stephens and Evans<sup>3</sup> obtained centriacinar regions for TEM by dissection of tissue in unpolymerized Araldite and for SEM by dissection in amyl acetate. Plopper et al.<sup>4</sup> recognized the advantages of using multiple types of microscopy on the identical tissue. In 30 $\mu$ m-thick sections from large epoxy blocks, they identified specific areas to be thin sectioned and examined in the TEM. The development of microtomes capable of cutting 1 $\mu$ m sections from large blocks of partially polymerized epoxy resin permitted examination of adjacent tissue slices by LM and TEM as in common use today. Much of our present information concerning the centriacinar responses to ozone inhalation was developed using these methods.<sup>5-9</sup> Recently Barry et al.<sup>10</sup> used Luer hubs as a punch to cut centriacinar regions from thin slices of rat lungs. This method proved to be a very useful approach for TEM morphometry of the centriacinar region.

Pawley and Nowell<sup>11</sup> recognized the advantages of finding focal lesions with the SEM and studying the identical tissue by TEM. They used a micromanipulator in the SEM column to select their tissue for TEM. Dissection in the SEM column proved tedious and others<sup>12</sup> developed simpler procedures for epoxy embedding of critical point dried tissues previously examined with SEM. The methods of Bastacky et al.<sup>13</sup> appear to result in the best quality TEM. Dissection of critical point dried tissue under a dissecting microscope can be used to provide additional centriacinar areas for study by SEM and TEM.<sup>14</sup>

Airway dissection of fixed lungs, based on the methods of Bastacky et al.<sup>13</sup> or Plopper et al.,<sup>15</sup> is at present the optimal way for relating lesions to specific airways. Dissection to the terminal bronchiole can be routinely done. Depending on the fixative used, these tissues are suitable for routine SEM or TEM or for cytochemical studies. Several authors of papers that follow used these techniques.

Epithelial lesions in the nasal cavity are useful indicators of damage in the lungs and biopsy samples of epithelium from exposed humans can be correlated with cells from experimentally exposed animals. For some studies, the nasal septum can simply be removed and processed for SEM and TEM in the usual manner.<sup>16</sup> More specific methods for fixation and sampling rodent nasal epithelium have been developed by Young<sup>17</sup> and by Popp and Martin.<sup>18</sup> Methods for EM of nonhuman primate nasal cavities were developed by Harkema et al.<sup>19</sup> Papers from two of these groups are presented below.

There are many choices of fixatives and several routes by which fixtures can be brought into contact with lung tissues and cells. Bullock<sup>20</sup> reviewed the current status of fixation for EM including some of the newer fixatives for immunocytochemistry, enzyme

---

The author is at the Department of Anatomy and California Primate Research Center, University of California, Davis, CA 95616. Some of the studies cited were supported in part by NIH Grants ES-00628 and RR-00169.

cytochemistry, and the problems of retaining materials for x-ray microanalysis. It is often necessary to fix the tissues so that they are suitable for LM, SEM, and TEM. We found a mixture of glutaraldehyde and formaldehyde in cacodylate buffer with calcium added at a final pH of 7.2-7.4 and osmolality of 550 mOsm to be very suitable for many studies.<sup>21</sup> Cytology of tracheal epithelium may best be done by use of a more isotonic solution of the same constituents.<sup>22</sup> Barry et al.<sup>10</sup> used 2% glutaraldehyde in 0.084 M cacodylate buffer for TEM morphometry of centriacinar cells. For most studies of the reaction of the respiratory system to inhaled vapors or gases, the fixative of choice is delivered to the cells and tissues by airway infusion at 20-30 cm H<sub>2</sub>O pressure. Respiratory system tissues fixed in this manner are suitable for LM, SEM, and TEM.

The specific needs of the study must determine both the type of fixation and the route by which the fixative is delivered to the cells and tissues. For studies using SEM, the extracellular surface coats must be removed so that surface details of the airway and alveolar cells can be seen.<sup>21</sup> This goal is most easily accomplished by fixation via the trachea. Extracellular surface coats and inflammatory cells in those coats can be left intact for morphological and cytochemical study by fixation via the pulmonary artery.<sup>23,24</sup> The methods of Brody and Craighead<sup>25</sup> are easy to use and very suitable for toxicologic studies. Extracellular surface coats are also maintained by rapid freeze methods.<sup>21,26</sup> Although rapidly frozen lung is not suitable for some EM morphometric studies,<sup>27</sup> it is very suitable for descriptive EM. Rapidly frozen lung is also very suitable for low-temperature SEM.<sup>28,29</sup>

#### *Approaches for Future Studies*

A major objective of toxicology must be the extrapolation from effects in experimental animals to hazards for man. Future EM studies of inhaled vapors and gases need to relate to mechanisms of cellular injury and repair. Mechanisms may extrapolate more readily than effects. There will be a need to correlate *in vitro* mechanistic studies with whole-animal exposures. Mechanisms that operate *in vitro* may or may not operate *in vivo*. The use of morphometry at the EM level<sup>10,30</sup> needs to be expanded and to include three-dimensional reconstructions.<sup>31,32</sup> There will be expanded use of immunocytochemistry for identification of specific components of cell secretions, of connective tissue fibers and matrix, and of functional groups of inflammatory cells. Many new reagents will be needed. Alternate methods of fixation which retain more antibody binding site activity need to be investigated. This aim may be accomplished by the use of fixatives containing imido-esters in place of aldehydes.<sup>20</sup> Changes in ionic surface charges of respiratory system cells<sup>33</sup> may be correlated with early functional changes. The use of morphometry for quantification of cytochemical final reaction products should provide additional information.

At the present we are using only a very small amount of the information available from the interaction of the electron beam with our lung specimens. Those studying inhaled particles are using more of that information, but most often to characterize the particles rather than the lung cells. There have been preliminary studies of lung using low-temperature SEM,<sup>29</sup> but the full potential of the instrumentation has not been applied to lung. HVEM has also been shown to have the potential of providing valuable information on lung cells<sup>29,34</sup> but has only been used in one preliminary study of ozone exposed animals.<sup>34</sup> Many more EM studies need to be done if we are to understand the reaction of the respiratory system to inhaled vapors and gases.

#### *References*

1. H. E. Stokinger, W. D. Wagner, and O. J. Dobrogorski, "Ozone toxicity studies: III. Chronic injury to lungs of animals following exposures at a low level," *Arch. Indust. Health* 16: 514, 1957.
2. P. Gross, L. D. Scheel, and H. E. Stokinger, "Ozone toxicity studies: Destruction of alveolar septa--a precursor of emphysema?" *Med. Thoe.* 22: 376-381, 1965.
3. R. J. Stephens and M. J. Evans, "Selection and orientation of lung tissue for scanning electron microscopy," *Envir. Res.* 6: 52-59, 1973.
4. C. G. Plopper, D. L. Dungworth, and W. S. Tyler, "Pulmonary lesions in rats exposed to ozone: A correlated light and electron microscopic study," *Amer. J. Pathol.* 71: 375-394, 1973.

5. L. W. Schwartz, D. L. Dungworth, M. G. Mustafa, B. K. Tarkington, and W. S. Tyler, "Pulmonary responses of rats to ambient levels of ozone," *Lab. Investigation* 34: 565-578, 1976.
6. R. J. Stephens, M. F. Sloan, M. J. Evans, and G. Freeman, "Early responses of lung to low levels of ozone," *Am. J. Pathol.* 74: 31-58, 1974.
7. R. J. Stephens, M. F. Sloan, M. J. Evans, and G. Freeman, "Alveolar Type I response to 0.5 PPM O<sub>3</sub> for short periods," *Exper. Molec. Path.* 20: 11-23, 1974.
8. P. W. Mellick, D. L. Dungworth, L. W. Schwartz, and W. S. Tyler, "Short term morphologic effects of high ambient levels of ozone on the lungs of rhesus monkeys," *Lab. Invest.* 36: 82-90, 1977.
9. W. L. Castleman, D. L. Dungworth, L. W. Schwartz, and W. S. Tyler, "Acute respiratory bronchiolitis: An ultrastructural and autoradiographic study of epithelial cell injury and renewal in rhesus monkeys exposed to ozone," *Am. J. Pathol.* 98: 811-827, 1980.
10. B. E. Barry, F. J. Miller, and J. D. Crapo, "Effects of inhalation of 0.12 and 0.25 ppm ozone on the proximal alveolar region of juvenile and adult rats," *Lab. Invest.* 53: 692-704, 1985.
11. J. B. Pawley and J. A. Nowell, "Microdissection of biological SEM samples for further study in the TEM," *SEM/1973*, 333-340.
12. M. E. G. Brummer, P. M. Lowrie, and W. S. Tyler, "A technique for sequential examination of specific areas of large tissue blocks using SEM, LM and TEM," *SEM/1975 I*, 333-340.
13. J. Bastacky, T. L. Hayes, and B. von Schmidt, "Lung structure as revealed by microdissection: Positional morphology of human lungs," *Amer. Rev. Respir. Dis.* 128: S7-S13, 1983.
14. W. S. Tyler, D. L. Dungworth, C. G. Plopper, D. M. Hyde, and N. K. Tyler, "Structural evaluation of the respiratory system," *Fund. Appl. Toxicol.* 5: 405-422, 1985.
15. C. G. Plopper, A. T. Mariassy, and L. O. Lollini, "Structures as revealed by airway dissection: A comparison of mammalian lungs," *Amer. Rev. Respir. Dis.* 128: S4-S7, 1983.
16. L. W. Schwartz, P. F. Moore, D. P. Chang, B. K. Tarkington, D. L. Dungworth, and W. S. Tyler, "Short-term effects of sulfuric acid aerosols on the respiratory tract: A morphological study in guinea pigs, mice, rats and monkeys," in S. D. Lee, Ed., *Biochemical Effects of Environmental Pollutants*, Ann Arbor, Mich.: Ann Arbor Science Pub., 1977, 257-272.
17. J. T. Young, "Histopathologic examination of the rat nasal cavity," *Fund. Appl. Toxicol.* 1: 309-312, 1981.
18. J. A. Popp and J. T. Martin, "Methods for the ultrastructural evaluation of rodent nasal mucosa," *Proc. 39th Mtg. EMSA*, 1981, 594-595.
19. J. R. Harkema, Ph.D. thesis, University of California, Davis.
20. G. R. Bullock, "The current status of fixation for electron microscopy: A review," *J. Microscopy* 133: 1-15, 1984.
21. J. A. Nowell and W. S. Tyler, "Scanning electron microscopy of the surface morphology of mammalian lungs," *Amer. Rev. Respir. Dis.* 103: 313-328, 1971.
22. C. G. Plopper, A. T. Mariasse, D. W. Wilson, J. L. Alley, S. J. Nishio, and P. Nettesheim, "Comparison of nonciliated tracheal epithelial cells in six mammalian species: Ultrastructural and population densities," *Exp. Lung Res.* 5: 281-294, 1983.
23. J. Gil and E. R. Weibel, "Improvements in demonstration of lining layer of lung alveoli by electron microscopy," *Respir. Physiol.* 8: 13-36, 1969.
24. J. D. Brain, P. Gehr, and R. I. Kavet, "The importance of the fixation method," *Am. Rev. Respir. Dis.* 129: 823-826, 1984.
25. A. R. Brody and J. F. Craighead, "A simple perfusion apparatus for lung fixation," *Proc. Soc. Exp. Biol. Med.* 143: 388-390, 1973.
26. R. W. Mazzone, C. M. Durand, and J. B. West, "Electron microscopic appearances of rapidly frozen lung," *J. Microscopy* 117: 269-284, 1979.
27. E. R. Weibel, W. Limacher, and H. Bachofen, "Electron microscopy of rapidly frozen lung: Evaluation on the basis of standard criteria," *J. Appl. Physiol.: Respirat. Environ. Exercise Physiol.* 53: 516-527, 1982.
28. G. Hook, C. Lai, J. Bastacky, and T. Hayes, "Conductive coatings studies on inflated lung in the frozen-hydrated and freeze dried states," *SEM/1980 IV*, 27-32.

29. J. Bastacky, T. L. Hayes, B. von Schmidt, S. B. Klein, J. Barr, G. L. Finch, M. McKoon, L. Baskin, and G. R. Hook, "Correlative microscopy of native surfaces of human lung: Color macrophotography, SEM, LM, TEM, HVEM, and low-temperature scanning electron microscopy," *Proc. 41st Mtg. EMSA*, 1983, 500-503.
30. H. Lum, W. S. Tyler, D. M. Hyde, and C. G. Plopper, "Morphometry of in situ and lavaged pulmonary alveolar macrophages from control and ozone-exposed rats," *Exp. Lung Res.* 5: 61-78, 1983.
31. J. D. Crapo, S. L. Young, E. K. Fram, K. E. Pinkerton, B. E. Barry, and R. O. Crapo, "Morphometric characteristics of cells in the alveolar region of mammalian lungs," *Am. Rev. Resp. Dis.* 128: S42-S46, 1983.
32. S. L. Young, E. K. Fram, and B. L. Craig, "Three-dimensional reconstruction and quantitative analysis of rat lung Type II cells: A computer-based study," *Am. J. Anat.* 174: 1-14, 1985.
33. R. E. Gordon, "The effects of NO<sub>2</sub> on ionic surface charge on Type 1 pneumocytes of hamster lungs," *Am. J. Pathol.* 121: 291-297, 1985.
34. W. Tyler, L. Schwartz, J. Pawley, and J. Nowell, "Effects of air pollutants on pulmonary cytology: A study using scanning electron microscopy, and high voltage electron microscopy," *XIXth Morphological Congress Symposia*, Charles University, Prague, 1978, 425-430.

## SPECIES VARIATION IN TRACHEOBRONCHIAL EPITHELIAL POPULATIONS: CONSIDERATIONS FOR SELECTING MODEL SPECIES FOR TOXICOLOGIC INVESTIGATIONS

C. G. Plopper, A. T. Mariassy, D. W. Wilson, J. A. St. George, N. K. Tyler, D. M. Hyde, Janet Heidsiek, and S. J. Nishio

A wide range of compounds are tested for their toxicity to the respiratory system. One of the primary routes of administration of these compounds is via inhalation. The site of impact of most inhaled toxins is the epithelial lining of conducting respiratory airways. The underlying assumption of inhalation toxicology studies is that data obtained in model species can be extrapolated to humans. The contention of this study is that the tracheobronchial epithelium of most mammalian species commonly used as models does not adequately reflect the condition in human conducting airways.

This study focuses on the epithelial population lining the tracheobronchial airway (trachea, bronchi, and bronchioles) of the mammalian respiratory system. At least eight epithelial cell types have been identified, each different in both function and sensitivity to inhaled toxins. This study considers the following questions concerning these populations: (1) Are the epithelial populations lining the same portion of the airway composed similarly in different species? (2) Do these epithelial populations vary in abundance in the same airway level in different species? (3) Is the epithelial population composition the same in all airway levels in the tracheobronchial tree of one species? (4) Are the secretory products contained in these epithelial cells similar in the same airway level in different species? (5) Does the cytochemical composition of the secretory product vary in cells in different portions of the tracheobronchial tree in the same species? (6) Is the architectural population organization the same as the centriacinar region of different species?

### *Centriacinar Region*

The centriacinar region is composed of nonalveolarized bronchioles (terminal bronchioles) and alveolarized bronchioles (respiratory bronchioles). Species vary in the organization of the centriacinar region, in the abundance of cell types composing the epithelial lining and in the ultrastructural characteristics of the lining epithelial cells, as follows.

Species with few or only one nonalveolarized noncartilaginous bronchiole and several generations of alveolarized bronchioles: Macaque monkey, dog, cat.

Species with several generations of nonalveolarized bronchioles and several generations of alveolarized bronchioles: Humans, ferret.

Species with several generations of nonalveolarized bronchioles and a single short or absent alveolarized bronchiole: Horse, ox, sheep, pig, rabbit, guinea pig, hamster, gerbil, rat, mouse.

Species in which nonciliated bronchiolar epithelial (Clara) cells compose more than 95% of the epithelial population: Dog, cat, Macaque monkey (non-blood vessel side).

Species in which nonciliated and ciliated bronchiolar epithelial cells are of about equal numbers in the epithelial populations: Horse, steer, sheep, rabbit, guinea pig, hamster, rat, mouse.

Species with Clara cells in which more than 40% of the cytoplasm is occupied by agranular endoplasmic reticulum: Horse, sheep, rabbit, guinea pig, rat, hamster, mouse.

Species with Clara cells in which glycogen occupies more than 60% of the cytoplasm: Ox, dog, cat.

Species with Clara cells containing little endoplasmic reticulum or glycogen: Humans, Macaque monkeys.

---

Author Mariassy is at Mount Sinai Medical Research Institute, Miami Beach, Fla.; the other authors are at the School of Veterinary Medicine, University of California, Davis, CA 95616. This work was supported by grants HL28978, ES00628, and DRR00169.

### *Tracheobronchial Tree*

The composition of the epithelium varies according to airway generation. Although only a few species have been evaluated, there are clearly strong distributional differences in the abundance of basal cells, mucous goblet cells, Clara cells, and ciliated cells. Figure 1 compares the differences in distribution between the cranial lobes of lungs from adult rabbits (Fig. 1a) and sheep (Fig. 1b).

### *Trachea*

Epithelial composition differs in the distal trachea of different species. The number of cells per millimeter of basal lamina and relative abundance of cell types varies widely between species, as follows.

Species variation in numerical density (#/mm) of epithelial cells lining the trachea: Sheep, 414; Macaque monkey, 266; cat, 273; rabbit, 211; rat, 148; hamster, 151.

Species variation in percent of tracheal epithelial population made up of mucous goblet cells: Sheep, 5; Macaque monkey, 8; cat, 20; rabbit, 1; rat, 0.5; hamster, 0; mouse, 0.

Species variation in percent of tracheal epithelial population made up of ciliated cells: Sheep, 31; Macaque monkey, 41; cat, 36; rabbit, 43; rat, 41; hamster, 48; mouse, 36.

Species variation in percent of tracheal epithelial population made up of basal cells: Sheep, 29; Macaque monkey, 31; cat, 37; rabbit, 28; rat, 13; hamster, 6; mouse, 8.

Clara cells were the predominant secretory cell type in three species: Rabbit, 18%; hamster, 41%; mouse, 36%. Serous cells predominate in rats, 39%.

### *Carbohydrate Cytochemistry*

The chemical nature of the secretory product produced by the cells of the trachea also varies. Standard carbohydrate histochemical methods--high iron diamine (HID) for sulfated glycoproteins, Alcian blue (AB) for acidic glycoprotein, and periodic acid Schiff (PAS) for neutral glycoproteins--show that the product in surface epithelium varies as follows.

Species in which the secretory product in tracheal epithelial cells is predominantly sulfated glycoconjugate include: Dog, cat, Macaque monkey.

Species in which the secretory product in tracheal epithelial cells is a mixture of sulfated glycoconjugates and sialomucin include: Human, sheep.

Species in which the secretory product in tracheal epithelium is predominantly neutral glycoconjugates or unreactive for carbohydrates include: Rabbit, rat, hamster, mouse.

The amount of secretory product that is stored in granules in the epithelium varies in different airway levels in the same species. Figure 2 is an example of quantitative differences in secretory products stored in surface epithelium in the trachea, lobar bronchus, and four generations of intrapulmonary airway including terminal and respiratory bronchioles in the adult rhesus monkey.

### *Conclusions*

A comparative overview of tracheobronchial epithelial composition emphasizes the high degree of diversity found in different species of mammals. Epithelial populations of the tracheobronchial tree vary (1) in different airway levels in the same species, (2) in the same airway level in different species, (3) in types of cells present, (4) in overall abundance of secretory product and number of cells, (5) in secretory granule carbohydrate content, and (6) in amount of stored secretory product.

### *Bibliography*

- P. K. Jeffrey, "Morphologic features of airway surface epithelial cells and glands," *Am. Rev. Resp. Dis.* 128: S14-S19, 1983.
- A. T. Mariassy and C. G. Plopper, "Tracheobronchial epithelium of the sheep: I. Quantitative light microscopic study of epithelial cell abundance and distribution," *Anat. Rec.* 205: 263-275, 1983.
- C. G. Plopper et al., "Distribution of nonciliated bronchiolar epithelial (Clara) cells in intra- and extrapulmonary airways of the rabbit," *Exper. Lung Res.* 5: 79-98, 1983.



- C. G. Plopper et al., "Comparison of nonciliated tracheal epithelial cells in six mammalian species: Ultrastructure and population densities," *ibid.*, pp. 281-294.
- C. G. Plopper, "Comparative morphologic features of bronchiolar epithelial cells: The Clara cell," *Am. Rev. Resp. Dis.* 128: S37-S41, 1983.
- S. S. Spicer et al., "Histochemical properties of the respiratory tract: Epithelium in different species," *ibid.*, pp. S20-S25.
- W. S. Tyler, "Comparative subgross anatomy of lungs: Pleuras interlobular septa and distal airways," *ibid.*, pp. S32-S36.
- J. G. Widdicombe and R. J. Pack, "The Clara cell," *Eur. J. Respir. Dis.* 63: 202-220, 1982.

FIG. 1.--Distribution and relative abundance of epithelial cell types in extra- and intrapulmonary airways of cranial lobe of (a) rabbit and (b) sheep. Airway generation number indicates number of times airway branches along one pathway. Relative percentages are based on direct nuclear counts.

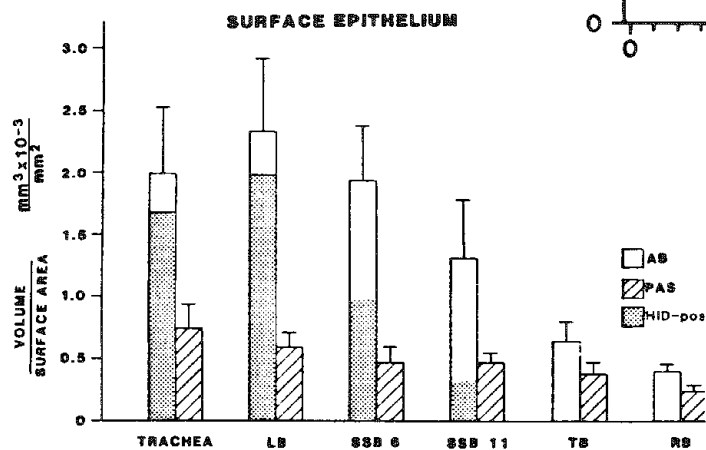
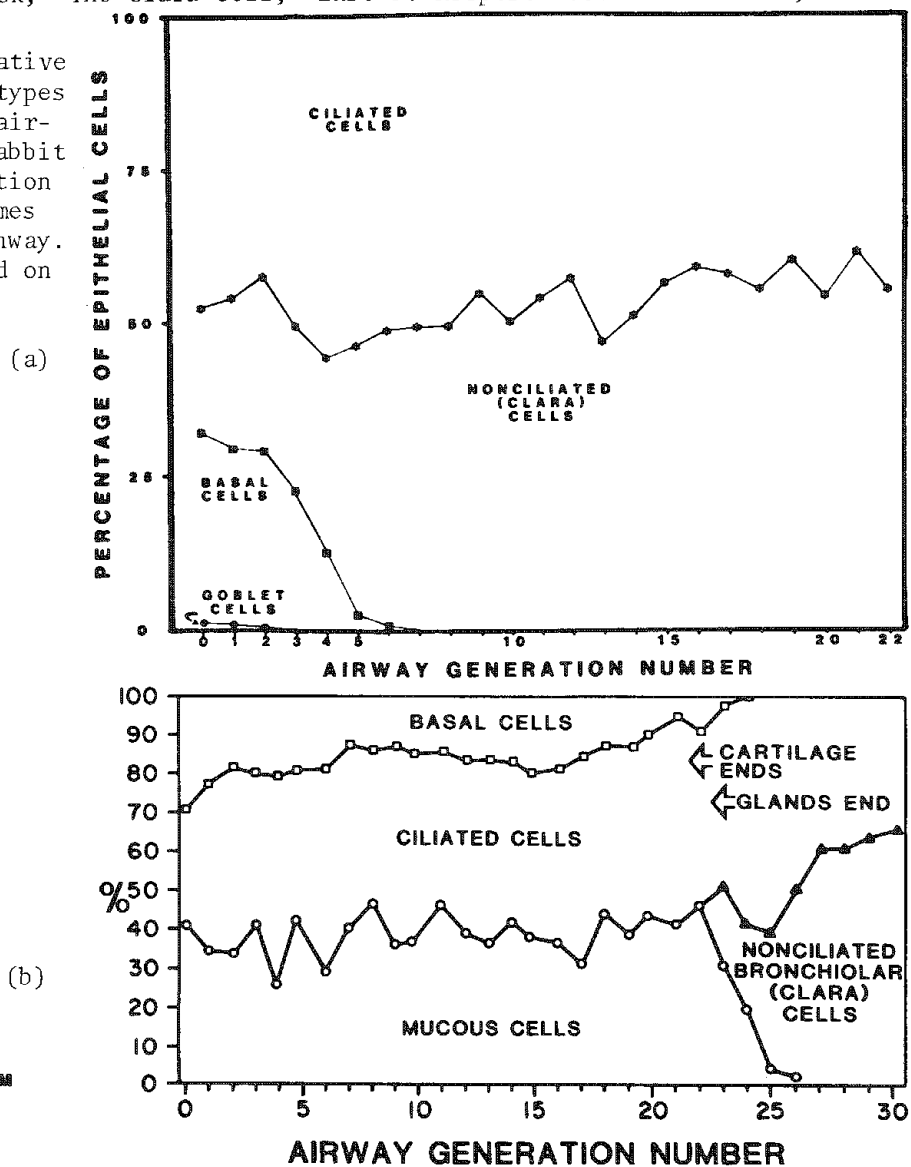


FIG. 2.--Computerized quantitation of volume of muco-substance stored in surface epithelial cells standardized to airway epithelial surface. Total amount of stored secretory product decreases in more distal airways. Trachea, lobar bronchus (LB), and proximal intrapulmonary bronchus (SSB6) have most stored product. Amount of sulfated product decreases in intrapulmonary bronchi (SSB6, SSB11) and is absent in terminal (TB) and respiratory bronchioles (RB).

## HISTOCHEMICAL AND CYTOCHEMICAL EVALUATION OF SECRETORY CELLS IN NONHUMAN PRIMATES EXPOSED TO OZONE

J. A. St. George, D. L. Cranz, S. J. Nishio, J. R. Harkema, D. L. Dungworth, and C. G. Plopper

Most studies on the pulmonary effects of ozone have focused on the centriacinar region and not the upper airways, where physiologists predict the impact of ozone would be the greatest.<sup>1</sup> Two studies have described a lesion in the trachea<sup>2,3</sup> and lower airways,<sup>3</sup> in response to high ambient concentrations of ozone. One of these studies, which focused on the trachea, described a lesion which appears in streaks and is characterized by loss of cilia and changes in epithelial cell types.<sup>2</sup> Ciliated cells decreased in number and often contained numerous granules. There was focal epithelial stratification that was associated with increased numbers of small mucous granule cells (SMG) and the appearance of intermediate cells, a cell type not seen in the controls. Intermediate cells also contained numerous granules. Several investigators have documented changes in the carbohydrate content of secretory granules within airway epithelium from laboratory animals exposed to various irritants.<sup>4</sup> We describe here histochemical and cytochemical methods that can be used to assess the effects of ambient and high ambient levels of ozone (0.15 and 0.64 ppm) on the carbohydrate content of secretory cells that comprise the surface epithelium of trachea and nasal cavity in a nonhuman primate.

### *Materials and Methods*

Bonnet monkeys *Macaca radiata* were exposed to filtered air or ozone. Three monkeys were exposed to filtered air, four were exposed for 7 h/day to 0.15 ppm for 90 days, and three were exposed for 23 h/day to 0.64 ppm ozone for 7 days. At the end of the exposure, the monkeys were anesthetized and exsanguinated, and the trachea was cannulated. Trachea and lungs were fixed by infusion of paraformaldehyde/glutaraldehyde at 30cm H<sub>2</sub>O pressure. The nasal cavities were fixed by flushing of fixative through the nasopharyngeal orifice. After this flush, the eyes, integument, and musculature were removed and the head was stored in the same fixative until processing. Samples were then embedded in glycol methacrylate for light microscopy (LM) or epoxy resin for transmission electron microscopy (TEM). One-micron serial methacrylate sections were stained in histochemical stains including Alcian blue-periodic acid Schiff (AB-PAS) or high iron diamine-Alcian blue (HID-AB).<sup>6</sup> Neutral sugars are distinguished from acid glycoconjugates by use of the AB-PAS stain. HID-AB differentiates sulfated from carboxylated acid glycoconjugates. For TEM, samples were stained *en bloc* with low iron diamine (LID),<sup>7</sup> HID,<sup>8</sup> MgCl<sub>2</sub> or buffer, then post-osmicated. Sections of unosmicated tissues were stained with periodic acid thiocarbohydrazide-silver proteinate (PTS).<sup>9</sup> We selected our specimens from the intercartilaginous area of the trachea where the focal lesion is observed.

### *Results*

In the area of the lesion, there is an increase in the cellularity of the epithelium and numerous cells contain carbohydrate with a concentration on the apical surface. By light microscopy, tracheal mucous cells and small mucous granule cells in control and ozone exposed monkeys were stained with PAS, AB, and HID.

By TEM, the cytochemical stains revealed more changes within the surface epithelium than seen at the light level. Figure 1 shows normal trachea stained with PTS. The PTS is analogous to PAS at the light level and recognizes adjacent hydroxyl groups of hexoses. The mucous cells contain granules that are darkly stained. The granules within mucous cells were of four morphological types (Fig. 2). Each granule consists of a matrix which may or may not surround a core. In the first type of granule, the matrix surrounds multiple cores (Fig. 2a). Triphasic granules are seen in the second morphological type, in which a mesh or matrix surrounds a biphasic core (Fig. 2b). The third type consists of

Authors St. George, Cranz, Nishio, and Plopper are at the Department of Anatomy, and Dungworth is at the Department of Pathology, both in the School of Veterinary Medicine, University of California, Davis, CA 95616; author Harkema is at the Inhalation Toxicology Research Institute, Albuquerque, N.M.

matrix only and in the fourth type a matrix surrounds a single core (Fig. 2d). In a previous study, changes in the morphology of the mucous granules in the ozone-exposed trachea were noted.<sup>2</sup> We quantified the differences between control and 0.64ppm ozone-exposed trachea by counting the number of cells with each morphological type while examining the granules with the electron microscope. In ozone-exposed trachea, more cells contained granules that were either uncored or biphasic with multiple cores. Figure 3 is a micrograph of an ozone lesion in the 0.64ppm exposed trachea. The SMG cells increase in number and intermediate cells which were not observed in normal trachea may contain either granules, signs of ciliogenesis, or both. The granules of an intermediate cell shown in Fig. 4 contain periodate-reactive material demonstrated with the PTS staining. In addition, ciliated cells contained in the trachea of an ozone-exposed animal frequently contain granules. As seen in Fig. 5, these granules contain periodate-reactive material that is acidic.

As reported previously, the nonolfactory nasal epithelium in monkeys was composed of three distinct epithelial populations: squamous, transitional (nonciliated), and respiratory (ciliated).<sup>10</sup> Secretory cells were present in the transitional and respiratory epithelium but absent in the stratified squamous epithelium. The nasal surface epithelium contained secretory cells that generally stained purple blue with AB-PAS or brown with HID-AB. However, more cells within the nasal cavity contained blue stain with HID/AB than in the trachea. When examined with the electron microscope, the mucous cells of ozone-exposed nasal cavity were found to contain dilated granular endoplasmic reticulum.<sup>11</sup> The material distending the structure was found to be relatively electron-lucent and was not stained with any of the cytochemical stains used in this study. The surrounding granules in these cells, as shown in Fig. 6, are stained strongly with the PTS stain.

### Conclusion

The histochemical and cytochemical stains on the various cell types from ozone-exposed trachea indicate that all cell types with granules, including mucous, SMG, intermediate, and ciliated cells, stain with all of the stains used, which shows that these cells contain periodate reactive, sulfated glycoconjugates. We have concluded from this study that tracheal mucous cells of Bonnet monkeys exposed to ozone were structurally different, but histochemically similar, to those in control trachea. This result does not agree with the results observed in laboratory animals, where changes were observed in the carbohydrate content upon irritant exposure. Our findings suggest that in mammals, such as humans, where sulfated respiratory mucins are present in the steady-state condition, histochemical or cytochemical changes such as those found in the rat do not occur but rather there are more cell types producing the sulfated mucins. The observation of mucous cells in nasal cavity with altered granular endoplasmic reticulum indicate a change in the biosynthetic or secretory capability of these cells upon exposure to ozone. However, it remains a question whether the increase in cell types producing complex carbohydrates or the change in biosynthetic capability of the mucous cells affects the amount of mucus contained in the mucous blanket or the rate of mucociliary clearance.

### References

1. W. L. Castleman *et al.*, "Lesions in respiratory bronchioles and conducting airways of monkeys exposed to ambient levels of ozone," *Exp. Mol. Pathol.* 26: 384-400, 1977.
2. D. W. Wilson *et al.*, "The response of the macaque tracheobronchial epithelium to acute ozone injury: A quantitative ultrastructural and autoradiographic study," *Am. J. Pathol.* 116: 193-206, 1984.
3. P. W. Mellick *et al.*, "Short term morphologic effects of high ambient levels of ozone on lungs on rhesus monkeys," *Lab. Invest.* 36: 82-90, 1977.
4. D. Lamb and L. Reid, "Mitotic rates, goblet cell increase and histochemical changes in mucus in rat bronchial epithelium during exposure to sulfur dioxide," *J. Pathol. Bacteriol.* 96: 97-111, 1968.
5. R. W. Mowry and C. H. Winkler, "The coloration of acidic carbohydrates of bacteria and fungi in tissue section with special reference to capsules of *Cryptococcus neoformans*, pneumococci, and *Staphylococci*," *Am. J. Pathol.* 32: 628-629, 1956.
6. S. S. Spicer, "Diamine methods for differentiating mucosubstances histochemically," *J. Histochem. Cytochem.* 13: 211-234, 1965.
7. M. Takagi *et al.*, "Ultrastructural localization of acidic glycoconjugates with the

low iron diamine method," *J. Histochem. Cytochem.* 30: 471-476, 1982.

8. S. S. Spicer *et al.*, "Ultrastructural visualization of sulfated complex carbohydrates in blood and epithelial cells with the high iron diamine procedure," *Histochem. J.* 10: 435-452, 1978.

9. J. P. Thiery, "Mise en évidence des polysaccharides sur corpus fine en microscopie électronique," *J. Microsc.* 6: 987-1018, 1967.

10. J. R. Harkema *et al.*, "Nonolfactory surface epithelium of the nasal cavity of the bonnet monkey: A morphologic and morphometric study of the transitional and respiratory epithelium," *Am. J. Anat.* (submitted).

11. J. R. Harkema *et al.*, "Response of the macaque nasal epithelium to ambient levels of ozone: A morphologic and morphometric study of the transitional and respiratory epithelium," *Am. J. Pathol.* (submitted).

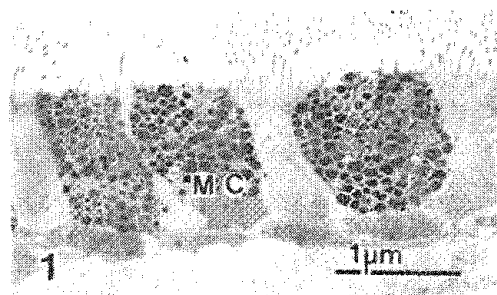


FIG. 1.--Mucous cells (MC) contain heavily stained granules with PTS. Control tracheal epithelium.

FIG. 2.--Four morphological types of mucous granules: (a) matrix surrounds multiple cores; (b) matrix with biphasic cores; (c) matrix with no cores; (d) matrix surrounds single core.

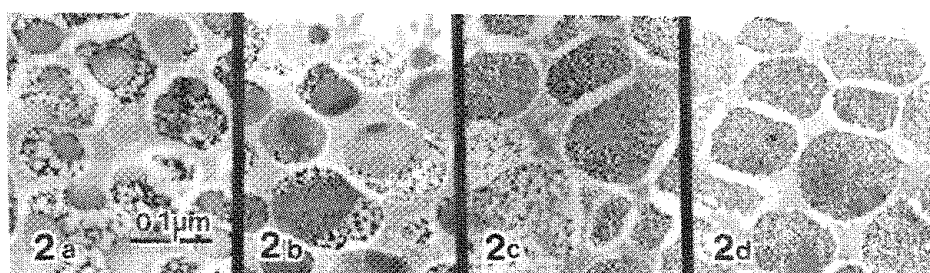


FIG. 3.--Tracheal lesion of 0.64ppm ozone-exposed monkey. Intermediate cell (IC) and small mucous granule cell (SMG).

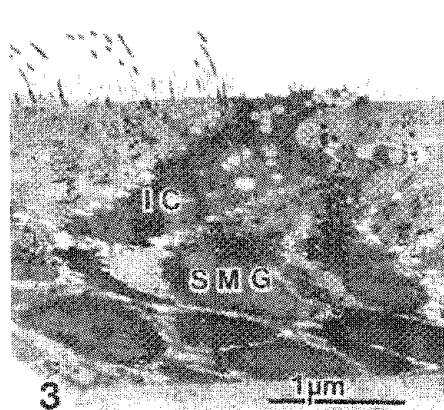
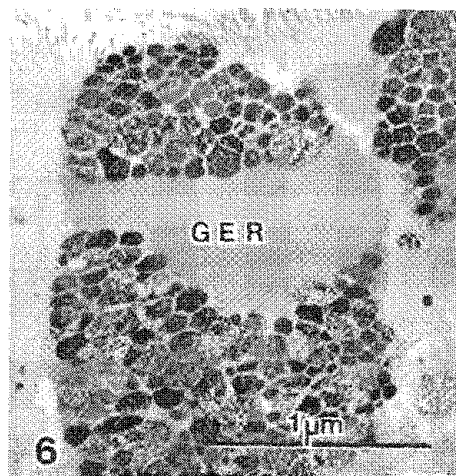
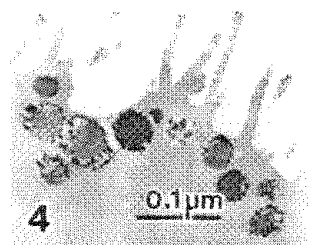


FIG. 4.--Intermediate cell containing granules with PTS staining.

FIG. 5.--Ciliated cell containing multiple granules stained with (a) LID and (b) PTS.



FIG. 6.--Mucous cell in nasal cavity of 0.15ppm ozone-exposed monkey. PTS stain reacts with granules surrounding unreactive, swollen granular endoplasmic reticulum (GER).



## OZONE-INDUCED INJURY TO TRACHEAL EPITHELIUM IN VITRO: MORPHOLOGIC CORRELATION OF INJURY WITH DOSE

K. J. Nikula and D. W. Wilson

The effects of airborne pollutants on the respiratory tract have been studied using in vivo inhalation exposures, organ implant systems, organ culture or explant systems, and cell culture systems.<sup>1-4</sup> The main disadvantages to the in vivo exposures are the uncertainty as to the actual dose of pollutant at specific sites in the respiratory tract, the complexity and expense of the exposure chambers, and the quantity of experimental toxicant required. With in vitro systems, a major problem is designing the exposure system to mimic in vivo exposure conditions where the luminal surfaces of respiratory epithelial cells are exposed almost directly to the inspired air, except for a mucous or surfactant layer of variable thickness.

A tracheal organ culture system for exposure of respiratory epithelium to ozone was developed in our laboratory which we feel appropriately resembles in vivo conditions, including direct exposure of epithelial cells. This system allows exposure of significant quantities of epithelium, so material can be harvested for light microscopy, for scanning and transmission electron microscopy, and for biochemical assays.

The purpose of this report is to characterize the morphologic response of rat tracheal epithelium to in vitro ozone exposure and to compare it with the in vivo response. By altering ozone exposure levels in the in vitro system, dose-response curves were established for morphological endpoints.

### *Materials and Methods*

*Animals.* Disease-free male Sprague-Dawley rats weighing 200-220 g were purchased from Bantin and Kingman (Fremont, Calif.), monitored serologically for infectious disease, and maintained on Purina rodent laboratory chow No. 5001 and water ad libitum.

*In Vitro Exposures.* The in vitro exposures were conducted with ten tracheal explants in each of three 24h trials. For each trial, the control group consisted of five explants exposed to a control atmosphere of 95% oxygen and 5% carbon dioxide, and the exposure group consisted of five explants exposed to the control atmosphere plus ozone (1, 2, or 3 ppm). The animals were anesthetized, had their tracheas removed and cut longitudinally through the cartilagenous portion, and placed epithelial side up on a stainless-steel grid in individual vials containing culture medium (Dulbecco's Minimal Eagle GIBCO, Grand Island, N.Y.) supplemented with gentamycin (20 µg/ml) and amphotericin B (2.5 µ/ml). Five vials containing the tracheas and 2 ml of medium were placed within each of two exposure vessels on a rocking platform (22 cycles/min), all inside a 37 C incubator. As the platform rocked, the tracheas were intermittently exposed to the experimental atmosphere. At the end of the incubation period, the explants were removed from culture and placed in 2% glutaraldehyde fixative in 0.1 molar cacodylic acid buffer, pH 7.3-7.4, 380-390 mOsm.

A limited 24h inhalation exposure trial (two rats each, 0 ppm O<sub>3</sub> and 1 ppm O<sub>3</sub> continuously) was conducted for comparison of the in vivo and in vitro ozone-induced lesions. After 24 h in the exposure chambers, the rats were euthanized and the trachea and lungs were fixed with 2% glutaraldehyde with 0.1 molar cacodylic acid buffer by airway perfusion at 30 cm of water pressure.

*Microscopic Analysis.* The fixed tracheas from both the in vitro and in vivo exposures were trimmed and examined in the same manner. The segment consisting of the distal 7 cartilage rings and associated membranous portion was dehydrated in a graded series of alcohols and amyl acetate, critical point dried with CO<sub>2</sub>, gold coated by use of a Denton Vacuum Sputter Coater, and examined by a stratified sampling method on an ETEC scanning

---

The authors are at the Department of Veterinary Pathology, University of California, Davis. American Lung Association support is acknowledged.

electron microscope. The entire section was photographed at 20 $\times$ , the length of the membranous portion was measured and divided by 6 so that 5 equally spaced locations along the center of the membranous portion were selected, and these locations were viewed at 800 $\times$ . Four morphologic criteria were evaluated and graded on a scale from 0 to 4 at each of these locations using the 800 $\times$  micrographs. Criteria evaluated were the percent of the surface occupied by ciliated cells, the quality of the cilia, the presence of large cell surface blebs and sloughed cells, and the presence of ruptured cell surface membranes.

Cartilage ring 10 was washed in Zetterquist's wash and postfixed in 1%  $O_5O_4$  Zetterquist's solution for 2 h at 25 C.<sup>5</sup> The tissues were washed and block stained in 2% uranyl acetate overnight. The specimens were dehydrated in a graded series of ethanols followed by propylene oxide and embedded in Epon Araldite. One-micron-thick sections were mounted on glass slides and stained with toluidine blue for light microscopy. The membranous portion was reembedded in beam capsules for ultrathin sectioning. Specimens were mounted on Formvar-coated slotted grids and viewed with a Zeiss model EM-10 transmission electron microscope, and montages were prepared by photographing the entire section at a magnification of 1600 $\times$ , followed by photographic enlargement to 2720 $\times$  on 5  $\times$  7 prints. Cell counts were based on counting the central 100 nuclear profiles in the epithelium. The linear density (cells/mm airway) was determined by a measurement of the length of the corresponding basement membrane by use of a quantitative digital image analysis system (MOP-3, Zeiss Inc., West Germany).

*Statistical Analysis of Data.* For the graded data from the scanning electron microscopic stratified sampling, the Mann-Whitney U test was used to test for significant differences between exposure groups at the 5% and 1% significance levels.

The data from the differential cell (nuclear) counts, expressed as percentages of cells and as cells per millimeter of airway, was analyzed by a one-way analysis of variance, and Fisher's least significant difference multiple comparison test at alpha levels of 0.05 and 0.01. Regression analyses were computed for categories for which the data suggested a linear relationship between ozone concentration and response, and the significance of the correlation coefficient was examined at the 0.05 and 0.01 levels.

## Results

*Serology.* The serologic tests indicated that the rats were free of infectious diseases.

*Light Microscopy.* In vitro control sections exhibited a pseudostratified columnar epithelium with a densely ciliated surface. The cilia were long and of relatively uniform height and density. Nuclear pyknosis was rare, and sloughing of cells was not observed. Epithelium from the ozone exposed tracheal explants exhibited mild to severe ciliary damage and loss. Nuclear pyknosis was frequently observed, and sloughing of cells was marked in some sections. The only difference apparent by light microscopy between the control and 1 ppm in vivo exposures was the presence of occasional ciliated cell without cilia in the exposed epithelia.

*Surface Morphology.* Table 1 lists the categories graded and the mean score for each exposure group.

The percentage of the surface occupied by ciliated cells and the quality of the cilia was significantly decreased in the three in vitro exposure groups compared to controls, but there was no significant difference among exposure groups. The control group had significantly fewer blebs and sloughed cells than the 3ppm exposures. The control, 1ppm, and 2ppm in vitro exposure groups had significantly fewer ruptured membranes than the 3ppm exposures.

For the in vivo exposures, the only significant difference was in the quality of cilia.

*Ultrastructural Changes, Quantification, and Dose-response Relationships.* By evaluation of transmission electron micrographs, 17 morphologic categories of normal or injured cells were distinguished. Summary data are presented in Table 2.

The data correlating morphologic injury with ozone concentration in the in vitro system indicate that two morphologic criteria show a linear change with increasing ozone concentration from 0 to 3 ppm. These criteria are normal basal cells, and cell surface blebs and sloughed cells. Six criteria (total abnormal ciliated cells,

total degenerate cells, degenerate serous cells, total abnormal serous cells, the ratio of total abnormal ciliated cells to total ciliated cells, and the ratio of total abnormal serous cells to total serous cells) show an increase in injury with increasing ozone concentration from 1 to 3 ppm. There is not a linear increase from 0 to 1 ppm; thus, 1 ppm is an apparent no-effect level. Necrotic cells, whether measured as unidentified necrotic cells or as total necrotic cells, showed a third type of relationship. There was a linear increase in necrotic cells with ozone concentration from 0 to 2 ppm ozone, but the line had a very shallow slope. From 2 to 3 ppm ozone, the line had a very steep slope because of the large increase in the necrotic cell population with 3ppm ozone exposure.

The category of total cells/mm airway does not show a significant change or trend with ozone exposure.

The results and dose-response relationships for the in vitro exposures were similar whether the population changes were measured as cell percentages or as cells per millimeter of airway.

### *Discussion*

This study illustrates the use of a rat tracheal explant system for examining the effects of oxidant gases on airway epithelium under precisely controlled exposure conditions. We found that in vitro exposure to oxidants causes injury to airway epithelium that is morphologically similar to that occurring in vivo, and that morphologic criteria can be used to establish dose-response relationships in oxidant injured airway epithelium.

Lesions observed with the in vitro exposures included a significant decrease in normal ciliated cells, and an increase in injured cilia, degenerate, and necrotic ciliated cells. These indications of ciliated cell injury, when added together, were measured as a significant increase in abnormal ciliated cells with 3ppm ozone exposure. With in vivo exposure, there was a significant increase in the population (percent) of ciliated cells with injured cilia, and the population (percent) abnormal ciliated cells. Surface morphology also indicated a significant decrease in ciliary quality for both the in vitro and in vivo exposures. These results illustrate the similarities between the morphologic injury induced by ozone exposure in vitro and in vivo and they correlate with the results of previous in vivo exposures.<sup>1,6</sup>

The ratio of abnormal ciliated cells to total ciliated cells is much greater than the comparable ratio for serous cells, which shows that ciliated cells are more susceptible to ozone induced injury, but serous cells are susceptible to injury at higher concentrations.

Basal cells, whether measured as normal basal cells or total basal cells, decreased significantly with exposure to 2 and 3 ppm ozone. Since degenerate or necrotic basal cells were not evident, this change may represent differentiation to other cell types as a response to injury.

Three techniques (light microscopy, scanning electron microscopy, and transmission electron microscopy) were used in this study. Scanning electron microscopy facilitated the examination of larger areas, and thus most readily revealed the increase in membrane blebs and sloughed cells as well as the ciliary damage. The quantitation and dose-response relationships relied upon the use of transmission electron microscopy. Cell types, and especially subcategories of injured cells, frequently cannot be differentiated by light microscopy. With the in vivo exposure where the lesion primarily consisted of subtle ciliary damage, ultrastructural examination and quantitation was especially important.

This system would be very useful in comparative studies of ozone-induced injury. In vitro exposures of human, nonhuman primate, and rodent tissues would be extremely useful in extrapolating pathophysiologic laboratory animal derived data from in vivo exposure to man.

### *References*

1. D. W. Wilson et al., "The response of the macaque tracheobronchial epithelium to acute ozone injury," *Am. J. Path.* 116: 192-206, 1984.
2. S. Mitsutoshi et al., "The effects of formaldehyde gas in a flow-through rat tracheal implant system," *Toxicology* 30: 317-325, 1984.
3. W. C. Eisenberg et al., "Biological effects of singlet delta oxygen in respiratory tract epithelium," *Experimentia* 40: 514-515, 1984.

4. R. E. Rasmussen, "In vitro systems for exposure of lung cells to  $\text{NO}_2$  and  $\text{O}_3$ ," *J. Tox. Environ. Health* 13: 397-411, 1984.

5. D. C. Pease, *Histological Techniques for Electron Microscopy*, New York: Academic Press, 1964, 2d ed., 38.

6. L. W. Schwartz et al., "Pulmonary responses of rats to ambient levels of ozone: Effects of 7-day intermittent or continuous exposure," *Lab. Invest.* 34: 565-578, 1976.

TABLE 1.--Surface morphology mean grades.

Category	In Vitro $\text{O}_3$ Exposures				In Vivo $\text{O}_3$ Exposures		Symbols for Tables 1 and 2: Different From Significance Level		
	0 ppm	1 ppm	2 ppm	3 ppm	0 ppm	1 ppm			
% ciliated	3.6	1.3 <sup>x</sup>	1.2 <sup>x</sup>	2.0 <sup>x</sup>	2.2	1.9		P<0.01	P<0.05
Quality cilia	3.8	2.2 <sup>x</sup>	2.0 <sup>x</sup>	2.2 <sup>x</sup>	3.8	2.7 <sup>x</sup>	Control	x	xx
Cell surface blebs and sloughed cells	0.0	0.9 <sup>x</sup>	0.6 <sup>xx</sup>	1.8 <sup>x, ++, *</sup>	0	0.1	1 ppm	+	++
Ruptured membranes	0.0	0.5	0.4	1.3 <sup>x, ++, *</sup>	0	0.1	2 ppm	*	**
							3 ppm	#	##

TABLE 2.--Summary data cells/mm airway mean  $\pm$  standard deviation.

Cell Type	In Vitro $\text{O}_3$ Exposures				In Vivo $\text{O}_3$ Exposures	
	0 ppm	1 ppm	2 ppm	3 ppm	0 ppm	1 ppm
Total cells	262.5 $\pm$ 43.9	222.0 $\pm$ 28.0	274.8 $\pm$ 59.9	255.6 $\pm$ 52.1	139.4 $\pm$ 36.4	177.5 $\pm$ 71.1
Total ciliated cells	42.7 $\pm$ 23.9	5.2 $\pm$ 5.8 <sup>x</sup>	10.4 $\pm$ 6.7 <sup>x</sup>	23.7 $\pm$ 19.3	11.7 $\pm$ 6.8	23.4 $\pm$ 15.2
Normal	40.2 $\pm$ 24.6	4.7 $\pm$ 4.9 <sup>x</sup>	5.1 $\pm$ 4.3 <sup>x</sup>	6.9 $\pm$ 6.1 <sup>x</sup>	11.0 $\pm$ 7.8	14.6 $\pm$ 11.6
Abnormal	2.4 $\pm$ 2.6	0.5 $\pm$ 0.9	5.3 $\pm$ 5.3	17.1 $\pm$ 13.2 <sup>x, +, **</sup>	0.7 $\pm$ 0.9	8.7 $\pm$ 3.5
Total serous cells	156.2 $\pm$ 16.7	150.3 $\pm$ 20.8	219.0 $\pm$ 47.1 <sup>xx, +</sup>	191.9 $\pm$ 41.2	95.0 $\pm$ 24.5	105.5 $\pm$ 37.6
Normal	154.0 $\pm$ 15.2	148.6 $\pm$ 20.2	211.1 $\pm$ 48.9	126.8 $\pm$ 77.3	95.0 $\pm$ 24.5	104.8 $\pm$ 38.5
Abnormal	2.2 $\pm$ 2.5	1.7 $\pm$ 1.2	7.9 $\pm$ 6.5	19.8 $\pm$ 11.1 <sup>x, +, **</sup>	0 $\pm$ 0	0.6 $\pm$ 0.9
Total basal cells	36.5 $\pm$ 12.9	36.0 $\pm$ 11.9	13.9 $\pm$ 13.0 <sup>x, +</sup>	9.6 $\pm$ 5.3 <sup>x, +</sup>	24.7 $\pm$ 2.3	23.4 $\pm$ 2.5
Total globular leukocytes	15.5 $\pm$ 5.0	18.1 $\pm$ 10.4	20.3 $\pm$ 12.4	12.6 $\pm$ 10.1	5.6 $\pm$ 6.0	10.8 $\pm$ 0.8
Total necrotic cells	2.0 $\pm$ 2.0	3.2 $\pm$ 1.8	6.0 $\pm$ 1.6	19.6 $\pm$ 6.0 <sup>x, +, *</sup>	0 $\pm$ 0	1.9 $\pm$ 2.7
Total degenerate cells	6.1 $\pm$ 5.6	4.6 $\pm$ 2.4	13.2 $\pm$ 8.0	33.6 $\pm$ 15.2 <sup>x, +, *</sup>	0.7 $\pm$ 1.0	8.9 $\pm$ 3.5
Abnormal ciliated/ Ratio Total Ciliated	0.1 $\pm$ 0.1	0.0 $\pm$ 0.1	0.5 $\pm$ 0.4 <sup>xx, +</sup>	0.7 $\pm$ 0.1 <sup>x, +</sup>	0.1 $\pm$ 0.1	0.4 $\pm$ 0.1
Abnormal Serous/ Ratio Total Serous	0.014 $\pm$ 0.015	0.011 $\pm$ 0.007	0.038 $\pm$ 0.03	0.108 $\pm$ 0.071 <sup>x, +, **</sup>	0.0 $\pm$ 0.0	0.008 $\pm$ 0.011
Cell surface blebs and sloughed cells	0.6 $\pm$ 1.3	4.4 $\pm$ 3.5	8.0 $\pm$ 9.2	9.2 $\pm$ 5.7	0.0 $\pm$ 0.0	0 $\pm$ 0



## OXYGEN FREE RADICALS STIMULATE SECRETION OF MUCIN BY RODENT AIRWAY EPITHELIUM IN VITRO

K. B. Adler, J. E. Schwarz, and J. E. Repine

Reactive oxygen metabolites can be generated in the lung subsequent to inhalation of many deleterious particulates and gases.<sup>1</sup> Oxygen free radicals are associated with a broad spectrum of pulmonary lesions, such as constriction of airway and vascular muscle, edema, and generalized cell injury.<sup>2</sup> Since obstruction of respiratory airways with mucus often accompanies pulmonary disorders associated with these same lesions, the possibility that oxygen free radicals could stimulate secretion of mucin by respiratory epithelium was investigated. We found that superoxide stimulated secretion of mucin by explants of rodent airways via a mechanism that may involve lipoxygenase metabolism of arachidonic acid within secretory cells of the respiratory mucosa. With the laser microprobe mass analyzer (LAMMA 500, Leybold Heraeus Co., Cologne, FRG) stimulation of secretion by lipoxygenase products of arachidonic acid metabolism was demonstrated to correlate with alterations in the differential distribution of intracellular calcium within epithelial secretory cells.

### Methods

Explants of trachea from male Hartley guinea pigs (300 g) were placed into organ culture as described previously.<sup>3</sup> The explants were exposed for 2 h to chemically generated oxidants: D-glucose (1%) + glucose oxidase (0.35–35  $\mu$ /ml) and resulted in generation of peroxides; or purine (0.02–2 mM) + xanthine oxidase (0.002–0.2  $\mu$ /ml) to generate superoxide.<sup>4</sup> At the end of the 2h period, secretion of mucin was monitored and compared to control (no oxidant addition) values for mucin secretion, with the use of uptake and release of radiolabeled glucosamine and acid precipitation, as described previously.<sup>3</sup> The effects of simultaneous addition of 100  $\mu$ g/ml of the free radical-scavenging enzymes catalase (scavenges hydrogen peroxide) and superoxide dismutase (SOD, scavenges superoxide) were evaluated, as were effects of inhibitors of arachidonic acid metabolism: indomethacin (cyclooxygenase inhibitor) and NDGA (cyclo- and lipoxygenase inhibitor), both at  $10^{-5}$  M.

Additional explants were exposed to stimulatory concentrations ( $10^{-8}$  M) of the lipoxygenase metabolite leukotriene  $C_4$  (LTC<sub>4</sub>) for 1 h. At that time, they were rapidly frozen in a liquid nitrogen based bounce-free system ("Genetleman Jim"; Ted Pella Inc., Tustin, Calif.) and freeze-substituted.<sup>5</sup> After they were embedded in Spurr's resin, sections of approximately 0.25 $\mu$ m thickness were placed on copper electron microscopic grids. The sections were examined at 320 $\times$  magnification in the LAMMA 500,<sup>6</sup> and the amounts of calcium in cytoplasm, nuclear membrane, and inner face of the plasmalemma were compared between secretory cells in control and leukotriene-stimulated tissues.

### Results

As illustrated in Table 1, H<sub>2</sub>O<sub>2</sub> generated by glucose and glucose oxidase did not affect secretion of mucin. However, superoxide, generated by purine (0.02–2 mM) plus xanthine oxidase (0.002–0.2  $\mu$ /ml), stimulated secretion of mucin by explants of rodent trachea in a concentration-dependent manner. The stimulatory effect was inhibited by simultaneous addition of the scavenging enzyme SOD, at 100  $\mu$ g/ml, but not by catalase at the same concentration. Indomethacin and NDGA, both at  $10^{-5}$  M, abolished the stimulatory response to superoxide, which suggests either involvement of arachidonic acid metabolites in the response to superoxide, or an antioxidant effect of these inhibitors.

To investigate further the possibility that arachidonate metabolites could be involved in stimulated secretion, secretory cells in explants of guinea pig trachea exposed to the

---

Authors Adler and Schwarz are at the University of Vermont (Department of Pathology), Burlington, Vt. Author Repine is at the Webb-Waring Lung Center, Denver, Colo. Support from the Council for Tobacco Research-USA, Inc., is acknowledged.

TABLE 1.--Effects of oxidants on secretion of mucin by guinea pig tracheal explants.

Agent	Conc	N	Mucin secretion (% control) *
purine + xanthine oxidase	(2mM)		
xanthine oxidase	(0.02 U/ml)	6	246 + 23**
xanthine oxidase	(0.002 U/ml)	12	163 + 7**
xanthine oxidase	(0.0002 U/ml)	6	98 + 8
purine + xanthine oxidase	(2mM)		
+ NDGA	(0.002 U/ml)		
	10 <sup>-5</sup> M	6	112 + 7
Indomethacin	10 <sup>-5</sup> M	6	102 + 3
SOD	(100 ug/ml)	6	115 + 7
Catalase	(100 ug/ml)	6	154 + 11**

\* = Mean + 1 S.E.

\*\* = Significantly increased over control values

TABLE 2.--Differential distribution of calcium within mucosal secretory cells of guinea pig tracheal explants.\*

Cellular Site	LTC4-exposed**	Control**
Cytoplasm	1419 + 150	759 + 229
Nuclear Membrane	1110 + 239	1101 + 234
Plasma Membrane	575 + 191	1226 + 114

\* = Calcium content measured as integrated peak at AMU 40, expressed in millivolts.

\*\* = All values are means + 1 S.E. N=12 at each point.

stimulatory peptidyl leukotriene LTC4 were examined in the LAMMA 500 for quantitative comparison of the calcium content at different intracellular sites. As illustrated in Table 2, LTC4-exposed cells had a significantly higher calcium content within cytoplasmic areas, and a significantly lower amount of calcium associated with the plasma membrane. This result would correlate well with the stimulatory effect of LTC4 on secretion, as an increase in cytoplasmic calcium (correlating with its release from intracellular membrane storage sites) could be the trigger for stimulation of mucin release in respiratory epithelium.

### Conclusions

The results of this study indicate chemically generated oxidants can stimulate secretion of respiratory mucin in vitro. The stimulatory effect may be mediated through activation of the lipooxygenase enzymatic pathway of arachidonic acid metabolism, as lipooxygenase products, specifically peptidyl leukotrienes, can stimulate mucin secretion. The differential distribution of calcium within secretory cells of leukotriene-exposed and control tissues suggests stimulation of secretion by leukotrienes may be triggered by release of calcium from storage sites on intracellular membranes.

## References

1. B. A. Freeman and J. D. Crapo, "Free radicals and tissue injury," *Lab. Invest.* 47: 412-426, 1982.
2. K. J. Johnson, J. C. Fantone II, J. Kaplan, et al., "In vivo damage of rat lungs by oxygen metabolites," *J. Clin. Invest.* 67: 983-993, 1981.
3. K. B. Adler, B. T. Mossman, G. B. Butler, et al., "Interaction of Mount St. Helens' volcanic ash with cells of the respiratory epithelium," *Environ. Res.* 35: 346-361, 1984.
4. R. M. Tate, H. G. Morris, W. R. Schroeder, et al., "Oxygen metabolites stimulate thromboxane production and vasoconstriction in isolated saline-perfused rabbit lungs," *J. Clin. Invest.* 74: 608-613, 1984.
5. A. R. Spurr, "Freeze-substitution additives for sodium and calcium retention in cells studied by x-ray analytical electron microscopy," *Bot. Gaz.* 133: 263-272, 1972.
6. H. J. Heinen, F. Hillenkamp, R. Kaufmann, et al., "LAMMA: A new laser microprobe mass analyzer for biomedicine and biological materials analysis," in A. Frigerio and M. McCamish, Eds., *Recent Developments in Mass Spectrometry in Biochemistry and Medicine*, Amsterdam: Elsevier, 1980, vol. 6, 435-451.

## ULTRASTRUCTURAL EVALUATION OF HUMAN NASAL EPITHELIUM: AN EXPERIMENTAL TOOL IN INHALATION TOXICOLOGY

J. L. Carson and A. M. Collier

The cellular lining of the large conducting airways of humans consists of a pseudostratified columnar epithelium.<sup>1</sup> Ciliated cells comprise the majority of the superficial cells of this layer with interspersed mucus-secreting and brush border cells. The action of mucus generated by the secretory cells to entrap inhaled particulates and endogenous cellular debris, and of the ciliated cells to sweep these contaminants physically from the airways, comprises a highly coordinated first line of defense for the airways known as the mucociliary escalator. Failure or compromised function of either component of the escalator may lead to enhanced susceptibility to infection or other pulmonary injury. Previous studies in our laboratory have demonstrated that the pseudostratified columnar epithelium lining the nasal turbinates of normal healthy human subjects shares a morphologic and physiologic identity with that of the lower large airways.<sup>2,3</sup> In addition, the epithelium lining the nasal turbinates can be conveniently and noninvasively retrieved with a minimum of discomfort to the subject. These samples may be used for direct structure/function analyses, maintained and manipulated as organ culture explants for experimental studies, or used to assess injury to the airway epithelium by toxic or infectious agents.

Because of the ease of acquisition of nasal epithelium and its similarity with that of the lower airways, and because the lining of the nasal cavities is the first site of interaction of the respiratory airways with the environment, we have directed our research efforts toward the use of nasal epithelium to gain additional insights into the biology of the respiratory airways, to obtain a perspective of general respiratory health, and to identify subtle pathologic changes that may be associated with infection or exposure to specific components of air pollution.

### *Experimental*

We have used two approaches for the acquisition of nasal epithelium from human subjects. The technique described by Alford et al.<sup>4</sup> retrieves the epithelium in a small intact mass in which a sense of anatomic orientation is preserved. This procedure particularly facilitates histological and ultrastructural analyses involving ultrathin sections or freeze-fracture replicas and greatly simplifies transfers of the sample to organ culture. The approach described by Rutland et al.,<sup>5</sup> on the other hand, has proved superior for examination of the epithelium by scanning electron microscopy. Nasal epithelium has been obtained by both these procedures from healthy human volunteers prior to and immediately following controlled exposure to 0.2 ppm nitrogen dioxide, 0.75 ppm sulfur dioxide, or 0.4 ppm ozone, for 1, 2, and 4 h, respectively, and from other subjects with various naturally acquired acute and chronic respiratory diseases. Nasal epithelium from normal healthy individuals processed by conventional ultrastructural methods retains its histologic integrity and relative anatomic orientation appearing as loose sheets or small rounded spheres of cells. Ciliated cells represent the preponderance of cell types in normal subjects although mucus-secreting cells and brush border cells are also readily identifiable. At the ultrastructural level, ciliogenic profiles are frequent in both ultrathin sections and in freeze-fracture preparations.<sup>6</sup> Previous studies have documented the incidence of abnormal cilia in normal airways to be of the order of 3-5%.<sup>7,8</sup> Compound cilia (cilia having two or more axonemes confined by a common membrane) are one of

---

The authors are at the Department of Pediatrics, Center for Environmental Medicine, and Frank Porter Graham Child Development Center, University of North Carolina, Chapel Hill, NC 27514. Support of the Pediatric Specialized Center of Research (SCOR) HL19171 from the National Heart, Lung, and Blood Institute and of Cooperative Agreements CR807392 and CR812738 from the U.S. Environmental Protection Agency is gratefully acknowledged. They also thank Nancy Hu and Todd Gambling for excellent technical assistance.

the more obvious forms of abnormal cilia seen in the airway epithelium. Because ciliary structure is well recognized to be requisite for optimal ciliary kinetics, the functional efficacy of compound cilia is questionable. Where the frequency of such abnormal cilia is small, compromised clearance is most likely negligible. However, more extensive ciliary injury due to infection or toxic inhalation may compromise collateral clearance and thus dispose the airways to further injury. We have used the incidence of compound cilia in the nasal epithelium as a measure of epithelial cell injury due to pollutant exposure. Our control specimens indicated no greater incidence of compound cilia than that reported by other laboratories. Examination of post-exposure samples from subjects exposed to ozone<sup>9</sup> or nitrogen dioxide<sup>10</sup> likewise indicated no appreciable increase in the prevalence of compound cilia. In contrast, samples obtained from seven subjects exposed to sulfur dioxide<sup>11</sup> exhibited a wide range of response relative to the incidence of compound cilia, with over half the subjects exhibiting a statistically significant increase in the frequency of compound cilia in the post-exposure interval.

### Conclusions

In summary, ultrastructural examination of human nasal epithelium, which can be conveniently obtained in either an experimental or clinical setting, represents a useful approach to the detailed characterization of airway epithelial cell fine structure. Additionally, this procedure is a reliable means for the evaluation of compromised structural and/or functional integrity of the airway epithelium that may be associated with acute air pollutant exposure and/or infection.<sup>12</sup> The mechanisms leading to the formation of compound cilia in the respiratory airways are not understood. Perhaps ciliary membrane integrity is compromised in such a way as to dispose them to fusion in the presence of some environmental insult, as was suggested by our experience with sulfur dioxide exposure. Also, the possibility that they are products of abnormal ciliogenic processes should not be overlooked. The goal of our future studies in air-pollution research is to achieve a better understanding of the direct, acute effects of inhaled toxic materials on the biology of human airway epithelial cell, particularly the identification of variant structure/function relationships that may be relevant to the development of chronic airways diseases.

### References

1. R. G. Breeze and E. B. Wheeldon, "The cells of the pulmonary airways," *Am. Rev. Respir. Dis.* 116: 705-777, 1977.
2. M. R. Knowles et al., "Measurements of nasal transepithelial electric potential differences in normal human subjects *in vivo*," *Am. Rev. Respir. Dis.* 124: 484-490, 1981.
3. J. L. Carson et al., "Ultrastructural characterization of epithelial cell membranes in normal human conducting airway epithelium: A freeze-fracture study," *Am J. Anat.* 173: 257-268, 1985.
4. B. R. Alford et al., "Atraumatic biopsy of nasal mucosa," *Arch. Otolaryng.* 90: 88-92, 1969.
5. J. Rutland et al., "Nasal brushing for the study of ciliary ultrastructure," *J. Clin. Pathol.* 35: 357-359, 1982.
6. J. L. Carson et al., "Morphometric aspects of ciliary distribution and ciliogenesis in human nasal epithelium," *Proc. Nat. Acad. Sci. (U.S.A.)* 78: 6996-6999, 1981.
7. C. M. Rossman et al., "Nasal ciliary ultrastructure and function in patients with primary ciliary dyskinesia compared with that in normal subjects with various respiratory diseases," *Am. Rev. Respir. Dis.* 129: 161-167, 1984.
8. C. L. Wissemann et al., "The prevalence of abnormal cilia in normal pediatric lungs," *Arch. Pathol. Lab. Med.* 105: 552-555, 1981.
9. J. L. Carson et al., "Response of human ciliated respiratory epithelium to brief *in vivo* ozone exposure: An ultrastructural study," *Environ. Res.* 37: 212-227, 1985.
10. J. L. Carson (unpublished results).
11. J. L. Carson et al., "The appearance of compound cilia in the nasal mucosa of normal human subjects following acute, *in vivo* exposure to sulfur dioxide," *Environ. Res.* (in press).
12. J. L. Carson et al., "Acquired ciliary defects in nasal respiratory epithelium of children with acute viral upper respiratory infections," *N. Engl. J. Med.* 312: 463-468, 1985.

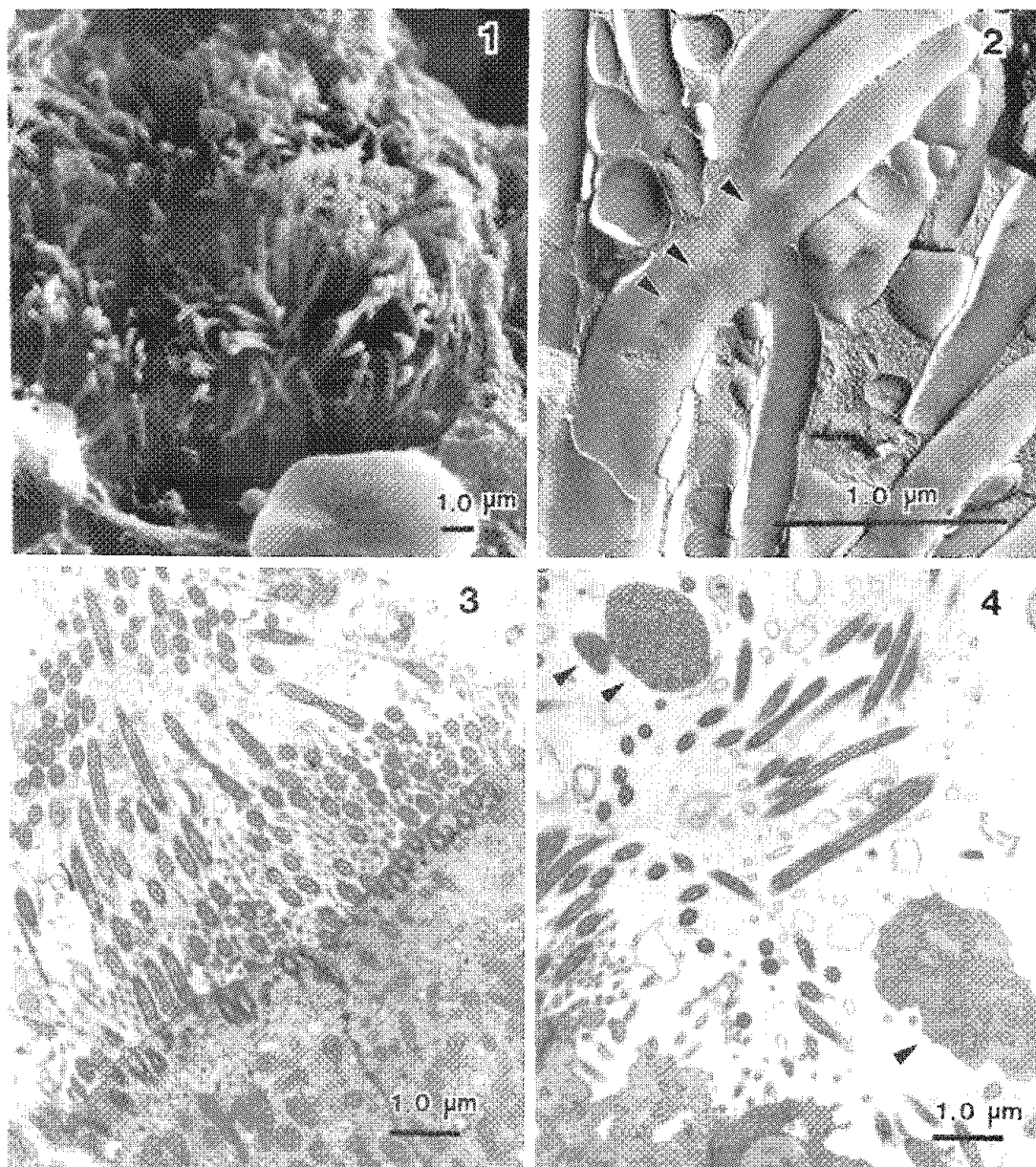


FIG. 1.--Scanning electron micrograph of bed of cilia in sample of nasal epithelium obtained by brush biopsy from normal, healthy human subject.

FIG. 2.--Transmission electron micrograph of freeze-fracture replica of nasal epithelium from subject exposed to sulfur dioxide. Arrows indicate sites of fusion of adjacent ciliary membranes leading to formation of compound cilia.

FIG. 3.--Transmission electron micrograph of ultrathin section of ciliated human nasal epithelium prior to controlled exposure to sulfur dioxide.

FIG. 4.--Transmission electron micrograph of ultrathin section of ciliated human nasal epithelium from same subject as Fig. 3 immediately following controlled exposure to sulfur dioxide. Arrows indicate compound cilia.

## ULTRASTRUCTURAL CHANGES IN NASAL EPITHELIUM OF MONKEYS EXPOSED TO AMBIENT LEVELS OF OZONE

J. R. Harkema, C. G. Plopper, D. M. Hyde, J. A. St. George,  
D. W. Wilson, and D. L. Dungworth

Ozone ( $O_3$ ) is the major oxidizing component in photochemical smog. Although  $O_3$ -induced bronchiolitis has been morphologically characterized,<sup>1-4</sup> effects of  $O_3$  on the upper airways have not been thoroughly investigated. The purpose of this study was to determine whether acute and subchronic exposures to ambient levels of  $O_3$  induce ultrastructural changes in the nasal epithelium. The specific objectives were to locate the site(s) of  $O_3$ -induced epithelial changes in the nasal cavity of monkeys and describe the ultrastructural features that characterize these nasal lesions.

### *Materials and Methods*

Eighteen male and 10 female, colony-born bonnet monkeys (*Macaca radiata*) were used in this study. The monkeys had been raised indoors and were placed in 4.3m<sup>3</sup> exposure chambers for 1 week prior to exposure. These animals were then exposed to 0.00, 0.15, or 0.30 ppm  $O_3$  for 6 or 90 days, 8 h/day. Ozone was generated by silent arc discharge and monitored every half-hour by a DASIBI UV  $O_3$  monitor which was calibrated by a DASIBI absolute  $O_3$  photometer. Recorded concentrations of  $O_3$  were based on the ultraviolet photometric scale. After exposure, animals were anesthetized with ketamine and sodium pentobarbitol and euthanatized by exsanguination via the abdominal aorta. Immediately after death, the head was removed from the carcass and both nasal airways were flushed retrograde through the nasopharyngeal orifice with 100-200 ml of 0.6% glutaraldehyde/0.45% paraformaldehyde in cacodylate buffer (440 mOsm, pH of 7.40). Eyes, integument, musculature, and brain were then removed and the head was stored in a large volume of the same fixative until processing.

After fixation, the left half of the nasal cavity from each monkey was split down the longitudinal midline from the anterior nares to the posterior end of the nasopharynx, which exposed the mucosal surfaces. The left septal wall was photographed for later recording of sample sites. Most of the mucosa from this left septal wall was removed from the underlying cartilaginous or bony tissue in thin strips. These strips were excised with fine scissors, razor blades, and forceps, while the tissue was viewed through a high resolution dissection microscope. The areas were coded and recorded on the photograph of the septal wall. Tissue strips were processed for scanning electron microscopy (SEM) or transmission electron microscopy (TEM).

Tissues for SEM were post-fixed in 1% osmium tetroxide in 0.1M cacodylate buffer, dehydrated in a graded series of ethanol solutions, critical-point dried with  $CO_2$ , mounted on aluminum stubs, and coated with gold in a vacuum sputter coater. They were examined in an ETEC scanning electron microscope.

Tissues for TEM were also post-fixed in 1% osmium tetroxide, dehydrated in a graded series of alcohol, infiltrated with propylene oxide solutions, and then embedded in epon araldite. One-micron sections were stained with toluidine blue for light microscopy. Strips ~1mm were cut from the large blocks, re-embedded in molds, and thin-sectioned with a diamond knife on a Sorvall MT2-B microtome. These sections were mounted on Formvar-coated single slotted copper grids, stained with uranyl acetate and lead citrate, and examined with a Zeiss EM 10 electron microscope.

### *Results*

$O_3$ -induced changes in nasal mucosa were restricted to the anterior portions of the nasal cavity. These changes were limited to the nonciliated transitional epithelium and

---

Dr. Harkema is at the Inhalation Toxicology Research Institute, Albuquerque, NM 87185; the other authors are at the departments of Pathology and Anatomy, School of Veterinary Medicine, University of California, Davis, CA 95616, and the California Primate Center at Davis. This study was supported by Grant PO1-ES00628 and in part by DRR00169 and HL28978.

the ciliated respiratory epithelium anterior to the level of the nasal turbinates. No significant lesions were observed in the respiratory or olfactory epithelium of the posterior nasal cavity or nasopharynx. Changes in the transitional epithelium (which lies between the squamous epithelium of the nasal vestibule and the respiratory epithelium of the main nasal chamber) and changes in the anterior respiratory epithelium were most severe in monkeys exposed for 90 days. There were no significant differences in the degree of these changes in monkeys exposed to 0.15 ppm O<sub>3</sub> compared to those exposed to 0.30 ppm.

The most consistent surface changes in the nonciliated, transitional epithelium was an increase in dome-shaped luminal cells with microvillar surfaces. Increase in these dome-shaped cells gave this epithelial surface a cobblestone appearance (Fig. 1). These luminal cells contained varying amounts of secretory granules and were less frequent in the transitional epithelium of animals exposed only to filtered air.

In the respiratory epithelium of the anterior nasal cavity from animals exposed to O<sub>3</sub>, there was multifocal loss of cilia and the presence of luminal cells with attenuated cilia and/or nonciliated cells with microvillar surfaces (Fig. 2). Some of the O<sub>3</sub>-exposed ciliated cells had very electron-dense cytoplasmic and nuclear staining, and condensed mitochondria characteristic of necrosis (Fig. 3). Other ciliated cells in these areas did not differ from normal ciliated cells in control animals. The nonciliated microvillar cells in these focal areas of O<sub>3</sub> damage in the anterior respiratory epithelium were not observed in control animals. These luminal cells were cuboidal with basal cytoplasm that did not extend beyond the midregion of the epithelium. Both basal bodies and secretory granules were often observed in their apical cytoplasm.

Secretory cells in the ciliated respiratory epithelium of the O<sub>3</sub>-exposed monkeys also had ultrastructural features that differed from those of control animals. In all of the O<sub>3</sub>-exposed monkeys fewer typical goblet cells with abundant secretory granules were present than in controls. Most of the secretory cells in O<sub>3</sub>-damaged respiratory areas had fewer and more widely scattered granules than those in mucous cells of monkeys exposed only to filtered air. In addition, half of the 90-day, 0.30ppm-exposed monkeys had anterior respiratory epithelium which contained numerous secretory cells with unusually dilated cisterna of granular endoplasmic reticulum (gER) (Fig. 3). These cisterna were not observed in the nasal epithelium of 6 day, O<sub>3</sub>-exposed animals or control animals exposed to 0.00 ppm O<sub>3</sub>.

In addition to changes in luminal cells with O<sub>3</sub> exposure, there were changes in the underlying epithelial cells. Small mucous granular cells were more prominent in the O<sub>3</sub>-affected areas, as were unique cuboidal cells with unusual intracytoplasmic lumina lined with microvilli and cilia. However, basal cells appeared to be unchanged by O<sub>3</sub> exposure.

### *Discussion*

This study demonstrates that exposures to ambient concentrations of O<sub>3</sub> can induce morphologic changes in the nasal epithelium of primates. These changes are restricted to the epithelium in the anterior nasal cavity. Some features of this lesion in the nasal epithelium are similar to those previously described in the trachea and terminal bronchioles after O<sub>3</sub>-exposure.<sup>1-5</sup> Deciliation is a common feature of the O<sub>3</sub> lesion in these other areas as it is in the anterior nasal cavity. Ciliated cell necrosis is also a feature of the O<sub>3</sub>-induced tracheal lesion,<sup>5</sup> but is not characteristic of the lesion in the pulmonary terminal bronchiole.

Other O<sub>3</sub>-induced responses in the nasal epithelium appear to be unique to this epithelial cell population. The alterations in secretory cells and the presence and proliferation of intracytoplasmic lumina in O<sub>3</sub>-exposed nasal epithelium have not been reported in other conducting airways. Therefore, it appears that the surface epithelial response to O<sub>3</sub> is extremely variable within the respiratory tract not only in the distribution of the lesions, but also in the character of these lesions at various levels of the respiratory airway.

The O<sub>3</sub>-induced ultrastructural changes described in this study may indicate alterations in normal physiological functions of the nasal mucosa (i.e., mucociliary clearance). These functions are important nasal defense mechanisms that defend the lungs from excessive burdens of harmful agents. Compromise of these defense mechanisms could increase insult to the lungs which would lead to pulmonary disease.



## References

1. W. L. Castleman, D. L. Dungworth, L. W. Schwartz, and W. S. Tyler, "Acute respiratory bronchiolitis: An ultrastructural and autoradiographic study of epithelial cell injury and renewal in rhesus monkeys exposed to ozone," *Am. J. Pathol.* 98: 811-840, 1980.
2. W. L. Castleman, W. S. Tyler, and D. L. Dungworth, "Lesions in respiratory bronchioles and conducting airways exposed to ambient levels of ozone," *Ex. Mol. Pathol.* 26: 384-400, 1977.
3. P. W. Mellick, D. L. Dungworth, L. W. Schwartz, and W. S. Tyler, "Short term morphologic effects of high ambient levels of ozone on lungs in rhesus monkeys," *Lab. Invest.* 36: 82-90, 1977.
4. S. L. Eustis, L. W. Schwartz, P. C. Kosch, and D. L. Dungworth, "Chronic bronchiolitis in nonhuman primates after prolonged ozone exposure," *Am. J. Pathol.* 105: 121-137, 1981.
5. D. W. Wilson, C. G. Plopper, and D. L. Dungworth, "The response of the macaque tracheobronchial epithelium to acute ozone injury: A quantitative ultrastructural and autoradiographic study," *Am. J. Pathol.* 116: 193-206, 1984.

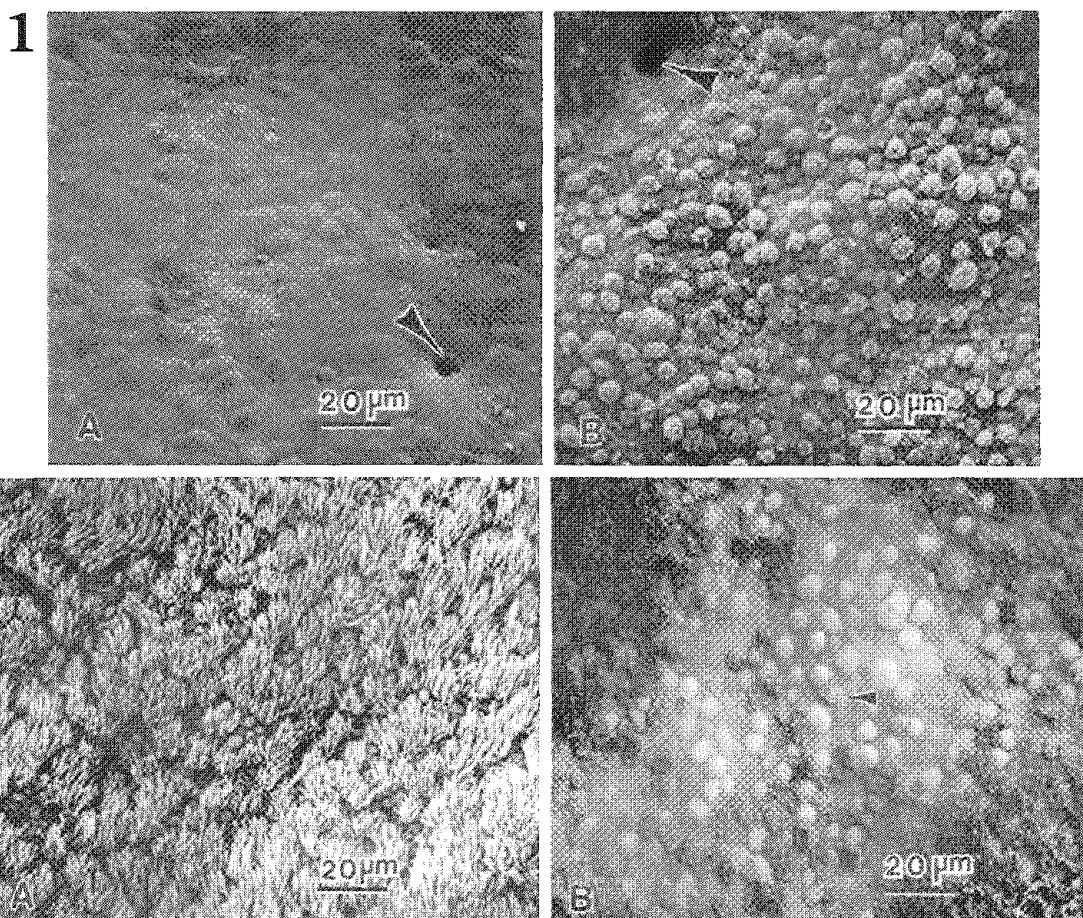


FIG. 1.--SEM micrographs of luminal surfaces of transitional epithelium from nasal septum of monkeys exposed to 0.00 ppm  $O_3$  (A) and 0.30 ppm  $O_3$  for 90 days (B). Marked increase in domed luminal cells after  $O_3$  exposure. Arrows point to openings of ducts from subepithelial glands.

FIG. 2.--SEM micrographs of luminal surface of anterior respiratory epithelium from nasal septum of animals exposed to 0.00 ppm  $O_3$  (A) and 0.30 ppm  $O_3$  for 90 days (B).  $O_3$ -exposed surfaces had loss of cilia and cells with shortened cilia (arrowheads) and nonciliated cells with domed luminal surfaces.

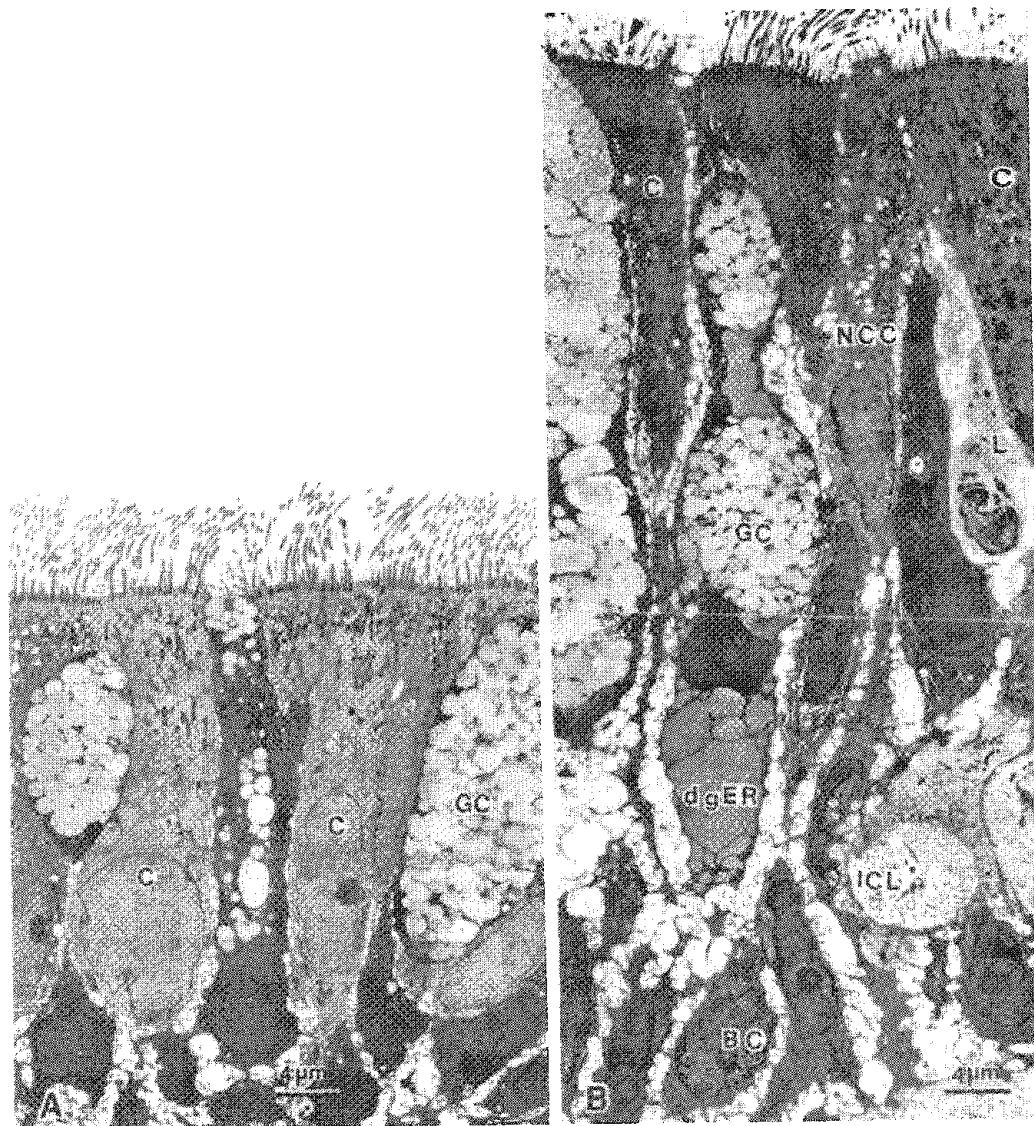


FIG. 3.--Montages of TEM micrographs of anterior respiratory epithelium from nasal septa of monkeys exposed to 0.00 ppm O<sub>3</sub> (A) and 0.30 ppm O<sub>3</sub> for 90 days (B). C = ciliated cell, GC = goblet cell, BC = basal cell, NCC = nonciliated cell, ICL = intracytoplasmic lumina, L = leukocyte, dgER = dilated cisterna of granulated endoplasmic reticulum. Arrowhead points to damaged cilia.

## MORPHOLOGIC CHANGES IN THE UPPER, RESPIRATORY TRACT OF RODENTS EXPOSED TO TOXICANTS BY INHALATION

J. A. Popp, K. T. Morgan, J. Everitt, X. Z. Jiang, and J. T. Martin

Although numerous studies have defined ultrastructural changes in the lung and trachea after inhalation exposure of laboratory rodents, similar evaluations of toxic responses in the upper respiratory tract have been described rarely. Before toxic responses could be evaluated, a thorough description of the normal mucosa of the laboratory rodent was necessary.

CDF (F-344)/Cr1Br rats, B6C3F1 mice, or Swiss Webster mice were used in all morphologic studies of the nose of control or toxin-exposed animals. Tissue was fixed by intravascular perfusion of Karnovsky's fixative in cacodylate buffer following a flush with 10% Dextran 40.<sup>1</sup> The nasal structures were trimmed and postfixed in 1% osmium tetroxide. The skulls were decalcified in 10% EDTA in 0.1 M cacodylate buffer. For transmission electron microscopy (TEM), selected areas of the nasal mucosa were embedded in epon-araldite. For scanning electron microscopy (SEM), either decalcified or undecalcified tissue was dehydrated, placed in acetone, and critical point dried with carbon dioxide.

Ultrastructural characterization of the rodent nasal respiratory epithelium by TEM has demonstrated 6 different cell types<sup>2</sup> and an electron-dense membrane on the luminal surface of the nasal mucus.<sup>3</sup> Although all these cells are similar to cells found at other levels of the respiratory tract, their identification in the nasal mucosa has revealed the complexity of the epithelial lining of the nasal cavity of rodents. SEM evaluation of the nasal respiratory epithelium has clearly shown an uneven distribution of the various cell types, particularly the ciliated and nonciliated cells.<sup>4</sup> Subsequent correlative studies of ciliated cell distribution with nasal mucous flow have demonstrated that ciliated cells form rows in the same direction as mucous flow in certain areas of the nasal mucosa (Fig. 1).

Recent inhalation studies of chlorine,<sup>5</sup> formaldehyde,<sup>6</sup> and dimethylamine have demonstrated the utility of electron microscopy in the evaluation of toxic effects in the upper respiratory tract of rodents. In rats exposed to formaldehyde (15 ppm, 6 h/day, 2 days) and mice exposed to chlorine (9 ppm, 6 h/day, 1, 3, and 5 days), injured epithelial cells were observed detached from the basement membrane (Fig. 2). SEM studies resulted in the identification of areas which were preferentially affected by the inhaled toxin. TEM studies identified numerous intracellular lesions. Many lesions were nonspecific indications of cellular injury and included dilated endoplasmic reticulum and autophagocytosis. However, TEM also demonstrated hypertrophy of goblet cells and ciliated cells as a very early response to formaldehyde exposure. TEM studies also proved that formaldehyde injury to the rodent nasal respiratory epithelium is not cell specific, which suggests that the uneven distribution of lesions may be due to uneven delivery of the toxin to the epithelium rather than localization of a sensitive cell type. SEM quickly and efficiently demonstrated the areas of cilia loss in chlorine studies. In formaldehyde studies, TEM evaluation of the tissue showed that many cilia were internalized within the cytoplasm where they were both free in the cytoplasm and contained within membrane-bound vacuoles. Chronic exposure to dimethylamine (175 ppm, 6 h/day, 2 years) resulted in an increase in eosinophilic globules in the cytoplasm of nasal epithelial cells. By TEM, 2 different lesions were identified. In some cells, massively dilated endoplasmic reticulum contained homogeneous electron-dense material (Fig. 3). In other cells, distinct crystalline structures were found (Fig. 4).

Although ultrastructural evaluation of the nasal cavity of rodents is still limited, available studies have proven the utility of both SEM and TEM to aid in the understanding of toxin-induced lesions. Ultrastructural evaluation of the nasal cavity has been hindered in the past by the relative inaccessibility of the epithelium, since it is encased

---

The authors are at the Department of Experimental Pathology and Toxicology, Chemical Industry Institute of Toxicology, Research Triangle Park, NC 27709.

in bone. With currently available preparative techniques, electron microscopy will become a more important tool in the future as we develop a better understanding of nasal toxicology in the rodent.

#### References

1. J. A. Popp and J. T. Martin, *Proc. 39th EMSA*, 1981, 594.
2. N. A. Monteiro-Riviere and J. A. Popp, *Am. J. Anat.* 169: 31, 1984.
3. K. T. Morgan et al., *Am. Rev. Respir. Dis.* 130: 275, 1984.
4. J. A. Popp and J. T. Martin, *Am. J. Anat.* 169: 425, 1984.
5. X. Z. Jiang et al., *Toxicol. Appl. Pharmacol.* 71: 225, 1983.
6. N. A. Monteiro-Riviere and J. A. Popp, *Fund. Appl. Toxicol.* (1986, in press).

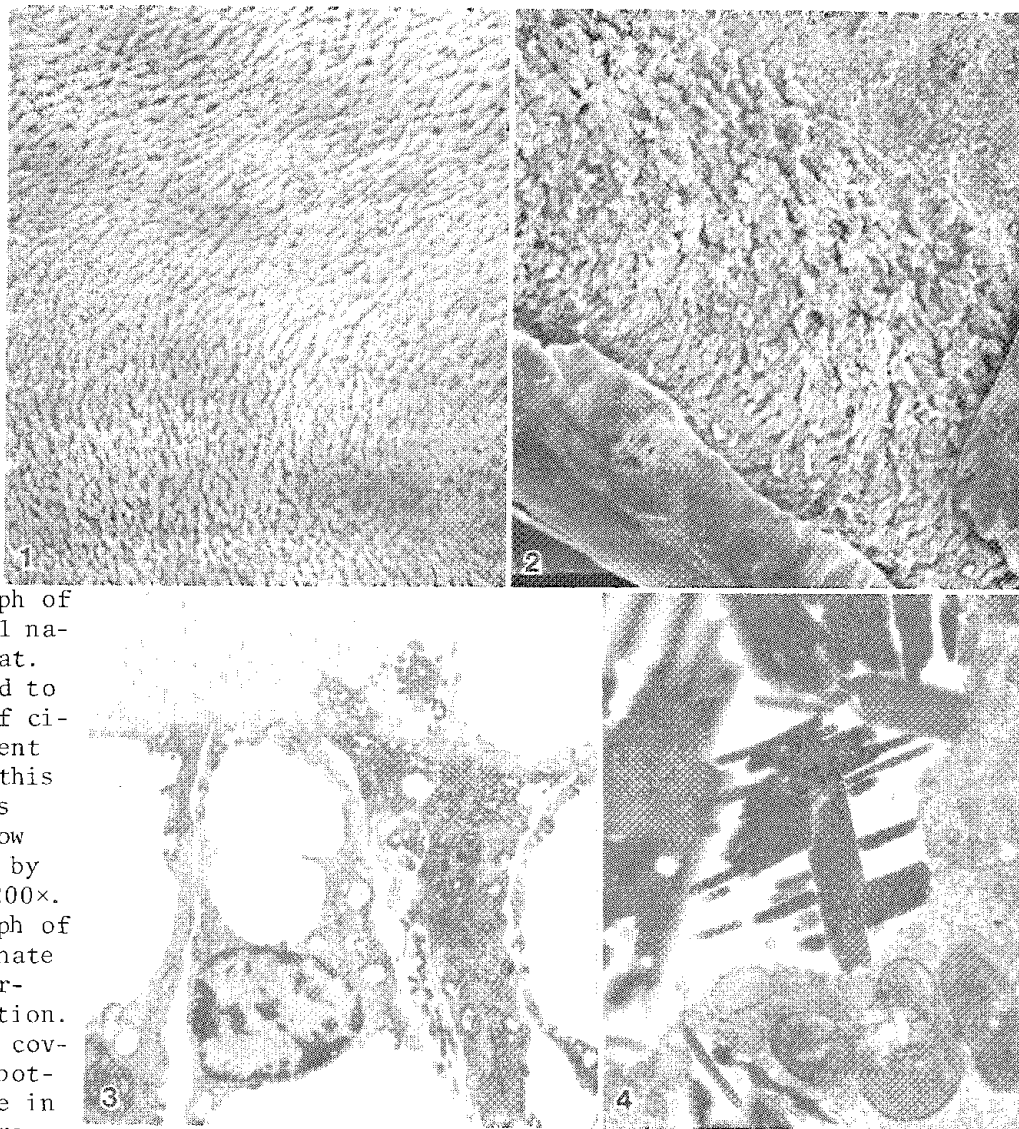


FIG. 1.--SEM micrograph of surface of mid-ventral nasal septum of F-344 rat. Mucus has been removed to reveal distribution of ciliated cells. Alignment of ciliated cells in this region of nose follows direction of mucus flow determined previously by in vitro techniques. 200 $\times$ .

FIG. 2.--SEM micrograph of largest ethmoid turbinate which lies in main air-stream during inspiration. Smooth adherent mucus covers ventral surface (bottom). Ciliated surface in this region normally resembles septum (cf. Fig. 1).

Exposure to 9.1 ppm chlorine gas for 3 days (6 h/day) resulted in exfoliation producing disorganized appearance (middle). A sharp line of demarcation between respiratory and olfactory epithelia is present (top). 325 $\times$ .

FIG. 3.--TEM micrograph of olfactory epithelium of F-344 rat exposed for 1 year to 2.5 ppm chlorine gas. Eosinophilic droplets are composed of amorphous floccular material lying in membrane-bound intracytoplasmic vacuoles. 3200 $\times$ .

FIG. 4.--TEM micrograph of crystals in olfactory epithelium of F-344 rat exposed to chlorine. By light microscopy, these crystals are often seen in association with intracytoplasmic droplets shown in Fig. 3. Electron microscopy demonstrated lack of periodic crystalline structure. 30 450 $\times$ .

## INORGANIC PARTICULATE MATTER FROM LUNGS OF INDIVIDUALS WITHOUT OCCUPATIONAL EXPOSURE

J. P. Mastin, W. J. Furbish, E. R. DeLong, V. L. Roggli, P. C. Pratt, and J. D. Shelburne

In an effort toward better understanding of the relationship between certain inhaled mineral particles and the diseases they cause, many investigators have analyzed the inorganic particulate matter in the lungs of individuals exposed to these minerals and looked for correlations between these data and severity of disease. The populations studied usually included individuals exposed in occupational settings, and the diseases studied were occupational pneumoconiosis (e.g., coal workers' pneumoconiosis and silicosis). However, few studies have been concerned with the pulmonary particulate burden in persons without an occupational history of exposure or clinical history of pneumoconiosis. Some studies have included such cases as controls, but made no attempt to correlate the analytical data with pathologic data. McNally quantitatively analyzed a series of lungs from an unexposed population for silica ( $\text{SiO}_2$ ),<sup>1</sup> and Lewis analyzed the total acid insoluble particulate burden gravimetrically from a similar population.<sup>2</sup> Again, no relationship to disease was mentioned in either of these studies. Churg compared the number of particles in lungs of patients with and without lung cancer and found the lung tissue from cancer patients to have more particles.<sup>3</sup>

In the current study, particulate matter from samples of lung tissue from randomly selected autopsy cases is analyzed gravimetrically and by qualitative and quantitative x-ray diffraction (XRD). Statistical analysis is used to determine whether correlations exist between the analytical data and demographic and pathologic data on individuals. The purposes here are to establish pulmonary particulate levels in a population not occupationally exposed as controls for possible future studies of exposed individuals, and to determine whether a relationship exists between the amount and type of particulate matter and severity of such common chronic lung conditions as emphysema, cancer, and changes in airways, both large and small.

### *Materials and Methods*

Lung tissue is obtained from randomly selected autopsy cases from the Duke University and Durham Veterans Administration Medical Center autopsy services and immediately frozen. Approximately 15 g of tissue, wet weight, is randomly selected from the upper and lower lobes. The weight of both lungs is recorded at this point. In every case, the tissue selected is not needed for diagnostic studies. Demographic and medical data are collected from the medical records for each case. These data include age, race, sex, occupational history, area of residence, pulmonary function test results, and medical history, including cause of death. In most cases, the lung not sampled is available to be fixed in an expanded state with formalin, and hilar slices from these lungs are used to estimate the severity of emphysema using the point-counting method described by Weibel<sup>4</sup> and Pratt.<sup>5</sup> Histologic sections are also available for assessment of chronic bronchitis by the method of Jamal et al.<sup>6</sup> and of changes in small airways, since these airways can show pathologic changes in individuals exposed to large amounts of mineral dust.<sup>7</sup> Blanks were prepared from fetal lung tissue not needed for diagnostic studies.

The partially frozen tissue is minced and dried at 100°C, and the particulate matter is isolated either by ashing at 450°C for 3 days, suspending the ash in 2.4 N HCl, and filtering onto a silver filter (0.45  $\mu\text{m}$  pore size); or by digesting in nitric acid for about 30 min and filtering onto a Nuclepore filter (0.4  $\mu\text{m}$  pore size). The weight of the particulate matter remaining on the filters ("dust") is determined gravimetrically. X-ray

---

Author Mastin's current address is the Division of Biomedical and Behavioral Science, National Institute for Occupational Safety and Health, Cincinnati, OH 45226; author Furbish is with Duke University, Department of Geology; author DeLong is with Health Services Research and Development, VA Medical Center, and Department of Community and Family Medicine, Duke University, Durham, N.C.; and authors V. L. Roggli, P. C. Pratt, and J. D. Shelburne are with the Department of Pathology, Duke University and VA Medical Center, Durham, N.C.

diffraction analysis is done on a Norelco/Phillips x-ray diffractometer with a copper target tube operated at 42 kV and 27 mA, a graphite crystal monochromator, a scintillation counter, and a count rate computer. Standards of quartz and kaolinite have been used for calibration and to insure that the treatments do not affect these minerals. Duplicate aliquots of tissue were taken from seven cases. One aliquot from each case was prepared by ashing and another by acid digestion. Analysis of the samples showed the techniques to give results that were not statistically different. Data from all cases, obtained by either technique, have therefore been combined.

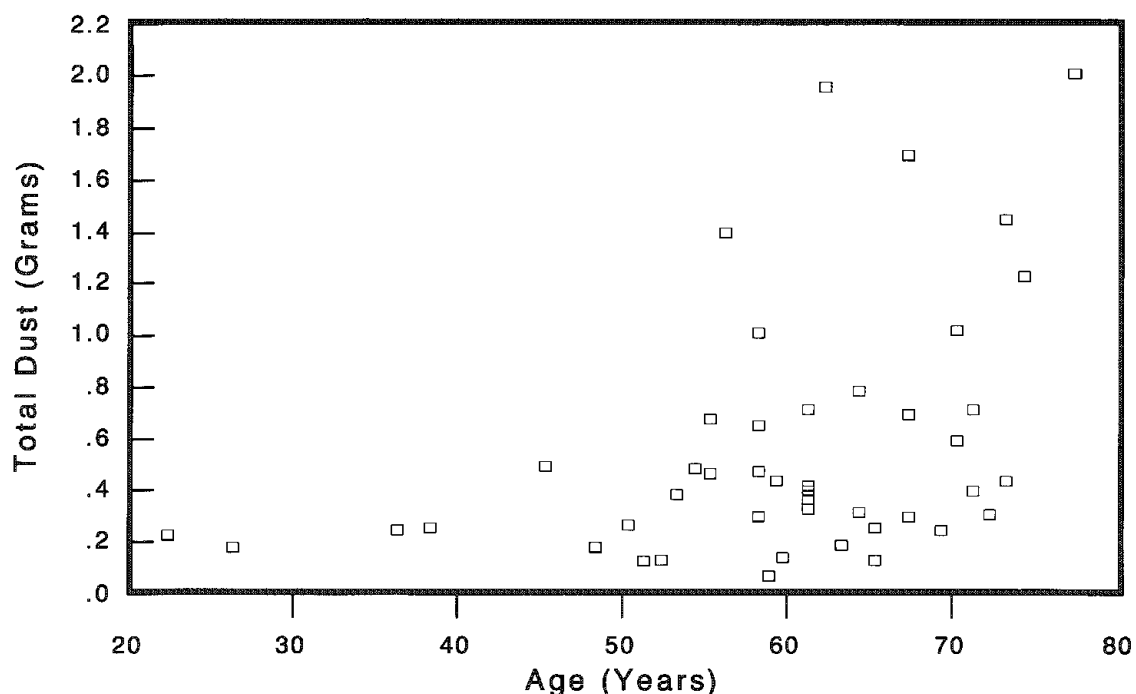


FIG. 1.--Total amount of dust (g) in both lungs, determined gravimetrically, vs age for 43 of 48 cases.

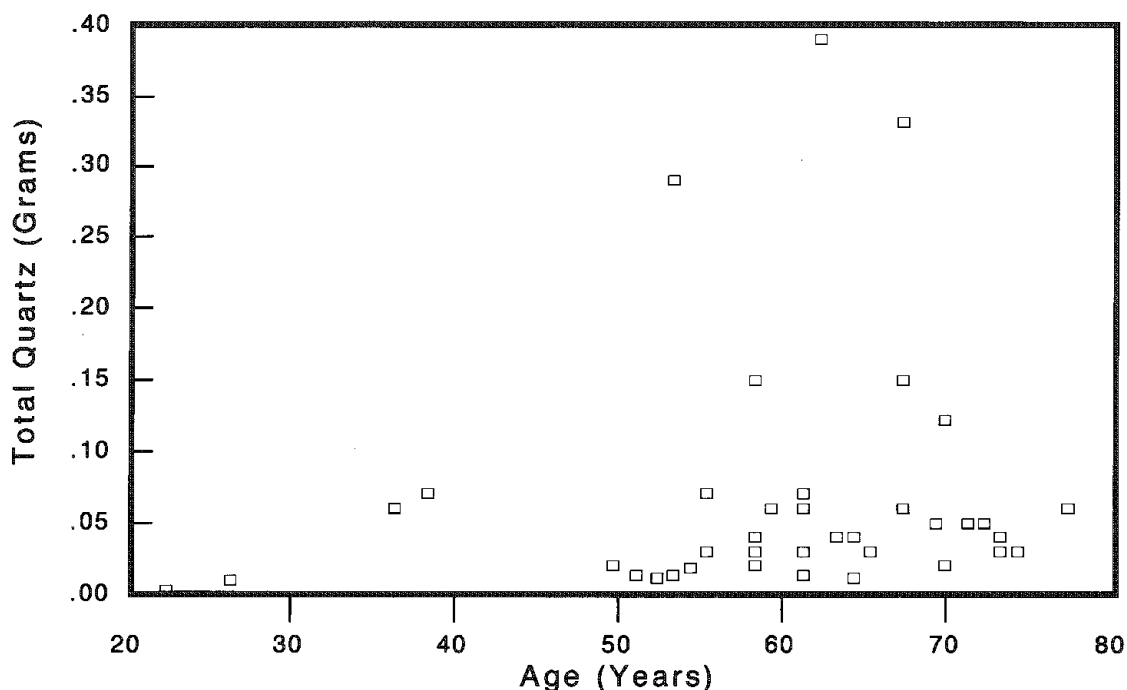


FIG. 2.--Total amount of quartz (g) in both lungs, determined by x-ray diffraction, vs age for 39 of 48 cases.



## Results and Discussion

To date, data from 48 cases have been collected. Quartz and talc were detected in all cases analyzed. Kaolinite was identified in all cases prepared by acid digestion, but in none of those prepared by ashing. High-temperature ashing, above about 400 C, changes the crystalline structure of kaolinite so that the diffraction peaks are weakened or lost altogether. Most of the cases also gave a peak in the 10Å region, suggesting the presence of phyllosilicate, possibly mica.

Table 1 gives the mean, standard deviation, median, and minimum and maximum values for age, smoking history (pack-years = packs per day × years smoked), dust, and quartz for the cases collected thus far. The quantities of dust and quartz are expressed as ratios to the dry weight of the samples and as total amounts in both lungs--e.g., total dust weight = total wet weight of both lungs × (sample dust weight/sample wet weight). Figure 1 shows a plot of total dust versus age; Fig. 2 is a plot of total quartz versus age. The plots indicate possible relationships between particulate matter and age, but obviously other factors are involved. Lewis reported an association between age and acid insoluble material in blue-collar but not white-collar workers.<sup>2</sup> Our analysis of the data reported by McNally indicated an association between age and silica, but this association was not discussed in that paper.<sup>1</sup>

The percent emphysema in this set of lungs ranges from 0 to 96%, with a mean and standard deviation of  $19.0 \pm 29.6\%$ . As expected, regression analysis showed a correlation between smoking and emphysema ( $r^2 = 0.59$  and  $p < 0.002$ ), which demonstrates the validity of this approach.

Continued collection of cases for this study is currently under way. The long-range goal of these studies is to be able to identify factors influencing the amount of particulate matter in these lungs, as well as pathologic effects these particles might have.

## References

1. W. D. McNally, "Silicon dioxide content of lungs in health and disease," *J. Amer. Med. Assoc.* 101: 584-587, 1983.
2. G. P. Lewis and L. Coughlin, "Lung 'soot' accumulation in man," *Atmos. Environ.* 7: 1249-1255, 1973.
3. A. Churg and B. Wiggs, "Mineral particles, mineral fibers, and lung cancer," *Environ. Res.* 37: 364-372, 1985.
4. E. R. Weibel, "Morphometrics of the lung," in H. Ralm and W. O. Fenn, Eds., *Handbook of Physiology*, Sec. 3, Respiration, Vol. I, p. 285, Washington, D.C.: American Physiological Society, 1964.
5. P. C. Pratt, R. T. Vollmer, and J. A. Miller, "Epidemiology of pulmonary lesions in nontextile and cotton textile workers: A retrospective autopsy analysis," *Arch. Environ. Health* 35: 133-138, 1980.
6. K. Jamal, T. P. Cooney, J. A. Fleetham, and W. M. Thurlbeck, "Chronic bronchitis: Correlation of morphologic findings to sputum production and flow rate," *Amer. Rev. Resp. Dis.* 129: 719-722, 1984.
7. A. Churg, J. L. Wright, B. Wiggs, P. D. Pare, and N. Lazar, "Small airways disease and mineral dust exposure," *Amer. Rev. Resp. Dis.* 131: 139-143, 1985.

TABLE 1.--Descriptive statistics.

	n†	Mean	Std deviation	Median	Minimum	Maximum
Age (year)	48	59	11.8	61	22	77
Smoking history (pack years)*	32	47.9	39.7	47.5	0	160
Dust/dry (mg/g)	47	2.4	1.8	2.0	0.47	9.5
Total dust** (g)	43	0.55	0.49	0.43	0.13	2.0
Quartz/dry (mg/g)	41	0.26	0.30	0.18	0.017	1.5
Total quartz**	39	0.061	0.086	0.048	0.01	0.4

\*Pack years = (packs/day × years smoked).

†Number of patients; data not available for some variables.

\*\*Total dust and total quartz refer to total weight in both lungs.

## ANALYTICAL SCANNING ELECTRON MICROSCOPY IN THE INVESTIGATION OF UNUSUAL EXPOSURES

V. L. Roggli

Analytical scanning electron microscopy has been extensively used in the characterization and identification of asbestos fibers isolated from lung tissue. However, this technique is also of value in the investigation of patients who have had unusual exposures. Often the nature of the exposure is suspected only after the analysis has been performed. Two examples of presentations of patients with unusual exposures are the subject of this report.

### *Case Histories*

*Case 1.* A 63-year-old woman presented to Duke University Medical Center with progressive shortness of breath and bibasilar interstitial markings on chest x ray. Bronchoscopy was normal, but bronchial washings showed numerous black fibers and gridlike structures, some of which were ferruginized. Open-lung biopsy was performed with a preoperative diagnosis of idiopathic pulmonary fibrosis. Histologic sections showed patchy interstitial fibrosis associated with black fibers. There was no history of occupational exposure to asbestos or other inorganic dusts.

*Case 2.* A 76-year-old man presented to the Durham Veterans Administration Medical Center for treatment of a large right upper lobe mass. He had a 50-pack-a-year smoking history and multiple strokes in the past three years. The patient's tumor was deemed inoperable, and he died during the admission. Autopsy confirmed a large cell carcinoma of the right upper lobe. In addition, there were bilateral parietal pleural plaques. Because of the author's interest in pleural plaques in relation to asbestos exposure, a portion of autopsy lung tissue was analyzed for mineral fiber content.

### *Materials and Methods*

In each case, wet formalin fixed lung tissue (from open biopsy in Case 1, from autopsy in Case 2) was weighed and then digested in 5.25% sodium hypochlorite solution as described.<sup>1</sup> The inorganic residue was collected on 0.4  $\mu$  pore-size 25mm-diameter Nuclepore filters. Filters were mounted on glass slides for light microscopic analysis after clearing in chloroform, and also on carbon planchets with colloidal graphite. The latter were sputter coated with gold for examination by scanning electron microscopy (JEOL JSM 35C at accelerating voltage of 20 kV) and energy-dispersive x-ray analysis (Kevex 7000 at 25 kV). The coated and uncoated fiber content of lung tissue was estimated, and 26 to 50 fibers were examined by EDXA in each case.

### *Results*

Digestion of a portion of the open biopsy tissue from Case 1 yielded 2.7 million black fibers per gram of wet lung tissue. Many fibers had sharp ends and angulated sides, giving a shard-like appearance. Some were bizarrely shaped. Approximately 0.2% of the fibers were coated--i.e., pseudoasbestos bodies (Fig. 1).<sup>2</sup> One hundred consecutive fibers were measured. The mean fiber length was 13  $\mu$ m ( $\pm$  6.6  $\mu$ m) and the mean fiber diameter was 2.1  $\mu$ m ( $\pm$  1.0  $\mu$ m). Twenty-six fibers were analyzed by EDXA, 22 of which contained no elements with atomic number above 11 (except for occasional traces of silicon, sodium, and chloride). One fiber contained a distinct peak for iron (Fig. 2). The other three fibers were sodium-aluminum-silicate, potassium-aluminum-silicate, and calcium only (one each). No asbestos fibers were identified. The morphology and composition of the black fibers is typical of woodstove dust,<sup>3</sup> and the source was traced to a poorly sealed wood stove in an inadequately ventilated trailer. Repeat bronchoscopy and bronchial washings six

---

The author is at Durham Veterans Administration and Duke University Medical Centers, Durham, NC 27710.



FIG. 1.--Dust recovered from bronchoalveolar lavage fluid on Nuclepore filter. Fiber in upper middle portion of field (arrow) is iron coated. Note grid-like structure left of center. Scale marker, 10  $\mu$ m.



FIG. 3.--Pseudo-asbestos body with black core fiber recovered from lungs of 76-year-old metal polisher. Scale marker, 10  $\mu$ m.

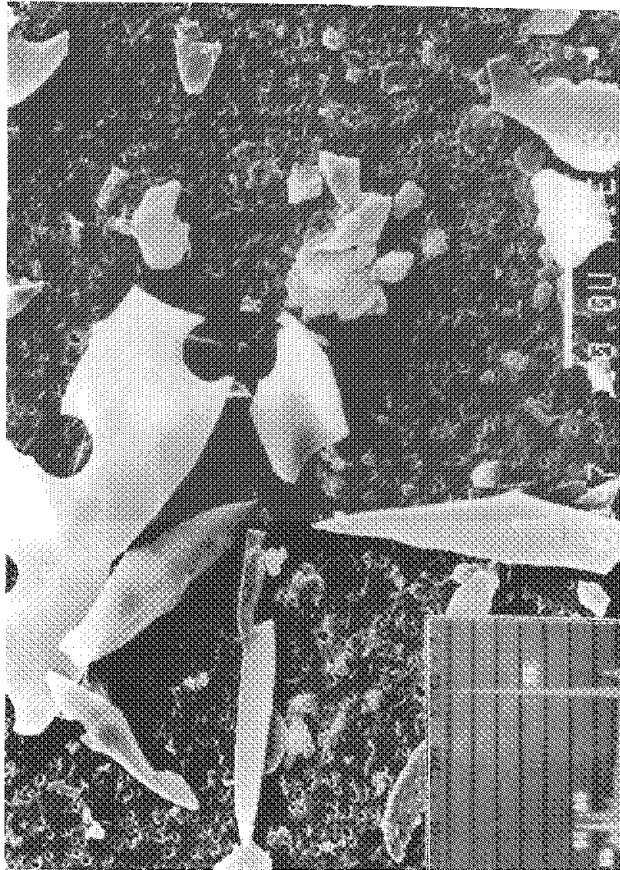


FIG. 2.--Scanning electron micrograph of dust recovered from lung, showing angulated particles and fibers, including grid-like structure at upper center. Inset: EDXA spectrum from iron-coated carbon fiber, showing prominent peak for iron. Scale marker, 10  $\mu$ m.

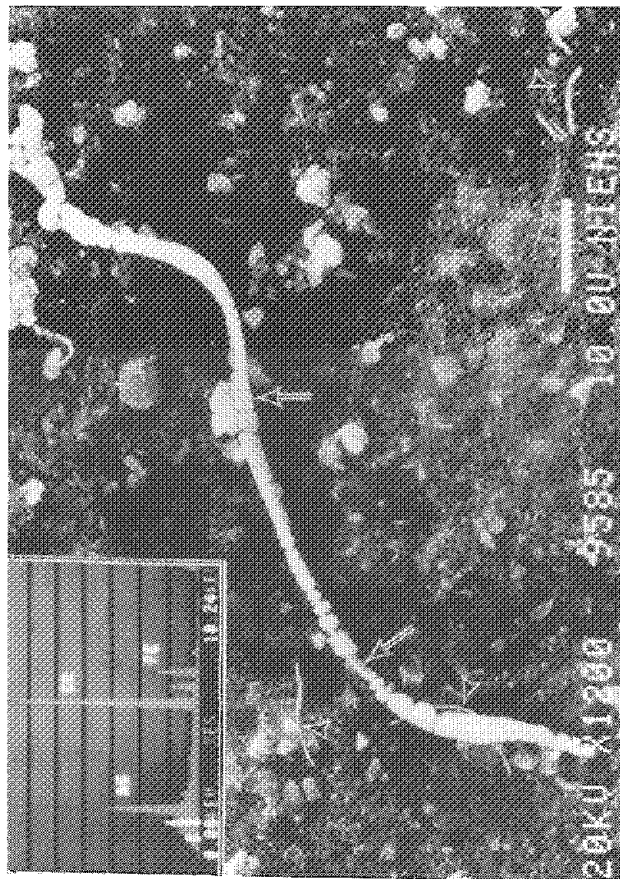


FIG. 4.--Scanning electron micrograph of pseudoasbestos body, showing beaded iron coating as well as bare area revealing core fiber (arrows). Additional uncoated fibers are present (arrowheads). Inset: EDXA spectrum from bare area of coated fiber, showing prominent peak for chromium, and smaller peak for iron. Au peak is due to sputter coating. Scale marker, 10  $\mu$ m.

months after the source of exposure had been removed showed no change in the numbers of fibers recovered. Similar fibers were recovered from bronchial washings from her asymptomatic spouse, but the fibers recovered were only 0.1-1.0% as numerous.

Digestion of a portion of left lung tissue from Case 2 demonstrated a modest number of ferruginous bodies (18 per gram of wet lung, normal range 0-20).<sup>4</sup> Some of the bodies had black cores and a curly morphology by light microscopy (Fig. 3). Many shorter uncoated black fibers were also observed. By scanning electron microscopy, there were 625 000 fibers per gram of wet lung, 92% of which were composed of chromium only by EDXA. These fibers were generally curved or semicircular, with serrated irregular borders. A few particularly long chromium fibers were iron coated (Fig. 4). Only about 0.5% of the fibers were coated. The remaining fibers identified were chrysotile (4%) and silica (4%). The mean fiber length of 100 consecutive fibers was 11.8  $\mu\text{m}$  ( $\pm$  7.9  $\mu\text{m}$ ), and the mean fiber diameter was 0.55  $\mu\text{m}$  ( $\pm$  0.25  $\mu\text{m}$ ). Occupational history obtained retrospectively from the wife indicated that the deceased had been a metal polisher for 30 years, last employed in 1973.

#### *Comments*

A variety of mineral fibers may become coated with iron when inhaled into the lung, and those bodies with nonasbestos cores can usually be distinguished from true asbestos bodies by light microscopy.<sup>2</sup> Indeed, pseudoasbestos bodies with carbon cores have been previously described, and the morphology of woodstove dust is also illustrated in the literature.<sup>3</sup> However, diffuse interstitial fibrosis as a consequence of exposure to woodstove dust has not been described, nor has the recovery of large numbers of coated and uncoated carbon fibers in bronchoalveolar lavage fluid and lung tissues. Similarly, pseudoasbestos bodies with chromium (presumably chromic oxide) cores have not been previously described. Epidemiologic studies have indicated an increased risk for lung cancer in chromate production workers,<sup>5</sup> but the author is not aware of any studies showing an increased lung cancer risk in metal polishers.

#### *References*

1. V. L. Roggli and A. R. Brody, "Changes in numbers and dimensions of chrysotile asbestos fibers in lungs of rats following short-term exposure," *Exptl. Lung Res.* 7: 133-147, 1984.
2. E. Crouch and A. Churg, "Ferruginous bodies and the histologic evaluation of dust exposure," *Am. J. Surg. Pathol.* 8: 109-116, 1984.
3. W. C. McCrone, *The Particle Atlas*, 2nd ed., vols. V and VI, Ann Arbor, Mich.: Ann Arbor Science Publishers, 1980, pp. 1336, 1634.
4. V. L. Roggli and J. D. Shelburne, "New concepts in the diagnosis of mineral pneumoconioses," *Sem. Respir. Med.* 4: 138-148, 1982.
5. J. C. Ives et al., "Environmental associations and histopathologic patterns of carcinoma of the lung: The challenge and dilemma in epidemiologic studies," *Am. Rev. Respir. Dis.* 128: 195-209, 1983.

## PULMONARY DAMAGE IN GUINEA PIGS CAUSED BY INHALED ULTRAFINE ZINC OXIDE: EVALUATION BY LIGHT AND ELECTRON MICROSCOPY AND ANALYSIS OF PULMONARY LAVAGE FLUID

M. W. Conner, W. H. Flood, A. E. Rogers and M. O. Amdur

Ash particles less than  $1\text{ }\mu\text{m}$  in diameter are important products of coal combustion because of the probability of their escape from collection devices, their long residence time in the atmosphere, their high content of surface-concentrated trace elements, and the expectation that, upon inhalation, they will be deposited deep within the lung. Zinc is particularly abundant in some coals and is present in high concentrations in the submicron ash produced when these coals are burned.<sup>1</sup> We have demonstrated that six exposures of guinea pigs to  $6\text{ mg/m}^3$  of freshly generated submicron zinc oxide (ZnO) causes centriacinar inflammation, elevated  $^3\text{H}$ -thymidine incorporation into nuclei of terminal bronchioles, and altered pulmonary function characterized by decreased lung volumes and diffusing capacity for carbon monoxide.<sup>2</sup> These findings are in contrast to the minimal changes produced by a single exposure to ZnO.<sup>3</sup> The purpose of this experiment was to study the development of the pulmonary lesions caused by ZnO by use of light and electron microscopy and analysis of pulmonary lavage fluid.

### *Experimental*

Male Hartley guinea pigs were exposed for 3h/day for 1 to 5 days in a nose-only exposure apparatus to  $6\text{ mg/m}^3$  ultrafine ZnO (projected area diameter of  $0.05\text{ }\mu\text{m}$ ) generated as previously described.<sup>3</sup> After each exposure, three guinea pigs were sacrificed and lungs were fixed by intratracheal instillation of glutaraldehyde. Centriacinar regions were selected for electron microscopic examination and additional lung sections from the left middle and left caudal lobes were examined by light microscopy. Three additional guinea pigs were sacrificed after the first, second, and third exposures and their lungs were washed twice with 4 ml of saline. The recovered fluid was analyzed for total and differential cell counts, protein and activities of angiotensin converting enzyme (ACE), beta glucuronidase, acid phosphatase and alkaline phosphatase. Control animals were exposed to particle-free furnace gases in the same apparatus.

### *Results*

Exposure to ZnO increased total cells, neutrophils, protein and activities of ACE, acid and alkaline phosphatases, and beta glucuronidase in pulmonary lavage fluid (Table 1). Centriacinar inflammation was detected by light microscopy after the second exposure and lesions increased in frequency and severity afterwards. Electron microscopic examination revealed only occasional blebbing of alveolar type 1 epithelial cells after the first exposure. After two exposures, type 1 epithelial cell blebbing and fragmentation were more frequent and endothelial cell swelling was noted in alveolar capillaries. Sloughing of type 1 cells and interstitial and intraalveolar infiltration with macrophages and neutrophils characterized the lesion after 3 exposures. After 5 exposures, considerable reepithelialization of centriacinar alveoli with cuboidal cells was evident and occasional ciliated cells were present along alveolar surfaces.

### *Discussion and Conclusions*

This study demonstrates that centriacinar type 1 epithelial cells are the cells most sensitive to injury by zinc oxide and that analysis of pulmonary lavage fluid is a useful method for detecting lung injury by ZnO.

---

Authors Conner, Flood, and Rogers are at the Department of Pathology, Boston University School of Medicine; author Amdur is at the Department of Applied Biological Sciences, Massachusetts Institute of Technology. The work was supported by U.S. Public Health Service Grant P01-ES02429 from the National Institute of Environmental Health Sciences.

## References

1. M. O. Amdur et al., "Coal combustion aerosols and SO<sub>2</sub>: An interdisciplinary analysis," *Environ. Sci. Technol.*, 138-145, 1986.
2. H. F. Lam et al., "Functional and morphologic changes in lungs of guinea pigs exposed to freshly generated ultrafine zinc oxide," *Toxicol. Appl. Pharmacol.*, 29-38, 1985.
3. M. W. Conner, A. E. Rogers, M. O. Amdur, "Response of guinea pig respiratory tract to inhalation of submicron zinc oxide particles generated in the presence of sulfur dioxide and water vapor," *Toxicol. Appl. Pharmacol.*, 434-442, 1982.

TABLE 1.--Effect of exposure to 6 mg/m<sup>3</sup> ZnO on pulmonary lavage fluids.<sup>a</sup>

Parameter	Group	Number of Exposures		
		1	2	3
Total Cells (10 <sup>6</sup> )	Control ZnO <sup>b</sup>	1.2 ± 0.1 2.8 ± 0.7	1.9 ± 0.4 2.7 ± 0.7	1.3 ± 0.3 2.5 ± 0.3
Neutrophils (10 <sup>5</sup> )	Control ZnO <sup>c</sup>	1.2 ± 0.6 8.7 ± 0.3	1.8 ± 1.0 98.5 ± 39.8	0.7 ± 0.4 53.1 ± 15.6
Angiotensin Converting Enzyme (units)	Control ZnO <sup>c</sup>	4.8 ± 0.6 2.2 ± 0.3	5.3 ± 0.3 13.1 ± 2.4	5.2 ± 0.9 16.3 ± 4.1
Acid Phosphatase (IU)	Control ZnO <sup>b</sup>	8.0 ± 0.5 10.8 ± 0.6	9.5 ± 0.4 15.2 ± 0.5	7.8 ± 0.6 13.1 ± 0.8
Alkaline Phosphatase (IU)	Control ZnO <sup>b</sup>	30 ± 6 28 ± 7	28 ± 5 66 ± 18	39 ± 4 91 ± 31
Beta glucuronidase (units)	Control ZnO <sup>d</sup>	38 ± 7 86 ± 12	28 ± 6 315 ± 23	31 ± 3 245 ± 90
Protein (mg)	Control ZnO <sup>b</sup>	0.9 ± 0.2 0.6 ± 0.1	0.7 ± 0.1 2.6 ± 0.6	0.8 ± 0.1 3.3 ± 0.6

<sup>a</sup> Mean ± Standard error

<sup>b</sup> P<0.05 vs Controls, ANOVA

<sup>c</sup> P<0.01 vs Controls, ANOVA

<sup>d</sup> P<0.005 vs Controls, ANOVA

## SEM OF TRACHEAL RESPIRATORY EPITHELIUM EXPOSED IN VITRO TO $\text{Ni}_3\text{S}_2$

G. L. Finch, T. L. Hayes, B. T. Mossman, M. J. W. Chang, and G. L. Fisher

Hamster tracheal explants maintained in tissue culture are useful models for the study of the interactions between toxic particles and the epithelium of the upper respiratory tract.<sup>1</sup> Advantages of using this system include easy manipulation of the culture environment and the ability to deliver quantifiable particulate doses. Our work involves scanning electron microscopic (SEM) studies of explant airway surfaces, and definition of alterations to epithelial morphology induced by nickel subsulfide ( $\text{Ni}_3\text{S}_2$ ) particle exposure. Nickel subsulfide has been identified as a potent metallic carcinogen and cytotoxic agent.<sup>2</sup>

### *Materials and Methods*

Male Golden Syrian hamsters, aged 4 to 6 weeks, were sacrificed and their tracheas were harvested, then cut into rings as described by Mossman and Craighead.<sup>1</sup> Tracheal rings were maintained in 35mm Petrie dishes containing 0.5 mL of culture medium (minimal essential medium, insulin, hydrocortisone, gentamycin, and mycostatin). Four explants were cultured in each dish. Cultures were incubated at 37°C for three days prior to exposure.

Nickel subsulfide ( $\text{Ni}_3\text{S}_2$ , as prepared by Fisher et al.<sup>2</sup>) was added to fresh medium and then subjected to ultrasonic agitation immediately before use. For each plate, the culture medium was removed then replaced with 2 mL of either fresh or  $\text{Ni}_3\text{S}_2$ -containing medium (20 mg/mL). Cultures were incubated for 1 h, then explants were removed to new culture dishes with fresh medium and cultured for 0, 0.25, 1, 4, and 20 h and 3 or 7 days. For SEM evaluation, sections were rinsed briefly in culture medium, immersed in room temperature fixative (2.3% glutaraldehyde in 0.05 M cacodylate; pH = 7.4; 360 mOsm), rinsed two times in 15min changes of fresh buffer (0.05 M cacodylate with added sucrose; pH = 7.4; 360 mOsm), dehydrated in a graded ethanol series, critical point dried through  $\text{CO}_2$ , coated with either evaporated carbon or sputtered platinum, and examined in an AMRay 1000A SEM with a Kevex 5100C x-ray spectrometer.

A low magnification micrograph was used for orientation and sample area selection (Fig. 1). For each explant, four areas were randomly selected for detailed morphological analysis at a magnification of 2000×. A conventional secondary electron image was used to assess morphology. The electron collector cage voltage was turned off, and the pseudo-backscattered image thus produced was used to locate test particles, which were then examined for the presence of Ni and S  $\text{K}\alpha$  x-ray peaks. Alternately, particles were located from x-ray maps made for the Ni  $\text{K}\alpha$  lines.

### *Results*

The surface of control explants appeared similar throughout the experimental time-course. The luminal surface was comprised of ciliated and nonciliated cells occurring with variable incidences (Fig. 2). Nonciliated cells were often gently rounded into the lumen with variable numbers of microvilli. Where ciliated cells were sparse, nonciliated cells often had polygonal profiles with well-defined cell boundaries. Cilia usually appeared as numerous, free-standing cylindrical projections from the epithelium, but were occasionally clumped due to incomplete rinsing of mucus.

In contrast to control explants,  $\text{Ni}_3\text{S}_2$ -exposed explants displayed a marked pattern of cell sloughing and regeneration of epithelium. Qualitatively, the normal differentiated epithelium appeared discontinuous immediately post-exposure, with both ciliated and non-

---

Author Hayes is at Donner Laboratory, Lawrence Berkeley Laboratory, Berkeley, CA 94720; Author Finch is at Lovelace ITRI, Box 5890, Albuquerque, NM 87185; author Mossman is at the Department of Pathology, University of Vermont, Burlington, Vt.; and authors Chang and Fisher are at the Toxicology Department, Battelle Columbus Division, Columbus, OH 43201. The authors acknowledge support from the U.S. Department of Energy, the Battelle Memorial Laboratory, and EPRI.

ciliated cells sloughed from the surface, revealing an underlying network of basal cells (Fig. 3). Many particles were observed at the surface at this time. Within hours, the luminal surface was characterized by more complete cell coverage. At this stage, no ciliated cells, typical dome-shaped nonciliated cells, or typical cell borders were evident. After 20 h to several days, recovery advanced to the point where the epithelium was either squamous in appearance, with flattened polygonal cells sharing raised cell borders, or essentially normal, with ciliated and nonciliated cells present.

Particles were observed predominantly on the exterior of the mucosal surface. Occasional internal particles were observed in both sloughing cells and residual basal cells. Although SEM examination revealed particles only very near the respiratory lumen, it was possible to document  $\text{Ni}_3\text{S}_2$  clearance and internalization within cells over time.

In order to describe temporal changes in explant morphology more rigorously, randomly selected fields of view were classified (Table 1). Score 1 (normal) epithelium consisted of both ciliated and nonciliated cells. Score 2 epithelium was essentially normal, but had less than 50% squamous-type cells covering the field of view. If more than 50% of an area was squamous but some normal ciliated areas were present, the area was classified as Score 3. Score 4 (squamous-type epithelium) was at least 50% squamous and contained only nonciliated cells.

TABLE 1.--Incidence (%) of epithelial types<sup>a</sup> in selected tracheal explant fields of view.

Treatment <sup>b</sup>	Score 1	Score 2	Score 3	Score 4	Desquamation	Basal Cell Replacement
Control	39	39	18	0	4	0
0 hr	0	0	0	0	88	12
.25, 1 hr	0	0	0	0	69	31
4, 20 hr	38	12	0	0	12	38
3, 7 days	50	25	12	12	0	0

a See text for a description of morphological classifications.

b Either control or  $\text{Ni}_3\text{S}_2$  (20  $\mu\text{g}/\text{mL}$ ); times are post-exposure.

Whereas scores 1 to 4 were used for apparently stable or end-type epithelia, the following descriptions characterized surfaces apparently undergoing transitions by either gaining or losing cells. Desquamating areas contained epithelium with holes between cells and sloughing cells at the surface. More pronounced desquamation was typified by remnant columnar cells rounded up from a superficial layer of basal cells. Cilia were not present at this stage. Basal cells resided upon the basement membrane and were usually elongated and frequently interdigitated among neighboring cells. Basal cell replacement was characterized by apparent basal cells that had either proliferated or recolonized the denuded luminal surface and then formed a flattened surface with or without cell boundaries. This classification appeared similar to Score 4-type epithelium; distinctions were based on the presence (Score 4) or absence (basal cell replacement) of microvilli covering the flattened superficial cells and lining cell borders.

An examination of Table 1 shows that explant surface morphology was severely affected by  $\text{Ni}_3\text{S}_2$  exposure. Immediately post-exposure to 1 h post-exposure, no fields of view appeared "normal." By 4 to 20 h post-exposure, a limited amount of normal epithelium was evident, and by 3 to 7 days post-exposure, most fields of view were indistinguishable from controls (Fig. 4). Thus, it appeared that ciliated epithelium was rapidly regenerated following a single 1 h exposure to  $\text{Ni}_3\text{S}_2$ .

### Discussion

Nickel subsulfide has been implicated by epidemiological studies as a potential causative factor in an observed increased incidence of nasal and pulmonary tumors in nickel workers. This compound has also been shown to be toxic in both in vivo and in vitro animal test systems.<sup>2</sup> Scanning electron microscopic studies of cultured tracheal explants demonstrated that 20  $\mu\text{g}/\text{mL}$  of particulate  $\text{Ni}_3\text{S}_2$  had a potent effect on the respiratory

epithelium. Although it is not possible to describe conclusively dynamic events by use of the "static world" of electron microscopy, it appeared that both desquamation of the normal columnar epithelium and basal cell replacement occurred rapidly after  $\text{Ni}_3\text{S}_2$  exposure. Epithelial sloughing and regeneration, or the induction of squamous metaplasia, are responses to external agents widely observed in the literature, and it is not clear to what extent such alterations are due to nonspecific particle insult or to effects that depend on the physical, chemical, or toxicologic parameters of the agents involved.

#### References

1. B. T. Mossman and J. E. Craighead, "Use of hamster tracheal organ cultures for assessing the cocarcinogenic effects of inorganic particulates of the respiratory epithelium," *Prog. Exp. Tumor Res.* 24: 36-47, 1979.
2. G. L. Fisher et al., "Mechanistic evaluation of the pulmonary toxicity of nickel subsulfide," in H. N. MacFarland et al., Eds., *The Toxicology of Petroleum Hydrocarbons*, Washington, D.C.: American Petroleum Institute, 1982, 87-96.

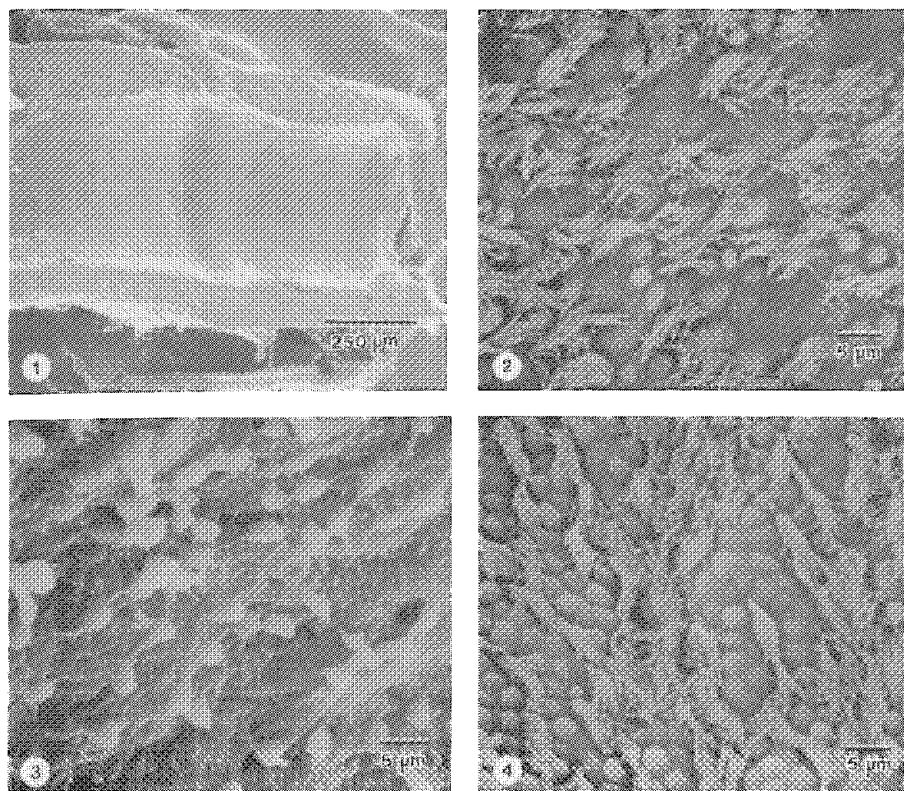


FIG. 1.--Low magnification SEM of hamster tracheal explant used for orientation and selection of fields of view for detailed morphological analysis (80 $\times$ ).

FIG. 2.--Field of view from control explant. Both ciliated and nonciliated cells are abundant (2000 $\times$ ).

FIG. 3.-- $\text{Ni}_3\text{S}_2$ -exposed explant 1 h post-exposure characterized by desquamation. Differentiated columnar epithelium is no longer present, revealing underlying network of cells (2000 $\times$ ).

FIG. 4.-- $\text{Ni}_3\text{S}_2$ -exposed explant 7 days post-exposure, exhibiting ciliated and nonciliated cells essentially indistinguishable from controls (2000 $\times$ ).

## MICROSCOPICAL EXAMINATIONS OF MUCOCILIAR EPITHELIUM OF RATS EXPOSED TO SODIUM COMBUSTION PRODUCTS

Anna Giovanetti and Piergiacomo Pagano

Sodium is used on a large scale as a coolant and heat-transfer medium in liquid metal fast reactors (LMFBR). It is also a very reactive metal that burns spontaneously in air to form oxides, which, with a strong exothermic reaction, combine with water to give sodium hydroxide. In the presence of carbon dioxide, reactions proceed rapidly, producing carbonate. All these compounds have been shown to be either caustic or merely irritant for the cellular tissues, depending on their alkalinity.<sup>1</sup> In a hypothetical severe reactor accident there is a probability of a mixed sodium-radioactive isotope release. Sodium combustion products can so damage the exposed cellular surface that they may modify the radioactive compounds behavior and affect respiratory clearance.

The mucous-ciliary system of the respiratory tract has been shown to be the target for a wide range of irritant chemicals.<sup>2</sup> In particular, after sodium inhalations in rats, the epithelium of the larynx and trachea is indicated as the seat of necrosis.<sup>3</sup> Accordingly, the aim of this investigation is to describe the relationship between sodium combustion products and morphological changes, with special attention to ciliated cells, which are the most susceptible to damage. With the use of scanning electron microscopy (SEM) it is possible to record either the number and extent of injured epithelium areas or the ultra-structural analysis of the cell surface.

### *Materials and Methods*

The generation was performed by heating sodium metal in inert gas ( $N_2$ ), by mixing it with air to obtain a gas-particle reaction and a final aerosol suitable for use and mainly composed of carbonate.

Two groups of 6 Sprague-Dawley rats (3 months old) were exposed in an appropriate stainless steel nose-only chamber,<sup>4</sup> for 30 min at two concentrations of aerosol, with concentration and aerodynamic size distribution being checked. Animals were housed under standard conditions and given food and water ad libitum.

Two rats for each group were killed 1 h, 24 h, and 7 days post-exposure. Anesthetized with a intraperitoneal injection of 1 ml sodium tiopentale (Farmitalia), the rats were opened and perfused via vena cava with Sørensen buffer (0.2 M pH 7.4) and with 2.5% gluteraldehyde (in Sørensen buffer 0.1 M pH 7.4) for 5 min each.

The larynx, trachea, and lungs were then removed en bloc, briefly rinsed in the buffer, and immersed for 2 h in 2.5% gluteraldehyde.

After they were dissected for SEM examination, the samples were placed overnight at 4 C dehydrated in graded ethanol (twice for 5 min at 50, 70, 90, 95, and 100%) and dried according to the critical-point method with carbon dioxide (CPD Bahlzer). All samples were coated with gold (Sputtering Coating S150B Edwards) and examined in a scanning electron microscope (Phillips SEM 505).

### *Results*

The conditions of the two experiments (Na2, Na3) were the following: Na2 mean concentration in Na = 115 mg/m<sup>3</sup>, MMAD = 1.5, Sg = 1.5; Na3 mean concentration in Na = 400 mg/m<sup>3</sup>, MMAD = 1.9, Sg = 1.4. In both the controls and in the exposed animals the individual difference in the ciliated/nonciliated cell ratio has been confirmed. nonciliated cells were noted in all the exposed rats. Na3 rats also showed cells with sparse cilia and cytoplasmic bundles (Fig. 1).

A major difference between the groups of rats of the two concentrations was observed 24 h post-exposure. In the Na3 rats 50% of the upper trachea (up to the 5th ring) was covered with nonciliated cells (flat, polygonal with raised borders; dendritic; dome-



FIG. 1.--Cells presenting ciliary loss and cytoplasmic bundles.

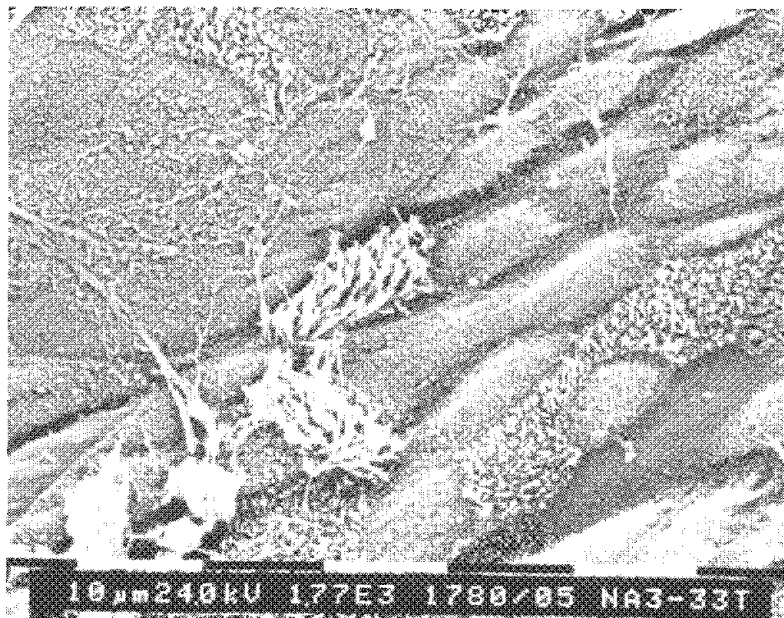
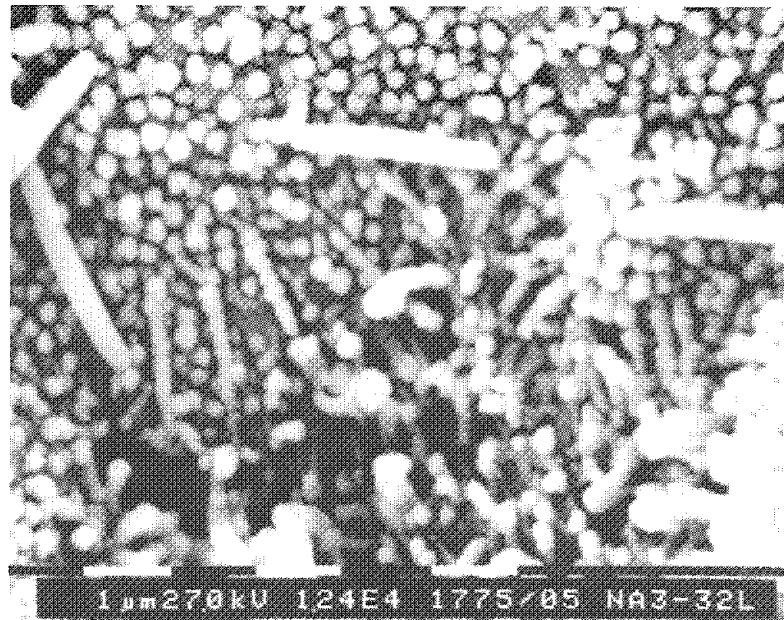


FIG. 2.--Types of nonciliated cells in tracheal epithelium of Na3 rat.

shaped) (Fig. 2), and cells with very few cilia. Moreover, an intermediate kind of cell presenting on its surface sparse cilia and mucous droplets was noted (Fig. 3). Of the two Na rats the epithelium was regularly ciliated except for a process of repair in the larynx of one rat, with swollen, partially undifferentiated cells spreading laterally over a previously denuded area.

After 7 days some little patches of nonciliated cells remain in Na3 rats only.

The nonciliated cells of the control animals were quite different from those of the exposed ones, being interspersed among ciliate cells, protruding and almost always secreting mucus. Likewise, the difference between cells undergoing ciliogenesis in the controls and cells losing cilia in the exposed rats (Fig. 1) appears clear.

### Conclusion

This study indicates that aerosol sodium combustion products induce injuries varying with the concentration on the mucous-ciliary epithelium. The degree of the damage was marked after 24 h, which indicates that it takes place gradually. Ciliary loss was not associated with cellular death. Where there was a lesion, recovery took place within 7 days.

Our observations agree with those reported in previous works on the cytotoxic effects of irritant gases,<sup>5</sup> recording ciliary loss and the presence of nonciliated cells of various types. Although we noted "intermediate" cells, they are quite different from those reported in the literature, presenting mature characteristics of ciliated and goblet cells.

### References

1. D. W. Cooper et al., *A Critical Review of Sodium Hydroxide Aerosol Toxicity*, Boston: Harvard School of Public Health (Environmental Health Sciences), HSPH/EPS (NuReg)-888, 1977.
2. In H. Witschi and P. Nettekheim, Eds., *Mechanisms in Respiratory Toxicology*, CRC Press, 1982, vol. 1.
3. G. M. Zwicker et al., "Toxicity of aerosols of sodium combustion reaction products," *J. Environ. Pathol. and Toxicol.* 2: 1139-1150, 1979.
4. M. Calamosca et al., "An exposure chamber for acute inhalation exposure," GAEP II Int. Aerosol Conference, Berlin, 1984.
5. D. W. Wilson et al., "The response of the macaque tracheobronchial epithelium to acute ozone injury," *Am. J. Pathol.* 116: 193-206, 1984.

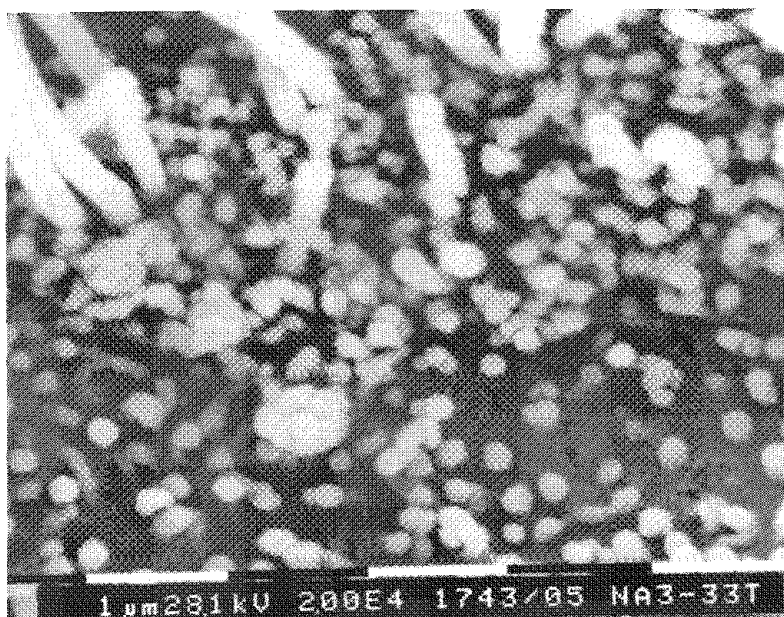


FIG. 3.--High magnification of epithelium of trachea from Na3 rat showing cell with scarce cilia and mucous droplets.

## MORPHOMETRIC ALTERATIONS IN THE LUNG INDUCED BY INHALED BACTERIAL ENDOTOXIN

R. C. Lantz, Robert Burrell, and D. E. Hinton

In order to determine the role of chemical mediators in the response to inhaled endotoxin hamsters were injected with pharmacological modifiers prior to inhalation of lipopolysaccharide (LPS) from a bacterium found in cotton and cotton mill dust. Blockage of complement activation abolished cell recruitment and changes in lung volume, and blockage of the cyclooxygenase pathway of arachidonic acid metabolism blocked cell recruitment and increases in numerical density of endothelial pinocytotic vesicles.

Previous work in this laboratory demonstrated that inhalation of LPS leads to recruitment of polymorphonuclear leukocytes (PMN) and platelets in the pulmonary capillary bed, to decreases in lung volume, and to increases in numerical density of endothelial pinocytotic vesicles.<sup>1</sup> Wedmore and Williams postulated that the inflammatory response involves two signals, one being complement activation and the second involving prostaglandins.<sup>2</sup> It is this hypothesis that we wish to test in the response to inhaled bacteria in the lung.

### *Methods and Materials*

Male Syrian golden hamsters were exposed for 5 h to a  $4\mu\text{g}/\text{m}^3$  concentration of LPS from *Enterobacter agglomerans*, a bacterium commonly found growing on cotton plants. Decomplementation of some animals was accomplished by intraperitoneal injections of cobra venom factor (CVE) (250 U/kg divided into 4 doses over 24 h prior to LPS exposure). Cyclooxygenase pathway was blocked by treatment with indomethacin (0.5 mg over a 24h period prior to LPS exposure). Animals were divided into two aerosol exposure groups (18 animals/group); one group received a saline aerosol, the second the LPS exposure. Within each group animals were further subdivided into no pretreatment (N = 6), prior CVP treatment (N = 6) and prior indomethacin treatment (N = 6). After aerosol exposure and a 6h waiting period, tissues were fixed by intratracheal instillation, removed, and processed for morphometric analysis at the light and electron microscopic levels. Standard morphometric point counting procedures were used throughout the studies (5 blocks/animal).<sup>3</sup> Differences between groups of animals were tested by a two-factor (aerosol exposure and type of pretreatment) analysis of variance.

### *Results*

Although no significant differences were seen in parameters measured at the light microscopic level, displacement volumes of fixed lungs from animals receiving LPS aerosol were significantly lower than volumes of lungs receiving saline aerosol (Table 1). Because the final volume of intratracheally fixed lungs depends on the rate of fixative entry, bronchconstriction and alteration of lung mechanics prior to fixation may be the cause of lower fixed lung volumes.<sup>4</sup> Both decompensation and indomethacin blocked this response.

At the electron microscopic level, recruitment of PMNs and platelets followed LPS inhalation. This response, typical of inflammatory processes, was also inhibited if the animals were decompensated or given indomethacin.

The presence of an inflammatory agent on the epithelial side of the air-blood barrier has led to recruitment of PMN and platelets from the capillary blood. For that to occur, some signal or mediator must cross the septal-tissue barrier, where alteration in one or more of the elements comprising the barrier might occur due to the presence of the mediator. No differences in the septal elements were found following LPS inhalation. Although the volume and number of endothelial cells did not change, the number of endothelial pinocytotic vesicles did. Table 1 shows estimates for the numerical density and average

---

The authors are at the Departments of Anatomy and of Microbiology, West Virginia University Medical Center, Morgantown, WV 26506. Supported by Project 82-521, Cotton Inc., Raleigh, NC.

volume of the endothelial pinocytotic vesicles. LPS inhalation led to an increase in the numerical density with no change in the size of the vesicles. Prior treatment with CVF had no effect while indomethacin abolished the increased number of vesicles. Neither pretreatment had an effect on the size of the vesicles (Table 1).

TABLE 1.--Effect of pharmacological modifiers on pulmonary response to LPS inhalation.

Parameter	Aerosol	Pretreatment		
		None	CVF-IP	INDO-IP
Lung volume (ml)	Saline	3.37±0.24	3.22±0.29	5.17±0.53
	LPS	2.65±0.36 <sup>A</sup>	3.56±0.38	5.12±0.45
Vol PMN in capillary blood (μl)	Saline	4.78±2.56	8.53±5.55	21.32± 6.08
	LPS	32.33±4.44 <sup>A</sup>	14.71±4.46	29.60±13.37
Vol platelet in capillary blood (μl)	Saline	1.72±0.60	4.76±1.05	5.88±1.60
	LPS	11.38±2.89 <sup>A</sup>	7.52±1.38	5.23±3.88
N <sub>V</sub> VES (μm <sup>-3</sup> )	Saline	155±16	135±14	194±20
	LPS	269±30 <sup>A</sup>	277±52 <sup>A</sup>	215±30
Vesicle volume (10 <sup>-4</sup> μm <sup>3</sup> )	Saline	1.51±0.16	0.99±0.13	0.95±0.10
	LPS	1.27±0.10	1.23±0.08	0.92±0.04

Values are means ± SEM.

Values are reported for absolute volume of PMNs and platelets in the distal lung capillary blood in order to correct for differences in blood volume between the various pretreatments.

N<sub>V</sub> is the numerical density of vesicles in endothelial cytoplasm.

Vesicle volume is average volume of endothelial pinocytotic vesicles.

A = significantly different from saline aerosol of same pretreatment (p < 0.05).

### Summary

Among the various mediators which have been implicated in inflammation are complement and prostaglandins. Wedmore and Williams have postulated that both an activated complement product and prostaglandins are necessary for exudation during inflammation.<sup>2</sup> In the present study, the role of these two mediators following LPS inhalation was tested and results indicate at least a partial role for complement and prostaglandins in the response. These results demonstrate the effectiveness of combining pharmacological and morphometric techniques in efforts to gain a better understanding of the pathogenesis of disease.

### References

1. R. C. Lantz et al., "Morphometric changes of the lung induced by inhaled bacterial endotoxin," *Exp. Mol. Path.* 43: 305-320, 1985.
2. C. V. Wedmore and T. J. Williams, "Control of vasculature permeability by polymorphonuclear leukocytes in inflammation," *Nature* 289: 646-650, 1981.
3. E. R. Weibel, *Stereological Methods, vol. 1: Practical Methods for Biological Morphometry*, London: Academic Press, 1979.
4. G. Hayatdavoudi et al., "Factors determining degree of inflation in intratracheally fixed rat lungs," *J. Appl. Physiol.* 48: 389-393, 1980.

## Applications in Chemical Processing

### THE Fe/MgO (001) SYSTEM STUDIED BY AES, XPS, AND TEM

R. A. Hubert and J. M. Gilles

In order to understand the metal-support interaction in Fe/MgO, which is a remarkable catalyst for ammonia synthesis and Fischer-Tropsch reactions, we have investigated the transformation into small particles of an ultrathin iron film deposited on MgO(001) faces. Experiments were performed in ultrahigh-vacuum (UHV) chambers or in transmission electron microscopes.

When annealed in UHV at 400 C, the iron film transforms into 80% metallic particles. Their diameter depends on the density of defects on the substrate and on the temperature; they usually lie in the 20nm range. Contact angles between the particles and the substrate have also been measured. Heating the system under  $10^{-4}$  mbar  $H_2$  minimizes the interaction between the metal and the oxide ( $\theta = 120^\circ$ ). Annealing in  $10^{-4}$  mbar  $O_2$  induces particle embedding and the contact angle falls to about  $70^\circ$ . Complete dissolution of the particles in the substrate is often observed when the system is heated directly in the electron microscope. This result is interpreted by the formation of a high-temperature stable (Fe,Mg)O solid solution.

#### *Experimental*

Air-cleaved MgO single crystals were used for the analysis of the samples by Auger Electron Spectroscopy (AES) and X-ray Photoelectron Spectroscopy (XPS). Transmission Electron Microscopy (TEM) experiments were performed either on cubic microcrystals or on thin platelets found in the smoke of burning Mg ribbons. These microsubstrates were collected on perforated organic microgrids presenting 1µm holes, or directly on copper electron microscope grids; they were observed in Philips EM300 and EM301 microscopes operating at 80 kV.

Iron films (0-10 nm thick) were deposited on the samples in UHV by evaporation from a hot metal filament.

Auger studies were performed with a RIBER OPC105 cylindrical mirror analyzer coupled with a grazing incidence 3keV electron beam in order to limit charging effects. XP spectra were measured with a VSW medium resolution apparatus with an Al target and an hemispherical analyzer. They were calibrated by setting of the binding energy of the O(1s) line to 530 eV.

#### *Results and Discussion*

The annealing of a Fe(2.5nm)/MgO(001) system was monitored by AES. As the temperature increased, a dramatic decrease of the iron signals occurred while the intensity of the oxygen and magnesium peaks increased. Figure 1 gives some details about this transformation. The ratios O/Fe and Mg/Fe, obtained from the corresponding Auger signals, are plotted versus time. The rates of variation were also computed and put in an Arrhenius plot. The activation energy was found to be about  $60 \text{ kJ.mol}^{-1}$ . This value is small compared with that obtained by Wuensch and Vasilos<sup>1</sup> for bulk diffusion of iron in MgO and evaluated at  $176 \text{ kJ.mol}^{-1}$ . Furthermore, the Mg/O Auger ratio, after annealing at high temperature, is characteristic of MgO. These observations show that the transformation is due to a surface diffusion of iron, leading to the formation of isolated particles. A great part of the MgO surface is thus uncovered after heating of the system, which explains the value of the Mg/O ratio.

In order to deduce the mean size of the particles from the Auger curves, we conducted a computer simulation based on the following assumptions: (1) the particles are hemispherical and have all the same radius; (2) the grazing incidence electron beam cannot access the whole part of the uncovered MgO surface because of the "shadows" associated

---

The authors are at the Facultés Universitaires Notre-Dame de la Paix, B-5000 Namur, Belgium.

with the particles; (3) parts of the oxide located under the particles or in the shadow zones are not detectable. This simulation indicated that the average radius of the particles lies around 15 nm.

XP spectra were recorded at room temperature (RT) after annealing of a Fe(5nm)/MgO(001) system. The evolution of the various signal intensities versus T are similar to that observed in AES. Figure 2 shows Fe(2p) spectra recorded at various temperatures; some of them are compared to a normalized RT spectrum. As T increases, the line at 706.9 eV, corresponding to the metal, decreases while peaks associated with oxidized iron ( $\text{Fe}^{2+}$  or  $\text{Fe}^{3+}$ ) are developing around 710 eV. The small peak appearing at 704.6 eV has not yet been satisfactorily interpreted. These results are compatible with the formation of metallic particles as suggested by AES. However, there is evidence for a partial oxidation of the iron surfaces.

Chains of cubic MgO microcrystals ( $100^3\text{nm}^3$ ) deposited across copper grids and covered with a 2.5nm iron film were treated in  $\text{H}_2$  and  $\text{O}_2$  atmospheres during 2 h at temperatures ranging from 300 to 500 C. They were then transferred in air to the electron microscope.

Figure 3(a) shows a typical result obtained after annealing at 450 C in  $\text{H}_2$ . A pronounced anisotropy is observed in the size distribution of the particles: the "top" faces of the microcrystals are supporting a single "drop" of metal, whereas the lateral faces are covered with many particles which are about five times smaller. This anisotropy is probably due to an anisotropy in the concentration of surface defects. Indeed, observations by Metois et al.<sup>2</sup> on the Au/MgO system show that particle sizes are smaller when the density of defects is increased. Some of our Auger results also confirm this assumption. The large particles sometimes show a well-defined profile from which the contact angle  $\theta$  can be deduced;  $\theta$  is always above  $90^\circ$  and can be as high as  $130^\circ$ .

Figure 3(b) presents the appearance of the sample after treatment in  $\text{O}_2$  at 440 C. In this case, we did not observe any anisotropy in the size distribution. The particles are often faceted and show a preferential orientation along the  $\langle 110 \rangle$  MgO direction, confirming the existence of epitaxy relationships. Contact angles are smaller than  $90^\circ$  and can be as small as  $60^\circ$ . In some cases, there is also evidence for lateral displacement of the particles as indicated by the trails resulting from partial diffusion of iron in the MgO lattice before particle movement. Diffusion had already been observed on MgO platelets supported on organic microgrids and heated in the microscope.<sup>3</sup> Sometimes, complete dissolution of iron even took place, but these experiments were not completely reproducible. We ascribed that to the presence of a surface contamination coming from the microgrids and probably due to carbon. As a matter of fact, the presence of carbon at the interface can induce a complete modification of the system morphology as the parameters determining the particle shape (surface energies, contact angle, etc.) are dramatically modified.

The contact angle values under  $\text{H}_2$  are close to those observed for liquid metallic iron on MgO.<sup>4</sup> They correspond to a sharp metal-oxide interface and indicate that the surface of the particles is not oxidized and that iron has not diffused into the MgO lattice. Indeed, diffusion only occurs for  $\text{Fe}^{2+}$  ions, leading to the formation of a substitutional (Fe,Mg)O solid solution. This situation is observed when the treatment is performed under  $\text{O}_2$ . In this case, the interface is diffuse and the contact angle is small. Furthermore, the particles are partly embedded in the substrate,<sup>5</sup> as observed in powder catalysts prepared by coprecipitation or by impregnation.<sup>6</sup>

### Conclusions

During the preparation of real catalysts, the reduction of the precursors leads to the formation of active metallic particles and to the diffusion of ferrous ions inside the oxide matrix. However, our study shows that those processes are antagonistic, as we have seen that the diffusion is inhibited by the annealing in hydrogen. On the other hand, annealing in oxygen favors diffusion. Hence the appropriate "blend" of both processes requires a careful control of the preparation parameters, as part of the metal has to diffuse in order to stabilize the particles, while the remainder must be reduced to get an active catalyst.

### References

1. B. J. Wuench and T. Vasilos, *J. Chem. Phys.* 36: 2917, 1962.
2. J. J. Metois, K. Heinemann, and H. Poppa, *Thin Solid Films* 41: 197, 1977.

3. R. A. Hubert and J. M. Gilles, *Appl. Surf. Sci.* 22/23: 631, 1985.
4. Ju. V. Naidich, *Prog. Surf. Membrane Sci.* 14: 353, 1981.
5. R. A. Hubert, Ph.D. thesis, Facultés Universitaires de Namur, Belgium, 1986 (unpublished).
6. M. Boudart et al., *J. Catal.* 37: 486, 1975.

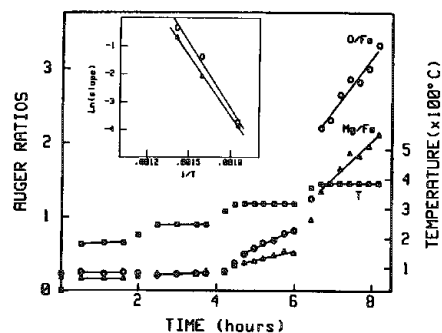


FIG. 1.--Evolution of O(510 eV)/Fe(703 eV) and Mg(1173 eV)/Fe(703 eV) Auger ratios with temperature and time for Fe (2.5nm)/MgO(001) system. (Inset: Arrhenius plot showing the rates of increase of both ratios.)

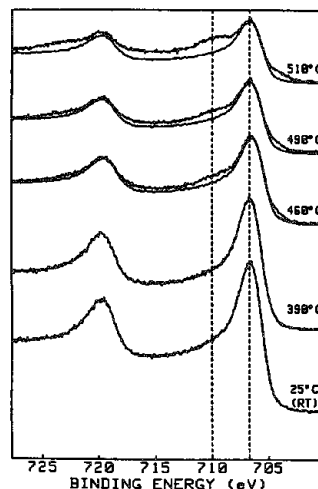


FIG. 2.--Evolution of Fe(2p) XPS line with temperature for Fe(5 nm)/MgO(001) system. In 3 cases, scaled RT-spectrum is shown for comparison.

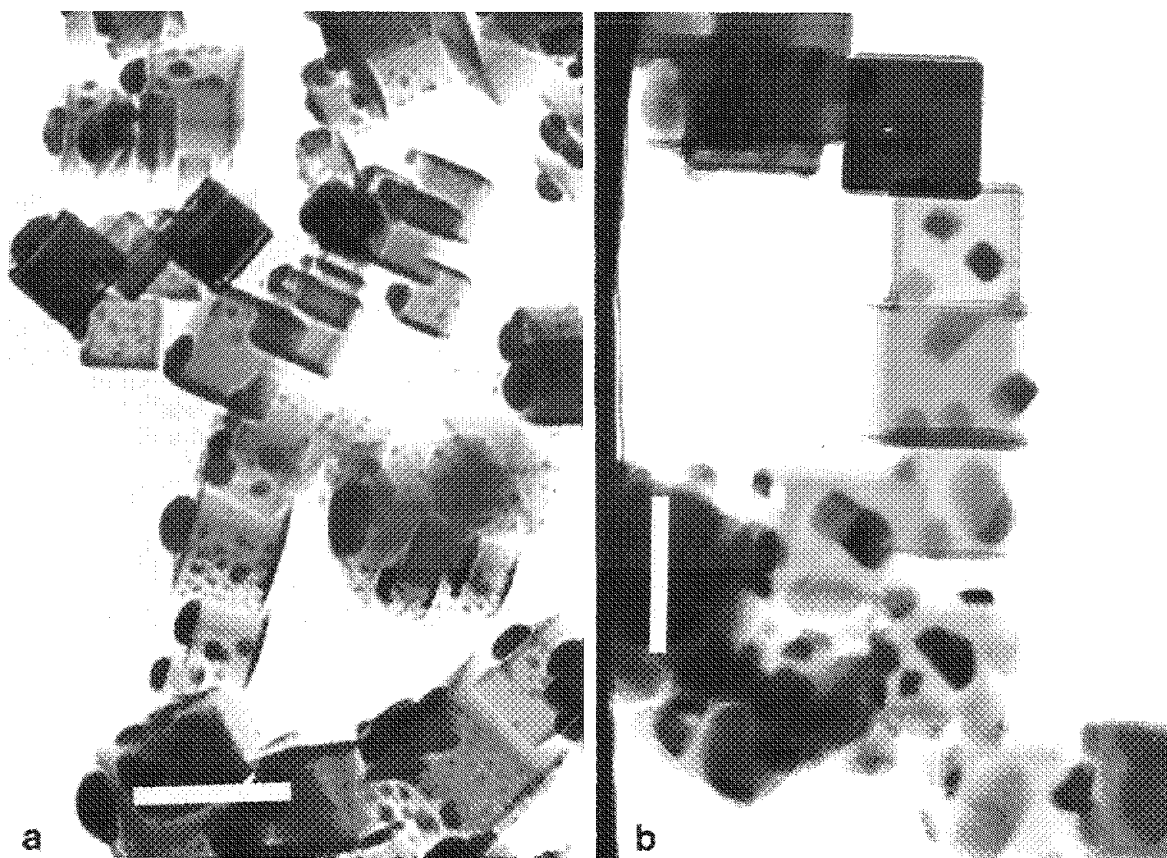


FIG. 3.--Typical morphology of a Fe(2.5 nm)/MgO(001) system after a 2h annealing: (a) in  $2 \times 10^{-4}$  mbar  $H_2$  at 450 C; (b) in  $2 \times 10^{-4}$  mbar  $O_2$  at 440 C. (Scale mark: 100 nm.)



## ELECTRON SPECTROSCOPY IN FUNDAMENTAL CATALYTIC STUDIES

D. W. Goodman and J. E. Houston

A detailed understanding of the chemical nature of surface impurities and overlayers is critical to many technologically important phenomena. Modern surface spectroscopies provide us with the capability to probe many subtleties of surface/adsorbate systems and have proved to be invaluable to the development of our understanding of surface catalyzed reactions and related phenomena. Here we wish to illustrate this point with two specific examples, the production of surface carbon in catalytic methanation over nickel and the modification of electronic properties of copper by an underlying ruthenium substrate.

### *Experimental*

The experimental systems used to acquire the chemical kinetics, Auger lineshape data, and photoemission data have been discussed in detail elsewhere.<sup>1,2</sup> The Auger/kinetic system consists of a microreactor that can analyze the products of catalytic reactions on single crystal surfaces for reactant pressures up to 1 atm. The product distribution is quantitatively determined by gas chromatography. One accomplishes surface analysis by introducing the sample into a ultrahigh vacuum (UHV) chamber through a vacuum interlock and performing Auger Electron Spectroscopy (AES).

The angular-resolved ultraviolet photoemission (ARUPS) data were measured by a Vacuum Generators ADES 400 system with a He discharge lamp.<sup>2</sup> The energy resolution was approximately 0.1 eV and the angular window was  $\pm 1^\circ$ . HeI photons ( $h\nu = 21.2$  eV) impinged on the surface along the surface normal and photoelectrons were detected at various positions along the  $\bar{\Gamma}$ -K line in the surface Brillouin zone (SBZ). The azimuthal orientation was established by Low Energy Electron Diffraction (LEED).

### *Discussion*

*Lineshape Analysis of Surface Carbon.* The production of surface carbon on transition metals is an important heterogeneous reaction. For example, the formation of surface carbon from CO dissociation has been shown to be the first step in the catalytic production of methane and higher hydrocarbons from CO and H<sub>2</sub> mixtures.<sup>1</sup> Kinetic measurements of the absolute rates of CO dissociation on Ni<sup>3</sup> and Ru<sup>4</sup> have confirmed this step to be sufficiently rapid to account for all the methane product. AES has been used to characterize the chemical nature of two types of carbon on Ni,<sup>3</sup> Ru,<sup>4</sup> and Rh<sup>5</sup>: a form active toward hydrogenation and an inactive form.<sup>5</sup> Based on comparisons with AES carbon lineshapes of bulk compounds, these carbon types have been classified as "carbide" and "graphitic," respectively.<sup>2</sup> An example of the characteristic Auger fingerprint for these two forms of carbon on nickel, together with spectra for nickel carbide and single crystal graphite, are shown in Fig. 1.

On Ni(100), CO dissociation at 24 Torr leads to an increasing coverage of carbide carbon (Fig. 1a) up to approximately one-half monolayer at ~650 K. With increasing reaction temperatures a carbon phase change to graphitic carbon (Fig. 1c) is observed. Under vacuum conditions, no thermal conversion of carbide to graphitic was found. The carbide carbon is associated with an active catalyst, whereas the graphitic form invariably indicates a deactivated catalyst. Similar conclusions have been drawn in studies carried out on Ru.<sup>4</sup>

The work on the surface carbon types on Ni(100) has been expanded to include studies of the Auger lineshapes for the graphite and carbide-like species on the Ni(111) and Rh(111) surfaces.<sup>5</sup> The loss deconvoluted<sup>5</sup> C(KVV) Auger lineshape for carbon deposited on

---

The authors are at the Sandia National Laboratories, Albuquerque, NM 87185. This work, performed at Sandia National Laboratories, was supported by the U.S. Department of Energy (Division of Chemical and Material Sciences) under contract DE-AC04-76DP00789.



the Ni(111) surface is shown in Fig. 2(a) directly compared to the C(KVV) lineshape from gas-phase  $\text{SiH}_3\text{-CH}_3$ .<sup>6</sup> In addition, Fig. 2(b) shows the C(KVV) lineshape for the graphitic form of carbon on this surface. Also shown on Fig. 2(b) is the direct comparison of the lineshapes of this graphitic form to that of clean, single-crystal graphite.<sup>6</sup> Finally, in Fig. 2(c) is shown the AES spectrum corresponding to the active form of carbon found on the Ni(100) surface. These results suggest that symmetry information regarding surface adsorbates can be obtained by use of similarly treated C(KVV) Auger lineshape data. The strong correlation found in Fig. 2(a) between the C(KVV) of surface "active" carbon on Ni(111) to the C(KVV) of  $\text{SiH}_3\text{-CH}_3$  suggests a carbon site in each case with a common bonding symmetry, i.e.,  $\text{C}_{3v}$ . This interpretation places the carbon in the threefold hollow sites essentially isolated from adjacent carbons. This bonding configuration is consistent both with chemical intuition as well as the known bonding scheme (in high coordination sites) of other adatoms on nickel.<sup>7</sup>

The spectrum of Fig. 2(c) is unique with respect to any known gas-phase analog<sup>6</sup> and is taken as indicative of the C occupying the unique four-fold sites on this surface. The isolated or localized bonding of these carbidic forms is responsible for the sharper contrast in the spectral features compared to the diffuse Auger spectrum of the graphitic form shown in Fig. 2(b).

The Auger lineshape data for Rh(111)<sup>5</sup> indicate in general a greater carbon propensity to polymerize on Rh(111) compared with Ni(100) and Ni(111). The Rh(111) surface, unlike Ni, does not form a pure carbide-like structure. AES lineshape data<sup>5</sup> invariably show that a mixture of a carbide-like and a graphitic type carbon is present. Furthermore, unlike the Ni case, the nongraphitic aspects of the carbon lineshape readily convert in vacuum to a graphitic form at temperatures in excess of 500 K.

*Photoemission of Copper on Ruthenium.* Monolayer (ML) and submonolayer (sub-ML) coverages of Cu adsorbed on the Ru(0001) surface have been found to alter the chemical behavior of the ordinarily inert Cu dramatically.<sup>8</sup> For example, it has been observed that 3/4 ML of Cu enhances the catalytic reaction rate for the dehydrogenation of  $\text{C}_6\text{H}_{12}$  to form  $\text{C}_6\text{H}_6$  by a factor of almost ten.<sup>9</sup> In addition, CO adsorption shows a binding strength intermediate between its weak level on pure Cu and the strong binding seen on Ru(0001). Obviously, at these levels of Cu coverage the Ru substrate is having a strong perturbing effect.

In studies aimed at observing the alterations in Cu electronic properties that give rise to this strong interaction, measurements have been undertaken of both the growth behavior of the Cu overlayer films by LEED<sup>9</sup> and the electronic properties by ARUPS.<sup>2</sup> In the sub-ML coverage range the Cu films were found to grow in the form of 2d islands in a structure pseudomorphic to the Ru surface under a tensile strain of about 5.5%; this structure is thermally stable against annealing to 900 K.

The ARUPS results, which are shown as a function of Cu coverage in Fig. 3, indicate several unique aspects in the sub-ML region. First, it has been shown that the feature at a binding energy of about 1.5 eV is the result of a Cu/Ru interface state (the first such state ever observed in a metal-metal system).<sup>2</sup> In addition, Fig. 3 demonstrates that the sharp d-band structure normally associated with Cu does not begin to appear until coverages greater than 1 ML. Prior to this point, the Cu overlayer electronic properties (with the exception of the interface state) appear very similar to those of the underlying Ru. Such effects have exciting potential in the sense of being able to tailor overall surface properties for predictable and specific chemical applications.

### Conclusions

Modern surface electron spectroscopies are playing a key role in defining the electronic properties of surface/adsorbate systems important in catalysis. For example, Auger line shape information provides a convenient method for assessing carbon types and bonding symmetry at surface sites. Photoemission, on the other hand, enables the measurement of specific electronic states uniquely related to the delocalized character of a metal overlayer at the metal/metal interface. This information is invaluable in relating surface electronic properties to catalytic activity.

## References

1. D. W. Goodman, "Model catalytic studies over metal single crystals," *Acct. Chem. Res.* 17: 194, 1984.
2. J. E. Houston, C. H. F. Peden, P. J. Feibelman, and D. R. Hamann, "Observations of a true interface state in strained-layer Cu adsorption on Ru(0001)," *Phys. Rev. Lett.* 56: 375, 1986.
3. D. W. Goodman, R. D. Kelley, T. E. Madey, and J. M. White, "Kinetics of the hydrogenation of CO over a single crystal nickel catalyst," *J. Catal.* 64: 479, 1980.
4. D. W. Goodman and J. M. White, "Measurement of carbide buildup and removal kinetics on Ni(100)," *Surf. Sci.* 90: 201, 1979.
5. J. E. Houston, D. E. Peebles, and D. W. Goodman, "Auger lineshape studies of carbon species on Rh and Ni surfaces," *J. Vac. Sci. Technol.* A1: 995, 1983.
6. R. R. Rye, unpublished data.
7. D. W. Goodman and M. Kiskinova, "Chemisorption and reactivity studies of H<sub>2</sub> and CO on sulfided Ni(100)," *Surf. Sci.* 105: L265, 1981.
8. C. H. F. Peden and D. W. Goodman, "Cyclohexane dehydrogenation over a strained-layer Cu/Ru catalyst," *J. Catal.* (in press).
9. J. E. Houston, C. H. F. Peden, D. S. Blair, and D. W. Goodman, "Monolayer and multilayer growth of Cu on the Ru(0001) surface," *Surf. Sci.* (in press).

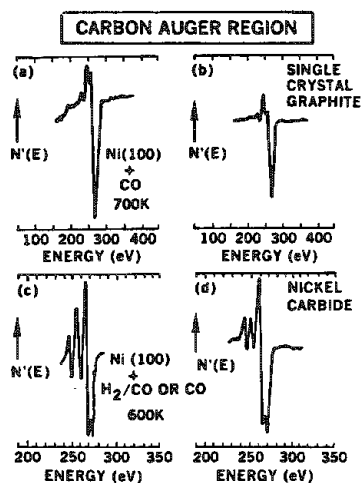


FIG. 1.--Comparison of AES carbon signals with those from single-crystal graphite and nickel carbide.

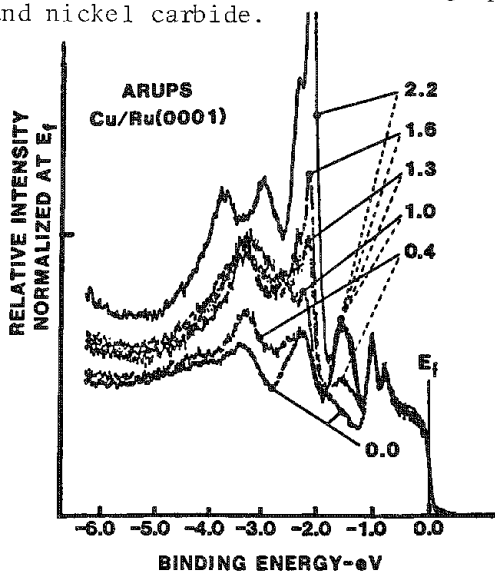


FIG. 3.--Angular resolved UV photoemission spectra (HeI) of Ru(001) surface for Cu over-layers of various coverages. Azimuthal and polar angles are such as to place observation at K point in surface Brillouin zone.

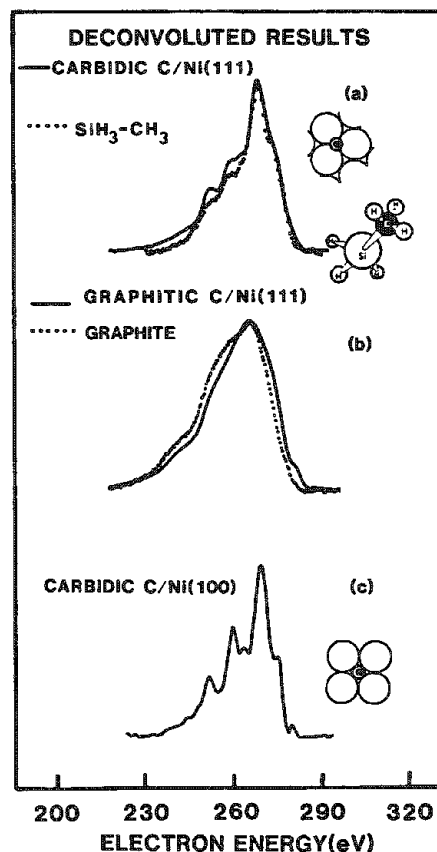


FIG. 2.--Comparison of various Ni surface carbon lineshapes: (a) solid curve, loss-deconvoluted C(KVV) lineshape for carbide carbon on Ni(111); dotted line, lineshape from gas phase SiH<sub>3</sub>-CH<sub>3</sub>; (b) solid line, loss-corrected lineshapes for graphitic carbon on Ni(111); dotted line, that obtained from bulk graphite; (c) corrected C(KVV) lineshape for carbide form of carbon on Ni(111) surface.

## APPLICATION OF AEM TO RUTHENIUM CATALYST SYNTHESIS

W. M. Targos and H. Abrevaya

Metals supported on high-surface-area metal oxides are used extensively in heterogeneous catalysis. The activity of these catalysts has been directly correlated with the size of the metal particles.<sup>1</sup> The selectivity of the reactions is directly related to electronic and structural properties of the reaction site.<sup>2</sup> Consequently, control over the size and structure of metals supported on metal oxides is a catalytic chemist's goal. A procedure for preparing small uniform-size metal particles has been disclosed in the literature.<sup>3</sup> Recently, an improved proprietary micelle procedure for preparing specific-size metal particles on supports was developed at The Signal Research Center (SRC). This new technology has provided the impetus for a group at SRC to develop selective Fischer-Tropsch catalysts under a program sponsored by the U.S. Department of Energy (Contract DE-AC22-84PC70023).

The catalysts discussed in this study contain ruthenium on  $\gamma$ -alumina made by the proprietary micelle method and conventional procedures. Since the analytical electron microscope (AEM) is particularly effective in characterizing 1-10nm supported metal crystallites,<sup>4</sup> it has been used interactively to characterize both the fresh and used catalysts investigated in this program. The objective of this work was to establish procedures for characterizing various types of ruthenium supported on  $\gamma$ -alumina by AEM. Future studies will focus on other characterization techniques as well as the test evaluation data for these catalysts.

### *Experimental*

The AEM used in this study was the Vacuum Generators HB-5. Elemental analysis was obtained by an energy-dispersive x-ray system (EDS). Elemental analyses were obtained in a scanning mode to limit radiation damage and maintain visual monitoring of the area during the analysis.

To prevent oxidation of the metal crystallites, special precautions were taken. All reduced catalysts were prepared for AEM analysis by grinding with a mortar and pestle in a nitrogen-purged glove bag. A carbon-coated nylon grid prewet with isopropanol was dipped into the powder and allowed to dry, and the excess powder was removed by gentle tapping and flexing of the grid. The grid was inserted into the specimen cartridge while still in the nitrogen-purged glove bag. The glove bag with specimen cartridge was taken to the microscope's delivery chamber, which was also under nitrogen purge. While nitrogen was purged through the glove bag, the bag was slipped over the delivery chamber, and the specimen cartridge was inserted into the instrument. The delivery chamber was evacuated within 15 min, at which time the specimen cartridge was inserted into the microscope.

Oxidized and used catalysts were prepared in air for microscopic analysis.

### *Results and Discussion*

In order rapidly to evaluate and screen a large number of catalysts, a procedure was followed which combined visual and EDS analyses to determine crystallite size distribution and estimate uniformity of ruthenium distribution among the alumina particles. The alumina particles analyzed by EDS were usually below 1  $\mu$ m in diameter and were quantitated by the Cliff-Lorimer thin-foil approximation. Although the thickness of the porous alumina particles was beyond acceptable limits for valid use of the thin-foil approximation to obtain quantitative results, the data were still valuable in making qualitative comparisons for optimizing catalyst formulations. All reduced catalysts were kept under nitrogen.

---

The authors are at the Signal Research Center, Des Plaines, IL 60017. They wish to acknowledge the assistance of S. Bradley for interpreting the microdiffraction patterns, and M. Akbarnejad for his assistance in preparing the catalysts.

### *Examination of Fresh Catalysts*

Three types of catalysts were obtained from the synthesis procedures used in this work: (1) highly agglomerated ruthenium, (2) highly dispersed ruthenium, and (3) ruthenium crystallites with a narrow size distribution.

Catalysts which exhibited highly agglomerated ruthenium were rapidly characterized because of their size, some as large as 2.5  $\mu\text{m}$  in diameter. Further analysis by EDS confirmed that the majority of the alumina particles did not contain ruthenium. It was not evident from this visual inspection that all the ruthenium could be accounted for. Bulk chemical analysis of these samples confirmed that the appropriate level of ruthenium, usually 1 wt.%, was present on the samples analyzed by AEM.

Examination of catalysts with highly dispersed ruthenium was made to insure that no ruthenium crystallites were present, and to determine the uniformity of ruthenium distribution among the alumina particles. Since the limit of detectability for ruthenium crystallites was 2 nm, additional data using hydrogen gas titration proved valuable in estimating the ruthenium dispersion. These catalysts were initially evaluated for large agglomerates of ruthenium. Usually 100-120 alumina particles were analyzed qualitatively for ruthenium to insure that the ruthenium was uniformly distributed among the alumina particles confirmed to have ruthenium. Twenty to thirty alumina particles were randomly selected for ruthenium analysis so that a semiquantitative result could be obtained. Typical data obtained from an evaluation of such a catalyst made by conventional aqueous impregnation technique are shown in Table 1. This catalyst did not show visible ruthenium particles and the ruthenium was uniformly distributed among the alumina particles.

Analysis of catalysts exhibiting narrow crystallite size distributions of 2-3 or 4-6 nm was more complex. These catalysts were made by the proprietary micelle procedure. Table 2 lists analyses that typify what was observed for catalysts made by this procedure. The distribution of ruthenium among alumina particles, in general, was not as uniform for the catalysts made by a conventional aqueous impregnation procedure.

Concern that the size distribution might be influenced by rapid and complete oxidation of the ruthenium crystallites during handling, which would make them less observable, was addressed. Although it was suspected that the measures taken might not be stringent enough to eliminate oxidation totally, it was anticipated that the effect of oxidation would be minimized. To verify this hypothesis, microdiffraction analysis of ruthenium crystallites on  $\gamma$ -alumina was performed and revealed that the major portion of the crystallites was metallic. Figure 1 shows an example of a microdiffraction pattern from a 12.5nm crystallite which corresponds to a [121] zone axis. Diffraction patterns for crystallites 4 nm in size were also obtained. These patterns usually had one diffraction spot and could not be readily indexed.

Determining crystallite sizes was also complicated by the wide number of orientation configurations of the alumina particles supported on the carbon film. Consequently, ruthenium crystallites only at the appropriate focus and diffracting conditions appeared visible. As the grid was tilted, some crystallites became visible and others disappeared from view.

A typical micrograph of the 4-6nm crystallites is shown in Fig. 2. Catalysts containing 4-6nm crystallites were not as difficult to detect and measure for size because the orientation was less critical for their observation. A hexagonal crystal shape was assumed for estimating crystallite sizes. Analysis of alumina particles in which no ruthenium crystallites could be visually observed in the 4-6nm size range did not contain ruthenium. It was important to establish that, because highly dispersed ruthenium was not desired. Hydrogen titration results indicated that the majority of the ruthenium must be in crystallite sizes 5 nm or slightly larger.

The analysis of catalysts containing 2-3nm ruthenium crystallites was not routine. No large ruthenium particles or intermediate size crystallites were observed. Only moderate quantities of 2-3nm crystallites were observed and they appeared raft-like. For the same weight percent of ruthenium on the catalyst, the quantity of 2-3nm crystallites should have been two to five times greater than the number of 4-6nm size ruthenium crystallites, depending on how much mass was in each crystallite. Failure to observe substantial quantities of 2-3nm crystallites may be due to reduced Z and diffraction contrast effects that might result from the low mass and partial oxidation of the raft-like particles. Attempts to enhance observation of these crystallites by tilting the specimen were not successful. Use of the annular dark field (ADF) detector to enhance observation of

these crystallites was not successful. A higher-angle detector such as that used by Penneycook<sup>5</sup> is needed to enhance observation of these crystallites. In future work, the mass of detectable crystallites will be estimated by monitoring x-ray counts of ruthenium generated from a crystallite as a function of time and normalizing these counts against the electron beam intensity.

Hydrogen titration data were obtained for the catalysts with 2-3nm ruthenium crystallites to determine whether highly dispersed ruthenium was present in appreciable quantities. The H<sub>2</sub> uptake for these catalysts was intermediate between those obtained for the highly dispersed catalysts and the catalysts with 4-6nm crystallites. Since the AEM data provided evidence that large crystallites were not present, the majority of the ruthenium should be present as approximately 2-3nm crystallites.

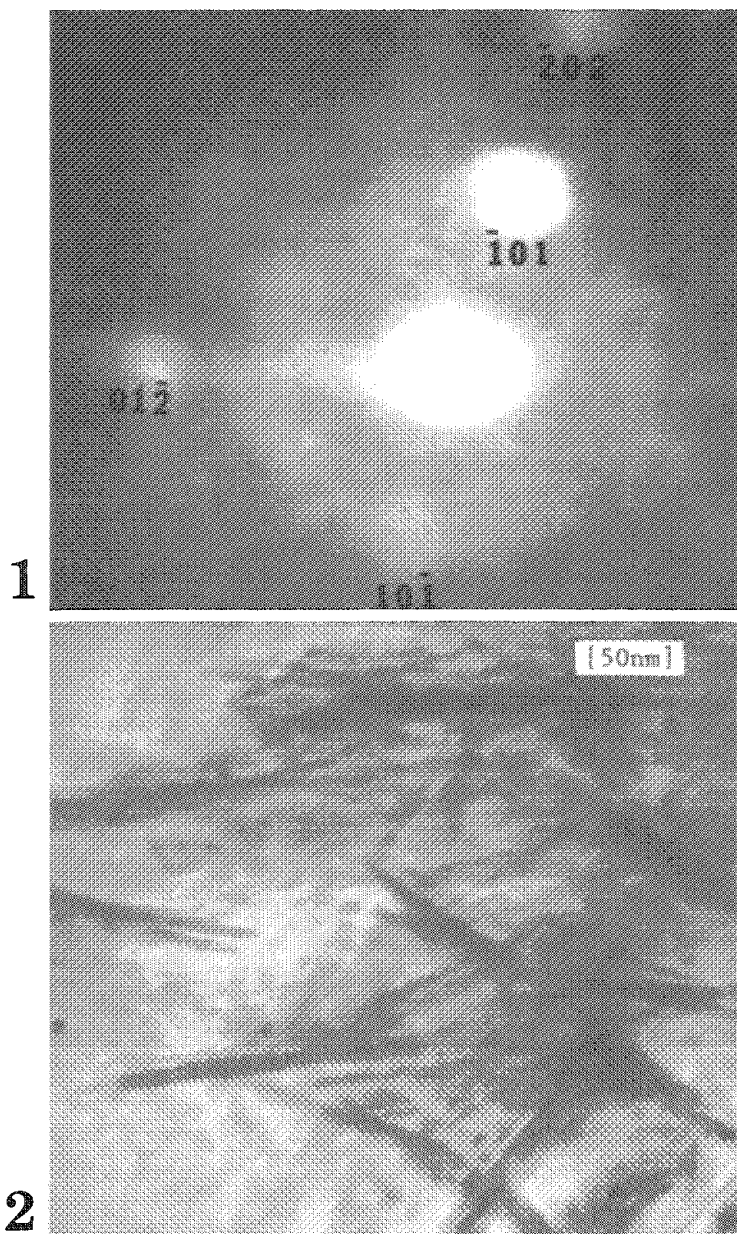


FIG. 1.--Microdiffraction pattern of 12.5nm ruthenium crystallite supported on  $\gamma$ -alumina.  
FIG. 2.--4-6nm ruthenium crystallites on  $\gamma$ -alumina.

### Examination of Used Catalysts

Catalysts that were exposed to testing conditions were given postmortem examination. No attempt was made to protect these catalysts from air exposure. It was suspected that the waxy hydrocarbon residue might protect the ruthenium from excessive oxidation. Attempts to obtain diffraction data from crystallites were impaired by rapid buildup of carbon at the point of beam contact. Also, because of the excessive hydrocarbon content, appreciable in situ reduction of these crystallites upon electron beam contact is anticipated.

Catalysts were taken from the top and bottom of the reactor to determine whether ruthenium was mobile during reaction conditions. Evaluation was made for crystallite growth and ruthenium content. In general, the quantitative results obtained by AEM were similar in trend to those obtained by bulk chemical analysis.

### Summary

The AEM was used as an integral part of the Fischer-Tropsch catalyst program. The information obtained from catalysts made in this program was interactively used to optimize formulations and testing conditions.

### References

1. P. J. Reucraft and H. Parekh, *Applied Catalyst* 3: 65, 1982.
2. M. J. Yacaman and J. M. Dominquez, *Growth and Properties of Metal Clusters*, Amsterdam: Elsevier, 1980, 493-503.
3. M. Boutonnet, J. Kzling, P. Stenius, *Colloids and Surfaces* 5: 209-225, 1982.
4. W. M. Targos, *Analytical Electron Microscopy--1984*, 201-204.
5. S. J. Pennycook, *J. Microscopy* 124(Pt 1): 15-22, 1981.

TABLE 1.--Analysis of ruthenium on individual  $\gamma$ -alumina particles made from conventional aqueous impregnation procedure.

Particle No.	Weight %	
	Al <sub>2</sub> O <sub>3</sub>	Ru
1	99.38	0.62
2	99.06	0.94
3	99.48	0.52
4	99.43	0.57
5	99.40	0.60
6	99.37	0.63
7	99.52	0.48
8	99.58	0.42
9	99.53	0.47
10	99.51	0.49
11	99.58	0.42
12	99.46	0.54
13	99.53	0.47
14	99.56	0.44
15	99.48	0.52
16	99.44	0.56
17	99.53	0.47

TABLE 2.--Analysis of ruthenium on individual  $\gamma$ -alumina particles made from a modified micelle procedure.

Particle No.	Weight %	
	Ru	Al <sub>2</sub> O <sub>3</sub>
1	1.48	98.52
2	1.78	98.22
3	0.23	99.77
4	--	100.00
5	0.26	99.74
6	1.62	98.38
7	1.10	98.90
8	1.10	98.89
9	2.05	97.95
10	1.90	98.10
11	1.31	98.69
12	0.95	99.05
13	0.78	99.22
14	--	100.00
15	0.15	99.85
16	--	100.00
17	1.10	98.90
18	--	100.00

## APPLICATION OF SECONDARY ION MASS SPECTROMETRY TO THE STUDY OF POTASSIUM AND COPPER PROMOTERS IN IRON OXIDE CATALYSTS

E. J. Karwacki, Jr.

The addition of promoters such as alkaline metals to iron-based catalysts has been found to be a means to improve product selectivity in Fischer-Tropsch synthesis.<sup>1-3</sup> However, surface characterization of these promoted catalysts by x-ray photoelectron spectroscopy (XPS) and Auger electron spectroscopy (AES) is often hindered because these techniques are not sensitive to surface dopant levels significantly below 1 at.%. The present study explored the potential application of secondary ion mass spectrometry (SIMS) for characterizing iron oxide catalysts promoted with copper and potassium. Both static SIMS and near-surface SIMS profiles suggest a redistribution of these promoters occurs after freshly prepared catalysts are activated and utilized for product synthesis.

### *Experimental*

Catalyst samples were prepared by coprecipitation of iron and copper nitrates in ammonium. The filtered cakes were subsequently doped with potassium salts and dried under atmospheric pressure at more than 373 K. Spent catalysts were removed from slurry reactors and the oil matrix stripped under inert atmosphere. The samples were stored before analysis within a nitrogen-filled glovebox.

SIMS analysis was performed on a Physical Electronics (PHI) model 560 spectrometer equipped with a SIMS II unit. Base pressures within the analysis chamber were routinely less than  $2 \times 10^{-10}$  Torr. A PHI model 04-303 differentially pumped ion gun, pumped by a Balzers 170 l/s turbomolecular pump, was used to generate the primary ions.

Catalyst samples were prepared for analysis by gently pressing of the powdered materials onto indium foil (Alfa Products) that had been precleaned by wiping with methanol. This supporting technique minimizes surface charging, a common problem with nonconductive materials. The prepared foils were mounted onto a 30° sample holder with stainless washers and screws.

Static SIMS measurements were performed with a 5keV primary ion beam of Ar<sup>+</sup>, defocused to a spot approximately 1 mm in diameter. Specimen current, measured with a picoammeter, was maintained at 4 nA. Though these conditions are not, by definition, truly "static" (ion dose < 10<sup>13</sup>/cm<sup>2</sup>), they were considered satisfactory because the spectra did not change appreciably in the time required to perform an analysis (<3 min). Near surface profiles were accomplished by an increase of the primary ion current to 0.4  $\mu$ A and rastering of the beam over a 4  $\times$  4mm region. These conditions resulted in an estimated sputter rate of 4 Å/min as measured vs a Ta<sub>2</sub>O<sub>5</sub> thin film standard. An oxygen jet was utilized during profiles to minimize matrix effects and stabilize ion yields, particularly the FeO<sup>+</sup>/Fe<sup>+</sup> ratio.

A secondary ion collection angle of approximately 20° (as measured from the surface normal) was utilized. The secondary ion energy prefilter was set at a bandpass center of 4 eV. Ion intensity measurements were performed using peak top mode. Data were collected, as depth profiles, on a PDP11/04 with the use of PHI MACS V6 software. The profiles were then transferred to a Vax11/750 for recalculation and display using RS/1® by Bolt, Beranek and Newman.

### *Results and Discussion*

Figures 1(a) and (b) depict typical static SIMS spectra obtained from unpromoted and promoted iron oxide catalysts, respectively. With promotion the K<sup>+</sup> signal increased by well over two orders of magnitude. The presence of potassium in the unpromoted catalyst

---

The author is at Air Products and Chemicals, Inc., Box 538, Allentown, PA 18105. DOE support (Grant DE-AC22-80PC30021) is acknowledged, as is the aid of Dr. Eamon Carroll, Ms. Nelly Cilen, and Mr. Steven Motika in supplying the catalysts used in this investigation.

illustrates the extreme sensitivity of the technique. Alkaline metals, because of their low ionization potentials, can be easily ionized, and hence detected at ppm and even ppb levels. No copper was observed on the unpromoted catalyst. After promotion, copper isotope lines were observed at  $m/e$  63 and 65. XPS and AES analyses of both types of catalysts could not detect the presence of either potassium or copper. Thus, the extreme sensitivity afforded by SIMS permits confirmation of the presence of these promoters on catalyst surfaces.

Although SIMS is quite sensitive, its inability to be made easily quantifiable has hindered its utilization as an analytical probe. In this study, rather than attempting to quantify promoter concentrations absolutely, we have emphasized the use of relative measurements (i.e., ion ratios) to compare results. Since iron oxide is the matrix, the  $K^+$ ,  $Cu^+$ , and  $FeO^+$  intensities are ratioed to the  $Fe^+$  intensity. These ratios are then plotted and used for sample-to-sample comparisons. As a criterion for considering these measurements reliable, the  $FeO^+/Fe^+$  ratio is required to be unchanged during analysis. If this ratio remains unchanged throughout the profiles, any variation in the  $Cu^+/Fe^+$  and  $K^+/Fe^+$  ratios is assumed to be due to changes in species concentration, rather than to matrix effects.

In Fig. 2(a)  $FeO^+/Fe^+$  profiles are plotted for three freshly prepared catalysts with varying amounts of potassium and copper promotion. All exhibit flat profiles throughout the analysis period. These data suggest that matrix effects during analysis have been minimized.  $K^+/Fe^+$  profiles obtained from the same three samples (Fig. 2b) indicate that after promotion a substantial enhancement ( $>1000$ ) occurs in the level of surface potassium present on iron oxide catalysts. Unpromoted precipitated iron oxides, identically profiled, showed  $K^+/Fe^+$  levels of 0.01 or less. These profiles show that after calcination there is a propensity for potassium to migrate to the surface. Figure 2(c) shows the corresponding  $Cu/Fe$  profiles. Unlike potassium, little if any tendency for copper migration during calcination is suggested by the fast flat  $Cu^+/Fe^+$  profiles are observed throughout the profile.

Promoter migration was further investigated by analyzing catalysts before and after use within a laboratory reactor. The  $FeO^+/Fe^+$  profiles, shown in Fig. 3(a), again indicate that matrix effects are minimized. The variation in both the fresh and spent profiles, during the first 2 min, is believed to be due to excessive carbon contamination on the surface. As discussed in the Experimental section, spent catalysts have to be removed from a slurry reactor and stripped of the oil matrix before analysis; however, not all the oil can be removed by this procedure. These profiles suggest a few monolayers of hydrocarbon still persist and must be sputter removed. After this period, the profiles settle down and agree very well.

The  $K^+/Fe^+$  profiles for the fresh and spent catalyst are depicted in Fig. 3(b). Neglecting the changes that occur during the first two minutes, significant potassium redistribution is indicated by the spent catalyst profile. Almost 2.5 times more potassium is observed near the surface of the catalyst after activation and use. Also, the spent profile tails downward as sputtering continues, reaching a base level near that of the fresh catalyst. Figure 3(c) likewise suggests that copper has also undergone some surface migration. The spent  $Cu^+/Fe^+$  profile closely resembles that exhibited by potassium. As Fig. 3(d) illustrates, the migration patterns of potassium and copper are similar because the  $Cu^+/K^+$  profile for the spent catalyst is almost identical to the fresh catalyst.

These SIMS observations, showing a strong tendency for potassium migration in activated and used catalysts, are supported by the recent work of Connell et al.<sup>4</sup> Using iron and aluminum foils whose surfaces were treated with KOH, it was shown by AES that potassium migration depends on gas-phase composition. Significantly less migration was observed on foils heated in oxygen than on foils heated in hydrogen or hydrogen-water atmospheres. The catalysts used in our study were also doped with potassium after coprecipitation of the oxide. By SIMS, potassium shows some tendency to concentrate near the surface after calcination. This redistribution is significantly enhanced after activation and use. During use in Fisher-Tropsch synthesis, the catalysts are subjected to a more reducing environment ( $CO + H_2$ ); in addition, water created by reduction of the catalyst surface, is also present. The earlier study by Connell also showed that a marked increase in potassium migration occurred after 0.53 mol % water was added to hydrogen.

Upon activation and use, copper migration is also suggested by the  $Cu^+/Fe^+$  SIMS profiles. Unlike potassium, copper nitrate is coprecipitated with iron nitrate and should



be evenly distributed throughout the catalyst after filtration. The fresh catalyst profile (Fig. 3c) indicates that after calcination, little copper redistribution occurs. After use, however, copper is observed to migrate to the surface. Therefore, similar transport driving forces are believed responsible for copper migration. Reducing environments appear significantly more conducive for copper migration in promoted iron oxide catalysts.

### Conclusions

This study illustrates the potential application for using SIMS as a catalyst probe. Both static SIMS and near surface SIMS profiles demonstrate the propensity for potassium and copper promoters to migrate to the surface of iron oxide. Some redistribution is due to calcination, as indicated by profiles of fresh catalysts, but a significantly higher tendency for surface migration is suggested by the profiles from activated and used catalysts. This enhancement is believed due to the presence of a reducing environment of hydrogen and water during activation and use. Though SIMS does not absolutely quantify these materials, this study has shown its potential as a qualitative and semiquantitative tool for evaluating promoters added at levels below the detection limits of more conventional surface techniques such as XPS and AES.

### References

1. M. E. Dry, in J. R. Andersen and M. Boudart, Eds., *Catalysts Science and Technology*, New York: Springer-Verlag, 1981, 1, 87.
2. D. W. Goodman, *Heterogeneous Catalysis Proc. Symp., Univ. Coop. Chem. Program, Dep. Chem. Texas A&M Univ.*, 2: 230-250, 1985.
3. G. Broden, G. Fafner, and H. P. Bonzel, *Surf. Sci.* 84: 119, 1975.
4. G. Connell and J. A. Dumesic, *J. of Catalysis* 92: 17, 1985.

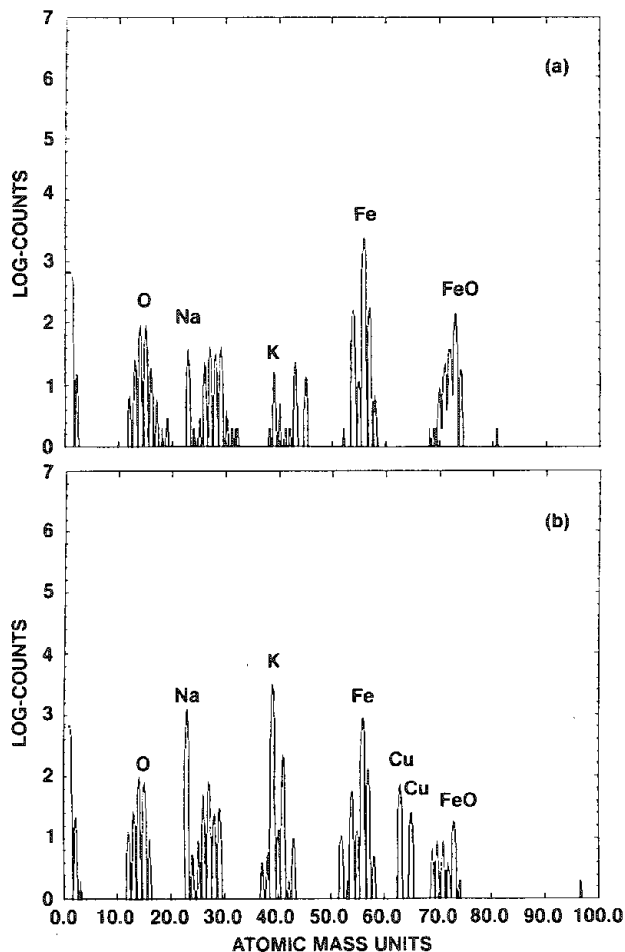


FIG. 1.--Typical static SIMS spectra obtained from (a) unpromoted precipitated iron oxide catalyst, (b) potassium and copper promoted iron oxide catalyst.

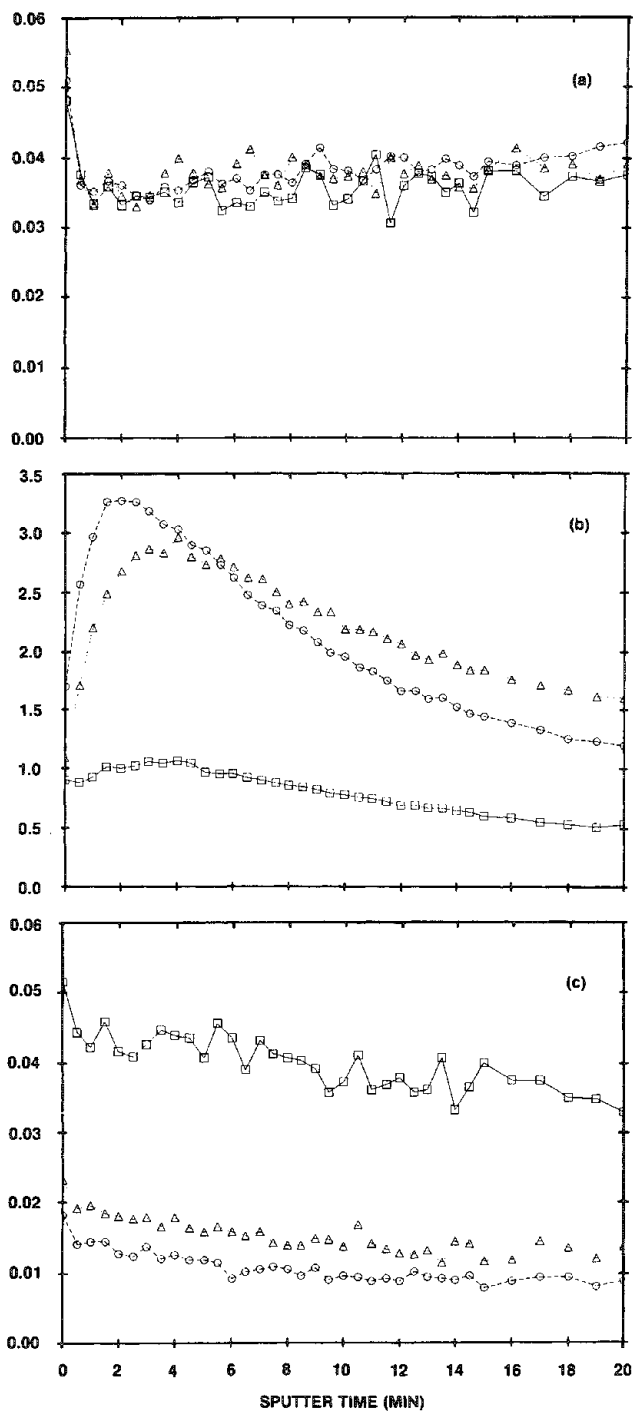


FIG. 2.--SIMS profiles for (a)  $\text{FeO}^+/\text{Fe}^+$ , (b)  $\text{K}^+/\text{Fe}^+$ , (c)  $\text{Cu}^+/\text{Fe}^+$  from three freshly prepared (calcined) catalysts; promoted with □ 1.5 wt% Cu, 0.1 wt% K; Δ 0.5 wt% Cu, 0.18 wt% K; ○ 0.5 wt% Cu, 0.1 wt% K.

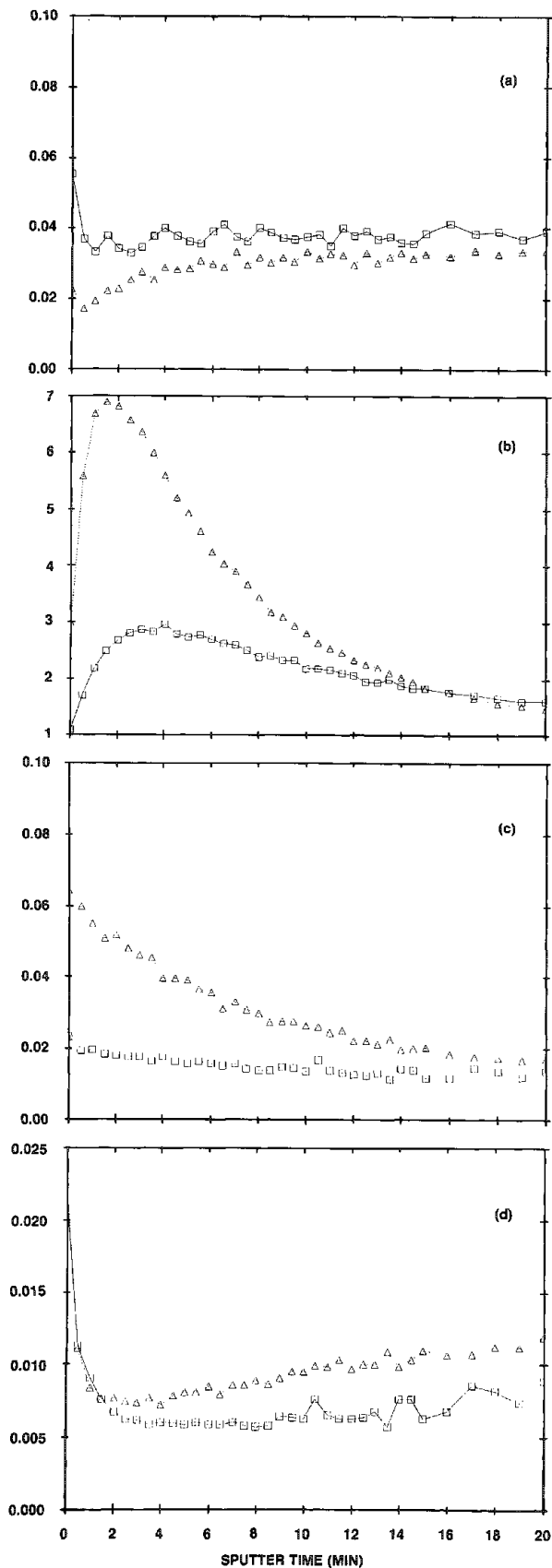


FIG. 3.--Result of SIMS profiles obtained from iron oxide catalyst promoted with 0.5 wt% Cu, 0.18 wt% K. Profiles for (a)  $\text{FeO}^+/\text{Fe}^+$ , (b)  $\text{K}^+/\text{Fe}^+$ , (c)  $\text{Cu}^+/\text{Fe}^+$ , (d)  $\text{Cu}^+/\text{K}^+$ . □ fresh (calcined) catalyst sample, Δ activated and used catalyst sample.

## MICRODISTRIBUTION OF KEROGEN AND MINERAL PHASES IN RAW AND RETORTED OIL SHALES

J. B. Hall, P. P. Hruskoci, T. L. Marker, and S. M. Polomchak

The microdistribution of the kerogen and mineral phase components of oil shale particles, both before and after retorting, can be useful information for devising and evaluating oil shale beneficiation and retorting schemes. Scanning electron microscopy and electron probe microanalysis procedures have been developed and applied to a wide range of raw and retorted oil shales. These data have provided insights into the limitations of physical beneficiation and aided in modeling the retorting process.

### *Procedure*

The samples analyzed were crushed shales (12 × 48 mesh), both raw and after retorting. The retort conditions ranged from mild (low temperature, short residence time) to severe (high temperature, long residence time). Polished cross sections of the particles were prepared by standard metallographic techniques,<sup>1</sup> except that sulfur was substituted for epoxy as the embedding medium to eliminate the possibility of confusing epoxy carbon for the kerogen carbon.

When polished cross sections are examined with a polarizing light microscope by incident illumination, the relative kerogen level in each particle is revealed by the darkness of the amber color.<sup>2</sup> However, such data can be misleading because iron sulfide inclusions also give a dark color to the oil shale particles. The scanning electron microscope (SEM) was used to image the polished cross sections in the backscattered electron (BSE) mode. By this technique, the lower-atomic-number kerogen material should appear darker than the higher-atomic-number mineral phases.<sup>3</sup> Carbon distribution maps were obtained by use of an SEM equipped with a wavelength-dispersive x-ray analyzer and heavy-element distribution maps were obtained with an SEM equipped with an energy-dispersive x-ray analyzer. The carbon maps reveal the distribution of the kerogen and carbonate carbon, but do not distinguish between them. The heavy element maps reveal the distribution of the different mineral phases.

### *Results and Discussion*

Numerous oil shale particles were analyzed, but data from only a few representative ones are included here to illustrate the type of information one obtains using these procedures.

Figures 1, 2, and 3 are data from raw oil shales. Figure 1 shows a backscattered electron (BSE) image and the corresponding carbon map of two raw shale particles. The scattered small bright inclusions were determined to be iron sulfide particles, the numerous darker inclusions were determined to be primarily silicate minerals with some carbonates, and the dark matrix is apparently the kerogen. The carbon map is consistent with the BSE image. It shows a greater density of carbon in the smaller oil shale particle for which the BSE image also shows more kerogen matrix. The data on these particles confirm that the oil shale particles are composed of mineral inclusions in a kerogen matrix. The larger oil shale particle has a greater density of mineral inclusions, and therefore less kerogen matrix. Figure 2 shows a BSE image and corresponding carbon map of a raw oil shale particle which has kerogen-rich bands running through it. This is also a very common feature in all the raw oil shales analyzed. Figure 3 shows a BSE image and corresponding carbon map of two raw oil shale particles with widely different kerogen levels. The left particle is a tight aggregate of mineral particles with very little kerogen, whereas the right particle appears to be almost pure kerogen except for the upper third of the particle. However, a closeup SEM view of even kerogen-rich particles show numerous well-dispersed mineral inclusions (Fig. 6a). The presence of these well-dispersed mineral inclusions in a kerogen matrix would limit physical beneficiation processes, although the

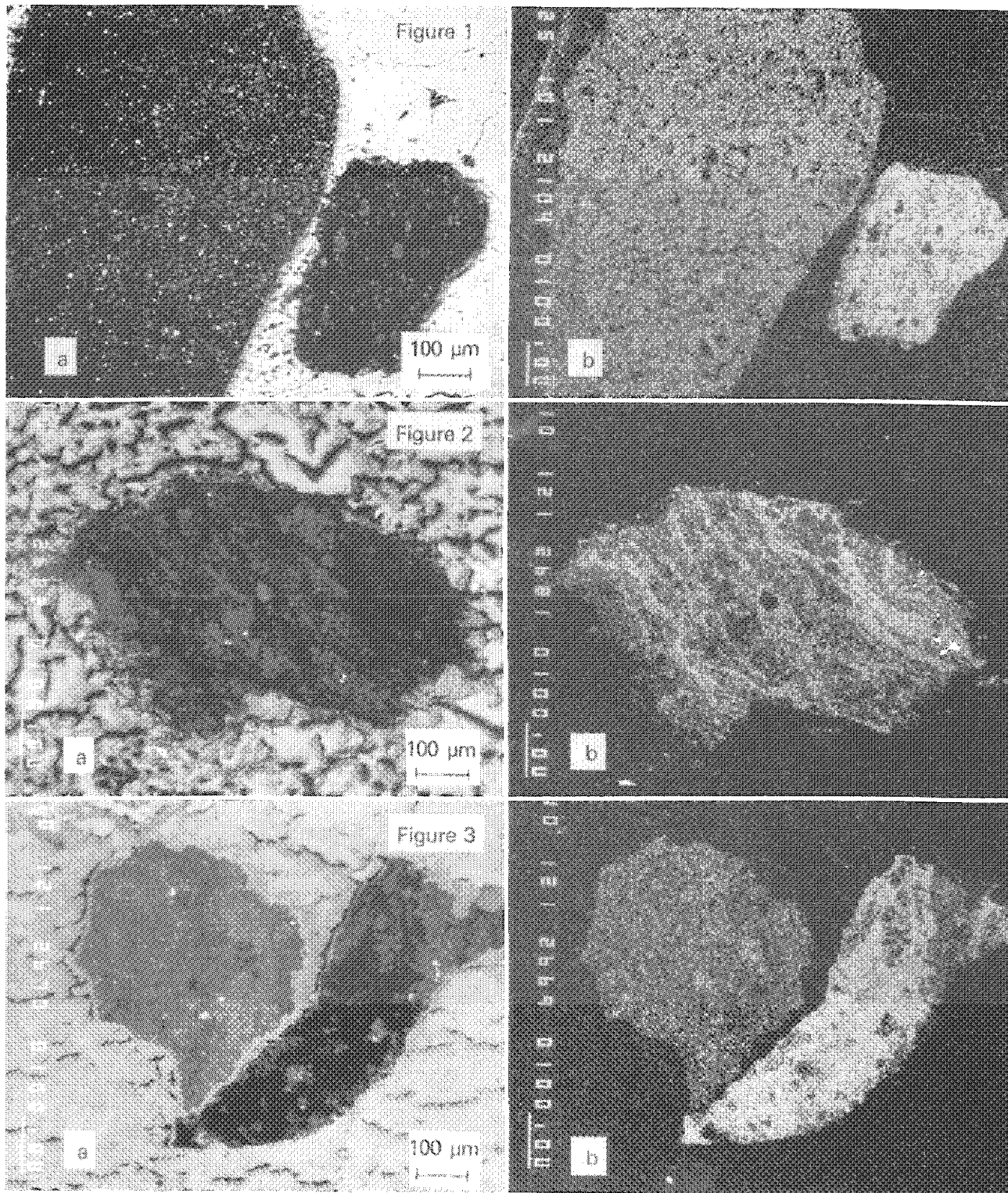


FIG. 1.--Raw oil shale (a) BSE image and (b) C map.  
 FIG. 2.--Raw oil shale (a) BSE image and (b) C map.  
 FIG. 3.--Raw oil shale (a) BSE image and (b) C map.

presence of very rich to very lean oil shale particles in the same oil shale does suggest that some kerogen enrichment should be possible.

Figure 4 shows a BSE image and carbon map of an oil shale retorted under mild conditions. This field of view, which is typical, shows retorted oil shale particles with a uniform low level of carbon. When the kerogen is heated it cracks to produce a coke residue and an oil product. The uniform distribution of this kerogen/carbon residue throughout the retorted oil shale particles suggests that at retorting temperatures the kerogen migrates and covers all the mineral phase surfaces. The mineral inclusions may be providing a reaction surface for the cracking of the kerogen. There was no evidence of a concentration of kerogen residue at the core of any of the incompletely retorted oil shale particles analyzed, which suggests that the retorting process is not diffusion limited.

Figure 5 shows a BSE image and carbon map of an oil shale retorted under severe conditions. This particle, which is typical, shows a uniformly dispersed very low carbon level. The original mineral inclusions appear to be tightly packed together without significant cavity formation. Although some evidence of cavity formation during retorting was observed, this closer packing of mineral inclusions dominated. Figure 6, which is a higher magnification SEM micrograph of a raw and retorted (medium severity) shale, shows this compaction more clearly. In the raw shale numerous mineral particles are scattered throughout a kerogen matrix, whereas in the retorted shale, mineral particles are compacted with very little kerogen matrix remaining. Although complete retorting does produce some mineral fines, apparently most of the mineral inclusions are held together as dense aggregates, which are easier to handle.

### *Conclusions*

Oil shale particles are composed of a kerogen matrix with mineral inclusions. The density of the mineral inclusions in individual raw oil shale particles varies widely, so that each crushed oil shale has particles that range in kerogen content from very rich to very lean. This finding suggests that a physical beneficiation process could be used to concentrate the kerogen-rich particles before retorting, but the kerogen enrichment process is substantially limited by the presence of well-dispersed mineral inclusions in even the most kerogen-rich particles. Retorting appears to redistribute the kerogen uniformly throughout the oil shale particles without any diffusion limitation and ultimately leads to a uniform distribution of carbon residue. It appears that the mineral inclusions may be providing the reaction surfaces for the cracking of the kerogen. As the kerogen cracks and the oil products leave the oil shale particles the remaining mineral inclusions become packed into dense, almost cavity-free aggregates.

### *References*

1. J. Dubois et al., *Metallography* 3: 337, 1970.
2. T. F. Yen, *Science and Technology of Oil Shale*, Ann Arbor, Mich.: Ann Arbor Science, 1976, 13-15.
3. J. I. Goldstein et al., *Scanning Electron Microscopy and X-Ray Microanalysis*, New York: Plenum Press, 1981, 75-77.

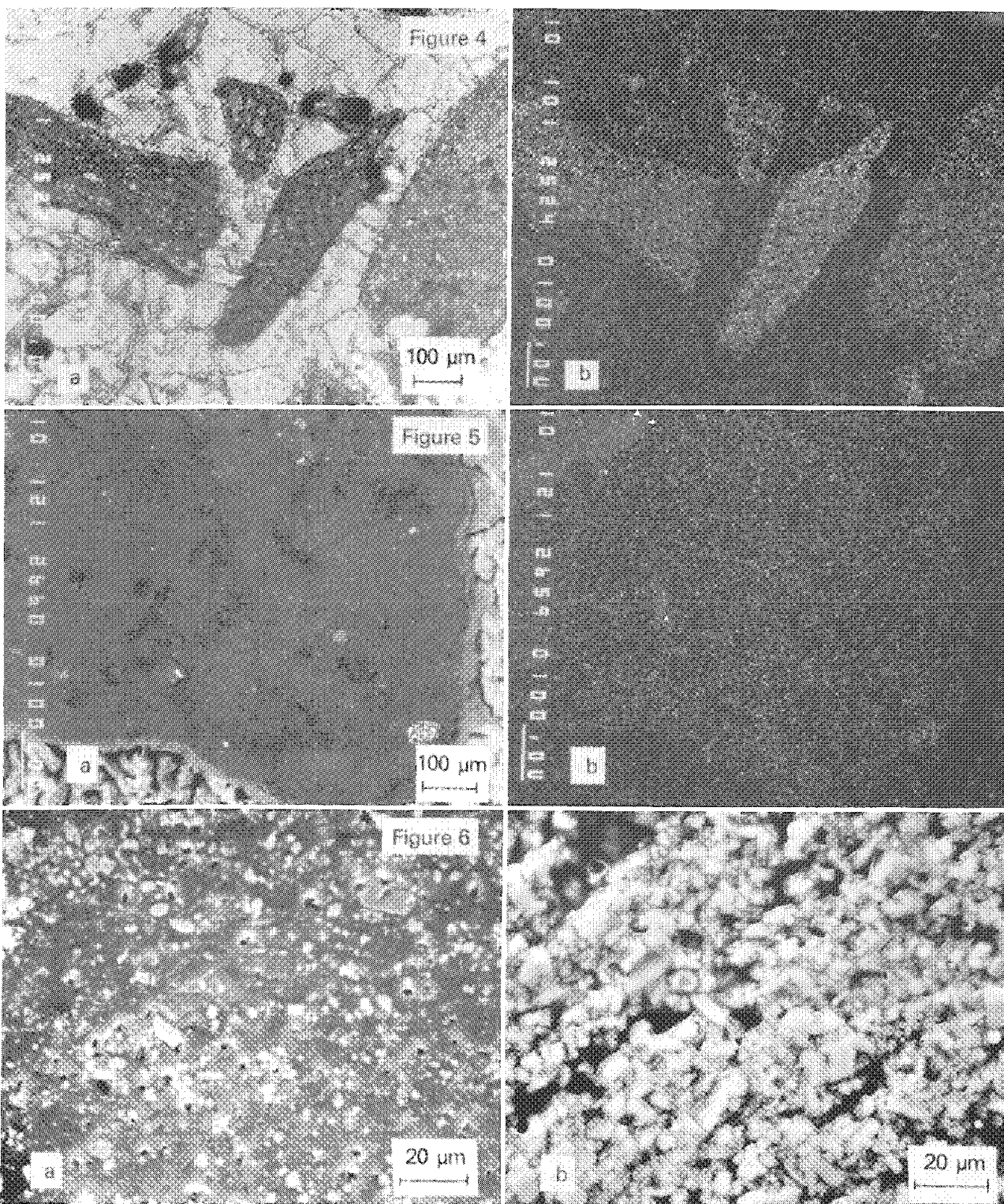


FIG. 4.--Retorted oil shale (a) BSE image and (b) C map.  
 FIG. 5.--Retorted oil shale (a) BSE image and (b) C map.  
 FIG. 6.--SEM images of (a) raw and (b) retorted oil shales.



# CONTROLLED ATMOSPHERE CATALYST CHARACTERIZATION BY X-RAY PHOTOELECTRON SPECTROSCOPY (XPS), X-RAY ABSORPTION SPECTROSCOPY (XAS), AND ANALYTICAL ELECTRON MICROSCOPY (AEM)

D. G. Castner and I. Y. Chan

In many industrial applications, cobalt-containing catalysts are activated by reduction and/or sulfidation of a cobalt oxide precursor. In order to understand how these catalysts function, it is informative to determine the geometric structure and oxidation state of these catalysts in their active state. This determination requires the coupling of controlled atmosphere and in situ treatment systems with physical characterization techniques.

It is desirable to use different characterization techniques on the same sample under the same conditions. A better understanding of the catalytic properties can be achieved by correlation of the results from the various techniques. In this paper, we demonstrate the complementary nature of controlled-atmosphere XPS, XAS, and AEM characterization techniques using an  $\text{SiO}_2$ -supported  $\text{Co}_3\text{O}_4$  catalyst. Table 1 lists the information readily obtainable with XPS, XAS, and AEM. It should be noted that phase identification using XPS and XAS is achieved by matching oxidation state, bond distances, and coordination numbers with known phases. There are cases where this method does not provide a unique determination.

TABLE 1.--Information readily available with XPS, XAS, and AEM.

XPS	Oxidation State Phase Identification Relative Surface Concentration of Phases Crystallite Size
XAS	Oxidation State Phase Identification Bond Distances Coordination Numbers Relative Bulk Concentration of Phases Transformation Rates of Phases
AEM	Phase Identification Microstructure (Morphology, Phase Distribution) Crystallographic Information

## Experimental

The cobalt-on-silica catalyst was prepared by pore-fill impregnation of  $\text{Co}(\text{NO}_3)_2$  on a Davison-grade 62 silica support. The nominal Co loading is 10 wt%. After drying at 100 C for 4 h, the catalyst was calcined at 250 C for 1 h and then at 450 C for 2 h.

The XPS experiments were performed with the catalyst treatment-surface analysis system at Chevron Research Co. The AEM studies were performed with a special specimen holder attachment for the JEOL 100CX microscope. The XAS experiments were performed at the Stanford Synchrotron Radiation Laboratory (SSRL). The methodologies for the controlled atmosphere XPS, XAS, and AEM experiments have been described elsewhere.<sup>1-3</sup>

## XPS Results

The  $\text{Co}_3\text{O}_4$  particle size determined from the Co/Si ratio was 10-30 nm.<sup>2</sup> They were the major, and probably the only, Co species present in the calcined catalyst. The complete reduction of  $\text{Co}_3\text{O}_4$  to metallic Co was observed after 1 h at 350 C in flowing hydrogen.

The authors are at Chevron Research Company, 576 Standard Avenue, Richmond, CA 94802. The contributions of R. O. Billman, T. M. Rea, and P. R. Watson are gratefully acknowledged.

### XAS Results

Figure 1 illustrates the results of the XAS temperature programmed reduction (TPR) experiment. It clearly revealed that CoO is an intermediate species in the reduction of  $\text{Co}_3\text{O}_4$  to Co. Previous studies have shown that the reduction rate of  $\text{Co}_3\text{O}_4$  to Co depends on the starting  $\text{Co}_3\text{O}_4$  crystallite size.<sup>2</sup>

### AEM Results

Individual  $\text{Co}_3\text{O}_4$  crystals were about 10-20 nm in size. They were present in hollow spherical agglomerates of about 500 nm in diameter. They appeared as doughnuts in the microtomed thin sections. These agglomerates were homogeneously distributed throughout the sample.

Cyclic oxidation and reduction reduced the average crystallite size and randomized the orientation (Fig. 2). The intermediate species CoO was detected by electron diffraction. Both hexagonal and cubic forms of Co were detected after reduction.

### Discussion

All three techniques were able to identify the phases that were present in the catalyst. The AEM results illustrated the morphologies and the crystallographic relationships of the crystallites, but the relative concentration of each phase was determined by the XAS/TPR experiment. By comparing the XPS and AEM results, we can ascertain the effects of surface enrichment, particle size, and particle distribution. The XPS and AEM experiments were end-point experiments; the XAS/TPR results were true in situ observations.

### Conclusions

Combined controlled-atmosphere XPS, XAS, and AEM study is a powerful approach to catalyst characterization. It provides a detailed description of the geometric structure and oxidation state of a catalyst. This study allows us to optimize and understand the performance of the catalyst system.

### References

1. D. G. Castner and D. S. Santilli, "XPS of Co catalysts: Correlation with carbon monoxide hydrogenation activities," in T. E. Whyte Jr. et al., Eds., *Catalytic Materials: Relationship Between Structure and Reactivity*, ACS Symposium Series No. 248, Washington, D.C.: American Chemical Society, 1984, 39-56.
2. D. G. Castner and P. R. Watson, "XPS and XAS characterization of Co catalysts: Reduction and sulfidation behavior," in M. L. Deviney and J. L. Gland, Eds., *Catalyst Characterization Science*, ACS Symposium Series, No. 288, Washington, D.C.: American Chemical Society, 1985, 144-152.
3. I. Y. Chan, "A controlled atmosphere specimen holder for transmission electron microscopy," *J. Elec. Micros.* 2: 525-532, 1985.

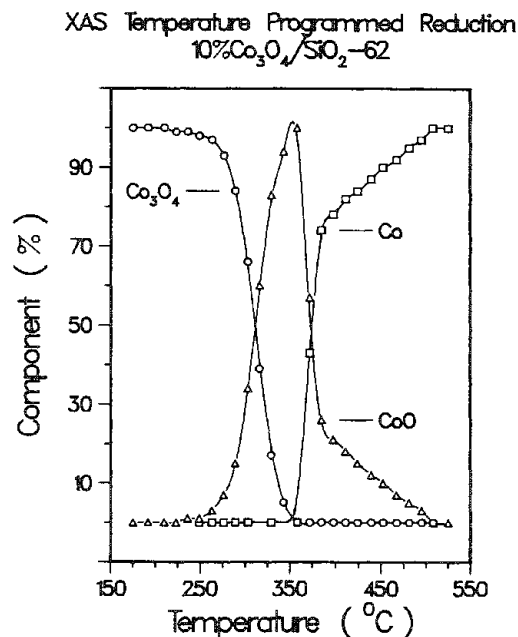


FIG. 1.--XAS/TPR results showing relative concentration of phases with increasing temperature.



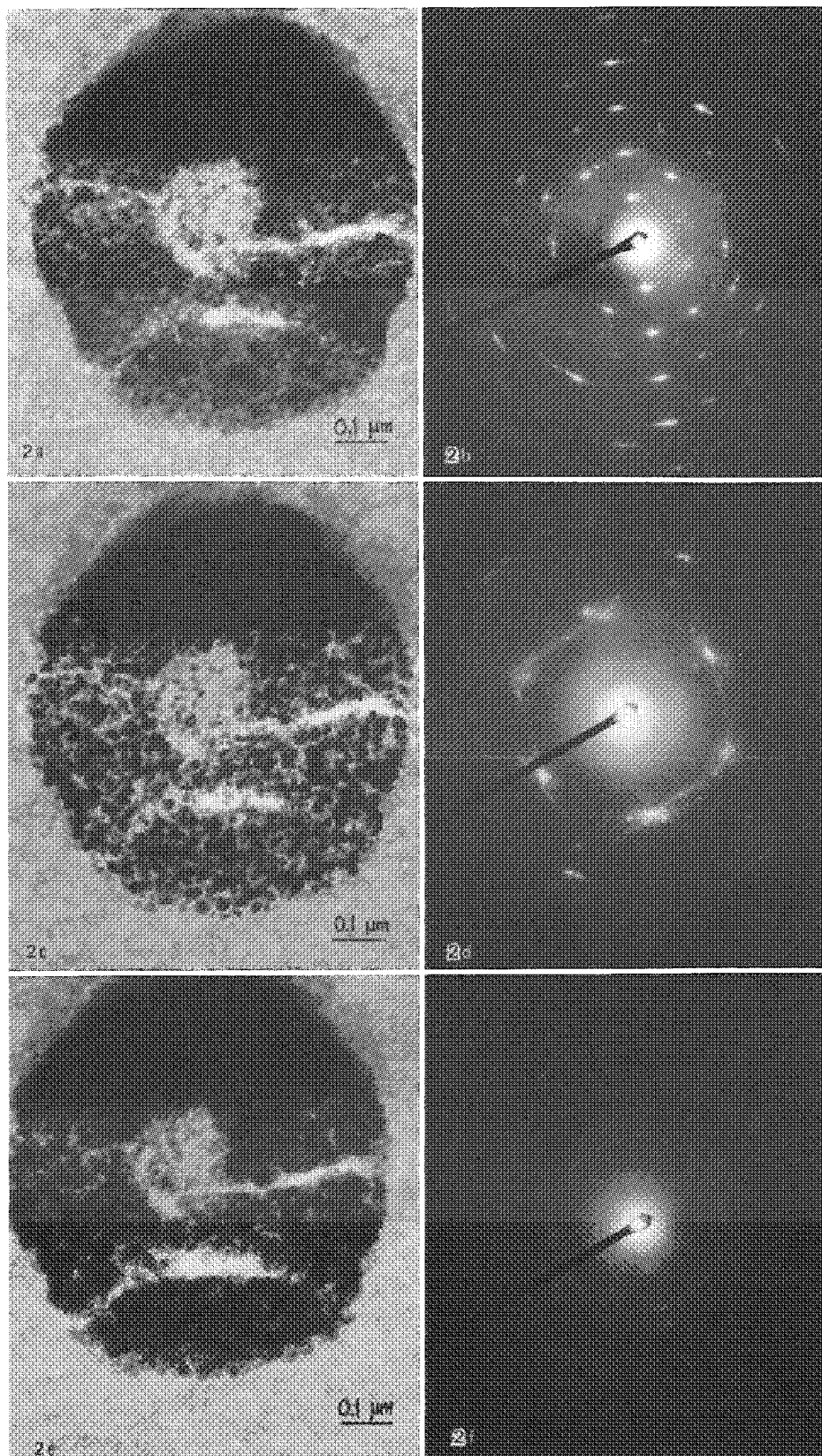


FIG. 2.--TEM images and diffraction patterns of same Co particle: (a) and (b) calcined; (c) and (d) reduced; (e) and (f) reoxidized.

## SURFACE ANALYSIS OF CATALYSTS

Naresh Shah, A. G. Dhere, P. J. Reucroft, and R. J. De Angelis

Obtaining a better understanding of metal-support interactions in supported metal catalysts and how this influences the surface concentration of active metal species is necessary for the development of more effective catalysts. In general, a more efficient coal gasification and liquefaction catalyst is a system with lower metal loading, higher activity, and greater thermal stability and resistance to poisons. ISS is the most direct method for estimating the surface concentration of the active metal. The surface atoms are the main participants in a catalytic reaction.

Ni/Al<sub>2</sub>O<sub>3</sub> catalyst systems are widely used as hydrogenation catalysts. The purpose of this paper is to demonstrate the usefulness of ISS as a surface analysis tool to determine the surface elemental composition.

### *Theory*

Ion Scattering Spectroscopy (ISS) is one of the most surface-sensitive tools available for surface analysis of a variety of materials. The chemical information obtained by ISS is highly surface specific, as it is obtained from only the top atomic layer, in contrast to other surface analysis techniques such as Auger electron spectroscopy and x-ray photoelectron spectroscopy.

In ISS a monoenergetic, well-collimated beam of singly charged noble gas ions (e.g., He, Ne, or Ar) of known mass  $M_1$  and energy  $E_0$  is directed toward a solid surface. The current  $I$  of ions backscattered from the surface after a perfect binary elastic collision is measured as a function of scattered ion energy  $E$ . Curves of  $I$  vs  $E/E_0$ , which are commonly known as ion scattering spectra, contain useful information about the top atomic layer of the surface. If the surface contains atoms of several different masses, the  $I$ -vs- $E$  curve consists of a series of current peaks at energies given by the following fundamental equation of ISS, which is derived from conservation of momentum and energy.

$$\frac{E}{E_0} = \frac{M_1^2}{(M_1 + M_2)^2} [\cos \theta + \sqrt{(M_2^2/M_1^2) - \sin^2 \theta}]^2$$

where  $\theta$  is the scattering angle (138°) fixed by instrument geometry.

An outstanding feature of ISS is its high degree of surface selectivity. The detected ions in ISS have scattered from only the first layer or two of atoms at the surface. This behavior results from a combination of two factors: (1) large scattering cross sections lead to attenuation or depletion of the ion beam as it penetrates the solid, and (2) more complete neutralization as particles penetrate more deeply. Both these effects reduce the yield of ions scattered from inside the solid and hence emphasize the peaks due to scattering from surface atoms.

### *Catalyst Preparation*

ISS studies have been carried out on a series of catalysts provided by United Catalysts Inc., Louisville. These catalysts (L series) were prepared by coprecipitation of varying amounts of Ni and Al carbonates from aqueous salt solutions. These carbonates were compacted into pellet forms and dried at 300–350 C for 16 h to remove moisture. After drying the pellets were sintered and calcined at 400 C for 2 h, which converted all the carbonates into oxides. The metal loading was varied from 10 to 40% by weight. These pellets were analyzed in the as-received form. In practice the catalysts are reduced in situ to get Ni particles on Al<sub>2</sub>O<sub>3</sub> substrate before methanation.

---

The authors are at the Department of Metallurgical Engineering and Materials and Science, University of Kentucky, Lexington, KY 40506. The research was sponsored by the Division of Materials Science, Office of Basic Energy Sciences, U.S. Department of Energy, under Grant DE-FG05-85ER45186.

## Experimental Procedure

All the samples were tested in the as-received condition. Ion scattering spectroscopy was carried out with a Model 525 ISS unit. TEM investigations were carried out on a Phillips EM400 Analytical Electron Microscope with EDAX.

Ion scattering spectroscopy was carried out with 2keV  $^4\text{He}^+$  ions at  $2 \times 10^{-5}$  Torr pressure. Before the chamber was back filled, it was evacuated to  $10^{-9}$  Torr. The beam current was 15 nA and ion beam size was 600  $\mu\text{m}$ .

TEM samples were prepared by crushing of the pellets. Crushed powder was suspended in alcohol and a drop was then placed on a holey carbon grid.

## Results and Discussion

Several ISS scans (Fig. 1) were taken for each sample and the Ni/Al intensity ratio was plotted as a function of time. Figure 2 is a plot of the steady-state Ni/Al intensity ratios as a function of Ni loading in the sample. ISS sensitivity for Ni was measured by Sparrow to be 4 times that of Al.<sup>1</sup> This information has been used to convert intensity ratio data into surface atomic ratios. Table 1 lists the ISS results. Also given in the table are the calculated values of atomic ratios as obtained from stoichiometric calculations with homogeneous composition assumed. The "near surface bulk" compositions were obtained from previous ESCA investigations.<sup>2</sup> The atomic ratios were calculated from observed intensity ratios and Al and Ni photoemission cross sections.<sup>3</sup> Table 1 also incorporates the ESCA results.

Figure 3 is a graphical representation of Table 1 showing the atomic ratios obtained from ISS and ESCA results as well as theoretical ratios (obtained from the bulk chemical composition) as a function of Ni loading. It is clear that ESCA atomic ratios are very close to the bulk values, which suggests that the nickel is dispersed homogeneously throughout the sample. However, ISS results show a dramatic difference. Since ISS is much more surface sensitive than ESCA, one can conclude that Ni tends to be depleted at the surface with low nickel loading. At concentration higher than 30% the nickel surface concentration approaches that of the bulk value.

Wu et al. have studied Ni/Al<sub>2</sub>O<sub>3</sub> systems prepared by impregnation techniques.<sup>4</sup> They observed a similar nonlinear dependence of the Ni/Al intensity ratio on Ni loading. Preferred occupation, by Ni atoms, of tetrahedral sites rather than the octahedral sites of  $\gamma\text{-Al}_2\text{O}_3$  was proposed at low metal loadings. In  $\gamma\text{-Al}_2\text{O}_3$  tetrahedral sites are considered to be farther removed from the surface in certain crystallographic directions.<sup>5</sup> At higher metal loadings, Wu et al. suggested the formation of new nickel species on top of a Ni monolayer.

Since the Al<sub>2</sub>O<sub>3</sub> systems shows no x-ray diffraction pattern, it is assumed to be amorphous. Hence the explanations based on an ordered crystalline structure do not apply to the present system. TEM observations were also carried out so that one could directly observe any such new phase formation in the co-precipitated samples. All efforts by high-resolution TEM were unsuccessful in identifying any spinel formation.

Lower than theoretical atomic ratios at lower Ni loadings may be due to coring phenomena during precipitation. It is proposed that Ni carbonate acts as a seed for aluminum carbonate and hence Ni is shadowed by Al. Beyond Ni concentrations the co-precipitation occurs at the same rate and the Ni/Al ratio then approach that of the bulk. This phenomenon is not observed under ESCA as it has a sampling depth about 50 to 100 times that of ISS, which samples only the top atomic layer.

## Conclusions

Surface concentration of Ni, as measured by ISS, remains constant with increasing bulk concentration up to certain loading and then increases dramatically. No large-scale spinel formation is observed.

1. G. R. Sparrow, Advanced R&D Inc., St. Paul, Minn., private communication.
2. R. B. Shalvoy and P. J. Reucroft, *J. Electron Spectroscopy and Related Phenomena* 12: 351-356, 1977.
3. P. J. Reucroft et al., *Surface Structure and Mechanisms of Gasification Catalyst Deactivation*, Annual Report for February 1976-January 1977 for the U.S. Energy Research and Development Administration, Contract EX-76-C-01-2229.
4. M. Wu, R. Chin, and D. M. Hercules, *Spectr. Lett.* 11: 615-623, 1978.
5. M. Shelef et al., *Surface Science* 47: 697-703, 1975.

TABLE 1.--Ni/Al intensity and atomic ratios.

Catalyst	Ni wt. %	ISS Ni/Al Intensity Ratio	ISS Ni/Al Atomic Ratio (meas.)	ESCA Ni/Al Intensity Ratio	ESCA Ni/Al Atomic Ratio (meas.)	Ni/Al Atomic Ratio (calc.)*
L141	10	0.37	0.093	0.29	0.153	0.099
L142	20	0.29	0.073	0.45	0.237	0.233
L143	30	0.20	0.050	0.92	0.484	0.422
L144	40	2.31	0.575	1.61	0.847	0.708

\* Calculated atomic ratios are obtained by assuming homogeneous bulk compositions.

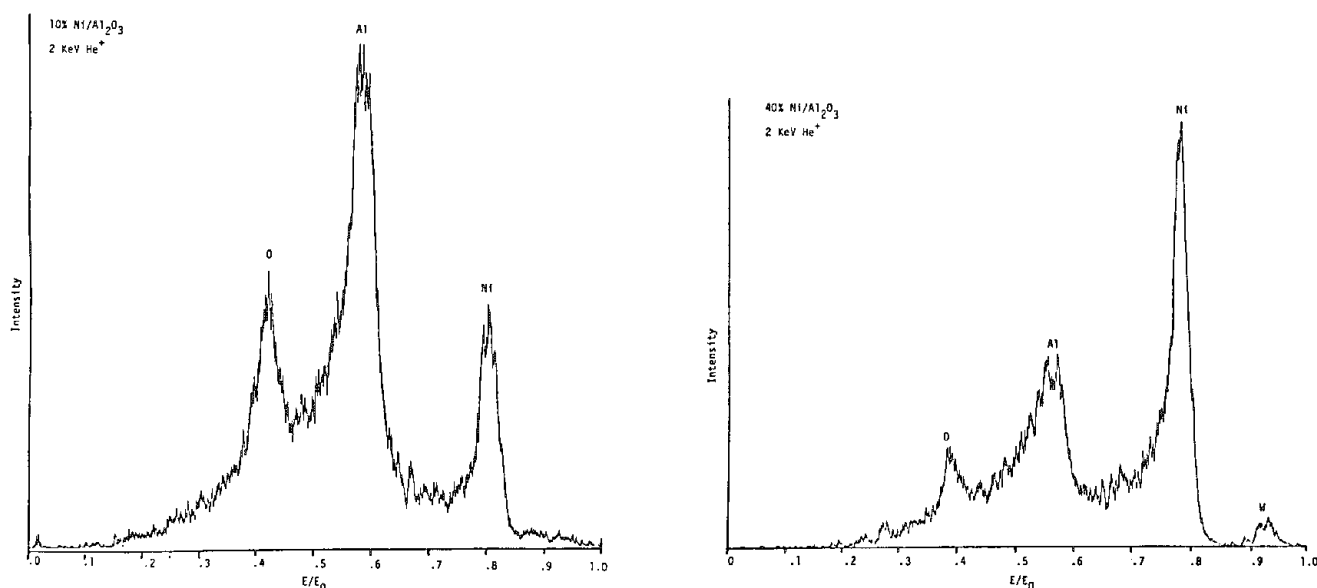


FIG. 1.--Typical ISS spectra of L141 and L144 catalysts.

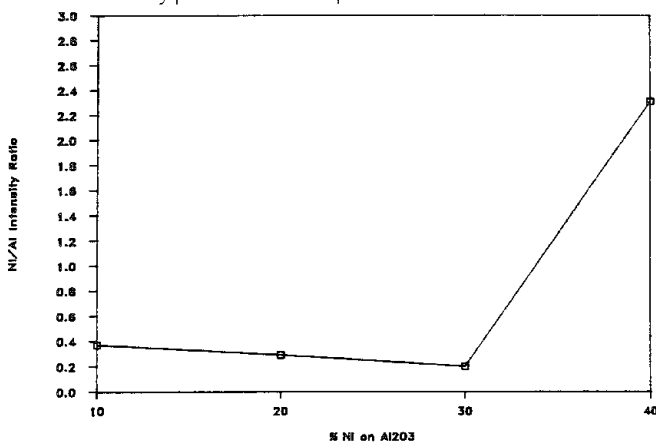


FIG. 2.--Variation in Ni/Al intensity ratios with Ni loading.

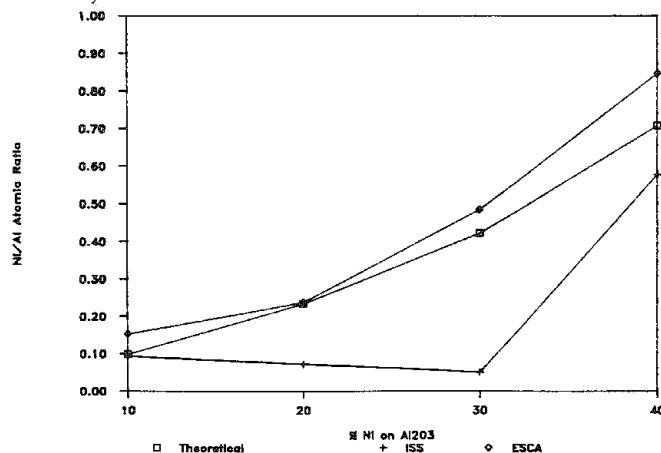


FIG. 3.--Variations in Ni/Al atomic ratios with Ni loading.

## MICROSTRUCTURE OF SMALL BIMETALLIC PARTICLES

A. O. Shastri and Johannes Schwank

Catalysts containing two metal components that do not form alloys in the bulk state are interesting model systems for examining the nature of catalytically active sites. There is considerable evidence in the catalysts literature for bimetallic "cluster" formation even with bulk-immiscible metal components. However, the structure and composition of such bimetallic particles remains the subject of intensive research. The composition of individual metal particles may depend on the particle size, and even in particles of the same size considerable compositional nonuniformities can exist.<sup>1</sup> The objective of this work was to investigate bimetallic Ru-Cu catalysts by analytical electron microscopy and compare them with previously studied Ru-Au catalysts. In terms of bulk-immiscibility and catalytic behavior, Ru-Cu closely resembles Ru-Au. There is considerable controversy in the literature with regard to the role of group IB metal in modifying the hydrogen adsorption behavior and catalytic activity of Ru.<sup>2,3</sup>

### *Experimental*

Two Ru-Cu/SiO<sub>2</sub> catalysts were prepared by coimpregnation of SiO<sub>2</sub> with aqueous precursor salt solutions, followed by drying and reduction in flowing H<sub>2</sub> at 673 K. Both catalysts had a total metal content of about 2.5 wt%. One catalyst contained 34 atom% Ru (code RCS034); the other catalyst contained 8 atom% Ru (code RCS008). The various catalyst specimens were investigated by means of TEM, EDS, and CBED in a JEOL 100CX TEM/STEM.

### *Results and Discussion*

A typical TEM micrograph and the corresponding CBED pattern for the catalyst RCS034 are shown in Figs. 1 and 2. In both catalysts RCS034 and RCS008, we did not find any metal particles larger than 7 nm. Figure 3 gives the EDS spectra obtained from two representative metal particles in RCS034. EDS clearly proved that in both catalysts RCS034 and RCS008 particles less than 5 nm in diameter were bimetallic, whereas particles from 4 to 7 nm consisted of monometallic Cu. All the Ru was contained in the small (<4 nm) particles. The CBED patterns from such bimetallic particles can be ascribed to either Ru or Cu without significant structural modification. This result indicates that the Ru-Cu bimetallic "clusters" observed in EDS may represent a random decoration of one metal component by the other without formation of "alloy" structures. Further corroboration for this hypothesis comes from the Cu-induced suppression of H<sub>2</sub> chemisorption on Ru, which indicates a break-up of Ru surface ensembles required for H<sub>2</sub> dissociation.<sup>4</sup>

No such suppression of H<sub>2</sub> chemisorption was found in SiO<sub>2</sub>-supported Ru-Au catalysts containing bimetallic particles of similar size (<4 nm). EDS spectra of these small metal particles consisted of a dominant signal of one metal component with only a trace signal of the other metal.<sup>1</sup> This finding suggests a different interdispersion of Cu or Au on the Ru surface. Despite these differences in interdispersion of the two metals in small bimetallic "clusters," the structure of SiO<sub>2</sub>-supported bimetallic Ru-Au and Ru-Cu particles can be described in terms of random decoration of one metal by the other.<sup>1,4</sup>

The poor x-ray signal/noise ratio and counting statistics obtained from such small metal particles preclude any exact compositional determination. Attempts to improve the counting statistics by prolonging the x-ray count time increase the risk of contamination and electron-beam damage. Quantification is further complicated by the lack of suitable calibration standards. Nevertheless, the combination of analytical electron microscopy with chemical probes such as surface-sensitive gas chemisorption and catalytic reactions can provide remarkable details about the nature of small bimetallic particles in supported

---

The authors are at Department of Chemical Engineering, University of Michigan, Ann Arbor, MI 48109. NSF and ARO support is acknowledged. The STEM used in this work was acquired under Grant No. DMR-77-09643 from NSF.

catalysts.

### References

1. A. K. Datye et al., "Analytical electron microscopy of supported bimetallic catalysts," *Analytical Electron Microscopy--1984*, 205-208.
2. J. H. Sinfelt et al., "Nature of ruthenium-copper catalysts," *J. Catalysis* 42: 227-237, 1976.
3. Rouco et al., "A comparative investigation of silica-supported Ru-Cu and Ru-Ag catalysts," *J. Catalysis* 84: 297-307, 1983.
4. A. G. Shastri and J. Schwank, "The microstructure of bimetallic Ru-Cu/SiO<sub>2</sub> catalysts: A chemisorption and analytical electron microscopy study," *J. Catalysis* (submitted).

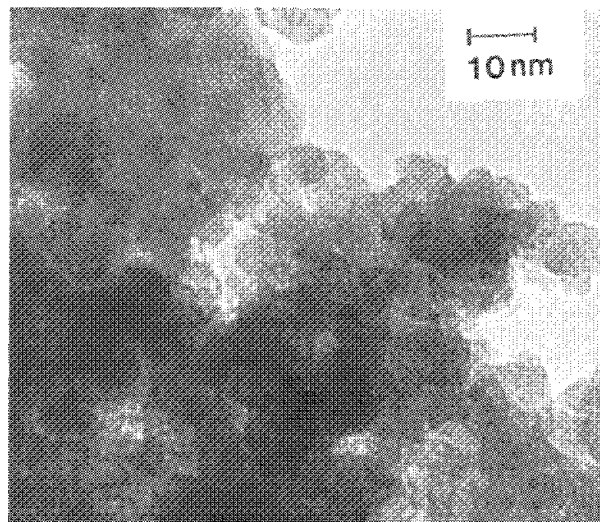


FIG. 1.--TEM image of catalyst RCS034.

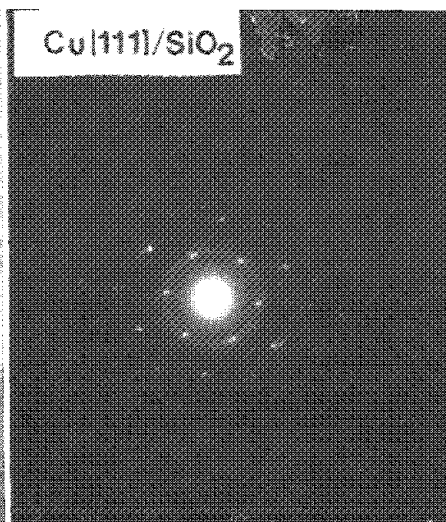
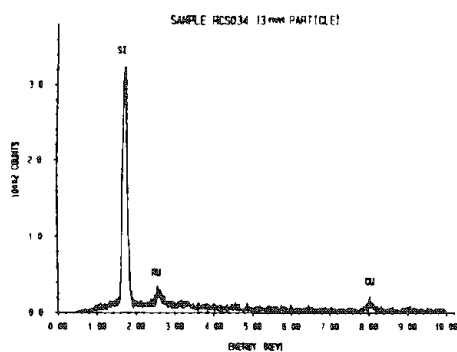
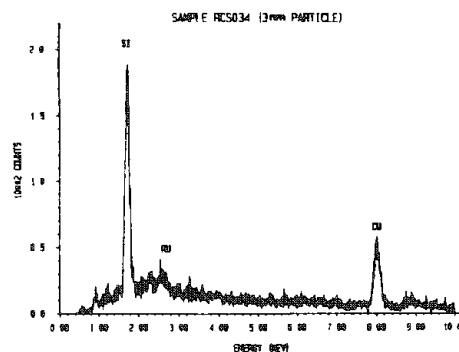


FIG. 2.--CBED pattern of 4nm metal particle in catalyst RCS034.



(a)



(b)

FIG. 3.--EDS spectra obtained from two different metal particles of similar size in RCS034 showing formation of (a) 1:1 Ru/Cu clusters, (b) Cu-rich bimetallic clusters.

## Microelectronics—Electron Beam Techniques

### ELECTRON-BEAM TECHNIQUES FOR STUDYING ELECTRONIC MATERIALS AND DEVICES

D. B. Wittry

The electron probe x-ray microanalyzer was developed in 1950 for local x-ray spectroscopic analysis by Castaing and Guinier at the University of Paris. Development of the scanning electron microscope for the study of surfaces began in 1948 in C. W. Oatley's laboratory at the University of Cambridge. Both instruments are based on local excitation by a focused electron beam and have become powerful tools for the study of electronic materials and devices by the use of a wide variety of signals that result from the interaction of the electron beam with a solid specimen. In this paper, we review some of the signals available and the type of information that can be derived from them.

#### *Characteristic X Rays*

Characteristic x rays are produced by the radiative decay of atoms excited in their inner shells. The probability of radiative decay is given by the fluorescence yield, a quantity that is very small for low atomic numbers and increases with increasing atomic number. Characteristic x rays are detected either by wavelength-dispersive spectrometry (WDS) with crystal diffractors, or energy-dispersive spectrometry (EDS) with a solid-state detector of the PIN configuration. In order to reduce noise and to provide improved energy resolution, the solid-state detectors (typically Li-drifted silicon) are cooled to liquid-nitrogen temperatures.

Characteristic x rays are useful for elemental analysis. Elements with atomic number greater than 4 are detectable by WDS and elements with atomic number greater than 10 are detectable with EDS if the detector has a beryllium window; lighter elements may be detected if the detector is operated with an ultrathin window or is windowless. The detection limits are typically 0.01 wt% for WDS and 0.1 wt% for EDS. The spatial resolution is of the order of 1  $\mu\text{m}$  for thick specimens and 500 Å for thin specimens in the transmission electron microscope.

Applications of x-ray spectroscopy to electronic materials include studies of the composition of alloy semiconductors, the composition of phosphors and magnetic materials, and studies of diffusion and segregation in a variety of materials.

#### *Auger Electrons*

Auger electrons result from the nonradiative decay of atoms excited in their inner shell. The probability of this process is given by  $(1 - \omega)$ , where  $\omega$  is the fluorescence yield. Auger electrons are detected by electron energy analyzers consisting of concentric hemispheres or concentric cylinders and an electron multiplier detector. Because Auger electrons may be distinguished from the background of backscattered electrons only if they have undergone negligible energy loss, Auger electron signals originate from only 10–20 Å below the surface. For this reason, Auger electron spectroscopy (AES) is useful only if contamination can be eliminated, which usually requires an ultrahigh-vacuum system.

Auger electrons are useful for elemental analysis of surfaces. All elements except H and He can be detected. Chemical bonding effects can also be sometimes observed and are more pronounced than in x-ray spectroscopy because the electrons involved are more weakly bound. Detection limits are typically 0.1% of a monolayer; and since this is basically a surface-analysis technique, the bulk detection limits are the same, i.e., 0.1% by volume. Modern AES systems are capable of lateral spatial resolution of the order of 500 Å.

Applications of Auger electron spectroscopy to solid-state electronics include the analysis of surface regions of integrated circuits, identification of surface contaminants, and determination of depth distribution of ion-implanted impurities in semiconductors.

---

The author is in the Departments of Materials Science and of Electrical Engineering, University of Southern California, Los Angeles, CA 90089-0241.

### *Backscattered Electrons*

Backscattered electrons are electrons scattered from the specimen with energies between 50 eV and the primary energy. They are detected with semiconductor detectors consisting of shallow diffused pn junctions or surface barriers or with scintillation-type detectors.

Backscattered electrons are useful for obtaining "atomic number" contrast in scanning electron microscopy because the fraction of backscattered electrons increases monotonically with atomic number of the specimen. Scintillation-type backscattered electron detectors using high-efficiency single phosphors can resolve an atomic number difference as small as 0.1. Spatial resolution is limited by the beam-specimen interaction and is of the same order as in x-ray microanalysis.

Applications of backscattered electron signals to solid-state electronics include studies of heterogeneous materials or structures, semiconducting binary alloys, epitaxially grown materials, and identification of oxide, carbide, and nitride inclusions in conjunction with EDS.

### *Secondary Electrons*

Secondary electrons are defined as electrons emitted from the specimen with energies below 50 eV. Unlike backscattered electrons, the secondary-electron yield does not vary systematically with atomic number. However, for a given specimen, it varies with the angle of incidence and the energy of the primary beam. The collection efficiency of the secondary-electron signal is affected by surface topography and by local electric or magnetic fields.

Secondary electrons are detected most efficiently by the Everhart-Thornley detector. This detector consists of a control grid, a scintillator biased at a large positive potential (typically 10-15 keV), a light guide for electrical isolation, and an electron multiplier phototube. Secondary-electron signals can provide a spatial resolution limited primarily by the escape depth of the secondary electrons, e.g., about 20 Å for semiconductors and metals and about 200 Å for insulators. The achievement of this limiting resolution with thick specimens results from the fact that it is possible to distinguish the secondary electrons due to the incident primary beam from the background of secondary electrons originating from the larger interaction volume.

Secondary electrons were the first signal to be used in scanning electron microscopy and are still one of the most important signals available in electron probe instruments. When used to reveal topographic information, secondary electrons have been used to indicate the nature of lead attachments, to measure linewidths on semiconductor devices, to show the results of electromigration at ledges, to indicate the presence of dust and contaminants on monolithic circuits, and to indicate particle size in magnetic recording media.

When used with special detector configurations to enhance the effects of local potentials, secondary-electron signals can provide voltage contrast, a property that has been used to reveal the presence of electrical discontinuities in conducting stripes and to indicate the potential of various regions of active devices. When active devices are used and the secondary-electron detection system is gated, stroboscopic techniques can be used to follow the movement of signals through various elements of an integrated circuit.

With detector configurations to enhance the effect of local magnetic fields, secondary electrons can provide magnetic contrast. This feature has been used to study magnetic domains in single crystals, to observe magnetization patterns on magnetic tape, and to study the field distribution of monolithic recording heads.

Crystallographic effects can be observed with secondary-electron signals, owing to anomalous penetration of the primary beam. This can yield a kind of diffraction pattern when the angle of incidence of the primary beam is scanned, for example, by a conventional deflection system scanning a large-area single crystal or a modified scanning mode in which the incident beam is rocked about a fixed point (SAD mode). The resulting patterns, originally called Coates patterns or pseudo-Kikuchi patterns, are usually referred to as electron channeling patterns and can provide information on crystal orientation and crystal perfection. They have been used for observation of grains and subgrains, stacking faults, and precipitates; studies of damage due to deformation or ion bombardment; and determination of dislocation density and the nature and position of defects.



### *Specimen Current*

Specimen current, sometimes called absorbed electron current, ideally represents the difference between the incident beam current and the current due to backscattered and secondary electrons. However, in most instruments the specimen current is complicated by additional currents due to interaction of backscattered and secondary electrons with the walls of the specimen chamber. By suitable biasing of the specimen, and addition or subtraction of signals, information similar to that obtained with backscattered electrons or secondary electrons can be obtained. However, because secondary or backscattered electrons can be observed with detectors that provide amplification, it is usually preferable to record these signals directly.

One application of specimen current to the study of electronic materials is the use of light-modulated specimen current to study photoconductivity. Light-modulated specimen current results when a semi-insulating specimen is bombarded simultaneously with light and an electron beam. Under the bombardment by electrons, the specimen's surface charges negatively for typical beam voltages used. The charging results from an unbalance between the secondary electron and backscatter currents and the incident beam current and its magnitude depends on the resistivity of the specimen. When the specimen is illuminated while being bombarded with electrons the resistivity of the specimen changes, the surface charging changes, and thus the specimen current changes. This effect has provided a basis for contactless studies of photoconductivity.

### *Electron-beam-induced Current*

Electron-beam-induced current (EBIC) results when the excess carriers generated by an electron beam are separated by drift across a pn junction or a surface barrier.

Electron-beam-induced currents are detected by measurement of the current between two ohmic contacts made to different parts of the specimen. For dc or low frequencies an operational amplifier can be connected in the "transresistance" mode, in which the two inputs are connected to the specimen and a feedback resistor is connected between the output and the inverting input. The OP amp then functions as a current-to-voltage converter and a voltage proportional to the short-circuit current of the junction appears at the output. For higher frequencies, if the OP amp cannot be located close to the specimen, it may be necessary to terminate the coaxial line to the specimen with a resistor to avoid reflections. In that case, a voltage is measured corresponding to the intercept of the load line (whose slope is  $1/R$ ) and the I-V characteristic of the junction.

Several geometries have been used depending on the orientation of the junction relative to the surface and the orientation of the surface relative to the direction of the electron beam. The two simplest cases have the beam normal to the surface and the junction either parallel or perpendicular to this surface. With the junction parallel to the surface, the electron-beam current is measured as a function of the beam accelerating voltage; with the junction perpendicular (or at a small angle) to the surface, the electron-beam current is measured as a function of beam position.

Electron-beam-induced currents have been used to locate junctions (either laterally or in depth), to measure carrier diffusion lengths in bulk materials and surface recombination velocities at grain boundaries, and to observe the effects of crystal imperfections on carrier recombination or carrier multiplication.

### *Ultrasonic or Thermal Waves*

The bombardment of a solid with an electron beam is accompanied by the generation of heat. Normally, this heat is either of no interest or is a source of potential damage to sensitive materials. However, if an ultrasonic transducer is coupled to the specimen so that sound can be transmitted across the interface between the transducer and the specimen, a signal is received that varies with the position of the electron beam, the properties of the region bombarded, and the properties of the specimen in the region between the beam impact point and the transducer.

In addition to an ultrasonic transducer, the practical use of thermal waves requires chopping the electron beam and detection of the fundamental frequency or its harmonics with a lock-in amplifier. The resulting technique has been called thermal wave scanning microscopy. Simple theory would indicate that the spatial resolution of this technique should be

limited by the wavelength of sound in the specimen. However, it has been found possible to obtain much better resolution in practice; the theoretical basis for this technique requires further investigation.

Thermal wave scanning microscopy provides information not only on the nature of the material directly bombarded but also on subsurface structure. It can reveal information on grain boundaries and inhomogeneities present in the bulk material.

Another technique that depends on thermal effects caused by electron bombardment may be described as follows. When a semiconductor is bombarded by a chopped electron beam, the optical reflectance of the specimen is modulated. If the modulated reflectance is studied as a function of the wavelength of light, a technique known as electron-beam-modulated reflectance results. Detailed experiments on the mechanism of electron-beam-modulated reflectance have indicated that the change in reflectance is due to thermal effects; therefore, this technique can be used to obtain information normally provided by thermorefectance but on smaller regions, and on materials difficult to study by thermorefectance, without the need for special specimen geometries.

### *Cathodoluminescence*

Cathodoluminescence results when light is produced by electron bombardment. The light may be in the visible, infrared, or ultraviolet region of the electromagnetic spectrum and may result from the radiative recombination of excess carriers or the radiative decay of excited luminescence centers.

Cathodoluminescence signals are detected by a large-aperture light collection system and a suitable detector placed at the conjugate focus of the collection system. Much of the early work was done with electron-probe microanalyzers that had an optical microscope for viewing the specimen; in that case, the objective lens or mirror of the microscope is used for collection of the light. For obtaining the spectral distribution, the light may be focused on the entrance slit of a scanning monochromator. The efficiency of light production and the spatial resolution depend on the mechanism for generation of light. For radiative recombination of excess carriers the efficiency may be low due to surface recombination unless relatively high beam voltages are used. In this case, the resolution is frequently limited by the beam size, which must be large to obtain enough current for adequate signals. The diffusion length of excess carriers can be a limiting factor if the beam size is less than a diffusion length. Then the resolution is determined by the signal level and by the contrast that can be obtained without excess noise. In cases where the luminescence is due to decay of excited luminescence centers, the spatial resolution may be better than when luminescence is due to radiative recombination of excess carriers.

Cathodoluminescence has been used to study the variation of energy band gap with composition in alloy semiconductors, to measure carrier diffusion lengths and surface recombination velocities in direct gap semiconductors, to study impurity levels in the forbidden energy gap due to point defects or complexes, to observe impurity concentration fluctuations, to observe precipitates, inclusions, dislocations, grain boundaries, and pn junctions, and to provide local measurements of temperature in semiconductor devices.

### *Brief Bibliography*

#### *Books*

- L. S. Birks, *Electron Probe Microanalysis*, New York: Wiley-Interscience, 1963, 1971.
- T. D. McKinley, K. T. J. Heinrich, and D. B. Wittry, Eds., *The Electron Microprobe*, New York: Wiley, 1966.
- P. R. Thornton, *Electron Microscopy: Applications to Materials and Device Science*, London: Chapman and Hall, 1968.
- C. W. Oatley, *The Scanning Electron Microscope Part I: The Instrument*, London: Cambridge University Press, 1972.
- C. A. Anderson, Ed., *Microprobe Analysis*, New York: Wiley, 1973.
- D. B. Holt, M. D. Muir, P. R. Grant, and I. M. Boswarva, Eds., *Quantitative Scanning Electron Microscopy*, New York: Academic Press, 1974.
- O. C. Wells, *Scanning Electron Microscopy*, New York: McGraw-Hill, 1974.
- S. J. B. Reed, *Electron Probe Analysis*, London: Cambridge University Press, 1975.

J. I. Goldstein and H. Yakowitz, Eds., *Practical Scanning Electron Microscopy*, New York: Plenum Press, 1975.

L. Reimer and G. Pfefferkorn, *Rasterelektronenmikroskopie*, Berlin: Springer-Verlag, 1977.

F. Maurice, L. Meny, and R. Tixier, Eds., *Microanalysis and Scanning Electron Microscopy*, Paris: Les Editions de Physique (Translation of *Microanalyse et microscopie électronique à balayage*), 1979.

J. J. Hren, J. I. Goldstein, and D. C. Joy, *Introduction to Analytical Electron Microscopy*, New York: Plenum Press, 1979.

K. F. J. Heinrich, *Electron Beam X-ray Microanalysis*, New York: Van Nostrand Reinhold, 1980.

J. I. Goldstein et al., *Scanning Electron Microscopy and X-ray Microanalysis*, New York: Plenum Press, 1981.

V. D. Scott and G. Love, *Quantitative Electron Probe Microanalysis*, London: Ellis Harwood, 1983.

D. F. Kyser, H. Niedrig, D. E. Newbury, and R. Shimizu, Eds., *Electron Beam Interactions with Solids for Microscopy, Microanalysis, and Microlithography*, Chicago: Scanning Electron Microscopy, 1984.

#### *Chapters and Reviews*

R. Castaing, "Electron probe microanalysis," *Advances in Electronics and Electron Physics* 13: 317-384, 1960.

D. C. Northrop, "Applications to solid state electronics," in J. W. S. Hearle, J. T. Sparrow, and P. M. Cross, Eds., *The Use of the Scanning Electron Microscope*, London: Pergamon Press, 1972.

D. B. Wittry, "Applications of electron microprobes to solid state electronics," in C. A. Andersen, Ed., *Microprobe Analysis*, New York: Wiley, 1973.

C. W. Oatley, "The early history of the scanning electron microscope," *J. Appl. Phys.* 53: R1-R13, 1982.

H. Niedrig, "Electron backscattering from thin films," *ibid.*, pp. R15-R49.

H. J. Leamy, "Charge collection scanning electron microscopy," *ibid.*, pp. R51-R80.

D. C. Joy, D. E. Newbury, and D. L. Davidson, "Electron channeling patterns in the scanning electron microscope," *ibid.*, pp. R81-R122.

H. Seiler, "Secondary electron emission in the scanning electron microscope," *ibid.*, 54: R1-R18, 1983.

B. G. Yacobi and D. B. Holt, "Cathodoluminescence scanning electron microscopy of semiconductors," *ibid.*, 59: 1986.

#### *Conference Proceedings*

##### *Institute of Physics*

*Microscopy of Semiconducting Materials*, Oxford, 1981 (Inst. Phys. Conf. Ser. 60).

*Microscopy of Semiconducting Materials*, Oxford, 1983 (Inst. Phys. Conf. Ser. 67).

*Microscopy of Semiconducting Materials*, Oxford, 1985 (Inst. Phys. Conf. Ser. 76).

##### *International Conferences on X-ray Optics and Microanalysis*

1. Cambridge, England, 1956

*X-ray Microanalysis and Microradiography*, V. E. Cosslett, Arne Engstrom and H. H. Pattee, Eds., New York: Academic Press, 1957.

2. Stockholm, Sweden, 1959

*X-ray Microscopy and X-ray Microanalysis*, A. Engstrom, V. E. Cosslett, and H. H. Pattee, Eds., New York: Elsevier Pub. Co., 1960.

3. Stanford, Calif., 1962

*X-ray Optics and X-ray Microanalysis*, H. H. Pattee, V. E. Cosslett, and Arne Engstrom, Eds., New York: Academic Press, 1963.

4. Orsay, France, 1965

*X-ray Optics and Microanalysis*, R. Castaing, P. Deschamps, and J. Philibert, Eds., Paris: Hermann, 1966.

5. Tübingen, Germany, 1968  
*Vth International Conference on X-ray Optics and Microanalysis*, G. Möllenstedt and K. H. Gaukler, Eds., Berlin: Springer-Verlag, 1969.
6. Osaka, 1971  
*Proceedings of the Sixth International Conference on X-ray Optics and Microanalysis*, G. Shinoda, K. Kohra, and T. Ichinokawa, Eds., Tokyo: University of Tokyo Press, 1972.
7. Moscow and Kiev, 1974  
*X-ray Optics and Microanalysis*, I. B. Borovskii and N. I. Komyak, Eds., English translation published by Amerind Pub. Co., 1985.
8. Boston, Mass., 1977  
*Eighth International Congress on X-ray Optics and Microanalysis*, D. R. Beaman, R. E. Ogilvie, and D. B. Wittry, Eds., Midland, Mich.: Pendell Publishing Co., 1980. (Available from San Francisco Press.)
9. The Hague, 1980  
*Proceedings of the Seventh European Congress on Electron Microscopy Including the Ninth International Conference on X-ray Optics and Microanalysis*, Vol. 3, P. Brederoo and V. E. Cosslett, Eds., Seventh European Congress on Electron Microscopy Foundation, Leiden, 1980.
10. Toulouse, France, 1983  
*10th International Congress on X-ray Optics and Microanalysis*, J. Sevely, F. Maurice, B. Jouffrey, and R. Tixier, Eds., Journal de Physique C2, Supplement au No. 2, Paris: Les Editions Physique, 1984.
11. London, Ontario, 1986  
*11th International Congress on X-ray Optics and Microanalysis*, J. D. Brown, Ed., San Francisco Press, 1987.

#### *International Conferences on Electron Microscopy*

International conferences on electron microscopy are sponsored by the Federation of Electron Microscopy Societies and are held every four years. The location of the conferences and publishers of the proceedings are as follows:

1. Delft, 1949
2. Paris, 1950, Editions de la Revue d'Optique Théoretique et Instrumentale
3. London, 1954, Royal Microscopy Society
4. Berlin, 1958, Springer Verlag
5. Philadelphia, 1962, Academic Press
6. Kyoto, 1966, J. Phys. Soc. Japan. Suppl.
7. Grenoble, 1970, Société Française Microscopie Electronique, Paris, 1970
8. Canberra, 1974, Australian Academy of Science, 1974
9. Toronto, 1978, Imperial, Canada
10. Hamburg, 1982, Deutsche Gesellschaft für Elektronenmikroskopie

#### *Scanning Electron Microscopy*

*Proceedings of the Annual Scanning Electron Microscope Symposium*, vol. 1, 1968, to vol. 10, 1977, Om Johari, Ed., IIT Research Institute. Proceedings from 1978 to the present are published by SEM Inc.

#### *Microbeam Analysis Society*

The first national conference of the Microbeam Analysis Society (MAS) was held in Silver Spring, Md., in 1966. At this meeting a committee was established to form a national society which was first known as the Electron Probe Analysis Society and later became the Microbeam Analysis Society. Since 1979 the annual proceedings have been published by San Francisco Press, which can also provide some of the earlier proceedings, as well as the proceedings of the MAS-sponsored tri-annual workshops on Analytical Electron Microscopy (1981, 1984).

#### *Electron Microscopy Society of America*

Meetings of the Electron Microscopy Society of America (EMSA) have been held since 1942. From 1967 to 1982 the annual proceedings were published by Claitors Press, Baton Rouge. Since 1983 the proceedings have been published by San Francisco Press.

## VOLTAGE CONTRAST FROM CLEAVED SILICON WAFERS IN THE SCANNING ELECTRON MICROSCOPE

O. C. Wells, B. B. Davari, and Catherine Wong

P-N junctions in angle-lapped silicon wafers can be examined by voltage contrast in the secondary electron (SE) image in the scanning electron microscope (SEM) to show the width of the depletion layer.<sup>1,2</sup> Here, the sample was cleaved rather than angle-lapped. The purpose of this work was to measure the position of the junction, and to determine the width of the depletion layer when it was reverse-biased. The possibility is discussed here of quantifying voltage contrast in the unmodified SEM if the potential difference between the different parts of the specimen surface does not exceed about 5 to 10 V. In this paper, the emphasis is on the development of measurement techniques.

### *Mounting the Sample*

A fixture was made to hold the specimen and associated electrodes (Fig. 1). Five of the wires on a ten-pin header were ground level with the upper surface so that the sample could be glued onto it close to the edge. Electrical connections were made to the pins that had not been ground away. The header was supported by inserting the wires into a socket.

An important requirement for voltage contrast is that all insulators must be properly shielded. Shielding was achieved by placement of a sheet metal electrode close to the header and with the upper edge parallel to the cleaved surface of the sample and ~0.5 cm away. Although that does not prevent the electron beam from reaching the insulators, it does shield the SE from the effects of the resulting charge potentials. This sheet of metal (which is referred to below as the *control electrode*) can be biased positively to reduce the edge penetration effect, as discussed below.

An upper electrode was connected to the specimen-touching alarm circuit.

### *Description of the Sample*

A n+ - p junction was formed by ion implantation with both As and P followed by diffusion to a depth of 0.25  $\mu\text{m}$  in a <100> p-type Si wafer with an acceptor (B) concentration  $N = 4 \times 10^{15} \text{ cm}^{-3}$ . The width  $W_d$  of the depletion region is then given by:

$$W_d = \sqrt{\frac{2e_s \phi_{\text{bias}}}{qN_A}} = \sqrt{\frac{\phi_{\text{bias}}}{3.2}} \mu\text{m}$$

where  $W_d$  = width of depletion layer,  $e_s$  = Si dielectric constant =  $10^{-12} \text{ F/cm}$ ,  $q$  = electronic charge =  $1.6 \times 10^{-19} \text{ coulomb}$ ,  $N_A$  = acceptor concentration ( $= 4 \times 10^{15} \text{ cm}^{-3}$  here),  $\phi_{\text{bias}}$  = electrostatic potential difference between the silicon on the two sides of the p-n junction (volts), or  $E_{\text{bi}} + E_{\text{rev}}$ ,  $E_{\text{bi}}$  = built-in voltage ( $\approx 0.7 \text{ V}$ ), and  $E_{\text{rev}}$  = reverse bias as measured between the wires to the device. Some calculated values of  $\phi_{\text{bias}}$  and  $W_d$  as a function of  $E_{\text{rev}}$  are as follows (where  $E_{\text{rev}} = -0.7$  refers to the forward-biased condition):

$E_{\text{rev}}$	= -0.7	0	1.0	2.0	3.0	4.0	5.0	10.0 (V)
$\phi_{\text{bias}}$	= 0	0.7	1.7	2.7	3.7	4.7	5.7	10.7 (V)
$W_d$	= 0	0.468	0.729	0.919	1.08	1.21	1.33	1.83 ( $\mu\text{m}$ )

The authors are at IBM Thomas J. Watson Research Center, Box 218, Yorktown Heights, NY 10598. They thank A. B. Fowler for helpful discussions, and J.-C. Gagnebin, J. Kuran, and P. McFarland for help in preparing the samples.

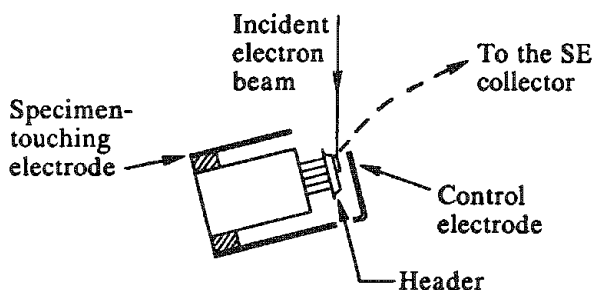


FIG. 1.--Fixture to hold specimen.

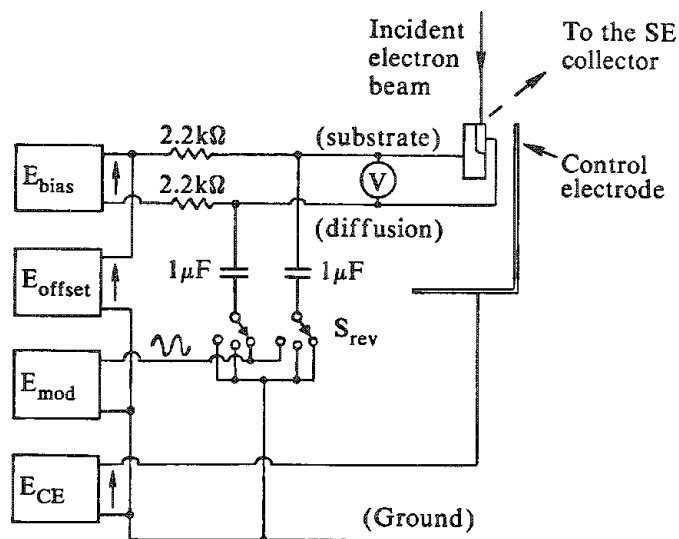


FIG. 2.--Method for biasing specimen.

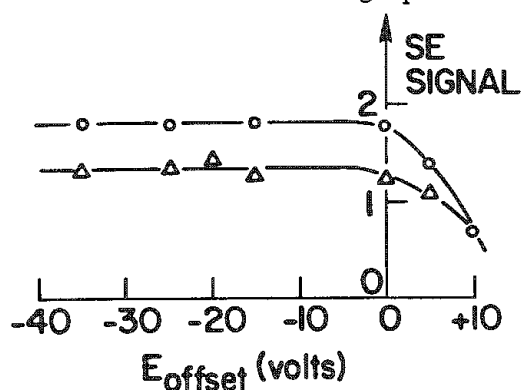
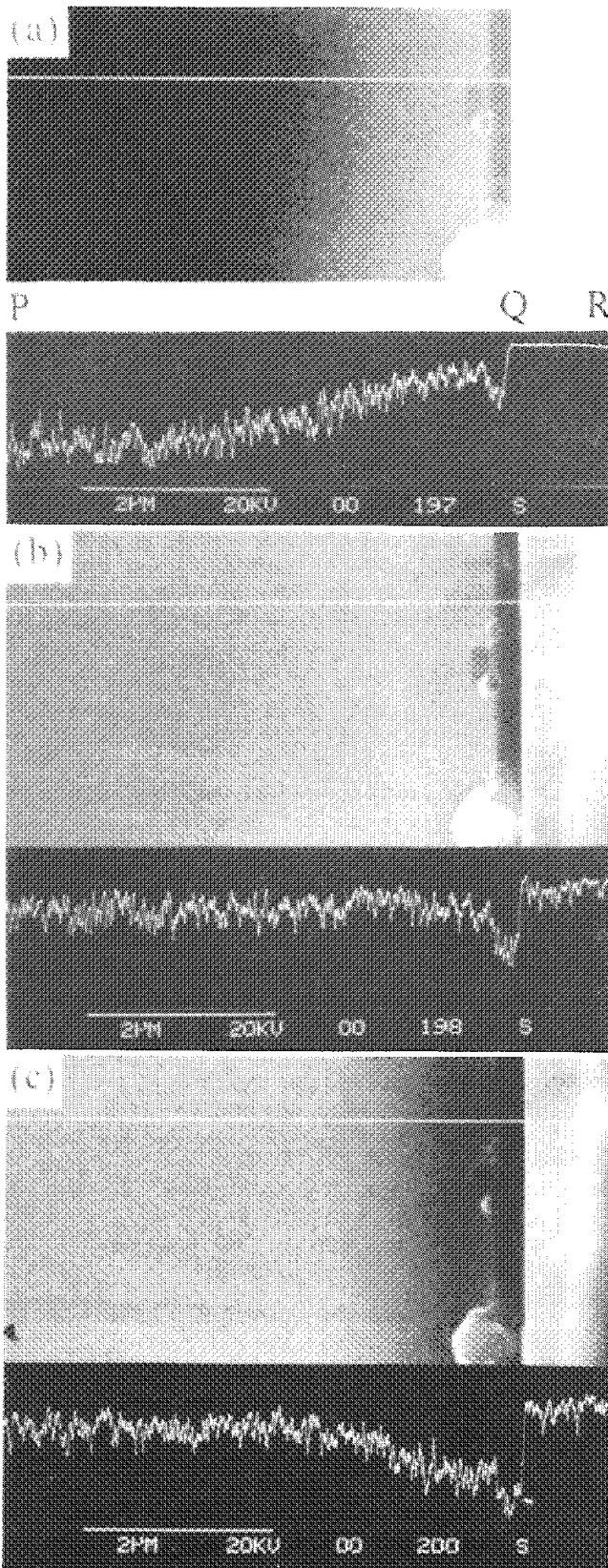


FIG. 4.--Upper and lower curves show modulation of video waveform caused by modulating  $E_{rev}$  from zero to 2 V reverse.

FIG. 3.--Silicon wafer cleaved to show diffused p-n junction. PQ = cleaved surface. QR = original upper surface of wafer. The video waveform was recorded at bright line. (a) For  $V_{CE} = 0$ , penetration effects make it difficult to form good image of cleaved surface. (b) For  $V_{CE} = +70$  V, cleaved surface can be seen more clearly. (c) The p-n junction is reverse biased by 2 V (diffusion positive). (Reproduced from Ref. 4.)



### *Biasing the Sample*

The sample was biased as shown in Fig. 2. The DC supply  $E_{\text{bias}}$  and the AC modulation signal  $E_{\text{mod}}$  are combined by means of an RC network to give the reverse voltage  $E_{\text{rev}}$  between the wires to do the device. A resistor of 2.2 k $\Omega$  is included in each lead from the  $E_{\text{bias}}$  supply for two reasons. First, this protects the sample when it is forward-biased. Second, it is part of the RC network that applies  $E_{\text{mod}}$  onto the chosen side of the device, as determined by the position of the switch  $S_{\text{rev}}$ . A high-resistance voltmeter is connected directly across the device to measure the DC component of  $E_{\text{rev}}$  and thus to show whether either  $E_{\text{bias}}$  or  $E_{\text{mod}}$  is being rectified by the device to change the DC bias.

$E_{\text{offset}}$  is applied between the device substrate and ground.

### *Eliminating the Edge Penetration Effect*

There are two problems when a cleaved sample tilted as in Fig. 1 is examined by the SE image in the SEM. First, there is a bright *penetration fringe* which obscures details on the cleaved surface close to the edge. Second, the steeply sloping surface is too bright, which makes it virtually impossible to see both surfaces properly in the SE image. The solution is to mount a *control electrode* at a positive potential  $E_{\text{CE}}$  close to the edge as shown in Figs. 1 and 2.<sup>3,4</sup> This electrode intercepts some of the SE from the steeply sloping surface of the wafer and solves both of these problems with the SE image. Figure 3(a) shows the SE image with no applied bias and with  $E_{\text{CE}} = 0$ . The video waveform recorded at the bright line shows a gently rising curve caused by electron penetration within several micrometers of the edge. This penetration fringe is essentially eliminated if  $E_{\text{CE}} = +70$  V (Fig. 3b). If the diffused region is made negative by 2 V, then the signal is reduced over approximately twice the calculated width of the depletion region (Fig. 3c). These micrographs show that the control electrode can improve the image contrasts in this case.

### *Adjusting the Offset Voltage*

The effect of varying  $E_{\text{offset}}$  is shown in Fig. 4. Here, the device was modulated sinusoidally from zero to a reverse bias of 2 V (i.e.,  $E_{\text{bias}} = -1$  V and  $E_{\text{mod}} = 2$  V peak-to-peak). The upper and lower curves show the maximum and minimum voltage levels from the head amplifier caused by this modulation. Thus, if  $-30$  V  $< E_{\text{offset}} < 0$ , the AC modulation of the video waveform (and with it, the voltage contrast in the recorded image) depends only on the relative voltage between the two sides of the junction, and is insensitive to the absolute potential of the specimen assembly. If  $E_{\text{offset}} > 0$ , then the signal decreases rapidly and the voltage contrast is less satisfactory.

The practical significance of these relationships is shown in Fig. 5. Here,  $E_{\text{bias}}$  and  $E_{\text{mod}}$  were adjusted as described above. This image is in three parts. In the upper part of Fig. 5, the switch  $S_{\text{rev}}$  was in the position shown in Fig. 2, so that the substrate potential was steady ( $= E_{\text{offset}} = -10$  V), while the diffused region was modulated with the sinusoidally varying potential. The frequency of  $E_{\text{mod}}$  was adjusted so that the wave drifted slowly across the screen as the image was recorded. The presence of voltage contrast can be seen by the sloping bars,<sup>5</sup> which extend across the depletion region.

In the central part of Fig. 5, the switch  $S_{\text{rev}}$  shown in Fig. 2 was moved into the center position, so that  $E_{\text{mod}}$  was no longer applied to the device. An additional switch contact on  $S_{\text{rev}}$ , not shown in Fig. 2, disconnected  $E_{\text{bias}}$  so as to remove the applied bias. In the lowest part of the image,  $S_{\text{rev}}$  was moved into the third position. The diffused region was therefore at a steady DC potential, while the substrate was connected to  $E_{\text{mod}}$ .

The following can be seen: First, the voltage contrast is essentially the same in the upper and lower regions in Fig. 5. This finding verifies that under these conditions it is the *potential difference* between the two sides of the p-n junction that causes voltage contrast, and not the absolute potential. Second, it can be seen that a positive relative potential reduces the collected SE current, whereas a negative relative potential of 2 V has no detectable effect. Finally, the edge of the wafer appears to be wavy when  $E_{\text{mod}}$  is applied to the substrate. That is because the substrate is connected to the header, which acts as a deflection plate for the incident electron beam.

If the above experiment is repeated with  $E_{\text{offset}} = +5$  V (which corresponds to the steeply sloping part of the curves in Fig. 4), then the contrast bars extend across the

total width of the micrograph, and it is not easy to interpret these contrasts in any simple way. It was concluded that it is simplest to work on a flat part of the curves shown in Fig. 4 and to interpret the voltage contrast in terms of the local fields which return the slower SE to the surface if there is a more negative part of the specimen nearby.

#### *Measurements of Voltage Contrast*

Video waveforms for  $E_{rev} = -0.7, 0, 1.2, 2.4, 4.8,$  and  $9.6$  V are shown in Fig. 6. (The DC background is *not* subtracted.) From the results that have been obtained so far (with the electron beam landing directly on the silicon), voltage contrast can be quite strong for a reverse bias of 2 or 3 V, is weak for zero applied bias, and is essentially zero if the junction is forward-biased. This is consistent with supposing that it is  $\Phi_{bias}$  that determines the motion of the SE in the region immediately above the specimen surface.

As compared with the above, it is to be expected that voltage contrast will be zero for applied bias if the measurement is made between two similar metal wires with ohmic contacts to the two sides of the p-n junction. It is also to be expected that if the silicon surface in an open-circuited p-n junction is examined in the SEM, then there might be zero observed contrast because the effect of the beam would then be to drive the junction into the forward-biased condition.

We have also verified that the voltage contrast can be enhanced by the AC-modulation technique.<sup>6-7</sup>

#### *Quantitative Voltage Contrast in the Unmodified SEM*

We are hoping that the voltage contrast in the unmodified SEM (and in the case when the applied bias is no greater than 5 to 10 V) can be quantified as follows. Suppose that both the SE coefficient and the SE energy distribution curve are uniform across the specimen surface. Suppose that the dominant mechanism for voltage contrast is that the slower SE on the more positive side of the junction are prevented from escaping by the retarding field from the nearby more negative part of the surface. Consider the energy distribution curve for SE shown in Fig. 7(a). The upper and lower dashed curves are the extreme curves plotted by Kollath.<sup>8</sup> An average curve has been drawn as a full line. The fraction of SE with energy greater than some value  $E_{filter}$  was calculated by counting squares and is shown in Fig. 7(b). According to mechanism described above, this will be the current collected from a point that is at a potential  $+E_{filter}$  relative to the most negative part of the specimen surface.

The expected distribution of  $\Phi_{bias}$  across the surface of a cleaved p-n junction with a uniformly doped region on the left and with a highly doped region on the right (and with no trapped surface charge) is shown in Fig. 7(c) for various values of the electrostatic potential difference  $\Phi_{bias}$ . The collected SE current is obtained by combining the curves shown in Figs. 7(b) and (c), as shown in Fig. 7(d). These curves are similar in form to the experimental waveforms shown in Fig. 6.

The accuracy with which data are recorded is now being improved, and preparations are being made to compare this more closely with the theory.

#### *References*

1. N. C. MacDonald and T. E. Everhart, "Direct measurement of the depletion layer width variation vs applied bias for a p-n junction," *Appl. Phys. Lett.* 7: 267-269, 1965.
2. N. C. MacDonald and T. E. Everhart, "Scanning electron microscope investigation of a planar diffused p-n junction profiles near the edge of a diffusion mask," *J. Appl. Phys.* 38: 3685-3692, 1967.
3. O. C. Wells and P. J. Bailey, "Reduction of penetration effect at sharp edges in the scanning electron microscope (SEM)," *J. Microscopy* 138 (Pt. 1): RP3-RP4, 1985.
4. O. C. Wells, "Reduction of edge penetration effect in the scanning electron microscope" (accepted for publication in *Scanning*).
5. G. V. Lukianoff and T. R. Touw, "Voltage coding: Temporal versus spatial frequencies," *SEM/1975*, 465-471.
6. G. V. Saporin, G. V. Spivak, and S. S. Stepanov, "Observation of the p-n junction



at small constant and alternating bias with the scanning electron microscope," *Sixth Int. Cong. El. Microsc.* (Kyoto), 1: 609-610, 1966.

7. C. W. Oatley, "Isolation of potential contrast in the scanning electron microscope," *J. Phys.* E2: 742-744, 1969.

8. R. Kollath, "On the energy distribution of secondary electrons" (in German), *Ann. Phys.* (Leipzig) 1: 357-380, 1947.

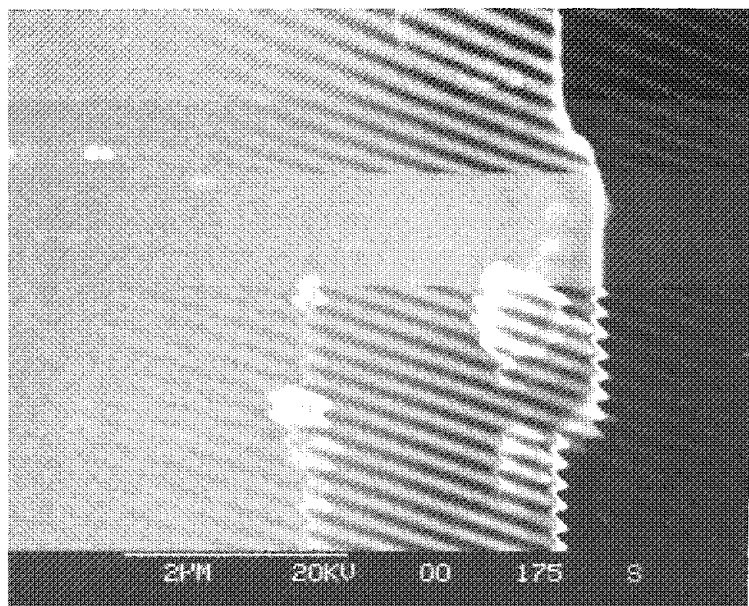


FIG. 5.--Micrograph in three parts. In upper part, LH part of surface is at constant potential, RH part is modulated sinusoidally. In center part, potential is everywhere constant. In lower part, potentials on RH and LH sides are reversed. Comparison of top and bottom shows it is potential difference, not absolute voltage that determines image contrast under these conditions.

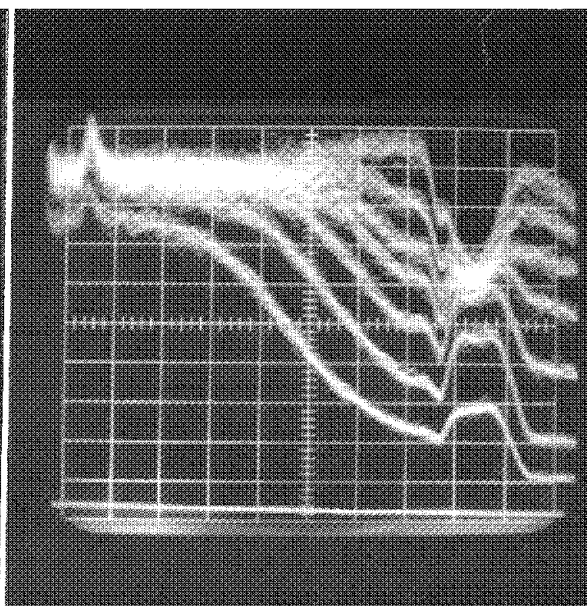


FIG. 6.--Video waveforms as function of  $E_{rev}$ .

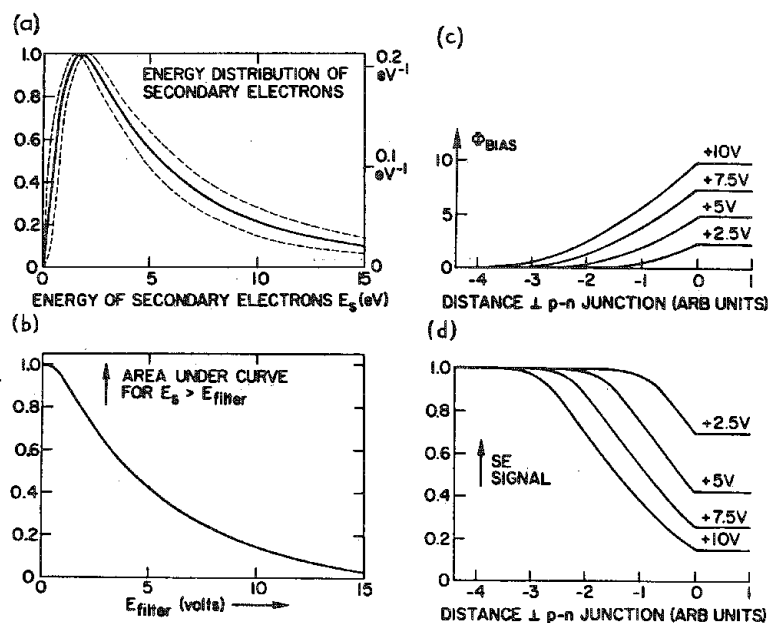


FIG. 7.--Curves relating to theoretical explanation of voltage contrast in unmodified SEM: (a) Energy distribution of SE (calibration on RH vertical axis is for unity area under full-line curve); (b) fraction of SE with energy exceeding  $E_{filter}$ ; (c) potential distribution across uniformly graded p-n junction; (d) expected waveform if  $E_{filter}$  is given by surface potential relative to most negative part.

## DIAGNOSTIC ANALYSIS OF GaAs HIGH-ELECTRON-MOBILITY DEVICES AND INTEGRATED CIRCUITS

A. Christou and W. T. Anderson

GaAs devices and circuits are at present realizing the promise that was predicted during 1978-1985. From a materials point of view GaAs, when compared with silicon, offers significant advantages: it has (a) higher low-field mobility, (b) a negative-resistance region, (c) a semi-insulating substrate which makes low-loss high-frequency device monolithic integration possible, and (d) lattice matching to other III-V compound semiconductors. With the additions of heterojunctions, electron mobility may be enhanced. The high-electron-mobility transistors (HEMTs) are based on a modulation-doped GaAs/AlGaAs heterostructure epitaxy in which the motions of the electrons are confined to a thin potential well in the GaAs buffer layer.<sup>1,2</sup> In the diagnostics of GaAs MESFET technology, the types of analysis must also include the material, the device and circuit as fabricated, and the degraded device and circuit. Table 1 lists the areas to be addressed in this paper, which is limited to beam-analysis techniques.

TABLE 1.--Types of analysis available for diagnostics of GaAs HEMT devices and circuits.

	Electrical	Electron Beam/Ion Beam
Materials Analysis	Mobility, Photoluminescence	e-beam DLTS, Scanning AES, SIMS, Auger, RBS, X-Ray Topography.
Device/Circuit Analysis, As Fabricated and Degraded	Magneto-transconductance, Circuit Parameters, DLTS	SIMS, Scanning AES, SEM

### *GaAs/GaAlAs Material Analysis*

Integrated circuits utilizing the HEMT structure are based on the field-effect transistor. Cross-sectional diagrams of depletion mode (D-mode) and enhancement mode (E-mode) HEMTs are shown in Fig. 1. The materials technology for the HEMT structure is molecular beam epitaxy (MBE). The performance and reliability of the HEMT structure is based on the quality of the GaAs material. Baseline requirements are: unintentional doping levels of less than  $1 \times 10^{14} \text{ cm}^{-3}$ , 77 K mobilities at less than  $5 \times 10^{14} \text{ cm}^{-3}$  of  $100\,000 \text{ cm}^2/\text{V-s}$ , and well-defined excitonic lines observed in the photoluminescence spectra at 4 K.

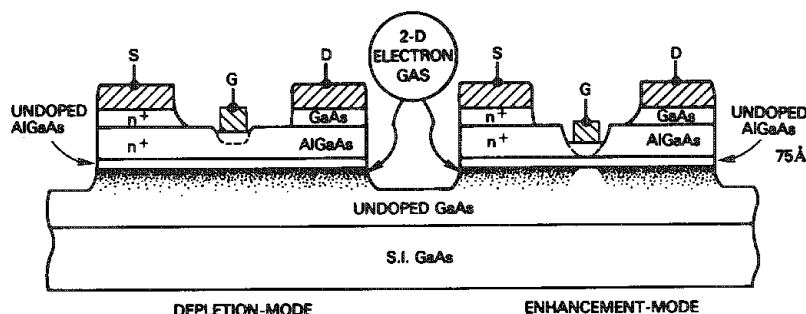


FIG. 1.--Cross-sectional diagrams of D-mode and E-mode HEMTs.

The GaAs/ $\text{Al}_x\text{Ga}_{1-x}\text{As}$  interface which confines the two-dimensional electron gas (2 DEG) must be of high quality, in that ideally the AlGaAs should be grown on an arsenic stabilized  $2 \times 4$  reconstructed surface. The interfacial requirements indicates that the crucial in situ diagnostic technique for epitaxial growth is reflection high-energy electron diffraction (RHEED), as shown in Fig. 2 for an epitaxial Ge film on GaAs.<sup>3</sup> The material properties which must be analyzed and achieved during MBE growth of  $\text{Al}_x\text{Ga}_{1-x}\text{As}$  are: unintentional doping levels of less than  $1 \times 10^{15} \text{ cm}^{-3}$ , controlled silicon doping, and a narrow half-width excitonic peak at 4 K observed by photoluminescence.

The authors are at the Naval Research Laboratory, Washington, D.C. 20375.

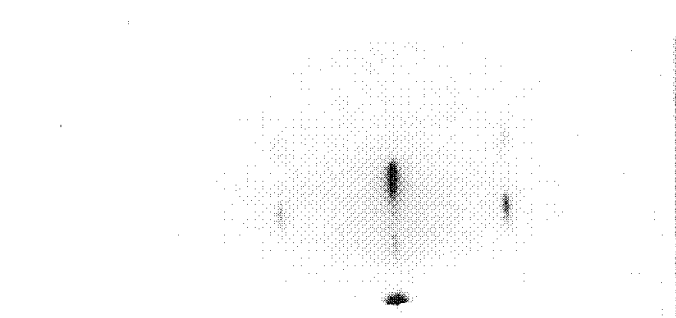


FIG. 2.--RHEED pattern showing growth of high-quality (100) germanium epitaxial layer on (100) GaAs substrate. Germanium layer is 1000 Å thick and was vacuum deposited at 425 C.

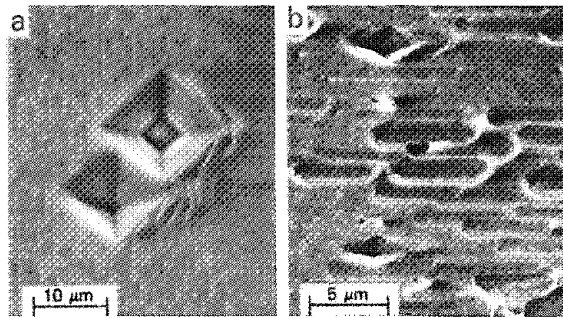


FIG. 3.--SEM micrographs<sup>4</sup> of GaAs surfaces etched by eutectic KOH + NaOH: (a) pyramid pattern caused by single dislocation, (b) rectangular pattern caused by tangled dislocation.

Superlattices in HEMT structures, consisting of many thin ( $\sim 100\text{\AA}$  thick) alternating layers of AlGaAs/GaAs, may be used as buffer layers and as a means of eliminating roughness at interfaces. Superlattice growth has been shown to eliminate roughness at interfaces in that defect structures tend to spread over the entire interface during multilayer growth. The basic diagnostic techniques include secondary ion milling spectroscopy (SIMS) and Auger electron spectroscopy (AES) for depth profiling, and Rutherford backscattering (RBS) for channeling and profile studies. Electron beam (E-beam) induced DLTS (deep-level transient spectroscopy) may be used to analyze traps in the band gap of the material. Surface defects<sup>4</sup> include pyramid type defects and dislocation induced rectangular patterns as shown in Fig. 3. Surface defect levels must be kept to less than  $200\text{ cm}^{-2}$  in order to achieve high yield circuits.

#### Device/Circuit Analysis

**Discrete Devices.** The primary failure modes of small-signal GaAs HEMTs are similar to GaAs MESFETs<sup>5</sup> in that the failures are related to ohmic contact migration (Ga outdiffusion, electromigration) at elevated temperatures, a gradual degradation in drain current  $I_{DS}$ , electromigration of the gate metal, gate burnout by electrostatic discharge (ESD), subsurface burnout, and a pulse burnout of the gate.<sup>6</sup> The electromigration failure mode is related to the initial outdiffusion of Ga which results in a Au-Ga top surface thereby reducing the electromigration resistance of the ohmic contact and gate. A similar outdiffusion of Al occurs in HEMTs. Figure 4 indicates that an enhanced migration of aluminum from the  $\text{Al}_{0.3}\text{Ga}_{0.7}\text{As}$  layers occurs during sintering. The relationship of the outdiffusion of Al to HEMT reliability must still be determined. Electromigration of the gate has been observed to be accompanied by void formation. At the present time state of the art

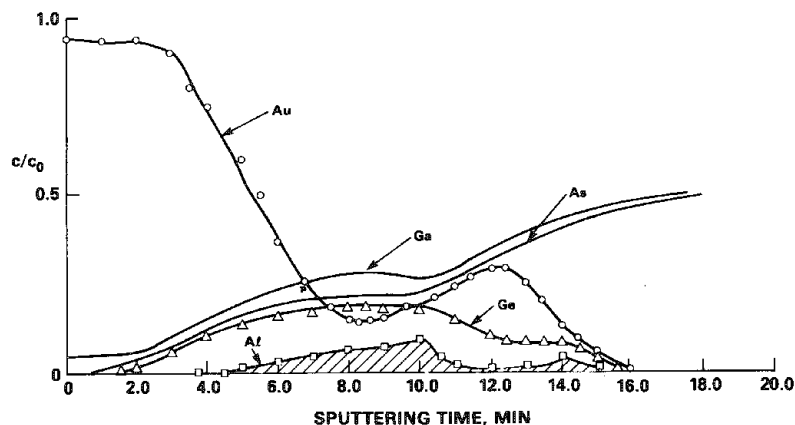


FIG. 4.--AES sputter profile showing enhanced outdiffusion of aluminum from HEMT ohmic contacts as a result of sintering at 350 C for 1 min.

TABLE 2.--Summary of discrete HEMT failure modes.

Device Part	Physical Changes	Electrical Changes
Ohmic Contact (AuGeNi)	Electromigration Ga outdiffusion Void formation	$R_{DS}$ increase decrease in $G_m$
Gate (Al, TiPtAu, TiWAu)	Al burnout Ga outdiffusion	$V_p$ and $G_m$ decrease decrease in $I_{DS}$ loss of channel control.
Channel/substrate	subsurface burnout	loss of channel control
MBE Epitaxial layers	Si, Al interdiffusion	Loss in 2 DEG confinement, decrease in $G_m$

$R_{DS}$  — drain to source resistance

$G_m$  — transconductance

$V_p$  — pinchoff voltage

$I_{DS}$  — drain current

MBE layers do not show any significant trapping phenomenon in the epitaxial layers; however, the persistent photoconductivity effect<sup>7</sup> continues to be observed in discrete HEMTs. Table 2 shows a summary of failure mechanisms as determined by diagnostic techniques for HEMTs.

The electromigration resistance of Al gates can be increased by several techniques.<sup>5</sup> In addition, gold-refractory gates, such as TiWAu, may be improved by doping the Au film and incorporating appropriate diffusion barriers.<sup>5</sup> These techniques have been incorporated in discrete HEMTs,<sup>8</sup> thereby improving the gate reliability. The activation energies measured for gate degradation vary from 0.5 to 1.0 eV and indicate that low-temperature grain-boundary-diffusion dominates. In analyzing electromigration failures, AES techniques have been successfully incorporated to assess Ga outdiffusion<sup>5</sup> and the presence of Ga on Au-refractory surfaces.

*Diagnostics of Discrete HEMTs After Alpha Particle Irradiation.* HEMTs fabricated at NRL having the structure shown in Fig. 1 were studied at the NRL microbeam facility which provided 1.1MeV alpha particles incident on devices. The methods used for irradiating the devices and measuring the resulting change in I/V characteristics were similar to those reported in a previous study<sup>9</sup> of GaAs FETs. All measurements were made with the devices biased with the gate bias  $V_G$  held typically near pinchoff, the source grounded,  $V_S = 0$ , and the drain bias  $V_D$  at 0 or varied up to 2.0V. An aperture 2.5  $\mu\text{m}$  in diameter was used to confine the beam to the gate region of the devices. The typical value of the alpha particle flux was 40 alphas per second through the aperture, or about  $3 \times 10^8/\text{sec-cm}^2$ , allowing for a spread in the beam to 4 $\mu\text{m}$ -diameter on the gate region. Charge collection measurements were made at various locations across the gate region by traversal of the device under the beam with a precision translation stage. The center of the gate and the edges of the source and drain could be clearly determined by the large reduction in collected charge when the beam impinged on the ohmic contact source/drain regions. In other cases, the entire device was irradiated with the full beam, without the aperture, to study the degradation in I-V characteristics.

The degradation in I/V characteristics and decreases in charge collection efficiency were similar to that observed<sup>9</sup> previously in GaAs FETs. A decrease was observed in the saturated drain current at zero gate bias,  $I_{DSS}$ , and the transconductance  $G_m$  also decreased as the alpha particle irradiation under the full beam increased, beginning at about 1 Mrad (GaAs). As the degradation was similar to that observed in GaAs FETs, the degradation was likely the result of carrier removal (decrease in the effective n-type carrier concentration) in the two-dimensional electron gas, formed in the lower undoped GaAs layer in Fig. 1, caused by displacement damage to the GaAs and AlGaAs crystal lattices.

During the period of measurement in which the beam was traversed from source to drain across the gate (about 60 s), it was found that the charge collection efficiency decreased. In the case of burnout, device degradation was evidenced by a large increase in noise from the charge sensitive preamplifier. The degradation in charge collection efficiency was typically 5% per 1000 alpha particles and was observed both when irradiated through the aperture and under the full beam.

During alpha particle irradiation of the entire device or through the aperture, all eight HEMTs were found to have had gate-to-source or gate-to-drain burnout. An example is shown in the SEM micrograph in Fig. 5. This device was irradiated through the aperture at a flux of  $3 \times 10^8/\text{s}\cdot\text{cm}^2$  while under bias conditions near pinchoff. When the device was examined after receiving a total of  $2 \times 10^5$  rad, it was found that subsurface burnout had occurred under the gate. This gate typically remained unmelted over the top of the burnout path. The devices that experienced this type of burnout exhibited degraded transistor characteristics and the gate rectification was considerably softened, as shown in Fig. 5. The total dose of alpha particles was  $2 \times 10^5$  rad. Burnout appeared to have originated under the gate, leaving a burnout path to the drain or source. The burnout path was more conducting than the active n-type GaAs of the channel, as evidenced by the softened gate I-V characteristics, but was not a complete metallic bridge.

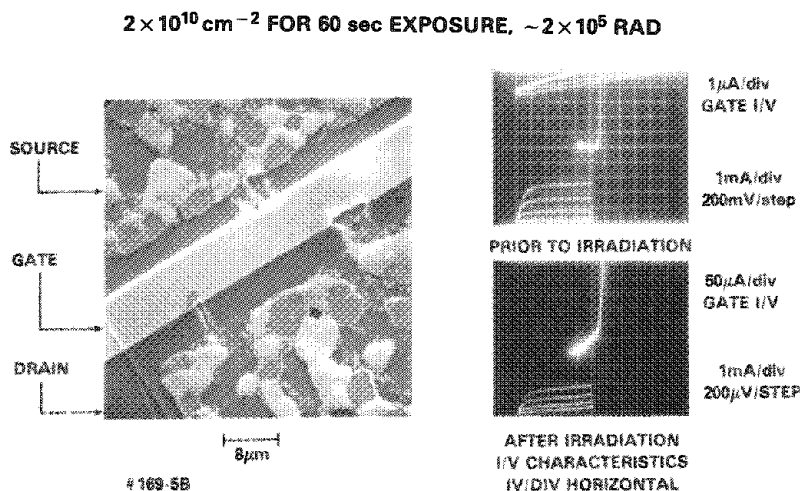


FIG. 5.--Typical gate burnout of HEMT irradiated by 1.1 MeV alpha particles through aperture at  $3 \times 10^8/\text{s}\cdot\text{cm}^2$  flux, under gate bias. I-V characteristics before and after irradiation: center of each figure is gate-to-source I-V, lower left of each figure is drain current vs drain bias (source grounded) for gate bias values in 200 mV steps.

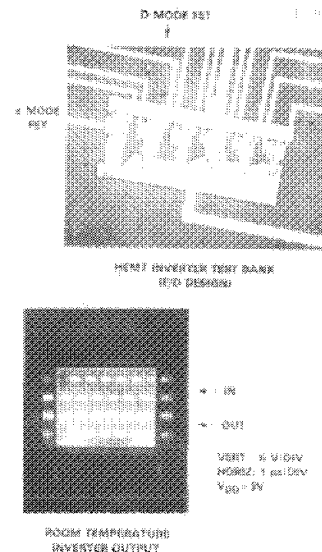


FIG. 6.--HEMT inverter circuit used in present reliability investigation, consisting of E-mode and D-mode HEMTs.

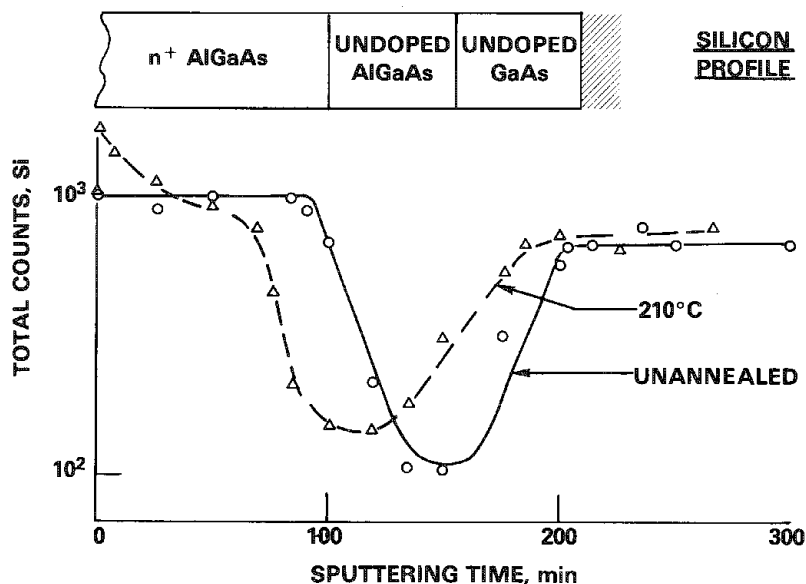


FIG. 7.--SIMS data for HEMTs annealed at 210 C for 500 h showing movement of silicon in channel area.

*Diagnostics of HEMT IC Degradation.* The reliability problems of HEMT integrated circuits can be divided into basic and process related. The basic reliability concerns are substrate defects, lateral diffusion of dopants, freezeout of carriers, persistent photoconductivity, I-V collapse in the dark, and ohmic contacts. The persistent photoconductivity is related to a defect center (DX) in the AlGaAs layer<sup>7,10</sup> and to the amount of undepleted  $\text{Al}_x\text{Ga}_{1-x}\text{As}$  layer between the gate and drain. The process-related reliability concerns are ohmic contacts, Schottky barrier formation, location of the 2 DEG layer, and passivation of the channel. The problems associated with the ohmic contact include the outdiffusion of aluminum, the lateral migration of ohmic contact constituents, and the nonuniform surface topography. The location of the 2-DEG layer is a further problem, which is introduced during accelerated life testing. Degradation of the heterojunction barrier results in a de-confinement of the 2 DEG. Table 1 summarizes the diagnostic techniques used to assess the above degradation mechanisms.

The photoconductivity effect as a reliability problem has been studied and the problem has been related to the mole fraction of aluminum in the structure. Accelerated stress tests of HEMT integrated circuits shown in Fig. 6 have been tested at elevated stress conditions in order to determine failure mechanisms.<sup>8</sup> The devices tested were depletion mode and enhancement mode HEMTs. The enhancement mode HEMTs were processed by etching the channel and recessing the gate. The gates utilized consisted both of Cr-Au and TiW-Au. The results of the accelerated life tests at 210 C resulted in a median time before failure (MTBF) of  $10^4$  h for TiW-Au gates and an MTBF of  $5 \times 10^3$  h for Cr-Au gates. In addition, a comparison of depletion-mode HEMTs with enhancement mode HEMTs showed that enhancement-mode HEMTs are less reliable.

The fundamental degradation mechanism was found to be the outdiffusion of Si from the  $n^+$  layer toward the channel. SIMS analysis of the FET structure indicates a migration of Si toward the channel as shown in Fig. 7. The movement of Si results in changes in channel characteristics such as pinchoff voltage and transconductance.

### Conclusions

Electron and ion beam diagnostic techniques are critical to the development of HEMT integrated circuits. The diagnostic techniques outlined in Table 1 and reviewed here include both material assessment and device/circuit evaluation. Although application of the diagnostic techniques has been emphasized, their generic natures may be applied to the evaluation of the problems related to the HEMT metal-semiconductor interface, surface, and bulk-related defects.

### References

1. R. C. Miller, and R. Dingle, *J. Appl. Phys.* 47: 4509, 1976.
2. H. Schichijo, K. Hess, and B. J. Streetman, *Solid State Electron.* 23: 817, 1980.
3. W. T. Anderson Jr., A. Christou, and J. E. Davey, Technical Digest, *Internat. Electron Devices Meeting*, 1977, 192-194.
4. W. F. Tseng, H. Lessoff, and R. Gorman, *J. Electrochem. Soc.* 132: 3067-3068, 1985.
5. J. E. Davey and A. Christou, "Reliability and degradation of active III-V semiconductor devices," in M. J. Howes and D. V. Morgan (Eds.), *Reliability and Degradation*, New York: Wiley, 1981.
6. W. T. Anderson, F. A. Buot, A. Christou, and Y. Anand, *Internat. Reliability Physics Symp.*, Anaheim, Calif., 1986.
7. R. Fischer, T. J. Drummond, W. Koop, H. Morkoc, K. Lee, and M. S. Shur, *Electronic Letts.* 19: 789, 1983.
8. A. Christou, W. Tseng, M. Peckerar, W. T. Anderson, D. M. McCarthy, and F. A. Buot, *Internat. Reliability Physics Symp.*, Orlando, Fla., 1985.
9. W. T. Anderson, A. B. Campbell, A. R. Knudson, A. Christou, and B. R. Wilkins, *IEEE Trans.* NS-31: 1124-1127, 1984.
10. H. Dambkas, W. Brokerhoff, and K. Heime, *Electronic Lett.* 20: 615, 1984.

## ELECTRON PROBE X-RAY MICROANALYSIS OF $\text{Al}_x\text{Ga}_{1-x}\text{As}$ EPITAXIAL LAYERS: TECHNIQUE AND ACCURACY CONSIDERATIONS

T. P. Rammel

Much attention has been focused in recent years on the development of III-V semiconductor compounds suitable for the fabrication of optoelectronic and microwave devices. Ternary and quaternary alloys of Al, Ga, As, In, and P are widely used in applications including light-emitting diodes, solid-state lasers, photodetectors, and high-frequency field-effect transistors.<sup>1-5</sup> Controlled epitaxial growth of these alloys tailored to specific composition and doping levels has been key to the rapid success of the III-V market. Liquid-phase epitaxy (LPE)<sup>6</sup> and more recently metalorganic chemical vapor deposition (MOCVD)<sup>1</sup> and molecular beam epitaxy (MBE)<sup>7</sup> offer the ability to grow multilayer structures having thicknesses ranging from tens of microns (LPE) down to tens of Å (MBE) with atomically abrupt interfaces. Knowledge of the stoichiometry of the individual layers is essential for successful process development and device performance assessment. Measurement techniques include photoluminescence, x-ray diffraction, electron probe x-ray microanalysis, Auger spectroscopy,<sup>8</sup> and ion-probe microanalysis.<sup>9</sup> Each technique has its advantages and limitations in terms of accuracy, depth resolution, and analysis time. This paper discusses in detail the use of electron probe x-ray microanalysis for quantitatively measuring the stoichiometry of epitaxial layers of the ternary  $\text{Al}_x\text{Ga}_{1-x}\text{As}$  system.

### *Experimental*

Composition profiles of the epitaxial layers were measured by acquisition of digital linescans across cleaved sections of the GaAs substrate/epitaxial layers. Cleaving GaAs results in a clean, smooth cross section of the layers. For thicker epitaxial structures (>50  $\mu\text{m}$ ), the digital stepping is accomplished via automated stage movement in 1  $\mu\text{m}$  (or greater) intervals with a stationary electron beam. For thinner structures, where a point-to-point resolution of better than 1  $\mu\text{m}$  is desired, high-resolution linescans were acquired by digital stepping of the electron beam across a stationary sample.

All x-ray detection was via wavelength spectrometers. TAP crystals were used for Al K $\alpha$  and Ga and As L $\alpha$  lines. Since only two TAP crystal spectrometers were available, two repetitions of the digital linescans are required, the first time to measure Al and Ga, the second to measure As. This procedure introduces uncertainties in beam/sample repositioning; however, methods were developed that yielded repositioning accuracies to within 0.1  $\mu\text{m}$ .

Accelerating voltages of 5, 10, and 20 kV have been used, with tradeoffs in spatial resolution, speed of analysis, and accuracy of results. At 20 kV it is possible to measure the K lines of Ga and As with LiF crystal spectrometers, which affords simultaneous monitoring of all three elements. However, the uncertainties in matrix corrections and loss of spatial resolution at higher accelerating voltages must be weighed against the benefits of simultaneous data acquisition.

Dwell times were typically 2 to 10 s per point, with total analysis times ranging from 5 to 35 min. Measurement of beam current was via a Faraday cup inserted into the beam path under computer control, with current-to-voltage-to-frequency conversion and digital scaling. Beam currents in the 10-100 nA range were typically used.

All analyses were performed on a JEOL 733 electron microprobe with four wavelength spectrometers, having 40° take-off angles. Automation of the stage and spectrometers was via a Tracor Northern TN-2000/TN-1310 system having digital beam control. Software is available to convert the raw data into quantitative profiles (k-ratio calculation and ZAF matrix corrections) in a matter of minutes.

---

The author is at Motorola, Inc., Semiconductor Research and Development Laboratory, Phoenix, AZ 85008.

## Results and Discussion

Shown in Figs. 1 and 2 are examples of quantitative profiles obtained with a 10kV accelerating voltage. The sample in Fig. 1 is a four-layer MOCVD  $\text{Al}_x\text{Ga}_{1-x}\text{As}/\text{GaAs}$  structure. Analysis was performed by the digital beam scanning technique. Total analysis time was approximately 15 min. The results were in excellent agreement with the x-values of 0.1/0.35/0/0.30 as predicted by growth kinetics. The two-layer LPE structure shown in Fig. 2 was analyzed by digital stage stepping in  $1\mu\text{m}$  increments. Note the graded Al composition in the layers. The ability to measure such gradients in epitaxial layers is an advantage of electron probe analysis over techniques such as photoluminescence. The compositions are plotted in atomic percent and afford easy conversion to stoichiometry (x-values). However, this method necessitates normalization to 100%. Typical total weight fractions for Al + Ga + As after ZAF matrix corrections were  $100 \pm 2\%$  for each point in the profile.

The accuracy of the quantitative profile depends on numerous factors, each of which introduces uncertainty in the results. These factors include statistical uncertainty in the raw data (standards and unknowns), dead-time effects in the proportional counter, instrument drift or instability, uncertainties in analytical parameters, and matrix correction errors.

Statistics dictate that the uncertainty in the raw data is equal to  $N^{-\frac{1}{2}}$ . For 1% precision,  $10^4$  counts are required for each element at each data point. Detector dead-time effects were corrected by use of the relation

$$N = N' / (1 - \tau N')$$

where  $N$  and  $N'$  are the true and measured countrates respectively and  $\tau$  is the deadtime in seconds.<sup>10</sup> This correction exceeds 10% for countrates of 40 000 cps, commonly encountered in measuring the aluminum standard.

Beam current drift was monitored via the Faraday cup/digital beam current monitor before, during, and after analysis. A word of caution regarding digital monitors: it was discovered that an error of about 8% was observed in the digital reading for each decade increase in beam current, apparently due to a zero offset/nonlinearity problem. As a result, measurement of standards and unknowns were taken at similar beam current conditions.

Matrix corrections (ZAF), particularly absorption, account for the greatest contribution to the uncertainty in the accuracy of the quantitative profiles (assuming the other sources of error are controlled). The fluorescence correction is virtually negligible for the  $\text{Al}_x\text{Ga}_{1-x}\text{As}$  system and the atomic number correction is of consequence only for Al. However, the absorption correction is significant for both Al and As, especially at higher accelerating voltages.

High mass absorption coefficients ( $\mu/\rho$ ) exist for Al  $K\alpha$  radiation in Ga and As and for As  $L\alpha$  in Ga. To complicate matters, there is significant disagreement in the literature regarding the absolute values of these coefficients. Relationships, usually of the form  $\mu/\rho = C\lambda^n$ , where  $\lambda$  is the wavelength of the radiation, have been derived by numerous investigators.<sup>11-16</sup> The values for the Al-Ga-As system calculated from these relationships are listed in Table 1. Note that differences of up to 25% exist for several of the coefficients.

There exist several different formulations for the absorption correction factor  $f(\chi)$ , which incorporate the mass absorption coefficients [ $\chi = (\mu/\rho) \csc \psi$ , where  $\psi$  is the take-off angle]. They include the Philibert-Duncumb-Heinrich (PDH) equation,<sup>17</sup> the Heinrich-Yakowitz (H-Y) expression,<sup>18</sup> and more recently those of Heinrich<sup>19</sup> and of Sewell, Love, and Scott (Love-Scott II).<sup>20</sup>

Listed in Table 2 are  $f(\chi)$  values derived from the various absorption models for  $\text{Al}_x\text{Ga}_{1-x}\text{As}$  with  $x = \phi$ . This composition represents the most extreme case of absorption for the system. The  $f(\chi)$  values were calculated at 5, 10, and 20 kV for a  $40^\circ$  take-off angle and  $\mu/\rho$  values of Henke et al. in Table 1. The absorption effects are greatest for Al and least for Ga. Note how the discrepancies among the various models increase as the overvoltage increases. Discrepancies of similar magnitude are evident when the  $\mu/\rho$  values of Henke et al. are compared with those of Heinrich using the same correction model.

Yakowitz and Heinrich<sup>21</sup> concluded in their work on error propagation in the absorption correction that if  $\mu/\rho$  is known within 5%, then for correction errors smaller than



FIG. 1.--Quantitative profile of four-layer MOCVD epitaxial  $\text{Al}_x\text{Ga}_{1-x}\text{As}$  structure in GaAs.

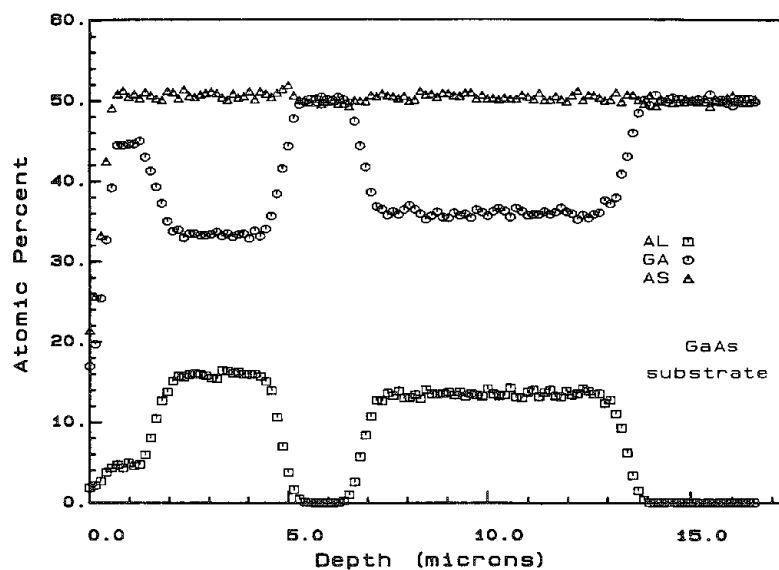


FIG. 2.--Quantitative profile of graded composition two-layer LPE  $\text{Al}_x\text{Ga}_{1-x}\text{As}$  on GaAs.

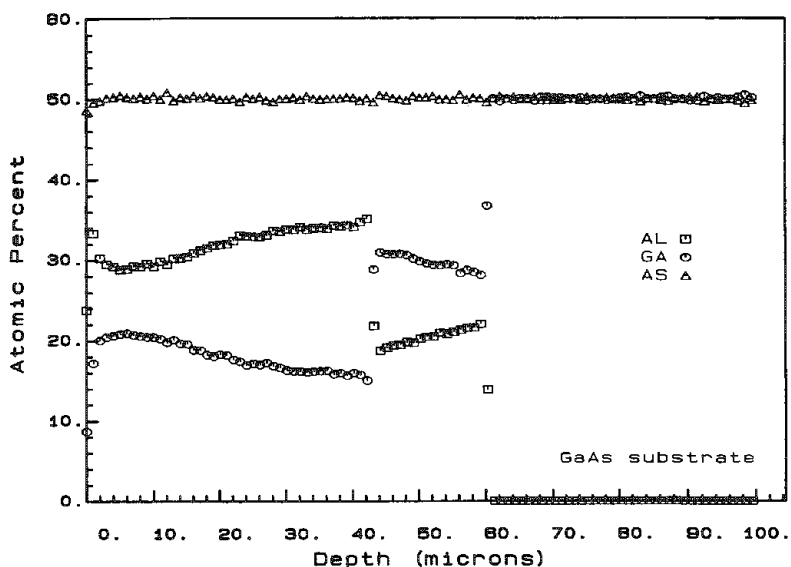


TABLE 1.--Mass absorption coefficients  $\mu/\rho$  ( $\text{cm}^2/\text{g}$ ) for Al-Ga-As system, interpolated or calculated from various sources.

Absorber	Al-K <sub>1</sub> $\lambda = 8.339\text{\AA}$	Ga-L <sub>1</sub> $\lambda = 11.292\text{\AA}$	As-L <sub>1</sub> $\lambda = 9.671\text{\AA}$	Source (Reference)
Al	386	888	578	Heinrich (11)
	405	915	600	Veigele (12)
	385	880	577	Springer/Nolan (13)
	404	930	590	Henke et al. (14)
	426	981	638	Kelly (15)
Ga	401	919	597	Mean
	17	40	25	Std. dev.
	6603	-	8455	(11)
	5230	1340	6450	(12)
	6574	1944	8421	(13)
As	5300	1380	6600	(14)
	6418	1887	7939	(15)
	6025	1638	7573	
	698	322	980	
	6782	-	1562	(11)
As	5300	1700	1170	(12)
	6769	2337	1562	(13)
	5400	1690	1170	(14)
	6283	2255	1560	(15)
	6107	1996	1405	
	720	349	214	

1%,  $f(x)$  should be  $\geq 0.8$ . Based on the results of their work, and considering the large uncertainty in several of the mass absorption coefficients, analysis of Al-Ga-As should be performed at low accelerating voltages to minimize the correction errors due to absorption effects.

Decreasing the accelerating voltage results in larger uncertainties associated with counting statistics due to the drop in x-ray production at the lower voltage (for constant current and time conditions). However, this increased uncertainty is more than offset by the decreased uncertainty due to the absorption correction, as is seen in Table 3. Shown are results comparing analysis of identical epitaxial layers with 5 and 10 kV beam voltages at similar beam current and time conditions. The compositions are the averages of those obtained when the four absorption correction models are applied to the raw data. The uncertainties listed include the contributions from the raw data, standards, mass absorption coefficients, and absorption correction models. These results are consistent with the work of Yakowitz and Heinrich on error propagation in the absorption correction,<sup>21</sup> from which it was calculated that the contributions from the mass absorption coefficient uncertainties for Al and As would be 1.5% and 1.0% at 5 kV and 3.8% and 2.7% at 10 kV (for a layer of composition similar to that of #1). The deleterious effect of the absorption correction uncertainty at the higher beam voltage for Al and As is obvious.

Regarding depth resolution in the quantitative profiles, using the relationship of Andersen and Hasler,<sup>22</sup> the x-ray ranges for Al K $\alpha$ , Ga L $\alpha$ , and As L $\alpha$  in GaAs are calculated to be about 0.16, 0.55 and 1.8  $\mu\text{m}$  at 5, 10 and 20 kV, respectively. The 85-to-15% interface widths for the profile shown in Fig. 2 were measured to be about 0.5  $\mu\text{m}$ . Analysis at 5 kV has yielded interface widths of less than 0.4  $\mu\text{m}$ . Under such conditions, epitaxial layers down to 1  $\mu\text{m}$  in thickness are resolvable and their stoichiometry is measurable.

### Conclusions

A method has been described to measure quantitatively the stoichiometry of  $\text{Al}_x\text{Ga}_{1-x}\text{As}$  epitaxial layers using electron probe microanalysis. The limiting factor in the accuracy of the results lies in the absorption correction uncertainty, particularly for Al and As. Uncertainty considerations indicate increased accuracy at accelerating voltages of 5 kV compared to 10 or 20 kV. Accuracies of better than 3% relative and depth resolution of less than 0.4  $\mu\text{m}$  are attainable within reasonable analysis times.

### References

1. R. Dupuis and P. D. Dapkus, " $\text{Ga}_{(1-x)}\text{As}/\text{Ga}_{(1-y)}\text{Al}_y\text{As}$  double heterostructure, room temperature lasers grown by metalorganic chemical vapor deposition," *Appl. Phys. Lett.* 31: 839-841, 1977.
2. E. E. Wagner et al., "Growth of high-quality  $\text{Al}_x\text{Ga}_{1-x}\text{As}$  by OMVPE for laser devices," *J. Electronic Mater.* 10: 239-253, 1981.
3. A. G. Milnes, "Semiconductor heterojunction topics: Introduction and overview," *Solid-State Electronics* 29: 99-121, 1986.
4. H. H. Weider, "Problems and prospects of compound semiconductor field-effect transistors," *J. Vac. Sci. Technol.* 17: 1009-1018, 1980.
5. H. Kroemer, "Heterostructure bipolar transistors and integrated circuits," *Proc. IEEE* 70: 13-25, 1982.
6. J. M. Blum and K. K. Shih, "Growth of smooth uniform epitaxial layers by liquid-phase-epitaxial method," *J. Appl. Phys.* 43: 1394-1396, 1972.
7. A. Y. Cho and J. R. Arthur, "Molecular beam epitaxy," *Prog. Solid State Chem.* 10: 157-191, 1975.
8. J. R. Arthur and J. J. LePore, "Quantitative analysis of  $\text{Al}_x\text{Ga}_{1-x}\text{As}$  by Auger electron spectroscopy," *J. Vac. Sci. Technol.* 14: 979-984, 1977.
9. T. S. Stewart et al., "Determination of Al in  $\text{Ga}_{1-x}\text{Al}_x\text{As}$  by Auger spectroscopy, ion microprobe and photoluminescence," *SPIE Semiconductor Growth Technology* 323: 164-173, 1982.
10. K. F. J. Heinrich et al., in *Advances in X-ray Analysis* 9: 208, 1966.
11. K. F. J. Heinrich, in T. D. McKinley et al., Eds., *The Electron Microprobe*, New York: Wiley, 1966, 196.

12. W. J. Veigele, in J. W. Robinson, Ed., *Handbook of Spectroscopy, Vol. I*, Cleveland: CRC Press, 1974, 28.
13. G. Springer and B. Nolan, "Mathematical expressions for the evaluations of x-ray emission and critical absorption energies and of mass absorption coefficients," *Can. J. Spectr.* 21: 134-138, 1976.
14. B. L. Henke et al., "Low energy x-ray interaction coefficients, photoabsorption, scattering and reflection," *Atomic Data and Nuclear Data Tables* 27: 1-144, 1982.
15. T. K. Kelly, "Mass absorption coefficients and their relevance to electron-probe microanalysis," *Trans. Inst. Min. Metall.* 75: B59-73, 1966.
16. J. T. Frazer, *A Computer Fit to Mass Absorption Coefficient Data*, La Jolla, Calif.: U.C. Institute for the Study of Matter, S.I.P reference number 67-29.
17. K. F. J. Heinrich, NBS Tech. Note 521, Washington, D.C.: National Bureau of Standards, 1970.
18. K. F. J. Heinrich et al., *Proc. 7th National Conference on Electron Probe Analysis*, EPASA, San Francisco, 1972, paper 3.
19. K. F. J. Heinrich, "A simple accurate absorption model," *Microbeam Analysis--1985*, 79-81.
20. D. A. Sewell et al., "Universal correction procedure for electron probe microanalysis: II. The absorption correction," *J. Phys.* D18: 1245-1268, 1985.
21. H. Yakowitz and K. F. J. Heinrich, "Quantitative electron probe microanalysis: Absorption correction uncertainty," *Mikrochim. Acta*, 1968, 182-200.
22. C. A. Andersen and M. F. Hasler, in R. Castaing et al., Eds., *X-Ray Optics and Microanalysis, 4th Int. Congr. on X-Ray Optics and Microanalysis*, Paris: Hermann, 1966, 310.

TABLE 2.--Absorption correction factors  $f(x)$  for  $Al_xGa_{1-x}As$  system ( $x = \phi$ ) calculated from four different models.

5 kV			10 kV			20 kV			Correction Model (Ref)
Al-K	Ga-L	As-L	Al-K	Ga-L	As-L	Al-K	Ga-L	As-L	
.803	.931	.850	.527	.800	.617	.234	.546	.316	PDH (17)
.765	.914	.819	.471	.761	.563	.198	.490	.271	H-Y (18)
.782	.922	.833	.461	.763	.557	.172	.472	.243	Heinrich (19)
.789	.930	.843	.491	.793	.593	.176	.503	.252	Love-Scott II (20)
.785	.924	.836	.488	.780	.583	.195	.503	.271	Mean
.016	.008	.013	.029	.020	.028	.028	.032	.033	Std. dev.

TABLE 3.--Comparison of 5 and 10kv analyses of identical epitaxial  $Al_xGa_{1-x}As$  layers.

Layer	5 kV			10 kV			
	Al	Ga	As	Al	Ga	As	
1	30.0	21.1	49.0	30.5	21.0	48.5	Mean Atomic Composition
	2.8%	1.8%	1.7%	6.1%	1.8%	3.2%	Relative Uncertainty
2	20.3	30.5	49.2	20.3	30.6	49.2	
	2.9%	1.6%	1.5%	6.8%	1.4%	2.6%	

## MICROBEAM QUANTITATIVE ANALYSIS OF MIXED OXIDES IN A TUNGSTEN MATRIX

R. R. Seaver and H. K. A. Kan

The technique of energy-dispersed x-ray spectrometry (EDXS) for quantitative analysis is compared with the standard technique of wavelength-dispersed x-ray spectrometry (WDXS). The sample configuration under consideration is that of mixed oxides of calcium-barium-aluminum embedded in a tungsten matrix. We have found that the results of the oxide composition obtained by the two techniques agree to better than 5%.

Our work was motivated by an interest in thermionic emitters used in high-power microwave transmitter tubes (traveling-wave tubes) for space communications. These emitters are the so-called impregnated cathodes that consist of porous tungsten structures of about 80% bulk density so that the pores form a connected network. The pores are impregnated with mixed oxides of barium, calcium, and aluminum from melt. In operation, the tungsten matrix reacts with the mixed oxide impregnants to produce a continuous supply of barium to the emitting surface, insuring a low work-function surface during the life of the satellite. The ability to make quantitative analyses of the embedded oxides or impregnants allows us to examine composition uniformity and identify the products of chemical reaction that accompany cathode operation.

EDXS is a convenient technique, but its ability to do quantitative analysis on samples having a complex geometry such as those containing embedded materials is often questioned. However, the findings described below indicate that with pore sizes of the order of a few micrometers and with suitable sample preparation, it is possible to obtain good quantitative agreements between EDXS and the standard technique of WDXS.

### *Experimental*

Each sample was sectioned so as to expose its interior, and was polished flat in order to establish a well-defined geometric relationship between the surface of the specimen and the analyzer system; this is an important procedure for obtaining quantitative results. The mixed oxide impregnant material is loosely held in the tungsten matrix, however, and must be rigidly supported during sectioning and polishing. A technique was developed to support the oxide material in place by infiltrating the entire structure with plastic so that the impregnants would not be smeared during polishing. The details of sample preparation are described elsewhere.<sup>1</sup>

A micrograph of a polished surface is shown in Fig. 1. The light area is tungsten and the dark regions are pores, which now contain impregnant materials supported by plastic. The features inside the pores represent different phases of oxides and will be described below in greater detail. Beam analysis is made directly on the supported materials, pore by pore. To avoid interference from the tungsten matrix, the analyzing beams were directed to the interior of the pores. The experimental conditions are described in Table 1 for both wavelength- and energy-dispersed analyses.

In addition to these techniques, it turned out that different oxide phases could also be distinguished by their gray scale as seen in ordinary secondary-electron SEM photographs. A "calibration," or the actual identification of regions having a particular gray level with a given oxide phase, of course requires actual quantitative analysis by WDXS. In Fig. 1, the oxide phases that were so identified are indicated. The gray-scale delineation was extremely helpful in directing the beam to perform analysis of the individual phases.

### *Results*

The results of measuring the oxide composition in 30 pores in one sample are shown in Fig. 2 in a phase diagram<sup>2</sup> for the system of BaO, CaO, and Al<sub>2</sub>O<sub>3</sub>. Each point on the

---

The authors are at the Chemistry and Physics Laboratory, The Aerospace Corporation, El Segundo, CA 90245.

TABLE 1.--Experimental conditions for wavelength- and energy-dispersal analysis.

Technique	WDXS	EDXS
Instrument	Cameca Camebax-Micro	Cambridge S 200, Tracor Northern 5500
Electron energy (kV)	15	15
Sample current (nA)	9	0.05-0.1
Take-off angle	40°	35°
Counting time (s)	20 (peak), 10 (background)	150
Analyzed element, line, standard	Ba, L, BaSO <sub>4</sub> Al, L, Al <sub>2</sub> O <sub>3</sub> Ca, K, CaSiO <sub>3</sub> W, M, W	Ba, L, BaSO <sub>4</sub> Al, K, Al <sub>2</sub> O <sub>3</sub> Ca, K, CaSiO <sub>3</sub> W, M, W

phase diagram represents the result obtained on one pore, and the average values of 30 pores are also indicated. The right portion of Fig. 2 shows the data obtained by EDXS; the left, the same results on the same sample in approximately the same region but obtained by electron microprobe. The scatter in the phase diagram in each case is attributed mostly to the nonuniformity of the sample itself. The agreement between the EDXS and the microprobe results is good; the methods agree to about 5%.

After a cathode is operated at elevated temperatures, the reaction of the oxide impregnants with the tungsten matrix results in the formation of different oxide phases; the details depend on the operating conditions and on the position of the phases in the sample because there is a continuously decreasing barium vapor pressure toward the emitting surface. The particular region in Fig. 1 shows the existence of several phases: dibarium calcium tungstate near the tungsten wall; calcium oxide (which has separated into sizable particles); and the remaining barium, calcium, and aluminum mixed oxides. When the beam was directed to these different regions, the results shown in Fig. 3 were obtained. The points scattered on the line joining the end points of barium aluminate and calcium oxide correspond to regions in the sample that contained a mixture of these two phases. Below that line are points corresponding to a composition close to that of the starting material (Fig. 2). The points at the lower portion of the phase diagrams have a ratio of barium oxide to calcium oxide of 2:1, and in each case a tungsten signal showing a material composition of dibarium calcium tungstate was observed. The similarity of the two sets of data shows that the two techniques gave very comparable results.

### Conclusion

EDXS can be used to obtain quantitative analysis results of oxides in a metal matrix that are in good agreement with results obtained by WDXS. Sample preparation that supports the embedded material and provides a well-defined geometry in the analysis chamber is essential to obtaining the favorable comparison. The analysis volumes were large enough in this case so as not to give significant signals from the matrix. In general the matrix can still absorb some of the x rays to affect the accuracy of the analysis, but the extent will depend on analysis geometry. In our case, the two techniques employed different take-off angles; the good agreement of the results suggests that the matrix absorption effect here is not large.

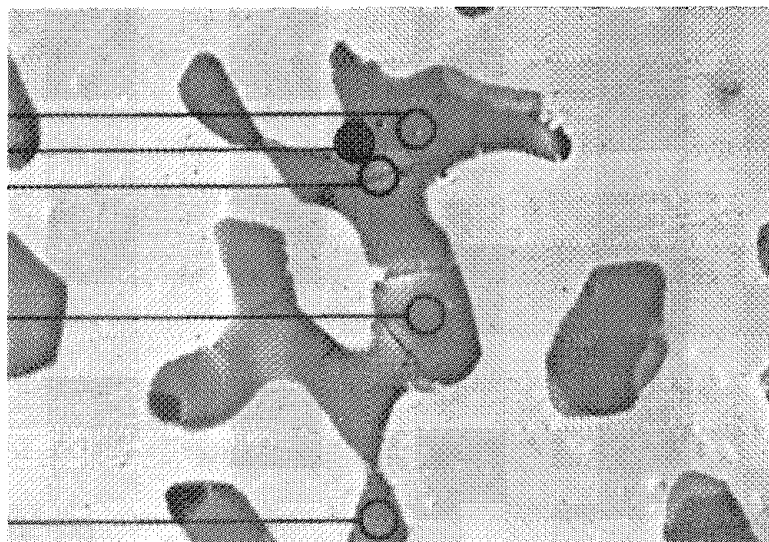
### References

1. H. K. A. Kan and R. R. Seaver, *Appl. Surf. Sci.* 25: 118-126, 1986.
2. G. M. Wolten, *An Appraisal of the Ternary System BaO-CaO-Al<sub>2</sub>O<sub>3</sub>*, Report SD-TR-80-67, Space Division, U.S. Air Force Systems Command, October 1980.

52.2:21.2:26.6  
15.0:79.6:5.4  
53.9:20.0:26.1

53.4:19.3:27.3

53.0:19.8:27.2



10  $\mu\text{m}$

FIG. 1.--Micrograph of polished cross section of impregnated cathode. Values are BaO:CaO:Al<sub>2</sub>O<sub>3</sub> ratio.

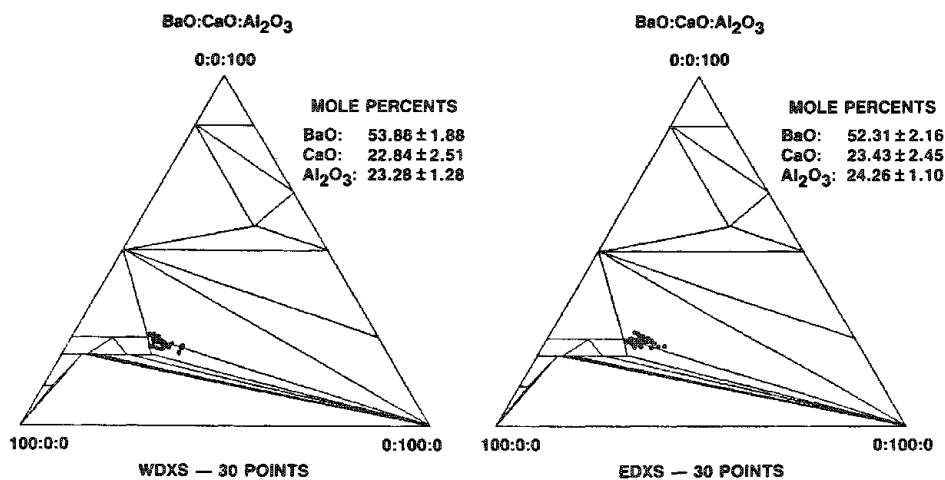


FIG. 2.--Analysis of unused cathode.

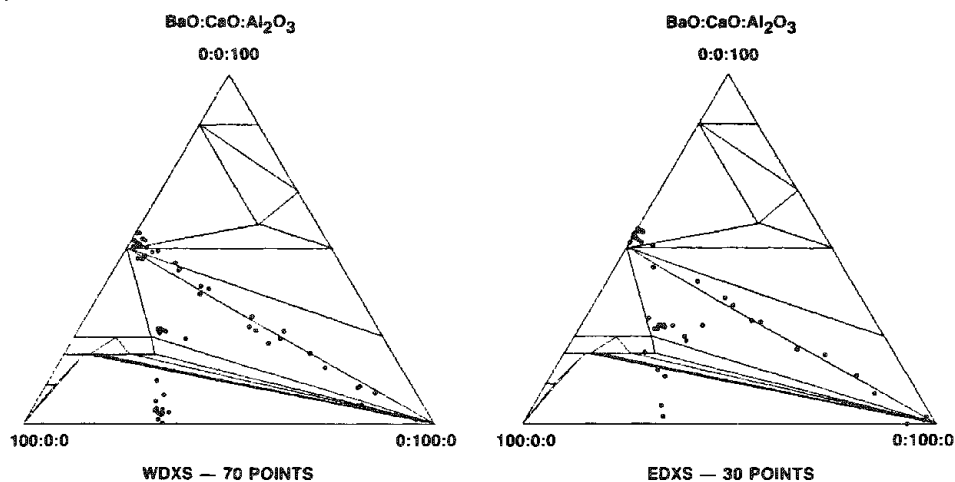


FIG. 3.--Analysis of used cathode.

## IN-PROCESS INSPECTION AND METROLOGY OF SEMICONDUCTOR WAFERS WITH THE USE OF AN AUTOMATED LOW-VOLTAGE SEM

M. H. Bennett and G. E. Fuller

Fabrication of shrinking integrated circuits in silicon has pushed inspection and measurement requirements beyond the resolving power of the optical microscope. Inspection and linewidth measurement (metrology) of submicron patterns now require the use of the scanning electron microscope (SEM). Inspection has several requirements:

1. It must be done in real time, while wafers are in process.
2. It must be nondestructive, which excludes conductive coating, so that wafers can be returned to the process flow and maintain maximum yield.
3. It must be low voltage to prevent radiation damage to transistor functions.

Instrumentation available until recently has used high accelerating voltage and required conductively coated small samples. It is now possible to perform whole-wafer, in-process inspection in a nondestructive manner.

### *Experimental*

The instrument used in these experiments is the Nanometrics CwikSCAN III-EZ. The instrument accommodates whole wafers and operates at a fixed beam voltage of 1 kV. The electron beam is generated in a thermally assisted field-emission source (a Schottky emitter) composed of a heated zirconiated tungsten crystal.<sup>1</sup> Inspection and metrology are highly computer controlled, accomplished through keyboard interaction rather than through a large array of front-panel controls.

Silicon wafers 4 in. in diameter coated with 0.5  $\mu\text{m}$  of chemically vapor-deposited polycrystalline silicon were used for the testing described here. Patterning of submicron lines in positive photoresist is done with a 10 $\times$  reduction stepper. After the wafer is loaded into the SEM and the area of interest is found, the SEM image is optimized through manual focusing and stigmatism. Then the image is digitally processed, stored in memory, and "frozen." A video intensity profile across the stored image can be obtained to aid in setting up optimum measurement parameters. Photoresist linewidth measurements are then made according to these parameters through automatic edge detection and calculation algorithms.<sup>2</sup> Included in the measurement algorithm is a calibration in which the system computer calculates slope and offset of the measured versus actual linewidth correlation based on measurements of two known linewidths. NBS traceable measurement standards are unavailable in the submicron regime. Therefore the "known" calibration standards are determined by comparison of the linewidths measured on high-quality conventional SEM micrographs with the pitch of multiple lines in the same micrographs. The pitch is carefully controlled by a laser interferometer on the electron-beam pattern generator used to produce the 10 $\times$  optical stepper reticles.

### *Results and Discussion*

The two principal uses for this SEM are inspection of patterned silicon wafers to determine the quality of the wafer processing and the measurement of pattern features, typically photoresist images, oxide openings, or metal leads.

For inspection purposes, SEM images obtained from a conventional instrument (JEOL JSM-845) operating at 15 kV on a gold-coated sample and the CwikSCAN images of an uncoated sample are comparable, as shown in Fig. 1. There is an obvious difference in contrast and sharpness, but all the important information about the photoresist profile is seen in both images. To satisfy the whole wafer inspection requirements described in the introduction, the nondestructive 1kV observation is mandatory.

The ability to image wafer pattern geometries clearly is also vital to accurate linewidth measurement. In addition, several other instrumental factors are important,

---

The authors are at Texas Instruments Inc., Box 225621 (MS 944), Dallas, TX 75265.

particularly the method of detecting the edges of pattern features, accurate rotational alignment of the sample, and optimum focus setting.

The linewidth measurements are obtained from the video image intensity profiles mentioned above. Three examples of such profiles and their corresponding images are shown in Fig. 2. The principal user variable in setting up the linewidth measurement procedure is the threshold. This variable describes the relative position along the rising or falling slope of the video profile which is declared to be the "edge" of the pattern feature. Possible choices of threshold are from 0 to 100%. The effect of various threshold percentages used to measure a 0.8 $\mu$ m photoresist line on a polycrystalline silicon-covered wafer is seen in Fig. 3. Three important features are seen: (1) the linewidth measurement changes monotonically with threshold setting, a direct result of the slope in the video profile and related to the resolution capability of the SEM; (2) the precision of the measurements is best in the range of thresholds from about 40% to 60%; and (3) the rate of change in measurement as a function of threshold is lowest in the 40%-60% threshold range.

This result demonstrates that the threshold is a variable that must be optimized to obtain the best precision and repeatability. The monotonic change in measurement with threshold is actually not an issue, since the correct linewidth is obtained through an independent calibration not directly involving threshold optimization. The independence of the measurement threshold from the calibration is very important. In some earlier instruments the only method for linewidth measurement calibration was the adjustment of the threshold. In numerous cases the required threshold was very low, less than 10%, which led to unacceptable measurement precision and repeatability.

The Cwikscan III-EZ is designed to give the best imaging and accurate linewidth measurements when the wafer is tilted at a substantial angle, typically 45°. Although it has been determined that accurate and precise measurements are indeed possible when the sample is tilted, it has also been noted that very careful adjustment of the rotational orientation of the patterns to be measured is required. In addition to the usual cosine error when oblique measurements are made on untilted samples, there is another error on tilted samples due to geometrical distortion of the image. The effect of wafer rotation on the video profile and linewidth measurement is seen in Fig. 2. When the wafer is measured as loaded with no intentional physical rotation, video profiles of the left and right edges of the photoresist pattern are slightly unequal (A). When the wafer is rotated by 2° CCW, left and right edge video profiles approximately equal (B). When the wafer is rotated an additional 5° CCW, video profiles are significantly distorted (C). These results show both the sensitivity of the imaging of tilted samples to physical sample rotation and the misalignment of the scan coil axis and stage tilt axis on this particular SEM instrument by about 2°. As expected, application of electronic scan rotation makes no difference to either video profile or measurement.

The impact of improper focus on the quality of linewidth measurements was determined by intentional overfocusing and underfocusing to a degree that even the most casual untrained observer would detect as poor focusing while still maintaining a clearly discernible image. Linewidth measurements made under these conditions do not vary from the measurement of an optimally focused image by more than a few nanometers.

### *Conclusions*

Previous limitations to nondestructive whole wafer inspection are now overcome.<sup>3</sup> However, some problems remain. Fixed-beam voltage is not optimum for all substrates used in semiconductor fabrication. At 1 kV, for example, photoresist charges slightly positive, and polysilicon and oxides charge slightly negative. Tilting minimizes charging effects, but at the 45° tilt used for these experiments wafer rotation becomes critical due to beam/wafer geometrical distortion and causes inaccuracy in measurement values. Instrument sensitivity to vibration and stray magnetic fields are a primary environmental concern. Stray fields cause "S" distortion of images (Fig. 2). Despite these issues to be resolved and the fact that this type of instrumentation is still evolving, our experience has shown this tool to be most valuable in semiconductor device fabrication. It has been implemented in a clean-room environment for use by minimally trained operators. This instrument has demonstrated nondestructive imaging and inspection capability nearly equal to that of a conventional high voltage SEM in the magnification range up to about 25 000 $\times$ . Although careful setup and calibration of the SEM are critically important to the quality of the



measurements, the automated linewidth measurement capability provides much better accuracy and precision than conventional optical linewidth measurement instruments in the range of one micron features and less.

#### References

1. D. W. Tuggle and S. G. Watson, *Proc. 42nd Meetg. EMSA*, 1984, 454.
2. W. R. Roth and V. J. Coates, *Proc. SPIE* 1984, 471.
3. M. H. Bennett and J. T. Truett, *TSEM J.* 15: 36, 1984.

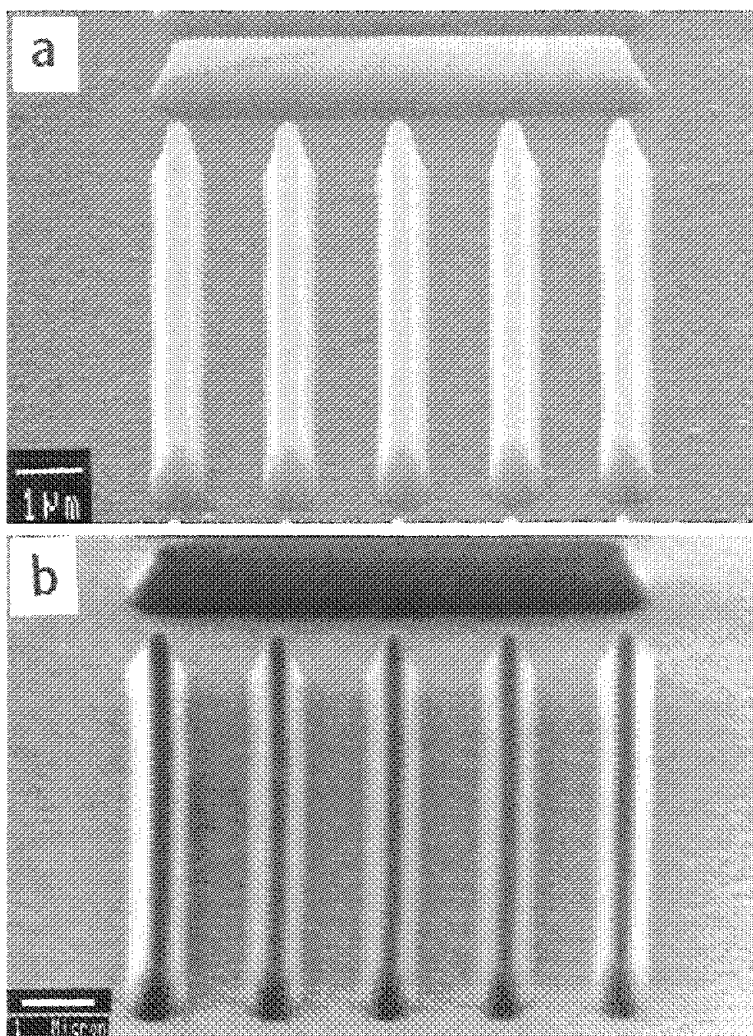


FIG. 1.--(a) Conventional SEM image of  $0.8\mu\text{m}$  resist lines on polysilicon at 15 kV; (b) comparable image of same lines at 1 kV.

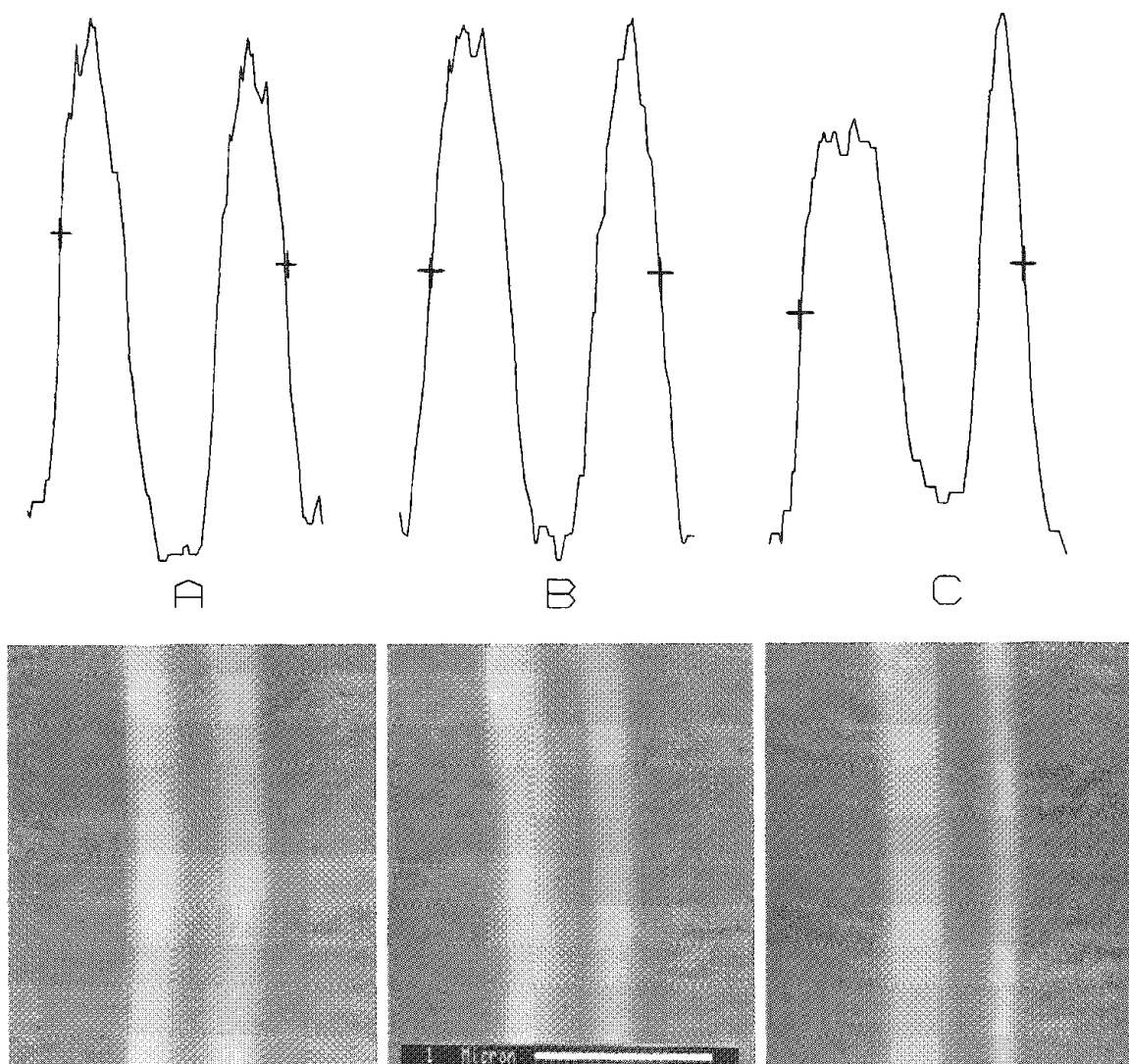


FIG. 2.--Effect of wafer rotation on video profiles and measurements of 0.8μm resist line on polysilicon: (a) no rotation, measures 0.766 μm; (b) 2° rotation, measures 0.773 μm; (c) 7° rotation, measures 0.759 μm. Crosses represent 50% thresholds determined by CWIK-SCAN measurement algorithm.

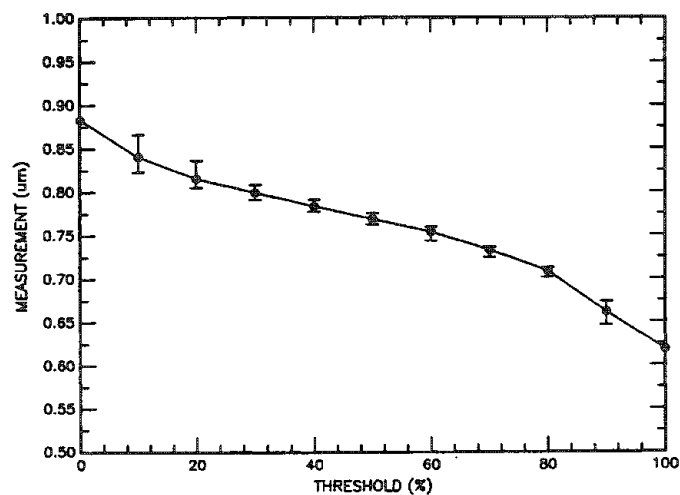


FIG. 3.--Effect of threshold percentage on measurements of 0.8μm resist line on polysilicon. Error bars represents maximum and minimum of 20 measurements.

## APPLICATIONS OF SEM AND XPS IN PLASMA ETCHING OF SINGLE CRYSTAL SILICON

Ram Sellamuthu, John Barkanic, Eugene Karwacki, and Ralph Jaccodine

Pattern transfer by plasma etching is a key step in the processing of semiconductor devices.<sup>1</sup> In this process, the substrate is etched both in the vertical and lateral directions. The lateral etching results in undercutting, an undesirable characteristic, as it gives rise to the loss of linewidth. Since the dimension of the pattern is in the micron range, we have used scanning electron microscopy (SEM) to observe the surface morphology and to characterize the undercut. In addition, SEM has been employed to determine the etch rate.

For certain plasma chemistries, a polymer is deposited on the exposed surface during etching.<sup>2</sup> The beneficial effect of the polymer film is that it acts as a sidewall passivating layer and so reduces the undercut.<sup>3</sup> In order to characterize the polymer, x-ray photoelectron spectroscopy (XPS) has been used.<sup>2,4</sup> However, the use of small-area XPS characterization has not been reported previously. Therefore, we have developed and used this procedure in this study so that the pattern surface can be analyzed without any interference from the mask region.

### *Experimental*

A parallel-plate, radial-flow, 13.56MHz plasma etching unit was used for etching single crystal Si wafers with  $\text{NF}_3$ - $\text{CF}_2\text{Cl}_2$ . The pressure, power density, and flow rate were maintained at 140 mTorr, 0.4 W/cm<sup>2</sup>, and 20 standard cm<sup>3</sup>/min while the concentration of  $\text{CF}_2\text{Cl}_2$  was varied. The etched wafer was cleaved and mounted on an SEM stub. The surface morphology was observed with an ETEC SEM at 20 kV. The etch rate was determined from the etch depth measured from the SEM micrograph divided by the etch time. A Perkin-Elmer PHI 5100 modified to perform small-area analysis was used for the XPS characterization. A Mg K $\alpha$  x-ray source was used with the voltage and the current was maintained at 15 kV and 20 mA, respectively. All spectra were collected at a collection angle of 45°. Small-area analysis was performed by a 600 $\mu\text{m}$ -diameter spot. The use of such a small area facilitated the analysis to be performed on the Si surface excluding the mask region.

### *Results and Discussion*

Figures 1 and 2 show the XPS survey spectra obtained on the Si region for experiments with 100%  $\text{NF}_3$  and  $\text{NF}_3$ -50%  $\text{CF}_2\text{Cl}_2$ , respectively. The F(1s) peak present in Fig. 1 is considered negligible, whereas the peak observed in Fig. 2 is very significant. Figures 3 and 4 show the C(1s) spectra obtained for the two cases, respectively. A peak position of 285 eV has been assigned to carbon present as hydrocarbon.<sup>5</sup> In the case of 100%  $\text{NF}_3$  etching, the peak position is shifted to about 286 eV. However, the absence of any significant amount of fluorine (Fig. 1) implies that the film is not polymeric.<sup>5</sup> Therefore, the shift is only due to a contaminating layer formed during the exposure of the wafer to the atmosphere. In addition to the hydrocarbon peak at 285 eV, the peaks at 288.5 and 295 eV shown in Fig. 4 were identified and characterized as those of CHF and  $\text{CF}_3$  groups, respectively.<sup>5</sup> This observation confirms that the nature of the film is polymeric. Figures 5 and 6 show the spectra obtained for the wafer etched with  $\text{NF}_3$ -40%  $\text{CF}_2\text{Cl}_2$ . In this case, the F(1s) peak height is small and the  $\text{CF}_3$  group is absent (Fig. 6). Therefore we may infer that the nature of the polymer formed during etching depends on the concentration of  $\text{CF}_2\text{Cl}_2$ .

Figures 7, 8, and 9 show the etch profiles for experiments with 100%  $\text{NF}_3$ ,  $\text{NF}_3$ -50%  $\text{CF}_2\text{Cl}_2$ , and  $\text{NF}_3$ -40%  $\text{CF}_2\text{Cl}_2$ , respectively. Figure 7 shows the presence of a significant

---

Authors Sellamuthu and Jaccodine are at the Department of Materials Science and Engineering, Lehigh University, Bethlehem, PA 18015; authors Barkanic and Karwacki are at Air Products and Chemical Company, Allentown, PA 18105. Support by Air Products and Chemicals Company and Ben Franklin Partnership Program is acknowledged.

undercut, whereas Fig. 8 shows a negligible undercut. The polymer film is expected to form on the sidewall as it forms on the bottom surface of the trench. It was possible to make such an inference only because we used a small-area XPS analysis. The polymer film on the sidewall is impervious to the penetration of etchant species, resulting in no lateral etching. In contrast, the vertical etching occurs because the ions bombarding the bottom surface break the film and make it easy for the etchant to reach the Si surface. As a result of sidewall passivation by the polymer film, the undercut is reduced for  $\text{NF}_3$ -50%  $\text{CF}_2\text{Cl}_2$  etching. Although a polymeric film has also been observed for the case of  $\text{NF}_3$ -40%  $\text{CF}_2\text{Cl}_2$  etching, the absence of  $\text{CF}_3$  group (Fig. 6) indicates that the film is not completely impervious to lateral etching.

The measured etch rates are 0.2, 0.4, and 0.8  $\mu\text{m}/\text{min}$  for 100%  $\text{NF}_3$ ,  $\text{NF}_3$ -50%  $\text{CF}_2\text{Cl}_2$ , and  $\text{NF}_3$ -40%  $\text{CF}_2\text{Cl}_2$ , respectively. The results of this work are considered applicable to the etching of monocrystalline and polycrystalline Si in the fabrication of high-density semiconductor chips.

### Conclusions

SEM has been used as an effective tool to study the surface morphology and to determine the etch rate of Si. A small-area XPS technique has been developed in this work to study the polymer film deposited during etching. Furthermore, this technique has been applied to identify and characterize the film. The polymer acts as a sidewall passivating layer, thereby reducing the undercut. The results are applicable to monocrystalline and polycrystalline Si etching in device processing.

### References

1. S. M. Sze, *VLSI Technology*, New York: McGraw-Hill Book Company, 1983.
2. D. L. Flamm, P. L. Cowan, and J. A. Golovchenko, *J. Vac. Sci. Technol.* 17: 1341-1347, 1980.
3. M. Kimizuka and K. Hirata, *J. Vac. Sci. Technol.* B3: 16-19, 1985.
4. C. G. Tuppen, R. Heckingbottom, M. Gill, C. Heslop, and G. J. Davies, *Surface and Interface Analysis* 6: 267-273, 1984.
5. G. E. Muilenberg, *Handbook of X-ray Photoelectron Spectroscopy*, Eden Prairie: Perkin-Elmer Corporation, 1978.

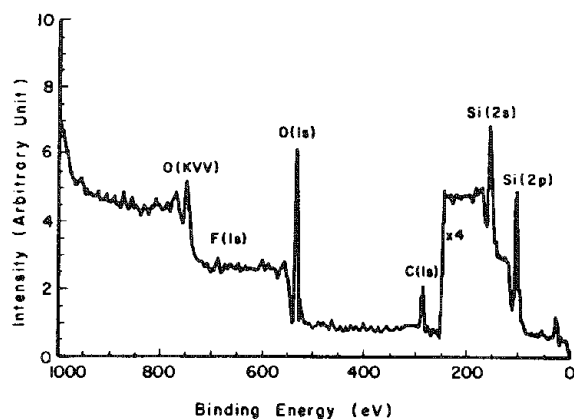


FIG. 1.--XPS survey spectrum for etching with 100%  $\text{NF}_3$

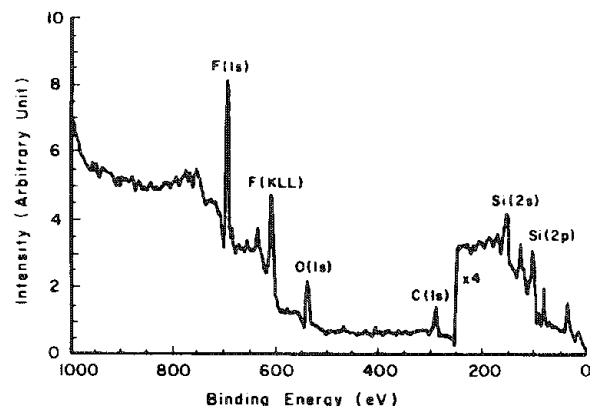


FIG. 2.--XPS survey spectrum for etching with  $\text{NF}_3$ -50%  $\text{CF}_2\text{Cl}_2$ .

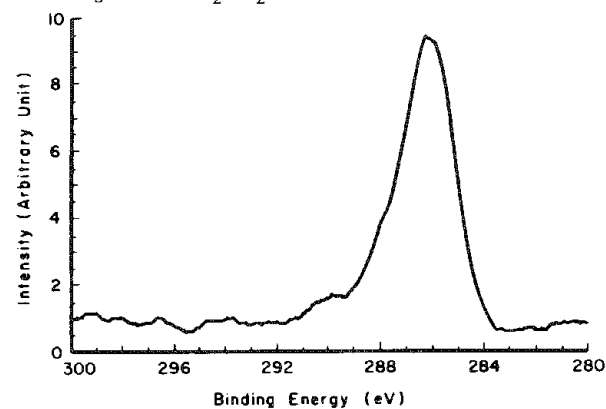


FIG. 3.--C(1s) spectrum for etching with 100%  $\text{NF}_3$ .

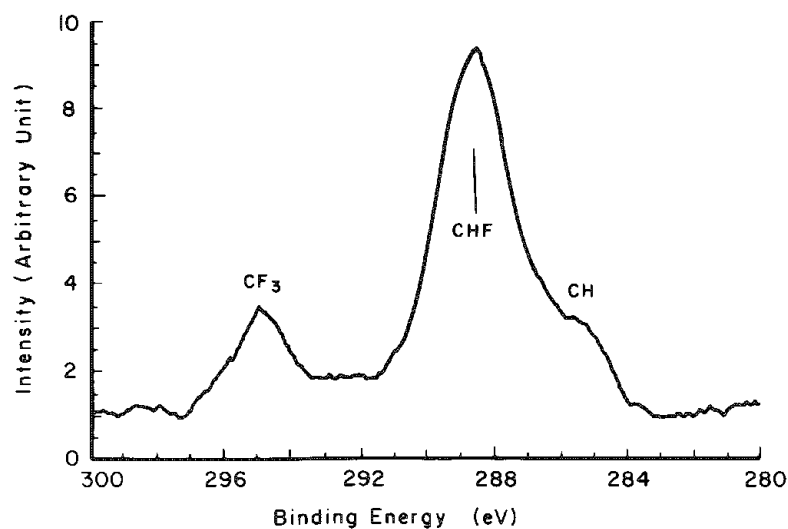


FIG. 4.--C(1s) spectrum for etching with  $\text{NF}_3$ -50%  $\text{CF}_2\text{Cl}_2$ .

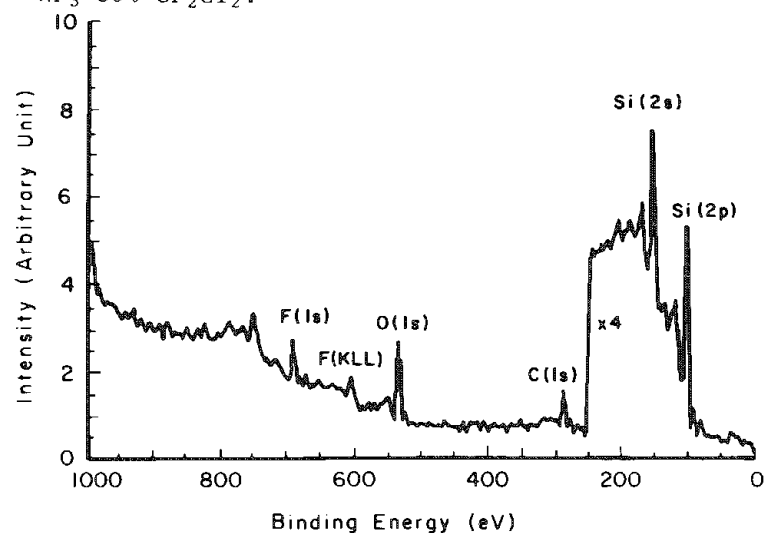


FIG. 5.--XPS survey spectrum for etching with  $\text{NF}_3$ -40%  $\text{CF}_2\text{Cl}_2$ .

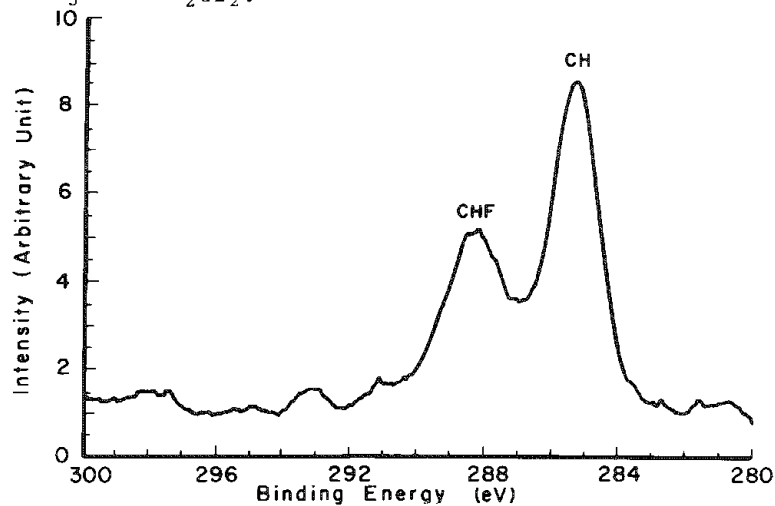
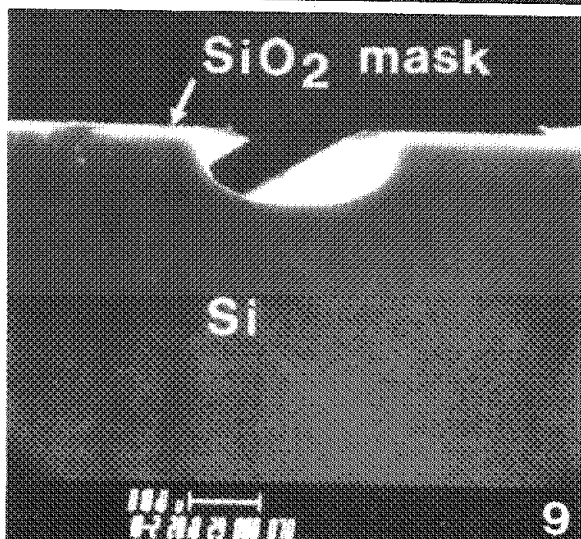
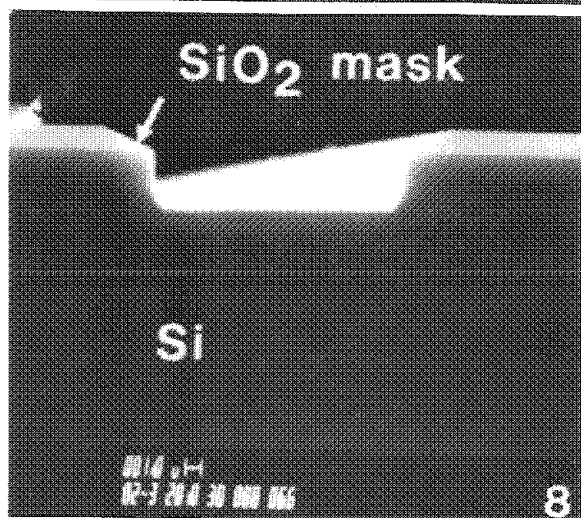
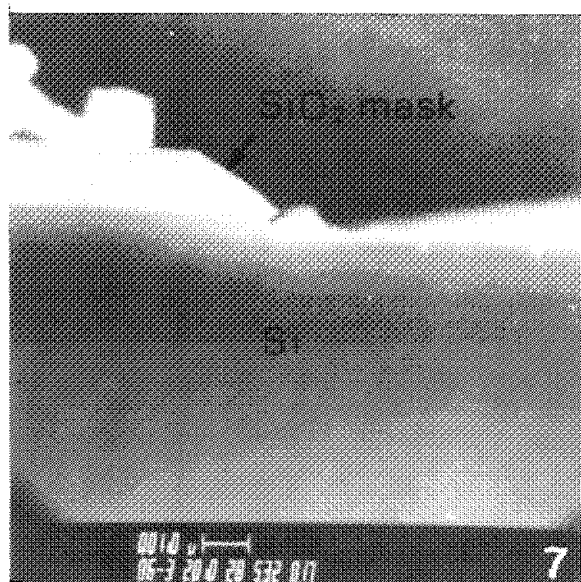


FIG. 6.--C(1s) spectrum for etching  $\text{NF}_3$ -40%  $\text{CF}_2\text{Cl}_2$ .



Electron micrographs showing: Fig. 7, large undercut (100%  $\text{NF}_3$ ); Fig. 8, small undercut ( $\text{NF}_3$ -50%  $\text{CF}_2\text{Cl}_2$ ); Fig. 9, large undercut ( $\text{NF}_3$ -40%  $\text{CF}_2\text{Cl}_2$ ).

## MICROCIRCUIT TRACE CUTTING WITH FOCUSED ION BEAMS

G. W. Stupian and M. S. Leung

When a failed microelectronic device is examined in a scanning electron microscope (SEM), several possible failure sites are often visible. Positive identification of the primary failure site, based on secondary electron micrographs alone, is difficult. Several other SEM imaging modes--e.g., electron beam induced current ("EBIC") and voltage contrast imaging--have been shown to be very helpful in identifying failure sites and clarifying failure mechanisms. These methods involve collecting current or supplying voltage signals through external leads connected to the specimen. Unfortunately, the application of these techniques is precluded if, as is often the case, shorting of device elements (traces) occurs as a result of catastrophic failure. Failure analysis is facilitated if trace metallizations can be cut selectively to isolate the electrically shorted portions of the device. By clearing of a short, failure sites can be identified. Measurements of circuit parameters of the remaining part of a device are also made possible, and may provide information about the degradation mechanism. In addition, the removal of electrical shorts by trace cutting permits the application of techniques such as EBIC to portions of a device where degradation may have occurred but where the "evidence" has not been obscured by catastrophic failure. Metallization widths in many microelectronic circuits are in the 1  $\mu\text{m}$  range; cutting techniques that can provide high spatial resolution are essential. Each method currently employed for trace cutting has certain advantages and limitations. We report here on the use of a focused ion beam from an ion microprobe for precision trace cutting. This cutting technique offers high spatial resolution and the opportunity of incorporating a sensitive method for end-point detection.

Trace-cutting techniques now in use include mechanical cutting with fine probes, chemical etching, and laser cutting. Mechanical cutting is a simple technique that requires only a microscope and a micromanipulator with a probe that has a sharp edge. However, probes small enough to afford good spatial resolution are difficult to manipulate. An additional complication is that soft metals, such as gold, simply smear when contacted by a mechanical probe and it is very difficult to break the conducting path completely. Chemical etching is difficult to apply selectively to narrow traces. Surface-tension effects are important with small drops, and liquid tends to flow where it is not wanted. The necessity for removal of etchant after use further complicates the procedure.

Laser-trace cutting is the technique most directly comparable with ion beam cutting.<sup>1</sup> Laser cutting is a thermal ablative process in which material is removed from the target by a series of pulses from a xenon or YAG laser. The minimum apparent size of the crater made by a laser cutter depends on the thickness of the metal being cut, but seems typically to be around 2  $\mu\text{m}$ . Certain features inherent to laser cutting make control of the process difficult. Light absorption, for example, varies among materials. On a passivated trace, laser light penetrates the oxide and is absorbed by the metal underneath to produce a small "explosion." Cuts made by ablation are often surrounded by debris, which can immensely complicate subsequent steps necessary in the analysis. In addition, compound semiconductors, such as gallium arsenide, decompose at the temperatures generated by laser cutting and on these materials the substrate beneath the target metal can be damaged.

Focused ion beam cutting can be accomplished by use of an ion microprobe designed primarily for elemental analysis. The incident ions sputter material from the specimen as gaseous ionic or molecular species, leaving little or no residue. Sputtered species are analyzed by a mass spectrometer to provide a chemical analysis of the specimen; in fact, mass analysis provides a convenient way of determining when a metallization has been severed. We have found that the trace-cutting capability of the ion probe, in combination

---

The authors are at the Aerospace Corp., Box 92957, Los Angeles, CA 90009. This work was supported in part by the U.S. Air Force under Space Division contract F04701-85-C-0086. The assistance of N. Marquez is also gratefully acknowledged.

with its capability for elemental analysis, makes it an especially useful instrument for the analysis of electronic devices.

### *Experimental*

The ion probe in our laboratory was manufactured by Applied Research Laboratories. Ions can be focused to a spot with a minimum diameter of about 2  $\mu\text{m}$  to provide elemental analyses with high spatial resolution. In addition to producing a small circular spot, the beam can be rastered along a line or over a rectangular area. The size and shape of a cut can thus be chosen with considerable freedom. The ion beam was positioned on the test circuit by a 200 $\times$  optical microscope, and the specimen was observed during the sputtering. Sputtering was continued until a trace appeared to have been severed, as evidenced first by the appearance of a metallic luster as overlying glassivation was removed, followed by the apparent disappearance of metal. The beam diameter was 2  $\mu\text{m}$ , the ion energy 20 keV, and the beam current was 0.5 nA. A commercial microwave power gallium arsenide field-effect transistor (GaAs FET) was employed as a test device in this study (Fig. 1). An FET is essentially a voltage controlled resistor which consists of a semiconducting channel connected to ohmic (source and drain) contacts at each end. The current flowing through the conducting channel is controlled by a voltage applied to a Schottky contact (the gate) placed between the drain and the source, and the gate is reverse biased in normal operation so that the input impedance is high. Two cuts were required to isolate a segment of the gate circuit because of a "wrap-around" gate geometry, and each required a sputtering time of about 5 min.

The electrical isolation of traces by ion cutting is demonstrated by use of the EBIC imaging mode in a scanning electron microscope (SEM). When an incident electron beam impinges on the gate of an FET, the electron-hole pairs generated by the beam are separated by the electric field intrinsic to the Schottky junction between the overlying gate metallization and the GaAs. The gate Schottky barrier acts as a solid-state electron multiplier. As the SEM beam rasters across the device, an EBIC image is formed by use of the current collected from the gate lead of the FET (with drain and source leads grounded) as the SEM display input. The regions of the gate that have both a functioning Schottky barrier and are electrically connected to the external gate lead appear bright in an EBIC micrograph.

### *Results and Discussion*

The connectivity of the gate metallization is shown by the EBIC picture of Fig. 2, taken before trace cutting. There are no gaps in the gate metallization, which appears as a bright pattern. A region of the gate was selected for isolation by ion trace cutting. The EBIC micrograph obtained after ion trace cutting (Fig. 3) clearly shows that the section of the gate between the ion beam cuts has been electrically isolated. Ion cutting did not leave much debris. The cuts are clean and well defined (Fig. 4).

Although the mass spectrum peaks from the metallization or substrate can in general be used as "end-point" detectors to minimize the amount of cutting needed, the spectrometer output was not monitored during trace cutting in this particular test case because of an unfavorable geometry of the device and our ion microprobe. The FET chip is at the bottom of a relatively narrow and deep package which interfered with positioning of the mass spectrometer pickup electrode.

A number of mechanisms can be involved in the degradation of GaAs FETs, including electromigration in both drain and source and gate metallizations, as well as electromigration across the channel. RF and DC characteristics may exhibit gradual degradation with some retention of function, but failure is often catastrophic. Traces melt, and the gate is usually shorted to the drain and source. If damage is not too excessive, shorted portions of the gate may be isolated by trace cutting. EBIC imaging can then provide information about the integrity of the remaining portions of the gate metallization, which can help in identifying the degradation mechanism.

Trace cutting with focused ion beams has other potential microelectronic applications besides failure analysis. One such application is the isolation of defective or redundant sections of circuits to improve yield as individual devices on a wafer become larger and more complex.



### Conclusion

In addition to providing elemental analyses with high spatial resolution, we have shown that an ion microprobe is a valuable tool for precision trace cutting in microcircuits. Trace cutting helps provide positive identification of failure sites and helps resolve ambiguities which may arise when several possible failure sites are found.

### References

1. R. L. Waters and J. K. Logan, "Methods of trace cutting for diagnostic probing of semiconductor devices," *Proc. 1984 International Symposium for Failure Analysis*, Los Angeles, Calif.

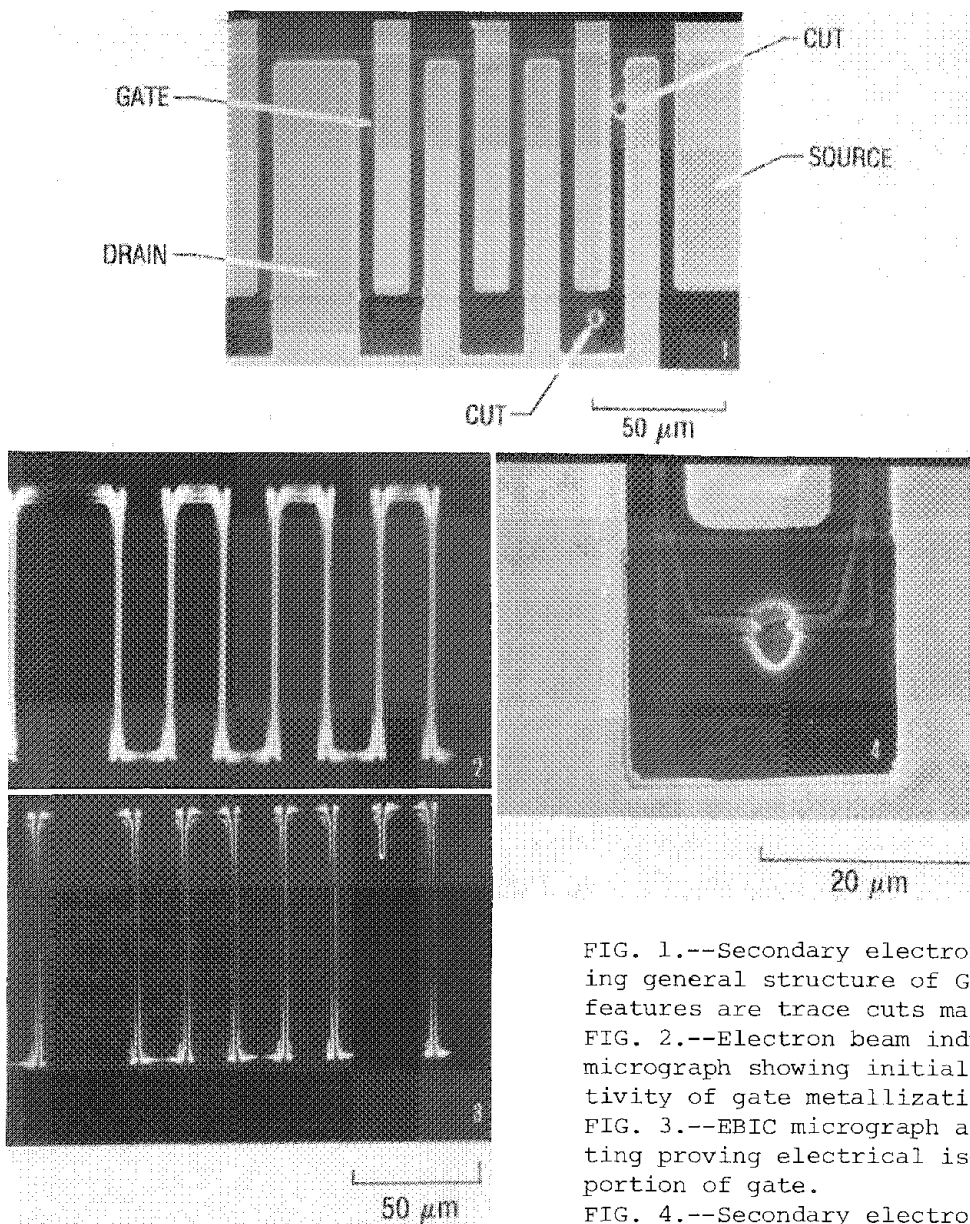


FIG. 1.--Secondary electron micrograph showing general structure of GaAs FET. Circular features are trace cuts made by ion beam.  
FIG. 2.--Electron beam induced current (EBIC) micrograph showing initial electrical connectivity of gate metallization.  
FIG. 3.--EBIC micrograph after ion trace cutting proving electrical isolation of target portion of gate.  
FIG. 4.--Secondary electron micrograph showing ion cut in more detail.



## MULTIPLE APPLICATIONS OF TEM/STEM TO THE INSPECTION OF COMPONENTS USED IN THE MANUFACTURE OF COMPUTERS

Richard Flutie and Normal Riel

The transmission electron microscope (TEM) has enjoyed a resurgence in electronics. The instrument has long been used to bridge the gap between the scanning electron microscope and the need for a higher-resolution imager. In electronics, the TEM has been mostly used for inspecting materials used in the wafer manufacture.<sup>2</sup>

At Digital Equipment we started again to utilize TEM on ion-milled cross sections and lateral sections.<sup>2</sup> However, it became evident that the high-resolution instrument could also be used in other applications where the SEM was less than perfect. It was at this point that management gave the professional staff the go-ahead to investigate and develop both new and existing methods of TEM applications to the electronics industry. We found that many of the older TEM techniques produced outstanding information when applied to the newer samples found in the high-tech industry.

This paper shows how we have found success by re-educating the scientific staff to the potential of older TEM methods applied to these newer components. It was almost as though the newer staff members had not been exposed to the potent microanalytical technique of the TEM/STEM. To those of us who had the experience, it was almost as though we had forgotten how powerful the instrument and its associated techniques could be.

### *Replication*

If the surface of the specimen is too flat to be properly characterized by the SEM, the replication technique is used (Fig. 1). In this method the surface is replicated with an electron-transparent material and then stripped so that we inspect the replica with the TEM. At DEC we have inspected wafer fab insulators this way. In some cases the SEM would have a charging problem. In general we have used the replica technique in IC wafer fab processing and media applications (heads and head substrates). Figure 2 is a replica of a treated head substrate. As we treat it we can determine changes in surface topology that affect the magnetic performance of the head, which is manufactured at a later step. The shadowing step in the replica (Fig. 1) if carefully controlled can be used to quantify surface texture. The shadow length can be measured on the final print. Using the shadow angle, the investigator can calculate the height of the features that cast the shadows. In Fig. 2, the surface texture is about 500 Å high (background surface detail). The original prints vary in magnification from 130 300× to 230 000× in these studies. These magnifications are required because the surface detail is so small and the sample is so flat.

### *Extraction Replication*

In some applications of wafer fab analysis, contamination can be extracted by use of a two-stage replication technique. In this case a cellulose acetate tape is moistened with acetone, placed directly onto the contaminated wafer (or finished device), and allowed to dry. Then we remove the replica by peeling the tape away, bringing with it the contamination. Then the contaminated side is coated with carbon and the tape is dissolved away. At this point one can shadow the side of the carbon that had the tape before the tape was dissolved away. One must be careful to shadow the correct side of the replica to obtain proper surface detail. After shadowing, the carbon replica can be TEM inspected and microanalyzed by EDX, WDX, or electron diffraction.

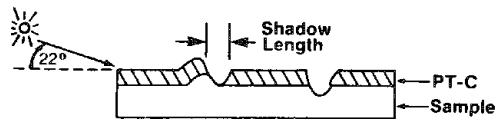
Figure 3 is a double-stage extraction replica of a contaminated wafer. The particles had not been identified by EDX on the wafer due to their small size. By properly performing this technique we were able to identify the particles and determine their origin to eliminate the problem. Shown in Fig. 3 is the diffraction pattern from one particle. This result is important because now we can identify smaller areas than we could with the SEM

---

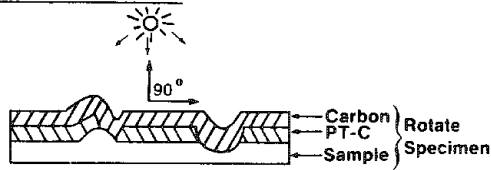
The authors are at the Digital Equipment Corp., 30 Forbes Road, Northboro, MA 01532.

# Replica Process For The Transmission Electron Microscope Inspection Of Smooth Surfaces

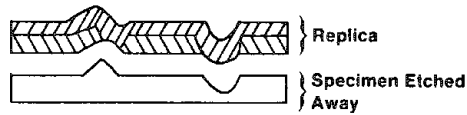
## 1 PT-C SHADOW:



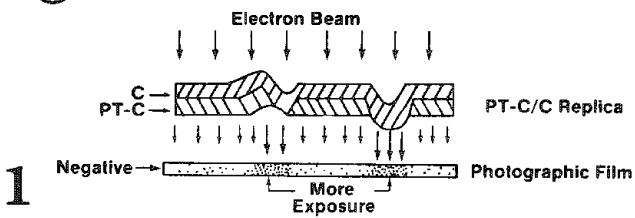
## 2 CARBON EVAPORATION:



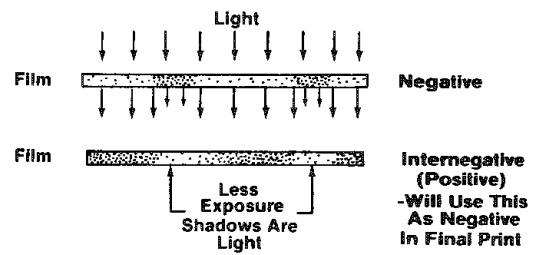
## 3 SEPARATE SPECIMEN:



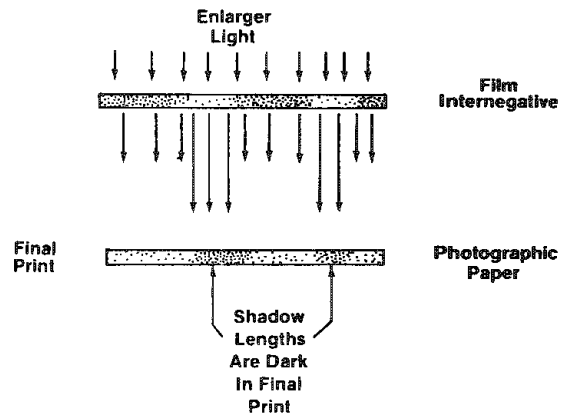
## 4 TEM INSPECT:



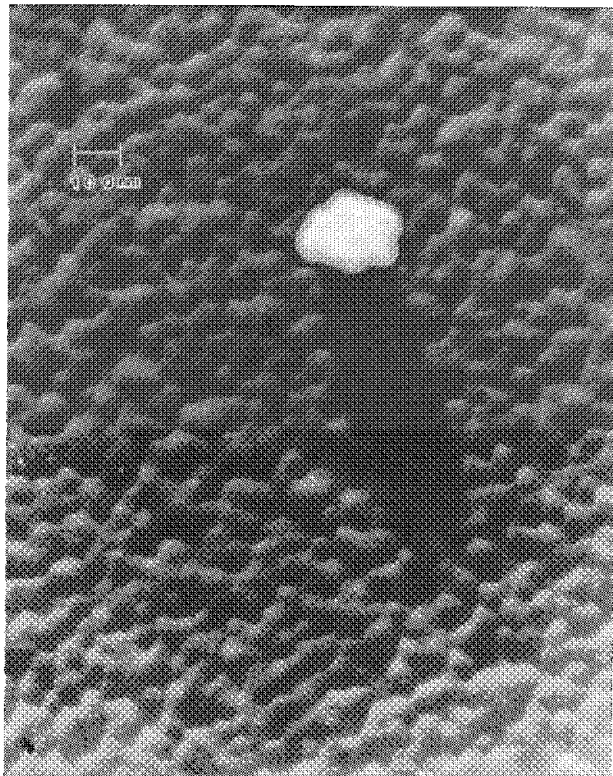
## 5 INTERNEGATIVE (POSITIVE)



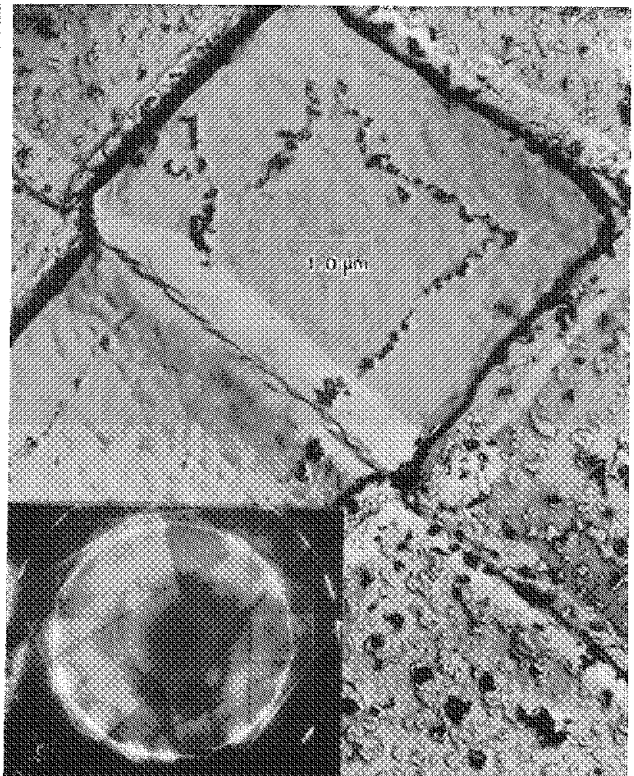
## 6 FINAL PRINT (PRINTED AS NEGATIVE):



1



2



3

EDX technique. EDX maps can be obtained at magnifications in excess of 50000 $\times$  when the STEM is used.

### *Microtome Methods*

Electron diffraction in the TEM/STEM mode of microtomed sliced sections of IC package leads, PC board metallization structures, and hard-surface disks reveals information that cannot be obtained any other way. Intermetallics formed between Cu and Sn on soldered connections can be identified uniquely. The problem is in the sample preparation. The analyzed specimen must be thin enough for the 100-200kV electron beam to penetrate (for electron diffraction).

We have been successful in slicing specimens with a diamond knife. The main object is to use an epoxy that sets up with the same hardness as the specimen. Figure 4 is a microtomed cross section of the very top surface of a hard surface disk. Microanalysis and structural studies can be performed on this specimen. We use these sliced sections to correlate ion milling rates on the Auger microprobe. That way we have more confidence in the depth profiles and the measured thickness obtained from the depth profile.

### *Grain Size Analysis*

By our previously described techniques<sup>3</sup> we can perform statistical size and grain analysis of thin films used in wafer processing. Figure 5 is a lateral section of Cu-Si doped aluminum. It was the actual metallization, in place on a finished device. The devices had been through a reliability test, current stressing the metal to determine the effect on the grain growth, which affects the long-term reliability. The TEM prints are measured on a graphics tablet and the data are used to calculate standard statistical parameters. We use the VIDS III display system manufactured by Optomax in Burlington, Mass. Figure 6 is a typical analysis of poly-silicon grain size.

### *Lateral and Horizontal Sections*

As described in the previous section, lateral sections are used for grain-size analysis. Figure 7 reveals the advantage of using the TEM over the SEM when individual fuse links in PROMs are inspected. To inspect with the SEM we must destroy the top and bottom environment of the fuse. Using TEM sample preparation methods,<sup>3</sup> we can inspect the fuse as it really is. At the same time we are inspecting it with much higher resolution, both in the imaging mode and the microanalytical mode.

Cross-section (vertical-section) TEM analysis has become an important tool in both wafer fab and finished devices.<sup>3</sup> Figure 8 shows how the TEM can be used to characterize VLSI structures, both in wafer fab and finished devices. Multilayered structures can be accurately measured and they can be microanalyzed with a resolution below 50 Å.

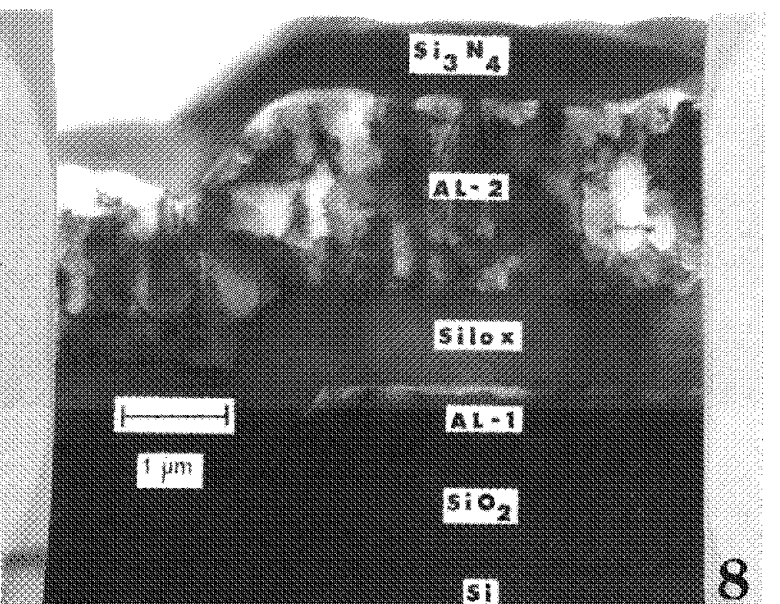
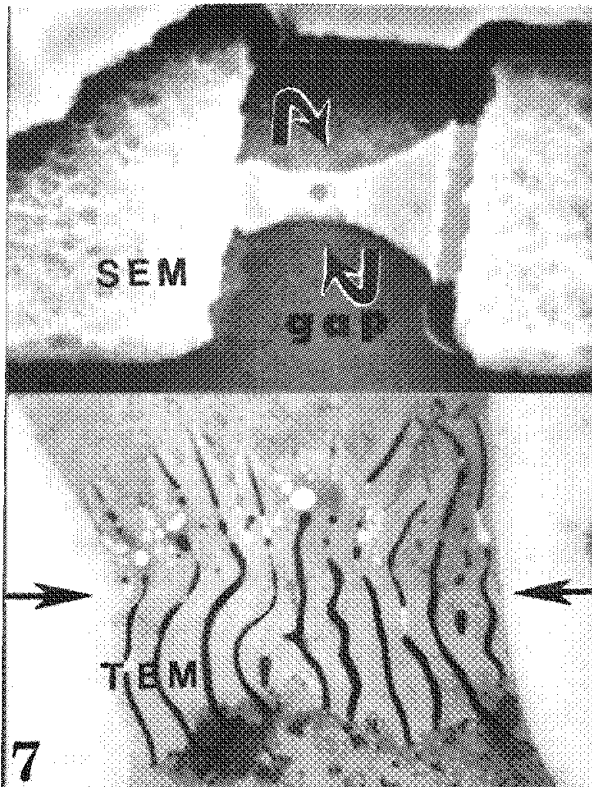
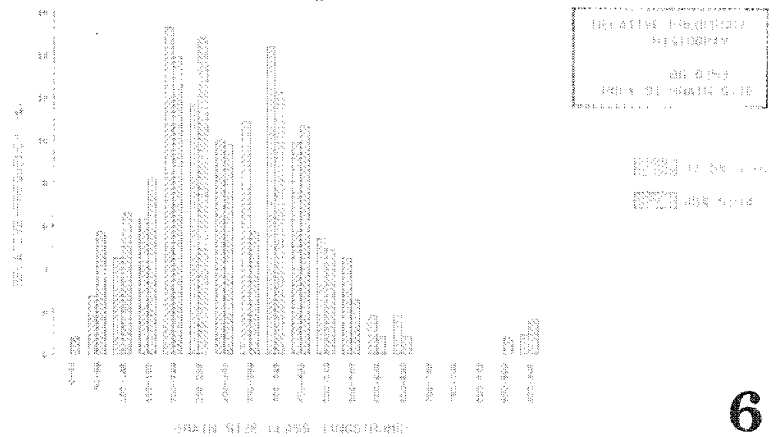
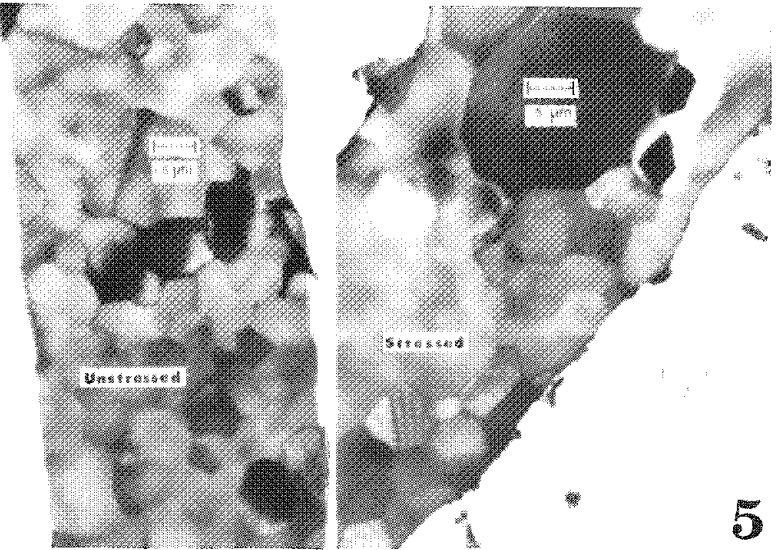
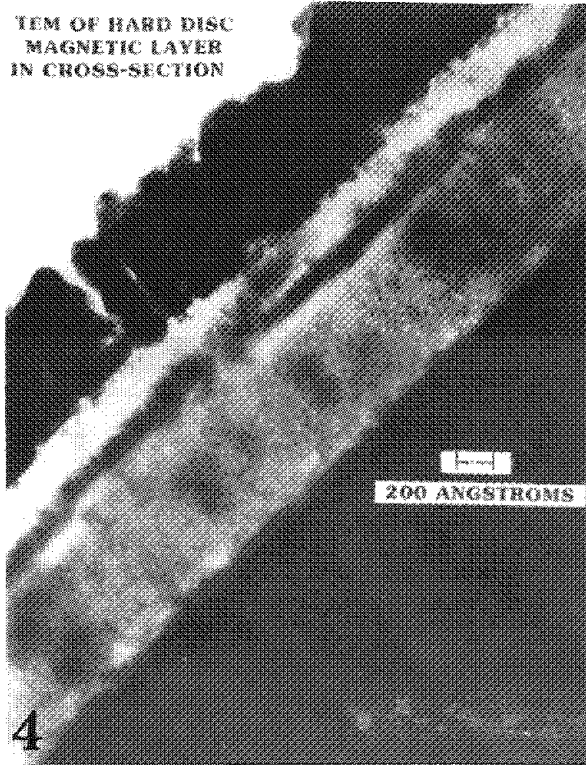
### *Summary*

Although the new popularity of the TEM in the electronics field came about from inspections of cross sections of VLSI structures, its use has been expanded by the application of older TEM methods to the newer electronic problems. This expansion of application is expected to continue in the future.

### *References*

1. W. E. Ham et al., *RCA Review* 38: 351, 1977.
2. R. Flutie, IEEE International Reliability Physics Symposium, Microsectioning Tutorial Proceedings, Las Vegas, Nev., 1984.
3. R. Flutie, Materials Research Society, Problem Solving with the TEM, Boston, 1985.

TEM OF HARD DISC  
MAGNETIC LAYER  
IN CROSS-SECTION



## ELECTRON BEAM LITHOGRAPHY WITH A CONVENTIONAL SEM

P. E. Russell, Tyler North, and Thomas M. Moore

The concept of modifying a standard SEM for use as an electron-beam lithography system has been explored many times. As early as 1965 Broers had reported the use of an SEM as a lithography tool to fabricate submicron metal lines on a silicon wafer.<sup>1</sup> Although electron beam lithography systems have evolved to a very highly refined level of dedicated manufacturing instruments, there has remained a need for microfabrication capabilities that use a conventional SEM as the basic tool. Such capabilities are required by resist chemists who are developing a new or improved e-beam resist material or resist processing procedure, for investigators studying the basic mechanisms of fine-line lithography, and for the fabrication of simple test-device structures of submicron dimensions. The basic requirements of such a system are the ability to control the electron-beam position in predefined patterns, beam blanking to avoid unintentional exposure, dosage control, and sample stage control. In this work, we describe the development and use of such a system with minimal modification to a conventional SEM equipped with the now typical digital image system of a modern x-ray analysis package. The system is based on a Tracor Northern TN5500 x-ray analysis automation system with a microscan digital imaging package. It has been successfully used as a submicron lithography tool on two different SEMs (JEOL JSM 840 and JSM 35C).

### *Basic System Requirements*

The most fundamental requirement of an e-beam lithography system is that of beam position control. A high resolution digital scan generator is preferred, with control of the pixel spacing and the dwell time of each pixel. One must have the capability of easily defining a pixel pattern to be exposed by the beam, and control of a beam blanking system to avoid unwanted beam exposure of specific pattern regions. In addition to defining patterns of exposure, one must control the electron beam dose each region receives, by varying either the beam current or the exposure time. One must be able reproducibly to set a known beam current, beam voltage, and spot size. Since this system is intended to be used for developmental work, one must also be able to vary individual parameters and move the sample to a new region to make another exposure. Typically, this method will be used to generate an exposure series by varying the dose on adjacent exposures and then carefully inspecting the resulting patterns after processing. The e-beam exposure requires a relatively high beam voltage (20-50 keV); the subsequent inspection of the finished exposure series, to determine resist latitude and sensitivity, requires good low-voltage (0.5-5.0 keV) imaging capabilities.<sup>2</sup> The system described in this work fulfills all the above-mentioned requirements with no adverse effects on the basic performance of the SEM, and requires only additions of software to existing SEM and (x-ray based) digital imaging and SEM control hardware.

### *System Description*

Figure 1 shows the basic system concept in block diagram form. The main system consists of an LSI 11/73 CPU with one megabyte of memory, dual floppy disk drives, and a color display monitor. This system provides all control functions for the peripheral units as well as pattern generation and display capabilities. The microscan control unit is used to provide a computer-generated, digital, external input to the scan generator. This system was originally designed to control the imaging functions of an SEM to

---

Author Russell is with the Materials Engineering Department, North Carolina State University, Raleigh, NC 27695; author North is with Tracor Northern, Inc., Middleton, WI 53562; author Moore is with Texas Instruments, Inc., MS147, Box 225936, Dallas, TX 75265. They acknowledge the assistance of Grant Baughman, Tracor Northern, for software development; Doug Shultz, TI, for SEM operation; Keith Bradshaw, TI, for resist preparation and for sharing his experience in e-beam lithography; and Kaz Ogura, JEOL, for artistic pattern generation.

facilitate x-ray mapping and/or image analysis. A software package (titled LITHO) has been developed that controls the following functions:

- (1) scanning pattern generation,
- (2) dwell time at each digital image pixel,
- (3) beam scanning coils,
- (4) beam blanking via blanking coils, and
- (5) stage motion via stepping motor controls.

The hardware units, in addition to the basic SEM, include the scan generator interface, the beam blanking interface, stage motor drives and control unit, and output drives to control the SEM viewing and photo CRTs, the color display screen, and a printer.

The control software has been organized into a menu-driven format. The main menu allows selection of setup functions, actual exposure functions, and other tasks such as input or storage of patterns to and from disks. The setup routines include pattern setup, which is used to create a binary pixel map of the pattern to be written. Patterns are generated by use of a variable sized and shaped box to sweep out the desired pattern features while the pattern is viewed on the color monitor. Patterns can be saved, copied, or modified by additions or deletions very easily. Also, Boolean logic functions are provided to modify quickly various combinations of patterns. The most common use of a Boolean logic function is to create a reverse contrast pattern by use of the NOT function. Pattern erosion and dilation functions are also provided. All patterns are stored as a  $256 \times 256$  array, but are written as a  $1024 \times 1024$  matrix on the sample. A total of seven patterns are retained in active memory at all times, which allows rapid pattern exchange without disk access. The additional capability of pattern storage on disk allows unlimited pattern storage capability.

Another group of setup functions allows the operator to enter the SEM magnification to be utilized, the SEM beam current, and the desired electron dose (in micro-Coulombs per square centimeter) or beam dwell time per pixel. When either of the dose or dwell time are chosen, the other is automatically adjusted to compensate, which provides a fixed beam current. Once all parameters are chosen, the e-beam writing is carried by the execution of a WRITE PATTERN command (via softkey or keyboard entry).

### *Exposure Examples*

Figure 2 is an example of a lithography test pattern created by the above described hardware. A 950 000 molecular weight polymethylmethacrylate (PMMA) resist was spun onto a GaAs substrate and baked at 180 C for 2 h. The wafers were exposed in a JEOL JSM 35C SEM and beam blanking was carried out with an electromagnetic blanking coil located just below the anode. The beam voltage used was 39 keV and the beam current was set as 1 pA. The SEM magnification was set at 2000 $\times$  and the beam dwell time was set at 5000  $\mu$ s per pixel with 9.5% of the pixels in a  $1024 \times 512$  array being exposed, corresponding to a total pattern exposure time of 5.5 min. The exposure was made as part of an exposure series over which the dose was controlled by variation of the dwell time at each exposure location. The dose in this case was approximately 100  $\mu$ C/cm<sup>2</sup>. After exposure, the resist was developed for 60 s in methyl isobutyl ketone (MIBK), followed by a 30s ultrasonic rinse in isopropyl alcohol.

The finished waver was then imaged using a JEOL JSM 840 SEM operating at 3keV accelerating voltage to avoid charging and resist damage. The pattern shows good resolution in both the x and y directions with well-defined edges. The resist is totally cleared from the bottom of the exposed regions. In the SEM image, the PMMA appears dark and the cleared areas appear bright. The average linewidth and linewidth uniformity was determined by means of the Tracor Northern software package LWM.<sup>3</sup> The average linewidth was found to be  $0.223 \pm 0.025$   $\mu$ m over a 20 $\mu$ m extension in the x-scan (horizontal) axis. The edge definition in the vertical lines (y-scan axis) is somewhat less reproducible, as is seen in the rightmost vertical line in Fig. 2. This outcome is related to our choice of the x direction for beam scanning. Improvements in this area are currently under investigation.

To demonstrate the capability of this system to generate and expose complex patterns, a more intricate pattern was generated and exposed by use of the parameters found to be appropriate in the preceding example. Figure 3 shows an SEM micrograph of this pattern etched into PMMA on GaAs. The linewidth in this example is 0.5  $\mu$ m. Notice that lines were successfully written at a width range of angles although the lines at angles other

than  $0^\circ$  or  $90^\circ$  show some discontinuity due to the pixel method of pattern generation. However, the two examples of Figures 2 and 3 clearly illustrate the capability of this system to perform high-quality submicron lithography.

### Conclusions

In this work, we have utilized many of the recent advances in both SEM and SEM control system hardware to develop an automated, easy-to-use e-beam lithography system. The system has been shown capable of producing submicron patterns of complex geometries. Due to the availability of commercial SEMs with both good low- and high-keV performance, it is possible to both expose and characterize resist materials in one SEM. The major requirements of the SEM (in addition to good high- and low-keV performance) are beam blanking availability, stage automation, and external input to the scan generator for digital beam control. The TN5500 control unit used for this work also provides, with available software, line-width measurement capabilities useful in characterizing finished lithography results. The modifications to a system originally designed for normal SEM and x-ray analysis is one of software only, so that the use of such a system is made readily available without the large investment typically required to obtain e-beam lithography capability.

This work has also identified some areas for improvement in the current system. A method for setting the beam size, through automation of the objective lens, is highly desirable. This advance is feasible as SEMs are beginning to have a digital objective-lens current control for autofocusing. Another desired feature not used in this work, but for which both hardware and software are available, is that of beam-current reading via a remote-controlled Faraday cup. This feature, as well as beam-current selection, has been reported in previous work on a similar system.<sup>4</sup>

### References

1. A. N. Broers, "Micromachining by sputtering through a mask of contamination laid down by an electron beam," R. A. Bakish, Ed., *First International Conference on Electron and Ion Beam Technology*, 1964, 191-204.
2. R. F. M. Thornley, "Recent developments in scanning electron microscopy," *Proceedings of the European Regional Conference on Electron Microscopy*, 1961, 173-176.
3. G. S. Fritz and A. T. Laudate, "Automated measurements of integrated circuit line-widths by electron microscopy," *Microbeam Analysis--1983*, 1-4.
4. P. E. Russell and C. R. Herrington, "Development and application of fully automated EBIC techniques for solar-cell measurements," *Microbeam Analysis--1982*, 449-454.

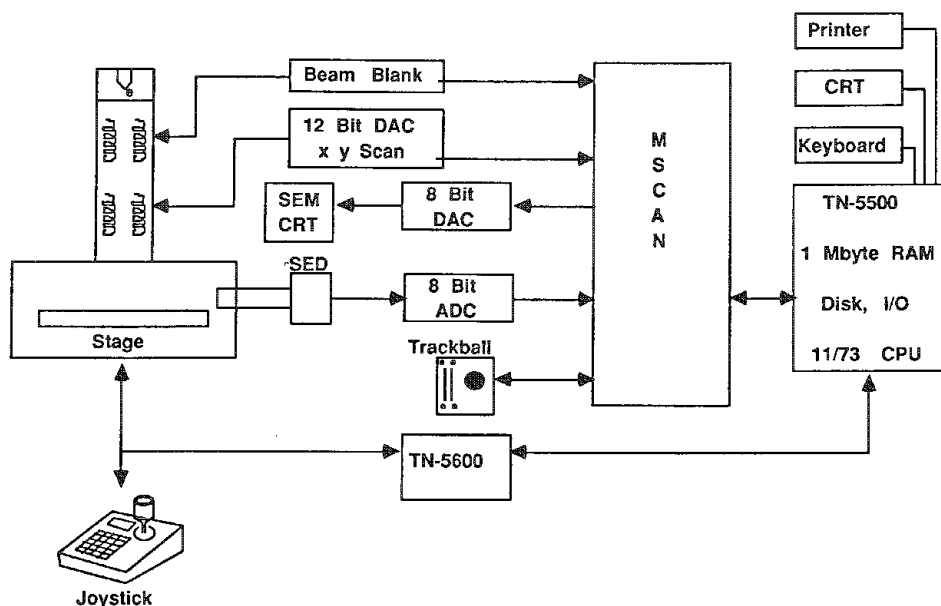


FIG. 1.--Basic hardware components used for electron-beam lithography system.





FIG. 2.--SEM image of e-beam lithography test pattern showing  $0.223\mu\text{m}$  lines and holes etched into PMMA on GaAs.

FIG. 3.--SEM image of e-beam lithography test pattern showing  $0.5\mu\text{m}$  lines at wide range of angles with complex shapes; PMMA on GaAs.



## Author Index

### A

Abend, G., 389  
 Abrevaya, H., 605  
 Adar, F., 22  
 Adler, K. B., 571  
 Aguilar, A., 164  
 Akiba, T., 251  
 Albee, A. L., 265  
 Allen, C. C., 135  
 AlShieb, Z., 29  
 Alvarez, A. R., 97  
 Amdur, M. O., 589  
 Anderson, W. T., 636  
 Austin, F. S., 104

### B

Baeslack, W. A., III, 64  
 Baker, R. T. K., 317  
 Barkanic, J., 653  
 Bastin, G. F., 285  
 Basu, S., 457, 461  
 Benjamin, T., 157  
 Bennett, M. H., 649  
 Bersch, M. G., 138  
 Block, J. H., 389  
 Bodart, F., 333  
 Bond, M., 199  
 Bovard, F. S., 303  
 Bovey, P., 251  
 Bowen, J. M., 29, 50  
 Bradley, J. G., 265  
 Bradshaw, R. W., 337  
 Brash, J., 22  
 Brenner, S. S., 363  
 Bright, D. S., 495, 517, 521  
 Brody, A. R., 541  
 Brown, W. E., 39  
 Budd, P. M., 409, 449  
 Burke, M. G., 363  
 Burns, M. S., 95, 107, 193  
 Burrell, R., 597

### C

Calvo, F. A., 164  
 Cantino, M. E., 226  
 Carson, J. L., 574  
 Caslavski, J. L., 29  
 Castner, D. G., 617  
 Cazaux, J., 527  
 Chabala, J., 107

Chaintreau, M., 78  
 Chan, I. Y., 617  
 Chang, M. J. W., 591  
 Christou, A., 636  
 Cieslak, M. J., 53, 69, 303  
 Collier, A. M., 574  
 Colonna, K. N., 214  
 Conley, J. M., 265  
 Conner, M. W., 589  
 Cowan, R., 131  
 Craig, B. L., 241  
 Cranz, D. L., 564  
 Crouch, R. L., 101

### D

Daniel, D., 78  
 Davari, B. B., 631  
 David, S. A., 53  
 De Angelis, R. J., 620  
 DeHoff, R. T., 479  
 DeLong, E. R., 583  
 Degischer, H. P., 375  
 Demortier, G., 333  
 Dennebouy, R., 78  
 Dhere, A. G., 620  
 Di Giacomo, G., 321  
 Dingle, T., 475  
 Disko, M. M., 429  
 Dodson, R. F., 551  
 Dörge, A., 209  
 Doyle, B. L., 15  
 Duffy, C. J., 157  
 Dungworth, D. L., 564, 577

### E

Eby, T. A., 238  
 Echlin, P., 6, 245, 248  
 Edwards, R. M., 254  
 Ehrlich, G., 382  
 Elin, R. J., 217  
 Etz, E. S., 39  
 Everitt, J., 581  
 Ewing, R. C., 131, 141, 145

### F

Farrow, L. A., 22  
 Fathers, D. J., 82  
 Finch, G. L., 591  
 Fiori, C. E., 183, 217, 482  
 Fisher, G. L., 591

Fleming, R. H., 148  
 Flood, W. H., 589  
 Flutie, R., 659  
 Friel, J. J., 303, 325  
 Fuller, G. E., 649  
 Furbish, W. J., 583

### G

Garrison, C. C., 331  
 Gillen, G., 109  
 Gilles, J. M., 599  
 Giovanetti, A., 594  
 Gómez de Salazar, J. M., 164  
 Goodhew, P. J., 409, 449, 602  
 Gooley, R. C., 117  
 Gordon, B. M., 175  
 Grant, I. P., 421  
 Greenberg, S. D., 539  
 Griffith, O. H., 180  
 Griffiths, B. W., 475  
 Groth, D. H., 547  
 Guilemany, J. M., 164

### H

Hagler, H. K., 231  
 Hall, E. L., 405, 411, 434, 613  
 Hall, T. A., 169  
 Hanson, A. L., 175  
 Hare, T. M., 513  
 Harkema, J. R., 539, 564, 577  
 Harris, A. W., 464, 467  
 Hawkey, L. A., 241  
 Hayes, T. L., 245, 591  
 Headley, T. J., 69, 73, 141  
 Heidsiek, J., 561  
 Heijligers, H. J. M., 285  
 Hein, W., 375  
 Heinrich, K. F. J., 268, 279  
 Hervig, R. L., 91  
 Heyman, R. V., 498  
 Higgins, K. L., 31  
 Hill, L. H., 541  
 Hills, C. R., 69  
 Hinton, D. E., 597  
 Hitzman, C. J., 101  
 Hlava, P. H., 117  
 Holcombe, C. E., 312  
 Hood, P. J., 487  
 Hook, G. R., 217

Horton, D. G., 127, 378  
 Hosseine, J. M., 217  
 Hounslow, A. W., 50  
 Houston, J. E., 115, 602  
 Howe, J. M., 405  
 Howitt, D. G., 299, 487  
 Hren, J. J., 343, 361  
 Hruskoci, P. P., 613  
 Hubert, R. A., 599  
 Humphreys, C. J., 421  
 Hyde, D. M., 561, 577

# I

Ikuta, T., 535  
 Inal, O. T., 343, 357  
 Ingram, P., 169, 205, 241  
 Isakozawa, S., 251  
 Ishimori, A., 473  
 Izutsu, K., 225

# J

Jaccodine, R., 653  
 Jiang, X. Z., 581  
 Johnson, D. E., 169, 225, 226  
 Johnson, W. L., III, 26  
 Jones, K. W., 175

# K

Kan, H. K. A., 646  
 Kanda, K., 525  
 Karnowsky, M. M., 357  
 Karwacki, E. J., Jr., 609, 653  
 Katon, J. E., 47  
 Kaufmann, R., 177  
 Keil, K., 123, 138  
 Kellogg, G. L., 343, 399  
 Kingham, D. R., 82, 99, 403  
 Kirkendall, T. D., 625  
 Knorovsky, G. A., 73  
 Kohler, V. L., 467  
 Kopf, D. A., 241  
 Kracher, A., 151  
 Krewer, J. A., 544  
 Kruit, P., 411  
 Kruse, N., 389  
 Kubic, T. A., 463  
 Kubozoe, M., 251  
 Kundmann, M. K., 417  
 Kurokawa, A., 113

# L

L'Esperance, G., 455  
 Laabs, F. C., 328  
 Lamartine, B. C., 88  
 Lang, P. L., 47  
 Lantz, R. C., 597  
 Lastra Q., R., 307  
 Lata, W., 64  
 LeFurgey, A., 205, 241  
 Leapman, R. D., 187  
 Lebiedzki, J., 254  
 Lee, R. J., 485  
 Legge, G. J. F., 170  
 Lehman, J. L., 251  
 Leigh, S. D., 289  
 Leung, M. S., 656  
 Levi-Setti, R., 107  
 Lewis, R. K., 78  
 Lieberman, M., 205  
 Lippold, J. C., 57  
 Liu, D-R, 425  
 Liu, S., 205  
 Liu, Y. K., 167, 302  
 Livi, R. P., 85  
 Love, G., 271  
 Lumpkin, G. R., 145, 451  
 Lyman, C. E., 434, 599

# M

McCaffrey, J., 455  
 McCarthy, J. J., 479, 485  
 McConville, R., 251  
 McKinley, J. P., 127  
 Mackinnon, I. D. R., 451  
 Mansker, W. L., 123, 126  
 Mariassy, A. T., 561  
 Marinenko, R. B., 495  
 Marker, T. L., 613  
 Martin, J. T., 581  
 Mase, H., 535  
 Mastin, J. P., 547, 583  
 Matsui, I., 525  
 Meeker, G. P., 148  
 Miller, M. K., 343, 370, 378  
 Millette, J. R., 544  
 Moore, T. M., 663  
 Morgan, K. T., 581  
 Morgan, N. E., 238  
 Mossman, B. T., 591  
 Mulford, R. A., 104

Mullock, S. J., 475  
 Myers, M. C., 238  
 Myklebust, R. L., 289, 495

# N

Nakaizumi, Y., 525  
 Newbury, D. E., 1, 268, 289, 495, 521  
 Nikula, K. J., 567  
 Nishi, S. J., 561  
 Nishikawa, O., 351  
 Nishio, S. J., 564  
 North, T., 663

# O

Oechsner, H., 79  
 Oliphant, G., 214

# P

Packwood, R., 268  
 Pagano, P., 594  
 Pak, H.-r., 357  
 Panessa-Warren, B. J., 233  
 Panitz, J. A., 196, 343  
 Pawley, J. B., 525  
 Pelton, A. R., 328  
 Peters, K.-R., 525  
 Pierson, M. L., 151  
 Piette, M., 333  
 Pinkerton, K. E., 553  
 Platek, S. F., 547  
 Plopper, C. G., 561, 564, 577  
 Polomchak, S. M., 613  
 Popp, J. A., 581  
 Pounds, J. G., 175  
 Powell, R. C., 29  
 Powers, C. R., 50  
 Pratt, P. C., 583

# R

Radicati di Brozolo, F., 471  
 Rajan, K., 455  
 Ratcliffe, A. E., 50  
 Rauch, F., 85  
 Rawson, S. A., 127, 135  
 Rammel, T. P., 641  
 Rempfer, G. F., 180  
 Repine, J. E., 571  
 Reucroft, P. J., 620

Rez, P., 421  
 Rick, R., 209  
 Riel, N., 659  
 Riley, R. D., 547  
 Rockley, M. G., 50  
 Rogers, A. E., 589  
 Rogers, J. W., Jr., 115  
 Rogers, P. S. Z., 157  
 Roggli, V. L., 539, 553, 583,  
 586  
 Romig, A. D., Jr., 57, 293  
 Roomans, G. M., 221  
 Rothenberg, S. J., 457, 539  
 Russ, J. C., 501, 505, 509,  
 513  
 Russ, J. Ch., 501, 505, 509  
 Russell, P. E., 663  
 Rye, R. R., 115

## S

Sandroff, C. J., 22  
 Sarikaya, M., 405  
 Sato, M., 525  
 Saubermann, A. J., 498  
 Schidlovsky, G., 175  
 Schwank, J., 623  
 Schwarz, J. E., 571  
 Scott, V. D., 271  
 Seaver, R. R., 646  
 Seidman, D. N., 348  
 Sellamuthu, R., 653  
 Semarge, R. E., 303, 337  
 Sewell, P. B., 455  
 Shah, N., 620  
 Shastri, A. G., 623  
 Shelburne, J. D., 583  
 Shelnutt, J. A., 35  
 Sherwood, R. D., 317  
 Shi, C., 85  
 Shimizu, R., 113, 535  
 Shuman, H., 199  
 Simons, D. S., 464  
 Slodzian, G. G., 78  
 Small, J. A., 289, 464  
 Smith, D. G. W., 153  
 Somlyo, A. P., 199  
 Somlyo, A. V., 199  
 Sorenson, W. R., 57  
 Spitzig, W. A., 328  
 Springfield, J. T., 123

St. George, J. A., 561, 564, 577  
 Statham, P. J., 281  
 Steel, E. B., 439, 517  
 Stein, C. L., 31  
 Stephens, J. J., 337  
 Stettler, L. E., 547  
 Stockton, C. M., 117  
 Stone, G., 254  
 Streit, L. A., 91  
 Stupian, G. W., 656  
 Swartout, W. M., 312  
 Sweeny, G. G., 97  
 Swyt, C. R., 482

## T

Targos, W. M., 605  
 Taylor, D. A., 238  
 Taylor, G. J., 138  
 Taylor, S. E., 248  
 Thompson, K. A., 312, 491  
 Thurnau, K., 209  
 Tomazic, B. B., 39  
 Tombrello, T. A., 85  
 Trahan, J. A., 532  
 Tyler, N. K., 561  
 Tyler, W. S., 557

## U

Ureña, A., 164

## V

Vale, S. H., 409  
 Van Deusen, S. B., 451  
 Venuti, G. S., 261  
 Vitek, J. M., 53

## W

Waddington, W. G., 421  
 Wagner, W., 375  
 Wahi, R. P., 375  
 Walck, S. D., 361  
 Walker, J. S., 485  
 Walker, L. R., 312, 491  
 Walker, T. M., 299  
 Wallach, E. R., 464, 467  
 Wang, E., 226  
 Wang, Y. L., 107  
 Warheit, D. B., 541  
 Warley, A., 227

Warner, R. R., 238, 261  
 Waugh, A. R., 82  
 Wells, O. C., 535, 631  
 Wilkinson, L. E., 226  
 Williams, D. B., 405, 411, 425,  
 434, 443  
 Williams, P., 91, 109  
 Wilson, D. W., 561, 567, 577  
 Wittry, D. B., 265, 631  
 Wollenberger, H., 375  
 Wong, C. Y., 631  
 Wrigley, J. D., 382  
 Wucher, A., 79

## X

Xiong, F., 85

## Y

Yamada, T., 473  
 Yamamoto, T., 473  
 Yu, J. F., 167

## Z

Zhang, Y. Q., 167  
 Zhou, S. T., 167

## NOTES

## NOTES

## NOTES